



NAM

A Database of Damaging Earthquakes of Moment Magnitude from 4.0 to 5.5 (Part 2)

**Cecilia I Nievas, Michail Ntinalexis, Danai Kazantzidou-Firtinidou,
Jovana Borozan, Marialuigia Sangirardi, Helen Crowley & Julian J
Bommer**

Datum March 2019

Editors Jan van Elk & Dirk Doornhof

General Introduction

Earthquakes are complex phenomena, which can have a large impact on the people living in the vicinity of the epicenter. This can include damage to buildings ranging from cracks to collapse, damage to infrastructure and psychological effects on the community. Case studies of historical earthquakes can therefore contribute to the understanding of the diversity of the effects earthquakes can have on the built environment, the natural environment, the local economy, the community and individual people. Case studies of earthquakes are therefore an element of the assurance of the risk assessment (Ref. 1).

Many case histories of earthquakes are available, but these focus primarily on larger earthquakes, like the 1906 earthquake in San Francisco and the 1960 earthquake in Chile. These tectonic earthquakes are considerably larger than the earthquakes expected to contribute to the hazard of induced earthquakes in Groningen.

Detailed case histories for earthquakes in the magnitude range relevant for Groningen are more difficult to find and often concentrate on the deep sub-surface seismological description and offer less insight into the effects of these earthquakes. NAM has therefore asked a team of academics to compile and compendium of earthquake case studies. The first report resulting from this effort (Ref. 2) was published mid-2016 and contained the first 6 case studies of earthquakes with magnitude in the range from 4 to 5.5. This was accompanied by an overview of all (potentially) human-induced earthquakes (Ref. 3).

The effort to compile a database of damaging earthquakes of moment magnitude from 4.0 to 5.5 and compendium of case studies has continued and is documented in the current report containing more than 18 additional case studies. In parallel, a statistical analysis is issued (Ref. 4) of the global occurrence and impact of small-to-medium magnitude earthquakes.

No single earthquake will be in all respects identical to the induced earthquakes in this study, but the collection of case studies of earthquakes is thought to provide additional insights. These reports (Ref. 2 to 4) document the activity to acquire an overview of earthquakes relevant for Groningen and to learn from these.

References

1. Groningen Meet- en Regelprotocol, NAM, May 2017
2. A Database of Damaging Earthquakes of Moment Magnitude from 4.0 to 5.5, Cecilia Inés Nievas, Helen Crowley, Michail Ntinalexis and Julian J Bommer, June 2016
3. Human-induced Earthquakes, Gillian R. Foulger, Miles Wilson, Jon Gluyas and Richard Davies, June 2016
4. Global Occurrence and Impact of Small-to-Medium Magnitude Earthquakes: A Statistical Analysis, Cecilia I. Nievas, Julian J. Bommer and Helen Crowley, March 2019



NAM

Title	A Database of Damaging Earthquakes of Moment Magnitude from 4.0 to 5.5 (Part 2)		Date	March 2019
			Initiator	NAM
Author(s)	Cecilia I Nievas, Michail Ntinalexis, Danai Kazantzidou-Firtinidou, Jovana Borozan, Marialuigia Sangirardi, Helen Crowley & Julian J Bommer	Editors	Jan van Elk Dirk Doornhof	
Organisation	Team of Academic Experts	Organisation	NAM	
Place in the Study and Data Acquisition Plan	<u>Study Theme:</u> Hazard and Risk Assessment <u>Comment:</u> Earthquakes are complex phenomena, which can have a large impact on the people living in the vicinity of the epicenter. This can include damage to buildings ranging from cracks to collapse, damage to infra-structure and psychological effects on the community. Case studies of historical earthquakes can therefore contribute to the understanding of the diversity of the effects earthquakes can have on the built environment, the natural environment, the local economy, the community and individual people. Case studies of earthquakes are therefore an element of the assurance of the risk assessment. Many case histories of earthquakes are available, but these focus primarily on larger earthquakes, like the 1906 earthquake in San Francisco and the 1960 earthquake in Chile. These tectonic earthquakes are considerably larger than the earthquakes expected to contribute to the hazard of induced earthquakes in Groningen. Detailed case histories for earthquakes in the magnitude range relevant for Groningen are more difficult to find and often concentrate on the deep sub-surface seismological description and offer less insight into the effects of these earthquakes. NAM has therefore asked a team of academics to compile and compendium of earthquake case studies. The first report resulting from this effort was published mid-2016 and contained the first 6 case studies of earthquakes with magnitude in the range from 4 to 5.5. This was accompanied by an overview of all (potentially) human-induced earthquakes. The effort to compile a database of damaging earthquakes of moment magnitude from 4.0 to 5.5 and compendium of case studies has continued and is documented in the current report containing more than 18 additional case studies. In parallel, a statistical analysis is issued of the global occurrence and impact of small-to-medium magnitude earthquakes.			

	No single earthquake will be in all respects identical to the induced earthquakes in this study, but the collection of case studies of earthquakes is thought to provide additional insights. These reports (Ref. 2 to 4) document the activity to acquire an overview of earthquakes relevant for Groningen and to learn from these.
Directly linked research	(1) Hazard and Risk Assessment (2) Meet – en Regelprotocol
Used data	Open Literature.
Associated organisation	Team of Academic Experts
Assurance	Report is based on compilation of academic papers and open literature.

A Database of Damaging Earthquakes of Moment Magnitude from 4.0 to 5.5

A report to NAM

Cecilia I Nievas, Michail Ntinalexis, Danai Kazantzidou-Firtinidou,
Jovana Borozan, Marialuigia Sangirardi, Helen Crowley & Julian J Bommer

Version 2

March 2019

Table of Contents

1. INTRODUCTION	3
2. COMPILATION OF THE DATABASE	7
2.1. General description	7
2.2. Sources	8
2.3. Magnitude	11
2.4. Clustering	14
2.5. Damage to buildings	16
2.6. Casualties and affected population	21
2.7. Economic losses	24
2.8. Other fields of the database	25
2.9. Incorporation of events from the Earthquake Impact Database	26
2.10. Example of interdependence of consequences of shocks within the same sequence and of the kind of consequences reported	33
2.11. Composition of the resulting database	41
2.11.1. Geographic distribution	41
2.11.2. Temporal distribution	42
2.11.3. Magnitude distribution	44
2.12. Insights on casualties and damage	46
2.12.1. Damaged and destroyed buildings	46
2.12.2. Infrastructure affected	55
2.12.3. Landslides and liquefaction	56
2.12.4. Casualties	57
3. STRUCTURE of CASE HISTORIES	68
3.1. Tectonic and seismic setting	68
3.1.1. Tectonic setting	68
3.1.2. Regional and local seismicity	68
3.1.3. Seismic hazard	68
3.2. Earthquake source characteristics	69
3.2.1. Location, depth and time	69
3.2.2. Magnitude	70
3.2.3. Style-of-faulting	70
3.2.4. Stress drop	70
3.2.5. Foreshocks and aftershocks	71
3.2.6. Nature of earthquake	71
3.3. Geology and ground conditions in the affected area	72
3.3.1. Regional geology and topography	72
3.3.2. Site conditions in the affected area	72
3.4. Ground motions	72
3.4.1. Intensity observations	73
3.4.2. Ground motion recordings	73
3.4.3. Inferred shaking levels	74
3.4.4. Duration of ground shaking	74
3.5. Collateral earthquake hazards	75
3.5.1. Surface rupture	76
3.5.2. Landslides	76
3.5.3. Liquefaction	77
3.5.4. Settlements	77
3.6. Exposed population	78
3.6.1. Socio-economic setting	78
3.6.2. Population density and distribution	78
3.6.3. Time of day of earthquake	79
3.7. Characteristics of exposed building stock	79
3.7.1. Seismic design codes	79
3.7.2. Building typologies	80

3.7.3. Prior damage and retrofit	80
3.8. Damage observations	81
3.8.1. Damage states	81
3.8.2. Damage statistics and description	82
3.8.3. Observed weaknesses	82
3.8.4. Damage distribution	83
3.9. Casualties and losses	83
3.9.1. Numbers of dead and injured	83
3.9.2. Causes of casualties	83
3.9.3. Estimates of economic losses	84
3.10. Discussion and conclusions	84
3.11. Note	84
4. OVERVIEW AND DISCUSSION OF CASE HISTORIES	85
5. CONCLUSIONS	93
6. ACKNOWLEDGEMENTS	98
7. REFERENCES	99
7.1. Bibliography	99
7.2. Web references	108
7.3. Other resources	110
APPENDIX I: Database of Damaging Small-to-Medium Magnitude Earthquakes	111
APPENDIX II: Damage and Macroseismic Intensity Scales	118
A2.1 The European Macroseismic Scale (EMS-98)	118
A2.2 The Medvedev-Sponheuer-Karnik scale (MSK-64)	122
A2.3 The Modified Mercalli Intensity scale (MMI)	123
APPENDIX III: Case histories of induced earthquakes	125
A3.1 December 2006 M3.2 Basel earthquake, Switzerland	125
A3.2 February 2011 M4.8 Guy-Greenbrier (Arkansas) earthquake, USA	160
A3.3 May 2011 M5.1 Lorca earthquake, Spain	190
A3.4 August 2011 M5.4 Trinidad (Colorado) earthquake, USA	243
A3.5 2011 M5.7, 2016 M5.8, 2016 M5.0 earthquakes in Oklahoma, USA	273
APPENDIX IV: Case histories of tectonic earthquakes	353
A4.1 March 1957 M4.8 Port Hueneme (California) earthquake, USA	353
A4.2 April 1966 M5.2 Tashkent earthquake, Uzbekistan	386
A4.3 1978 M5.1 Albstadt and 2014 M3.6 Darmstadt earthquakes, Germany	436
A4.4 November 1983 M4.8 Liège earthquake, Belgium	514
A4.5 December 1989 M5.4 Newcastle earthquake, Australia	563
A4.6 April 1992 M5.4 Roermond earthquake, The Netherlands	609
A4.7 March 1993 M5.4 Pyrgos earthquake, Greece	658
A4.8 July 1996 M4.8 Épagny-Annecy earthquake, France	710
A4.9 April 2002 M5.1 Au Sable Forks (New York) earthquake, USA	759
A4.10 April 2002 M4.8 Tbilisi earthquake, Georgia	800
A4.11 November 2004 M5.0 Salò earthquake, Italy	847
A4.12 April 2007 M4.0 Folkestone earthquake, United Kingdom	888
A4.13 August 2017 M3.9 Ischia earthquake, Italy	934

1. INTRODUCTION

Gas production in the Groningen field in the northern Netherlands is leading the occurrence of earthquakes in a region for which there is no evidence for any perceptible levels of natural seismicity. The largest induced event to date occurred on 16th August 2012 near the village of Huizinge and was reported by KNMI to have a local magnitude of 3.6. In response to these induced earthquakes, NAM is conducting probabilistic assessments of the seismic hazard and risk. These studies have been initiated both to support the gas production license applications (Winningsplan) and to inform the programme for structural upgrading of vulnerable buildings in and around the gas field.

The Groningen seismic hazard and risk assessments differ from seismic hazard and risk studies conducted for natural (tectonic) earthquakes in a number of regards. One of the key differences is the consideration of earthquakes that are much smaller than those usually included in the assessment of hazard and risk due to tectonic earthquakes. This raises questions concerning the smallest earthquakes of relevance and the need for a frame of reference for the impact that small-to-moderate earthquakes may have on the built environment. While the Groningen hazard and risk modelling effort aims to answer these questions for the gas field, the purpose of this report is to provide answers from empirical observations elsewhere.

In probabilistic seismic hazard analyses (PSHA) conducted to define seismic design loads for new structures, the integrations are truncated at a lower magnitude limit, M_{\min} , which is selected on the basis of smaller earthquakes producing insufficiently energetic motions to pose a threat to engineered structures (Bommer & Crowley, 2017). The rationale for M_{\min} (sometimes referred to as m_0) was stated in the landmark paper by Cornell (1968) that set out the basic formulation for PSHA:

“....and m_0 is some magnitude small enough, say 4, that events of lesser magnitude may be ignored by engineers.”

Numerous statements conveying the same rationale can be found in basic texts on engineering seismology and earthquake engineering, such as Reiter (1990):

“The lower bound, or minimum, magnitude represents that level of earthquake size below which there is no engineering interest.”

The textbook on *Geotechnical Earthquake Engineering* by Kramer (1996) makes the following statements:

“For engineering purposes, the effects of very small earthquakes are of little interest and it is common to disregard those that are not capable of causing significant damage.”

The imposition of an abrupt truncation of the magnitude distribution does not mean that all earthquakes of M_{\min} or greater are potentially damaging to engineered structures, but rather

that no earthquake smaller than this level could be considered capable of causing distress to the structures being designed. In essence, therefore, it is about the nature of the motions generated rather than the absolute size of the earthquakes. Reiter (1990) stated the following in his discussion of minimum magnitude:

“If, for example, probabilistic seismic hazard analysis were sufficiently sophisticated to allow separation between non-damaging peak accelerations from small earthquakes and more damaging peak accelerations from large earthquakes, lower bound magnitudes could be extended as low as the data allowed.”

Such an approach, based on a ground-motion filter rather than a magnitude cut-off, is precisely what is involved with the use of CAV (cumulative absolute velocity) filters as an alternative to M_{\min} . Based on values of CAV predicted as conditional on PGA (peak ground acceleration), all M-R- ϵ (magnitude-distance-epsilon, where the latter refers to the number of standard deviations above the median prediction from a ground-motion prediction equation, or GMPE) contributions leading to motions that fall below a specified level of CAV, are excluded from the calculation of annual exceedance frequency of PGA and spectral accelerations (EPRI, 2005).

Values of M_{\min} used in practice are generally in the range from 4 to 5, with the upper limit being common to PSHA studies for nuclear sites. The value of 5 for M_{\min} was recommended in EPRI (1989), a 360-page document arising from a 3-day workshop conducted by the Electric Power Research Institute specifically *“to establish a lower-bound earthquake magnitude, below which the potential for damage to nuclear plants is negligible.”* The approach that EPRI adopted to address this goal was summarised as follows:

“The objective of the workshop was to consider a broad range of issues that could provide insight to the engineering significance of ground motion generated by small-magnitude earthquakes. Based on the presentations at the meeting it was intended to develop a strategy to select a lower-bound magnitude for use in seismic hazard assessments. An Advisory Committee reviewed the information presented at the workshop and provided recommendations concerning the level of earthquake magnitude that may be damaging to nuclear power plant structures and equipment and a strategy to establish a sound basis to determine the lower bound magnitude.”

The use of 5.0 as the lower bound of magnitude is not, however, limited to nuclear applications: this same value of M_{\min} is used, for example, in the hazard mapping that forms the basis of seismic design codes in the USA (Petersen *et al.*, 2008). The European hazard map produced in the SHARE project (Woessner *et al.*, 2015) was generated with a lower magnitude limit of 4.5.

The rationale for not inflating high-frequency design accelerations with contributions from frequent small-magnitude earthquakes—producing motions of very short duration and low energy content—is perfectly defensible when considering new engineered structures. For the assessment of risk to existing buildings, however—and in particular buildings whose design did not include any consideration of earthquake loading, as is the case for dwellings

in the Groningen region—it would not be justifiable to exclude earthquakes in the range from magnitude 4-5 from consideration. Consequently, in the hazard and risk calculations for the Groningen field, the range of magnitudes considered is currently from **M3.5** to **M7.25**. The upper limit is the maximum value on the logic-tree for M_{\max} derived by an expert panel appointed to assess the available data and models for the Groningen field to infer estimates of the largest possible event (Bommer & van Elk, 2017). The lower limit is based on the fact that the threshold for catalogue completeness is $M_L 1.5$, but sensitivity analyses have shown that contributions to both hazard and risk from the first two units of magnitude are practically negligible. Given that a Monte Carlo approach is being used to perform the calculations, the computational burden of considering these very small earthquakes is worth avoiding if possible.

Disaggregations of the hazard (at the 475-year return period) and risk (in terms of ‘inside local personal risk’) estimates at the centre of the compaction bowl indicate dominant contributions from earthquakes in the range from **M4** to **M5** and a little higher. This is not a surprising result given that the contrary trends of earthquake recurrence rates decreasing with increasing magnitude (and doing so very sharply as M_{\max} is approached) and accelerations increasing with increasing magnitude (at a diminishing rate due to non-linearity in the scaling) generally lead to dominant contributions from earthquakes somewhere in the middle of the considered range, depending on the annual exceedance frequency being considered.

The primary focus of both the risk modelling and the structural upgrading programmes for Groningen, at least at this stage, is life safety. In other words, the key focus of the risk model is to estimate the numbers of people who could be killed by structural damage caused by ground shaking. The motivation for compiling this database of damaging earthquakes with magnitudes in the same range as those dominating the hazard and risk estimates is to provide a basis for comparing and evaluating the estimated losses, or in other words, to provide a ‘sanity check’. The Database of Damaging Small-to-Medium Magnitude Earthquakes should provide insight to the precedents for loss of life and damage due to earthquakes of moderate magnitude, which will be helpful in assessing the reliability of the risk calculations. This is not to say that if greater losses are estimated than have been observed in other earthquakes of comparable magnitude it would automatically invalidate the risk model, but rather it would require explanation of the specific features of the Groningen field—whether related to the seismicity rates, the ground motions, or the fragility of the exposed building stock—leading to exceptionally high estimates of expected losses. Similarly, for those cases where small-to-moderate earthquakes elsewhere in the world have resulted in unexpectedly high impact in terms of damage and casualties, the study will attempt to identify the specific features that led to this outcome; the team responsible for developing the Groningen hazard and risk model would then need to address the question of whether any of these same features could be expected to be present in the Groningen case. While this purpose of providing a basis for assessing the estimated seismic risk in terms of precedents is the primary objective of this database, the information gathered will also be of benefit in informing the development of various elements of the hazard and risk models.

The information for the compilation of the database was retrieved from a wide variety of sources, of varying degrees of reliability, but all earthquakes for which a report of damage or casualties is encountered are included in the listing, providing the magnitude falls within the specified range. Details on all challenges faced and decisions made during the compilation of the database are given in Chapter 2, together with resulting statistics and insights, while the database itself is available as a spreadsheet that can be downloaded from the NAM website¹ and a detailed description of its fields is presented in Appendix I. The database should not be considered as a static final product, as it may be expanded and enhanced as new sources of information are found, and should not be interpreted detached from the discussions contained herein.

For earthquakes of interest about which some degree of detailed information is available, case histories are presented summarising the nature of the event, the characteristics of the affected region, and the nature of the damage and other consequences. These case histories are presented in Appendix III for induced earthquakes and in Appendix IV for tectonic earthquakes. The distinction is made since it may be expected that induced earthquakes provide a better analogy for the Groningen field for two main reasons: firstly, induced earthquakes are generally of shallower focal depth than most tectonic events, which places the source of energy release closer to exposed buildings, on the one hand, but may also mean that the earthquakes have lower stress drops (e.g., Hough, 2014); secondly, induced earthquakes often occur in regions of relatively low natural seismicity and hence impact on built environments of low earthquake resistance. The reports on these earthquakes share a common format, which is explained in Chapter 3 of this report. Chapter 4 presents a brief overview and discussion of the case histories. The report closes with a summary of the findings in Chapter 5.

¹ <https://nam-onderzoeksrapporten.data-app.nl/reports/download/groningen/en/e4fd80e4-2e86-495c-97a4-d00954abcdff>

2. COMPILATION OF THE DATABASE

The core of this study is the database of earthquakes with magnitudes in the range from 4.0 to 5.5 that are reported to have caused appreciable damage or casualties, to which the name “Database of Damaging Small-to-Medium Magnitude Earthquakes” is given. The process and criteria followed for its compilation is described in detail herein. A thorough description of the contents of each field is provided in Appendix I. The resulting composition and statistics on the consequences observed are presented in Sections 2.11 and 2.12.

2.1. General description

The database consists of earthquakes that occurred from the year 1900 through 2017 for which reports of damage and/or casualties have been found, with magnitudes in the range of interest (**M**4.0-5.5). In order to include an event in the database, at least one of the following criteria had to be met:

- At least one death or injury of any kind (slight or serious).
- At least one building with some kind of damage to its structural or non-structural (but architectural) components. Cases in which mentions were oriented only to damage to falling china, bottles or other contents did not qualify.
- Damaged infrastructure.
- Reports exist of damage insurance claims.
- Reports exist of economic losses (measured or estimated).

The event could be later excluded if:

- It was part of an earthquake series with any shocks above **M**5.5 and it was not unambiguously clear which shocks caused the reported damage.
- The damage and/or casualties were not a direct or indirect result of the earthquake. For example, explosions and mine collapses get often reported as earthquakes, and the casualties and losses related to them are usually a consequence of the explosion or the collapse itself and not of the earthquake that followed. These cases were excluded. However, if the earthquake was the cause of the damage, even if one of the consequences was the collapse of a mine, then it was included. Cases in which the damage or casualties were due to phenomena triggered by the earthquakes (e.g., landslides) were included. It is noted that, in many cases, there is not enough information to understand whether the earthquake was originated in a source external to the mine, yet with slip potentially induced by mining-related stress changes, or whether it was originated by a collapse or explosion in the mine itself and only caused damage in the mine. The former would be included in the database, while the latter would not.

Regarding the first exclusion criterion, it is noted that it can also happen that an earthquake is part of a series for which all the shocks are smaller than **M**5.5 and it might still not be clear

how the damage evolved with the different shocks. Whenever situations like this have been identified, note has been taken that the consequences might refer to more than one event.

The kind of information that was sought for the compilation of the database was the following:

- City/province/state/small administrative subdivision, country and region in which the event occurred and/or where the consequences were observed.
- Date and time (UTC) of occurrence.
- Hypocentral coordinates (latitude, longitude, depth).
- Magnitude: **M** (direct or proxy), M_L , m_b , M_s and/or unknown (M_{unk}).
- Whether the earthquake belongs to a cluster, is a main shock, foreshock or aftershock.
- Whether the consequences are expected to correspond only to the listed earthquake or may include those of other earthquakes in the series.
- Maximum intensity.
- Nature of the event (induced or tectonic).
- Population exposed to the ground shaking.
- Total number of people affected.
- Total number of deaths.
- Number of deaths due to shaking.
- Number of injured people.
- Number of homeless and evacuated people.
- Causes of death and/or injury.
- Number of damaged buildings.
- Number of destroyed buildings.
- Whether infrastructure was affected or not.
- Occurrence of landslides and/or liquefaction.
- Monetary losses.

Peculiarities of these parameters are discussed in what follows.

2.2. Sources

Information regarding the consequences of destructive large magnitude earthquakes is usually abundant, but this is generally not true for their small-to-medium magnitude counterparts. One of the main reasons for this is the natural preference to invest resources in the assessment of events that have a greater impact in society. It has been only in more recent years that the earthquake engineering community has started to recognise that, in certain areas of the world, expected annual losses due to seismic events tend to be more influenced by frequent shaking that causes small damage than by the rarer catastrophic events. Moreover, the impact of smaller earthquakes that occur in areas of high seismicity is likely to be perceived as minimal by a population who is used to the effects of earthquakes. Nobody writes about common, usual events. Still, large databases dedicated to the

consequences of natural hazards and other threats are a relevant source of data for the present work. The three biggest databases used herein were:

- The International Events Database (referred to as well as the Emergency Events Database) of the Université Catholique de Louvain, Belgium (EM-DAT in what follows).
- The Significant Earthquake Database of the National Centers for Environmental Information of the National Oceanic and Atmospheric Administration (NOAA) of the United States (NOAA in what follows).
- The EXPO-CAT catalogue of human population exposure (Allen *et al.*, 2009b) and the PAGER-CAT losses database (Allen *et al.*, 2009a).

Other large databases such as the Cambridge Earthquake Impact Database, Desinventar or the GEM Earthquake Consequences Database are, of course, of general interest, but tend to focus on events with magnitudes outside our range of study.

Though not organised per-se as databases of damage and casualties, the earthquake catalogue of the United States Geological Survey (USGS) and the Bulletin of the International Seismological Centre (ISC) served as well as large sources of information. While longer descriptions are available for a small number of earthquakes, this information consists, in most cases, of one or two sentences describing the consequences, sometimes providing numbers of damaged buildings and/or casualties. Phrases include expressions like “minor damage in [place]”, “some buildings damaged at [place]” or “buildings damaged or destroyed in [place]”, among others. Short comments on consequences available in the ISC Bulletin usually correspond to contributions from the USGS itself, but it is noted that many cases have been found in which a comment regarding damage occurrence is available in the ISC Bulletin but not directly on the website of the USGS. As many local agencies publish reports on damaging events that occurred within their area of influence on their websites, these were consulted when relevant to specific earthquakes.

Scientific journal papers and reports are, with no doubt, another source of relevant information, in spite of their natural focus on larger-magnitude events. Additionally to those focusing on a particular earthquake or earthquake sequence, extensive compilations of damage descriptions for complete earthquake catalogues and periodical summaries of observed seismicity were extremely useful as well. Examples of this are Part C of the EK DAG earthquake catalogue for Germany and adjacent areas (Schwarz *et al.*, 2010), a list of relevant Peruvian earthquakes by the National Civil Defense Institute of Peru (INDECI), and the newsletters of the Society for Earthquake and Civil Engineering Dynamics (SECED).

While all of the above were of great relevance for this work, a peculiarity of working with small-to-medium magnitude earthquakes is that a lot of the information does not get systematically reported in scientific sources. In this sense, the more recent work of Earthquake-Report.com is noteworthy, as they aim at reporting live on the consequences of all earthquakes that occur worldwide, irrespective of their extent. Summaries of catastrophe relief actions from ReliefWeb, the digital service of the United Nations Office for the Coordination of Humanitarian Affairs (OCHA) were incredibly valuable as well. Finally, online

newspapers and news agencies, as well as blogs, personal websites and social media (e.g., Twitter), were of great help, as it is sometimes only here that comments about very minor or isolated damage can be found.

In direct connection with the work of Earthquake-Report.com, the Earthquake Impact Database (EID) available online as spreadsheet files for the years 2013-2017 was of significant relevance for the present work. The EID is an initiative that describes itself as a community who “*collects information and provides statistics about damaging earthquakes in the whole world*”. It differs from all other sources in the fact that information regarding damage and casualties due to earthquakes occurring worldwide is gathered and published online in near-real time via a network of collaborators. Their sources are the media and the reports that people who have felt an earthquake leave using their online questionnaire, as well as seismological institutions. This allows for even the smallest of events to be taken into consideration as the data remains accessible. As time goes by after each earthquake, media reports of small events get buried under the large flow of information of the Internet and it becomes more difficult to distinguish the effects from different earthquakes in a sequence. When earthquakes strike within some hours of each other, the latter is impossible, but if they occur some days or weeks apart, immediate reports might be able to make this distinction to some degree, while final reports tend to refer to the whole sequence. Consequently, many databases do not have an entry per event but rather one report summarising all the observations collectively, while the EID appears to generate separate entries. This clearly results in a much larger number of earthquakes being reported by the EID than in other databases, as illustrated by Table 2.1 for the years 2013-2017.

Table 2.1. Number of earthquakes per year in the Earthquake Impact Database (EID), the International Events Database (EM-DAT; Université Catholique de Louvain) and the NOAA database (NOAA). No filters of magnitude or location applied.

Year	EID	EM-DAT	NOAA
2013	389	29	52
2014	376*	26	55
2015	354	23	37
2016	323	30	43
2017	279	19	49

* Nine additional earthquakes are listed for 2014 under the heading “earthquakes with uncertain/unconfirmed damage reports”. These were not considered for the present work.

With the number of earthquakes in the EID being so large, manual verification of each individual event would incur the need for a very significant number of man-hours. For this reason, a computer code was written in Python to make the process as automated as possible. The way in which events from the EID were incorporated to the Database of Damaging Small-to-Medium Magnitude Earthquakes is discussed in detail in Section 2.9.

Turning to local media and secondary sources of information introduced the challenge associated with dealing with local languages. The amount and quality of information in the present work may thus be biased towards earthquakes that occurred in areas of the world where English, Spanish, Italian, French, Portuguese or German are spoken. We were able to gain access to texts in Serbian, Russian, Greek, Hindu, Nepalese and Chinese in a more sporadic fashion, thanks to collaborators to whom we are grateful. Once a relevant source has been identified, online translation services can be of use to retrieve information, notwithstanding their often limited accuracy. Carrying out a full search in an unfamiliar language is, however, very challenging.

2.3. Magnitude

While simple to describe, determining whether an earthquake lies in the range **M**4.0-5.5 is not always straightforward, for three main reasons. Firstly, seismic moments are not routinely calculated for smaller earthquakes. Secondly, different agencies/authors often arrive to different estimates of moment magnitude. For earthquakes whose magnitude lies close to the lower (**M**4.0) or upper (**M**5.5) bound, some estimates might lie in the range while others lie outside. Thirdly, proxy moment magnitude values—*i.e.*, moment magnitude values calculated by means of empirical conversion models from other magnitude scales or relevant parameters—have uncertainties associated with the variability of the empirical models used to determine them and the quite frequent lack of data used to derive them in the lower-magnitude range.

The magnitude scales compiled in the database were: moment magnitude (**M**), surface-wave magnitude (M_s), body-wave magnitude (m_b), and local magnitude (M_L). The value of moment magnitude reported in the first magnitude-related column of the database is that with which the inclusion or not of the earthquake in the database was decided, while alternative values found are reported in the field “Mw (alt)”. An additional field was created for unknown magnitude scales, M_{unk} , as there are cases in which the scale of the magnitude reported is not clear (*e.g.*, events from the EID), or in which the sources themselves specify that the scale is unknown (*e.g.*, some events in the NOAA database). The magnitude values reported by the EID were always included in this M_{unk} field. Estimates of magnitude were retrieved mostly from the ISC Bulletin, the USGS catalogue, the ISC-GEM catalogue (v4.0) (Storchak *et al.*, 2013) and the world catalogue of Weatherill *et al.* (2016) (v3.0c), referred to as WPG16v3c hereafter. The Parametric Catalogue of Italian Earthquakes (CPTI15 v1.5; Rovida *et al.*, 2016), the Italian web portal of macroseismic intensities of the INGV (Tosi *et al.*, 2015), the catalogues of the Spanish National Geographic Institute (Instituto Geográfico Nacional, IGN), the Mexican National Seismological Service (Servicio Sismológico Nacional, SSN), the French seismic catalogue (FCAT-17; Manchuel *et al.*, 2018), the Colombian Geological Service (Servicio Geológico Colombiano, SGC), Geoscience Australia (GA), the China Earthquake Networks Center (CENC; Mignan *et al.*, 2013), the earthquake catalogue for Germany and adjacent areas (EKDAG; Schwarz *et al.*, 2010), and the earthquake database of the British Geological Survey (BGS) were also consulted when necessary.

The source of the reported moment magnitudes is indicated within the database in the field “Mw Case”. Acronyms of seismological agencies as per the list available on the website of the ISC² are used when **M** values are those reported in the ISC Bulletin and attributed to those agencies, with the exception of the catalogues and agencies listed above. In the case of values of moment magnitude stemming from the ISC-GEM, the WPG16v3c, the CPT115, or the FCAT-17 catalogues, the words “direct” and “proxy” indicate whether they are directly calculated values or estimated from other magnitude scales or observations of macroseismic intensities, respectively.

When neither direct nor proxy values of **M** could be found, empirical conversion models were used to make an estimate of **M** by means of one of the values of magnitude available in other scales, with order of preference of M_s over m_b over M_L over M_d as source value. For M_s and m_b , linear piece-wise models that average those of Scordilis (2006), the Generalised Orthogonal Regression models of Di Giacomo *et al.* (2015), and those of Weatherill *et al.* (2016) were used (Figure 2.1), while a one-to-one equivalence was assumed for $M_L=M_d=\mathbf{M}$. Details on these average models and assumptions can be found in Nievas *et al.* (2019). Whenever the reported moment magnitude stems from the application of these conversions, the field “Mw Case” of the database contains the text “*Converted from [original scale]=[value in original scale]*”. Values of **M** directly calculated from inversion were always preferred over proxy **M** values retrieved from existent catalogues, which were, in turn, preferred over the application of conversion models.

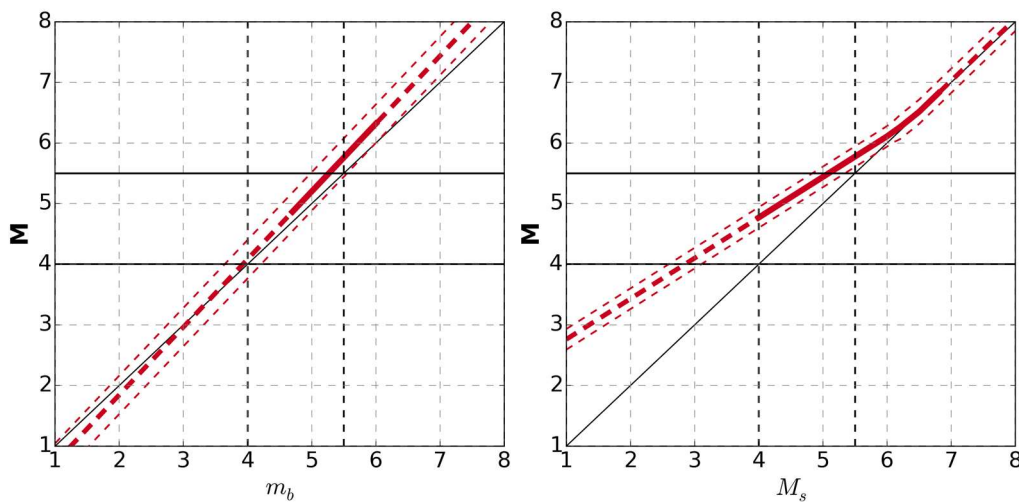


Figure 2.1. Average relation between m_b and **M** (left) and M_s and **M** (right) used to obtain proxy **M** values for the database. Thick dashed lines indicate extrapolation beyond the magnitude range where all source models were derived. Thin dashed lines indicate plus/minus one standard deviation.

Hierarchies were established in order to deal with lack of agreement in the values of **M**. Due to its global coverage and its longevity as a dataset, the **M** estimates from the Global Centroid Moment Tensor catalogue (GCMT; Dziewonski *et al.*, 1981; Ekström *et al.*, 2012) were preferred, when available, over all other estimates, in line with the ISC-GEM catalogue (Storchak *et al.*, 2013) and the work of Weatherill *et al.* (2016), who took it as the reference scale for harmonisation (which means as well that the proxy **M** values retrieved from these

² <http://www.isc.ac.uk/iscbulletin/agencies/>

sources were originally calculated with the GCMT-**M** value as a target). Estimates of **M** by the USGS were taken in second order of preference, as they tend to be similar in value to those of the GCMT, though with some variability (see, for example, Weatherill *et al.*, 2016). Large international organisations were prioritised over smaller local ones, except when rigorously compiled local catalogues such as the Parametric Catalogue of Italian Earthquakes (CPTI15 v1.5; Rovida *et al.*, 2016) were available. The latter took precedence over the USGS, though they were still considered after GCMT. In the case of proxy **M** values, the order of preference was ISC-GEM over WPG16v3c over local catalogues (CPTI15 for Italy and FCAT-17 for France). Similar criteria were applied to magnitude estimates in other scales used to estimate **M** by means of conversion models as described above and in Figure 2.1, with M_s and m_b calculated by the ISC or, if not available, by the USGS, being preferred over those calculated by local agencies. Local agencies relevant to the area in which the earthquakes occurred were always prioritised over local agencies from other areas. Whenever available, detailed studies published in the scientific literature were preferred over magnitude estimates reported by agencies, as it is expected that a specific study be able to take into consideration information unavailable to automatic processing algorithms used by the agencies.

It is noted that the use of hierarchies of agencies and magnitude scales does not eliminate the problem of borderline cases for which some magnitude estimates might dictate inclusion (in the **M**4.0-5.5 range) while some others might dictate exclusion. An interesting example of this currently in the database is the 1917 **M**5.5 Monterchi (High Tiber Valley, Italy) earthquake, for which the CPTI15 catalogue reports moment magnitudes of 6.09 ± 0.10 (from macroseismic data), 5.74 ± 0.16 (converted from an uncertainty-weighted average of M_s and m_b), and 5.99 ± 0.08 (uncertainty-weighted average of the other two), while a moment tension inversion of the digitised analogue records of this earthquake by Bernardi *et al.* (2016) yields a moment magnitude of 5.5 ± 0.2 . This last value was adopted for the database in view of the detailed study carried out by the authors to compute the moment tensor from historical data known to be subject to important constraints, and the inherent limitations of the other intensity-derived magnitude estimates. Apart from this case, there are currently twelve other earthquakes in the database for which the alternative value of **M** (reported in “Mw (alt)”) is larger than **M**5.5. However, as explained earlier, decisions on inclusion were taken based on the primary reported value of **M**.

Borderline cases also arise when the median estimates of proxy **M** obtained by means of empirical conversion models are slightly above **M**5.5 but within a reasonable margin when considering the uncertainty that stems from both, the measurement error of the magnitude in the original scale and the uncertainty of the conversion model applied to it. For example, it is not uncommon to find earthquakes whose magnitudes in various scales (except **M**) fall within the 4.0-5.5 range but whose (median) proxy **M** is above the upper-bound threshold, due to, for example, the tendency for models that convert from M_s into **M** to yield larger numerical values of **M** than those of M_s (e.g., Scordilis, 2006; Di Giacomo *et al.*, 2015; Weatherill *et al.*, 2016). The uncertainty associated with proxy **M** was not taken into consideration for deciding on the inclusion of earthquakes to the present database, as this could lead to an apparent contradiction in the magnitude range considered. It is noted, however, that earthquakes of magnitudes close to the **M**5.5 upper bound tend to have

directly-calculated values of **M** and, as a consequence, the number of earthquakes affected by this decision is relatively small.

During the compilation of the database it was possible to observe that there are cases for which the value of moment magnitude obtained from the seismic moment (M_0) reported by the GCMT appears to be reported truncated to the first decimal place instead of rounded. For example, the reported seismic moment might indicate an **M5.57**, but it is reported by the same GCMT as **M5.5** instead of **M5.6**. For the sake of consistency with the lower- and upper-bound limits defined for this work, the values reported in the Database of Damaging Small-to-Medium Magnitude Earthquakes are those obtained from the seismic moment as $M = \frac{2}{3} \log_{10} M_0 - 10.7$ (Hanks & Kanamori, 1979). The downside of this decision is the existence of damaging earthquakes reported as **M5.5** by the GCMT that do not form part of the database. An example of this is the **M5.57** shock of 18th May 2013 in southern Iran ($M_0 = 2.53 \times 10^{24}$ dyn·cm), reported to have caused damage (Earthquake-Report, 2013; USGS, 2014; GCMT event ID 201305181003A).

Closely related with this last observation is the fact that cut-off values needed to be selected for inclusion or not of an event. With magnitudes often reported to just one decimal place (e.g., in the ISC Bulletin), it was decided to translate the range **M4.0-5.5** into $3.95 \leq M < 5.55$, as 3.95 would be rounded up to 4.0 and values approaching but still below 5.55 would be rounded down to 5.5.

2.4. Clustering

Determining whether an earthquake is part of a cluster or not helps understand the extent to which its reported consequences might be related to those of other earthquakes or not. Small-to-medium magnitude earthquakes might end up associated with structural collapses due to pre-weakening or progressive damage phenomena that make the consequences more severe than they could have been, had the same earthquake stricken alone. Two fields have been placed in the database with this aim: “Clustering”, in which the earthquake is classified as being a main shock (MS), a foreshock (FS), an aftershock (AS) or part of a swarm (SWARM), and “Consequences”, in which direct comments are made regarding the extent to which the consequences listed have been influenced by other events. The category SWARM is used herein to refer to events that form part of a sequence in which the largest earthquakes of the sequence are of similar magnitude, and it is thus not possible to identify a main shock. The possible contents of these two fields are explained in detail in Appendix I. The “Consequences” field contains phrases such as “additional damage”, if the same area had been recently damaged by a previous event, “possibly of many”, when several earthquakes of similar magnitude have occurred within a short period of time but the sources do not report consequences individually for each of them, “seem separate”, if the consequences seem to be due only to the earthquake being listed, and others of the like. “Additional damage” is an expression often found within the USGS catalogue and/or the ISC Bulletin. In many cases both sources specify that the consequences of a certain event are included in those of another one. This information was retrieved and reported in the “Consequences” field whenever possible.

Two remarks need to be made regarding the implications of the statement “seem separate” in the Consequences field of the database. First, the use of the word “seem” is deliberate, as it is difficult to have absolute certainty in this respect. Second, it was assigned based on information available regarding other shocks that may have occurred close in time and space. However, not finding other earthquakes in a catalogue does not guarantee that the earthquakes did not occur. This is particularly true for older events, for which only larger, more relevant earthquakes have been properly registered.

Interpretation of the implications of these fields is not straightforward either, due to the nature of the problem itself. A complete understanding of the extent of the interdependence between the consequences of different earthquakes requires access to additional information, including:

- whether different shocks of the same sequence affected the same site/s or different ones;
- whether structures affected by a previous earthquake had been retrofitted or replaced by new ones before a subsequent earthquake;
- what the fragility of structures that have suffered some minor structural damage but are not repaired at all is.

All these matters are very specific to the particular location and time at which the earthquake/s under study occurred and are greatly influenced by factors such as the seismicity of the area, the policies of maintenance of the building stock and, in more general terms, the socio-economic setting as a whole. The only way to determine the consequences of each particular earthquake with certainty would be to have access to detailed information on both post-earthquake assessments, assuming these were carried out immediately after each event, thus further assuming the time in between was such that allowed for this to be possible, and the state of the building stock before the first earthquake in the sequence. Due to all of this, the content of the fields “Clustering” and “Consequences” should be interpreted with care and be considered only as a guideline.

Whenever possible, the participation or not of an earthquake in a cluster was determined manually, by observing a sufficiently long time-window of seismicity in the area of interest, or from the existing literature. This information was complemented with the results obtained from declustering the catalogue of Weatherill *et al.* (2016) using the declustering algorithm of Gardner & Knopoff (1974) as implemented in the OpenQuake Hazard Modeller's Toolkit (Weatherill 2014), with Gardner & Knopoff (1974) time and distance windows and the same time span considered for both foreshocks and aftershocks. It should be noted that declustering algorithms are not perfect, as they work only in terms of the distance between different earthquakes in time and space, and the assumption that the main shock is the event with the largest magnitude in a certain cluster, and they do not take into account the structural geology close to the site. Moreover, due to the existence of a main shock premise, they are not designed to identify swarms and treat them as such. Swarms are still classified as clusters, but a main shock is selected even if 0.1 units in magnitude above several other events in the swarm. Square brackets in the fields “Clustering” and “Consequences” (e.g.,

[AS]) indicate that the classification is that resulting from the declustering algorithm and no manual verification has been carried out.

Visual inspection of seismic clusters is not definite either, as the time window selected plays a fundamental role in the observation. Seismically active areas are particularly hard in this regard, with earthquakes happening everywhere all the time. Moreover, not finding other earthquakes in a catalogue cannot be equated with other earthquakes not having occurred, as there are many other reasons for which they might not be listed, especially when talking about older events. The only way of determining with a higher degree of accuracy if an earthquake is a foreshock or aftershock of another event is to carry out an in-depth analysis, probably needing to apply relocation techniques to the whole set of earthquakes under study and to investigate in detail the active faults of the area. This is clearly not possible when compiling a database of the dimensions of that being compiled herein. Consequently, notes made regarding the clustering of the earthquakes in the database should be handled with care. Moreover, even if a perfect classification of earthquake clusters was feasible, it is unlikely that information about damage and previous repairs be available to complement it, the result being still imperfect for the purpose of understanding the effects of each individual event.

2.5. Damage to buildings

The database contains two different fields to report damage to buildings, categorising it into “damaged” and “destroyed” buildings. These can contain (i) a specific number, (ii) a range of numbers, (iii) a verbal description, or (iv) nothing. A reported specific number implies that such number was found in all consulted sources, or that there is enough reason to believe that any discrepancy between numbers found is due to the evolution of the earthquake aftermath in time (*i.e.*, newer reports replacing older reports). A range of numbers can refer either to the lower and upper bounds of damaged/destroyed buildings found in the sources or to an estimation of values retrieved from the NOAA database. The two cases can be distinguished from each other in two ways. Firstly, the database contains a series of flags to indicate that reported values are estimates from NOAA, namely the fields “NOAA damaged” and “NOAA destroyed” for the case of buildings, and “NOAA economic”, “NOAA deaths” and “NOAA injuries” for other parameters. Secondly, the ranges used by NOAA are standard, as shown in Table A1.1 of Appendix I. Whenever a source was found stating a specific number *X* and NOAA reported an estimated range, the specific value *X* was adopted instead of the estimated range from NOAA. As numbers or ranges of damaged or destroyed buildings were not always available, the “damaged” and “destroyed” fields may contain verbal descriptions such as “several”, “some, minor”, “limited”, “extensive”, etc., which were adopted as found in the sources. Whenever a simple phrase such as “Damage in [Place]” was found, the word “Some” was written under the damaged buildings field. Finally, lack of availability of data in any of these fields (*i.e.*, empty fields) can be due either to no buildings having been damaged/destroyed as well as simple lack of information (for example, when a value of economic loss is given but no details can be found regarding the kind of damage observed). Based on the experience obtained from the compilation of this database, the authors believe that whenever a number of damaged buildings or a damage description in

verbal terms is available, a lack of mention of destroyed buildings is likely an indication of no destroyed buildings observed. However, this may not always be the case, as the different interpretations of “damaged” and “destroyed” may play a role, as will be discussed below. Moreover, many cases of no data for either damaged or destroyed buildings do have a reported economic loss, which likely implies that damage did occur but was not accurately recorded.

It is noted that care is needed to interpret ranges of numbers stemming from different values found in different sources, as the ranges of damaged and destroyed may overlap. For example, source A might report 80 buildings damaged and 20 destroyed, while source B might report 95 buildings damaged and 15 destroyed, the database finally saying 80-95 damaged and 15-20 destroyed. Assuming that the two upper bounds can be taken together (*i.e.*, saying that the earthquake damaged 95 buildings and destroyed 20) may thus result in the overall consequences being unrealistically inflated (or deflated, if taking the two lower-bound values instead).

Ideally, damage should be reported using proper damage scales, such as the European Macroseismic Scale EMS-98 (Grünthal, 1998; see Appendix II for a description), for example. While keeping their broadness, damage scales are more detailed than a rough damaged vs. destroyed classification, and thus allow to differentiate between some hairline cracks in a few walls and large extensive cracks in many walls, for example, two cases that would fall under the “damaged” category of the present database. The reason for using the simple damaged vs. destroyed distinction herein is the lack of availability of detailed information for most of the earthquakes that make up the database. Just to give an overall impression, of a sample of 105 earthquakes for which a large effort was invested to gather detailed information, statistics in terms of a standard damage scale were only found for two, and statistics in terms of more detailed verbal descriptions (*e.g.*, no damage, minor damage, serious damage) were available for another five. Moreover, sources like the USGS and NOAA use “damaged” and “destroyed” as their two categories, though the former may sometimes include descriptors such as “minor” or “extensive”.

While, in general terms, a certain degree of equivalence between “damaged” and grades 1 through 3 of EMS-98 as well as between “destroyed” and grades 4 and 5 could be expected, it should be noted that the interpretation of damage by those writing the original descriptions and any subsequence processing of the latter has a large influence in this and any classification. The problem of subjectivity is not automatically eliminated by the use of standardised damage scales either, but the more detailed a scale is, the more it is reduced. In this regard, Musson *et al.* (2010), for example, highlights that the differences that exist between different macroseismic intensity scales are often less significant than the differences that arise from different people assigning different intensities to the same site. This naturally extends to and includes damage estimation.

In order to illustrate the kind of information that might be available for earthquakes for which some kind of post-earthquake assessment report was found, a series of examples are discussed in what follows. The first example will illustrate the rare case in which a certain amount of relevant information can be found, but it is not summarised in terms of damage

scales. This example is that of the **M5.0** Koyna (Maharashtra, India) earthquake of 16th September 2008 (21.47 UTC), whose impact the USGS describes as *“One person killed in the Daund area. At least 20 people injured, over 1,500 buildings damaged and several roads damaged by rockfalls in Satara. Buildings also damaged at Bombay”*³. The Amateur Seismic Centre (ASC) website, which focuses on earthquakes that occur in the Indian Subcontinent, provides a longer description⁴:

“A 6-month old baby was killed and 5 injured in the collapse of a mud wall at Nathachiwadi in Yevat taluka in Pune district. At least 12 people were injured, one with a serious fracture injury at Ambwade, in Patan taluka in Satara district including 3 at Ambewadi, 3 at Ambeghar Tarphe Marli, 2 at Sanbur, 2 at Tamhine and 1 at Patan.

In Satara district, nearly 606 buildings were damaged in 110 villages including 573 buildings in 92 villages in Patan taluka, ... [...]. Serious damage (numbers more than 1 in parenthesis) reported to over 606 buildings in 110 villages in Satara district included buildings at Ambeghar (21), Ambwade Khurd (6), ... [...]. 221 wall collapses were reported from the Dhebewadi region. Minor damage was reported to more than 1,000 buildings in Patan taluka. The greatest damage occurred the Dhebewadi area where 309 buildings were damaged in 37 villages and in the Marli area were 134 buildings were damaged in 23 villages. The worst affected village was Sanbur with as many as 37 damaged buildings. A rock fall on the Dhebewadi-Salve road disrupted traffic for much of the 17th. In the Chaphal area, buildings were damaged at Dervan (12), ... [...]. Damage to buildings also occurred in Radhanagari and Shahuwadi in Kolhapur district.

Outside the epicentral region, a wall collapse resulted in one death at Nathachiwadi in Yewat taluka, Pune district. Other minor damage was also reported from Yevat taluka. Minor cracks developed in buildings at Dhabol and Panchgani. At Valva, the kalash (pinnacle) of the Maruti Temple near the S.T. Stand was knocked down and the temple itself was badly cracked. In Mumbai, a minor rock fall was reported behind a Toyota showroom on LBS Road at Gurunanaknagar in Ghatkopar while at Kambekar Street in Dongri, part of the wall & slab of a 3rd floor balcony was dislodged onto the balcony on the lower floor. In the Hubli-Dharwad area in north Karnataka, minor damage was reported from the IT Park in Hubli where walls developed cracks and part of the ceiling fell in some buildings”.

As can be observed, damage is described in terms of broad categories such as “serious damage”, “wall collapses”, “minor damage”, or “damage”. From the text, it is not possible to infer how serious the damage in the first case was, or what kind of wall collapsed in the second case, for example. A wall collapsing can be a partial collapse of a house, but it can also be the collapse of a free-standing fence wall not designed to resist earthquake loading, whose consequences are those related only to the people, animals and/or property standing by it at the moment of the earthquake instead of a significant compromise to the structural integrity of a house. The overall description suggests that 606 plus around three buildings were severely damaged, 222 walls collapsed, over 720 buildings suffered from generic

³ <https://earthquake.usgs.gov/earthquakes/eventpage/usp000gh63#impact>

⁴ <http://asc-india.org/lib/20080917-koyna.htm>

“damage”, and over 1,000 were damaged to a minor extent. When summarising this kind of information into a damaged vs. destroyed distinction, the result will be dependent on the interpretation of the text. This subjectivity is not only introduced in the present work, but also in concise summaries like that of the USGS.

For some earthquakes, it can occur that some detailed information may be available, but certain fundamental data to interpret it is missing, as this second example will show. For the **M4.6** Tuscany (Italy) earthquake of 6th February 1971, the ISC Bulletin contains reports of “*much property damage*”, “*major damage in Tuscania area*” and “*damage estimated at 1 million dollars*”⁵, while the NOAA database specifies 1678 houses damaged and 40 houses destroyed⁶. There exists, however, a more detailed study by Console & Sonaglia (1972) that provides statistics for 1,271 assessed buildings, classified into four main structural typologies:

- I) Reinforced concrete frames and masonry infills of clay or tuff bricks.
- II) Masonry buildings in clay or tuff bricks, with or without reinforced concrete ring beams.
- III) Masonry buildings in Roman style or of unknown construction technique, with or without reinforced concrete ring beams.
- IV) Dry--joint masonry buildings.

Table 2.2 shows the damage results presented by Console & Sonaglia (1972). As can be observed, each column sums up to 100%, which indicates that proportions have been calculated per building typology. However, information regarding how many buildings of each typology were assessed is missing, and only the total summation of all types (*i.e.*, 1,271) is given. From the data available, it is not possible to infer what was the total number of buildings per damage grade. If it is assumed that heavy damage should be classified as “destroyed”, comparison of this table against the values reported by NOAA suggests that the number of buildings of type IV was probably not that large, as the total number of buildings with heavy damage should be equal to or smaller than 40. In order to be able to make better-informed inferences from this data, one would need to deepen the investigation to try to characterise the composition of the building stock at the time. While this might be possible for some earthquakes, information like this is not widely available at a world scale and, even if it was, it would be extremely time-consuming to conduct an investigation of this extent for each of the thousands of earthquakes that make up the database.

Something similar occurs, for example, with information regarding the **M5.0** Zigong (China) earthquake of 29th March 1985. While the USGS simply mentions “*some damage in the Neijiang area*”⁷, Zezhen & Dinggen (1988) provided more detailed statistics, but in terms of surface area of the living space: “*The total floor area of buildings is about 9.2 million square meters. During the earthquake, 2.10 million square meters of floor area of buildings were damaged. Among them, 165 thousand square meters were severely damaged or collapsed, 601 thousand square meters damaged, and 1.34 million square meters were slightly*

⁵ http://www.isc.ac.uk/cgi-bin/web-db-v4?event_id=786944&out_format=IMS1.0&request=REVIEWED

⁶ https://www.ngdc.noaa.gov/nndc/struts/results?eq_0=4556&t=101650&s=13&d=22,26,13,12&nd=display

⁷ <https://earthquake.usgs.gov/earthquakes/eventpage/usp0002d9q#impact>

damaged. As regards (sic) strengthened buildings (totalled 540,000m²), 92% of them were intact, only 8% of them suffered moderate or slight damage". Not knowing the average floor area of dwellings and the average number of dwellings per building in the affected area, it is not possible to transform these values into number of buildings. However, it is possible to sum up the damaged surface areas and determine that they represent around 21% of the 9.2 million m², while the destroyed surface area accounts for 1.8%. A report for the United Nations Office for Disaster Risk Reduction mentions that the earthquake destroyed 400 houses and damaged over 2.5 million square metres (RADIUS, 1999). The agreement between the latter and the areas reported by Zezhen & Dinggen (1988) suggests that the 400 houses might correspond to the 165,000 m². If this relation were true in general terms, the remaining 1.94 million m² mentioned as damaged by Zezhen & Dinggen (1988) would be equivalent to around 4,700 houses. However, it is noted that this is an assumption whose degree of accuracy is difficult to gauge without a deeper investigation.

Table 2.2. Proportion of buildings presenting different damage grades per building typology after the 6th February 1971 Tuscany (Italy) earthquake, according to Console & Sonaglia (1972).

Damage	Typology			
	I	II	III	IV
No Damage	86%	43%	8%	7%
Slight Damage	14%	44%	35%	11%
Medium Damage	0%	11%	33%	12%
Heavy Damage	0%	2%	24%	70% ^(*)

(*) Source says 7% but the column does not add up to 100% and the remaining information in the source suggests this is probably a typo.

While the example of the **M5.0** Koyna (Maharashtra, India) earthquake illustrated the difficulties associated to determining how severe damage was and whether it should be classified as plain damage or as destruction, similar challenges exist at the other extreme of the spectrum. Different sources might use the expression "minor damage" in different ways. In some cases, it is clear from additional descriptions that minor damage refers to hairline cracks in non-structural partition walls or even in structural masonry walls, damage to ceilings and plaster, *etc.*, while in others it is possible that it refers only to contents being knocked off shelves, with no actual damage to the property. Earthquakes for which it was possible to determine that damage only consisted on contents falling off were not included in the database. However, reports of "minor damage" without further specification were included, simply because the risk of discarding events that did cause consequences to the built environment would be too large otherwise.

Some inconsistencies were noted when confronting the numbers of damaged and destroyed buildings reported in the NOAA database against those contained in the USGS catalogue or in the ISC Bulletin. These were:

- Cases in which the USGS/ISC report X damaged or destroyed, and NOAA reports X damaged and X destroyed.

- Cases in which the USGS/ISC report X damaged and Y destroyed, and NOAA reports Y damaged and X destroyed.
- Cases in which the USGS/ISC report damage with descriptions such as “*minor damage to some buildings*” or “*X buildings slightly damaged*” and NOAA reports 0 buildings damaged and 1 to 50 destroyed.

As the source of these inconsistencies remains unclear, it was decided that written descriptions from the USGS or the ISC Bulletin (as well as other potential sources) would take precedence over and inform the numbers reported in the NOAA database. For the first of the cases enumerated above, repetition of the same number under both categories in the NOAA database was interpreted as that number being the total number of buildings that were either damaged or destroyed, and that the exact proportion in which these number falls into each category is not known. In these cases, the number was assigned to “damaged buildings”, while “some of” was written under “destroyed buildings”, implying that some of the buildings listed as damaged were actually destroyed.

Finally, it is noted that numbers of damaged and destroyed buildings may sometimes refer to dwellings or homes, which may coincide or not with the number of buildings, depending on the number of dwellings typically contained within a building in a certain region. As the latter may not be immediately known without further investigation, such cases were noted in the Comments field of the database. Moreover, it is often not clear if the word “homes” refers to “houses” as buildings inhabited by one family, or to dwellings, that is, housing units inhabited by one family, many of which may exist within the same building.

2.6. Casualties and affected population

Fields related to human impacts are: total affected, total deaths, shaking deaths, injuries, homeless and evacuated. The two latter refer to people whose residence became permanently affected by the earthquake and could not return, and those who had to leave their residences for a limited period of time but could finally return, respectively. The definition of “affected people” appears to be more undefined, with many sources reporting, for example, “5,000 people were affected by this earthquake” without specifying if this includes any person for whom the earthquake and/or its consequences had effects on their everyday life, even if to different extents, or to only injured and dead. The values reported herein correspond to those found in the sources under the same wording.

The distinction between total deaths and shaking deaths is made to separately identify those caused by the response of buildings or their contents to the ground shaking, which would be *shaking deaths*, as opposed to other earthquake-related deaths such as those that could be caused by stampedes, accidents occurred while trying to flee from a building, heart attacks, earthquake-triggered landslides, etc. By definition, the number of shaking deaths is equal to or smaller than the number of total deaths. The same classification could not be applied for injuries, as information on the latter tends to be significantly scarcer and more imprecise than that on deaths. Just like for the case of damaged/destroyed buildings, standard ranges estimated by NOAA can be found in the total deaths and injuries fields too. When this is the

case, the corresponding flag “NOAA deaths” or “NOAA injuries” is set to “Y” (“yes”). Non-standard ranges and/or ranges not accompanied by these flags simply reflect discrepancy in the numbers found in the sources. Whenever a source was found stating a specific number X and NOAA reported an estimated range, the specific value X was adopted instead of the estimated range from NOAA, as the latter stems from the assignment of values from verbal descriptors.

Whenever information regarding the causes of death and/or injury were found, they were added to the database in the “Causes of death/injury” field. The keyword “PAGERshaking” was used to indicate those cases for which the specific causes of death were not found but the deaths were listed as being shaking deaths in PAGER-CAT (Allen *et al.*, 2009a). As explained by Allen *et al.* (2009a), deaths were assumed to be shaking deaths if no indication of a different origin could be found. The same criterion was applied herein: whenever no specific data was available but extensive damage was known to have occurred, the causes of death were indicated as “possibly due to structural failures”. If the extent of the damage was not totally clear from the sources so as to make such an inference, causes of death were left as unknown.

Within the collected causes of fatalities, it was not uncommon to find, apart from those due to structural damage, deaths associated with the reaction of people to the earthquake (e.g., stampedes, accidents occurring while trying to flee from a building, jumping off balconies, etc.), others caused by secondary hazards such as earthquake-triggered landslides, and others due to heart attacks or cardiorespiratory failures. Having identified 55 earthquakes (around 15% of those in the database associated with deaths) with reported fatal victims associated with deaths due to heart attacks (2.7-3.8% of number of deaths), a special effort was put into better understanding the relationship between earthquakes and fatal cardiac events. In approximately 77% of these 55 earthquakes the only reported deaths were those attributed to heart attacks, while for 6 of these earthquakes the heart attacks were the only reported consequence found (*i.e.*, no reports on damage, injuries or the occurrence of liquefaction or landslides).

Results from existing studies on the link between seismic events and deadly acute coronary syndromes have often reached conflicting results (e.g., Kloner, 2006; Bartels & VanRooyen, 2012; Bazoukis *et al.*, 2018). While a statistically significant increase in the number of cardiac-related deaths after an earthquake or a positive correlation between this number and epicentral distance or seismic intensity of the aftershock sequence have been observed (e.g., Trichopoulos *et al.*, 1983; Leor & Kloner, 1996; Leor *et al.*, 1996; Tanaka *et al.*, 2015), establishing an univocal connection between the occurrence of a small-to-medium magnitude earthquake and a heart attack is difficult due to several reasons:

- The frequency with which cardiac-related deaths occur is extremely high. According to Leor *et al.* (1996), for example, 300,000 sudden deaths from cardiac causes occur per year in the United States, which translates into more than 800 deaths per day. These high daily rates do not allow for the small numbers of heart-attack deaths due to small-to-medium magnitude earthquakes to be distinguishable from the baseline.

- Deaths due to heart attacks may not necessarily occur simultaneously or right after the ground shaking (Trichopoulos *et al.*, 1983). For example, the 25 sudden deaths that occurred on the day of the 1994 M6.7 Northridge earthquake investigated by Leor *et al.* (1996) took place along the whole of the day, even though the earthquake occurred at 4.31 am local time.
- Heart failures can have many causes and be influenced by many factors, such as time of the day, day of the week, season, physical exertion, emotional upset, consumption of psychotropic substances, sexual activity, etc. (Kloner, 2006). Consequently, some of the cardiac-related deaths that occur (sufficiently) concurrently with an earthquake might be related, for example, to unusual physical exertion, like escaping from a building during the ground shaking or cleaning up earthquake debris. In these cases, the question of whether the emotional distress caused by the earthquake had a decisive influence or not over the heart failure may be left unanswered (Leor *et al.*, 1996). Existing studies have focused as well on the influence of the time of the day of the earthquake, with earthquakes occurring in the morning (e.g., 1994 Northridge, 1995 Hanshin-Awaji/Kobe, 2010 Christchurch) having a seemingly larger impact in terms of cardiac-related deaths than those occurring in the afternoon (e.g., 1989 Loma Prieta, 2011 Christchurch) (Suzuki *et al.*, 1995; Brown, 1999; Chan *et al.*, 2013). All this would suggest that the stress caused by an earthquake might only represent one additional trigger that, in combination with other triggers or conditions, may result in an increased number of heart-related deaths.
- People with conditions of high heart failure risk exist in all large populations. It is thus possible that a stressor such as the emotional distress caused by an earthquake could accelerate the timing of a heart failure that otherwise would have happened later, the earthquake emerging like a trigger and not a cause in itself. The observation of increased numbers of cardiac-related deaths after earthquakes followed by smaller-than-average such deaths in the period following the earthquake support this hypothesis (Leor *et al.*, 1996; Bazoukis *et al.*, 2018). However, the potential effects of ischemic preconditioning⁸ on the reduced number of cardiac-related deaths after an earthquake have been mentioned by Kloner (2006).
- The occurrence of a cardiac-related death on the day of an earthquake might also be influenced by other factors such as limited or delayed access to medical attention due to damage to roads, traffic cut-off after disasters and even damage to hospitals themselves. This can occur irrespective of whether the earthquake acted as a trigger or not (e.g., Tanaka *et al.*, 2015; Bazoukis *et al.*, 2018).

Due to the uncertainty and ambiguities associated with the interpretation of cardiac-related deaths in close proximity in time with an earthquake, deaths reported as heart attacks, cardiorespiratory arrests, fright, or any similar wording were removed from the statistics on the database that are presented later on.

⁸ Ischemic preconditioning is an experimental technique consisting in causing short periods of shortage of blood supply with the purpose of ultimately producing resistance to the latter (Wikipedia).

The number of injuries is, in general, much more uncertain than deaths, due to a combination of factors, starting with the difficulties of defining the degree or type of injury to be counted as an earthquake-related injury. There is also the influence of the lack of reporting of minor injuries due to the primary focus on people who need urgent medical treatment right after an earthquake (Alexander, 1985). This is clearly influenced as well by the overall aftermath of the event, with a proportionately larger number of light injuries likely to be counted when consequences are limited in extent than when more serious casualties have occurred. In this sense, the recording of deaths is much more systematic, as it needs to be carried out officially and is evidently a binary state.

Interpretation of information stemming from different kinds of sources had its own challenges as well. For example, the following has been found for the **M**5.2 earthquake that occurred on 11th March 1978 in the vicinity of the Strait of Messina, in Italy:

- The NOAA database and the comment by the USGS reported in the ISC Bulletin mention two deaths.
- An online article states that “a woman died in Messina due to a heart attack caused by the fear”, and makes no further comments on any other deaths (Caridi, 2011).
- PAGER-CAT reports two deaths for this event and labels them both as shaking deaths.

In view of the above, the question is whether the two deaths reported by NOAA, the USGS and PAGER-CAT are the same two shaking deaths to which one non-shaking (heart attack) death needs to be added, or whether one of the two deaths reported by all those sources is the non-shaking death due to a heart attack. In this specific case, it was decided to assume that only two deaths had occurred, one of which was the heart attack, and that PAGER-CAT mistakenly assigned it to a shaking death. The same approach was followed with other cases in which the overall number of deaths seems to be in agreement across different sources but there is disagreement regarding the causes. Doing otherwise carries the potential risk of artificially inflating the number of deaths.

2.7. Economic losses

Losses in monetary terms are reported in United States dollars at the time of the earthquake, unless noted otherwise. Whenever values were found reported in local currencies, historic exchange rates for the particular currency were retrieved from online sources (FXTOP, 2018) and used to transform the values to US dollars at the time of the earthquake. In these cases, losses are expressed as round numbers, taking an approximate average conversion rate within the year in which the earthquake occurred.

The NOAA database states that its economic losses correspond to United States dollars at the time of the earthquake when they are specific values, but 1990 United States dollars when they are reported as estimated ranges. The latter were assigned by NOAA from verbal descriptors when a specific amount could not be found in the literature, as per the equivalences presented in Table A1.1 of Appendix I. As for the case of damage to buildings

and casualties, the “NOAA economic” flag is set to “Y” when the economic losses reported are estimates retrieved from the NOAA database.

It is, however, not always possible to be certain of the currency that the sources are referring to when reporting economic losses, especially when new papers and studies are published regarding older earthquakes. Furthermore, there are even cases in which previous conversions are likely already implicit within the sources. An example of this is the M_L 5.4 Adelaide (Australia) earthquake of 28th February 1954, for which Denham (1992) reports an economic loss of 8.8 million Australian dollars at the time of the earthquake. However, it is likely that this value be already a conversion from British pounds, as Australian dollars were first introduced in 1966, 12 years after the earthquake. In this case, the economic loss reported in the present database was obtained using the 1966 conversion rate between Australian and US dollars.

Ideally, economic losses should be subdivided into material losses (*i.e.*, repairing, rebuilding, etc.), downtime losses, and losses due to the “value of life” (*i.e.*, the economic value assigned to fatalities). What exactly has been included in the value reported by the sources is seldom clear, as it is not clear whether the value was a first estimate in the immediate aftermath of the earthquake or a balance made after some time. In cases related to induced seismicity in the United States, for example, it is common to find values associated with monetary claims made in court.

Due to the major uncertainties associated with the origin of these figures, reported estimates are to be taken more as an indicative guide of the extent of the damage caused by the earthquake than as a definite value.

2.8 Other fields of the database

Hypocentral coordinates (latitude, longitude, depth) as well as date and time of occurrence were mostly retrieved from the USGS, the ISC Bulletin or local agencies of relevance, with a smaller number of cases—usually of older events—having their origin in journal papers or any of the other sources considered herein, when the earthquakes could not be found listed by seismological agencies.

Suspected anthropogenic origins have been indicated in the database by means of the “Induced Flag” field, whenever possible, relying mainly on existing evaluations rather than attempting to make such assessments as part of this work. Sources have been mostly scientific publications, comments included within the ISC Bulletin, the Human-induced Earthquakes Database (HiQuake, Foulger *et al.*, 2018), and comments listed in the EID. Cases for which the earthquakes were not flagged in the EID as having an anthropogenic origin but whose location was the same as other earthquakes in the EID that were flagged, as well as earthquakes that correspond to areas of known induced seismicity such as Oklahoma (USA) were considered to be anthropogenic too. It is noted, however, that the distinction between natural and induced seismicity can often be unclear and a matter of contention.

The field “Exposed Population” serves the purpose of giving an idea of the number of people that could have been potentially affected. This is relevant because the severity of the consequences of the earthquake are directly linked to the proportion of people injured/killed/affected to the total number of people expected to have been exposed (e.g., it is not the same to say that there were 10 people injured in a cite of 1 million than in a small town of 1,000). For this purpose, the population estimated to have been exposed to Modified Mercalli Intensities equal to or larger than IV, according to EXPO-CAT (Allen *et al.*, 2009b) or PAGER (Wald *et al.*, 2008) was reported in this field. When these are not available, particularly for older events, the values are those reported by the sources as being the population of the most affected settlements. It is relevant to note that numbers retrieved from EXPO-CAT or PAGER are not observations but estimations based on intensity prediction equations and models for population distribution.

The maximum seismic intensity attributed to the earthquake is reported in the field “Max. Intensity”. This can be either a value reported by the sources from direct observations or polling, or have been retrieved from the USGS ShakeMaps (Worden & Wald, 2016).

Apart from the number of damaged buildings, destroyed buildings and economic losses, consequences to the physical environment are reported in terms of three flags indicating the occurrence of landslides (which include landslides, rockslides, mudslides and snow slides), liquefaction, and whether infrastructure was affected. The latter can refer to damaged roads, bridges and/or dams, damaged lifelines, as well as simple reports of interruption of services, even if the causes are unknown, as sources are often not explicit regarding the kind of the interruption observed.

The “ID” field contains an identifier that is unique for each earthquake in the database. Those IDs starting with the letter E and followed by a number and a hyphen (e.g., E13-xxx) correspond to earthquakes that were automatically processed and retrieved from the EID, as described in the upcoming Section 2.9. The “From EID” flag also serves the purpose of identifying those events, and it does not indicate whether the earthquake can be found in the EID or not but rather whether it was included in the present database by means of the algorithm described in Section 2.9.

Any relevant additional information is contained in the “Comments” field. This can be related to a clarification regarding the damage observed, additional data regarding the main shock of the sequence if the reported earthquake is an aftershock, the uncertainty associated with the reported proxy moment magnitude, the occurrence of other shocks closely spaced in time, the currency conversion rate used for the economic losses, etc.

2.9. Incorporation of events from the Earthquake Impact Database

As mentioned in Section 2.2, the Earthquake Impact Database (EID) differs from other sources in the fact that information regarding damage and casualties due to earthquakes occurring worldwide is gathered and published online in near-real time via a network of

collaborators, a strategy that results in a much larger number of entries than any other database of earthquake consequences. In order to facilitate the handling of such a large volume of data, a Python code was written so as to provide a certain degree of automatization to the process. The challenges of this automatisisation were, mainly: (i) identifying the earthquake that each entry of the EID is making reference to, knowing only the country, sometimes a region within it, the date, but not the time, and a magnitude in an unspecified scale; and (ii) retrieving as much information as possible from a database format not conceived for automatic processing.

The EID is available online from the year 2013 onward. The exact format of the database has changed with time but, in all cases, earthquakes are reported in terms of their date of occurrence (not the time), the country and region within the country in which they occurred, their magnitude (in an unspecified scale), their depth, their maximum Modified Mercalli Intensity, and the number of fatalities and injuries. For the years 2015-2017, numbers of damaged and destroyed buildings are provided as well, while for 2013-2014 the consequences to the built environment are given in broad terms of the code scale presented in Table 2.3. Within the EID spreadsheets, the scale is defined by a main description and a comment, transcribed herein under the “Secondary Description” column. For the years 2015 and 2016, consequences in terms of the code scale and reported numbers of damaged and destroyed buildings complement each other. In many cases, comments to the cells containing the number of damaged and/or destroyed buildings specify that the number is an estimation, which is inferred to be carried out by people compiling the EID, though the specific method is not described.

As the EID does not provide epicentral coordinates but only names of regions within countries and, sometimes, only names of countries, the first task consisted in transforming this information into a search area within which the code would attempt to retrieve earthquakes. This was carried out by means of Google Maps APIs. The precision and success of this task was directly linked to the quality and specificity of the location description in the EID. Several search areas were sought for each event, trying to range from smaller regional locations to broader ones. Depending on the kind of area found, the Google Maps APIs could provide the coordinates of a bounding box (*i.e.*, a rectangle around the region) or a longitude-latitude pair corresponding to the centre of the region. For each defined area, a search was carried out within the ISC Bulletin, either within a rectangle or a circle defined from the longitude-latitude pair and a 50-km radius (which was also used to expand the rectangle so as to cover events that might fall too close to a regional boundary). As the EID does not specify the time of occurrence of the events, the search was carried out for the whole day reported.

Table 2.3. Damage levels defined by the Earthquake Impact Database.

Level	Main Description	Secondary Description
1	Non-structural damage	Examples: windows broken, cracked and fallen plaster, falling objects, damaged chimneys, garden wall collapsed, landslide without damage or other secondary effects, etc. (in a few cases).
1-2	Very limited structural damage	or extensive non-structural damage. Many broken windows / cracked plaster / etc., or very few cracked walls or ceilings.
2	Some houses damaged, mainly minor damage	Example: (small) cracks in walls and/or ceiling of some houses, limited communication network affected, etc or single collapsed house and (nearly) no other damage.
2-3	Some houses severely damaged	A few collapsed walls / partially collapsed ceilings.
3	Some houses collapsed, others damaged	Example: some houses completely destroyed / uninhabitable. Dozens others with structural damage.
3-4	Dozens of houses collapsed	Hundreds of houses with structural damage.
4	Many houses collapsed and others damaged	Example: many dozens / hundreds of houses collapsed or uninhabitable, hundreds more damaged. Damaged roads by ground fissures and destroyed water and power supply.
4-5	Many hundred houses collapsed	Thousands of houses damaged, most affected villages / towns nearly completely damaged.
5	Massive destruction	Thousands of houses collapsed, many more damaged. Also massive damage to infrastructure and communication.
5+	More than 20.000 houses destroyed	Villages completely destroyed, massive damage in dozens of locations around the epicenter. 100,000s and more houses affected.

All events found in the ISC Bulletin for all the search areas defined were then filtered in terms of their magnitude. The magnitude value reported in the EID, whose scale is unspecified, played two main roles. Firstly, it was used to determine whether an earthquake in the EID was worth analysing in detail or not. The maximum magnitude for this was set to 5.8, inclusive, to account for the variability that may exist in estimates of magnitude, particularly when different scales are mixed together. Earthquakes with reported magnitudes above this limit (around 15% of the total) were not assessed any further. Secondly, the magnitude value from EID was used to filter out events found within the search areas. For each potential event found in the ISC Bulletin, the minimum and maximum reported magnitudes were determined. If the value reported in the EID fell within the range defined by these minimum and maximum, minus/plus 1.0 unit respectively, it was kept as the potentially sought event. If outside that range, it was concluded that the event was not relevant for the search.

Once a set of potential earthquakes was identified, each of these were compared against the Database of Damaging Small-to-Medium Magnitude Earthquakes being compiled herein, with the purpose of determining whether the event was already part of it. Distance and time

windows of 100 km and 60 seconds were used for this purpose. This means that if an event potentially matching the EID entry of interest fell within 100 km and 60 seconds of an event in the Database of Damaging Small-to-Medium Magnitude Earthquakes, it was assumed that said event was already in the latter. If no match between any of the potential earthquakes found for a certain EID entry and the Database of Damaging Small-to-Medium Magnitude Earthquakes was found, it was concluded that the EID event needed to be added to the latter. In this case, all potential earthquakes were exported as output, and the final earthquake was selected after a visual inspection of the results, as any automatization in this regard would be extremely difficult. For each potential earthquake, one set of hypocentral coordinates and one magnitude estimate were selected according to the criteria defined in Nievas *et al.* (2017), the absolute priority being for moment magnitudes. Additionally, body-wave and surface-wave magnitude estimates authored by the ISC or the USGS were retrieved.

The manual inspection of entries for which several potential earthquakes were considered in the output allowed for the possibility to flag possible swarms or cases in which the consequences listed in the EID may correspond to more than one earthquake that occurred very close in time. Cases like this were flagged as “possibly of X” or “possibly of many” in the “Consequences” field of the database. Only if the EID explicitly mentioned the occurrence of more than one event or in the cases in which it was obvious, the more certain “of X” (X=number of events) was written instead. Neither “possibly of X” nor “of X” should be interpreted as X being the only possible number of earthquakes whose consequences are being reported, but as the number of seemingly individual events with magnitudes above approximately 4.0 (with flexibility, defined on a case-by-case basis) that appear to have occurred at the same location and were found by the Python code. It is noted that this approach does not allow to consider earthquakes that occurred the day before or the day after, in UTC, as the search is carried out only within one specific day.

For each entry in the EID database, the outcome of this process could be any of the following:

- Not assessed: The entry had a magnitude value above 5.8 and was not assessed.
- No date: The entry had a problem in its definition of the date. For example, some entries mention a whole month, or say “swarm” and a month.
- No ISO country code: Some of the tools from Google Maps require the specification of the country ISO code. The reasons why the ISO code might not have been found could be many: misspelling of the country name, spelling of the country name in the country’s language instead of English, etc.
- No geocode: The Google Maps API and the code could not define any region from the information provided.
- Not found in ISC: The Google Maps API and the code were able to define search areas, but no events were found within these areas for the specified day in the ISC Bulletin.
- Found in the ISC and the Database of Damaging Small-to-Medium Magnitude Earthquakes: Potential matching earthquakes were identified and comparison against

the Database of Damaging Small-to-Medium Magnitude Earthquakes led to conclude that the event was already a part of it.

- Found in the ISC but not in the Database of Damaging Small-to-Medium Magnitude Earthquakes: Potential matching earthquakes were identified but none of them were found within the Database of Damaging Small-to-Medium Magnitude Earthquakes. Events falling under this category were selected to be added to the latter.

Entries from the EID database classified as either “no date”, “no ISO country code” or “no geocode” were manually inspected so as to identify the issues that led to the assigned classification. Once corrected (for example, if it was a spelling problem), the Python code was re-run. After this assessment no events were left under these categories. Entries classified as “not found in the ISC” were collected and subject to a second round of investigation in which the time window was expanded to include the day before and the day after that indicated in the corresponding EID entry. This was done to cover not only cases in which local times are misreported as UTC, but also general date errors that can arise from dating the earthquakes based on damage reports. Earthquakes that remained unidentified after this second automatic processing were later assessed manually. Those that were finally found through this last manual processing were mostly cases in which the epicentres fell slightly outside the search area defined by the automatic code, or the latter was completely inappropriate (due, for example, to the region assigned in the EID being interpreted as a very specific locality instead of a broader area), or the code encountered issues when handling non-ASCII characters. Around 6% of the total of entries from the EID could not be matched with earthquakes reported in the ISC Bulletin even after the second round and the manual check. These were not included in the Database of Damaging Small-to-Medium Magnitude Earthquakes.

While carrying out the second automatic search it was noted that some earthquakes that had not been found in the ISC Bulletin before were found, and their date was exactly that reported in the EID. As there was a lapse of some months in between the first and second round of processing, this is probably due to the fact that the ISC Bulletin is dynamic, particularly before it is reviewed. Not all data from all contributing agencies arrives instantaneously and the grouping of events can change as new data becomes available. This is a problem inherent to dealing with relatively recent events of small magnitude.

Entries classified as having been found in the ISC Bulletin but not in the Database of Damaging Small-to-Medium Magnitude Earthquakes were then re-filtered according to their magnitude. Whenever moment magnitudes had not been retrieved by the automatic algorithm, a search for values of **M** (direct or proxy) was carried out as per the rest of the earthquakes of the Database of Damaging Small-to-Medium Magnitude Earthquakes, and the same criteria were applied to decide their final inclusion or not.

While the process of adding events from the EID was kept as automatic as possible, there were cases in which manual adjustments were made as inconsistencies were found during the manual selection of the sought earthquake within the potential ones.

The consequences of each earthquake from the EID, namely, the number of fatalities, injuries, homeless, damaged buildings, and destroyed buildings, were taken at face-value due to the impossibility of manually checking every single entry. There are several reasons behind this decision. Firstly, the large number of earthquakes involved. Secondly, the fact that many of the sources listed by the EID are written in local languages, and the quality of the translations that can be achieved with online translation services is not always satisfactory. Thirdly, the fact that the sources of the EID are websites that may become inaccessible after a certain period of time. Finally, even if an attempt was made to carry out a new search to avoid the second and third issues, it is not always possible to find relevant sources of small magnitude events with limited impact, as they get buried among information on larger and more devastating events as time passes by. A brief check-up of some randomly-selected cases revealed that, while many entries are easily verifiable in the original sources listed by the EID, some discrepancies may exist as well. For example, a case was identified in which the telephone number to which the population needed to call to request for official verification of potential damage in their properties appears to have been misinterpreted as being the number of damaged buildings (Umbria, Italy, 2nd January 2017, first entry of the EID for 2017) (Umbria 24, 2017). In a different case, that of an earthquake with $m_b=4.7$ in Colombia, the information reported by the EID coincides with what is stated in the source cited therein, but a deeper analysis suggests the original data may be inaccurate. This earthquake is reported to have caused the collapse of the roof of a jail located over 300 km away from the epicentre (RCN Radio, 2017). Even if the ground shaking generated by this event had been unusually large, it is unlikely that this roof was in good conditions and collapsed exclusively due to the earthquake. However, no final answer can be given to this matter without an in-depth investigation that is clearly beyond the scope and possibilities of any database effort. This last case serves as well as an example of the issue of coverage versus reliability of which no database is exempt.

For the cases in which damage was reported in terms of a scale and not numbers of damaged/destroyed buildings, the descriptions provided by the EID (Table 2.3) were used to fill in the corresponding fields in the database. For this purpose, the equivalences shown in Table 2.4 were established. For damage level 3, for example, which is described as *“Some houses collapsed, others damaged. Example: some houses completely destroyed/uninhabitable. Dozens of others with structural damage.”*, the words “dozens” and “some” were assigned to the damaged and destroyed buildings fields, respectively.

It is important to note that having found an earthquake in the ISC Bulletin that potentially matches the entry in the EID does not guarantee that it is the right earthquake. This is particularly true in the cases in which a whole country was specified as the location in the EID instead of a region within it (relatively common for the years 2013-2014), and the country happened to cover a large area and have high levels of seismicity, a great example of which is Turkey. Even if the search areas were reasonably constrained, it is also possible that the code finds earthquakes that are not the desired one, as not all earthquakes that occur in the world are reported in the ISC Bulletin.

Table 2.4. Equivalence between damage levels defined by the Earthquake Impact Database and numbers of damaged/destroyed buildings in the resulting Database of Damaging Small-to-Medium Magnitude Earthquakes.

Level	Damaged Buildings	Destroyed Buildings
1	Non-structural	0
1-2	Limited	0
2	Some, Minor	0
2-3	Some, Severe	0
3	Dozens	Some
3-4	Hundreds	Dozens
4	Hundreds	Dozens to hundreds
4-5	Hundreds	Hundreds
5	Thousands	Thousands
5+	Thousands	>20,000

To illustrate the process of determining which of the potential earthquakes is the one that the EID refers to, the $m_b=4.7$ (proxy **M4.79**) Sichuan (China) earthquake of 22nd September 2015 is used as an example. Table 2.5 shows the corresponding entry in the EID, while Table 2.6 lists the four potential earthquakes identified by the computer code. As shown in Figure 2.2, two of them fall within Sichuan itself, while another had its epicentre in Yunnan, around 50 km away from the boundary with Sichuan, and the fourth one falls in Myanmar. Based on the magnitude value of 4.0 reported in the EID, one could imagine that the earthquake being sought is the $m_b=4.2$ that occurred at 00.10.55 UTC, as the other event that falls within Sichuan has an m_b magnitude of 4.7. However, a link to a Chinese news website⁹ provided in the EID as a comment to the “Source” field allows to know, via Google Translate, that the sought earthquake occurred in Qingchuan County, located in north-eastern Sichuan. As a consequence, it is concluded that the 18.01.35 UTC $m_b=4.7$ is the correct one.

Table 2.5. Entry for the $m_b=4.7$ Sichuan earthquake of 22nd September 2015 in the Earthquake Impact Database.

Date (UTC)	Country, Region (Epicenter)	Mag.	Depth (km)	Intensity (MMI)	Fatalities	Injuries	Damage level	Buildings damaged	Buildings destroyed	Source
22/09/2015	China, Sichuan	4.0	11		--	--	1	2	0	

⁹ http://news.china.com.cn/rollnews/news/live/2015-09/23/content_34335910.htm



Figure 2.2. Potential earthquakes identified by the computer code as the possible Sichuan earthquake of 22nd September 2015. Selected event marked with a circle.

Table 2.6. Potential earthquakes identified by the computer code as the possible Sichuan earthquake of 22nd September 2015. Selected event marked in grey.

Date	UTC	Lat.	Lon.	Depth	Mw	ML	mb	Ms
22/09/2015	00:10:55	28.150	100.330	10.0			4.2	
22/09/2015	00:10:56	25.691	97.243	0.0				3.8
22/09/2015	06:01:11	27.587	100.030	0.0				3.1
22/09/2015	18:01:35	32.464	105.321	0.0			4.7	3.4

2.10. Example of interdependence of consequences of shocks within the same sequence and of the kind of consequences reported

Being the question of whether the consequences of an event are completely independent from preceding earthquakes or not so relevant, an example will be used to illustrate the kind of information available for different earthquakes in a series, as well as the easiness (or lack of) with which this information can be retrieved. This example will focus on the earthquakes that hit Central Nepal between 2015 and 2017.

A devastating **M7.8** earthquake hit Nepal on 25th April 2015, and a second **M7.3** shock stroke some weeks later, on 12th May 2015. Abundant aftershock activity was recorded in the area. The EID contains 17 entries related to this series. Of these, two are the largest shocks, another two have magnitudes above **M5.5** as well, one is the **M5.27** earthquake on 27th November 2016, already within the Database of Damaging Small-to-Medium Magnitude Earthquakes, another is a magnitude 3.2 earthquake on 21st June 2017, below the **M4.0** threshold, and the other eleven were incorporated to the Database of Damaging Small-to-Medium Magnitude Earthquakes after processing of the EID. Tables 2.7 and 2.8 summarise the characteristics and the consequences reported in the EID and sources therein cited for the 17 shocks, while Figure 2.3 shows the locations of their epicentres. For the same period of time and geographical area, the NOAA database contains only four entries: two for the **M7.8** and **M7.3** events, and other two for the 27th November 2016 and 21st June 2017 earthquakes. The consequences of the four shocks with magnitudes larger than **M5.5** will not be discussed in detail herein, as it is clear that they caused extensive damage and a very large number of casualties.

Table 2.7 Hypocentral coordinates and magnitude estimates for 17 earthquakes that caused damage and/or casualties in Central Nepal between 2015 and 2017. The two larger shocks are marked in bold italics. **M** in [] are proxy values.

ID	Date (UTC)	Time (UTC)	Latitude	Longitude	Depth	M	M _L	m _b	M _s	M _{unk}
1	25/04/2015	06:11:25	28.231	84.731	8.2	7.8	-	7.1	7.9	7.8
2	26/04/2015	07:09:09	27.737	85.979	13.4	6.8	-	6.6	7	6.7
3	02/05/2015	05:35:50	28.266	84.747	33.0	[5.0]	-	4.9	3.7	5.1
4	05/05/2015	10:38:45	27.596	85.742	0.0	[4.1]	4.1	4.1	-	4
5	10/05/2015	09:38:33	27.564	85.502	0.0	[4.3]	4.0	4.3	-	4.2
6	12/05/2015	07:05:19	27.809	86.066	15.0	7.3	-	6.8	7.6	7.3
7	12/05/2015	07:36:53	27.525	86.142	13.8	6.1	-	6.1	-	-
8	15/05/2015	01:42:46	27.886	84.770	29.9	[5.0]	-	4.9	4.1	5.5
9	16/05/2015	11:34:12	27.370	86.260	12.0	5.4	-	5.7	-	5.5
10	20/08/2015	06:02:53	27.919	85.521	0.0	[4.3]	4.7	-	3.3	4.8
11	05/02/2016	16:20:11	27.878	85.338	23.5	[5.4]	-	5.2	4.0	5.5
12	21/02/2016	18:10:03	27.808	84.631	35.7	[5.3]	-	5.1	3.7	5.5
13	09/04/2016	13:20:11	27.471	85.080	0.0	[4.1]	3.8	4.1	-	4.5
14	11/05/2016	08:52:51	28.036	84.659	45.8	[4.6]	-	4.5	3.2	4.5
15	27/11/2016	23:35:21	27.802	86.532	10.0	5.3	-	5.4	5.4	5.6
16	27/02/2017	03:37:51	27.411	86.061	41.1	[4.6]	-	4.7	3.7	4.7
17	21/06/2017	-	-	-	-	[3.2]	-	-	-	3.2

Table 2.8 Casualties and damage caused by the 17 earthquakes listed in Table 2.7 that stroke Central Nepal between 2015 and 2017, according to the Earthquake Impact Database. Texts inside [] in italics indicate information not readily available in the EID but accessible via the website links provided therein. Inj.= injured. L. = landslides.

ID	Deaths		Inj.	Causes of death/injury	Buildings		L.
	Tot.	Shaking			Damaged	Destroyed	
1	9124	-	23790	-	300,000	800,000	-
2	8	-	83	-	Hundreds	Dozens to Hundreds	-
3	4	-	1	-	Dozens	Some	[Y]
4	1	[1]	0	[collapse of pre-damaged house]	Non-structural	[1]	-
5	1	[0]	0	[running out of house]	-	-	-
6	228	-	3680	-	Thousands	Thousands	-
7	1	-	0	-	-	-	-
8	1	[0]	-	[heart attack during estampede]	-	-	-
9	4	[1]	0	[1 wall collapse, 1 heart attack, 1 drowned in agitated river, 1 fell when running]	Dozens	1	-
10	1	[0]	0	[landslide]	Non-structural	0	Y
11	1	-	66	[15 injuries for running away from houses in panic]	-	-	-
12	0	0	1	-	Some, Minor	0	-
13	0	0	5	[stampede]	Non-structural	0	-
14	0	0	3	[panic reactions]	-	0	-
15	1	-	2	-	Dozens	1	-
16	0	0	0	-	15	0	-
17	1	[1]	1	[bricks (of pile) falling on head of worker]	0	0	-

A first fact of interest is that the distance between the epicentres of the two large shocks is around 140 km. With this information alone, one could conclude that the consequences of the two might not be related. However, when plotting the finite fault solutions for the two earthquakes it can be noted that not only do the two partially overlap, but they also enclose most of the remaining epicentres as well (see Figure 2.3). As a consequence, many of the aftershocks may have hit areas that had been previously damaged, even when many of them seem to have occurred relatively far away from the larger main shocks. It is also interesting to note that the declustering of the merged catalogue (see Section 4.2) treats both large earthquakes as main shocks with their own series of aftershocks. This could lead to neglecting the effect of the previous earthquakes and thinking, for example, that all the damage caused by the **M7.3** 12th May 2015 was independent from that caused by the **M7.8** 25th April 2015, when the overlapping of the finite fault solutions suggests this is not necessarily the case. It is unquestionable that discussions in terms of epicentral distances are irrelevant for such large earthquakes. However, this example illustrates the possible misinterpretations that might arise from simply looking at a list of earthquakes within a database.

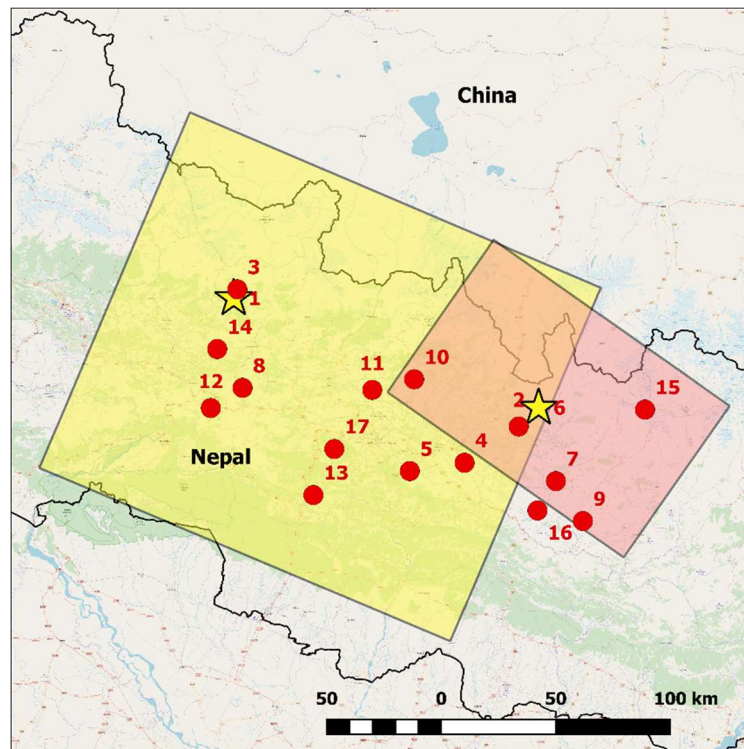


Figure 2.3. Epicentres of the 17 earthquakes listed in Tables 2.7 and 2.8. Stars indicate the epicentres of the two large **M7.8** and **M7.3** shocks. The yellow and red rectangles indicate the projection of the finite fault solution for each of the two, respectively, according to the USGS (USGS, 2017a; USGS, 2017b). Epicentre of earthquake 17 defined approximately from news report (The Himalayan Times, 2017). Administrative boundaries from GADM maps and data (GADM). Background map from OpenStreetMap (OpenStreetMap).

For the aftershock labelled 3 in Tables 2.7 and 2.8 and Figure 2, the EID reports 4 deaths, 1 injury and no specific number of damaged or destroyed buildings but an overall rating of damage level 3. The latter is described as “some houses collapsed, others damaged” and the example provided by the EID makes reference to “some houses completely destroyed/uninhabitable, dozens of others with structural damage”. The sources cited in EID for this event are three. The first one is a report from Earthquake-Report, which does not provide any specific information but only a comment regarding damage to be expected, as “a number of houses have such structural damage that even a lesser shock can reduce them to rubble” (Earthquake-Report, 2015b). The second one is a newspaper article (The Kathmandu Post, 2015b) that reports the occurrence of landslides and one woman having been injured, though it is not clear if the latter is a consequence of the former. The landslide was not directly mentioned in the EID. The third source is a tweet by the Search and Rescue Dog Handlers Academy of Nepal (SAR Dogs Nepal, 2015), saying that their teams reported 4 dead and 32 missing. From these sources, it is not possible to know how the damage level 3 was assigned to this earthquake, or if the reported damage to the built environment was also due to the landslides.

According to the EID, aftershock 4 caused one death and damage level 1, which translates into simply non-structural damage. No number of damaged buildings is provided, but zero destroyed ones is specifically mentioned. The news website cited by the EID (Xinhua Net, 2015) reports the death of a woman whose house had been damaged by the 25th April main shock and collapsed after this aftershock, without specifying if the death was due to said

collapse, though it may be inferred. In this case, the link between the main shock and the consequences of the aftershock is completely clear. The website also mentions that the earthquake occurred on Wednesday morning, which may potentially mean that the earthquake found by the algorithm, occurring on Tuesday at 16.23 local time, may not be the sought one (though wrong dates and times have been spotted in news websites as well). However, the epicentre of the assigned earthquake falls within Kavre district, which is mentioned in the article as the location at which the death occurred. It is surprising that the damage caused by this earthquake was classified in the EID as non-structural (level 1) and that the collapsed house was not reported as a destroyed building. It is, thus, possible that the damage scale adopted by the EID may not always be used literally. Speculating with an explanation, it is possible that this may be due to the reporter attempting to convey somehow the fact that the consequences of this earthquake were not independent from those of the main shock, which would reflect the difficulties associated with applying a standardised damage scale to a case of incremental damage due to repeated shaking.

The automatic algorithm identified seven different shocks as potential earthquake 5, as shown in Figure 2.4, none of which coincided in time with the one mentioned in the Earthquake-Report site referenced by the EID (Earthquake-Report, 2015a). Of the seven, the one at 09.38.33 UTC was selected not only because its magnitude appeared to be the closest to that reported in the EID, but also because it matches the time of occurrence reported in the second reference cited by the EID, a local newspaper (The Kathmandu Post, 2015a), taking into consideration the time difference between UTC and Nepal. The 09.23.00 UTC event mentioned by Earthquake-Report could not be found either in the USGS catalogue or the ISC Bulletin. The only consequence reported by the EID for this earthquake is one fatality, with no details on the circumstances. According to the article in the local newspaper, this fatality corresponds to a 72-year-old person who fell down while running out of their house, which *“had developed cracks after the April 25 devastating earthquake”*. In contrast with aftershock 4, for which the death appears to have been caused by the collapse of a pre-damaged house, the death associated with aftershock 5 appears to have been due only to the reaction of the person to the shaking.

For aftershock 8, the EID only reports one death, without details on the circumstances under which it occurred. The source cited is a newspaper article (Business Standard, 2015) that states that the death was due to a heart attack during a stampede.

For aftershock 9, the EID reports 4 deaths with unspecified causes, one destroyed building and damage level 3, described as “some houses collapsed, others damaged”. The only source cited is a newspaper article written in Hindi (Live Hindustan, 2015), which states that the causes of the deaths were: (i) the collapse of a wall at a rice mill, (ii) a heart attack, (iii) large earthquake-generated waves in the Gandak river causing a person to drown, and (iv) a person tripping over and falling while trying to run away during the shaking. Interestingly, Google Translate (Hindi-English) only made it possible to understand the first three. This clearly illustrates the importance of being able to access reports written in local languages when dealing with the consequences of small-to-medium magnitude events, as it was only with the aid of a colleague that the correct meaning of the text in Hindi could be understood.

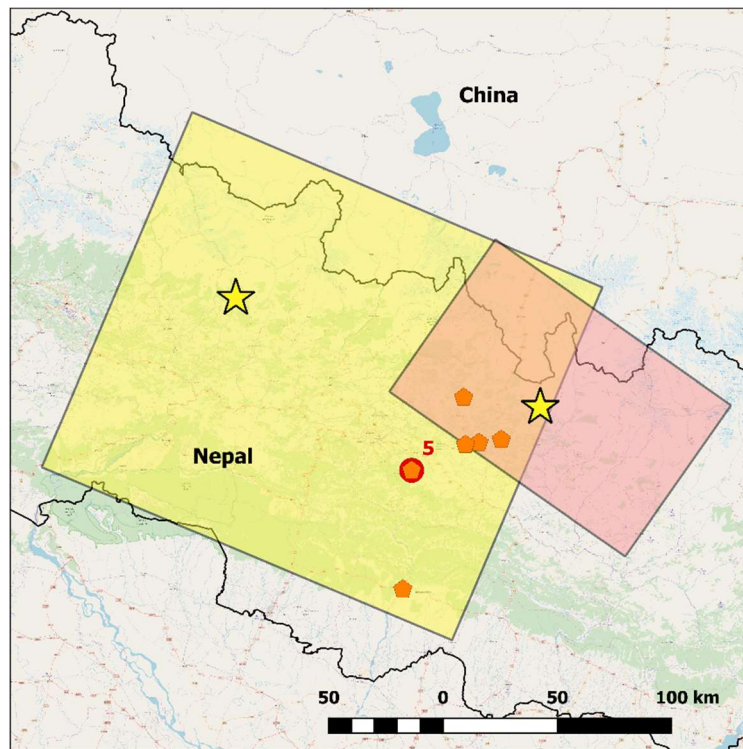


Figure 2.4. Potential earthquakes (orange pentagons) found for aftershock 5 in Tables 2.7 and 2.8. Selected one marked with red circle. Administrative boundaries from GADM maps and data (GADM). Background map from OpenStreetMap (OpenStreetMap).

One death, zero buildings damaged or destroyed and a landslide are the consequences enumerated by the EID for aftershock 10. The original source, a report from a website dedicated to natural disasters named Disaster Report, specifies that the death was due to a landslide that occurred in Kaule, in the district of Nuwakot, around 40 km away from the epicentre of the identified earthquake. The local time mentioned in the report is in agreement with the UTC of the earthquake identified within the ISC Bulletin as aftershock 10. The authors of the present work had access to the aforementioned website at the time of carrying out this analysis. However, at the time of writing, the link to the website leads to a message stating that the domain name expired. Though unintended, this illustrates how easily information on small earthquakes can vanish and how difficult it is to retrieve it as time passes by.

While the EID reports one death and 66 injured for Earthquake 11, the only source cited by the EID that can be accessed at the moment of writing indicates that 15 people were injured when running away from their houses in panic (Daily News and Analysis India, 2016). The other two sources correspond to broken links, one of which is that of the Disaster Report website mentioned above.

The consequences reported by the EID for earthquake 12 consist of one injury, zero buildings destroyed, unspecified number of buildings damaged, and overall damage level 2. From the only source (Nagarik News, 2016) cited by the EID it is possible to know that the injury corresponded to a 26-year old man who severely sprained his foot whilst running away during the earthquake. The source does not mention anything about damage or fatalities.

For aftershock 13, the consequences listed in the EID are 5 injuries (unspecified reasons), zero buildings damaged or destroyed, and overall damage level 1. The only source cited is a news website (My Republica, 2016) that reports the occurrence of a stampede that caused said 5 injuries, but does not mention anything about damage. Therefore, it is not known how the damage level 1 was assigned in the EID.

For aftershock 14, the EID reports 3 injuries (unspecified reasons), zero buildings destroyed, unspecified damaged buildings and unspecified damage level. The one source to which reference is made is Disaster Report, which was, as for the case of aftershock 10, accessed at the time of carrying out this analysis but is not available at the time of writing. The report stated that the three injuries were due to panic reactions, like jumping from a second floor during the shaking. Two earthquakes had been identified by the automatic algorithm as potential aftershock 14, one of which being the one listed in Table 2.7, the other one having an m_b of 4.5 as well, with epicentral coordinates 29.4 km away. The location and time of the former coincide with those reported in the original source. Without confronting the two against the on-line report it would have been impossible to determine which of the two was the earthquake that the EID was making reference to.

The aftershock that took place on 27th November 2016, that is, earthquake 15 in Tables 2.7 and 2.8, was already in the Database of Damaging Small-to-Medium Magnitude Earthquakes and, thus, did not need to be added from the EID. For said earthquake, the NOAA database reports one death, one injured and two houses destroyed, and estimates losses of less than 1 million USD. The EID reports one death, two injured and one building destroyed, instead, and classifies it as damage level 3, that is, “some houses collapsed, others damaged”, without citing any source. The reason for which the consequences of this aftershock made it to the NOAA database while those of other shocks did not is not known. The EM-DAT database does not report on this earthquake either.

The EID reports 15 damaged buildings and no other consequence for aftershock 16. The original source is an on-line news article (News X, 2017) that states the occurrence of two earthquakes of similar magnitude within less than one hour, which caused damage to an unspecified number of old structures. It is not known if the EID took the number of 15 from a different unknown source or if it is an estimate of their own. The local times reported for the two earthquakes on the news article correspond to the two events identified by the automatic algorithm.

The last earthquake of the list, number 17, is an interesting case. First of all, it was not possible to find an earthquake matching the characteristics described for this one either in the ISC Bulletin or the USGS Catalogue or the catalogue of the National Seismological Centre of Nepal (Government of Nepal - National Seismological Centre). The EID indicates one death and one injury for this event, and refers to one on-line source, which specifies that the death was that of a worker of a brick factory who was piling up a stack of bricks and was hit by the bricks falling on him when the earthquake hit. The injured person was his son. While the trigger of the event that led to these casualties was (allegedly) the earthquake, it was the particular circumstances that led to the consequences observed and these should not be regarded as standard or typical. The fact that the casualties occurred at a manufacturing site means as well that they are related to work safety standards more than

they are to the earthquake, as the former should account for the possibility of ground shaking causing an accident in the work place. The source does not specify if the worker was wearing a helmet, protective shoes or any other safety equipment.

Having gone one by one in detail through these events, the following summary of the twelve aftershocks listed in Tables 2.7 and 2.8 that lie within the **M4.0-5.5** range can be made:

- Three earthquakes (ID 5, 8, 14) caused only deaths and/or injuries as a consequence of people's reactions and not due to the response of buildings. This was verified in the original sources. While the criteria used by databases such as NOAA or EM-DAT to include or not events is not known, it is not surprising that these three earthquakes are not mentioned in those databases.
- One earthquake (ID 11) caused only deaths and/or injuries, though from the sources it was only possible to know that some of those injuries were due to people's reactions to the shaking, the remaining injuries and one death being of unknown nature.
- One earthquake (ID 10) only caused a landslide that killed one person, as reported by the original source.
- Of the remaining seven earthquakes that are reported to have caused damage, the number of damaged/destroyed buildings could only be fully verified in one case (ID 4, collapse of house pre-damaged by the main shock) and partially verified in another, assuming that the one building destroyed by earthquake 9 is the one that killed one person. For the latter, the remaining three deaths were not associated to the performance of buildings. For the only other case in which a specific number of damaged buildings was reported in the EID (earthquake 16), only a generic comment regarding "damage to old structures" was found within the cited original source. For earthquake 15, which was already in the database, the number of injuries and destroyed houses does not match by one unit the values reported in the NOAA database. For the remaining three (ID 3, 12, 13), the number of dead/injured could be verified from the sources, but not the damage to buildings.

This example has illustrated a series of important points. Firstly, how the consequences of any particular earthquake might be influenced by the consequences of previous earthquakes in a sequence. Secondly, that a quick look at a list of earthquakes and their declustering information in a database might lead to erroneous interpretations on the connections across different events. Thirdly, how easy it is to lose access to online sources within a relatively short period of time. This last point highlights, once more, the reasons for which the identification of earthquakes causing minor damage becomes so difficult shortly after the earthquake occurs.

2.11. Composition of the resulting database

At the time of writing, the Database of Damaging Small-to-Medium Magnitude Earthquakes consists of 1,960 events. This section looks in detail into its composition.

It is noted that the expression “from the EID” is used herein to refer to the earthquakes retrieved from the EID by means of the algorithm described in Section 2.9. This does not imply that other earthquakes may not have been reported in the EID as well, but simply that they had already been incorporated to the Database of Damaging Small-to-Medium Magnitude Earthquakes before the application of said procedure.

2.11.1. Geographic distribution

Figures 2.5 and 2.6 show the epicentral locations of the earthquakes of the database, with the latter focusing on those retrieved from the EID as per the procedure described in Section 2.9 and the former showing those retrieved from all other sources. As can be observed, both maps are quite similar in their distribution and follow, in general, the patterns of global seismicity. However, it is noted that areas known to have high seismicity rates but very low population density are largely absent from both maps, clearly due to their very low exposure. Examples of this are Alaska (northwest North America), Tierra del Fuego (south tip of South America) and the Kurile Islands (northeast Asia). In contrast, lower-seismicity areas such as the north-eastern USA and Brazil acquire greater prominence in the database, possibly due to the higher social impact of smaller events (and subsequent tendency to report them) in areas for which seismic shaking is perceived as unusual, as well as a likely higher vulnerability of the building stock (broadly speaking, notwithstanding socio-economic factors).

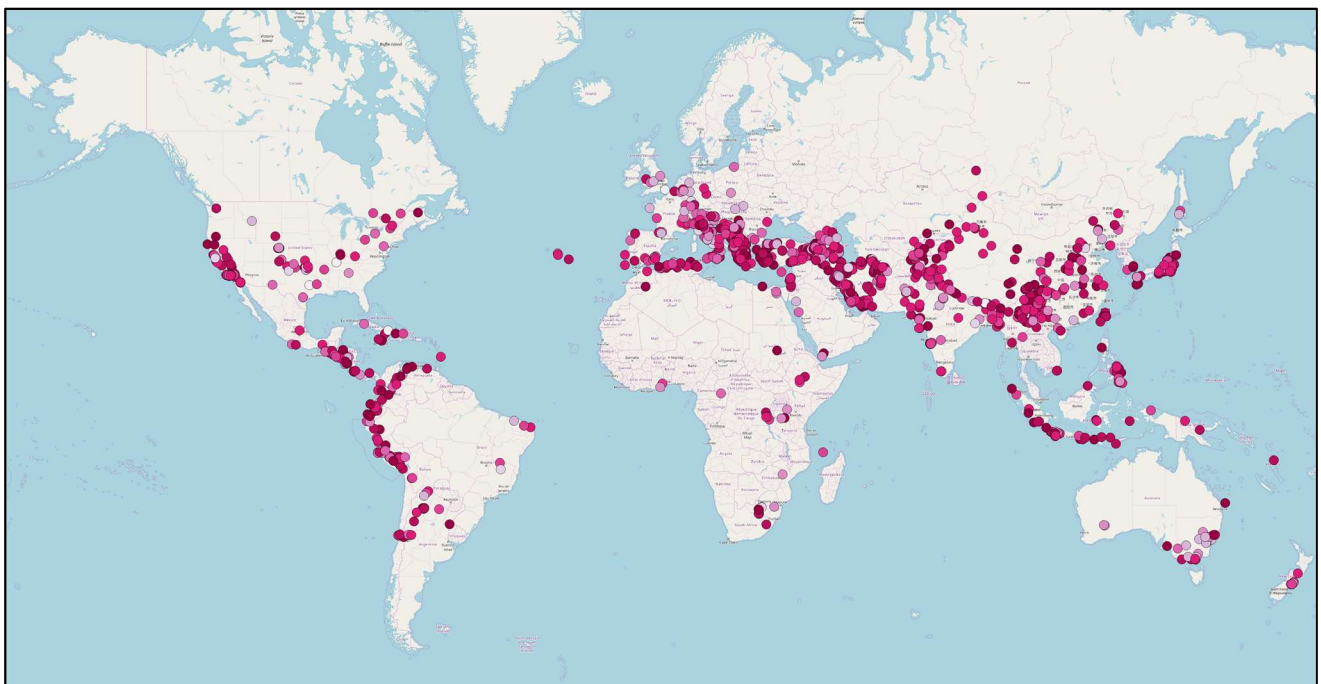


Figure 2.5. The Database of Damaging Small-to-Medium Magnitude Earthquakes: earthquakes not retrieved from the EID (1,092 out of 1,960). Colour scale indicates moment magnitude (white: lowest, magenta: highest).

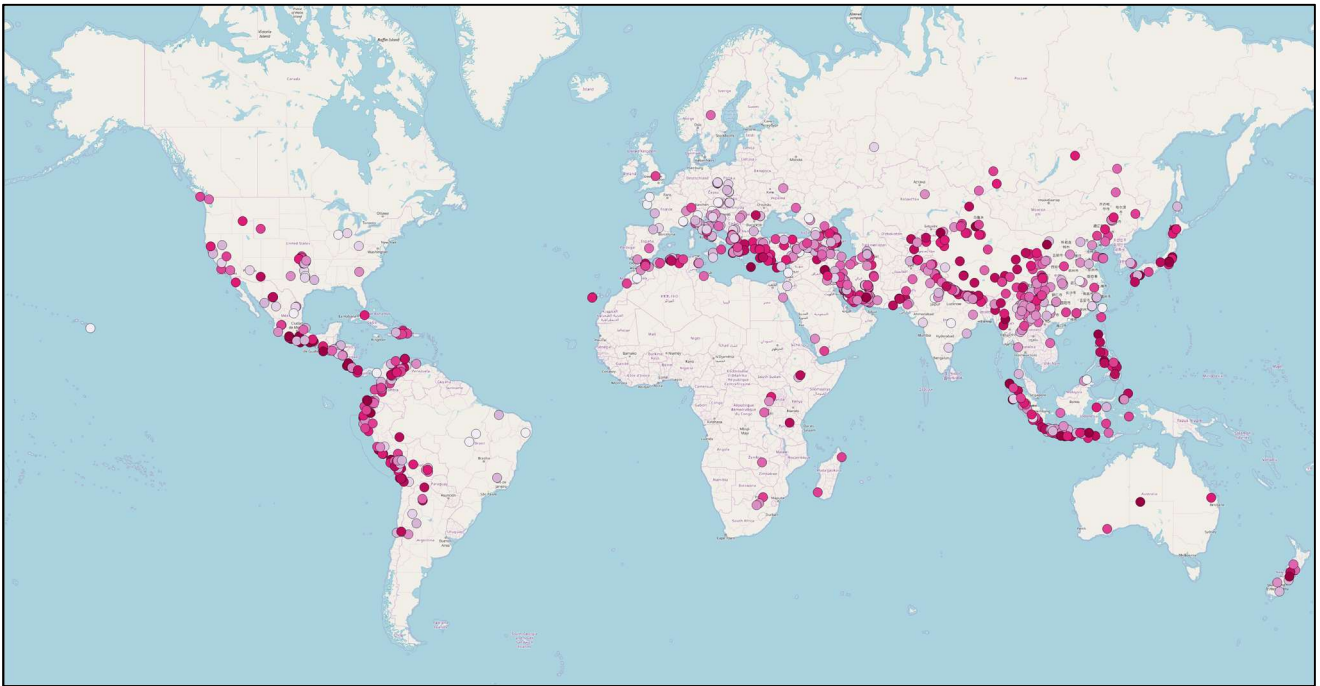


Figure 2.6. The Database of Damaging Small-to-Medium Magnitude Earthquakes: earthquakes retrieved from the EID (868 out of 1,960). Colour scale indicates moment magnitude (white: lowest, magenta: highest).

2.11.2. Temporal distribution

Due to the influence of data availability, the distribution in time of the earthquakes of the database is not uniform, with the number of earthquakes per decade increasing as shown in the plot on the left of Figure 2.7. This increase is not homogeneous either. A first noticeable jump can be observed in the 1960s and is possibly due to an increase in the resources with which large volumes of earthquake data could be systematically processed, thanks to the establishment of the World-Wide Standardized Seismograph Network (WWSSN) around that time and the creation of the International Seismological Centre (ISC) in 1964 (Adams 2010; ISC). Another distinct jump occurs at the beginning of the 2000s, possibly associated with the boost in the ability to communicate and access news and reports associated with the global embrace of on-line technologies. The most extreme jump is, undoubtedly, that of the 2010s, which is clearly related to the existence of the EID from 2013 onward (see plot on the right of Figure 2.7). This illustrates how data accessibility can play a fundamental role in the perception of the impact of non-catastrophic hazards such as low-to-medium magnitude earthquakes and serves as an indication of the completeness of the present database.

Table 2.9 further illustrates the impact of adding the events contained in the EID on the total number of earthquakes in the database. Of the five years for which earthquakes were retrieved from the EID, 2017 is the one for which the proportion of events stemming from the latter is the lowest. Interestingly, 2017 was one of the years for which more data for the Database of Damaging Small-to-Medium Magnitude Earthquakes was collected almost in real time, an observation that illustrates the effects of near-real time reporting and recording.

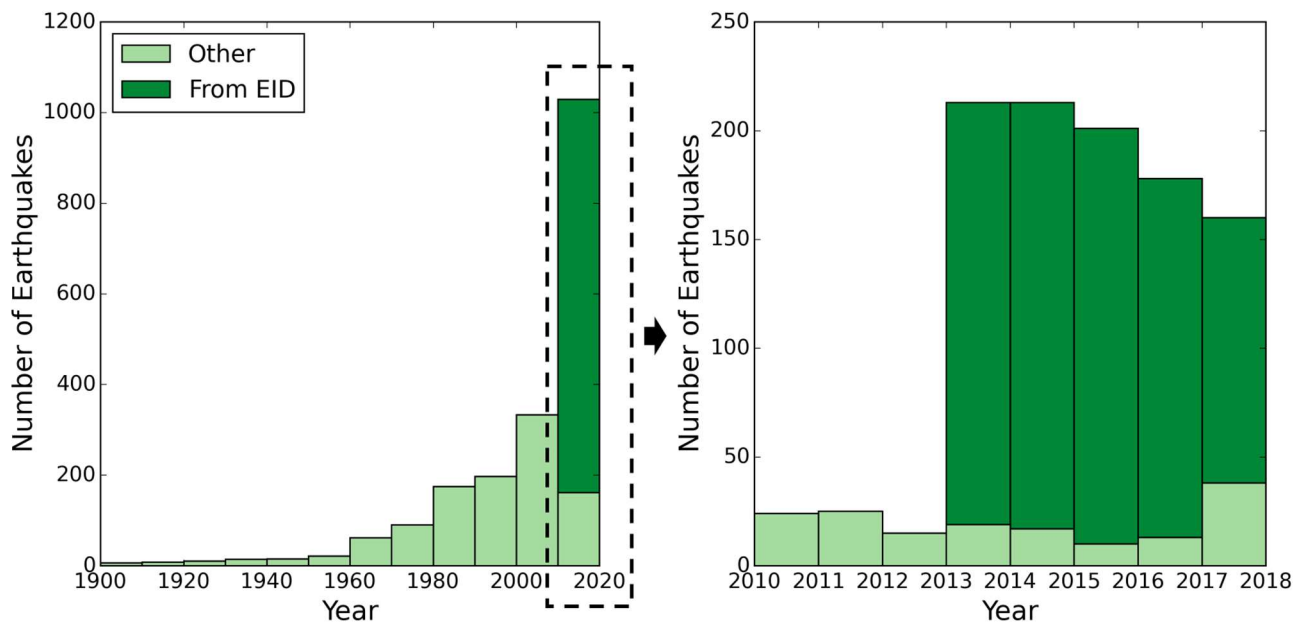


Figure 2.7. Distribution of dates of the earthquakes that make up the whole of the Database of Damaging Small-to-Medium Magnitude Earthquakes (1900-2017). The plot on the right shows a detail of the period 2010-2017.

Table 2.9. Number of events in the Database of Damaging Small-to-Medium Magnitude Earthquakes.

Year	Other Sources	From EID	All
1900-2012	995	0	995
2013	19	194	213
2014	17	196	213
2015	10	191	201
2016	13	165	178
2017	38	122	160
TOTAL	1,092	868	1,960

The clear variation in the annual rate of damaging earthquakes raises the question of whether that of the years 2013-2017 could be assumed to be closer to the “real” value in all years. The average for this short period is around 190 damaging earthquakes per year. If this were to apply generally, it would imply, for example, that less than 20% of the damaging earthquakes of the 2000s may have been captured in the database, with this percentage reducing even more further back in time. There is the issue, of course, of five years of seismicity being a relatively short time for generalisations to be made, as fluctuations in the overall seismicity rates exist naturally as well. The latter can be observed when noting the overall decrease in the rate of events not retrieved from the EID reported for the 2010s in the plot on the left of Figure 2.7. Even if assuming the same rate for the two years that are missing from the whole decade (2018 and 2019) the final number would still be much lower than the 333 cases for 2000-2009. A first hypothesis could be the possible delay between the occurrence of damaging earthquakes, the publication of studies about them, and the point in time at which they become part of databases, though the fact that NOAA tends to

incorporate new events relatively fast would rule out this explanation. Looking at the merged world catalogue of Nievas *et al.* (2017) it can be noted that it contains an average of 82,556 earthquakes per year for the period 1st January 2010 - 31st December 2014, and an average of much fewer 51,970 for the period 1st January 2015 - 30th June 2017. This suggests that the decrease might be simply due to the natural randomness associated with the occurrence of earthquakes.

A point worth of noting is that a large proportion of the earthquakes incorporated from EID is associated with only non-structural or very limited structural damage, the implication being that it does not appear likely that this 190 earthquakes-per-year rate be in reality so much larger. Nevertheless, it is not possible to assert that all damaging earthquakes have been captured by the EID, and around 6% of the entries of the EID were not included in the database due to the impossibility of matching them with earthquakes reported in the ISC Bulletin. How close or not this 190 earthquakes-per-year rate is to the “real” value is difficult to quantify.

2.11.3. Magnitude distribution

The distribution of moment magnitudes of earthquakes that make up the whole database is depicted in Figure 2.8, which shows primary values of **M** used to define the inclusion or not of the earthquakes in the database. Due to the rounding up of magnitudes in the range $3.95 \leq \mathbf{M} < 4.00$ to 4.0 and rounding down of the range $5.5 < \mathbf{M} \leq 5.55$ to 5.5, the first and last bins are slightly wider than the rest, the former containing earthquakes in the range $3.95 \leq \mathbf{M} < 4.25$ and the latter $5.25 \leq \mathbf{M} \leq 5.55$. All other bins are as indicated and include their lower boundary but not their upper one.

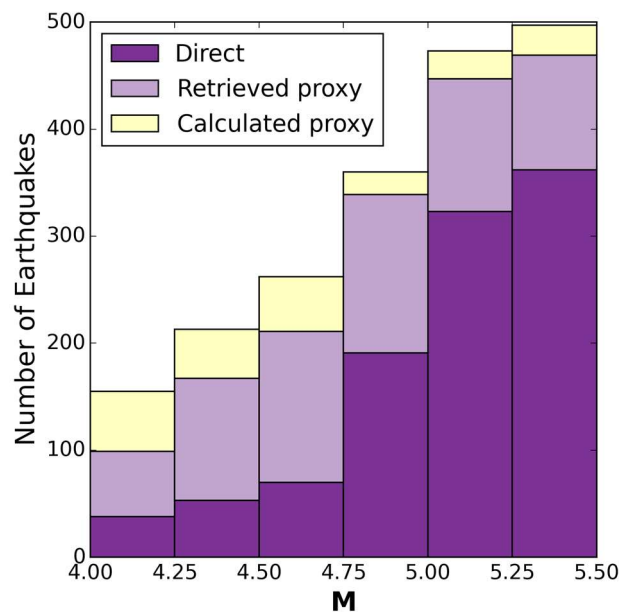


Figure 2.8. Distribution of moment magnitudes of the whole of the Database of Damaging Small-to-Medium Magnitude Earthquakes. Direct = **M** directly calculated from inversion (retrieved from seismological agencies, scientific literature, etc.). Retrieved proxy = proxy **M** retrieved from existing catalogues. Calculated proxy = proxy **M** calculated from other magnitude scales within the context of this work.

The number of damaging earthquakes in each magnitude bin increases steadily and reaches its maximum within the 5.25-5.50 bin of Figure 2.8. This is not unexpected, as larger-magnitude earthquakes have a larger damage potential, notwithstanding the influence of distance, site effects, vulnerability and other factors. However, the relative increase from the 5.00-5.25 to the 5.25-5.50 bin is very small (around 5%) with respect to the relative increase from all other bins up to that point. Moreover, because of the rounding procedure explained above, the 5.25-5.50 is slightly wider than the previous one. If the upper bound of the bin was a strict 5.5 (included), there would be 61 earthquakes less in it, as their M falls in the range $5.5 < M < 5.55$. Subtracting these 61 earthquakes to the 497 in the bin leaves 436, which is less than the 473 cases with $5.00 \leq M < 5.25$. All this suggests that the Gutenberg-Richter law (Gutenberg & Richter, 1944) appears to take over for magnitudes above around 5.25, as there are 1.8 times more earthquakes in the range 5.00-5.25 than in the range 5.25-5.50 in a given period of time, assuming a b-value of 1.0. In other words, Figure 2.8 shows that the higher likelihood of larger earthquakes to cause damage or casualties is counterbalanced by the decreasing frequency with which these events occur.

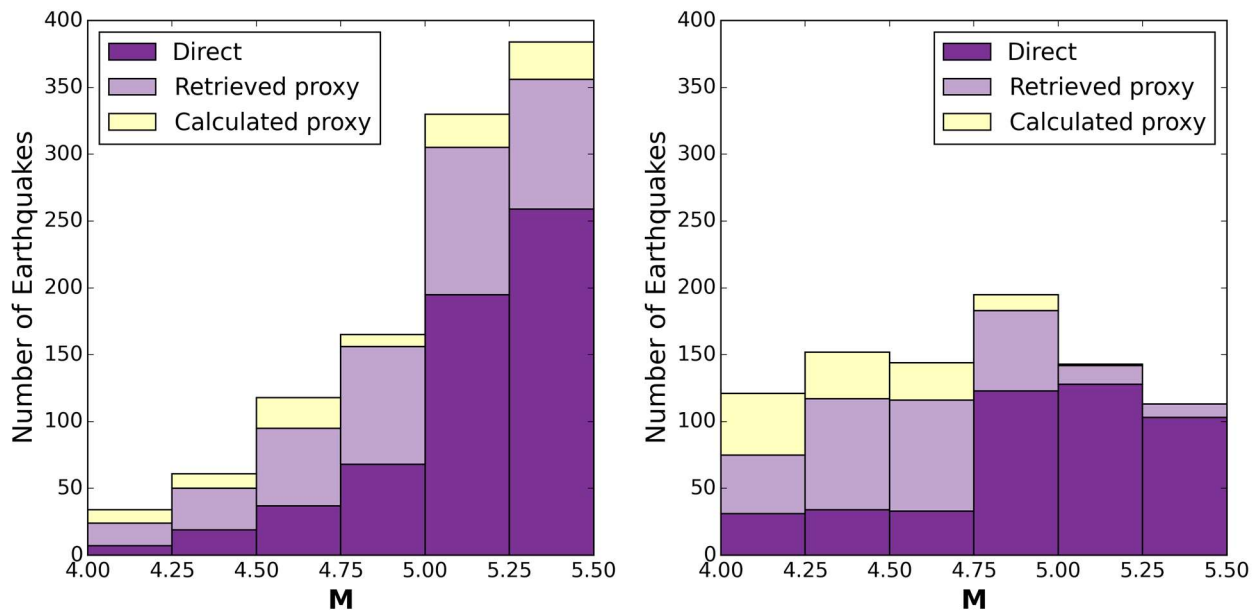


Figure 2.9. Distribution of magnitudes of the earthquakes that make up the Database of Damaging Small-to-Medium Magnitude Earthquakes and were not automatically processed from the EID (left), and those from the EID (right). Direct, Retrieved proxy, Calculated proxy as per description of Figure 2.8.

It is noted that it is possible that accessibility to data on damage/casualties be playing a role as well in the magnitude distribution of the database. For sources other than the EID, it is the larger-magnitude earthquakes with relatively noticeable consequences that get reported. It is thus possible that the earthquakes that appear as “missing” for the years before 2013 (see Figure 2.7) have magnitudes on the lower side of the $M4.0$ - 5.5 range and could thus change the magnitude distribution increasing the relative contribution of the smaller-magnitude bins.

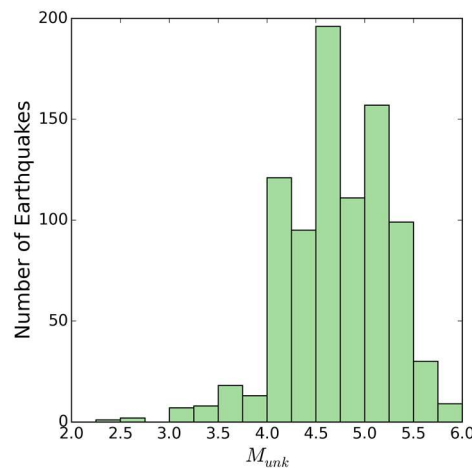


Figure 2.10. Distribution of magnitudes of the earthquakes from the EID added to the Database of Damaging Small-to-Medium Magnitude Earthquakes, as reported in the EID (unknown scale Munk).

2.12. Insights on casualties and damage

The following subsections provide statistics on casualties and damage that stem from the 1,960 earthquakes that make up the Database of Damaging Small-to-Medium Magnitude Earthquakes at the time of writing. For their interpretation, it is fundamental to note, once more, that the database contains, by nature, information from various sources of undetermined reliability. Consequently, these statistics cannot be deemed to represent verified scientific measurements or observations. It is noted as well that the earthquakes contained in the database result from a series of choices made during its compilation (and explained in the previous sections) and that the application of different criteria could lead to the inclusion or exclusion of events and a change in the subsequent analyses.

2.12.1. Damaged and destroyed buildings

As explained in Section 2.5, the “damaged buildings” and “destroyed buildings” fields of the database contain different kinds of data, including numbers, number ranges and verbal descriptions. The proportion of the total that each kind of data represents is depicted in Figure 2.11 for the whole database (top plots) and for the two subsets of earthquakes retrieved from the EID (centre plots) and from all other sources (bottom plots). The possible categories are:

- Number: one specific number of damaged or destroyed buildings found.
- EID estimation: number reported in the EID as their own estimate.
- NOAA range: range of values estimated by NOAA based on verbal descriptions.
- Other range: a range of numbers found in different sources, excluding estimates from the NOAA database.
- Text: only a verbal description was found. This includes verbal descriptions assigned to EID-retrieved events for which damage levels were processed as per Table 2.4
- Not available: no data found.

- Some of: only for destroyed buildings. It implies that some of the buildings reported as damaged were, in fact, destroyed, but the proportion is not known.

Due to the existence of this mix of data types, results are presented in two groups: one gathering cases labelled as “number”, “EID estimation”, “NOAA range”, “other range” and “some of”, in Figures 2.12 and 2.13, and another for the cases labelled as “text”, in Figures 2.15 and 2.16.

Figures 2.12 and 2.13 show results for damaged and destroyed buildings, respectively. Ranges of values are decomposed into lower and upper bounds. Whenever a specific number is available, the two are the plotted as the same. The “some of” cases of destroyed buildings were translated into a lower bound of 1 and an upper bound equal to the number of damaged buildings, when available, or the upper bound of damaged buildings when these were given as a range. The reader is reminded, nevertheless, that a scenario in which all lower-bound values or all upper-bound values apply is very unlikely, reality most likely lying in between. The increasing destructive power of increasingly larger magnitude events is visible in all plots. While the two right-most plots of Figures 2.12 and 2.13 appear to not comply with this last statement, the reason for this lies most likely in the magnitude distribution of each subgroup (Figure 2.9), as it is clear that the most destructive earthquakes had been already incorporated to the database before the retrieval of events from the EID. It is likely for this same reason that 684 of the 696-697 cases of zero reported destroyed buildings correspond to earthquakes retrieved directly from the EID.

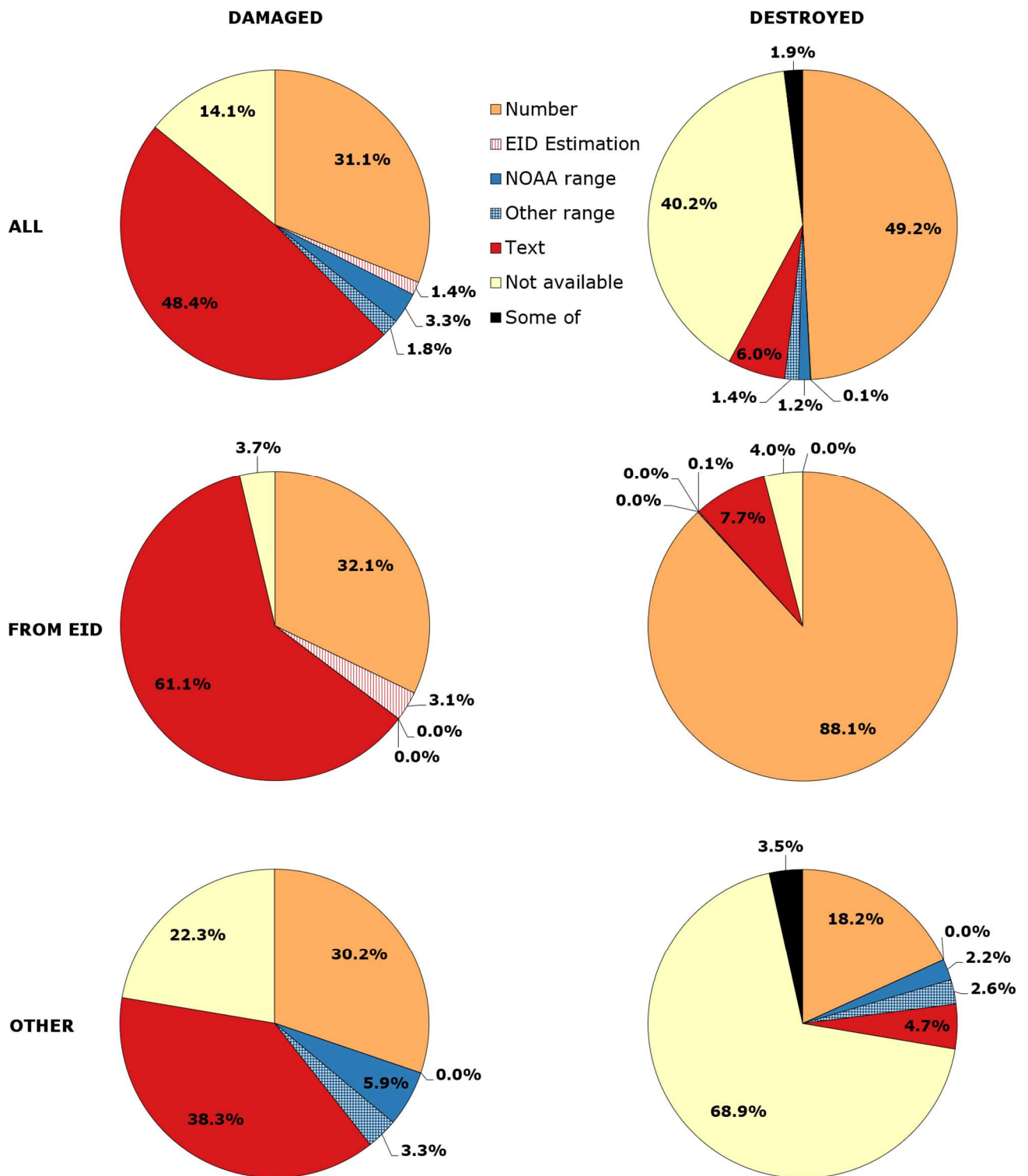


Figure 2.11. Kind of information available regarding damaged (left) and destroyed (right) buildings for the whole of the Database of Damaging Small-to-Medium Magnitude Earthquakes (top) and for earthquakes retrieved from the EID (centre) and all other sources (bottom).

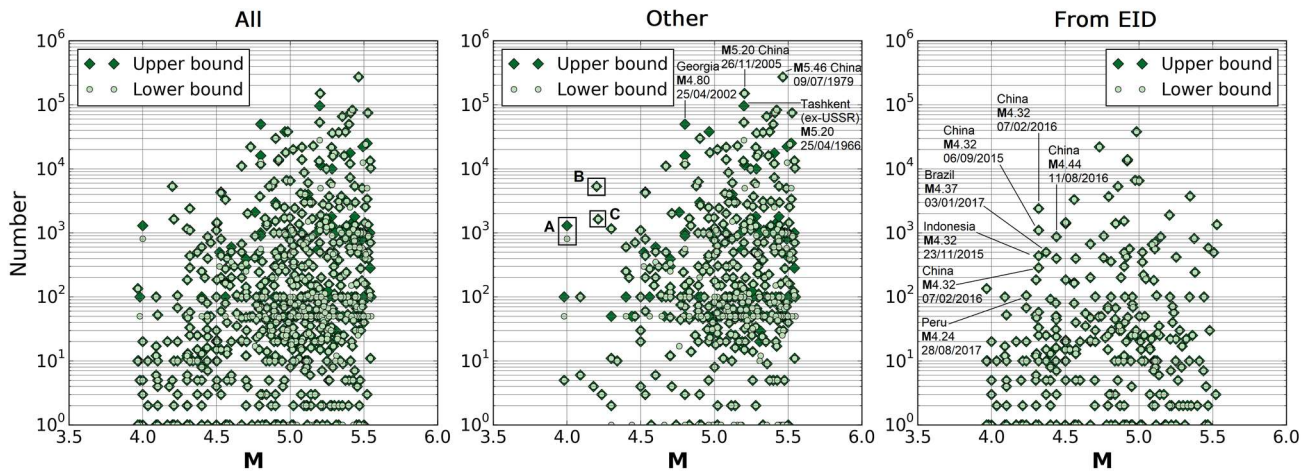


Figure 2.12. Number of damaged buildings as a function of magnitude for the whole of the Database of Damaging Small-to-Medium Magnitude Earthquakes (left), for the events taken from EID (right) and elsewhere (centre), for the cases in which data was available as “Number”, “EID estimation”, “NOAA range”, “Other range”, and “Some of”, as per Figure 2.11 (736 total earthquakes). Zero values not shown (26 total cases).

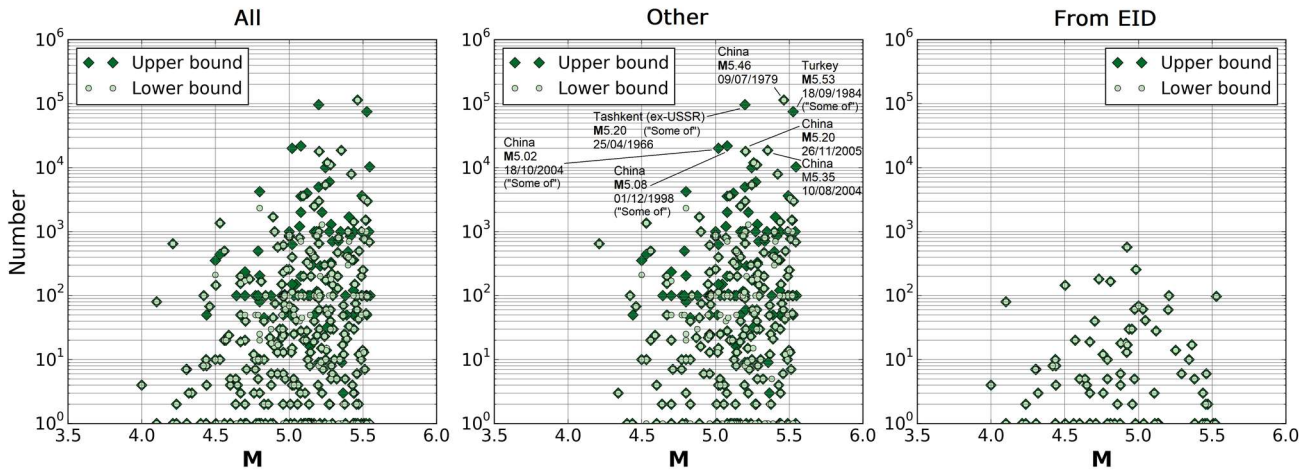


Figure 2.13. Number of destroyed buildings as a function of magnitude for the whole of the Database of Damaging Small-to-Medium Magnitude Earthquakes (left), for the events taken from EID (right) and elsewhere (centre), for the cases in which data was available as “Number”, “EID estimation”, “NOAA range”, “Other range”, and “Some of”, as per Figure 2.11 (1,055 total earthquakes). Zero values not shown (696-697 total cases).

From Figure 2.12 it appears that only earthquakes with magnitudes above around 4.7 seem to have resulted in 10,000 or more damaged buildings, while Figure 2.14 suggests that a slightly larger magnitude of 4.8 marks the start of numbers of destroyed buildings above 2,000. However, not all numbers can be considered equally reliable. Figure 2.14 shows the locations of the 45 earthquakes for which the lower- and/or upper-bound number of destroyed buildings is larger than 1,000, all with moment magnitude larger than 4.5. Of these, twelve are cases of “Some of”, one of which has a NOAA range estimate of 100-1,000 as number of damaged buildings. Seven of the remaining 33 cases correspond to NOAA estimates of the same range as well. The problem with these is not only that they are estimates and not observations, but also that the range is quite broad, with a difference of one order of magnitude between the lower and upper bound. It is thus likely that the

(unknown) real number of destroyed buildings be considerably smaller than depicted in Figure 2.13 in all eight cases.

The earthquake with the largest reported number of destroyed buildings is a **M5.46** earthquake that occurred in Liyang, China, on 9th July 1979, as depicted in Figure 2.13. According to Chung *et al.* (1995), who cite a Chinese source, this earthquake resulted in 272,000 damaged and 113,909 collapsed houses. The same publication studied as well the **M5.28** event of 22nd April 1974 that also occurred in Liyang and is another of the eleven cases with numbers of destroyed buildings larger than 10,000 that can be observed in Figure 2.13. Much smaller numbers of 21,709 damaged and 11,081 collapsed houses are attributed to this earthquake. Through their study, Chung *et al.* (1995) concluded that the stress drop of the 1979 event had been above average for intraplate events, while that of the 1974 event had been much lower. Interestingly, almost half of the 45 earthquakes with lower- and/or upper-bound number of destroyed buildings larger than 1,000 were located in China (see Figure 2.14).

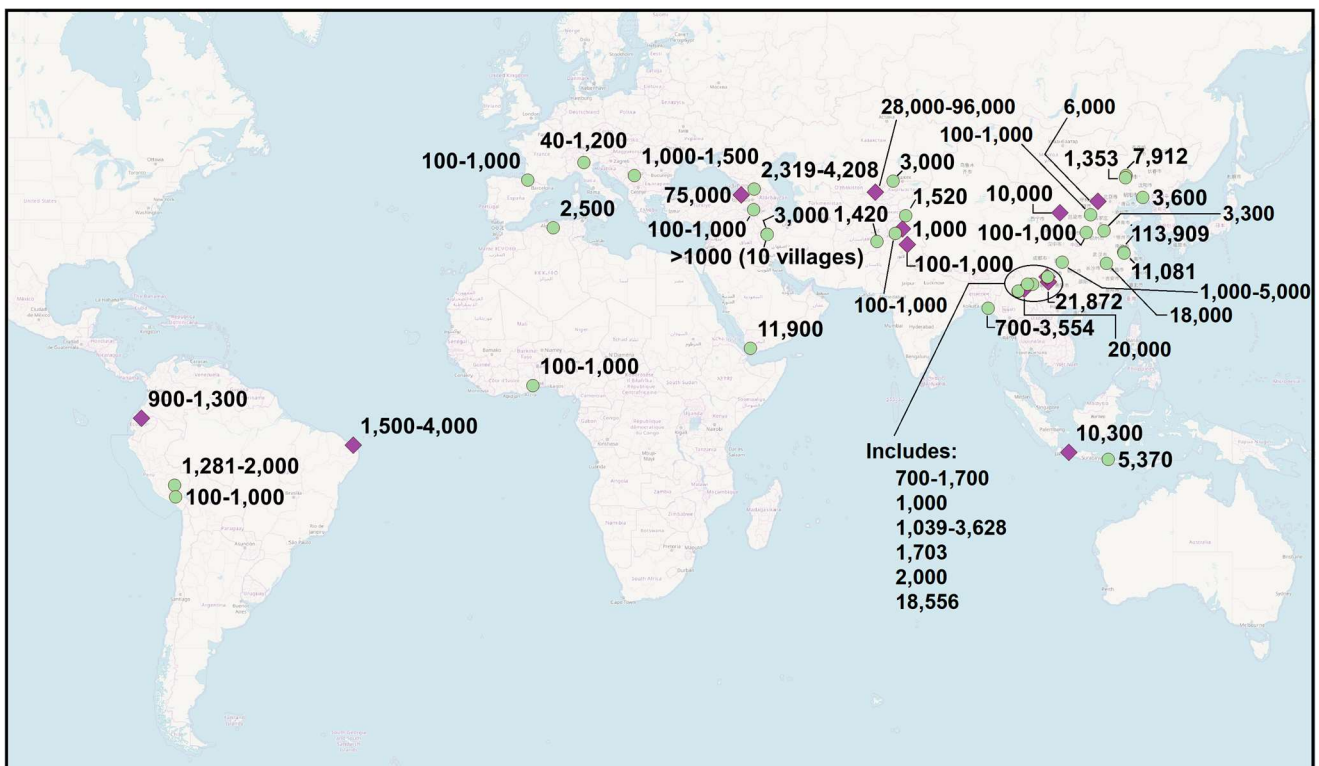


Figure 2.14 Reported numbers of destroyed buildings for the 45 earthquakes for which there are reports indicating at least 1,000 destroyed buildings. Green circles indicate cases in which a number or range of numbers are available, while purple rhombuses indicate the “Some of” cases with their corresponding lower- and upper-bound numbers of damaged buildings.

Apart from the two Liyang earthquakes of 1974 and 1979, the cases of reported destroyed buildings of 10,000 and above are:

- The 1966 **M5.20** Tashkent (Uzbekistan, ex-USSR) earthquake. This is one of the “Some of” cases, with the number of reported damaged buildings ranging from 28,000 to 96,000 (e.g., Earthquake-Report, 2013a; Wright, 1971). Most sources indicate the occurrence of instances of destruction, but Rasskazovsky &

Abdurashidov (1969) explicitly mention that all buildings were heavily damaged but not destroyed.

- The **M5.35** event of 10th August 2004 in Ludian (China). According to NOAA and the USGS, it resulted in 65,601 damaged and 18,556 destroyed buildings. It affected the same area as a quite damaging **M5.6** earthquake that occurred in November 2003.
- The **M5.20** earthquake of 26th November 2005 in Jiujiang/Ruichang (China). The numbers reported for this earthquake in different sources are somewhat contradictory. While the USGS and NOAA report 150,000 houses destroyed and no numbers of damage, a report of ReliefWeb (2005a) of the same day of the earthquake mentions 18,000 collapsed and 15,000 damaged houses, citing the Ministry of Civil Affairs as the source, while a report from two days later (ReliefWeb 2005b) speaks of 18,000 collapsed and 150,000 damaged “rooms” (which has been interpreted herein as dwellings) citing information provided by the United Nations Resident Coordinator’s Office in Beijing. Given that this last number is the same one reported by the USGS and NOAA as destroyed houses, which seems unlikely, 18,000 destroyed and 150,000 damaged were adopted for the database. It is noted that the consequences reported might result from the combined effect of this earthquake and two other ($m_b=4.6$ and $m_b=4.3$) that occurred in the area on the same day.
- The **M5.26** earthquake of 22nd November 1991 in Ibb (Yemen). This is an interesting case of uncertainty associated with potential progressive damage caused by earthquakes in a sequence. A series of reports from ReliefWeb (1991) show how the estimates of damaged and destroyed buildings build up from 17 destroyed and 87 partially-collapsed houses one day after the earthquake (which are the values reported by the USGS and NOAA for this earthquake) all the way through 11,900 houses needing to be reconstructed and 2,600 houses deemed to be repairable, two and a half months later. The report makes reference as well to an abundant number of aftershocks, but their magnitudes do not appear to have been large (smaller than 3.5 on the Richter scale, according to ReliefWeb, though none of them appear in the ISC Bulletin). In view of this and the fact that assessing the exact number of damaged/destroyed buildings after an earthquake takes time, the estimates from one day later were interpreted as preliminary results, and those of two and a half months later as the final numbers to report.
- Five “Some of” cases: 1984 **M5.53** in Turkey (75,000), 1988 **M5.24** in China (10,000), 1990 **M5.55** in Indonesia (10,300), 1998 **M5.08** in China (21,872), and 2004 **M5.02** in China (20,000).

While some of these cases appear to be related to relatively solid reporting of damage, others illustrate the uncertainties that come inevitably associated with these figures. This occurs as well with the numbers of damaged buildings shown in Figure 2.12, in which cases of earthquakes with **M** smaller than 4.5 and more than 100 reported damaged buildings for which the sources are somewhat uncertain are marked. These include:

- Four earthquakes retrieved from the EID (2015 **M4.32** China, 2016 **M4.32** China, 2016 **M4.32** China, 2017 **M4.24** Peru) for which the original sources could not be accessed, possibly due to the websites being no longer available.
- A **M4.37** earthquake in 2017 in Brazil, for which the EID specifies that the number provided is an estimate and not an observation.
- A **M4.44** earthquake that occurred on 11th August 2016 in Chongqing, Chin, retrieved from the EID as well but which the EID and the original source do not match. While the EID reports 873 damaged buildings, the source cited therein vaguely describes damage to around 34+ (Eastday.com, 2016). It may be possible that the number reported by the EID stem from other uncited sources.
- A **M4.32** earthquake that occurred on 23rd November 2015 in North Molukka, Indonesia. The EID reports 437 damaged buildings, but an article in the online news portal Tempo.co (Siswadi, 2019) says “the earthquake also caused 934 houses to be damaged, namely 237 heavily damaged, 193 moderately damaged and 504 slightly damaged”. However, it is difficult to understand if these numbers correspond to this earthquake or many, as the statement appears after referring to the earthquake sequence having started one week earlier. Moreover, the number reported by the EID, 437, nearly matches the sum of 237 and 193, which is suspicious, as it suggests that the 504 slightly damaged houses were not considered by the EID. It is noted, though, that the original source is being interpreted with the aid of Google Translate and, consequently, inaccuracy in translation might have an influence as well, since such automatic translation algorithms do not yet capture all the nuances of the original language.

Some other earthquakes reported to have caused damage to large numbers of buildings have been marked in the plots of Figure 2.12 too. Three of these have already been discussed above, as they are associated as well with large estimates of numbers of destroyed buildings: the 1966 **M5.20** Tashkent earthquake, the **M5.46** earthquake of 9th July 1979 in China, and the **M5.2** earthquake of 26th November 2005 in China. In the case of the **M4.80** Tbilisi, Georgia, earthquake of 25th April 2002, the number of damaged buildings ranges from 11,780 to 50,000. While Gabrichidze *et al.* (2004) presents detailed damage statistics for around 16,000 damaged buildings, reported to be a subset of a stock of around 45,000 buildings, Varazanashvili *et al.* (2008) suggests that around 50,000 buildings were damaged, and that this number represents 40% of the total. It is quite difficult to interpret these contradictory pieces of information, as neither of the two sources specifies the exact extent of the area over which damage was observed or assessed. The two simply mention “Tbilisi”, whose administrative boundaries have changed through the years (e.g., Salukvadze & Golubchikov, 2016).

The case of a **M4.0** earthquake reported to have caused damage to 807-1,300 buildings in Figure 2.12 (label “A”) is the 2007 Folkestone earthquake in the United Kingdom, for which most of the damage consisted of dislodgement/cracking/collapse of chimney clay pots and/or bricks, with instances of damage inflicted to roof tiles and, rarely, roof structures, and

cracking/falling of plaster. Infrequent minor structural damage was only observed within the most damaged area (e.g., vertical cracking of walls and lintels, the fall of free-standing walls, partial collapses of house walls) (Sargeant *et al.*, 2008). This case illustrates the fact that seemingly large numbers of damaged buildings should be interpreted bearing in mind that the simple damaged/destroyed classification cannot reflect the degree of damage observed, which may be quite low. The case labelled “B” in Figure 2.12 corresponds to a $M_L=4.2$ rockburst that occurred at Mentougou coal mine in Beijing on 19th May 1994, for which Li *et al.* (2007) report 5,318 damaged houses, while the case labelled “C” is a **M4.21** earthquake that took place in Sanshui, China, on 26th September 1997, which reportedly resulted in 1,639 damaged and 648 inhabitable houses (South China Morning Post, 1997).

The database contains 26 cases for which zero damaged buildings are specifically reported, none of which contain details on economic losses, and 24 of which were directly retrieved from the EID. Four of the 26 have numbers of destroyed buildings reported. Of the remaining 22, three are reported to have affected infrastructure (one of which caused one injury as well), and the remaining 19 are only associated with injuries in 17 cases and/or deaths in two cases. The two deaths were reportedly caused by a landslide and a heart attack allegedly attributed to the earthquake.

As mentioned earlier, Figures 2.15 and 2.16 gather information on the cases for which only verbal descriptions were available: 948 earthquakes in the case of damaged buildings and 118 earthquakes in the case of destroyed buildings. There are five and one earthquakes with verbal descriptions of damaged and destroyed buildings, respectively, that are not depicted in Figures 2.15 and 2.16 due to their descriptions being too specific. These are four cases in which a percentage of damaged buildings is given and two cases in which the name of a village considered to have suffered damage/destruction to 100% of its buildings is provided.

In Figure 2.15, the topmost nine descriptions (from “Widespread” until “Some”, inclusive) refer only to quantities of buildings, while the rest make reference as well to the kind of damage. It is clearly difficult to draw sound conclusions from verbal descriptions. However, it is noted that, in general terms, the most negative wording (e.g., severe, serious, significant, heavy, extensive, considerable, etc.) appears to be more commonly associated with larger magnitudes than lower magnitudes, as would be expected. Of the 410 earthquakes for which the description regarding damaged buildings is either “Non-structural”, “Limited” or “Some, Minor” (which represent 43% of the total cases depicted in Figure 2.15), 97% correspond to cases retrieved directly from the EID. It is interesting to note that, in general, these three expressions—which correspond to translations from damage levels 1, 1-2 and 2 as per Table 2.4—are associated with the complete range of magnitudes, while “some, severe” and “dozens”—damage levels 2-3 and 3—appear to cover the whole range as well but become more dense for $M>4.5$, and there are only a few instances of “hundreds”—damage levels 3-4 and 4—all with $M>4.7$.



Figure 2.15. Descriptions of damage of damaged buildings as a function of moment magnitude for the whole of the Database of Damaging Small-to-Medium Magnitude Earthquakes for which only verbal descriptions were found (948 earthquakes). Green and lilac indicate events retrieved from the EID and all other sources, respectively.

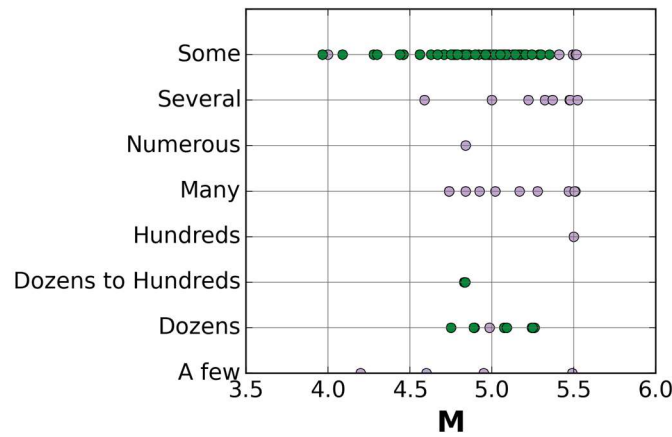


Figure 2.16. Descriptions of damage of destroyed buildings as a function of moment magnitude for the whole of the Database of Damaging Small-to-Medium Magnitude Earthquakes for which only verbal descriptions were found (118 earthquakes). Green and lilac indicate events retrieved from the EID and all other sources, respectively.

2.12.2. Infrastructure affected

The Database of Damaging Small-to-Medium Magnitude Earthquakes contains 177 earthquakes reported to have affected infrastructure, though it is noted that many sources used for its compilation do not often report damage to infrastructure explicitly. It is therefore possible that the number of earthquakes that have affected infrastructure may be larger.

Figure 2.17 shows the magnitude distribution of these 177 earthquakes. As can be observed, around 75% of the cases correspond to events with magnitudes equal to or larger than 5.0.

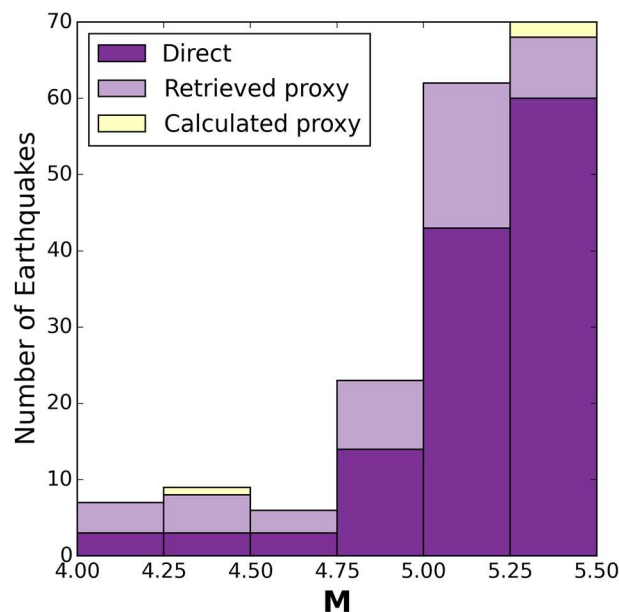


Figure 2.17. Distribution of magnitudes of the 177 earthquakes from the Database of Damaging Small-to-Medium Magnitude Earthquakes reported to have affected infrastructure. Direct, Retrieved proxy, Calculated proxy as per description of Figure 2.8.

2.12.3. Landslides and liquefaction

Figure 2.18 depicts the magnitude distribution of the 158 earthquakes in the database reported to have caused landslides, rockslides, mudslides and/or snow avalanches. As in the case of infrastructure, over 75% of these events had magnitudes equal to or larger than 5.0, which is consistent with the global database of earthquake-induced landslides compiled by Rodriguez *et al.* (1999). A range of 577-871 deaths are associated with these 158 earthquakes, of which 339-393 deaths (45-59%) are attributed to the landslides themselves while the rest reportedly had other causes. However, only around 21% of the 158 earthquakes are associated with landslide-caused deaths.

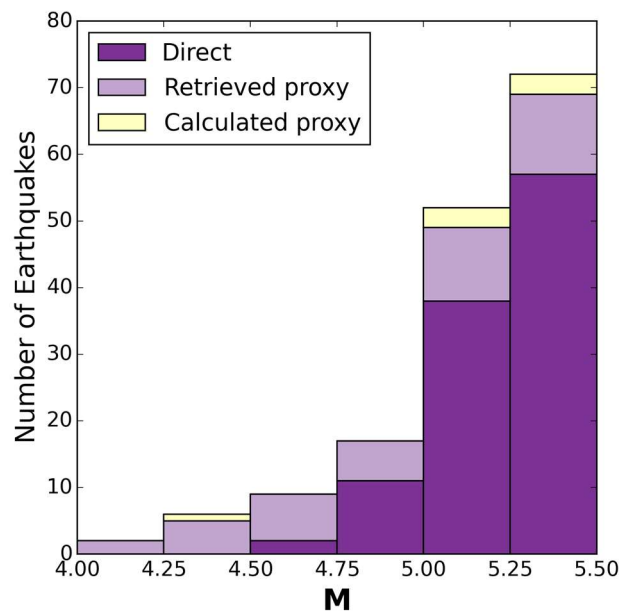


Figure 2.18. Distribution of magnitudes of the 158 earthquakes from the Database of Damaging Small-to-Medium Magnitude Earthquakes reported to have caused landslides, rockslides, mudslides and/or snow avalanches. Direct, Retrieved proxy, Calculated proxy as per description of Figure 2.8.

The occurrence of liquefaction has been reported for only ten earthquakes in the database. This is consistent with the findings of Green & Bommer (2019) regarding the smallest earthquakes that cause liquefaction. These ten earthquakes are:

- 1903 Warrnambool (Australia, M_L 5.30),
- 1989 Newcastle (Australia, M 5.40),
- 1992 Milos (Greece, M 5.19),
- 1992 Roermond (the Netherlands, M 5.38),
- 1993 Pyrgos (Greece, M 5.44),
- 1996 Épagny-Annecy (France, M 4.80),
- 2002 Au Sable Forks (United States, M 5.16),
- 2004 Garda Lake (Italy, M 5.07),
- 2009 Olancho (United States, M 5.26), and
- 2010 Vitanovac/Kraljevo (Serbia, M 5.52).

As shown in Figure 2.19, all but one of these had magnitudes equal to or larger than 5.0. The one case with magnitude smaller than 5.0, the 1996 Épagny-Annecy earthquake, appears to have caused only small-scale liquefaction at one of the ends of the airport's runway, in spite of the whole affected area being susceptible to liquefaction effects (Dominique *et al.*, 2008). It should be noted as well that there is lack of agreement regarding the moment magnitude of this earthquake, with Dufumier (2002) estimating **M**4.80 and the European-Mediterranean Seismological Centre (EMSC) and Bock (1997) reporting **M**5.30. However, Dufumier (2002) state that the latter results from fixing the hypocentral depth to an unrealistically shallow value, and results in the focal mechanism to be incompatible with the local tectonics.

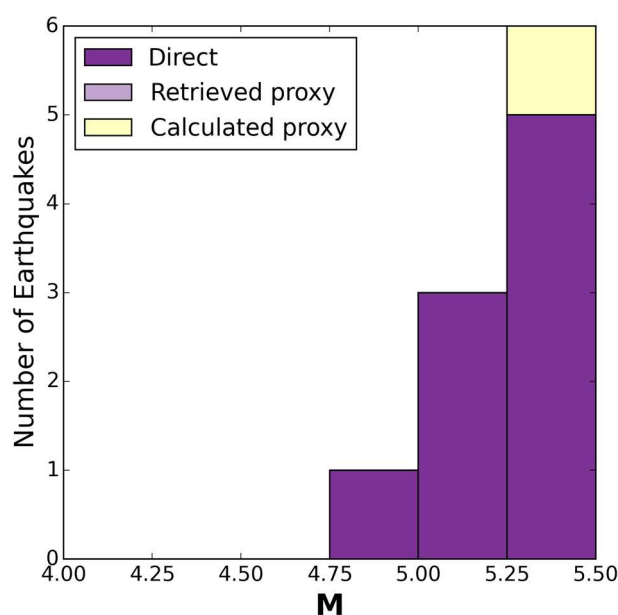


Figure 2.19. Distribution of magnitudes of the 10 earthquakes from the Database of Damaging Small-to-Medium Magnitude Earthquakes reported to have caused liquefaction. Direct, Retrieved proxy, Calculated proxy as per description of Figure 2.8.

2.12.4. Casualties

Table 2.10 summarises the number of total deaths and injuries contained in the Database of Damaging Small-to-Medium Magnitude Earthquakes. Lower and upper bounds emerge from the existence of ranges of values, either because different values were found in different sources or because they stem from an estimate made by NOAA. The total numbers were obtained by considering all lower and all upper bounds simultaneously, which clearly represents to unlikely extreme scenarios. In the case of injuries, descriptive words such as “a few”, “some”, etc., were assigned ranges according to the criteria used in the NOAA database (Table A1.1 of Appendix I). “Slight” and “minor” were considered synonymous with “few”, and “several” was considered synonymous with “some”. Deaths attributed to heart attacks were withdrawn from the results presented hereafter for the reasons discussed in Section 2.6.

As can be observed from Table 2.10, the whole database comprises a total of 2,307-3,125 deaths (excluding 87-88 heart attacks) and 33,718-46,940 injuries. As discussed earlier, uncertainty is present in reported deaths and injuries of many earthquakes, usually more in the latter than in the former. However, there is a particularly peculiar case worth of notice: the 1966 **M**5.2 Tashkent (Uzbekistan) earthquake. Due to the secrecy with which the Soviet Union treated information of this kind, the exact number of casualties due to this earthquake was never known. While the official death toll was only of 8-15, some estimates go up to figures as large as 5,500-7,500 (Gurenko & Dumitru, 2009; Hutchings, 1987; Sims, 2007). However, as it appears that these numbers may include at least hundreds of people who died from traumatic stress and heart attacks during the aftershock sequence (Geo-Storm, 2013; Fergana News, 2006; RIA Novosti, 2016), only the 8-15 deaths were considered in Table 2.10 and all the plots and statistics that follow hereafter.

Table 2.10. Summary of casualties observed for the whole database, excluding heart attacks attributed to earthquakes.

Casualties	Without EID		From EID		All	
	Lower	Upper	Lower	Upper	Lower	Upper
Total Deaths	2,269	3,087	38	38	2,307	3,125
Injuries	32,210	44,429	1,508	2,511	33,718	46,940

Figures 2.20 and 2.21 show the frequency with which an individual earthquake was associated with a specific number of injuries and total deaths, respectively, and reveal that zero deaths and/or zero injuries (per earthquake) are by far the most frequent outcome. This outcome is in agreement with Table 2.11, which classifies earthquakes into four mutually-exclusive groups: earthquakes causing (1) no casualties, (2) no deaths but some injuries, (3) some deaths but no non-lethal injuries, and (4) both deaths and injuries. As can be observed, around 59% of the total number of earthquakes that make up the whole of the database are not reported to have caused human casualties at all. The proportion is larger for earthquakes taken directly from the EID (78%) than for those taken from elsewhere (43%), which may be expected, given that earthquakes that have caused no casualties and only minor damage are less likely to appear in sources other than the EID. In this sense, it is noticeable that the proportion of earthquakes from the EID that have caused deaths is very small, 2.6%, against 14% of the total, or 23% of the non-EID events. Table 2.11 shows as well that the proportion of earthquakes that have caused no deaths but some injuries (27% of the total, 33% of the non-EID events) is larger than the proportion of earthquakes causing deaths (14% of the total, 23% of the non-EID events).

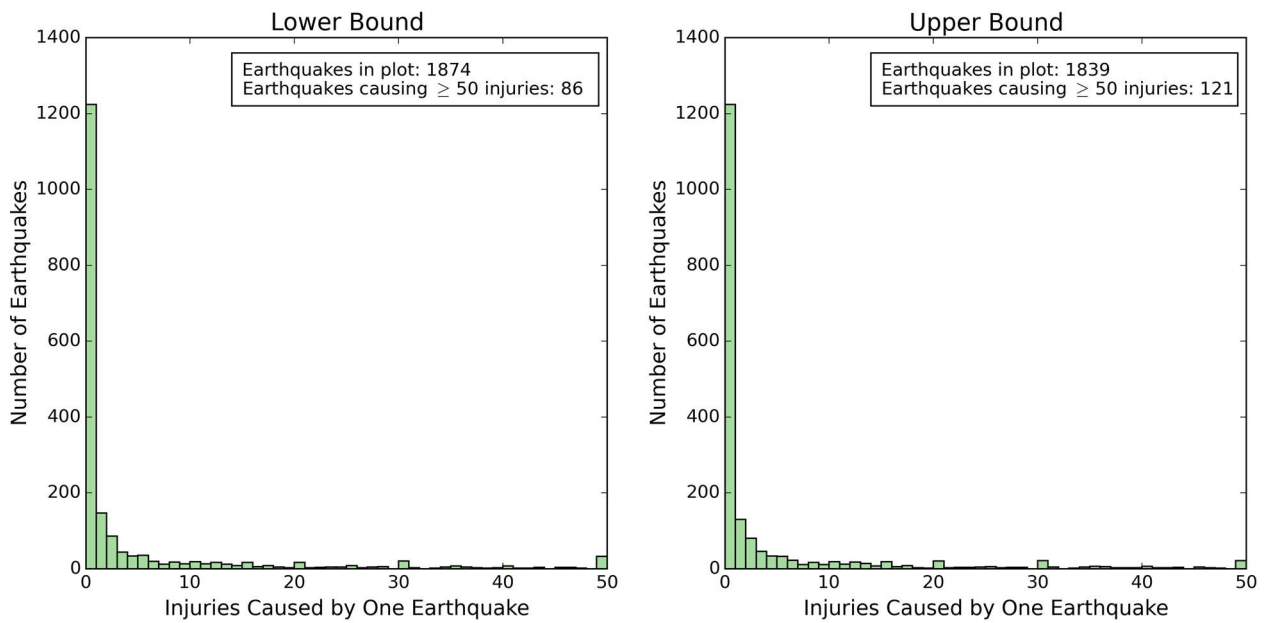


Figure 2.20. Number of earthquakes in the Database of Damaging Small-to-Medium Magnitude Earthquakes causing a particular number of injuries, lower (left) and upper (right) bound. The horizontal axis has been truncated at 50 but values go up to 8,000, albeit with very low frequencies. Number of earthquakes not shown due to this truncation: 86 (left) and 121 (right).

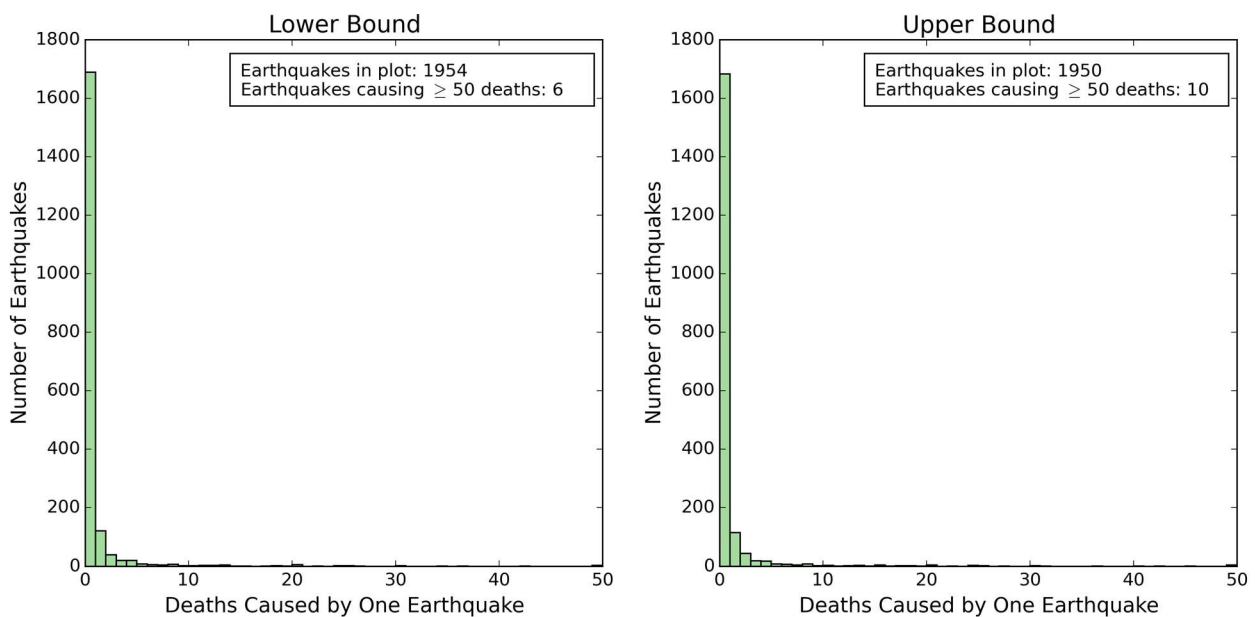


Figure 2.21. Number of earthquakes in the Database of Damaging Small-to-Medium Magnitude Earthquakes causing a particular number of total deaths, lower (left) and upper (right) bound. The horizontal axis has been truncated at 50 but values go up to 500, albeit with very low frequencies. Number of earthquakes not shown due to this truncation: 6 (left) and 10 (right).

Table 2.11. Classification of earthquakes according to the existence or not of associated casualties(*).

Casualties	Number of Earthquakes						Percentage (%) of Earthquakes					
	Without EID		From EID		All		Without EID		From EID		All	
	Low	Up	Low	Up	Low	Up	Low	Up	Low	Up	Low	Up
No deaths & no injuries	475	475	676	676	1,151	1,151	43.5	43.5	77.9	77.9	58.7	58.7
No deaths & some injuries	369	362	170	170	539	532	33.8	33.2	19.6	19.6	27.5	27.1
Some deaths & no injuries	62	62	11	11	73	73	5.7	5.7	1.3	1.3	3.7	3.7
Some deaths & some injuries	186	193	11	11	197	204	17.0	17.7	1.3	1.3	10.1	10.4

(*) The existence of cases in which the number of earthquakes is larger for the case in which lower bound values of deaths and injuries are used than for the case in which upper bound values are used instead is not an error. It stems from the simple fact of having ranges of values and different conditions applying to each of them. For example, the table reports 539 and 532 earthquakes that caused some injuries but no deaths. The difference is due to seven earthquakes for which the number of total deaths is reported as a range from zero to up to three, all of which have non-zero lower and upper bound injuries. When upper bounds are considered, these seven earthquakes do not fall under this category and are removed, but are included when lower bounds are used instead.

Analogous to Figures 2.12 and 2.13, the plots in Figures 2.22 and 2.23 depict the number of injured and dead against magnitude for the whole of the database. As can be observed, very few earthquakes with magnitudes smaller than 4.5 are reported to have caused over 50 injuries, and most cases of earthquakes with $M < 4.5$ lie significantly below this value. The same magnitude appears to mark a jump between earthquakes causing less or more than 10 total deaths. The increase in the number of casualties with magnitude is clear in both figures. As for the case of damaged/destroyed buildings, the plots concerning earthquakes retrieved from the EID should be interpreted considering their magnitude distribution and the fact that earthquakes with larger consequences tend to be reported in other sources besides the EID. Figure 2.24 shows the magnitude distribution of the earthquakes reportedly associated with injuries (top) and deaths (bottom). As can be observed, the number of earthquakes associated with either of the two increases with magnitude.

In view of this, it is of interest to go back to an observation made in Section 2.3 regarding cases of moment magnitudes equal to or larger than 5.5 but reported as a truncated 5.5 by the GCMT, as these would fall in the right-most bins of the plots in Figure 2.24. A set of 30 earthquakes that fall into this category was identified, with values of M derived from the GCMT seismic moment in the range 5.55-5.59. If included, this set would add 41-47 deaths and 837-1,763 injuries to the database. Except for one heart attack, almost all of these deaths are attributed or likely due to structural failures. This example illustrates the potential impact of the uncertainty in magnitude discussed in Section 2.3, particularly around the upper bound of the magnitude range.

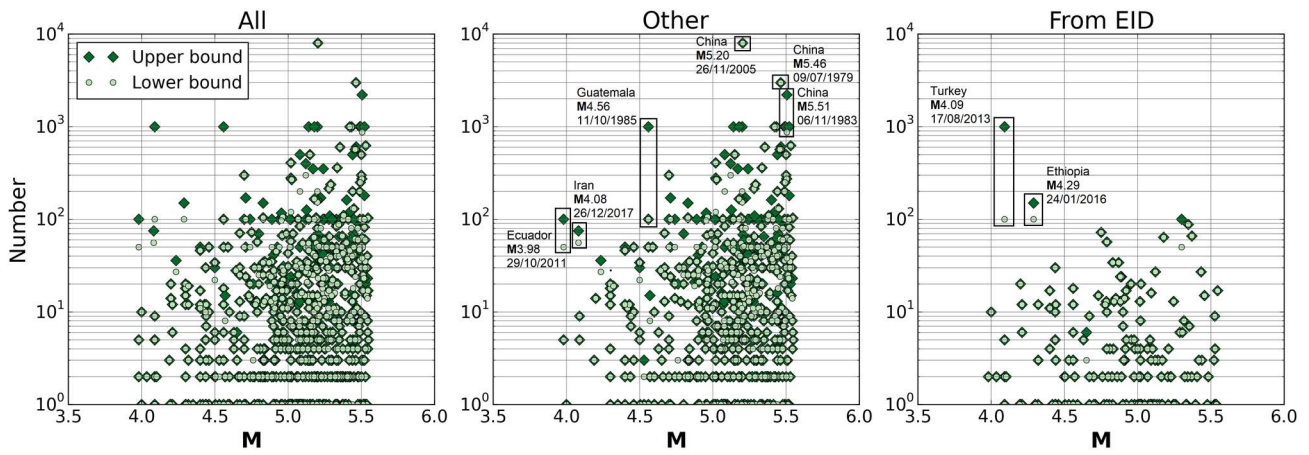


Figure 2.22. Number of injuries as a function of moment magnitude for the whole of the Database of Damaging Small-to-Medium Magnitude Earthquakes (left), for the events taken from EID (right) and elsewhere (centre). Zero values not shown (1,224 earthquakes with zero reported injuries).

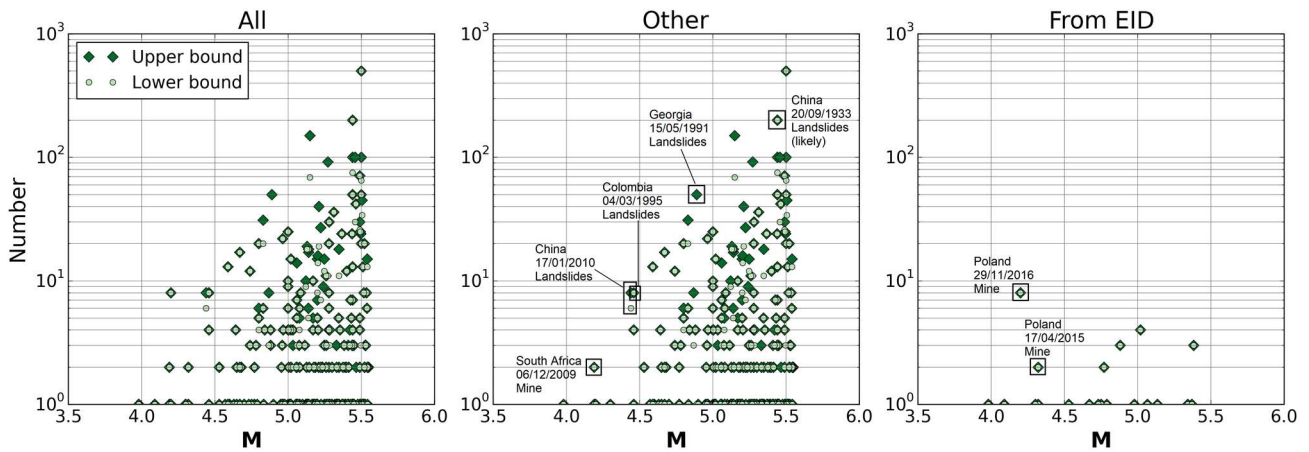


Figure 2.23. Number of total deaths as a function of moment magnitude for the whole of the Database of Damaging Small-to-Medium Magnitude Earthquakes (left), for the events taken from EID (right) and elsewhere (centre). Zero values not shown (1,683-1,690 earthquakes with zero reported deaths).

Some earthquakes reported to have caused relatively large numbers of injuries despite their small magnitude are marked in the plots of Figure 2.22. These include:

- A **M3.98** (proxy, $M_L=m_b=4.0$) earthquake in Ecuador, which is reported to have caused an unspecified number of minor injuries due to broken glass (El Telégrafo, 2011). This was translated into 50-100 injuries.
- A **M4.08** (proxy, $m_b=4.0$) seismic event in Iran, reportedly associated with 56 to 75 injuries due to escaping in panic (22 reported hospitalised) and one heart-attack death (Breaking The News, 2017; Iran Front Page, 2017; News.am, 2017),
- A **M4.09** (proxy, $m_b=3.8-4.1$) earthquake in Turkey, which is reported to have resulted in “many” injuries associated with people fleeing their homes or jumping off balconies or out of windows. According to Earthquake-Report (2013b), the fact that it occurred

on the 14th anniversary of the Izmit earthquake is likely to have had an influence on the reaction of the population. This “many” injuries were translated into 100-1,000.

- A **M4.29** (± 0.30 , Wilks *et al.*, 2017) earthquake that occurred in Ethiopia, for which the EID reports 150 injuries but sources cited therein point only at 100, reportedly due to a stampede at a university campus (Earthquake-Report, 2016).
- A **M4.56** (proxy, $m_b=4.5$) earthquake in Guatemala, to which NOAA attributes an estimate of 100-1,000 injuries.

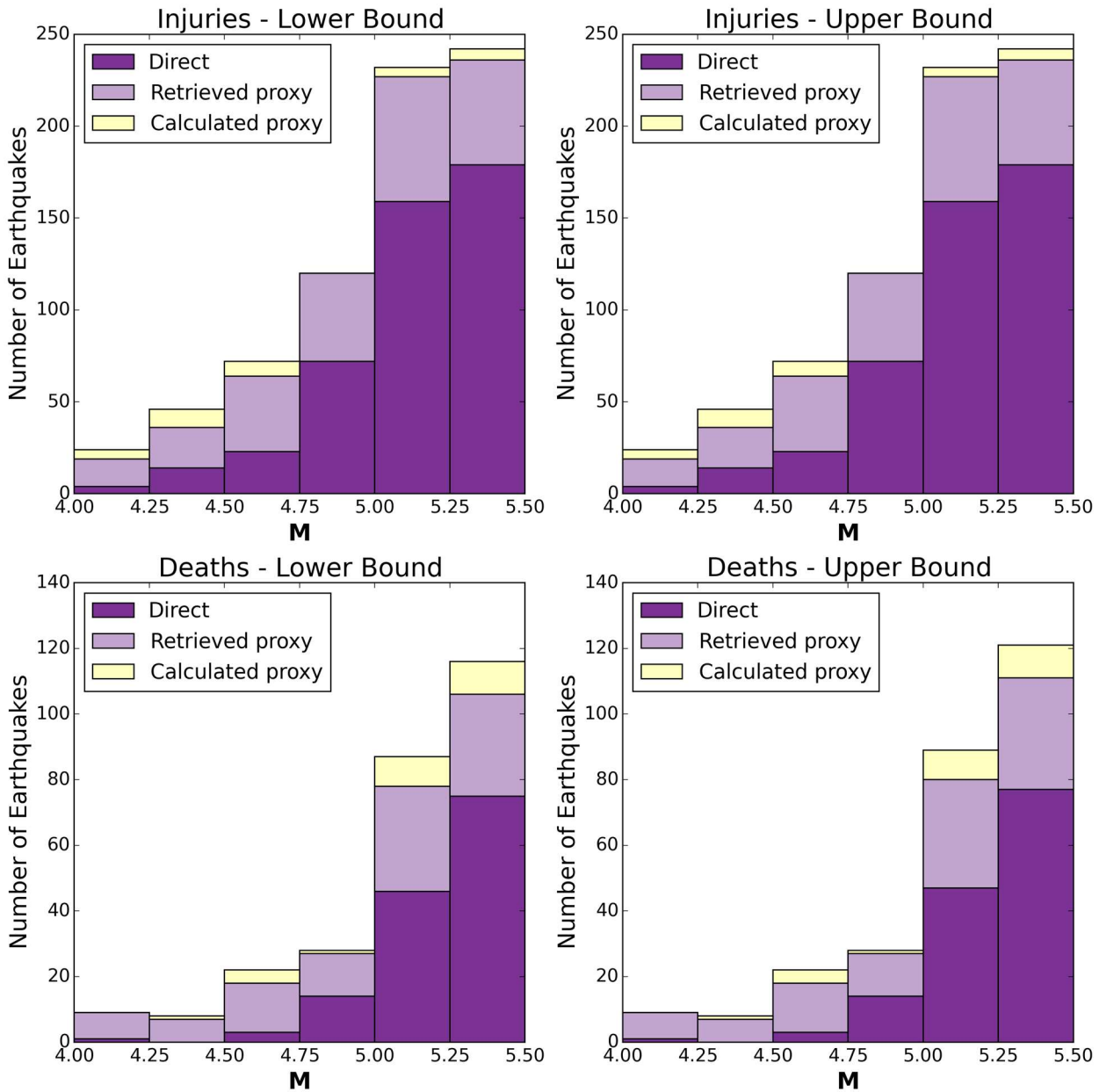


Figure 2.24. Magnitude distribution of the earthquakes with associated injuries (top) and total deaths excluding heart attacks (bottom), considering lower- (left) and upper-bound (right) figures. Direct, Retrieved proxy, Calculated proxy as per description of Figure 2.8.

As can be observed, the numbers plotted in Figure 2.22 correspond to the assignation of an estimated range in three out of these five cases. Based on the descriptions for the first and third cases (Ecuador and Turkey), it seems likely that the numbers may have been significantly smaller. The only case of the five in which the injuries are likely to have been related to damage to structures is that of the earthquake in Guatemala.

Something similar occurs with the total number of deaths depicted in the plots of Figure 2.23, in which outlying cases of higher fatalities due to causes other than structural failures are marked. As can be observed, they correspond to either landslides or the consequences of damage to mines. There are ten cases of earthquakes with magnitudes equal to or smaller than 4.4 with one reported death. Of these, five are either attributed or likely due to structural failures, one is a death due to falling from a bridge, another one is due to running out of the house, and two others are due to snow- or landslides, while the cause of the tenth event is unknown.

The database contains three cases of upper-bound deaths equal to or larger than 200. One of them is a **M**5.5 earthquake that occurred in Iran in 1925, with 500 reported deaths. According to PAGER-CAT (Allen *et al.*, 2009a), these were shaking deaths. As its moment magnitude value has been converted from $M_{\text{unk}}=5.50$, which was retrieved from the NOAA database, it is possible that its actual moment magnitude may have been larger. Another one is a **M**5.44 (proxy, $M_s=5.00$) earthquake that occurred in Peru in 1943, with 75-200 reported deaths due to unknown causes. The third one is a **M**5.44 (proxy, $M_s=5.00$) earthquake that occurred in China in 1933, with 200 reported deaths, most of which were possibly due to landslides. It is noticeable how the three are relatively old events. This tendency for larger numbers of reported deaths to seem to be associated with older events can be observed in Figure 2.25.

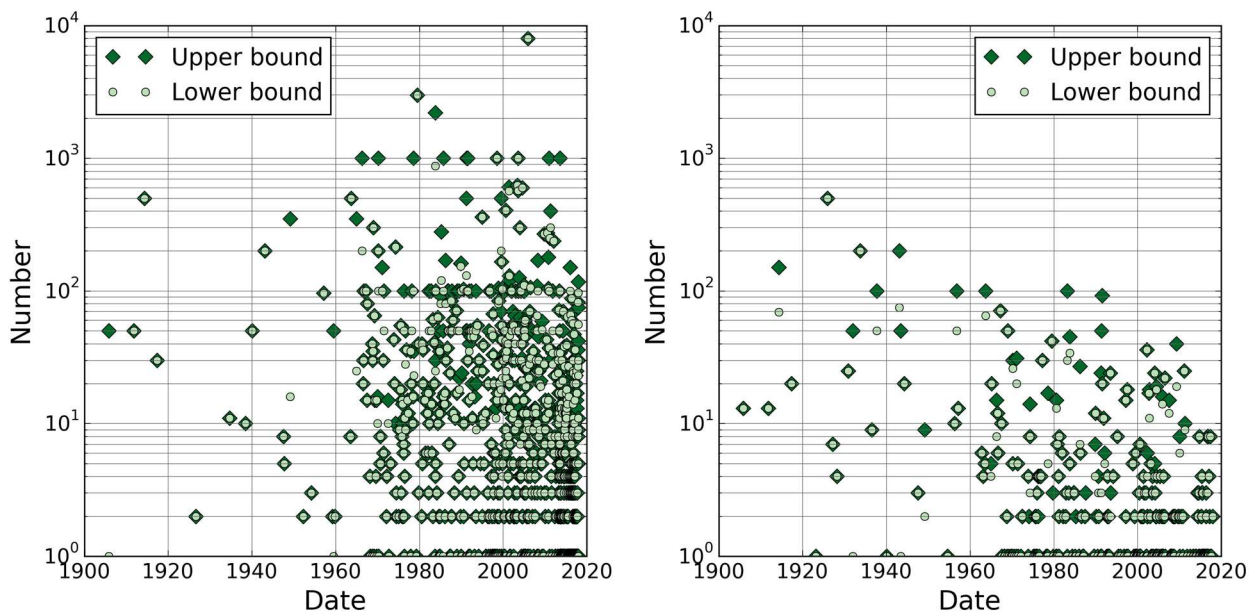


Figure 2.25 Number of injuries (left) and total deaths (right) as a function of date for the whole of the Database of Damaging Small-to-Medium Magnitude Earthquakes. Zero values not shown.

Though more unlikely, it is still possible to identify earthquakes with magnitudes smaller than 4.0 associated with deaths, even if they are not part of the present database. A quite outstanding case is that of the 2017 **M**3.9 Ischia (Italy) earthquake, which caused extensive damage, 39-42 injured, and the death of two people. Other earthquakes include the 2001 **M**3.2 Lorraine (France), the 2005 $M_L=3.7$ and 2014 $M_L=2.3$ South Africa, 2014 $M_L=3.1$ Czech Republic and 2016 $M_L=2.6$ Silesia (Poland) ones, reportedly associated with 1, 5, 9, 3 and 1 deaths, respectively. While all of the latter occurred in mines rather than buildings, those of Ischia were attributed to structural failures. However, the disproportionately large consequences of the Ischia earthquake appear to have resulted not only to unusually large ground motions and site effects but also to the extreme vulnerability of the building stock (see Appendix A4.13).

The causes of death were gathered and classified under ten categories:

- Landslides: movements of masses of soil, rocks and/or snow.
- Structural failures: the behaviour of structural and non-structural components (e.g., ceilings) when subject to ground shaking.
- Mines: treated separately from structural failures due to them involving a very specific kind of structure.
- Falling objects/debris: falling plaster or bricks (fall of small fragments, as opposed to the collapse of a brick structure), as well as other elements falling from shelves.
- Escaping: jumping off balconies and out of windows, running out of buildings, “panic reactions”.
- Tsunami: named as a cause in only one case, that of a **M**5.49 earthquake that occurred in Indonesia in 1967.
- Other: other rather unusual known causes. Examples: four intoxications due to the collapse of chimneys due to the 1983 Liège earthquake, one construction worker who died electrocuted when the scaffolding swayed and hit an electric post during an earthquake in the Philippines in 1999, one death due to falling off a bridge during the shaking generated by an earthquake in India in 2011, etc.
- Probably structural failures: cases in which the extent of damage reported suggests that the most likely cause of death was damage to buildings, but no specific statements have been found.
- PAGER shaking: cases categorised as shaking deaths by PAGER-CAT (Allen *et al.*, 2009a).
- Unknown: no causes were found and details on the extent of damaged deemed as insufficient to be classified as “probably structural failures”.

Whenever it occurred that deaths were categorised as shaking deaths by PAGER-CAT (Allen *et al.*, 2009a) and it was also possible to make a similar inference from the reported extent of damage, the deaths were assigned to the “probably structural failures” category.

Figure 2.26 shows the proportions of deaths attributed to each cause, while Figure 2.27 shows the proportions of instances of deaths instead (in both cases excluding heart attacks). Instances are defined herein as a mention of a cause. Deaths attributed to a particular

earthquake may be all due to one cause, which translates into one instance, or X different causes, which translates into X instances. For example, if a single earthquake is reportedly associated with ten deaths, six due to structural failures and two due to landslides, then there are two instances associated with this earthquake. An alternative approach could have been that of introducing a category labelled “more than one cause (per earthquake)”. However, such a category would obscure the specific causes involved and it was thus preferred to present results in terms of instances. It is noted that there are only 17 (lower bound) – 23 (upper bound) earthquakes with more than one cause listed (23-30 if heart attacks were considered), which implies that the difference between the total number of instances and total number of earthquakes is 17-23.

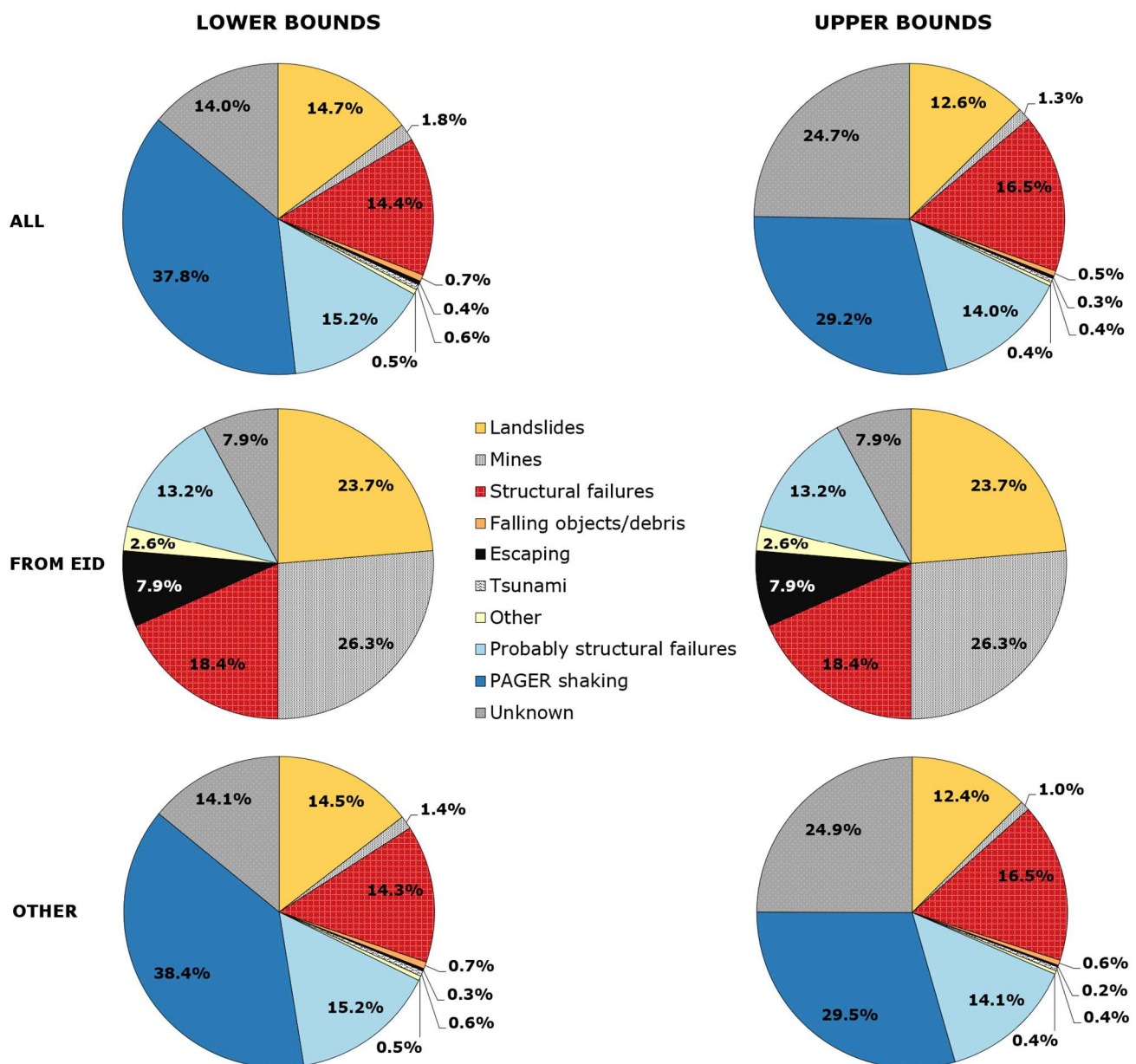


Figure 2.26 Causes of death for all total deaths excluding deaths attributed to heart attacks reported in the Database of Damaging Small-to-Medium Magnitude Earthquakes (top) and for earthquakes retrieved from the EID (centre) and all other sources (bottom), in terms of proportions of the number of deaths. Lower- and upper-bound values shown on the left and right, respectively. Total number of deaths (for the whole database): 2,307, lower bounds; 3,125, upper bounds.

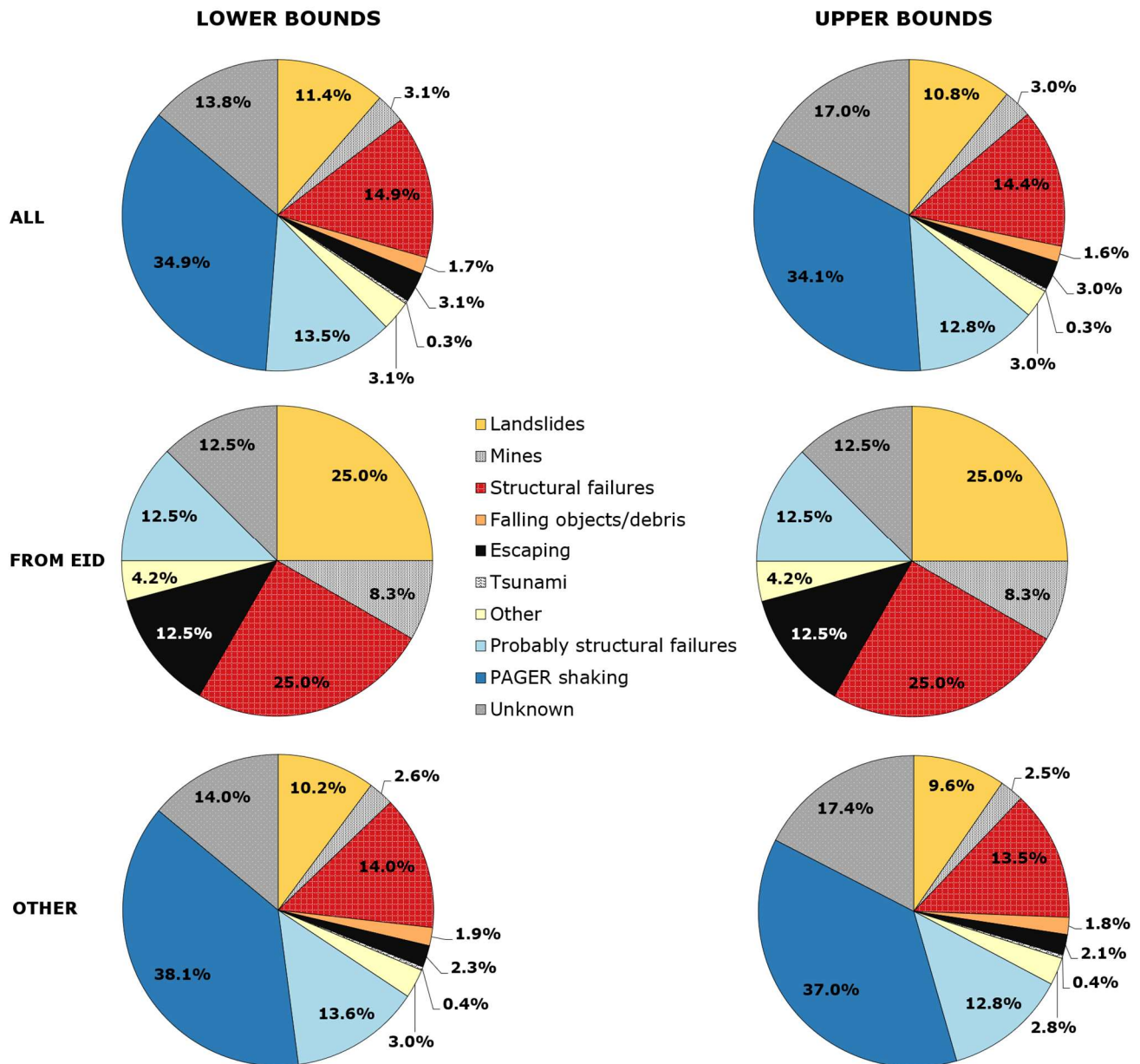


Figure 2.27 Causes of death for all total deaths excluding deaths attributed to heart attacks reported in the Database of Damaging Small-to-Medium Magnitude Earthquakes (top) and for earthquakes retrieved from the EID (centre) and all other sources (bottom), in terms of proportions of the number of instances. Lower- and upper-bound values shown on the left and right, respectively. Total number of instances (for the whole database): 289, lower bounds; 305, upper bounds.

As can be observed from the plots on the top of Figure 2.26, structural failures account for 14.4 to 16.5% of the total number of deaths, with an additional 14.0-15.2% probably due to the same reason, and 29.2-37.8% identified as shaking deaths by PAGER-CAT (Allen *et al.*, 2009). If the deaths classified as “probably structural failures” and “PAGER shaking” were, indeed, due to structural failures, the latter would account for 59.7-67.4% of the total number of deaths. Proportions change slightly when considering number of instances of causes of death instead of number of deaths, as in Figure 2.27. The participation of causes such as falling objects/debris, escaping and others acquire somewhat greater prominence. This suggests that these causes tend to be associated with fewer deaths per instance than landslides or damage to mines, which is expected.

Given that most deaths are associated with earthquakes not retrieved from the EID (see Table 2.10), the proportions stay relatively stable when only the latter are considered, both in terms of number of deaths (Figure 2.26) and number of instances (Figure 2.27). They do change significantly for those earthquakes retrieved from the EID, though, with only a total 31.6% of the deaths (37.5% of the instances) attributed to structural failures or likely structural failures. It is noted, however, that the earthquakes retrieved from the EID represent only 38 deaths and 24 instances, quite low numbers to be statistically sound.

3. STRUCTURE OF CASE HISTORIES

In Appendices III and IV of this report, numerous case histories of damaging earthquakes are described in some detail. In this Chapter, the information presented for each earthquake case history is briefly described together with an explanation of why the information is relevant to the objectives of this study.

3.1. Tectonic and seismic setting

This section introduces the geographical setting of the earthquake in terms of the tectonics of the region and the characteristics of the natural seismicity, if any, of the area affected by the earthquake.

3.1.1. Tectonic setting

The tectonic setting of the earthquake is noted in simple terms such as whether the event occurred in an active or stable region, and providing a brief description of the tectonic structures present in the area of the earthquake. The location and characteristics of any well-known faults are noted. The local stress field, if known at all from focal mechanisms or other sources, is reported; this is of particular relevance for those cases reported as being induced or triggered by anthropogenic activities.

3.1.2. Regional and local seismicity

The previous seismicity in the immediate vicinity of the earthquake, as well as in the broader region, is summarised. Here again the information is to provide context for the reported event, since in an active or elevated seismicity it is less likely that a moderate magnitude earthquake would attract much attention or be reported. Moreover, in a seismically active area, building practices are likely to take some account of seismic loading thus reducing the likelihood of damage from smaller earthquakes. On the contrary, events—particularly induced earthquakes—that occur in seismically quiet areas are more likely to affect vulnerable building stock and to be considered worthy of reporting.

3.1.3. Seismic hazard

A summary of existing seismic hazard assessments for the area, region or country where the earthquake occurred fulfils a similar role of providing context. Seismic hazard studies and seismic zonation maps are published for most parts of the world now, and wherever such information can be retrieved it should be reported. In addition to stand-alone seismic hazard maps, another source of relevant information are national building codes where these include specifications for seismic design loads.

For ease of comparison, however, it is valuable to also include the hazard estimates provided in regional maps such as that produced for Europe in the SHARE project (Woessner *et al.*, 2015), and global studies such as GSHAP (Giardini *et al.*, 1999). While

this provides global coverage, some caution should be applied since the map was compiled from various national and regional studies of varying quality. Moreover, some areas were not covered by these studies, such as the United Arab Emirates, and in order to fill these gaps some interpolations and extrapolations were made that may have resulted in very unreliable hazard estimates (e.g., Aldama-Bustos *et al.*, 2009).

3.2. Earthquake source characteristics

This section presents the basic features that characterise the earthquake and which are essential for its interpretation.

3.2.1. Location, depth and time

The location of the earthquake is defined by the geographical coordinates of the epicentre and the focal depth reported in kilometres below the Earth's surface. Estimates of these parameters are generally be available from multiple sources, including national, regional and global seismological agencies. The latter category includes the USGS and the ISC, the latter providing source characteristics about two years after the occurrence of each event but using more data and generally providing more reliable estimates. Additionally, there may be estimates provided in special studies of the individual earthquake. All of the relevant estimates are reported, together with their source, in the form of a table as well as a map together with the affected locations.

The parameter that is generally most difficult to constrain is the focal depth, for which it is necessary to have recordings from nearby seismographs. For this reason, a local network may often provide the most reliable estimate of the focal depth even if the other source parameters are more reliably determined by regional or global agencies. It is common to find focal depths reported as 5, 10 or 33 km—without associated errors—which reflects the practice of constraining the depth to one of these values in order to obtain convergence in the location calculations. These values are not reliable indicators of the depth at which the earthquake occurred. For larger earthquakes in which the fault ruptures through the full depth of the seismogenic crust, the significance of the focal depth is relatively minor, but for small-magnitude earthquakes where the rupture dimensions are small in comparison to the seismogenic thickness, the depth can be a controlling factor in the nature of the surface motions.

The origin time of the earthquake is presented in both UTC and local time, the former (which is equivalent to GMT) being the global standard for reporting earthquakes. Local time is also important, however, for interpreting the impact of the event, especially since the number of casualties will be related to where the population is located, and may be more numerous at night for example, particularly in those cases where damage was experienced mainly by dwellings. This is discussed further in Section 3.6.3.

3.2.2. Magnitude

The basic measure of the strength of an earthquake, in terms of the total seismic energy radiated from the source, is the magnitude or the seismic moment. Magnitudes may be reported by several agencies and also on multiple scales, including local (or Richter) magnitude, M_L , and its variants based on the length of the signals, coda magnitude, M_C , and duration magnitude, M_D . These measures are commonly available for small earthquakes that are only recorded by local or regional seismograph networks. In some cases, regional and global agencies also report magnitudes on teleseismic scales such as body-wave magnitude, m_b , and surface-wave magnitude, M_s . The best indication of earthquake size is generally considered to be seismic moment, M_0 , which may be converted to moment magnitude, which is represented by the symbol **M** or M_w (the former being strictly more correct for smaller earthquakes). All of the magnitude values reported for the earthquake in terms of **M**, m_b , M_s and M_L by relevant sources are reported, again in tabular form.

No attempt has been made to homogenise the magnitudes of the different case histories. The moment magnitude value used to characterise the earthquake (for example, in the title of each report) has been selected based on the relevance of the different sources for each particular earthquake and discussions found in the literature regarding their precision and credibility.

3.2.3. Style-of-faulting

Should centroid moment tensor (CMT) of fault plane solutions be available for the earthquake, these are clearly reported. Although it is now common practice to include style-of-faulting in predictive equations for tectonic earthquakes (e.g., Bommer *et al.*, 2003), the significance of style-of-faulting on the resulting motions from small-magnitude earthquakes has not been clearly established. However, knowledge of the style-of-faulting—and if known, the strike, dip and rake of the fault rupture—is useful for placing the earthquake in the context of the tectonic environment and the inferred causes of the event.

3.2.4. Stress drop

Inversions of the Fourier amplitude spectra of earthquake recordings can be used to estimate the source, path and site parameters that characterise the attenuation source spectrum defined according to a model such as that of Brune (1970). These parameters include the stress parameter, $\Delta\sigma$, often—and not entirely correctly (Atkinson & Beresnev, 1997)—referred to as the stress drop. The value of the stress parameter is an indicator of the strength of the high-frequency radiation from the source (Figure 3.1). Since the parameters estimated from such inversions are invariably subjected to various trade-offs (e.g., Edwards *et al.*, 2008), the extraction—and even more so, comparison between one inversion study and another—of individual parameter values requires some caution. However, whenever the stress drop has been estimated, it is reported given its implications for the strength of the resulting ground motions. This is particularly relevant for induced seismicity, since a number of studies have suggested that shallow earthquakes—both

induced and tectonic—tend to be associated with lower than average stress drops (e.g., Allen, 2012; Hough, 2014).

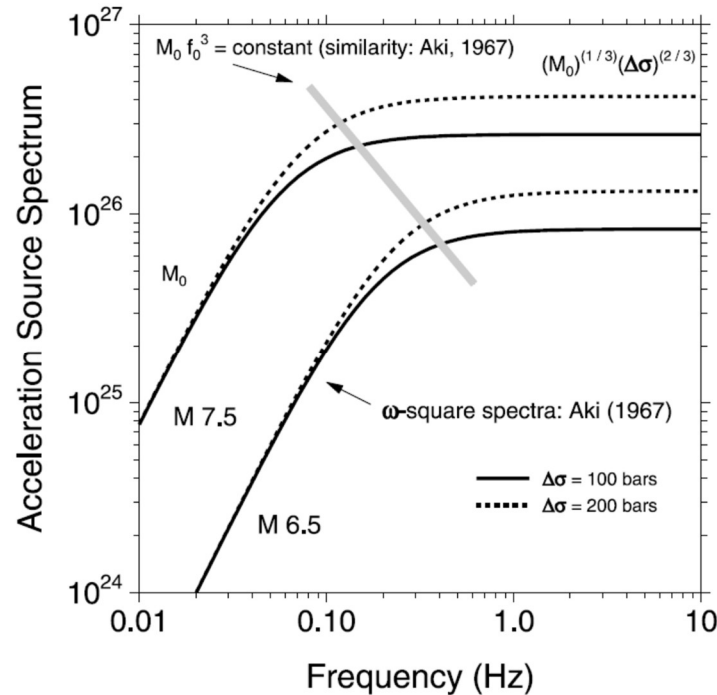


Figure 3.1. Fourier amplitude spectra of acceleration for earthquakes of **M** 6.5 and 7.5 and two values of stress drop (Boore, 2003)

3.2.5. Foreshocks and aftershocks

The document notes any felt foreshocks and aftershocks. When possible, the locations are shown on a map. The primary reason for identifying felt foreshocks is that such events can prompt evacuation of buildings that results in fewer casualties when the main event strikes. The interest in aftershocks stems from both the possibility that these may compound any damage from the main shock and the fact that any prolongation of the disturbance is more likely to make it worthy of attention and reporting. Both foreshocks and aftershocks are useful to constrain the source location of the main shock, and to delineate the causative fault.

3.2.6. Nature of earthquake

In this section, we simply note whether the event was natural (*i.e.*, of tectonic, or possibly volcanic, origin) or whether it was reported to have been induced or triggered. The report does not attempt to make the discrimination between events of natural and anthropogenic origin—following published guidelines such as those proposed by Dahm *et al.* (2013)—but rather accept on face value the conclusions made in the available reports. However, in those cases where the classification has been controversial, this is noted.

3.3. Geology and ground conditions in the affected area

The geological context of the earthquake is summarised very briefly, the focus being primarily on how this may influence the effects of the earthquake rather than its bearing on the origin of the earthquake; the latter is already addressed in Section 3.1.1.

3.3.1. Regional geology and topography

The general geological setting of the earthquake location and the affected areas is briefly described. If there are well-known faults mapped in the area, these are noted—and shown in map form where possible—with a note as to whether any role of these structures in the event has been inferred. The key features of interest, however, are the general age and nature of the local geology and the setting of the affected areas (e.g., valleys, mountainside, plains, *etc.*). These factors are significant since they can influence both the nature and intensity of the ground shaking (Section 3.4) and can lead to collateral hazards triggered by it (Section 3.5).

3.3.2. Site conditions in the affected area

In addition to noting the general geological and topographical setting of the earthquake, this section focuses specifically on the nature of the surface materials in the affected areas. This is important because of the influence of the site conditions—whether hard rock or deep layers of soft soils—can have on the nature of the ground motions. The subsequent interpretation of the earthquake effects is greatly enhanced when the recorded motions and/or the structural damage can be related to the near-surface geo-materials.

If the descriptions of the near-surface deposits in the vicinity of the epicentre and/or the affected areas indicates the presence of sand deposits, whether at the surface or at some depth, this is noted, together with any available information regarding the depth to the phreatic level (water table). The key interest here is related to liquefaction, since it has been raised as a potential hazard in the Groningen field. Reporting of liquefaction from small-to-moderate magnitude earthquakes is rather rare (e.g., Holzer *et al.*, 2010) hence a very useful by-product of this database may be ‘negative evidence’ regarding liquefaction triggered by such earthquakes. If in this section the presence of potentially liquefiable deposits is recorded but no liquefaction is reported (Section 3.5.3), then this may be interpreted to indicate that either liquefaction did not occur or else that the impact of any liquefaction was sufficiently small to pass unnoticed.

3.4. Ground motions

Damage due to earthquake shaking reflects that the seismic demand (*i.e.*, strength of the shaking) exceeded the seismic capacity (or resistance) of the exposed buildings. Damage may therefore occur under low levels of shaking if the affected buildings are exceptionally susceptible, just as damage to buildings of high seismic resistance would be indicative of

very intense shaking. Therefore, meaningful interpretation of damage reports is greatly enhanced by information regarding the strength and nature of the induced shaking.

3.4.1. Intensity observations

Macroseismic intensities are reported, whether these are just mentions of values at specific locations, mapped intensity data points (IDP) or isoseismal maps. The origin of such macroseismic data is clearly identified since practices related to the assigning of intensities varies greatly from country to country and from agency to agency, and these procedures often diverge appreciably from what might be considered good practice as defined, for example, by Musson & Cčić (2002). There have even been cases of authors of reports on a single earthquake documenting their divergent views on the assessment of intensity (e.g., Sargeant *et al.*, 2008; see Folkestone earthquake in Appendix 4.9).

The scale on which the intensities have been defined is also recorded since there are subtle differences among the various scales in use globally. Even if most of the 12-point scales are broadly comparable in their definitions, it has been found that some tend to yield different results in their application, particularly the MCS scale widely used in Italy (Musson *et al.*, 2010). In view of such differences, no attempt is made to convert intensity observations to a common scale in the database; each data set is reported in the scale in which the original assessment was made.

While macroseismic intensities determined from a combination of field surveys and questionnaires distributed among the population are ideal, these are not always available. In these cases, the ShakeMaps (Worden *et al.*, 2017) elaborated by the USGS become particularly useful for gaining some understanding on the intensities that might have been experienced. However, ShakeMaps should be interpreted with caution, as they combine information coming from: (i) Did You Feel It? (DYFI) questionnaires, *i.e.*, online macroseismic questionnaires spontaneously filled in by the public when they have felt an earthquake, and from which intensity is inferred; (ii) macroseismic intensity questionnaires or specific macroseismic studies, particularly for older earthquakes; (iii) conversion of instrumental ground motion into intensities at stations where the earthquake has been recorded; (iv) ground motion and intensity prediction models. Whenever there is not enough data in terms of the first two or three sources, the ShakeMap is dominated by predictive models and, thus, does not necessarily represent observed effects. When showing ShakeMaps in this section, as much information as possible is provided so as to understand the quality of the intensity estimates.

3.4.2. Ground motion recordings

Clearly, the best possible insights that can be obtained regarding the nature of the ground shaking are obtained from accelerograph recordings. If such instruments were installed and operational in the affected areas, the characteristics of the recorded motions are reported together with as much information as possible regarding the locations of the recording instruments and the site conditions at those locations. The proximity of the recordings to both the earthquake epicentre and to the areas where damage is reported to have occurred

is a key piece of information in this regard. Whenever possible, this information is summarised on a map.

When accelerograms can be accessed, acceleration histories as well as response spectra are calculated and presented, but failing this any published plots of acceleration and velocity time-series and response spectra are reproduced in the report, as well as any comparisons against relevant ground motion prediction models.

3.4.3. Inferred shaking levels

In the absence of any recordings of ground shaking in the epicentral region, there is a temptation to infer levels of ground shaking. One option would be to use empirical correlations between macroseismic intensity and instrumental ground-motion parameters to infer values of PGA, PGV and even spectral accelerations from the intensities (Dangkua & Cramer, 2011; Worden *et al.*, 2012). However, the uncertainties associated with such correlations is such as to render the results of limited value and very possibly to make them misleading. This is particularly the case when the correlations of intensity and ground-motion parameters have been derived using recordings of larger magnitude earthquakes. For this reason, this approach has not been followed herein.

Other options for inferring ground-motion levels include ShakeMap approaches (Worden *et al.*, 2017) and the application of GMPEs judged to be applicable to the region and magnitude range of the earthquakes. All such practices are subject to great uncertainty and with the possible exception of a well-established (and hence well calibrated) local ShakeMap facility, are likely to yield results of limited value. Nevertheless, ShakeMaps in terms of peak ground acceleration are included in the reports when available, acknowledging that their limitations are related to the origin of the information and their associated uncertainties, as described in Section 3.4.1, with the additional issue that DYFI and macroseismic intensity points need to be converted into PGA using a conversion model.

In some cases it has been possible to find acceleration histories derived from physical modelling of the source and rupture process and these have been included in the reports, together with any inferences on ground shaking made by others, including a brief explanation of how these inferences were made.

3.4.4. Duration of ground shaking

For both the assessment of damage to structures that experience degradation of strength and stiffness under cycling loading (*e.g.*, Bommer *et al.*, 2004) and the assessment of liquefaction hazard, the duration of the ground shaking is an important parameter. Therefore, reports of the duration of shaking are a useful addition to the case history and are included when available. However, it is only when these have been directly calculated from recordings that they hold their greatest value, as reports based on subjective experiences of the shaking tend to exaggerate its length. Given how many definitions of duration have been proposed and how different are the results that these can yield even from a single accelerogram (Bommer & Martinez-Pereira, 1999), the definition of duration is clearly stated.

Where possible, data on the duration of shaking observed during the seismic event under study is compared with the significant duration predicted by the models of Bommer *et al.* (2009) and Afshari & Stewart (2016). As described by Bommer *et al.* (2009), the significant duration of a waveform is defined as the time lapse between the instants at which the release of certain specified values of Arias intensity is attained. These values are, most commonly, 5% and 75%, or 5% and 95%, the former being more representative of the energy from the body waves, and the latter corresponding to the full wave train. The 5-75% of Arias definition is used in the case histories, and estimations are provided irrespective of whether measured values are available or not.

3.5. Collateral earthquake hazards

While the primary focus in this study is damage due to ground shaking—since this is generally the main cause of building damage (Bird & Bommer, 2004) and is also expected to be the primary hazard in Groningen—it is worthwhile giving brief consideration to other earthquake hazards (Figure 3.2). Some of these—in particular liquefaction in the case of Groningen—could pose a threat to infrastructure and lifelines (Bird & Bommer, 2004).

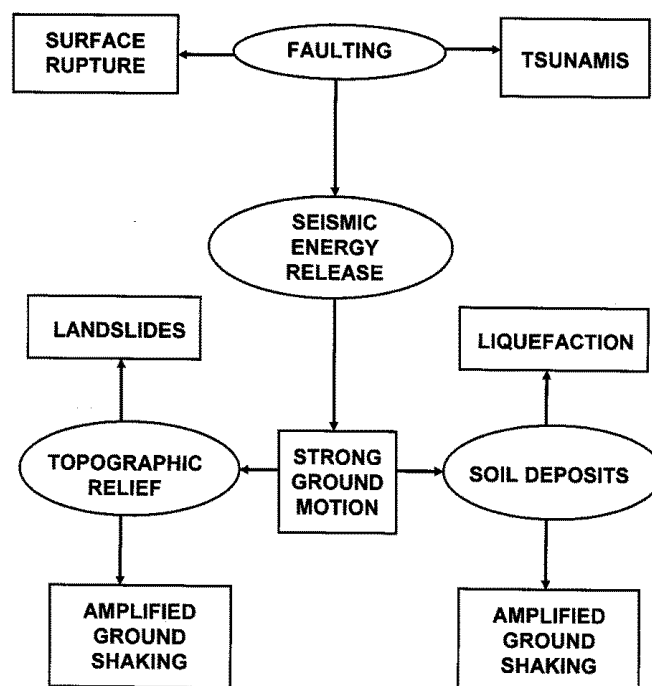


Figure 3.2. Potentially damaging earthquake effects (rectangles) associated with earthquake processes (ellipses). From Bommer & Boore (2004).

Amplified ground shaking is already covered by Sections 3.3.2 and 3.4. Clearly the possibility of tsunami hazard in the Groningen field can be safely dismissed and it is well established that the magnitude threshold for tsunamigenic earthquakes is larger than the upper limit of 5.5 considered in this review. However, the other collateral hazard are worthy of consideration and these are briefly discussed in the following three sub-sections.

3.5.1. Surface rupture

If the fault rupture associated with an earthquake reaches the Earth's surface, the resulting offsets can pose a very serious threat to any structures straddling the fault trace, particularly if the offset is vertical. However, the probability of surface rupture associated with earthquakes in the magnitude range covered by this study is rather low (Figure 3.3) hence this hazard is not reported very often for the earthquakes studied herein. Even in those rare cases where such surface expression of the faulting was noted, it is possible that the actual displacements may be sufficiently small to not necessarily pose a particularly onerous threat. Nonetheless, for each earthquake in the database it is noted whether or not any surface rupture was reported and, in any cases where this phenomenon was observed, if it contributed to the reported damage. The observation of ground fractures is also reported in this section, even if not directly related to the fault rupture.

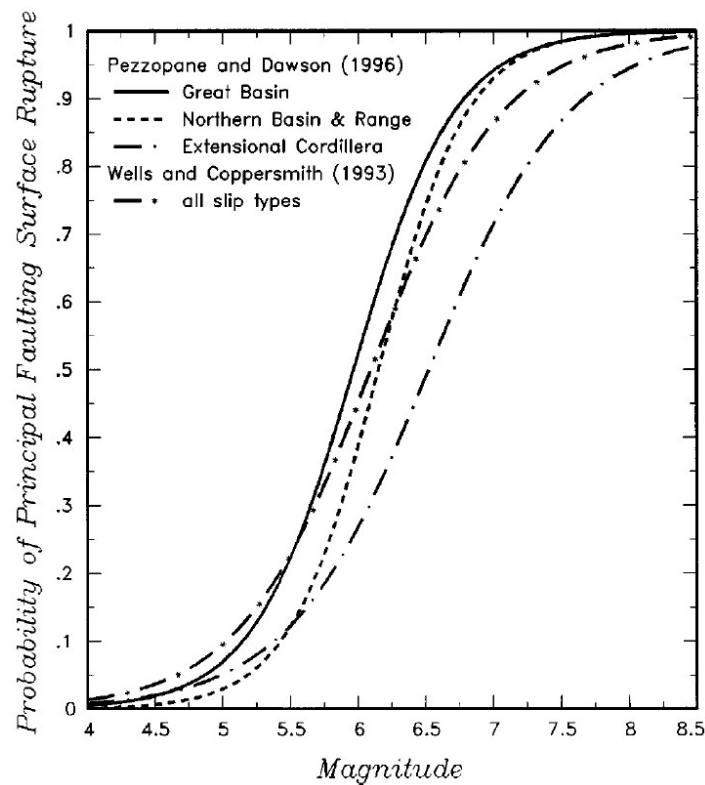


Figure 3.3. Probabilities of surface rupture as a function of earthquake magnitude. From Youngs *et al.* (2003).

3.5.2. Landslides

Earthquake-triggered landslides can lead to additional damage if they affect the foundations of any structures located on the slope that becomes unstable or if they impact on or bury structures located downslope from the instability. Given the very flat landscape in the Groningen region—and indeed in the whole of the Netherlands—landslides are not expected to be a relevant hazard. Therefore, any damage or casualties that were associated with

landsliding can be noted as examples of events that would not be expected to manifest in Groningen.

Overall relatively few landslides would be expected from earthquakes in the magnitude range of interest to this study (Figure 3.4) but this does not mean that they are impossible. Indeed, given that landslides can and do occur under static conditions, the lower bound magnitude of earthquakes that could trigger slope instability is likely to be rather small, provided that the geotechnical and hydrological conditions in the slope were sufficiently unfavourable. In summary, any landslides associated with the earthquake are reported, with as much information as possible regarding their location, size, run out or volume, and the material in the slide as well. Any damage directly associated with landslides is clearly documented. Otherwise, this section simply records the absence of such reports.

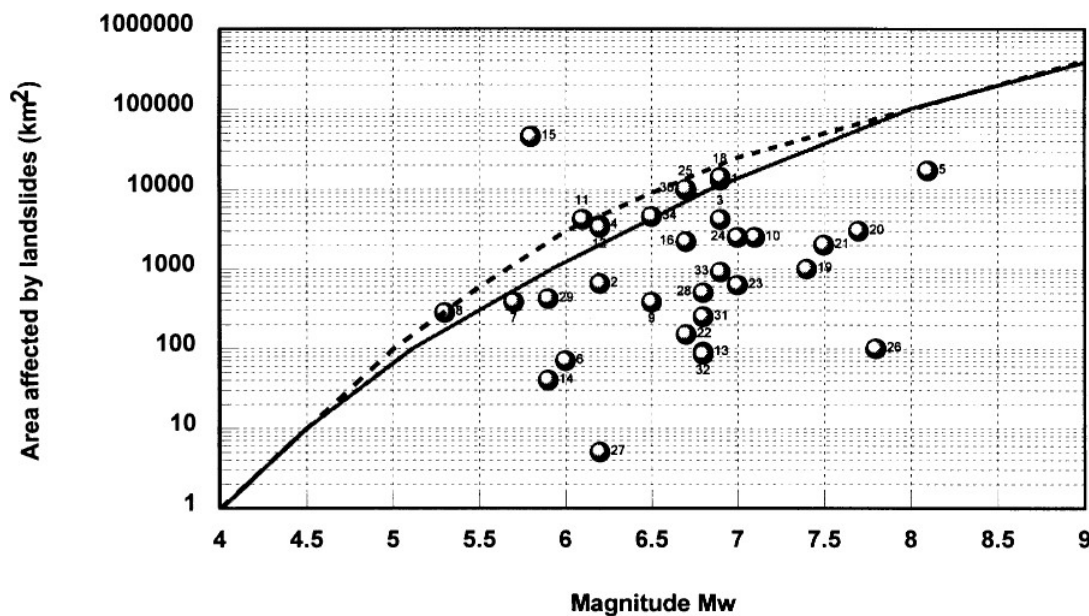


Figure 3.4. Areas affected by landsliding as a function of earthquake magnitude. From Rodriguez *et al.* (1999)

3.5.3. Liquefaction

This section records any observations of liquefaction and, should such cases be encountered, the nature of any damage attributable to liquefaction. For those earthquakes where the presence of potentially liquefiable soils was noted (Section 3.3.2), the absence of liquefaction reports may also be noted since this contributes useful data for the characterisation of liquefaction hazard in the Groningen field.

3.5.4. Settlements

Another possible effect of ground shaking on soil deposits is the further compaction of different strata. Uneven settlements below a certain structure can lead to damage as a consequence of the stresses developed in the structure when accommodating such relative displacements. Foundation settlements can result from liquefaction, but also from simple re-accommodation of the soil layers and/or deformation of underground structures such as coal

mines. Whenever reported, information regarding observed settlements is included in this section.

3.6. Exposed population

This section presents the main characteristics of the population that was exposed to the seismic event under consideration.

3.6.1. Socio-economic setting

The socio-economic conditions of the population of a certain region can exert a significant influence on the quality of construction of buildings and infrastructure. In prosperous regions and countries, people and authorities tend to carry out appropriate maintenance work, which is sometimes poor or even non-existent in under-developed areas. Further, other needs such as water, employment or security generally take precedence over seismic safety in poor regions. The socio-economic setting can thus end up controlling the vulnerability of the building stock and, by extension, whether it represents or not a threat to life. Nevertheless, the relationship between prosperity and maintenance can be far more complex than this. It is not uncommon to find less well-maintained buildings in prosperous regions with low seismicity, simply because of the lack of awareness that not being exposed to high levels of hazard can entail. This latter factor can be of particular relevance for putting the influence of socio-economic settings in context when studying regions of low natural seismicity like the Netherlands.

Defining the socio-economic setting is not a trivial task. For the sake of simplicity, the Human Development Index (HDI) and the Inequality-adjusted Human Development Index (IHDI) are the two main indices used herein as main indicators. The HDI is a composite statistic that combines indicators of life expectancy, education and per capita income. Its inequality-adjusted version takes into consideration inequality in these three indicators among the population. In addition to these, a brief description regarding the economic development of the region is provided, including data such as gross domestic product (GDP) per capita and unemployment rates.

3.6.2. Population density and distribution

Interpretation of the impact of an earthquake obviously depends on the number of people and buildings exposed to the strong ground shaking. The distribution of the population and population density need not only be described in broad regional and epicentral terms but also, and more importantly, in terms of occupancy of the different building typologies within the affected areas. If the majority of the population lives and works in modern buildings constructed using a modern seismic design code, it is possible that the number of casualties observed would be less than if the population was concentrated within old pre-seismic-code constructions. However, this information is seldomly available for small-to-medium magnitude earthquakes and, thus, this section focuses on describing the population density in simple terms that provide sufficient context to understand the level of exposure to the earthquake.

The main sources of data for this section are, consequently, national and regional censuses, as well as global data sets of population distribution such as Gridded Population of the World (GPW; CIESIN 2005; CIESIN 2016). In some cases, specific journal publications or technical reports can contain information on the exposed population as well. Where relevant, information regarding population density and distribution is presented on a map.

Whenever available, the number of people estimated to have been exposed to different macroseismic intensities according to the EXPO-CAT catalogue of human population exposure Allen *et al.* (2009b) is also reported. It is highlighted, though, that these numbers are not observations but estimations based on intensity prediction equations and models for population distribution.

3.6.3. Time of day of earthquake

The time of the day at which an earthquake occurs has a large influence on the number of people exposed within building typologies of varying vulnerability. For example, it is broadly recognized that the 2011 Christchurch earthquake could have caused many more casualties had it occurred during the daytime, as most of the buildings that collapsed were located in the business district of the city (e.g., Galloway *et al.*, 2014). By contrast, the opposite was true in the case of the 2003 Bam earthquake, which also occurred during night time but during which residential buildings were heavily damaged and thus a high number of casualties was observed (Ibrion *et al.*, 2015). Further, climate and seasons can have an analogous effect, with warm pleasant weather encouraging more people to be outside and, therefore, less exposed to structural failure, or holiday periods resulting in low occupancy of industrial buildings and offices. This information is relevant for understanding whether a large/small number of dead or injured people is due to the characteristics of the seismic event and the exposed building stock, or to the daily and seasonal variation of occupancy of the different structures.

3.7. Characteristics of exposed building stock

A description of the buildings exposed to the seismic events under study is provided herein.

3.7.1. Seismic design codes

Whether the building stock has been designed to some seismic code or not has a significant influence on the level of damage to be expected during a seismic event. Structural engineering practice evolved during centuries from not explicitly considering any kind of seismic load, to prescribing that buildings should be able to resist a lateral load equivalent to a pre-established percentage of its own weight, to developing proper seismic design codes based on more advanced knowledge of hazard and structural dynamics. The latter only became common practice in the second half of the twentieth century. This means that a very large proportion of the building stock worldwide has not been designed following a seismic code and, therefore, can be found to be relatively vulnerable to seismic actions. Relevant

exceptions to this conclusion are those regions for which strong winds have always represented a significant hazard: buildings in these areas can be found to be able to withstand low-to-moderate levels of ground shaking due to their lateral load resistance coming from wind design considerations. All this is particularly relevant for the case of the Groningen field, a region with a low level of natural seismic hazard but constant relatively strong winds. However, the existence of seismic design codes does not necessarily translate into safe buildings, for lack of official governmental control of code-compliance can be a fundamental failure in the seismic design process and contribute significantly to the vulnerability of the building stock, as pointed out by Gülkan (2000).

Determining whether the status of the building stock exposed to the seismic events under study is comparable to that of the Netherlands in terms of the implementation of seismic design codes and exposure to other kinds of hazard is relevant to understanding to what extent the consequences observed for these events could be expected in the Groningen field.

3.7.2. Building typologies

Not all buildings are expected to behave in the same way during a seismic event. Combinations of different factors such as types of materials, geometry and construction quality, will lead to buildings with different degrees of vulnerability and different replacement/repair costs. This sub-section contains detailed descriptions of the building typologies present at the time of the seismic events under study, at the site of interest. This information is used to understand if the building stock of the Netherlands is comparable to that of the events in the database in terms of vulnerability, which will dictate the level of damage to be expected.

Numerous building taxonomies (*i.e.*, building classification schemes) have been proposed and used to describe building stocks in different countries and at different points in time. HAZUS (FEMA, 2003), EMS-98 (Grünthal, 1998), the World Housing Encyclopedia (EERI, 2000), and the GEM Building Taxonomy (Brzev *et al.*, 2013) are only some of the many examples. Damage statistics are directly related to the taxonomy used, as the percentages of buildings in each damage state will normally be sub-classified according to each building type, and damage scales may be specific to the typology. Given the difficulties that trying to re-classify buildings starting from a certain taxonomy entails, the original data being usually inaccessible, the exposed building stocks are characterised in this section as found in the literature.

3.7.3. Prior damage and retrofit

When describing the characteristics of the exposed building stock, it is not only relevant to include information on the buildings as they were designed, but also to understand if that original design has been strengthened by some degree of retrofit or weakened by un-repaired prior damage or lack of maintenance. This is very difficult to assess in many cases, though there are others in which such observations were made by those carrying out the field study after the earthquake. Whenever available, this information is reported herein.

3.8. Damage observations

This section, together with the upcoming one, are the core of the present study. All the information gathered in previous sections acquires a more significant meaning in light of the consequences of the events being described. Damage to the exposed building stock is extensively described herein, with the aim of achieving a comprehensive understanding of the impact of these small-to-moderate earthquakes and the factors contributing to the extent of their consequences.

3.8.1. Damage states

The damage state of buildings affected by seismic events is better described by means of standardised damage scales, such as the European Macroseismic Scale (EMS-98; Grünthal, 1998), FEMA 356 (FEMA, 2000) and HAZUS (FEMA, 2003), just to name some. It is not unusual to find publications from older events that do not report damage levels directly but describe the severity of the shaking by means of macroseismic intensity scales such as the Medvedev-Karnik-Sponheuer (MSK; Musson & Cčić, 2012) scale, the Mercalli-Cancani-Sieberg scale (MCS-1930; Sieberg, 1930) and the Modified Mercalli scale (MMI; Musson & Cčić, 2012). If no detailed information is available, macroseismic intensity can be used to infer the level of damage.

Depending on the location and date of the events under study, information is available in terms of one scale or another. In view of the potential drawbacks of converting reported damage from one scale to a different one, no attempt has been made to carry out such conversion. As in the case of Section 3.4.1, damage state data is reported in the scale in which the original assignment was made. Sufficient description of the scale used is provided, so that the meaning of each damage state can be fully understood from the contrast against the whole range of damage states covered by the scale.

Immediately after a damaging earthquake has occurred, it is common practice that trained engineers carry out a visual inspection of the building stock in order to determine the degree of habitability of each structure. This is indicated by means of a colour tag, which can be green, yellow or red, each symbolizing unrestricted, restricted and no access, respectively. A green tag is assigned to a structure that has either not suffered any damage or has suffered only from minor superficial damage. A yellow tag indicates that significant actions need to be put in place for the building to be fully inhabitable again but that, until that occurs, occupants can access it briefly to gather essential belongings, and technicians and engineers can access it to carry out the reparations. Finally, a red (or sometimes black) tag is assigned to those structures which have suffered extensive damage and are at risk of imminent collapse.

The European Macroseismic Scale (EMS-98; Grünthal, 1998) classifies damage into five grades, defined separately for masonry and reinforced concrete buildings. The Medvedev-Sponheuer-Karnik scale (MSK-64; Medvedev *et al.*, 1965) scale defines five grades as well, though these are defined without consideration of the structural typologies. Details on these two damage scales and on the relationship between macroseismic intensity levels and

damage to buildings for the two and for the Modified Mercalli Intensity scale are provided in Appendix II of this report.

3.8.2. Damage statistics and description

The proportion of buildings that can be assigned to each damage state are reported here. Due note is taken of whether the damage observed was caused directly by ground shaking or if it was a consequence of collateral earthquake hazards such as those listed in Section 3.5. Given that landslides are not expected to represent a significant hazard in Groningen, while liquefaction could be, and other forms of collateral hazards may be totally discarded in the Groningen field, this distinction is of great relevance for the present study.

It is noted that the proportion of the total building stock that is damaged during an earthquake is often not reported. Nevertheless, an effort has been made to describe as thoroughly as possible the damage observed as well as to convey the extent of the impact of the earthquake in the affected area.

Apart from specific publications that can exist reporting the consequences of each seismic event in the database, relevant sources of information for this section are the International Events Database (EM-DAT), the Significant Earthquake Database of the National Centers for Environmental Information of the National Oceanic and Atmospheric Administration (NOAA) of the United States, the PAGER-CAT losses database of Allen *et al.* (2009a), and the descriptions found in the USGS catalogue and the ISC Bulletin.

As reports on damage in terms of statistics and damage scale cannot always be found, this section is used as well to qualitatively describe the damage observed. Even in the cases where statistics are available, qualitative descriptions are relevant to convey more details regarding the consequences of the earthquake and an encompassing picture.

While for many of the case histories information on damage is scarce, for some others the opposite is true. It should be noted that, in those cases, a summary of the most relevant findings is presented herein.

3.8.3. Observed weaknesses

In those cases for which information regarding specific structural weaknesses that might have had a significant influence on the extent of damage observed is available, this information is included herein. Structural weaknesses to be considered include, but are not limited to, soft-storeys (*i.e.*, the stiffness of one storey being significantly lower than the others), vertical and horizontal irregularities, insufficient width of seismic joints leading to pounding of neighbouring buildings, short-column effects (*i.e.*, columns with shorter effective heights than others in the structure, and consequently more prone to shear failure), lack of verticality of walls, lack of anchorage of façades, out-of-plane failure of unreinforced masonry walls, inadequate confinement of reinforced concrete members, and corrosion of reinforcement. In addition, special attention is paid to damage of non-structural components such as chimneys and parapets, which are commonplace in ordinary buildings in the

Netherlands, in view of the potential threat these elements can pose to human life. The influence of eventual systematic weaknesses on the damage observed for a specific event needs to be accounted for when interpreting the possible extrapolation of consequences from earthquakes of the database to the case of the Groningen field.

3.8.4. Damage distribution

The geographical distribution of physical damage caused by the seismic event is reported here, in the form of a map when sufficient data are available. Due note is taken of cases in which a concentration of damage was observed within a certain area, identifying, where possible, the reasons for such trend. For example, if more extensive damage was observed in structures located over a hill than in those of similar characteristics located at a similar distance from the epicentre but on a plain, the influence of topographic effects may be suspected. Furthermore, even though there is still some controversy around the question of whether small-to-moderate magnitude earthquakes can be associated to directivity effects, a number of recent publications has shown that there is evidence of high frequency directivity for moderate magnitude earthquakes (e.g. Chen *et al.*, 2014; Boatwright, 2007). No attempt has been made to study the potential directivity effects of the earthquakes in the present database, but note has been taken of those cases for which bibliographical sources suggest their existence.

3.9. Casualties and losses

As the primary focus of this study is life safety, this is one of the core sections of the present study. The number and causes of casualties, as well as estimates of the overall economic losses, are provided. Relevant sources are the same as those used for the description of damage to buildings.

3.9.1. Numbers of dead and injured

The number of people who died or were injured by the seismic event is reported here, ideally related to building typologies and their damage states, or to any other relevant context, though this information is seldom available. These numbers should be interpreted jointly with the causes reported in the next sub-section.

3.9.2. Causes of casualties

The causes of the observed casualties are fundamental to understanding what sort of intervention would be needed to reduce the induced seismic risk in the Netherlands, if any. As a first step, it is established whether the casualties were a direct consequence of ground shaking or of a collateral hazard such as landslides or surface ruptures, or, even further, if they were due to subsequent physical and/or emotional trauma triggered by the stress and panic caused by the seismic event. Within those caused directly by ground shaking, it is then further determined if they had their origin in the severe structural damage or collapse of specific structural typologies, or if they were the consequence of non-structural elements or

equipment moving or falling. The first case would suggest the possible need for some kind of structural intervention in the building stock, while the latter would indicate that attention should be focused more on non-structural components than on structural ones.

3.9.3. Estimates of economic losses

Estimates of economic losses made by others are reported here, and no attempt is made to make new estimates. Monetary values are given, in most cases, as originally calculated at the time of the event, though it is not always possible to be certain of what the sources themselves are reporting, especially when new papers and studies are published regarding older earthquakes.

Ideally, the overall economic losses should be subdivided into material losses (*i.e.*, repairing, rebuilding, etc.), downtime losses (*i.e.*, losses due to the period of time in which industries and businesses of the region affected by the seismic event could not continue normally with their economic activities) and losses due to the "value of life" (*i.e.*, the economic value assigned to fatalities). However, this kind of information is rarely available.

3.10. Discussion and conclusions

In this closing section, a brief summary is given of the impact of the particular earthquake, and an attempt is made to explain the main factors contributing to damage, casualties and losses associated with the event.

3.11. Note

The compilation and analysis of all the case histories presented in this work was carried out over a period of some years. Consequently, values and references to the *present time* cover, approximately, the years 2015-2018. Whenever the time of writing is of relevance to what is being stated, it has been clearly noted.

4. OVERVIEW AND DISCUSSION OF CASE HISTORIES

Twenty-one earthquakes have been studied in detail in the present report, including eight believed to be of induced origin. Their locations and magnitudes are depicted in Figure 4.1 and Tables 4.1 and 4.2. This is too small a sample to allow any general conclusions to be drawn that would be applicable to the potential effects of moderate-magnitude seismicity, but nonetheless several significant observations can be made regarding the nature and impact of these earthquakes. The detailed case histories are contained in Appendices III and IV.



Figure 4.1. Epicentral locations of the earthquakes studied in detail as case histories. Rhombuses and circles indicate induced/triggered and tectonic origins, respectively. Colour scale indicates moment magnitude, from **M**3.4 (light purple) through **M**5.8 (dark purple).

Of the seven cases of anthropogenically-caused earthquakes, six were triggered by high-pressure fluid injection and one by groundwater extraction. The latter was the 2011 **M**5.1 earthquake that occurred close to the town of Lorca, Spain, and which caused the most damage and casualties of the seven. It should be acknowledged, though, that, apart from Basel, which deserves a separate comment, it was also the one event of this group that occurred close to a large human settlement, as opposed to the five induced earthquakes that occurred in relatively scarcely populated areas of the United States. A peak ground acceleration of 0.36 g was recorded on firm soil in the town of Lorca itself, and it is believed that both directivity effects and site amplification had an important influence on the level of shaking to which the structures were subject. The most affected typologies were mainly the city's aged building stock as well as a few more modern buildings with significant structural deficiencies. The earthquake left 9-10 dead and hundreds of injured, nearly all of these the result of the collapse of non-structural elements. While causing landslides, these do not

seem to have greatly influenced the extent of damage, as they only affected roads and a courtyard wall. Despite being attributed to triggering as a result of groundwater extraction, it occurred in a region with appreciable natural seismicity.

Table 4.1. Summary of consequences observed for the induced/triggered earthquakes studied in detail, as reported in the Database of Damaging Small-to-Medium Magnitude Earthquakes.

Date & Time (UTC)	Place	M	Deaths		Injured	Buildings		Losses (10 ⁶ USD)
			Total	Shaking		Damaged	Destroyed	
08/12/2006 16:48	Basel, Switzerland	3.2	0	0	0	40-2,000	0	6.5-8.3
28/02/2011 05:00	Guy-Greenbrier (Arkansas), USA	4.8	0	0	0	14	0	1.0
11/05/2011 16:47	Lorca, Spain	5.1	9-10	9-10	300-400	6,052	331	200.0 -1,600.0
23/08/2011 05:46	Trinidad (Colorado), USA	5.4	0	0	0	44	2	0.1-5.0
06/11/2011 03:53	Prague (Oklahoma), USA	5.7	0	0	2	14-94 (*)	0	1.0 -12.0
03/09/2016 12:02	Pawnee (Oklahoma), USA	5.8	0	0	1	14	0	> 0.6
07/11/2016 01:44	Cushing (Oklahoma), USA	5.0	0	0	1	50-80	2	1.0 -20.0

(*) Upper bound likely includes the effects of a **M4.8** aftershock.

The five induced earthquakes from the United States studied herein occurred in three areas known to be experiencing significantly high rates of seismicity in the last years: Oklahoma, north Arkansas and the Raton Basin (Colorado/New Mexico) (Petersen *et al.*, 2017). As shown in Table 4.1, there are no deaths associated with any of these five events, and no injuries associated with the 2011 **M4.7** Guy-Greenbrier (Arkansas) and 2011 **M5.3** Trinidad (Colorado) earthquakes. Four injuries are associated with the three Oklahoma earthquakes, only that of the 2016 **M5.8** Pawnee shock being the consequence of damage inflicted to buildings (collapse of a chimney). The two injuries reported for the 2011 **M5.7** Prague earthquake were the case of a person hitting their head when trying to flee a building and a case of a foot cut by broken glass, while that of the 2016 **M5.0** Cushing event is a hand laceration of unknown origin. It is noted that both the 2011 Prague and 2016 Pawnee earthquakes are above the upper limit of the magnitude range for this study but were included nonetheless because of their importance as highly-publicised cases of induced seismicity. Interestingly, only the **M5.8**, whose energy release is 2.8 times that of a **M5.5**, caused an injury due to a structural failure. The **M5.8** Pawnee earthquake was also the only one of the five to cause sand blows associated to liquefaction, though these do not seem to have caused significant damage. A reduced number of rockfalls affected some roads after the **M5.3** Trinidad and **M5.7** Prague earthquakes.

Table 4.2. Summary of consequences observed for the tectonic earthquakes studied in detail, as reported in the Database of Damaging Small-to-Medium Magnitude Earthquakes.

Date & Time (UTC)	Place	M	Deaths		Injured	Buildings		Losses (10 ⁶ USD)
			Total	Shaking		Damaged	Destroyed	
18/03/1957 18:56	Port Hueneme (California), USA	4.8 (M _L)	0	0	0	Some	1	N/A
25/04/1966 23:22	Tashkent, Uzbekistan (USSR)	5.2	8-15 (*)	N/A	200 -1000	28,000 -96,000	Some of (^)	300.0
03/09/1978 05:08	Albstadt, Germany	5.2	0	0	23-35	5,000 -11,500	1-60	140.0 -170.0
08/11/1983 00:49	Liège, Belgium	4.8	6	1	25-30	13,000 -16,000	25-205	50.0 -80.0
27/12/1989 23:26	Newcastle, Australia (x)	5.4	13	12	100 -162	50,000	300 -486	1,000 -2,500
13/04/1992 01:20	Roermond, the Netherlands	5.4	1	0	45	1,300	5-100	125.0 -206.0
26/03/1993 11:58	Pyrgos, Greece	5.4	1	0	2-16	600 - 1,800	100 - 360	160.0
15/07/1996 00:13	Épagny-Annecy, France	4.8	0	0	1	11,800	3	70.0 -100.0
20/04/2002 10:50	Au Sable Forks (New York), USA	5.1	0	0	0	900	0	16.0
25/04/2002 17:41	Tbilisi, Georgia	4.8	6-8	4	30-70	11,780 -50,000	2,319 - 4,208	180.0 -350.0
24/11/2004 22:59	Garda Lake/Salò, Italy	5.0	0	0	5-12	4,147	40 - 1,200	150.0 -260.0
28/04/2007 07:18	Folkestone, United Kingdom	4.0	0	0	1	807 -1,300	0	60.0
17/05/2014 16:46	Darmstadt, Germany	3.6	0	0	0	154	0	1.36
21/08/2017 18:57	Ischia (Napoli), Italy	3.9	2	2	39-42	349 - 1,000	688	8.0 -140.0

(*) 8-15 are the official numbers. Some estimates reach 5,500-7,500, but these probably include many occurred during the aftershock period and/or related to secondary effects (e.g. deaths due to heart attacks).

(^) "Some of" implies that the reported number of damaged buildings includes those destroyed.

(x) It has been suggested by Klose (2007) that the 1989 Newcastle earthquake may have been induced by the de-watering of coal mines in the region, but the idea has been challenged by other scientists (see Appendix A4.5).

It is interesting to note that the **M5.0** Cushing earthquake, with the second smallest magnitude after Guy-Greenbrier, appears to have caused more damage than the other four, as the upper bound of 94 damaged buildings for Prague might be an overestimation (see Table 4.). The **M5.3** Trinidad (Colorado) earthquake could, perhaps, be deemed as the closest case in terms of magnitude and damage, the one of Cushing being smaller but

closer to urbanised areas and the latter being bigger but farther away. The **M4.7** Guy-Greenbrier event of 2011 in Arkansas was smaller in magnitude than the other four in Colorado and Oklahoma and caused only very minor damage, likely due not only to its smaller magnitude but also to it occurring in a scarcely populated area.

All these five earthquakes were triggered by wastewater injection and caused shaking that was damaging to local buildings mostly in quite sparsely-populated areas. The damage was almost exclusively to unreinforced masonry and was consistent with classical patterns of seismic response for such buildings observed in many earthquakes. Damage include the collapse of gable walls, parapets, chimneys and brick façades, as well as cracking of plaster and drywalls. Accelerations generated by the 2011 Guy-Greenbrier and Trinidad earthquakes are somewhat uncertain, as near-field records do not exist for the former and very low values were recorded for the latter over 25 km from the epicentre; estimates from USGS ShakeMaps seem to vary significantly whenever their background calculations are reviewed and a new map is generated. For the 2011 Prague and the 2016 Pawnee earthquakes, PGA values of around 0.06 and 0.09 g were recorded at 25 and 50 km from the epicentres, respectively, and the USGS ShakeMaps suggest maximum median accelerations of around 0.45 g in both cases. The 2016 Cushing earthquake is the best recorded of all these five, with values around 0.6 g registered in the very near-field, but no records available within the city of Cushing itself, though the epicentral distance to the record and to the city are comparable.

The final induced case is the 2006 Basel earthquake, which was associated with an enhanced geothermal project in this Swiss city and for which a geometric mean horizontal PGA of 0.1 g was recorded around 7 km away from the epicentre. With a local magnitude of only 3.4 (**M3.2**), this earthquake is actually below the range to be considered in this study, but it was included since it has been a high-profile and controversial case, which has raised significant concerns regarding anthropogenically-generated seismicity. The Basel earthquake is often cited as an example of a damaging small-magnitude shallow-focus earthquake. However, the detailed study of this event has shown that at most it caused a large number of non-structural—and generally very superficial—cracking, and the large insurance claims paid out following this earthquake grossly exaggerated the actual physical impact of this earthquake on the built environment. Together with the 2012 **M3.5** Huizinge earthquake in the Netherlands, Basel is an example of the concept of “moral hazard”, that is, the punishment of companies carrying out seismically-inducing activities by claiming damage of unknown origin was caused by a particular earthquake (e.g., Bommer *et al.*, 2015).

Except for the 2016 Pawnee event, for which there were almost no foreshocks and fewer than expected aftershocks, the aforementioned earthquakes occurred within a sequence of foreshocks and aftershocks or a swarm, in some cases with the total number of events numbering tens or even hundreds.

The fourteen tectonic earthquakes studied herein are varied in terms of their locations and consequences, those occurring in Roermond (the Netherlands), Liège (Belgium), Albstadt (Germany), Darmstadt (Germany), Folkestone (UK), Épagny/Annecy (France) and

Newcastle (Australia) being the most representative for Groningen in terms of their relatively similar building stock and socio-economic settings. Of these, the **M3.6** Darmstadt earthquake caused no casualties, while the **M4.0** Folkestone and **M4.8** Épagny earthquakes only caused one injury each, due to falling masonry and broken glass, respectively. Dislodged, cracked or collapsed chimneys were one of the most frequent forms of damage in all three earthquakes, together with dislodged roof tiles and cracked plasterwork and masonry, their extent clearly increasing with magnitude. A maximum horizontal PGA of 0.12 g was recorded during the Folkestone earthquake, 5 to 8 km away from its epicentre.

The remaining four earthquakes, **M4.8** Liège, **M5.2** Albstadt, **M5.4** Roermond and **M5.4** Newcastle, were more significant in terms of their casualties. The Albstadt earthquake only caused injuries, two dozen of which were reportedly due to the collapse of walls during an aftershock that occurred a couple of hours after the main shock. One death due to a heart attack is attributed to the Roermond earthquake, while its 45 injuries are believed to be due to falling chimneys, masonry and tiles, as well as broken windows. The death toll is higher for Liège, but only one out of the six deaths reported was due to a falling ceiling, while four occurred after the earthquake, as a consequence of intoxications with carbon monoxide due to the collapse of chimneys, and one is a heart attack. Most of its 25-30 injured were allegedly hit by masonry elements falling on the roads and while running out of buildings. Of the four, the Newcastle earthquake certainly caused the largest number of casualties. Having caused the notorious collapse of a 17-year-old structure housing an auditorium, it resulted in the death of nine people due to this cause. Three additional deaths attributed to this earthquake were caused by the collapse of parapets and awnings, while a last one was associated to a heart attack. Hundreds of injuries were likely due to similar causes. It is noted, though, that the aforementioned auditorium was found to have significant structural deficiencies, and that the death toll would have probably been much larger had the earthquake occurred during a performance with a full audience.

These four earthquakes also caused the cracking or collapse of chimneys and parapets, as well as the cracking of masonry and plaster, though the extent of the damage appears to have been much larger than for Darmstadt, Folkestone and Épagny. Moreover, the collapse of roofs and walls as well as the complete collapse of roof tiles instead of simple dislodgements appear to have been more common for Liège, Albstadt and Roermond. This is not surprising, considering that the magnitudes of the former range between **M3.6** and **M4.8**, while those of the latter group range from **M4.8** to **M5.4**. In the case of Newcastle, the dislodgement and overturning of chimneys appears to have been relevant only for older structures, as newer ones did not tend to possess them. The failure of suspended awnings stood out in Newcastle instead. However, all these seven earthquakes share one additional feature. In all cases, the most damaged typologies have been masonry structures built before the introduction of seismic codes in the respective areas, while more modern reinforced concrete structures and better-built masonry buildings are only reported to have suffered from more than non-structural damage in cases in which poor design or construction errors were relatively apparent. Additional factors that were mentioned to have an effect on the extent of the damage observed were poor maintenance (e.g., Folkestone, Newcastle) and the introduction of structural modifications in time (e.g., Épagny/Annecy, Newcastle).

One important feature of the Roermond earthquake was that the shaking caused significant liquefaction, which is a factor of relevance to Groningen, although it is important to keep in mind that the Roermond earthquake was almost two units in magnitude greater than the largest induced earthquake in Groningen to date and, hence, several hundred times more energetic. In any case, no building damage at all was attributed to liquefaction due to the Roermond earthquake, which is also an important observation for the Groningen case. Of the other six earthquakes, only that of Épagny/Annecy appears to have caused small-scale liquefaction at one of the ends of the airport's runway, in spite of the whole affected area being susceptible to liquefaction effects. In the case of Newcastle, settlements believed to have caused damage to buildings have been attributed to liquefaction, though no sand boils were observed. A general finding from an independent study is that liquefaction that could pose a threat to the built environment has generally been limited to earthquakes of **M5** and greater (Green & Bommer, 2018).

It is interesting to note that the 2014 Darmstadt earthquake, only 0.4 magnitude units above Basel and still below the **M4.0** threshold, is documented to have caused damage to more buildings and to a greater extent than the latter, despite its monetary loss estimate being much lower. This observation, together with the almost no damage reported for the geothermally-induced **M3.4** St. Gallen (Switzerland) earthquake of 20th July 2013 (Edwards *et al.*, 2015; not studied herein), supports what was said before about the consequences reported for Basel being unrealistically high.

On the other extreme of the spectrum of the fourteen tectonic earthquakes studied lie the 1966 **M5.2** Tashkent (Uzbekistan) and the 2002 **M4.8** Tbilisi (Georgia) earthquakes, both having taken place in ex-Soviet nations, albeit very different from each other and distant in time and space. The consequences of these two earthquakes appear as significantly more extreme than those of all other earthquakes studied. During the 1966 Tashkent earthquake, it was mostly pre-1917 adobe houses with shallow or no foundations and fired brick masonry buildings that suffered the most, all of which are suspected to have sustained previous damage, besides not having been designed for seismic action and being built with poor-quality materials and workmanship skills. Similarly, pre-1950 masonry buildings with no seismic design, lack of maintenance and frequent low-quality vertical extensions were the most affected by the 2002 Tbilisi earthquake, for which a maximum horizontal PGA of 0.11 g was recorded on bedrock within the city itself, 6 km away from the epicentre. Many of these buildings are expected to have been damaged already by armed conflicts that took place in the 1990s as well as the consequences of subsidence. It is acknowledged, though, that the consequences reported for the 2002 Tbilisi earthquake may have been aggravated by continuous heavy rains that followed the earthquake with the arrival of the summer and subsequent snow in the winter, in the same way that the long sequence of aftershocks that followed the 1966 Tashkent earthquake are believed to be responsible for additional damage to buildings. While many other factors have a role in the consequences of seismic events, the relevance of these cases to Groningen lies in that they both highlight the influence of the quality of construction and maintenance on the performance of structures subject to seismic loading. Most of the buildings affected by the six European earthquakes discussed above also lacked seismic design and were still more capable of withstanding the shaking.

Regarding casualties, the 2002 Tbilisi earthquake caused three deaths due to falling debris, one death due to the collapse of a roof, and two deaths due to heart attacks, as well as 30 to 70 injuries due to unspecified reasons. For the 1966 Tashkent earthquake the number of people reported injured varies from 200 to 1,000. More than half of the 200 reported by some sources are attributed to impulsive reactions of people as a consequence of fear, such as jumping out of windows, while one third were caused by falling plaster or bricks, as well as household items, and only one tenth was reported to be due to the collapse of roofs or walls. The official death toll for Tashkent was 8-15, but the Soviet authorities never revealed the real figures, and estimates rise to several thousands. The composition of such numbers is, however, not clear in the sources. Statements regarding hundreds of elderly people dying from post-traumatic stress and especially from heart attacks during the occurrence of aftershocks suggest that figures in the order of thousands might be including a large number of deaths only indirectly related to the earthquake (and possibly hard to verify).

Similar to the six European earthquakes already discussed, the 1993 **M5.4** Pyrgos (Greece) and 2004 **M5.0** Garda/Salò (Italy) affected mostly relatively old masonry structures. In the first case, adobe, mixed masonry and stone masonry buildings lacking a seismic design philosophy were the most damaged, while the second greatly affected pre-World War II non-engineered masonry buildings, in some cases up to 200-300 years old. Cracking of masonry and plaster, partial (and total only in Pyrgos) collapses were observed. A maximum horizontal PGA of 0.43 g and a maximum vertical PGA of 0.15 g were recorded on rock 3 km away from the epicentre of Pyrgos earthquake. For Salò, a maximum horizontal PGA of 0.07 g was recorded on rock around 13 km from the epicentre, relatively close to several of the affected towns, though simulations suggest a possible maximum of 0.2-0.25 g that could have been amplified even further due to site effects. In both earthquakes, engineered structures performed better, though they were not fully exempt of damage. No deaths occurred during the Salò earthquake, and the one death reported for Pyrgos appears to have occurred while a person was trying to flee a building, though it is not clear if the death was due to falling debris, for example, or to an accident that occurred during the act of fleeing itself. Between two and sixteen people were injured during the Pyrgos earthquake due to unknown causes, though the damage extent suggests they may have been related to the performance of the buildings. Some of the injuries associated to the Salò earthquake appear to have occurred while people tried to prevent paintings or furnishings to get damaged, while others were due to running away and falling debris. Both earthquakes are reported to have caused liquefaction, Salò only at one location that resulted in localised lateral spreading and a crack along the harbour, Pyrgos more extensively and influencing the extent of damage, particularly due to the resulting subsidence. The relatively large magnitude of Pyrgos earthquake (the same as that of Roermond) needs to be highlighted in this respect, together with the very high susceptibility to liquefaction of the affected area. The landslides and rockfalls associated to these two events do not appear to have had a large influence on the damage suffered by buildings.

While the consequences of the **M5.0** Salò earthquake are not extremely surprising for an earthquake of that magnitude in northern Italy, those of the much smaller and recent 2017 **M3.9** Ischia (southern Italy) earthquake were disproportionately high and enough reason to include it in this study despite its magnitude being lower than the considered range. A

maximum horizontal PGA of 0.28 g and vertical PGA of 0.27g were recorded less than 1 km away from the epicentre, within one of the most affected urban settlements. At least three total collapses and several partial collapses occurred, amongst many other instances of extensive diagonal cracking and failure of chimneys, cornices and connections between perpendicular walls. While site effects and large ground motions are largely responsible for the damage observed, it is the vulnerability of the building stock, which consisted mostly of unreinforced masonry, that is pointed out as one of the main reasons for the damage having been so extensive. Discussions in the media, political and scientific circles refer to the lack of control of construction activities in the region, which led to many illegal extensions and new structures being built with poor-quality materials and lack of proper structural design. Two deaths occurred due to damage to buildings, and 42 injured are likely to have been consequence of the same. As with Salò and Pyrgos, the landslides caused by the **M3.9** Ischia earthquake do not appear to have influenced the extent of damage to buildings.

Quite different from all the earthquakes already described is the case of the $M_L=4.8$ Port Hueneme event of 1957, which may join Basel (and Huizinge) in the list of earthquakes with potentially misinterpreted consequences, though for very different reasons. The Port Hueneme earthquake has been often described as having caused “heavy” damage, though a closer look reveals that such a statement was most likely only related to contents falling off shelves in stores. Damage to buildings appears to have consisted mostly on cracks in walls and plaster, and the fall of the latter as well as loose bricks or cornices. Due to a lack of more detailed information, it is difficult to compare the Port Hueneme earthquakes against the rest, though the descriptions found suggest that the consequences were much more limited.

Finally, the 2002 **M5.1** Au Sable Forks (New York, USA) earthquake provides an interesting example in which the consequences to the road and electrical infrastructure appear to have accounted for a very large percentage of the overall monetary losses, though the minor to moderate damage suffered by around 900 buildings in a very vast area should not be overlooked. Several roads were affected by the occurrence of liquefaction in the filling soils used beneath them. The electricity supply was interrupted for up to 10 hours in some areas, as three transmission towers were severely damaged by a rockslide, and several pieces of equipment were damaged due to the shaking. While rockslides are not a problem in Groningen, liquefaction and the failure of electrical equipment could be.

It is worth noticing that, besides the evident influence of the quality of construction, maintenance and overall (lack of) seismic design philosophy, site amplification due to loose unconsolidated deposits is a common factor in most of the case histories studied, an observation that is of great importance for Groningen, in view of its own susceptibility to site effects (e.g., Rodriguez-Marek *et al.*, 2017).

5. CONCLUSIONS

The compilation of the Database of Damaging Small-to-Medium Magnitude Earthquakes alongside the study of 21 case-history earthquakes has provided some interesting insights on the characteristics of these kinds of events. It is noted, however, that the statistics presented herein cannot be deemed to represent verified scientific measurements or observations but are rather those resulting from various sources of undetermined reliability. Moreover, they are dependent on the criteria used to compile the database, as different choices regarding, for example, the treatment of unknown magnitude scales or moment magnitudes derived empirically from other parameters could lead to the inclusion or exclusion of events and, thus, to a change in the statistics presented. In this sense, it should be noted as well that the database is organic and can grow both as time goes by and as new information regarding past events emerges.

To begin with, it has been noted that the geographical distribution of events that make up the database follows, overall, the patterns of global seismicity, except for the fact that areas with high seismicity but low exposure are missing and some areas with low seismicity, such as the north-eastern USA and Brazil, acquire more prominence. The distribution of the damaging earthquakes in time clearly illustrates the influence of both, detectability of small-magnitude earthquakes and availability and accessibility to damage records. The biggest jump in the number of earthquakes is observed in 2013, the first year for which the Earthquake Impact Database (EID) has been compiled in near-real time. The rate of around 190 damaging earthquakes in the range **M**4.0-5.5 per year reported for the 2013-2017 period suggests, for example, that less than 20% of the damaging earthquakes of the 2000s may have been captured in the database for said decade, with this percentage reducing further back in time. While it is not possible to know if the rate observed for 2013-2017 is “complete” or even accurate in the long-term, and around 6% of the total of entries from the EID could not be matched with earthquakes reported in the ISC Bulletin (and were thus not included in the database), it is noted that the EID appears to contain even earthquakes that caused minimal damage.

The number of damaging earthquakes contained in the database increases with magnitude and reaches its maximum within the **M**5.25-5.50 bin. However, when considering that this bin is slightly wider than the preceding one due to the rounding of events with $5.5 < \mathbf{M} < 5.55$ down to 5.5, the peak occurs in the **M**5.00-5.25 bin instead. In any of the two cases, either the latter in which the peak is slightly shifted or the former, in which the relative increase from the 5.00-5.25 to the 5.25-5.50 bin is very small, this suggests that the higher likelihood of larger earthquakes to cause damage or casualties appears to be counterbalanced by the decreasing frequency with which these larger events occur. The magnitude distribution of the database may potentially be influenced by accessibility to data, as it is likely that unreported damaging earthquakes not included in the database be on the lower side of the **M**4.0-5.5 range.

For those earthquakes for which numerical data is available, only earthquakes with magnitudes above around **M**4.7 appear to have caused 10,000 or more buildings to be

damaged, and very few values above 1,000 are observed below this magnitude as well. More than 2,000 destroyed buildings are observed only for magnitudes of almost **M4.8** and above. Six out of the 21 case-history earthquakes are associated with 10,000 damaged buildings or more: 1966 **M5.2** Tashkent, 1978 **M5.2** Albstadt (upper bound only), 1983 **M4.8** Liège, 1989 **M5.4** Newcastle, 1996 **M4.8** Épagny-Annecy, and 2002 **M4.8** Tbilisi. Only two of the case-histories are reported to have resulted in more than 2,000 destroyed buildings: 1966 **M5.2** Tashkent, for which the exact number and/or the extent of damage is not really known, and 2002 **M4.8** Tbilisi. The lack of proper seismic design, the poor quality of workmanship and construction materials and the existence of previous damage and/or weaknesses—due to settlements and/or preceding seismic events and/or armed conflicts—prior to the earthquake feature in both cases as having had an influence over the extent of the resulting damage.

Less than 10% of the earthquakes in the database are reported to have affected infrastructure, though it is noted that many sources used for its compilation do not often report damage to infrastructure explicitly and it is thus possible that the real number be larger. Of the 177 identified earthquakes, around 75% have magnitudes equal to or larger than **M5.0**. The 2002 **M5.1** Au Sable Forks (USA) case-study is an excellent example of an earthquake whose consequences to the road and electrical infrastructure appear to have accounted for a very large percentage of the overall monetary losses.

A similar proportion of earthquakes with magnitude above **M5.0** can be observed within the 158 earthquakes reported to have caused landslides. These 158 earthquakes are reported to have caused 339-393 deaths due to the landslides themselves and are associated with 577-871 deaths overall, including seven heart attacks. Liquefaction has been reported only for ten of the 1,960 earthquakes of the database, all of which had magnitudes equal to or larger than **M5.0** except for one, the 1996 **M4.8** Épagny-Annecy earthquake, which is reported to have caused only small-scale liquefaction at one of the ends of the airport's runway, in an area clearly prone to such phenomena. Apart from Épagny-Annecy, other five of the 21 case-studies are within the 10 earthquakes identified within the database as having caused liquefaction: **M5.1** Au Sable Forks Yes, involving geotechnical fillings and possibly influenced by a previous flood, **M5.0** Salò, after which a 30-cm fissure was attributed to lateral spreading due to liquefaction, **M5.4** Newcastle, for which no sand boils or mud volcanoes were observed but settlements of houses were attributed to liquefaction, **M5.4** Roermond for which sand boils were observed at three sites (though they did not cause structural damage), and **M5.4** Pyrgos, for which sandboils were observed and subsidence affected the extent of damage. A report for the **M5.4** Trinidad earthquake mentions a description of the ground seemingly rotating as a sign of possible liquefaction, but most likely being Rayleigh waves. As a consequence, the **M5.4** Trinidad case was not flagged as causing liquefaction in the database. Clearly above the upper-bound magnitude of **M5.5**, the **M5.8** Pawnee was reported to have caused sand blows at two or three locations.

Within the whole database it was possible to identify 55 earthquakes with reported fatal victims associated with deaths due to heart attacks (87-88 deaths). These represent around 15% of the earthquakes in the database associated with deaths and 2.7-3.8% of the number of deaths. In approximately 77% of these 55 earthquakes the only reported deaths were

those attributed to the heart attacks, while for six of these earthquakes the heart attacks were the only reported consequence found (*i.e.*, there were no further reports on damage, injuries or the occurrence of liquefaction or landslides). In view of this, a brief literature research was carried out to understand the extent to which heart attack deaths can be unequivocally linked to earthquakes. While some existing studies have identified a statistically significant increase in the number of cardiac-related deaths after an earthquake or a positive correlation between this number and epicentral distance or seismic intensity of the aftershock sequence, establishing an unambiguous connection between the occurrence of a small-to-medium magnitude earthquake and a heart attack appears to be difficult. Due to this, deaths reported as heart attacks, cardiorespiratory arrests, fright, or any similar wording were removed from the statistics presented in this report.

Apart from the aforementioned 87-88 heart attacks, the Database of Damaging Small-to-Medium Magnitude Earthquakes comprises a total of 2,307-3,125 deaths and 33,718-46,940 injuries. However, around 59% of the earthquakes caused neither injuries nor deaths. A further 27% caused no deaths but some injuries, while 4% caused some deaths but are not reported to have caused further injuries, and only around 10% reportedly caused both deaths and injuries. As would be expected, the number of earthquakes that have reportedly caused injuries and/or deaths increases progressively with magnitude. For example, 46 earthquakes with magnitudes $3.95 \leq M < 4.25$ are reported to have caused injuries, but the number of earthquakes with magnitudes in the range $5.25 \leq M < 5.55$ is over five times larger. The difference between these two extreme bins is bigger in the case of deaths, with 9 and 116-121 earthquakes reported to have caused fatalities in each case. The number of injuries and deaths caused by any individual earthquakes also tends to increase for increasing magnitudes. Very few earthquakes with magnitudes below **M4.5** are associated with more than 50 injuries or 10 total deaths. Albeit with some exceptions, outlying large numbers of injuries or deaths for the corresponding earthquake magnitudes are generally not associated with structural failures but rather to secondary effects or reasons such as cuts due to broken glass, scaping in panic, jumping off balconies or out of windows, landslides, or the collapse of mines. Based on the available information, structural failures account for 14.4 (lower bound) to 16.5% (upper bound) of the total number of deaths, although these values could be as large as 59.7-67.4%, if suspicions regarding the remaining cases—for which existing reports allow to infer structural failures as a cause—were true. Other causes of death apart from the aforementioned landslides, damage to mines and accidents occurred while escaping are falling objects/debris and a tsunami associated with a **M5.49** earthquake in Indonesia. Causes of death were not found for 14.0-24.7% of the deaths. Proportions change slightly when considering number of instances instead of number of deaths, with causes such as falling objects/debris, escaping and others acquiring somewhat greater prominence.

The 21 detailed case-history earthquakes studied herein can aid to achieve a deeper understanding of the specific features that may lead to deaths or injuries. The four total injuries associated with the **M4.8** Épagny-Annecy, **M5.7** Prague and **M5.0** Cushing earthquakes were reportedly due to broken glass (2), hitting the head while running outside (1) and a hand laceration of unknown origin (1), while the one death reported for the **M5.4** Pyrgos earthquake is that of an elderly woman trying to flee from a building. No deaths were

reported for any of those three earthquakes either, just as neither deaths nor injuries were reported for the **M4.8** Port Hueneme, **M5.1** Au Sable Forks, **M3.2** Basel, **M4.8** Guy-Greenbrier, **M5.4** Trinidad and **M3.6** Darmstadt earthquakes. For other earthquakes such as **M5.2** Tashkent, **M4.8** Liège, **M5.4** Roermond, **M4.8** Tbilisi and **M5.0** Salò, causes of death and/or injury appear as a mix of structural and non-structural reasons. Perhaps the most unusual within this group include at least one injured while attempting to prevent damage to paintings or furnishings (Salò) and four deaths due to intoxications with carbon monoxide after the collapse of chimneys (Liège). Within the remaining six cases (**M5.2** Albstadt, **M5.4** Newcastle, **M4.0** Folkestone, **M5.1** Lorca, **M5.8** Pawnee and **M3.9** Ischia), the collapse of parapets and a chimney as well as falling debris feature prominently alongside the collapse of walls and buildings. While the failure of structures is a clear cause of injuries and deaths in these examples and the database as a whole, the role played by the training of the population on how to react in case of an earthquake (*i.e.*, calmly, seeking protection, etc.) should not be underestimated.

Factors contributing to the extent of the damage observed that appeared repeatedly in the different case-studies include:

- the vulnerability of the building stock, often not designed to withstand earthquake loading, and/or built with poor-quality materials and workmanship, and/or lacking proper maintenance, and/or modified in time without the supervision of an engineer;
- the larger vulnerability of particular components of buildings, such as chimneys, parapets, suspended awnings (in the case of the Newcastle earthquake) and non-structural façades;
- the proximity of the hypocentre to the built environment;
- site amplification of ground motions.

Where a mix of older and newer building typologies were exposed to one of the 21 case-study earthquakes, a better performance of the more modern structures designed with some kind of earthquake-resistant philosophy was observed, with extreme exceptions usually due to design or construction flaws, such as the case of the collapse of a 10-year old reinforced concrete building during the **M5.1** Lorca earthquake due to short-column effect or the collapse of the 17-year-old auditorium of the Workers Club—later found to have suffered from significant structural deficiencies—during the **M5.4** Newcastle event.

The 21 case-study earthquakes shed some light as well over the need to interpret the number of damaged buildings with caution. Very prominent examples of this are the up to 2,000 damage claims resulting from the geothermally-induced 2006 **M3.2** Basel earthquake, or the up to 1,300 buildings reported damaged by the 2007 **M4.0** Folkestone earthquake. For the former, it is extremely difficult to prove whether the very minor non-structural damage observed was caused by seismic shaking or not, and it is thus misleading to refer to unverified insurance claims as ‘damage’. For the latter, most of the damage consisted of dislodgement/cracking/collapse of chimney clay pots and/or bricks, instances of damage to roof tiles and, rarely, roof structures, cracking/falling of plaster, and infrequent minor structural damage such as vertical cracking of walls and lintels, with very few falls of free-standing walls and partial collapses of house walls reported only within the most damaged

area. These two examples illustrate that large numbers of reported damaged buildings can refer to relatively mild damage. Moreover, the distinction between damaged and destroyed buildings made in the database should only be considered as indicative, as most sources do not describe in detail what is meant by one term or the other. Developed countries with low levels of natural seismicity tend to classify as damage what in many countries with higher seismic activity or many developing countries would not even receive attention. The media reflects this tendency quite clearly, often finding extensive non-structural damage being described as “destruction”, even when the structure has remained mostly unaffected. The seemingly objective numbers of the monetary losses should not be taken as the final word either, as these are usually estimations and it is often not clear what kind of losses they include. In the case of induced seismicity the relevance of the concept of “moral hazard”—which played a significant role in the number of insurance claims after the Basel earthquake—should not be overlooked, as societies tend to pay more attention to the consequences of earthquakes when the hazard is perceived as non-natural and, consequently, avoidable (e.g., Bommer *et al.*, 2015).

Along similar lines, plots of resulting damaged and destroyed buildings for the whole of the database should be handled with care. For example, of the 45 earthquakes for which the reported lower- and/or upper-bound number of destroyed buildings is larger than 1,000, all of which have magnitudes larger than 4.5, twelve (26.7%) are cases in which no actual number is specified in the source but it is reported that “some of” the damaged buildings would be better described as destroyed. Another eight (17.8%) of these 45 cases are not associated with an observed number of destroyed buildings but with an estimate by NOAA in the range of 100 to 1,000, which is very broad and, still, an estimate.

In closing, it is important to emphasise that while this work is of great value for providing a frame of reference for the management of induced seismic risk in the Groningen field, none of the cases can ever be considered a direct analogue. We therefore counsel against the use of such information as the basis for empirical risk assessments, supporting instead the development of analytical models for hazard and risk calibrated to data and measurements from Groningen. However, the results presented in this report provide a frame of reference for assessing the credibility of results of either scenario-based estimates of earthquake damage in Groningen or of dominant scenarios contributing to probabilistic risk estimates.

The present database is a key component of a statistical study carried out separately (Nievas *et al.*, 2017, 2019a, 2019b), in which the percentage of all the earthquakes that occur globally in the 4.0-5.5 magnitude range and sufficiently close to human settlements do have some kind of consequence has been investigated.

6. ACKNOWLEDGEMENTS

The authors would like to thank Dr. Anirudh Rao and Dr. Yen-Shin Chen for aiding with translations into English of some newspaper articles. The authors are grateful as well to Dr. Graeme Weatherill for his assistance in the use of the GEM Catalogue Toolkit https://github.com/GEMScienceTools/catalogue_toolkit. We also express our appreciation to Jens Skapski and all of the contributors to the Earthquake Impact Database, for making their valuable work available to the public through their website.

This work was funded by Nederlandse Aardolie Maatschappij B.V. (NAM) as part of the Study and Data Acquisition Program for induced seismicity in Groningen.

7. REFERENCES

7.1. Bibliography

- Adams, R. (2010). *Notes on the history of the International Seismological Centre*. Available online at: <http://www.isc.ac.uk/about/history/radams/>. Last accessed: 7th April 2018.
- Afshari, K. & J.P. Stewart (2016). Physically parametrised prediction equations for significant duration in active crustal regions. *Earthquake Spectra* **32**(4), 2057-2081.
- Aldama-Bustos, G., J.J. Bommer, C.H. Fenton & P.J. Stafford (2009). Probabilistic seismic hazard analysis for rock sites in the cities of Abu Dhabi, Dubai and Ra's Al Khaymah, United Arab Emirates. *Georisk* **3**(1), 1-29.
- Alexander, D. (1985). Death and injury in earthquakes. *Disasters* **9**(1), 57-60.
- Allen, T.I. (2012). *Stochastic ground motion prediction equations for southeastern Australian earthquakes using updated source and attenuation parameters*. Record 2012/69, Geoscience Australia, Canberra, Australia.
- Allen, T.I., K.D. Marano, P.S. Earle & D.J. Wald (2009a). PAGER-CAT: A composite earthquake catalog for calibrating global fatality models. *Seismological Research Letters* **80**(1), 1325–1345.
- Allen, T.I., D.J. Wald, P.S. Earle, K. D. Marano, A. J. Hotovec, K. Lin & M. G. Hearne (2009b). An Atlas of ShakeMaps and population exposure catalog for earthquake loss modeling. *Bulletin of Earthquake Engineering* **7**(3), 701–718.
- Atkinson, G.M. & I. Beresnev (1997). Don't call it stress drop. *Seismological Research Letters* **68**(1), 3-4.
- Bartels, S.A. & M.J. VanRooyen (2012). Medical complications associated with earthquakes. *The Lancet* **379**(9817), pp.748-757.
- Bazoukis, G., G. Tse, K.K. Naka, V. Kalfakakou, K. Vlachos, A. Saplaouras, K.P. Letsas, P. Korantzopoulos, C. Thomopoulos, P. Michelongona, X. Bazoukis, V. González-Salvado, T. Liu, L.K. Michalis, A. Baranchuk, T. Itoh, M. Efremidis, C. Tsioufis & S. Stavrakis (2018). Impact of major earthquakes on the incidence of acute coronary syndromes – A systematic review of the literature. *Hellenic Journal of Cardiology*, in press. <https://doi.org/10.1016/j.hjc.2018.05.005>
- Bernardi, F., M.G. Ciaccio, B. Palombo & G. Ferrari (2016). Moment tensor inversion of early instrumental data: application to the 1917 High Tiber Valley, Monterchi earthquake. *Annals of Geophysics* **59**(3), S0318, pp. 13.
- Bird, J.F. & J.J. Bommer (2004). Earthquake losses due to ground failure. *Engineering Geology* **75**(2), 147-179.
- Boatwright, J. (2007). The persistence of directivity in small earthquakes. *Bulletin of the Seismological Society of America* **97**(6), 1850–1861.
- Bock, G. (1997). *A Rapid Warning System for Earthquakes in the European-Mediterranean region*. GeoForschungsZentrum (GFZ) 1st Year Progress report, European Commission, DG XIII, 54-60.
- Bommer, J.J. & A. Martinez-Pereira (1999). The effective duration of earthquake strong motion. *Journal of Earthquake Engineering* **3**, 2, 127-172.

- Bommer, J.J. & D.M. Boore (2004). Engineering Seismology. *In: Encyclopaedia of Geology*, Academic Press, vol. 1, pp.499-514.
- Bommer, J.J. & H. Crowley (2017). The purpose and definition of the minimum magnitude limit in PSHA calculations. *Seismological Research Letters* **88**(4), 1097-1106.
- Bommer, J.J., H. Crowley & R. Pinho (2015). A risk-mitigation approach to the management of induced seismicity. *Journal of Seismology* **19**(2), 623–646.
- Bommer, J.J., J. Douglas & F.O. Strasser (2003). Style-of-faulting in ground motion prediction equations. *Bulletin of Earthquake Engineering* **1**(2), 171-203.
- Bommer, J.J., G. Georgallides & I.J. Tromans (2001). Is there a near-field for small-to-moderate magnitude earthquakes? *Journal of Earthquake Engineering* **5**(3), 395-423.
- Bommer, J.J., G. Magenes, J. Hancock & P. Penazzo (2004). The influence of strong-motion duration on the seismic response of masonry structures. *Bulletin of Earthquake Engineering* **2**(1), 1-26.
- Bommer, J.J., P.J. Stafford & J.E. Alarcón (2009). Empirical equations for the prediction of the significant, bracketed, and uniform duration of earthquake ground motion. *Bulletin of the Seismological Society of America* **99**(6), 3217-3233.
- Bommer, J.J. & J. van Elk (2017). Comment on “The maximum possible and the maximum expected earthquake magnitude for production-induced earthquakes at the gas field in Groningen, the Netherlands” by Gert Zöller and Matthias Holschneider. *Bulletin of the Seismological Society of America* **107**(3), 1564–1567.
- Boore, D.M. (2003). Simulation of ground motion using the stochastic method. *Pure & Applied Geophysics* **160**, 635-676.
- British Geological Survey (BGS) Earthquake Database. <http://www.earthquakes.bgs.ac.uk/earthquakes/dataSearch.html>. Last accessed: 5th September 2018.
- Brown, D.L. (1999). Disparate effects of the 1989 Loma Prieta and 1994 Northridge earthquakes on hospital admissions for acute myocardial infarction: importance of superimposition of triggers. *American Heart Journal* **137**(5), 830-836.
- Brzev S., C. Scawthorn, A.W. Charleson, L. Allen, M. Greene, K. Jaiswal & V. Silva (2013). *GEM building taxonomy version 2.0*. GEM Technical Report 2013-02 V1.0.0, 188 pp., GEM Foundation, Pavia, Italy, doi: 10.13117/GEM.EXP-MOD.TR2013.02.
- Business Standard (2015). *Toll in Nepal quakes reaches 8,502*. https://www.business-standard.com/article/news-ians/toll-in-nepal-quakes-reaches-8-502-115051501298_1.html. Last accessed: 5th September 2018.
- Caridi, P. (2011). *I terremoti di 1975 e 1978 nello Stretto di Messina: quelle scosse così forti ma dimenticate da tutti (The earthquakes of 1975 and 1978 in the Strait of Messina: such strong shocks forgotten by everyone, in Italian)*. Available online at: <http://www.meteoweb.eu/2011/12/i-terremoti-di-1975-e-1978-nello-stretto-di-messina-quelle-scosse-cosi-forti-ma-dimenticate-da-tutti/100743/>. Last accessed: 15th November 2018.
- Center for International Earth Science Information Network - CIESIN - Columbia University, United Nations Food and Agriculture Programme - FAO, and Centro Internacional de Agricultura Tropical - CIAT (2005). *Gridded Population of the World, Version 3 (GPWv3)*. Palisades, NY: NASA Socioeconomic Data and Applications Center (SEDAC). <http://dx.doi.org/10.7927/H4639MPP>.

Center for International Earth Science Information Network - CIESIN - Columbia University (2016). *Gridded Population of the World, Version 4 (GPWv4)*. Palisades, NY: NASA Socioeconomic Data and Applications Center. <http://dx.doi.org/10.7927/H4NP22DQ>.

Chan, C., J. Elliott, R. Troughton, C. Frampton, D. Smyth, I. Crozier & P. Bridgman (2013). Acute myocardial infarction and stress cardiomyopathy following the Christchurch earthquakes. *PloS one* **8**(7), e68504.

Chan, C.W.-H. (2015). *Acute cardiac admissions after natural disasters - Insight from the Christchurch earthquakes*. Thesis, Master of Medical Science, University of Otago. Retrieved from: <http://hdl.handle.net/10523/5628>. Last accessed: 8th April 2018.

Chen, Y., J. Letort, F. Cotton & S. Drouet (2014). High-frequency directivity effects: evidence from analysis of the Les Saintes records. *Journal of Seismology* **18**(3), 457-466.

Console, R. & A. Sonaglia (1972). Studio del terremoto di Toscana (A study of the earthquake occurred in Toscana, February 1971, in Italian). *Annals of Geophysics* **25**(3), 367-390.

Cornell, C.A. (1968). Engineering seismic risk analysis. *Bulletin of the Seismological Society of America* **58**(5), 1583-1606.

Dahm, T., D. Becker, M. Bschoegg, S. Cesca, B. Dost, R. Frisch, S. Hainzl, C.D. Klose, D. Kühn, S. Lasocki, Th. Meier, M. Ohrnberger, E. Rivalta, U. Wegler & S. Husen (2013). Recommendation for the discrimination of human-related and natural seismicity. *Journal of Seismology* **17**(1), 197-202.

Daily News and Analysis India (2016). *Moderate quake jolts Nepal, 15 injured*. <http://www.dnaindia.com/world/report-52-magnitude-quake-jolts-nepal-2174475>. Last accessed: 5th September 2018.

Dangkua, D.T. & C.H. Cramer (2011). Felt intensity versus instrumental ground motion: A difference between California and Eastern North America? *Bulletin of the Seismological Society of America* **101**(4), 1847-1858.

Denham, D. (1992). Intraplate earthquakes – why? *Proceedings of the Australian Earthquake Engineering Society Conference*. Available online at: <https://aees.org.au/wp-content/uploads/2013/11/Page-03-Denham.pdf>. Last accessed: 7th November 2018.

Di Giacomo, D., I. Bondár, D.A. Storchak, E.R. Engdahl, P. Bormann & J. Harris (2015). ISC-GEM: Global Instrumental Earthquake Catalogue (1900–2009), III. Re-computed M_s and m_b , proxy M_w , final magnitude composition and completeness assessment. *Physics of the Earth and Planetary Interiors* **239**, 33-47.

Dominique, P., A. Evans, B. Le Brun, J.L. Nédélec, T. Winter, N. Zornette, C. Mirgon & M. Imbault (2008). *Plan de prévention des risques naturels prévisibles - PPR de la commune d'Epagny - Premier livret: Présentation (Natural risk prevention plan for the communes of Epagny – PPR of the Commune of Epagny – First book: Presentation, in French)*. Bureau des recherches Géologiques et Minières (BRGM), 84 pp.

Dufumier, H. (2002). Synthesis of magnitude and focal mechanism computations for the $M \geq 4.5$ earthquakes in France for the period 1995-2000. *Journal of Seismology* **6**, 163–181.

Dziewonski, A.M., T.-A. Chou & J. H. Woodhouse (1981). Determination of earthquake source parameters from waveform data for studies of global and regional seismicity. *Journal of Geophysical Research* **86**, 2825-2852.

Earthquake-Report (2015a). *Moderate earthquake - Kavre, Nepal on May 10, 2015*. <https://earthquake-report.com/2015/05/10/moderate-earthquake-kavre-nepal-on-may-10-2015/>. Last accessed: 5th September 2018.

Earthquake-Report (2015b). *Strong aftershock in Nepal*. <https://earthquake-report.com/2015/05/02/moderate-earthquake-nepal-on-may-2-2015/>. Last accessed: 5th September 2018.

Edwards, B., A. Rietbrock, J.J. Bommer & B. Baptie (2008). The acquisition of source, path and site effects from micro-earthquake recordings using Q tomography: applications to the UK. *Bulletin of the Seismological Society of America* **98**(4), 1915-1935.

Edwards, B., T. Kraft, C. Cauzzi, P. Kästli & S. Wiemer (2015). Seismic monitoring and analysis of deep geothermal projects in St Gallen and Basel, Switzerland. *Geophysical Journal International* **201**, 1022-1039.

Ekström, G., M. Nettles & A. M. Dziewonski (2012). The global CMT project 2004-2010: Centroid-moment tensors for 13,017 earthquakes. *Physics of the Earth and Planetary Interiors* **200-201**, 1-9.

EPRI (1989). *Engineering characterization of small-magnitude earthquakes*. EPRI Report NP-6389, Electric Power Research Institute, Palo Alto, California,

EPRI (2005). *Use of minimum CAV in determining effects of small magnitude earthquakes on seismic hazard analyses*. EPRI Report 1012965, Electric Power Research Institute and US Department of Energy.

FEMA (2000). *Prestandard and commentary for the seismic rehabilitation of buildings*. Report No. 356. Federal Emergency Management Agency, Washington DC

FEMA (2003) *HAZUS-MH MR4 Technical Manual*, Federal Emergency Management Agency. http://www.fema.gov/media-library-data/20130726-1716-25045-6422/hazus_mr4_earthquake_tech_manual.pdf

Foulger, G.R., M.P. Wilson, J.G. Gluyas, B.R. Julian & R.J. Davies (2018). Global review of human-induced earthquakes. *Earth-Science Reviews* **178**, 438-514. Database available online at: <http://inducedearthquakes.org/>. Last accessed: 29th June 2018.

FXTOP (2018). *Historical rates*. <http://fxtop.com/en/historical-exchange-rates.php>. Last accessed: 7th November 2018.

Gabrichidze, G., G. Lomidze, T. Mukhadze, A. Odisharia & I. Timchenko (2004). April 2002 epicentral earthquake in Tbilisi, Georgia. *Proceedings of the 13th World Conference on Earthquake Engineering*, August 1-6, Vancouver, B.C., Canada. Available online at (last accessed 30th October 2017): http://www.iitk.ac.in/nicee/wcee/article/13_1063.pdf.

Galloway, B., J. Hare, D. Brunson, P. Wood, B. Lizundia & M. Stannard (2014). Lessons from the post-earthquake evaluation of damaged buildings in Christchurch. *Earthquake Spectra* **30**(1), 451-474.

Gardner, J. K. & L. Knopoff (1974). Is the sequence of earthquakes in Southern California, with aftershocks removed, Poissonian? *Bulletin of the Seismological Society of America* **64**(5), 1363-1367.

Geoscience Australia (GA) - Commonwealth of Australia (2018) Earthquake Catalogue. <https://earthquakes.ga.gov.au/>. Last accessed: 5th September 2018.

- Giardini, D., G. Grünthal, K.M. Shedlock & P. Zhang (1999). The GSHAP global seismic hazard map. *Annali di Geofisica* **42**(6), 1225-1230. Data available at: <http://www.seismo.ethz.ch/static/gshap/>.
- Government of Nepal - National Seismological Centre. *Earthquake catalogue*. <http://seismonepal.gov.np/earthquakes>. Last accessed: 5th September 2018.
- Green, R.A. & J.J. Bommer (2018). What is the smallest earthquake magnitude that can trigger liquefaction? *Earthquake Spectra*, under review.
- Grünthal, G. (ed.) (1998). *European Macroseismic Scale 1998 (EMS-98)*. Cahiers du Centre Europeen de Geodynamique et de Seismologie 15, Centre Europeen de Geodynamique et de Seismologie, Luxembourg.
- Gülkan, P. (2000). Building code enforcement prospects: the failure of public policy. *Earthquake Spectra*: **16**(1), 351-374.
- Gurenko, E. & D. Dumitru (2009). *Mitigating the adverse financial effects of natural hazards on the economies of Central Asia. A study of catastrophe risk financing options*. Available at: http://siteresources.worldbank.org/FINANCIALSECTOR/Resources/CACDRM-Component2_CatRiskFinancingReport.pdf. Last assessed 28th September 2017.
- Gutenberg, B. & C.F. Richter (1944). Frequency of earthquakes in California. *Bulletin of the Seismological Society of America* **34**, 185-188.
- Hanks T, Kanamori H (1979) A magnitude moment scale. *Journal of Geophysical Research* **84**, 2348-2351.
- Holzer, T.L., A.S. Jayko, E. Hauksson, J.P.B. Fletcher, T.E. Noce, M.J. Bennett, C.M. Dietel, K.W. Hudnut (2010). Liquefaction caused by the 2009 Olancho, California (USA), **M5.2** earthquake. *Engineering Geology* **116**, 184-188.
- Hough, S.E. (2014). Shaking from injection-induced earthquakes in Central and Eastern United States. *Bulletin of the Seismological Society of America* **104**(5), 2619-2626.
- Hutchings, R. (1987). *Soviet secrecy and non-secrecy*. Barnes & Noble Books, Totowa, New Jersey, USA.
- Ibrion, M., M. Mokhtari, F. Parsizadeh & F. Nadim (2015). Timescape of the earthquake disasters in Iran: the intricacies of earthquake time and earthquake disaster risk reduction. *Geografiska Annaler: Series A, Physical Geography* **97**(1), 197-216.
- Instituto Nacional de Defensa Civil (INDECI) Sismos ocurridos en Perú a través del tiempo (Earthquakes that have occurred in Peru through time). Available online at: https://www.indeci.gob.pe/compend_estad/2006/7_otras_estad/7.1_sismos/7.1.4_hist_sismos.pdf. Last accessed 31st October 2018.
- Instituto Geográfico Nacional (IGN). *Spanish earthquake catalogue*. <http://www.ign.es/web/ign/portal/sis-catalogo-terremotos>. Last accessed: 5th September 2018.
- International Seismological Centre. ISC Bulletin. <http://www.isc.ac.uk/iscbulletin/search/>. Last accessed: 5th September 2018.
- Kario, K., B.S. McEwen & T.G. Pickering (2003). Disasters and the heart: a review of the effects of earthquake-induced stress on cardiovascular disease. *Hypertension Research* **26**(5), 355-367.
- Kloner, R.A. (2006). Natural and unnatural triggers of myocardial infarction. *Progress in cardiovascular diseases* **48**(4), 285-300.

Klose, C.D. (2007). Geomechanical modeling of the nucleation process of the 1989 Newcastle earthquake in Australia. *Earth and Planetary Science Letters* **256**, 547–553.

Kramer, S.L. (1996). *Geotechnical Earthquake Engineering*. Prentice Hall.

Leor, J. & R.A. Kloner (1996). The Northridge earthquake as a trigger for acute myocardial infarction. *The American journal of cardiology* **77**(14), 1230-1232.

Leor, J., W.K. Poole & R.A. Kloner (1996). Sudden cardiac death triggered by an earthquake. *New England Journal of Medicine* **334**(7), 413-419.

Li, T., M.F. Cai & M. Cai (2007). A review of mining-induced seismicity in China. *International Journal of Rock Mechanics & Mining Sciences* **44**, 1149–1171.

Live Hindustan (2015). *Four days after the earthquake, four people died in Bihar (in Hindi)*. <https://www.livehindustan.com/news/national/article1-Bihar-earthquake:-State-shaken-by-fresh-5.7-magnitude-quake-480452.html>. Last accessed: 5th September 2018.

Manchuel, K., P. Traversa, D. Baumont, M. Cara, E. Nayman & C. Durouchoux (2018). The French seismic CATalogue (FCAT-17). *Bulletin of Earthquake Engineering* **16**, 2227-2251.

Mignan, A., C. Jiang, J. Zechar, S. Wiemer, Z. Wu & Z. Huang (2013). Completeness of the mainland China earthquake catalog and implications for the setup of the China earthquake forecast testing center. *Bulletin of the Seismological Society of America* **103**(2A), 845-859.

Musson, R.M.W. & I. Cčić (2002). Macroseismology. In: International Handbook of Earthquake and Engineering Seismology, W.H.K. Lee, H. Kanamori, P.C. Jennings and C. Kisslinger (eds.), *International Geophysics* **81**: Part A, 49, 807-822.

Musson, R.M.W. & I. Cčić (2012). Intensity and intensity scales. In: Bormann, P. (Ed.), *New Manual of Seismological Observatory Practice 2 (NMSOP-2)*, Potsdam: Deutsches GeoForschungsZentrum GFZ, p. 1-41.

Musson, R.M.W., G. Grünthal & M. Stucchi (2010). The comparison of macroseismic intensity scales. *Journal of Seismology* **14**, 413-428.

My Republica (Nepal Republic Media) (2016). *Five injured in stampede during earthquake*. <http://admin.myrepublica.com/feature-article/story/40261/five-injured-in-stampede-during-earthquake.html>. Last accessed: 5th September 2018.

Nagarik News (2016). *Earthquake with epicentre in Gorkha, people run helter-skelter in the middle of the night (in Nepali)*. <http://archive.nagariknews.com/society/nation/story/56812.html>. Last accessed: 5th September 2018.

News X (2017). *Two earthquakes jolt Nepal on Monday*. <https://www.newsx.com/world/57143-two-earthquakes-jolt-nepal-on-monday>. Last accessed: 5th September 2018.

Nievas, C.I., J.J. Bommer & H. Crowley (2017). *Global occurrence and impact of small-to-medium magnitude earthquakes: a statistical analysis*. Report for the Nederlandse Aardolie Maatschappij BV (NAM), The Netherlands.

Nievas, C.I., J.J. Bommer & H. Crowley (2019a). *Global occurrence and impact of small-to-medium magnitude earthquakes: a statistical analysis – Version 2*. Report for the Nederlandse Aardolie Maatschappij BV (NAM), The Netherlands.

Nievas, C.I., J.J. Bommer, H. Crowley & J. van Elk (2019b). Global occurrence and impact of small-to-medium magnitude earthquakes: A statistical analysis. *Bulletin of Earthquake Engineering*, under review.

Petersen, M.D., A.D. Frankel, S.C. Harmsen, C.S. Mueller, K.M. Haller, R.L. Wheeler, R.L. Wesson, Y. Zeng, O.S. Boyd, D.M. Perkins, N. Luco, E.H. Field, C.J. Wills & K.S. Rukstales (2008). *Documentation for the 2008 update of the United States national seismic hazard maps*, USGS Open-File Report 2008-1128, US Geological Survey, Reston, VA. 61 pp.

Petersen, M.D., C.S. Mueller, M.P. Moschetti, S.M. Hoover, A.M. Shumway, D.E. McNamara, R.A. Williams, A.L. Llenos, W.L. Ellsworth, A.J. Michael, J.L. Rubinstein, A.F. McGarr & K.S. Rukstales (2017). 2017 one-year seismic-hazard forecast for the Central and Eastern United States from induced and natural earthquakes. *Seismological Research Letters* **88**(3), 772-783.

RADIUS (Zigong) Workgroup (1999). *Radius case study in Zigong, China*. Report for the United Nations Office for Disaster Risk Reduction. Available online at (last accessed 30th March 2018): https://www.unisdr.org/files/2724_Zigongreportrevised.pdf.

Rasskazovsky, V. & K. Abdurashidov (1969). Restoration of stone buildings after earthquake. *Proceedings of the Fourth World Conference on Earthquake Engineering*. Santiago de Chile.

RCN Radio (2017). *Temblor tumbó techo en cárcel Las Mercedes (Earthquake knocked down roof in Las Mercedes jail, in Spanish)*. <https://www.rcnradio.com/colombia/temblor-tumbo-techo-carcel-las-mercedes>. Last accessed: 21st November 2018.

Reiter, L. (1990). *Earthquake Hazard Analysis: Issues and Insights*. Columbia University Press, New York. 254 pp.

Rodríguez, C.E., J.J. Bommer & R.J. Chandler (1999). Earthquake-induced landslides 1980-1997. *Soil Dynamics & Earthquake Engineering* **18**(5), 325-346.

Rodriguez-Marek, A., P.P. Kruiver, P. Meijers, J.J. Bommer, B. Dost, J. van Elk & D. Doornhof (2017). A regional site-response model for the Groningen gas field. *Bulletin of the Seismological Society of America* **107**(5), 2067-2077.

Rovida, A., M. Locati, R. Camassi, B. Lolli & P. Gasperini (2016). *CPTI15, the 2015 version of the Parametric Catalogue of Italian Earthquakes*. doi:<http://doi.org/10.6092/INGV.IT-CPTI15>.

Salukvadze, J. & O. Golubchikov (2016). City as a geopolitics: Tbilisi, Georgia—A globalizing metropolis in a turbulent region. *Cities* **52**, 39-54.

Sargeant, S.L., R. Lawley, P.J. Stafford, G. Weatherill, A-J.S. Weston, J.J. Bommer, P. Burton, M. Free, R.M.W. Musson & T. Rossetto (2008). The felt effects of the Folkstone, UK, earthquake of 28 April 2007. *Seismological Research Letters* **79**(5), 672-687.

Schwarz, J., S. Beinersdorf, H. Meidow & L. Ahorner (2010). *Magnitudenorientierter Erdbebenkatalog für deutsche und angrenzende Gebiete EK DAG - erweiterter Ahorner-Katalog (Magnitude-oriented earthquake catalog for Germany and adjacent areas EK DAG – extended Ahorner catalog, in German)*. Tech. rep., Bauhaus University, Weimar, Germany. Available online: <https://www.edac.biz/projekte/erdbebenkatalog/kontakt-download/>. Last accessed: 31st October 2018.

Scordilis, E.M. (2006). Empirical global relations converting M_s and m_b to moment magnitude. *Journal of Seismology* **10**, 225-236.

Search and Rescue Dog Handlers Academy of Nepal (SAR Dogs Nepal) at Twitter (2015). <https://twitter.com/sardogsnepal/status/594465740788404224>. Last accessed: 5th September 2018.

Servicio Geológico Colombiano (SGC). *Colombian seismic catalogue (in Spanish)*. <https://www2.sgc.gov.co/sgc/sismos/Paginas/catalogo-sismico.aspx>. Last accessed: 5th September 2018.

Servicio Sismológico Nacional (SSN) Mexican seismic catalogue. <http://www2.ssn.unam.mx:8080/catalogo/>. Last accessed: 5th September 2018.

Sieberg, A. (1930). Geologie der Erdbeben, *Handbuch der Geophysik* **2**(4), 552-555

Sims, J. (2007). Natural disasters and the role of women. In Stoltman, J. P., J. Lidstone & L. M. DeChano (eds.): *International perspectives on natural disasters*. Springer, Dordrecht, The Netherlands.

Siswadi, A. (2019). *This is the source of the Pangalengan earthquake (in Indonesian)*. Tempo.co. Available online at: <https://tekno.tempo.co/read/1169530/ini-sederet-potensi-bencana-sepanjang-puncak-musim-hujan>. Last accessed: 28th January 2019.

Storchak, D.A., D. Di Giacomo, I. Bondár, E. R. Engdahl, J. Harris, W.H.K. Lee, A. Villaseñor & P. Bormann (2013). Public release of the ISC-GEM Global Instrumental Earthquake Catalogue (1900-2009). *Seismological Research Letters* **84**(5), 810-815.

Suzuki, S., S. Sakamoto, T. Miki, *et al.* (1995). Hanshin-Awaji earthquake and acute myocardial infarction. *The Lancet* **345**(981), 974-977.

Tanaka, F., S. Makita, T. Ito, T. Onoda, K. Sakata & M. Nakamura (2015). Relationship between the seismic scale of the 2011 northeast Japan earthquake and the incidence of acute myocardial infarction: a population-based study. *American Heart Journal* **169**(6), 861-869.

The Himalayan Times (2017). *One dies in tremor in Dhading*. <https://thehimalayantimes.com/nepal/one-dies-tremor-dhading/>. Last accessed: 5th September 2018.

The Kathmandu Post (2015a). *One dies in latest aftershock*. <http://kathmandupost.ekantipur.com/news/2015-05-10/one-dies-in-latest-aftershock.html>. Last accessed: 5th September 2018.

The Kathmandu Post (2015b). *Tremor triggers landslides in Barpak*. <http://kathmandupost.ekantipur.com/news/2015-05-02/tremor-triggers-landslides-in-barpak.html>. Last accessed: 5th September 2018.

Tosi, P., P. Sbarra, V.D. Rubeis & C. Ferrari (2015). Macroseismic intensity assessment method for web questionnaires. *Seismological Research Letters* **86**(3), 985–990.

Trichopoulos, D., X. Zavitsanos, K. Katsouyanni, A. Tzonou & P. Dalla-Vorgia (1983). Psychological stress and fatal heart attack: the Athens (1981) earthquake natural experiment. *The Lancet* **321**(8322), 441-444.

Umbria 24 (2017). *Terremoto, scossa di magnitudo 4.1: crolli e danni nello Spolefino (Earthquake of magnitude 4.1: collapses and damage in Spolefino, in Italian)*. <http://www.umbria24.it/attualita/terremoto-nuova-forse-scossa-nel-cuore-della-notte>. Last accessed: 21st November 2018.

United States Geological Survey (2017a). *Preliminary finite fault results for the Apr 25, 2015 Mw 7.8 28.1300,84.6500 earthquake (Version 1)*. <https://earthquake.usgs.gov/earthquakes/eventpage/us20002926#finite-fault>. Last accessed: 5th September 2018.

- United States Geological Survey (2017b). *Preliminary finite fault results for the May 12, 2015 Mw 7.3 27.8428,86.1535 earthquake (Version 1)*.
<https://earthquake.usgs.gov/earthquakes/eventpage/us20002ejl#finite-fault>. Last accessed: 5th September 2018.
- Varazanashvili, O., N. Tsereteli, S. Adamia, N. Butikashvili & T. Mukhadze (2008). Seismotectonic features of the April 25, 2002 Tbilisi, Georgia earthquake (Ms=4.6). *Journal of the Georgian Geophysical Society* **12**(A), 33–45.
- Wald, D.J., P.S. Earle, T.I. Allen, K. Jaiswal, K. Porter & M. Hearne (2008). Development of the U.S. Geological Survey's PAGER system (Prompt Assessment of Global Earthquakes for Response). *Proceedings of the 14th World Conference on Earthquake Engineering*. Beijing, China, 8 pp.
- Weatherill, G. A. (2014). *OpenQuake Hazard Modeller's Toolkit - User Guide*. Global Earthquake Model (GEM), Technical Report.
- Weatherill, G.A., M. Paganì & J. García (2016). Exploring earthquake databases for the creation of magnitude-homogeneous catalogues: tools for application on a regional and global scale. *Geophysical Journal International* **206**, 1652–1676. WPG16v3c World Catalogue version of 21st July 2017, pers. comm..
- Woessner, J., D. Giardini, H. Crowley, F. Cotton, G. Grünthal, G. Valensise, R. Arvidsson, R. Basili, M. B. Demircioglu, S. Hiemer, C. Meletti, R. W. Musson, A. N. Rovida, K. Sesetyan, M. Stucchi & The SHARE Consortium (2015). The 2013 European Seismic Hazard Model: Key Components and Results. *Bulletin of Earthquake Engineering* **13**(12), 3553–3596. Website of the project: <http://www.share-eu.org/>. Data available online at: <http://www.efehr.org/en/home/>.
- Worden, C.B., M.C. Gerstenberger, D.A. Rhoades & D.J. Wald (2012). Probabilistic relationships between ground-motion parameters and Modified Mercalli Intensity in California. *Bulletin of the Seismological Society of America* **102**(1), 204–221.
- Worden, C.B., E.M. Thompson, M. Hearne & D.J. Wald (2017). *ShakeMap V4 Manual: technical manual, user's guide, and software guide*. United States Geological Survey. Available online at: <http://usgs.github.io/shakemap/>.
- Worden, C.B. & D. Wald (2016). ShakeMap Manual Release. *United States Geological Survey*. 109 pp.
- Wright, J.R. (1971). *Industrialized building in the Soviet Union*. Report of the U.S. Delegation to the U.S.S.R. National Bureau of Standards Special Publication 334, Washington D.C.
- Wyss, M. & G. Trendafiloski (2009). Trends in the casualty ratio of injured to fatalities in earthquakes. *Second International Workshop on Disaster Casualties*, University of Cambridge, 15–16 June, United Kingdom.
- Youngs, R.R., W.J. Arabasz, R.E. Anderson, A.R. Ramelli, J.P. Ake, D.B. Slemmons, J.P. McCalpin, D.I. Doser, C.J. Fridrich, F.H. Swan, A.M. Rogers, J.C. Yount, L.W. Anderson, K.D. Smith, R.L. Bruhn, P.L.K. Knuepfer, R.B. Smith, C.M. dePolo, D.W. O'Leary, K.J. Coppersmith, S.K. Pezzopane, D.P. Schwartz, J.W. Whitney, S.S. Olig & G.R. Toro (2003). A methodology for probabilistic fault displacement hazard analysis (PFDHA). *Earthquake Spectra* **19**(1), 191–219.
- Zezen, N. & L. Dinggen (1988). Seismic performance of strengthened buildings in 1985 Zigong, Sichuan earthquake. *Proceedings of the Ninth World Conference on Earthquake Engineering*, August 2–9, Tokyo-Kyoto, Japan. Available online at (last accessed 30th March 2018): http://www.iitk.ac.in/nicee/wcee/article/9_vol7_433.pdf.

7.2. Web references

Amateur Seismic Centre (ASC): www.asc-india.org.

Breaking The News (2017). *Iran earthquake injures 57, kills 1*. Available online at: <https://www.breakingthenews.net/iran-earthquake-injures-57-kills-1/news/details/41604422?ts=1514380546366>. Last accessed: 20th December 2018.

Cambridge Earthquake Impact Database: <http://www.ceqid.org/CEQID/Home.aspx>.

Colombian Geological Service (Servicio Geológico Colombiano) earthquake search: <http://200.119.88.135/RSNC/index.php/consultas/consulexp>. Last accessed: 5th April 2018.

Desinventar Database: <http://www.desinventar.org/en/database>. Last accessed: 30th April 2018.

Did You Feel It? (DYFI): <https://earthquake.usgs.gov/data/dyfi/>. Last accessed: 30th April 2018.

Earthquake Impact Database (EID):

Facebook page: <https://www.facebook.com/earthquakeimpactdatabase/>. Last accessed: 27th March 2018.

Database files:

https://docs.google.com/spreadsheets/d/1oveZ42OLdJFnKu2aZfMg4aV1AR_OgHftxRm-65bJw4w/edit#gid=0. Last accessed: 5th January 2018 (year 2017), 22nd November 2017 (years 2013-2016).

Earthquake-Report: <https://earthquake-report.com/>. Last accessed: 27th March 2018.

Earthquake-Report (2013a). *Strong earthquake in Eastern Uzbekistan damages buildings*. Available online at: <https://earthquake-report.com/2013/05/24/strong-earthquake-eastern-uzbekistan-on-may-24-2013/>. Last accessed: 29th November 2018.

Earthquake-Report (2013b). *Moderate earthquake in Western Turkey (near Bursa) – Panic caused many injuries*. Available online at: <https://earthquake-report.com/2013/08/17/moderate-earthquake-western-turkey-on-august-17-2013/>. Last accessed: 20th December 2018.

Earthquake-Report (2016). *150 people injured due to an earthquake in Awassa, Ethiopia*. Available online at: <https://earthquake-report.com/2016/01/24/moderate-earthquake-ethiopia-on-january-24-2016-2/>. Last accessed: 20th December 2018.

Eastday.com (2016). *4.4 earthquake in Dianjiang, Chongqing, strikes historical area. No aftershock activity recorded (in Chinese)*. Available online at: <http://news.eastday.com/s/20160811/u1ai9622345.html>. Last accessed: 28th January 2019.

El Telégrafo (2011). *Earthquake in Quito caused cracks in houses and landslides (in Spanish)*. Available online at: <https://www.eltelegrafo.com.ec/noticias/informacion/1/sismo-de-4-grados-sacudio-quito>. Last accessed: 20th December 2018.

EM-DAT – The Emergency Events Database (Université Catholique de Louvain, Brussels, Belgium; Cred. Prof. Dr. D. Guha-Sapir): <http://www.emdat.be/>. Last accessed: 15th April 2018.

Fergana News (Фергана) (2006). *Tashkent earthquake. Legends and facts of 26 April 1966 (in Russian)*. [http://www.\(Fergana News 2006\).com/articles/4367](http://www.(Fergana News 2006).com/articles/4367). Last accessed: 29th November 2018.

GEM Earthquake Consequences Database: <https://gemecd.org/>.

Geo-Storm (2013) Tashkent earthquake of 1966 (in Russian). Available online at: <http://geo-storm.ru/priroda-i-klimat/stihii/tashkentskoe-zemletrjasenie-1966-goda/>. Last accessed: 29th November 2018.

Global Centroid Moment Tensor Project (GCMT): <http://www.globalcmt.org>. Last accessed: 9th May 2018.

Global Rural-Urban Mapping Project (GRUMP): <http://sedac.ciesin.columbia.edu/data/collection/grump-v1>

Google Maps APIs: <https://developers.google.com/maps/>.

International Disaster Database: <http://www.emdat.be/>

International Seismological Centre (ISC):

Main website: <http://www.isc.ac.uk/>. *Internatl. Seismol. Cent.*, Thatcham, United Kingdom, 2014.

History: <http://www.isc.ac.uk/about/history/>.

Online Bulletin: <http://www.isc.ac.uk/iscbulletin/search/>.

Iran Front Page (2017). *Mild earthquake in Tehran, Alborz kills 1, wounds 75*. Available online at: <https://ifpnews.com/exclusive/mild-quake-tehran-alborz-kills-1-wounds-75/>. Last accessed: 20th December 2018.

Munich Re's NatCatSERVICE: <http://www.munichre.com/natcatservice>

National Geophysical Data Center / World Data Service (NGDC/WDS): Significant Earthquake Database. National Geophysical Data Center, National Oceanic and Atmospheric Administration (NOAA). DOI:10.7289/V5TD9V7K. <https://www.ngdc.noaa.gov/hazard/earthqk.shtml>. Last accessed: 15th April 2018.

Nederlandse Aardolie Maatschappij BV (NAM) research reports: <https://www.nam.nl/feiten-en-cijfers/onderzoeksrapporten.html#iframe=L2VtYmVkl2NvbXBvbmVudC8/aWQ9b25kZXJ6b2Vrc3JhchHBvcnRlbg==>. Last accessed: 30th April 2018.

News.am (2017). *One killed, several injured in Iran earthquake*. Available online at: <https://news.am/eng/news/428739.html>. Last accessed: 20th December 2018.

ReliefWeb (United Nations Office for the Coordination of Humanitarian Affairs): <https://reliefweb.int/>.

ReliefWeb (1991). *Yemen Earthquake Nov 1991 UNDRO Situation Reports 1-5*. Available online at: <https://reliefweb.int/report/yemen/yemen-earthquake-nov-1991-undro-situation-reports-1-5>. Last accessed: 25th January 2019.

ReliefWeb (2005a). *China: Earthquake OCHA Situation Report No. 1*. Available online at: <https://reliefweb.int/report/china/china-earthquake-ocha-situation-report-no-1-3>. Last accessed: 25th January 2019.

ReliefWeb (2005b). *China: Earthquake OCHA Situation Report No. 2*. Available online at: <https://reliefweb.int/report/china/china-earthquake-ocha-situation-report-no-2-2>. Last accessed: 25th January 2019.

RIA Novosti (PIA Новости) (2016). *Tashkent earthquake (1966) (in Russian)*. Available online at: <https://ria.ru/spravka/20160426/1419855458.html>. Last accessed: 29th November 2018.

South China Morning Post (1997). *Thousands homeless after earthquake*. Available online at: <https://www.scmp.com/article/213469/thousands-homeless-after-quake>. Last accessed: 4th February 2019.

United States Geological Survey (USGS): <https://earthquake.usgs.gov/earthquakes/search/>.

World Housing Encyclopedia. www.world-housing.net

Xinhua Net (2015). *A woman dies in the minor quake in Nepal's Kavre district*. http://www.xinhuanet.com/english/2015-05/06/c_134215552.htm. Last accessed: 5th September 2018.

7.3. Other resources

When no external source is indicated for a map, it is implied that it was elaborated by the authors of the present report, using either of these two software:

- QGIS free and open source Geographic Information System: <http://qgis.org/>.
- The Generic Mapping Tools (GMT) open source collection: <http://gmt.soest.hawaii.edu/>.
Academic reference:
Wessel, P. & W.H. Smith (1998). New, improved version of Generic Mapping Tools released. *Eos, Transactions American Geophysical Union* **79**(47), 579-579.

In maps elaborated with QGIS or GMT, shapefiles of countries' administrative boundaries are from:

- DIVA-GIS: <http://www.diva-gis.org/gdata>.
- GADM: <https://gadm.org/data.html>.

In maps elaborated with QGIS, world maps data comes from either of these two sources:

- OpenStreetMap: <https://www.openstreetmap.org>.
- OpenCycleMap: <https://www.opencyclemap.org>.

When no external source is indicated for a beachball showing the focal mechanism, it is implied that it was elaborated by the authors of the present report, using the OpenQuake Hazard Modeller's Toolkit (Weatherill, 2014). Academic reference:

Weatherill, G. A. (2014). *OpenQuake Hazard Modeller's Toolkit - User Guide*. Global Earthquake Model (GEM), Technical Report.

I. APPENDIX I: The Database of Damaging Small-to-Medium Magnitude Earthquakes

The pages that follow contain a description of the fields that make up the Database of Damaging Small-to-Medium Magnitude Earthquakes compiled within the context of this work. Further explanations and examples regarding how it was compiled can be found in Chapter 2 of this report.

The fields of the database are the following:

- 1) **Date (UTC)**
- 2) **Time (UTC)**
- 3) **Country**
- 4) **Name/Location**
- 5) **Latitude of epicentre**
- 6) **Longitude of epicentre**
- 7) **Depth (km)**
- 8) **Mw**: moment magnitude.
- 9) **Mw (alt)**: an alternative estimate of moment magnitude, if more than one value of moment magnitude is found in the literature.
- 10) **ML**: local (Richter) magnitude.
- 11) **mb**: body-wave magnitude.
- 12) **Ms**: surface-wave magnitude.
- 13) **Munk**: unknown magnitude scale. There are cases in which the reports of damage are not clear in stating the magnitude scale reported. The NOAA database of significant earthquakes, for example, contains events for which the magnitude scale is marked as unknown. For events added from the Earthquake Impact Database (EID), this column contains the values of magnitude reported therein.
- 14) **Mw case**: Source of the moment magnitude values reported, in order, first for Mw, then for Mw (alt). Agencies' acronyms as listed in the ISC Bulletin. "Direct" and "proxy" used with ISC-GEM, WPG16, CPTI15 and FACT-17 sources to indicate direct calculation or calculation via other parameters. "Converted from [original scale]=[value in original

scale]” implies that the conversion into moment magnitude was conducted using the models described in Section 2.3.

- 15) Max. Intensity:** Modified Mercalli Intensity (MMI), unless specified otherwise. Caution is needed when intensities are below IV as they are likely to be erroneous, given that the first degrees of MMI do not imply damage or even the fall of objects. Whenever detailed studies of macroseismic intensity were readily available, the reported maximum intensity corresponds to these. In all other cases this column refers to values from the USGS ShakeMaps or reported in the ISC Bulletin or any other relevant agency. Possible intensity scales other than MMI are:

EMS-98: European Macroseismic Scale (Grünthal, 1998)

MSK-64: Medvedev-Sponheuer-Karnik scale (Medvedev *et al.*, 1965)

MCS: Mercalli-Cancani-Sieberg scale (Sieberg, 1932), predecessor of the MMI and used in Italy, for example.

GOST-52: official seismic scale used in the Soviet Union until 1995, consisting of macroseismic intensities VI through IX of the GEOFIAN seismic scale of Medvedev (1953) (Gorshkov & Shenkareva, 1960).

- 16) Induced Flag:** If “I”, the earthquake has been reported as having an anthropogenic origin.
- 17) Exposed Population:** In most cases, the values reported correspond to the population estimated to have been exposed to MMI equal to or larger than IV (according to EXPO-CAT, Allen *et al.*, 2009, or PAGER). In some cases, particularly for older events, the values are those reported by the sources as being the population of the most affected localities.
- 18) Total Affected:** As the definition of “affected” can be subjective, this column contains the number of people reported as “affected” in the sources, where this exact term has been used.
- 19) Total Deaths:** The number of people reported as having died due to the earthquake, either directly or indirectly, related to ground shaking or not. The kinds of deaths include, but are not limited to, deaths due to the collapse of structures, the fall of non-structural components, heart attacks, running in panic, and landslides.
- 20) Shaking Deaths:** The number of people reported to have died as a consequence of the behaviour of engineering structures (including non-structural components) during the earthquake, but not due to secondary effects (such as landslides), panic reactions or heart attacks. By definition, this number is equal to or smaller than that of Total Deaths.

- 21) Injured:** The number of people reported as injured. The causes of the injuries can be any, including panic reactions, landslides, and, of course, the behaviour of engineered structures.
- 22) Homeless:** The number of people whose residences have been damaged beyond repair.
- 23) Evacuated:** The number of people who have left their residences due to the earthquake. This number may include those that can safely return after structural inspections have been carried out to determine the integrity of the buildings.
- 24) Causes of Death/Injury:** Not all deaths and injuries should be interpreted as being due to the failure of buildings. This field aims at clarifying the circumstances under which the casualties occurred. Apart from the structural failure of buildings, common causes of death/injury include falling objects and/or non-structural elements, heart attacks, landslides, cuts with broken glass and accidents occurred while reacting in panic to the shaking (falling, jumping out of windows, hitting heads against walls while running, stampedes, etc). "Panic reactions" in this field should, thus, not be interpreted as post-traumatic consequences of the earthquake but as the latter. The keyword "PAGERshaking" implies that no sources specifying the cause of the deaths were found, but that they were listed as shaking deaths in PAGER-CAT (Allen *et al.*, 2009a). "possibly due to structural failures" implies that the causes of death were not found but the extent of the damage observed suggests that structural failures is the likely cause. If the extent of the damage was not totally clear from the sources so as to make such an inference, causes of death were left as unknown.
- 25) Buildings Damaged:** The number of buildings reported as damaged. For earthquakes retrieved from the EID by means of the algorithm described in Section 2.9 and for which specific numbers of damaged and destroyed buildings were not reported therein, damage levels were converted into damaged and destroyed buildings as per the equivalences shown in Table 2.4.
- 26) Buildings Destroyed:** The number of buildings reported as destroyed. For earthquakes retrieved from the EID by means of the algorithm described in Section 2.9 and for which specific numbers of damaged and destroyed buildings were not reported therein, damage levels were converted into damaged and destroyed buildings as per the equivalences shown in Table 2.4.

Note that the number of damaged and destroyed buildings should be interpreted with care, as most of the sources used for the compilation of the database do not provide sufficient information about the damage states observed. Of the many factors that may influence the consideration or not of a building as damaged, its location is probably one of the main ones. In more developed countries, what is reported as damaged buildings is more often the damage claims, while in developing countries what is referred to as damaged buildings will more often be more significantly damaged (*e.g.*, cracks would

not be referred to as damage). In countries with censorship (for example, ex-Soviet nations), these numbers are unlikely to be accurate.

The keyword “Some of” is used in this field to denote that *some of* the buildings enumerated as damaged were destroyed, though the exact number is unknown.

- 27) Economic Loss:** In United States dollars at the time of the earthquake, unless specified otherwise.
- 28) Infrastructure Affected:** If Y (yes), reports have been found stating that either transportation, electricity, telephone, internet, gas, water, and/or sewage networks, as well as healthcare facilities, were affected, even if momentarily or with minor damage.
- 29) Landslides:** If Y (yes), reports have been found stating the occurrence of landslides, rockslides, mudslides or snow avalanches.
- 30) Liquefaction:** If Y (yes), reports have been found stating the occurrence of liquefaction.
- 31) Clustering:** By means of different keywords, this field indicates whether the event should be considered a main shock (MS, this includes events that are not part of clusters), a foreshock (FS), an aftershock (AS) or part of a swarm (SWARM), the latter implying a series of earthquakes of relatively similar magnitude that are not an aftershock sequence of a larger main shock. If AS or FS are followed by the ID of another earthquake of the database, the named earthquake is the corresponding main shock. If AS or FS are followed by NULL, the corresponding main shock is not part of the damaging database due to its magnitude being too large. If followed by ND, the corresponding main shock is not part of the damaging database because, despite lying within the magnitude range of interest, it has not been found to have caused any damage. This could be due to different reasons: (i) the original damage report might be assigning all damage and casualties to an aftershock even though both aftershock and main shock caused damage, but it is difficult to separate the effects of the two (*i.e.*, cumulative damage); (ii) the locations and depths were such that the main shock was sufficiently distant from urbanised areas but an aftershock/foreshock was not; (iii) a misclassification of the event due to the inherent limitations of the clustering algorithm. If SWARM is followed by the ID of other earthquakes in the database, the latter are earthquakes that belong to the same cluster. Square brackets (*e.g.*, [AS]) indicate that the classification is that resulting from the declustering algorithm and no manual verification has been carried out. This field should be interpreted together with **Consequences**.
- 32) Consequences:** The purpose of this column is to convey whether the consequences reported for an event were only caused by said event or if they were related to others. A detailed discussion can be found in Chapter 2, the following being a summary of possible contents of this field:

Additional damage: The damage reported occurred after a previous event had already caused damage in the same area.

Additional damage likely: The sources do not explicitly mention the occurrence of damage over an already damaged area, but visual inspection of the characteristics of past events suggests that this is likely.

Pre-weakened: This is very similar to “additional damage”. The difference lies in the level of damage observed in the previous event. “Pre-weakened” would make reference to cases in which previous events are suspected to have caused minor damage, and that this minor damage had an influence on the consequences of the second event being larger than could have been. “Additional damage” is then reserved to more explicit and significant damage having been observed during the first event, or cases in which separate reports exist for each event.

Seem separate: The consequences appear to be due only to the earthquake listed, within reasonable limits.

Possibly of many: The consequences are likely to be due to more than one earthquake.

Of many: Same as above, but with a higher level of certainty.

Of [number]: The number makes reference to the number of events believed to have caused the consequences reported.

Includes aftershocks/foreshocks: The earthquake in the database is a main shock, but the consequences correspond as well to at least one of the aftershocks/foreshocks.

May include aftershocks/foreshocks: When the aforementioned is suspected, but not found explicitly stated.

Includes main shocks: The earthquake in the database is a foreshock or an aftershock, but the consequences correspond as well to the main shock. This is more common for foreshocks, as for aftershocks it is more common to find the main shock being reported with its consequences covering some of the aftershocks.

Nothing: Nothing is stated.

33) Comments: Any additional information that might be of relevance for interpreting the characteristics of a particular earthquake.

34) NOAA deaths: If Y (yes), the range given in the “Total Deaths” column is an estimation made by NOAA whenever actual values were not available in their sources. See explanation below and Table A1.1

- 35) NOAA injuries:** If Y (yes), the range given in the “Injured” column is an estimation made by NOAA whenever actual values were not available in their sources. See explanation below and Table A1.1
- 36) NOAA damaged:** If Y (yes), the range given in the “Buildings Damaged” column is an estimation made by NOAA whenever actual values were not available in their sources. See explanation below and Table A1.1
- 37) NOAA destroyed:** If Y (yes), the range given in the “Buildings Destroyed” column is an estimation made by NOAA whenever actual values were not available in their sources. See explanation below and Table A1.1
- 38) NOAA economic:** If Y (yes), the range given in the “Economic Loss” column is an estimation made by NOAA whenever actual values were not available in their sources. See explanation below and Table A1.1
- 39) From EID:** If Y (yes), the earthquake has been incorporated from the Earthquake Impact Database, as per the procedure described in Section 2.9. Data on damage and casualties has been taken at face value from EID, and the entry has been associated with an event from the ISC Bulletin by means of an automatic computer code designed for this purpose.

A reported number of 0 (zero) implies that sources have been found sustaining zero is the corresponding number, while an empty field implies that no explicit statements have been found. For example, many reports say “15 injured”, but do not say anything about deaths. While it would be possible to infer that if injuries have been reported but deaths have not then there were probably no deaths, the fields have been left blank. This is even more important for the case of the potential difference between total deaths and shaking deaths. In many cases it is not possible to know the causes of the deaths and, consequently, whether the number of shaking deaths is equal to the number of total deaths. In these cases, the number has been reported under “Total Deaths”, without specifying anything under “Shaking Deaths”.

Deaths, injuries, monetary losses, damaged and destroyed buildings reported in terms of standard ranges correspond to estimates made by NOAA whenever actual values were not available in their sources, as per the criteria described in Table A1.1. Other ranges reported in the database that do not conform to this scheme correspond to different estimates found in different sources for a particular earthquake. The columns “NOAA deaths”, “NOAA injuries”, “NOAA damaged”, “NOAA destroyed” and “NOAA economic” indicate whether the values shown correspond to estimates from the NOAA database. Monetary losses estimated by NOAA correspond to 1990 United States dollars (*i.e.*, not at the time of occurrence of the earthquake).

Table A1.1. Ranges of deaths, injuries, damaged buildings and destroyed buildings (left) as well as monetary losses (right) used by the Significant Earthquakes Database of the National Centers for Environmental Information of the National Oceanic and Atmospheric Administration (NOAA).

Code	Description	Range	Code	Description	Range (USD)
0	None	0	0	None	0
1	Few	~ 1 - 50	1	Limited	~ <1,000,000
2	Some	~ 50 - 100	2	Moderate	~ 1,000,000 - 5,000,000
3	Many	~ 100 - 1,000	3	Severe	~ 5,000,000 - 25,000,000
4	Very Many	~ >1,000	4	Extreme	~ >25,000,000

To download the database:

The Database of Damaging Small-to-Medium Magnitude Earthquakes can be downloaded from the NAM website:

<https://nam-onderzoeksrapporten.data-app.nl/reports/download/groningen/en/e4fd80e4-2e86-495c-97a4-d00954abcdff>

References

Earthquake Impact Database (EID):

Facebook page: <https://www.facebook.com/earthquakeimpactdatabase/>. Last accessed: 27th March 2018.

Database files:

https://docs.google.com/spreadsheets/d/1oveZ42OLdJFnKu2aZfMg4aV1AR_OgHftxRm-65bJw4w/edit#gid=0. Last accessed: 5th January 2018 (year 2017), 22nd November 2017 (years 2013-2016).

Gorshkov, G.P. & G.A. Shenkareva (1960). On the correlation of seismic scales – USSR. *Transactions of the Institute of Earth Physics of the Academy of Sciences USSR* 1(168), 44-64. Translation into English by the United States Joint Publications Research Service, New York, USA. Available online at: <http://www.dtic.mil/dtic/tr/fulltext/u2/a362451.pdf>. Last accessed: 20th February 2018.

Medvedev, S.V. (1953). A new seismic scale. *Transactions of the Institute of Earth Physics of the Academy of Sciences USSR* 21, 110.

Medvedev, S., W. Sponheuer & V. Karnik (1965). *Seismic intensity scale, MSK 1964*. Academy of Sciences of the U.S.S.R., Soviet Geophysical Community, 13 pp.

Sieberg, A. (1932). Geologie der Erdbeben. *Handbuch der Geophysik* 2(4), 550-555.

II. APPENDIX II: Damage and Macroseismic Intensity Scales

Macroseismic intensity scales are only described herein in terms of their relationship with vulnerability classes and damage scales. For full descriptions of the intensity scales please refer to the original publications.

A2.1 The European Macroseismic Scale (EMS-98)

The European Macroseismic Scale (EMS-98; Grünthal, 1998) classifies structures into six vulnerability classes labelled from A (most vulnerable) through F (least vulnerable). For each kind of structure, a most likely vulnerability class and a probable and less-probable range are given, as per Figure A2.1.1.

Type of Structure		Vulnerability Class					
		A	B	C	D	E	F
MASONRY	rubble stone, fieldstone	○					
	adobe (earth brick)	○—					
	simple stone	—○					
	massive stone		—○—				
	unreinforced, with manufactured stone units	—○—					
	unreinforced, with RC floors		—○—				
	reinforced or confined			—○—			
REINFORCED CONCRETE (RC)	frame without earthquake-resistant design (ERD)		—○—				
	frame with moderate level of ERD			—○—			
	frame with high level of ERD				—○—		
	walls without ERD		—○—				
	walls with moderate level of ERD			—○—			
	walls with high level of ERD				—○—		
STEEL	steel structures			—○—			
WOOD	timber structures		—○—				

○ most likely vulnerability class; — probable range;
 range of less probable, exceptional cases

Figure A2.1.1. Classification of structural typologies into vulnerability classes. From Grünthal (1998).

Damage is classified into five grades, defined separately for masonry and reinforced concrete buildings. Figures A2.1.2 and A2.1.3, extracted from Grünthal (1998), define said damage grades.






Classification of damage to masonry buildings	
	<p>Grade 1: Negligible to slight damage (no structural damage, slight non-structural damage) Hair-line cracks in very few walls. Fall of small pieces of plaster only. Fall of loose stones from upper parts of buildings in very few cases.</p>
	<p>Grade 2: Moderate damage (slight structural damage, moderate non-structural damage) Cracks in many walls. Fall of fairly large pieces of plaster. Partial collapse of chimneys.</p>
	<p>Grade 3: Substantial to heavy damage (moderate structural damage, heavy non-structural damage) Large and extensive cracks in most walls. Roof tiles detach. Chimneys fracture at the roof line; failure of individual non-structural elements (partitions, gable walls).</p>
	<p>Grade 4: Very heavy damage (heavy structural damage, very heavy non-structural damage) Serious failure of walls; partial structural failure of roofs and floors.</p>
	<p>Grade 5: Destruction (very heavy structural damage) Total or near total collapse.</p>

Figure A2.1.2. Definition of EMS-98 damage grades for masonry buildings. From Grünthal (1998).

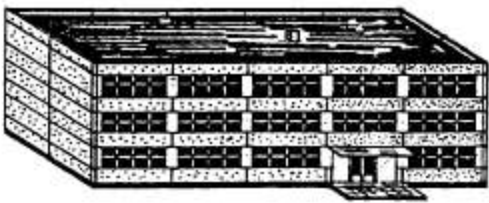
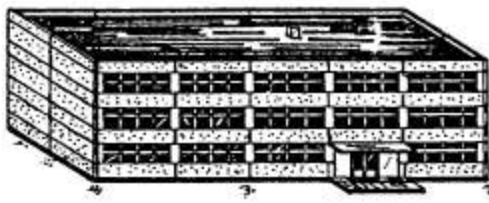

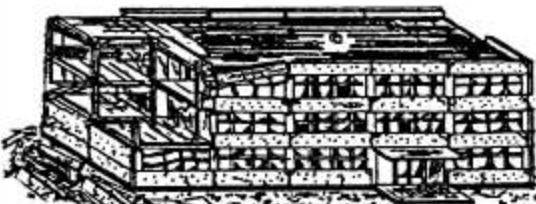

Classification of damage to buildings of reinforced concrete	
	<p>Grade 1: Negligible to slight damage (no structural damage, slight non-structural damage) Fine cracks in plaster over frame members or in walls at the base. Fine cracks in partitions and infills.</p>
	<p>Grade 2: Moderate damage (slight structural damage, moderate non-structural damage) Cracks in columns and beams of frames and in structural walls. Cracks in partition and infill walls; fall of brittle cladding and plaster. Falling mortar from the joints of wall panels.</p>
	<p>Grade 3: Substantial to heavy damage (moderate structural damage, heavy non-structural damage) Cracks in columns and beam column joints of frames at the base and at joints of coupled walls. Spalling of concrete cover, buckling of reinforced rods. Large cracks in partition and infill walls, failure of individual infill panels.</p>
	<p>Grade 4: Very heavy damage (heavy structural damage, very heavy non-structural damage) Large cracks in structural elements with compression failure of concrete and fracture of rebars; bond failure of beam reinforced bars; tilting of columns. Collapse of a few columns or of a single upper floor.</p>
	<p>Grade 5: Destruction (very heavy structural damage) Collapse of ground floor or parts (e. g. wings) of buildings.</p>

Figure A2.1.3. Definition of EMS-98 damage grades for reinforced concrete (RC) buildings.
From Grünthal (1998).

Depending on the number of buildings that fall into each damage grade, macroseismic intensities can then be assigned. EMS-98 intensities I through IV imply no damage, and intensities V and above relate to damage grades and vulnerability classes as described in Table A2.1.1. Definitions for “few”, “many” and “most” are given in Figure A2.1.4.

Table A2.1.1. Relation between macroseismic intensity levels and number of buildings of different vulnerability classes suffering from different damage grades in EMS-98 (Grünthal, 1998).

EMS-98 Intensity	Description
V (Strong)	Damage of grade 1 to a few buildings of vulnerability class A and B.
VI (Slightly damaging)	Damage of grade 1 is sustained by many buildings of vulnerability class A and B; a few of class A and B suffer damage of grade 2; a few of class C suffer damage of grade 1.
VII (Damaging)	Many buildings of vulnerability class A suffer damage of grade 3; a few of grade 4. Many buildings of vulnerability class B suffer damage of grade 2; a few of grade 3. A few buildings of vulnerability class C sustain damage of grade 2. A few buildings of vulnerability class D sustain damage of grade 1.
VIII (Heavily damaging)	Many buildings of vulnerability class A suffer damage of grade 4; a few of grade 5. Many buildings of vulnerability class B suffer damage of grade 3; a few of grade 4. Many buildings of vulnerability class C suffer damage of grade 2; a few of grade 3. A few buildings of vulnerability class D sustain damage of grade 2.
IX (Destructive)	Many buildings of vulnerability class A sustain damage of grade 5. Many buildings of vulnerability class B suffer damage of grade 4; a few of grade 5. Many buildings of vulnerability class C suffer damage of grade 3; a few of grade 4. Many buildings of vulnerability class D suffer damage of grade 2; a few of grade 3. A few buildings of vulnerability class E sustain damage of grade 2.
X (Very destructive)	Most buildings of vulnerability class A sustain damage of grade 5. Many buildings of vulnerability class B sustain damage of grade 5. Many buildings of vulnerability class C suffer damage of grade 4; a few of grade 5. Many buildings of vulnerability class D suffer damage of grade 3; a few of grade 4. Many buildings of vulnerability class E suffer damage of grade 2; a few of grade 3. A few buildings of vulnerability class F sustain damage of grade 2.
XI (Devastating)	Most buildings of vulnerability class B sustain damage of grade 5. Most buildings of vulnerability class C suffer damage of grade 4; many of grade 5. Many buildings of vulnerability class D suffer damage of grade 4; a few of grade 5. Many buildings of vulnerability class E suffer damage of grade 3; a few of grade 4. Many buildings of vulnerability class F suffer damage of grade 2; a few of grade 3.
XII (Completely devastating)	All buildings of vulnerability class A, B and practically all of vulnerability class C are destroyed. Most buildings of vulnerability class D, E and F are destroyed.

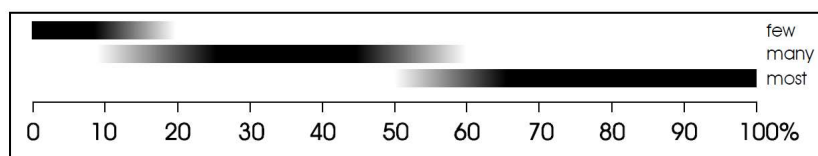


Figure A2.4. Definitions of quantity in EMS-98. From Grünthal (1998).

A2.2 The Medvedev-Sponheuer-Karnik scale (MSK-64)

The Medvedev-Sponheuer-Karnik scale (MSK-64; Medvedev *et al.*, 1965) defines three structural typologies, as per Table A2.2.1, and five damage grades, as per Table A2.2.2.

Table A2.2.1. Structural typologies as per MSK-64 scale (Medvedev *et al.*, 1965).

Structural typologies	Description
Type A	Buildings in field-stone, rural structures, adobe houses, clay houses.
Type B	Ordinary brick buildings, buildings of the large block and prefabricated type, half-timbered structures (<i>i.e.</i> , load-bearing timber frames with infills), buildings in natural hewn stone.
Type C	Reinforced buildings, well-built wooden structures.

Table A2.2.2. Classification of damage as per MSK-64 scale (Medvedev *et al.*, 1965).

Damage grades		Damage description
Grade 1	Slight damage	Fine cracks in plaster; fall of small pieces of plaster.
Grade 2	Moderate damage	Small cracks in walls; fall of fairly large pieces of plaster; pantiles slip off; cracks in chimneys; parts of chimneys fall down.
Grade 3	Heavy damage	Large and deep cracks in walls; fall of chimneys.
Grade 4	Destruction	Gaps in walls; parts of buildings may collapse; separate parts of the buildings lose their cohesion; inner walls and filled-in walls of the frame collapse.
Grade 5	Total damage	Total collapse of buildings.

Similar to EMS-98, macroseismic intensities are assigned as a function of the number of buildings that fall into each damage grade, quantities being defined in Table A2.2.3. MSK-64 intensities I through IV imply no damage, and intensities V and above relate to damage grades and vulnerability classes as described in Table A2.2.4.

Table A2.2.3. Definitions of quantity in MSK-64 (Medvedev *et al.*, 1965).

Descriptor	Meaning
Single, few	About 5%
Many	About 50%
Most	About 75%

Table A2.2.4. Relation between macroseismic intensity levels and number of buildings of different vulnerability classes suffering from different damage grades in the MSK-64 scale. From Medvedev et al. (1965).

MSK-64 Intensity	Description
V (Awakening)	Slight damage of grade 1 in buildings of type A possible.
VI (Frightening)	Damage of grade 1 is sustained in single buildings of type B and in many of type A. Damage in a few buildings of type A is of grade 2.
VII (Damage to buildings)	Many buildings of type C suffer damage of grade 1; in many buildings of type B damage is of grade 2. Many buildings of type A suffer damage of grade 3, few of grade 4.
VIII (Destruction of buildings)	Many buildings of type C suffer damage of grade 2, few of grade 3. Many buildings of type B suffer damage of grade 3 and a few of grade 4, and many buildings of type A suffer damage of grade 4 and a few of grade 5.
IX (General damage to buildings)	Many buildings of type C suffer damage of grade 3, a few of grade 4. Many buildings of type B suffer damage of grade 4 and a few of grade 5, and many buildings of type A suffer damage of grade 5.
X (General destruction of buildings)	Many buildings of type C suffer damage of grade 4, a few of grade 5. Many buildings of type B suffer damage of grade 5. Most buildings of type A suffer damage of grade 5.
XI (Catastrophe)	Severe damage even to well-built buildings, bridges, water dams and railway lines.
XII (Landscape changes)	Practically all structures above and below ground are greatly damaged or destroyed.

A2.3 The Modified Mercalli Intensity scale (MMI)

The classification of structural typologies in the Modified Mercalli Intensity scale (Richter, 1958) focuses only on four types of masonry, which are described in Table A2.3.1.

Table A2.3.1. Structural typologies as per the MMI scale (Richter, 1958).

Structural Typologies	Description
Masonry A	Good workmanship, mortar, and design; reinforced, especially laterally, and bound together by using steel, concrete, etc.; designed to resist lateral forces.
Masonry B	Good workmanship and mortar; reinforced, but not designed in detail to resist lateral forces.
Masonry C	Ordinary workmanship and mortar; no extreme weaknesses like failing to tie in at corners, but neither reinforced nor designed against horizontal forces.
Masonry D	Weak materials, such as adobe; poor mortar; low standards of workmanship; weak horizontally.

Modified Mercalli intensities equal to or below V do not imply damage to buildings, while intensities VI and above relate to the damage suffered by different typologies of masonry as described in Table A2.3.2. The Modified Mercalli scale does not define damage grades.

Table A2.3.2. Relation between macroseismic intensity levels and the damage sustained by different typologies of masonry, according to Richter (1958).

MMI Scale	Description
VI	Weak plaster and masonry D cracked.
VII	Damage to masonry D, including cracks. Weak chimneys broken at roof line. Fall of plaster, loose bricks, stones, tiles, cornices (also unbraced parapets and architectural ornaments). Some cracks in masonry C.
VIII	Damage to masonry C; partial collapse. Some damage to masonry B; none to masonry A. Fall of stucco and some masonry walls. Twisting, fall of chimneys, factory stacks, monuments, towers, elevated tanks. Frame houses moved on foundations if not bolted down; loose panel walls thrown out.
IX	Masonry D destroyed; masonry C heavily damaged, sometimes with complete collapse; masonry B seriously damaged. (General damage to foundations.) Frame structures, if not bolted, shifted off foundations.
X	Most masonry and frame structures destroyed with their foundations. Some well-built wooden structures and bridges destroyed.

References

Grünthal, G. (ed.) (1998). *European Macroseismic Scale 1998 (EMS-98)*. Cahiers du Centre Europeen de Geodynamique et de Seismologie 15, Centre Europeen de Geodynamique et de Seismologie, Luxembourg.

Medvedev, S., W. Sponheuer & V. Karnik (1965). *Seismic intensity scale, MSK 1964*. Academy of Sciences of the U.S.S.R., Soviet Geophysical Community, 13 pp.

Richter, C.F. (1958). *Elementary seismology*. W. H. Freeman and Company, San Francisco and London, viii + 768 pp.

III. APPENDIX III: Case histories of induced earthquakes

A3.1 December 2006 M3.2 Basel Earthquake, Switzerland

This earthquake occurred on 8th December 2006, at 16.48 UTC (17.48 local time), right under the city of Basel, northern Switzerland, six days after the start of the injection of a large volume of water at high pressures for the creation of an enhanced geothermal system (EGS) for the Deep Heat Mining Project in said city. It was the largest of a series of events that were induced in the area, and was preceded by a M_L 2.6 event that occurred in the early morning of the same day, and which led to the premature halt of the injection, and by a M_L 2.7 event in the afternoon. The creaking of woodwork and rattling of doors and windows caused by the main shock alarmed the population, though consequent damage was limited mostly to hairline cracks. The geothermal project was finally cancelled in December 2009.

A3.1.1 Tectonic and seismic setting

A3.1.1.1 Tectonic setting

Basel is located in the triple frontier comprising Switzerland, France and Germany, in the southern end of the Upper Rhine Graben, which is part of the European Cenozoic rift system (Häring *et al.*, 2008). It is limited to the east by the tabular Jura, which is related to the extensional movements of the graben (Laubscher, 2001), and to the south by the folded Jura, associated to the Alpine compression (Ferry *et al.*, 2005). The overall seismotectonic regime of Switzerland is related to the collision of the African and the European plates (Wiemer *et al.*, 2009), whose average total convergence rate is around 0.9-0.94 cm/year (Giardini *et al.*, 2004).

The stress field in the southern end of the Upper Rhine Graben is characterised by an overall strike-slip regime (Häring *et al.*, 2008). The average direction of the regional maximum compressive horizontal stress is around N144 (Deichmann & Ernst, 2009, reporting results of Kastrup, 2004) to N162 (Plenefisch & Bonjer, 1997), *i.e.*, it corresponds to a NNW-SSE orientation.

Given that Switzerland lies in a transition zone between areas of high and low seismicity in Europe, its tectonic structure is quite complex (Wiemer *et al.*, 2009). Several authors report a predominance of strike-slip and normal mechanisms (*e.g.*, Deichmann & Ernst, 2009) within the seismic catalogues, but the faults system in the area around Basel is far more heterogeneous and involves a large variety of mechanisms and orientations, as can be observed in Figure A3.1.1 and Figure A3.1.2. The distinction between active and inactive faults and the determination of the deformation rates of the former are some of the most difficult issues associated to defining the tectonics of this area.

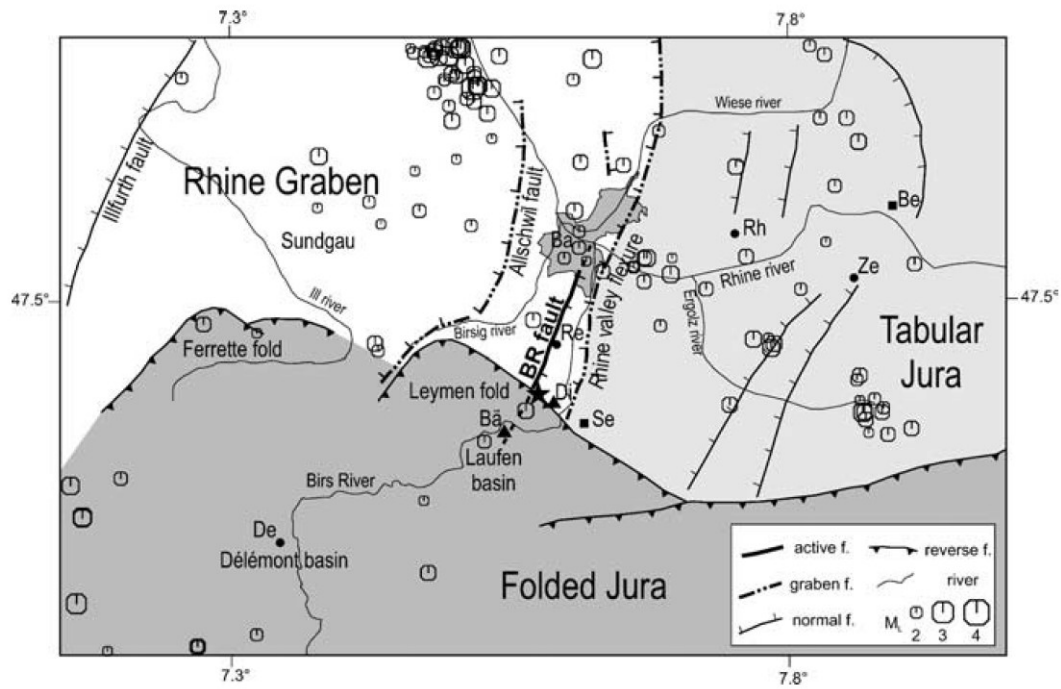


Figure A3.1.1. Seismotectonic setting of the southern end of the Upper Rhine Graben. BR: Basel-Reinach fault. Ba: Basel. Fault mechanisms shown as indicated in embedded legend. (Ferry *et al.*, 2005).

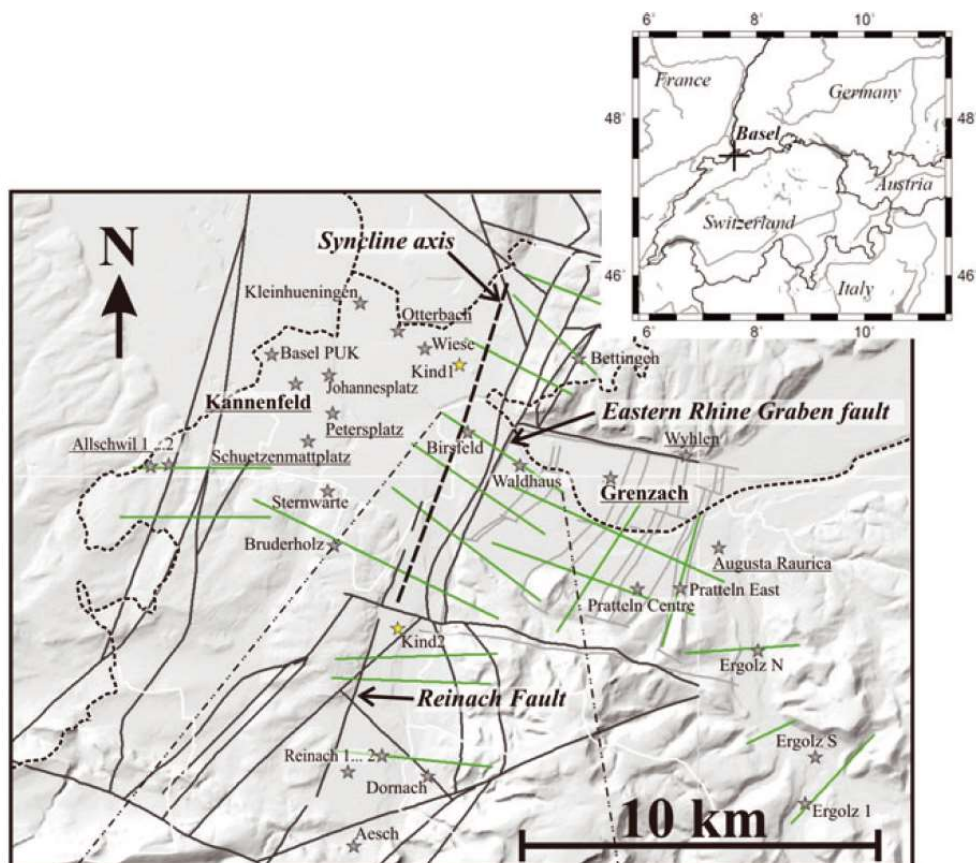


Figure A3.1.2. Seismotectonic setting of the southern Upper Rhine Graben. Dashed lines: country borders. White lines: Basel canton borders. Dark grey lines: main graben structure. Light grey lines: graben and horst structure. (Ignore green lines) (Havenith *et al.*, 2007).

A3.1.1.2 Regional and local seismicity

The area of the Upper Rhine Graben presents one of the highest seismic activity rates in Switzerland (Becker *et al.*, 2002). It sees persistent small-to-moderate seismicity and infrequent destructive events (Häring *et al.*, 2008; Wiemer *et al.*, 2009). According to the website of the Swiss Seismological Service (SED), approximately ten earthquakes with M_L between 3 and 4 occur per year in Switzerland, while an earthquake with M_L of at least 5 usually occurs every 10-20 years, and earthquakes with M_L larger than or equal to 6 occur every 100-150 years. The M_L 6.5-6.9 earthquake which severely damaged the city of Basel in 1356 is the largest known to have occurred in central-northern Europe (Häring *et al.*, 2008; Majer *et al.*, 2007). The exact return period of an event like this is not clear. Giardini *et al.* (2004) and the Swiss Seismological Service report it to be around 1,000-1,500 years, while Becker *et al.* (2002) believe it is more likely to be around 1,500-3,000 years instead.

The map in Figure A3.1.3 shows the epicentres of relevant earthquakes observed around the Basel area, while the plots in Figure A3.1.4 show the strongest earthquake magnitude and the number of earthquakes with M_L larger than 2.5 observed per year between 1975 and 2012. It is noted that the years 2006 and 2007 do not present neither the largest magnitudes nor the largest number of events with M_L larger than 2.5 of the last decades.

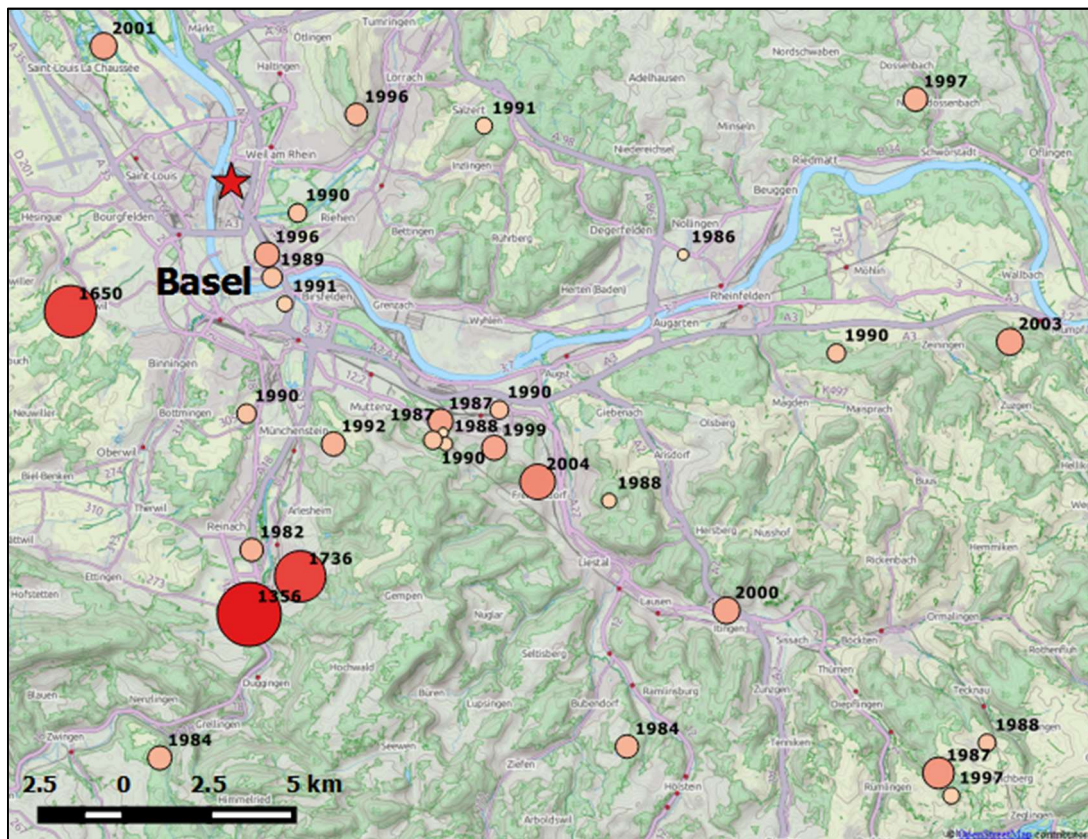


Figure A3.1.3. Epicentres of relevant earthquakes around the area of the city of Basel. The colour and diameter of the symbols is proportional to the (estimated) moment magnitude of the events. The red star corresponds to the 2006 main shock.

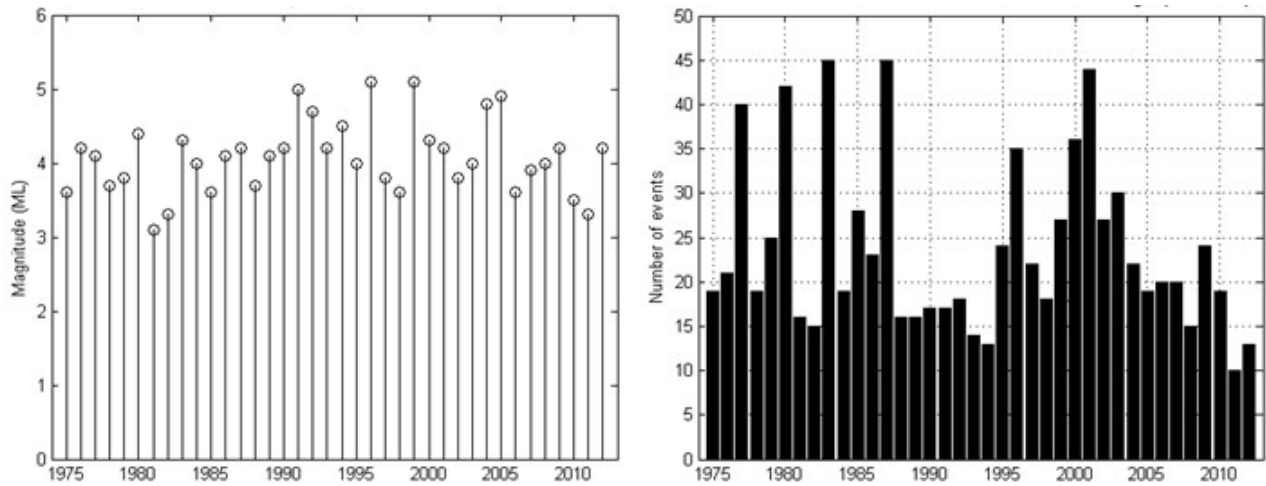


Figure A3.1.4. Magnitudes of the strongest earthquakes from 1975 to 2012 (left), and number of earthquakes with a magnitude M_L of 2.5 or greater from 1975 to 2012 (right) (Swiss Seismological Service, 2015).

A3.1.1.3 Seismic hazard

At the time of writing (August 2015), Switzerland is finishing the preparation of an update to its seismic hazard maps (Wiemer *et al.*, 2014). The current hazard map was elaborated in 2004, and was the first to be the product of a fully probabilistic model to replace the previous intensity-based maps of 1978 (Wiemer *et al.*, 2009; Giardini *et al.*, 2004). The 2004 seismic hazard model provides expected pseudo-spectral accelerations for oscillator periods between 0.1 and 2.0 seconds, with a 5% damping value, for different return periods. The map in Figure A3.1.5 shows the pseudo-spectral accelerations corresponding to a 10% probability of exceedance in 50 years for an oscillator period of 0.2 seconds. As can be observed, values range between 0.05 g and 0.15 g, and, for Basel, it is around 0.12 g. Figure A3.1.6 shows the 5% damped uniform hazard spectra for Basel for different return periods.

The Eurocode-based Swiss Structural Standard SIA 261:2003 does not make direct use of the hazard maps mentioned above but, instead, divides the whole country into four seismic zones (Z1, Z2, Z3a and Z3b) and assigns a design peak ground acceleration value to each of them. For the case of Basel, this is equal to 1.3 m/s^2 (0.13 g, zone Z3a). This design peak ground acceleration value corresponds to a return period of 475 years, on rock, and is later used to define the design pseudo-acceleration spectrum, which also takes into consideration the soil type of the construction site.

Figure A3.1.7 shows the 5% damped uniform hazard spectrum on rock from the SHARE (Seismic Hazard Harmonization in Europe) project (Woessner *et al.*, 2015) for a point with coordinates 47.600° N and 7.582° E , which correspond approximately to the city of Basel. As can be observed, the expected pseudo-spectral acceleration for a 0.2 seconds oscillator on rock with a 10% probability of exceedance in 50 years is 0.52 g, which is significantly higher than the value provided by the Swiss seismic hazard model of 2004.

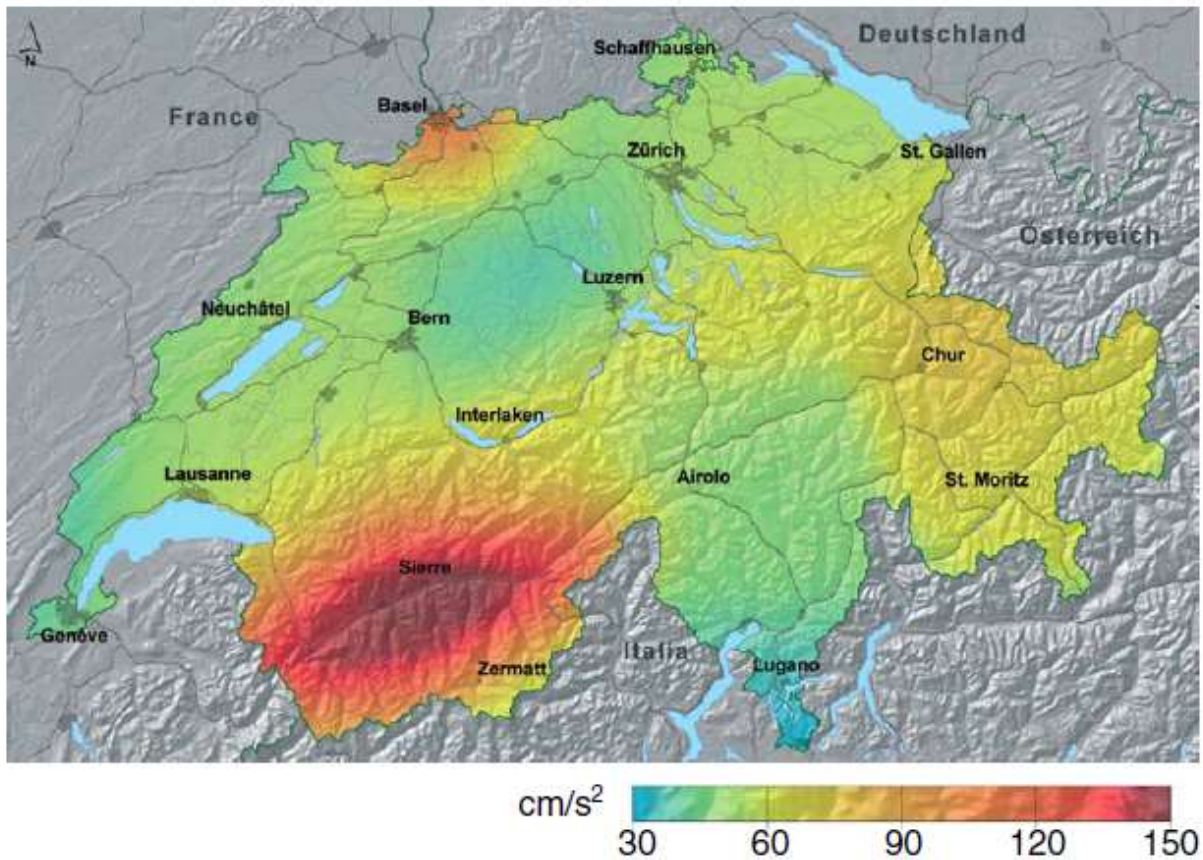


Figure A3.1.5. Seismic hazard map of Switzerland. Values correspond to 5% damped pseudo-spectral accelerations in rock for an oscillator period of 0.2 seconds with a 10% probability of exceedance in 50 years (Wiemer *et al.*, 2009).

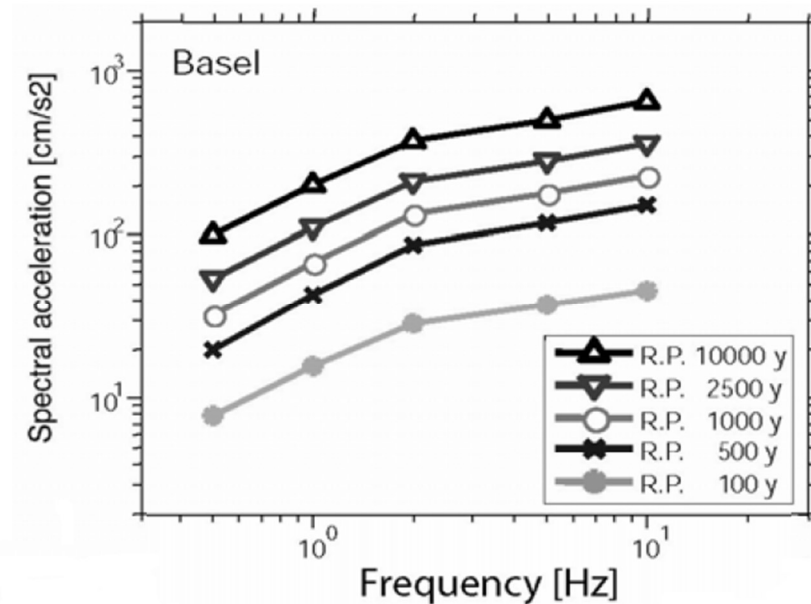


Figure A3.1.6. 5% damped uniform hazard spectra for Basel for different return periods, from Giardini *et al.* (2004).

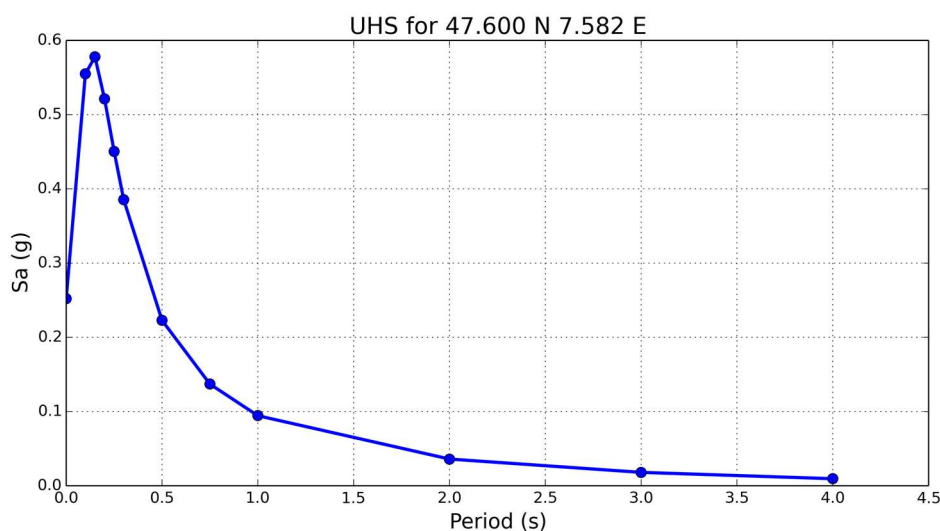


Figure A3.1.7. Uniform Hazard Spectrum for point 47.600° N 7.582° E (closest available to the city of Basel) according to SHARE (5% critical damping). Values correspond to PGA and spectral acceleration in rock with a 10% probability of exceedance in 50 years (mean).

Results from the Global Seismic Hazard Assessment Program (GSHAP) yield an expected PGA on rock with a 10% probability of exceedance in 50 years of about 0.15 g (1.47 m/s^2) for the region around the city of Basel (Giardini *et al.*, 1999).

The Worldwide Seismic Design Tool of the United States Geological Survey (USGS) make use of the results from GSHAP to estimate the spectral accelerations at 0.2 and 1.0 seconds with a 2% probability of exceedance in 50 years, which, for the case of Basel, are 0.75 g and 0.30 g, respectively. It should be noted that these values result from significant approximations and are therefore classified within the lowest reliability category of the USGS database.

A3.1.2 Earthquake source characteristics

A3.1.2.1 Location, depth and time

The main shock occurred on 8th December 2006, at 16.48 UTC (17.48 local time).

Several organizations and agencies report their own estimations of the epicentral coordinates and hypocentral depth. The information reported in the websites of the Swiss Seismological Service (SED), the French Laboratoire de Détection et de Géophysique Bruyères-le-Châtel (CEA), the National Earthquake Information Center (NEIC) of the United States Geological Service (USGS), the European-Mediterranean Seismological Centre (EMSC) and the International Seismological Centre (ISC) is summarized in Table A3.1.1. Cells marked as (*f) correspond to parameters that were held fixed while inversion was carried out to retrieve those that remain. Epicentral coordinates reported by SED, NEIC, CEA and Deichmann & Ernst (2009) are relatively consistent with each other, while those reported by the EMSC and the ISC seem to be the most inaccurate.

Table A3.1.1. Epicentral coordinates and hypocentral depths from different sources.

Agency / Publication		Latitude	Longitude	Depth (km)
ZUR	Swiss Seismological Service (SED)	47.5820 ° N	7.6000 ° E	5.00
NEIC	National Earthquake Information Center, USGS	47.5800 ° N	7.6000 f ° E	5.00 (*f)
EMSC	European-Mediterranean Seismological Centre	47.6100 ° N	7.6800 ° E	6.00
ISC	International Seismological Centre (inversion)	47.5821 ° N	7.5302 ° E	0.00 (*f)
DASE/CEA	Laboratoire de Détection et de Géophysique Bruyères-le-Châtel, France	47.5800 ° N	7.6000 ° E	7.00 (*f)
Deichmann & Ernst (2009) / Deichmann & Giardini (2009)		47.5840 ° N	7.5930 ° E	4.70

(*f) fixed parameter used for inversion

The map in Figure A3.1.8 shows the different estimations of the epicentral coordinates enumerated above, together with the epicentral locations of the 28 strongest events of the series, as reported by Deichmann & Ernst (2009) and Deichmann & Giardini (2009). According to these authors, the hypocentres of these events are located at depths between 4 and 5 km, always inside the stimulated rock volume. These depths are similar to those reported by Häring *et al.* (2008), and shown in Figure A3.1.9.

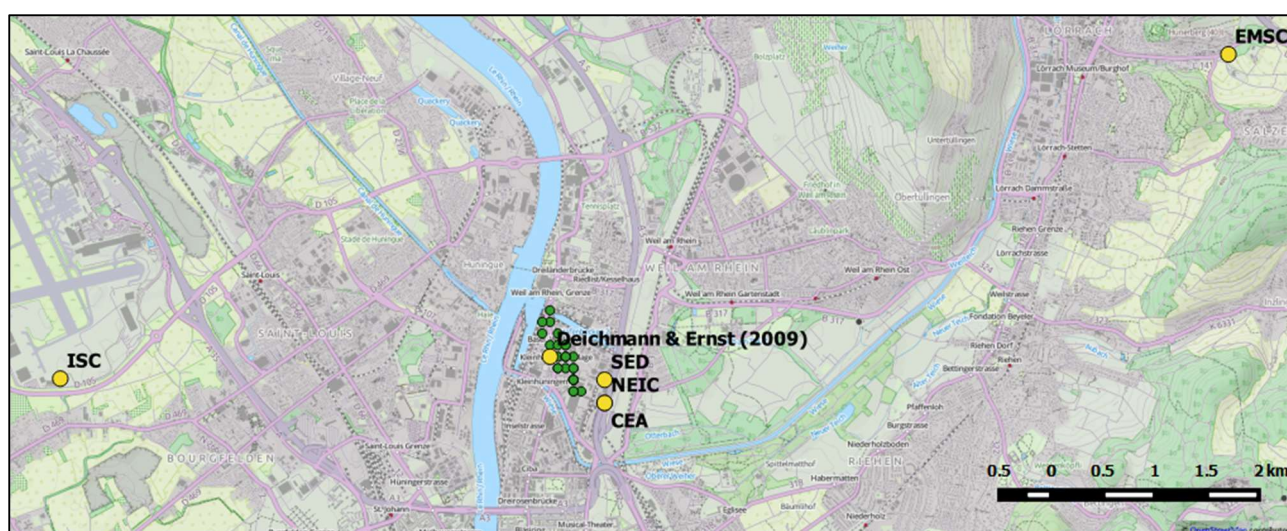


Figure A3.1.8. Estimation of epicentral coordinates (yellow circles). Green circles correspond to the epicentres of the 28 strongest events of the series, as reported by Deichmann & Ernst (2009) and Deichmann & Giardini (2009).

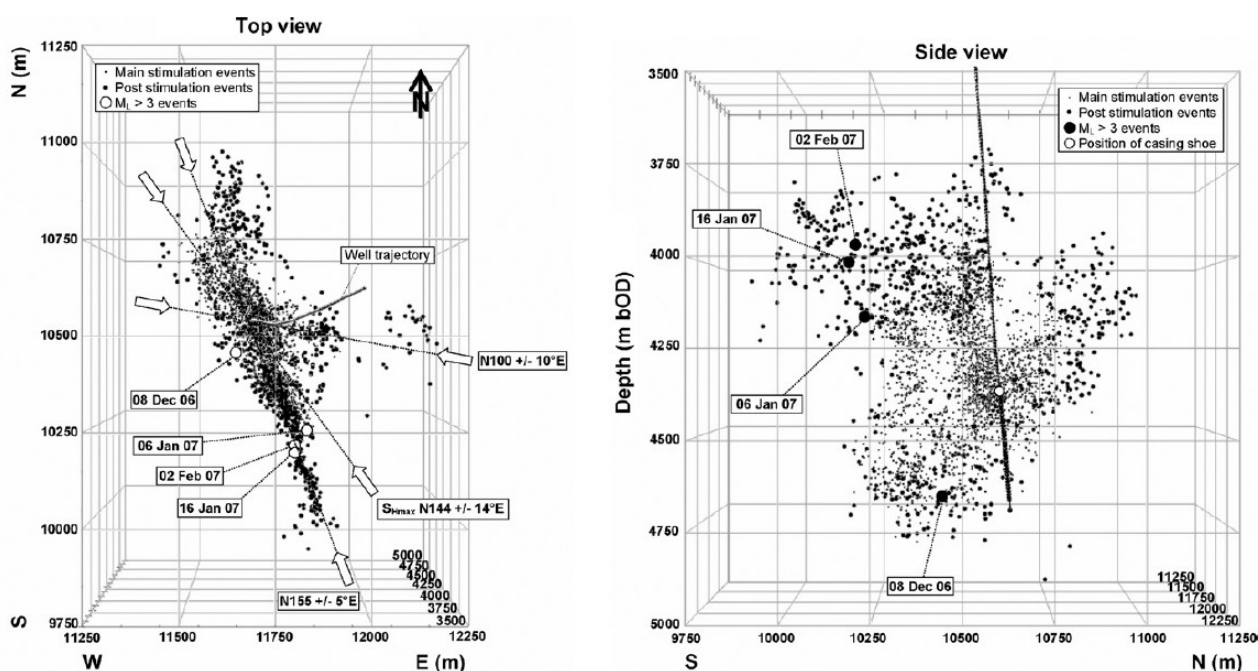


Figure A3.1.9. Locations of the seismic events that occurred between 2nd December 2006 and the end of November 2007. Depths are given in meters below Ordnance Datum (bOD), which is at 250 m depth. (Häring *et al.*, 2008).

A3.1.2.2 Magnitude

Estimations of magnitude made by the main agencies and reported by two significant studies are reported in Table A3.1.2.

Table A3.1.2. Estimations of moment magnitude (**M**) and local magnitude (**M_L**).

Agency		M	M _L
ZUR	Swiss Seismological Service (SED)	3.17	3.4
EMSC	European-Mediterranean Seismological Centre	-	3.8
DASE/CEA	Laboratoire de Détection et de Géophysique Bruyères-le-Châtel, France	-	3.87
NEIC	National Earthquake Information Center, USGS	-	3.90
Deichmann & Ernst (2009) / Deichmann & Giardini (2009)		-	3.4
Bethmann <i>et al.</i> (2011)		2.95	-

A3.1.2.3 Style-of-faulting

Häring *et al.* (2008), Deichmann & Ernst (2009) and Deichmann & Giardini (2009) report the faulting mechanism of the main shock as being mostly right-lateral strike-slip, with a small normal component, as shown in Figure A3.1.10. Their fault plane solutions are summarized in Table A3.1.3. Deichmann & Giardini (2009) conclude that the main shock occurred on the WNW–ESE striking fault plane, which they say is optimally oriented with respect to the tectonic principal stress axes of the area.

Table A3.1.3. Fault plane solutions from different sources. Fault planes marked in gray are the preferred solution in each case.

Fault Plane 1			Fault Plane 2			Source
Strike	Dip	Rake	Strike	Dip	Rake	
12	75	-13	105	77	-165	Deichmann & Ernst (2009) / Deichmann & Giardini (2009)
12	73	-13	106	78	-163	Häring <i>et al.</i> (2008)

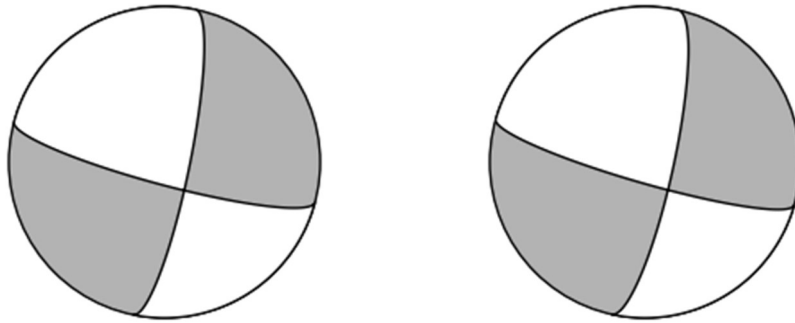


Figure A3.1.10. Fault plane solutions for the main shock, according to Deichmann & Ernst (2009)/Deichmann & Giardini (2009) (left) and Häring *et al.* (2008) (right).

Most of the fault mechanisms of the most significant events in the series analyzed by Häring *et al.* (2008) and Deichmann & Ernst (2009) are strike-slip, and only a few have strong normal components. According to Häring *et al.* (2008), these observations provide evidence that the place of the injection is located in a strike-slip dominated regime. It should be noted, however, that the strike of the fault plane solutions of the various events in the series reveal a complex spatial pattern that seems to be better explained by small-scale heterogeneities of the fractured rock mass and the stress field than by the activation of a single fault (Kraft & Deichmann, 2014; Deichmann *et al.*, 2014). Nevertheless, according to Deichmann & Giardini (2009), these heterogeneities would most likely correspond to pre-existing faults and not to cracking of the rock mass occurring during the water injection (hydrofracking).

A3.1.2.4 Stress drop

Goertz-Allmann *et al.* (2011) calculated the stress drop of about 1,000 earthquakes of the series. It is possible to see in Figure A3.1.11 that the estimated stress drop for the **M**2.95 (M_L 3.4) main shock is approximately 1.3 MPa, though the uncertainty is large and indicates that the true value probably lies between somewhere between 0.2 and 3.6 MPa. For the whole series, the median stress drop is 2.3 MPa. The authors note that the stress drops of individual events have been smoothed using a median filter over the closest ten events. Edwards *et al.* (2015) mention a median value closer to the upper bound of Goertz-Allmann *et al.* (2011), around 3.5 MPa, acknowledging it might vary between 0.76 and 10.4 MPa, accounting for a \pm 5% variation in the corner frequency.

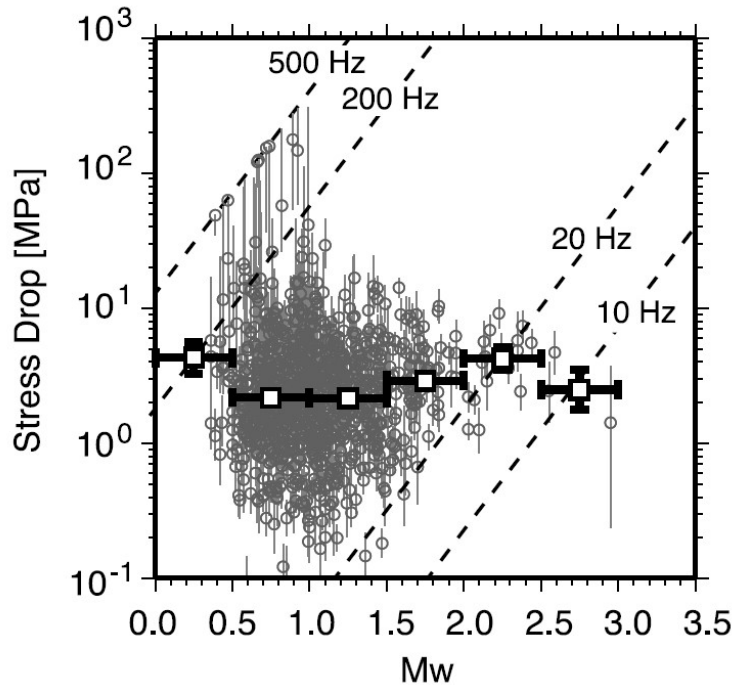


Figure A3.1.11. Stress drop versus moment magnitude for 1,000 events of the series. Thin vertical bars indicate the estimated uncertainty of the stress drop calculated for each event, due to the uncertainty in the corner frequencies. From Goertz-Allmann *et al.* (2011).

In contrast, Häring *et al.* (2008) state a stress drop of approximately 300 bar (30 MPa) for the main shock is not unlikely, given that the estimated source radius and rupture area are significantly smaller than the expected for a natural event of the same magnitude, for which typical stress drops range between 1 and 100 bar (0.1-10 MPa).

A3.1.2.5 Foreshocks and aftershocks

The M3.2 (M_L 3.4) event was the strongest of a large series of events directly linked to the injection of a large volume of water at high pressures for the creation of an enhanced geothermal system (EGS) in the area. According to Häring *et al.* (2008), approximately 11,200 events were detected during the phase of active stimulation, from 2nd December to 8th December 2006. In the early morning of this day, a M_L 2.6 event occurred and the injection was halted. Over 12 hours later, a M_L 2.7 event took place, and was followed one hour later by the M_L 3.4 main shock, after which the water was allowed to flow back from the well (Deichmann & Giardini, 2009). About 3,700 additional events occurred afterwards, up to the end of November 2007, three of which had magnitudes M_L larger than 3.0 (Häring *et al.*, 2008). An additional M_L 0.6 was detected in 2010, five events with M_L between 0.9 and 1.2 were detected in 2012, and two events with M_L 1.8 and 1.0 were recorded in 2013 (Deichmann *et al.*, 2014). The plot in Figure A3.1.12 shows the number of events of each magnitude recorded by the Swiss Seismological Service between 3rd December 2006 and 30th November 2007.

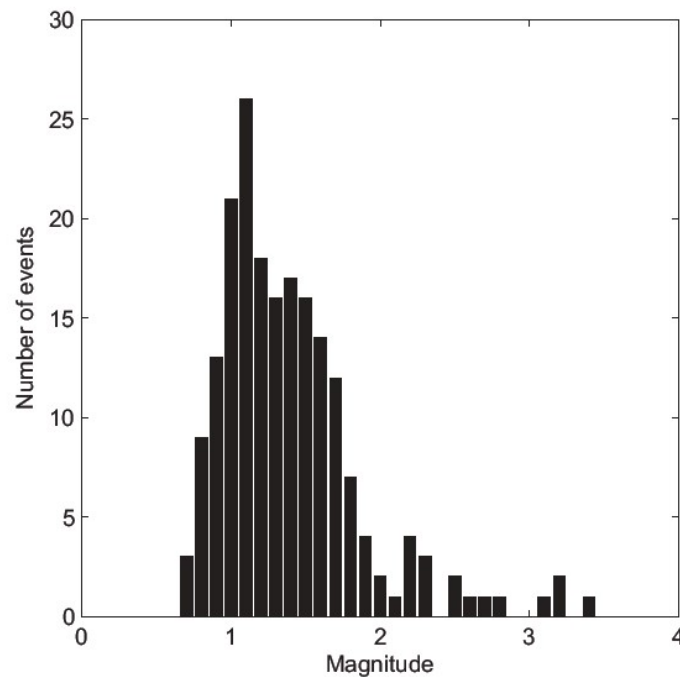


Figure A3.1.12. Number of events of each magnitude (M_L) recorded by the Swiss Seismological Service between 3rd December 2006 and 30th November 2007. From Deichmann & Giardini (2009).

A3.1.2.6 Nature of earthquake

This seismic series was induced by the injection of a large volume of water at high pressures for the creation of an enhanced geothermal system (EGS) for the Deep Heat Mining Project in Basel. As Häring *et al.* (2008) explain, an EGS consists in drilling the underground at great depths until reaching hot dry rock or magma, and injecting pressurized water into it with the aim of generating steam that can drive turbines or even be used for heating. The Basel 1 well was drilled between May and October 2006 up to a depth of 5 km, and approximately 11,500 m³ of water were injected at high pressures between 2nd December and 8th December 2006. The injection was stopped after the occurrence of a M_L 2.6 event in the early morning of 8th December 2006, and the well was opened so as to let water flow back after a M_L 2.7 and M_L 3.4 event in the afternoon/evening, following a pre-approved seismic response plan (Häring *et al.*, 2008). The increased seismic activity continued well after bleeding off the well, with around 15,000 events having been detected over the whole process (refer to the *Foreshocks and aftershocks* section above).

Deichmann & Giardini (2009) note, however, that these induced earthquakes do not seem to correspond to a case of hydrofracking (fracturing of the rock due to the water injection), but were caused instead by the ambient tectonic stress and shear dislocations on pre-existing faults, only triggered by the increase in pore pressure. As supporting evidence, these authors point out that, according to Häring *et al.* (2008), the water pressure within the rock mass did not reach the minimum stress threshold needed for hydrofracking to occur, and most of the seismic activity preceded the time at which the pressure in the well reached its maximum, and persisted for a significant duration afterwards. Nevertheless, as

Catalli *et al.* (2013) point out, the temporary evolution of the seismic activity followed the injection rate and pressure variations in the well.

A3.1.3 Geology and ground conditions in the affected area

A3.1.3.1 Regional geology and topography

The city of Basel is located within a deep sedimentary basin, the Upper Rhine Graben. It is limited by the Black Forest massif to the north-east, the Vosges massif to the north-west, and the Jura mountains to the south-west (Figure A3.1.13). It is close to the Eastern Rhine Graben Fault (Figure A3.1.2), which presents a throw of about 1400 m. According to Fähr *et al.* (1997), on the (west) down-thrown side, the Mesozoic strata (Triassic to Jurassic) are covered by 500 to 1,000 m of Tertiary sediments, of which there are very few outcrops, and above which there are 5 to 50 m thick unconsolidated deposits of (Quaternary) Pleistocene and Holocene gravels. There are no Tertiary sediments to the east, where the Mesozoic sediments of the Tabular Jura (Figure A3.1.1) are covered directly by 5 to 50 m of Pleistocene and Holocene gravels and, in some parts, with an additional layer of marls. Figure A3.1.14 shows a schematic NW-SE section cutting through the Eastern Rhine Graben Fault.



Figure A3.1.13. Geographical features around the area of Basel. Image from Wikipedia

The drilling of the Basel 1 well passed through over 2.4 km of Quaternary, Tertiary, Mesozoic and Permian sediments, approximately 100 m of Permian siltstone and weathered granite, and finally entered the crystalline basement at a depth of over 2.5 km (Häring *et al.*, 2008).

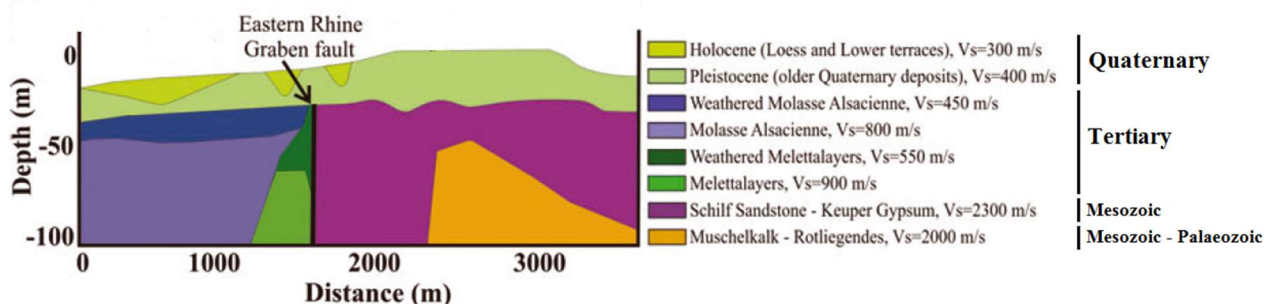


Figure A3.1.14. Geological section across the Eastern Rhine Graben Fault. (Havenith *et al.*, 2007)

A3.1.3.2 Site conditions in the affected area

The map in Figure A3.1.15 shows the surficial geology of the Canton of Basel City (Basel-Stadt) and nearby areas, according to the Swiss Seismological Service. As can be observed, a large part of the city consists of gravel terraces, but there is also a significant surface covered by loess and clay.

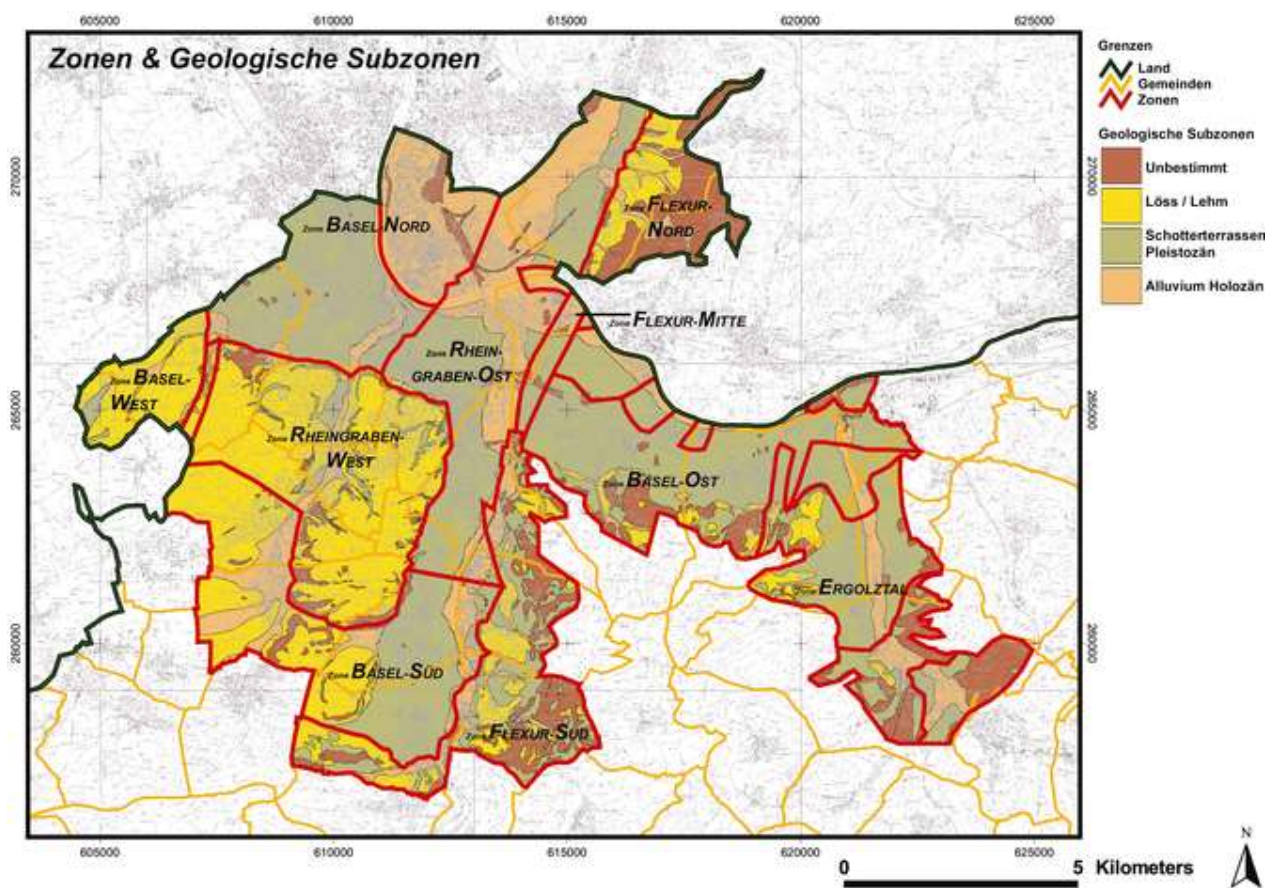


Figure A3.1.15. Surficial geology of the Canton of Basel City and nearby areas. Dark brown: rock. Yellow: loess / clay. Green: Pleistocene gravel terraces. Light brown: Holocene alluvium. Swiss Seismological Service (2015).

The online Geoportal of Basel (Basel Geoportal, 2015) contains an interactive version of the aforementioned map and all the associated information needed to define the design pseudo-acceleration and displacement spectra, which is summarized by Wenk & Fäh

(2012). Figure A3.1.16 shows the 5%-damped design elastic pseudo-acceleration response spectra for the different microzones of the Basel area. The spectrum corresponding to the area where the Basel 1 well was located is indicated. As can be observed, the design accelerations increase significantly when taking into consideration the site conditions.

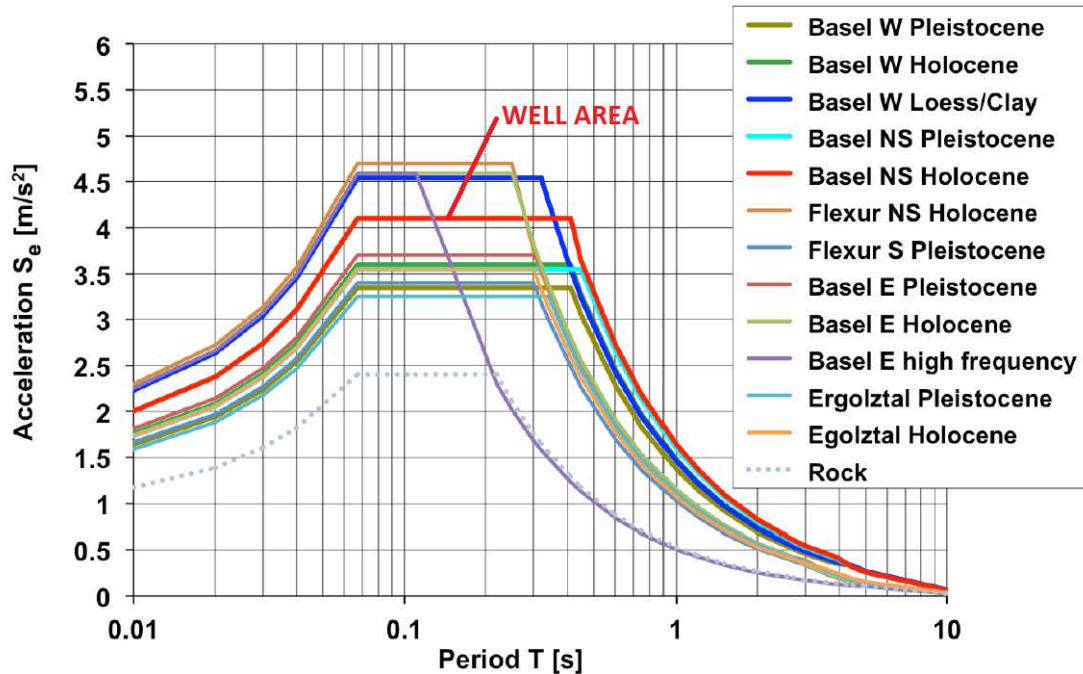


Figure A3.1.16. 5%-damped design elastic pseudo-acceleration response spectra for the microzones of the Basel area. (Wenk & Fäh, 2012).

Figure A3.1.17 shows a qualitative microzonation map of the Canton of Basel City (Basel-Stadt) presented by Fäh *et al.* (2001). The colour scale represents the degree of susceptibility of each area to site amplification effects, with red indicating an increased susceptibility and blue showing a reduced susceptibility with respect to a regional value.

According to Noack & Fäh (2015), liquefaction hazard is of minor importance for the Basel area, given that saturated sands can be found only at very few places.

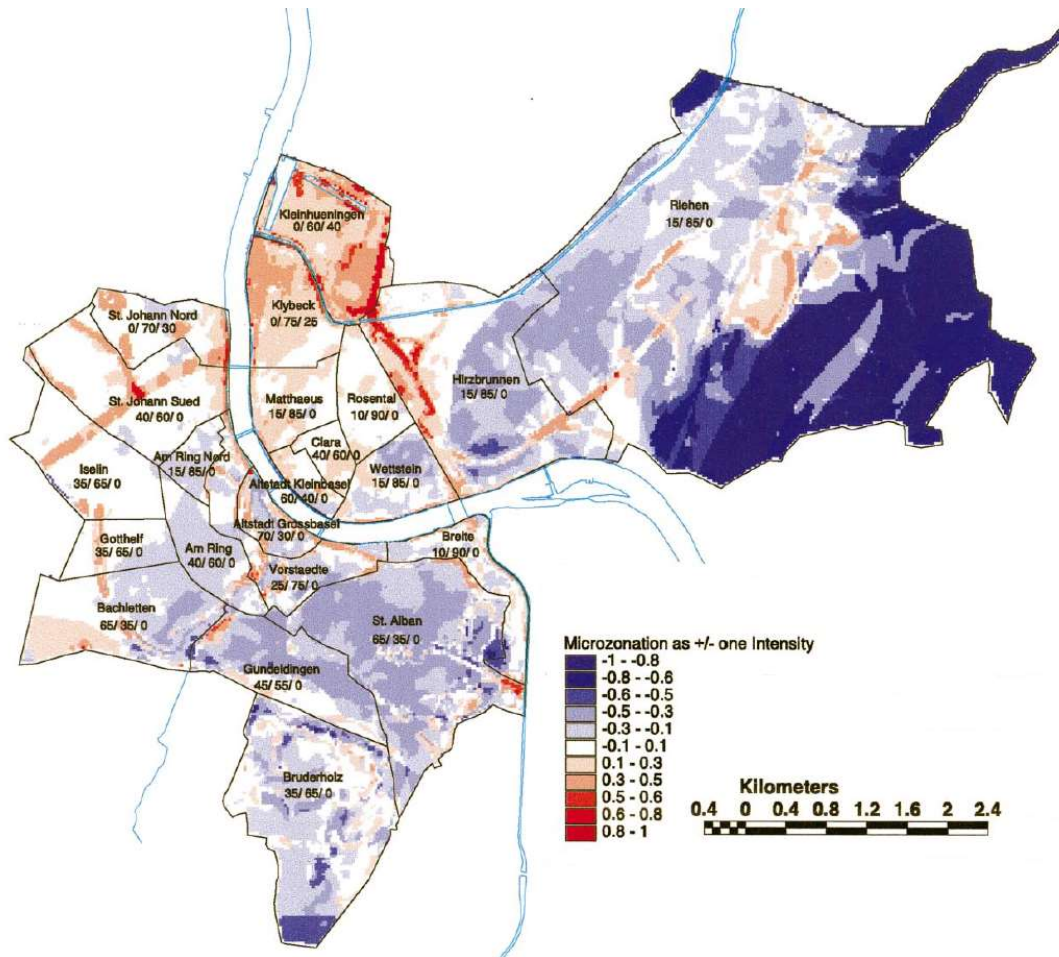


Figure A3.1.17. Qualitative microzonation map of the Canton of Basel City. Areas marked in red are more susceptible to site amplification effects (Fäh *et al.*, 2001).

A3.1.4 Ground motions

A3.1.4.1 Intensity observations

Baer *et al.* (2007), Deichmann & Giardini (2009) and the Swiss Seismological Service report a maximum EMS-98 (European Macroseismic Scale, Grünthal, 1998) intensity of V, which define the event as "strong", and means that it was felt indoors by most and outdoors by a few, causing some fear, and that some slight non-structural damage to the most vulnerable structures was observed. Creaking of woodwork and rattling of doors and windows were systematically reported (Deichmann & Giardini, 2009), while swinging of suspended objects and oscillations in liquid-filled containers were less frequently mentioned (Baer *et al.*, 2007). The radius of the area for which the intensity was equal to or larger than IV was 10 km, with peaks in the SSW direction and towards the east. Baer *et al.* (2007) believe the first peak is consistent with the radiation pattern expected from the focal mechanism of the event, while the second one is likely to be the consequence of site amplification due to loose alluvial terraces.

Figure A3.1.18 shows the EMS-98 macroseismic intensities determined from 865 observations of people who either filled in the online questionnaire or replied to emails

directly sent to them by the Swiss Seismological Service. It should be noted that intensities assigned in French and German territories are not reliable, due to the lack of reports from these areas.

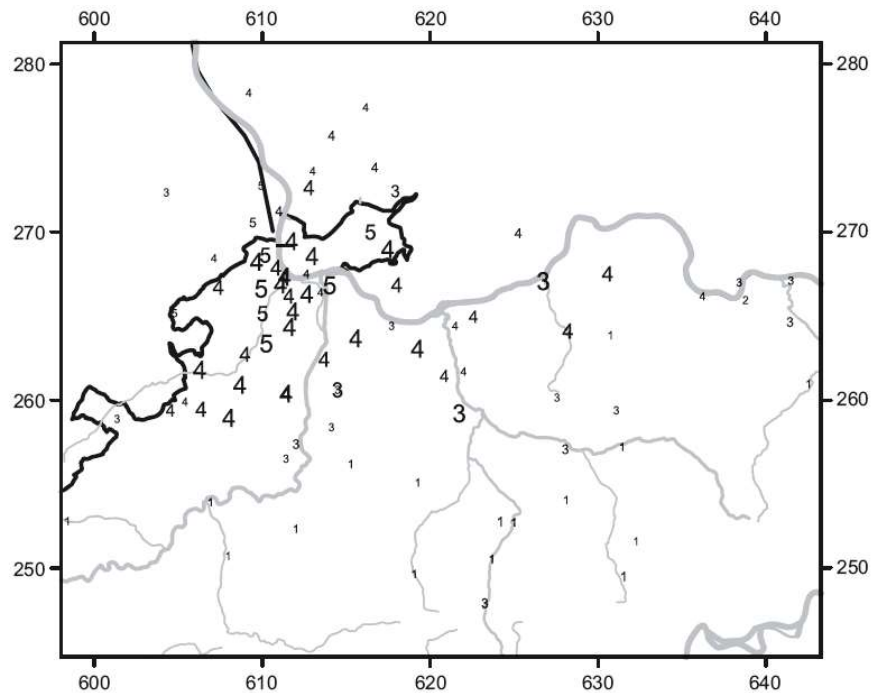


Figure A3.1.18. EMS-98 macroseismic intensities for the main shock, based on reports communicated to the Swiss Seismological Service. It is not representative of the shaking in Germany and France. The size of the number reflects the quality of the data, which can range from very poor (1-2 reports) to very good (15-60 reports). From Baer *et al.* (2007).

The observed macroseismic intensities are plotted against epicentral distance in Figure A3.1.19, and compared against median expected values from intensity prediction equations. As can be observed, many observations are higher than the expected values, especially at short distances from the epicentre.

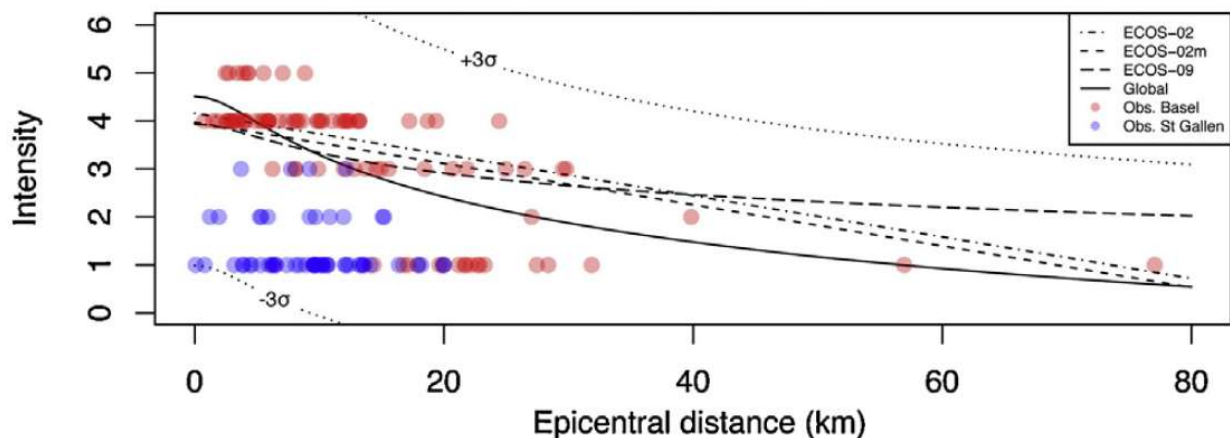


Figure A3.1.19. EMS-98 intensity versus epicentral distance: observations (red dots) and predictions from intensity prediction equations by ECOS-02 (Fäh *et al.*, 2003), ECOS-02m (Álvarez-Rubio *et al.*, 2012), ECOS-09 (Fäh *et al.*, 2011) and Global (Allen *et al.*, 2012). From Mignan *et al.* (2015).

A3.1.4.2 Ground motion recordings

The main shock of this series of events was recorded by a large number of permanent and temporary strong motion stations, even at large distances. The largest geometric mean peak ground acceleration and peak ground velocity recorded were 0.1 g and around 2 cm/s, as can be observed in Figure A3.1.20. The largest geometric mean pseudo-spectral acceleration values for oscillator periods of 0.3 and 1.0 second were 0.1 g and 0.004 g, respectively. Based on the work of Worden *et al.* (2012), Edwards *et al.* (2015) point out that these ground motions are around the onset of damage. Figure A3.1.20 also provides a comparison with respect to the median attenuation curves predicted by the Swiss stochastic model of Edwards & Fah (2013) as modified by Cauzzi *et al.* (2015) to consider an intermediate soil condition (V_{s30} of around 620 m/s), since the recorded data corresponds to several soil classes. As can be observed, the recorded data easily exceeds the median predictions, especially in the near-field. Edwards *et al.* (2015) believe that this is due to significant site amplification effects combined with the shallow depth of the hypocentre.

The largest geometric mean spectral values were observed at station SBEG (Figure A3.1.23), located in the area of Bettingen, around 5.6 km to the ESE of the epicentre, over soil with V_{s30} around 440 m/s. As can be observed in Figure A3.1.21, the geometric mean spectral acceleration and displacement demands present significant peaks in the short period range, typical of low-rise buildings. This amplification becomes more evident in Figure A3.1.22, where the geometric mean spectral acceleration is compared to the design acceleration spectra for the three types of soil that can be found in the area close to the station (10% probability of exceedance in 50 years, data obtained from the online Geoportal of Basel geoviewer, 2015, and Wenk & Fäh, 2012). Other stations, such as OTTER (1.1 km from the epicentre) and CHBRI (4.8 km from the epicentre) present spectral acceleration values of individual as-recorded components of around 0.10 and 0.06 g, respectively, at a 0.05 seconds oscillator period (Ripperger *et al.*, 2009), but do not exhibit the large amplification around 0.1 seconds as the geometric mean values of station SBEG.

Ripperger *et al.* (2009) calculated the maximum resultant PGV from the velocity time-history of 29 stations, which range from 0.043 cm/s (CHBDO station, 12.0 km away from the epicentre) to 1.389 cm/s (SBAJ station, 2.1 km away from the epicentre). As shown in Figure A3.1.23, larger values are observed to the south and to the east of the epicentre, an observation that matches the peaks in macroseismic intensity discussed earlier (Figure A3.1.18). Figure A3.1.24 shows the velocity time histories of the four stations (out of the 29) with the largest maximum resultant PGV.

Based on the observation of some of the waveforms recorded for the largest events of the series, Häring *et al.* (2008) suggest that it is possible that these may have formed by a cascade-like rupture process either on single continuous structures or almost synchronously on several closely adjacent structures instead. Figure A3.1.25 shows how this can be observed in the waveform recorded at the OTER2 station during the main shock. A number of successive events occurring a few milliseconds apart can be

distinguished after the first P-wave arrival. This staggering becomes undistinguishable at stations located farther away from the epicentre.

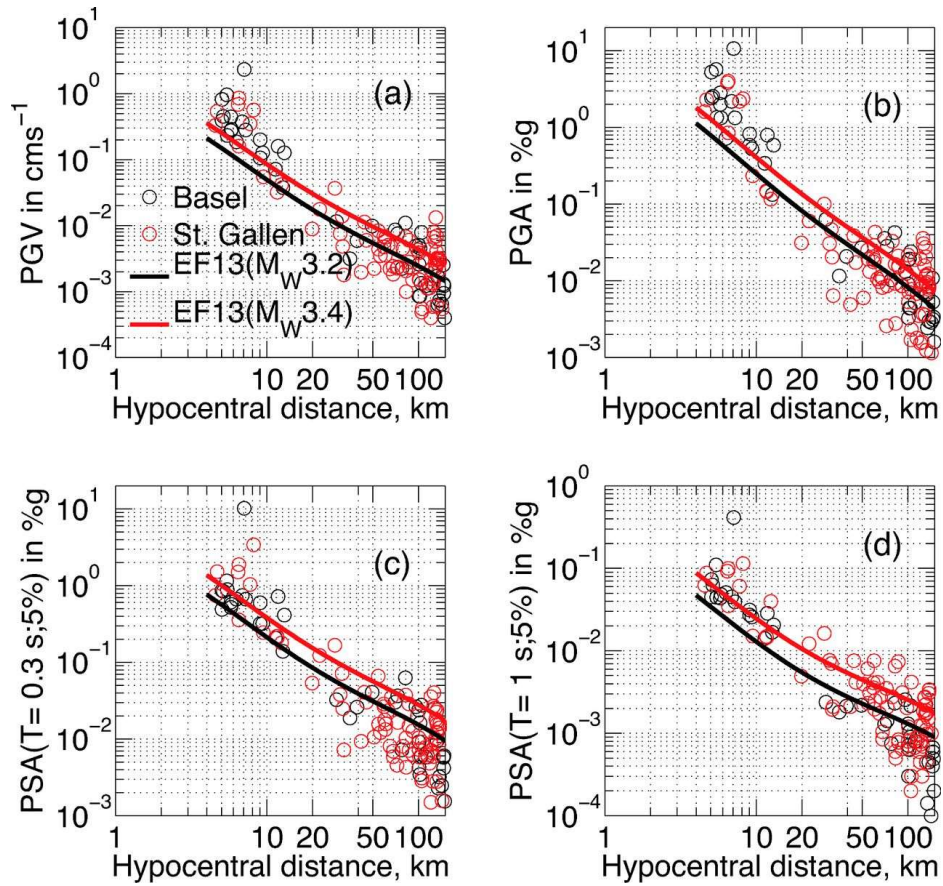


Figure A3.1.20. Attenuation of PGV (a), PGA (b) and 5%-damped pseudo-spectral acceleration at $T = 0.3$ s (c) and $T = 1$ s (d), as a function of hypocentral distance. Black circles show the geometric mean of the two horizontal components for the Basel 2006 main shock. The thick black line labeled EF13 is the median attenuation curve for events occurring in the Swiss foreland (Edwards & Fäh, 2013; Cauzzi *et al.*, 2015). Ignore red dots and red lines. (Edwards *et al.*, 2015).

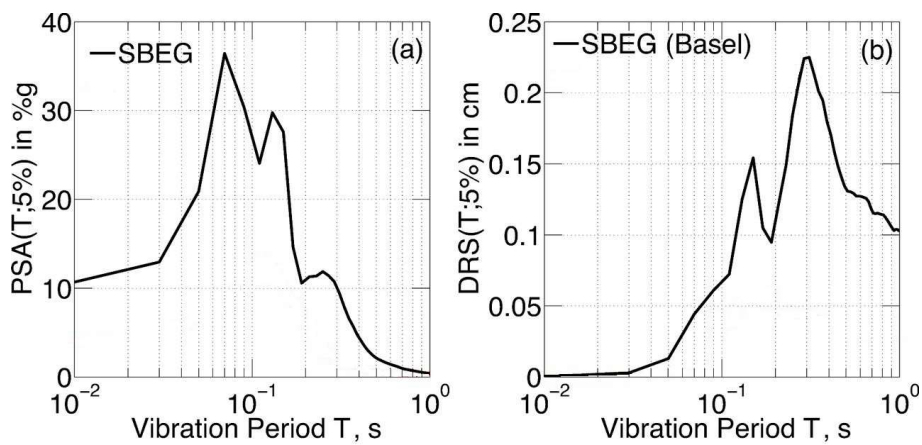


Figure A3.1.21. 5%-damped pseudo-acceleration (PSA) and displacement (DRS) spectra (geometric mean of the horizontal components) observed at station SBEG. From Edwards *et al.* (2015).

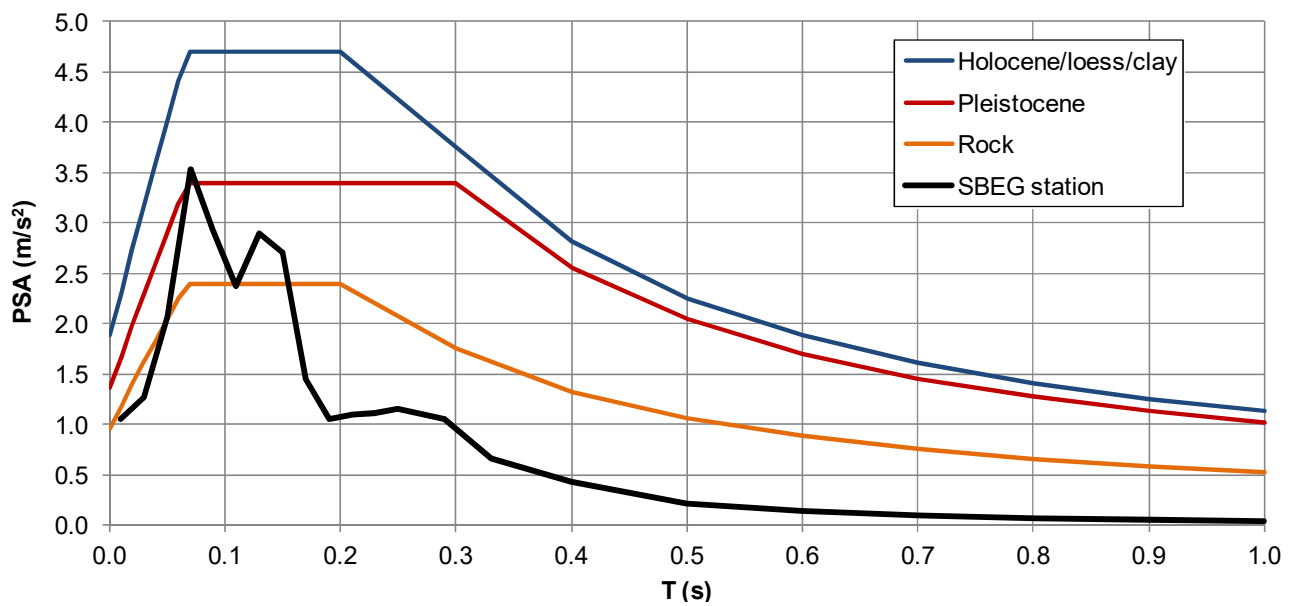


Figure A3.1.22. 5%-damped pseudo-acceleration (PSA) spectra (geometric mean of the horizontal components) observed at station SBEG compared against the design spectra for the three soil types that can be found in the area close to the station. Data for station SBEG: Edwards *et al.* (2015)

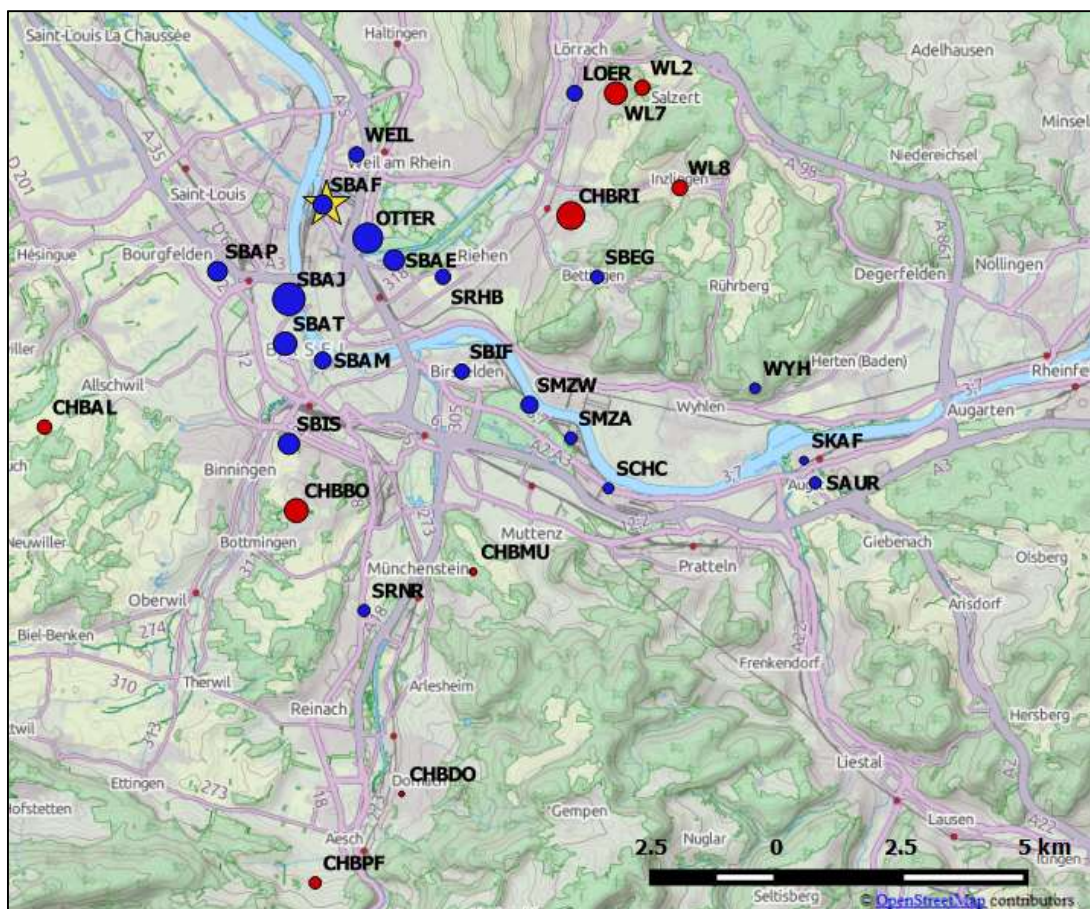


Figure A3.1.23. Maximum resultant PGV in 29 recording stations (red: temporary, blue: permanent), shown proportionally to the size of the location circles (data from Ripperger *et al.*, 2009). The yellow star shows the location of the epicentre according to Deichmann & Ernst (2009). Maximum resultant PGV: 1.389 cm/s, at SBAJ station (2.1 km from the epicentre).

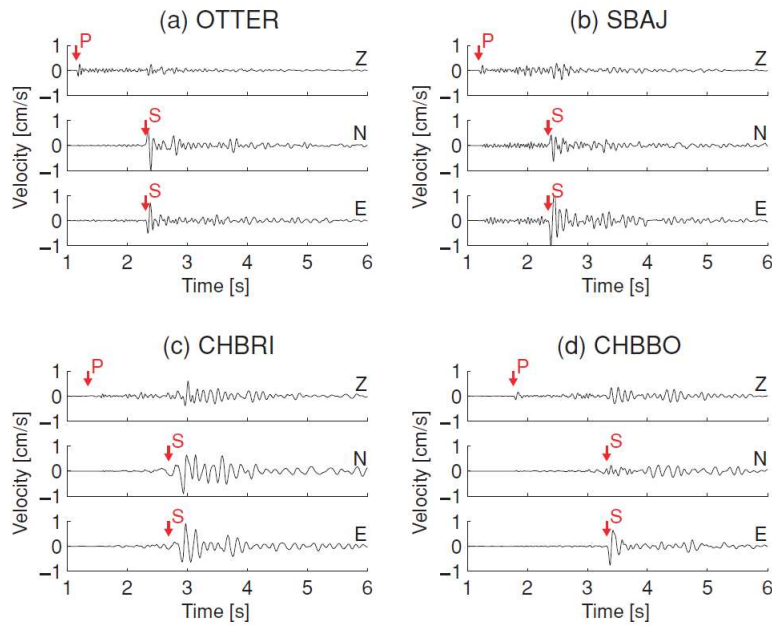


Figure A3.1.24. Velocity time histories for four stations located 1.1 km (OTTER), 2.1 km (SBAJ), 4.8 km (CHBRI) and 6.2 km (CHBBO) away from the epicentre. Stations CHBRI and CHBBO are placed over unconsolidated sediments. (Ripperger *et al.*, 2009).

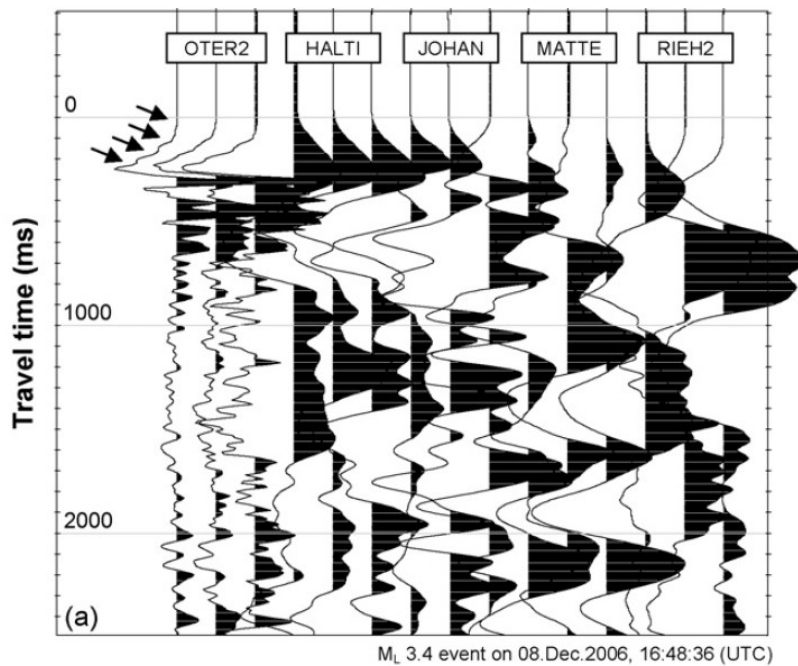


Figure A3.1.25. Raw unfiltered traces recorded during the main shock, aligned at the P-wave picks. Multiple arrivals are indicated by arrows (Häring *et al.*, 2008).

A3.1.4.3 Inferred shaking levels

As pointed out above, there is significant agreement between the maximum resultant PGV values calculated by Ripperger *et al.* (2009) and the EMS-98 intensities reported by the Swiss Seismological Service (Figure A3.1.18). Further, it is relevant to note that stations CHBRI and CHBBO, which presented two of the highest resultant PGV values, are located over unconsolidated sediments, while the other two, OTTER and SBAJ, are very close to

the epicentre. Station SBEG, which experienced the largest geometric mean spectral values, is also placed over soils with a significant amplification potential.

No attempts to infer ground shaking levels within the city of Basel from macroseismic intensities have been found in the literature.

A3.1.4.4 Duration of ground shaking

According to Deichmann & Giardini (2009), people reported a short, high-frequency shaking which lasted from one to three seconds.

Estimations of earthquake significant durations can be obtained by means of prediction equations such as those of Bommer *et al.* (2009) and Afshari & Stewart (2016), whose results for the 5-75% of Arias intensity definition of significant duration are shown in Figure A3.1.26. Given that no details are available with respect to the locations at which the 1-3 seconds shaking was observed, a range of distances to the rupture and soil types are considered. A 0.1 km radius, as suggested by Häring *et al.* (2008), and the 4.7 km hypocentral depth of Deichmann & Ernst (2009) are assumed. As the microzonation map of Basel (Figure A3.1.15; Basel Geoportal, 2015) shows a variety of site conditions, values of V_{s30} corresponding to the bounding limits of the definitions of soil types according to Eurocode 8 (CEN, 2004) are used. The estimations obtained using the model of Afshari & Stewart (2016) are more consistent with the one-to-three second range reported by Deichmann & Giardini (2009) than those obtained with that of Bommer *et al.* (2009). It is noted, however, that the model of Bommer *et al.* (2009) is being applied significantly outside the range of magnitudes for which it was derived ($M_{4.8-7.9}$). In any case, both Deichmann & Giardini (2009) and all estimations seem to suggest that this was most likely a very short duration event.

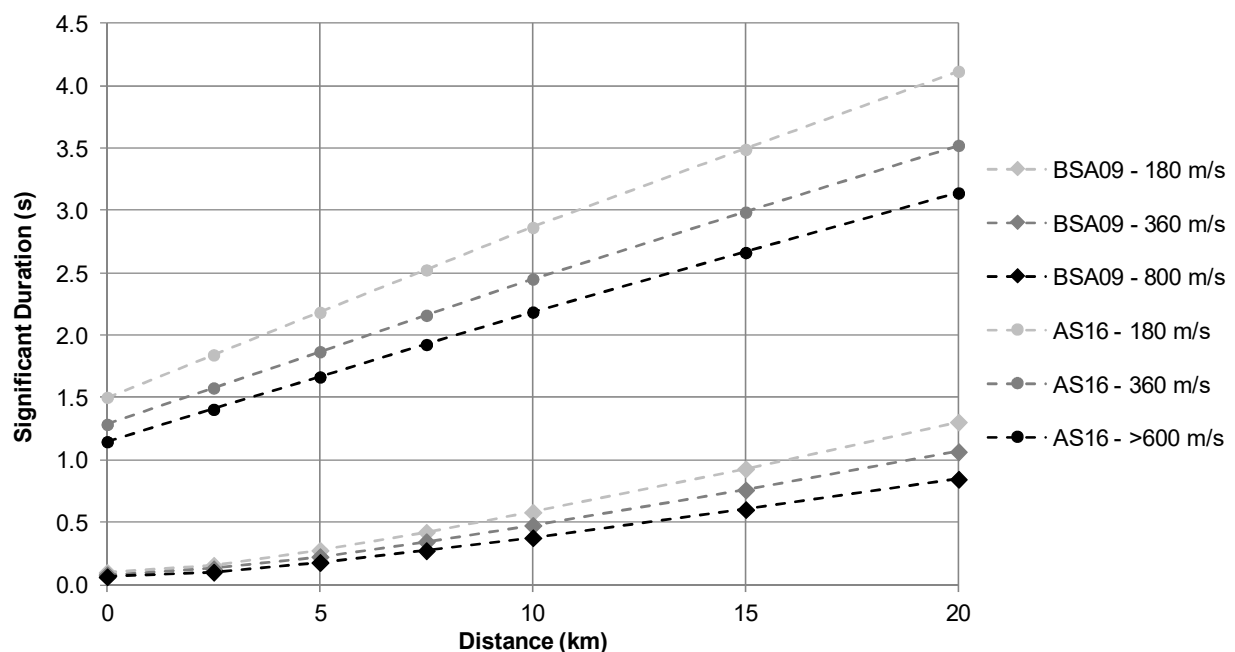


Figure A3.1.26. Estimation of the significant duration of the main shock, using prediction equations by Bommer *et al.* (2009, BSA) and Afshari & Stewart (2016, AS).

A3.1.5 Collateral earthquake hazards

A3.1.5.1 Surface rupture

No surface rupture reported.

A3.1.5.2 Landslides

No landslides reported.

A3.1.5.3 Liquefaction

No liquefaction reported.

A3.1.5.4 Settlements

No settlements reported.

A3.1.6 Exposed population

A3.1.6.1 Socio-economic setting

According to the 2014 Human Development Report (United Nations, 2014), the Human Development Index (HDI) for Switzerland in 2013 was 0.917, while its Inequality-adjusted HDI (IHDI) was 0.847. This located Switzerland in the 3rd place in the world's ranking, while the Netherlands ranks 4th. Table A3.1.4 compares the HDI and IHDI for both countries for a series of Human Development Reports (2006; 2008; 2009; 2014). IHDI values are not available for reports generated before 2010. The column "Adj. HDI" provides the HDI values given in the 2014 report for previous years, adjusted for data consistency in time. As can be observed, both countries present similar levels of human development.

Table A3.1.4. Human Development Index and Inequality-adjusted Human Development Index for Switzerland and the Netherlands.

Report	Data	Switzerland				Netherlands			
		HDI	IHDI	Rank	Adj. HDI	HDI	IHDI	Rank	Adj. HDI
2006	2004	0.947	-	9	-	0.947	-	10	-
2007/2008	2005	0.955	-	7	0.901	0.953	-	9	0.888
2009	2007	0.960	-	9	0.903	0.964	-	6	0.901
2014	November 2013	0.917	0.847	3	-	0.915	0.854	4	-

Switzerland has a powerful growing economy, its most important economic sectors being manufacturing and finance. Specialist chemicals, machines and electronics, and precision instruments are its main exportation products (Wikipedia). Basel, in particular, is host to

several chemical and pharmaceutical industries, and is one of the main financial centres of Switzerland (Steimen *et al.*, 2004). In 2008, the Canton of Basel City had the largest gross domestic product (GDP) per capita in Switzerland, with it being around double of the national value (Wikipedia).

Table A3.1.5 presents a comparison between Switzerland and the Netherlands in terms of GDP, GDP per capita and unemployment rate.

Table A3.1.5. Gross domestic product (GDP), GDP per capita and unemployment rate for Switzerland and the Netherlands, according to the World Economic Outlook Database (2015).

Indicator	Units	Switzerland		Netherlands	
		2006	2014	2006	2014
Gross domestic product, current prices	Billions of US dollars	377.240	712.050	663.119	866.354
Gross domestic product per capita, current prices	US dollars	51,770.607	87,475.464	40,571.399	51,372.963
Unemployment rate	% of total labor force	3.400	3.164	3.900	7.395

A3.1.6.2 Population density and distribution

The tri-national metropolitan area of Basel has a population of around 829,000 people, 65%, 8% and 27% of which live in Swiss, French and German municipalities (Figure A3.1.27). The municipality of the city of Basel itself has a population of around 170,000 inhabitants which, along with the populations of Bettingen and Riehen, make up the around 197,000 inhabitants of the Swiss Canton of Basel City (Basel-Stadt).

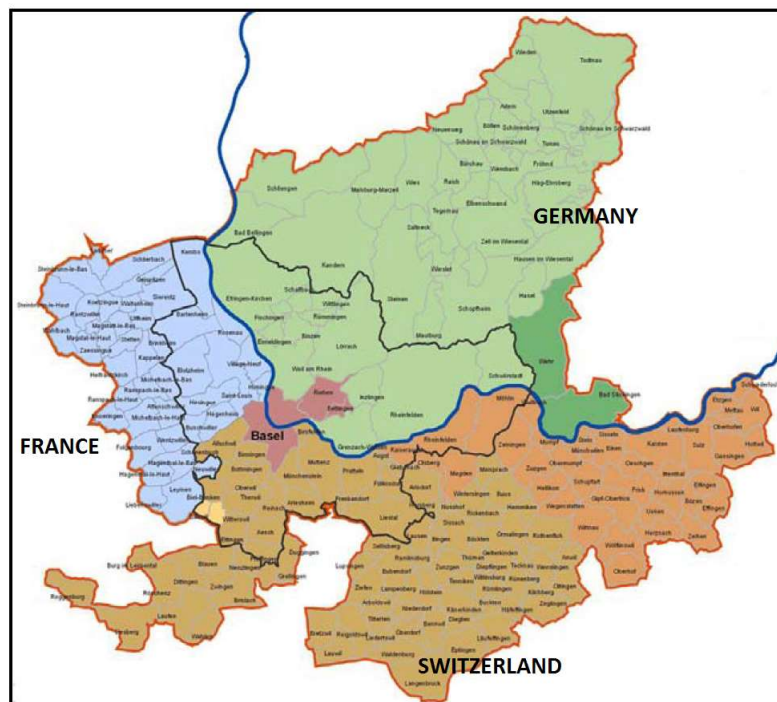


Figure A3.1.27. Basel metropolitan area: Swiss (brown), French (blue) and German (green) regions. Marked in red is the Swiss Canton of Basel City (Basel-Stadt) (Driscoll *et al.*, 2010).

A3.1.6.3 Time of day of earthquake

Given that no injuries were reported, the time at which the main shock occurred did not have any influence in its consequences for the population.

A3.1.7 Characteristics of exposed building stock

A3.1.7.1 Seismic design codes

According to Wenk & Fähr (2012), seismic requirements are generally the dominating design action for new buildings in Switzerland, though wind design codes were introduced several decades earlier than seismic ones (Badoux & Peter, 2000). As Wenk (2014) points out, the first Swiss seismic regulations were contained in the Swiss Structural Standard SIA 160:1970 introduced in 1970. They were based on allowable stress design concepts, and specified that all ordinary buildings in Switzerland be designed for a minimum horizontal load equal to 2% of their weight. They recommended that a minimum 5% be used in the regions of higher seismicity but, given that the ultimate decision was left in the hands of the local authorities, only the Canton of Basel City adopted the 5% value.

The SIA 160:1970 standards were revised in 1989, and they were modified to incorporate the first probabilistic hazard map of Switzerland, which was based on macroseismic intensity. As a result, the SIA 160:1989 standards incorporated a seismic zoning map which contained four zones, each of them finally related to a design value of horizontal ground acceleration. In this map, Basel belonged to zone 2, and was therefore associated to a design horizontal acceleration of 0.1 g. Badoux & Peter (2000) point out that, in general, the 1989 update of the standards resulted in a significant increase in the required lateral load resistance of structures.

By 1998, the Swiss Seismological Service started the process that would lead to the 2004 non-intensity based fully-probabilistic seismic hazard assessment (PSHA) of Switzerland (Wiemer *et al.*, 2009; Giardini *et al.*, 2004). Its outcome was incorporated in the Eurocode-based new generation of Swiss Structural Standard SIA 261:2003, which replaced SIA 160:1989. Probabilistic hazard maps were generated in terms of pseudo-spectral accelerations at a number of oscillator frequencies (not peak ground accelerations), which were then combined to produce an equivalent design value of horizontal ground acceleration. The resulting seismic zoning map again divided the country into four zones, whose design acceleration values remained the same as those of SIA 160:1989, but for which the zone boundaries changed, significantly increasing the area corresponding to the higher seismicity zones. In this map, Basel belongs to zone 3a, and is thus associated to a design horizontal acceleration of 0.13 g.

According to Wenk (2014), the SIA 260:2003 - SIA 267:2003 standards were partially revised in the years 2012 to 2014, but no changes were introduced to the seismic zoning map. At the time of writing (August 2015), Switzerland is finishing the preparation of an update to its seismic hazard maps (Wiemer *et al.*, 2014).

A3.1.7.2 Building typologies

According to Fähr *et al.* (2001), most of the buildings in the city of Basel were built within the last 150 years, with the exception of the old downtown area, which dates back to the Middle Ages. In general, they are mostly three to five storeys high residential buildings, with the exception of the industrial area in the north-east and two areas to the west and south in which family housing is the predominant typology (see Figure A3.1.28).

As can be observed in Figure A3.1.29, around 57% of the buildings in the metropolitan area of Basel are masonry buildings, while around 38% are made of reinforced concrete, according to the data from Mignan *et al.* (2015). Brick masonry is the most frequent type of masonry. Reinforced concrete (RC) moment-resisting frames are very infrequent, and most concrete structures consist of RC walls, either alone or combined with masonry walls too. Steel and wood structures represent a very small percentage of the overall building stock (5.6%).

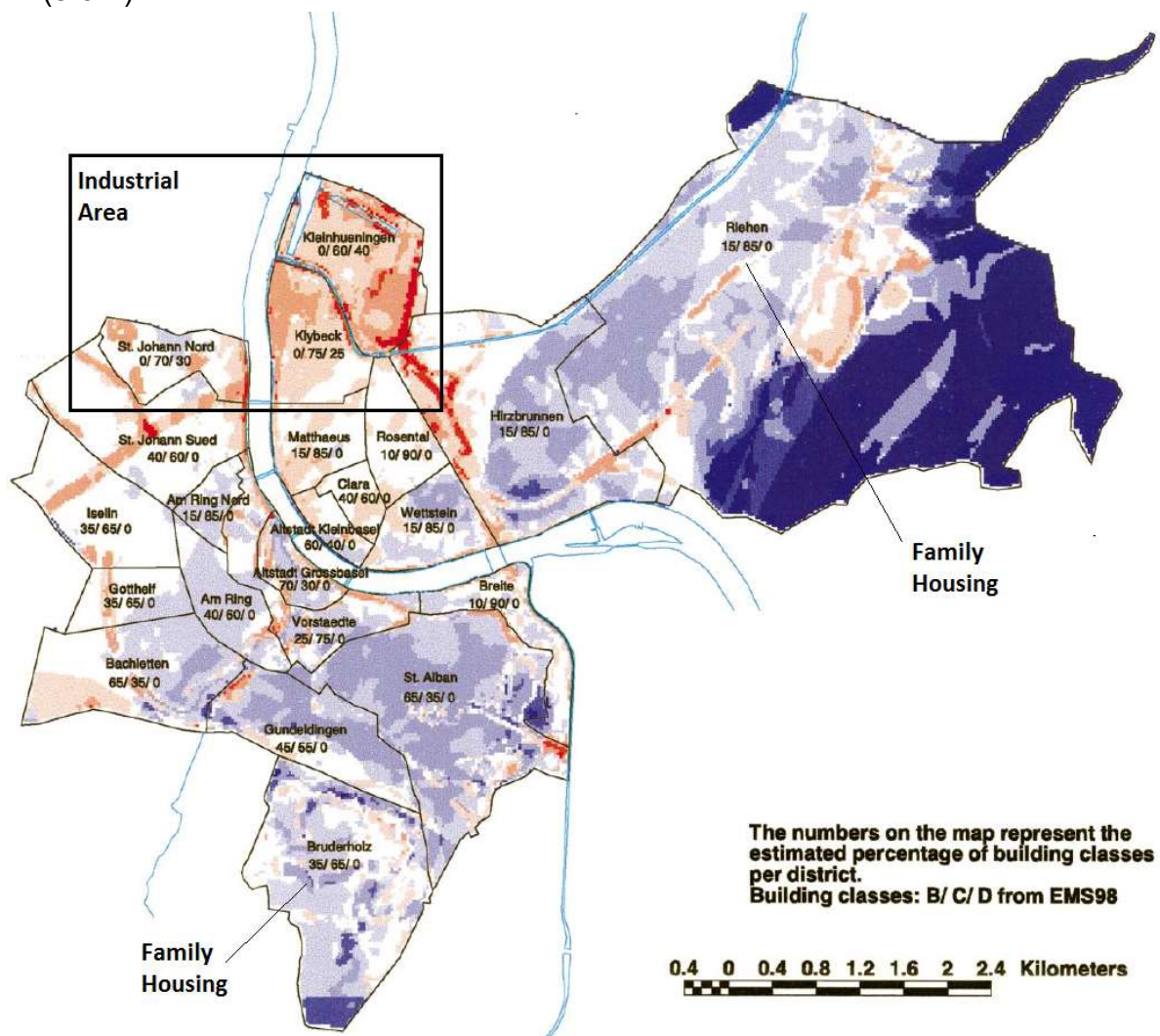


Figure A3.1.28. Distribution of EMS-98 building vulnerability classes (given in percentage with the format B/C/D). From Fähr *et al.* (2001).

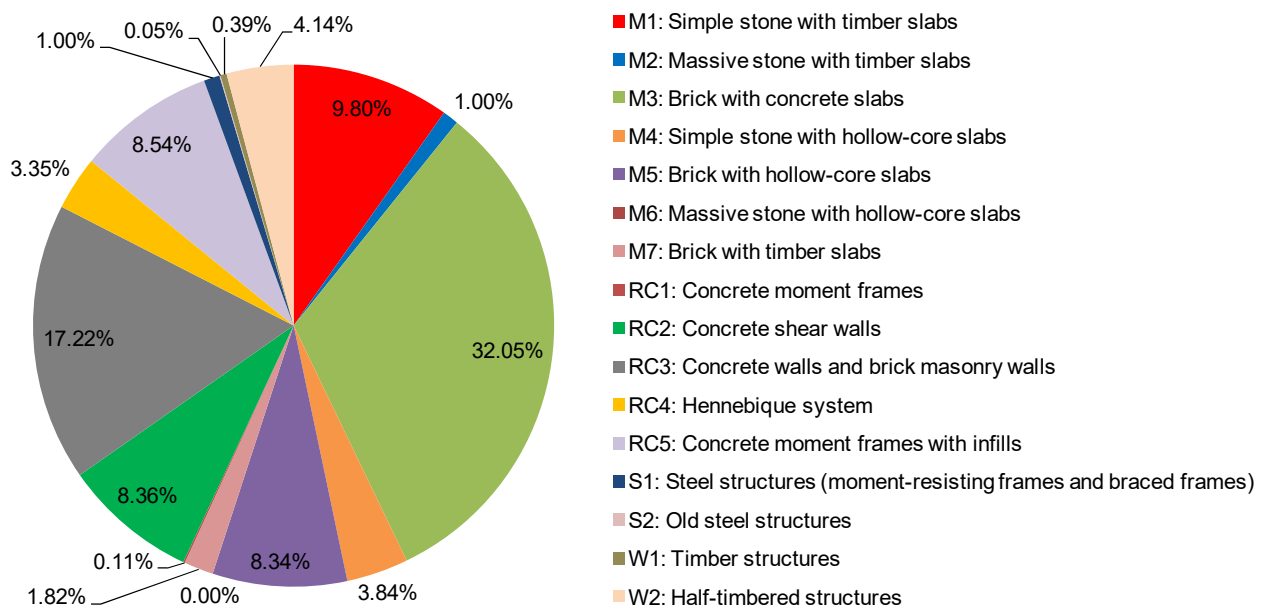


Figure A3.1.29. Percentage of buildings per building typology (data from Mignan *et al.*, 2015).

The European Macroseismic Scale (EMS-98) classifies buildings into six vulnerability classes, from A through F, with the former and the latter corresponding to the most and least vulnerable, respectively. According to Fähr *et al.* (2001) and Mignan *et al.* (2015), most of the buildings in the metropolitan area of Basel fall between classes B and D. Figure A3.1.28 shows the percentage of buildings of each district that belong to each vulnerability class (B, C or D), determined by visual inspection by Fähr *et al.* (2001). According to this map, only buildings in the industrial area are assigned to vulnerability class D. According to Mignan *et al.* (2015), typologies RC1, RC2, RC3, RC5, S2, W1 and W2 belong to this class. Masonry buildings only belong to classes B or C.

Figure A3.1.30 shows the number of buildings per administrative district of the area around the city of Basel, while Figure A3.1.31 shows the number of masonry and reinforced concrete buildings (typologies M1 to M7 and RC1 to RC5 altogether).

Lang & Bachmann (2004) evaluated the vulnerability of eighty-seven residential buildings of Basel using a non-linear static approach. From their results, they concluded that buildings whose structure combines reinforced concrete walls with unreinforced masonry are more vulnerable than pure unreinforced masonry buildings. They attribute this to the unfavourable layouts in plan and elevation of the former, which have very open façade planes and a very small number of lateral resisting elements, and to the practice of using unreinforced masonry in the upper storeys and reinforced concrete in the bottom ones.

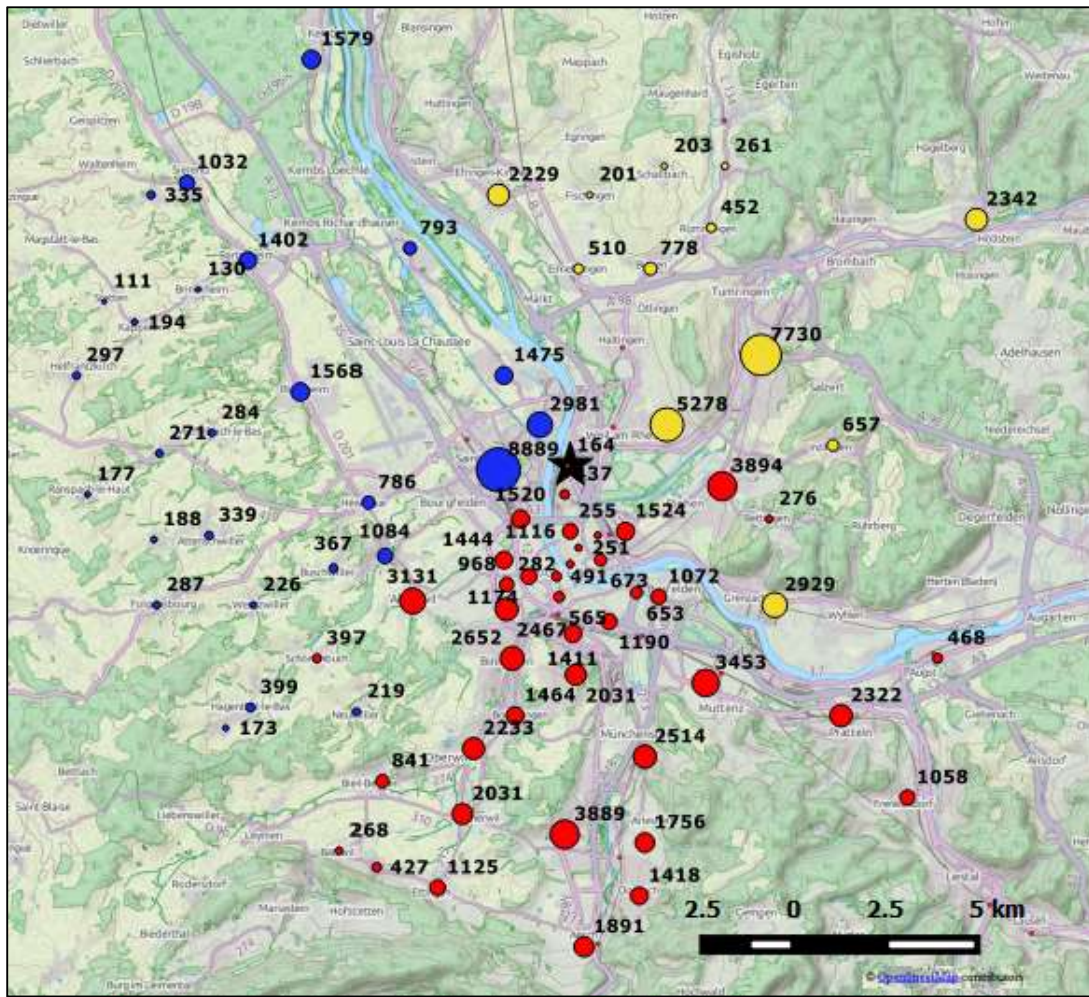


Figure A3.1.30. Total number of buildings per administrative district of Switzerland (red), France (blue) and Germany (yellow) (data from Mignan *et al.*, 2015). The black star shows the epicentre, as determined by Deichmann & Ernst (2009).

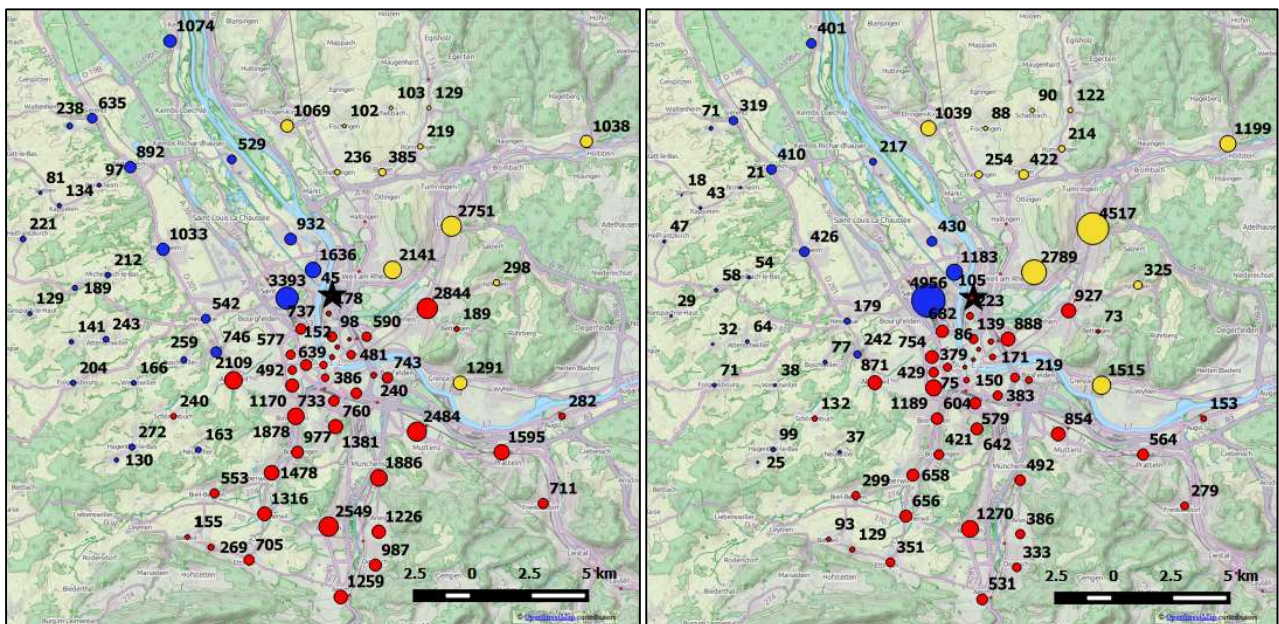


Figure A3.1.31. Number of masonry (left) and reinforced concrete (right) buildings per administrative district of Switzerland (red), France (blue) and Germany (yellow) (data from Mignan *et al.*, 2015). The black star shows the epicentre, as determined by Deichmann & Ernst (2009).

Badoux & Peter (2000) studied the seismic vulnerability of Swiss RC buildings constructed between 1945 and 1989. In their assessment of a series of case studies, they observed that the thinnest RC walls found in existing buildings were 140 mm thick, slabs were 180 mm and thicker, the horizontal and vertical reinforcement ratios of RC walls was between 0.2-0.4% and 0.4-0.7%, respectively, the edges of walls were always confined with U-shaped stirrups, the overlap of the reinforcement bars was usually around 40 bar diameters, and until 1968 the anchorage of reinforcement bars was usually carried out with hooks. Based on these observations, they concluded that the basic conditions required for reinforced concrete to behave in a ductile manner appear to be met.

A3.1.7.3 Prior damage and retrofit

No information has been found regarding prior damage and retrofit.

A3.1.8 Damage observations

A3.1.8.1 Damage states

Given the low level of damage observed, there are no reports making use of standardised damage scales for this earthquake. However, from the qualitative descriptions, it is possible to believe that all damage observed corresponded to Grade 1 in the European Macroseismic Scale (EMS-98; Grünthal, 1998; see Appendix II). This inference is in agreement with what is implied for an EMS-98 intensity of V, for which only damage of Grade 1 to a few buildings of the two lowest vulnerability classes is observed, as described in Table A2.1.1 of Appendix II.

A3.1.8.2 Damage statistics and description

Due to the mild nature of the resulting damage and the relatively old building stock predominant in Basel, it has been very difficult to draw solid conclusions on the total number of damaged buildings. Four main statements on this matter can be found in the literature. Firstly, Deichmann & Giardini, (2009) report hundreds of buildings being affected by very slight non-structural damage such as fine hairline cracks to the plaster and damage to the paint at building junctions. Secondly, Ripperger *et al.* (2009) refer to more than 2,000 damage claims having been filed, of which around 900 were originated within the city of Basel (4.7% of the building stock of the city). Thirdly, Ripperger *et al.* (2009) report as well on the results obtained from 865 interpretable reports gathered by the SED with the purpose of assessing macroseismic intensity. Of the 865 observations, 40 (4.6%) included reports of non-structural damage to buildings: 31 cases of haircracks in walls and 9 cases of minor pieces of plaster falling down. This percentage is larger (5.7%) if only the reports coming from the area of Basel city are considered (403 reports). Fourthly, doubt is casted over how many of the damage claims actually correspond to damage caused by the earthquake. In this regard, Deichmann & Giardini (2009) express that “a significant share of the [hundreds of] reported instances of damage is presumed to be a direct consequence of the earthquake”, implying that an unknown portion of them is not.

Similarly, Bommer *et al.* (2015) state that the number of insurance claims may have been influenced by pre-existing non-structural damage (only noticed once attention was drawn to damage after the earthquake) and potential cases of “moral hazard”, that is, the punishment of companies carrying out seismically-inducing activities by claiming damage of unknown origin was caused by a particular earthquake.

Figures A3.1.32 through A3.1.34 show examples of the kind of damage observed.



Figure A3.1.32. Crack in connection between wall and timber roof (left). Cracks in corner of a window (right).



Figure A3.1.33. Hairline cracks in plaster (left). Minor plaster spalling (right).



Figure A3.1.34. Crack in intersection of two perpendicular masonry elements (left). Crack parallel to the orientation of fibres in a timber element (right).

A3.1.8.3 Observed weaknesses

No particular weaknesses reported.

A3.1.8.4 Damage distribution

As pointed out earlier, the distribution of observed macroseismic intensities (Figure A3.1.18) presents peaks in the SSW direction and towards the east. According to Baer *et al.* (2007), the peak in the SSW direction is consistent with the radiation pattern associated with the focal mechanism of the event, while the peak generated towards the east was probably caused by site amplification due to the presence of poorly compacted alluvial terraces.

A3.1.9 Casualties and losses

A3.1.9.1 Numbers of dead and injured

No casualties were reported for this earthquake.

A3.1.9.2 Causes of casualties

No casualties were reported for this earthquake.

A3.1.9.3 Estimates of economic losses

Figures for economic losses vary between 7 million and 9 million CHF, or around 6.5 to 8.3 million USD (Baisch *et al.*, 2009; Edwards *et al.*, 2015; Giardini, 2009; Kraft *et al.*, 2009).

Similar numbers are reported by newspapers such as *The New York Times* and *The Guardian*.

Giardini (2009) and Kraft *et al.* (2009) point out that these figures seem disproportionately high for a M_L 3.4 event. The two main factors contributing to a real estimation of the damage being so challenging to make are the lack of data from past small earthquakes (Giardini, 2009) and the difficulties in determining which instances of damage can be directly associated to the earthquake and which cannot, given its small magnitude. However, according to Kraft *et al.* (2009), the insurance company did not make an effort to question possibly unjustified claims.

Though the damage in each building never exceeded the usual insurance deductible value of more than 10% of the insured property, all the damage claims were paid by the liability insurance of Geopower Basel, due to the damage having been generated by a manmade event (Giardini, 2009).

A3.1.10 Discussion and conclusions

This M_L 3.4 earthquake occurred on 8th December 2006, at 16:48 UTC (17:48 local time), right under the city of Basel, northern Switzerland, six days after the start of the injection of a large volume of water at high pressures for the creation of an enhanced geothermal system (EGS) for the Deep Heat Mining Project led by Geopower Basel in said city. It was the largest of a series of little less than 15,000 events that were induced in the area, and was preceded by a M_L 2.6 event that occurred in the early morning of the same day, and which led to the premature halt of the injection, and by a M_L 2.7 event in the afternoon. The geothermal project was finally cancelled in December 2009.

The creaking of woodwork and rattling of doors and windows caused by the main shock alarmed the population, though consequent damage was limited mostly to hairline cracks in plaster and paint. Nevertheless, the company in charge of the project received more than two thousand damage reports some days after the event. The exact number of cases corresponding to damage undoubtedly caused by the earthquake is unknown. Figures for economic losses vary between 7 million and 9 million CHF (6.5 to 8.3 million USD), which seem to be surprisingly high for a M_L 3.4 event. All damage claims were paid by the liability insurance of Geopower Basel.

Though the occurrence of these earthquakes was clearly related to the water injection process for the EGS, the tectonics of the area of Basel are not incapable of naturally producing seismic events of the magnitudes observed during this series and much larger. Further, they do not seem to have been the consequence of hydrofracking (fracturing of the rock due to the water injection) but of the induced activation of a complex pre-existing fault pattern.

A3.1.11 References

A3.1.11.1 Bibliography

- Afshari, K. & J.P. Stewart (2016). Physically parametrised prediction equations for significant duration in active crustal regions. *Earthquake Spectra* **32**(4), 2057-2081.
- Badoux, M. & K. Peter (2000). Seismic vulnerability of older Swiss RC buildings. In *Proceedings of the 12th World Conference on Earthquake Engineering*, Auckland, New Zealand, 30 January - 4 February.
- Baer, M., N. Deichmann, J. Braunmiller, J. Clinton, S. Husen, D. Fäh, D. Giardini, P. Kästli, U. Kradolfer & S. Wiemer (2007). Earthquakes in Switzerland and surrounding regions during 2006. *Swiss Journal of Geosciences* **100**, 517–528.
- Baisch, S., D. Carbon, U. Dannwolf, B. Delacou, M. Devaux, F. Dunand, R. Jung, M. Koller, C. Martin, M. Sartori, R. Secanell & R. Vörös (2009). *Deep heat mining basel: seismic risk analysis*. Ser. Group Departement Für Wirtsch. Soz. Umw. Kantons Basel-Stadt Basel. Available online at: http://wsu.bs.ch/dms/wsu/download/abgeschlossene-dossiers/serianex_teil_1_english.pdf. Last accessed: 20th April 2017.
- Becker, A., C.A. Davenport & D. Giardini (2002). Palaeoseismicity studies on end-Pleistocene and Holocene lake deposits around Basle, Switzerland. *Geophysical Journal International* **149**, 659–678.
- Bommer, J.J., H. Crowley & R. Pinho (2015). A risk-mitigation approach to the management of induced seismicity. *Journal of Seismology* **19**(2), 623–646.
- Bommer, J.J., P.J. Stafford & J.E. Alarcón (2009). Empirical equations for the prediction of the significant, bracketed, and uniform duration of earthquake ground motion. *Bulletin of the Seismological Society of America* **99**(6), 3217-3233.
- Catalli, F., M.-A. Meier & S. Wiemer (2013). The role of Coulomb stress changes for injection-induced seismicity: the Basel enhanced geothermal system. *Geophysical Research Letters* **40**, 72–77.
- Cauzzi, C., B. Edwards, D. Fah, J. Clinton, S. Wiemer, P. Kastli, G. Cua & D. Giardini (2015). New predictive equations and site amplification estimates for the next-generation Swiss ShakeMaps. *Geophysical Journal International* **200**, 421–438.
- CEN (2004). *Eurocode 8: Design of structures for earthquake resistance - Part 1: General rules, seismic actions and rules for buildings*. European Committee for Standardization, Brussels, Belgium.
- Deichmann, N. & J. Ernst (2009). Earthquake focal mechanisms of the induced seismicity in 2006 and 2007 below Basel (Switzerland). *Swiss J. Geosci.* **102**, 457–466.
- Deichmann, N. & D. Giardini (2009). Earthquakes induced by the stimulation of an Enhanced Geothermal System below Basel (Switzerland). *Seismol. Res. Lett.* **80**, 784–798.
- Deichmann, N., T. Kraft & K.F. Evans (2014). Identification of faults activated during the stimulation of the Basel geothermal project from cluster analysis and focal mechanisms of the larger magnitude events. *Geothermics* **52**, 84–97.

- Driscoll, J., F. Vigier & K. Leith (2010). *The Basel Metropolitan Area: three borders - one metropolitan area*. International Centre for Local and Regional Development (ICLRD), Northern Ireland.
- Edwards, B. & D. Fah (2013). A stochastic ground-motion model for Switzerland. *Bull. Seismol. Soc. Am.* **103**, 78–98.
- Edwards, B., T. Kraft, C. Cauzzi, P. Kästli & S. Wiemer (2015). Seismic monitoring and analysis of deep geothermal projects in St Gallen and Basel, Switzerland. *Geophysical Journal International* **201**, 1020–1037.
- Fäh, D., E. Rüttener, T. Noack, T. & P. Kruspan (1997). Microzonation of the city of Basel. *J. Seismol.* **1**, 87–102.
- Fäh, D., F. Kind, K. Lang & D. Giardini (2001). Earthquake scenarios for the city of Basel. *Soil Dyn. Earthq. Eng.* **21**, 405–413.
- Ferry, M., M. Meghraoui, B. Delouis & D. Giardini (2005). Evidence for Holocene palaeoseismicity along the Basel-Reinach active normal fault (Switzerland): a seismic source for the 1356 earthquake in the Upper Rhine graben. *Geophysical Journal International* **160**, 554–572.
- Giardini, D. (2009). Geothermal quake risks must be faced. *Nature* **462**, 848–849.
- Giardini, D., G. Grünthal, K.M. Shedlock & P. Zhang (1999). The GSHAP global seismic hazard map. *Annali di Geofisica* **42**(6), 1225-1228.
- Giardini, D., S. Wiemer, D. Fäh & N. Deichmann (2004). *Seismic Hazard Assessment of Switzerland, 2004*. Swiss Seismological Service, ETH Zurich.
- Goertz-Allmann, B.P., A. Goertz & S. Wiemer (2011). Stress drop variations of induced earthquakes at the Basel geothermal site. *Geophysical Research Letters* **38**, 5 pp.
- Grünthal, G. (ed.) (1998). *European Macroseismic Scale 1998 (EMS-98)*. Cahiers du Centre Europeen de Geodynamique et de Seismologie 15, Centre Europeen de Geodynamique et de Seismologie, Luxembourg.
- Häring, M.O., U. Schanz, F. Ladner & B.C. Dyer (2008). Characterisation of the Basel 1 enhanced geothermal system. *Geothermics* **37**, 469–495.
- Havenith, H.-B., D. Fäh, U. Polom & A. Roullé (2007). S-wave velocity measurements applied to the seismic microzonation of Basel, Upper Rhine Graben. *Geophysical Journal International* **170**, 346–358.
- Kastrup, U. (2004). Stress field variations in the Swiss Alps and the northern Alpine foreland derived from inversion of fault plane solutions. *J. Geophys. Res.* **109**, 22 pp.
- Kraft, T. & N. Deichmann (2014). High-precision relocation and focal mechanism of the injection-induced seismicity at the Basel EGS. *Geothermics* **52**, 59–73.
- Kraft, T., P.M. Mai, S. Wiemer, N. Deichmann, J. Ripperger, P. Kästli, C. Bachmann, D. Fäh, J. Wössner & D. Giardini (2009). Enhanced geothermal systems: mitigating risk in urban areas. *Eos Trans. Am. Geophys. Union* **90**, 273–274.
- Lang, K. & H. Bachmann (2004). On the seismic vulnerability of existing buildings: a case study of the city of Basel. *Earthq. Spectra* **20**, 43–66.

- Laubscher, H. (2001). Plate interactions at the southern end of the Rhine graben. *Tectonophysics* **343**, 1–19.
- Majer, E.L., R. Baria, M. Stark, S. Oates, J. Bommer, B. Smith & H. Asanuma (2007). Induced seismicity associated with enhanced geothermal systems. *Geothermics* **36**, 185–222.
- Mignan, A., D. Landtwing, P. Kästli, B. Mena & S. Wiemer (2015). Induced seismicity risk analysis of the 2006 Basel, Switzerland, Enhanced Geothermal System project: Influence of uncertainties on risk mitigation. *Geothermics* **53**, 133–146.
- Noack, T. & D. Fäh (2015) *Earthquake Microzonation: site effects and local geology. A case study for the Kanton of Basel-Stadt*. Unpublished report.
- Plenefisch, T. & K.-P. Bonjer (1997). The stress field in the Rhine Graben area inferred from earthquake focal mechanisms and estimation of frictional parameters. *Tectonophysics* **275**, 71–97.
- Ripperger, J., P. Kästli, D. Fäh & D. Giardini (2009). Ground motion and macroseismic intensities of a seismic event related to geothermal reservoir stimulation below the city of Basel - observations and modelling. *Geophysical Journal International* **179**, 1757–1771.
- SIA 261 (2003). *Actions on Structures*. Swiss Standard SIA 261, Swiss Society of Engineers and Architects, Zurich.
- Steimen, S., D. Fäh, D. Giardini, M. Bertogg & S. Tschudi (2004). Reliability of building inventories in seismic prone regions. *Bull. Earthq. Eng.* **2**, 361–388.
- United Nations, ed. (2006). *Human Development Report 2006 - Beyond scarcity: power, poverty and the global water crisis*. Report of the United Nations Development Programme (UNDP), New York, United States.
- United Nations, ed. (2008). *Human Development Report 2007/2008 - Fighting climate change: human solidarity in a divided world*. Report of the United Nations Development Programme (UNDP), New York, United States.
- United Nations, ed. (2009). *Human Development Report 2009 - Overcoming barriers: human mobility and development*. Report of the United Nations Development Programme (UNDP), New York, United States.
- United Nations, ed. (2014). *Human Development Report 2014 - Sustaining human progress: Reducing vulnerabilities and building resilience*. Report of the United Nations Development Programme (UNDP), New York, United States.
- Wenk, T. (2014). *Seismic zoning map of Switzerland*. DGEB Workshop: Results of the European Project SHARE: Seismic Harmonization in Europe, pp. 43–52.
- Wenk, T. & D. Fäh (2012). Seismic microzonation of the Basel area. In *Proceedings of the 15th World Conference on Earthquake Engineering*, Lisbon, Portugal, September 24–28.
- Wiemer, S., D. Giardini, D. Fäh, N. Deichmann & S. Sellami (2009). Probabilistic seismic hazard assessment of Switzerland: best estimates and uncertainties. *J. Seismol.* **13**, 449–478.
- Wiemer, S., S. Hiemer, J. Woessner, L. Danciu, D. Fäh, B. Edwards, C. Cauzzi, C. Michel, V. Poggi, E. Kissling, P. Kästli & D. Giardini (2014). The 2014 update of the Swiss national seismic hazard model - Key science issues. In *Proceedings of the Second European Conference on Earthquake Engineering and Seismology*, Istanbul, Turkey, August 25–29.

Woessner, J., D. Giardini, H. Crowley, F. Cotton, G. Grünthal, G. Valensise, R. Arvidsson, R. Basili, M. B. Demircioglu, S. Hiemer, C. Meletti, R. W. Musson, A. N. Rovida, K. Sesetyan, M. Stucchi & The SHARE Consortium (2015). The 2013 European Seismic Hazard Model: Key Components and Results. *Bulletin of Earthquake Engineering* **13**(12), 3553–3596. Online data source: <http://www.efehr.org/en/home/>. Last accessed: 3rd December 2017.

Worden, C.B., M.C. Gerstenberger, D.A. Rhoades & D.J. Wald (2012). Probabilistic relationships between ground-motion parameters and Modified Mercalli Intensity in California. *Bull. seism. Soc. Am.* **102**, 204-221.

A3.1.11.2 Web references

European-Mediterranean Seismological Centre (EMSC): <http://www.emsc-csem.org>.
Website for this event (last accessed 9th February 2017):
<http://www.emsc-csem.org/Earthquake/earthquake.php?id=37096>.

Microzonation of Basel at the Basel Geoportal (2015): <http://www.stadtplan.bs.ch/geoviewer/>.
Last accessed: 11th August 2015.

Swiss Seismological Service (SED): <http://www.seismo.ethz.ch/>.
Website for this event (last accessed 9th February 2017):
<http://hitseddb.ethz.ch:8080/ecos09/detail.html?id=30217904.00000&locale=en>.

United States Geological Survey (USGS): <http://earthquake.usgs.gov/>.
Renovated website for this event (last accessed 9th February 2017):
<http://earthquake.usgs.gov/earthquakes/eventpage/usp000eztf#executive>.

Wikipedia (last accessed 11th August 2015):
<https://en.wikipedia.org/wiki/Switzerland>
https://en.wikipedia.org/wiki/Cantons_of_Switzerland

World Economic Outlook Database 2015 (2015):
<http://www.imf.org/external/pubs/ft/weo/2015/01/weodata/index.aspx>.
Last accessed: 11th August 2015.

A3.2 February 2011 M4.8 Guy-Greenbrier (Arkansas) Earthquake, USA

This earthquake occurred on 28th February 2011, at 05.00 UTC (27th February 2011, 23:00 local time), and is one of the largest to have been registered in Arkansas outside of the New Madrid Seismic Zone. It was part of a large earthquake swarm that started around 2009 and which is believed to have been triggered by the injection of waste water at disposal wells in the vicinity of a previously unknown fault. The main shock and other strong events in the sequence were felt across a broad area, but caused only minor damage to houses, mainly in the town of Greenbrier, and no casualties.

A3.2.1 Tectonic and seismic setting

A3.2.1.1 Tectonic setting

This earthquake occurred within the Arkoma basin, in the centre of the state of Arkansas, around 60 km to the north of Little Rock, the state capital. The Arkoma basin is located just north of the Ouachita Mountains frontal faults (Figure A3.2.1), and it is bounded to the north by the Ozark Uplift (Abd *et al.*, 2012; Horton, 2012). The whole area lies within the large stable continental region of the central and eastern United States, which is characterised by a relatively lower seismic activity and low strain rates than active continental regions (Klose & Seeber, 2007), and by the fact that earthquakes tend to be felt over much larger areas (USGS).

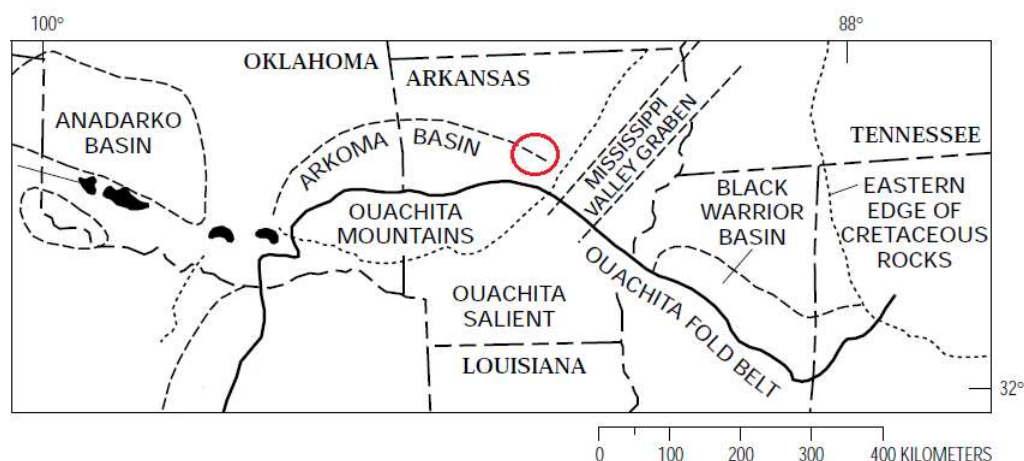


Figure A3.2.1. Tectonic map of Arkansas and surrounding areas. The red circle encloses the area around the epicentre of the 2011 Guy-Greenbrier earthquake. Modified from Perry Jr (1997).

The most relevant tectonic features of the Arkoma basin consist of normal faults, thrust faults and folds striking approximately east-west (Figure A3.2.2), originated in alternating tensional and compressional stress fields at different geological stages (Abd *et al.*, 2012). The 2011 Guy-Greenbrier earthquake sequence revealed the existence of an unknown fault striking about N30E (Figure A3.2.2) at depths between 3.0 and 7.0 km, extending from the Precambrian basement up into the Palaeozoic sedimentary rock, named "the Guy-Greenbrier" fault by Horton (2012). This fault is suitably oriented with respect to the

N60E direction of the principal compression axis of the present-day stress field in the mid-continental area for strike-slip failure (Abd *et al.*, 2012; Horton, 2012). It is noted that its orientation is similar to that of the northern segment of the New Madrid Seismic Zone, the most relevant seismic source of the state, located around 300 km to the north-east. No known seismogenic faults have surface traces within Arkansas.

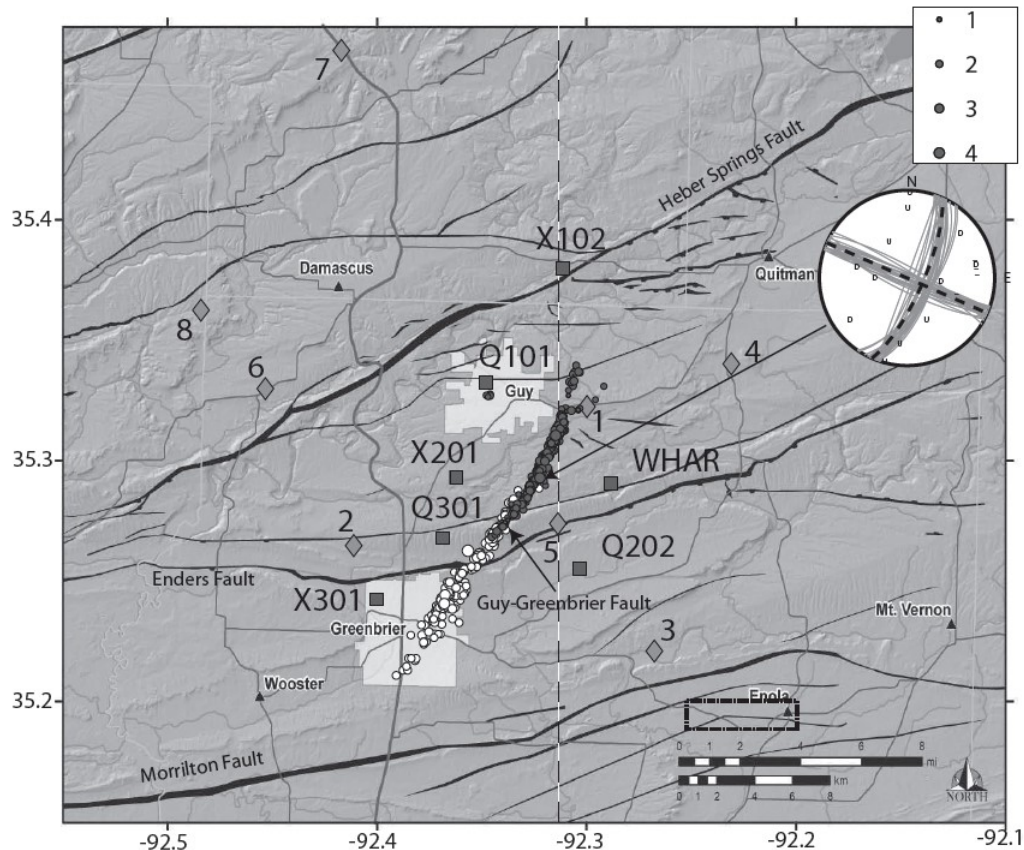


Figure A3.2.2. Known faults around the epicentral area and the newly-identified Guy-Greenbrier fault (Horton, 2012). Circles indicate the epicentres of events that occurred between 1st October 2010 and 15th February 2011 (dark gray filled) and between 16th February 2011 and 8th March 2011 (white filled). Numbered diamonds indicate waste disposal wells. First-motion focal mechanism for **M**4.0 event on 11th October 2010 shown. From Horton (2012).

A3.2.1.2 Regional and local seismicity

Seismicity rates in the area known as the central and eastern United States (CEUS) are generally low (Hough & Page, 2015). With the exception of the north-east corner of the state, which belongs to the New Madrid Seismic Zone, most of Arkansas is subject only to diffuse seismic activity consisting of scattered, isolated earthquakes, and occasional swarms (Dart & Ausbrooks, 2011; Horton, 2012). Figure A3.2.3 presents the earthquake archive catalogue of the Arkansas Geological Survey, which includes events from 1699 until 26th December 2015.

The New Madrid Seismic Zone (NMSZ) is the most hazardous fault zone to the east of the Rocky Mountains (Ausbrooks, 2010; Horton, 2012; McFarland, 2001). Four large earthquakes with estimated magnitudes **M**7.5, **M**7.0, **M**7.3 and **M**7.5 took place in the

NMSZ between 16th December 1811 and 7th February 1812, and caused extensive rise and subsidence of lands, fissures, sand blows, and large landslides, as well as damage to buildings, though limited due to the low exposure in the area. According to the United States Geological Survey (USGS), the NMSZ has produced other sequences of major earthquakes over the past 4,500 years, including several events of **M7.0** to **M8.0** (USGS, 2016).

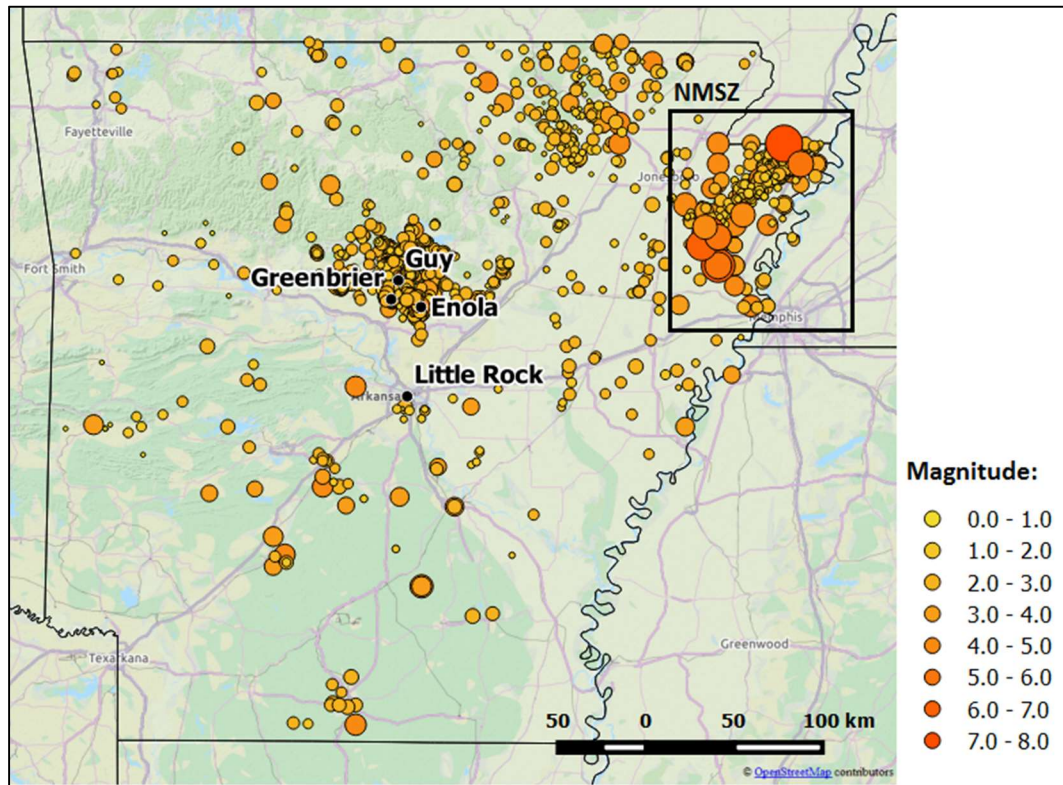


Figure A3.2.3. Earthquake catalogue (1699-2015) for Arkansas, according to the Arkansas Geological Survey. New Madrid Seismic Zone (NMSZ) marked (Arkansas Geological Survey, 2016).

Outside of the NMSZ, no earthquakes with magnitude larger than **M4.9** have ever been recorded. Between 1699 and 2010, only twelve events with magnitudes between **M4.0** and **M4.9** were identified, and they actually occurred in a much narrower period of time, between 1883 and 1974. Within the Faulkner county, where Guy and Greenbrier are located, three main earthquake swarms are known to have occurred: (i) the 1982 Enola swarm, which lasted for many years and produced over 40,000 events, of which the largest was a **M4.5**, (ii) the 2001 swarm, which occurred in the same area as the 1982 one, and whose largest event was a **M4.4**, (iii) and the 2011 Guy-Greenbrier swarm itself (Abd *et al.*, 2012; Ausbrooks, 2010; Horton, 2012; McFarland, 2001). The Enola swarms were located around 15.0 km to the south-east of the Guy-Greenbrier swarm. There are no reports of damage from either the 1982 or the 2001 Enola swarms (Ausbrooks, 2010; McFarland, 2001; The Encyclopedia of Arkansas History & Culture, 2015).

Huang & Beroza (2015) point out that even though observed seismicity along the Guy-Greenbrier fault decayed gradually after injection at the wells closer to the fault was

stopped in March 2011, it did not end abruptly but became more diffuse, and remained higher than the background seismicity rate before the 2011 sequence.

According to Horton (2012), the rupture of the entire (estimated) surface of the Guy-Greenbrier fault is capable of causing earthquakes with magnitudes up to **M5.5-6.0**, but their likelihood is unknown.

A3.2.1.3 Seismic hazard

Figure A3.2.4 shows extracts of the probabilistic seismic hazard maps for the United States of 2008 and 2014, elaborated by the United States Geological Survey (USGS; Petersen *et al.*, 2008; Petersen *et al.*, 2014). Values shown correspond to peak ground acceleration (PGA) on rock with a 10% probability of exceedance in 50 years. The area affected by the 2011 Guy-Greenbrier earthquake and the state of Arkansas are marked in red.

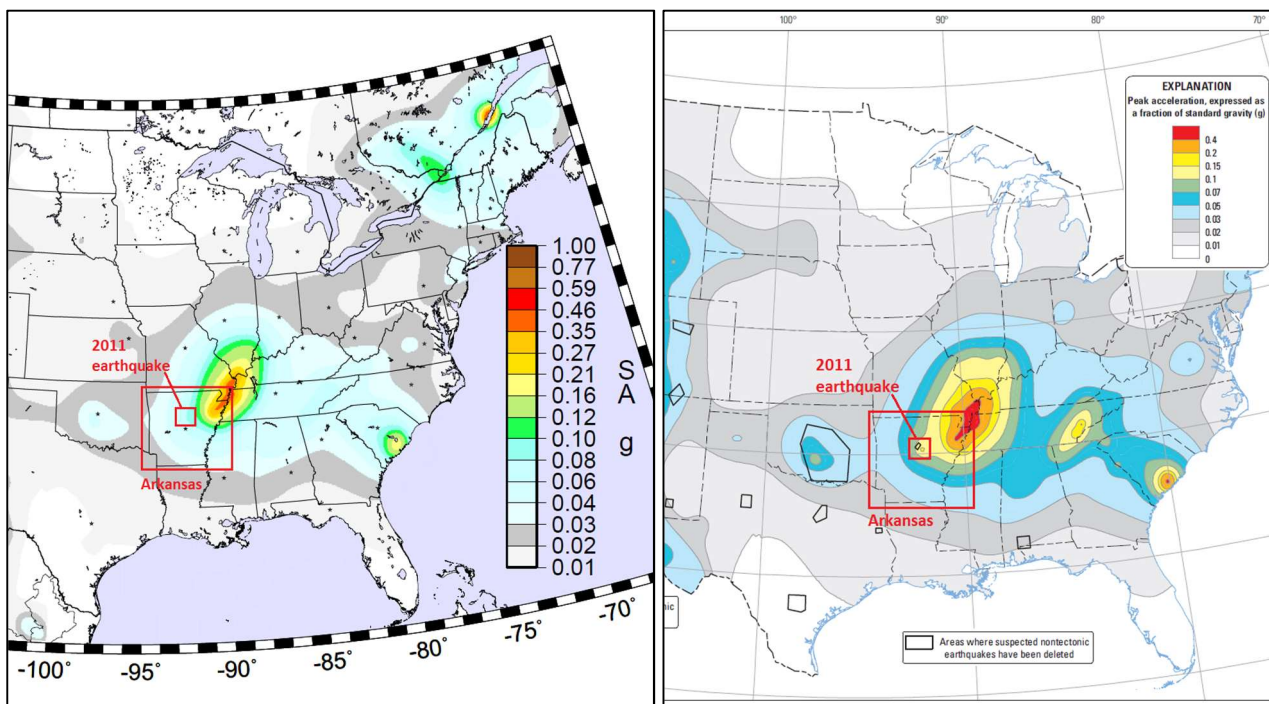


Figure A3.2.4. Extract of the 2008 (left) and 2014 (right) hazard maps for the United States, elaborated by the USGS (2016). Values correspond to peak ground acceleration (g) on rock with a 10% probability of exceedance in 50 years.

Table A3.2.1 presents a summary of the PGA values expected at Guy, Greenbrier and Little Rock. As can be observed, the expected PGA values of Guy and Greenbrier have suffered an increase of about 50% in the 2014 hazard map. The table also reports the corresponding values obtained from the Global Seismic Hazard Assessment Program (GSHAP; Giardini *et al.*, 1999), which are around 10% smaller than those of 2008. In spite of the discrepancies, all values support the idea that seismic hazard is moderate to low in the affected area. It should be noted that the USGS national seismic hazard maps do not take into consideration induced seismic activities (please refer to the *Seismic hazard* section of Appendix A3.6 for a discussion on the topic).

Table A3.2.1. Peak ground acceleration (PGA, g) values on rock with a 10% probability of exceedance in 50 years according to the 2008 and 2014 USGS hazard maps, and results from the Global Seismic Hazard Assessment Program (GSHAP), at relevant locations in Arkansas.

PLACE	USA 2008	USA 2014	GSHAP
Guy	0.0750	0.1124	0.0669
Greenbrier	0.0731	0.1118	0.0641
Little Rock	0.0653	0.0802	0.0590

A3.2.2 Earthquake source characteristics

A3.2.2.1 Location, depth and time

The main shock occurred on 28th February 2011, at 05.00 UTC (27th February 2011, 23.00 local time).

Several organizations and agencies report their own estimations of the epicentral coordinates and hypocentral depth. The information reported in the websites of the National Earthquake Information Center (NEIC) of the United States Geological Service (USGS), the Global Centroid Moment Tensor Project (GCMT; Dziewonski *et al.*, 1981; Ekström *et al.*, 2012) and the International Seismological Centre (ISC) is summarized in Table A3.2.2. The Arkansas Geological Survey reports the same coordinates and depth as the USGS. Cells marked as (*f) correspond to parameters that were held fixed while inversion was carried out to retrieve those that remain.

Table A3.2.2. Epicentral coordinates and hypocentral depths from different sources.

Agency / Publication		Latitude	Longitude	Depth (km)
NEIC	National Earthquake Information Center, USGS	35.2650 ° N	92.3440 °W	3.80
GCMT	Centroid Global Centroid Moment Tensor Project (**)	35.3800 ° N	92.3700 °W	12.00 (*f)
ISC	International Seismological Centre - GEM catalogue	35.3264 ° N	92.3004 °W	10.00 (*f)

(*f) fixed parameter used for inversion

(**) centroid (not-hypocentral) location

According to Horton (2012), the events recorded between late September 2010 and 4th March 2011 occurred at depths between 3.00 and 7.00 km, and the hypocentre of the main shock in particular was located at a depth of around 6.00 km. Abd *et al.* (2012) give a range of hypocentral depths between 1.00 and 7.00 km for events recorded between September 2009 and August 2011.

The map in Figure A3.2.5 shows the different estimations of the epicentral coordinates enumerated above, together with the faults identified by the USGS around the area (Stoeser *et al.*, 2007). The Guy-Greenbrier fault (shown in red) is not yet part of the USGS database because its existence was not known until after the 2011 sequence (Horton,

2012). Note that coordinates reported by the GCMT correspond to the location of the centroid, and not the hypocentre.

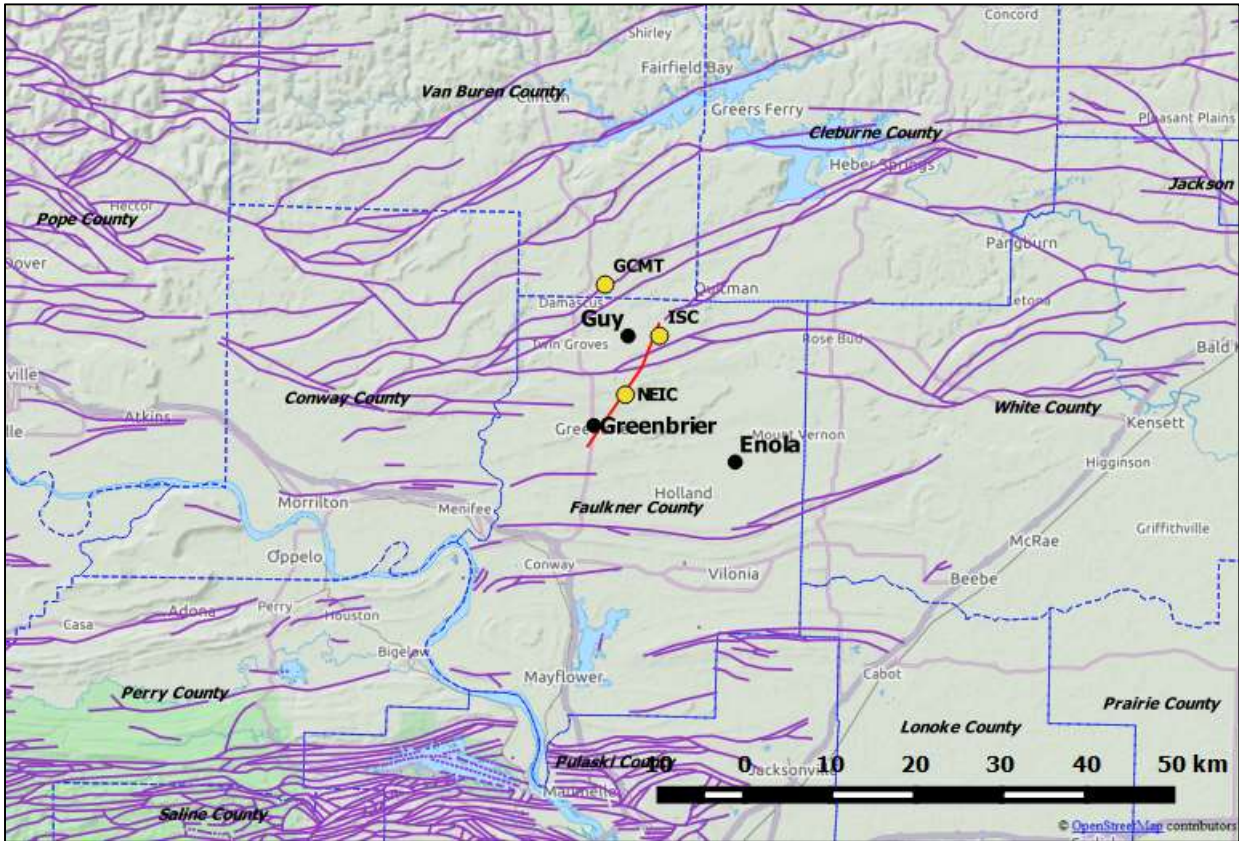


Figure A3.2.5. Estimation of epicentral coordinates (yellow circles). Faults in the area marked in violet, according to the USGS (Stoeser *et al.*, 2007; USGS, 2016). Approximate trace of the Guy-Greenbrier fault, as suggested by Horton (2012), shown in red.

A3.2.2.2 Magnitude

Estimations of magnitude made by the same agencies are reported in Table A3.2.3.

Table A3.2.3. Estimations of moment magnitude (**M**), body-wave magnitude (**mb**) and surface-wave magnitude (**Ms**).

Agency		M	mb	Ms
NEIC	National Earthquake Information Center, USGS	4.7	4.4	-
GCMT	Global Centroid Moment Tensor Project	4.8	4.4	4.8
ISC	International Seismological Service (inversion)	-	4.5	4.2

A3.2.2.3 Style-of-faulting

The fault plane solutions for the main shock indicate a right-lateral strike-slip mechanism, with a small extensional component. The Centroid Moment Tensor is significantly non-double couple, which is typical of fluid-injection triggered events, for it is an indicator of a volumetric change.

Table A3.2.4 summarizes the fault plane solutions calculated by the USGS and the GCMT, while Figure A3.2.6 shows the corresponding beachball representations. Note that, being the dip very close to 90° in all cases, a 26° strike and a 211° strike are practically equivalent.

Table A3.2.4. Fault plane solutions and fault planes from different sources. Fault planes marked in grey are the preferred solution in each case.

Fault Plane 1			Fault Plane 2			Source
Strike	Dip	Rake	Strike	Dip	Rake	
295	80	-5	26	85	-170	Regional Moment Tensor NEIC (USGS)
301	71	1	211	89	161	GCMT

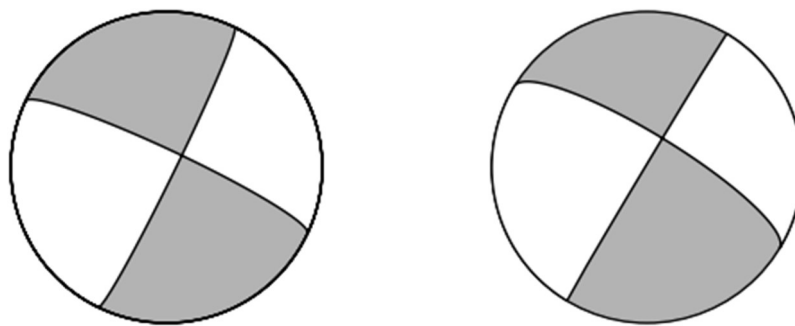


Figure A3.2.6. Fault plane solutions according to the USGS (left) and GCMT (right).

A3.2.2.4 Stress drop

No information could be found regarding the stress drop of the main shock. However, Huang *et al.* (2016) calculated the stress drops for 25 earthquakes of the sequence with magnitudes in the range **M**2.17-2.57 by means of the spectral ratio method, and report median values of 10.57 and 3.54 MPa for the Brune and Boatwright spectral models, respectively. Taking into consideration the uncertainties associated to the calculation of stress drops, they conclude that the results obtained are comparable with the values corresponding to tectonic earthquakes in California that occur at similar shallow depths.

A3.2.2.5 Foreshocks and aftershocks

The exact moment at which the Guy-Greenbrier earthquake swarm started is not clear, though it is believed to be directly related to the first waste disposal well of the area becoming operational in April 2009. According to Horton (2012), there was a noticeable change in the number of earthquakes with magnitudes equal to or larger than 2.5, which increased from one in 2007 and two in 2008, to ten in 2009, 54 in 2010 and 157 in 2011. Nevertheless, Horton (2012) believes that no earthquakes occurred along the Guy-Greenbrier fault itself prior to the start of injection at well number 1 (Figure A3.2.2) on 7th July 2010. Three of the most relevant foreshocks occurred shortly after well number 5 (Figure A3.2.2) was activated in September 2010. These were a **M**4.0, a **M**3.8 and a **M**3.9,

which occurred on 11th October, 15th October and 20th November, respectively, and were widely felt across northern Arkansas and southern Missouri. After a two-month halt, seismic activity resumed by mid-February 2011. The largest foreshock of the series was a **M4.1** event that took place on 18th February 2011.

Wells 1 and 5 were shut down on 4th March 2011, but the Guy-Greenbrier swarm did not come to a full stop immediately (Horton, 2012). The observed seismicity decayed steadily during the three months that followed but, according to Huang & Beroza (2015), it remained higher during 2012-2014 than the background seismicity rate before the 2011 sequence. Huang & Beroza (2015) detected more than 460,000 earthquakes between July 2010 and October 2011 by means of single-station template matching, a technique that allows to detect particularly small earthquakes in areas of sparse instrumentation.

A3.2.2.6. Nature of earthquake

In spite of the difficulties that exist in establishing an unequivocal link between seismic events and waste disposal wells, several authors agree that the 2011 Guy-Greenbrier earthquake sequence was a triggered swarm (Abd *et al.*, 2012; Horton, 2012; Huang & Beroza, 2015; Llenos & Michael, 2013).

Abd *et al.* (2012), found a strong correlation between fluid injection at wells 1 and 5 (Figure A3.2.2) and seismic activity. Horton (2012), Huang & Beroza (2015) and Llenos & Michael (2013) concluded that the change in seismicity rates observed in the Guy-Greenbrier area since 2009 is too significant to be due to random fluctuations in seismicity rates. In particular, Huang & Beroza (2015) observed that, during the operation of nearby injection wells, seismicity around the Guy-Greenbrier area deviated from the Gutenberg-Richter law, but returned to it after injection was halted. Apart from this temporal correlation, Horton (2012) points out that 98% of the earthquakes that occurred in the area in 2011 occurred within 6 km of one of three waste disposal wells, after the start of injection at those wells.

Within the earthquake archive catalogue of the Arkansas Geological Survey (Figure A3.2.3), the earthquakes that make up the Guy-Greenbrier earthquake sequence are tagged as "probable triggered" events.

A.2.2.3 Geology and ground conditions in the affected area

A3.2.3.1 Regional geology and topography

Guy and Greenbrier lie over the Arkansas River Valley, one of the five physiographic regions of the state (Figure A3.2.7). It is a low-lying region surrounding the Arkansas River and its major tributaries. Its Precambrian crystalline basement is overlain by thick layers of Palaeozoic sedimentary rocks (Horton, 2012). These consist of a sequence of coal-bearing sandstones and shale arranged into east-west trending open folds (anticlines and synclines) and faults, which are a consequence of the compression stresses the area was

subject to during the formation of the Ouachita orogenic system (Arkansas Geological Survey). The Arkansas River Valley region serves as a transition zone between the Ozark plateaus, an area of fairly flat-lying rock formations, and the latter.

The sedimentary layers at the Arkansas River Valley region are part of the buried section of the Ozark aquifer, which is mainly formed by dolostone, limestone and sandstone. The Guy-Greenbrier fault partially cuts the Ozark aquifer, and penetrates 2.0-3.0 km into the Precambrian basement rock.

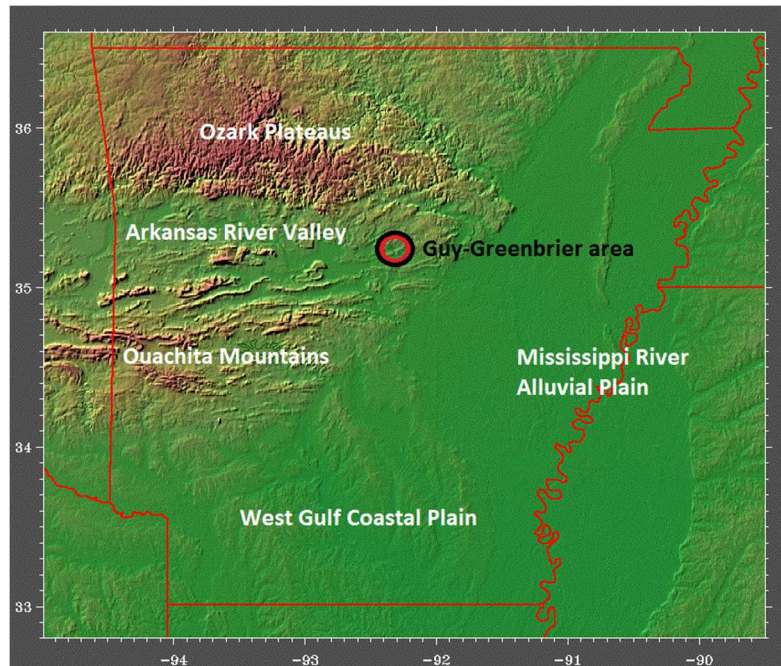


Figure A3.2.7. Topographic map and physiographic regions of the state of Arkansas. Topographic map by Ray Sterner, Applied Physics Laboratory, Johns Hopkins University (1995).

A3.2.3.2 Site conditions in the affected area

The map in Figure A3.2.8 shows the National Earthquake Hazards Reduction Program (NEHRP) soil classification map of Arkansas (Ausbrooks & Doerr, 2008a). As can be observed, the towns of Guy and Greenbrier are located over soil type B, which corresponds to rock with V_{s30} values between 760 and 1500 m/s. The map also shows that soils around the Arkansas river and in the Mississippi river alluvial plain are susceptible to liquefaction. Within the HAZUS scheme, the Guy-Greenbrier area belongs to a liquefaction susceptibility level of 1, corresponding to "very low", on a scale that goes from 0, "none", to 5, "very high" (Ausbrooks & Doerr, 2008b).

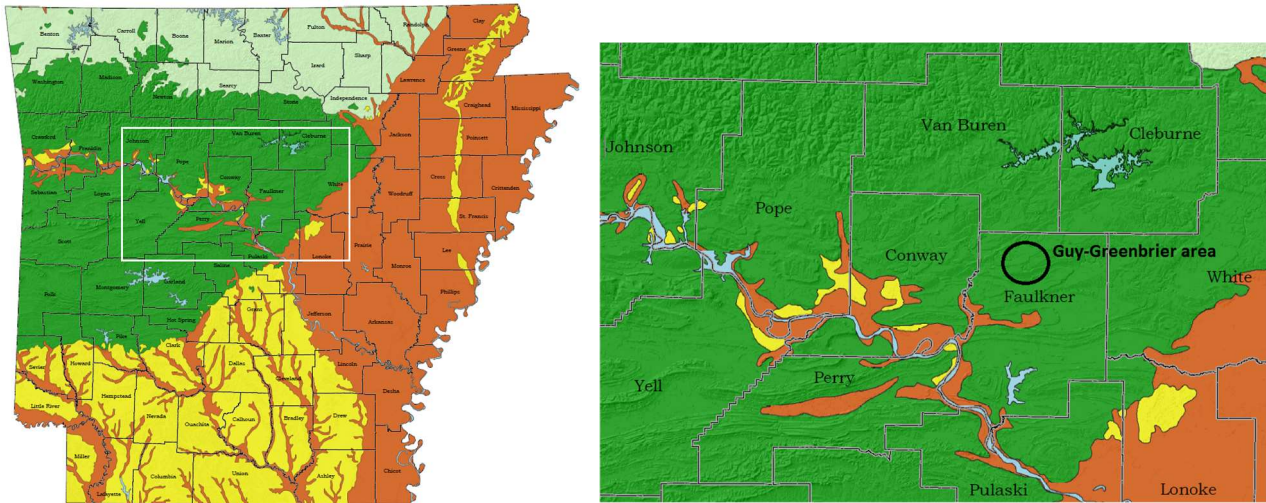


Figure A3.2.8. NEHRP soil classification map of Arkansas, by the Arkansas Geological Survey (Ausbrooks & Doerr, 2008a): rock (soil type B, dark green), regolith, weathered shales, cemented gravels, hard and/or stiff/very stiff soils (soil type C, light green), sands, silts and/or stiff/very stiff clays, loess, gravels (soil type D, yellow), and soils vulnerable to potential failure or collapse under seismic loading such as liquefiable soils, quick and highly sensitive clays, collapsible, weakly cemented soils (soil type F, brown).

A3.2.4 Ground motions

A3.2.4.1 Intensity observations

According to the written report at the USGS website, the Modified Mercalli Intensities (MMI) observed were the following: V (moderate shaking, minor damage) at Greenbrier, IV (light shaking) at Bee Branch, Clinton, Concord, Conway, Damascus, Edgemont, Enola, Glencoe, Higden, Hindsville, Judsonia, Kingston, Lepanto, Lockesburg, Oil Trough, Onia, Parthenon, Quitman, Roland, Timbo, Tuckerman, West Helena and Witts Springs, and III (weak shaking) in much of central and northern Arkansas, in parts of eastern Oklahoma and southern Missouri, and in the Memphis, Tennessee area. It was also felt in parts of Alabama, Illinois, Indiana, Kansas, Kentucky, Louisiana, Mississippi and Texas. Figure A3.2.9 shows the corresponding automatically calculated USGS ShakeMap (Worden *et al.*, 2017).

Based on the intensity versus distance plot elaborated by the USGS that gathers the data points obtained by means of the Did You Feel It macroseismic intensity questionnaire, it appears that the map shown in Figure A3.2.9 may be more heavily influenced by estimations from intensity prediction equations than by observed data points. The old version of the USGS website listed only five stations used to generate the ShakeMaps, all of them over 400 km away from the epicentre.

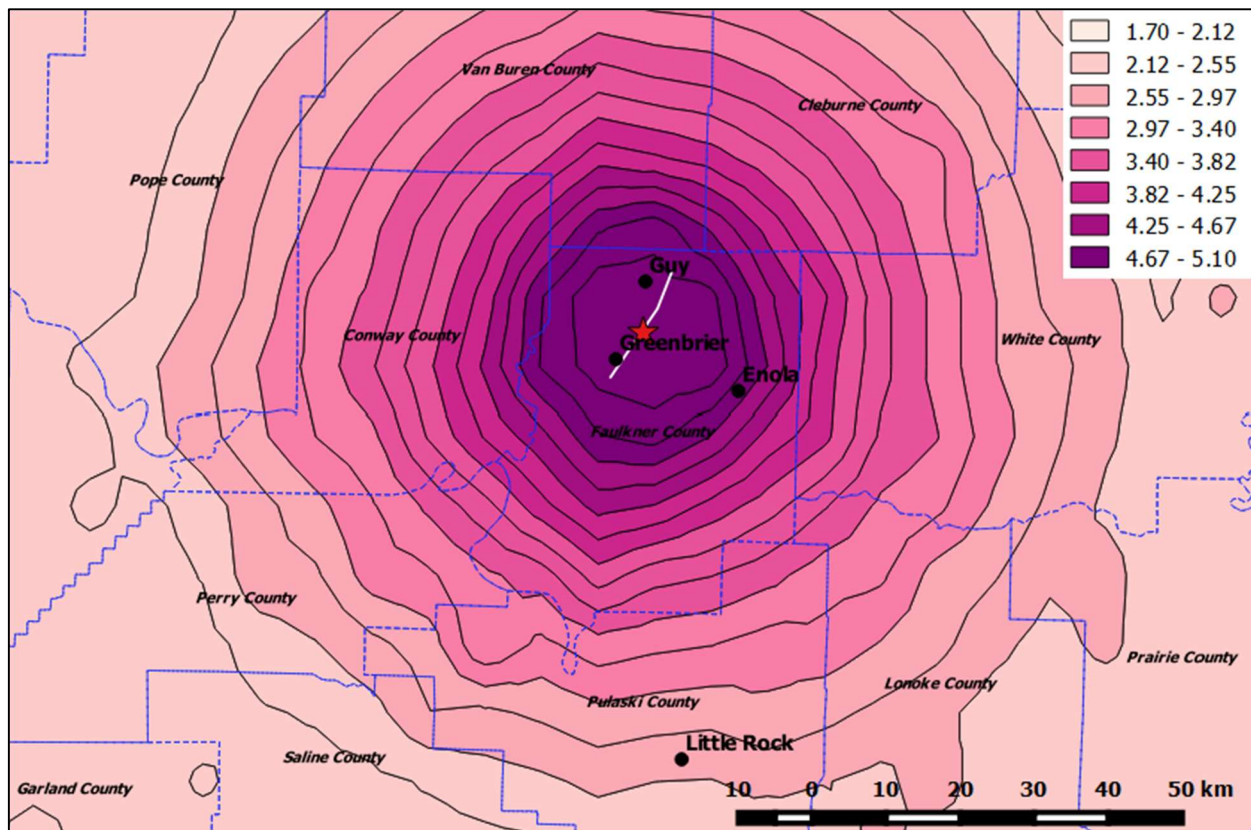


Figure A3.2.9. USGS ShakeMap in terms of Modified Mercalli Intensities (MMI), initial automatic calculation. The red star is the epicentre of the main shock, according to the USGS. Approximate trace of the Guy-Greenbrier fault shown in white.

A3.2.4.2 Ground motion recordings

Five three-component accelerograms are available for this event from the Center for Engineering Strong Motion Data (CESMD), with epicentral distances between 180 and 420 km. Peak ground acceleration (PGA) values for other five stations with epicentral distances between 440 and 470 km are available at the website of the USGS. The location, epicentral distance and recorded PGA values for the ten stations are summarized in Table A3.2.5. As can be observed, motion at these stations was extremely weak. As an example, the plots for the acceleration time-histories recorded at station 7404, located in Memphis, Tennessee, 211 km away from the epicentre, are shown in Figure A3.2.10. Unfortunately, no records are readily available for the near-field.

Table A3.2.5. Main characteristics of waveforms and recording stations for ten records of the main shock, available from the CESMD and the USGS. Epicentral distances: as reported by source (A) and calculated with the OpenQuake Hazard Library (Pagani *et al.*, 2014) for source (B) with respect to epicentral coordinates reported by the USGS.

Station	Station Name	Latitude	Longitude	Epi. Dist. (km)	PGA (cm/s ²)			Source
					Horiz. 1	Horiz. 2	Vertical	
2459	Paragould - Post Office	36.0570 ° N	90.4880 °W	189.3	1.546	1.945	1.089	(A)
7404	TN Memphis - VAMC, Bldg 6	35.1440 ° N	90.0260 °W	211.1	1.708	2.309	1.194	(A)
2454	Campbell - Fire Station	36.4940 ° N	90.0760 °W	245.8	1.163	1.339	0.587	(A)
2457	Dexter- Fire Station 2	36.7960 ° N	89.9660 °W	273.2	1.592	2.055	0.521	(A)
2491	St. Louis - Visitors Ctr	38.6260 ° N	90.1910 °W	419.2	1.280	1.528	0.405	(A)
OK002	Wilshire Boulevard, Harrah, OK	35.5490 ° N	97.1970 °W	440.9	0.076	0.082	0.148	(B)
OK005	Luther Middle School, Luther, OK	35.6550 ° N	97.1910 °W	441.1	0.061	0.068	0.143	(B)
OK001	Jones High School, Jones, OK	35.5610 ° N	97.2890 °W	449.3	0.061	0.071	0.103	(B)
OK009	Oakdale Elementary School, Edmond, OK	35.5810 ° N	97.4230 °W	461.5	0.418	0.282	0.560	(B)
OK004	Oklahoma Science Museum, OK	35.5230 ° N	97.4750 °W	465.9	0.055	0.076	0.097	(B)

(A) Processed records downloaded from the CESMD Strong Motion Center (<http://www.strongmotioncenter.org>).

(B) Data from the USGS (<http://earthquake.usgs.gov/earthquakes/shakemap/global/shake/022811a/download/stationlist.txt>).

Waveforms not directly available.

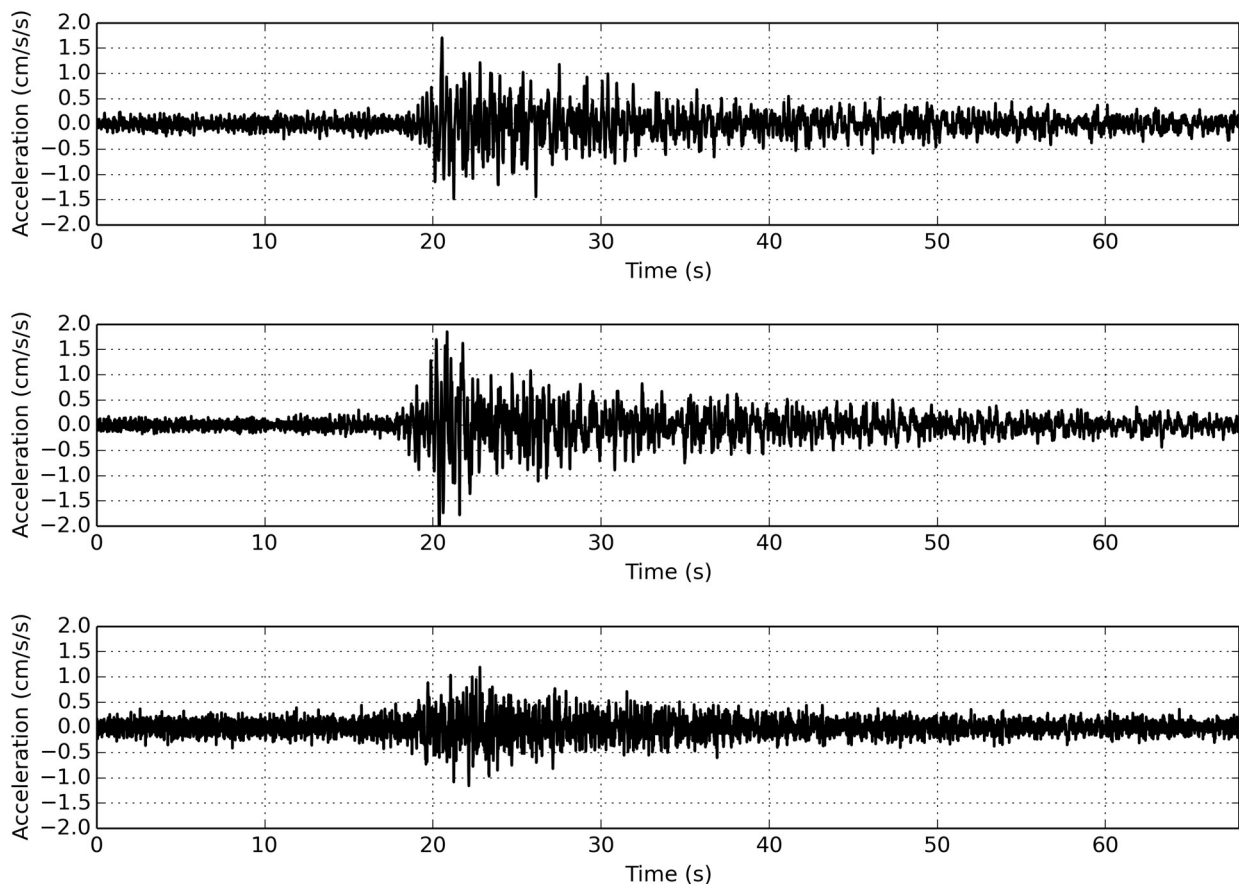


Figure A3.2.10. Horizontal (top and centre) and vertical (bottom) acceleration time-histories recorded for the main shock at station 7404, located in Memphis, Tennessee, 211 km away from the epicentre. Waveform data from the Center for Engineering Strong Motion Data (CESMD, 2016).

Figure A3.2.11 and Figure A3.2.12 show the pseudo-acceleration and displacement response spectra for the five records whose waveforms are available from the CESMD, obtained using the OpenQuake ground motion toolkit (Weatherill, 2014).

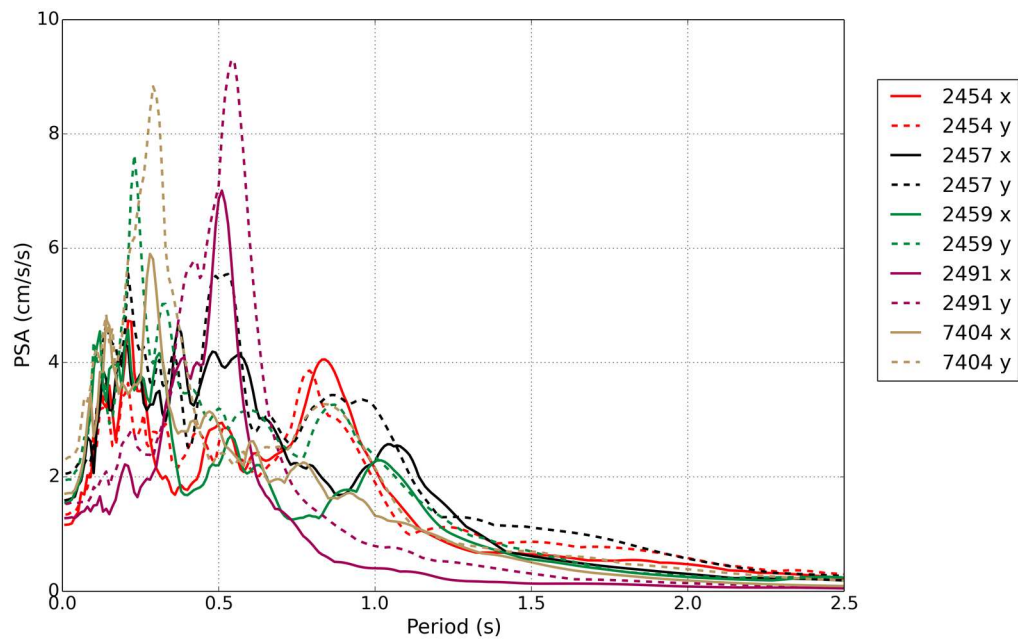


Figure A3.2.11. Pseudo-acceleration response spectra (5% damping) for each of the two horizontal components (x, y) of the five available accelerograms. Waveform data from the CESMD.

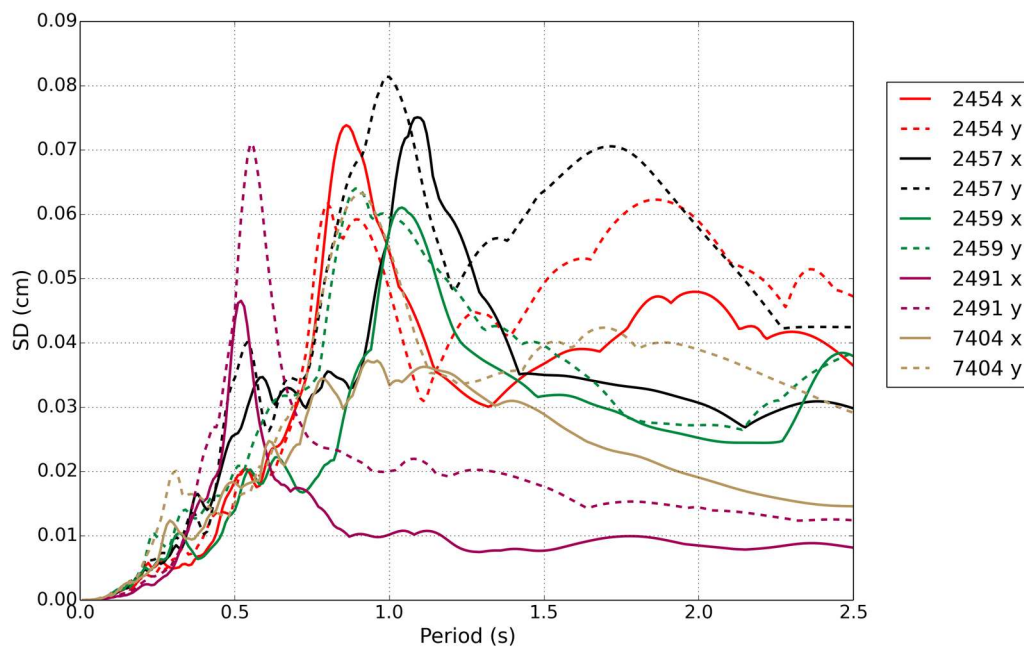


Figure A3.2.12. Pseudo-displacement response spectra (5% damping) for each of the two horizontal components (x, y) of the five available accelerograms. Waveform data from the CESMD.

A3.2.4.3 Inferred shaking levels

In their website, the USGS provides an estimation of the peak ground acceleration values expected to have been observed during the earthquake, based on information from reports of felt intensity and recording stations, where available. This estimation results of special interest for this event for which direct information from records is only available for epicentral distances larger than 180 km. The map on the left of Figure A3.2.13 shows the acceleration ShakeMap (Worden *et al.*, 2017) automatically generated by the USGS soon after the event, while the map on the right shows the acceleration contours that can be downloaded from the website at the time of writing (January 2016). Given the difference in scale, the map on the right allows for higher values of PGA to be better appreciated. According to these maps, Guy and Greenbrier may have been subject to PGA values of around 10% g. An updated version of this ShakeMap dated 30th March 2017 reaches a much larger value of 57% g at the epicentre, and values of around 30% g and 22% g at Greenbrier and Guy, respectively. The reasons for these discrepancies are not clear. Moreover, it is not clear why the USGS website reports the availability of 7,423 Did You Feel It responses and, at the same time, zero of these responses used to generate the ShakeMaps. Given the lack of information it is not possible to determine which of these values are more realistic.

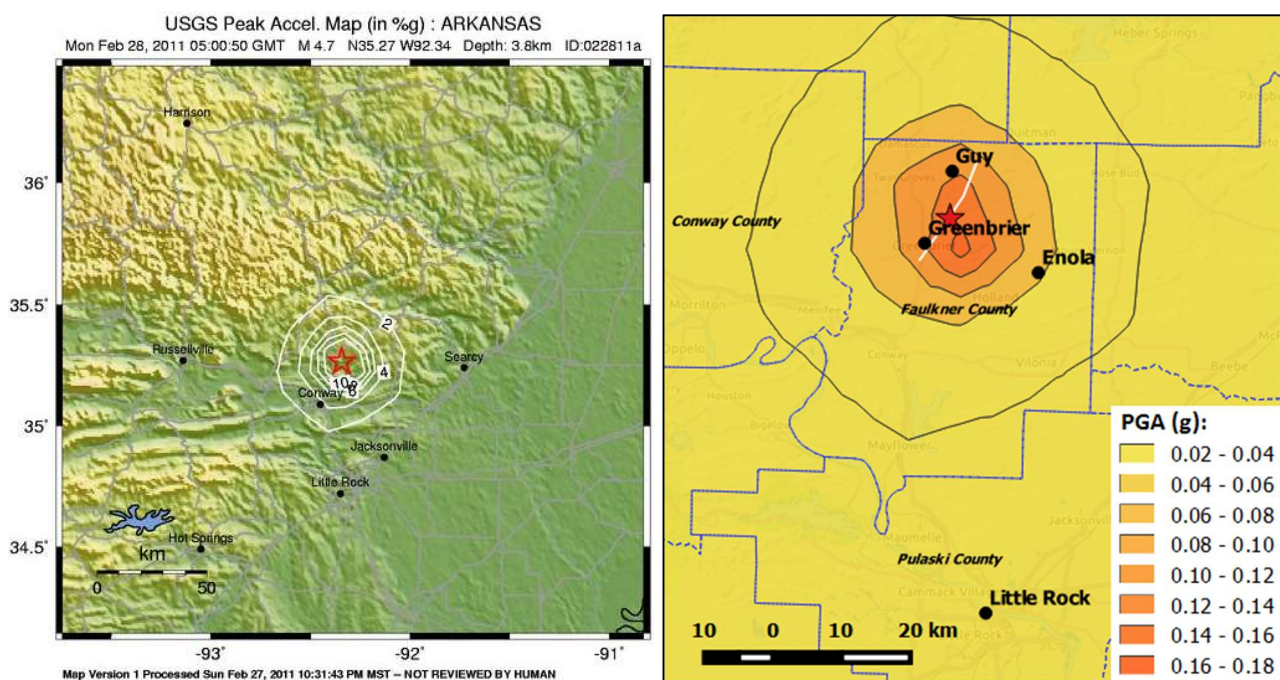


Figure A3.2.13. USGS ShakeMaps in terms of peak ground acceleration: initial automatic calculation, as reported on the old USGS website (left), and contour lines shapefile downloaded from the website in January 2016 (right). Note the difference in scale between the two figures (USGS, 2016).

A3.2.4.4 Duration of ground shaking

The 5%-75% definition of the significant duration of the five records from the CESMD database was calculated for each as-recorded horizontal component using the OpenQuake ground motion toolkit (Weatherill, 2014). Results are shown in Table A3.2.6.

Table A3.2.6. Significant duration (5%-75% of Arias intensity, in seconds) of the ground motions available from the CESMD database (2016).

Station	Station Name	Latitude	Longitude	Repi (km)	X component	Y component
2459	Paragould - Post Office	36.0570 ° N	90.4880 °W	189.3	11.3	8.7
7404	TN Memphis - VAMC, Bldg 6	35.1440 ° N	90.0260 °W	211.1	13.7	12.2
2454	Campbell - Fire Station	36.4940 ° N	90.0760 °W	245.8	15.9	17.8
2457	Dexter- Fire Station 2	36.7960 ° N	89.9660 °W	273.2	16.8	13.9
2491	St. Louis - Visitors Ctr	38.6260 ° N	90.1910 °W	419.2	11.4	5.5

Estimations of earthquake significant durations can be obtained by means of prediction equations such as those of Bommer *et al.* (2009) and Afshari & Stewart (2016). Horton (2012) estimated that the area that ruptured during the main event was less than 4 km², which can be approximated by a square with a 2 km side, or a circle with a 2.25 km diameter. Based on these numbers, it seems reasonable to estimate the depth to the top of the rupture as the hypocentral distance minus 1 km. Two alternative values were finally considered to be used with the equation of Bommer *et al.* (2009), using the hypocentral depth reported by the USGS (3.8 - 1.0 = 2.8 km), on one hand, and that estimated by Horton (2012) (6.0 - 1.0 = 5.0 km), on the other. A series of distances were considered, including an approximation to the epicentral distances to the towns of Guy and Greenbrier (~6.00 km), and values covering the stations for which information on significant duration is available. In view of the lack of information regarding the site conditions at the recording stations, two extreme values of V_{s30} were considered: 180 m/s, the lower bound for NEHRP soil type D, which may be the soil type of station 2459, based on the NEHRP soil classification map of Arkansas (Ausbrooks & Doerr, 2008a), and 1500 m/s, the upper bound for NEHRP soil type B, which corresponds to that of Guy and Greenbrier (see Figure A3.2.8). Results obtained are plotted in Figure A3.2.14¹.

As can be observed, V_{s30} has a stronger influence on the results than the depth to the top of the rupture when using the equation of Bommer *et al.* (2009). When compared to the values yielded by this equation, the significant durations of the records from stations 2459, 7404, 2454 and 2457 are closer to the curves obtained using a V_{s30} of 1500 m/s, and significantly below the curves for a V_{s30} of 180 m/s. However, when applying the equation of Bommer *et al.* (2009) using the epicentral distances to these stations, the two alternative depths to the top of the rupture as before, and values of V_{s30} between 200 and 300 m/s, estimated from the USGS V_{s30} Map Server (Wald & Allen, 2007) and the NEHRP soil classification map of Arkansas (Ausbrooks & Doerr, 2008a, Figure A3.2.8), observed durations (Table A3.2.6) are within the range of [-1.08,-0.18] standard deviations of the

¹ Calculated as per a previous version of this report with **M4.7** instead of **M4.8**.

predicted ones. The case of Station 2491 is more extreme, as analogous calculations place its observed durations in the range of $[-3.53, -2.00]$ standard deviations. These normalised residuals indicate that the significant durations at these locations were shorter than could be expected. It is anyway noted that the model of Bommer *et al.* (2009) is being applied outside its distance range, and just below the minimum magnitude that was used for its derivation.

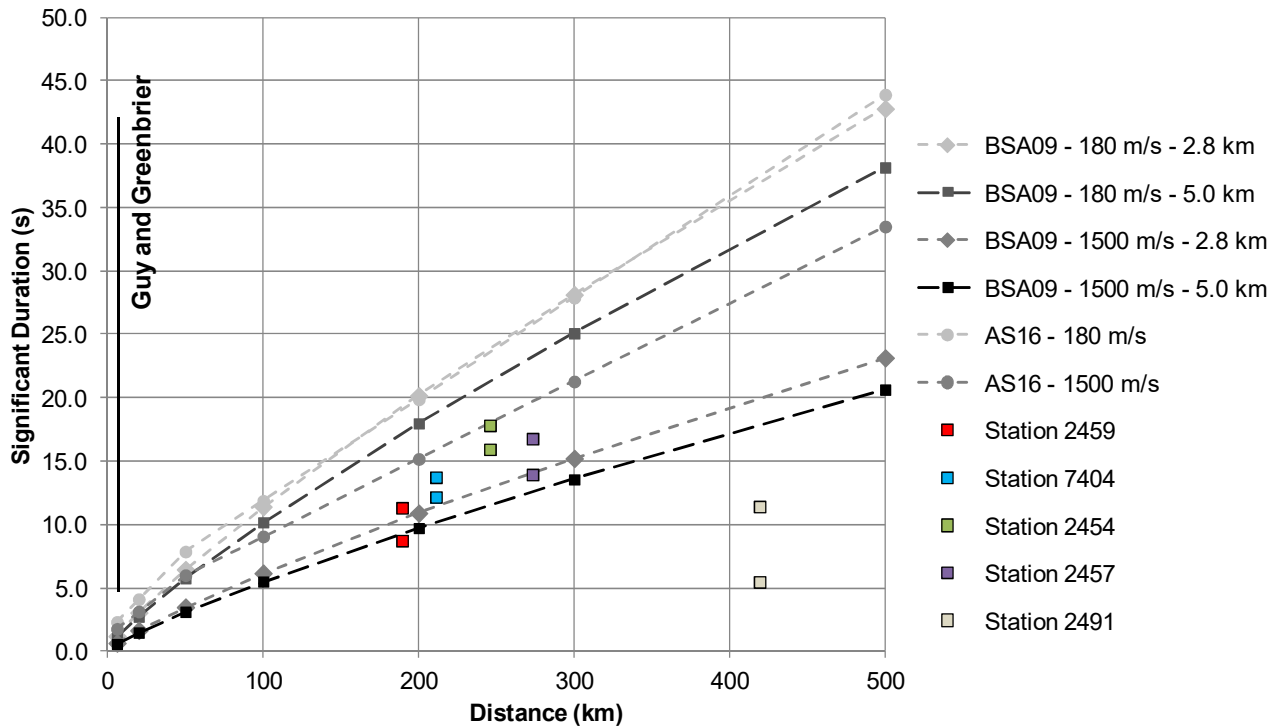


Figure A3.2.14. Estimation of the significant duration of the main shock, using prediction equations by Bommer *et al.* (2009, BSA) and Afshari & Stewart (2016, AS), and significant duration calculated for the two as-recorded horizontal components of the five available accelerograms.

Values observed for all stations lie systematically below the predictions of Afshari & Stewart (2016) for the whole range of V_{s30} considered (180-1500 m/s). However, comparisons analogous to those carried out above show that significant durations observed for stations 2459, 7404, 2454 and 2457 lie in the range of $[-1.04, -0.21]$ standard deviations from the predicted ones, a range very similar than that obtained for the model of Bommer *et al.* (2009). The situation with Station 2491 is similar as well, with observed values lying in the range of $[-3.23, -2.02]$ standard deviations from the predicted ones. The range of distances and magnitudes for the application of the model of Afshari & Stewart (2016) should not be a problem.

The Arkansas Democrat-Gazette (2011) reports dispatchers having said that the shaking in Greenbrier lasted for about 2 seconds. The equation of Bommer *et al.* (2009) yields values of significant duration between 0.58 and 0.79 seconds, for depths to the top of the rupture of 2.8 and 5.0 km, for a closest distance to the fault rupture of 6.00 km, and V_{s30} between 760 and 1500 m/s, which are the lower and upper bounds for NEHRP soil type B, which is expected in Greenbrier (Ausbrooks & Doerr, 2008a). For a V_{s30} of 180 m/s, these values change to 1.20 and 1.07 seconds. The equation of Afshari & Stewart (2016) yields

1.77 seconds for V_{s30} larger than 600 m/s, and 2.32 seconds for 180 m/s, values that strongly agree with the perception reported in the Arkansas Democrat-Gazette (2011).

A3.2.5 Collateral earthquake hazards

A3.2.5.1 Surface rupture

According to the characterisation of the geometry of the rupture provided by Horton (2012), which can be summarized in Figure A3.2.15, this earthquake did not reach the surface. As mentioned earlier, Horton (2012) estimated that the area that ruptured during the main event was less than 4 km².

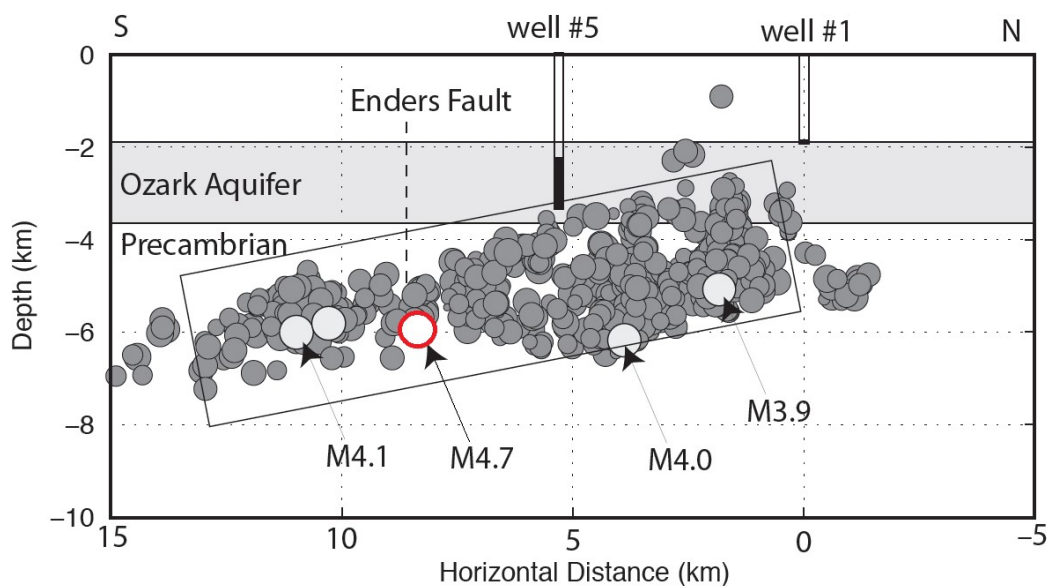


Figure A3.2.15. Cross section along the Guy-Greenbrier fault, showing the hypocentres of the **M4.8** main shock and three foreshocks (Horton, 2012).

A3.2.5.2 Landslides

No landslides reported for this event.

A3.2.5.3 Liquefaction

No liquefaction reported for this event.

A3.2.5.4 Settlements

No direct reference to the occurrence of settlements has been found. However, in the scarce information on damage it is mentioned that damage to foundations, cracks in driveways and cracks in walkways were observed, without any details on their origin, which may have been the settlement of the soils over which they lied.

A3.2.6 Exposed population

A3.2.6.1 Socio-economic setting

According to the 2014 Human Development Report (United Nations, 2014), the Human Development Index (HDI) for the United States in 2013 was 0.914, while its Inequality-adjusted HDI (IHDI) was 0.755. This located the USA in the 5th place in the world's ranking, while the Netherlands ranks 4th. The following table compares the HDI and IHDI for both countries from the last three Human Development Reports (United Nations, 2011; United Nations, 2013; United Nations, 2014). The column "Adj. HDI" provides the HDI values given in the 2014 report for previous years, adjusted for data consistency in time.

Table A3.2.7. Human Development Index and Inequality-adjusted Human Development Index for the United States and the Netherlands.

Report	Data	Unites States of America				Netherlands			
		HDI	IHDI	Rank	Adj. HDI	HDI	IHDI	Rank	Adj. HDI
2011	May 2011	0.910	0.771	4	0.911	0.910	0.846	3	0.914
2013	October 2012	0.937	0.821	3	0.914	0.921	0.857	4	0.915
2014	November 2013	0.914	0.755	5	-	0.915	0.854	4	-

Table A3.2.8 presents a comparison between the United States and the Netherlands in terms of GDP, GDP per capita and unemployment rate. During 2011, the unemployment rate in Arkansas was around 0.5% smaller than that of the US as a whole (US Bureau of Labor Statistics, 2016).

Table A3.2.8. Gross domestic product (GDP), GDP per capita and unemployment rate for the United States and the Netherlands, according to the World Economic Outlook Database 2015.

Indicator	Units	Unites States		Netherlands	
		2011	2014	2011	2014
Gross domestic product, current prices	Billions of US dollars	15,517.925	17,418.925	894.576	866.354
Gross domestic product per capita, current prices	US dollars	49,724.999	54,596.653	53,589.909	51,372.963
Unemployment rate	% of total labor force	8.942	6.150	4.980	7.395

Though employing only 3% of its population, the agricultural sector remains fundamental to the economy of Arkansas. According to the 2012 Census of Agriculture (United States Department of Agriculture, 2014), 40.6% of its surface is dedicated to farming, and the state ranks 14th in the country with respect to the total value of agricultural products sold. The main industries in Arkansas include food processing, electric equipment, fabricated metal products, and paper products. According to the United States Energy Information Administration (EIA, 2016), marketed natural gas production in Arkansas has experienced a nearly six-fold increase between 2005 and 2014. The state ranked 8th in the national natural gas marketed production during 2014, accounting for 4.1% of the total marketed production of the country, and 15th in the total national energy production in 2013.

The large economic crisis that began in 2008 had a significant impact on the United States, causing high unemployment, an increasing federal debt and inflation. In 2011, the Gross Domestic Product (GDP) increased in 43 of the 50 states of the USA. The state of Arkansas was not amongst the states with the largest growth, and experienced just a 0.3% increase in its GDP, a value that positioned it within the second to lowest quintile (Bureau of Economic Analysis, U.S. Department of Commerce, 2012). During the year 2012, the state of Arkansas ranked 48th with respect to GDP per capita, with a value that was a 25% lower than that of the USA as a whole. Nevertheless, it was also the 5th cheapest state to live in and the 2nd cheapest state to do business during that same year, according to CNBC's America's Top States for Business 2012 (2012).

A3.2.6.2 Population density and distribution

The area around the epicentre of this event is sparsely populated. Table A3.2.9 shows the population by 1st April 2010 of some relevant towns around the epicentral area. According to the United States Census 2010 (U.S. Census Bureau, 2012), population density in the year 2010 for Faulkner County, where the epicentre was located, was 67.5 people/km², while the overall density for the state of Arkansas is 21.6 people/km². The density of housing units per area is around 29 housing units /km² for Faulkner County and 10 housing units /km² for the whole of Arkansas.

Table A3.2.9. Population of some relevant towns in the epicentral area (only urban population considered) (Quickfacts, 2016).

City	Population 1 st April 2010
Guy	708
Greenbrier	4,712
Conway	58,908
Damascus	382
Enola	338
Quitman	762
Holland	557
Wooster	860
Vilonia	3,815
Meniffee	302
Center Ridge	388

The USGS PAGER exposure report generated around 30 minutes after the main shock estimates that approximately thirty-five and ninety-four thousand people were exposed to shaking of intensities V and IV in the Modified Mercalli Intensity (MMI) scale, respectively, while around 1.3 million people were exposed to intensities between II and III (Figure A3.2.16). Note that these numbers are much larger than those of Table A3.2.9 because Table A3.2.9 reports strictly on the urban population of the enumerated towns, while the USGS PAGER exposure report considers all of the exposed population.

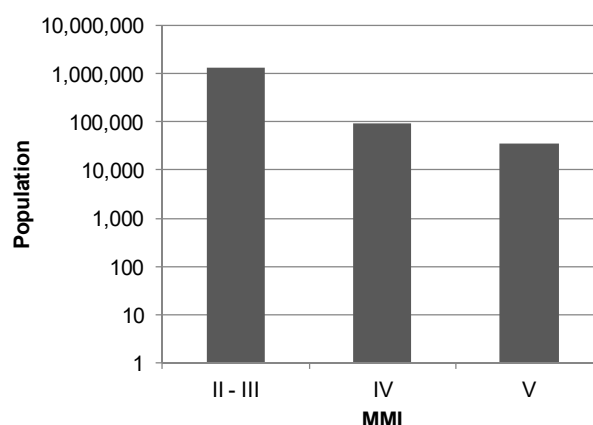


Figure A3.2.16. Estimation of total population exposed to different Modified Mercalli Intensities (MMI) 35 hours after the main shock (USGS, 2016)

A3.2.6.3 Time of day of earthquake

The main shock occurred on 28th February 2011, 23.00 local time. Given the type of damage and the absence of casualties, the time of occurrence of the event did not have a significant impact over its consequences.

A3.2.7 Characteristics of exposed building stock

A3.2.7.1 Seismic design codes

While Cutcliffe (2000) believes that it was the 1906 San Francisco earthquake which marked the start of a real interest in earthquake engineering and seismic design in the United States, Freeman (1932) stated a quarter of a century later that "the art of constructing earthquake-resisting buildings is still in the formative stage, that there are differences of opinions among experts and that there is much deficiency in important data". Further, he points at the 1925 Santa Barbara earthquake to have been more significant in raising awareness on the subject. It was this devastating event that prompted the first edition of the Uniform Building Code (UBC) in 1927, which contained the first written seismic design provisions for a regional level, but which did not become mandatory until 1961 (Beavers, 2002).

As recapitulated by Beavers (2002), the origin of seismic design codes and building codes in general in the USA started in a fragmented fashion, by regions or states. For example, the Uniform Building Code (UBC) just mentioned above was typically used west of the Mississippi river. The National Building Code of the Building Officials and Code Administrators (BOCA) (known as the BOCA Code) was, instead, used in the upper midwest and northeast. It was first published in 1950, including seismic design provisions. In the south, the Standard Building Code (SBC) of the Southern Building Code Congress International (SBCCI) was used. Seismic design provisions were included in the SBC in 1976, by referencing ANSI A58.1, but "were not mandatory unless local authorities

required seismic design, which was rarely the case", until 1988. The 1987 edition of the BOCA Code also incorporated the provisions of ANSI A58.1, and made them mandatory.

The ANSI A58.1 standard of the American National Standards Institute (ANSI) was first published in 1945, and was the first standard to consider earthquake loads (Beavers, 2002). However, seismic hazard did not have a role in ANSI A58.1, which only had a map showing the locations of destructive earthquakes of the past until its 1972 edition, in which a seismic hazard description similar to the 1949 USCGS (United States Coast and Geodetic Survey) map was incorporated. The 1972 edition of ANSI A58.1 was also the first one to outline modern wind design provisions (Fratinaro & Schroeder, 2015; Ghosh, 2008), evolving from more basic guidelines developed in the 1950s (Huston, 2007).

The 1949 hazard map was the first one to encompass the whole of the contiguous USA, and it was based on "the premise that similar earthquakes will occur in the future where they have occurred in the past" (Beavers, 2002). For reasons that are not fully clear, this map was withdrawn in 1952, and replaced with a map that only showed the location of known past significant earthquakes. In the 1970s, the responsibility of producing hazard maps passed on to the USGS (United States Geological Survey), who published the first map developed in the form of probabilistic estimates of maximum acceleration contours on rock in 1976, and which, as highlighted by Beavers (2002), represented a significant paradigm shift. It should be noted, however, that the first edition of the ATC3-06, which in 1985 evolved into the National Earthquake Hazards Reduction Program (NEHRP) Recommended Provisions for Seismic Regulations for New Buildings and Other Structures, used a truncated version of this map in 1978, not allowing for values above 0.4g to be considered. This map was used for almost 20 years, given the inability to reach consensus on a different map that took place in between 1988 and 1994. It was finally updated by the USGS in 1997, after a four-year project called Project 97, during which large efforts were invested in giving a voice to all the professionals and sectors involved. Since then, the USGS hazard map has been updated in 2002, 2008 and 2014.

The way in which seismic loads were considered evolved significantly from the simple use of a 7.5%-10.0% of the building's weight as a lateral load (1927 edition of the UBC), with the progressive incorporation of significant factors such as soil type and capacity, seismic zonation, natural period of vibration of the structure, and importance of the building.

In 1988, ANSI combined with ASCE to update and re-designate ANSI A58.1-1982 to ASCE 7, which is now the most significantly recognised standard by all earthquake regulations, codes, standards, procedures and guidelines for basic seismic design in the USA (Beavers, 2002). Furthermore, ASCE 7 is also the "de facto" national wind design standard (Fratinaro & Schroeder, 2015). The International Building Code (IBC), whose first edition in 2000 was based in the NEHRP Provisions, makes reference to ASCE 7 for the definition of seismic and wind loads. According to FEMA-543 (FEMA, 2007), the area around Guy and Greenbrier has seen around 26 tornadoes of categories F3 to F5 ("severe" to "incredible") per 10,000 km² between 1950 and 1998, one of the highest rates across all of the USA.

As mentioned in Section A3.2.1.3, it is noted that the national seismic hazard maps of the United States (and all other countries in the world) do not take into consideration induced seismic activities and, consequently, areas for which most ground shaking is believed to have an anthropogenic origin might be seismically designed but for ground motion levels that might not reflect the short-term likelihoods being currently experienced.

Building practise in Arkansas is regulated by the Arkansas Fire Prevention Code, which is divided into three volumes: (I) Fire, (II) Building, and (III) Residential. It is based on the International Fire Code, the International Building Code and the International Residential Code, with some adjustments carried out by local experts (Arkansas Contractors Licensing Board, 2016; Construction Market Data, 2016; Arkansas Building Authority, 2012).

The Building Code Effectiveness Grading Schedule (BCEGS), developed by the Insurance Services Office (ISO), indicates that the overall level of code enforcement across the state of Arkansas is relatively low when compared to the country as a whole and to states like California, in which awareness with respect to seismic risk is much greater. Figure A3.2.17 shows the distribution of communities by BCEGS class number for the United States as a whole and for the state of Arkansas. Within this classification schedule, classes 1-3 correspond to the maximum enforcement levels, while class 10 indicates no enforcement at all. These figures agree with statements of Beavers (2002) and Cutcliffe (2000), who highlight that, due to their relative lack of seismic activity, the effort to incorporate good seismic design practises in building codes has been more challenging in the central and eastern USA, when compared to other areas of the country.

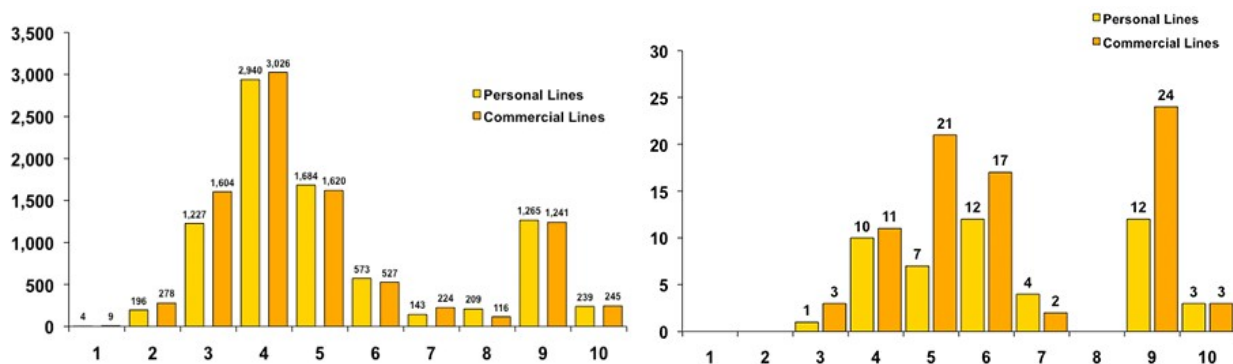


Figure A3.2.17. Distribution of communities by BCEGS class number for the whole of the United States (left) and the state of Arkansas (right). Personal lines include 1- and 2-family dwellings. Commercial lines include all other buildings. Classes 1-3: maximum enforcement. Class 10: no enforcement (ISO Mitigation, 2015).

A3.2.7.2 Building typologies

Information regarding building typologies in the state of Arkansas is scarce to null. For this reason, data regarding typologies at the country level were collected from the PAGER Inventory Database v2.0 (Jaiswal & Wald, 2008). Figure A3.2.18 shows that the structure of most of the buildings in the USA consists of light wood frames (61.2%), and unreinforced brick masonry (19.3%) in a smaller proportion. The remaining 19.4% is mostly made up of heavy wood frames and mobile homes (Figure A3.2.19). From visual

inspection by means of Google Street View and from the description of damage caused by the 2011 Guy-Greenbrier earthquake that could be found, it seems possible to infer that light wood frames and unreinforced brick masonry are probably the most likely building typologies in the affected area.

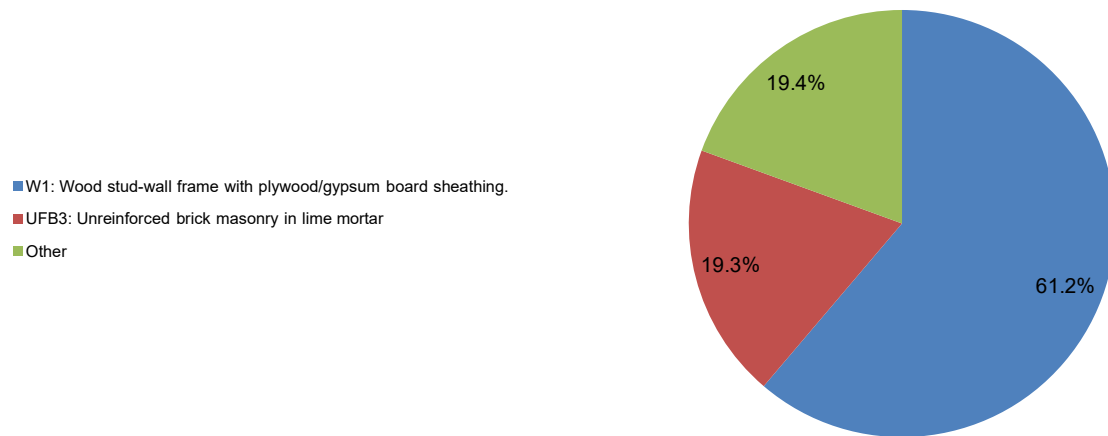


Figure A3.2.18. Proportion of buildings in the United States belonging to each typology. The subcategories within class "Other" are expanded upon in the figure below. Data from Jaiswal & Wald (2008).

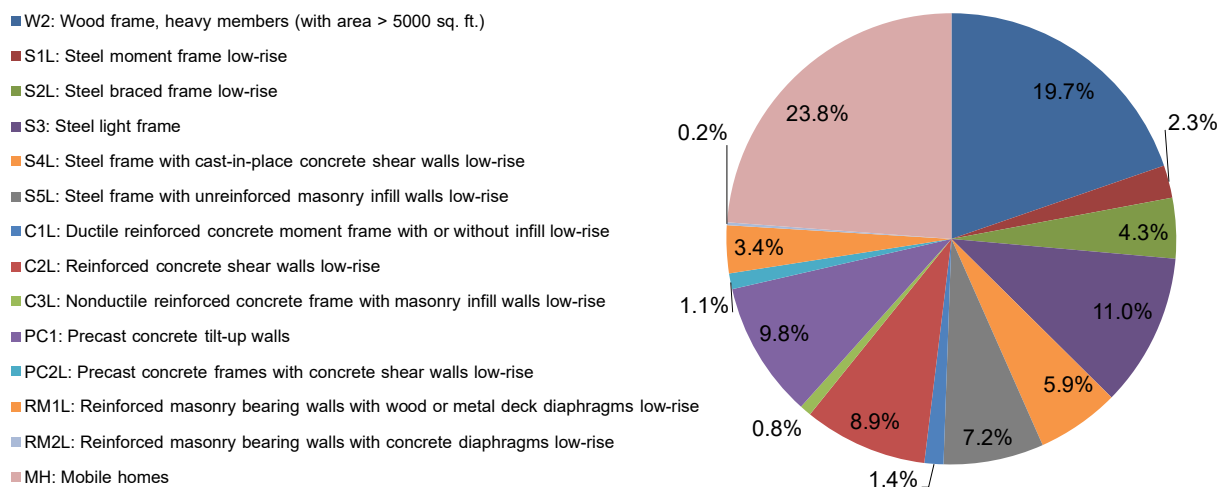


Figure A3.2.19. Breakdown of the "Other" class in the figure above. To determine the percentage that each of these sub-categories represents of the total in the USA, multiply the value in this figure by 0.194. Data from Jaiswal & Wald (2008).

A3.2.7.3 Prior damage and retrofit

No details on prior damage or retrofit available.

A3.2.8 Damage observations

A3.2.8.1 Damage states

Neither engineering reports nor relevant photographs of the damage caused by the 2011 Guy-Greenbrier earthquake seem to be publicly available. However, the qualitative descriptions found appear to correspond to Grade 2 damage in the European Macroseismic Scale (EMS-98; Grünthal, 1998). For details regarding the latter, please refer to Section 3.8.1 of Chapter 3 and Appendix II. The maximum Modified Mercalli Intensity of V reported by the USGS appears as low when comparing the damage observed by this earthquake and the relationship between MMI and damage described in Table A2.3.2 of Appendix II.

A3.2.8.2 Damage statistics and description

Information regarding damage caused by the 2011 Guy-Greenbrier earthquake is scarce. The NEHRP report for the year 2011 (FEMA *et al.*, 2012) says that "the earthquake caused little damage", a statement that is supported by The New York Times' report of no "major damage" (The New York Times, 2011). Nevertheless, several lawsuits were filed, mostly by residents of Greenbrier. Case number 23CV-14-84, entitled "*2010-2011 Guy-Greenbrier Earthquake Swarm Victims v. Chesapeake Operating, Inc. and BHP Billiton Petroleum (Fayetteville) LLC*", available via the archive of THV11 (2014) is a relevant source of information, for it gathers descriptions of damage suffered by 14 houses. Table A3.2.10 summarizes the types of damage described in the 14 cases of said lawsuit and from two additional sources, one of which mentions damage to foundations of a house located around 500 metres away from the epicentre (Reuters, 2013), and another one that simply shows the picture of cracked bricks (Arkansas Fracking, 2011). Fifteen of the sixteen cases considered in Table A3.2.10 correspond to properties in Greenbrier, 6.3 km away from the epicentre, while the remaining case is from Perryville, Perry County, 61.6 km to the south-west of the epicentre. According to a litigation summary available at the website of the University of Dayton (2016), case number 23CV-14-84 was dismissed with prejudice, which means that the plaintiffs are barred from filing another case on the same claim.

A3.2.8.3 Observed weaknesses

Given the lack of information regarding damage caused by this event, no observations of systematic weaknesses can be made.

A3.2.8.4 Damage distribution

There are no details available with respect to the distribution of damage within the towns. Nevertheless, it should be noted that Greenbrier, which suffered the most damage, is a small town with a population of less than five thousand people.

Table A3.2.10. Type and number of cases of damage observed, from the available sources.

Type of damage	N°
Cracks in drywall	11
Cracks in exterior mortar	8
Pulling away of moulding	7
Cracks in exterior brick	7
Damage to foundations	5
Cracks in driveway	5
Cracks in walkways	5
Doorframes out of plumb	3
Damaged doors	3
Floor cracks	3
Damaged doorframes	2
Ceiling cracks	2
Front porch pulling away from the house	1
Window frames out of plumb	1
Un-levelling of front porch pillars	1
Un-levelling of interior columns	1
Waterline leaks and mold	1

A3.2.9 Casualties and losses

A3.2.9.1 Numbers of dead and injured

According to the all-hazards mitigation plan of the state of Arkansas (Arkansas Department of Emergency Management, 2013), there were no reports of casualties for this earthquake. This information matches what was reported by CNN (2011) and The Huffington Post (2011).

A3.2.9.2 Causes of casualties

No report of casualties found (Arkansas Department of Emergency Management, 2013).

A3.2.9.3 Estimates of economic losses

Not much information is readily available regarding the overall economic loss caused by this event.

Apart from case number 23CV-14-84 mentioned earlier, several other lawsuits were filed claiming for compensation for the damage suffered as a consequence of the 2011 Guy-Greenbrier earthquake swarm. Case 23CV-14-84 was filed in the Court of Faulkner County, Arkansas, and the amount pleaded per each of the 14 properties is 75,000 USD. According to a local newspaper, The Log Cabin Democrat (2014), 75,000 USD is the cut-off for Federal Court Jurisdiction. The newspaper also reports on complaints filed by about a dozen of other Greenbrier residents in Federal Court, for damages in excess of 75,000 USD each. An article by Reuters (2013) with date 27th August 2013, states that Emerson

Poynter lawyers, who represented the plaintiffs of case 23CV-14-84, represented 35 homeowners at that point in time.

According to the estimation from USGS PAGER, the **M4.8** main shock was most likely to cause economic losses of less than one million US dollars (65% probability), and had only a 30% chance of causing losses between one and ten million US dollars instead.

A3.2.10 Discussion and conclusions

This **M4.8** earthquake occurred on 28th February 2011, at 05.00 UTC (27th February 2011, 23.00 local time), and is one of the largest to have been registered in Arkansas outside of the New Madrid Seismic Zone. It was part of a large earthquake swarm that started around 2009 and which is believed to have been triggered by the injection of waste water at disposal wells in the vicinity of a previously unknown fault. Earthquakes in the area are not frequent, but three swarms have been known to occur between 1982 and 2011, including the Guy-Greenbrier sequence itself.

The main shock and other strong events in the sequence were felt across a broad area. Nevertheless, and in spite of the lack of official systematic damage and economic losses reports, it seems that the swarm caused only relatively minor damage to houses, mainly in the town of Greenbrier. Information on a lawsuit available online allows to account for damage reported for 14 houses, whose structures are likely to have been either low-rise wooden light frames or bearing unreinforced masonry. The most common descriptions found make reference to cracks in drywalls, masonry and moulding, and, to a lesser extent, damage to foundations, driveways and walkways. No casualties were reported.

A3.2.11 References

A3.2.11.1 Bibliography

Abd, N., H. Mahdi, H. Al-Shukri, A. Catakli, H. Chlaib & M. Su (2012). Induced Seismicity of Central Arkansas. *International Geophysical Conference and Oil & Gas Exhibition*, Istanbul, Turkey, 2012, pp. 1–4.

Afshari, K. & J.P. Stewart (2016). Physically parametrised prediction equations for significant duration in active crustal regions. *Earthquake Spectra* **32**(4), 2057-2081.

Arkansas Building Authority (2012). *Minimum standards & criteria*. Arkansas, USA. Available at <http://aba.arkansas.gov/aboutUs/Documents/Final%202012%20Revision.pdf>. Last accessed: 9th February 2017.

Arkansas Department of Emergency Management (2013). *State of Arkansas all-hazards mitigation plan*. Arkansas, USA, 725 pp.

Ausbrooks, S.M. (2010). *The May 2001 Faulkner County earthquakes, 2nd edition*. Arkansas Geological Survey, USA.

- Ausbrooks, S.M. & E. Doerr (2008a). *NEHRP Soil Classification Map of Arkansas*. Arkansas Geological Survey, USA.
- Ausbrooks, S.M. & E. Doerr (2008b). *Liquefaction susceptibility map of Arkansas*. Arkansas Geological Survey, USA.
- Ausbrooks, S.M. & S. Horton (2012). *Disposal of hydrofracking-waste fluid by injection into subsurface aquifers triggers earthquake swarm in central Arkansas with potential for damaging earthquakes*. Arkansas Geological Survey and the University of Memphis, USA. Available online from http://www.gwpc.org/sites/default/files/event-sessions/Ausbrooks_Scott.pdf. Last accessed: 27th January 2016.
- Beavers, J.E. (2002). A review of seismic hazard description in US design codes and procedures. *Prog. Struct. Eng. Mater.* **4**, 46–63.
- Beavers, J.E. (2002). A review of seismic hazard description in US design codes and procedures. *Prog. Struct. Eng. Mater.* **4**, 46–63.
- Bommer, J.J., P.J. Stafford & J.E. Alarcón (2009). Empirical equations for the prediction of the significant, bracketed, and uniform duration of earthquake ground motion. *Bulletin of the Seismological Society of America* **99**(6), 3217–3233.
- Cutcliffe, S.H. (2000). Earthquake resistant building design codes and safety standards: The California experience. *GeoJournal* **51**, 259–262.
- Dart, R.L. & S.M. Ausbrooks (2011). *Earthquakes in Arkansas and vicinity 1699–2010*. U.S. Geological Survey, Open-File Report 2011–1118.
- Dziewonski, A.M., T.-A. Chou & J. H. Woodhouse (1981). Determination of earthquake source parameters from waveform data for studies of global and regional seismicity. *Journal of Geophysical Research* **86**, 2825–2852.
- Ekström, G., M. Nettles & A. M. Dziewonski (2012). The global CMT project 2004–2010: Centroid-moment tensors for 13,017 earthquakes. *Physics of the Earth and Planetary Interiors* **200–201**, 1–9.
- FEMA (2007). *FEMA 543, Design Guide for Improving Critical Facility Safety from Flooding and High Winds: Providing Protection to People and Buildings*.
- FEMA, NIST, NSF & USGS (2012). Annual report of the National Earthquake Hazards Reduction Program for fiscal year 2011. United States, 56 pp.
- Fratinaro, V.F. & S.A. Schroeder (2015). Historical study of the wind design provisions of ASCE 7. *Structures Congress 2015*, 829–839.
- Freeman J.R. (1932). *Earthquake Damage and Earthquake Insurance*. 1st edition. New York: McGraw-Hill.
- Ghosh, S.K. (2008). Searching for simplicity: The evolution of wind provisions in standards and codes in the United States. *RCI Interface*, 13–21.
- Giardini, D., G. Grünthal, K.M. Shedlock & P. Zhang (1999). The GSHAP global seismic hazard map. *Annali di Geofisica* **42**(6), 1225–1228.
- Grünthal, G. (ed.) (1998). *European Macroseismic Scale 1998 (EMS-98)*. Cahiers du Centre Europeen de Geodynamique et de Seismologie 15, Centre Europeen de Geodynamique et de Seismologie, Luxembourg.

- Horton, S. (2012). Disposal of Hydrofracking Waste Fluid by Injection into Subsurface Aquifers Triggers Earthquake Swarm in Central Arkansas with Potential for Damaging Earthquake. *Seismol. Res. Lett.* **83**, 250–260.
- Hough, S.E. & M. Page (2015). A Century of Induced Earthquakes in Oklahoma? *Bull. Seismol. Soc. Am.* **105**(6): 2863–2870.
- Huang, Y. & G.C. Beroza (2015). Temporal variation in the magnitude-frequency distribution during the Guy-Greenbrier earthquake sequence: Variation in MFD for Induced Seismicity. *Geophys. Res. Lett.* **42**, 6639–6646.
- Huang, Y., G.C. Beroza & W.L. Ellsworth (2016). Stress drop estimates of potentially induced earthquakes in the Guy-Greenbrier sequence. *Journal of Geophysical Research: Solid Earth*, **121** (9), 6597–6607.
- Huston, E. (2007). SEAW's handbook of a rapid-solutions methodology for wind design. *Struct. Mag.*, 61–64.
- Jaiswal, K. & D.J. Wald (2008). Creating a Global Building Inventory for Earthquake Loss Assessment and Risk Management. USGS Open File Report 2008-1160. Available electronically at <http://pubs.usgs.gov/of/2008/1160/>. Last accessed: 9th February 2017.
- Klose, C.D. & L. Seeber (2007). Shallow seismicity in stable continental regions. *Seismol. Res. Lett.* **78**, 554–562.
- Llenos, A.L. & A.J. Michael (2013). Modeling Earthquake Rate Changes in Oklahoma and Arkansas: Possible Signatures of Induced Seismicity. *Bull. Seismol. Soc. Am.* **103**, 2850–2861.
- McFarland, J.D. (2001). *The May 2001 Faulkner County earthquakes, 1st edition*, Arkansas Geological Survey, USA.
- Perry Jr, W.J. (1997). Structural settings of deep natural gas accumulations in the conterminous United States. *Geologic Controls of Deep Natural Gas Resources in the United States*, *US Geological Survey Bulletin* **2146**, 41–46.
- Petersen, M.D., A.D. Frankel, S.C. Harmsen, C.S. Mueller, K.M. Haller, R.L. Wheeler, R.L. Wesson, Y. Zeng, O.S. Boyd, D.M. Perkins, N. Luco, E.H. Field, C.J. Wills & K.S. Rukstales (2008). *Documentation for the 2008 update of the United States National Seismic Hazard Maps*. USGS Open-File Report 2008-1128, 61 pp.
- Petersen, M.D., M.P. Moschetti, P.M. Powers, C.S. Mueller, K.M. Haller, A.D. Frankel, Y. Zeng, S. Rezaeian, S.C. Harmsen, O.S. Boyd, N. Field, R. Chen, K.S. Rukstales, N. Luco, R.L. Wheeler, R.A. Williams & A.H. Olsen (2014). *Documentation for the 2014 update of the United States National Seismic Hazard Maps*. USGS Open-File Report 2014-1091, 243 pp.
- Stoeser, D.B., G.N. Green, L.C. Morath, W.D. Heran, A.B. Wilson, D.W. Moore & B.S. Van Gosen (2007). *Preliminary integrated geologic map databases for the United States*. U.S. Geological Survey, Open-File Report 2005-1351. Available online at <http://pubs.usgs.gov/of/2005/1351/>. Last accessed: 27th January 2016.
- United Nations, ed. (2011). *Human Development Report 2011 - Sustainability and equity: A better future for all*. Report of the United Nations Development Programme (UNDP), New York, United States.
- United Nations, ed. (2013). *Human Development Report 2013 - The rise of the South: Human progress in a diverse world*. Report of the United Nations Development Programme (UNDP), New York, United States.

United Nations, ed. (2014). *Human Development Report 2014 - Sustaining human progress: Reducing vulnerabilities and building resilience*. Report of the United Nations Development Programme (UNDP), New York, United States.

Wald, D.J. & T.I. Allen (2007). Topographic slope as a proxy for seismic site conditions and amplification. *Bulletin of the Seismological Society of America* **97**, 1379–1395. Slope-based online map viewer available at:

<http://usgs.maps.arcgis.com/apps/webappviewer/index.html?id=8ac19bc334f747e486550f32837578e1>. Data used herein downloaded from deprecated version last accessed on 7th December 2015.

Weatherill, G. A. (2014). *OpenQuake ground motion toolkit - User guide*. Global Earthquake Model (GEM). Technical Report.

Worden, C.B., E.M. Thompson, M. Hearne & D.J. Wald (2017). *ShakeMap V4 Manual: technical manual, user's guide, and software guide*. United States Geological Survey. Available online at: <http://usgs.github.io/shakemap/>.

A3.2.11.2 Web references

Arkansas Contractors Licensing Board (2016):
<http://aclb.arkansas.gov/Pages/BuildingCodes.aspx>.
Last accessed: 27th January 2016.

Arkansas Democrat-Gazette (2011):
<http://www.arkansasonline.com/news/2011/feb/27/47-magnitude-quake-hits-central-arkansas/>.
Last accessed: 9th February 2017.

Arkansas Fracking (2011): http://www.arkansasfracking.org/june24_2011_012.JPG.
Last accessed: 9th February 2017.

Arkansas Geological Survey: <http://www.geology.arkansas.gov/>.

Arkansas Geological Survey earthquake archive:
http://www.geology.arkansas.gov/xl/Earthquake_Archive.xlsx. Last accessed: 21st January 2016.

Center for Engineering Strong Motion Data (CESMD): <http://www.strongmotioncenter.org/>.
Last accessed: 19th November 2015.

CNBC's America's Top States for Business 2012 (2012): <http://www.cnbc.com/id/100003143>.
Last accessed: 9th February 2017.

CNN (2011): <http://edition.cnn.com/2011/US/02/28/arkansas.quake/>.
Last accessed: 9th February 2017.

Construction Market Data (2016): <http://www.cmdgroup.com/building-codes/arkansas/>.
Last accessed: 9th February 2017.

Global Centroid Moment Tensor Project (GCMT): <http://www.globalcmt.org>.
Last accessed: 9th May 2018.

ISO Mitigation (2015):
<http://www.isomitigation.com/index.php/bcegs/facts-and-figures-about-bcegs-grades-around-the-country>. Last accessed: 24th October 2015.

Quickfacts (2016): <http://quickfacts.census.gov/>. Last accessed: 27th January 2016.

Reuters (2013):

<http://www.reuters.com/article/us-usa-energy-quakes-insight-idUSBRE97Q05N20130827>.

Last accessed: 9th February 2017.

The Encyclopedia of Arkansas History & Culture (2015):

<http://www.encyclopediaofarkansas.net/encyclopedia/entry-detail.aspx?entryID=5912>.

The Huffington Post (2011):

http://www.huffingtonpost.com/2011/02/28/earthquake-in-arkansas_n_829048.html.

Last accessed: 9th February 2017.

The Log Cabin Democrat (2014): <http://thecabin.net/news/local/2014-02-13#.Vqh3CjHF-Oc>.

Last accessed: 9th February 2017.

The New York Times (2011): http://www.nytimes.com/2011/03/01/us/01earthquakes.html?_r=0.

Last accessed: 9th February 2017.

THV11 archives (2014):

http://archive.thv11.com/assetpool/documents/140214060946_Earthquake%20Damage%20Lawsuit.pdf. Last accessed: 27th January 2016.

United States Bureau of Economic Analysis (2012):

https://www.bea.gov/newsreleases/regional/gdp_state/2012/pdf/gsp0612.pdf.

Last accessed: 9th February 2017.

United States Bureau of Labor Statistics, Economy at a Glance (2016):

<http://www.bls.gov/eag/eag.ar.htm>. Last accessed: 27th January 2016.

United States Department of Agriculture, 2012 Census of Agriculture (2014):

<http://www.agcensus.usda.gov/Publications/2012/>. Last accessed: 9th February 2017.

United States Energy Information Administration (EIA, 2016): <http://www.eia.gov/state/rankings/>.

Last accessed: 25th January 2016.

United States Geological Survey (USGS): <http://earthquake.usgs.gov/>

Outdated website for this event (last accessed 27th January 2016):

<http://earthquake.usgs.gov/earthquakes/eqinthenews/2011/nm022811a/#summary>.

Renovated website for this event (last accessed 27th January 2016):

<http://earthquake.usgs.gov/earthquakes/eventpage/nm608509#executive>.

University of Dayton, Hydraulic Fracturing Tort Litigation Summary (2016):

https://www.udayton.edu/directory/law/documents/watson/blake_watson_hydraulic_fracturingprimer.pdf. Last accessed: 27th January 2016.

USGS, New Madrid 1811-1812 earthquakes (2016):

<http://earthquake.usgs.gov/earthquakes/states/events/1811-1812.php>.

Last accessed: 27th January 2016.

A3.3 May 2011 M5.1 Lorca Earthquake, Spain

This earthquake occurred on 11th May 2011, at 16.47 UTC (18.47 local time), very close to the city of Lorca, south-eastern Spain, preceded by a **M**4.5 foreshock at 15.05 UTC (17.05 local time), which caused only minor damage. The main shock, on the other hand, caused significant losses to the city of Lorca, most possibly due to a combination of the proximity of the epicentre to the town, the shallowness of the hypocentre, directivity and site amplification effects, and the vulnerability of the building stock.

A3.3.1 Tectonic and seismic setting

A3.3.1.1 Tectonic setting

The epicentre of the earthquake was located in the proximity of the city of Lorca, in the autonomous community of Murcia, south-eastern Spain, very close to the boundary between the Eurasian and the African tectonic plates, whose relative positioning is shortening in the north-northwest to south-southeast direction (Gaspar-Escribano & Benito, 2007) at an approximate rate of 4.5-5.6 mm per year (Masana *et al.*, 2004). This area constitutes the east sector of the Cordillera Bética, and it presents the highest seismic activity rate of the Iberian peninsula (Rodríguez-Escudero *et al.*, 2014). Nevertheless, this activity is quite diffuse and spread over a large number of geological structures (Masana *et al.*, 2004) with a combination of normal, strike-slip and reverse behaviour. The main southwest to northeast structures comprise over 450 km of oblique left-lateral slip faults running from Almería to Alicante, which can be subdivided into five main ones, as shown in Figure A3.3.1, which are: Carboneras fault, Palomares fault, Alhama de Murcia fault, Carrascoy fault and Bajo Segura fault. The Alhama de Murcia fault, believed by many (Alfaro *et al.*, 2012; Rodríguez-Escudero *et al.*, 2014; Rodríguez-Peces *et al.*, 2014; Cabañas Rodríguez *et al.*, 2011; Alguacil *et al.*, 2014; López-Comino *et al.*, 2012) to be responsible for the 2011 **M**5.1 Lorca earthquake, is composed, in turn, of four segments: Goñar-Lorca, Lorca-Totana, Totana- Alhama de Murcia and Alhama de Murcia-Alcantarilla (please refer to Figure A3.3.2). According to Rodríguez-Escudero *et al.* (2014), the two first segments and their inter-segment area are the ones which ruptured in May 2011.

Within the context of a seismic risk study carried out for the whole of the Murcia region, Martínez Díaz *et al.* (2005) investigated the changes in Coulomb stress induced in the area by earthquakes with **M** larger than 4.5 which occurred in between the years 1000 and 2005, and concluded that all the previous seismicity considered had increased the probability of seeing new seismic events along the westernmost segments of the Alhama de Murcia fault.

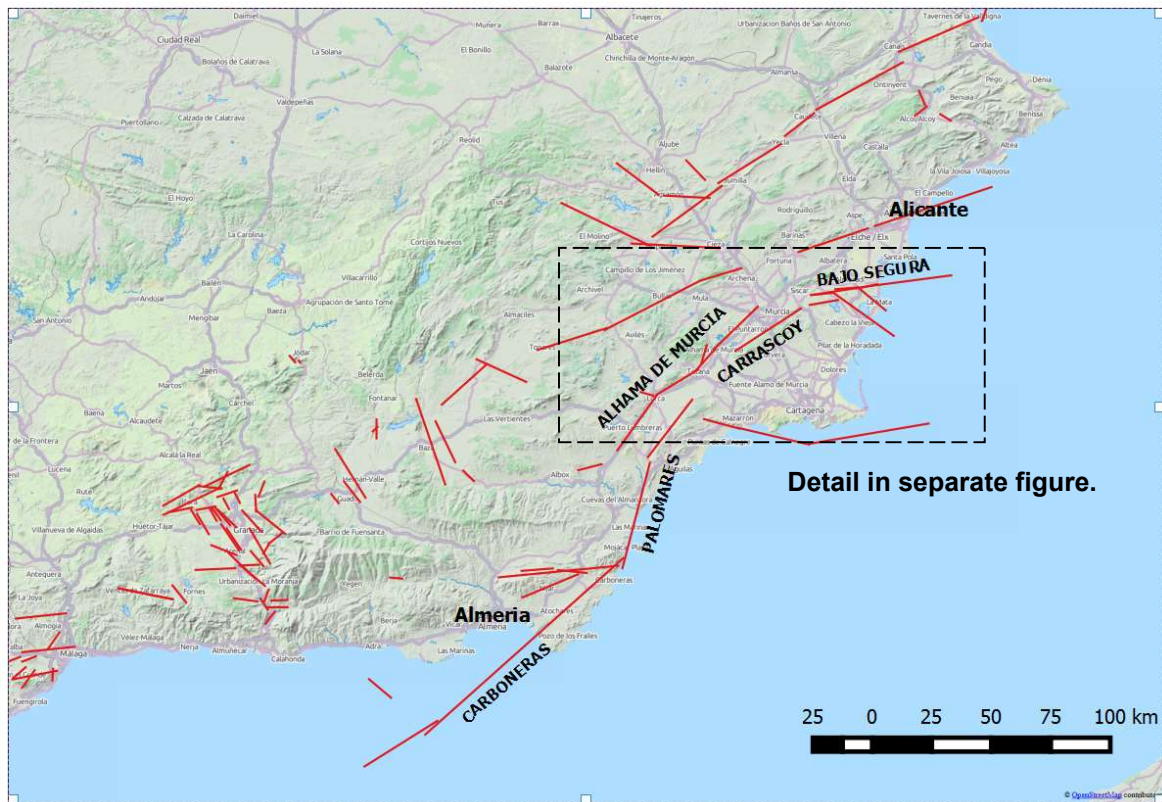


Figure A3.3.1. Main southwest to northeast structures running from Almería to Alicante. Location and dimension of faults in digital format obtained from García-Mayordomo *et al.* (2012)



Figure A3.3.2. Segments that make up the Alhama de Murcia fault. The red star shows the location of the epicentre of the 11th May 2011 main shock, as reported by the Spanish National Geographic Institute (Instituto Geográfico Nacional, IGN). Location and dimension of faults in digital format obtained from García-Mayordomo *et al.* (2012)

It should be noted that other researchers (e.g., Pro *et al.*, 2014), indicate that the 2011 Lorca earthquake was not originated within the Alhama de Murcia fault itself, but along a secondary fault parallel to the latter, located to the north of the city of Lorca, called the Cejo de los Enamorados fault. Its location is not reported in the Quaternary Active Faults Database of Iberia (QAFI, García-Mayordomo *et al.*, 2012) and it is therefore not shown in Figure A3.3.2, but it approximately coincides with the epicentre reported by the Spanish National Geographic Institute (Instituto Geográfico Nacional, IGN) shown in the figure.

A3.3.1.2 Regional and local seismicity

As mentioned above, south-eastern Spain presents the highest seismic activity rate of the Iberian peninsula. The area has experienced several seismic events that have caused a significant level of damage in the past. The city of Lorca, in particular, has experienced damage similar to that of the 2011 earthquake in 1579 and 1674 (Martínez Guevara & Fernández Navarro-Soto, 1986; Martínez Solares & Mezcuca, 2002). The EMS-98 intensity of these events in the city of Lorca is estimated to have been VII ("damaging") and VIII ("heavily damaging"), respectively (Rodríguez-Escudero *et al.*, 2014). Similarly to the 2011 event, the 1674 one was preceded by a foreshock of intensity V to VI, *i.e.*, "strong" to "slightly damaging" (Cabañas Rodríguez *et al.*, 2011).

In more recent years, three significant events occurred in the vicinity of Lorca: the 1999 **M4.7** Mula earthquake, the 2002 **M5.0** Bullas earthquake, and the 2005 **M4.8** La Peca sequence, which presented EMS-98 macroseismic intensities of VI ("slightly damaging"), V ("strong") and VII ("damaging"), respectively (Alfaro *et al.*, 2012; Cabañas Rodríguez *et al.*, 2011; Morales *et al.*, 2014). The epicentres of these and other relevant events can be observed in the map of Figure A3.3.3, in which the 2011 main shock is highlighted.

In spite of the moderate magnitudes of the aforementioned events, a paleoseismic study by Masana *et al.* (2004) reports the occurrence of a minimum of two but possibly three large earthquakes with moment magnitudes in between 6.1 and 7.0 along the Alhama de Murcia fault in the last 27,000 years.

A3.3.1.3 Seismic hazard

Figure A3.3.4 shows an extract of the probabilistic seismic hazard map for Spain, according to the Spanish National Geographic Institute (Instituto Geográfico Nacional, IGN). It shows the PGA values on rock with a 10% probability of exceedance in 50 years, *i.e.*, with a 475-year return period. This map was elaborated after the Lorca earthquake of 2011 and, therefore, specifies a larger design PGA than the one in force at the time of the earthquake, which was 0.12 g (NCSE-02, 2002). The current map indicates that this value should be 0.18-0.19 g instead.

Figure A3.3.5 shows the uniform hazard spectrum on rock from the SHARE (Seismic Hazard Harmonization in Europe) project (Woessner *et al.*, 2015) for a point with coordinates 37.700° N and 1.718° W, which correspond approximately to the city of Lorca. As can be observed, the expected PGA on rock with a 10% probability of exceedance in

50 years is 0.14 g, around 17% higher than that of NCSE-02 at the time of the earthquake, but 22% smaller than that of the newest national seismic hazard map for Spain.

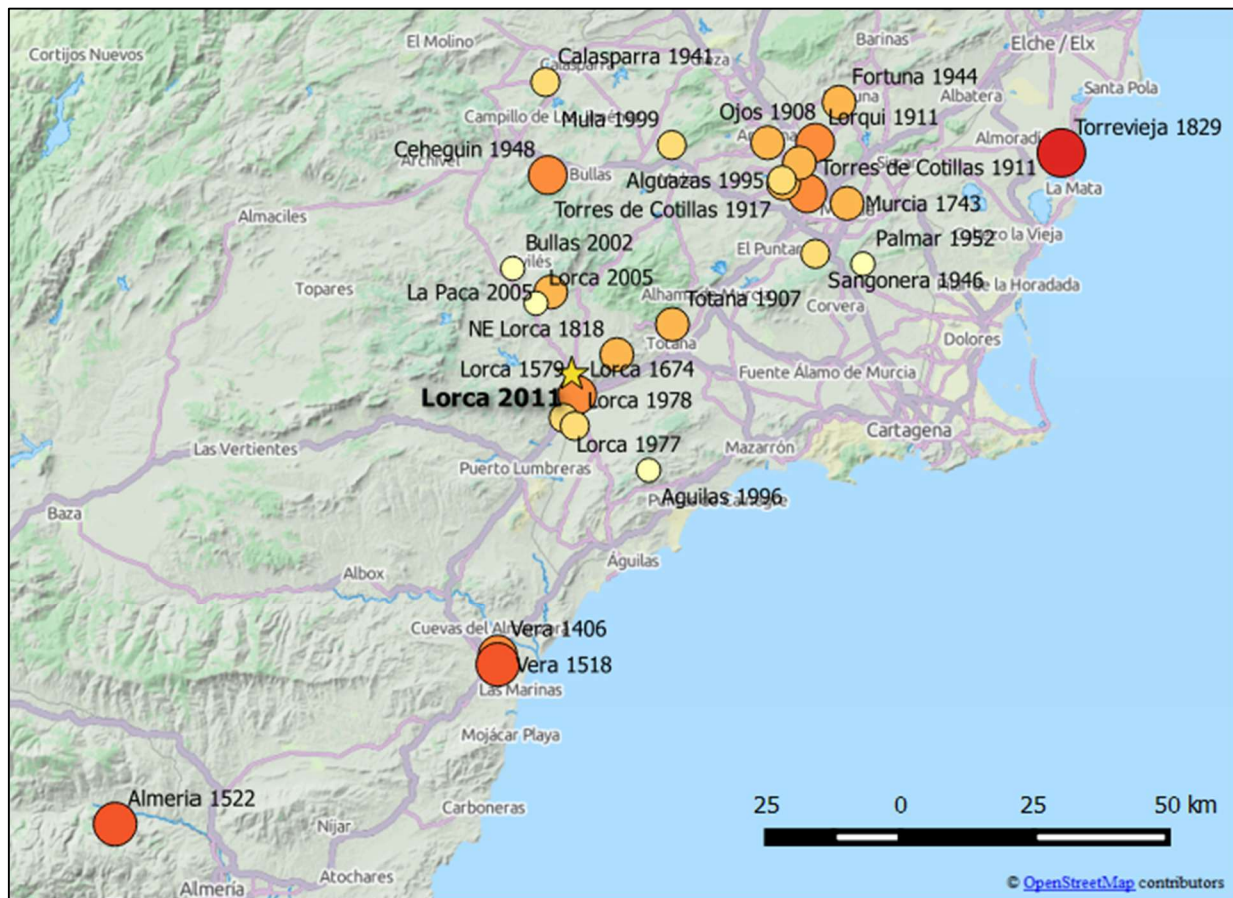


Figure A3.3.3. Epicentres of relevant earthquakes around the area of the city of Lorca. The colour and diameter of the symbols is proportional to the maximum macroseismic intensity of the event.

Results from the Global Seismic Hazard Assessment Program (GSHAP) yield an expected PGA on rock with a 10% probability of exceedance in 50 years of about 0.15 g (1.479 m/s²) for the region around the city of Lorca (Giardini *et al.*, 1999). This value is around 25% higher than that of NCSE-02 at the time of the earthquake, but 17% smaller than that of the newest national seismic hazard map for Spain.

The Worldwide Seismic Design Tool of the United States Geological Survey (USGS) make use of the results from GSHAP to estimate the spectral accelerations at 0.2 and 1.0 seconds with a 2% probability of exceedance in 50 years, which, for the case of Lorca, are 0.75 g and 0.30 g, respectively. It should be noted that these values result from significant approximations and are therefore classified within the lowest reliability category of the USGS database.

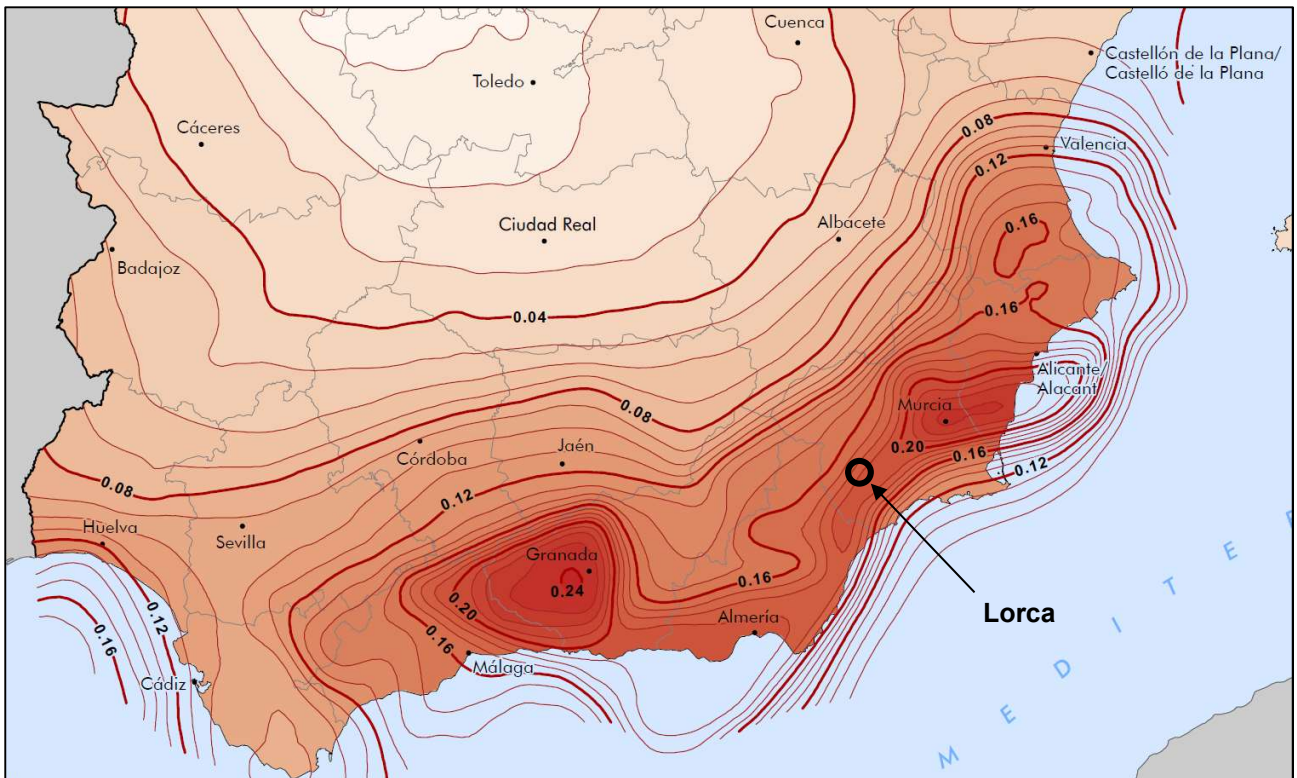


Figure A3.3.4. Extract of the seismic hazard map for Spain, according to the IGN. Values correspond to PGA on rock with a 10% probability of exceedance in 50 years (Spanish National Geographic Institute, 2016).

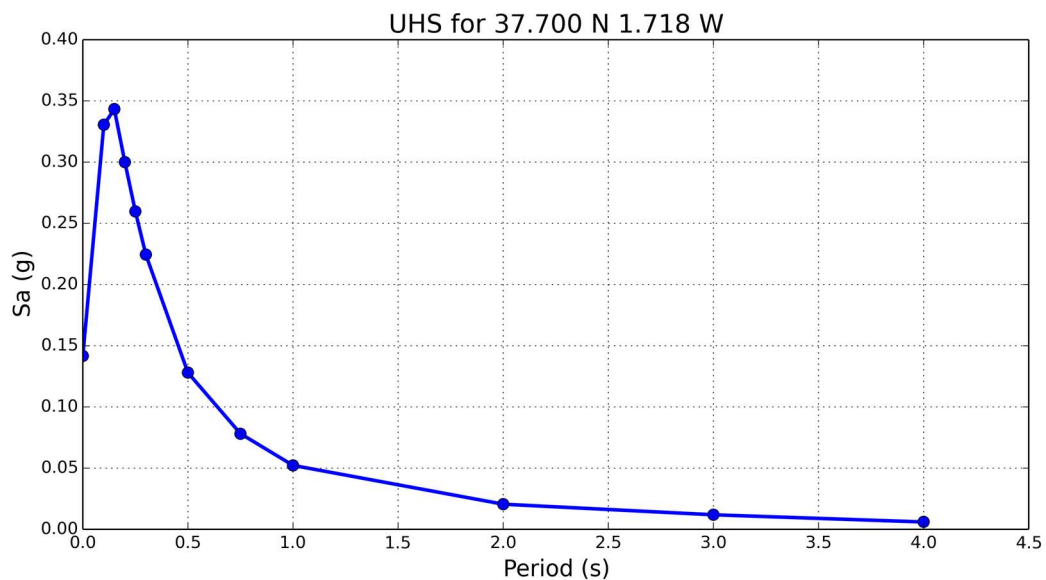


Figure A3.3.5. Uniform Hazard Spectrum for point 37.700° N 1.718° W (closest available to the city of Lorca) according to SHARE (5% critical damping). Values correspond to PGA and spectral acceleration in rock with a 10% probability of exceedance in 50 years (mean).

A3.3.2 Earthquake source characteristics

A3.3.2.1 Location, depth and time

The main shock occurred on 11th May 2011, 16.47 UTC (18.47 local time).

Several organizations and agencies report their own estimations of the epicentral coordinates and hypocentral depth. The information reported in the websites of the Spanish National Geographic Institute (IGN), the National Earthquake Information Center (NEIC) of the United States Geological Service (USGS), the Global Centroid Moment Tensor Project (GCMT; Dziewonski *et al.*, 1981; Ekström *et al.*, 2012), the European-Mediterranean Seismological Centre (EMSC) and the International Seismological Centre (ISC) is summarized in Table A3.3.1. Cells marked as (*f) correspond to parameters that were held fixed while inversion was carried out to retrieve those that remain. Some discrepancy can be observed amongst the different agencies, especially regarding the hypocentral depth which is, in fact, the parameter that is most difficult to constrain. Recognizing this difficulty, Morales *et al.* (2014) and López-Comino *et al.* (2012) carried out a large effort to relocate all the events in the series, finally arriving to the values reported in Table A3.3.1.

Table A3.3.1. Epicentral coordinates and hypocentral depths from different sources.

Agency / Publication		Latitude	Longitude	Depth (km)
IGN	Instituto Geográfico Nacional (MDD)	37.7175 ° N	1.7114 ° W	4.00 (*f)
NEIC	National Earthquake Information Center, USGS	37.6990 ° N	1.6720 ° W (*f)	1.00 (*f)
GCMT	Global Centroid Moment Tensor Project	37.7000 ° N	1.6500 ° W	12.00 (*f)
EMSC	European-Mediterranean Seismological Centre	37.6800 ° N	1.6800 ° W	2.00
ISC	International Seismological Centre (inversion)	37.6494 ° N	1.6938 ° W	6.70
Morales <i>et al.</i> (2014)		37.7300 ° N	1.6900 ° W	4.60
López-Comino <i>et al.</i> (2012)		37.7270 ° N	1.6860 ° W	4.60

(*f) fixed parameter used for inversion

Note that in some cases it is not clear whether the reported coordinates correspond to the epicentre or to the centroid of the moment tensor solution. However, given the small magnitude of the event, the difference between the two is not expected to be significant.

In spite of the large variability that can be found in the estimations regarding hypocentral depth, most journal publications regarding this earthquake make reference to a shallow event, less than 6 km below the surface (Alfaro *et al.*, 2012; Alguacil *et al.*, 2014; Basset-Salom and Guardiola-Víllora, 2014; Cabañas Rodríguez *et al.*, 2011; Feriche *et al.*, 2012; González *et al.*, 2012; López-Comino *et al.*, 2012; Morales *et al.*, 2014; Pro *et al.*, 2014; Rodríguez-Peces *et al.*, 2014; Romão *et al.*, 2013).

The map in Figure A3.3.6 shows the different estimations of the epicentral coordinates enumerated above. The Quaternary Active Faults Database of Iberia (García-Mayordomo *et al.*, 2012), indicates that the Lorca-Totana segment of the Alhama de Murcia fault is striking in the WSW direction, dipping towards the NNW. As shown in Figure A3.3.6,

hypocentral locations from the local networks (IGN) and reported in subsequent studies (López-Comino *et al.*, 2012; Morales *et al.*, 2014) are consistent with this information.

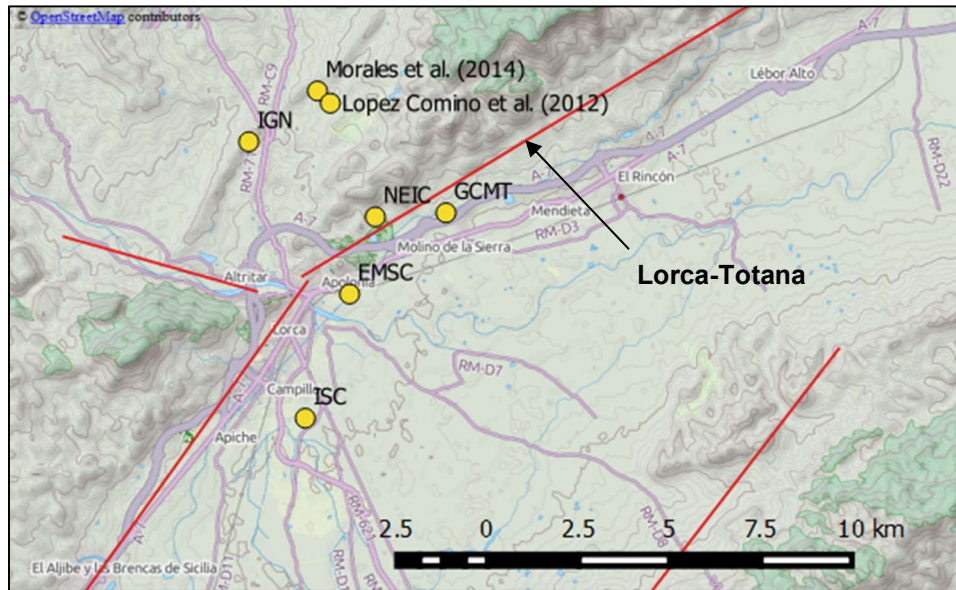


Figure A3.3.6. Estimations of the epicentral coordinates. Red lines represent the fault traces. Location and dimension of faults in digital format obtained from García-Mayordomo *et al.* (2012)

A3.3.1.1 Magnitude

Estimations of magnitude made by the main agencies are reported in Table A3.3.2. Most organizations agree on the moment magnitude **M** being 5.1, though several journal publications report 5.2 instead (Alguacil *et al.*, 2014; López-Comino *et al.*, 2012; Martínez-Díaz *et al.*, 2012; Rodríguez-Escudero *et al.*, 2014).

Table A3.3.2. Estimations of moment magnitude (**M**), body-wave magnitude (**mb**), local magnitude (**M_L**) and surface-wave magnitudes (**M_s**).

Agency		M	mb	ML	Ms
IGN	Instituto Geográfico Nacional (MDD)	5.1	5.4 (*)	-	-
NEIC	National Earthquake Information Center, USGS	5.1	5.3	-	-
GCMT	Global Centroid Moment Tensor Project	5.1	-	-	-
EMSC	European-Mediterranean Seismological Centre	5.1	5.3	5.4	-
ISC	International Seismological Centre (inversion)	-	5.1 - 5.2	-	4.6 - 4.7

(*) mbLg

A3.3.2.3 Style-of-faulting

All the centroid moment tensor solutions from diverse sources indicate an oblique-reverse mechanism (López-Comino *et al.*, 2012; Pro *et al.*, 2014), as shown in Table A3.3.3. Based on the known tectonics and active faults in the region, nodal planes aligning to ENE-WSW would represent the likely fault plane (Martínez-Díaz *et al.*, 2012). The distribution of aftershocks supports this assertion (please refer to Foreshocks and

aftershocks section). Figure A3.3.7 plots the moment tensor solutions calculated immediately after the earthquake.

Table A3.3.3. Centroid moment tensor solutions from different sources. Fault planes marked in gray match the orientation of the Alhama de Murcia fault and parallel secondary structures in the area.

Fault Plane 1			Fault Plane 2			Source
Strike	Dip	Rake	Strike	Dip	Rake	
234	45	43	111	61	126	GCMT
245	65	58	120	40	138	GeoAzur
294	58	140	47	57	39	GFZ, reported by EMSC
230	69	33	127	59	156	IGN
220	75	50	113	42	157	NEIC (USGS)
310	76	159	45	70	15	NEIC (USGS)
238	54	59	104	46	26	Pro et al. (2014)
302	45	152	52	71	48	INGV

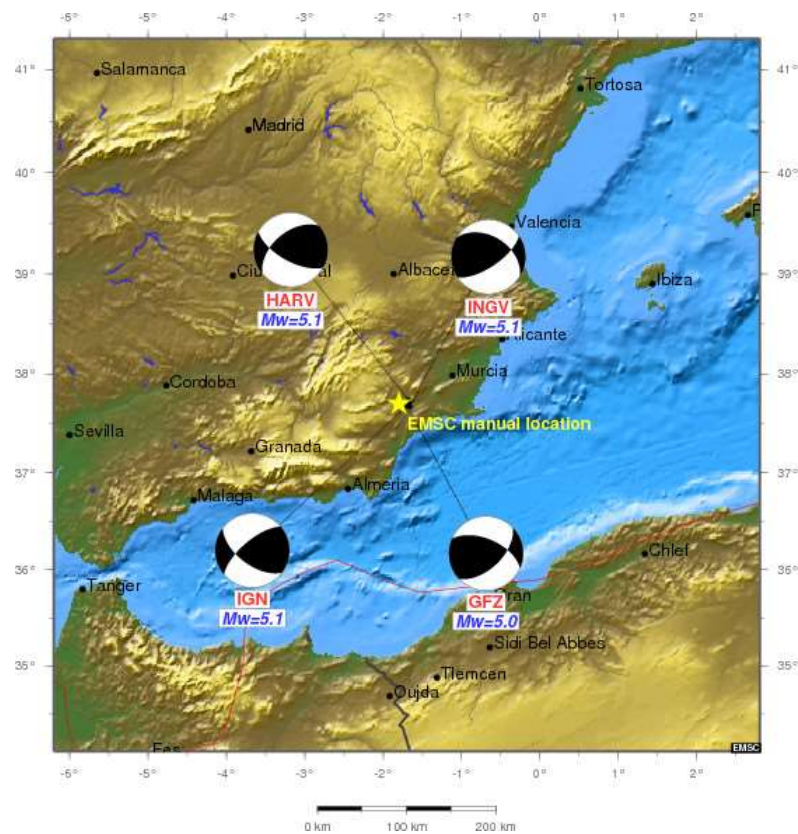


Figure A3.3.7. Moment tensor solutions calculated immediately after the earthquake, from the website of the European-Mediterranean Seismological Centre (2016).

A3.3.2.4 Stress drop

Pro *et al.* (2014) report a stress drop of 2.70 MPa, while Avouac (2012) says it has been calculated to be between 0.5 and 2.0 MPa. Morales *et al.* (2014), on the other hand, report that the dynamic stress drop was somewhere between 5.8 and 8.5 MPa.

A3.3.2.5 Foreshocks and aftershocks

The **M** 5.1 main shock was preceded by a **M** 4.5 event that occurred less than two hours earlier, on 11th May 2011, at 15.05 UTC (17.05 local time), which caused only minor damage (Alguacil *et al.*, 2014). According to Morales *et al.* (2014), the maximum EMS-98 intensity of this foreshock was VI. In between the two events, the IGN reports the occurrence of six minor events with moment magnitudes ranging from 1.3 to 2.6 (Cabañas Rodríguez *et al.*, 2011).

Several aftershocks followed the main shock. According to the IGN, around 140 earthquakes occurred in the area between 11th May and 14th July 2011, out of which sixteen were felt, one of them reaching a maximum EMS-98 intensity of IV (Cabañas Rodríguez *et al.*, 2011; Pro *et al.*, 2014). The largest aftershock was a **M**3.9 event on 11th May at 20.37 UTC (Morales *et al.*, 2014). A peak in the number of events registered per day occurred on 14th May, and a drastic decrease was observed after 16th May (Cabañas Rodríguez *et al.*, 2011; Morales *et al.*, 2014). Figure A3.3.8 shows the distribution in time of the events of the sequence, while Figure A3.3.9 shows all the events registered by the IGN between 11th May and 31st August 2011, for the region enclosed by meridians 2.0°W and 1.2°W and parallels 37.5°N and 38.0°N.

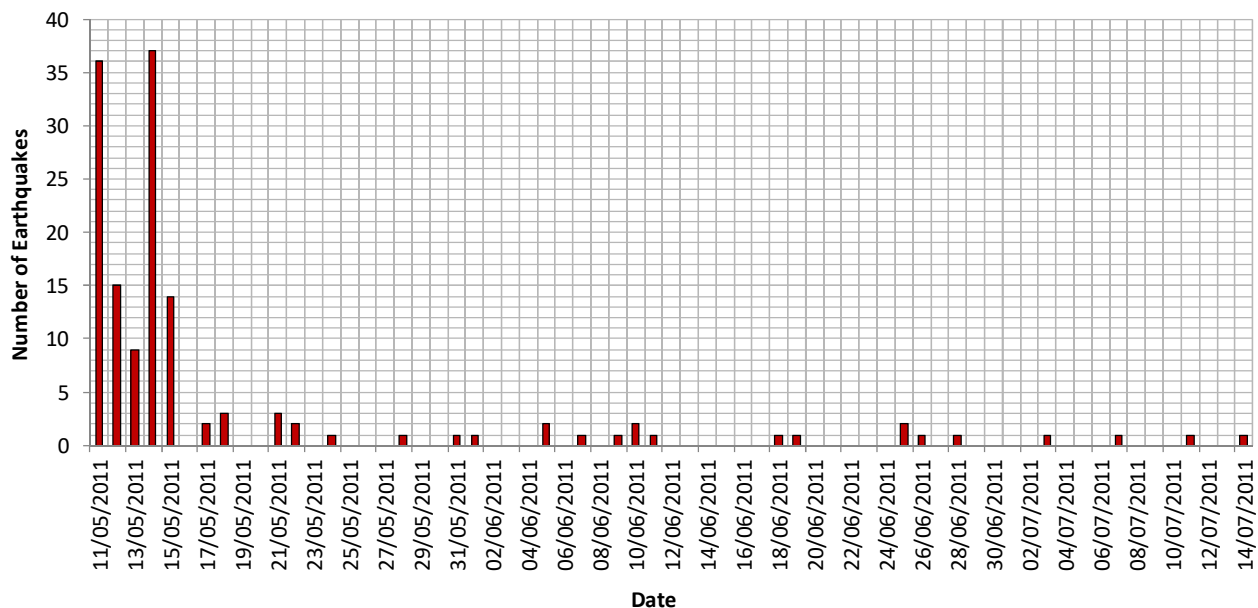


Figure A3.3.8. Distribution in time of the earthquake sequence. Data from Cabañas Rodríguez *et al.* (2011).

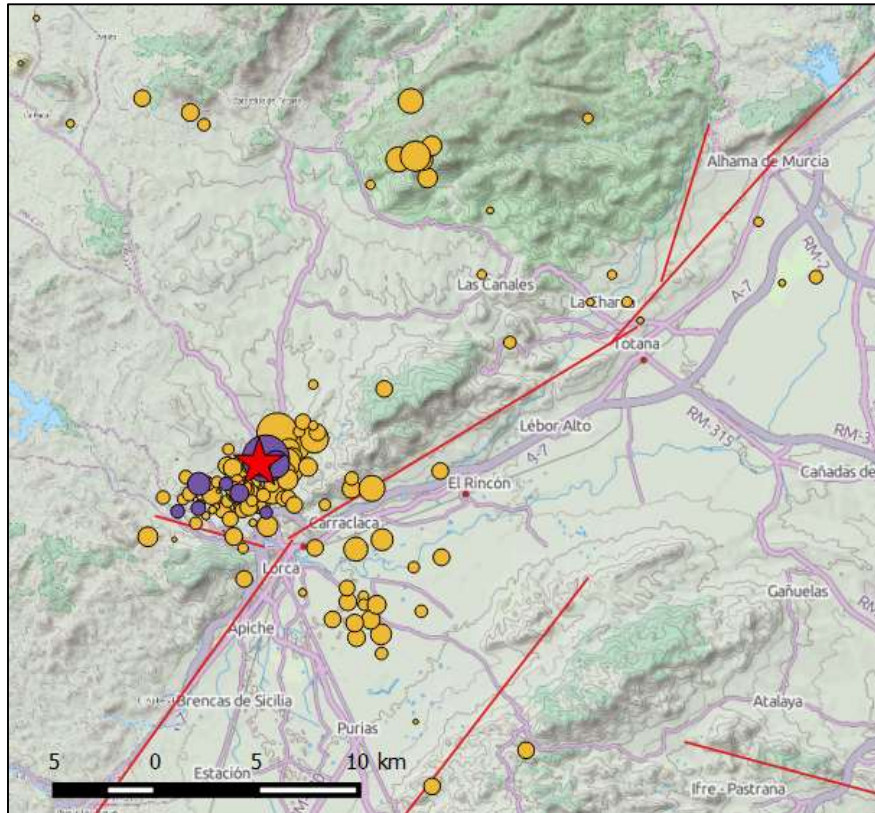


Figure A3.3.9. Epicentres of the seismic series according to the Spanish National Geographic Institute (IGN). Purple and orange circles correspond to events which occurred before and after the main shock (red star), respectively.

A3.3.2.6 Nature of earthquake

A study by González *et al.* (2012) suggests that the 2011 Lorca earthquake was triggered by the effects of groundwater extraction. These authors report a drop of around 250 metres in the phreatic level in the area of Lorca between 1960 and 2010. Furthermore, González & Fernández (2011) have determined that the Alto Guadalentín basin presents a subsidence rate of more than 10 cm per year due to long-term sustained water extraction from the underground aquifers. By means of a model of the ground deformation resulting from crustal unloading due to water extraction, González *et al.* (2012) calculated the three-dimensional Coulomb stress change and concluded that it can reasonably explain the observed fault slip pattern as well as the dynamics of the rupture.

Though agreeing with González *et al.* (2012) regarding the relevance of the influence of water extraction on the 2011 Lorca earthquake, Avouac (2012) draws attention to the fact that the stresses released during the earthquake, 0.5 to 2.0 MPa, are significantly larger than those that could have been induced by removal of underground water, and suggests that the released stresses probably built up over several centuries due to tectonic deformations, and that the role of water extraction was most likely limited to influencing the rate at which these stresses were accumulated and when and how they were released.

A3.3.3 Geology and ground conditions in the affected area

A3.3.3.1 Regional geology and topography

As described by Alfaro *et al.* (2012) and Martínez-Díaz *et al.* (2012), two mountain ranges, the Peña Rubia and Tercia ranges, are located to the northwest of the Alhama de Murcia fault, and are constituted by sedimentary and metamorphic rocks which are mainly Triassic, though some Palaeozoic and Jurassic rocks can be found as well. These two ranges are separated from each other by a pull-apart basin with sedimentary infill from the Miocene and Quaternary, known as the Lorca basin, which is where the homonymous city is located. The basin formed during an extensional phase in the Middle to Late Miocene, period in which some segments of the Alhama de Murcia fault behaved as normal faults. As described above (please refer to the Tectonic and Seismic Setting section), this sedimentary basin is subject to a NNW–SSE compressive stress field since the Upper Miocene, which causes it to be folded. The river running through the basin is called Guadalentín.

A3.3.3.2 Site conditions in the affected area

Given its location within the Lorca basin, the town of Lorca is mostly lying over sedimentary soils with a very heterogeneous structure. Navarro *et al.* (2014) carried out an extensive geological study in the area and produced a soil classification map of the city using the soil type categories of Eurocode 8 - Part 1 (CEN, 2004). As can be observed in Figure A3.3.10, a large part of the city is founded over soils type B2 and C.

Navarro *et al.* (2014) present as well two cross sections (marked as A-A' and B-B' in Figure A3.3.10, shown in Figure A3.3.11) that expose the complexity of the geology of the basin. Navarro *et al.* (2014) and Martínez-Díaz *et al.* (2011) conclude that the alluvial deposits of the basin can be responsible for amplification of ground motions.

Within the context of the RISMUR project ("Seismic Risk of the Autonomous Community of the Murcia Region", "Riesgo Sísmico de la Comunidad Autónoma de la Región de Murcia" in Spanish), Tsige Aga & García Flores (2005) produced a soil classification map for the whole of the Murcia region, according to which Lorca falls within a mid-level amplification category with respect to the whole of the autonomous community of Murcia. The authors also investigated the potential for liquefaction and concluded that though this phenomenon can take place in the region, its occurrence is expected to be isolated and non-frequent. Regarding the city of Lorca itself, the liquefaction hazard is low, especially because the phreatic level is located around 250 meters below the surface (González *et al.*, 2012). Figure A3.3.12 shows the map produced by Tsige Aga & García Flores (2005) for the whole region.

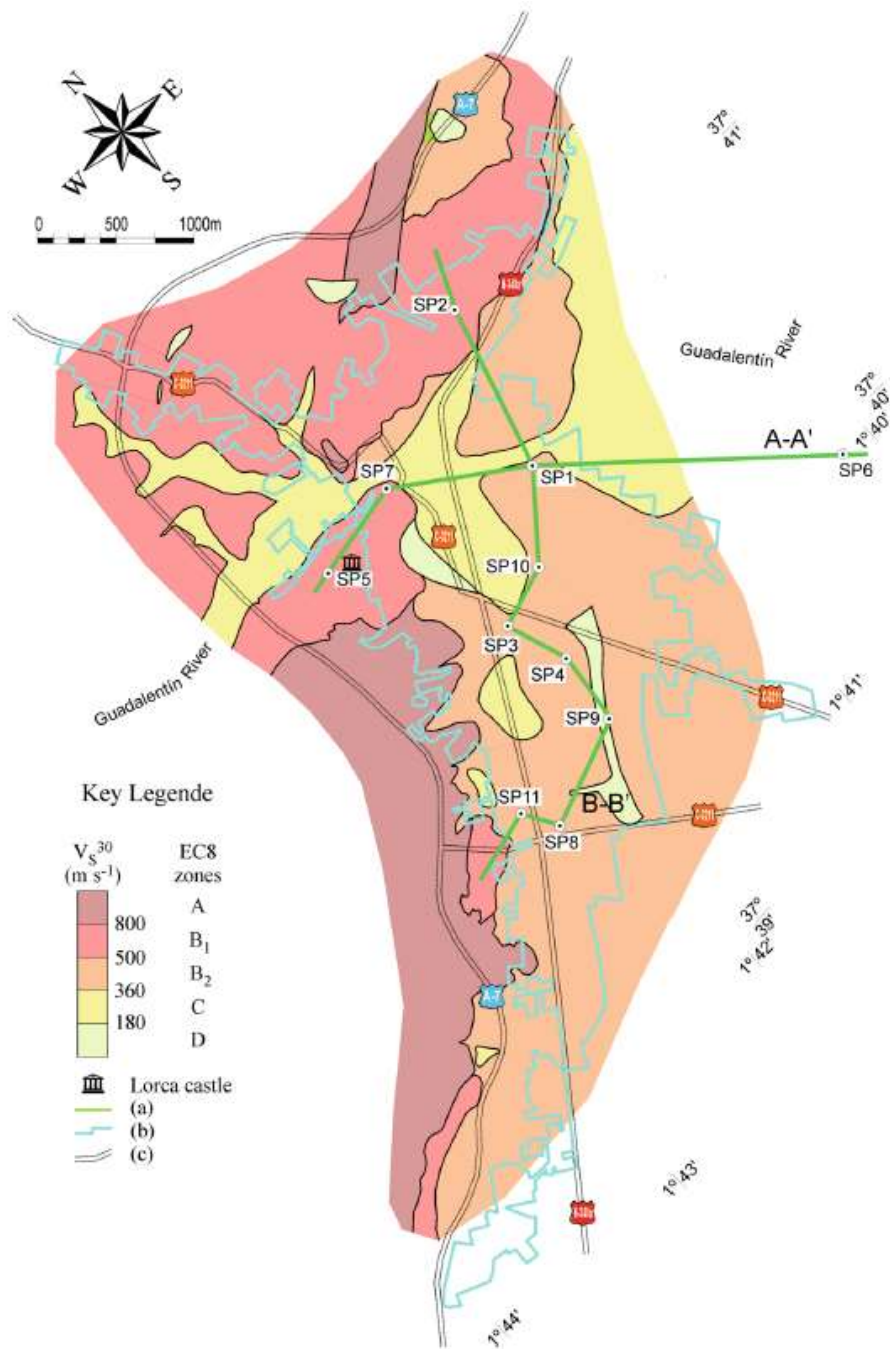


Figure A3.3.10. Soil classification map of the city of Lorca, from Navarro *et al.* (2014). The light-blue solid line shows the urban boundary. Points marked as SP(·) correspond to the location of ambient noise arrays used in the study by Navarro *et al.* (2014).

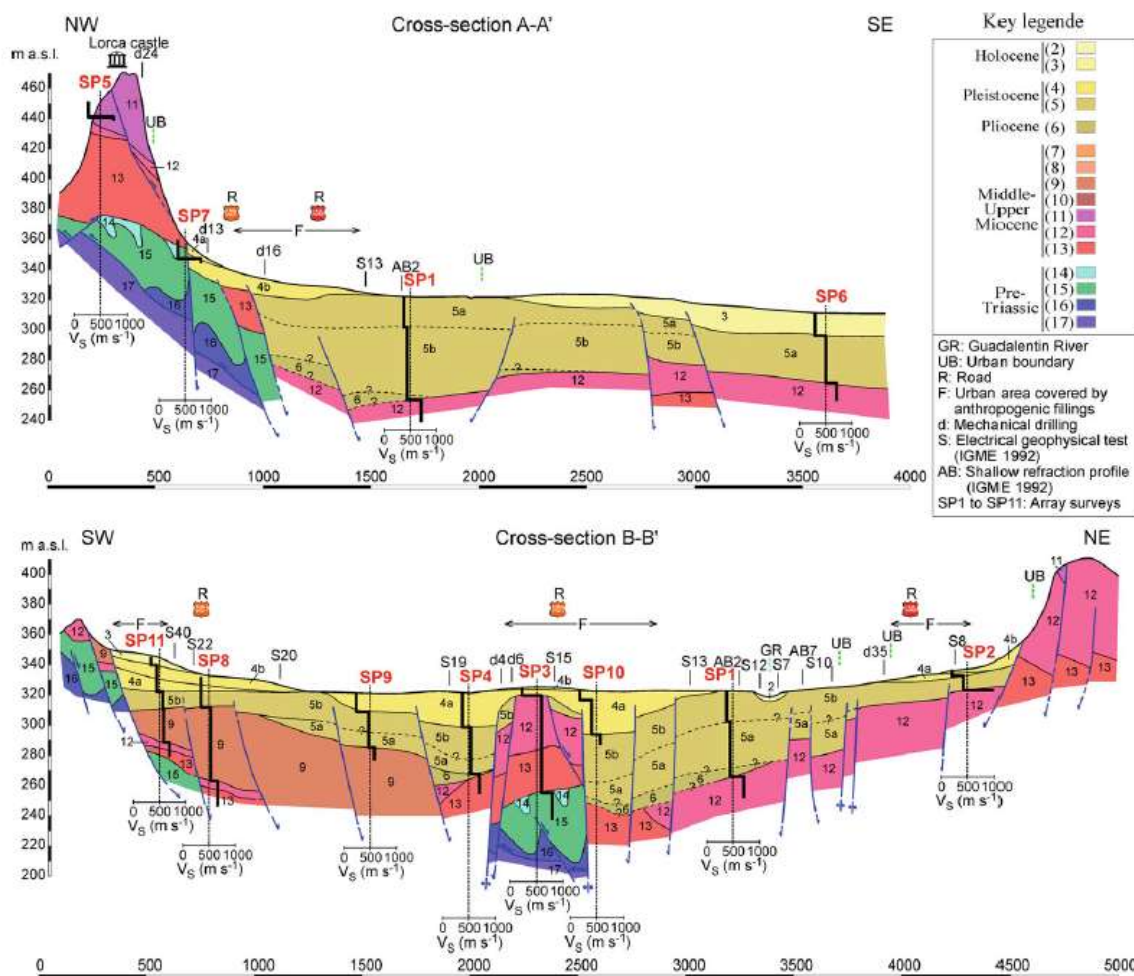


Figure A3.3.11. Geological cross sections of the city of Lorca, from Navarro *et al.* (2014).

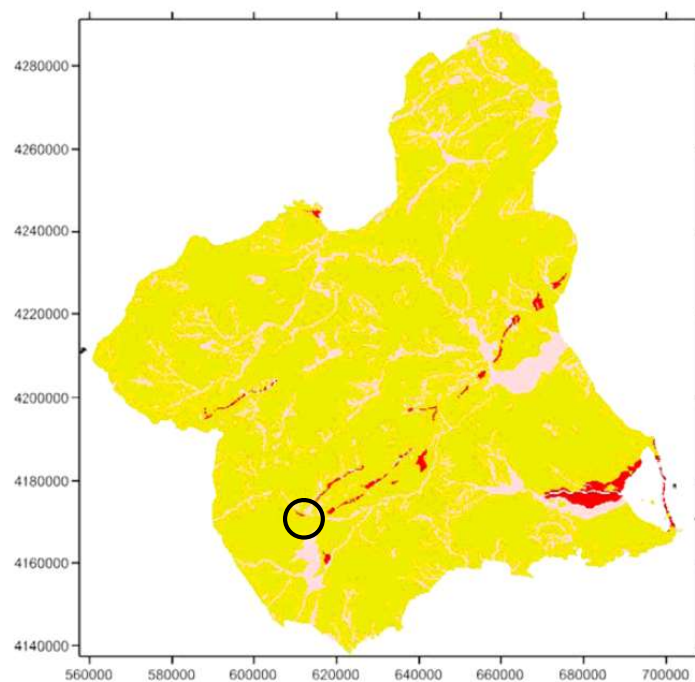


Figure A3.3.12. Liquefaction hazard map for the Murcia region, from Tsige Aga and García Flores (2005). Red: susceptible; pink: rather susceptible; yellow: not susceptible. Black circle: area around the city of Lorca.

A3.3.4 Ground motions

A3.3.4.1 Intensity observations

The IGN reports a maximum EMS-98 (European Macroseismic Scale, Grünthal, 1998) intensity of VII, which defines the event as "damaging". The distribution of felt intensities, as calculated from the online feedback of around six hundred users, is shown in Figure A3.3.13. The IGN provides no indication of how these intensities are calculated.

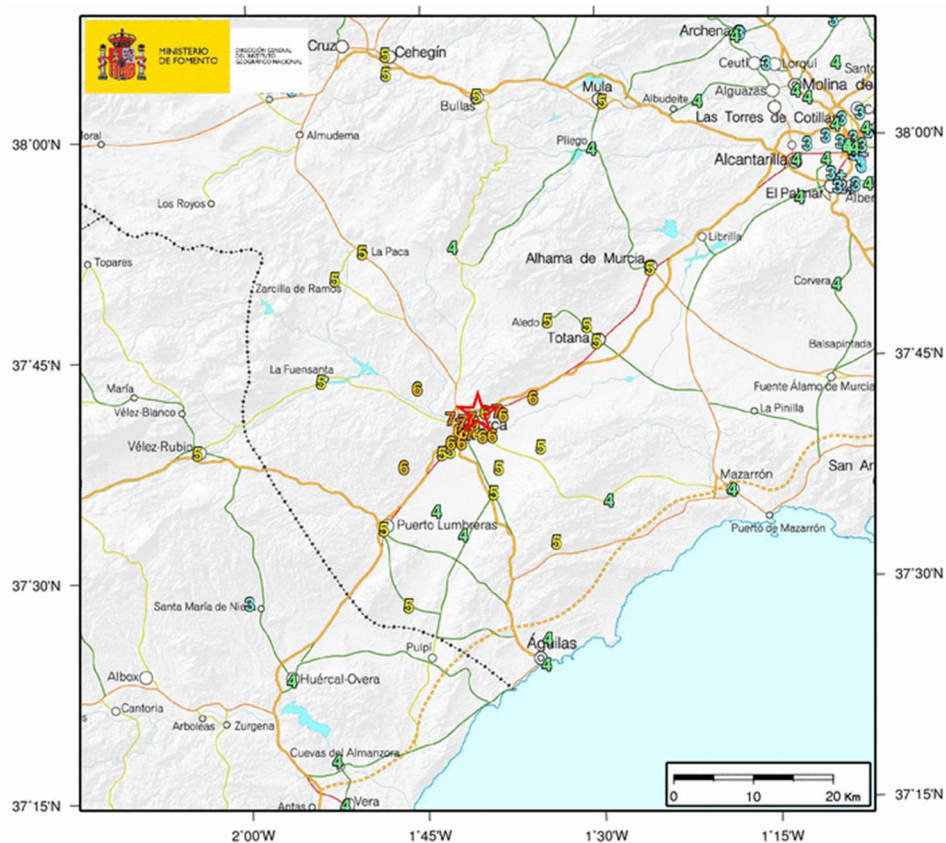


Figure A3.3.13. EMS-98 intensity levels for the 2011 Lorca main shock, from the website of the Spanish National Geographic Institute (2016), updated on 22nd March 2012. Enlargement of the area marked in the previous figure.

In its summary of the significant earthquakes of the world which occurred during 2011, the United States Geological Service (USGS) reports a maximum MMI (Modified Mercalli Scale) intensity of VI at the city of Lorca, which corresponds to strong shaking and slight damage. Intensities assigned to other nearby locations are V ("moderate") at Alhama de Murcia and IV ("light") at Huercal-Overa, Mazarron, Murcia, Lumbreras and Totana. No details are given with respect to the computation of these values. However, the ShakeMap (Worden *et al.*, 2017) of this earthquake reaches values of almost VIII (2017 version) and, within the "Did You Feel It?" report of the earthquake, an MMI of VII is assigned to the city of Lorca, as shown in Figure A3.3.14. This and the other intensity values shown on the map were calculated combining data points in terms of intensity as well as from seismic stations and intensity prediction models. Figure A3.3.15 shows the MMI intensities as a function of distance, as reported by the USGS. Note that the minimum distance considered in this plot is 10 km and, thus, information regarding the city of Lorca is not included.

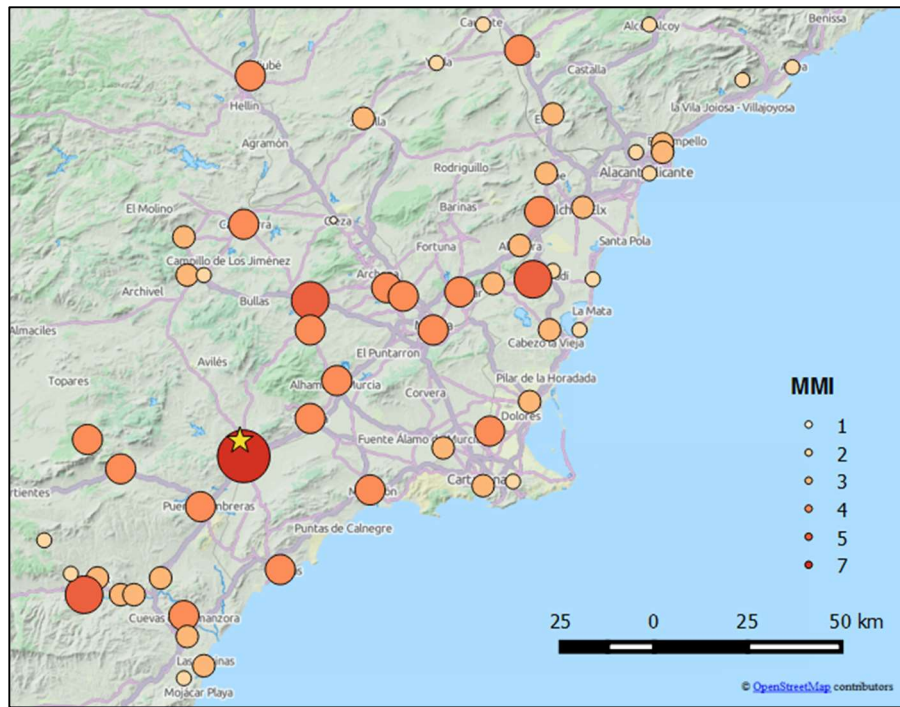


Figure A3.3.14. MMI intensity values calculated for each city from the responses to the "Did You Feel It?" questionnaire at the website of the United States Geological Service (USGS, 2016).

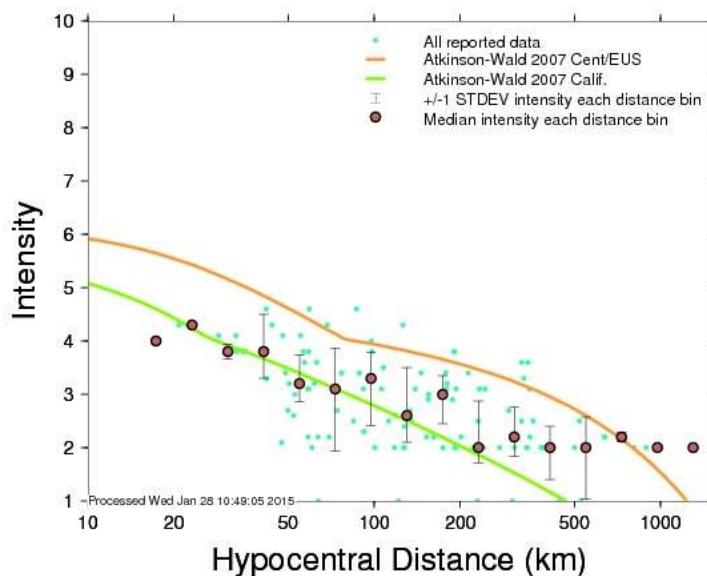


Figure A3.3.15. MMI intensity values vs. hypocentral distance, from the website of the United States Geological Service (USGS, 2016).

A3.3.4.2 Ground motion recordings

According to Cabañas Rodríguez *et al.* (2011), the foreshock was registered by five IGN stations at epicentral distances between 3 and 40 km, while the main shock was registered by seventeen IGN stations at epicentral distances between 3 and 185 km (Figure A3.3.16). The largest PGA values registered within Lorca for the foreshock and main shock were 0.275 g and 0.365 g, respectively, and they are the largest values ever recorded in the Iberian peninsula (Alfaro *et al.*, 2012). Table A3.3.4 shows the values of peak ground

acceleration (PGA) and peak ground velocity (PGV) recorded at the seventeen stations for the main shock. Note that the epicentral distances provided are those reported by Cabañas Rodríguez *et al.* (2011) and they can vary depending on the estimation of the epicentral coordinates.

Table A3.3.4. Corrected PGA and PGV values recorded for the main shock, from Cabañas Rodríguez *et al.* (2011). Soil types according to classification by Mezcua *et al.* (2008): (2) firm soil, Quaternary consolidated deposits, (3) soft sedimentary deposits.

STATION	Epicentral Dist.(km)	Soil Type	E-W Component		N-S Component		Vertical Component	
			PGA(cm/s ²)	PGV(cm/s)	PGA(cm/s ²)	PGV(cm/s)	PGA(cm/s ²)	PGV(cm/s)
LORCA	3	2	150.3	14.2	357.9	35.6	114.9	8.0
ZARCILLA DE RAMOS	24	2	31.4	2.1	25.4	2.2	25.8	1.3
ALHAMA DE MURCIA - 02	27	3	44.3	2.1	41.1	1.3	23.5	0.8
ALHAMA DE MURCIA - 01	28	N/A	7.7	0.2	9.8	0.4	9.1	0.4
VELEZ-RUBIO	36	2	9.3	0.6	10.6	0.5	5.9	0.4
MULA	42	3	41.5	1.4	35.7	1.5	20.2	0.9
VERA	53	3	7.1	0.4	5.8	0.4	4.5	0.3
LORQUÍ	57	3	7.8	0.3	7.9	0.3	3.7	0.2
MURCIA	58	3	8.4	0.4	7.0	0.4	2.6	0.1
CIEZA	64	3	2.8	0.2	2.4	0.1	1.4	0.1
OLULA DEL RÍO	67	2	4.4	0.3	2.2	0.3	1.7	0.2
FORTUNA	73	N/A	7.5	0.3	6.4	0.3	3.5	0.2
JUMILLA	92	2	5.1	0.4	3.8	0.3	3.5	0.3
GUARDAMAR DEL SEGURA	100	3	1.4	0.1	2.0	0.2	0.6	0.1
ELDA	116	2	2.7	0.2	1.7	0.2	0.9	0.1
ALBOLOTE	182	3	1.4	0.2	2.3	0.2	0.8	0.1
JAEN	186	2	2.8	0.2	2.1	0.2	1.3	0.1

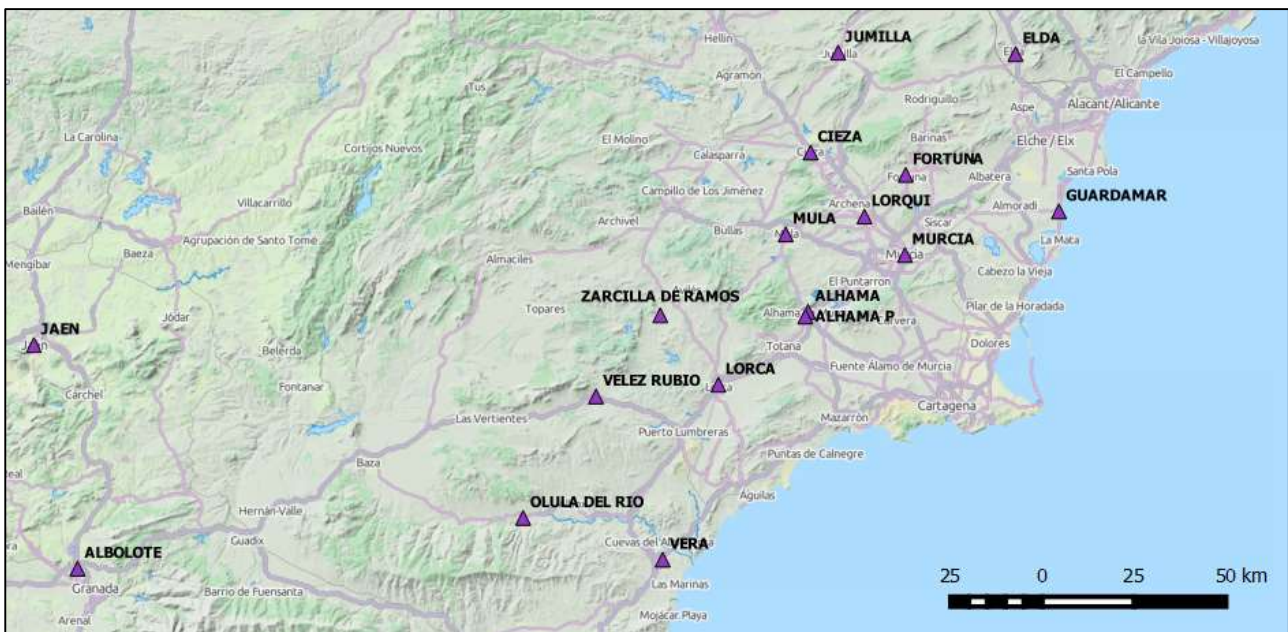


Figure A3.3.16. Location of the seventeen stations that recorded the 2011 Lorca main shock, from the website of the Spanish National Geographic Institute (2016).

According to Cabañas *et al.* (2014), most of the accelerographs deployed in South-Eastern Spain are installed in the ground floor or basement of buildings, usually no more than two or three storeys high. Detailed information regarding the type of soil in these locations is lacking, and all the available information is based on geological mapping and approximate designations. These authors assert that Lorca station can be considered to be located over soil type B (Eurocode 8), which matches what is shown in Figure A3.3.10, and that the Alhama de Murcia 02 and Mula stations are located over soil types B-C and C-D (Eurocode 8), respectively. This appears to be in reasonable agreement with the classification of Mezcua *et al.* (2008), presented in Table A3.3.4, who classified the soil types of a series of Spanish stations based on "a crude qualitative description provided for each station". However, Belvaux *et al.* (2015) state that the Lorca station is placed in the basement of a former jail in the elevated part of the ancient city, where conglomerate bedrock is seen to outcrop, and, therefore, the soil conditions might be considered to better match those of a soil type A (Eurocode 8).

The maximum recorded horizontal acceleration, 0.365 g, occurred in the N30W direction of the Lorca station (Cabañas Rodríguez *et al.*, 2011), which is almost perpendicular to the strike of the Alhama de Murcia fault (Cabañas *et al.*, 2014). This feature is interpreted as a consequence of rupture directivity in the near-field (Alguacil *et al.*, 2014). To confirm this observation, Alguacil *et al.* (2014) plot the maximum acceleration and velocity from the horizontal accelerograms recorded at the Lorca station at every possible angle, and highlight that both the maximum PGA and maximum PGV occur in the direction perpendicular to the strike of the Alhama de Murcia fault, as shown in Figure A3.3.17.

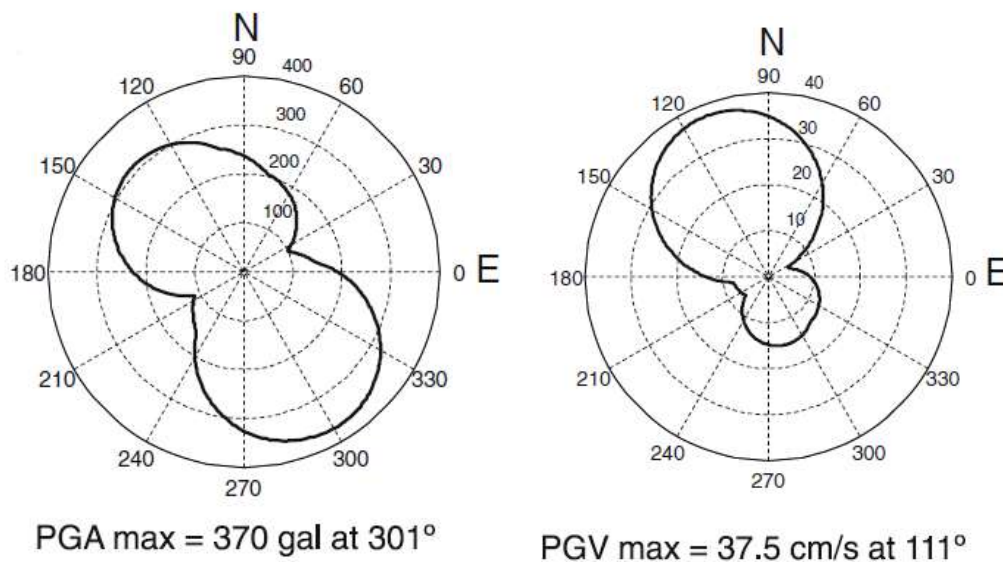


Figure A3.3.17. Polar diagrams of acceleration (left) and velocity (right) as a function of axis orientation, for the accelerograms recorded at the Lorca station, from Alguacil *et al.* (2014).

The acceleration, velocity and displacement time histories for the two components of the records with the largest PGA values are shown in the figures that follow (figures taken from Cabañas *et al.*, 2014).

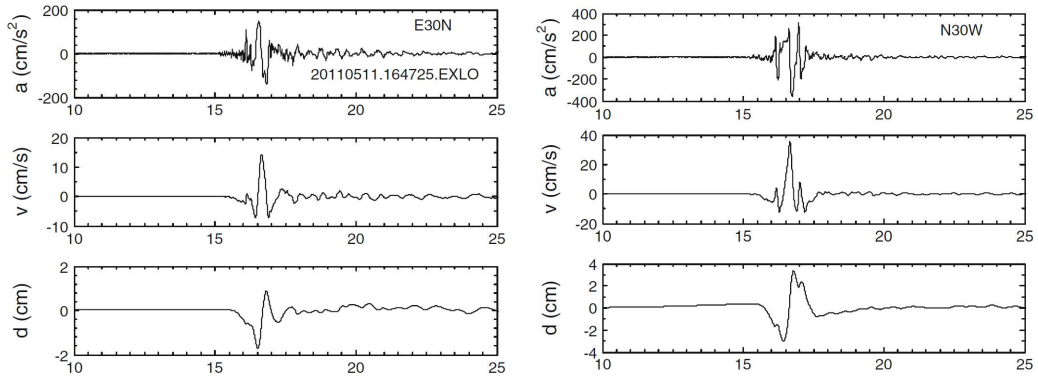


Figure A3.3.18. Horizontal corrected acceleration (top), velocity (middle) and displacement (bottom) for the two components of the Lorca station, from Cabañas *et al.* (2014).

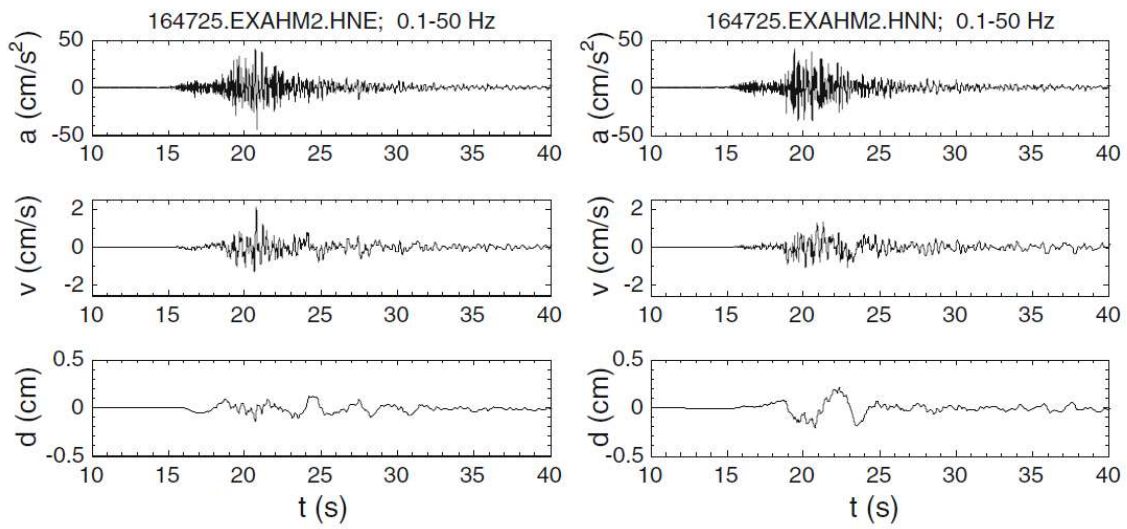


Figure A3.3.19. Horizontal corrected acceleration (top), velocity (middle) and displacement (bottom) for the two components of the Alhama de Murcia 02 station, from Cabañas *et al.* (2014).

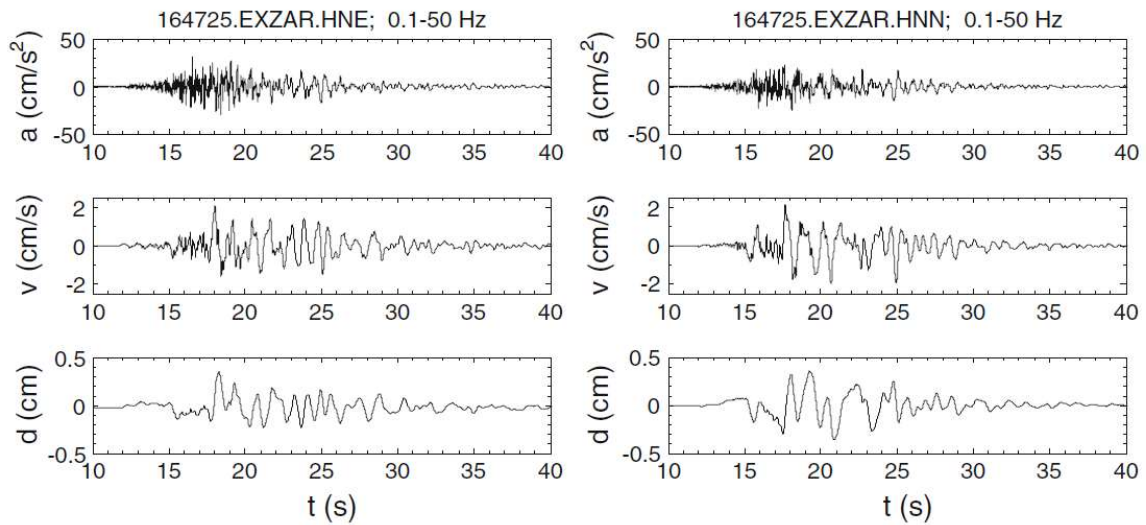


Figure A3.3.20. Horizontal corrected acceleration (top), velocity (middle) and displacement (bottom) for the two components of the Zarcilla de Ramos station, from Cabañas *et al.* (2014).

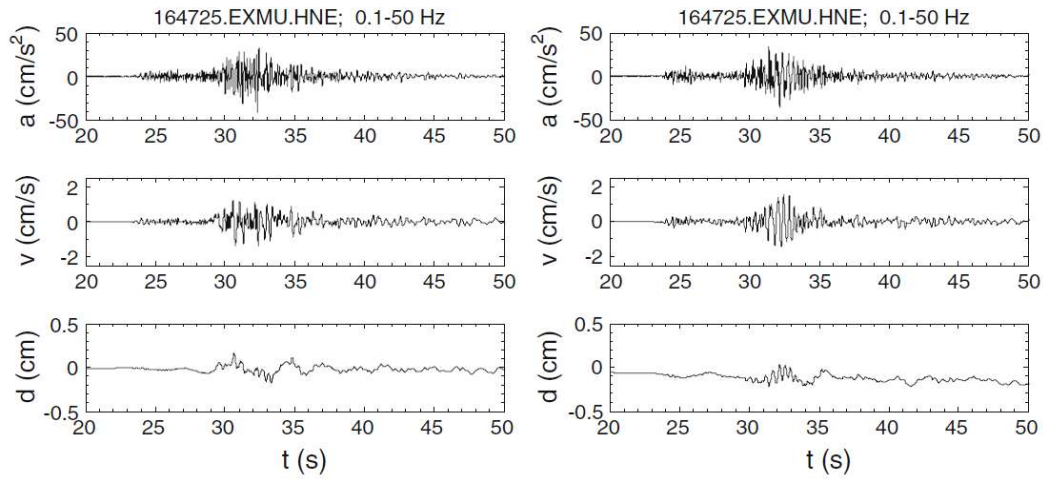


Figure A3.3.21. Horizontal corrected acceleration (top), velocity (middle) and displacement (bottom) for the two components of the Mula station, from Cabañas *et al.* (2014).

Figure A3.3.22 presents the comparisons carried out by Benito Oterino *et al.* (2012) for the PGA values recorded in the different stations with respect to those predicted by four different ground motion prediction equations (GMPEs): Abrahamson & Silva (AS08, 2008), Chiou & Youngs (CY08, 2008), Campbell & Bozorgnia (CB08, 2008) and Akkar & Bommer (AB10, 2010). All of these GMPEs consider the geometric mean of the two horizontal components: geometric mean of as-recorded components in the case of AB10, and GMRot150 in the other three cases. In order to make the comparisons, the authors have used a V_{s30} value of 1100 m/s. In general, and with the exception of the Mula station, acceleration values recorded at distances larger than 20 km are equal to or smaller than those predicted by the GMPEs. For the case of the Lorca station, the geometric mean of the as-recorded components matches the predictions of CB08 and CY08, but each individual component is significantly different from this value.

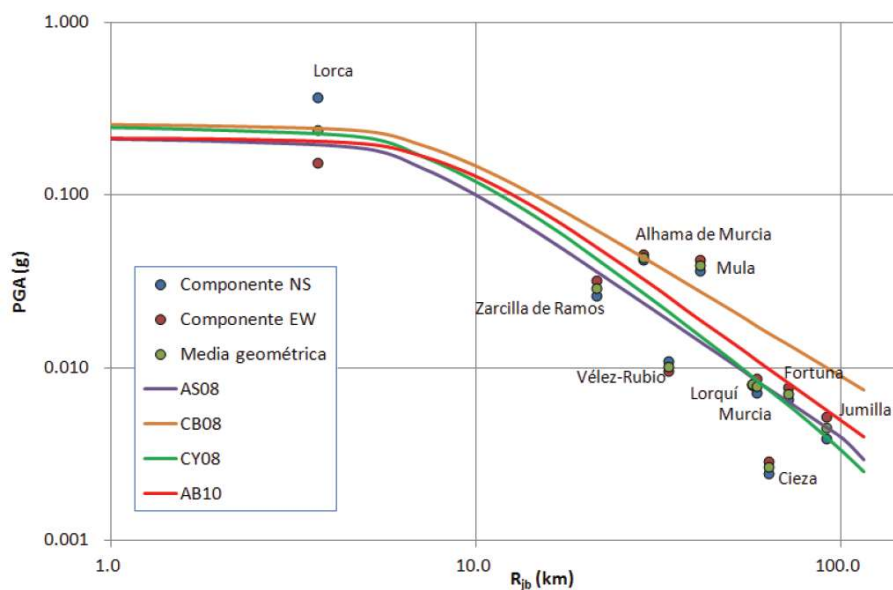


Figure A3.3.22. PGA values recorded at different stations during the main shock against estimations from ground motion prediction equations, from Benito Oterino *et al.* (2012). Blue, red and green dots correspond to north-south, east-west and geometric mean values for each record.

Results of the previous comparison are similar to those obtained by Belvaux *et al.* (2015) (Figure A3.3.23) using GMPEs developed for Spain: Cabañas *et al.* (1999), Tapia *et al.* (2007) and Mezcua *et al.* (2008).

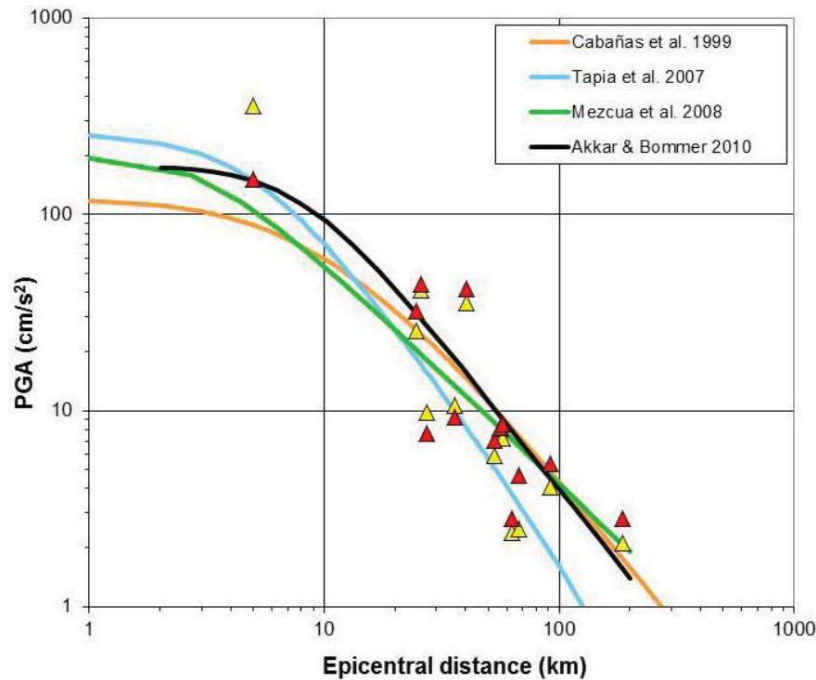


Figure A3.3.23. PGA values recorded at different stations during the main shock against estimations from ground motion prediction equations, from Belvaux *et al.* (2015).

Cabañas *et al.* (2014) have compared the pseudo-acceleration response spectra (5% critical damping) of the accelerograms recorded at the Lorca, Alhama de Murcia 02 and Mula stations with the elastic design spectra from the NCSE-02 Spanish building code for the soil types they consider representative of the site conditions at those locations. As can be observed in Figure A3.3.24, the pseudo-spectral accelerations of the N30W component of the Lorca station record largely exceed those of the design spectra in the low-period range. Some of the spectral accelerations for the E30N component exceed the design spectra as well, albeit to a lesser extent. On the other hand, both components of the Alhama de Murcia 02 and Mula stations do not exceed the spectral accelerations from the corresponding design spectra (Figure A3.3.25). It should be noted that this comparison is more appropriate for the spectral shape than for the actual values of the ordinates themselves.

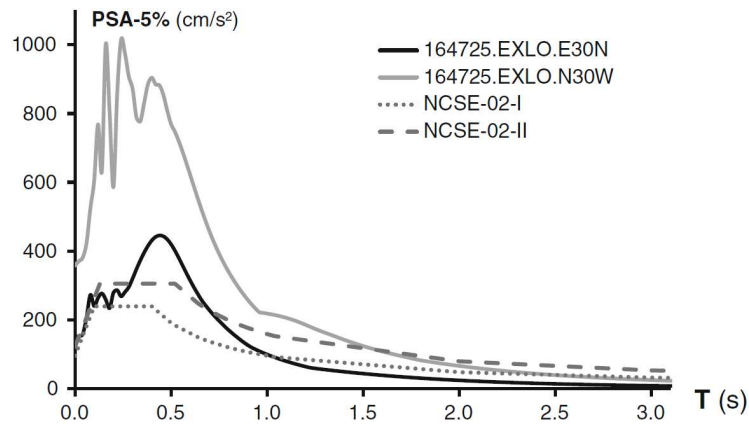


Figure A3.3.24. Pseudo-acceleration response spectra (5% critical damping) from the accelerograms recorded at the Lorca station, compared with the elastic design spectra from the NCSE-02 Spanish building code for soil types I and II (equivalent to soil classes A and B in Eurocode 8), from Cabañas *et al.* (2014).

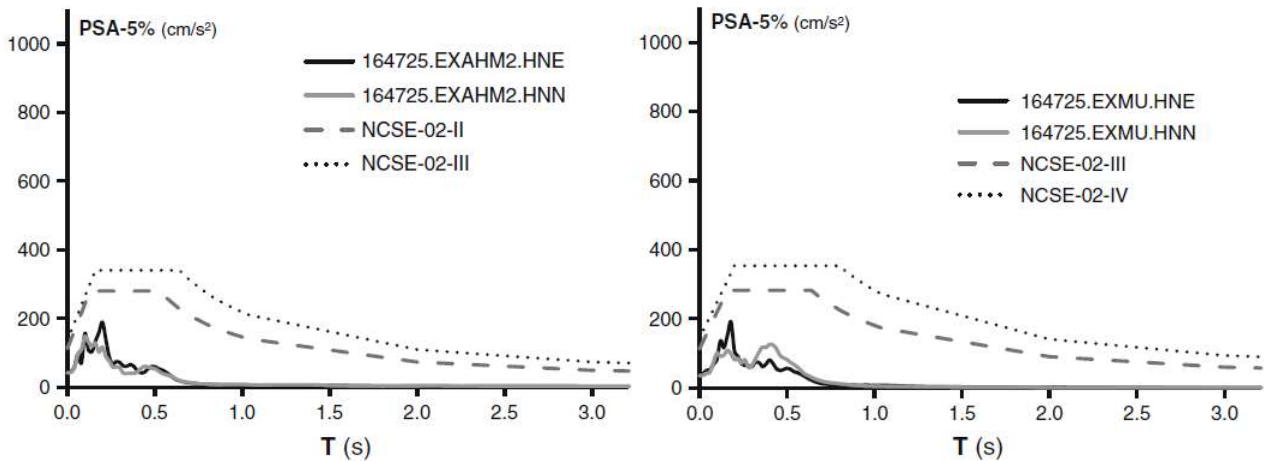


Figure A3.3.25. Pseudo-acceleration response spectra (5% critical damping) from the accelerograms recorded at the Alhama de Murcia 02 (left) and Mula (right) stations, compared with the elastic design spectra from the NCSE-02 Spanish building code for soil types II and III (equivalent to soil classes B and C in Eurocode 8, top) and III and IV (equivalent to soil classes C and D in Eurocode 8, bottom), from Cabañas *et al.* (2014).

Cabañas Rodríguez *et al.* (2011) have compared the pseudo-acceleration response spectrum of the N30W component of the Lorca station accelerogram with the median spectra obtained from several GMPEs for the corresponding magnitude, distance and local conditions. As can be observed in Figure A3.3.26, the spectrum of the recorded component easily exceeds all those obtained with the GMPEs.

Cabañas Rodríguez *et al.* (2011) draw attention to the fact that the two stations located in Alhama de Murcia are located at similar distances from the epicentre of the main shock but have recorded very different PGA levels (see Table A2.2.4). The authors believe that this is probably due to one of the stations (the one with the largest recorded motion) being located over softer soils than the other one, though they acknowledge the need for a more detailed analysis.

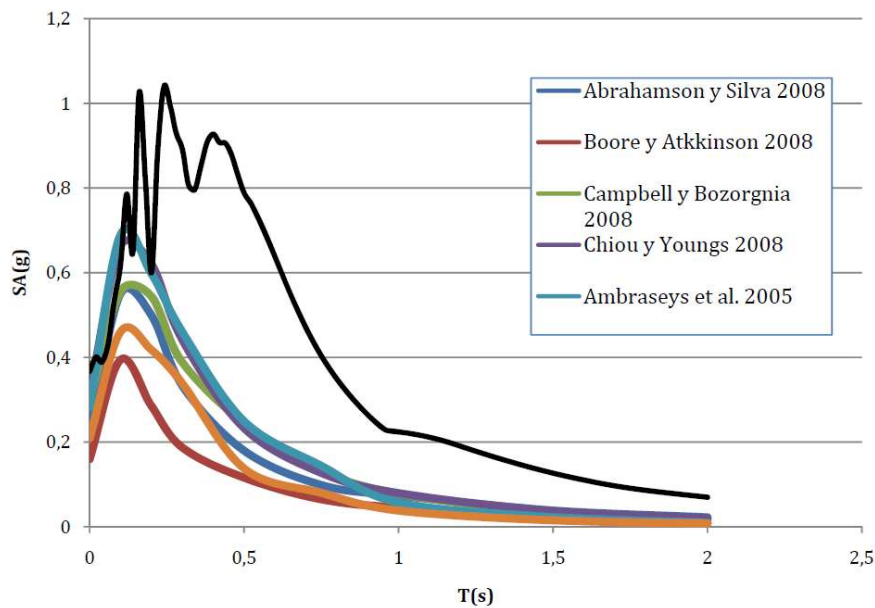


Figure A3.3.26. Pseudo-acceleration response spectra (5% critical damping) from the N30W component of the accelerogram recorded at the Lorca station, compared with mean spectra from different GMPEs, from Cabañas Rodríguez *et al.* (2011).

Several authors believe that directivity effects contributed to the significant level of damage that occurred within the city of Lorca (López-Comino *et al.*, 2012; Pro *et al.*, 2014; Rueda *et al.*, 2011). Unusually well-defined pulses can be easily observed in the two components of the record from Lorca station (Figure A3.3.18). In spite of the common belief that directivity effects only take place with events larger than **M**6.5, they have been observed in other small-to-moderate magnitude events, such as the **M**5.7 1986 San Salvador earthquake (Bommer *et al.*, 2001).

Rueda *et al.* (2011) used the wavelet transform technique of Baker (2007) and identified velocity pulses due to directivity in the three components of the accelerograms recorded at the Lorca station. Figure A3.3.27 shows the pulses extracted from the recorded ground motions. A pulse period of 0.67 seconds was calculated, though this value does not match the peaks observed in both components in the response spectrum, which occur at a period of around 0.4 seconds, as shown in Figure A3.3.24 (Belvaux *et al.*, 2015).

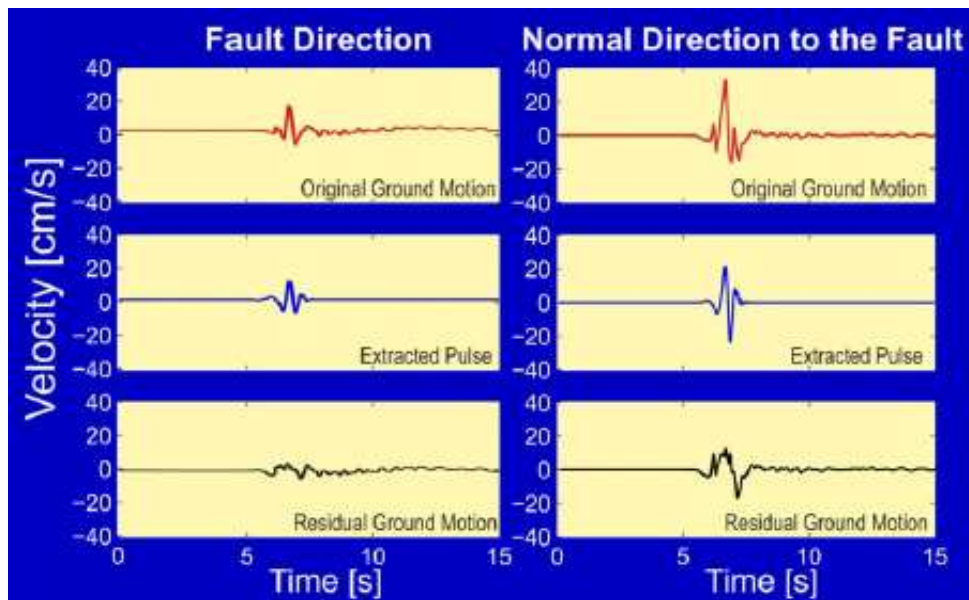


Figure A3.3.27. Original velocity time-history (top), extracted velocity pulse (middle) and residual velocity time-history (bottom) for the E30N (left) and N30W (right) components of the accelerogram recorded by the Lorca station, from Rueda *et al.* (2011).

A3.3.4.3 Inferred shaking levels

The only recording station within the city of Lorca is the Lorca station which, as mentioned earlier, is located on an elevated part of the city, over soils that could be classified as rock or very dense soil, according to different sources. As will be described later on, the most damaged areas of the city correspond to those in which softer soils are predominant, at lower altitudes. Based on the soil types and on the possible amplification due to basin effects, it is thus possible to believe that the structures might have experienced larger ground motions than those recorded at Lorca station. However, it is known that hills and ridges can cause significant amplification of ground motions as well (e.g. 1994 Northridge earthquake, California, Bouchon & Baker, 1996), and therefore it is also possible that the accelerations recorded at Lorca station be actually larger than those affecting the structures in the valley.

Figure A3.3.28 depicts the USGS ShakeMap (Worden *et al.*, 2017) in terms of peak ground acceleration, derived using a combination of recorded values, conversions from intensity data and ground motion prediction models. While the maximum value shown is 0.42 g, it is noted that the region shaded in this colour is very small, while the 0.38-0.40 g range covers a larger area. According to this map, values slightly larger than the 0.365 g recorded at Lorca station were to be expected.

No further attempts to infer ground shaking levels within the city of Lorca from macroseismic intensities have been found in the literature.

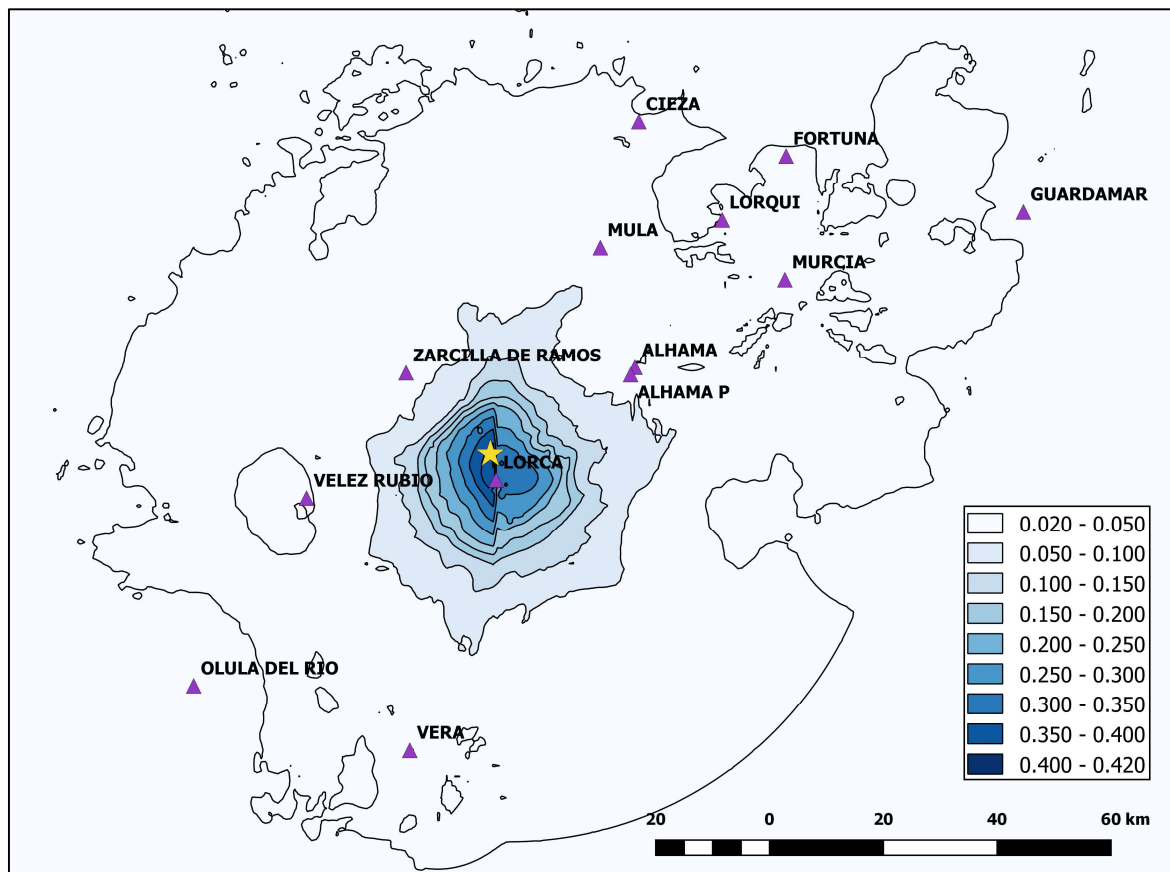


Figure A3.3.28. USGS ShakeMap in terms of peak ground acceleration (g, colour scale) and location of stations that recorded the 2011 Lorca main shock, according to the IGN.

A3.3.4.4 Duration of ground shaking

Benavent-Climent *et al.* (2014) report that the significant duration of the main shock, defined as the time lapse between the release of the 5% and 95% of the Arias Intensity, was 0.935 seconds, a value that is in agreement with the 1.00 second specified by Alfaro *et al.* (2012), though the latter give no indication with respect to which definition of duration they are referring to. Neither of the two publications indicates the location of these durations either, though it is assumed that they are talking of that observed within the city of Lorca. These values are small and suggest that buildings had to absorb most of the energy of the earthquake in a very short period of time, a situation which is quite common in the near-field.

Estimations of earthquake significant durations can be obtained by means of prediction equations such as those of Bommer *et al.* (2009) and Afshari & Stewart (2016). Using the rupture plane defined by Martínez-Díaz *et al.* (2012), a range of shear wave velocities corresponding to the boundaries of the soil types used for the soil classification map of the city of Lorca (Figure A3.3.10), and the 5%-75% of Arias intensity definition of significant duration, the estimated durations shown in Figure A3.3.29 are obtained. As Benavent-Climent *et al.* (2014) report the 5%-95% of Arias intensity definition of significant duration instead, estimations for this definition are included as well for the site of the Lorca station, which is located over soil type B1 (V_{s30} between 500 and 800 m/s, Figure A3.3.10). As can be observed, the resulting durations range between 1.91 and 2.68 seconds, significantly

longer than those reported by Benavent-Climent *et al.* (2014) and Alfaro *et al.* (2012), though very small still. The latter are within [-2.21,-1.73] and [-1.55,-1.30] standard deviations of the models of Bommer *et al.* (2009) and Afshari & Stewart (2016), respectively, for the parameters considered herein. This suggests that the significant duration of the Lorca earthquake at Lorca station may have been shorter than usually expected for an event of this kind.

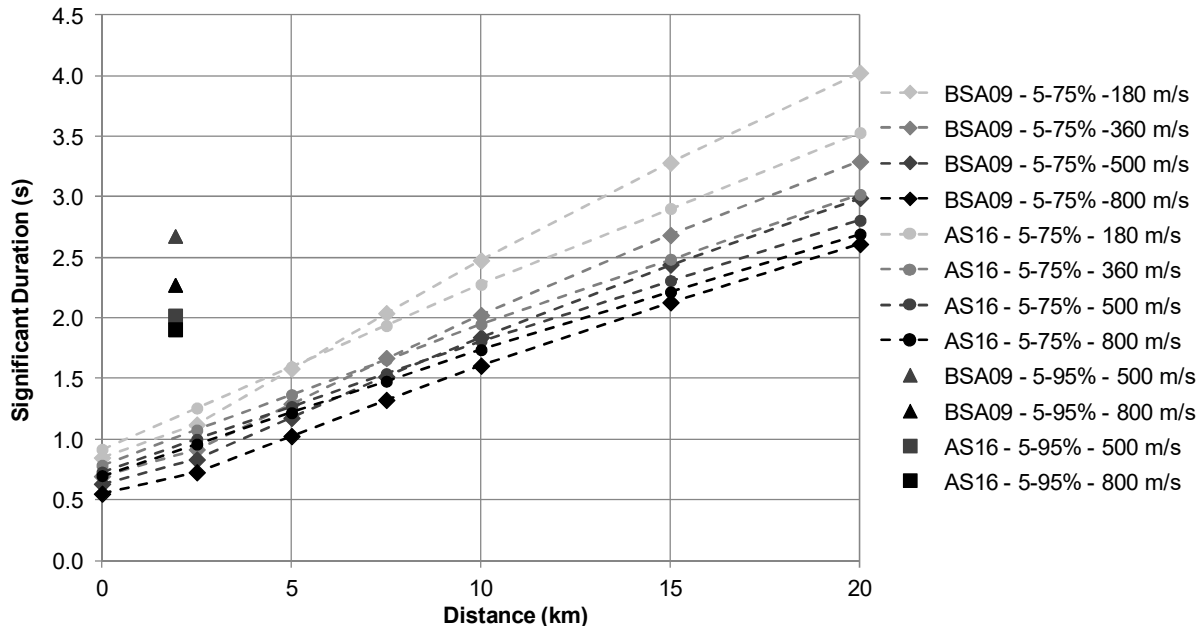


Figure A3.3.29. Estimation of the significant duration of the main shock, using prediction equations by Bommer *et al.* (2009, BSA) and Afshari & Stewart (2016, AS).

A3.3.5 Collateral earthquake hazards

A3.3.5.1 Surface rupture

Martínez-Díaz *et al.* (2011) and Cabañas Rodríguez *et al.* (2011) report that a field survey carried out during three days soon after the main shock found no signs that would indicate the existence of surface rupture due to the earthquake sequence.

Detailed studies of the rupture process carried out by Pro *et al.* (2014), López-Comino *et al.* (2012) and Martínez-Díaz *et al.* (2012) support these observations and conclude that the rupture did not reach the surface, though it stopped propagating quite close to it, at a depth of around 1.5 km, an observation that can explain the strong ground motions observed. Pro *et al.* (2014) and Martínez-Díaz *et al.* (2012) report rupture planes of 12.5 km² and 9.0 km², respectively, with associated maximum slips of 27 cm and 15 cm.

A3.3.5.2 Landslides

In the 1,000 km² that make up their study area, Alfaro *et al.* (2012) identified 256 areas in which landslides had been induced by the earthquake sequence, with a total affected area of around 104 km². The authors report a prevalence of disrupted instabilities (*i.e.*, relatively

highly-fragmented rocks and soil) over coherent (*i.e.*, unfragmented) ones, as defined by Keefer (1984), and highlight the fact that neither of them can be attributed to a singular event within the seismic sequence. Further, they also observed some instabilities along the Guadalentín river, which crosses the city. Those observed upstream were clearly earthquake-induced, while those downstream seemed to be the consequence of previous heavy rains, as explained by local land-owners. The maximum observed distances from the epicentre of the main shock to the landslides was 13.3 km for disrupted landslides and 4.4 km for coherent ones. Figure A3.3.30 shows the landslides they identified.



Figure A3.3.30. Landslides identified by Alfaro *et al.* (2012). "LOR" makes reference to Lorca station. From Alfaro *et al.* (2012).

Alfaro *et al.* (2012) and Rodríguez-Peces *et al.* (2014) coincide in saying that landslides were more common in Miocene materials such as calcareous sandstones, conglomerates and marls, followed by argillites, gypsums, fine-grained soil, phyllite/slate, and coarse-grained soil.

Alfaro *et al.* (2012) do not report any damage to the building stock or casualties directly associated to the landslides, and only mention disruption in roads and communications between the city of Lorca and rural areas nearby. Rodríguez-Peces *et al.* (2014) and Martínez-Díaz *et al.* (2011) make reference to these disruptions as well and describe some damage in buildings and civil structures attributable to these instabilities. In particular, they mention that part of a wall enclosing the courtyard of a house was destroyed by a fallen rock, at the easternmost point of the Lorca's castle cliff, and that the pavement of the road leading to the castle as well as that on the road to the Pantano de Puentes dam were seriously damaged by rock falls. Martínez-Díaz *et al.* (2011) believe that some of these areas might be related to instabilities prior to the 2011 earthquake, and highlight that both roads were open to traffic again ("with relative normality") between 24 and 48 hours after

the main shock. However, Cabañas Rodríguez *et al.* (2011) indicate that circulation along the road to the Pantano de Puentes dam was still disrupted by July 2011.

Martínez-Díaz *et al.* (2011) describe that some sections of the external wall of the north face of Lorca's castle collapsed due to ground instability. They also take notice that stabilization work had been carried out along the south face of the castle about three years before the earthquake, and that precautionary measures taken at that time were fundamental in avoiding further damage and losses during the 2011 events.

A3.3.5.3 Liquefaction

Liquefaction not reported for this earthquake.

A3.3.5.4 Settlements

Settlements not reported for this earthquake.

A3.3.6 Exposed population

A3.3.6.1 Socio-economic setting

According to the 2014 Human Development Report (United Nations, 2014), the Human Development Index (HDI) for Spain in 2013 was 0.869, while its Inequality-adjusted HDI (IHDI) was 0.775. This located Spain in the 27th place in the world's ranking, while the Netherlands ranks 4th. The following table compares the HDI and IHDI for both countries from the last three Human Development Reports (United Nations, 2011; United Nations, 2013; United Nations, 2014). The column "Adj. HDI" provides the HDI values given in the 2014 report for previous years, adjusted for data consistency in time.

Table A3.3.5. Human Development Index and Inequality-adjusted Human Development Index for Spain and the Netherlands.

Report	Data	Spain				Netherlands			
		HDI	IHDI	Rank	Adj. HDI	HDI	IHDI	Rank	Adj. HDI
2011	May 2011	0.878	0.799	23	0.868	0.91	0.846	3	0.914
2013	October 2012	0.885	0.796	23	0.869	0.921	0.857	4	0.915
2014	November 2013	0.869	0.775	27	-	0.915	0.854	4	-

The autonomous community of Murcia, where Lorca is located, is the region which experienced the largest economic growth between 1995 and 2008 in Spain. The mean annual growth of its gross domestic product (GDP) was 4.3% for this period, while that of Spain was 3.5% (data from the Strategic Plan of the Murcia Region 2014-2020, "Plan Estratégico de la Región de Murcia 2014-2020", 2012). This situation changed drastically in 2008, due to the significant crisis that hit Europe.

Said crisis also affected the unemployment levels significantly in the years before the 2011 Lorca earthquake. From a 7.56% unemployment rate in 2007, Murcia moved to 12.63%, 20.73% and 24.49% in 2008, 2009 and 2011, respectively. For the same years, the unemployment rates in Spain as a whole were 8.26%, 11.34%, 18.01% and 20.89%. (Sources: Wikipedia, citing the website of the Spanish National Statistics Institute (INE) website, and INE's press releases).

Figure A3.3.31 shows that, in the year 2012, the GDP per capita of Murcia was ranked 15th amongst all of the Spanish autonomous communities, and it was below the national average (data from the Spanish National Statistics Institute, Instituto Nacional de Estadística, INE).

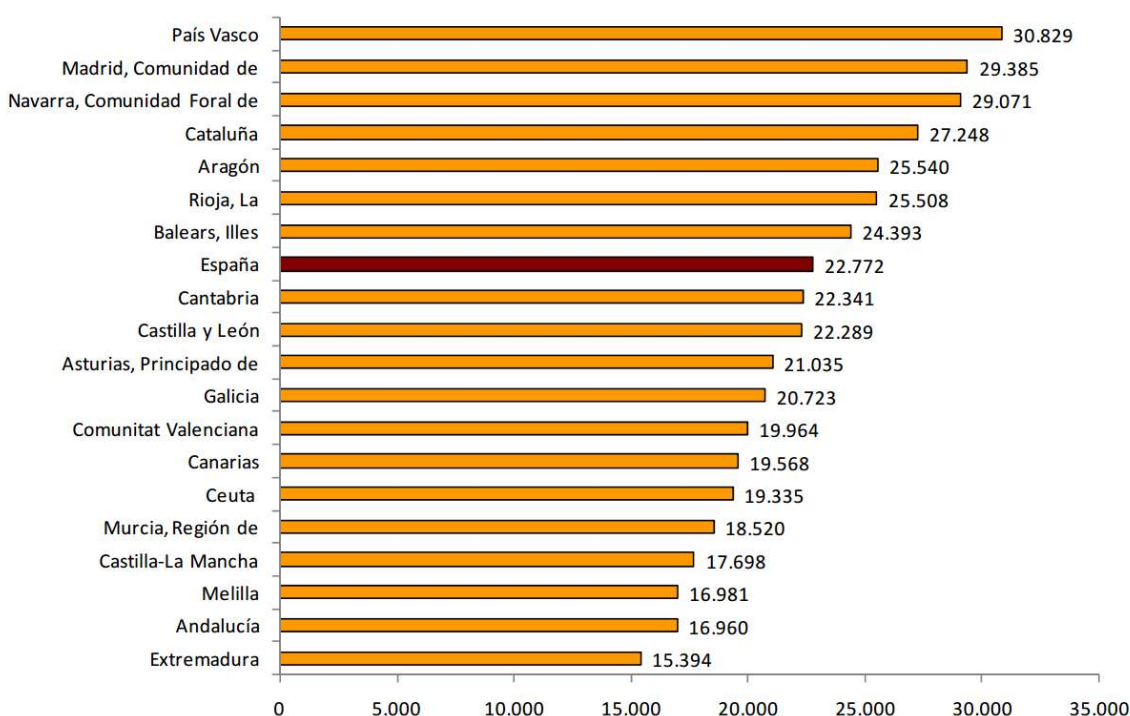


Figure A3.3.31. GDP per capita for all the autonomous communities of Spain, compared with that of the whole country (red bar), from the Spanish National Statistics Institute (2016).

A3.3.6.2 Population density and distribution

According to the INE, the population of the municipality of Lorca was 92,694 in 2010 and 92,869 in 2011. Around 60% and 25% of the population is located within the city of Lorca itself and its surrounding parishes (pedanías, in Spanish, Figure A3.3.32), respectively.

A3.3.6.3 Time of day of earthquake

The foreshock occurred on 11th May 2011 at 17.05 local time, while the main shock occurred on the same day at 18.47 local time. According to Goula *et al.* (2011), public offices and schools were already closed at the time of the main shock and, therefore, the number of people exposed inside these kinds of buildings was reduced. Further, said

authors highlight that the foreshock played a significant role in creating concern in the population and encouraging them to stay in open areas outside of buildings.



Figure A3.3.32. Parishes ("pedanías") of the municipality of Lorca. The zone marked as 1 corresponds to the city of Lorca itself. Around 85% of the population of the whole municipality are located within the red circle.

A3.3.7 Characteristics of exposed building stock

Basset-Salom and Guardiola-Villora (2014) give a brief overview of the building stock in the city of Lorca saying:

"Lorca [...] is characterized by a very rich historic heritage including not only monumental or religious buildings (towers, mansions, palaces, churches or monasteries) but also a residential stock varied in age and styles".

And:

"The city was seriously damaged by the strong 1674 earthquake which was the starting point of a long period of reconstruction: most of the building stock of the city centre, the monumental buildings and its actual urban structure belong to the following 200 years".

A3.3.7.1 Seismic design codes

The first Spanish seismic code was published in 1962, and it was updated in 1968 and 1974. In all these versions, the whole country is subdivided in seismic regions according to expected levels of macroseismic intensity. The 1962 code uses the Modified Mercalli Scale (MMS; Musson & Cencić, 2012), and assigns Lorca an intensity level of VIII. The

1968 and 1974 codes use the Medvedev-Karnik-Sponheuer scale (MSK; Musson & Cčić, 2012) instead, and the numeric value of VIII is maintained for Lorca. In all cases, the macroseismic intensity assigned to Lorca is above the threshold for which the codes needed to be applied. Seismic design was static, very basic, and carried out only for structural elements (Cabañas Rodríguez *et al.*, 2011).

The NCSE-94 code of 1994 abandoned the use of macroseismic intensities and provided, for the first time, design acceleration values calculated by means of a probabilistic seismic hazard analysis. As with modern codes, this value was used to scale a pseudo-acceleration spectrum. For the case of Lorca, the design PGA on rock with a 10% probability of exceedance in 50 years was 0.12 g. This value remained unchanged in the NCSE-02 code of 2002, the most recent seismic code of Spain, and was clearly exceeded during the 2011 Lorca earthquake. Based on a study regarding the ground motions registered during the 1999 Mula and 2005 La Peca earthquakes, Gaspar-Escribano & Benito (2007) had warned that pseudo-spectral accelerations at the intermediate-high frequencies could exceed those indicated by NCSE-02 in the Murcia region. Interestingly, a new hazard map was elaborated by the National Geographic Institute (IGN) in 2012, in which a new design PGA value in rock of around 0.18 g is specified for the city of Lorca.

After their analysis of the consequences of the 2011 Lorca earthquake, Cabañas Rodríguez *et al.* (2011) highlight as a major shortcoming of the current Spanish seismic design code (NCSE-02) the fact that it does not limit the maximum displacement of buildings in terms of absolute values.

Eurocode 8 is not yet in force for application in Spain, though it can be voluntarily applied by engineers, as long as they comply with NCSE-02 as well. According to Arnedo Pena (2010), by mid-2010 the translation of Eurocodes into Spanish had almost been finished, while the phase of elaborating the National Annex had partially started already, though 2010 was supposed to be the year for their complete implementation. The proposal for the National Annex containing the National Determined Parameters (NDPs) for the application of Eurocode 8 can be downloaded from the website of the Ministerio de Fomento of Spain.

In a presentation given at the University of Costa Rica, Patrick Murphy Corella (Spanish architect, practitioner, member of the Asociación Española de Ingeniería Sísmica, AEIS) pointed out that very little seismic design concepts could be observed in the reinforced concrete (RC) buildings that suffered the most damage in Lorca. Similar comments can be found in the report by Regalado & Lloret (2011).

From personal communications with Spanish civil engineers, it appears that compliance with the NCSE-02 code is duly verified by official entities, but that this does not always translate into a well-elaborated seismic concept design of the structures.

A3.3.7.2 Building typologies

Most sources coincide in the most basic classification of the types of buildings in the city of Lorca at the time of the earthquake being a simple division between heritage (mostly churches), masonry and reinforced concrete (RC) buildings.

In their report on the 2011 Lorca earthquake, Cabañas Rodríguez *et al.* (2011) provide the most useful classification that could be found in the literature, given that they relate the six basic typologies that they describe to their equivalents in the EMS-98 (Grünthal, 1998), HAZUS (FEMA, 2003) and RISK-UE BTM (Milutinovic & Trendafiloski, 2003) classification schemes. The six typologies which, according to Cabañas Rodríguez *et al.* (2011), comprise most of the building stock of Lorca are:

- EMM: ordinary masonry walls with timber floors/roof without diaphragm effect, usually built before the 20th century
- EML: brick masonry walls with timber floors/roof without diaphragm effect, typical of the period 1921-1940
- EMH: brick masonry walls with RC floors/roof with diaphragm effect, usually built between 1941 and 1964
- EHP: RC frames constructed between 1965 and 1996
- EHP94: RC frames constructed between 1997 and 2004 (NCSE 94 building code)
- EHP02: RC frames constructed after 2004 (NCSE 02 building code)

For evident reasons, Cabañas Rodríguez *et al.* (2011) group the first and last three typologies under the names of "traditional" and "technological" constructions, respectively.

The European Macroseismic Scale (EMS-98) classifies buildings into six vulnerability classes, from A through F, with the former and the latter corresponding to the most and least vulnerable, respectively. Cabañas Rodríguez *et al.* (2011) classify their six typologies according to the EMS-98 vulnerability scale as follows:

Table A3.3.6. EMS-98 vulnerability classes of the six building typologies identified for Lorca, according to Cabañas Rodríguez *et al.* (2011).

Typology	EMS-98
EMM	A
EML	B
EMH	C
EHP	C
EHP94	D
EHP02	D

Cabañas Rodríguez *et al.* (2011) provide as well the relationship between the typologies in Lorca and those defined by the RISK-UE Building Typology Matrix (RISK-UE BTM, Milutinovic & Trendafiloski, 2003), as well as their associated vulnerability index. Within the RISK-UE vulnerability classification scheme, each typology is assigned a basic

vulnerability index between 0 and 1, which represents the vulnerability level expected for the buildings that belong to that typology. This basic vulnerability index can then be adjusted to account for the peculiarities of each building, as well as regional differences. Values close to 1 correspond to the greatest vulnerability, while values close to 0 are assigned to structures designed to high code standards. Table A3.3.7 presents the vulnerability indices and equivalence of building typologies established by Cabañas Rodríguez *et al.* (2011).

Table A3.3.7. RISK-UE typologies and vulnerability indices for the different typologies in Lorca, according to Cabañas Rodríguez *et al.* (2011).

Typology	Storeys	RISK-UE BTM and Vulnerability Index	
EMM	1-2	0.85 M11L	Rubble stone and/or fieldstone, low-rise
	3-5	0.89 M11M	Rubble stone and/or fieldstone, mid-rise
	+6	0.93 M11H	Rubble stone and/or fieldstone, high-rise
EML	1-2	0.72 M31L	Wooden slabs and unreinforced masonry, low-rise
	3-5	0.76 M31M	Wooden slabs and unreinforced masonry, mid-rise
	+6	0.80 M31H	Wooden slabs and unreinforced masonry, high-rise
EMH	1-2	0.59 M34L	RC slabs and unreinforced masonry, low-rise
	3-5	0.61 M34M	RC slabs and unreinforced masonry, mid-rise
	+6	0.67 M34H	RC slabs and unreinforced masonry, high-rise
EHP	1-2	0.59 M34L	RC slabs and unreinforced masonry, low-rise
	3-5	0.60 RC1M	RC moment frames, mid-rise
	+6	0.68 RC1H	RC moment frames, high-rise
EHP94	1-2	0.40 RC1L	RC moment frames, low-rise
	3-5	0.44 RC1M	RC moment frames, mid-rise
	+6	0.48 RC1H	RC moment frames, high-rise
EHP02	1-2	0.40 RC1L	RC moment frames, low-rise
	3-5	0.44 RC1M	RC moment frames, mid-rise
	+6	0.48 RC1H	RC moment frames, high-rise

Basset-Salom & Guardiola-Víllora (2014) provide a detailed description of the main characteristics of the unreinforced masonry non-heritage buildings in Lorca at the time of the earthquake, which are summarized below:

- Load bearing walls form the street façades of a corner building, or the main façade and the interior courtyard façade, and load bearing party walls.
- Façade walls are between 30 and 80 cm thick.
- Walls between adjacent buildings (party walls) are between 20 and 30 cm thick, usually shared by the two structures, with the consequence of these behaving as a whole.
- In general, interior walls are non-structural, thinner and poorly connected to exterior and party walls.
- The following fabric typologies can be found:
 - Small or medium sized rubble or poorly cut stone with lime-mortar, typical of the 18th and 19th centuries, for one or two storeys buildings.

- Brick masonry fabric (20x10x3/4 cm bricks before 1950, 24x12x4/5 cm bricks afterwards) with lime or cement mortar, typical of the 19th and 20th centuries, for buildings of up to four storeys.
- Isolated cases of rubble stone masonry with binding brick courses.
- Horizontal systems are usually one of the following:
 - Timber beams for lintels, beams and joists.
 - Lightweight masonry vaults, or a traditional covering made out of a reed and plaster deck, or brick deck under ceramic curved tiles (for the case of roofs).
 - RC beams and joists with ceramic vaults.
- The following elements can be found to be used for adding strength to the buildings:
 - Quoins (solid corner masonry/stone blocks).
 - Plinths (square slabs at base of columns).
 - Floor and wall timber ties or timber ring beams.
 - Timber lintels.
 - Stone frames around openings.
 - Iron ties.
- A large percentage of the façades have balconies with a usual depth of 0.4 m.

Basset-Salom & Guardiola-Villora (2014) highlight that uniformly squared stone blocks can be found almost exclusively in monumental buildings and mansions.

Regarding the churches that could be found in Lorca at the time of the earthquake, most of which were built between the 15th and 18th centuries, Romão *et al.* (2013) bring attention to the complexity of their structural configuration and geometry, as well as to the heterogeneity of their materials. Further, they emphasize that their degree of maintenance is variable, but often poor. Finally, they describe the use of five types of masonry:

- Small and medium size irregular stones with mortar.
- Two-leaf (*i.e.*, two-layered) wall with an outer leaf made of regular cut stone and an internal one made of small and medium size irregular stones with mortar.
- Brickwork.
- Regular cut stone.
- Three-leaf wall with regular cut stone leaves of similar thickness.

According to Romão *et al.* (2013), the reinforced concrete (RC) buildings in Lorca are mostly residential, but commercial spaces located at street level are frequently observed. Further, basements (often partially-underground) used for parking purposes are common as well. The number of storeys is usually between three and six, and only very few buildings are taller than ten storeys. From the structural point of view, Romão *et al.* (2013) describe two cases: RC columns and beams with floors made by one-way precast concrete joists with RC topping, on one hand, and RC columns, no beams, and floors consisting in flat or waffle slabs, on the other. Benavent-Climent *et al.* (2014) mention the use of wide (flat) beams as being common practice too. External walls, parapets and interior partition walls are usually made of masonry.

In spite of the very detailed descriptions of the building typologies that could be found in Lorca at the time of the earthquake, information regarding the relative quantities of each typology is scarce in publications directly related to the earthquake. It is possible, however, to combine the information contained in the RISMUR ("Seismic Risk of the Autonomous Community of the Murcia Region") and SISMIMUR ("Civil Protection Special Plan in view of the Seismic Risk in the Murcia Region") projects together with data from the 2011 census to get an idea of the overall level of vulnerability of the building stock in Lorca. The resulting distribution of buildings by year of construction and EMS-98 vulnerability class are shown in Figure A3.3.33 and 34. As can be observed, it is estimated that slightly more than 50% of the residential buildings in Lorca belonged to the two most vulnerable classes (A and B).

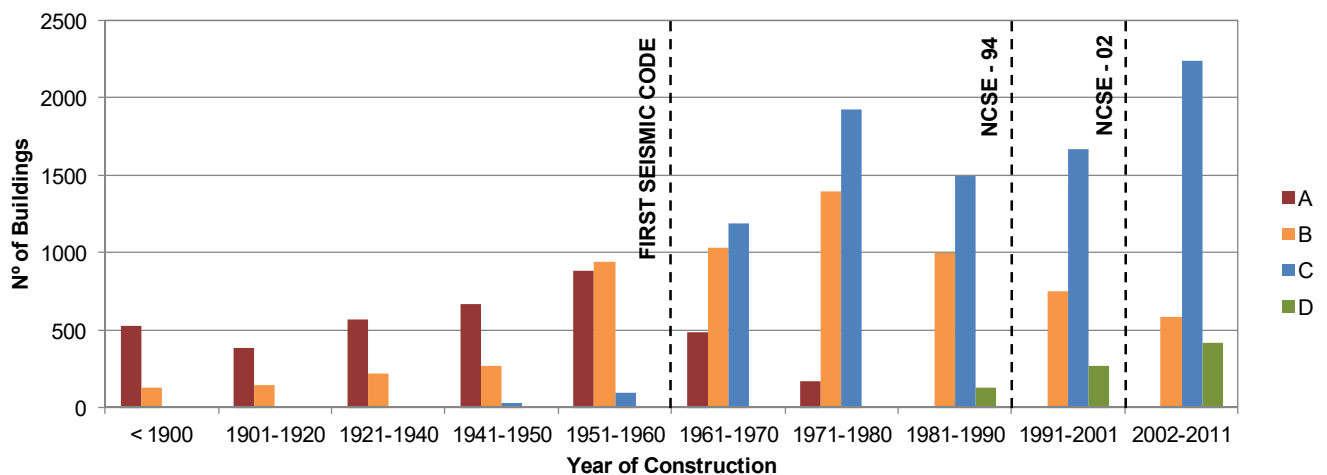


Figure A3.3.33. Number of residential buildings in the municipality of Lorca per year of construction and EMS-98 vulnerability class, estimated from the available data. Vertical dashed lines indicate the introduction of the first Spanish seismic code (1962) and the codes of 1994 and 2002.

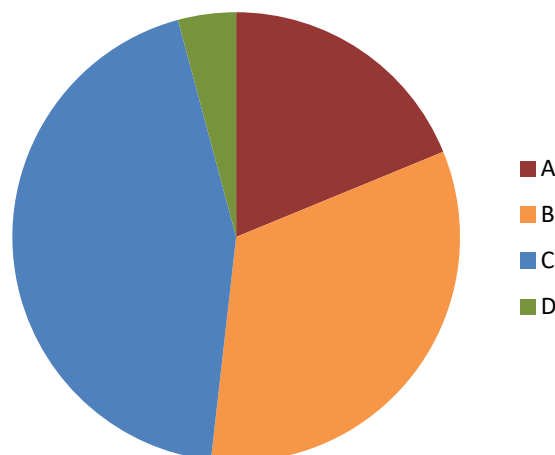


Figure A3.3.34. Estimated percentage of residential buildings belonging to each EMS-98 vulnerability class at the moment of the 2011 Lorca earthquake.

It should be noted that the quantities shown in Figure A3.3.33 correspond to the whole municipality of Lorca, and not just to the city of Lorca itself, and therefore their significance lies in the overall distribution among different categories and not in the absolute values themselves. While the whole municipality of Lorca comprised over 19,000 buildings, the

city of Lorca itself and, in particular, the area in which the damage of the earthquake was more severe, comprises only around 8,000 buildings.

Regarding their representativeness, it should be noted that the 2011 census took place after the earthquake, in November 2011. Nevertheless, this information is used because it is probably closer to the situation in May 2011 than the equivalent information from the 2001 census. Further, the information corresponds only to residential buildings. Murphy Corella (2005) reports that these make up 95.64% of the total building stock of the Murcia region. Finally, work carried out by Murphy Corella (2005) was based on the whole of the Murcia region, and it is being assumed herein that this applies directly to the municipality of Lorca, and that all of Lorca's building stock corresponds to an urban environment.

In order to assign overall vulnerability levels within smaller districts in the Murcia region, the SISMIMUR project establishes the following criteria:

- High vulnerability: more than 45% of the building stock corresponds to class A.
- Medium vulnerability: more than 50% of the building stock corresponds to classes A or B combined.
- Low vulnerability: more than 40% of the building stock corresponds to class C.

According to these criteria, the SISMIMUR project assigns a medium vulnerability level to the area in which Lorca is located.

A3.3.7.3 Prior damage and retrofit

Feriche *et al.* (2012) mention that some heritage buildings, particularly churches, have undergone restoration interventions during the last century with some detrimental consequences. For example, the addition of a compression layer of reinforced concrete in the roofs of heritage buildings has probably increased the stresses over the masonry and, at the same time, increased the mass of the building. Further, the incorporation of metallic braces that have afterwards become rusty has caused the rocks in which they are embedded to break.

Romão *et al.* (2013) make similar observations regarding the church of Santiago, whose dome and transept area were strengthened in the 1960s using reinforced concrete with the aim of providing some kind of diaphragm action. This church suffered quite significant damage.

In contrast, Basset-Salom & Guardiola-Víllora (2014) mention that the residential and commercial unreinforced stone or brick masonry of Lorca's city centre have seldom had any intervention to improve their seismic vulnerability. Exceptions to these observations include the use of ring beams, quoins and iron ties in a reduced number of buildings.

As an interesting detail of a damaging intervention, the Master Plan for the Recovery of Lorca's Cultural Patrimony (Ayuntamiento de Lorca, 2011) makes reference to the merlons

of the battlements of the tower of Lorca's castle, which were only added in 1972 and were the first elements to fail, even during the foreshock (Jurado Jiménez, 2012).

A3.3.8 Damage observations

A3.3.8.1 Damage states

Most information regarding damage caused to buildings by the 2011 Lorca earthquake makes use of the European Macroseismic Scale (EMS-98; Grünthal, 1998), which classifies damage into five grades. Further, numerous statistics regarding the post-earthquake tagging are available as well. For details regarding the European Macroseismic Scale and the tagging codes, please refer to Section 3.8.1 of Chapter 3 and Appendix II.

A3.3.8.2 Damage statistics and description

It is relevant to point out the existing level of discrepancy amongst the different statistics that can be found in the literature. In some cases, this is clearly due to the different dates in time in which these were developed (especially those referring to the aftermath soon after the main shock), but in others the cause of differences is unknown.

According to Goula *et al.* (2011), 7,839 buildings had been assessed by 21st May 2011 for fast tagging (assignment of green, yellow and red tags, for damage ranging from null or negligible to serious and extensive). As can be observed in Table A3.3.8, around 10% of the assessed buildings were classified as having moderate to heavy damage. It should be noted that a green tag does not imply absence of damage, and green tagged buildings can present cracks and several other minor problems.

Table A3.3.8. Post-earthquake tagging by 21st May 2011, according to Goula *et al.* (2011). Gray tagging corresponds to buildings which were in ruins before the earthquake.

Tag	N° Buildings	% Buildings
Green	6998	89.3%
Yellow	465	5.9%
Red	309	3.9%
Gray	67	0.9%

Numbers are slightly different within the report prepared by Cabañas Rodríguez *et al.* (2011), who also report the tagging corresponding to 7,839 buildings, but for whom buildings with yellow and red tags represent 8.1% and 4.8% of the total, respectively. They present the information disaggregated by districts. Four districts out of a total of thirty-five suffered damages in over 40% of their building stock, and around 45% of the districts had more than 20% of their building stock tagged as yellow or red. Even though the number of

"traditional" and "technological" buildings is provided, tagging information is not separated according to this classification.

The most encompassing statistics can be found in Feriche *et al.* (2012), Benavent-Climent *et al.* (2014) and Donaire Ávila *et al.* (2012), who express that at least 80% of the building stock of the city of Lorca was affected by the earthquake to some extent. All authors coincide in the fact that these statistics correspond to 6,416 inspected buildings out of the 7,852 to 7,890 existing buildings in the area. According to Feriche *et al.* (2012), the damage to the building stock in terms of the European Macroseismic Scale (EMS-98) was as summarized in Table A3.3.9 (left), while according to Benavent-Climent *et al.* (2014) and Donaire Ávila *et al.* (2012), the damage observed for the same set of buildings was as summarized in Table A3.3.9 (right).

Table A3.3.9. Damage grades of 6,416 inspected buildings, according to Feriche *et al.* (2012), left, and Benavent-Climent *et al.* (2014) and Donaire Ávila *et al.* (2012), right.

N° Buildings	Damage Grade	Authors' Description
4035	1 - 2	Minor damage.
1328	2 - 3	Moderate damage.
689	3 - 4	Moderate to serious damage.
329	4 - 5	Had to be demolished.

N° Buildings	Damage Grade	Authors' Description
4035	2	-
1328	3	-
689	4	Mostly the case of four-storey buildings.
329	5	

The information contained in the tables above is briefly summarized by Rodríguez-Escudero *et al.* (2014) and Martínez-Díaz *et al.* (2012), who report serious damage observed in 1,164 buildings (slightly above the sum of 689 and 329 in the tables), according to data from the Municipality of Lorca by November 2011. Regarding the over 300 buildings that needed to be demolished, Alfaro *et al.* (2012) report that demolition work "was still in progress several months after the main event".

Donaire Ávila *et al.* (2012) provide some insight with respect to the damage suffered by RC buildings built from 1994 to 2002, *i.e.*, according to the NCSE-94 code, and from 2003 to 2008, *i.e.*, built according to the NCSE-02 code. They report 755 and 373 damaged buildings for each group. Figure A3.3.35 shows the number of damaged buildings with EMS-98 damage grade equal to or larger than 3. The authors highlight that the number of buildings designed to code which suffered substantial to very heavy damage is clearly not negligible.

The vulnerability of RC buildings was clearly demonstrated by the two complete collapses observed, as described by Romão *et al.* (2013). Only one of these occurred during the main shock, while the other took place almost a week after the earthquake when it was about to be demolished. This latter structure, called the "Grial" building, suffered from excessive residual deformations, and from inadequate confinement at the top extreme of the ground storey columns.

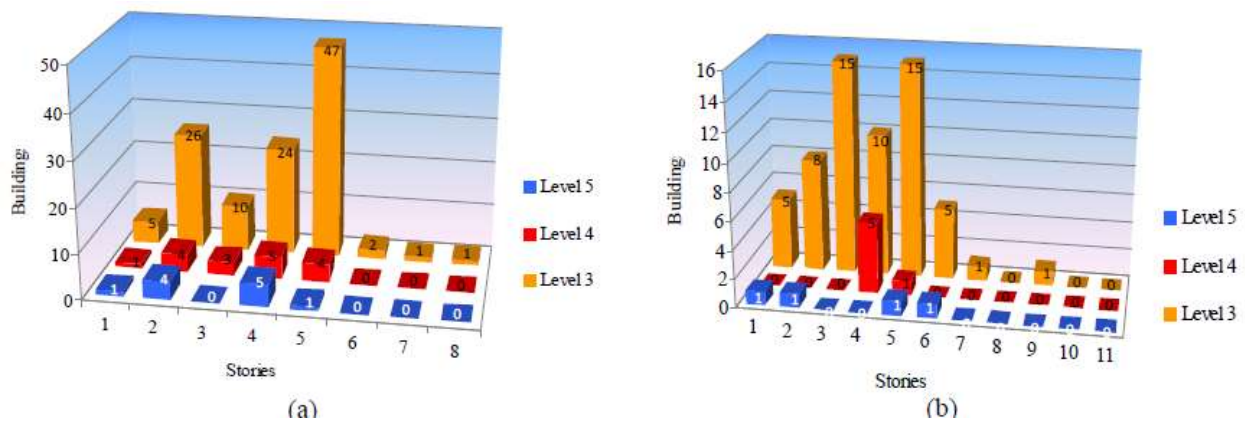


Figure A3.3.35. Number of damaged buildings with EMS-98 damage grade equal to or larger than 3: (a) built between 1994 and 2002; (b) built between 2003 and 2008. (Donaire Ávila *et al.*, 2012).

The RC building that collapsed during the main shock was located in La Viña neighbourhood, an area that was particularly damaged, as reported in the Damage Distribution section. This building was a 10-year old, 3-storey residential structure, with a partially subterranean parking lot constructed on a slope. The collapse was due to the short column effect of the parking level columns, as it became clear from a neighbouring building with similar characteristics whose columns exhibited damage associated to this phenomenon (Cabañas Rodríguez *et al.*, 2011). While collapsing, the building across the street was hit and damaged. Figure A3.3.36 shows the collapsed building.



Figure A3.3.36. Building located in La Viña neighbourhood which collapsed during the main shock (Meteoweb, 2016). A street runs in between the two buildings shown.

Basset-Salom & Guardiola-Víllora (2014) studied in some detail 65 façades from 50 unreinforced masonry residential buildings located within the historic city centre, 93% of which had timber floors while only 7% had RC floors (RC beams and joists with ceramic vaults) instead. Of these buildings, 46% suffered negligible or slight damage (EMS-98 grade 1), 36% suffered moderate damage (EMS-98 grade 2), 18% suffered substantial to heavy damage (EMS-98 grade 3); worse levels of damage, corresponding to EMS-98 grades 4 and 5, were not observed. The authors report as well the types of failure mechanism that prevailed in each case, based on the classification catalogue developed by D'Ayala & Speranza (2003). As can be observed in Figures A3.3.37 and A3.3.38, most

of the assessed buildings suffered from in-plane mechanisms H or H2. Figure A3.3.39 shows examples provided by the same authors of buildings classified as having suffered EMS-98 damage grades 3 and 4.

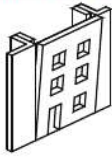
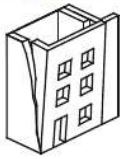

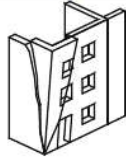
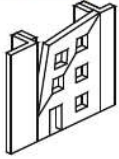
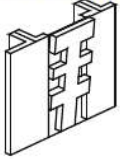
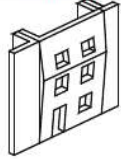
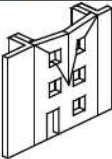
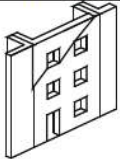
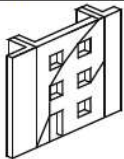
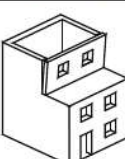
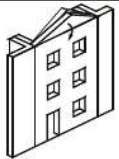

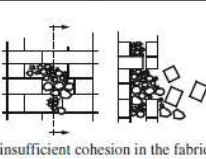
A	B1	B2	C	D	E	F
vertical overturning	overturning (1 side wing)	overturning (2 side wings)	corner failure	partial overturning	vertical strip overturning	vertical arch
						
FURTHER PARTIAL FAILURES						
G	H	H2	I	L	ASSOCIATED FAILURES	
horizontal arch	in plane failure	in plane pier failure	vertical addition	gable overturning	roofs/floors failure	masonry failure
						 insufficient cohesion in the fabric

Figure A3.3.37. Classification of failure mechanisms in masonry according to D'Ayala & Speranza (2003), from Basset-Salom & Guardiola-Villora (2014).

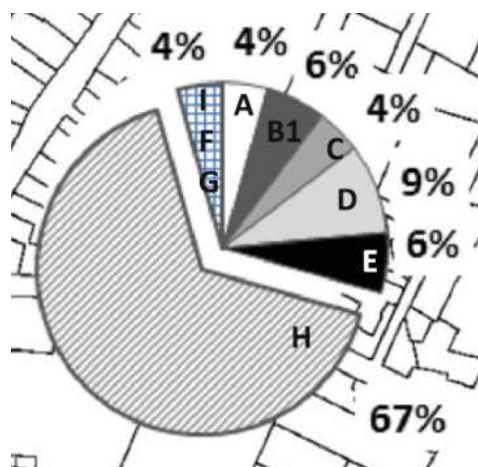


Figure A3.3.38. Failure mechanisms observed in the 50 buildings studied by Basset-Salom & Guardiola-Villora (2014).

Heritage buildings suffered significant damage during the earthquake. Feriche *et al.* (2012) and Romão *et al.* (2013) describe in detail the most common types of damage observed in churches and other types of historical buildings, which are:

- Partial or total collapse of roofs, towers and walls.
- Significant damage or collapse of belfries.
- Cracking within a wall and in between perpendicular walls.
- Partial or total collapse of arches, vaults and walls.

- Detachment of façades and ornaments.
- Cracking of buttresses and arches.
- Vertical displacement of the keystones in arches.

Basset-Salom & Guardiola-Víllora (2014) highlight that some of the heritage buildings that had to be demolished were listed in the Catalogue of Protected Buildings of 1994.



Figure A3.3.39. Examples of masonry buildings that suffered EMS-98 damage grade 3 (left) and 4 (right). From Basset-Salom & Guardiola-Víllora (2014).

The possible examples of damages in churches are several, but that of the Church of Santiago is of particular interest not only due to its severity but also to the fact that said building had been retrofitted in the 1960s. At that time, the dome and transept area were strengthened using reinforced concrete with the aim of providing some kind of diaphragm action (Romão *et al.*, 2013; Feriche *et al.*, 2012). During the main shock, the dome, roof and vaults collapsed, as shown in Figure A3.3.40.

As mentioned in the Damage States section, non-structural elements such as masonry infills, parapets and ledges, were particularly vulnerable during the earthquake and their failure was responsible for deaths and severe damage. Collapses of non-structural walls surrounding elevator shafts were reported, as well as severe deformation of elevator door frames (Goula *et al.*, 2011). Detachment of air conditioning units due to failure of the façades that were holding them was observed.



Figure A3.3.40. Collapse of the transept area of the Church of Santiago (Wikipedia).

Goula *et al.* (2011) report that seven out of seventeen (41%) pre-school and primary school buildings and three out of eight (38%) secondary school buildings suffered from damage that limited their re-occupation after the earthquake. Three out of four health centers suffered from significant non-structural damage, while the fourth one presented severe structural problems. In view of this, Goula *et al.* (2011) highlight the need for decreasing the vulnerability of primary importance constructions in the area.

Finally, and as reported earlier in the Landslides section, some of the damage observed can be attributed to soil and rocks instability, though not on a significant scale.

A3.3.8.3 Observed weaknesses

Numerous publications make reference to systematic weaknesses observed in the different kinds of constructions. According to Feriche *et al.* (2012), the following weaknesses were systematically observed in heritage buildings (mostly churches): excessive stiffness, low ductility and lack of connection between vertical and horizontal elements.

With regards to unreinforced masonry residential buildings, Romão *et al.* (2013) put emphasis on their geometrical irregularities, heterogeneity of their materials and their frequent lack of conservation, while Basset-Salom & Guardiola-Víllora (2014) report observation of poor quality rubble stones, inadequate bond between stones and mortar, and weak connections between the different leafs of the same wall. Cabañas Rodríguez *et al.* (2011) highlight the poor connection between perpendicular walls.

Romão *et al.* (2013), Cabañas Rodríguez *et al.* (2011) and Goula *et al.* (2011) extensively describe the weaknesses found in RC buildings, which can be summarized as follows:

- Soft storeys at ground level, mainly due to the architectural regulations of the city, which impose that commercial spaces have greater interstorey heights than residential ones, and to the use of masonry exterior walls in all floors except the ground level.
- Short column effects due both to partially underground basements and interaction with masonry infills.
- Inadequate shear reinforcement in columns: a typical spacing of the transverse reinforcement of around 20 to 30 cm and no densification in plastic hinge regions was observed.
- Non-structural masonry infills interacting with structural ones and attracting seismic forces due to their stiffness and lack of separation from the latter, while not being designed for it.
- Insufficient building separation leading to pounding between adjacent buildings.

Regarding non-structural elements such as exterior masonry walls and parapets, Romão *et al.* (2013) report an inadequate seismic performance related to inadequate connection of these elements to the structures, and the interaction between structural and non-structural elements clearly not having been accounted for during the design stage, as mentioned above. Cabañas Rodríguez *et al.* (2011) explain that the NCSE-94 building code, which was in force between 1996 and 2004, only required parapets and ledges to be confined with concrete in areas where the design PGA (in rock) was above 0.16 g, which was higher than that corresponding to Lorca in the same code. This threshold was reduced to 0.12 g in the NCSE-02 code and, therefore, buildings designed after 2004 should have complied with this requirement.

A3.3.8.4 Damage distribution

Several authors highlight the uneven distribution of damage within the city of Lorca (e.g., Alguacil *et al.*, 2014). Cabañas Rodríguez *et al.* (2011) and Benito Oterino *et al.* (2012) report a concentration of damage in some districts of La Viña neighbourhood (southwestern zone of the city, districts 1013 and 1024 of Figure A3.3.41), and district 1027 of the neighbourhood of the Fuerzas Armadas avenue. These authors find a significant correlation between the number of damaged buildings and the soil type, and they observe an increase of damage for buildings located on soft sedimentary soils of the Guadalentín valley. Around 20% of the buildings located on this type of soil were damaged, as shown in Table A3.3.10, in which soils are classified into four categories, IA, IB, II and III, ranging from hard to soft. Figure A3.3.41 superimposes the yellow and red tagged buildings with this soil classification and the administrative districts of the city. Note that this soil classification is slightly different from that shown previously in Figure A3.3.10 (Navarro *et al.*, 2014), but there exists overall consistency between the two. Further, Navarro *et al.* (2014) coincide as well on the influence of unconsolidated Quaternary formations on the level of damage observed, and highlight the case of the neighbourhoods of La Viña (to the south) and La Alberca and La Alameda (close to the Guadalentín river), also shown in the figure below.

Table A3.3.10. Number of damaged buildings per soil type, from Cabañas Rodríguez *et al.* (2011).

Soil Type	N° Buildings	Damaged Buildings	% of Buildings Damaged
IA (hard)	369	24	6.50%
IB	1006	74	7.36%
II	2013	127	6.31%
III (soft)	3374	664	19.68%
All	6762	889	13.15%

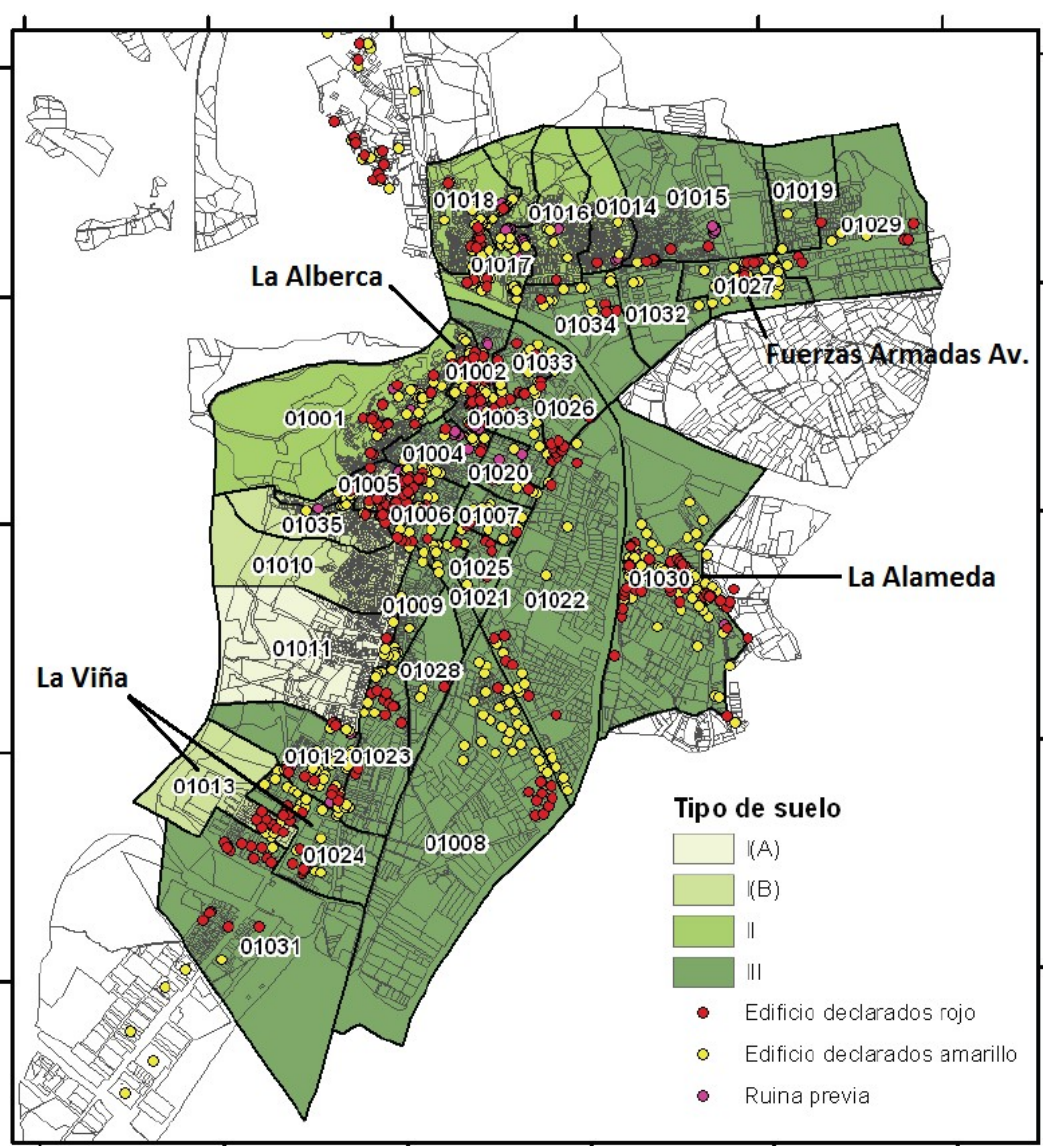


Figure A3.3.41. Yellow and red tagged buildings superimposed to the basic soil types in the city (darker shades of green correspond to softer soils) and its administrative districts, from Benito Oterino *et al.* (2012).

Several authors coincide as well in believing that directivity effects contributed to the significant level of damage that occurred within the city of Lorca, despite the small

magnitude of the main shock (López-Comino *et al.*, 2012; Pro *et al.*, 2014; Rueda *et al.*, 2011).

A3.3.9 Casualties and losses

A3.3.9.1 Numbers of dead and injured

Most sources, including the website of the National Geographic Institute (Instituto Geográfico Nacional, IGN) of Spain, indicate that 9 people died due to the 2011 Lorca earthquake (Cabañas Rodríguez *et al.*, 2011; Cabañas *et al.*, 2014; López-Comino *et al.*, 2012; Rodríguez-Escudero *et al.*, 2014), though reference to 10 casualties can be found as well (e.g., EM-DAT International Disaster Database).

Discrepancy can also be observed in what regards the number of injuries, though most sources coincide in citing a number around 300 and 400 people (Cabañas Rodríguez *et al.*, 2011; Cabañas *et al.*, 2014; López-Comino *et al.*, 2012; Rodríguez-Escudero *et al.*, 2014; EM-DAT International Disaster Database).

Regarding those left homeless, the number raises to 15,000, according to the EM-DAT International Disaster Database.

A3.3.9.2 Causes of casualties

Most of the deaths and injuries observed were due to falling objects and non-structural elements such as parapets, external masonry walls and cornices (Pro *et al.*, 2014; Romão *et al.*, 2013), whose failure was systematically observed during this event. In particular, Regalado & Lloret (2011) report that seven out of the nine fatalities can be attributed to this cause.

Several authors (e.g., Alfaro *et al.*, 2012) suggest that the death toll would have been a lot higher had the foreshock that alarmed the population not occurred.

Information regarding the number of casualties associated to the RC building which collapsed during the main shock have not been found. Nevertheless, a local newspaper makes reference to one woman having died due to this collapse, and her son having been found still alive under the debris (Laverdad, 2011).

A3.3.9.3 Estimates of economic losses

Figures for economic losses are quite varied and, in many cases, it is not clear exactly which kind of losses are being considered.

Martínez-Díaz *et al.* (2012) and Rodríguez-Escudero *et al.* (2014) make reference to an estimation of economic losses from the Municipality of Lorca by November 2011 of more

than 1,200 million Euros (around 1,600 million US dollars at the time). No details are given of whether these losses are direct or integral.

In a series of press releases, the European Commission (2011) says that a request from Spain for 21.1 million Euros from the European Union Solidarity Fund was approved, and that the total direct cost of the damage caused by the earthquake was estimated in 842.8 million Euros.

This value is similar to the 700 million Euros reported by Olcina Cantos (2011), who specifies that 50 million of which correspond to losses in the historic or artistic patrimony of the city.

A more recent document (2014) from the Spanish Insurance Compensation Consortium (Consortio de Compensación de Seguros), a public corporate entity attached to the Ministry of Economy and Competitiveness, reports a total value of insurance claims for damage due to the earthquake of around 498 million Euros. Table A3.3.11 shows the disaggregation of the insured losses.

Table A3.3.11. Disaggregation of insured losses by type of damage, from Consorcio de Compensación de Seguros (2014). Values are given in Euros updated to December 2013.

Type of Damage / Risk Class	N° Files	Claims	
		Euros	%
Death	4	136,322	0.0%
Permanent Disability	5	75,854	0.0%
Dwellings and Dwelling Communities	24,996	415,172,739	83.4%
Offices	365	7,362,734	1.5%
Commerces	2,096	67,573,680	13.6%
Industries	202	6,911,276	1.4%
Cars	375	704,168	0.1%
Civil Engineering Works	1	25,241	0.0%
TOTAL	28,044	497,962,014	

It should be noted that a newspaper from the region of Murcia highlights that a big percentage of the properties were not insured, and that this additional demolition and reconstruction costs are falling on the government (Murcia Today, 2015).

All the figures provided above are well above the 200 million US dollars losses reported by the International Disaster Database (EM-DAT).

A3.3.10 Discussion and conclusions

This **M**5.1 earthquake occurred on 11th May 2011, at 16.47 UTC (18.47 local time), very close to the city of Lorca, south-eastern Spain, preceded by a **M**4.5 foreshock at 15.05 UTC (17.05 local time), which caused only minor damage. The main shock, on the other hand, reached a maximum EMS-98 intensity of VII and caused losses of around one thousand million Euros to the city of Lorca, nine deaths, and injuries to hundreds of people. The main reasons for the high losses were:

- the proximity of the epicentre to the town (1.8 to 6.0 kilometres, depending on the estimation of the epicentral coordinates),
- the shallowness of the hypocentre (less than 6 km deep),
- directivity effects,
- site amplification effects, and
- vulnerability of the building stock.

Regarding the latter, it is relevant to highlight that, in spite of there being a history of evolution of the Spanish seismic design building codes since the 1960s, a series of weaknesses were systematically observed in the building stock. In particular, reinforced concrete buildings suffered from short column effects and soft storeys, as well as from a lack of adequate seismic gaps in between adjacent structures. Of particular relevance was that their masonry infills and parapets proved to be poorly linked to the structure, either in default or in excess, for failure of these elements was the cause of most casualties. Similarly, structural masonry structures presented problems related to the inadequate bond between stones and mortar, weak connections between the different leafs of the same wall and between vertical and horizontal elements, as well as a combination of excessive stiffness and low ductility. Furthermore, it should also be noted that around 25% of the building stock existing in the municipality of Lorca at the time of the earthquake had been built before the publication of the first code.

Neither surface ruptures nor liquefaction were observed, as expected from its low hazard around the epicentral area. Hundreds of slope instabilities were identified. These were responsible for some very localized damage to buildings, but were not the cause of the widespread losses that took place.

This earthquake was triggered by the effects of groundwater extraction, though the characteristics of the event are consistent with the natural seismicity of the area. This means that human activity may have had an influence on the time and way in which accumulated tectonic stresses were released, but these had nevertheless most likely been building up naturally over several centuries.

A3.3.11 References

A3.3.11.1 Bibliography

Abrahamson, N. & W. Silva (2008). Summary of the Abrahamson & Silva NGA ground-motion relations. *Earthquake Spectra* **24**(1), 67-97.

Afshari, K. & J.P. Stewart (2016). Physically parametrised prediction equations for significant duration in active crustal regions. *Earthquake Spectra* **32**(4), 2057-2081.

Akkar, S. & J.J. Bommer (2010). Empirical Equations for the prediction of PGA, PGV, and spectral accelerations in Europe, the Mediterranean region, and the Middle East. *Seismological Research Letters* **81**, 195-206.

Alfaro, P., J. Delgado, F.J. García-Tortosa, L. Lenti, J.A. López, C. López-Casado & S. Martino (2012). Widespread landslides induced by the Mw 5.1 earthquake of 11 May 2011 in Lorca, SE Spain. *Engineering Geology* **137-138**, 40–52.

Alguacil, G., F. Vidal, M. Navarro, A. García-Jerez & J. Pérez-Muelas (2014). Characterization of earthquake shaking severity in the town of Lorca during the May 11, 2011 event. *Bulletin of Earthquake Engineering* **12**(5), 1889–1908.

Armijo, R. (1977). *La zona des failles Lorca-Totana (Cordillères Bétiques, Espagne). Étude tectonique et neotectonique (The Lorca-Totana faults zone, Betic Cordillera, Spain. Tectonic and neotectonic study, in French)*. Thèse IIIème cycle (thesis), Univ. Paris VII: 229 p.

Arnedo Pena, A. (2010). *How does the system of implementation of European standards works in Spain*. Polish Road Congress Conference, Warsaw, Poland, June 2010. Available online at: http://www.pkd.org.pl/pliki/eurokody_Arnedo.pdf. Last accessed: 18th June 2015.

Avouac, J.P. (2012). Earthquakes: Human-induced shaking. *Nature Geoscience* **5**(11), 763–64.

Baker, J.W. (2007). Quantitative classification of near-fault ground motions using wavelet analysis. *Bulletin of the Seismological Society of America* **97**, 1486-1501.

Basset-Salom, L. & A. Guardiola-Víllora (2014). Seismic performance of masonry residential buildings in Lorca's city centre, after the 11th May 2011 earthquake. *Bulletin of Earthquake Engineering* **12**(5), 2027–48.

Belvaux, M., A. Macau, S. Figueras, X. Goula & T. Susagna (2015). Recorded ground motion and estimated soil amplification for the May 11, 2011 Lorca earthquake. *Earthquake Spectra* **31**(4), 2301-2323.

Benavent-Climent, A., A. Escobedo, J. Donaire-Avila, E. Oliver-Saiz & A.L. Ramírez-Márquez (2014). Assessment of expected damage on buildings subjected to Lorca earthquake through an energy-based seismic index method and nonlinear dynamic response analyses. *Bulletin of Earthquake Engineering* **12**(5), 2049–73.

Benito Oterino, M.B., M.E. Jiménez Peña, M.J. García Rodríguez, J.M Gaspar Escribano & J. García Mayordomo (2005). *Riesgo sísmico en la región de Murcia RISMUR - Volumen 5: Evaluación del riesgo sísmico (Seismic risk in the Murcia region RISMUR – Volume 5: Seismic risk evaluation, in Spanish)*. RISMUR Report, 103 pp.

Benito Oterino, B., A. Rivas Medina, J.M. Gaspar Escribano & P. Murphy (2012). El terremoto de Lorca (2011) en el contexto de la peligrosidad y el riesgo sísmico en Murcia (The 2011 Lorca

- earthquake within the context of seismic hazard and risk in Murcia, in Spanish). *Física de La Tierra* **24**, 255-287.
- Bommer, J.J., G. Georgallides & I.J. Tromans (2001). Is there a near-field for small-to-moderate magnitude earthquakes? *Journal of Earthquake Engineering* **5**(3), 395-423.
- Bommer, J.J., P.J. Stafford & J.E. Alarcón (2009). Empirical equations for the prediction of the significant, bracketed, and uniform duration of earthquake ground motion. *Bulletin of the Seismological Society of America* **99**(6), 3217-3233.
- Bouchon, M. & J. Baker (1996). Seismic response of a hill; the example of Tarzana, California. *Bulletin of the Seismological Society of America* **86**(1, A), 66-72.
- Bousquet, J.C. & H. Phillip (1976). Observations micro-tectoniques sur la compression nord-sud quaternaire des Cordillères Bétiques Orientales (Espagne Méridional - Arc de Gibraltar). *Bull. Soc. Géol. France* **18**, 711-724.
- Cabañas, C., B. Benito, M. López, M.E. Jiménez, P. Gómez González, S. Alvarez & L. Cabañas Rodríguez (1999). Banco de datos de movimiento fuerte del suelo: aplicaciones (Strong ground motion database: applications, in Spanish). *Física de la Tierra* **11**, 113-139.
- Cabañas, L., J.M. Alcalde, E. Carreño & J.B. Bravo (2014). Characteristics of observed strong motion accelerograms from the 2011 Lorca (Spain) earthquake. *Bulletin of Earthquake Engineering* **12**(5), 1909-32.
- Cabañas Rodríguez, L., E. Carreño Herrero, A. Izquierdo Álvarez, J.M. Martínez Solares, R. Capote del Villar, J.J. Martínez-Díaz, B. Benito Oterino, J. Gaspar Escribano, A. Rivas Medina, J. García Mayordomo, R. Pérez López, M.A. Rodríguez Pascua & P. Murphy Corella (2011). *Informe del sismo de Lorca del 11 de Mayo de 2011 (Report on the Lorca earthquake of 11 May 2011, in Spanish)*. Report of the Instituto Geográfico Nacional, Madrid, Spain. Available online at: <http://digital.csic.es/handle/10261/62381>.
- Calais, E., C. DeMets, J-M. Nocquet (2003). Evidence for a post-3.16-Ma change in Nubia-Eurasia-North America plate motions? *Earth and Planetary Science Letters* **216**, 81-92.
- Campbell K.W. & Y. Bozorgnia (2008). NGA ground motion model for the geometric mean horizontal component of PGA, PGV, PGD and 5% damped linear elastic response spectra for periods ranging from 0.01 to 10 s. *Earthquake Spectra* **24**(1), 139-171.
- CEN (2004). *Eurocode 8: Design of structures for earthquake resistance - Part 1: General rules, seismic actions and rules for buildings*. European Committee for Standardization, Brussels, Belgium.
- Chiou B.S.-J. & R.R. Youngs (2008). An NGA Model for the average horizontal component of peak ground motion and response spectra. *Earthquake Spectra* **24**(1), 173-215.
- Consorcio de Compensación de Seguros (2014). *Estadística riesgos extraordinarios. Serie 1971-2013 (Extraordinary risks statistics. 1971-2013 series, in Spanish)*. Available online at: http://www.consorseguros.es/web/c/document_library/get_file?uuid=548d4f59-b6c5-40dd-b06b-98dbcefd790f&groupId=10124. Last accessed: 18th June 2015.
- D'Ayala, D. & E. Speranza (2003). Definition of collapse mechanisms and seismic vulnerability of historic masonry buildings. *Earthquake Spectra* **19**(3), 479-509.
- DeMets, C., R.G. Gordon, D.F. Argus & S. Stein (1994). Effect of recent revisions to the geomagnetic reversal time scale on estimates of current plate motions, *Geophysical Research Letters* **21**, 2191-2194.

d'Estevou, P. & C. Montenat (1985). Evolution structurale de la zone Betique orientale (Espagne) du Tortonian à l' Holocène (Structural evolution of the Eastern Betic Zone (Spain) from Tortonian to Holocene, in French). *Comptes-rendus des séances de l'Académie des sciences. Série 2, Mécanique-physique, chimie, sciences de l'univers, sciences de la terre* **300**(8), 363-368.

Donaire Ávila, J., A. Benavent Climent, A. Escobedo Ruiz, E. Oliver Saiz, A.L. Ramírez Márquez & M. Feriche Fernández-Castanys (2012). Damage assessment on building structures subjected to the recent near-fault earthquake in Lorca (Spain). In *Proceedings of the 15th World Conference on Earthquake Engineering*, Lisbon, Portugal, September 24-28.

Dziewonski, A.M., T.-A. Chou & J. H. Woodhouse (1981). Determination of earthquake source parameters from waveform data for studies of global and regional seismicity. *Journal of Geophysical Research* **86**, 2825-2852.

Ekström, G., M. Nettles & A. M. Dziewonski (2012). The global CMT project 2004-2010: Centroid-moment tensors for 13,017 earthquakes. *Physics of the Earth and Planetary Interiors* **200-201**, 1-9.

Feriche, M., F. Vidal, G. Alguacil, C. Aranda, J. Pérez-Muelas, M. Navarro & A. Lemme (2012). Performance of cultural heritage of Lorca (Spain) during the two small earthquakes of May 11th, 2011. In *Proceedings of the 15th World Conference on Earthquake Engineering*, Lisbon, Portugal, September 24-28.

García-Mayordomo, J., J.M. Insua-Arévalo, J.J. Martínez-Díaz, A. Jiménez-Díaz, R. Martín-Banda, S. Martín-Alfageme, J.A. Álvarez-Gómez, M. Rodríguez-Peces, R. Pérez-López, M.A. Rodríguez-Pascua, E. Masana, H. Perea, F. Martín-González, J. Giner-Robles, E.S. Nemser, J. Cabral, QAFI compilers (2012). The quaternary active faults database of Iberia (QAFI v.2.0). *Journal of Iberian Geology* **38**(1), 285-302.

Gaspar-Escribano, J. M. & B. Benito (2007). Ground-motion characterization of low-to-moderate seismicity zones and implications for seismic design: Lessons from recent Mw 4.8 damaging earthquakes in southeast Spain. *Bulletin of the Seismological Society of America* **97**(2), 531-44.

Giardini, D., G. Grünthal, K.M. Shedlock & P. Zhang (1999). The GSHAP global seismic hazard map. *Annali di Geofisica* **42**(6), 1225-1228.

González, P.J. & J. Fernández (2011). Drought-driven transient aquifer compaction imaged using multitemporal satellite radar interferometry. *Geology* **39**(6), 551-54.

González, P.J., K.F. Tiampo, M. Palano, F. Cannavó & J. Fernández (2012). The 2011 Lorca earthquake slip distribution controlled by groundwater crustal unloading. *Nature Geoscience* **5**(11), 821-25.

Goula, X., J. Irizarry, S. Figueras, A. Macau, A.H. Barbat, L.M. Carreño, N. Lantada, J. Valcarcel (2011). *El terremoto de Lorca del 11 de Mayo de 2011. Informe de la inspección y de los trabajos de campo realizados (The Lorca earthquake of 11 May 2011. Report on the carried out assessment and field work, in Spanish)*. Monografies tècniques, Barcelona, IGC.

Grünthal, G. (ed.) (1998). *European Macroseismic Scale 1998 (EMS-98)*. Cahiers du Centre Europeen de Geodynamique et de Seismologie 15, Centre Europeen de Geodynamique et de Seismologie, Luxembourg.

Jiménez-Munt, I., R. Sabadini, A. Gardi (2003). Active deformation in the Mediterranean from Gibraltar to Anatolia inferred from numerical modeling and geodetic and seismological data. *Journal of Geophysical Research* **108**.

- Jurado Jiménez, F. (2012). Torre del Espolón: de ruina a primer monumento recuperado en Lorca (Murcia) (Torre del Espolón: from ruin to the first recovered monument in Lorca, Murcia, in Spanish). *Alberca: Revista de La Asociación de Amigos Del Museo Arqueológico de Lorca* **10**, 39–52.
- Keefer, D.K. (1984). Landslides caused by earthquakes. *Geological Society of America Bulletin* **95**(4), 406–421.
- Khazaradze, G., J. Gárate, E. Suriñach, J.M. Davila, E. Asensio (2008). Crustal deformation in south-eastern Betics from CuaTe-Neo GPS network. *Geo-Temas* **10**, 1023-1026.
- Koulali, A., D. Ouazar, A. Tahayt, R.W. King, P. Vernant, R.E. Reilinger, S. McClusky, T. Mourabit, J.M. Davila & N. Amraoui (2011). New GPS constraints on active deformation along the Africa–Iberia plate boundary. *Earth and Planetary Science Letters* **308**, 211–217.
- López-Comino, J.A., F.L. Mancilla, J. Morales & D. Stich (2012). Rupture directivity of the 2011, Mw 5.2 Lorca earthquake (Spain). *Geophysical Research Letters* **39**(3): n/a–n/a.
- Martínez-Díaz, J.J. (2002). Stress field variety related to fault interaction in a reverse oblique-slip fault: the Alhama de Murcia fault, Betic cordillera, Spain. *Tectonophysics* **356**, 291-305.
- Martínez-Díaz, J.J., E. Masana & M. Ortuño (2012). Active tectonics of the Alhama de Murcia fault, Betic Cordillera, Spain. *Journal of Iberian Geology* **38**(1), 253-270.
- Martínez Díaz, J.J., C. Canora Catalán & J.A. Álvarez Gómez (2005). *Riesgo sísmico en la región de Murcia RISMUR - Volumen 4: Mapa de representación de máxima acumulación de esfuerzos en las fallas activas de la comunidad autónoma de la región de Murcia (Seismic risk in the Murcia region RISMUR – Volume 4: Map of the maximum accumulation of stress along the active faults of the autonomous community of Murcia region, in Spanish)*. RISMUR Report, 50 pp.
- Martínez-Díaz, J.J., M. Bejar-Pizarro, J.A. Álvarez-Gómez, F.L. Mancilla, D. Stich, G. Herrera & J. Morales (2012). Tectonic and seismic implications of an intersegment rupture. *Tectonophysics* **546-547**, 28–37.
- Martínez-Díaz, J.J., M.A. Rodríguez-Pascua, R. Pérez López, J. García Mayordomo, J.L. Giner Robles, F. Martín-González, M. Rodríguez Peces, J.A. Álvarez Gómez & J.M. Insua Arévalo (2011). *Geological preliminary field report of the Lorca earthquake (5.1 Mw, 11th May 2011)*. Report of the Instituto Geológico y Minero de España (IGME), Spanish Group of Tectónica Activa, Paleosismicidad y Riesgos Asociados de la Universidad Complutense de Madrid (UCM), Universidad Autónoma de Madrid (UAM) and Universidad Rey Juan Carlos de Madrid (URJC).
- Martinez Guevara, J.B. & S. Fernandez Navarro-Soto (1986). *Catálogo sísmico de la región de Murcia (Sismicidad histórica hasta el siglo XVIII) (Seismic catalogue of the Murcia región – Historic seismicity until the 18th century, in Spanish)*. Report of the Instituto Geografico Nacional, Spain.
- Martinez Solares, J.M. & J. Mezcuca (2002). *Catálogo sísmico de la Península Ibérica (880 a.C. - 1900) (Seismic catalogue of the Iberian Peninsula – 880 B.C. – 1900, in Spanish)*. Monography of the Instituto Geográfico Nacional, Spain.
- Masana, E., J.J. Martínez-Díaz, J.L. Hernández-Enrile & P. Santanach (2004). The Alhama de Murcia fault (SE Spain), a seismogenic fault in a diffuse plate boundary: Seismotectonic implications for the Ibero-Magrebien region. *Journal of Geophysical Research* **109**(B1), n/a-n/a.
- Mezcua, J., R.M. Garcia Blanco, & J. Rueda (2008). On the strong ground motion attenuation in Spain. *Bulletin of the Seismological Society of America* **98**(3), 1343-1353.

- Milutinovic, Z.V. & G.S. Trendafiloski (2003). *RISK-UE - An advanced approach to earthquake risk scenarios with applications to different European towns - WP4: Vulnerability of current buildings*. RISK-UE Report, 110 pp.
- Montenat, C., P.O. D'Estevou & P. Masse (1987). Tectonic-sedimentary characters of the Betic Neogene Bassins evolving in a crustal transcurrent shear zone (SE Spain). *Bull. Centres Rech. Explo. Prod. Elf Aquitaine* **11**, 1-22.
- Morales, J., J.V. Cantavella, F.L. Mancilla, L. Lozano, D. Stich, E. Herraiz, J.B. Martín, J.A. Lopez-Comino & J.M. Martínez-Solares (2014). The 2011 Lorca seismic series: Temporal evolution, faulting parameters and hypocentral relocation. *Bulletin of Earthquake Engineering* **12**(5), 1871–1888.
- Morel, J.L. & M. Meghraoui (1996). Gorringe-Alboran-Tell tectonic zone: a transpression system along the Africa-Eurasia plate boundary. *Geology* **24**, 755-758.
- Murphy Corella, P. (2005). *Riesgo sísmico en la región de Murcia RISMUR - Volumen 3: La vulnerabilidad de la edificación de la región de Murcia (Seismic risk in the Murcia region RISMUR – Volume 3: vulnerability of the building stock in the Murcia region, in Spanish)*. RISMUR Report, 60 pp.
- Navarro, M., A. García-Jerez, F.J. Alcalá, F. Vidal & T. Enomoto (2014). Local site effect microzonation of Lorca town (SE Spain). *Bulletin of Earthquake Engineering* **12**(5), 1933–1959.
- NCSE-02 (2002). *Norma de Construcción Sismorresistente: Parte general y edificación - Real decreto 997/2002, de 27 de Septiembre (Seismic building code: general and constructions – Royal decree 997/2002 of 27 September, in Spanish)*. Published in BOE **244**, 35898-35967.
- Olcina Cantos, Jorge (2011). Lecciones tras el desastre de Lorca (terremotos del 11 de Mayo de 2011) (Lessons after the Lorca disaster (earthquakes of 11 May 2011), in Spanish). *Estudios Geográficos* **72**(271), 717–724.
- Pro, C., E. Buforn, S. Cesca, C. Sanz de Galdeano & A. Udías (2014). Rupture process of the Lorca (southeast Spain) 11 May 2011 (M W = 5.1) earthquake. *Journal of Seismology* **18**, 481–95.
- Regalado, F. & V. Lloret (2011). *Análisis y reflexiones sobre los terremotos del 11 de mayo del 2011 acontecidos en Lorca (sugerencias para el futuro) (Analysis and reflections on the Lorca earthquakes of 11 May 2011 (recommendations for the future), in Spanish)*. Report of the Equipo Técnico de Florentino Regalado y Asociados y Regalado Arquitectos.
- Rodríguez-Escudero, E., J.J. Martínez-Díaz, J.A. Álvarez-Gómez, J.M. Insua-Arévalo & R. Capote del Villar (2014). Tectonic setting of the recent damaging seismic series in the southeastern Betic Cordillera, Spain. *Bulletin of Earthquake Engineering* **12**(5), 1831–1854.
- Rodríguez-Peces, M.J., J. García-Mayordomo & J.J. Martínez-Díaz (2014). Slope instabilities triggered by the 11th May 2011 Lorca earthquake (Murcia, Spain): Comparison to previous hazard assessments and proposition of a new hazard map and probability of failure equation. *Bulletin of Earthquake Engineering* **12**(5), 1961–1976.
- Romão, X., A.A. Costa, E. Paupério, H. Rodrigues, R. Vicente, H. Varum & A. Costa (2013). Field observations and interpretation of the structural performance of constructions after the 11 May 2011 Lorca earthquake. *Engineering Failure Analysis* **34**, 670–692.
- Rueda, J., J. Mezcua, R.M. García-Blanco (2011). Directivity effects of the May 11, 2011 Lorca (Spain) Mw=5.1 earthquake. In AGU Fall Meeting Abstracts **1**, p. 2277.

Serpelloni, E., G. Vannucci, S. Pondrelli, A. Argnani, A. Casula, M. Anzidei, P. Balde & P. Gasperini (2007). Kinematics of the Western Africa-Eurasia plate boundary from focal mechanisms and GPS data. *Geophysical Journal International* **169**, 1180-1200.

Tapia, M., T. Susagna & X. Goula (2007). Curvas predictivas del movimiento del suelo en el oeste del Mediterráneo (Western Mediterranean ground motion predictive curves, in Spanish). *3er Congreso Nacional de Ingeniería Sísmica*, Girona, Spain, May 2007.

Tsige Aga, M. & I. García Flores (2005). *Riesgo sísmico en la región de Murcia RISMUR - Volumen 2: Caracterización geotécnica y análisis de efecto local (Seismic risk in the Murcia region RISMUR – Volume 2: geotechnical and site effects characterisation, in Spanish)*. RISMUR Report, 39 pp.

United Nations, ed. (2011). *Human Development Report 2011 - Sustainability and equity: A better future for all*. Report of the United Nations Development Programme (UNDP). Palgrave Macmillan, New York, United States.

United Nations, ed. (2013). *Human Development Report 2013 - The rise of the South: Human progress in a diverse world*. Report of the United Nations Development Programme (UNDP), New York, United States.

United Nations, ed. (2014). *Human Development Report 2014 - Sustaining human progress: Reducing vulnerabilities and building resilience*. Report of the United Nations Development Programme (UNDP), New York, United States.

Woessner, J., D. Giardini, H. Crowley, F. Cotton, G. Grünthal, G. Valensise, R. Arvidsson, R. Basili, M. B. Demircioglu, S. Hiemer, C. Meletti, R. W. Musson, A. N. Rovida, K. Sesetyan, M. Stucchi & The SHARE Consortium (2015). The 2013 European Seismic Hazard Model: Key Components and Results. *Bulletin of Earthquake Engineering* **13**(12), 3553–3596. Online data source: <http://www.efehr.org/en/home/>. Last accessed: 3rd December 2017.

Worden, C.B., E.M. Thompson, M. Hearne & D.J. Wald (2017). *ShakeMap V4 Manual: technical manual, user's guide, and software guide*. United States Geological Survey. Available online at: <http://usgs.github.io/shakemap/>.

A3.3.11.2 Web references

Ayuntamiento de Lorca (2011): Plan Director para la recuperación del patrimonio cultural de Lorca (Lorca City Council - Master Plan for the recovery of the cultural heritage of Lorca, in Spanish): <http://www.lorca.es/concejaliasyservicios/concejaliasyservicios.asp?id=1547>. Last accessed: 9th February 2017.

European Commission (2011): http://europa.eu/rapid/press-release_IP-11-1361_en.htm, http://europa.eu/rapid/press-release_PRES-11-456_en.htm?locale=en. Last accessed: 9th February 2017.

GeoAzur: <https://geoazur.oca.eu>. Last accessed: 18th June 2015.

GeoForschungsZentrum: <http://geofon.gfz-potsdam.de/>. Last accessed: 18th June 2015.

Global Centroid Moment Tensor (GCMT) Project: <http://www.globalcmt.org/>. Last accessed: 18th June 2015.

Instituto Geográfico Nacional (IGN, Spanish National Geographic Institute): <http://www.ign.es/>. Last accessed: 18th June 2015.

Instituto Nacional de Estadística (INE, Spanish Statistics National Institute): <http://www.ine.es/>. Last accessed: 18th June 2015.

International Seismological Centre: <http://www.isc.ac.uk/>. Last accessed: 18th June 2015.

Laverdad (2011):
<http://www.laverdad.es/murcia/20110511/local/lorca/terremoto-lorca-201105111711.html>.
Last accessed: 9th February 2017.

Ministerio de Fomento: <http://www.fomento.gob.es/>. Last accessed: 18th June 2015.

Murcia Today (2015):
http://murciatoday.com/reconstruction-work-still-in-progress-4-years-after-lorca-earthquake_25885-a.html. Last accessed: 9th February 2017.

Quaternary Active Faults Database of Iberia (QAFI) v.2: <http://info.igme.es/qafi/>.
Last accessed: 18th June 2015.

RISMUR Project: <http://www.112rm.com/dgsce/planes/rismur.php>. Last accessed: 18th June 2015.

SISMIMUR Project: <http://www.112rm.com/dgsce/planes/sismimur/sismimur.php>.
Last accessed: 18th June 2015.

United States Geological Survey (USGS): <http://earthquake.usgs.gov/>.
Website for this event (last accessed 18th June 2015):
<http://earthquake.usgs.gov/earthquakes/eventpage/usp000j1en#executive>.

A3.4 August 2011 M5.4 Trinidad (Colorado) Earthquake, USA

This earthquake occurred on 23rd August 2011, at 05.46 UTC (22nd August 2011, 23.46 local time), and was the largest to take place in Colorado in around half a century. It was part of a sequence that started with a series of small foreshocks the day before, was followed by over 500 events in the following four months, and is believed to have been induced by deep injection of wastewater in the Raton Basin. The main shock was widely felt and caused damage to masonry buildings in the scarcely populated towns of Segundo, Valdez, Cokedale and Trinidad, all located within 20 km of the epicentre.

A3.4.1 Tectonic and seismic setting

A3.4.1.1 Tectonic setting

The epicentre of this earthquake was located within the Raton sedimentary Basin, at the base of the Sangre de Cristo Mountains, the southernmost sub-range of the Rocky Mountains, along the border of the states of Colorado and New Mexico. The Rocky Mountains make up an effective boundary between the active shallow regions of the United States, to the West, and the stable continental regions, to the East. Overall, the state of Colorado is subject to a regional tectonic setting of east–west extension (Rubinstein *et al.*, 2014).

The most relevant fault in the area is the extensional Sangre de Cristo fault, over the Rockies (Figure A3.4.1), which is part of the Rio Grande Rift system and is the closest known to be active during the Quaternary Period (Rubinstein *et al.*, 2014). Quaternary deposits around the area of this fault and to its West show the occurrence of multiple paleoseismic events with individual displacements of 1.7 to 2.9 metres, and fourteen faults around the state of Colorado are believed to be capable of generating maximum credible earthquakes with magnitudes ranging from **M**6.25 to 7.5 (Sheehan *et al.*, 2003).

In spite of this significant tectonic activity across the western side of the state of Colorado, there is little evidence for faulting within the low-lying Raton Basin, except for some isolated buried faults reported by Rubinstein *et al.* (2014), making reference to Johnson (1969), Robson & Banta (1987), and Scott & Pillmore (1993), which are not part of the U.S. Geological Survey (USGS) Quaternary Fault and Fold Database (2015), and are believed by the authors to be inactive. As shown in Figure A3.4.2, the lineation of the foreshocks, main shock and aftershocks is consistent with the strike of one of these faults. Nevertheless, Rubinstein *et al.* (2014) believe that the 2011 earthquake swarm had its origin along the planes of unknown faults, not expected to be directly related to these previously mapped ones, though both structures are consistent with the regional tectonic stresses.

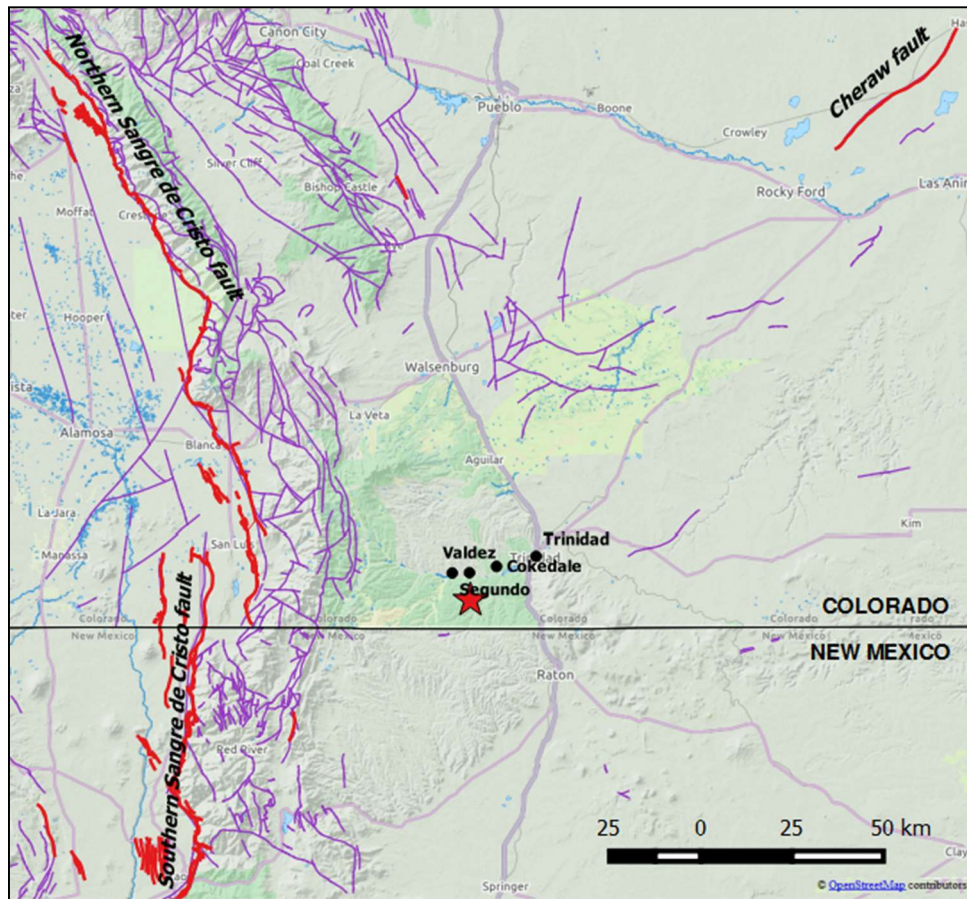


Figure A3.4.1. Quaternary faults (red) and fault traces (violet) close to the Raton Basin. The four locations marked are those at which damage was observed during the 2011 Trinidad earthquake. Faults locations from the Quaternary Fault and Fold Database of the United States (USGS) and the Mineral Resources Online Spatial Data (USGS).

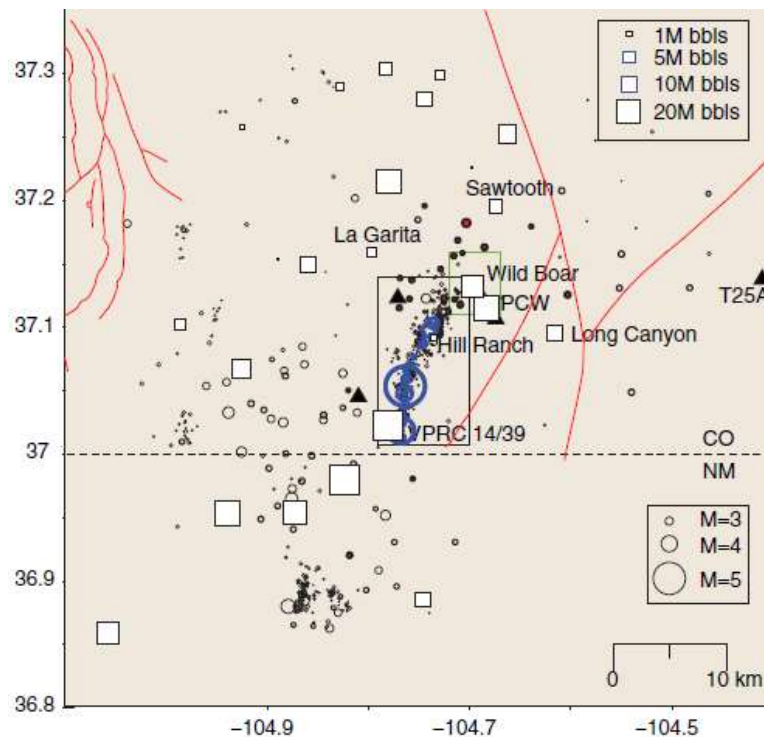


Figure A3.4.2. Seismicity from August 2011 to 15th December 2011 (blue circles), and location of injection wells (white squares). Faults (red lines) to the East of the epicentres shown are those believed to be buried and inactive. From Rubinstein *et al.* (2014).

A3.4.1.2 Regional and local seismicity

In spite of having faults believed to be capable of generating earthquakes of magnitudes up to 7.5 (Sheehan *et al.*, 2003), Colorado is usually considered a region of minor seismic activity. In particular, the Raton Basin is, or was before the turn of the century, one of the most aseismic areas of the state.

According to the United States Geological Service (USGS), the first known reference to an earthquake in Colorado dates from 7th December 1870. During this event, an observer in Fort Reynolds, 30 km to the east of Pueblo, noticed that bottles which were originally separated by over 2 cm, were suddenly pulled together. The largest known historical earthquake to have taken place in Colorado occurred on 7th November 1882, had an estimated moment magnitude of 6.6 ± 0.6 , and was the first ever to cause damage at Denver, where walls cracked and plaster fell from walls (USGS; Sheehan *et al.*, 2003). A large increase in the seismic activity within the state of Colorado was observed during the 1960s, after a well was drilled for the disposal of waste fluids at the Rocky Mountain Arsenal, northeast of Denver (USGS). These and most of the significant earthquakes in the state had their epicentres around the north-central or western areas.

Within the Raton Basin, the most relevant earthquakes observed before 2011 were the August-September 2001 and August-September 2005 sequences, whose epicentres were located on the Colorado side and on the New Mexico side of the central region of the basin, respectively. The 2001 swarm included eight shocks with magnitudes larger than or equal to 4.0, with the two largest being M_{bLg} 4.0 and 4.5. The largest earthquake ever recorded in the basin before the **M5.4** 2011 event was a **M5.0** which occurred as part of the 2005 sequence, in August that year (USGS; Rubinstein *et al.*, 2014). These sequences represented a significant change in the seismic behaviour of the Raton Basin, whose activity before August 2001 was widely distributed and infrequent, and observed mostly around its north-eastern margin (Rubinstein *et al.*, 2014). Sixteen earthquakes with magnitudes equal to or larger than 3.8 occurred within the basin between August 2001 and 2013, while only one had taken place in the preceding three decades. Rubinstein *et al.* (2014) believe that this increase in the seismic activity in the area can be linked to wastewater injection, but Matthews (2011) highlights that analysis carried out by the USGS and the Colorado Geological Service were not conclusive.

Before 2001, relevant earthquakes in the area include a **M4.6** event on 2nd October 1966 northeast of Trinidad, the 1973 swarm, whose two largest events were a **M3.1** and a **M4.2**, west or northwest of Trinidad, a **M3.2** in 1983, northeast of Trinidad, and three events with magnitudes equal to or larger than 3.2 in 1996, also to the northeast of Trinidad (USGS; Matthews, 2011).

Figure A3.4.3 shows the seismicity in Colorado between 1870 and 1992, as reported by Sheehan *et al.* (2003).

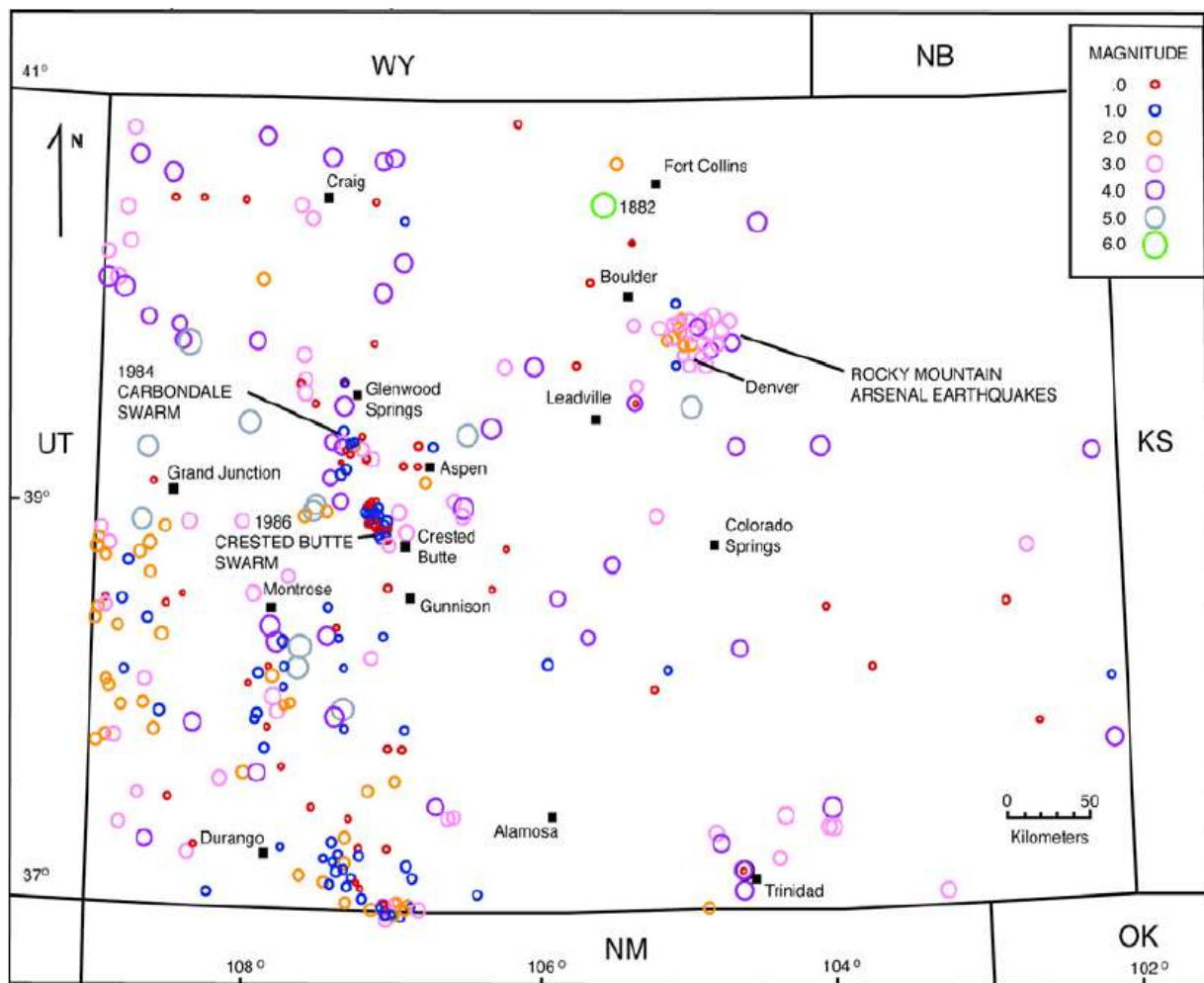


Figure A3.4.3. Seismicity of the state of Colorado between 1870 and 1992. From Sheehan *et al.* (2003), after Bott & Wong (1995).

A3.4.1.3 Seismic hazard

Figure A3.4.4 shows extracts of the probabilistic seismic hazard maps for the United States of 2008 and 2014, elaborated by the USGS (USGS; Petersen *et al.*, 2008; Petersen *et al.*, 2014). Values shown correspond to peak ground acceleration (PGA) on rock with a 10% probability of exceedance in 50 years. The Raton Basin area is marked in red. Table A3.4.1 presents a summary of the PGA values expected at Segundo, Valdez, Cokedale and Trinidad, which are the locations that experienced damage during the 2011 Trinidad earthquake. The table also reports the corresponding values obtained from the Global Seismic Hazard Assessment Program (GSHAP; Giardini *et al.*, 1999), which are closer to those of the 2014 USGS hazard map than to those of the 2008 one. In any case, all values support the idea that seismic hazard is moderate to low in the area of the Raton Basin. It should be noted that the USGS national seismic hazard maps do not take into consideration non-tectonic seismic activities and, therefore, the 2011 Trinidad sequence had no effect over the change from the 2008 map to the 2014 one (please refer to the *Seismic hazard* section of Appendix A3.6 for a discussion on the incorporation of induced seismicity to seismic hazard calculations).

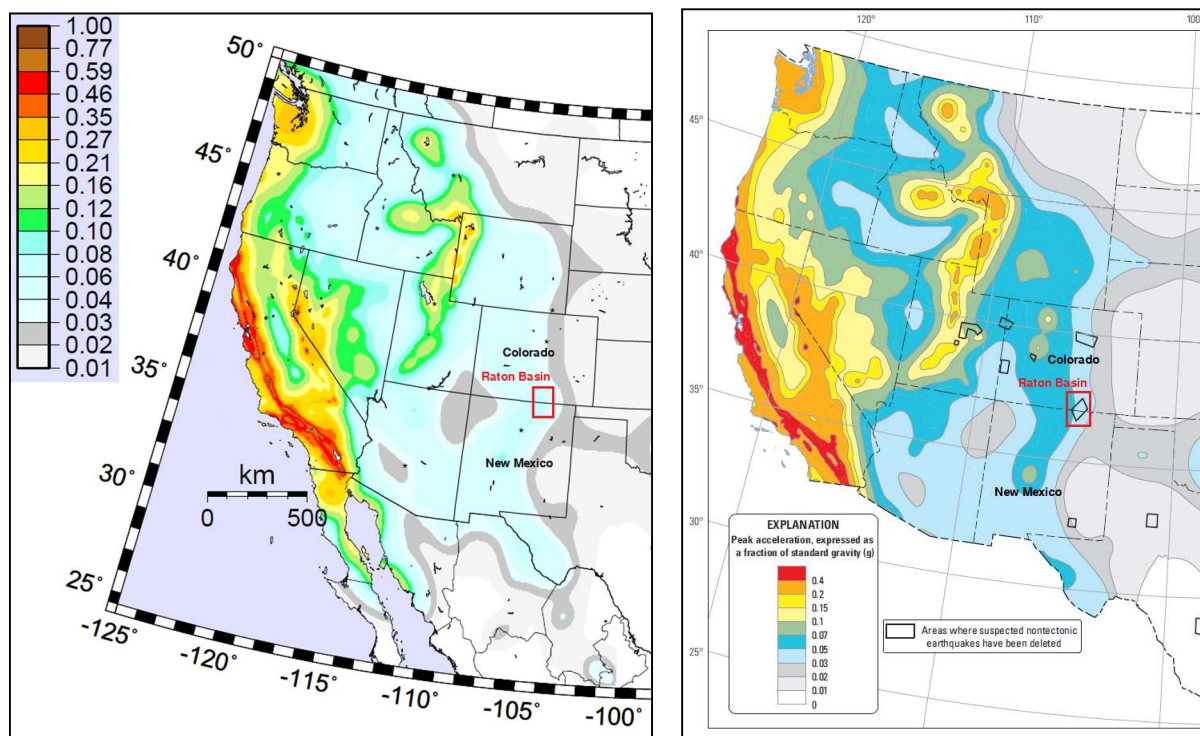


Figure A3.4.4. Extract of the 2008 (left) and 2014 (right) hazard maps for the United States, elaborated by the USGS (2015). Values correspond to peak ground acceleration (g) on rock with a 10% probability of exceedance in 50 years.

Table A3.4.1. Peak ground acceleration (PGA, g) values on rock with a 10% probability of exceedance in 50 years according to the 2008 and 2014 USGS hazard maps, and results from the Global Seismic Hazard Assessment Program (GSHAP), at locations in which damage was observed after the 2011 Trinidad earthquake.

PLACE	USA 2008	USA 2014	GSHAP
Segundo	0.0648	0.0417	0.0466
Valdez	0.0629	0.0405	0.0431
Cokedale	0.0590	0.0383	0.0395
Trinidad	0.0551	0.0365	0.0367

A3.4.2 Earthquake source characteristics

A3.4.2.1 Location, depth and time

The main shock occurred on 23rd August 2011, at 05.46 UTC (22nd August 2011, 23.46 local time).

Several organizations and agencies report their own estimations of the epicentral coordinates and hypocentral depth. The information reported in the websites of the National Earthquake Information Center (NEIC) of the United States Geological Service (USGS), the Global Centroid Moment Tensor Project (GCMT; Dziewonski *et al.*, 1981; Ekström *et al.*, 2012) and the International Seismological Centre (ISC) is summarized in Table A3.4.2. Cells marked as (*f) correspond to parameters that were held fixed while

inversion was carried out to retrieve those that remain. Table A3.4.2 also includes the epicentral coordinates and hypocentral depths calculated by Barnhart *et al.* (2014) and Rubinstein *et al.* (2014).

Table A3.4.2. Epicentral coordinates and hypocentral depths from different sources.

Agency / Publication		Latitude	Longitude	Depth (km)
NEIC	National Earthquake Information Center, USGS	37.0630 ° N	104.7010 °W	4.00
GCMT	Centroid Global Centroid Moment Tensor Project (**)	37.1200 ° N	104.5900 °W	12.00
ISC	International Seismological Service (inversion)	37.0680 ° N	104.6482 °W	10 (*f)
Barnhart <i>et al.</i> (2014)		37.0381 ° N	104.7530 °W	5.10 (*f)
Rubinstein <i>et al.</i> (2014)		37.0540 ° N	104.7600 °W	3.50

(*f) fixed parameter used for inversion

(**) centroid (not-hypocentral) location

Rubinstein *et al.* (2014) shed some light over the variability observed in the estimations of the hypocentral depths. According to the authors, standard arrival-time location techniques place the main shock hypocenter at 4.3 km depth, though with a two standard deviation uncertainty of ± 15.0 km. Analyses of In-SAR images support this small value, indicating that slip was concentrated within a zone of approximately 2.5 to 6.0 km in depth. Finally, computed synthetic seismograms for two well-recorded smaller earthquakes that were close to the main shock match best the recorded surface waves when hypocentral depths of 3.0 and 4.0 km are used for their generation. Based on all these observations and on the fact that most aftershocks have hypocentral depths between 4.0 and 8.0 km, and these are better constrained than for the main shock due to the availability of more stations, Rubinstein *et al.* (2014) conclude that a hypocentral depth of the main shock between 3.0 and 4.0 km is most likely.

The map in Figure A3.4.5 shows the different estimations of the epicentral coordinates enumerated above. Note that coordinates reported by the GCMT correspond to the location of the centroid, and not the hypocentre.

A3.4.2.2 Magnitude

Estimations of magnitude made by the same agencies are reported in Table A3.4.3.

Table A3.4.3. Estimations of moment magnitude (**M**), body-wave magnitude (**mb**) and surface-wave magnitude (**Ms**).

Agency		M	mb	Ms
NEIC	National Earthquake Information Center, USGS	5.3	5.0	-
GCMT	Global Centroid Moment Tensor Project (1)	5.4	5.0	5.4
ISC	International Seismological Service (inversion)	-	5.1	5.0

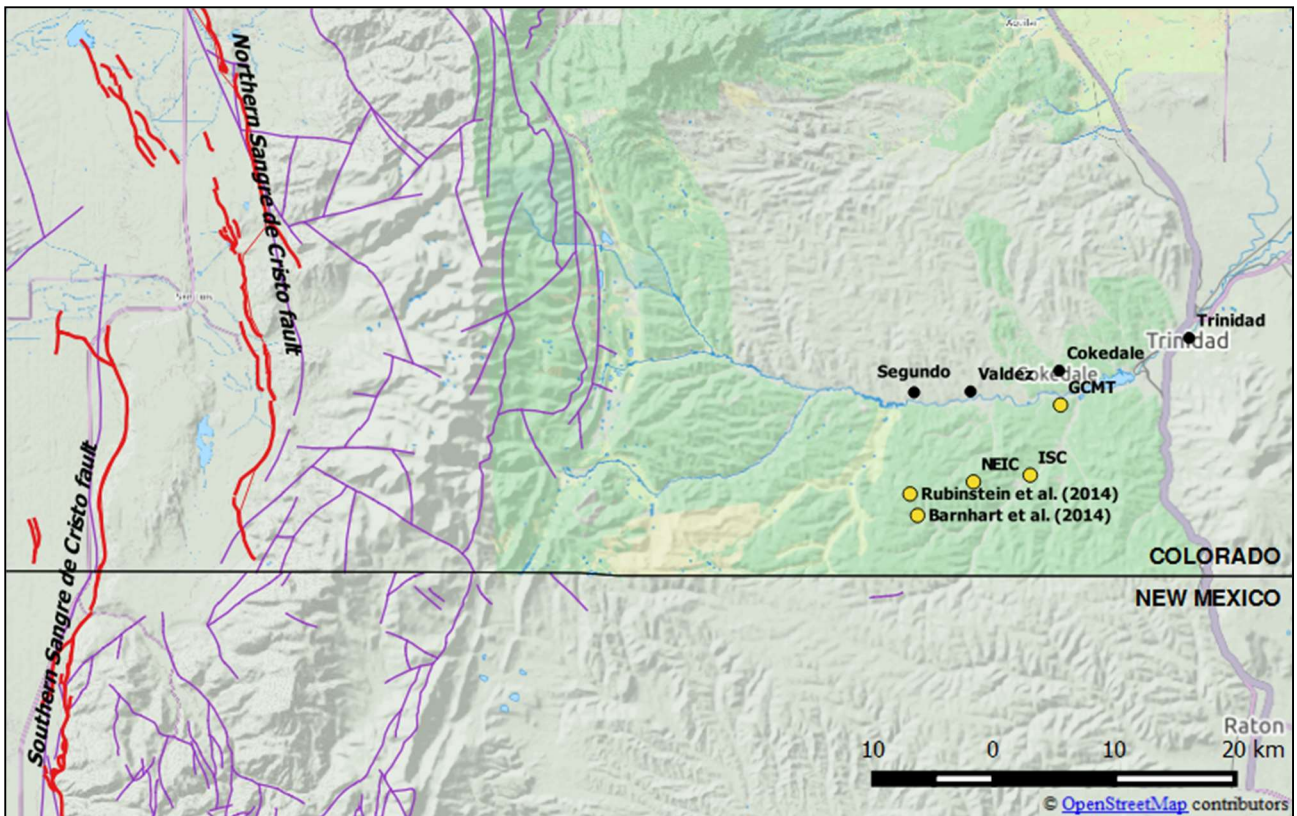


Figure A3.4.5. Estimation of epicentral coordinates (yellow circles). Faults in the area marked in red and violet, as described earlier.

A3.4.2.3 Style-of-faulting

All sources indicate a normal mechanism on a fault striking to the north-northeast (USGS; Barnhart *et al.*, 2014; Rubinstein *et al.*, 2014). According to Rubinstein *et al.* (2014), the main shocks of the swarms that took place in 2001 and 2005 in the Raton Basin also presented the same mechanism at a similar strike, which is consistent with the ambient stress. Said authors also note that the whole 2011 sequence had epicentres along two intersecting lineations. While the southern lineation strikes nearly north-south, the northern one strikes closer to northeast-southwest. The authors believe that these planes are faults different from the ones with similar strikes lying to the East of the basin (Figure A3.4.2). Further, they suggest that it is possible that the different lineations be a consequence of lack of precision in the localization of the events. Table A3.4.4 summarizes the fault plane solutions calculated by the USGS and the GCMT, while Figure A3.4.6 shows the corresponding beachball representations.

Table A3.4.4. Fault plane solutions and fault planes from different sources. Fault planes marked in gray are the preferred solution in each case.

Fault Plane 1			Fault Plane 2			Source
Strike	Dip	Rake	Strike	Dip	Rake	
185	38	-103	21	53	-80	Regional Moment Tensor NEIC (USGS)
203	38	-75	4	53	-101	GCMT

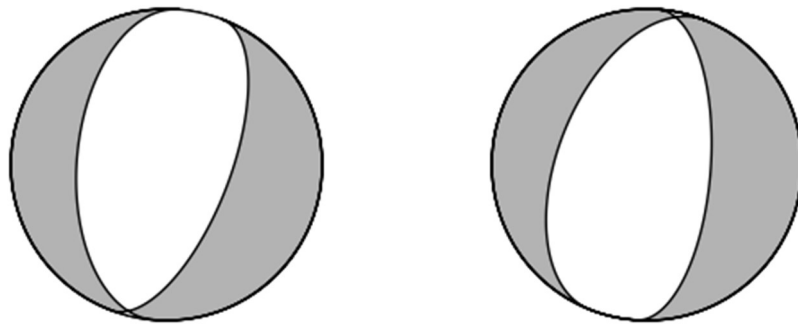


Figure A3.4.6. Fault plane solutions according to the USGS (left) and GCMT (right).

A3.4.2.4 Stress drop

Barnhart *et al.* (2014) report a stress drop of 0.07 MPa, which they say is much lower than expected for intraplate normal faulting events.

A3.4.2.5 Foreshocks and aftershocks

The **M**5.4 main shock was preceded by a foreshock sequence which started on 21st August 2011. By means of a manual scanning of the seismic records at a station to the southeast of Trinidad, Rubinstein *et al.* (2014) identified 36 foreshock events, the first of which was a **M**~1.1, which was the smallest detected. The three strongest foreshocks (Figure A3.4.7) were a **M**4.7 and two events of ML 2.9 and 3.0, all of which occurred within the 24 hours before the main shock (Barnhart *et al.*, 2014; Morgan & Morgan, 2011; Rubinstein *et al.*, 2014). According to the USGS, the **M**4.7 event reached a MMI of IV at La Junta, Manzanola, Trinidad and Weston. According to Rubinstein *et al.* (2014), the earliest foreshocks had epicentres towards the north, while foreshocks following the **M**4.7 event were mostly concentrated to the south.

After the **M**5.4 main shock, the USGS located 584 aftershocks that took place within the Raton Basin between 23rd August and 15th December 2011. Rubinstein *et al.* (2014) point out that the sequence decayed quickly, and most aftershocks occurred within approximately one month of the main shock. According to Barnhart *et al.* (2014), the aftershock sequence exhibits statistical properties (such as the b-value of the Gutenberg-Richter relation and the Omori-Utsu decay constant) expected for intraplate earthquakes. Most of the aftershocks occurred at very shallow depths (Rubinstein *et al.*, 2014). The location of some of the most significant ones, according to the USGS, is shown in Figure A3.4.7. The largest reported macroseismic intensity for these events was MMI V, which corresponds to moderate shaking and very light damage (Did You Feel It?, USGS).

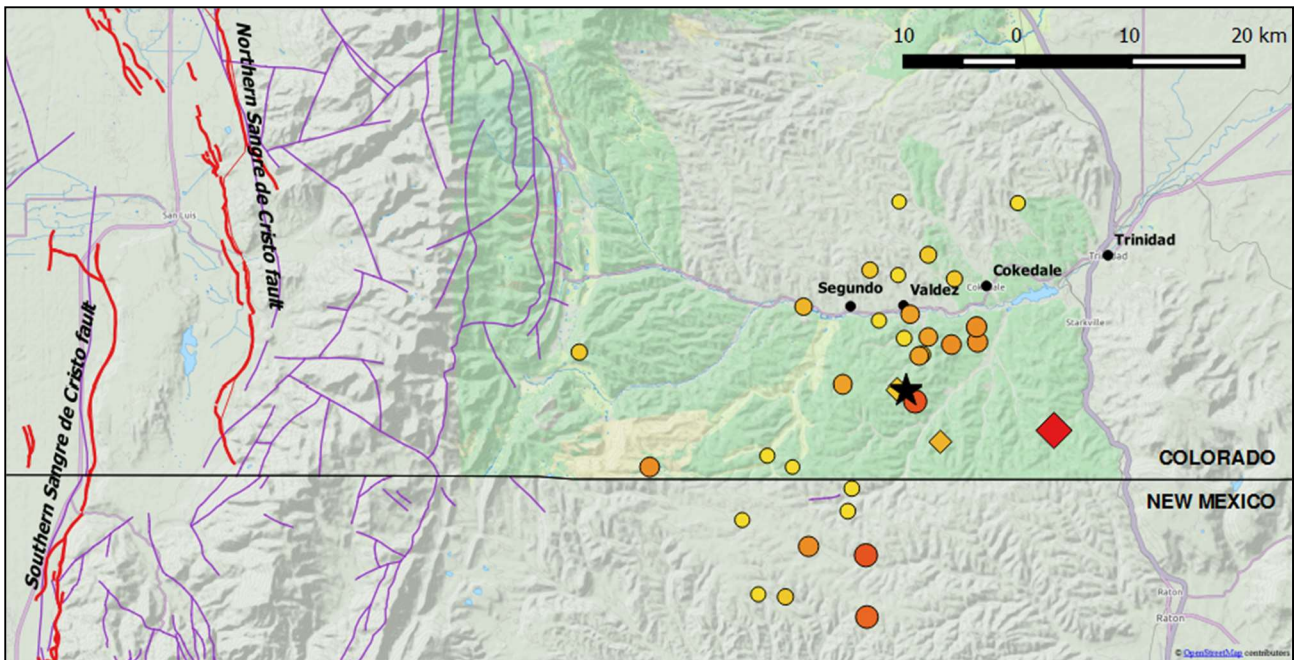


Figure A3.4.7. Most significant foreshocks (rhombuses) and aftershocks (circles), with colour scale representing magnitude (2.5: yellow, 4.7: red). The black star is the epicentre of the main shock, according to the USGS. Epicentral coordinates of all events according to the USGS. Faults in the area marked in red and violet, as described earlier.

A3.4.2.6 Nature of earthquake

While some authors are cautious in labelling the 2011 Trinidad earthquake sequence as induced (e.g., Matthews, 2011) others present significant arguments supporting this hypothesis (Barnhart *et al.*, 2014; Rubinstein *et al.*, 2014). In any case, it is well known that the Raton Basin is a coal-bearing sedimentary basin which is being actively exploited for the production of gas and the disposal via injection of wastewater (Matthews, 2011). However, according to Rubinstein *et al.* (2014), increased seismic activity in the basin since 2001 is directly related only to deep injection of wastewater and not to gas production. They get to this conclusion by means of three separate analyses. Firstly, a statistical analysis of the change in the earthquake rate that occurred in the area in 2001 suggests that it is highly unlikely that such a change be due to random fluctuations of the ambient seismicity. Secondly, they observed a significant spatial correlation between the location of the injection wells and the epicentres of the seismic events taking place since 2001, an observation which matches that of Barnhart *et al.* (2014), who found a strong correlation between the seismicity in the Raton Basin and regions of subsidence observed in InSAR time series analysis. Finally, Rubinstein *et al.* (2014) note that total injection volumes and the number of earthquakes taking place present similar trends.

A3.4.3 Geology and ground conditions in the affected area

A3.4.3.1 Regional geology and topography

This earthquake occurred within the Raton Basin, a coal-bearing sedimentary basin in which 2.0-2.5 km of Cretaceous and Tertiary sedimentary rocks overlie a Precambrian crystalline basement (Barnhart *et al.*, 2014). The basin itself presents a flat topography, but lies at the base of the Sangre de Cristo Mountains, the southernmost subrange of the Rocky Mountains. It is approximately 150 km long in the north–south direction, and 75 km wide at its maximum (Rubinstein *et al.*, 2014).

A3.4.3.2 Site conditions in the affected area

Figure A3.4.8 presents an east-west stratigraphic cross section across the southern part of the Raton Basin, while Figure A3.4.9 describes the corresponding formations and soil types. As can be observed, sandstone and shale, two types of clastic sedimentary rock, are predominant in all formations.

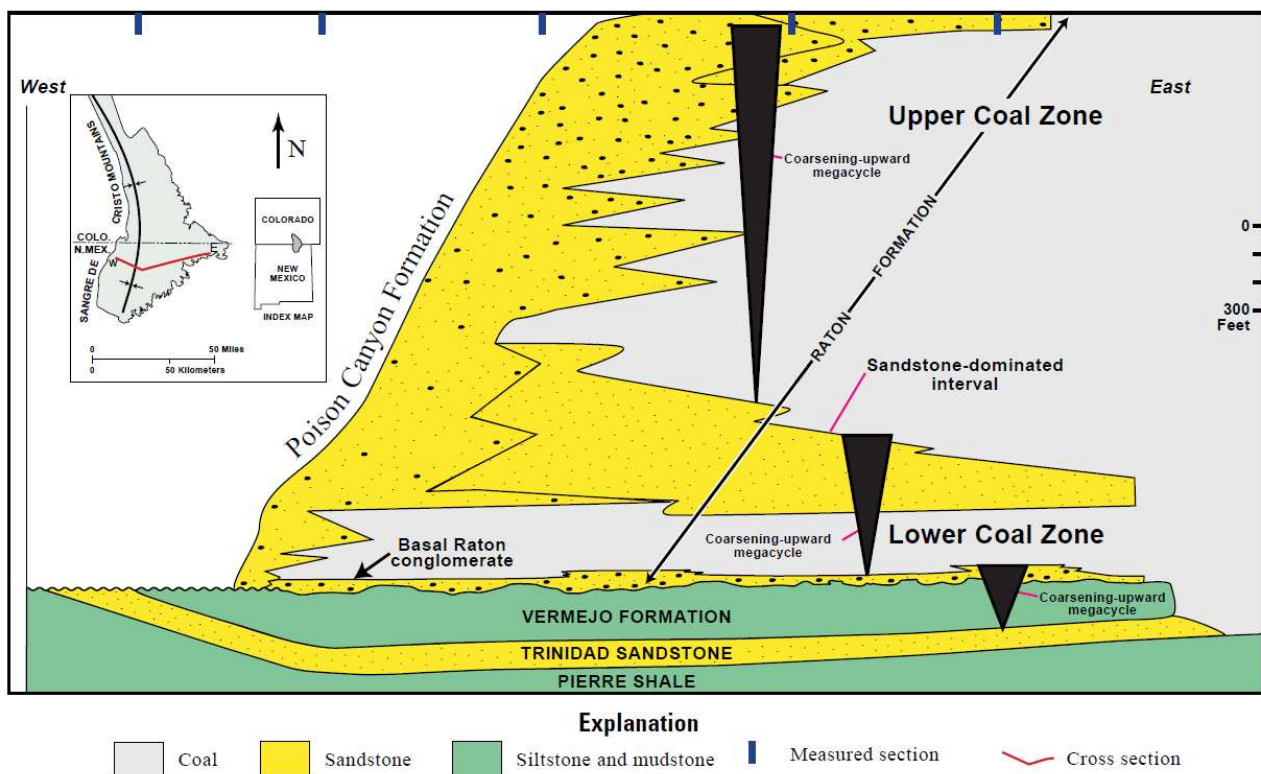


Figure A3.4.8. East-west stratigraphic cross section across the southern part of the Raton Basin. From Flores (1987) and Flores & Bader (1999), in Johnson & Finn (2001).

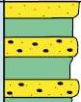




AGE		FORMATION NAME	GENERAL DESCRIPTION	LITH- OLOGY	APPROX. THICKNESS IN FEET
TERTIARY	PALEOCENE	POISON CANYON FORMATION	SANDSTONE—Coarse to conglomeratic beds 13–50 feet thick. Interbeds of soft, yellow-weathering clayey sandstone. Thickens to the west at expense of underlying Raton Formation		500+
		RATON FORMATION	Formation intertongues with Poison Canyon Formation to the west UPPER COAL ZONE—Very fine grained sandstone, siltstone, and mudstone with carbonaceous shale and thick coal beds BARREN SERIES—Mostly very fine to fine-grained sandstone with minor mudstone, siltstone, with carbonaceous shale and thin coal beds LOWER COAL ZONE—Same as upper coal zone; coal beds mostly thin and discontinuous. Conglomeratic sandstone at base; locally absent		0(?)–2,100 ← K/T boundary
MESOZOIC	UPPER CRETACEOUS	VERMEJO FORMATION	SANDSTONE—Fine to medium grained with mudstone, carbonaceous shale, and extensive, thick coal beds. Local sills		0–380
		TRINIDAD SANDSTONE	SANDSTONE—Fine to medium grained; contains casts of <i>Ophiomorpha</i>		0–300
		PIERRE SHALE	SHALE—Silty in upper 300 ft. Grades upward to fine-grained sandstone. Contains limestone concretions		1800-1900

Figure A3.4.9. Generalised stratigraphic column for Cretaceous and Tertiary rocks in the Raton Basin. From Flores & Bader (1999), modified from Pillmore (1969), Pillmore & Flores (1987), and Flores (1987), in Johnson & Finn (2001).

To our knowledge, measured V_{s30} values for the Raton Basin area are not readily available in the literature. However, based on the work by Wills & Silva (1998), Wills & Clahan (2006) report a series of relationships between Californian geologic units and their corresponding V_{s30} values, which can be used as a reference herein. Table A3.4.5 summarizes those corresponding to geologic units which can be comparable to those of the Raton Basin. As can be observed, V_{s30} values can be expected to range approximately between 300 and 600 m/s. These values are in agreement with those estimated by the United States Geological Survey (USGS) V_{s30} Map Server (Figure A3.4.10) using topographic slope as a proxy (Wald & Allen, 2007). The map in Figure A3.4.10 was generated using the correlations derived by Wald & Allen (2007) for active tectonic regions. These were preferred here over those for stable shield regions given the proximity to the Rocky Mountains which suggests conditions might be closer to those of western and not eastern USA.

According to Rubinstein *et al.* (2014), the hydraulic head within the Cretaceous layers lies, on average, approximately 500 m below the surface, and is approximately 4.9 MPa naturally underpressured. Due to this, wastewater injection throughout much of the Colorado portion of the Raton Basin can be done via gravity feed.

Table A3.4.5. Relationship between geologic units comparable to those of the Raton Basin and their shear-wave velocities (Wills & Clahan, 2006).

Geologic description	Mean V_{s30}
Tertiary (mostly Miocene and Pliocene) shale and siltstone units such as the Repetto, Fernando, Puente, and Modelo Formations of the Los Angeles area	390
Tertiary (mostly Miocene, Oligocene, and Eocene) sandstone units such as the Topanga Formation in the Los Angeles area and the Butano sandstone in the San Francisco Bay area	515
Cretaceous sandstone of the Great Valley Sequence in the central Coast Ranges	566

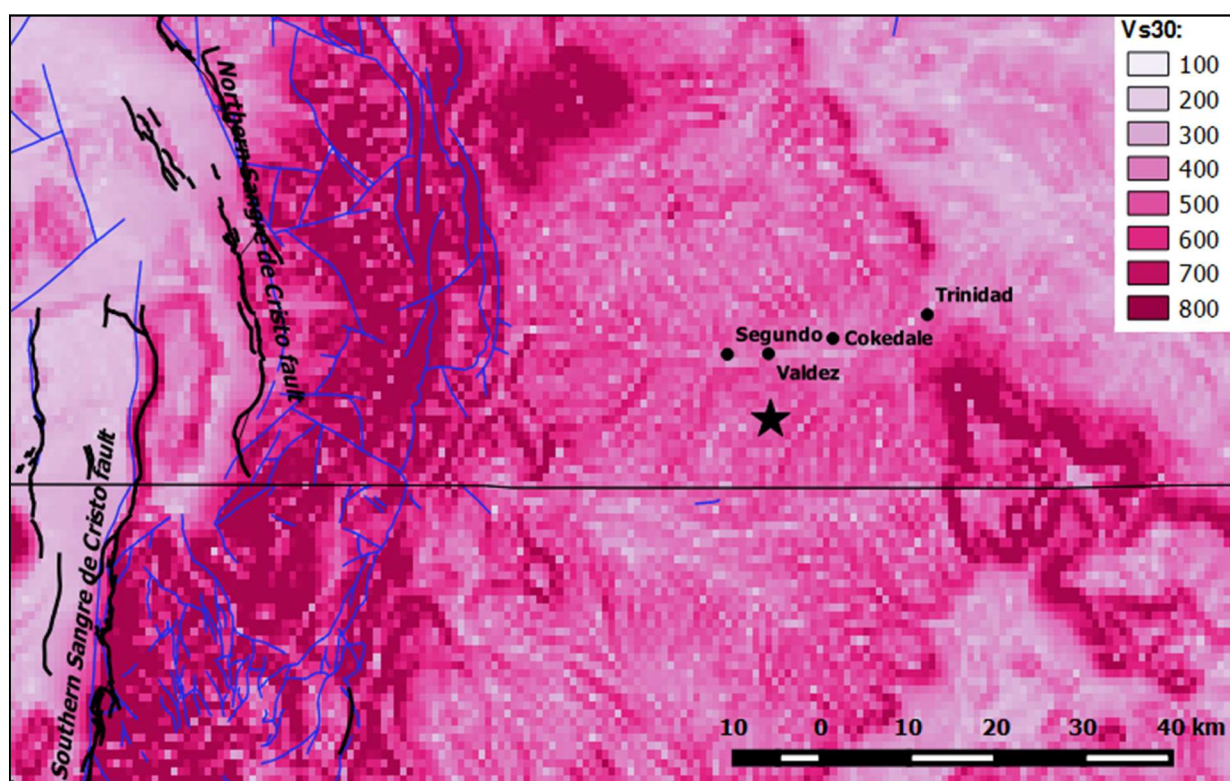


Figure A3.4.10. Estimation of V_{s30} in the Raton Basin using topographic slope as a proxy. From the USGS V_{s30} Map Server (Wald & Allen, 2007).

A3.4.4 Ground motions

A3.4.4.1 Intensity observations

Four locations were reported to have suffered structural damage in their building stocks. From most severe to least, these are: Segundo, Valdez, Cokedale and Trinidad (Morgan & Morgan, 2011). According to the written report at the USGS website, the Modified Mercalli Intensities (MMI) at these sites were VII (very strong shaking, moderate damage) at Segundo, VI (strong shaking, minor damage) at Cokedale and Valdez, and V (moderate shaking, minor damage) at Trinidad. The main shock was felt in most of eastern and central Colorado and in parts of south-western Colorado. It was also felt widely in south-western Nebraska, western Kansas and north-eastern New Mexico, and felt in a few places in Texas, at Cheyenne, Wyoming and at Omaha, Nebraska.

In spite of the intensity at Segundo being reported as VII, the two MMI ShakeMaps produced by the USGS (Worden *et al.*, 2017) do not reach this intensity level. Figure A3.4.11 (top) shows the automatically calculated ShakeMap, while Figure A3.4.11 (bottom) presents the revised version (dated October 2014). As can be observed, the automatically calculated version reaches values closer to VII, while the revised one only gets to IV-V. This difference is most likely due to aggregation of Did You Feel It? reports by zip codes and the incorporation of instrumental intensities derived from recorded peak ground acceleration values. In any case, and as it will become clear in the section regarding damage observations, the MMI VII value assigned to Segundo probably has its origin in the damage assessment carried out by the Colorado Geological Survey, and reported in Morgan & Morgan (2011). According to the website of the USGS, the newer ShakeMap has been calculated using 34 Did You Feel It? Points and data from 44 seismic stations, all of the latter located over 100 km away from the epicentre except for station T25A (27 km), in combination with relevant intensity prediction models.

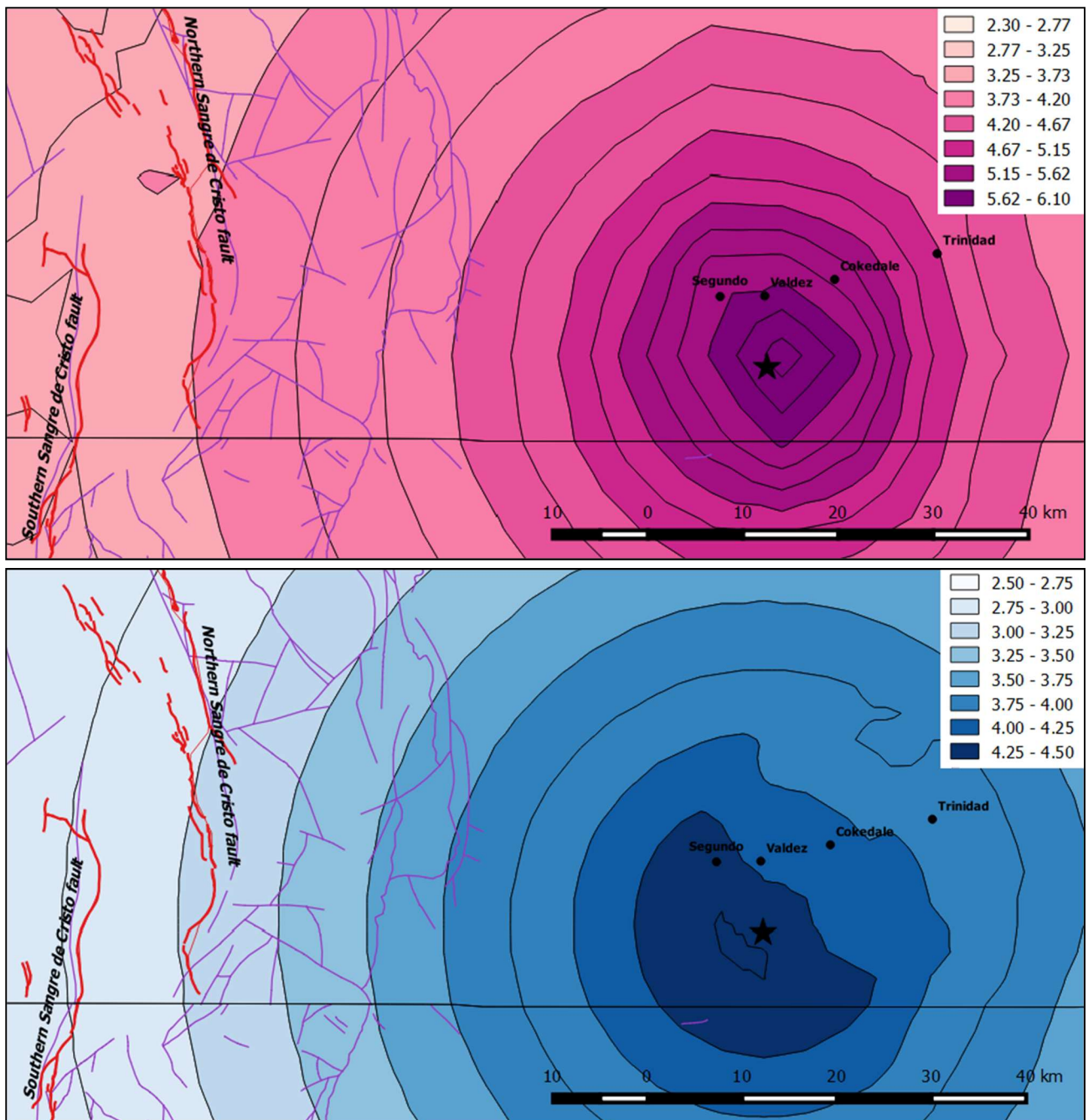
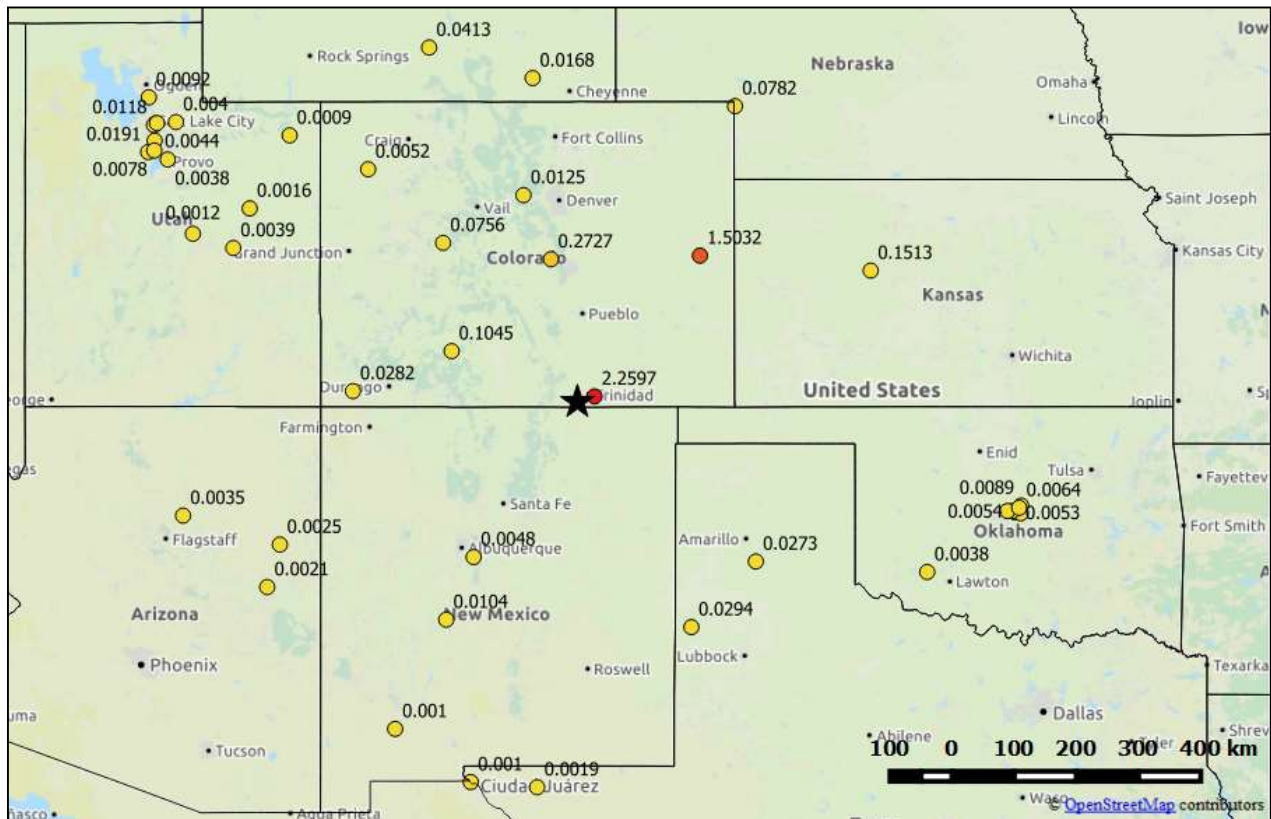


Figure A3.4.11. USGS ShakeMaps in terms of Modified Mercalli Intensities (MMI): initial automatic calculation (top), and revised calculation (bottom, version dated October 2014). The black star is the epicentre of the main shock, according to the USGS.

A3.4.4.2 Ground motion recordings

Information on ground motion recordings for this earthquake is scarce. The website of the USGS provides information on peak ground acceleration (PGA), peak ground velocity (PGV) and pseudo-spectral acceleration at 0.3, 1.0 and 3.0 seconds at some locations. The maximum recorded PGA was 2.26% g, and was observed at station T25A, around 27 km away from their estimated epicentral coordinates, close to the city of Trinidad. The list of highest recorded PGA values continues with 1.50% g registered over 280 km away (station KSCO). All remaining recorded values are smaller than 0.27% g (station Q24A, 213 km). The two largest values of PGV were 1.43 and 1.23 cm/s, registered at KSCO and

T25A stations, respectively. The maximum observed pseudo-spectral acceleration values were 4.26% g, 2.14% g and 0.53% g, at 0.3, 1.0 and 3.0 seconds, respectively.



A3.4.4.3 Inferred shaking levels

The initial automatically calculated ShakeMap (Figure A3.4.13, left) suggests a maximum 10% g PGA within a 15 km diameter circle around the epicentre, slightly shifted to the East. Values provided in the revised map dated October 2014 (Figure A3.4.13, right) are significantly higher. Values within the same 15 km diameter circle around the epicentre are larger than 36% g. Station T25A, with its 2.26% g, lies within an area of this map in which a value of 6% g is estimated. An updated version of this ShakeMap dated March 2018 reaches a maximum 15% g, which is more in agreement with the initial version than with that of October 2014. The lack of stability of the results from the ShakeMap are probably due to the availability of only one seismic station and very few Did You Feel It? Responses

in the near-field. Comments regarding these discrepancies have not been found in the literature.

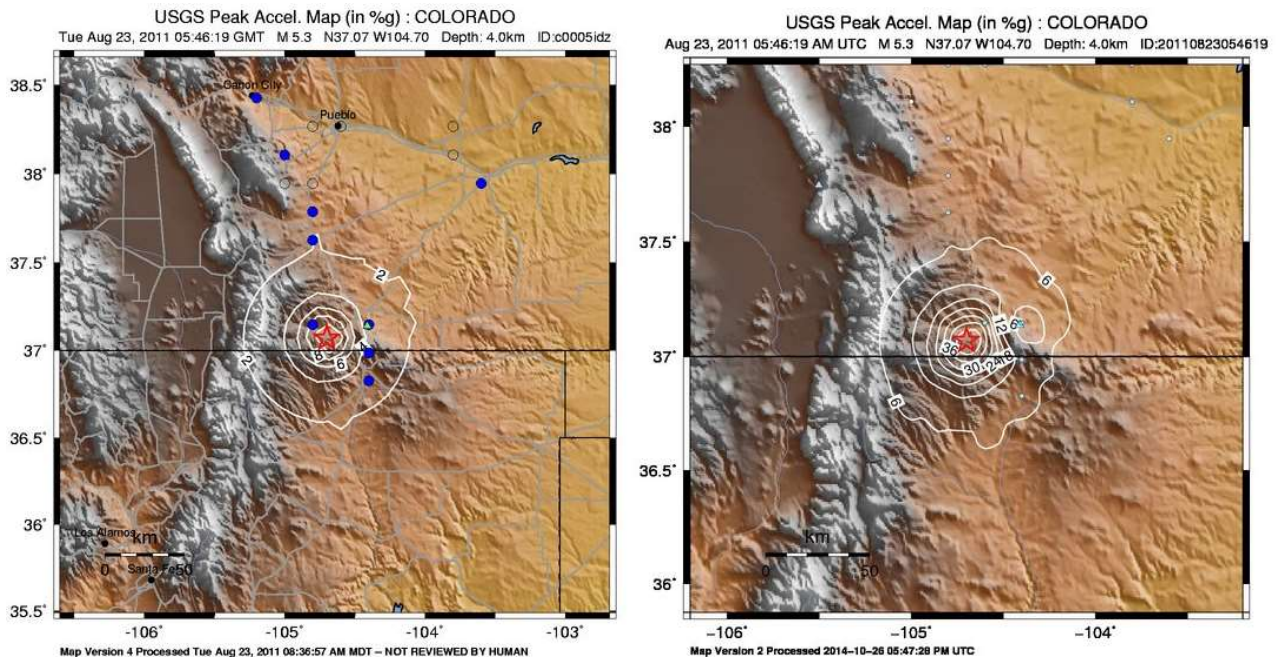


Figure A3.4.13. USGS ShakeMaps in terms of peak ground acceleration: initial automatic calculation (left), and revised calculation dated October 2014 (right). Note the difference in scale between the two figures (USGS, 2015).

A3.4.4.4 Duration of ground shaking

According to Morgan & Morgan (2011), in Segundo, the most severely-hit town, the resident whose house experienced the most severe damage said the earthquake lasted for "about a minute".

Estimations of earthquake significant durations can be obtained by means of prediction equations such as those of Bommer *et al.* (2009) and Afshari & Stewart (2016), whose results for the 5-75% of Arias intensity definition of significant duration are shown in Figure A3.4.14. V_{s30} values reported by Wills & Clahan (2006) for Californian geologic units comparable to those of the Raton Basin are used (Figure A3.4.5), though a larger range from 180 to 800 m/s is included in Figure A3.4.14 for completeness. Closest distances from the fault rupture are not known with precision, so epicentral distances to Segundo (6.80 km) and station T25A (26.35 km), as well as an arbitrary 50.00 km case are used to estimate the significant duration of this earthquake. A 1.50 km depth to the top of rupture is used, based on the work by Barnhart *et al.* (2014). Results¹ shown in Figure A3.4.14 are well below the duration reported by Morgan & Morgan (2011). While it is noted that the perception of the general public of the duration of a seismic event tends to be exaggerated, this agrees with the observations of Barnhart *et al.* (2014), who reported that the main shock was "unexpectedly long for a M5.3 event".

¹ Calculated as per a previous version of this report with M5.3 instead of the finally adopted M5.4.

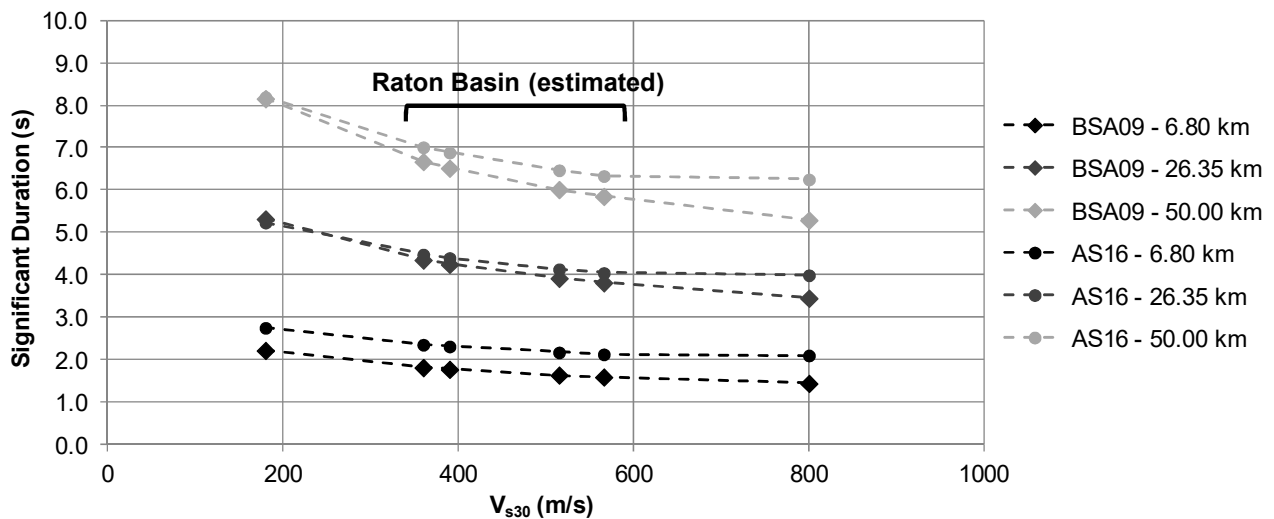


Figure A3.4.14. Estimation of the significant duration of the main shock, using prediction equations by Bommer *et al.* (2009, BSA) and Afshari & Stewart (2016, AS).

A3.4.5 Collateral earthquake hazards

A3.4.5.1 Surface rupture

Surface rupture not reported for this earthquake.

A3.4.5.2 Landslides

Morgan & Morgan (2011) report rockfalls covering the State Highway 12, a road approximately 1.5 km east of Segundo. Some of the rock fragments were larger than 1.8 m, but damage to the pavement seems to have been null or minimum. The rocks were quickly removed.

A3.4.5.3 Liquefaction

In their report on the damage assessment carried out by the Colorado Geological Survey, Morgan & Morgan (2011) raise the question of whether the house that suffered the most severe damage had experienced issues associated to liquefaction. The authors report that the residents said the ground "seemed to rotate" and interpret this as a possible consequence of liquefaction. However, given the extremely low phreatic level (500 m, according to Rubinstein *et al.*, 2014), liquefaction seems unlikely, and the residents' description most likely refers to the motion of the ground due to Rayleigh waves.

A3.4.5.4 Settlements

Settlements not reported for this earthquake.

A3.4.6 Exposed population

A3.4.6.1 Socio-economic setting

According to the 2014 Human Development Report (United Nations, 2014), the Human Development Index (HDI) for the United States in 2013 was 0.914, while its Inequality-adjusted HDI (IHDI) was 0.755. This located the USA in the 5th place in the world's ranking, while the Netherlands ranks 4th. Table A3.4.6 compares the HDI and IHDI for both countries from the last three Human Development Reports (United Nations, 2011; United Nations, 2013; United Nations, 2014). The column "Adj. HDI" provides the HDI values given in the 2014 report for previous years, adjusted for data consistency in time.

Table A3.4.6. Human Development Index and Inequality-adjusted Human Development Index for the United States and the Netherlands.

Report	Data	Unites States of America				Netherlands			
		HDI	IHDI	Rank	Adj. HDI	HDI	IHDI	Rank	Adj. HDI
2011	May 2011	0.910	0.771	4	0.911	0.910	0.846	3	0.914
2013	October 2012	0.937	0.821	3	0.914	0.921	0.857	4	0.915
2014	November 2013	0.914	0.755	5	-	0.915	0.854	4	-

Table A3.4.7 presents a comparison between the United States and the Netherlands in terms of GDP, GDP per capita and unemployment rate.

Table A3.4.7. Gross domestic product (GDP), GDP per capita and unemployment rate for the United States and the Netherlands, according to the World Economic Outlook Database 2015.

Indicator	Units	Unites States		Netherlands	
		2011	2014	2011	2014
Gross domestic product, current prices	Billions of US dollars	15,517.925	17,418.925	894.576	866.354
Gross domestic product per capita, current prices	US dollars	49,724.999	54,596.653	53,589.909	51,372.963
Unemployment rate	% of total labor force	8.942	6.150	4.980	7.395

During the mid-19th century, mining was the most significant economic activity in the state of Colorado, but it was slightly overshadowed when irrigated agriculture developed and raising livestock acquired importance by the late 19th century (Wikipedia). Early industries grew around these activities. Nowadays, agricultural products produced in Colorado include cattle, wheat, dairy products, corn, and hay. Industrial and service sectors, as well as scientific research, expanded significantly during the second half of the 20th century. Modern industries in the state include food processing, transportation equipment, machinery, and chemical products. Furthermore, the state of Colorado ranked seventh of all the United States in total energy production in 2014, and sixth in natural gas marketed production in 2015, according to the United States Energy Information Administration (EIA, 2016).

The large economic crisis that began in 2008 had a significant impact on the United States, causing high unemployment, an increasing federal debt, and inflation. In 2011, the Gross Domestic Product (GDP) increased in 43 of the 50 states of the USA. The state of Colorado presented a 1.9% increase in its GDP, a value that positioned it within the second to highest quintile (Bureau of Economic Analysis, U.S. Department of Commerce, 2012). During the year 2012, the state of Colorado ranked 15th with respect to GDP per capita, whose value was an 8% higher than that of the USA as a whole.

A3.4.6.2 Population density and distribution

The Raton Basin is sparsely populated (Matthews, 2011). Table A3.4.8 shows the population by 1st April 2010 of the four most affected towns. According to Gridded Population of the World v.3.0 (CIESIN, 2005), population density in the year 2010 around Segundo and Valdez and the Raton Basin in general was estimated to be less than 10 people per square kilometre. Around Cokedale, values are closer to 20 people/km². Trinidad is more populated, and reaches a density of around 100 people/km² in average².

Table A3.4.8. Population of the four towns which were most affected by this earthquake. Data from American Fact Finder (2016).

City	Population 1 st April 2010
Segundo	98
Valdez	47
Cokedale	129
Trinidad	9,096

As Segundo, Valdez and Cokedale are extremely small towns, their population density is very uneven (55, 11 and 249 people/km², respectively), as it is highly sensitive to the area assigned to each. This sensitivity becomes evident when looking at the case of the city of Trinidad against the census county division (CCD) of Trinidad: 378 people/km² for the former, but 8 people/km² for the latter, with a total population of 9,096 and 12,017 people, respectively (American Fact Finder, 2016). In any case, it is clear from the values presented in Table A2.4.8 that the area most severely hit by this event is scarcely populated. It is perhaps the density for the whole of Las Animas county, where Segundo, Valdez, Cokedale and Trinidad are located, that works as the best indicator: 1.25 people/km² and 0.66 housing units/km². The towns of Segundo, Valdez and Cokedale, and the city of Trinidad had 82, 26, 94 and 4,375 housing units each.

In the same way there is disagreement between the initial automatically calculated ShakeMaps and intensity estimations, the USGS PAGER exposure report generated within the first hour of the earthquake differs slightly from its revised version, generated

² Due to the extremely small spatial extent of Segundo, Valdez and Cokedale, the resolution of GPW v3.0 (2.5 arc-minutes) was too coarse to provide accurate values, as confirmed by the contrast with the values reported by the US Census. The more recent GPW v4.0, with a 30 arc-sec resolution, gives densities of 4, 17 and 183 people/km² for Valdez, Segundo and Cokedale, respectively. The average and maximum density in the city of Trinidad are 88 and 1241 people/km² according to GPW v4.0 too.

after nine hours of the event. As shown in Figure A3.4.15 (left), initial estimations included an exposure of 23 people to MMI VII, while adjusted estimations eliminate this exposure level altogether (Figure A3.4.15, right).

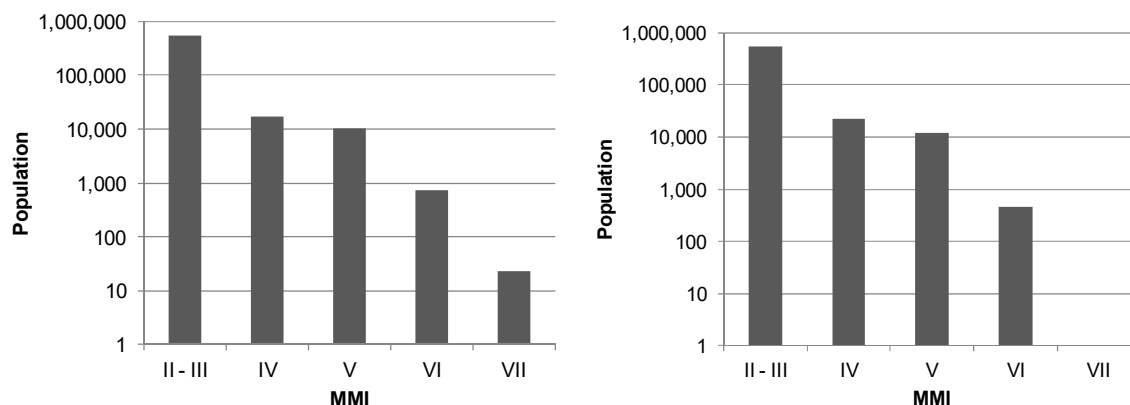


Figure A3.4.15. Estimation of total population exposed to different Modified Mercalli Intensities (MMI) one hour after the main shock (left) and nine hours after the main shock (right) (USGS, 2015).

A3.4.6.3 Time of day of earthquake

The main shock occurred on 22nd August 2011, 23.46 local time. Given the type of damage and the absence of casualties, the time of occurrence of the event did not have a significant impact over its consequences.

A3.4.7 Characteristics of exposed building stock

A3.4.7.1 Seismic design codes

While Cutcliffe (2000) believes that it was the 1906 San Francisco earthquake which marked the start of a real interest in earthquake engineering and seismic design in the United States, Freeman (1932) stated a quarter of a century later that "the art of constructing earthquake-resisting buildings is still in the formative stage, that there are differences of opinions among experts and that there is much deficiency in important data". Further, he points at the 1925 Santa Barbara earthquake to have been more significant in raising awareness on the subject. It was this devastating event that prompted the first edition of the Uniform Building Code (UBC) in 1927, which contained the first written seismic design provisions for a regional level, but which did not become mandatory until 1961 (Beavers, 2002).

As recapitulated by Beavers (2002), the origin of seismic design codes and building codes in general in the USA started in a fragmented fashion, by regions or states. For example, the Uniform Building Code (UBC) just mentioned above was typically used west of the Mississippi river. The National Building Code of the Building Officials and Code Administrators (BOCA) (known as the BOCA Code) was, instead, used in the upper midwest and northeast. It was first published in 1950, including seismic design provisions.

In the south, the Standard Building Code (SBC) of the Southern Building Code Congress International (SBCCI) was used. Seismic design provisions were included in the SBC in 1976, by referencing ANSI A58.1, but "were not mandatory unless local authorities required seismic design, which was rarely the case", until 1988. The 1987 edition of the BOCA Code also incorporated the provisions of ANSI A58.1, and made them mandatory.

The ANSI A58.1 standard of the American National Standards Institute (ANSI) was first published in 1945, and was the first standard to consider earthquake loads (Beavers, 2002). However, seismic hazard did not have a role in ANSI A58.1, which only had a map showing the locations of destructive earthquakes of the past until its 1972 edition, in which a seismic hazard description similar to the 1949 USCGS (United States Coast and Geodetic Survey) map was incorporated. The 1972 edition of ANSI A58.1 was also the first one to outline modern wind design provisions (Fratinaro & Schroeder, 2015; Ghosh, 2008), evolving from more basic guidelines developed in the 1950s (Huston, 2007).

The 1949 hazard map was the first one to encompass the whole of the contiguous USA, and it was based on "the premise that similar earthquakes will occur in the future where they have occurred in the past" (Beavers, 2002). For reasons that are not fully clear, this map was withdrawn in 1952, and replaced with a map that only showed the location of known past significant earthquakes. In the 1970s, the responsibility of producing hazard maps passed on to the USGS (United States Geological Survey), who published the first map developed in the form of probabilistic estimates of maximum acceleration contours on rock in 1976, and which, as highlighted by Beavers (2002), represented a significant paradigm shift. It should be noted, however, that the first edition of the ATC3-06, which in 1985 evolved into the National Earthquake Hazards Reduction Program (NEHRP) Recommended Provisions for Seismic Regulations for New Buildings and Other Structures, used a truncated version of this map in 1978, not allowing for values above 0.4g to be considered. This map was used for almost 20 years, given the inability to reach consensus on a different map that took place in between 1988 and 1994. It was finally updated by the USGS in 1997, after a four-year project called Project 97, during which large efforts were invested in giving a voice to all the professionals and sectors involved. Since then, the USGS hazard map has been updated in 2002, 2008 and 2014.

The way in which seismic loads were considered evolved significantly from the simple use of a 7.5%-10.0% of the building's weight as a lateral load (1927 edition of the UBC), with the progressive incorporation of significant factors such as soil type and capacity, seismic zonation, natural period of vibration of the structure, and importance of the building.

In 1988, ANSI combined with ASCE to update and re-designate ANSI A58.1-1982 to ASCE 7, which is now the most significantly recognised standard by all earthquake regulations, codes, standards, procedures and guidelines for basic seismic design in the USA (Beavers, 2002). Furthermore, ASCE 7 is also the "de facto" national wind design standard (Fratinaro & Schroeder, 2015). The International Building Code (IBC), whose first edition in 2000 was based in the NEHRP Provisions, makes reference to ASCE 7 for the definition of seismic and wind loads. Regarding the latter, it should be noted that,

according to ASCE 7-05 (ASCE, 2005), the area affected by the 2011 Trinidad earthquake corresponds to a so-called "special wind region", prone to tornado-like wind speeds.

As mentioned in Section A3.4.1.3, it is noted that the national seismic hazard maps of the United States (and all other countries in the world) do not take into consideration induced seismic activities and, consequently, areas for which most ground shaking is believed to have an anthropogenic origin might be seismically designed but for ground motion levels that might not reflect the short-term likelihoods being currently experienced.

The IBC 2012 is currently in force in the state of Colorado and is "to be applied to all state-owned buildings and physical facilities including capital construction and controlled maintenance construction projects" (State of Colorado, 2014). No regulation referring to privately-owned buildings has been found.

The Building Code Effectiveness Grading Schedule (BCEGS), developed by the Insurance Services Office (ISO), indicates that the overall level of code enforcement across the state of Colorado is relatively low when compared to the country as a whole and to states like California, in which awareness with respect to seismic risk is much greater. Figure A3.4.16 shows the distribution of communities by BCEGS class number for the United States as a whole and for the state of Colorado. Within this classification schedule, classes 1-3 correspond to the maximum enforcement levels, while class 10 indicates no enforcement at all. These figures agree with statements of Beavers (2002) and Cutcliffe (2000), who highlight that, due to their relative lack of seismic activity, the effort to incorporate good seismic design practises in building codes has been more challenging in the central and eastern USA, when compared to other areas of the country.

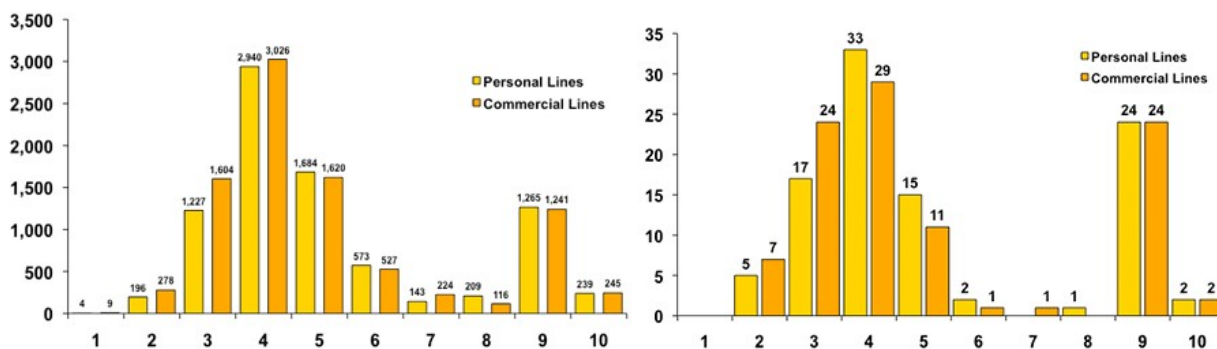


Figure A3.4.16. Distribution of communities by BCEGS class number for the whole of the United States (left) and the state of Colorado (right). Personal lines include 1- and 2-family dwellings. Commercial lines include all other buildings. Classes 1-3: maximum enforcement. Class 10: no enforcement ISO Mitigation (2015)

A3.4.7.2 Building typologies

Information regarding building typologies in the state of Colorado is scarce to null. For this reason, data regarding typologies at the country level were collected from the PAGER Inventory Database v2.0 (Jaiswal & Wald, 2008). Figure A3.4.17 shows that the structure of most of the buildings in the USA consists of light wood frames (61.2%), and

unreinforced brick masonry (19.3%) in a smaller proportion. The remaining 19.4% is mostly made up of heavy wood frames and mobile homes (Figure A3.4.18). From available pictures of damage caused by the 2011 Trinidad earthquake it seems possible to infer that light wood frames and unreinforced brick masonry are probably the most likely building typologies in the affected area.

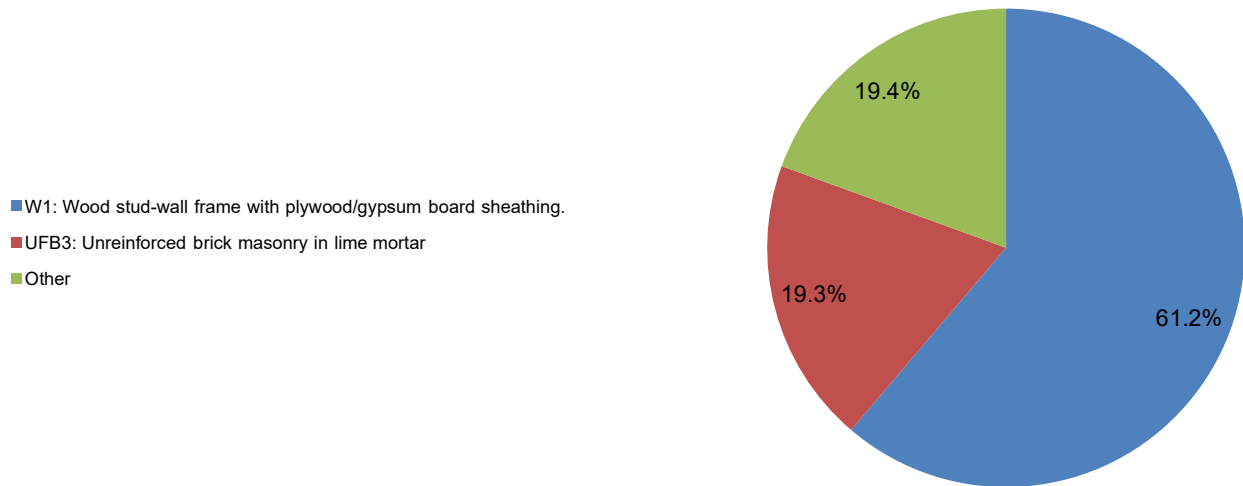


Figure A3.4.17. Proportion of buildings in the United States belonging to each typology. The subcategories within class "Other" are expanded upon in the figure below (Jaiswal & Wald, 2008).

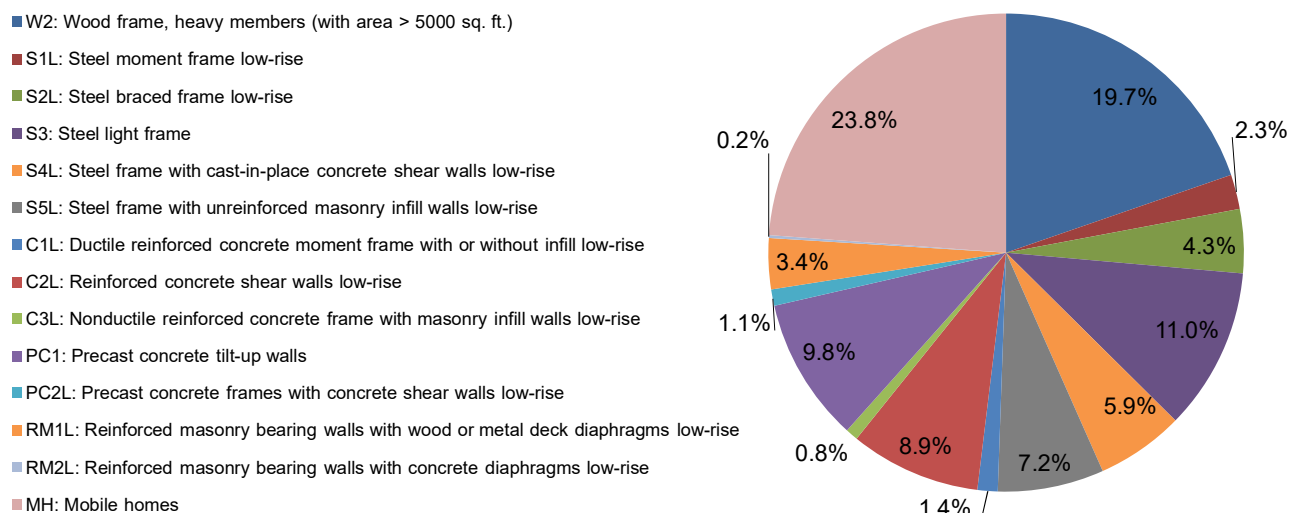


Figure A3.4.18. Breakdown of the "Other" class in the figure above. To determine the percentage that each of these sub-categories represents of the total in the USA, multiply the value in this figure by 0.194 (Jaiswal & Wald, 2008).

A3.4.7.3 Prior damage and retrofit

No details on prior damage or retrofit available.

A3.4.8 Damage observations

A3.4.8.1 Damage states

Given the relatively low level of damage observed, there are no reports making use of standardised damage scales for this earthquake. However, from the qualitative descriptions, it is possible to believe that most damage observed corresponded to Grade 2 in the European Macroseismic Scale (EMS-98; Grünthal, 1998). For details regarding the latter, please refer to Section 3.8.1 of Chapter 3 and Appendix II. The damage observed appears to be in agreement with the maximum MMI of VII reported, when considering its implications for damage (Table A2.3.2 of Appendix II).

A3.4.8.2 Damage statistics and description

As mentioned earlier, the four locations in which structural damage was observed were, from most severe to least, Segundo, Valdez, Cokedale, and Trinidad (Morgan & Morgan, 2011, see locations in Figure A3.4.11). According to Matthews (2011), forty-six structures were damaged, beyond repair in only two cases. It seems that one of these cases was reported in Segundo, but Morgan & Morgan (2011) state that this could not be verified, due to the will of the owners of the property to remain anonymous.

Located at approximately 6.8 km from the epicentre, both Segundo and Valdez saw several displaced/pulled-away façades and chimneys, significant cracks in masonry walls, and masonry blocks and bricks collapsing and causing additional damage due to their fall. Offsets of façades and walls reported by Morgan & Morgan (2011) range from 1 cm to 5 cm. Figs. II.4.19 and 20 show some examples of this kind of damage.

Cracked plaster was observed in all four towns mentioned, being the case of the 3 metres vertical crack at the Cokedale post office/city hall building the worst (Figure A3.4.21). Nevertheless, the town mayor of Cokedale (located at approximately 11.5 km from the epicentre) reported "no significant damage" to the residences in the area (Morgan & Morgan, 2011).

Regarding Trinidad, located at approximately 21 km from the epicentre, Morgan & Morgan (2011) only report a plaster and metal siding fall from the front of a coffee shop.

A3.4.8.3 Observed weaknesses

No reports of systematic weaknesses were found in the literature. However, the kind of damage observed and the statements by Beavers (2002) and Cutcliffe (2000) regarding the challenges faced by the efforts to incorporate good seismic design practises in the central and eastern USA suggest that the lack of seismic design of masonry structures was the main cause of the damage observed.

A3.4.8.4 Damage distribution

There are no details available with respect to the distribution of damage within the towns. Nevertheless, it should be noted that the towns which suffered the most damage are significantly small (less than 100 people in Segundo, and less than 50 people in Valdez).



Figure A3.4.19. Damage observed at Segundo: on the left, the exterior wall pulled away approximately 2.5 cm from the interior wall; on the right, the front of this brick building collapsed (Morgan & Morgan, 2011).



Figure A3.4.20. Major brick damage to a home in Segundo (left) and to a garage in Valdez (right) (Morgan & Morgan, 2011).



Figure A3.4.21. A 3 metres long vertical crack in the building of the Cokedale post office/city hall (left); cracked plaster on a façade in Segundo (Morgan & Morgan, 2011).

A3.4.9 Casualties and losses

A3.4.9.1 Numbers of dead and injured

No casualties reported.

A3.4.9.2 Causes of casualties

No casualties reported.

A3.4.9.3 Estimates of economic losses

According to Morgan & Morgan (2011), none of the damaged structures were covered by earthquake insurance, and the economic loss was expected to exceed 100,000 US dollars. This figure is in agreement with the estimation from USGS PAGER (2015) according to which the economic loss was not expected to exceed one million US dollars. The Significant Earthquake Database of the National Centers for Environmental Information of the National Oceanic and Atmospheric Administration (NOAA) of the United States places the loss estimates between 1 and 5 million US dollars.

A3.4.10 Discussion and conclusions

This M5.4 earthquake occurred on 23rd August 2011, at 05.46 UTC (22nd August 2011, 23.46 local time), and was the largest to take place in Colorado in around half a century. It was part of a sequence that started with a series of small foreshocks the day before and was followed by over 500 events in the following four months. Whilst tectonic earthquakes have been known to occur in the Raton Basin area, this event is believed to have been induced by deep injection of wastewater in the Raton Basin.

The main shock was widely felt and caused damage to around 46 buildings (two of which were deemed unrepairable) in the scarcely populated towns of Segundo, Valdez, Cokedale and Trinidad, all located within 20 km of the epicentre. These structures are likely to have been either low-rise wooden light frames or bearing unreinforced masonry. Common instances of damage included displaced façades and chimneys, the out-of-plane collapse of masonry gables, cracks in bearing and non-bearing masonry, and cracks in plaster. Rockfalls occurred at the State Highway 12, a road approximately 1.5 km east of Segundo, causing minimum disruption and no damage to buildings. No casualties were reported.

In spite of there being some disagreement amongst different estimations of the ground motion level to which the damaged structures were subject, an accelerogram recorded near the town of Trinidad suggests that it was not particularly high. It is thus likely that the significant damage observed be due to the lack of seismic design of masonry structures in the area, in spite of their (possible) wind design.

A3.4.11 References

A3.4.11.1 Bibliography

Afshari, K. & J.P. Stewart (2016). Physically parametrised prediction equations for significant duration in active crustal regions. *Earthquake Spectra* **32**(4), 2057-2081.

American Society of Civil Engineers, Structural Engineering Institute (2005). *Minimum Design Loads for Buildings and Other Structures*, ASCE/SEI 7-05. Reston, VA, United States.

Barnhart, W.D., H.M. Benz, G.P. Hayes, J.L. Rubinstein & E. Bergman (2014). Seismological and geodetic constraints on the 2011 M_w 5.3 Trinidad, Colorado earthquake and induced deformation in the Raton Basin. *Journal of Geophysical Research: Solid Earth* **119**, 7923–7933.

Beavers, J.E. (2002). A review of seismic hazard description in US design codes and procedures. *Progress in Structural Engineering and Materials* **4**, 46–63.

Bommer, J.J., P.J. Stafford & J.E. Alarcón (2009). Empirical equations for the prediction of the significant, bracketed, and uniform duration of earthquake ground motion. *Bulletin of the Seismological Society of America* **99**(6), 3217-3233.

Bott, J.D.J. & I.G. Wong (1995). The 1986 Crested Butte earthquake swarm and its implications for seismogenesis in Colorado. *Bulletin of the Seismological Society of America* **85**, 1495-1500.

Center for International Earth Science Information Network - CIESIN - Columbia University, United Nations Food and Agriculture Programme - FAO, and Centro Internacional de Agricultura Tropical - CIAT (2005). *Gridded Population of the World, Version 3 (GPWv3)*. Palisades, NY: NASA Socioeconomic Data and Applications Center (SEDAC). <http://dx.doi.org/10.7927/H4639MPP>.

Cutcliffe, S.H. (2000). Earthquake resistant building design codes and safety standards: The California experience. *GeoJournal* **51**, 259–262.

Dziewonski, A.M., T.-A. Chou & J. H. Woodhouse (1981). Determination of earthquake source parameters from waveform data for studies of global and regional seismicity. *Journal of Geophysical Research* **86**, 2825-2852.

Ekström, G., M. Nettles & A. M. Dziewonski (2012). The global CMT project 2004-2010: Centroid-moment tensors for 13,017 earthquakes. *Physics of the Earth and Planetary Interiors* **200-201**, 1-9.

Flores, R.M. (1987). Sedimentology of Upper Cretaceous and Tertiary siliciclastics and coals in the Raton Basin, New Mexico and Colorado, in Lucas, S.G. & Hunt, A.P., eds., *Northeastern New Mexico*. New Mexico Geological Society 38th Annual Field Conference, 255–264.

Flores, R.M. & Bader, L.R. (1999). A summary of Tertiary coal resources of the Raton Basin, Colorado and New Mexico, chap. SR of Fort Union Coal Assessment Team, 1999 Resource Assessment of Selected Tertiary Coal Beds and Zones in the Northern Rocky Mountains and Great Plains Region. U.S. Geological Survey Professional Paper 1625-A [available only on CD-ROM].

Fratinaro, V.F. & S.A. Schroeder (2015). Historical study of the wind design provisions of ASCE 7. *Structures Congress 2015*, 829–839.

Freeman J.R. (1932). *Earthquake Damage and Earthquake Insurance*. 1st edition. New York: McGraw-Hill.

- Ghosh, S.K. (2008). Searching for simplicity: The evolution of wind provisions in standards and codes in the United States. *RCI Interface*, 13–21.
- Giardini, D., G. Grünthal, K.M. Shedlock & P. Zhang (1999). The GSHAP global seismic hazard map. *Annali di Geofisica* **42**(6), 1225-1228.
- Grünthal, G. (ed.) (1998). *European Macroseismic Scale 1998 (EMS-98)*. Cahiers du Centre Europeen de Geodynamique et de Seismologie 15, Centre Europeen de Geodynamique et de Seismologie, Luxembourg.
- Huston, E. (2007). SEAW's handbook of a rapid-solutions methodology for wind design. *Struct. Mag.*, 61–64.
- Jaiswal, K. & D.J. Wald (2008). Creating a Global Building Inventory for Earthquake Loss Assessment and Risk Management. USGS Open File Report 2008-1160. Available electronically at <http://pubs.usgs.gov/of/2008/1160/>. Last accessed: 9th February 2017.
- Johnson, R. (1969). *Geologic map of the Trinidad quadrangle, south-central Colorado*. U.S. Geol. Surv. Misc. Geol. Investig. Map I-558.
- Johnson, R.C. & T.M. Finn (2001). *Potential for a basin-centered gas accumulation in the Raton Basin, Colorado and New Mexico - Geologic studies of basin-centered gas systems*. U.S. Geological Survey Bulletin 2184-B, US Department of the Interior, US Geological Survey. Available only online: <http://geology.cr.usgs.gov/pub/bulletins/b2184-b/>. Last accessed: 9th February 2017.
- Matthews, V. (2011). The Trinidad, Colorado earthquakes. *Colorado Geological Survey*. Available online at: <http://2fdpn7hy0ht206jws2e9og41.wpengine.netdna-cdn.com/wp-content/uploads/2013/08/Trinidad-2011.pdf>. Last accessed 20th August 2018.
- Morgan, M.L. & K.S. Morgan (2011). Preliminary damage report of the August 22, 2011 Mw 5.3 earthquake near Trinidad, Colorado. *Colorado Geological Survey*. Available online at: <http://coloradogeologicalsurvey.org/wp-content/uploads/2013/08/Preliminary-Damage-Report-of-the-Mw-5-3-Trinidad-Earthquake.pdf>. Last accessed 20th August 2018.
- National Geophysical Data Center / World Data Service (NGDC/WDS): Significant Earthquake Database. National Geophysical Data Center, National Oceanic and Atmospheric Administration (NOAA). DOI:10.7289/V5TD9V7K. <https://www.ngdc.noaa.gov/hazard/earthqk.shtml>. Last accessed: 24th December 2017.
- Petersen, M.D., A.D. Frankel, S.C. Harmsen, C.S. Mueller, K.M. Haller, R.L. Wheeler, R.L. Wesson, Y. Zeng, O.S. Boyd, D.M. Perkins, N. Luco, E.H. Field, C.J. Wills & K.S. Rukstales (2008). *Documentation for the 2008 update of the United States National Seismic Hazard Maps*. USGS Open-File Report 2008-1128, 61 pp.
- Petersen, M.D., M.P. Moschetti, P.M. Powers, C.S. Mueller, K.M. Haller, A.D. Frankel, Y. Zeng, S. Rezaeian, S.C. Harmsen, O.S. Boyd, N. Field, R. Chen, K.S. Rukstales, N. Luco, R.L. Wheeler, R.A. Williams & A.H. Olsen (2014). *Documentation for the 2014 update of the United States National Seismic Hazard Maps*. USGS Open-File Report 2014-1091, 243 pp.
- Pillmore, C.L. (1969). Geology and coal deposits of the Raton coal field, Colfax County, New Mexico. *The Mountain Geologist* **6**, 125–142.
- Pillmore, C.E. & R.M. Flores (1987). Stratigraphy and depositional environments of the Cretaceous-Tertiary boundary clay and associated rocks, Raton Basin, New Mexico and Colorado, in Fassett, J.E. & Rigby, J.K., Jr., eds., *The Cretaceous-Tertiary Boundary in the San Juan and Raton Basins, New Mexico and Colorado*. *Geological Society of America* **209**, 111–130.

Robson, S. & E. Banta (1987). *Geology and hydrology of deep bedrock aquifers in eastern Colorado*. USGS Water-Resources Investig. Rept. 85-4240, 22 pp.

Rubinstein, J.L., W.L. Ellsworth, A. McGarr & H.M. Benz (2014). The 2001-present induced earthquake sequence in the Raton Basin of northern New Mexico and southern Colorado. *Bulletin of the Seismological Society of America* **104**, 2162–2181.

Sheehan, A.F., J.D. Godchaux & N. Hughes (2003). Colorado Front Range seismicity and seismic hazard. *Engineering Geology in Colorado: Contributions, Trends and Case Histories*.

Scott, G. R. & C. L. Pillmore (1993). *Geologic and structure-contour map of the Raton 30'x 60' quadrangle, Colfax and Union Counties, New Mexico, and Las Animas County, Colorado*. U.S. Geol. Surv. Misc. Geol. Investig. Map I-2266.

State of Colorado (2014). *Building code compliance policy: Coordination of approved building codes, plan reviews and building inspections*. Office of the State Architect, State Buildings Programs, Policies and Procedures, Colorado, United States.

United Nations, ed. (2011). *Human Development Report 2011 - Sustainability and equity: A better future for all*. Report of the United Nations Development Programme (UNDP), New York, United States.

United Nations, ed. (2013). *Human Development Report 2013 - The rise of the South: Human progress in a diverse world*. Report of the United Nations Development Programme (UNDP), New York, United States.

United Nations, ed. (2014). *Human Development Report 2014 - Sustaining human progress: Reducing vulnerabilities and building resilience*. Report of the United Nations Development Programme (UNDP), New York, United States.

Wald, D.J. & T.I. Allen (2007). Topographic slope as a proxy for seismic site conditions and amplification. *Bulletin of the Seismological Society of America* **97**, 1379–1395. Slope-based online map viewer available at: <http://usgs.maps.arcgis.com/apps/webappviewer/index.html?id=8ac19bc334f747e486550f32837578e1>. Data used herein downloaded from deprecated version last accessed on 6th November 2015.

Wills, C.J. & K.B. Clahan (2006). Developing a map of geologically defined site-condition categories for California. *Bulletin of the Seismological Society of America* **96**, 1483–1501.

Wills, C.J. & W. Silva (1998). Shear wave velocity characteristics of geologic units in California. *Earthquake Spectra* **14**, 533–556.

Worden, C.B., E.M. Thompson, M. Hearne & D.J. Wald (2017). *ShakeMap V4 Manual: technical manual, user's guide, and software guide*. United States Geological Survey. Available online at: <http://usgs.github.io/shakemap/>.

A3.4.11.2 Web references

American Fact Finder – United States Census Bureau (2016): <http://factfinder.census.gov/faces/nav/jsf/pages/index.xhtml>. Last accessed: 4th December 2016.

Colorado Geological Survey: <http://coloradogeologicalsurvey.org/>

Global Centroid Moment Tensor Project (GCMT): <http://www.globalcmt.org>. Last accessed: 9th May 2018.

ISO Mitigation (2015):
<http://www.isomitigation.com/index.php/bcegs/facts-and-figures-about-bcegs-grades-around-the-country>. Last accessed: 24th October 2015.

United States Bureau of Economic Analysis (2012):
https://www.bea.gov/newsreleases/regional/gdp_state/2012/pdf/gsp0612.pdf.
Last accessed: 9th February 2017.

United States Energy Information Administration (EIA, 2016): <http://www.eia.gov/state/rankings/>.
Last accessed: 25th January 2016.

United States Geological Survey (USGS): <http://earthquake.usgs.gov/>.
Outdated website for this event (last accessed 6th November 2015):
<http://earthquake.usgs.gov/earthquakes/eqinthenews/2011/usc0005idz/#summary>.
Renovated website for this event (last accessed 6th November 2015):
<http://earthquake.usgs.gov/earthquakes/eventpage/usp000j6wm#executive>.

United States Geological Survey (USGS) Mineral Resources Online Spatial Data (2015):
<http://mrdata.usgs.gov/geology/state/>. Last accessed: 26th September 2015.

United States Geological Survey (USGS) Quaternary Fault and Fold Database (2015):
<http://earthquake.usgs.gov/hazards/qfaults/>. Last accessed: 28th September 2015.

Wikipedia: <https://en.wikipedia.org/wiki/Colorado>. Last accessed 6th November 2015.

World Economic Outlook Database 2015 (2015):
<http://www.imf.org/external/pubs/ft/weo/2015/01/weodata/index.aspx>.
Last accessed: 17th October 2015.

A3.5 2011 M5.7, 2016 M5.8, 2016 M5.0 Earthquakes in Oklahoma, USA

Being all part of a likely man-made recent increase in the seismicity observed in the state of Oklahoma, this chapter studies three earthquakes: the **M5.7** one that occurred on 6th November 2011, at 03.53 UTC (5th November 2011, 22.53 local time) in the vicinity of Prague, the **M5.8** one of 3rd September 2016 at 12.02 UTC (07.02 local time) close to Pawnee, and the **M5.0** event that took place on 7th November 2016 at 01.44 UTC (6th November 2016, 19.44 local time) approximately 4 km to the north-west of Cushing. All of them (whose locations can be observed in Figure A3.5.1) together with their foreshocks and aftershocks, are believed to have been induced by the activities of deep injection of wastewater that have been going on in the area for decades.

These three are clearly not the only earthquakes that the state of Oklahoma has experienced recently. Amongst the thousands that have been occurring, two other stand out for having been felt particularly strongly: the **M5.1** Fairview event of 13th February 2016 (17.07 UTC) and the **M4.4** Pawnee event of 2nd November 2016 (04.26 UTC). However, as none of the two appear to have caused relevant damage, they are not studied in detail herein (Fairview: CNN, 2016a; Fox News, 2016; News On 6, 2016a; The Weather Company, 2016; Pawnee: KFOR, 2016a; News OK, 2016c; News On 6, 2016b; RT, 2016).

All three studied events were extensively felt and caused significant fear in the population. The 2011 **M5.7** Prague earthquake was the largest to have ever occurred in the history of Oklahoma until the 2016 **M5.8** Pawnee one took place. The former caused damage in the area enclosed by the cities/towns of Prague, Sparks, Meeker and Shawnee, while the latter affected mostly the city of Pawnee and surrounding areas. Though with a much smaller magnitude, the 2016 **M5.0** Cushing earthquake caused widespread damage in the city of Cushing.

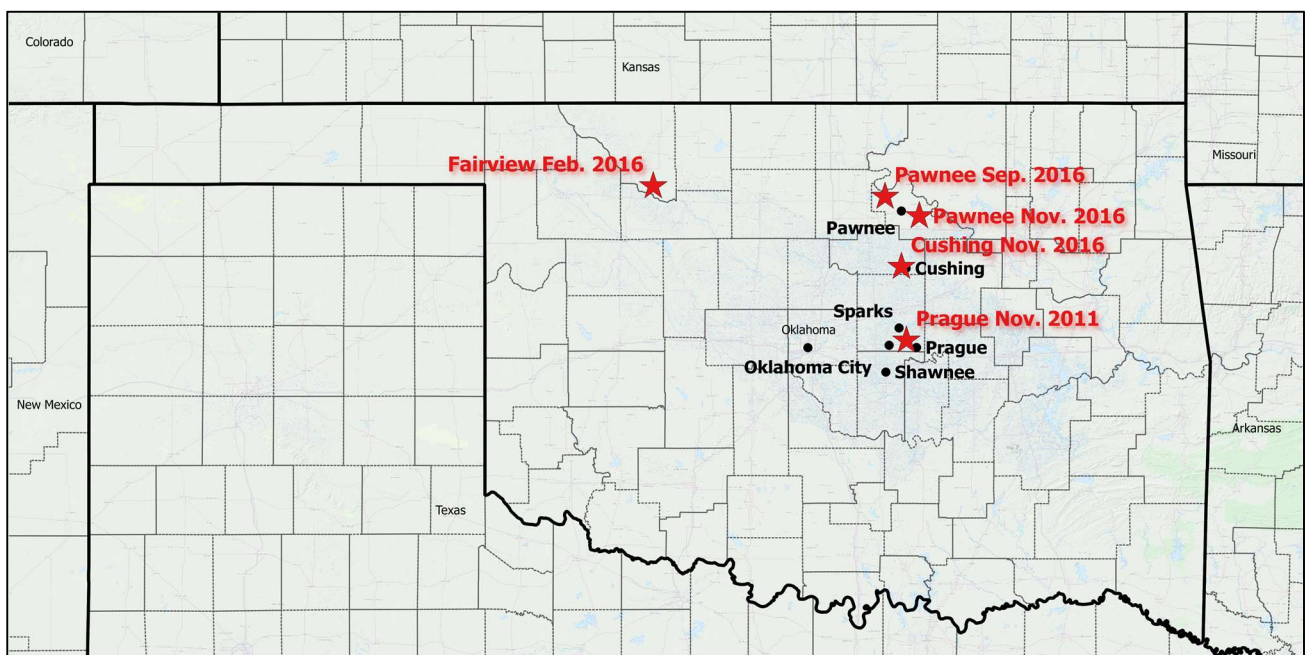


Figure A3.5.1. Epicentres of the three earthquakes under study and two additional relevant events within the state of Oklahoma.

A3.5.1 Tectonic and seismic setting

A3.5.1.1 Tectonic setting

These three earthquakes occurred within the Cherokee Platform, in the centre of the state of Oklahoma, to the east and north-east of Oklahoma City. The whole area belongs to the large stable continental region of the central and eastern United States. In contrast with active continental regions, stable continental areas are characterised by a relatively lower seismic activity and low strain rates (Klose & Seeber, 2007), and by the fact that earthquakes tend to be felt over much larger areas (USGS).

The state of Oklahoma is subject to a horizontal compressive stress oriented from east to west (Darold & Holland, 2015; Witze, 2015). Witze (2015) determined a mean and a median orientation of the maximum horizontal stress of N83.2°E and N84.8°E, respectively, with a standard deviation of 21.3°. This direction of horizontal stresses causes faults oriented northwest to southeast or northeast to southwest to be more likely to rupture than faults with orientations significantly different from these.

The slow rates of deformation and limited knowledge of the fault geometry that characterise stable continental regions often prevent unambiguous attribution of an earthquake to a given fault structure. According to Yeck *et al.* (2017), all three events occurred on previously unmapped faults (or segments of faults) within the shallow Precambrian basement that are near optimally oriented with respect to the present state of stress in Oklahoma.

The 2011 **M5.7** Prague earthquake occurred on an unmapped extension of a previously known splay of the Wilzetta fault system (Keranen *et al.*, 2013, McNamara *et al.*, 2015a; Walsh & Zoback, 2016; Yeck *et al.*, 2017). While the main 200-km long fault runs in the NNE-SSW direction, the unmapped segment that gave rise to this event strikes closer to the NW-SW direction instead, as shown in Figure A3.5.2, and is consequently more favourably oriented for rupture than the former.

Similarly, the 2016 **M5.8** Pawnee earthquake occurred on an unknown splay of the Labette fault (Manga *et al.*, 2016; Yeck *et al.*, 2017), now named the Pawnee fault by Yeck *et al.* (2017), and the 2016 **M5.0** Cushing earthquake, together with its 2014 predecessors, occurred on two unmapped fault structures that appear to be conjugate to the Wilzetta-Whitetail fault zone (McNamara *et al.*, 2015b; Yeck *et al.*, 2017), as shown in Figure A3.5.2.

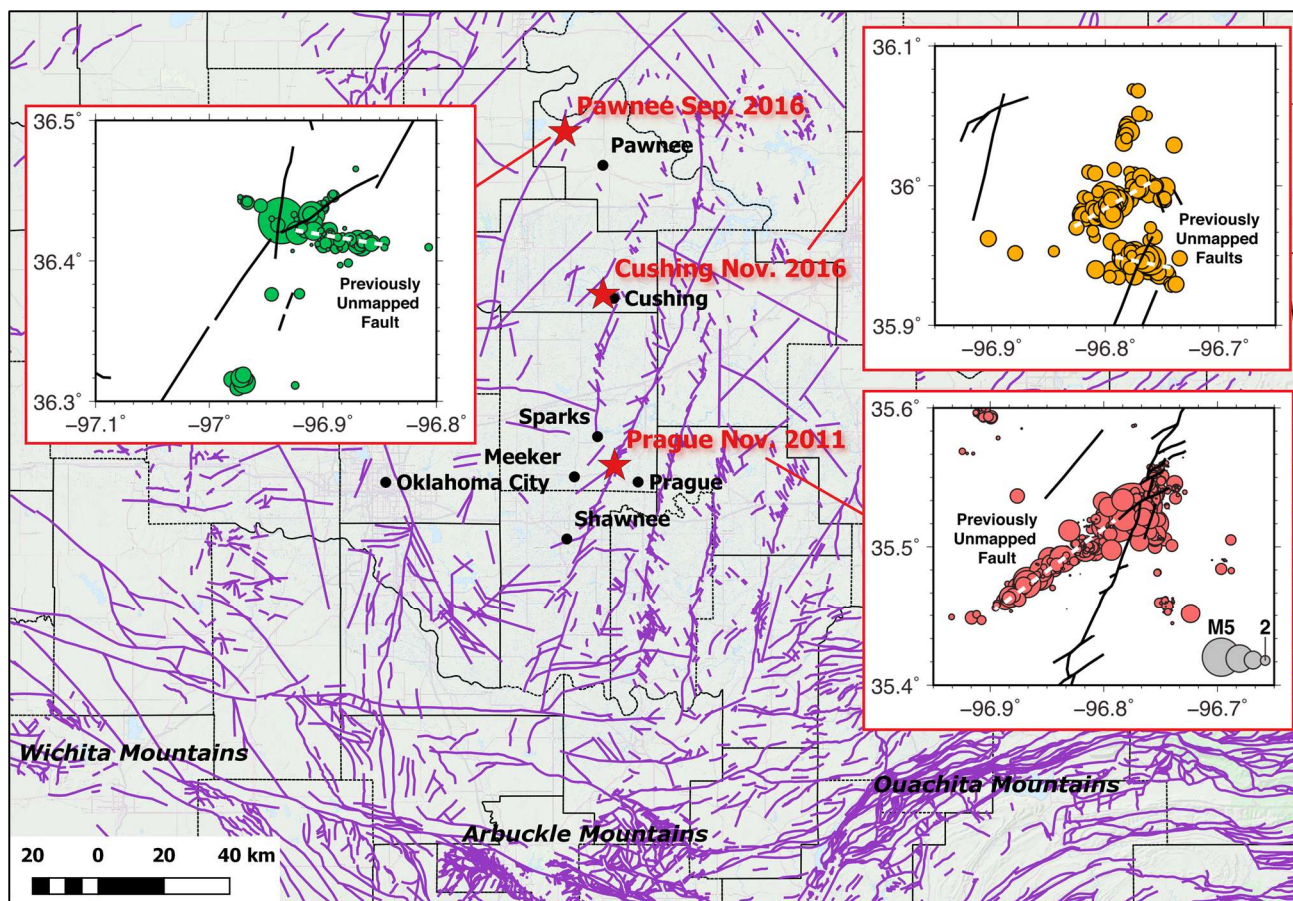


Figure A3.5.2. Epicentres of the three earthquakes under study (red stars, according to the USGS) and details of the faults that caused them. Insets from Yeck *et al.* (2017). Interpretative fault map of Oklahoma (purple lines) according to Marsh & Holland (2016).

A3.5.1.2 Regional and local seismicity

Seismicity rates in the area known as the central and eastern United States (CEUS), to which Oklahoma belongs, are generally low, as should be expected for such low intraplate strain rates (Hough & Page, 2015). The Meers fault, located along the Wichita mountains (Figure A3.5.2), is the only fault within the state of Oklahoma with documented Quaternary surface rupture. According to Hough & Page (2015), there is evidence of two earthquakes of **M**6.5-7.0 having occurred along this fault within the past 3,400 years, though modern seismicity rates associated with it have been extremely low.

A recent study by Hough & Page (2015) indicates that the earliest earthquake known to have occurred within Oklahoma according to the recently compiled Central and Eastern United States Seismic Source Characterization for Nuclear Facilities (CEUS-SSC) catalogue occurred on 22nd October 1882, and had its epicentre in eastern Oklahoma. Hough & Page (2015) believe that this event was associated to the Ouachita structural belt (Figure A3.5.2). The CEUS-SSC catalogue estimates a moment magnitude of **M**5.6 for this event, while Hough & Page (2015) estimate a significantly lower **M**4.8 instead.

Only six events larger than **M**3.5 occurred in Oklahoma between 1900 and 1940, and no events larger than **M**3.5 occurred between 1940 and 1950 (Hough & Page, 2015). A

relevant **M**5.5 event took place on 9th April 1952, with epicentre to the west of Oklahoma City. Although damage was not extensive, people located close to the epicentral area were noticeably alarmed (USGS).

The relatively low seismicity rates inferred from the information above support the affirmation by Taylor *et al.* (2017), who state that most of the faults in Oklahoma were inactive until 2009. From 2009 onwards, seismicity started to increase dramatically due to deep injection of wastewater (e.g., Ellsworth *et al.*, 2015; Petersen *et al.*, 2017; Taylor *et al.*, 2017). Interpretation of the quantification of this increase by different sources in the literature is not straightforward, as different authors use different minimum magnitudes and time spans (e.g., Keranen *et al.*, 2013; Hough & Page, 2015; Petersen *et al.*, 2016; Petersen *et al.*, 2017). However, all numbers reflect a drastic change in the observed seismicity, which becomes evident in Figures A3.5.3 and A3.5.4 generated by the USGS, the first of which illustrates the number of earthquakes with magnitude **M**3.0 or larger observed in Oklahoma per year until 31st December 2016, while the latter shows the epicentres of events in the same magnitude range registered from 1973 to 24th June 2016 (*i.e.*, the 2016 Pawnee and Cushing events are not included) grouped by their time of occurrence. According to McGarr *et al.* (2015), the annual rate of earthquake sequences with at least one event with **M**3.0 or larger of Oklahoma has now exceeded that of California.

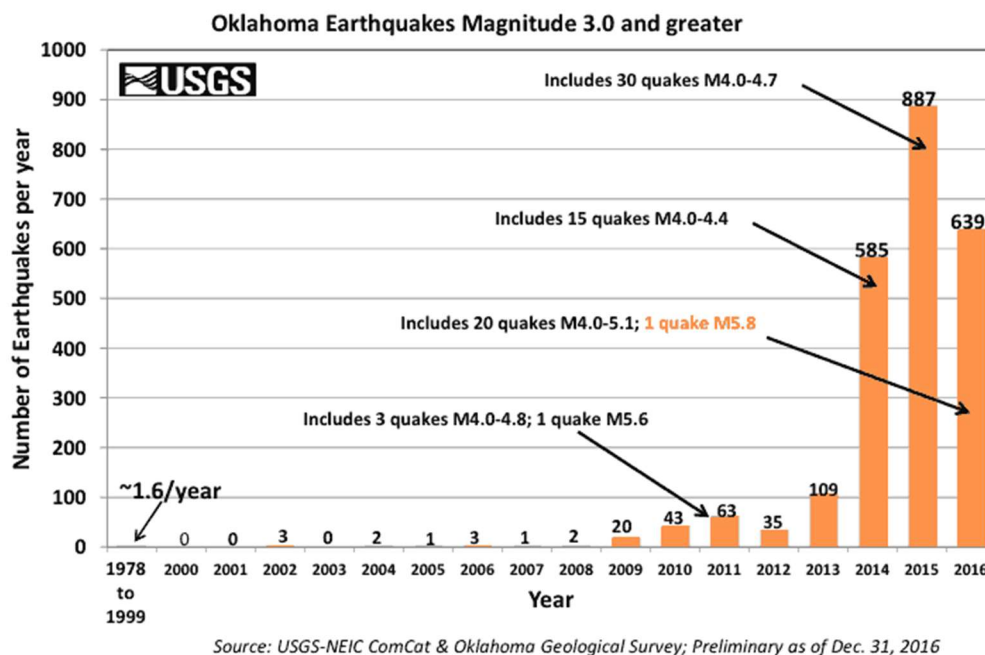


Figure A3.5.3. Number of earthquakes with magnitude **M**3.0 or larger observed in Oklahoma per year (USGS, 2016).

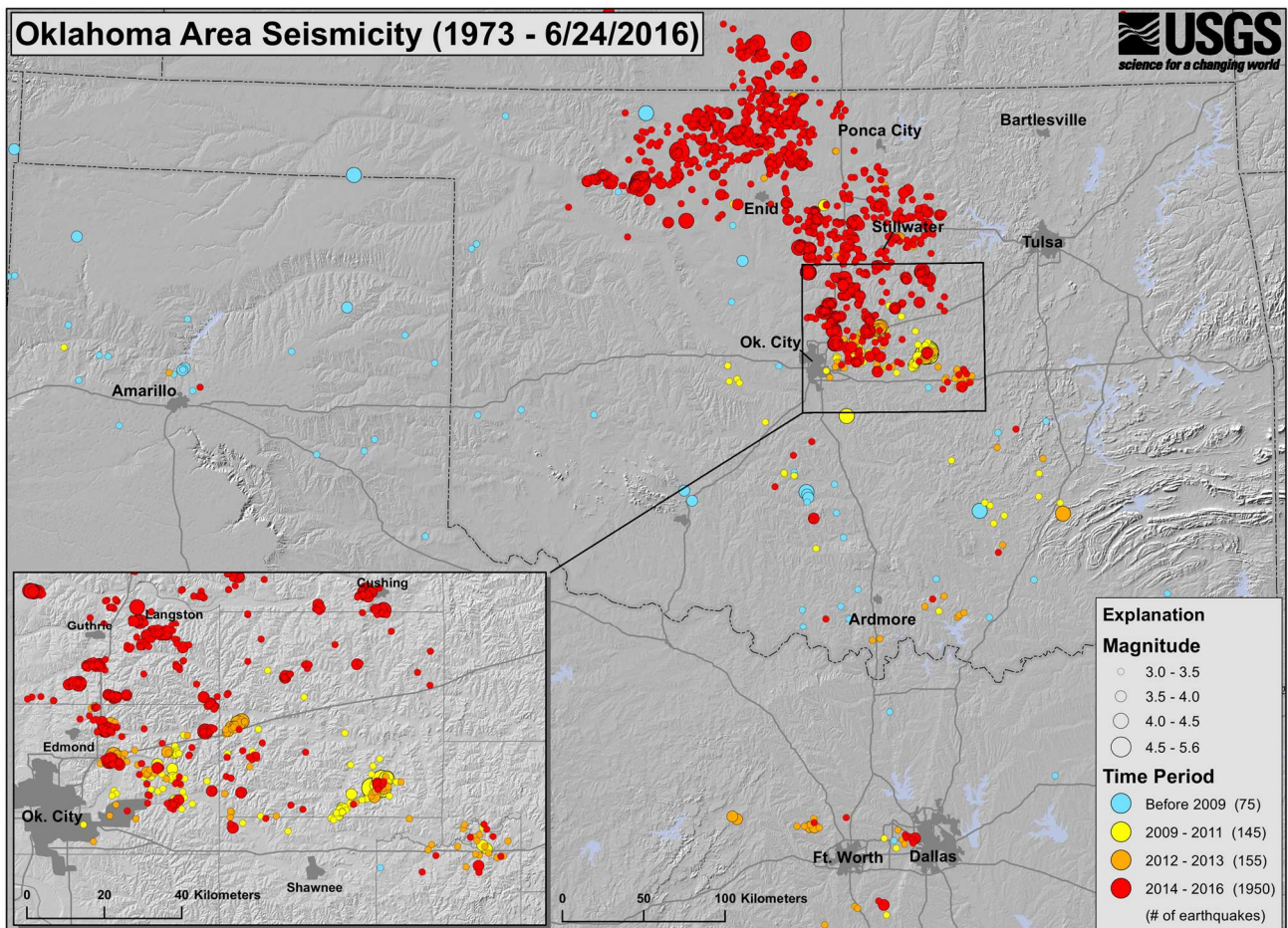


Figure A3.5.4. Seismicity map of Oklahoma according to the United States Geological Survey. Events between 1973 and 24th June 2016 are grouped by colours (USGS, 2016).

A3.5.1.3 Seismic hazard

Figure A3.5.5 shows extracts of the probabilistic seismic hazard maps for the United States of 2008 and 2014, elaborated by the United States Geological Survey (USGS; Petersen *et al.*, 2008; Petersen *et al.*, 2014). Values shown correspond to peak ground acceleration (PGA) on rock with a 10% probability of exceedance in 50 years. The area affected by the 2011 Prague earthquake and the state of Oklahoma are marked in red. Table A3.5.1 presents a summary of the PGA values expected at Meeker, Prague, Shawnee and Sparks, which are the most relevant locations to describe the damage experienced as a consequence of the 2011 **M**5.7 Prague earthquake, and those at Pawnee and Cushing. The table also reports the corresponding values obtained from the Global Seismic Hazard Assessment Program (GSHAP; Giardini *et al.*, 1999), which are very close to the average between those of the 2014 USGS hazard map and those of the 2008 one. In spite of the discrepancies, all values support the idea that seismic hazard is moderate to low in the affected area.

It should be noted that the USGS national seismic hazard maps (and those of any other country in the world) do not take into consideration anthropogenic seismic activities and, therefore, the 2011 events around the area of Prague had no effect over the change from the 2008 map to the 2014 one. The issue of how to incorporate ground motions generated

by induced seismicity to building design codes is currently under debate, not only due to the fact that only recently has the international community started to dedicate more efforts in this direction, but also because the rates of induced seismicity usually change rapidly within a few years, in a much shorter time span than that required for the approval of new building codes or the expected lifespan of civil engineering structures (Petersen *et al.*, 2017). In an attempt to start addressing this challenge, the USGS has started producing one-year seismic hazard forecasts combining tectonic and induced events (Petersen *et al.*, 2016; Petersen *et al.*, 2017). Figure A3.5.6 shows values of peak ground acceleration with a 1% probability of exceedance in one year (approximately 39.5% probability of exceedance in 50 years, assuming a Poisson process) resulting from the 2017 one-year seismic hazard model for the Central and Eastern United States. The increase in seismic hazard arising from including induced seismicity in the model is evident.

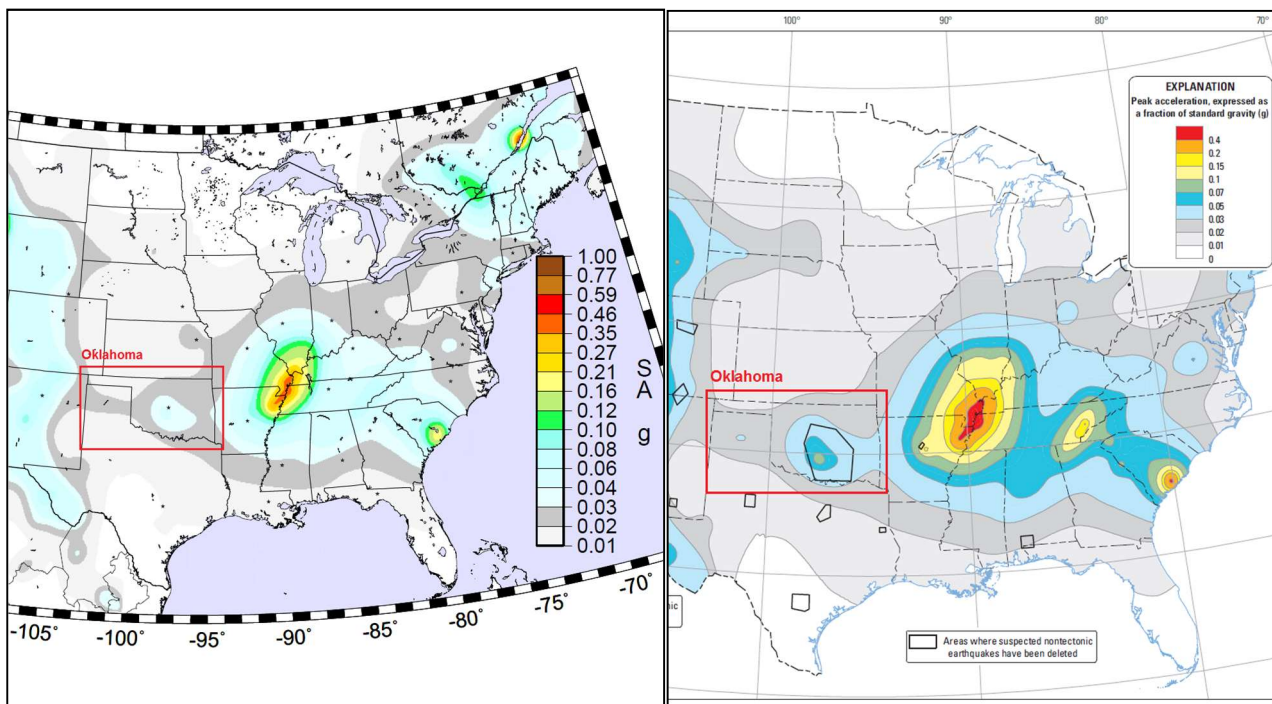


Figure A3.5.5. Extract of the 2008 (left) and 2014 (right) hazard maps for the United States, elaborated by the USGS (2015). Values correspond to peak ground acceleration (g) on rock with a 10% probability of exceedance in 50 years.

Table A3.5.1. Peak ground acceleration (PGA, g) values on rock with a 10% probability of exceedance in 50 years according to the 2008 and 2014 USGS hazard maps, and results from the Global Seismic Hazard Assessment Program (GSHAP), at locations in which damage was observed after the 2011 **M**5.7 Prague, 2016 **M**5.8 Pawnee and 2016 **M**5.0 Cushing earthquakes.

PLACE	USA 2008	USA 2014	GSHAP
Meeker	0.0328	0.0412	0.0371
Prague	0.0312	0.0390	0.0349
Shawnee	0.0342	0.0444	0.0394
Sparks	0.0310	0.0382	0.0350
Pawnee	0.0240	0.0282	0.0257
Cushing	0.0269	0.0317	0.0295

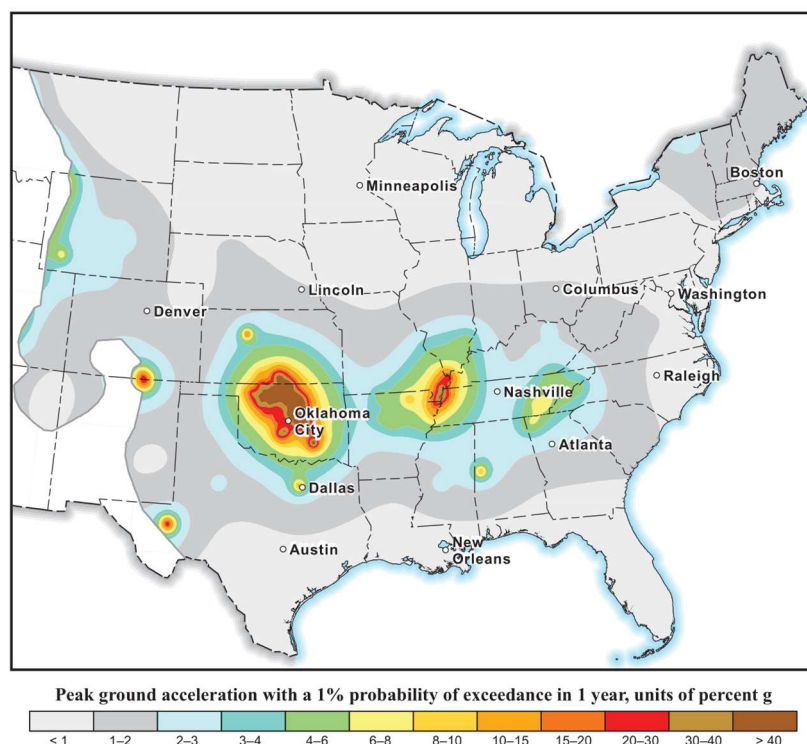


Figure A3.5.6. Peak ground acceleration (% of g) on rock with a 1% probability of exceedance on 1 year, according to the 2017 one-year seismic hazard model for the Central and Eastern United States. From Petersen *et al.* (2017).

A3.5.2 Earthquake source characteristics

A3.5.2.1 Location, depth and time

The Prague main shock occurred on 6th November 2011, at 03.53 UTC (5th November 2011, 22.53 local time). The Pawnee main shock occurred on 3rd September 2016, at 12.02 UTC (07.02 local time). The Cushing main shock occurred on 7th November 2016, at 01.44 UTC (6th November 2016, 19.44 local time).

Several organizations and agencies report their own estimations of the epicentral coordinates and hypocentral depths. The information reported in the websites of the National Earthquake Information Center (NEIC) of the United States Geological Service (USGS), the Global Centroid Moment Tensor Project (GCMT; Dziewonski *et al.*, 1981; Ekström *et al.*, 2012), the International Seismological Centre (ISC), the International Data Centre (IDC) and the Oklahoma Geological Service (OGS) is summarized in Tables A3.5.2, A3.5.3 and A3.5.4. Cells marked as (*f) correspond to parameters that were held fixed while inversion was carried out to retrieve those that remain. It is noted that the ISC-GEM catalogue (Storchak *et al.*, 2013) only covers earthquakes until 2013, and thus information regarding the 2016 Pawnee and Cushing events is not available from this source. Also included are the epicentral coordinates and hypocentral depth calculated by Holland (2013), Sun & Hartzell (2014), Grandin *et al.* (2017) and Yeck *et al.* (2017).

Table A3.5.2. Epicentral coordinates and hypocentral depths for the 2011 **M5.7** Prague earthquake from different sources.

Agency / Publication		Latitude	Longitude	Depth (km)
NEIC	National Earthquake Information Center, USGS	35.5320 ° N	96.7650 °W	5.20
GCMT	Global Centroid Moment Tensor Project (**)	35.6100 ° N	96.7200 °W	12.00 (*f)
ISC	International Seismological Centre - GEM catalogue	35.5330 ° N	96.7050 °W	10.00
IDC	International Data Centre, CTBTO	35.5293 ° N	96.7495 °W	0.00 (*f)
OGS	Oklahoma Geological Service	35.5316 ° N	96.7714 °W	3.1 - 5.2
Holland (2013)		35.5220 ° N	96.7800 °W	3.10
Sun & Hartzell (2014)		35.5301 ° N	96.7773 °W	5.00

(*f) fixed parameter used for inversion

(**) centroid (not-hypocentral) location

Table A3.5.3. Epicentral coordinates and hypocentral depths for the 2016 **M5.8** Pawnee earthquake from different sources.

Agency / Publication		Latitude	Longitude	Depth (km)
NEIC	National Earthquake Information Center, USGS	36.4250 ° N	96.9290 °W	5.60
GCMT	Global Centroid Moment Tensor Project (**)	36.5400 ° N	96.8600 °W	18.20
IDC	International Data Centre, CTBTO	36.4587 ° N	96.8684 °W	0.0 (*f)
OGS	Oklahoma Geological Service	36.4259 ° N	96.9293 °W	5.56
Grandin <i>et al.</i> (2017)		36.4250 ° N	96.9060 °W	5.60
Yeck <i>et al.</i> (2017)		36.4292 ° N	96.9351 °W	4.69

(*f) fixed parameter used for inversion

(**) centroid (not-hypocentral) location

Table A3.5.4. Epicentral coordinates and hypocentral depths for the 2016 **M5.0** Cushing earthquake from different sources.

Agency / Publication		Latitude	Longitude	Depth (km)
NEIC	National Earthquake Information Center, USGS	35.9910 ° N	96.8030 °W	4.40
GCMT	Global Centroid Moment Tensor Project (**)	36.1600 ° N	96.7300 °W	12.00 (*f)
IDC	International Data Centre, CTBTO	36.0473 ° N	96.7532 °W	0.00 (*f)
OGS	Oklahoma Geological Service	35.9907 ° N	96.8030 °W	4.14

(*f) fixed parameter used for inversion

(**) centroid (not-hypocentral) location

Regarding the variability in the estimated depths, a shallow hypocentre seems the most likely for the three events. For the 2011 **M5.7** Prague earthquake, Keranen *et al.* (2013) report the depths of 83% of the aftershocks being less than 5 km, and highlight that 30% of the early aftershocks (which represent 20% of the total) were located within the sedimentary units into which fluids are injected. Furthermore, Sun & Hartzell (2014) infer a slip model for the 2011 main shock in which a first patch of highly-concentrated slip is located at a depth range between 3.0 and 5.5 km, and a second deeper one can be observed between 7.5 and 9.5 km.

For the 2016 **M**5.8 Pawnee earthquake, the 18.2 km estimated by the Global Centroid Moment Tensor Project (GCMT) seem particularly inaccurate, though the USGS reports an uncertainty of ± 6.1 km on their 5.6 km estimated depth, which would yield a final 11.7 km depth in an extreme case. The idea of a shallow hypocentre is strongly supported by the work of Yeck *et al.* (2017), who carried out an extensive relocation of this event and its aftershocks, with the aim of characterising their causative fault, and report a depth of 4.69 ± 1.00 km for the main shock and between 5 and 7 km for the majority of the aftershocks.

For the 2016 **M**5.0 Cushing earthquake, the USGS reports an uncertainty of ± 1.8 km on their 4.4 km estimation, suggesting a shallow hypocentre is the most likely for this event as well.

The maps in Figure A3.5.7 show the different estimations of the epicentral coordinates enumerated above. Note that coordinates reported by the GCMT correspond to the location of the centroid, and not the hypocentre. For the 2016 **M**5.8 Pawnee and **M**5.0 Cushing events, the USGS reports uncertainties in their epicentral coordinates of ± 1.2 and ± 0.5 km, respectively (there is no specification of uncertainty for the 2011 **M**5.7 Prague event).

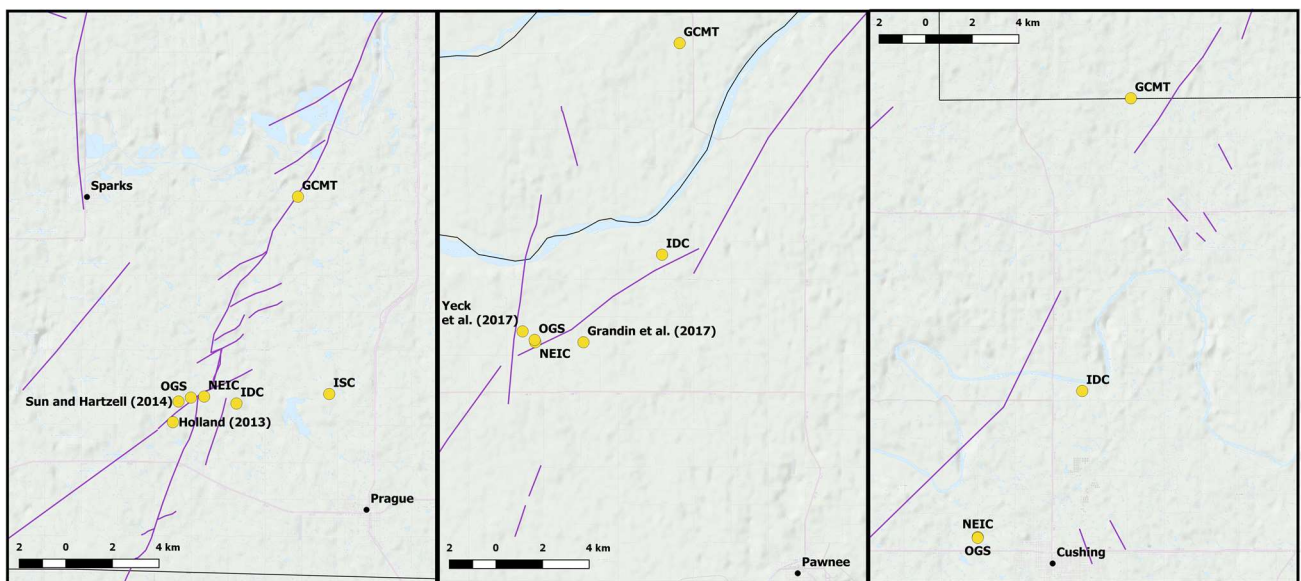


Figure A3.5.7. Estimation of epicentral coordinates (yellow circles). Faults in the area marked in violet, according to Marsh & Holland (2016).

A3.5.2.2 Magnitude

Estimations of magnitude made by the same agencies are reported in Tables A3.5.5, A3.5.6 and A3.5.7. The USGS had originally estimated the moment magnitude of the 2011 Prague and 2016 Pawnee earthquakes in 5.6 for both events, but updated them on 7th September 2016 to **M**5.7 and **M**5.8, respectively (USGS Press Release, 2016). For the **M**5.8 Pawnee earthquake, Grandin *et al.* (2017) estimate **M**5.64 and **M**5.71 with point source and finite fault inversions, respectively.

Table A3.5.5. Estimations of moment magnitude (**M**), body-wave magnitude (**mb**) and surface-wave magnitude (**Ms**) for the 2011 **M5.7** Prague earthquake.

Agency		M	mb	Ms
NEIC	National Earthquake Information Center, USGS	5.7	5.2	5.6
GCMT	Global Centroid Moment Tensor Project	5.7	5.2	5.7
ISC	International Seismological Service	-	5.2	5.7
IDC	International Data Centre, CTBTO	-	4.8	5.5
OGS	Oklahoma Geological Service	5.6	5.2	5.6
Holland (2013) and Sun & Hartzell (2014)		5.6	-	-

Table A3.5.6. Estimations of moment magnitude (**M**), body-wave magnitude (**mb**) and surface-wave magnitude (**Ms**) for the 2016 **M5.8** Pawnee earthquake.

Agency		M	mb	Ms
NEIC	National Earthquake Information Center, USGS	5.8	5.6	5.7
GCMT	Global Centroid Moment Tensor Project	5.7	-	5.8
IDC	International Data Centre, CTBTO	-	5.3	5.5
OGS	Oklahoma Geological Service	5.5	-	-
Grandin <i>et al.</i> (2017)		5.7	-	-
Yeck <i>et al.</i> (2017)		-	-	5.7

Table A3.5.7. Estimations of moment magnitude (**M**), body-wave magnitude (**mb**) and surface-wave magnitude (**Ms**) for the 2016 **M5.0** Cushing earthquake.

Agency		M	mb	Ms
NEIC	National Earthquake Information Center, USGS	5.0	4.6	4.8
GCMT	Global Centroid Moment Tensor Project	5.0	-	5.0
IDC	International Data Centre, CTBTO	-	4.4	4.5
OGS	Oklahoma Geological Service	4.6	-	-

A3.5.2.3 Style-of-faulting

According to the USGS and other sources, all three events presented strike-slip mechanisms, with variable levels of double-couple component, as can be observed in Figure A3.5.8.

For the case of the 2011 **M5.7** Prague earthquake, all sources indicate a strike-slip mechanism on a fault striking to the northeast. Furthermore, Holland (2013) demonstrates that the vast majority of the events that made up the 2011 Prague sequence, as well as the vast majority of the events occurring in the area in general, are the result of strike-slip motion on steeply dipping faults, as shown in Figure A3.5.9. Table A3.5.8 summarizes the fault plane solutions calculated by the USGS, the GCMT, Holland (2013) and Sun & Hartzell (2014) for this event. Note that, being the dip very close to 90° in all cases, a 55° strike and a 235° strike are practically equivalent.

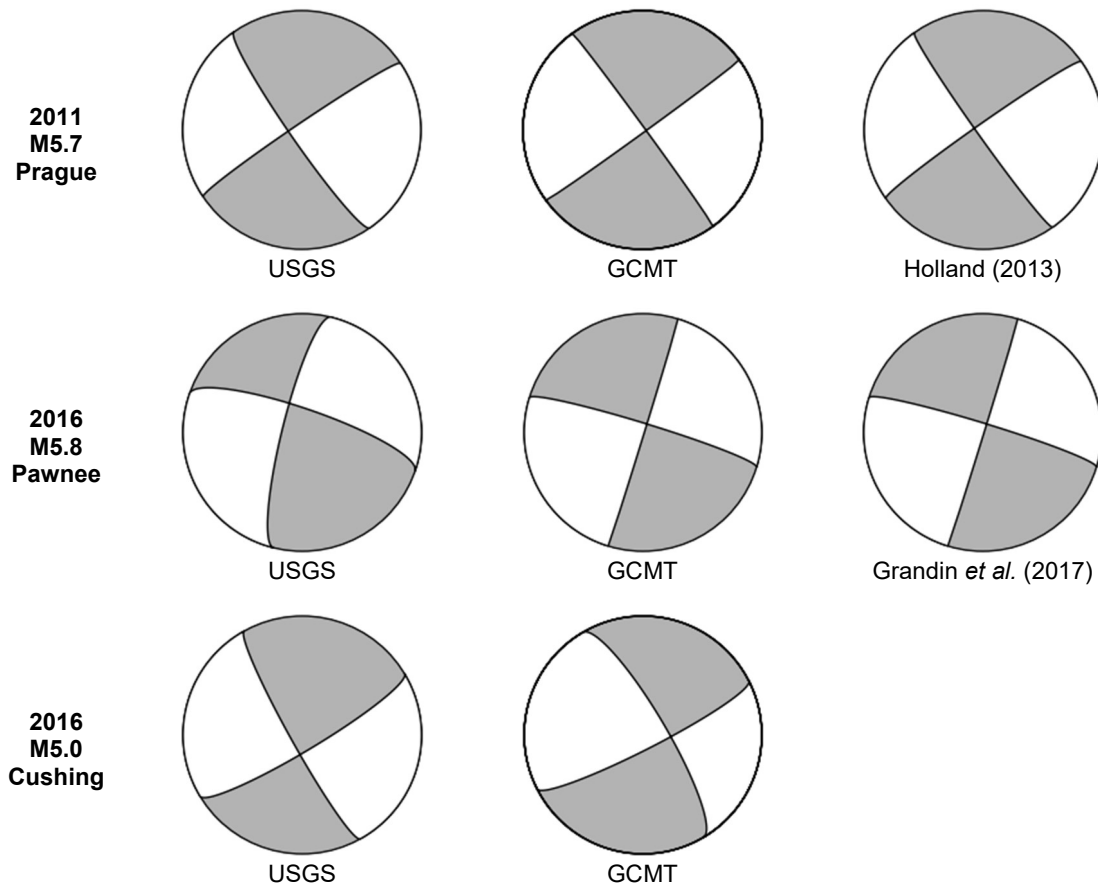


Figure A3.5.8. Focal mechanisms for the three events according to different sources.

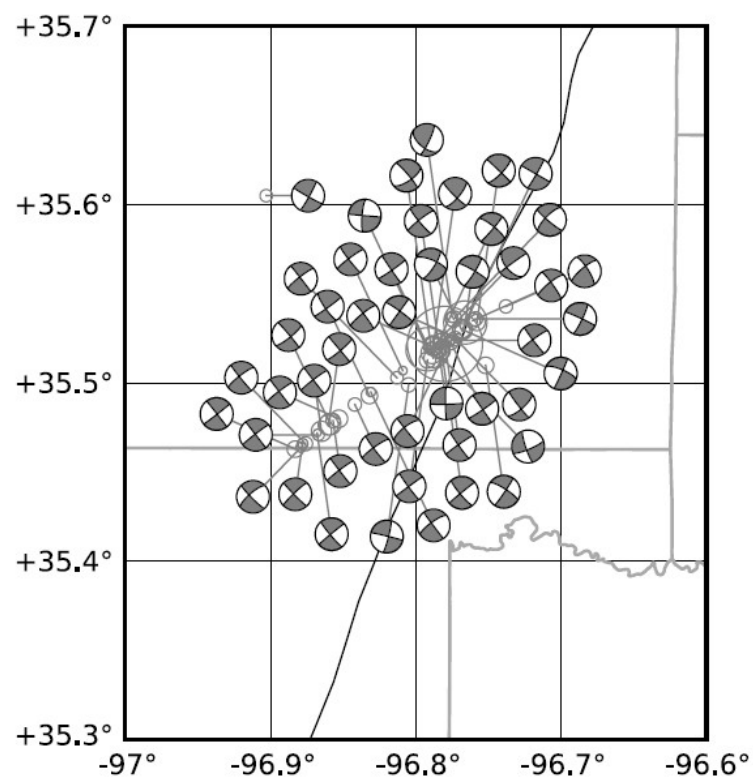


Figure A3.5.9. Focal mechanisms of 47 events of the 2011 Prague earthquake sequence following the M4.8 foreshock of 5th November 2011. From Holland (2013).

Table A3.5.8. Fault plane solutions and fault planes from different sources for the 2011 **M5.7** Prague earthquake. Fault planes marked in grey are the preferred solution in each case.

Fault Plane 1			Fault Plane 2			Source
Strike	Dip	Rake	Strike	Dip	Rake	
236	85	-171	146	81	-5	Regional Moment Tensor NEIC (USGS)
324	88	-2	54	88	-178	GCMT
235	85	-175	-	-	-	Holland (2013) and Sun & Hartzell (2014)

Similarly, Yeck *et al.* (2017) observe that the 2016 Pawnee series, including the **M5.8** main shock, present strike-slip focal mechanisms with near-vertical nodal planes whose epicentral coordinates delineate a fault with an ESE-WNW orientation (Grandin *et al.*, 2017). Table A3.5.9 gathers the fault plane solutions calculated by various sources.

At the time of writing (March 2017), the literature regarding the 2016 **M5.0** Cushing event is still quite scarce. However, both the USGS and the GCMT Project indicate strike-slip mechanisms, as shown in Table A3.5.10. Moreover, McNamara *et al.* (2015b) observed strike-slip mechanisms for the 2014 series of events that are now considered foreshocks of the 2016 main shock (Yeck *et al.*, 2017).

Table A3.5.9. Fault plane solutions and fault planes from different sources for the 2016 **M5.8** Pawnee earthquake. Fault planes marked in grey are the preferred solution in each case.

Fault Plane 1			Fault Plane 2			Source
Strike	Dip	Rake	Strike	Dip	Rake	
289	72	16	194	74	161	Regional Moment Tensor NEIC (USGS)
287	83	-1	17	89	-173	GCMT
288	88	0	18	90	-178	Grandin <i>et al.</i> (2017)

Table A3.5.10. Fault plane solutions and fault planes from different sources for the 2016 **M5.0** Cushing earthquake. Fault planes marked in grey are the preferred solution in each case.

Fault Plane 1			Fault Plane 2			Source
Strike	Dip	Rake	Strike	Dip	Rake	
151	81	12	59	78	171	Regional Moment Tensor NEIC (USGS)
329	72	-11	63	79	-162	GCMT

A3.5.2.4 Stress drop

According to the slip model inferred by Sun & Hartzell (2014) for the 2011 **M5.7** Prague earthquake, two large slip patches could be identified for the main shock: one located around the hypocentre, at a depth range between 3.0 and 5.5 km, and a second one between 7.5 and 9.5 km (Figure A3.5.10). The average stress drops were 9 MPa (90 bars) for the shallower patch and 1.6 MPa (16 bars) over all areas of slip. The latter is the closest to the 2.01 MPa (20.1 bars) reported by Darragh *et al.* (2015), who also indicate 1.75 MPa (17.5 bars) for the **M4.8** foreshock.

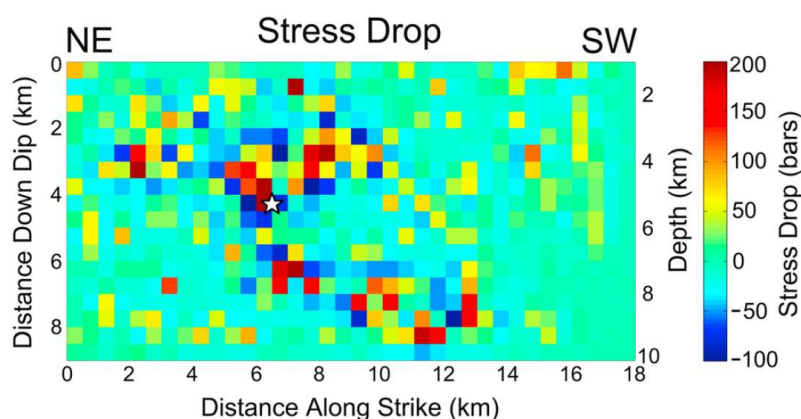


Figure A3.5.10. Static stress drop (1 bar = 0.1 MPa) on the fault due to the 2011 **M**5.7 Prague main shock. From Sun & Hartzell (2014).

At the time of writing (March 2017), no reports on the stress drops associated to the 2016 **M**5.8 Pawnee and **M**5.0 Cushing events have been found.

A3.5.2.5 Foreshocks and aftershocks

The **M**5.7 Prague earthquake of 6th November 2011 was preceded by multiple foreshock events that started in February 2010 (Keranen *et al.*, 2013), the largest of which was a **M**4.8 which occurred around 21 hours earlier (Oklahoma Geological Survey, OGS). It was then followed by thousands of aftershocks, including a **M**4.0 that occurred only 10 minutes after the main shock and a **M**4.8 on 8th November 2011, which was the biggest. Yeck *et al.* (2017) report that 35 aftershocks with (assumed local) magnitude equal to or larger than 3.0 occurred within the first 15 days after the main shock, two of which had magnitudes above 4.0, which clearly are the **M**4.0 and **M**4.8 just mentioned. The OGS reports that the aftershocks in the Prague area followed the normal Omori Law time--decay that is typical of natural seismicity.

Keranen *et al.* (2013) report the occurrence of 1183 aftershocks. During the whole sequence, they observe the progressive rupture of three fault planes, and believe that the **M**4.8 foreshock of 5th November 2011 triggered the rest of the sequence, including the main shock. Figure A3.5.11 shows their reported locations for several of the events in the sequence.

As opposed to the Prague case, the 2016 **M**5.8 Pawnee earthquake presented almost no foreshock activity. Yeck *et al.* (2017) report the occurrence of only one event with (local) magnitude above 3.0 in the 60 days before the main shock. A query on the USGS database confirms this and allows to see that the number of events rises only to three if the time window is extended to 90 days. Similarly, the number of aftershocks was significantly lower than for Prague, with only eleven events with (local) magnitude equal to or larger than 3.0 in the first 15 days after the main shock, the largest of which had a magnitude of 3.9 (Yeck *et al.*, 2017, type of magnitude not specified, possibly M_L). The aftershock seismicity was concentrated along some 7.5 km of a previously unmapped fault striking ESE-WNW, at a depth of approximately 6 km (Grandin *et al.*, 2017; Yeck *et al.*,

2017), but also along the Labette fault, which lies to the north of the latter, as shown in Figure A3.5.12.

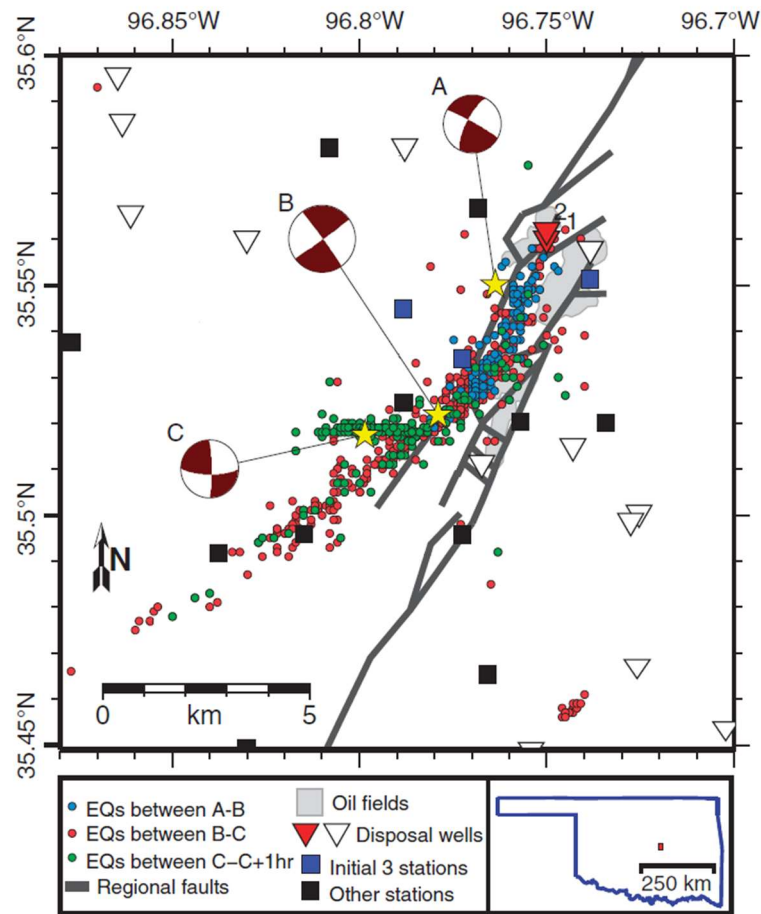


Figure A3.5.11. Location of the main **M**4.8 foreshock (marked as A), the **M**5.7 main shock (marked as B), the **M**4.8 aftershock (marked as C), and several other foreshocks (blue dots) and aftershocks (red and green dots). From Keranen *et al.* (2013).

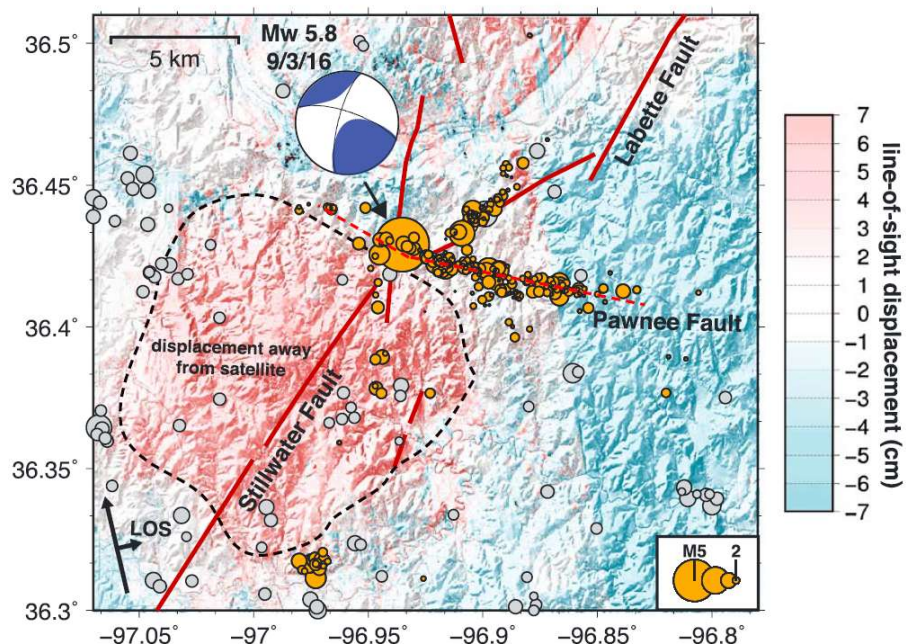


Figure A3.5.12. Location of the main shock of the 2016 **M**5.8 Pawnee earthquake and its foreshocks (grey circles) and aftershocks (orange circles). From Yeck *et al.* (2017).

The 2016 **M**5.0 Cushing earthquake was preceded by five foreshocks with **M**4.0 or larger since 7th October 2014, the last of which occurred over a year before the main shock, on 10th October 2015 (Yeck *et al.* 2017). Querying the USGS online database confirms this and shows that, within two months of the main shock, the largest foreshock was a **M**_L 3.3 on 4th October 2016.

McNamara *et al.* (2015b) and Yeck *et al.* (2017) show that the first two **M**4.0 or larger foreshocks, which occurred in October 2014, and most of the events that occurred around that time took place along approximately 5 km on a previously unmapped fault striking N80W, and not on the one that generated the 2016 **M**5.0 Cushing earthquake. Seismicity seemed to migrate to the latter around 2015, during which the other three larger foreshocks occurred. The trace of these two faults can be observed in Figure A3.5.2.

At the time of writing (March 2017), no publications focus on a thorough description of the aftershocks of the 2016 **M**5.0 Cushing earthquake, though their locations are illustrated in the work of Yeck *et al.* (2017) (see Figure A3.5.2). A query on the USGS database for all **M**1.5 and larger events after the main shock until 20th March 2017 suggests that around 25 aftershocks have occurred so far, out of which the largest is a **M**_L 3.6 on 24th November 2016.

A3.5.2.6 Nature of earthquake

A significant number of studies link the 2011 Prague earthquake sequence to deep fluid injection of waste water (Ellsworth *et al.*, 2015; Hough & Page, 2015; Keranen *et al.*, 2013; Llenos & Michael, 2013; Sumy *et al.*, 2014; Sun & Hartzell, 2014; Weingarten *et al.*, 2015; Witze, 2015). In particular, Sun & Hartzell (2014) point out that the relatively low peak slip and stress drop support this assertion. A statement by the Oklahoma Geological Survey from March 2013 (OGS, 2013) exposes the original lack of agreement on the issue, for it concludes that "the interpretation that best fits current data is that the Prague earthquake sequence was the result of natural causes", based mainly on the fact that tectonic earthquakes have been known to occur in the area and that measurements carried out by the Oklahoma Corporation Commission (OCC) indicate that the geological formations in the area are under-pressured. However, a joint statement of the Oklahoma Geological Survey and the United States Geological Survey from May 2014 (OGS & USGS, 2014) states their conviction that the recent changes in earthquake rates in Oklahoma do not seem to be due to typical natural fluctuations, and that they are likely linked to waste water injection. Regarding the reference to previous seismicity observed in the area, Hough & Page (2015) acknowledge the evidence that natural intraplate earthquakes tend to be temporally clustered, but also believe that the apparent cluster of activity in Oklahoma since 2009 is not consistent with the level of natural rate fluctuations seen in the past.

Though claiming that the 2011 Prague sequence was induced, Keranen *et al.* (2013) believe that the faults were heavily loaded with tectonic stress and that fluid injection acted as a trigger, for the scalar moment released exceeds the value expected as a function of the volume of injected fluid by several orders of magnitude. Sumy *et al.* (2014) support this view and suggest that it was the **M**4.8 foreshock that was directly induced by fluid injection

and then triggered the main shock and its aftershocks. Langenbruch & Zoback (2016), however, state that the 2011 Prague sequence does not fit their overall model to characterise the relationship between volume of injected fluids and seismicity, and therefore cannot conclude whether it was triggered by injection or not.

For the development of their 2016 one-year hazard model including induced seismicity, the USGS grouped most of the seismic events in Oklahoma and southern Kansas within a region classified as having induced seismicity (Petersen *et al.*, 2016). Similarly, Langenbruch & Zoback (2016) show that the majority of earthquakes with magnitude equal to or larger than 3.0 that have occurred between 2009 and September 2016 have had their epicentres in areas where very large volumes of saltwater had been injected, as can be observed in Figure A3.5.13. Based on this evidence, Yeck *et al.* (2017) suggest that “it is probable, but not certain, that the (2016) Pawnee sequence was induced”. A similar statement is made by Manga *et al.* (2016), and both sources highlight the need for a more detailed analysis on the matter. Yeck *et al.* (2017) emphasise that if the suspected anthropogenic origins of the 2016 **M**5.8 Pawnee earthquake were to be confirmed, it would become the largest event to have occurred as a consequence of fluid injection to this time. On a more moderate perspective, Grandin *et al.* (2017) believe that this earthquake was, effectively, induced, but also suggest that the Oklahoma region might be seismically active in the long term and that wastewater injection might be acting as an accelerator of a natural tectonic process.

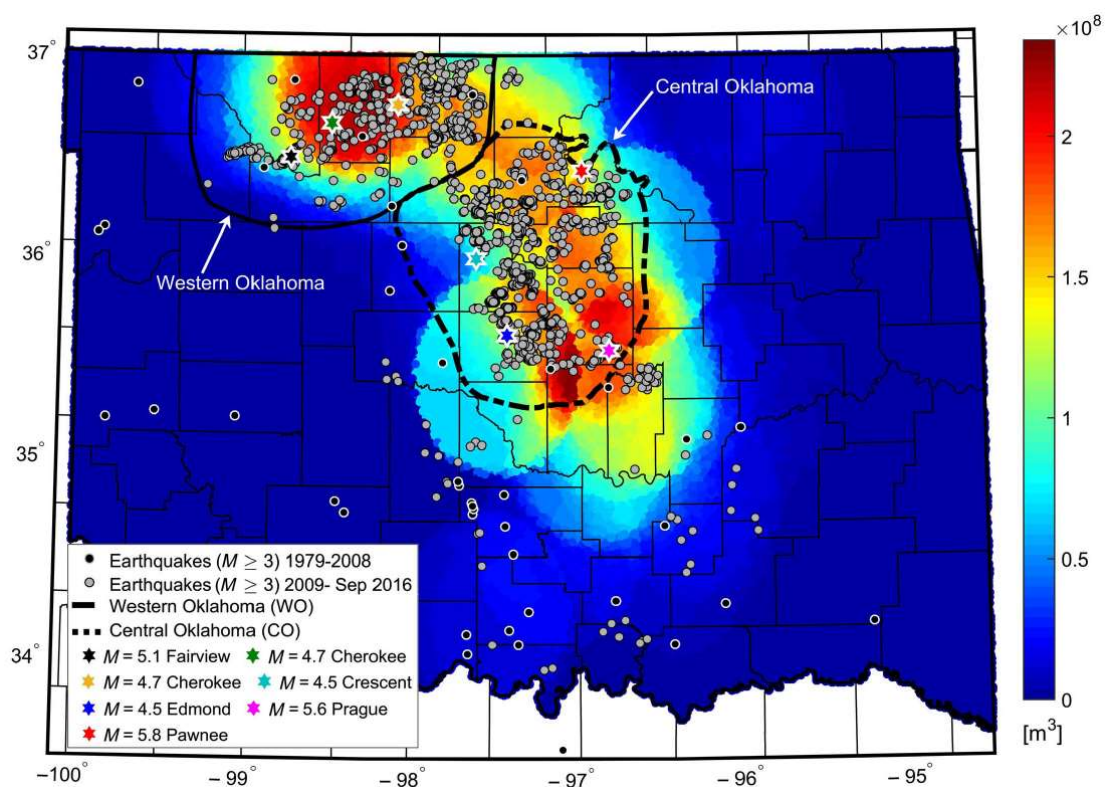


Figure A3.5.13. Historic earthquakes (1979-2008, black circles) and recent earthquakes (2009-September 2016, grey circles) over background colour scale indicating the cumulative volume (m³) of saltwater injected between 2009 and December 2015. From Langenbruch & Zoback (2016).

Due to the 2016 **M5.0** Cushing earthquake being so recent at the time of writing (March 2017), studies on its link with anthropogenic activities are not yet available. However, it is clear that its epicentre lies well within the area marked as having received large volumes of wastewater between 2009 and December 2015 in Figure A3.5.13.

A3.5.3 Geology and ground conditions in the affected area

A3.5.3.1 Regional geology and topography

The regions affected by these three events are located in a low-lying area in the middle of the state of Oklahoma, within the geologic province known as the Cherokee Platform (Northcutt & Campbell, 1995). The whole state slopes gradually downwards from west to east, and its main topographic features are the Wichita mountains, the Arbuckle mountains, the Ouachita mountains and the Ozark mountains, marked in the map of Figure A3.5.14 as the Wichita, Arbuckle, Ouachita and Ozark uplifts, respectively. The western part of the state is part of the United States' High Plains, a large relatively flat region lying at a significantly high altitude.

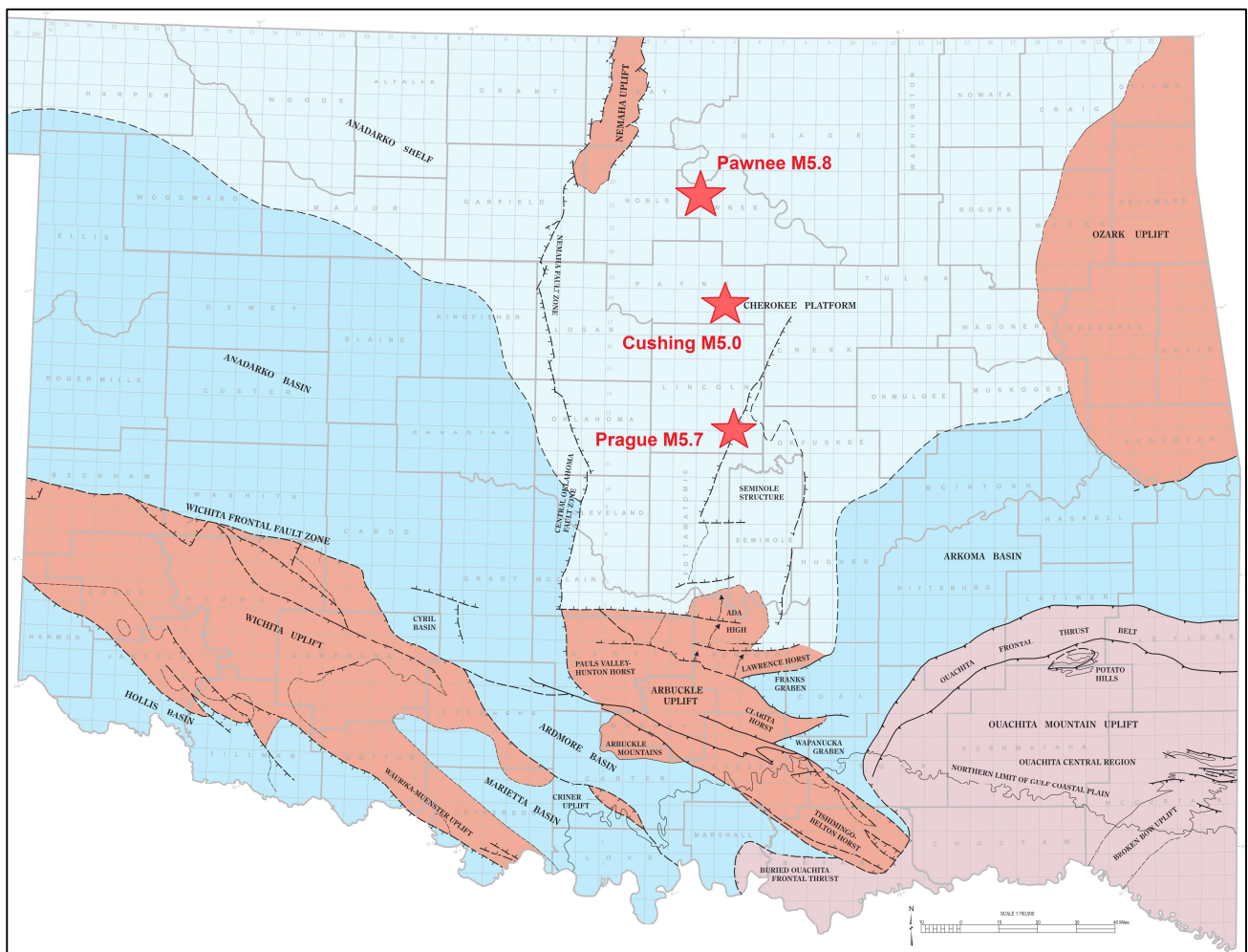


Figure A3.5.14. Geologic provinces of Oklahoma, from Northcutt & Campbell (1995). The red circles mark, approximately, the location of the three epicentres according to the USGS.

As shown in the map in Figure A3.5.15, different affected cities lie over different kinds of geologic units (Johnson, 2008). The cities of Prague and Cushing lie over Pennsylvanian sediments, which consist mostly of marine shale, with interbedded sandstone, limestone, and coal, and whose thickness can vary between 0.6 and 1.5 km. The cities of Meeker and Pawnee are located in an area where a relatively thin layer (~300 m) of Permian sediments consisting of shallow-marine, deltaic and alluvial deposits of red sandstone and shale, overlays the Pennsylvanian sediments. Clayton *et al.* (2016) specify that the Permian sediments observed in Pawnee are mostly shale, but also sandstone and limestone. Due to their proximity to two rivers, the cities of Sparks and Shawnee, as well as some of the areas affected by the 2016 M5.8 Pawnee earthquake lie over quaternary deposits of sand, silt, clay and gravel, whose thickness varies between 8.0 and 30.0 metres.

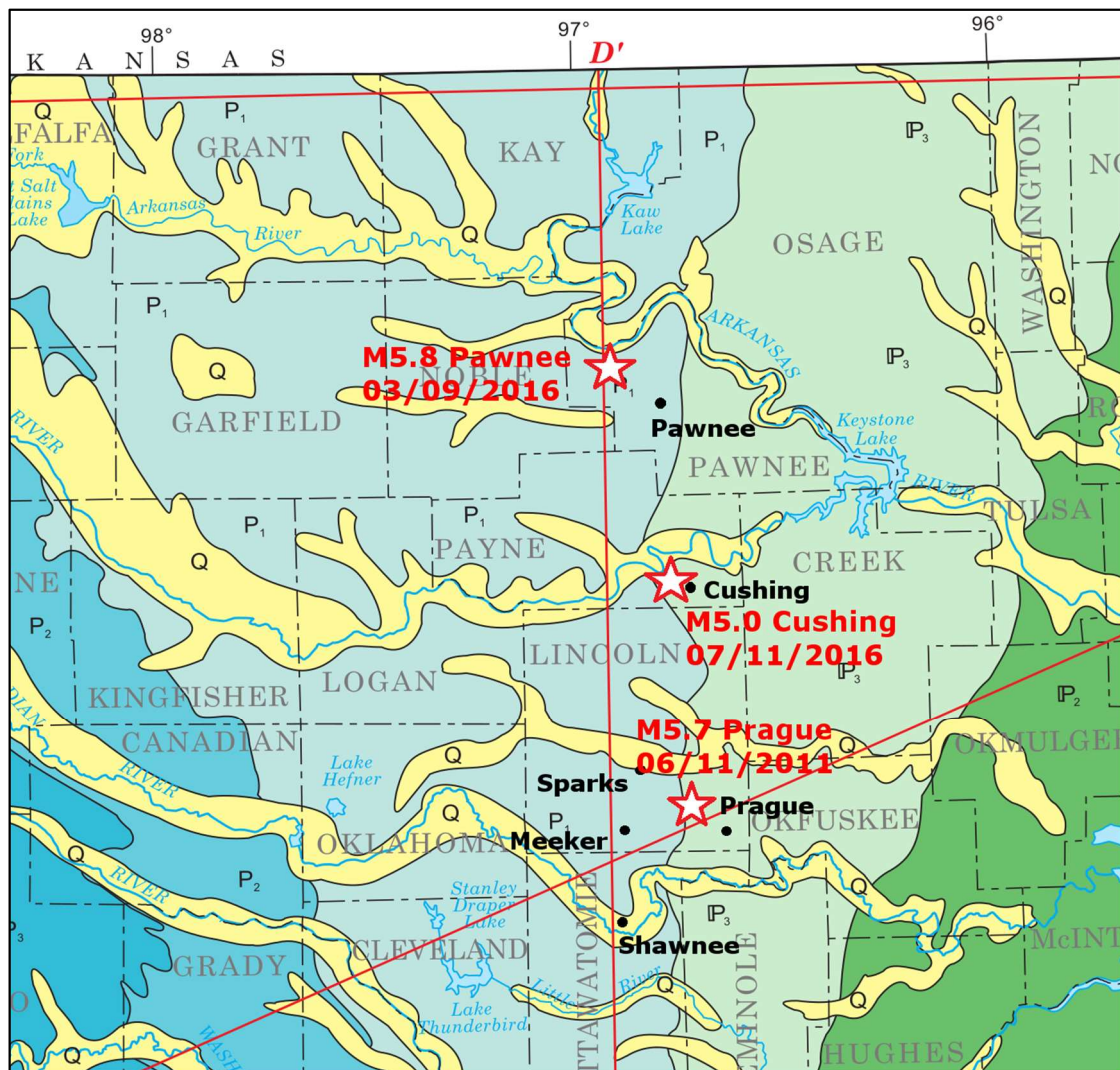


Figure A3.5.15. Geologic map of sediments and sedimentary rocks of the areas affected by the three events. Permian (P): shallow-marine, deltaic and alluvial deposits of red sandstone and shale predominate, generally between 0.3 and 2.0 km thick; subdivided into lower (P1) and upper (P2, P3 and P4) units. Pennsylvanian (IP): mostly marine shale, with interbedded sandstone, limestone, and coal, generally between 0.6 and 1.5 km thick; subdivided into lower (IP1), middle (IP2) and upper (IP3) units. Quaternary (Q): sand, silt, clay and gravel in flood plain and terrace deposits of major rivers, generally 8.0 to 30.0 m thick. Epicentres according to the USGS (stars) and location of cities affected by the three earthquakes (black dots) marked approximately over original geologic map from Johnson (2008).

A3.5.3.2 Site conditions in the affected area

Figure A3.5.16 presents a schematic cross section across the Wilzetta fault system, which is believed to be where the 2011 **M**5.7 Prague event was originated. According to the figure, a top layer of interbedded sandstone and shale overlays an alternation of clay, clay shale and limestone (Keranen *et al.*, 2013). This cross section is consistent with the geologic units described above.

Clayton *et al.* (2016) report that most of the area affected by the 2016 **M**5.8 Pawnee earthquake, with the exception of the river banks, is covered by residual clay soil of varying thickness. Clayton *et al.* (2016) also report that the existence of sporadic bedrock outcrops, which could be an indication of the depth to bedrock being generally small. This idea is supported by Grandin *et al.* (2017), who generated the map shown in Figure A3.5.17 using well data from Campbell & Weber (2006). The map suggests a depth to bedrock of approximately 2 km around Pawnee, the same or even slightly shallower around Cushing, and slightly deeper around Prague.

Clayton *et al.* (2016) characterise the susceptibility to liquefaction of the area around Pawnee as low, except along the Quaternary alluvial sediments around the Arkansas River and its major streams.

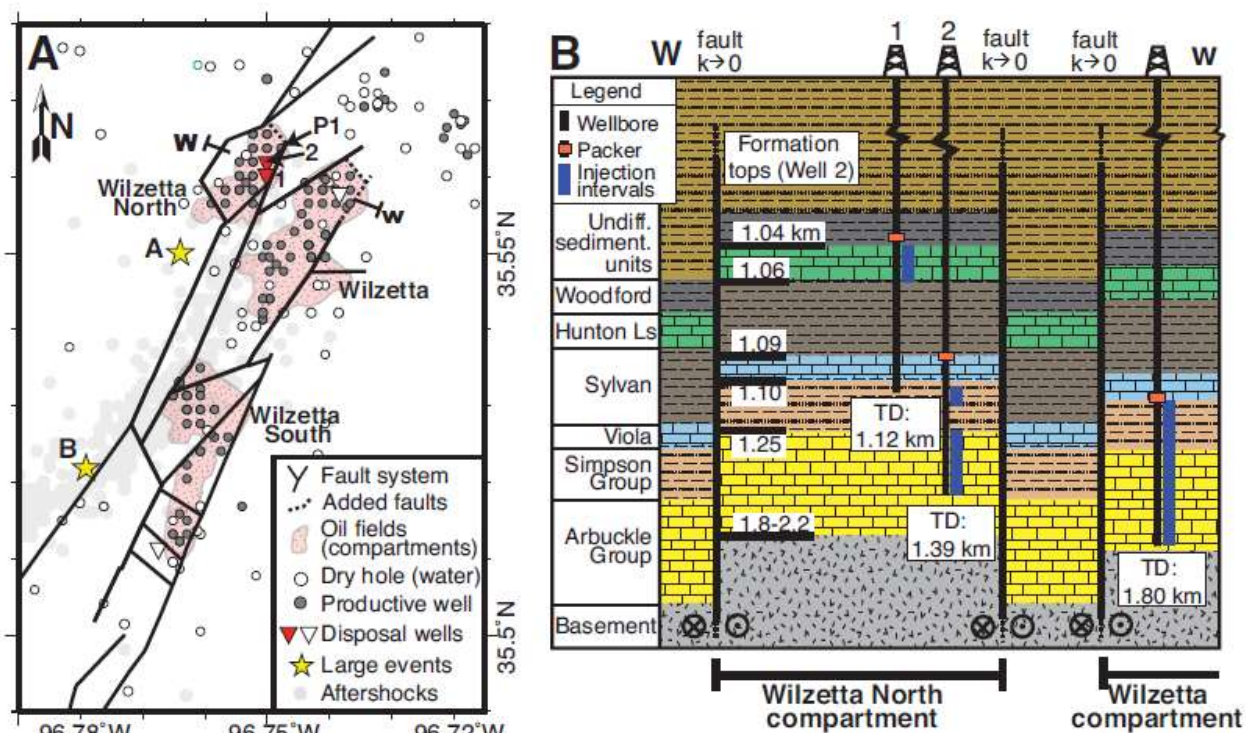


Figure A3.5.16. Schematic cross section across the Wilzetta fault system. Location of crossed section is marked over the map on the left. Starts marked as A and B are the epicentres of the **M**4.8 foreshock and the main event, respectively. The city of Prague lies to the southeast of this structure, while the city of Sparks lies to its northwest. Oil fields and wells are indicated as well.

From Keranen *et al.* (2013).

Taylor *et al.* (2017) outline a typical borehole description for the area around Cushing, based on two borehole logs obtained during the reconnaissance mission after the 2016 **M**5.0 Cushing earthquake. As can be observed in Figure A3.5.18, there is a very shallow top layer of unconsolidated soil or clay overlaying numerous alternating layers of shale, sandstone, limestone, and sandy layers of various rock types. While the information is not enough to develop detailed shear velocity profiles in depth, Taylor *et al.* (2017) use ranges of depth (2-7 m) and shear-wave velocity (200-300 m/s) for the top layer to estimate a fundamental period of the soil column between 0.027 and 0.14 seconds, with an average of around 0.09 s.

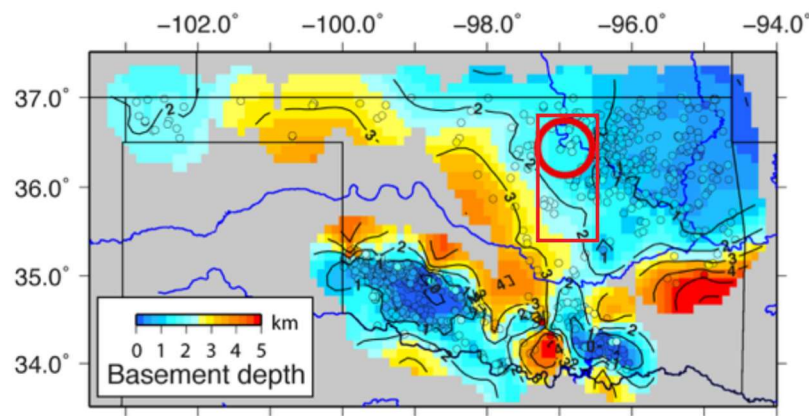


Figure A3.5.17. Depth to the basement in Oklahoma deduced from well data. Area affected by 2016 **M**5.8 Pawnee earthquake and all three events marked with red circle and red rectangle. From Grandin *et al.* (2017).

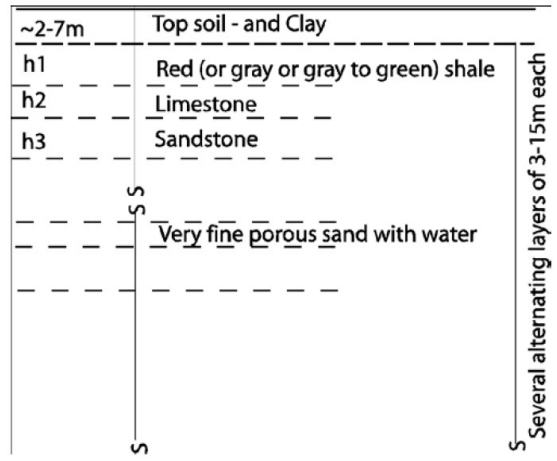


Figure A3.5.18. Typical borehole description for Cushing. From Taylor *et al.* (2017).

Measurements of V_{s30} are extremely scarce for central Oklahoma. Yong *et al.* (2015) and Parker *et al.* (2017) report values measured at seven seismological stations across the whole state, six of which correspond to sites surrounding Oklahoma city, over 50 km to the West of Prague, and even farther away from Cushing and Pawnee. These range between 304 and 761 m/s. Besides these, two values of V_{s30} are available in the report by Holland *et al.* (2013) on the probabilistic seismic hazard assessment of the Arcadia Dam, located to the northeast of Oklahoma city. Shear wave velocities vary from 300 m/s at the top to 800 m/s at a depth of 30 metres and yield a V_{s30} value of 621 m/s, in one case, while in the

other the variation goes from 180 m/s at the surface to 400 m/s at a depth of 30 metres, and yield a much lower V_{s30} value of 281 m/s. All these are marked as circles on Figure A3.5.19.

Due to the lack of direct measurements of V_{s30} in the area of interest, values estimated through different methodologies can be of interest as well. The variability inferred from the values reported above is somehow in agreement with the map generated by the United States Geological Survey (USGS) V_{s30} Map Server (Wald & Allen, 2007) (Figure A3.5.19) using topographic slope as a proxy, by means of the correlations derived by Wald & Allen (2007) for stable shield regions. According to this map, Prague and Shawnee would be characterised by V_{s30} values of around 350 to 400 m/s, and Pawnee of approximately 600 m/s, with some lower-velocity areas of around 400 m/s nearby to the West, while the area around Sparks seems to vary along a larger range between 450 and 700 m/s, and that of Cushing between 300 and 700 m/s. Along similar lines to those of Wald & Allen (2007), Parker *et al.* (2017) use a hybrid geology-slope approach to estimate values of V_{s30} , and their method yields an estimated 684 m/s for the region affected by the three events under study. All these ranges of values are consistent with the relationships between Californian geologic units and their corresponding V_{s30} values reported by Wills & Clahan (2006), which, despite of the different setting, can be used as a reference. Not all the geologic formations reported by Keranen *et al.* (2013) can be represented by the aforementioned study, but those of relevance are summarized in Table A3.5.11. As can be observed, V_{s30} values can be expected to range approximately between 300 and 600 m/s according to this source.

As an alternative to proxy methods like those of Wald & Allen (2007) and Parker *et al.* (2017), Zalachoris *et al.* (2017) developed estimates of V_{s30} for the states of Texas, Oklahoma and Kansas using fundamentals of wave propagation by means of the P-wave seismogram method. Figure A3.5.20 presents the resulting median V_{s30} map, from which values between 600 and 800 m/s could be assigned to the areas of interest. These are larger than those described above. In their work, Zalachoris *et al.* (2017) point out that their results tend to be, in general, larger than those obtained with the method of Parker *et al.* (2017) for these states. Median estimations for three stations are shown as squares on Figure A3.5.19, while estimations reported by Clayton *et al.* (2016) based on the results of Parker *et al.* (2017) and Zalachoris *et al.* (2017) for eight stations are shown as rhombuses on the same map.

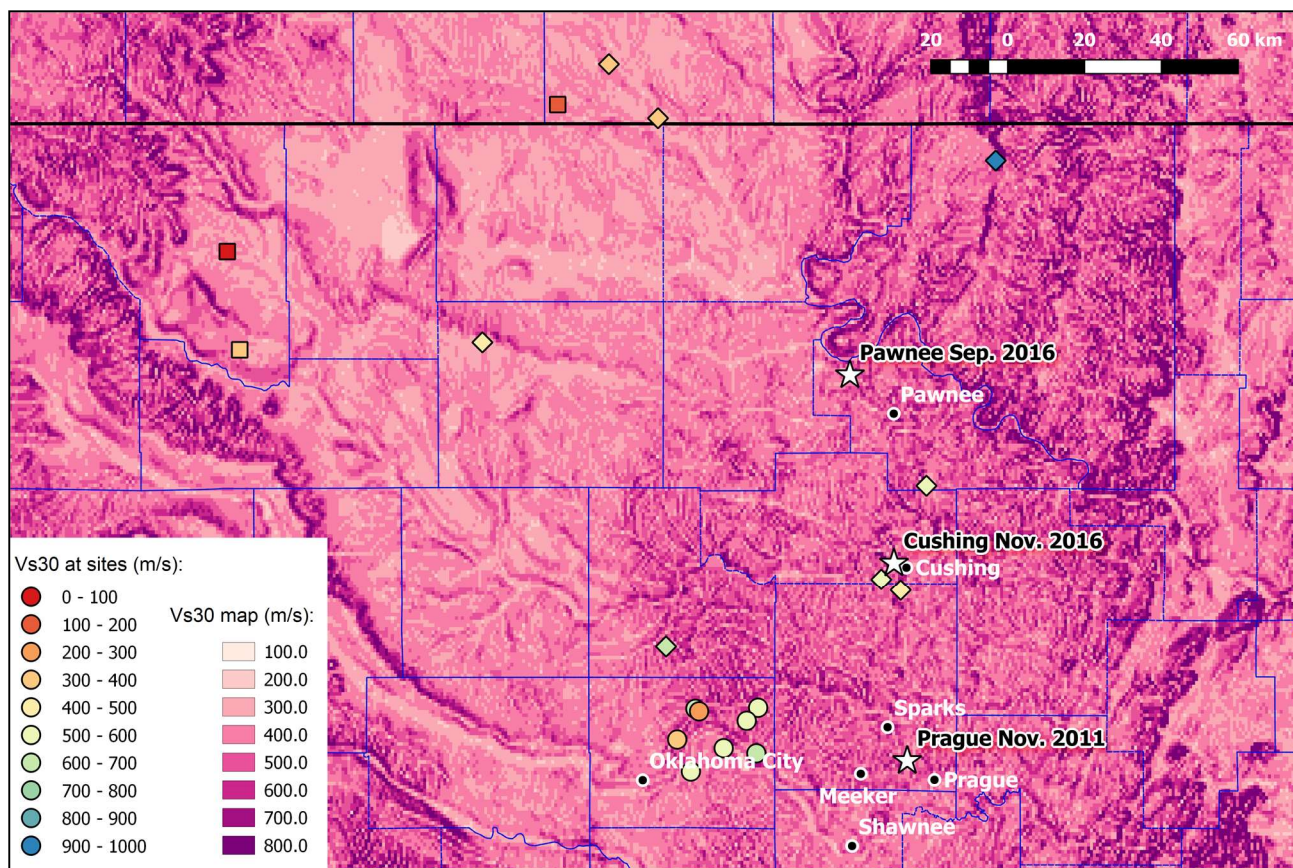


Table A3.5.11. Relationship between geologic units comparable to those of the area affected by the 2011 Prague earthquake and their shear-wave velocities. From Wills & Clahan (2006).

Geologic description	Mean V_{s30}
Tertiary (mostly Miocene and Pliocene) shale and siltstone units such as the Repetto, Fernando, Puente, and Modelo Formations of the Los Angeles area	390
Tertiary (mostly Miocene, Oligocene, and Eocene) sandstone units such as the Topanga Formation in the Los Angeles area and the Butano sandstone in the San Francisco Bay area	515
Cretaceous sandstone of the Great Valley Sequence in the central Coast Ranges	566

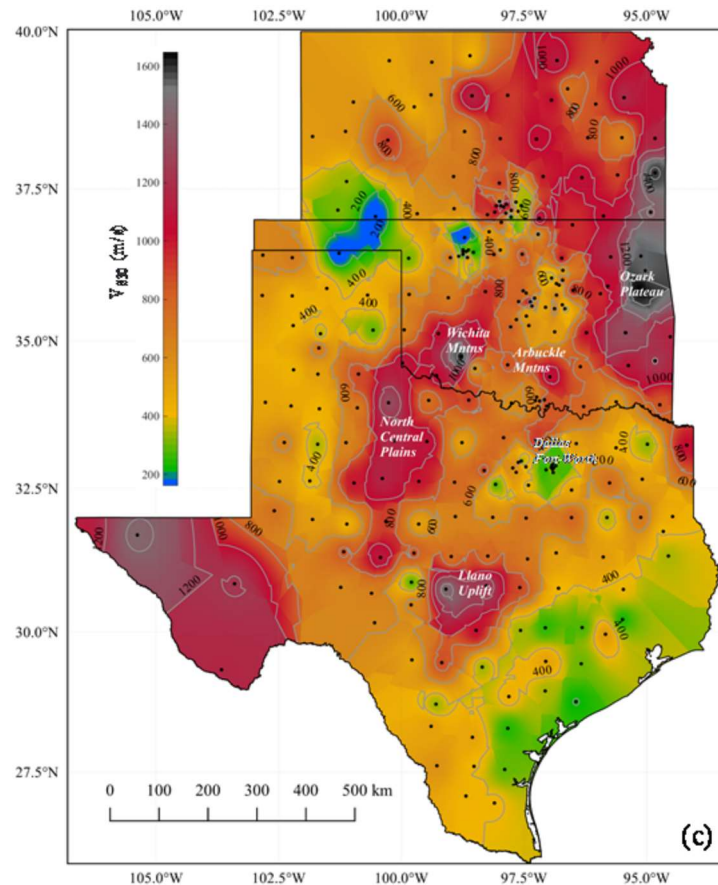


Figure A3.5.20. Median V_{s30} estimates for Texas, Oklahoma and Kansas using the P-wave seismogram method. From Zalachoris *et al.* (2017).

A3.5.4 Ground motions

A3.5.4.1 Intensity observations

According to Keranen *et al.* (2013) and the USGS, an area of approximately 65 km² in the immediate vicinity of the epicentre of the 2011 **M**5.7 Prague earthquake experienced shaking of intensity VIII (severe shaking, extensive damage in poorly built constructions) in the Modified Mercalli scale. The USGS reports the largest damage to have occurred in the area between the cities of Shawnee and Sparks. The Modified Mercalli Intensity (MMI) at these sites and at Castle, Indianola, McLoud, Sentinel and Tupelo was VI (strong shaking, minor damage), while intensity VII (very strong shaking, moderate damage) is reported for Meeker and Prague. It was felt in at least seventeen states of the central United States, from southern Wisconsin to southern Texas, and from eastern Colorado to the Memphis, Tennessee area. A resident of Shawnee told Fox News that him and his family felt it strongly, and that it was hard to keep their balance and walk (Fox News, 2011). The USGS ShakeMap (Worden *et al.*, 2017) for this event (Figure A3.5.21) reaches a MMI of VII around the epicentre and the city of Prague. Meeker, Sparks and Shawnee are indicated as having reached MMI VI, while Oklahoma city falls close to the border between IV and V.

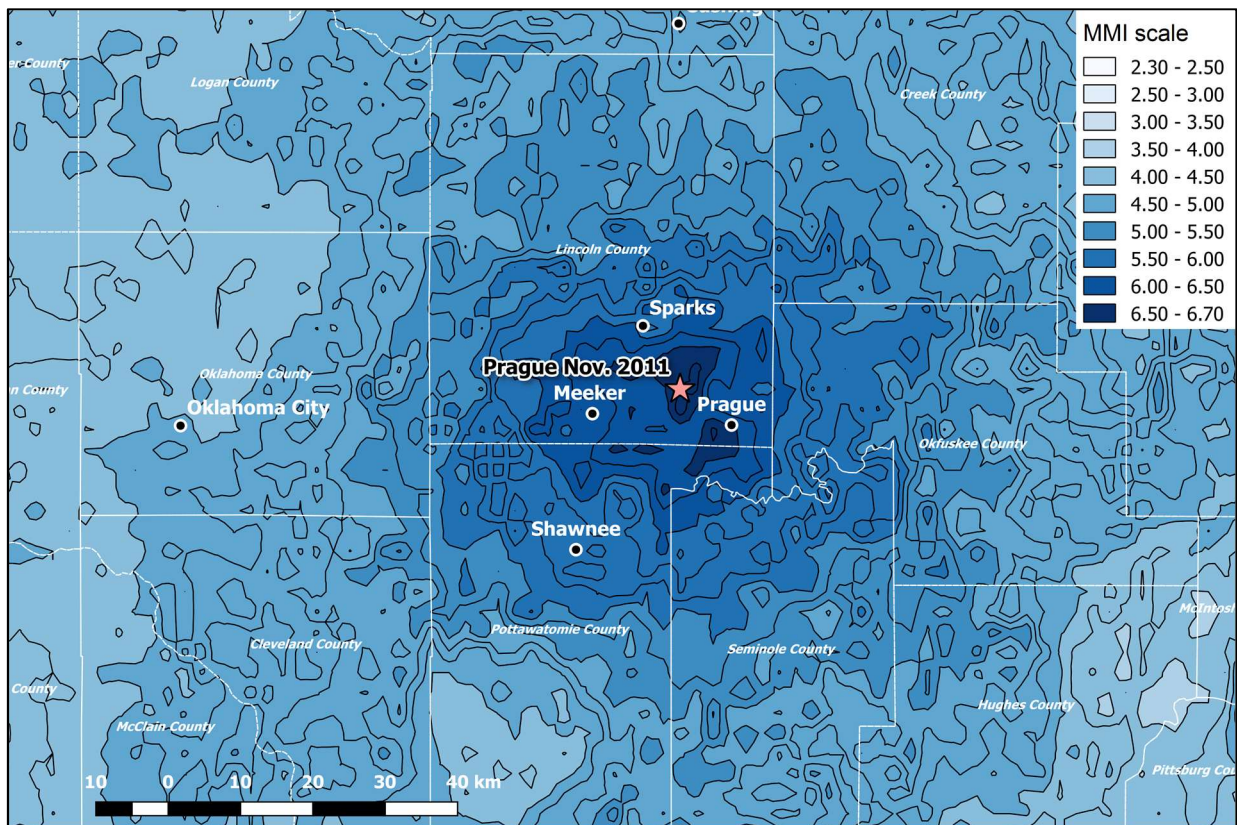


Figure A3.5.21. USGS ShakeMap (revised calculation, 10/03/2017) in terms of Modified Mercalli Intensities (MMI) for the 2011 M5.7 Prague earthquake.

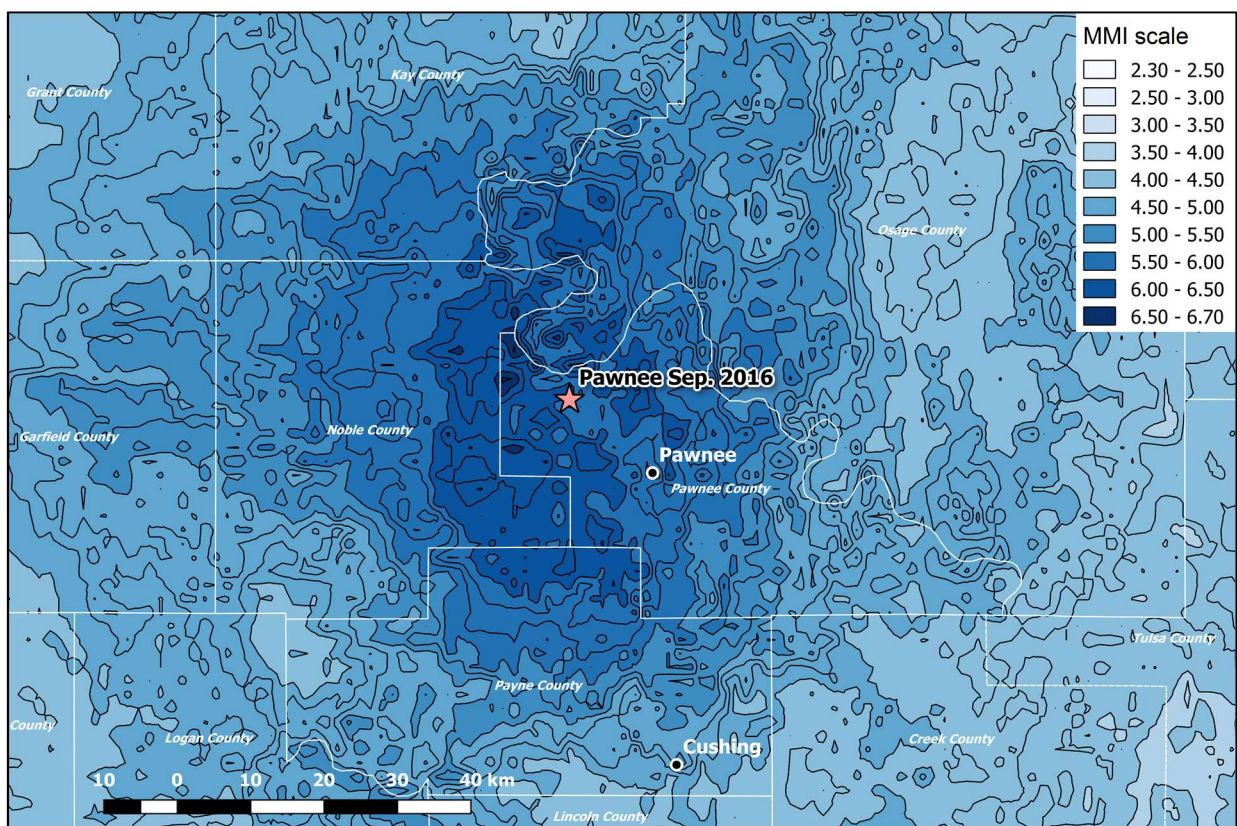


Figure A3.5.22. USGS ShakeMap (revised calculation, 03/12/2016) in terms of Modified Mercalli Intensities (MMI) for the 2016 M5.8 Pawnee earthquake.

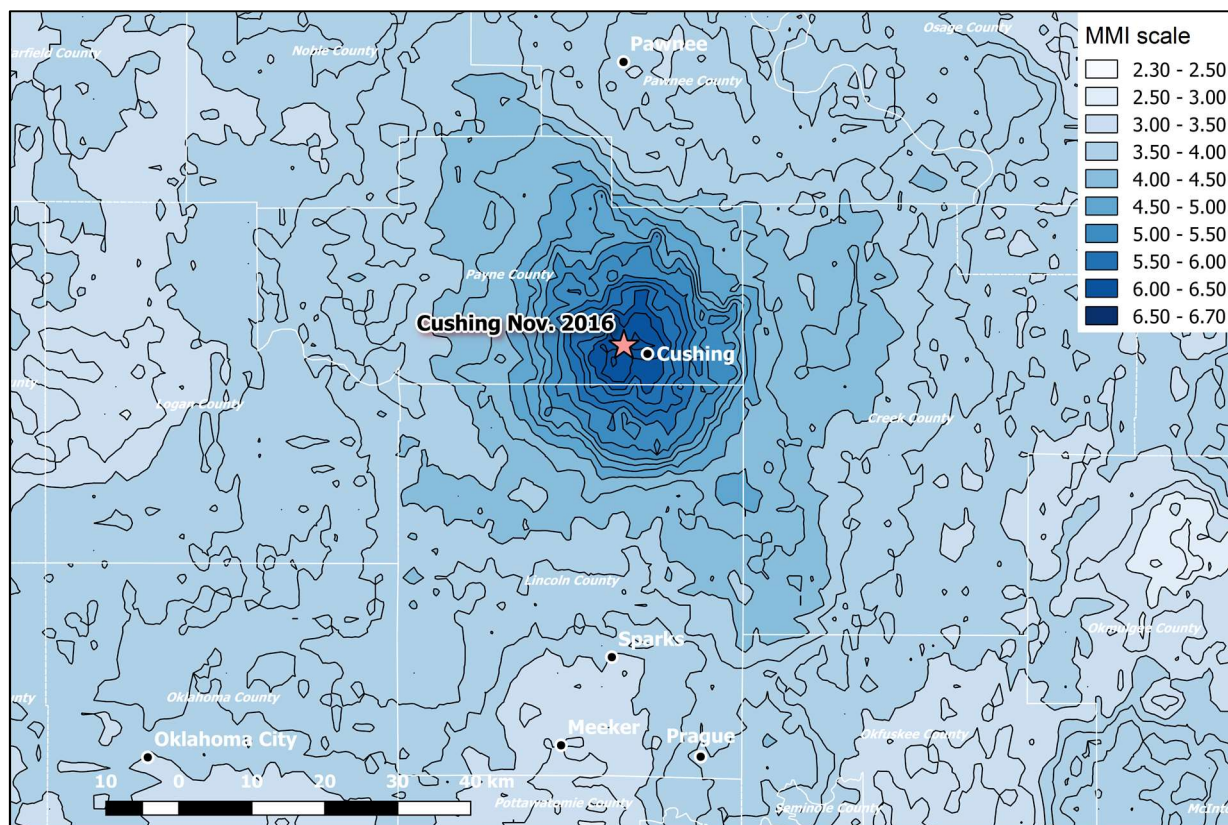


Figure A3.5.23. USGS ShakeMap (revised calculation, 18/12/2016) in terms of Modified Mercalli Intensities (MMI) for the 2016 **M**5.0 Cushing earthquake.

The 2016 **M**5.8 Pawnee earthquake was felt in a large area stretching from Denver, Colorado, to Chicago, Illinois, and from Texas to South Dakota, up to distances over 1500 km (Yeck *et al.*, 2017; NBC News, 2016; Reuters, 2016). Yeck *et al.* (2017) report MMI between VI and VIII in the epicentral region. The USGS reports MMI of VII at Glencoe and Osage, VI at Carney, Dacoma, Morrison, Shidler and Spencer, and V at Wichita and in more than 30 other towns in Kansas, and that it was felt in parts of Alabama, Arizona, Colorado, Georgia, Illinois, Indiana, Kentucky, Louisiana, Michigan, Minnesota, Mississippi, New Mexico, North Dakota, Ohio, South Dakota, Tennessee and Wisconsin. The USGS ShakeMap for this event (Figure A3.5.22) reaches a MMI of VII only in very localised spots, while most of the epicentral area, including the city of Pawnee, would fall under MMI VI.

For the 2016 **M**5.0 Cushing earthquake, the USGS reports a MMI of VI at Cushing and Mounds, V at Drumright, Piedmont, Stroud and Wellston, and IV in many locations in Kansas, Arkansas, Missouri and Texas, and that it was also felt in parts of Illinois, Indiana, Iowa and Nebraska. The USGS ShakeMap for this event (Figure A3.5.23) reaches a MMI between VI and VII in the epicentral area, including the city of Cushing. Visual inspection of Figures A3.5.21 through A3.5.23 suggests that the 2016 **M**5.0 Cushing event was felt in a much more reduced area than the other two, which is expected, given that all three are similarly shallow events, but the magnitude of the Cushing earthquake is much smaller.

A3.5.4.2 Ground motion recordings

There is a variety of sources for information regarding ground motion records from these three events, of which the two main ones are three-component waveforms available at the website of the Center for Engineering Strong Motion Data (CESMD), and horizontal (and, in some cases, vertical) peak ground accelerations (PGA) and spectral demands for lists of recording stations used by the USGS to generate the corresponding ShakeMaps (Worden *et al.*, 2017). Figure A3.5.24 summarises the PGA values from these sources and plots them against their corresponding epicentral distances, calculated with respect to the epicentral coordinates estimated by the USGS using the OpenQuake Hazard Library (Pagani *et al.*, 2014), together with vertical lines that indicate, in an approximate fashion, the range of distances in which damage was observed. For the 2011 **M**5.7 Prague event, the USGS reports only one value per station without specifying which component it corresponds to. For the other two events, as well as for the waveforms from the CESMD, values for the three components are available and shown with different markers and colours. As can be observed it is for the 2016 **M**5.0 Cushing event for which more near-field records are available. The PGA values attained by the four closest recordings of this earthquake are notably large, 58.5% g being the largest as-recorded horizontal component of the four. For the 2011 **M**5.7 Prague and 2016 **M**5.8 Pawnee events, all available data correspond to PGA values below 10% g.

Taylor *et al.* (2017) present a comparison between ground motions from five stations located in the near-field of the 2016 **M**5.0 Cushing earthquake (which include the four mentioned above) and expected median ground motions from two ground motion prediction models, one for induced seismicity and the other for tectonic events in the central and eastern USA, and conclude that the peak ground accelerations observed for Cushing are significantly larger than the expected median for a **M**5.0 event.

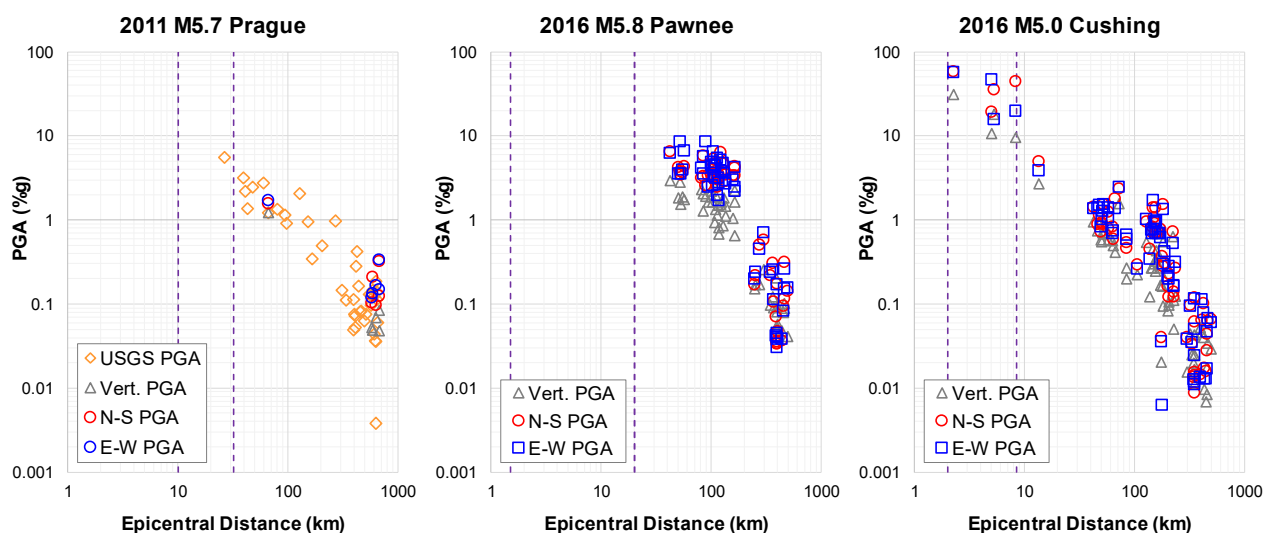


Figure A3.5.24. Recorded PGA (%g) versus epicentral distance for the three events. Data from the list of physical stations used by USGS's ShakeMap and calculated from waveforms available from the CESMD. Vertical dashed lines indicate, approximately, the distances at which damage was observed.

Figures A3.5.25 and A3.5.26 show the pseudo-acceleration and displacement response spectra for the six records whose waveforms are available at the CESMD for the 2011 **M**5.7 Prague earthquake. Given that the epicentral distances are quite large, the motion observed is weak. Yenier *et al.* (2017) compared the ground motions generated by 291 earthquakes within the 2011 Prague sequence with those of events in central and eastern North America in terms of the geometric mean of the two as-recorded components and concluded that, in average, the former decay at a rate similar to that of the latter.

The 2016 **M**5.8 Pawnee earthquake is the one for which the largest number of waveforms are available at the CESMD. Figures A3.5.27 and A3.5.28 show their corresponding pseudo-acceleration and displacement response spectra. Clayton *et al.* (2016) show similar plots for five of these stations and for five others whose waveforms were not accessible to the authors. Of the latter, station OK.DEOK shows marked peaks similar to many of those shown in Figure A3.5.27 around $T=0.1$ s, while four other stations (OK.QUOK, N4.T35B, OK.CROK and OK.CHOK) show motions with more numerous peaks at other periods.

As shown in Figures A3.5.29 and A3.5.30, pseudo-acceleration spectra of records from the 2016 **M**5.0 Cushing earthquake also feature a peak at a similar period. Taylor *et al.* (2017) observe these peaks as well, and point out that periods around 0.1 seconds are expectable for low-rise buildings of the kind that can be found in Cushing. Taylor *et al.* (2017) also carry out a comparison between the pseudo-acceleration spectra of these five records and the ASCE 7-10 design spectrum corresponding to Cushing, as well as spectra anchored to the 0.2 and 1.0 second values with 1% in 1-year and 2% in 50-years probabilities of exceedance spectra of Petersen *et al.* (2016) and Petersen *et al.* (2014) hazard models for the United States. They conclude that the observed motions were much larger than the ASCE 7-10 design spectrum and generally exceed the 1% in 1-year spectrum as well, though they seem to be below those of the 2% in 50-years one.

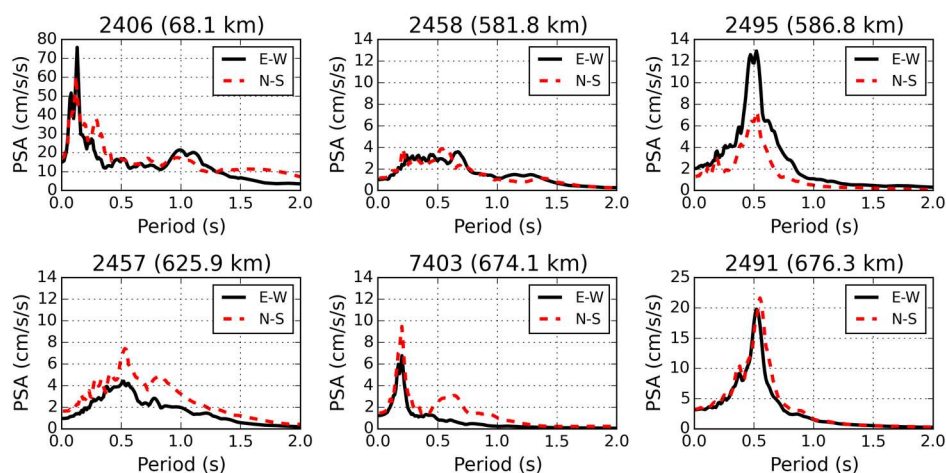


Figure A3.5.25. Pseudo-acceleration spectra (5% of critical damping) of the two horizontal components of the six waveforms available at the CESMD for the 2011 **M**5.7 Prague earthquake. Epicentral distances (as reported by the CESMD) shown in parentheses.

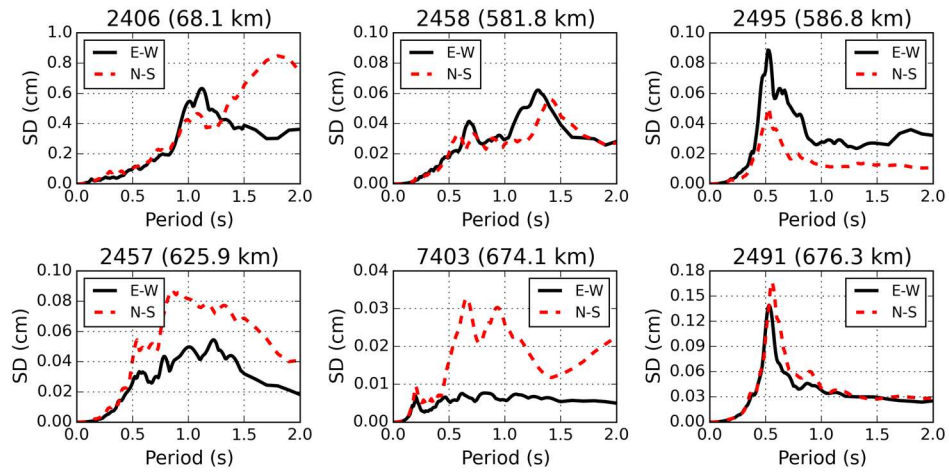


Figure A3.5.26. Displacement spectra (5% of critical damping) of the two horizontal components of the six waveforms available at the CESMD for the 2011 **M**5.7 Prague earthquake. Epicentral distances (as reported by the CESMD) shown in parentheses.

Figure A3.5.31 shows the waveforms recorded at three stations located very close to the 2016 **M**5.0 Cushing earthquake. Two features strike the eye: firstly, that the duration of the motion is relatively short and, secondly, the two bulges separated by a low energy time interval. Taylor *et al.* (2017) made these observations as well. It is noted here that the two bulges are apparent in all three components of station OK914, which is located almost directly to the south of the epicenter (as estimated by the USGS), but seem stronger in the E-W component of station OK915 and the N-S component of station OK031, each located to the south-west and south-east of the epicentre, respectively. The difference or similarity between the amplitude of the motion of the two horizontal components of each station follows the same pattern.

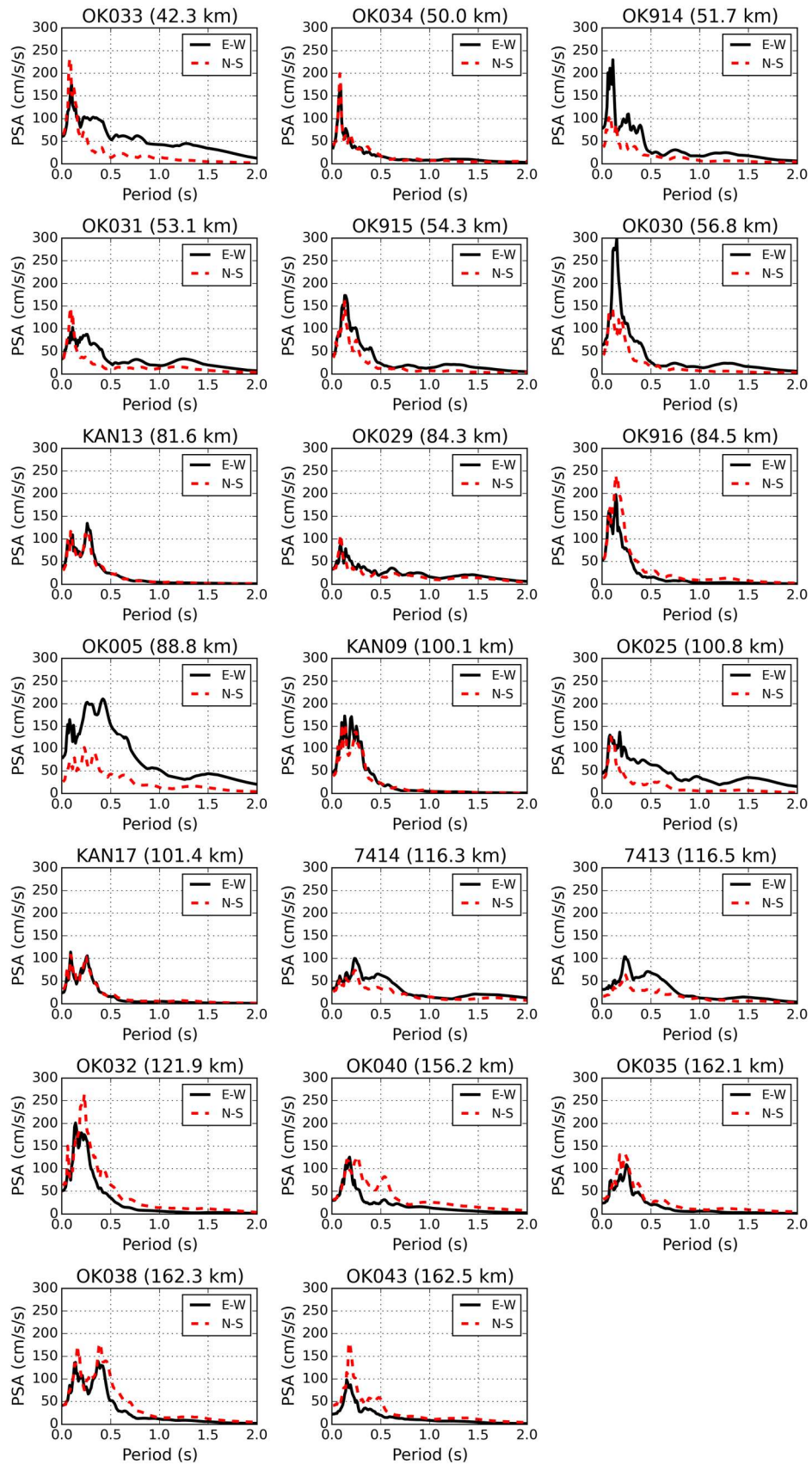


Figure A3.5.27. Pseudo-acceleration spectra (5% of critical damping) of the two horizontal components of the twenty waveforms available at the CESMD for the 2016 **M**5.8 Pawnee earthquake. Epicentral distances (with respect to epicenter coordinates estimated by the USGS, calculated with the OpenQuake Hazard Library (Pagani *et al.*, 2014)) shown in parentheses.

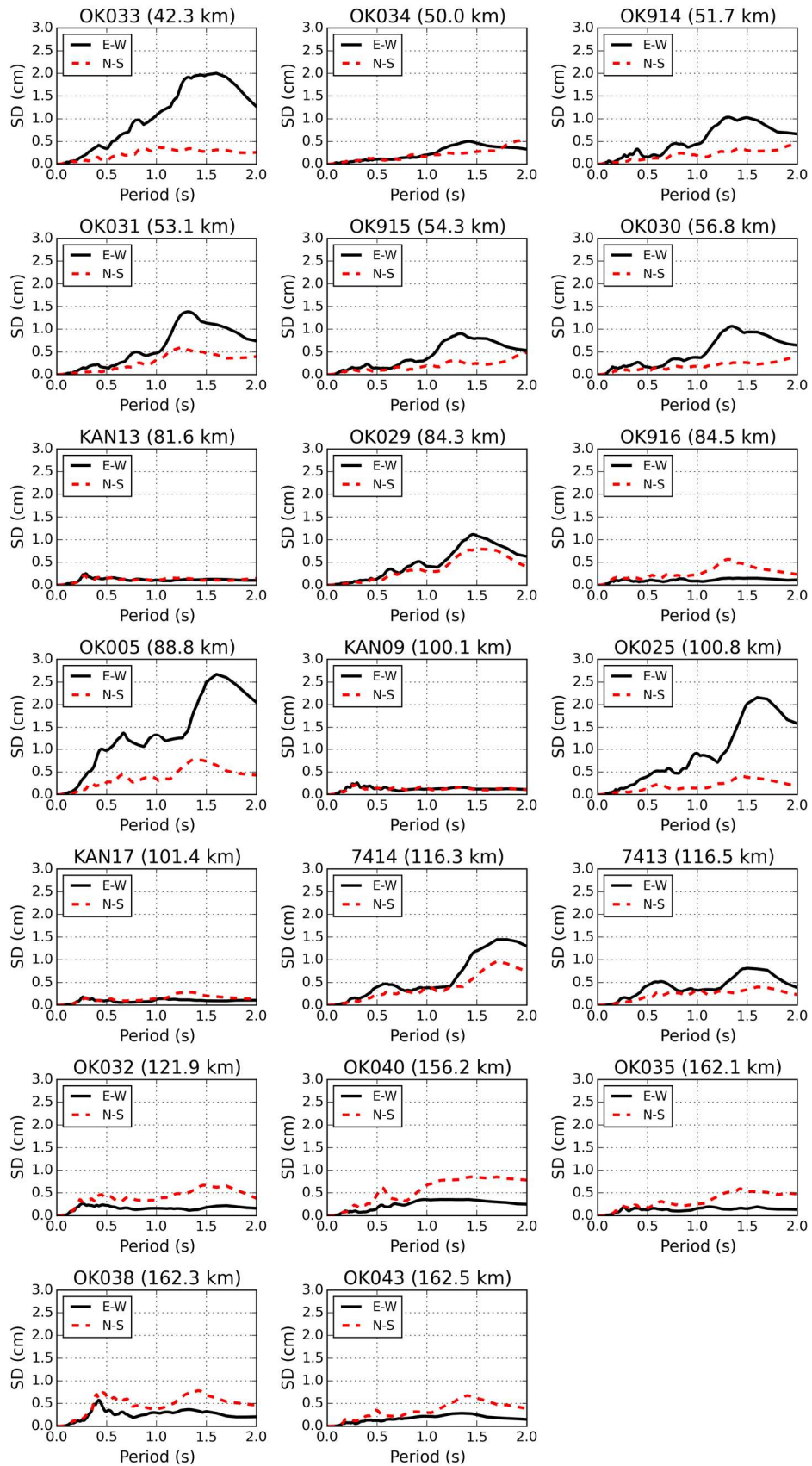


Figure A3.5.28. Displacement spectra (5% of critical damping) of the two horizontal components of the twenty waveforms available at the CESMD for the 2016 **M**5.8 Pawnee earthquake. Epicentral distances (with respect to epicenter coordinates estimated by the USGS, calculated with the OpenQuake Hazard Library (Pagani *et al.*, 2014)) shown in parentheses.

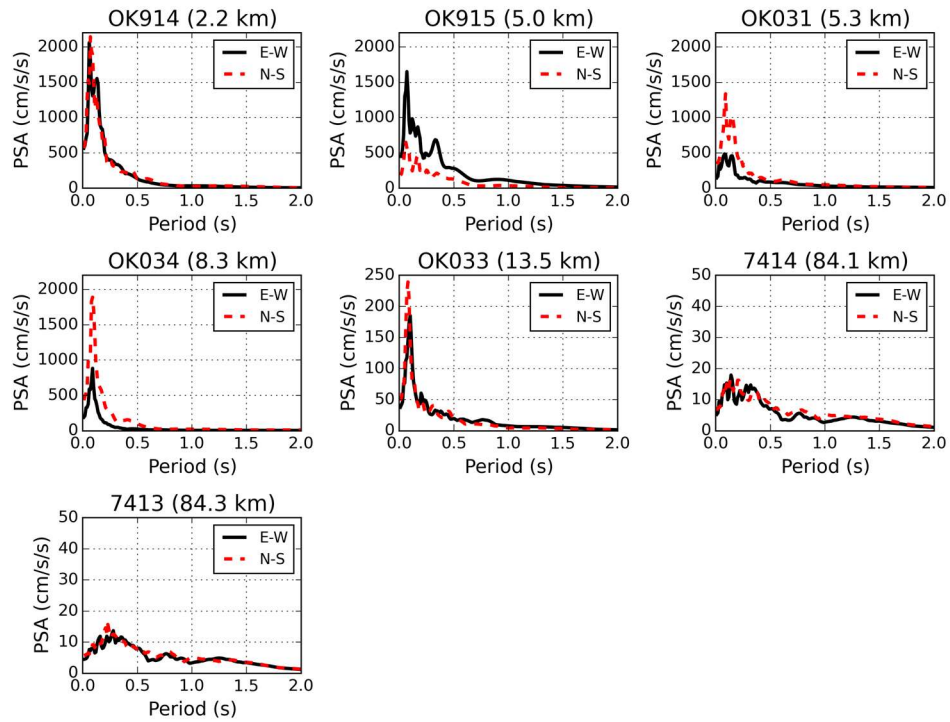


Figure A3.5.29. Pseudo-acceleration spectra (5% of critical damping) of the two horizontal components of the seven waveforms available at the CESMD for the 2016 **M**5.0 Cushing earthquake. Epicentral distances (with respect to epicenter coordinates estimated by the USGS, calculated with the OpenQuake Hazard Library (Pagani *et al.*, 2014)) shown in parentheses.

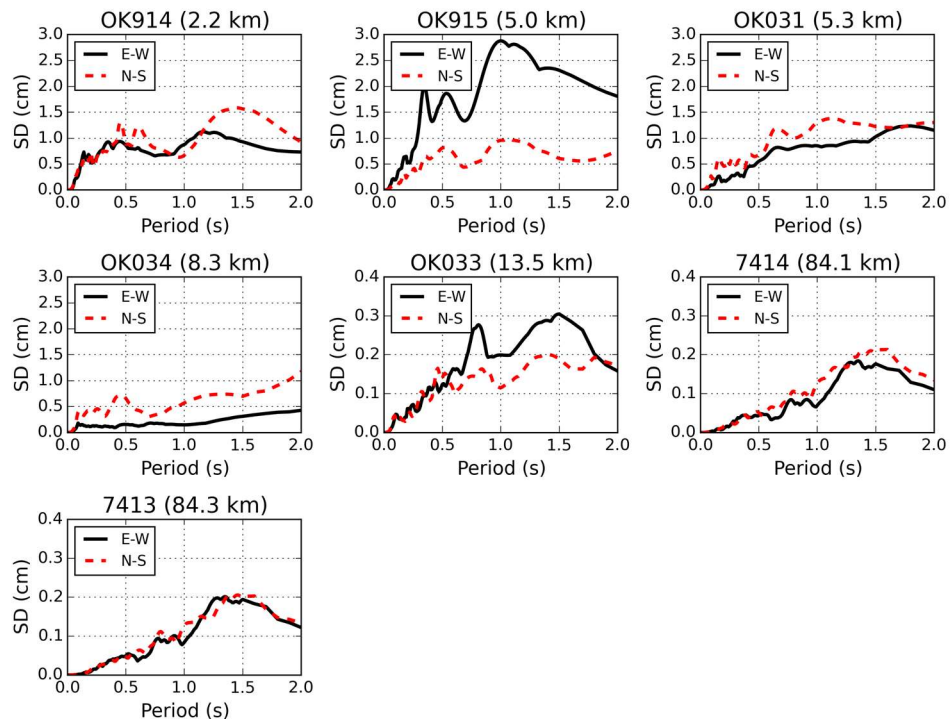


Figure A3.5.30. Displacement spectra (5% of critical damping) of the two horizontal components of the seven waveforms available at the CESMD for the 2016 **M**5.0 Cushing earthquake. Epicentral distances (with respect to epicenter coordinates estimated by the USGS, calculated with the OpenQuake Hazard Library (Pagani *et al.*, 2014)) shown in parentheses.

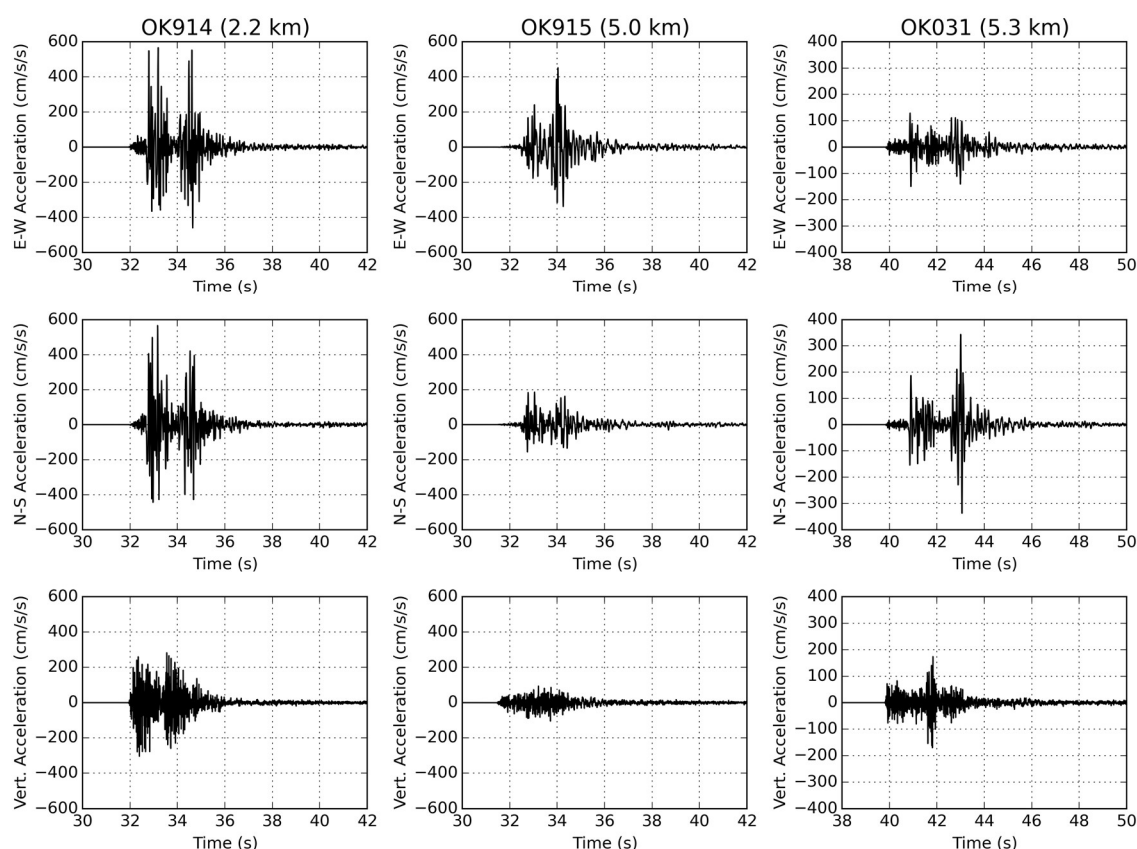


Figure A3.5.31. Acceleration time-histories of the 2016 **M**5.0 Cushing earthquake recorded at three stations. Time windows corresponding to strong motion shown from the complete accelerograms available at the CESMD, different records not synchronised.

A3.5.4.3 Inferred shaking levels

In order to generate a more complete characterisation of the earthquake, the USGS combines information from recording stations and reports of felt intensity to produce ShakeMaps (Worden *et al.*, 2017) in terms of Modified Mercalli Intensity, as seen above, peak ground accelerations (PGA) and velocities (PGV) and pseudo-spectral accelerations at 0.3, 1.0 and 3.0 seconds. These estimations of ground motion are of particular relevance when near-field recordings are missing or scarce. The overall quality of the data feeding the ShakeMaps for these three earthquakes seems to be quite good, given the many recording stations and Did You Feel It? points that appear to have been used.

For the 2011 **M**5.7 Prague earthquake, the closest station for which recorded values are publicly available is located 26 km away from the epicentre. The map in Figure A3.5.32 shows the PGA ShakeMap generated by the USGS, together with available recorded PGA values. According to these estimations, the city of Prague may have experienced around 40-42% g, Sparks and Meeker 20-25% g, and Shawnee 10-15% g. Figure A3.5.33 shows the equivalent map for the 2016 **M**5.8 Pawnee earthquake, for which the closest reported PGA value is even farther away. For the city of Pawnee itself, the estimated PGA values are around 15-20% g, though locations assessed by the GEER team (Clayton *et al.*, 2016) closer to the epicentre may have experienced between 25% and 42% g according to this estimation.

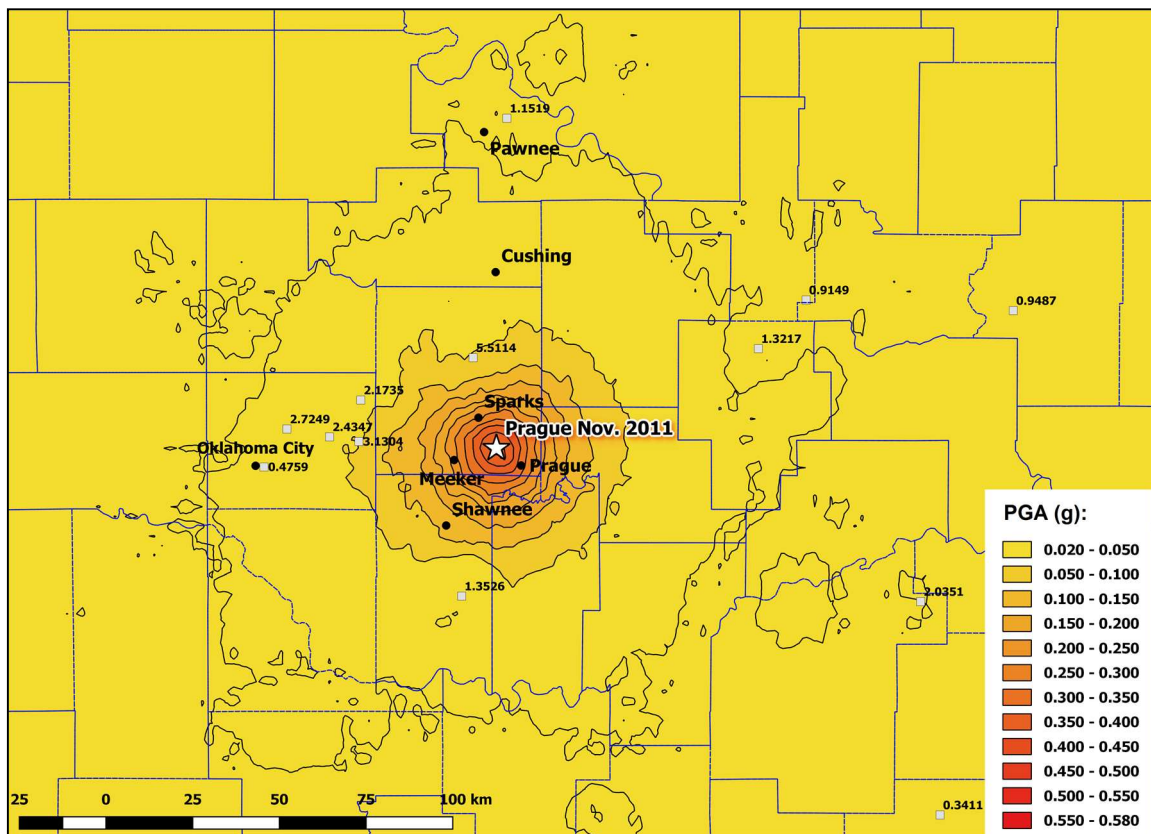


Figure A3.5.32. USGS ShakeMap (revised calculation, 10/03/2017) in terms of peak ground accelerations (PGA, g) for the 2011 **M**5.7 Prague earthquake. Squares indicate PGA values recorded at stations (%g).

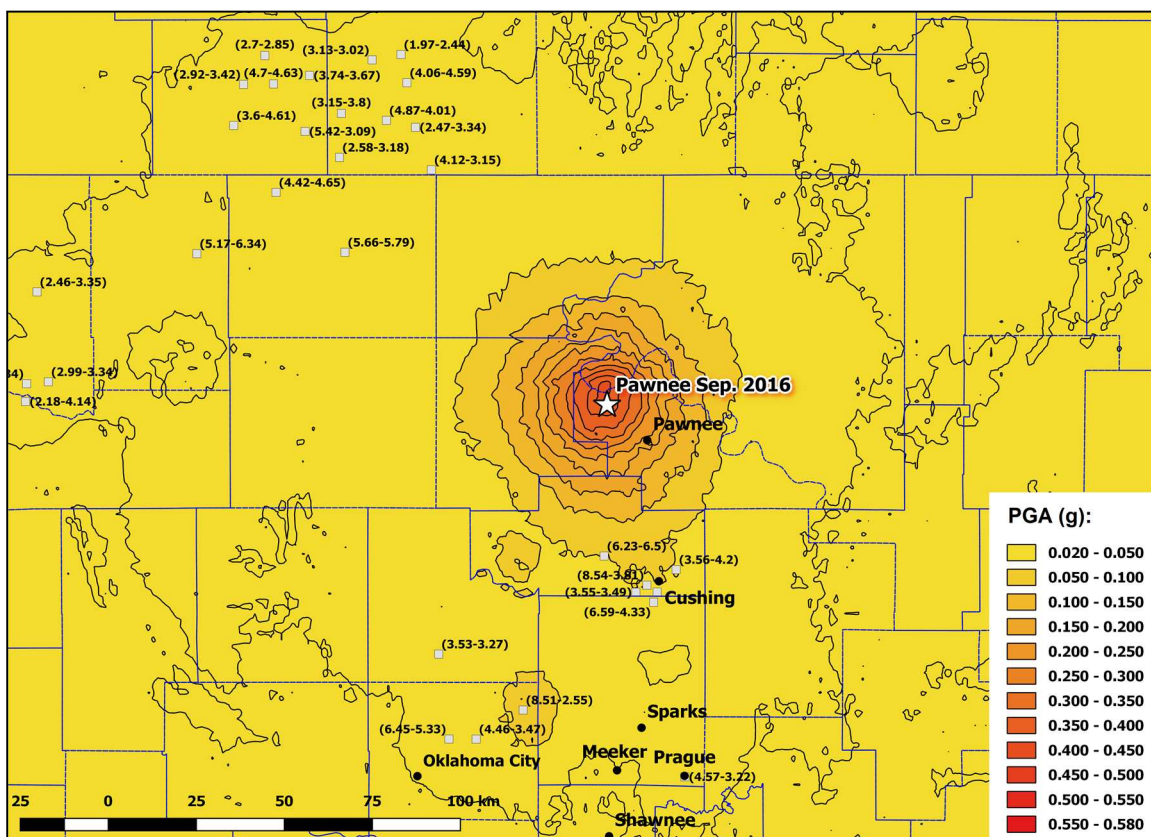


Figure A3.5.33. USGS ShakeMap (revised calculation, 03/12/2016) in terms of peak ground accelerations (PGA, g) for the 2016 **M**5.8 Pawnee earthquake. Squares indicate PGA values recorded at stations (%g, first value E-W, second value N-S components).

Based on their observation of sporadic bedrock outcrops, which they suspect suggests an overall generally small depth of sedimentary deposits, Clayton *et al.* (2016) believe that there were no substantial site amplification effects influencing the ground motion levels for this earthquake.

As mentioned earlier, a series of near-field records are available for Cushing, facilitating the estimation of observed ground motions around the epicentral area. As shown in Figure A3.5.34, the city of Cushing is likely to have experienced peak ground accelerations of between 45% and 58% g, this upper-bound corresponding to the N-S as-recorded component of station OK914, located 2.25 km south of the epicentre, to the west of the city.

As the four stations closest to Cushing (OK914, OK915, OK031 and OK034) present spectral amplification around the 0.1 second period (Figure A3.5.29), a value that is consistent with the estimation of the natural period of the soil column of Taylor *et al.* (2017), it is likely that a large part of the city of Cushing experienced ground motions with similar frequency contents.

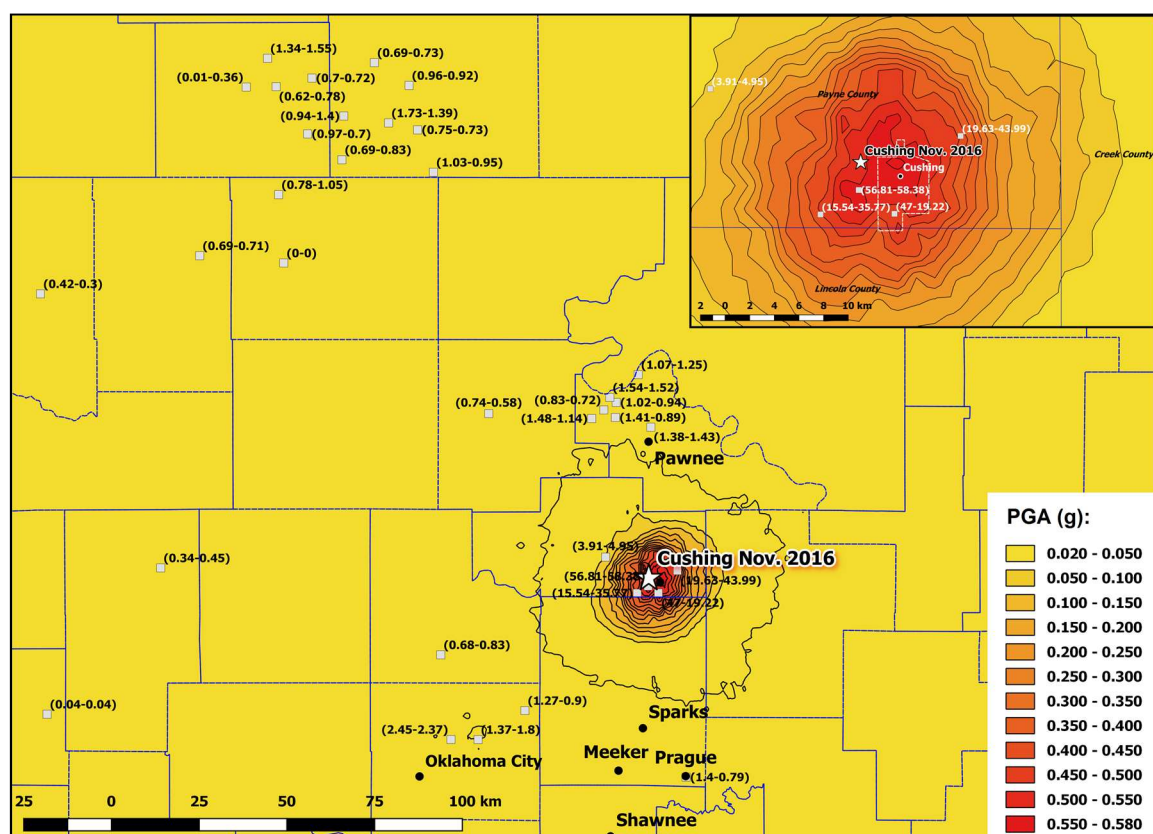


Figure A3.5.34. USGS ShakeMap (revised calculation, 18/12/2016) in terms of peak ground accelerations (PGA, g) for the 2016 M5.0 Cushing earthquake. Squares indicate PGA values recorded at stations (%g, first value E-W, second value N-S components). Dashed lines in the inset approximately delineate the contours of Cushing's urban area.

A3.5.4.4 Duration of ground shaking

The 5%-75% definition of the significant duration of the six records of the 2011 **M5.7** Prague earthquake available from the CESMD database was calculated for each as-recorded horizontal component using the OpenQuake ground motion toolkit (Weatherill, 2014). Results are shown in Table A3.5.12.

Table A3.5.12. Significant duration (5%-75% of Arias intensity, in seconds) of the ground motions available for the 2011 **M5.7** Prague earthquake from the CESMD database (2016).

Station	Station Name	Latitude	Longitude	Repi (km)	X component	Y component
2406	OK Oklahoma City - VAMC, Bldg 3	35.4840 ° N	97.4950 °W	66.3	18.3	17.3
2458	AR Lepanto - FS	35.6130 ° N	90.3300 °W	582.0	22.6	21.2
2495	MO Poplar Bluff - FS	36.7370 ° N	90.3980 °W	587.2	14.8	33.2
2457	Dexter- Fire Station 2	36.7960 ° N	89.9660 °W	626.2	22.1	17.8
7403	MO St. Louis - Cochran VAMC, Bldg 6	38.6430 ° N	90.2320 °W	674.6	36.5	34.4
2491	St. Louis - Visitors Ctr	38.6260 ° N	90.1910 °W	676.8	31.3	30.9

Estimations of earthquake significant durations can be obtained by means of prediction equations such as those of Bommer *et al.* (2009) and Afshari & Stewart (2016). For the former, a 1.5 km depth to the top of the rupture was used, based on the slip model of Sun & Hartzell (2014) and the fact that Keranen *et al.* (2013) reports that there was no surface rupture for this event. A series of distances were considered, including an approximation to the distances to the cities of Sparks, Prague and Meeker, as well as the distance to recording station 2406, located in Oklahoma City, and an average 600 km distance to represent the remaining five stations for which the significant duration could be calculated. In view of the lack of information regarding the site conditions at the recording stations, a range of values of V_{s30} was also considered, including the known values for ADOK station (620 m/s) and Arcadia dam (280 m/s), and values that would approximately correspond to the cities of Prague and Shawnee (375 m/s) and some locations in Sparks (700 m/s), according to the V_{s30} map generated by the United States Geological Survey (Figure A3.5.19). Results obtained are plotted in Figure A3.5.35.

As can be observed, the significant duration calculated for Station 2406 (around 18 seconds) is double than estimated for a distance of 66 km in all soil conditions considered. It is interesting to note that these 18 seconds are quite in agreement with what was reported by the Earth Institute at Columbia University as being a statement by seismologist Katie Keranen, who said the shaking of the 2011 **M5.7** Prague earthquake lasted "for about 20 seconds" (The Earth Institute, Columbia University, 2013). A resident of the town of Broken Arrow, located approximately 100 km away from the epicentre, told the CNN (2011) that the ground shaking lasted "for a full minute", a value that is significantly larger than that predicted by the Bommer *et al.* (2009) and Afshari & Stewart (2016) equations, and the significant duration calculated for Station 2406, at 66 km from the epicentre. It is noted that reports of duration coming from the general public have a tendency to exaggerate the length of the shaking episode.

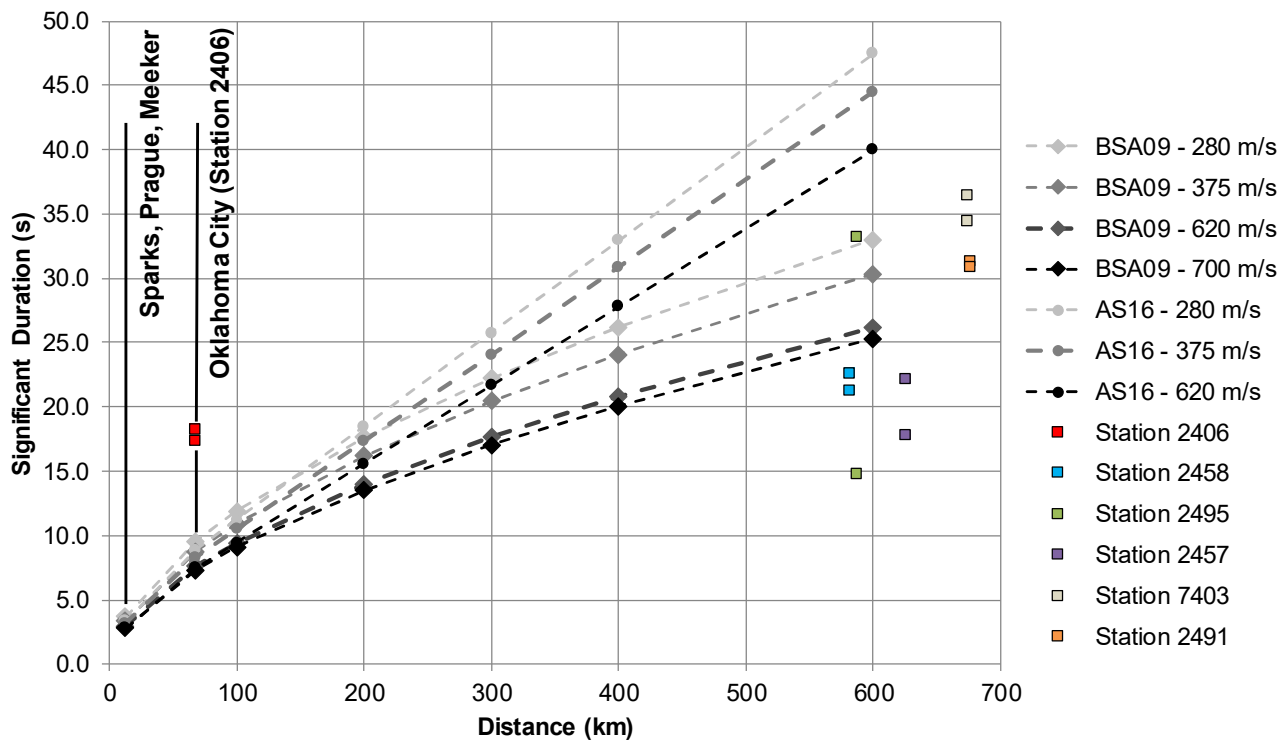


Figure A3.5.35. Estimation of the significant duration of the main shock of the 2011 **M**5.7 Prague earthquake, using prediction equations by Bommer *et al.* (2009, BSA) and Afshari & Stewart (2016, AS), and significant duration calculated for the two as-recorded horizontal components of the six available accelerograms.

Noting that both predictive models are being applied outside of the distance range for which they were fitted, it is observed that calculated values for the remaining five stations are significantly closer to the predictions of the Bommer *et al.* (2009) equation than to those of the Afshari & Stewart (2016) one. Applying the predictive models using the epicentral distances to all the stations, a 1.5 km depth to the top of the rupture as before, and values of V_{s30} estimated from the V_{s30} USGS map (Wald & Allen, 2007) (Figure A3.5.19), observed durations (Table A3.5.12) are within the range of [-1.75,+1.20] and [-2.49,+1.41] standard deviations of the models of Bommer *et al.* (2009) and Afshari & Stewart (2016), respectively.

Table A3.5.13 is the equivalent of Table A3.5.12 for the case of the 2016 **M**5.8 Pawnee event, while Figure A3.5.36 shows analogous comparisons to estimations of significant durations obtained by means of the prediction equations of Bommer *et al.* (2009) and Afshari & Stewart (2016) to those of Figure A3.5.35. The latter were carried out for a range of distances that cover those of the available accelerograms, and for three values of V_{s30} : 400 and 600 m/s, as suggested by the United States Geological Survey (USGS) V_{s30} Map Server (Wald & Allen, 2007), estimated using topographic slope as a proxy (see Section A3.5.3.2), and 100 m/s, added in view of the values calculated from the available accelerograms being much larger than those predicted, with the aim of providing additional reference. A depth to the top of rupture of 3 km was adopted, in agreement with the rupture slip model developed by Grandin *et al.* (2017). Figure A3.5.36 suggests that observed values of significant duration for this earthquake tend to be larger than the

predictions for distances up to 100 km, approximately, and smaller than the predictions at larger distances. While it could be thought that this observation might be due to the model of Bommer *et al.* (2009) being applied outside of its distance range, this is not the case for the model of Afshari & Stewart (2016), for which the tendency is the same. This trend becomes even more evident when plotting the normalised residuals (*i.e.*, number of standard deviations that the median estimation differs from the “real” value) of the estimations from Bommer *et al.* (2009) and Afshari & Stewart (2016) with respect to the observed values for the available accelerograms, against closest distances to the fault rupture, as shown in Figure A3.5.37. The estimations were carried out with the same 3 km as depth to the top of rupture as before and the closest distances from the fault rupture to the sites calculated using the slip model of Grandin *et al.* (2017) and the OpenQuake Hazard Library (Pagani *et al.*, 2014). A measured value of V_{s30} was available only for Station OK005 (596 m/s, Yong *et al.*, 2015) and the medians of values calculated via wave propagation considerations by Zalachoris *et al.* (2017) were available for three stations (KAN17, OK035 and OK040), while estimations assigned by Clayton *et al.* (2016) based on the proxy method of Parker *et al.* (2017) and calculations of Zalachoris *et al.* (2017) were used for five other stations. For the remaining eleven stations, V_{s30} values were approximately estimated from the United States Geological Survey (USGS) V_{s30} Map Server (Wald & Allen, 2007). While it is clear that the predicted durations are based on important assumptions regarding the shear-wave velocity at the site, the trend might still be worth noting.

Table A3.5.13. Significant duration (5%-75% of Arias intensity, in seconds) of the ground motions available for the 2016 **M**5.8 Pawnee earthquake from the CESMD database (2017).

Station	Station Name	Latitude	Longitude	Repi (km)	X component	Y component
OK033	Mehan, Oklahoma, USA	36.0440 ° N	96.9380 °W	42.3	13.9	14.5
OK034	N. Norfolk Rd., Cushing, OK	36.0100 ° N	96.7130 °W	50.0	20.0	18.9
OK914	W 9th St, Cushing, OK	35.9710 ° N	96.8050 °W	51.7	12.6	16.4
OK031	2598 S Brethren Rd, Cushing, OK	35.9530 ° N	96.8390 °W	53.1	15.1	14.5
OK915	CUH Airport, Cushing, OK	35.9540 ° N	96.7730 °W	54.3	14.8	15.3
OK030	Cody Creek RV Park, Cushing, OK	35.9280 ° N	96.7840 °W	56.8	11.0	17.1
KAN13	Rinehart Farm	37.0130 ° N	97.4780 °W	81.6	18.0	17.8
OK029	Liberty Lake, Oklahoma, USA	35.7970 ° N	97.4550 °W	84.3	11.8	11.6
OK916	City of Medford, OK	36.8070 ° N	97.7480 °W	84.5	13.4	10.3
OK005	Luther Middle Sch, Luther, OK	35.6550 ° N	97.1910 °W	88.8	3.4	7.9
KAN09	Ward Farm, Argonia, KS, USA	37.1530 ° N	97.7590 °W	100.1	15.9	15.4
OK025	Westminster-Hefner, OK City, OK	35.5810 ° N	97.3380 °W	100.8	8.4	10.6
KAN17	Caldwell, KS (west of town)	37.0440 ° N	97.7650 °W	101.4	23.1	15.7
7414	OK: Oklahoma City; VAMC, FF	35.4850 ° N	97.4960 °W	116.3	7.2	8.5
7413	OK: Oklahoma City; VAMC, Bld 1	35.4830 ° N	97.4960 °W	116.5	5.1	6.6
OK032	Salt Plains WLR near Rte 11, OK	36.8040 ° N	98.2100 °W	121.9	7.7	6.4
OK040	E2430 & Blaine Rds, Waynoka, OK	36.4830 ° N	98.6740 °W	156.2	11.1	6.3
OK035	E0210 Rd & N2420 Rd, Alva, OK	36.7080 ° N	98.7100 °W	162.1	11.5	11.5
OK038	West end E0370 Rd, Waynoka, OK	36.4780 ° N	98.7420 °W	162.3	13.5	9.9
OK043	N2390 & E0400 Rds, Waynoka, OK	36.4330 ° N	98.7460 °W	162.5	11.1	8.9

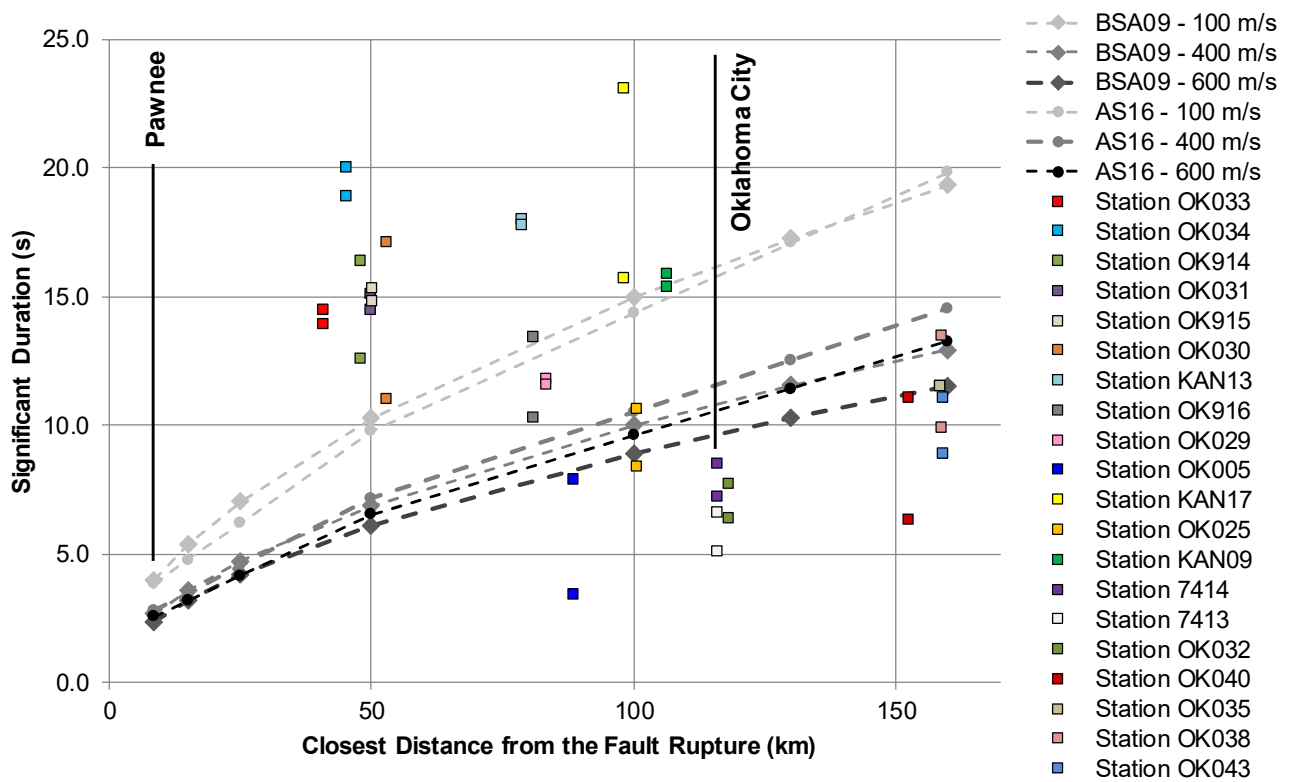


Figure A3.5.36. Estimation of the significant duration of the main shock of the 2016 **M**5.8 Pawnee earthquake, using prediction equations by Bommer *et al.* (2009, BSA) and Afshari & Stewart (2016, AS), and significant duration calculated for the two as-recorded horizontal components of the twenty available accelerograms.

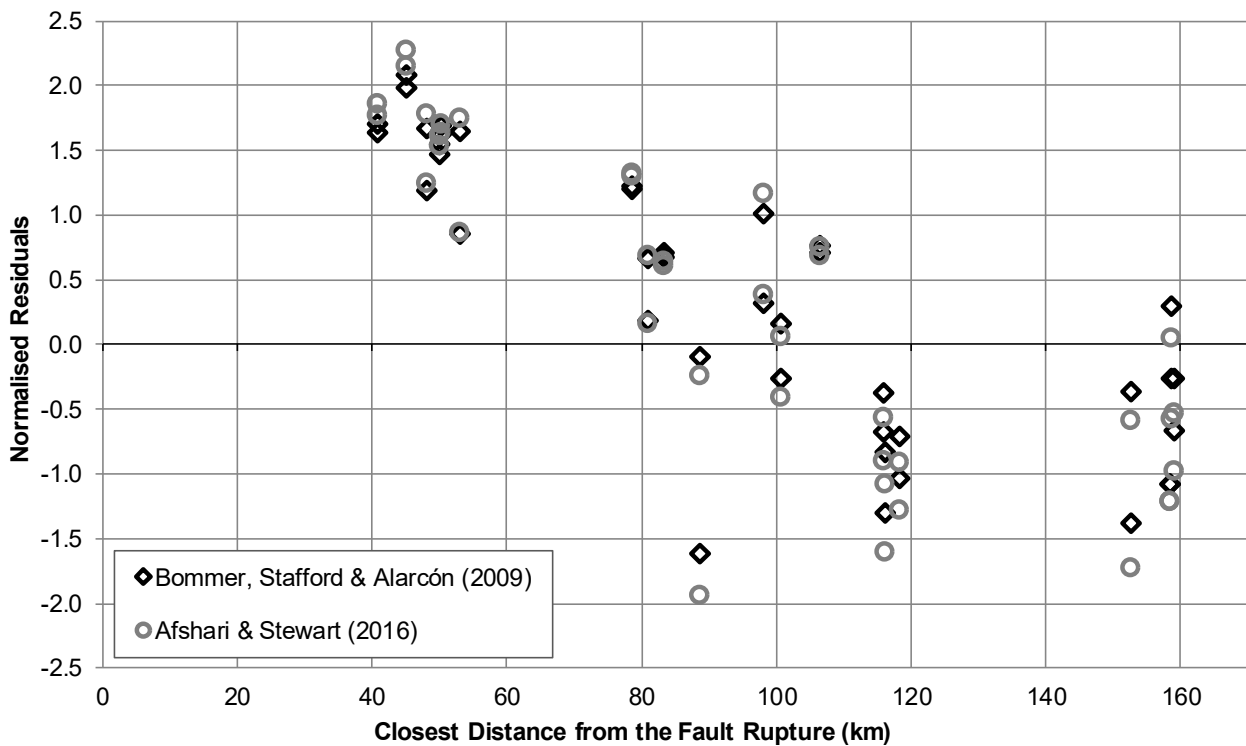


Figure A3.5.37. Normalised residuals of the predictions of significant duration using the models of Bommer *et al.* (2009, BSA) and Afshari & Stewart (2016, AS) against closest distance from the fault rupture for the available accelerograms of the 2016 **M**5.8 Pawnee earthquake.

Finally, Table A3.5.14 and Figure A3.5.38 present analogous results for those presented above, but for the case of the 2016 **M**5.0 Cushing earthquake. For the comparison against estimations of significant durations obtained by means of the prediction equations of Bommer *et al.* (2009) and Afshari & Stewart (2016), four values of V_{s30} are used: 100 m/s, as an extreme reference value, 300 and 700 m/s, identified as the lower and upper bounds for the area around Cushing from the United States Geological Survey (USGS) V_{s30} Map Server, and 509 m/s, the value estimated by Clayton *et al.* (2016) for Station OK031. As at the time of writing (March 2017) there are no details on the finite rupture available in the literature, a value of 1.5 km is assumed for the depth to the top of the rupture, in view of the shallow depth of this event, and epicentral distances are used to compare predicted durations to those shown in Table A3.5.14. Except for Station OK034, for both models, and Station OK915 for the model of Afshari & Stewart (2016), all observed values are larger than the predictions. Observed durations (Table A3.5.14) are within the range of [-1.76,+1.67] and [-2.14,+1.17] standard deviations of the models of Bommer *et al.* (2009) and Afshari & Stewart (2016), respectively. As can be observed, this event had a relatively short duration within the city of Cushing.

It is interesting to note that for both the 2016 Pawnee and Cushing events the perception of the population regarding the duration seems to be, in many cases, that it was significantly longer than the 5-75% of Arias intensity significant duration values calculated both from the available waveforms and the prediction models (e.g., News On 6, 2016b; News OK, 2016e).

Table A3.5.14. Significant duration (5%-75% of Arias intensity, in seconds) of the ground motions available for the 2016 **M**5.0 Cushing earthquake from the CESMD database (2017).

Station	Station Name	Latitude	Longitude	Repi (km)	X component	Y component
OK914	W 9th St, Cushing, OK	35.9710 ° N	96.8050 °W	2.2	1.8	1.8
OK915	CUH Airport, Cushing, OK	35.9540 ° N	96.7730 °W	5.0	1.3	1.6
OK031	2598 S Brethren Rd, Cushing, OK	35.9530 ° N	96.8390 °W	5.3	2.1	2.2
OK034	N. Norfolk Rd., Cushing, OK	36.0100 ° N	96.7130 °W	8.4	1.5	0.6
OK033	Mehan, Oklahoma, USA	36.0440 ° N	96.9380 °W	13.5	5.2	4.7
7414	OK:Oklahoma City;VAMC, FF	35.4850 ° N	97.4960 °W	84.1	14.6	15.4
7413	OK:Oklahoma City;VAMC, Bld 1	35.4830 ° N	97.4960 °W	84.3	15.9	16.5

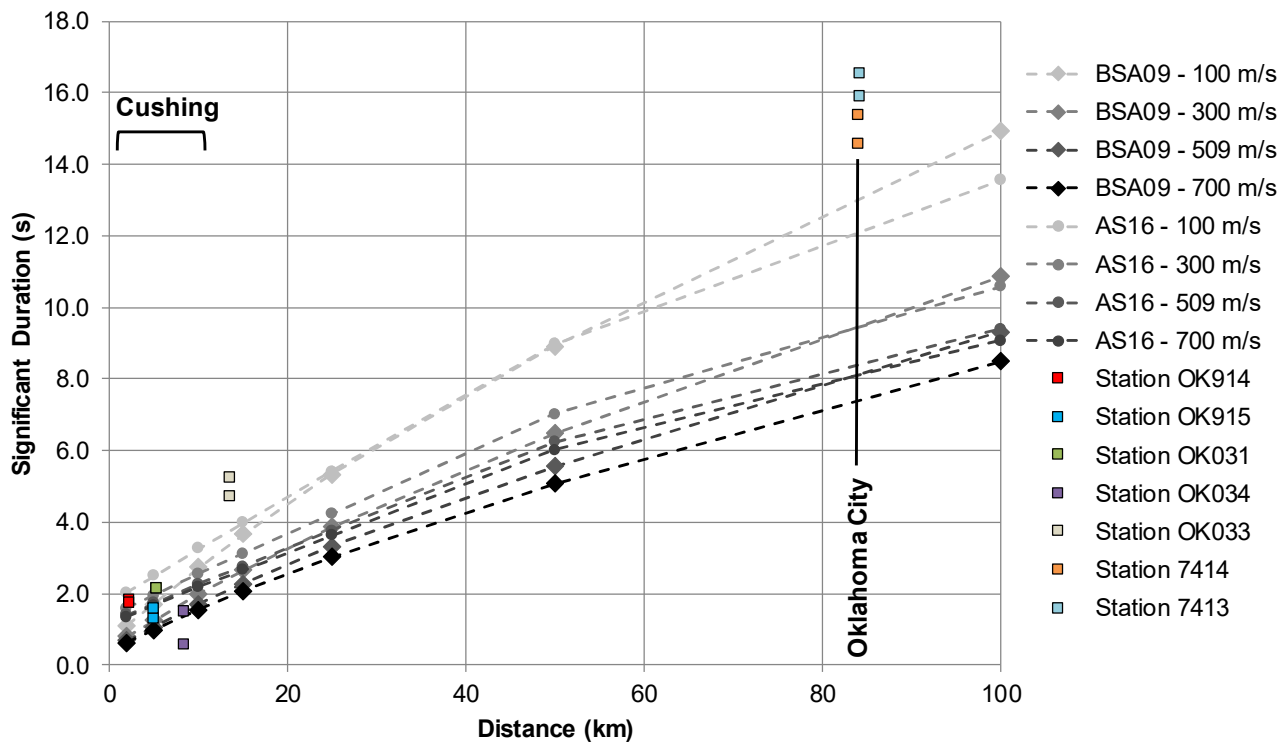


Figure A3.5.38. Estimation of the significant duration of the main shock of the 2016 **M**5.0 Cushing earthquake, using prediction equations by Bommer *et al.* (2009, BSA) and Afshari & Stewart (2016, AS), and significant duration calculated for the two as-recorded horizontal components of the seven available accelerograms.

A3.5.5 Collateral earthquake hazards

A3.5.5.1 Surface rupture

According to Keranen *et al.* (2013), there was no surface rupture for the 2011 **M**5.7 Prague earthquake. Sun & Hartzell (2014) report a peak slip at the hypocentre of 70 cm, though the slip distribution is quite heterogeneous.

Similarly, Grandin *et al.* (2017) state that there was no surface rupture either for the 2016 **M**5.8 Pawnee earthquake, and that the slip, whose maximum was around 40-50 cm, occurred deep into the crystalline basement, and not in the sedimentary cover. However, spaceborne InSAR satellite observations revealed that this event did generate detectable surface deformation (Grandin *et al.*, 2017).

At the time of writing (March 2017), no reports of surface rupture from the 2016 **M**5.0 Cushing earthquake are available.

A3.5.5.2 Landslides

The Christian Science Monitor (2011) reports a rock fall of the size of a sport-utility vehicle along a rural county road caused by the 2011 **M5.7** Prague earthquake.

For the case of the 2016 **M5.8** Pawnee earthquake, Clayton *et al.* (GEER report, 2016) describe a small slump failure that caused a 4-cm settlement of a private house (marked as “Porche settlement” in Figure A3.5.40). The property owner expressed that the site had been experiencing ground displacements before the earthquake, but that the shaking had played a role in aggravating the situation. Figure A3.5.39 shows photos of the settlement (left) and the slope failure (right).



Figure A3.5.39. Porch settlement (left) and slump failure causing it (right) due to the 2016 **M5.8** Pawnee earthquake. From GEER report (Clayton *et al.*, 2016).

No landslides or slump failures appear to have been caused by the 2016 **M5.0** Cushing earthquake.

A3.5.5.3 Liquefaction

No liquefaction phenomena have been reported for either the 2011 **M5.7** Prague or the 2016 **M5.0** Cushing events. However, the 2016 **M5.8** Pawnee earthquake generated sand blows at two locations, according to Clayton *et al.* (GEER report, 2016) and Petersen *et al.* (2017). Clayton *et al.* (2016) highlight that the GEER (Geotechnical Extreme Events Reconnaissance) team that visited the area on 7th-8th September 2016 were not able to observe any signs of liquefaction by themselves, but were provided information by the local community and members of reconnaissance teams sent by the USGS, the Oklahoma State University and the University of Oklahoma. At both of these sites the soil profile consisted of tilled clay layers overlying sand river deposits (Clayton *et al.*, 2016). Petersen *et al.* (2017) indicate a diameter of approximately 2 metres for the sand blow to the south of the epicentre (Figure A3.5.40). The GEER report (Clayton *et al.*, 2016) makes reference

as well to indications of lateral spreading at a third site, which could be due either to liquefaction or a slump failure of the river bank.

Figure A3.5.40 shows the location at which the sand blows and other geotechnical effects were observed, as found in the GEER report (Clayton *et al.*, 2016) and the associated files, which are available as a separate download. These contain photos of a third small sand blow occurring nearby an inactive water well and minor cracks in the ground somewhere else, of which there is no mention in the report. As can be observed, all these phenomena seem to have occurred at distances smaller than 10 km from the epicentre. These locations are similar, though not exactly the same as those indicated by Manga *et al.* (2016), who point out five sites at which liquefaction has been reported.

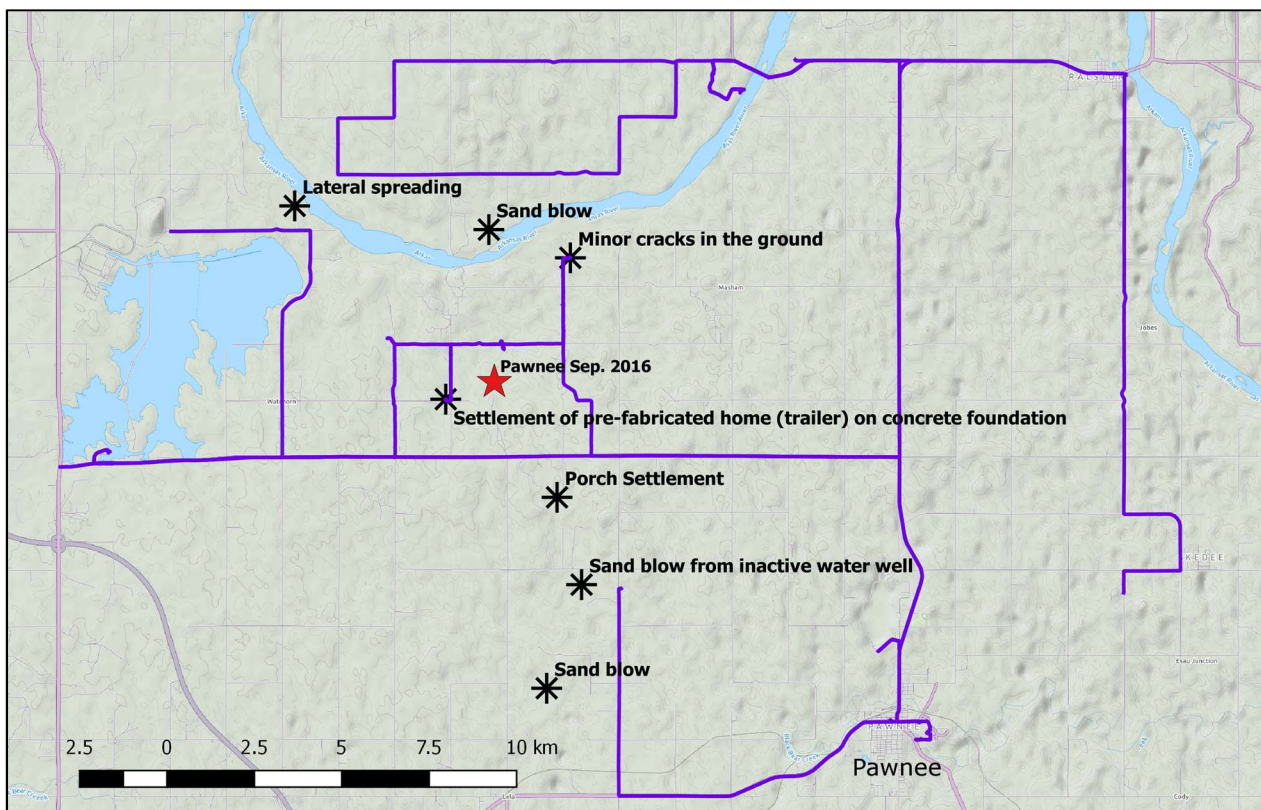


Figure A3.5.40. Locations at which geotechnical effects were observed after the **M5.8** Pawnee earthquake of 3rd September 2016, according to the GEER report and associated downloadable files (Clayton *et al.*, 2016). Purple lines indicate routes followed by the reconnaissance team. Red star indicates location of the epicentre according to the USGS.

A3.5.5.4 Settlements

No reports of settlements have been found for the 2011 **M5.7** Prague or the 2016 **M5.0** Cushing events. However, some instances of settlements have been reported for the 2016 **M5.8** Pawnee, mostly associated with observed liquefaction and, in one case, with a small lump failure (see Section A3.5.5.2). Damage potentially associated to these settlements does not appear to have been significant.

A3.5.6 Exposed population

A3.5.6.1 Socio-economic setting

According to the 2016 Human Development Report (United Nations, 2016), the Human Development Index (HDI) for the United States in 2015 was 0.920, while its Inequality-adjusted HDI (IHDI) was 0.796. This located the USA in the 10th place in the world's ranking, while the Netherlands ranks 7th. The following table compares the HDI and IHDI for both countries from the last five Human Development Reports (United Nations, 2011, 2013, 2014, 2015 and 2016). The column "Adj. HDI" provides the HDI values given in the 2016 report for previous years, adjusted for data consistency in time.

Table A3.5.15. Human Development Index and Inequality-adjusted Human Development Index for the United States and the Netherlands.

Report	Data	Unites States of America				Netherlands			
		HDI	IHDI	Rank	Adj. HDI	HDI	IHDI	Rank	Adj. HDI
2011	May 2011	0.910	0.771	4	0.913	0.910	0.846	3	0.921
2013	October 2012	0.937	0.821	3	0.915	0.921	0.857	4	0.922
2014	November 2013	0.914	0.755	5	0.916	0.915	0.854	4	0.923
2015	April 2015	0.915	0.760	8	0.918	0.922	0.861	5	0.923
2016	September 2016	0.920	0.796	10	-	0.924	0.861	7	-

Table A3.5.16 presents a comparison between the United States and the Netherlands in terms of GDP, GDP per capita and unemployment rate. Some of the main economic sectors of Oklahoma include energy production, manufacturing (e.g., oil field machinery, construction machinery, aircraft and aerospace equipment, electronic components, etc), agriculture and cattle-ranching (Netstate, 2017). Oklahoma possesses two of the one-hundred largest oilfields in the country (Doerflinger & Bajema, 2014). In 2014, the state of Oklahoma ranked third in the national natural gas marketed production and fourth in the national production of dry natural gas (dry natural gas production equals the marketed production minus the extraction loss), according to the United States Energy Information Administration (EIA, 2016). Furthermore, it ranked fifth in the total national energy production in 2013. Cushing, in particular, is regarded as one of the United States' "largest oil hubs" (Doerflinger & Bajema, 2014), and often called the "pipeline crossroads of the world" (Taylor *et al.*, 2017). Overall, the trade, transportation and utilities sector accounts for 18.3% of Oklahoma's GDP, followed by mining, the government sector and financial activities, which represent 15.0%, 14.9% and 13.1% of the GDP, respectively (Evans, 2017). Though agriculture, forestry, fishing and hunting represent only 1.3% of the GDP, Oklahoma ranks fifth in cattle production and fourth in production of wheat in the whole of the United States (Evans, 2017; Netstate, 2017).

Table A3.5.16. Gross domestic product (GDP), GDP per capita and unemployment rate for the United States and the Netherlands, according to the World Economic Outlook Database 2016.

Indicator	Units	Unites States			Netherlands		
		2011	2015	2016 (*)	2011	2015	2016 (*)
Gross domestic product, current prices	Billions of US dollars	15,517.93	18,036.65	18,561.93	894.58	750.70	769.93
Gross domestic product per capita, current prices	US dollars	49,725.00	56,083.97	57,293.79	53,589.91	44,322.83	45,210.24
Unemployment rate	% of total labor force	8.933	5.283	4.895	4.984	6.700	6.500

(*) Estimation by the International Monetary Fund (IMF)

Information specific to the business sectors in Cushing is available from Taylor *et al.* (2017), who point out that 26% and 21% of the around 400 for-profit businesses in Cushing are in the retail sector and the service sector, respectively. The construction sector follows in importance with a 13% of the businesses, while the finance, insurance and real estate sector as well as the transportation, communications, electric, gas and sanitary services sector hold 10% of the businesses each.

The large economic crisis that began in 2008 had a significant impact on the United States, causing high unemployment, an increasing federal debt, and inflation. In 2011, the Gross Domestic Product (GDP) increased in 43 of the 50 states of the USA. The state of Oklahoma presented a 1.0% increase in its GDP, a value that positioned it within the third to highest quintile (Bureau of Economic Analysis, U.S. Department of Commerce, 2012). During the year 2012, the state of Oklahoma ranked 37th with respect to GDP per capita, whose value was a 15% lower than that of the USA as a whole. However, Oklahoma's economy and employment levels were affected by the sharp drop in oil prices by mid-2014, just like all other states whose main economic activity is related to oil and gas extraction, though Oklahoma has performed relatively well in comparison (Doerflinger & Bajema, 2016; Wilkerson, 2016). According to Doerflinger & Bajema (2016), the growth rate of Oklahoma's GDP is one of the strongest in the USA, with a 2.5% average annual growth since the 2009 recession, larger than the 1.9% national average. However, looking at quarterly variations, Oklahoma has experienced contractions of its GDP in 2016 (Bureau of Economic Analysis, U.S. Department of Commerce, 2017), as mining declined 20.4% at the national level during the second quarter of 2016.

A3.5.6.2 Population density and distribution

The area around the epicentres of the three events under study is sparsely populated. Table A3.5.17 shows the population by 1st April 2010 of some of the most affected towns. According to the United States Census 2010 (U.S. Census Bureau, 2012; USBoundary, 2017), population density in the year 2010 around the areas of Prague, Sparks and Meeker was between 14 and 20 people/km² (37 and 53 people/mi²), taking into consideration the area and population of the census county divisions, instead of just the urban areas. Similarly, the population density around Pawnee is 4.8 people/km² (12.5

people/mi²). The area around the town of Shawnee is more densely populated, with an average of around 50 people/km² (131 people/mi²), while that around Cushing follows in density, with 38 people/km² (98.5 people/mi²). The density of housing units is between 6.4 and 8.6 housing units/km² and 20.9 housing units /km² (16.9 to 22.5 housing units /mi² and 54.5 housing units/mi²) for the area around Prague, Sparks and Meeker, and Shawnee, respectively. For the area around Pawnee and Cushing, values are 2.4 and 17.2 housing units/km² (6.0 and 44.5 housing units/mi²), respectively. Figure A3.5.41 shows the population density in the area according to Gridded Population of the World (GPW v4.0, CIESIN, 2016). While the values do not match those of the United States Census due to the differences that arise from resolution of GPW and the definition of census county divisions, the map in Figure A3.5.41 gives a picture of how sparsely populated the areas affected by these three events are.

Table A3.5.17. Population and number of housing units of relevant towns and cities in the epicentral areas of the three events as of 1st April 2010 (only urban population considered) (U.S. Census Bureau, 2012).

City	Population	Housing Units
Oklahoma	580,008	256,930
Shawnee	29,857	13,205
Sparks	169	80
Meeker	1,145	521
Prague	2,386	1,147
Pawnee	2,196	1,049
Cushing	11,784	3,591

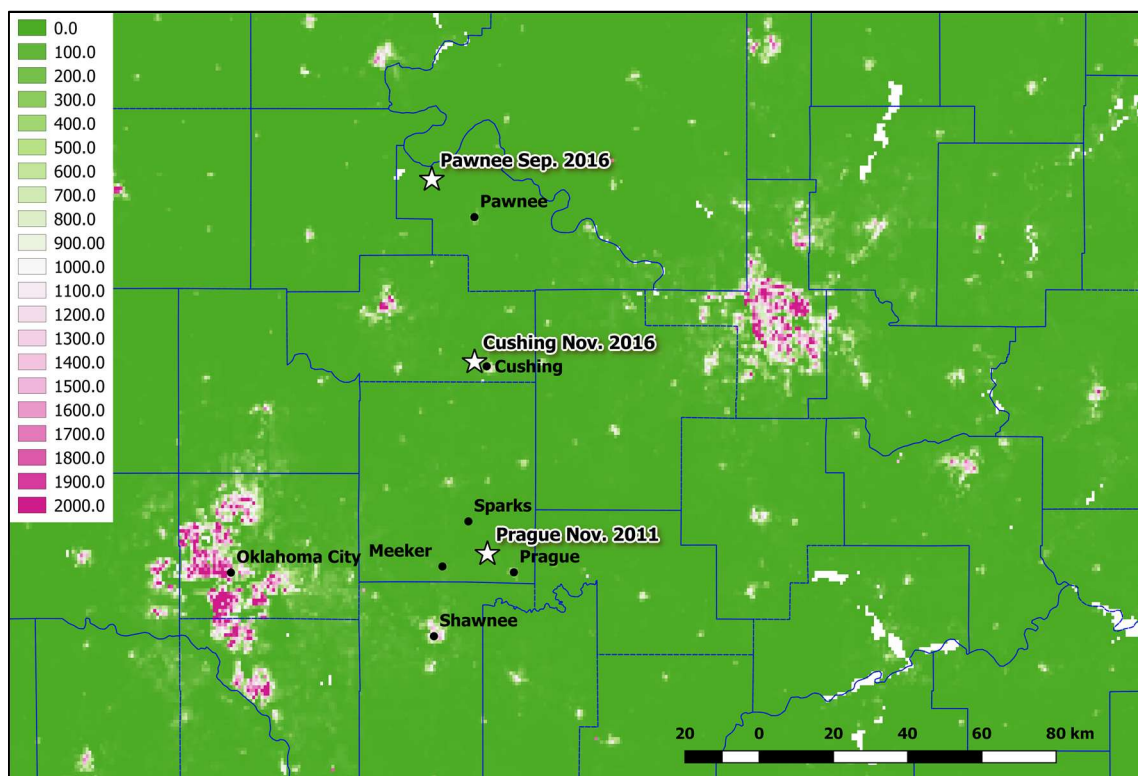


Figure A3.5.41. Population density (people/km²) in the affected areas as of 2010 according to Gridded Population of the World (GPW v4.0, CIESIN, 2016).

The USGS PAGER exposure report generated 35 hours after the 2011 **M5.7** Prague earthquake estimates that approximately eight thousand people were exposed to shaking of intensity between VII and VIII in the Modified Mercalli Intensity (MMI) scale, while seventy-nine thousand and around 2.6 million were exposed to MMI VI and V, respectively (Figure A3.5.42, left). For the 2016 **M5.8** Pawnee earthquake, the USGS PAGER exposure report estimates that around four hundred thousand people were exposed to shaking of intensity between V and VI (Figure A3.5.42, centre), while the figure is only of eighteen thousand for the 2016 **M5.0** Cushing event (Figure A3.5.42, right). Note that these numbers are much larger than those of Table A3.5.17 because Table A3.5.17 reports strictly on the urban population of the enumerated towns, while the USGS PAGER exposure report considers all of the exposed population.

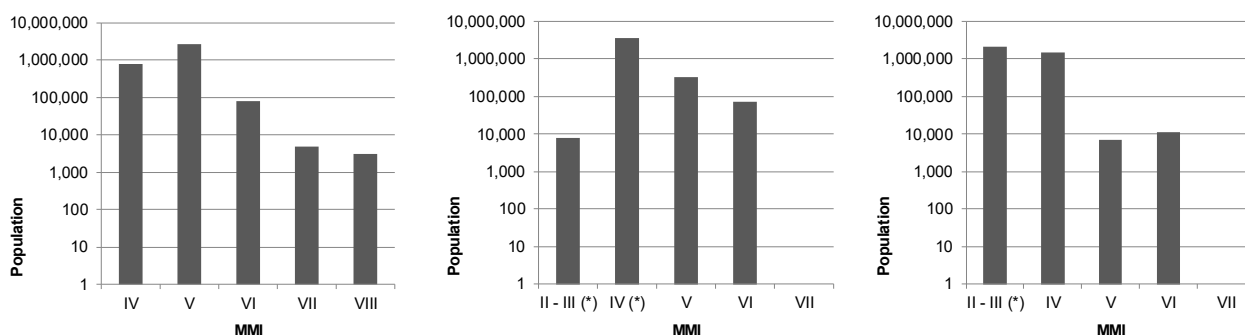


Figure A3.5.42. Estimation of total population exposed to different Modified Mercalli Intensities (MMI) for the three events: 2011 **M5.7** Prague (left), 2016 **M5.8** Pawnee (centre) and 2016 **M5.0** Cushing (right). Data from PAGER (USGS, 2015, 2016). An (*) indicates that the estimated exposure only includes population within a certain analysed area.

A3.5.6.3 Time of day of earthquake

The main shock of the 2011 Prague sequence occurred on Saturday 5th November 2011, 22.53 local time. In general, the time of occurrence of the event does not appear to have had a significant impact over its consequences. Nevertheless, it should be noted that the occupants of a house in Sparks whose chimney collapsed and caused severe damage to the roof (Figure A3.5.47) did not suffer any injuries because they were sleeping in their bedroom and the chimney caused damage to the living room. The time of occurrence of the **M4.8** aftershock of 8th November 2011 02.46 UTC was slightly more relevant, for it having taken place at night prevented the occurrence of multiple injuries as a consequence of ceiling tiles falling inside classrooms at Meeker High School.

The 2016 **M5.8** Pawnee earthquake occurred on Saturday 3rd September 2016, at 07.02 local time. While it is not clear if the time of occurrence had a direct relation with its consequences, it might be thought that the chances of a person getting hurt by façade blocks falling from a building like that of the Arkansas Valley National Bank (Figure A3.5.52) would have been higher at a busier street hour.

The 2016 **M5.0** Cushing main shock occurred on Sunday 6th November 2016, 19.44 local time. As suspended ceilings suffered damages at some schools, it was fortunate that the earthquake did not occur on a week day during school hours, as children could have been

injured. Similar to the case of the Pawnee earthquake, it is possible that more injuries could have resulted from the failure of façades onto sidewalks had the shaking occurred at a more busy time of the week.

A3.5.7 Characteristics of exposed building stock

A3.5.7.1 Seismic design codes

While Cutcliffe (2000) believes that it was the 1906 San Francisco earthquake which marked the start of a real interest in earthquake engineering and seismic design in the United States, Freeman (1932) stated a quarter of a century later that "the art of constructing earthquake-resisting buildings is still in the formative stage, that there are differences of opinions among experts and that there is much deficiency in important data". Further, he points at the 1925 Santa Barbara earthquake to have been more significant in raising awareness on the subject. It was this devastating event that prompted the first edition of the Uniform Building Code (UBC) in 1927, which contained the first written seismic design provisions for a regional level, but which did not become mandatory until 1961 (Beavers, 2002).

As recapitulated by Beavers (2002), the origin of seismic design codes and building codes in general in the USA started in a fragmented fashion, by regions or states. For example, the Uniform Building Code (UBC) just mentioned above was typically used west of the Mississippi river. The National Building Code of the Building Officials and Code Administrators (BOCA) (known as the BOCA Code) was, instead, used in the upper midwest and northeast. It was first published in 1950, including seismic design provisions. In the south, the Standard Building Code (SBC) of the Southern Building Code Congress International (SBCCI) was used. Seismic design provisions were included in the SBC in 1976, by referencing ANSI A58.1, but "were not mandatory unless local authorities required seismic design, which was rarely the case", until 1988. The 1987 edition of the BOCA Code also incorporated the provisions of ANSI A58.1, and made them mandatory.

The ANSI A58.1 standard of the American National Standards Institute (ANSI) was first published in 1945, and was the first standard to consider earthquake loads (Beavers, 2002). However, seismic hazard did not have a role in ANSI A58.1, which only had a map showing the locations of destructive earthquakes of the past until its 1972 edition, in which a seismic hazard description similar to the 1949 USCGS (United States Coast and Geodetic Survey) map was incorporated. The 1972 edition of ANSI A58.1 was also the first one to outline modern wind design provisions (Fratinaro & Schroeder, 2015; Ghosh, 2008), evolving from more basic guidelines developed in the 1950s (Huston, 2007).

The 1949 hazard map was the first one to encompass the whole of the contiguous USA, and it was based on "the premise that similar earthquakes will occur in the future where they have occurred in the past" (Beavers, 2002). For reasons that are not fully clear, this map was withdrawn in 1952, and replaced with a map that only showed the location of known past significant earthquakes. In the 1970s, the responsibility of producing hazard

maps passed on to the USGS (United States Geological Survey), who published the first map developed in the form of probabilistic estimates of maximum acceleration contours on rock in 1976, and which, as highlighted by Beavers (2002), represented a significant paradigm shift. It should be noted, however, that the first edition of the ATC3-06, which in 1985 evolved into the National Earthquake Hazards Reduction Program (NEHRP) Recommended Provisions for Seismic Regulations for New Buildings and Other Structures, used a truncated version of this map in 1978, not allowing for values above 0.4g to be considered. This map was used for almost 20 years, given the inability to reach consensus on a different map that took place in between 1988 and 1994. It was finally updated by the USGS in 1997, after a four-year project called Project 97, during which large efforts were invested in giving a voice to all the professionals and sectors involved. Since then, the USGS hazard map has been updated in 2002, 2008 and 2014.

The way in which seismic loads were considered evolved significantly from the simple use of a 7.5%-10.0% of the building's weight as a lateral load (1927 edition of the UBC), with the progressive incorporation of significant factors such as soil type and capacity, seismic zonation, natural period of vibration of the structure, and importance of the building.

In 1988, ANSI combined with ASCE to update and re-designate ANSI A58.1-1982 to ASCE 7, which is now the most significantly recognised standard by all earthquake regulations, codes, standards, procedures and guidelines for basic seismic design in the USA (Beavers, 2002). Furthermore, ASCE 7 is also the "de facto" national wind design standard (Fratinaro & Schroeder, 2015). The International Building Code (IBC), whose first edition in 2000 was based in the NEHRP Provisions, makes reference to ASCE 7 for the definition of seismic and wind loads. Regarding the latter, it should be noted that most of the state of Oklahoma is located within an area of the United States known as "tornado alley", characterised by the frequent occurrence of tornadoes due to the interaction between big masses of air with significantly different humidity contents and temperature. According to FEMA-543 (FEMA, 2007), the area around Oklahoma City has seen over 26 tornadoes of categories F3 to F5 ("severe" to "incredible") per 10,000 km² between 1950 and 1998, one of the highest rates across all of the USA.

As mentioned in Section A3.5.1.3, it is noted that the national seismic hazard maps of the United States (and all other countries in the world) do not take into consideration induced seismic activities and, consequently, areas for which most ground shaking is believed to have an anthropogenic origin might be seismically designed but for ground motion levels that might not reflect the short-term likelihoods being currently experienced.

In 2009, the state of Oklahoma created the Oklahoma Uniform Building Code Commission (OUBCC), whose purpose was and continues to be to develop state minimum-requirement building codes. All jurisdictions in the state of Oklahoma can either adopt these minimum requirements or more restrictive ones. The OUBCC has adopted (with some modifications) the International Building Code (now in its 2015 version) and the 2009 edition of the International Residential Code (IRC), a stand-alone code addressing the requirements for residential one- and two-family homes and town houses.

The Building Code Effectiveness Grading Schedule (BCEGS), developed by the Insurance Services Office (SO), indicates that the overall level of code enforcement across the state of Colorado is relatively low when compared to the country as a whole and to states like California, in which awareness with respect to seismic risk is much greater. Figure A3.5.43 shows the distribution of communities by BCEGS class number for the United States as a whole and for the state of Oklahoma. Within this classification schedule, classes 1-3 correspond to the maximum enforcement levels, while class 10 indicates no enforcement at all. These figures agree with statements of Beavers (2002) and Cutcliffe (2000), who highlight that, due to their relative lack of seismic activity, the effort to incorporate good seismic design practises in building codes has been more challenging in the central and eastern USA, when compared to other areas of the country. Furthermore, this is also consistent with the statement by Witze (2015), who points out that the buildings in Oklahoma in particular might not be constructed to standards that consider seismic risk.

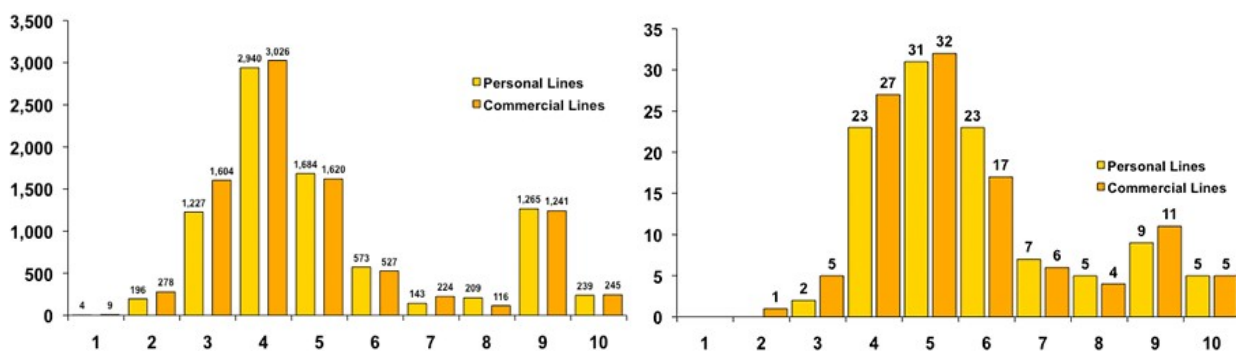


Figure A3.5.43. Distribution of communities by BCEGS class number for the whole of the United States (left) and the state of Oklahoma (right). Personal lines include 1- and 2-family dwellings. Commercial lines include all other buildings. Classes 1-3: maximum enforcement. Class 10: no enforcement (ISO Mitigation, 2015)

A3.5.7.2 Building typologies

Information regarding building typologies in the state of Oklahoma is scarce to null. For this reason, data regarding typologies at the country level were collected from the PAGER Inventory Database v2.0 (Jaiswal & Wald, 2008). Figure A3.5.44 shows that the structure of most of the buildings in the USA consists of light wood frames (61.2%), and unreinforced brick masonry (19.3%) in a smaller proportion. The remaining 19.4% is mostly made up of heavy wood frames and mobile homes (Figure A3.5.45).

From available pictures of damage caused by the 2011 Prague earthquake it seems possible to infer that light wood frames and unreinforced brick masonry are probably the most likely building typologies in the affected area. Furthermore, Witze (2015) makes direct reference to the latter, when she states that "*many scientists [...] are concerned about how old brick-and-mortar structures would hold up in a large earthquake*" in Oklahoma.

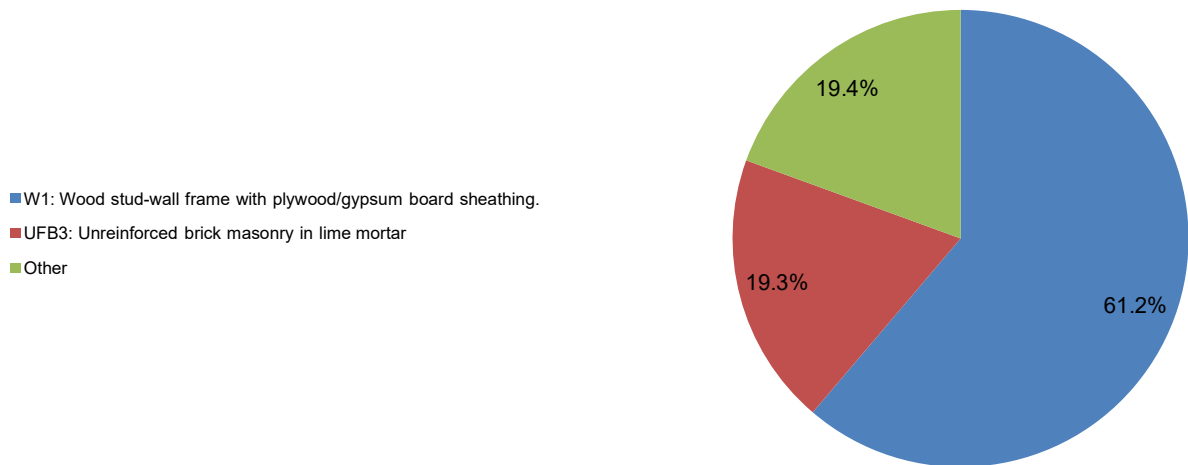


Figure A3.5.44. Proportion of buildings in the United States belonging to each typology. The subcategories within class "Other" are expanded upon in the figure below. Data from Jaiswal & Wald (2008).

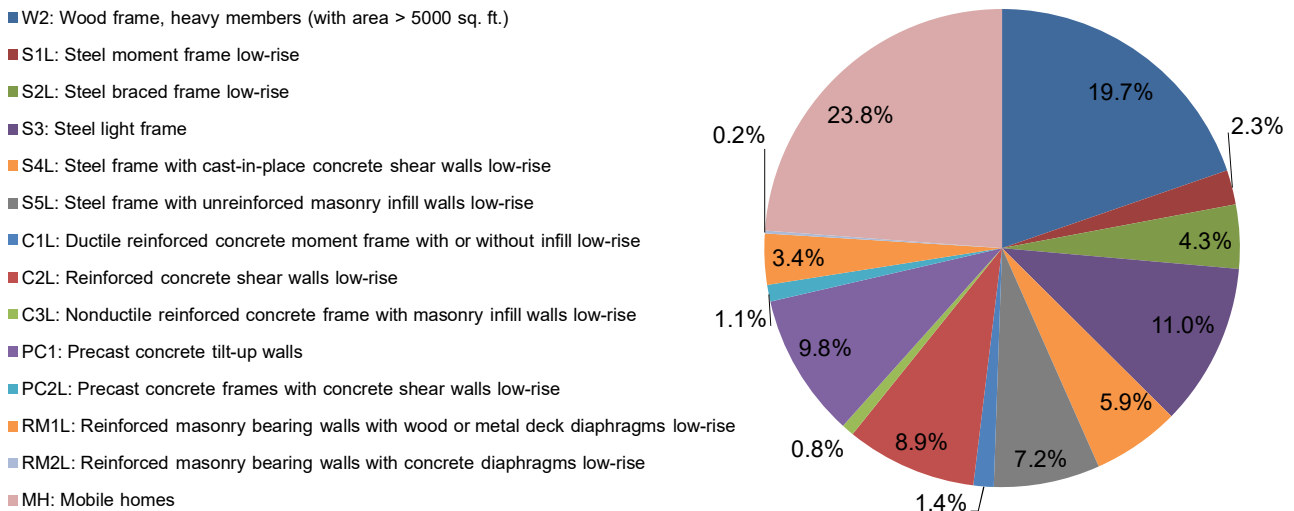


Figure A3.5.45. Breakdown of the "Other" class in the figure above. To determine the percentage that each of these sub-categories represents of the total in the USA, multiply the value in this figure by 0.194 (Jaiswal & Wald, 2008).

According to Taylor *et al.* (2017), unreinforced brick masonry buildings built between 1910 and 1940 seem to be predominant in the Central Business District (CBD) of Cushing, while light wood frame houses of one or two storeys are more common in the more residential areas. The former usually contain flexible wood diaphragms and timber collector elements, and were not designed to resist lateral wind or seismic forces (Taylor *et al.*, 2017). From their report it can be inferred that reinforced concrete and steel frame buildings are not common in Cushing, as observations on only one building of each kind are made.

For the case of Pawnee, it is not clear exactly what the proportions of the two most common typologies are. However, the description and photos of damage available (e.g., Clayton *et al.*, 2016) seem to indicate that stone (non-structural) façades, possibly attached to a light wood frame structure, are more common than in Prague or Cushing.

In what regards dams, P. Bassal, from GEER (Geotechnical Extreme Events Reconnaissance), states that most of the approximately 4,700 that exist in the state of Oklahoma were built before the 1970s, without seismic design (Bassal, 2016, EERI Oklahoma USA Earthquakes Clearinghouse).

A3.5.7.3 Prior damage and retrofit

No details on prior damage or retrofit available for the 2011 Prague or the 2016 Pawnee earthquakes.

There is no detailed information available either for the 2016 Cushing earthquake, except for a comment by McNamara *et al.* (2015a) regarding the Cushing regional airport and community youth centre having sustained minor damage during the **M4.0** and **M4.3** earthquakes of 7th and 10th October 2014. No information regarding further damage to the airport due to the 2016 **M5.0** Cushing earthquake could be found, but the youth centre did sustain some damage again. It is not clear if the minor damage suffered in 2014 had any effect on the consequences observed two years later, in 2016.

A3.5.8 Damage observations

A3.5.8.1 Damage states

The Oklahoma Geological Survey does not know of any publicly available report on damage caused by the 2011 **M5.7** Prague earthquake that makes use of standardised damage scales (OGS, 2015, personal communication). However, from the qualitative descriptions found in online media it is possible to believe that most damage observed would correspond to Grades 2 and 3 in European Macroseismic Scale (EMS-98; Grünthal, 1998). This appears to be in agreement with what would be implied by a maximum Modified Mercalli Intensity of VIII (see Table A2.3.2 in Appendix II).

Though more systematic gathering and reporting of damage data was carried out for the 2016 **M5.8** Pawnee and **M5.0** Cushing events, no description of damage by means of a standardised scale was found at the time of writing (March 2017). From the available information, it is estimated that most cases would correspond to Grade 2 in EMS-98 for Pawnee and Grade 3 in EMS-98 for Cushing. The maximum MMI of VII to VIII in Pawnee and this description of damage seem reasonable, but a maximum MMI of VI seems low for Cushing, VII appearing as more appropriate (see Table A2.3.2 in Appendix II).

For details regarding the European Macroseismic Scale (EMS-98; Grünthal, 1998), please refer to Section 3.8.1 of Chapter 3 and Appendix II.

A3.5.8.2 Damage statistics and description

Information regarding damage caused by the 2011 **M5.7** Prague earthquake is scarce in comparison with that available for the 2016 **M5.8** Pawnee and **M5.0** Cushing events, for

which the Earthquake Engineering Research Institute (EERI) set up an online clearinghouse (EERI Oklahoma USA Earthquakes Clearinghouse, 2016) to gather data and make it readily available. While detailed descriptions of the observed damage will come in the paragraphs that follow, Table A3.5.18 presents a summary of the types of damage caused by each of the three events, in broad terms, generated combining all the information available at the time of writing (March 2017). It is noted that some of the differences observed are due to the different kinds of structures existing at each of the affected locations, as described earlier.

Table A3.5.18. Summary of types of damage observed for each event.

Type of Damage	6 th Nov. 2011 M5.7 Prague	3 rd Sep. 2016 M5.8 Pawnee	7 th Nov. 2016 M5.0 Cushing
Cracks in plaster or plasterboards	Yes	Yes	Yes
Cracks in floor tiles	Yes	No	Yes
Cracks in masonry non-structural infills	No	No	Yes
Damage to brick non-structural façades	Yes	No	Yes
Damage to rock non-structural façades	No	Yes	No
In-plane failure of structural masonry	No	No	Yes
Out-of-plane failure of structural masonry	No	No	Yes
Failure of masonry parapets	Yes	No	Yes
Full or partial collapse of chimneys	Yes	Yes	Yes
Damage to suspended ceilings	Yes ⁽¹⁾	No	Yes
Damage to pipes in buildings	No	Yes	Yes
Damage to pipe main lines	No	No	Yes
Building settlement	No	Yes	No
Damage to roads	Yes	No	No
Damage to bridges	No	No ⁽²⁾	No
Damage to concrete dams	No	No	No
Damage to earthen dams	No	Yes ⁽³⁾	No

(1) Not due to the main shock but to the M4.8 aftershock.

(2) According to the GEER-051 Report, damage was observed in an old bridge, but it was unclear if the damage was earthquake-related.

(3) According to the GEER-051 Report, cracks in the soil structure were observed, but it was unclear if the damage was earthquake-related.

Data on the damage caused by the 2011 M5.7 Prague earthquake is not only scarce but also contradictory at some points. According to the USGS, fourteen houses were "destroyed" in the Shawnee-Sparks area (Figure A3.5.21), but other reports and the images available from online media suggest damage was significantly less than implied by the description of the USGS. According to a situation update by the Oklahoma Department of Emergency Management with date 6th November 2011 04.30 pm local time (*i.e.*, 17-18 hours after the main shock), twelve houses in the Lincoln County "sustained minor damage", most of which involved cracks in plasterboards, damage to brick façades, and toppling of chimneys. This statement is in agreement with that of Joey Wakefield, from the Lincoln County Emergency Management team, who told News 9 that most of the damage observed was superficial, and specified "we are seeing a lot of fireplaces falling over, bricks falling, sheet rock cracked" (News 9, 2011).

Some of the instances of damage most encountered in the media are the collapse of one of the towers of Benedictine Hall at St. Gregory's University in Shawnee, a chimney which toppled and damaged the roof of a house in Sparks, a house whose façade bricks almost completely detached from the wood-frame structure, and the buckling of US Highway 62 between Meeker and Prague.

Figure A3.5.46 shows the damage to Benedictine Hall, a five-storey administrative building at St. Gregory's University, in Shawnee, built in 1915, one of whose 7-8 metre four towers collapsed (Reuters, 2011). According to Brad Collins, spokesman for the University, and as can be observed in Figure A3.5.46, the other three towers also sustained damage (Fox News, 2011).



Figure A3.5.46. Damage to one of the towers of Benedictine Hall at St. Gregory's University in Shawnee after the **M5.7** 2011 Prague main shock. Photos by Jim Beckel, from News OK (2011).

The roof of a house in Sparks was damaged due to the chimney toppling over it during the main shock (Figure A3.5.47). According to News OK (2011), the occupants of the house were not in the room at that moment and were not injured. Numerous cracks can be observed on the walls as well.

As shown in Figure A3.5.48, the façade bricks of a house in Sparks almost completely detached from its wood-frame structure. News 9 (2011) reports quite extensively on this case, but does not mention any structural damage to the house.

A lawsuit filed by one resident of Lincoln County (case number CJ-2015-24, Court of Lincoln County, Oklahoma, State of Oklahoma, 2015) describes in detail the damage sustained by her house during the foreshock and main shock. According to said document, the **M4.8** foreshock caused the sheetrock above most doors of the house to crack, and numerous small items located in cabinets and on shelves to fall and break. As for the **M5.7** main shock itself, the document enumerates the following consequences: falling of the chimney, cracking and partial detachment of the brick façade, cracking of floor tiles, ceilings and sheetrock, cracking and breaking of studs of the wood walls, displacement of brick columns, and loosening of window frames and bathtubs. Cracking of concrete is mentioned as well, though it is not clear as to whether it refers to structural concrete or pavement.



Figure A3.5.47. Damage to a house in Sparks. The chimney toppled over the roof. Photos by Sue Ogrocki (News OK, 2011).



Figure A3.5.48. Façade bricks detached from the wood-frame structure of a house in Sparks. Photo by AP PHoto as in ABC News (2015).

The 2011 main shock also caused US Highway 62 to buckle in three locations between Meeker and Prague (USGS; CNN, 2011; The Earth Institute, Columbia University, 2013). According to The Christian Science Monitor (2011), the road was rapidly patched and reopened to traffic some hours after the earthquake.

According to the Oklahoma Department of Emergency Management (2011), by 6th November 2011 04.30 pm local time the Oklahoma Department of Transportation had found no damage to bridges within a 80-km radius of the epicentre, and the U.S. Army Corps of Engineers had reported no problems at dam sites within an approximate 120-km radius of the epicentre.

The total number of houses damaged due to the 2011 main shock is not clear, for the only numerical reference is the 12-14 homes mentioned earlier. Besides the cases described above, online media report numerous broken windows and mirrors, cracks to masonry and plasterboards, and collapsed chimneys. However, Joey Wakefield, from the Lincoln County Emergency Management team, reported a much larger number of homes affected with earthquake-related damage following the strongest **M4.8** aftershock of 8th November 2011 02.46 UTC. According to Mr. Wakefield, his office had received reports of 94 homes damaged due to the "recent earthquakes". Gibson & Medley (2011) highlight the possible influence of cumulative damage on these numbers. The Significant Earthquake Database of the National Centers for Environmental Information of the National Oceanic and Atmospheric Administration of the United States (NOAA) reports 14 destroyed houses and an estimate of 100 to 1,000 damaged houses. The latter appears as an overestimation, but no sources have been found reporting a sound final figure.

The **M4.8** aftershock of 2011 caused damage to ceiling tiles and metal framework in five classrooms, the library, the auditorium and the cafeteria at Meeker High School. The Meeker City Hall and two other structures were reported to have experienced some kind of damage as a consequence of this aftershock as well.

It is noted that Clayton *et al.* (2016) characterised both the 2011 **M5.7** Prague and the 2016 **M5.1** Fairview earthquakes as having caused "very light to light damage". However, searching through media sources it becomes clear that while all the information just presented is available for the 2011 **M5.7** Prague event, articles regarding the 2016 **M5.1** Fairview only make reference to it having been felt strongly but no significant damage having been reported (CNN, 2016a; Fox News, 2016; News On 6, 2016a; The Weather Company, 2016).

To the authors' knowledge, the most complete compendium on damage caused by the 2016 **M5.8** Pawnee earthquake to the date of writing (March 2017) is that of the GEER report (Clayton *et al.*, 2016) and its associated files, which are available as a separate download that contains photos and a KML file. Information from the three types of files (the written report, the photos and the KML file), which does not fully coincide, is gathered and presented in Figure A3.5.49.

As can be observed, bridges (green squares), dams and levees (brown triangles) located around the area of Ponca City and Kaw City did not show visible indications of damage. These include the bridges of Ferguson Road on Kaw Lake, Oklahoma Highway 11 on Kaw Lake, Lake Ponca, Kalley Ave. over Arkansas River, U.S. 60 over Arkansas River and U.S. 177 over Salt Fork Arkansas River, the Ponca Lake levee and the Kaw Lake dam. Closer to the epicentre, the Sooner Lake southern levees presented no damage, while the

boat ramp had some cracks, believed to be unrelated to the earthquake by the reconnaissance team. While access to the Sooner Lake dam (northeast of the lake) was not possible, personnel of Oklahoma Gas & Electric indicated that it presented no damage.

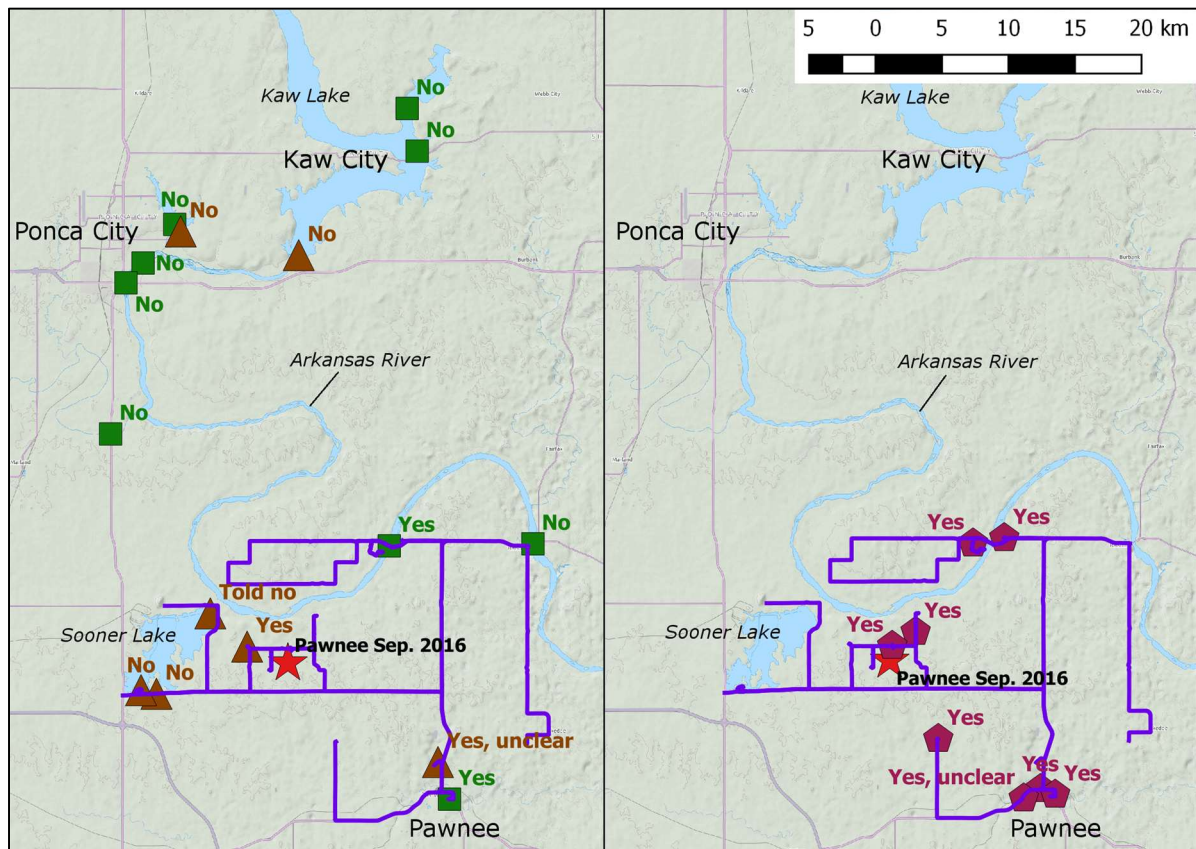


Figure A3.5.49. Locations assessed by the GEER reconnaissance team: earthen dams/levees (brown triangles) and bridges (green squares), on the left, and buildings (burgundy pentagons), on the right. Texts make reference to the existence of damage or not. Purple lines indicate routes followed by the team. Red star indicates location of the epicentre according to the USGS. Locations according to the GEER report and associated files (Clayton *et al.*, 2016).

The two cases in which damage may have occurred in earthen dams were that of Pawnee Lake (around 3 km to the north of the city of Pawnee) and of a watering pond dam 4 km north-west of the epicentre (to the east of Sooner Lake), approximately. In both, the damage consisted only of cracks along the downstream earth slopes of the dams. Though looking recent, Clayton *et al.* (2016) note that it is uncertain whether they were caused by the 2016 **M**5.8 Pawnee earthquake or not. Manga *et al.* (2016) report that the dam at Pawnee Lake did not suffer any damage.

The lack of damage to dams observed by the GEER reconnaissance team is supported by a statement by Bassal (2016) on the EERI Oklahoma USA Earthquakes Clearinghouse (2016) saying that the Army Corps of Engineers had inspected seven dams, including the large Keystone Dam, located in between Pawnee and Tulsa, and no damage had been observed.

Two bridges located within a 20 km radius of the epicentre presented some kind of damage. The Catlette Rd. over Black Bear Creek bridge, a 3-span pre-stressed concrete

girder bridge built in 2012 to the east of Pawnee, suffered from minor cracking in a sidewalk over the approach slab, but no damage to the bridge structure itself. The Belford Bridge, a 5-span steel truss bridge over the Arkansas river, presented spalling of cover concrete on top of the abutments, which may be due to pounding between the latter and the deck, gapping between the backfill soil and the abutment backwall, and 1-2 cm wide cracks in the soil beneath the bridge at both abutments (Figure A3.5.50). According to the meta-data of the photo and KML files of Clayton *et al.* (2016), fractured anchored bolts were observed too, but corrosion appeared to be severe and the bolts may have broken before the earthquake. The bridge on Oklahoma Highway 18 over the Arkansas river, to the east of the Belford Bridge, did not suffer any damage.



Figure A3.5.50. Damage at the west abutment of Belford Bridge, which may be due to the 2016 M5.8 Pawnee earthquake: spalling of concrete (left and centre) and 4-cm wide gap between backfill soil and abutment. From GEER report (Clayton *et al.*, 2016).

According to Clayton *et al.* (2016), the most common forms of damage to buildings observed were the detachment of stones from façades, partial or complete collapse of chimneys, and cracking of interior plaster and/or drywall finishes. The GEER report and its associated files (Clayton *et al.*, 2016) refer to damage to buildings at eight locations, three of which correspond to historic constructions located within Pawnee city: the Pawnee Nation building, the Pawnee County Courthouse, and the Pawnee Bill House. As shown in Figure A3.5.51, the first two presented cracking of interior plaster finishes, while the last one showed evidence of settlement, but the site has already suffered from slope stability issues for a long time and the GEER team noted that it was “difficult to tell how much settlement, if any, has occurred due to (the) earthquake”. When describing the Pawnee Nation building, the metadata of the photos of Clayton *et al.* (2016) refers to this building and other three similar ones nearby (also belonging to the Pawnee Nation complex) dating back to the 1920s-1930s and being made of structural stone masonry with plaster on lath interior finishes. It also notes that a piece of plaster ceiling of approximately 1 ft² had completely fallen off the ceiling of one of these buildings, and that cracks in interior plaster were observed in all of them. The GEER team highlights that there were no reports of damage to suspended tile ceilings.

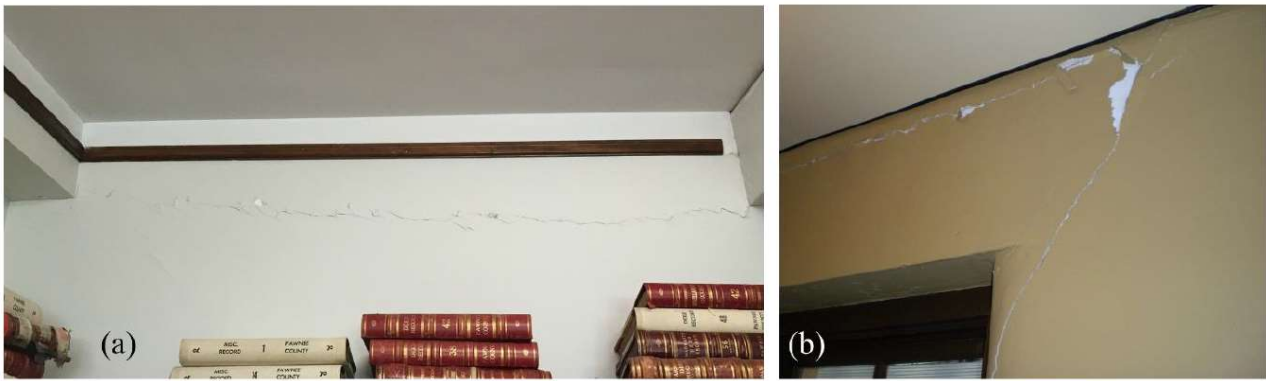


Figure A3.5.51. Cracking of interior plaster finishes at the Pawnee County Courthouse (left) and the Pawnee Nation building (right). From GEER report (Clayton *et al.*, 2016).

Though not mentioned in the GEER report (Clayton *et al.*, 2016), a fourth historic building in downtown Pawnee suffered from damage. The Arkansas Valley National Bank building, which is more than 110 years old, had several of its hand-cut sandstone façade blocks fallen over the sidewalk, as shown in Figure A3.5.52 (News OK, 2016b). This building is the one that seems to have received the most media coverage, possible due to its accessible location and the damage being visible from the outside (e.g., CNN, 2016b; NBC News, 2016; News OK, 2016b).



Figure A3.5.52. Examples of failures of stone façades: Arkansas Valley National Bank building (left, photo by Paul Hellstern, The Oklahoman, available from News OK (2016a), and a single-family residential house (right, photo from GEER report, Clayton *et al.*, 2016).

The GEER team did, however, observe failures of stone façades of residential buildings and noted that the stones tended to either have no mechanical connection with the structure or had an insufficient number of anchors. For example, the façade shown in Figure A3.5.52 (right) had metal strap anchors spaced at 1 to 3 metres intervals. Leaving aside the three historic sites mentioned above, two out of the five remaining buildings marked in in Figure A3.5.49 experienced façade failure, three had collapsed chimneys, and two had cracks in interior walls and finishes. In addition, one seemed to have

experienced settlement, and another presented cracks on the sidewalks, which appeared to have become separated from the façade in around 2.5 cm, though it was unclear if this was due to the earthquake or not.

While quite detailed and comprehensive, the GEER report (Clayton *et al.*, 2016) does not present statistics of number of buildings damaged. Figure A3.5.49 (right) shows eight locations where damage was observed, one of which possible accounts for four buildings altogether (those of Pawnee Nation), making a total of 12 buildings when adding the Arkansas Valley National Bank building, whose damage was not documented by Clayton *et al.* (2016). This number seems to be consistent with the statement of NBC News (2016) saying that “at least 14 buildings were damaged”, or that of CNN (2016b) citing Governor Mary Fallin saying that “rural Pawnee County and the city of Pawnee had at least six buildings damaged” and describing the damage as “minimal”. However, according to News OK (2016d) Curt Marshall, an attorney for the residents of Pawnee, “estimated that hundreds of homes in Pawnee have been affected by the quakes, sustaining damage ranging from cracks in walls, foundations and storm shelters to short-circuited electrical outlets”. It is noted that this estimation is being made within the context of a lawsuit filed on 17th November 2016 by residents of Pawnee against 27 energy companies, and not as part of a scientific assessment. Similarly, another article in News OK (2016b) cites the Oklahoma Insurance Department stating that by 30th September 2016 only four out of 247 insurance claims had been paid, as 39 were closed without payment and 17 were denied due to either the damage being less than the deductible or concluding that it had not been caused by the earthquake, while 212 were still open. Finally, Yeck *et al.* (2017) cite an article by Bustillo & Strum (2016) in the Wall Street Journal that makes reference to six buildings in Osage County having been reported as uninhabitable after the earthquake. This statement is surprising when contrasted against the information contained in the GEER report (Clayton *et al.*, 2016), as only one of the instances of damage reported by the latter is located in Osage County, which lies to the north-east of the epicentre and the town of Pawnee, both located within Pawnee County.

At the time of writing (March 2017), the equivalent of the GEER report (Clayton *et al.*, 2016) for the 2016 **M**5.0 Cushing earthquake is the Earthquake Engineering Research Institute (EERI) reconnaissance team report by Taylor *et al.* (2017), which contains an encompassing characterisation of the type of damage undergone by each type of construction and statistics regarding the assessment of the downtown area. Alongside this report, the EERI Oklahoma USA Earthquakes Clearinghouse (2016) contains a very large collection of photographs with their corresponding description of the damage observed.

Figure A3.5.53 summarises the damage reported for Cushing in different sources: the EERI report (Taylor *et al.*, 2017), the EERI Oklahoma USA Earthquakes Clearinghouse photo gallery (2016), the Cushing Public Schools Facebook page (Cushing Public Schools, 2017) and several news websites (KFOR, 2017; News OK, 2016f, 2016g, 2016h; Stillwater News Press, 2017). Figure A3.5.53 does not intend to be an exhaustive description of the damage caused by the 2016 **M**5.0 Cushing earthquake but simply aims at gathering information available at the time of writing in an organised way. The red square indicates the downtown area surveyed by Taylor *et al.* (2017), within which

damage was relatively widespread (e.g., News OK, 2016h), while the green rectangle indicates the approximate location of the East Main Street business corridor, which Taylor *et al.* (2017) describe as having suffered little to no damage. Circles indicate locations outside the downtown area marked in red for which information was available. Those in green correspond to sites with minor or no damage, while those in purple represent sites with damage other than minor of any kind. No circles are used within the downtown area, except for the two red ones shown, which mark the position of two buildings for which the need for demolition was found reported. One of these is the Lion's Den, the Cushing Lions Club, a nearly one-century old building that sustained damage during the 2016 **M**5.0 earthquake and was left with a visible residual deformation (EERI Oklahoma USA Earthquakes Clearinghouse, 2016), as shown in Figure A3.5.54. Its façade collapsed in March 2017 (1600KUSH, 2017; KFOR, 2017), perhaps due to loss of seating of the beam supporting the masonry above it, as may be inferred from the photos. The other is the American Legion building, built in 1924, whose masonry back wall suffered out-of-plane failure and whose chimney, parapets and structural walls were severely cracked during the earthquake, and was demolished in March 2017 (EERI Oklahoma USA Earthquakes Clearinghouse, 2016; Stillwater News Press, 2017).

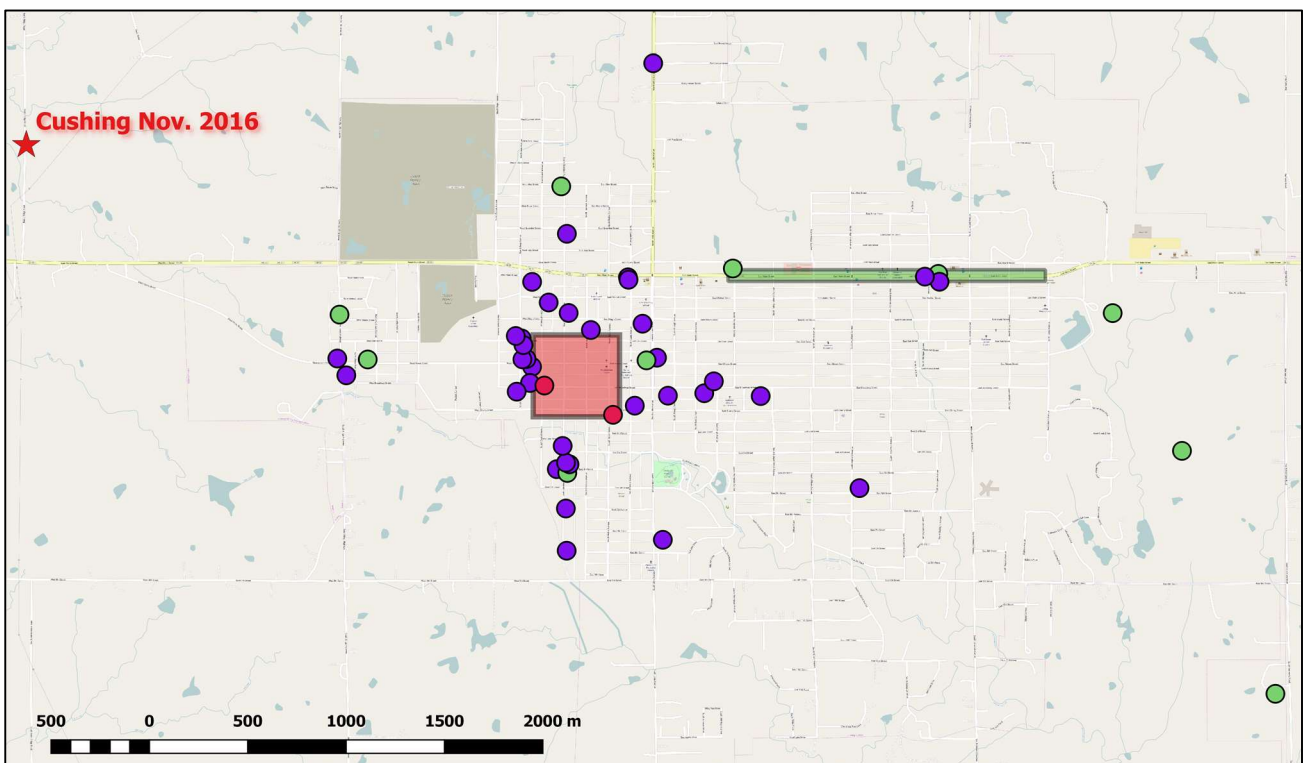


Figure A3.5.53. Sites with little to no damage (green circles), damage (purple circles) and that require demolition (red circles). Red square indicates downtown area surveyed by Taylor *et al.* (2017), within which damage was relatively widespread. Green rectangle indicates approximately the East Main Street business corridor, along which buildings suffered little to no damage. Red star indicates epicentral coordinates according to the USGS.



Figure A3.5.54. Damage sustained by the Lion's Den: (a) Residual deformation (photo by E. Jampole, from EERI Oklahoma USA Earthquakes Clearinghouse, 2016); (b) severe cracking in structural masonry wall (photo by A. Masroor, from EERI Oklahoma USA Earthquakes Clearinghouse, 2016); (c) failure of outer wythe of façade brickwork on side wall (photo by A. Masroor, from EERI Oklahoma USA Earthquakes Clearinghouse, 2016); (d) failure of façade in March 2017 (from 1600KUSH, 2017); (e) failure of façade in March 2017 (KFOR, 2017).

The EERI reconnaissance team surveyed 52 commercial buildings within the downtown area marked in red in Figure A3.5.53 and concluded that around 29% of these had sustained either moderate or severe damage, and 59.6% had only minor damage, as shown in Table A3.5.19 (Taylor *et al.*, 2017). Business owners were also asked to self-report the extent of the damage that their properties had suffered. While being clearly subjective, results from this survey shown in Figure A3.5.55 can serve as a guidance to summarise the severity of the damage in the area. More than half of these business owners reported having lost electricity immediately after the earthquake, while 9% had neither water nor gas either, and 6% had no internet. One week after the event only 6% remained with some kind of lifeline loss (Taylor *et al.*, 2017).

Table A3.5.19. Assessment of commercial buildings in downtown Cushing carried out by the EERI reconnaissance team (Taylor *et al.*, 2017).

Damage	Number of Buildings	Percentage
No damage	6	11.5%
Minor damage	31	59.6%
Moderate damage	9	17.3%
Severe damage	6	11.5%

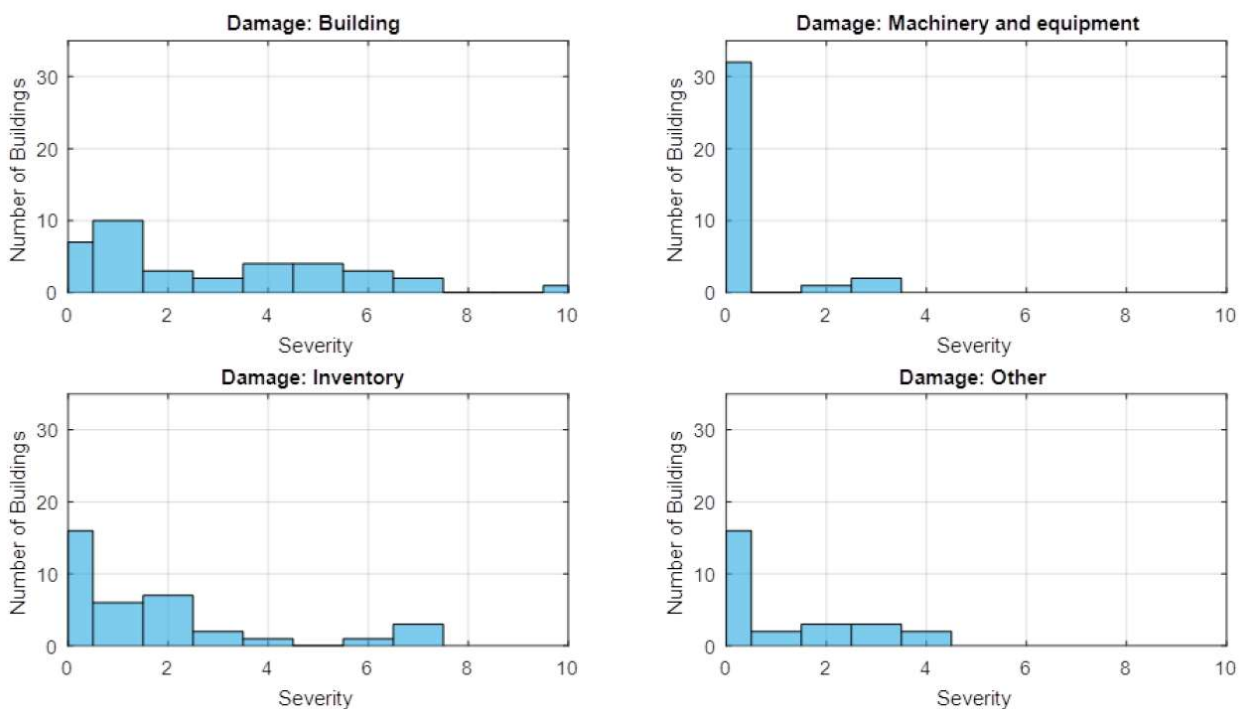


Figure A3.5.55. Extent of damage to their buildings self-reported by business owners in downtown Cushing. From Taylor *et al.* (2017).

According to KFOR (2016b), 40 to 50 buildings were “substantially damaged” by the 2016 M5.0 Cushing earthquake. Similarly, the USGS reports “at least 40” severely damaged buildings and the NOAA database says 50. Although the damage scales used for these statements are not objectively specified, these numbers seem to be in general overall agreement with the information gathered in Figure A3.5.53 and the statistics of Taylor *et al.* (2017) for the downtown area. However, the points marked in purple in Figure A3.5.53 (*i.e.*, outside the downtown area) can easily add around 30 more.

According to Taylor *et al.* (2017), the most common types of damage observed by the EERI reconnaissance team in unreinforced masonry buildings, typical of the business area in downtown Cushing, were cracking of mortar joints and brick units near openings, out-of-plane collapse and bulging of outer wythes on multi-wythe walls, and fallen brick units from parapets, while less common forms of damage to these buildings include collapse of parapets, out-of-plane collapse of entire wall sections, and residual lateral deformations. Figure A3.5.56 shows some examples of these kinds of damage.



Figure A3.5.56. Examples of damage of unreinforced masonry buildings: (a) out-of-plane failure of an entire wall section of the Cushing Publishing building (not in use, photo by A. Masroor); (b) out-of-plane collapse and bulging of outer wythe (photo by E. Jampole); (c) brick façade separated from concrete masonry wall inner wythe at former St. Peter and Paul Catholic Church (photo by E. Jampole); (d) step cracks in brick wall (photo by A. Greer); (e) step cracks in concrete masonry wall (photo by E. Wilson). All photos from EERI Oklahoma USA Earthquakes Clearinghouse (2016).

For the Cimarron Tower, the only building referred to as being a reinforced concrete frame, Taylor *et al.* (2017) report the cracking of masonry infills and the failure of masonry parapets and terra cotta cornices, as shown in Figure A3.5.57, as well as the breaking of several water supply pipes inside. They mention that the EERI team was not able to directly access the building due to safety reasons.

Cushing's (seemingly) only steel frame building, the Cushing Municipal Tower Plant, sustained only minor damage, primarily associated to the cracking of masonry infill walls adjacent to the steel frames, fallen ceiling panels, and minor damage to equipment (Taylor *et al.*, 2017).



Figure A3.5.57. Damage to the roof parapet and cornices of 7-storey reinforced concrete Cimarron tower: before (left, Google Street View) and after the 2016 **M**5.0 Cushing earthquake (right, photo by Jim Beckel, The Oklahoman, from News OK photo gallery, 2016g).

Similarly, damage to light wood frame residential homes consisted mostly on cracking of partition walls in corners and near openings, as well as damage to non-structural brick façades and masonry chimneys, with structural damage being rare (Taylor *et al.*, 2017).

Besides the cracking of partition walls and failure of masonry parapets and chimneys, other instances of damage to non-structural components include the cracking of floor tiles, the falling of ceiling tiles and/or their supporting sub-structures, which was quite common (e.g., Figure A3.5.58), and some isolated reports of damage to heating, ventilation and/or air-conditioning systems in commercial buildings (EERI Oklahoma USA Earthquakes Clearinghouse, 2016; Taylor *et al.*, 2017).

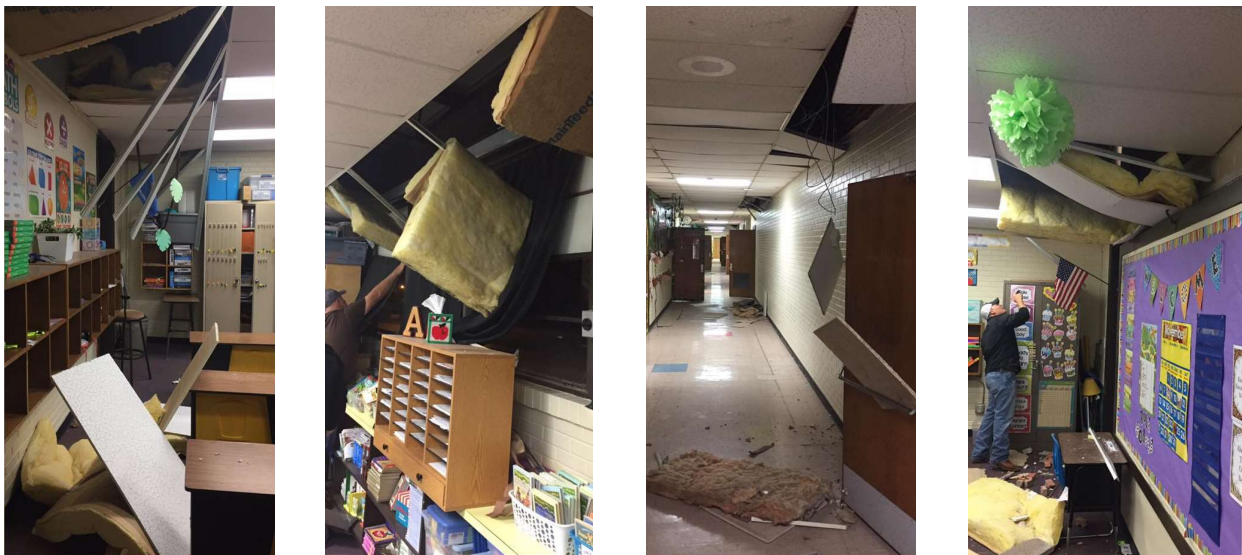


Figure A3.5.58. Examples of damage to ceiling tiles and their supporting grids at Cushing Upper Elementary School. Photos from the Cushing Public Schools Facebook page (Cushing Public Schools, 2017).

According to News On 6 (2016c), the town's hospital and hotels were not amongst the damaged structures. According to the Cushing Public Schools Facebook page (2016), the three public schools located on the East side of the city (Cushing High School, Cushing Middle School and Harmony Lower Elementary) suffered little to no damage. The Cushing Upper Elementary School, located close to the downtown area, had several fallen ceiling

tiles and insulation blocks, as well as damage to the grids supporting them (Cushing Public Schools Facebook page, 2016; Taylor *et al.*, 2017), as shown in Figure A3.5.58. The Cushing Pre-Kindergarten (ex Sunnyside Elementary), located to the south-west of the city, also had fallen ceiling tiles and associated supporting structures, as well as cracks in mortar joints and brick units, according to Taylor *et al.* (2017). A steel canopy structure in its main entrance sustained some moderate damage and moved away from the building, resulting in an unstable condition. Taylor *et al.* (2017) point out that the nuts of the anchor of the steel baseplate to the concrete sidewalk were likely not fully tightened before the earthquake. According to a series of tweets linked by KFOR (2016c), the Cushing Youth and Community Center also had several ceiling tiles and supporting grids fallen.

Three water main pipes were reported as damaged by the earthquake around Cushing (News OK, 2016f; Taylor *et al.*, 2017). One of them was located along Highway 18, to the North of the city, and showed holes and signs of corrosion, according to Taylor *et al.* (2017). Part of the downtown area was evacuated shortly after the earthquake for the fear of possible natural gas lines having been damaged, though officials later reported that there had been no problems with major lines and that “other minor leaks” had been sealed (Taylor *et al.*, 2017). Storage tanks, pipelines and other infrastructure related to the oil industry appeared to have been able to withstand the motion without any consequences (News OK, 2016f), as too have roads and bridges in a 15-mile inspection radius (Taylor *et al.*, 2017).

A3.5.8.3 Observed weaknesses

No reports of systematic weaknesses were found in the literature in relation to the 2011 Prague earthquake. However, the kind of damage observed and the statements by Beavers (2002) and Cutcliffe (2000) regarding the challenges faced by the efforts to incorporate good seismic design practises in the central and eastern USA suggest that the lack of seismic design of masonry structures and, perhaps, non-structural components, was the main cause of the damage observed.

It should be noted that a commonly observed failure was the toppling or complete collapse of masonry chimneys/fireplaces. Apart from the case reported above (Figure A3.5.47), other chimneys were also severely damaged, as shown in Figure A3.5.59. This is also true for the 2016 Pawnee and Cushing earthquakes.

With respect to the 2016 Pawnee event, Clayton *et al.* (2016) point out that the lack of appropriate mechanical anchorage between stone façades and structures appears to be frequent around the area of Pawnee. Given that a large proportion of the damage observed was related to the failure of stone façades, it can be inferred that this weakness had a decisive role in the aftermath of this earthquake. From the report by Taylor *et al.* (2017) and the photo gallery of the EERI Oklahoma USA Earthquakes Clearinghouse (2016) it can be inferred that something similar occurred in Cushing with the lack of connection between the inner and outer wythes of unreinforced masonry walls, which resulted in the outer wythes easily undergoing out-of-plane failures.



Figure A3.5.59. Complete collapse of a fireplace in the interior of a house in Sparks (left, News 9, 2011), and collapse of the top of a chimney of a house (right, Wikipedia).

Having been the failure of ceiling tiles and their supporting structures a relatively common type of damage observed for Cushing, it may also be inferred that the lack of appropriate design of suspended ceilings is likely to have played a role. It is noted, however, that seismic design of non-structural components is an area of earthquake engineering that has only started to receive increasing attention in recent times (e.g., Filiatrault & Sullivan, 2014).

A3.5.8.4 Damage distribution

There are no details available with respect to the distribution of damage due to the 2011 **M5.7** Prague earthquake within the towns. Joey Wakefield, from the Lincoln County Emergency Management team, highlighted that though damage reports were being received from all over Lincoln County, the area with a higher concentration was around the epicentre, as expected (Gibson & Medley, 2011).

The distribution of damage due to the 2016 **M5.8** Pawnee earthquake is shown in Figures A3.5.40 and A3.5.49. The geotechnical information of the area is not detailed enough to infer site effects. Moreover, though it can be noted that, according to Grandin *et al.* (2017), the WNW-ESE striking fault ruptured from West to East, and that a big proportion of the observed damage seems to have occurred more to the East than to the West of the epicentre, the lack of population and building exposure in the area and the lack of availability of near-field records makes it difficult to assess whether directivity may have played a role on the consequences of this earthquake.

For the 2016 **M5.0** Cushing earthquake, the map in Figure A3.5.53 clearly shows more instances of damage on the West side of the city than on the East. One reason for this might simply be that the epicentre was located to the north-west of Cushing. However, another one might be related to the kinds of construction that can be found in different parts of town. While details on the exact exposure are not available, it was mentioned earlier that Taylor *et al.* (2017) make reference to unreinforced brick masonry buildings being predominant in the downtown business area and light wood frame houses being more common in the residential areas, and a quick browse over the city using Google Maps and Google Street View strongly suggest that the areas that suffered the most

damage may have probably had a larger proportion of the former than the latter kind of structure. The risk of bias is nevertheless present, as the EERI reconnaissance team focused on investigating the consequences around the central business district (Taylor *et al.*, 2017). Moreover, damage to unreinforced masonry structures can often be observed from the outside, while the kind of non-structural damage to internal partitions that many light wood frame houses may have suffered is only visible when accessing the property. In this sense, it is possible that the EERI Oklahoma USA Earthquakes Clearinghouse (2016) may contain more photos of damage that could be observed from the outside than other, though it is noted that plenty of interior photographs are available as well.

A3.5.9 Casualties and losses

A3.5.9.1 Numbers of dead and injured

The USGS and the Oklahoma State Department of Health report at least two injured in the Shawnee-Sparks area due to the 2011 **M5.7** Prague earthquake: one in Lincoln County (where the epicentre was located), and the other one in Pottawatomie County, to the south of the above (Figure A3.5.21). Reuters (2011) highlights that the Oklahoma Health Department reported that there were no serious injuries, that the two injuries that occurred were minor, and that neither of them required hospitalization. However, CNN (2011) reports at least one person having been taken to a hospital in Prague with minor injuries. Ellsworth *et al.* (2015) confirm that there were no deaths.

For the 2016 **M5.8** Pawnee earthquake, Clayton *et al.* (2016), NBC News (2016) and CNN (2016b) report one injury, while Reuters (2016) states that there were no injuries.

For the 2016 **M5.0** Cushing earthquake, the USGS reports one person injured, which probably corresponds to the same person that Taylor *et al.* (2017) report as having been taken to hospital with a laceration on the back of their hand after having been evacuated from the Cimarron Tower (Figure A3.5.57). In contrast, News On 6 (2016c) cites the Cushing Fire Department saying that it had not transported anyone to the hospital for injuries. News OK (2016i) speaks of no major injuries, though this does not necessarily contradict the USGS and Taylor *et al.* (2017).

A3.5.9.2 Causes of casualties

According to a situation update by the Oklahoma Department of Emergency Management with date 6th November 2011 04.30 pm local time (OEM, 2011), the cause of the injury at Lincoln County after the 2011 **M5.7** Prague earthquake was that the person involved hit his head when trying to run out of his home during the main shock, while the victim of the injury at Pottawatomie County cut her foot on broken glass after the earthquake.

For the 2016 **M5.8** Pawnee earthquake, Clayton *et al.* (2016) report that the injury was caused by a collapsing chimney.

It is not clear what caused the hand laceration to the person injured by the 2016 **M5.0** Cushing earthquake.

A3.5.9.3 Estimates of economic losses

According to the International Business Times (2015), the 2011 **M5.7** Prague earthquake caused losses of around one million U.S. dollars (USD). This figure is significantly smaller than the estimation from USGS PAGER (2015), according to which losses were expected to range between ten and one-hundred million USD instead. This range of losses had a 33% probability, while losses smaller than one million and between one and 10 million had a 4% and a 17% probability. The estimation from USGS PAGER is somehow in agreement with the 12 million insured losses reported by Daniell & Vervaeck (2012) and the over 10 million insured losses mentioned by Ellsworth *et al.* (2015), which contrast quite significantly with the statement by Bankrate.com (2016), according to which less than 1% of Oklahomans had proper earthquake insurance. However, a recent newspaper article citing the Oklahoma Insurance Department as a source reports that the 2011 **M5.7** Prague earthquake has been the most expensive earthquake in Oklahoma as of March 2017, with insurances companies having paid a total of 1,669,100 USD to cover 118 claims, while other 220 claims have been denied (Tulsa World, 2017).

This same source reports 423 insurance claims filed for damage due to the 2016 **M5.8** Pawnee earthquake, of which 296 were denied, 52 received payments for a total of 253,100 USD and 75 remain open as of March 2017 (Tulsa World, 2017). Another newspaper article explains that the closure of claims without payment is due, in general, to the damage amounting to less than the deductible, or the inspection resulting in the conclusion that the damage was not caused by the earthquake (News OK, 2016b).

According to Tulsa World (2017), 108 insurance claims were filed after the 2016 **M5.0** Cushing earthquake, of which 30 have been defined, 8 received payments for a total of 90,300 USD, and 70 were still open as of March 2017. These numbers do not seem to include the “more than a million dollars in damage” to insured buildings belonging to the city of Cushing reported by KFOR (2017), as the figures clearly do not match. The Significant Earthquake Database of the National Centers for Environmental Information of the National Oceanic and Atmospheric Administration of the United States (NOAA, 2017) also reports damage for about 1 million USD, while the Emergency Events Database (EM-DAT, 2017) report a much larger sum of 20 million USD instead.

It is not clear either whether the numbers for Cushing or Pawnee include losses reported for the Oklahoma State University by the University newspaper, which reports about 320,000 USD of damage due to the **M5.8** Pawnee event, and an original estimate of about 40,000 USD brought down to 13,352 USD for damage due to the **M5.0** Cushing event (OColly, 2017). Whether all the damage corresponds to the main campus in Stillwater, located at approximately 35 and 28 km from the epicentres of the **M5.8** Pawnee and the **M5.0** Cushing events, respectively, or if it includes other University buildings within the state as well, is not specified. As it is stated that the University has a 50,000 USD

deductible, it may be inferred that all of the reparations needed after Cushing were paid by the University, while those due to Pawnee were partially paid by the University insurance.

According to Tulsa World (2017), insurance companies have paid 5.1 million USD in claims related to earthquake damage in the state of Oklahoma from 2010 through 2016, with an approval rate of about 3 in 20 claims. It is worth noting, once more, that several sources point out that most residents in Oklahoma do not have earthquake insurance, and that even those who do are subject to deductibles (e.g., KFOR, 2017; News OK, 2016b; Taylor *et al.*, 2017). Consequently, insured losses reported above are clearly not the total direct material losses from these three earthquakes.

A3.5.10 Discussion and conclusions

The three earthquakes studied herein occurred on 6th November 2011, at 03.53.10 UTC (5th November 2011, 22.53.10 local time), 3rd September 2016 at 12.02.44 UTC (07.02.44 local time), and 7th November 2016 at 01.44.24 UTC (6th November 2016, 19.44.24 local time). The first one, the **M5.7** Prague event, was the largest to have ever occurred in the history of Oklahoma until the **M5.8** Pawnee of 3rd September 2016 one took place. The former caused damage in the area enclosed by the cities/towns of Prague, Sparks, Meeker and Shawnee, while the latter affected mostly the city of Pawnee and surrounding areas. Though with a much smaller magnitude, the **M5.0** Cushing earthquake of 7th November 2016 caused widespread damage in the city of Cushing, possibly due to the epicentre being so much closer to the city itself than in the previous two cases.

Whilst tectonic earthquakes have been known to occur in Oklahoma, including a **M5.5** in 1952, the sharp increase in seismicity observed since 2009 is widely believed to have been induced by the activities of deep injection of wastewater that have been going on in the area for decades.

The **M5.7** main shock of the 2011 Prague sequence and other strong events were extensively felt and caused significant fear in the population, who were not used to ground shaking. The overall extent of the damage is somehow unclear, for some sources describe around 14 houses being "destroyed", while some others only talk about "minor damage". Up to 94 homes were reported as damaged due to the "recent earthquakes", but this number is likely to include buildings affected by the aftershocks, the strongest of which had a magnitude of **M4.8**. Given the lack of official systematic damage and economic losses reports it is difficult to reach to a conclusion on the matter. However, descriptions and images available through online media suggest that most damage was related to cracks in plasterboards, floor tiles and ceilings, cracks/detachment of brick façades, and toppling of chimneys, while the most significant instances were the collapse of a small spire from a university building, a toppled chimney that damaged the roof over which it fell, a house with almost all façade (non-bearing) bricks detached, and the buckling of a highway.

With a slightly larger magnitude but located farther away from the affected sites, the 2016 **M5.8** Pawnee event also seems to have caused damage to around 14 buildings, though a

much larger number of insurance claims have been made. Most of the damage seems to be related to the failure of non-structural stone façades (likely due to a lack or insufficiency of mechanical anchors between façade and structure that was systematically observed), the partial or full collapse of chimneys, and the cracking of interior plaster or drywall finishes. Some geotechnical phenomena were observed, including liquefaction at a few locations, cracking of soil backfills and earthen dams, a small slump failure that caused settlement of a private house, and spalling of cover concrete on the abutments of a bridge. In many cases, it was not clear to the reconnaissance teams if the damage pointed out by the inhabitants of the area had actually been caused by the earthquake.

Numerically, the effects of the 2016 **M**5.0 Cushing event seem more extensive at first glance, an observation that is supported by the fact that the consequences of this event are reported within the EM-DAT and NOAA databases, while those of the 2016 **M**5.8 Pawnee one are not. This is probably due to the combined effect of a much larger number of buildings being located very close to the epicentre and ground motions appearing to have been particularly large in the area (0.585 g PGA), though it is noted that no ground motion records sufficiently close to the locations damaged by the 2011 Prague and 2016 Pawnee are available to make a proper comparison. Unreinforced masonry structures from the first half of the 20th century seem to have been the most affected ones, with two undergoing demolition as a consequence of the damage sustained, some suffering from out-of-plane collapse of parapets and entire wall sections, and many others having cracks of mortar joints and brick units near openings, out-of-plane collapse and bulging of outer wythes on multi-wythe walls, and brick units falling from parapets. Damage to non-structural components such as partition walls, brick façades, chimneys, ceiling tiles and their supporting structures was observed quite frequently in many kinds of structures. Overall, around 40-50 buildings are described as having been “substantially damaged”, though an accurate description of the meaning of this expression has not been found. Within the downtown area of Cushing, comprising approximately a 350 m-side square, 15 out of 52 buildings assessed suffered from moderate to severe damage, and 31 out of 52 had some kind of minor damage instead. At least 36 instances of some kind of damage can be counted outside of the area assessed as “downtown”, the total number of damaged buildings likely raising at least to 80.

A3.5.11 References

A3.5.11.1 Bibliography

Afshari, K. & J.P. Stewart (2016). Physically parametrised prediction equations for significant duration in active crustal regions. *Earthquake Spectra* **32**(4), 2057-2081.

Beavers, J.E. (2002). A review of seismic hazard description in US design codes and procedures. *Prog. Struct. Eng. Mater.* **4**, 46–63.

Bommer, J.J., P.J. Stafford & J.E. Alarcón (2009). Empirical equations for the prediction of the significant, bracketed, and uniform duration of earthquake ground motion. *Bulletin of the Seismological Society of America* **99**(6), 3217-3233.

- Bustillo, M. & B. Strum (2016). Oklahoma earthquake felt in several U.S. states, as oil wells draw scrutiny, *Wall Street Journal*.
- Campbell, J. A. & J. A. Weber (2006). *Wells drilled to basement in Oklahoma*. Oklahoma Geological Survey Special Publication 2006-1.
- Center for International Earth Science Information Network - CIESIN - Columbia University (2016). Gridded Population of the World, Version 4 (GPWv4): Population Density. Palisades, NY: NASA Socioeconomic Data and Applications Center (SEDAC). Available online at (last accessed 12th April 2017): <http://sedac.ciesin.columbia.edu/data/set/gpw-v4-population-density>.
- Clayton P., G. Zalachoris, E. Rathje, T. Bheemasetti, S. Caballero, X. Yu & S. Bennett (2016). *The Geotechnical Aspects of the September 3, 2016 M5.8 Pawnee, Oklahoma Earthquake*. GEER-051 report. Available online at (last accessed 13th March 2017): http://www.geerassociation.org/component/geer_reports/?view=geerreports&id=78&layout=default.
- Cutcliffe, S.H. (2000). Earthquake resistant building design codes and safety standards: The California experience. *GeoJournal* **51**, 259–262.
- Daniell, J. & A. Vervaeck (2012). *CATDAT Integrated Historical Global Catastrophe Database - Damaging Earthquakes Database 2011- The Year in Review*. Available online at <http://earthquake-report.com/2012/01/09/catdat-damaging-earthquakes-database-2011-annual-review/>. Last accessed: 9th February 2017.
- Darold, A.P. & A.A. Holland (2015). *Preliminary Oklahoma optimal fault orientations*. Open File Report OF4-2015, Oklahoma Geological Survey. 1 pp.
- Darragh R., N. Abrahamson, W. Silva & N. Gregor (2015). Development of hard rock ground-motion models for Region 2 of central and eastern North America. In *NGA-East Ground Motion Models for the Central and Eastern North America Region*, PEER Technical Report 2015/04, Pacific Earthquake Engineering Research, Berkeley, USA.
- Doerflinger, P. L. & L. Bajema, L. (2014). *Oklahoma 2016: Comprehensive annual financial report for the fiscal year ended June 30, 2014*. Office of Management and Enterprise Services, Oklahoma City, Oklahoma, USA. Available online at: <https://www.ok.gov/OSF/documents/cafr14.pdf>. Last accessed: 12th April 2017.
- Doerflinger, P. L. & L. Bajema, L. (2016). *Oklahoma 2016: Comprehensive annual financial report for the fiscal year ended June 30, 2016*. Office of Management and Enterprise Services, Oklahoma City, Oklahoma, USA. Available online at: <https://www.ok.gov/OSF/documents/cafr16.pdf>. Last accessed: 12th April 2017.
- Dziewonski, A.M., T.-A. Chou & J. H. Woodhouse (1981). Determination of earthquake source parameters from waveform data for studies of global and regional seismicity. *Journal of Geophysical Research* **86**, 2825-2852.
- Ekström, G., M. Nettles & A. M. Dziewonski (2012). The global CMT project 2004-2010: Centroid-moment tensors for 13,017 earthquakes. *Physics of the Earth and Planetary Interiors* **200-201**, 1-9.
- Ellsworth W. L., A. L. Llenos , A. F. McGarr , A. J. Michael , J. L. Rubinstein , C. S. Mueller , M. D. Petersen & E. Calais (2015). Increasing seismicity in the U. S. midcontinent: Implications for earthquake hazard. *The Leading Edge* **34**(6), 618–626.
- Evans, M. (2017). *Oklahoma economic indicators*. Oklahoma Employment Security Commission - Economic Research and Analysis Division. 32 pp. Available online at (last accessed 12th April 2017): https://www.ok.gov/oesc_web/documents/ImiEconIndPub.pdf.

- FEMA (2007). *FEMA 543, Design Guide for Improving Critical Facility Safety from Flooding and High Winds: Providing Protection to People and Buildings*.
- Filiatrault, A. & T. Sullivan (2014). Performance-based seismic design of nonstructural building components: The next frontier of earthquake engineering. *Earthquake Engineering and Engineering Vibration* **13**(1), 17-46.
- Fratinaro, V.F. & S.A. Schroeder (2015). Historical study of the wind design provisions of ASCE 7. *Structures Congress 2015*, 829–839.
- Freeman J.R. (1932). *Earthquake Damage and Earthquake Insurance*. 1st edition. New York: McGraw-Hill.
- Ghosh, S.K. (2008). Searching for simplicity: The evolution of wind provisions in standards and codes in the United States. *RCI Interface*, 13–21.
- Giardini, D., G. Grünthal, K.M. Shedlock & P. Zhang (1999). The GSHAP global seismic hazard map. *Annali di Geofisica* **42**(6), 1225-1228.
- Gibson, T. & R. Medley (2011). Monday earthquake rocks Lincoln County, damages high school. News OK. Available online at <http://newsok.com/article/3621379>. Last accessed: 9th February 2017.
- Grandin, R., M. Vallée & R. Lacassin (2017). Rupture Process of the Oklahoma Mw5.7 Pawnee Earthquake from Sentinel-1 InSAR and Seismological Data. *Seismological Research Letters*, IN PRESS.
- Grünthal, G. (ed.) (1998). *European Macroseismic Scale 1998 (EMS-98)*. Cahiers du Centre Europeen de Geodynamique et de Seismologie 15, Centre Europeen de Geodynamique et de Seismologie, Luxembourg.
- Holland, A.A. (2013). Optimal Fault Orientations within Oklahoma. *Seismological Research Letters* **84**, 876–890.
- Holland, A.A., C.R. Toth & E.M. Baker (2013). *Probabilistic seismic hazard assessment and observed ground motions for the Arcadia, Oklahoma, Dam site*. Oklahoma Geological Survey, The University of Oklahoma, Special Publication 2013-01. Available online at http://wichita.ogs.ou.edu/documents/SP2013-01/SP2013-01_PSHA-Arcadia.pdf. Last accessed: 9th February 2017.
- Hough, S.E. & M. Page (2015). A century of induced earthquakes in Oklahoma? *Bulletin of the Seismological Society of America* **105**(6), -.
- Huston, E. (2007). SEAW's handbook of a rapid-solutions methodology for wind design. *Struct. Mag.*, 61–64.
- Jaiswal, K. & D.J. Wald (2008). Creating a Global Building Inventory for Earthquake Loss Assessment and Risk Management. USGS Open File Report 2008-1160. Available electronically at <http://pubs.usgs.gov/of/2008/1160/>. Last accessed: 9th February 2017.
- Johnson, K.S. (2008). *Geologic history of Oklahoma*. Educational Publication 9: 2008, Oklahoma Geological Survey.
- Keranen, K.M., H.M. Savage, G.A. Abers & E.S. Cochran (2013). Potentially induced earthquakes in Oklahoma, USA: Links between wastewater injection and the 2011 Mw 5.7 earthquake sequence. *Geology* **41**, 699–702.

- Klose, C.D. & L. Seeber (2007). Shallow seismicity in stable continental regions. *Seismological Research Letters* **78**, 554–562.
- Langenbruch, C. & M. D. Zoback (2016). How will induced seismicity in Oklahoma respond to decreased saltwater injection rates? *Science Advances* **2**, e1601542.
- Llenos, A.L. & A.J. Michael (2013). Modeling Earthquake Rate Changes in Oklahoma and Arkansas: Possible Signatures of Induced Seismicity. *Bulletin of the Seismological Society of America* **103**, 2850–2861.
- Manga, M., C.-Y. Wang & M. Shirzaei (2016). Increased Stream Discharge after the 3 September 2016 M_w 5.8 Pawnee, Oklahoma Earthquake: Stream Response to an Induced Earthquake. *Geophysical Research Letters* **43**(22): 11,588–11,594.
- Marsh, S. & A. Holland (2016). *Comprehensive fault database and interpretive fault map of Oklahoma*. Open File Report OF2-2016, Oklahoma Geological Survey. 15 pp. GIS-compatible files available at <http://www.ou.edu/content/ogs/data/fault.html>. Last accessed: 18th February 2017.
- McGarr, A., B. Bekins, N. Burkardt, J. Dewey, P. Earle, W. Ellsworth, S. Ge, S. Hickman, A. Holland, E. Majer, J. Rubinstein, A. Sheehan (2015). Coping with earthquakes induced by fluid injection. *Science* **347**(6224): 830–831.
- McNamara, D. E., H. M. Benz, R. B. Herrmann, E. A. Bergman, P. Earle, A. Holland, R. Baldwin, & A. Gassner (2015a). Earthquake hypocenters and focal mechanisms in central Oklahoma reveal a complex system of reactivated subsurface strike-slip faulting: earthquake source parameters in Oklahoma. *Geophysical Research Letters* **42** (8): 2742–2749.
- McNamara, D. E., G. P. Hayes, H. M. Benz, R. A. Williams, N. D. McMahon, R. C. Aster, A. Holland, T. Sickbert, R. Herrmann, R. Briggs, G. Smoczyk, E. Bergman & P. Earle (2015b). Reactivated faulting near Cushing, Oklahoma: increased potential for a triggered earthquake in an area of United States strategic infrastructure. *Geophysical Research Letters* **42**(20): 8328–8332.
- Northcutt, R.A. & J.A. Campbell (1995). *Geological provinces of Oklahoma*. Open-File Report OF5-95, Oklahoma Geological Survey.
- Pagani, M., D. Monelli, G. Weatherill, L. Danciu, H. Crowley, V. Silva, P. Henshaw, L. Butler, M. Nastasi, L. Panzeri, M. Simionato & D. Viganò (2014). OpenQuake Engine: an open hazard (and risk) software for the Global Earthquake Model. *Seismological Research Letters* **85**(3), 692–702.
- Parker, G. A., J. A. Harmon, J. P. Stewart, Y. M. A. Hashash, A. R. Kottke, E. M. Rathje, W. J. Silva & K. W. Campbell (2017). Proxy-based V_{s30} Estimation in Central and Eastern North America. *Bulletin of the Seismological Society of America* **107**(1), 117–131.
- Petersen, M.D., A.D. Frankel, S.C. Harmsen, C.S. Mueller, K.M. Haller, R.L. Wheeler, R.L. Wesson, Y. Zeng, O.S. Boyd, D.M. Perkins, N. Luco, E.H. Field, C.J. Wills & K.S. Rukstales (2008). *Documentation for the 2008 update of the United States National Seismic Hazard Maps*. USGS Open-File Report 2008-1128, 128 pp.
- Petersen, M.D., M.P. Moschetti, P.M. Powers, C.S. Mueller, K.M. Haller, A.D. Frankel, Y. Zeng, S. Rezaeian, S.C. Harmsen, O.S. Boyd, N. Field, R. Chen, K.S. Rukstales, N. Luco, R.L. Wheeler, R.A. Williams & A.H. Olsen (2014). *Documentation for the 2014 update of the United States National Seismic Hazard Maps*. USGS Open-File Report 2014-1091, 243 pp.
- Petersen, M.D., C.S. Mueller, M.P. Moschetti, S.M. Hoover, A.L. Llenos, W.L. Ellsworth, A.J. Michael, J.L. Rubinstein, A.F. McGarr & K.S. Rukstales (2016). Seismic-hazard forecast for 2016 including induced and natural earthquakes in the Central and Eastern United States. *Seismological Research Letters* **87**(6), 1327–1341.

Petersen, M.D., C.S. Mueller, M.P. Moschetti, S.M. Hoover, A.M. Shumway, D.E. McNamara, R.A. Williams, A.L. Llenos, W.L. Ellsworth, A.J. Michael, J.L. Rubinstein, A.F. McGarr & K.S. Rukstales (2017). 2017 One-Year Seismic-Hazard Forecast for the Central and Eastern United States from Induced and Natural Earthquakes. *Seismological Research Letters* **88**(3), 1–12.

Storchak, D.A., D. Di Giacomo, I. Bondár, E. R. Engdahl, J. Harris, W.H.K. Lee, A. Villaseñor & P. Bormann (2013). Public Release of the ISC-GEM Global Instrumental Earthquake Catalogue (1900-2009). *Seismological Research Letters*, **84**(5), 810-815. Version 4.0 of the catalogue available at <http://www.isc.ac.uk/iscgem/download.php>. Last accessed: 17th March 2017.

Sumy, D.F., E.S. Cochran, K.M. Keranen, M. Wei & G.A. Abers (2014). Observations of static Coulomb stress triggering of the November 2011 M 5.7 Oklahoma earthquake sequence. *Journal of Geophysical Research: Solid Earth* **119**, 1904–1923.

Sun, X. & S. Hartzell (2014). Finite-fault slip model of the 2011 M_w 5.6 Prague, Oklahoma earthquake from regional waveforms. *Geophysical Research Letters* **41**, 4207–4213.

Taylor, J., M. Çelebi, A. Greer, E. Jampole, A. Masroor, S. Melton, D. Norton, N. Paul, E. Wilson, & Y. Xiao (2017). *EERI Earthquake Reconnaissance Team Report: M5.0 Cushing, Oklahoma, USA Earthquake on November 7, 2016*. Earthquake Engineering Research Institute, Oakland, California, USA. Available online at: <http://www.eqclearinghouse.org/2016-09-03-oklahoma/2017/02/15/eeri-reconnaissance-team-report-on-the-cushing-oklahoma-earthquake-is-now-available/>. Last accessed: 11th February 2017.

United Nations, ed. (2011). *Human Development Report 2011 - Sustainability and equity: A better future for all*. Report of the United Nations Development Programme (UNDP), New York, United States.

United Nations, ed. (2013). *Human Development Report 2013 - The rise of the South: Human progress in a diverse world*. Report of the United Nations Development Programme (UNDP), New York, United States.

United Nations, ed. (2014). *Human Development Report 2014 - Sustaining human progress: Reducing vulnerabilities and building resilience*. Report of the United Nations Development Programme (UNDP), New York, United States.

United Nations, ed. (2015). *Human Development Report 2015 – Work for Human Development*. Report of the United Nations Development Programme (UNDP), New York, United States.

United Nations, ed. (2016). *Human Development Report 2016 – Human Development for Everyone*. Report of the United Nations Development Programme (UNDP), New York, United States.

U.S. Census Bureau (2012). *United States 2010 Census of Population and Housing - Population and Housing Unit Counts - Oklahoma*. U.S. Department of Commerce - Economics and Statistics Administration - U.S. Census Bureau, Washington D.C. Data available online at (last accessed 23rd March 2017): <https://factfinder.census.gov/faces/nav/jsf/pages/index.xhtml>.

Wald, D.J. & T.I. Allen (2007). Topographic slope as a proxy for seismic site conditions and amplification. *Bulletin of the Seismological Society of America* **97**, 1379–1395. Slope-based online map viewer available at: <http://usgs.maps.arcgis.com/apps/webappviewer/index.html?id=8ac19bc334f747e486550f32837578e1>. Data used herein downloaded from deprecated version last accessed on 26th April 2017.

Walsh, F. R. & M. D. Zoback (2016). Probabilistic assessment of potential fault slip related to injection-induced earthquakes: Application to north-central Oklahoma, USA. *Geology* **44**(12): 991-994.

Weatherill, G. A. (2014). *OpenQuake ground motion toolkit - User guide*. Global Earthquake Model (GEM). Technical Report.

Weingarten, M., S. Ge, J. W. Godt, B. A. Bekins & J. L. Rubinstein (2015). High-rate injection is associated with the increase in U.S. mid-continent seismicity. *Science* **348**, 1336-1340.

Wills, C.J. & K.B. Clahan (2006). Developing a map of geologically defined site-condition categories for California. *Bulletin of the Seismological Society of America* **96**, 1483–1501.

Wilkerson, C. (2016). *How is Oklahoma's economy performing relative to other oil and gas states?* Federal Reserve Bank of Kansas City. Available online at (last accessed: 12th April 2017): <https://www.kansascityfed.org/publications/research/oke/articles/2016/comparing-oklahomas-economy>.

Witze, A. (2015). Artificial quakes shake Oklahoma. *Nature* **520**, 418–419.

Worden, C.B., E.M. Thompson, M. Hearne & D.J. Wald (2017). *ShakeMap V4 Manual: technical manual, user's guide, and software guide*. United States Geological Survey. Available online at: <http://usgs.github.io/shakemap/>.

Yeck, W. L., G. P. Hayes, D. E. McNamara, J. L. Rubinstein, W. D. Barnhart, P. S. Earle, and H. M. Benz (2017). Oklahoma experiences largest earthquake during ongoing regional wastewater injection hazard mitigation efforts: The 3 September 2016, M w 5.8 Pawnee Earthquake. *Geophysical Research Letters* **44**(2): 711–717. Catalog of relocated earthquake hypocenters available digitally at <https://www.sciencebase.gov/catalog/item/586c08c6e4b0f5ce109fa810>. Last accessed: 17th March 2017.

Yenier, E., G. M. Atkinson & D. F. Sumy (2017). Ground motions for induced earthquakes in Oklahoma. *Bulletin of the Seismological Society of America* **107**(1): 198–215.

Yong, A., E. M. Thompson, D. Wald, K. L. Knudsen, J. K. Odum, W. J. Stephenson & S. Haefner (2015). *Compilation of Vs30 data for the United States: U.S. Geological Survey Data Series 978*. United States Geological Service, 8 p. Available online at: <https://pubs.er.usgs.gov/publication/ds978> . Last accessed: 10th April 2017.

Zalachoris, G., E. M. Rathje & J. G. Paine (2017). Vs30 characterization of Texas, Oklahoma, and Kansas using the P-wave seismogram method. *Earthquake Spectra* **33**(3), 943-961.

A3.5.11.2 Web references

1600KUSH (2017):
<http://1600kush.com/wp/2017/04/11/cushing-lions-den-nearing-its-final-days-until-demolition/>.
Last accessed: 14th April 2017.

ABC News (2015):
<http://abcnews.go.com/US/oklahoma-admits-oil-gas-industry-responsible-dramatic-rise/story?id=30502267>. Last accessed: 9th February 2017.

Bankrate (2016):

<http://www.bankrate.com/finance/insurance/earthquake-insurance-sturdier-home-coverage-1.aspx>

Last accessed: 9th February 2017.

Bassal, P. (2016) *Oklahoma Dams Survive September 3rd Quake*. Available online at:

<http://www.eqclearinghouse.org/2016-09-03-oklahoma/2016/09/18/oklahoma-dams-lucky-to-survive-september-3rd-quake/>. Last accessed: 10th March 2017.

Center for Engineering Strong Motion Data (CESMD): <http://www.strongmotioncenter.org/>. Last accessed: 26th March 2017.

Central and Eastern United States Seismic Source Characterization for Nuclear Facilities (CEUS-SSC) Project: <http://www.ceus-ssc.com/>. Last accessed: 9th February 2017.

CNN (2011): <http://edition.cnn.com/2011/11/06/us/oklahoma-earthquake>.

Last accessed: 9th February 2017.

CNN (2016a):

<http://edition.cnn.com/2016/02/13/us/oklahoma-earthquake/>. Last accessed: 16th March 2017.

CNN (2016b):

<http://edition.cnn.com/2016/09/03/us/oklahoma-earthquake/>. Last accessed: 14th March 2017.

Court of Lincoln County, Oklahoma, State of Oklahoma (2015):

<http://op.bna.com.s3.amazonaws.com/txlr.nsf/r%3FOpen%3Dphas-9zzlug>.

Last accessed: 9th February 2017.

Cushing Public Schools Facebook page (2017): <https://www.facebook.com/CushingSchools/>. Last accessed: 10th March 2017.

EERI Oklahoma USA Earthquakes Clearinghouse (2016):

<http://www.eqclearinghouse.org/2016-09-03-oklahoma/>. Last accessed: 26th April 2017.

Photo gallery (last accessed on 13th April 2017): <http://www.eqclearinghouse.org/2016-09-03-oklahoma/maps-and-photos/photo-gallery/>.

EM-DAT – The Emergency Events Database (Université Catholique de Louvain, Brussels, Belgium; Cred. Prof. Dr. D. Guha-Sapir): <http://www.emdat.be/>. Last accessed: 4th December 2017.

Fox News (2011):

<http://www.foxnews.com/us/2011/11/06/52-magnitude-earthquake-strikes-oklahoma/>.

Last accessed: 9th February 2017.

Fox News (2016):

<http://www.foxnews.com/us/2016/02/13/magnitude-5-1-earthquake-recorded-near-fairview-oklahoma.html>. Last accessed: 16th March 2017.

Geotechnical Extreme Events Reconnaissance (GEER): <http://www.geerassociation.org/>.

Global Centroid Moment Tensor Project (GCMT): <http://www.globalcmt.org/>. Last accessed: 16th March 2017.

International Business Times (2015):

<http://www.ibtimes.com/oklahoma-earthquake-swarm-2015-sharp-turnaround-oklahoma-officials-confirm-link-1892086>. Last accessed: 9th February 2017.

International Seismological Centre (ISC): <http://www.isc.ac.uk/>.

ISO Mitigation (2015):

<http://www.isomitigation.com/index.php/bcegs/facts-and-figures-about-bcegs-grades-around-the-country>. Last accessed: 24th October 2015.

KFOR (2016a): <http://kfor.com/2016/11/02/magnitude-4-5-earthquake-shakes-oklahoma/>.

Last accessed: 16th March 2017.

KFOR (2016b):

<http://kfor.com/2016/12/06/residents-file-lawsuit-over-november-earthquake-in-cushing/>.

Last accessed 13th April 2017.

KFOR (2016c):

<http://kfor.com/2016/11/07/cushing-earthquake-downgraded-as-pictures-of-damage-flood-in/>.

Last accessed 14th April 2017.

KFOR (2017):

<http://kfor.com/2017/03/16/there-was-a-near-catastrophic-situation-concerns-rise-after-another-downtown-cushing-building-collapses/>. Last accessed 13th April 2017.

National Geophysical Data Center / World Data Service (NGDC/WDS): Significant Earthquake Database. National Geophysical Data Center, National Oceanic and Atmospheric Administration (NOAA, 2017). DOI:10.7289/V5TD9V7K. <https://www.ngdc.noaa.gov/hazard/earthqk.shtml>. Last accessed: 4th December 2017.

NBC News (2016): <http://www.nbcnews.com/news/us-news/state-emergency-declared-oklahoma-after-magnitude-5-6-earthquake-n642676>. Last accessed: 14th March 2017.

Netstate (2017): http://www.netstate.com/economy/ok_economy.htm.

Last accessed 12th April 2017.

News 9 (2011):

<http://www.news9.com/story/15972293/earthquake-rattles-communities-in-lincoln-county>.

Last accessed: 9th February 2017.

News OK (2011): <http://newsok.com/gallery/articleid/3621379/pictures/1555036>.

Last accessed: 9th February 2017.

News OK (2016a):

<http://newsok.com/gallery/articleid/5525184/1/pictures/4510808?embeddedLinkType=gallery>.

Last accessed: 14th March 2017.

News OK (2016b): <https://newsok.com/most-damage-from-5.8-magnitude-pawnee-earthquake-not-covered-by-insurance/article/5524515>. Last accessed: 14th March 2017.

News OK (2016c): <http://newsok.com/article/5525184>. Last accessed: 16th March 2017.

News OK (2016d):

<https://newsok.com/hit-by-earthquakes-pawnee-oklahoma-residents-sue-27-energy-companies/article/5527619>. Last accessed: 14th March 2017.

News OK (2016e): <http://newsok.com/article/5525795>. Last accessed: 11th April 2017.

News OK (2016f):

<https://newsok.com/cushing-oil-infrastructure-suffers-no-damage-in-earthquake/article/5525916>.

Last accessed: 14th April 2017.

News OK photo gallery (2016g):

<https://newsok.com/gallery/articleid/5526026/1/pictures/?embeddedLinkType=gallery>.

Last accessed: 14th April 2017.

News OK (2016h):

<https://newsok.com/cushing-cleaning-up-from-earthquake-damage/article/5525917>.

Last accessed: 14th April 2017.

News OK (2016i):

<https://newsok.com/official-40-to-50-buildings-damaged-in-oklahoma-quake/article/5525830>

Last accessed: 14th April 2017.

News On 6 (2016a):

<http://www.newson6.com/story/31215265/fairviewearthquakefeltacrossnortheastoklahoma>.

Last accessed: 16th March 2017.

News On 6 (2016b):

<http://www.newson6.com/story/33602048/pawnee-residents-worry-a-bigger-earthquake-is-yet-to-come>. Last accessed: 16th March 2017.

News On 6 (2016c):

<http://www.newson6.com/story/33643549/earthquake-centered-in-payne-county-rattles-oklahoma>.

Last accessed: 14th April 2017.

OColly (2017):

http://www.ocolly.com/news/earthquake-repairs-at-osu-total-more-than/article_dd012f00-1f0d-11e7-9d8e-efd88d4099ca.html. Last accessed: 18th April 2017.

Oklahoma Department of Emergency Management, Situation Update (OEM, 2011):

[https://www.ok.gov/OEM/Emergencies & Disasters/2011/Earthquake Event - November 6, 2011/20111106 Earthquake Situation Update .html](https://www.ok.gov/OEM/Emergencies%20&%20Disasters/2011/Earthquake%20Event%20-%20November%206,%202011/20111106%20Earthquake%20Situation%20Update.html).

Last accessed: 9th February 2017.

Oklahoma Geological Survey (OGS): <http://www.ou.edu/ogs/>

Oklahoma Geological Survey (2013):

http://www.ogs.ou.edu/earthquakes/OGS_PragueStatement201303.pdf.

Last accessed: 9th February 2017.

Oklahoma Geological Survey and United States Geological Service (OGS & USGS, 2014):

http://earthquake.usgs.gov/contactus/golden/newsrelease_05022014.php

Last accessed: 21st December 2015.

Oklahoma Uniform Building Code Commission (OUBCC): <https://www.ok.gov/oubcc/>

Reuters (2011):

<http://www.reuters.com/article/2011/11/07/us-quake-usa-oklahoma-idUSTRE7A50A020111107#wfgJM5G1CcKDqvtL.97>. Last accessed: 9th February 2017.

Reuters (2016) : <http://www.reuters.com/article/us-oklahoma-quake-idUSKCN11D2QR>.

Last accessed: 14th March 2017.

RT (2016): <https://www.rt.com/usa/365042-tulsa-earthquake-reports-oklahoma/>.

Last accessed: 16th March 2017.

Stillwater News Press (2017):

http://www.stwnewspress.com/news/local_news/cushing-loses-historic-american-legion-building/article_7df65ad4-6bba-50ea-b4ef-c24fca65e019.html. Last accessed: 13th April 2017.

The Christian Science Monitor (2011):

<http://www.csmonitor.com/USA/Latest-News-Wires/2011/1106/Rare-Oklahoma-earthquake-damages-14-buildings>. Last accessed: 9th February 2017.

The Earth Institute, Columbia University (2013): <http://www.earth.columbia.edu/articles/view/3072>. Last accessed: 9th February 2017.

The Weather Company (2016):

<https://weather.com/safety/earthquake/news/tulsa-oklahoma-fairview-earthquake-aftershock-usgs>. Last accessed: 16th March 2017.

Tulsa World (2017):

http://www.tulsaworld.com/earthquakes/earthquake-insurance-in-claims-approved-in-oklahoma-since/article_de588725-1475-592c-9025-bdcfb9b8bcd.html. Last accessed: 18th April 2017.

USBoundary (2017): <http://www.usboundary.com/>. Last accessed: 23rd March 2017.

United States Bureau of Economic Analysis (2012):

https://www.bea.gov/newsreleases/regional/gdp_state/2012/pdf/gsp0612.pdf. Last accessed: 9th February 2017.

United States Bureau of Economic Analysis (2017):

https://faq.bea.gov/scb/pdf/2017/01%20January/0117_gdp_by_state.pdf. Last accessed: 12th April 2017.

United States Energy Information Administration (EIA, 2015): <http://www.eia.gov/state/rankings/>. Last accessed: 21st December 2015.

United States Geological Survey (USGS): <http://earthquake.usgs.gov/>.

Outdated website for the 5-Nov-2011 Prague event (last accessed 21st December 2015):

<http://earthquake.usgs.gov/earthquakes/eqinthenews/2011/usb0006klz/#details>.

Renovated website for the 5-Nov-2011 Prague event (last accessed 26th April 2017):

<http://earthquake.usgs.gov/earthquakes/eventpage/usp000jadn#executive>.

Website for the 13-Feb-2016 Fairview event (last accessed 26th April 2017):

<http://earthquake.usgs.gov/earthquakes/eventpage/us20004zy8#executive>.

Website for the 3-Sep-2016 Pawnee event (last accessed 26th April 2017):

<http://earthquake.usgs.gov/earthquakes/eventpage/us10006jxs#executive>.

Website for the 2-Nov-2016 Pawnee event (last accessed 26th April 2017):

<http://earthquake.usgs.gov/earthquakes/eventpage/us100073m6#executive>.

Website for the 7-Nov-2016 Cushing event (last accessed 26th April 2017):

<http://earthquake.usgs.gov/earthquakes/eventpage/us100075y8#executive>.

United States Geological Survey (USGS) Oklahoma Area Seismicity Map (2016):

https://earthquake.usgs.gov/earthquakes/byregion/oklahoma/OKquakes1973_062642016v3.pdf.

Last accessed: 16th March 2017.

United States Geological Survey (USGS) Oklahoma Earthquakes Magnitude 3.0 and Greater (2016):

<https://earthquake.usgs.gov/earthquakes/byregion/oklahoma/OKeq-graph.qif>.

Last accessed: 16th March 2017.

United States Geological Survey (USGS) PAGER (2015):

<http://earthquake.usgs.gov/earthquakes/pager/events/us/b0006klz/index.html>.

Last accessed: 21st December 2015.

United States Geological Survey (USGS) Press Release (2016):
<https://www.usgs.gov/news/magnitudes-oklahoma-earthquakes-shift-upward>.
Last accessed: 17th March 2017.

World Economic Outlook Database 2016 (2016):
<https://www.imf.org/external/pubs/ft/weo/2016/02/weodata/download.aspx>.
Last accessed: 12th April 2017.

IV. APPENDIX IV: Case histories of tectonic earthquakes

A4.1 March 1957 M4.8 Port Hueneme (California) Earthquake, USA

This earthquake occurred on 18th March 1957, at 18.56 UTC (10.56 local time), in Port Hueneme, Ventura County, California, and affected mostly Port Hueneme, Oxnard and San Buenaventura (usually referred to as Ventura), all within the same county. It was the first earthquake for which a strong motion record consisting of one pulse was recorded. Details on the damage caused are scarce, being described as relatively large for the magnitude of the event. No casualties were reported.

A4.1.1 Tectonic and seismic setting

A4.1.1.1 Tectonic setting

The tectonic setting of California is dominated by the San Andreas fault system, whose right-lateral strike-slip behaviour is responsible for most of the relative motion that occurs between the Pacific and the North American plates (Wallace, 1990; Hauksson, 1991). However, the predominant fault structures in the area around Port Hueneme are the Transverse Ranges, which in their western section delimit the Ventura basin, within which Port Hueneme and the whole area affected by this earthquake are located. The Transverse Ranges owe their name to their predominantly E-W orientation, transverse to the prevailing NW-SE San Andreas system (USGS, 2006). According to the Ventura Basin Study Group (VBSG) of the Institute for Crustal Studies (ICS) of the University of California at Santa Barbara, the Ventura basin is one of the most active tectonic regions of the world and is characterised by the presence of blind active faults that do not outcrop and structures that have undergone a complex history of tectonic deformation. Its location is depicted in Figure A4.1.1.

Figure A4.1.2 shows the fault-zone polygons used for the determination of hazard levels within the Uniform California Earthquake Rupture Forecast v3.0 (UCERF3; Field *et al.*, 2013) and the fault traces according to the Quaternary Fault and Fold Database of the United States (United States Geological Survey, USGS), around the epicentral area.

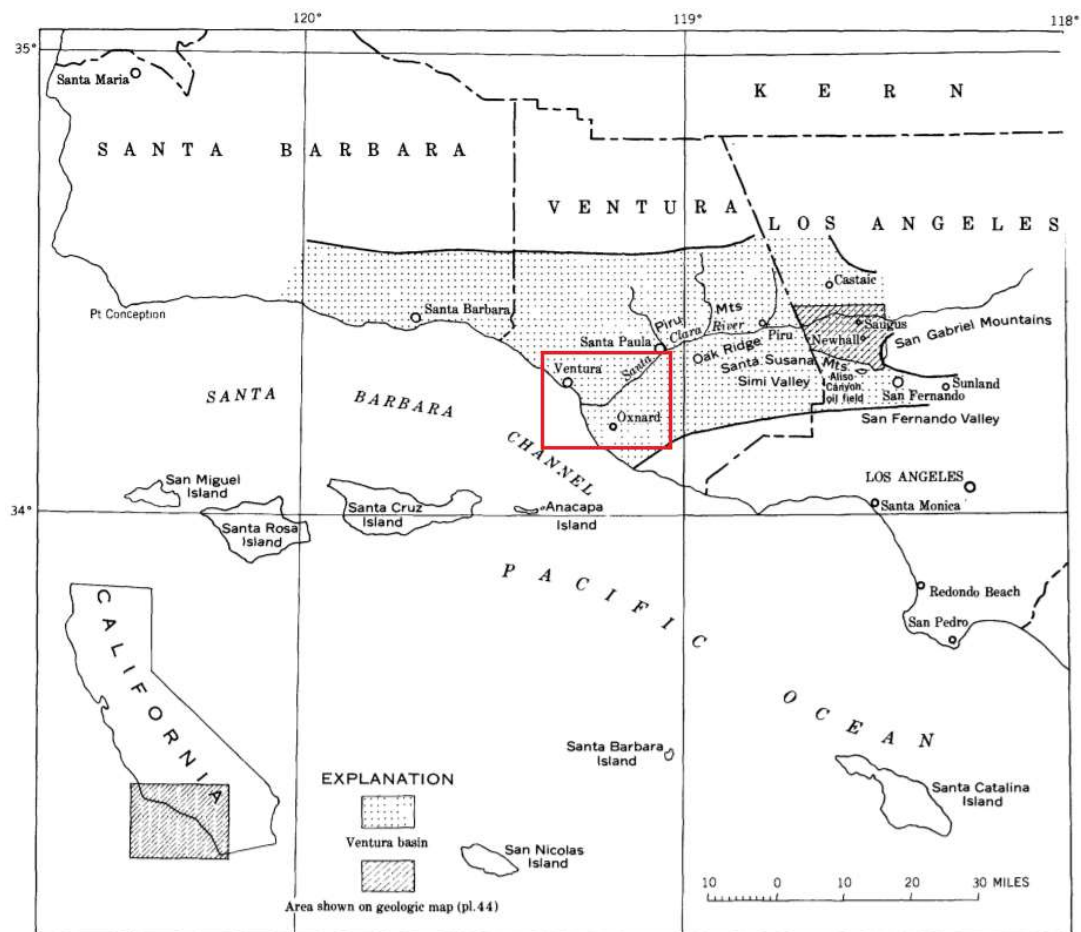


Figure A4.1.1. Location of the Ventura basin within Southern California. The red rectangle encloses the area affected by the 1957 earthquake. From Winterer & Durham (1962).

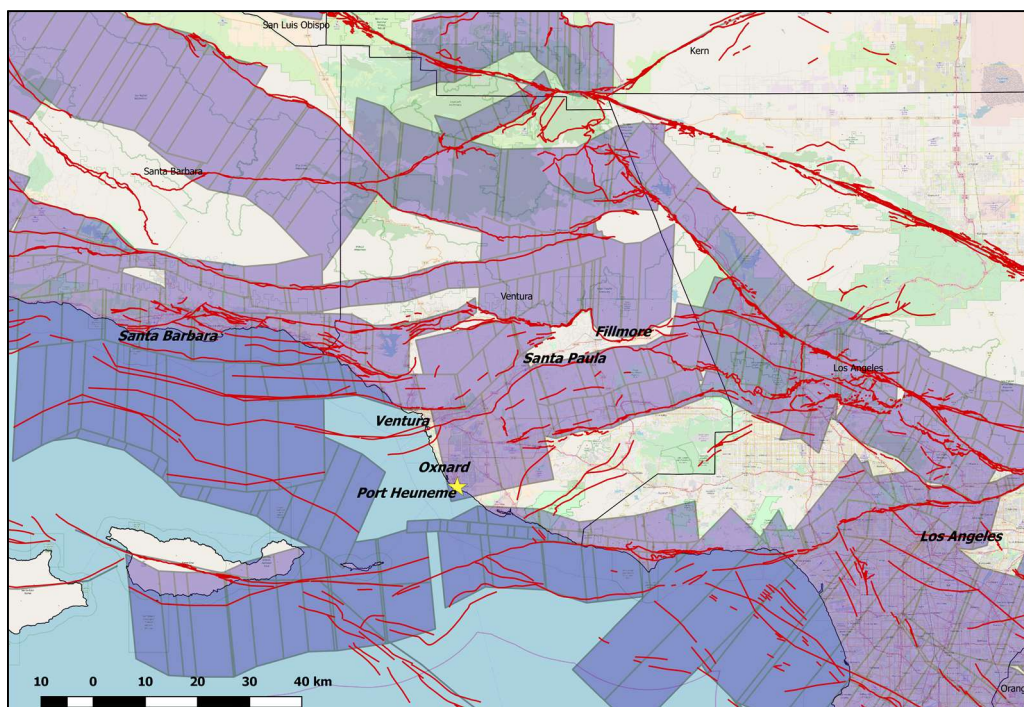


Figure A4.1.2. Fault-zone polygons (purple) from the Uniform California Earthquake Rupture Forecast v3.0 (UCERF3; Field *et al.*, 2013) and traces (red lines) according to the Quaternary Fault and Fold Database of the United States (data from USGS). Yellow star denotes 1957 epicentre according to the USGS.

A4.1.1.2 Regional and local seismicity

According to the USGS, southern California has the highest level of seismic risk of the United States, with around 10,000 earthquakes occurring per year. Of these, several hundred have magnitudes greater than 3.0, while between 15 and 20 have magnitudes greater than 4.0 (USGS). However, the damage experienced by the cities located in Ventura county, such as Ventura, Oxnard and Camarillo, has generally been minor, as the more damaging earthquakes of 1812 and 1857 occurred at a time in which the population level was still relatively low (Weber & Kiessling, 1978). Nevertheless, both these earthquakes caused severe damage to the San Buenaventura (Ventura) mission (Weber & Kiessling, 1978).

Figure A4.1.3 depicts a series of significant earthquakes to have occurred in the area around Port Hueneme, as selected by the Southern California Earthquake Data Center (SCEDC, 2012) for their map of southern California. As can be observed, the two closest to the area affected by the 1957 Port Hueneme earthquake are the 1973 Point Mugu and the 1941 Santa Barbara earthquakes. The former has been assigned a moment magnitude of 5.3 with a 0.545-unit error by the California Integrated Seismic Network, though much larger values are reported in other magnitude scales (M_L 6.0, m_b 5.6, M_s 5.8; ISC Bulletin; Stierman & Ellsworth, 1976). It caused at least five injuries and damage mostly to windows, ceilings, plaster, chimneys and shelved goods, though there were reports of structural damage and broken pipes, as well as of loss of electricity supply (SCEDC, 2012). The 1941 Santa Barbara earthquake is reported to have had a local magnitude M_L of 5.5 and have reached a Modified Mercalli Intensity of VIII, causing water main pipes to break, the cracking and falling of walls and the breaking of the tops of streetlights (SCEDC, 2012).

According to Weber & Kiessling (1978), earthquakes that occurred outside of Ventura county but caused damage in it were those of 1925 (Santa Barbara, **M6.8**), 1927 (Point Arguello, M_L 7.1), 1933 (Long Beach, **M6.4**), 1941 (Santa Barbara, M_L 5.5), 1952 (Arvin-Tehachapi, Kern County, **M7.5**), and 1971 (San Fernando, **M6.6**), while damaging events that occurred within the county itself were those of 1950 (north of Ojai, magnitude 4.7), 1957 (Port Hueneme, M_L 4.8), 1963 (Camarillo, magnitude 3.7), and 1973 (Point Mugu, **M5.3**, M_L 6.0), the latter being the strongest of the four. In Oxnard, the effects of the **M6.4** 1933 Long Beach and the M_L 5.5 1941 Santa Barbara earthquake appear to have been milder than those of the **M6.8** 1925 Santa Barbara one.

It is of interest to note that while the 1957 Port Hueneme earthquake is reported as damaging by Weber & Kiessling (1978), it is not shown in the selection of significant earthquakes in southern California of the Southern California Earthquake Data Center (SCEDC, 2012).

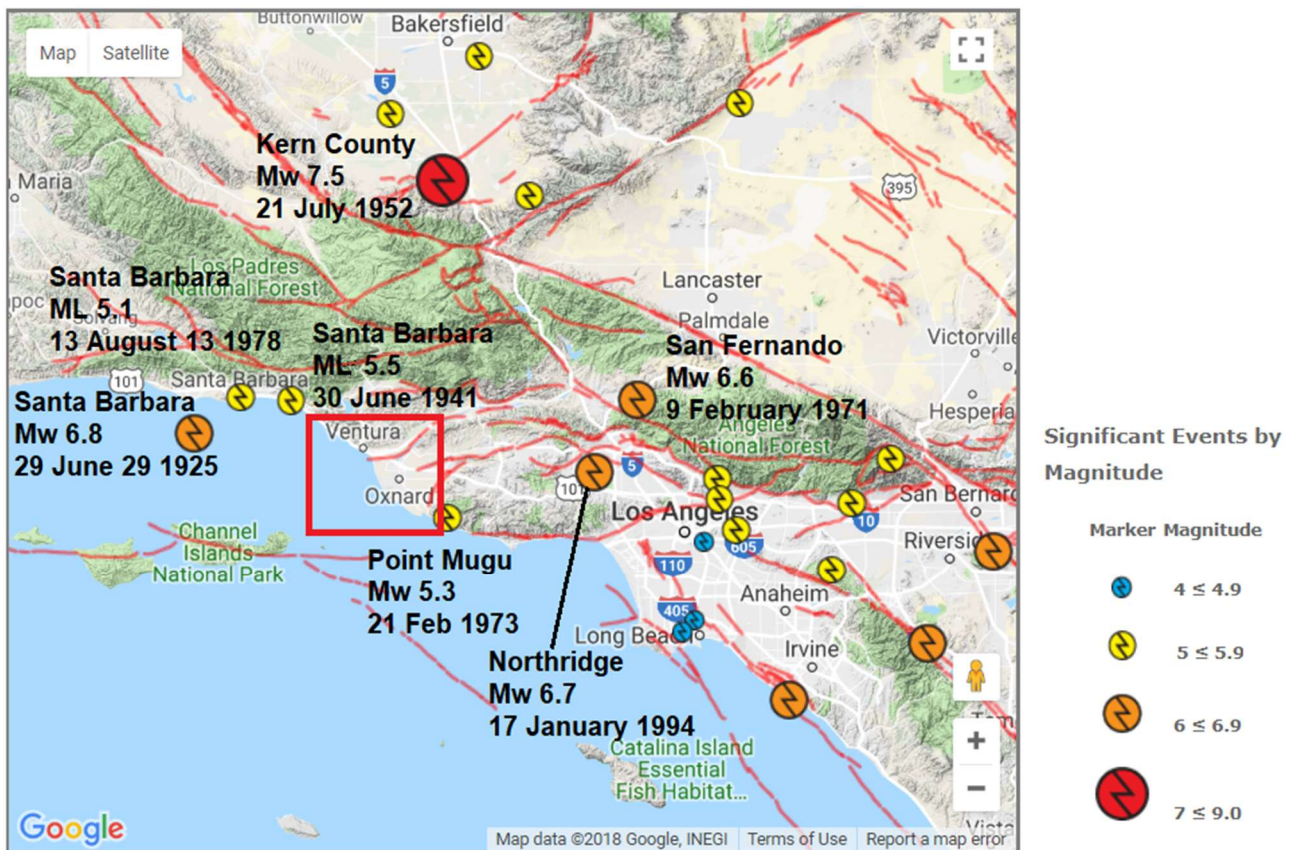


Figure A4.1.3. Significant earthquakes and faults in the area around Port Hueneme. The red rectangle encloses the area affected by the 1957 earthquake. Modified from Southern California Earthquake Data Center (SCEDC, 2012).

A4.1.1.3 Seismic hazard

Figure A4.1.4 shows the 2014 National Hazard Map of the United States, elaborated by the USGS (Petersen *et al.*, 2014). According to this map, the area around Port Hueneme presents PGA values on rock with a 10% probability of exceedance in 50 years between 0.2 and 0.4 g. The Unified Hazard Tool of the USGS (see web references) allows to read a more specific value of 0.335 g for Port Hueneme, and spectral acceleration values of 0.757 and 0.225 g at 0.2 and 1.0 seconds, respectively, for the same probability.

Being located along the west coast in California, the area affected by this earthquake is clearly one of high seismic hazard, though it is not the absolute highest of the state. However, old seismic hazard maps of the United States from 1933, 1948 and 1949 assigned this area and the most seismically active regions of California the same hazard level, designated as zone 3 (Beavers, 2002). It is thus clear that the perception of seismic hazard has been that of a seismically active area for at least 85 years.

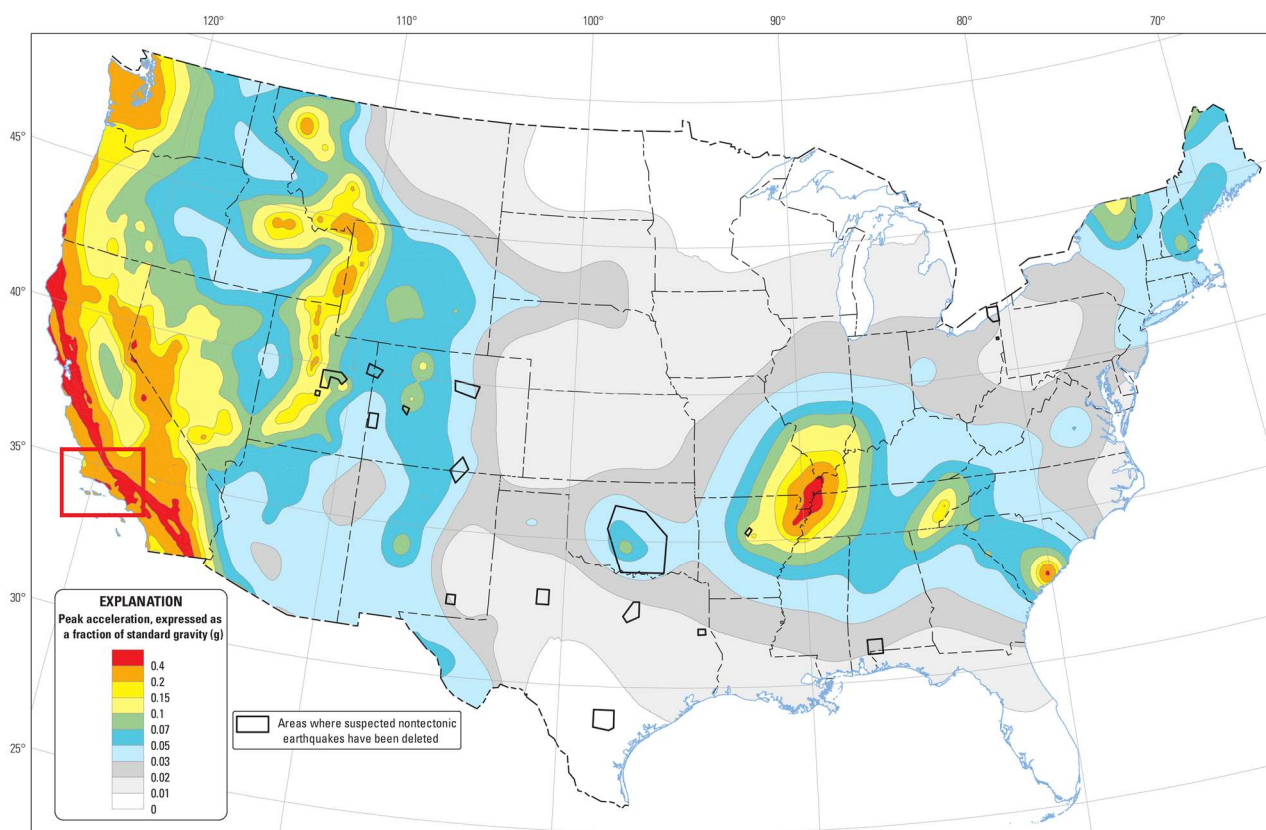


Figure A4.1.4. 2014 hazard map of the United States, elaborated by the USGS (Petersen *et al.*, 2014). Values correspond to peak ground acceleration (g) on rock with a 10% probability of exceedance in 50 years. Red rectangle encloses the area around Port Hueneme, California.

A4.1.2 Earthquake source characteristics

A4.1.2.1 Location, depth and time

The main shock occurred on 18th March 1957, at 18.56 UTC (10.56 local time). Table A4.1.1 and Figure A4.1.5 show the hypocentral locations according to three sources. McGuire & Barnhard (1977) report that the epicentral distance to Port Hueneme was 6 km, but do not specify the epicentral coordinates themselves. Figure A4.1.5 shows a 6 km-radius circle around Port Hueneme, to represent the potential location of the epicentre according to this source.

Table A4.1.1. Epicentral coordinates and hypocentral depths from different sources.

Agency / Publication		Latitude	Longitude	Depth (km)
NEIC	National Earthquake Information Center, USGS	34.1460 °N	119.2030 °W	6.00
VDC	Strong-Motion Virtual Data Center	34.1180 °N	119.0520 °W	13.80
Kanamori & Jennings (1978)		34.1183 °N	119.2183 °W	-

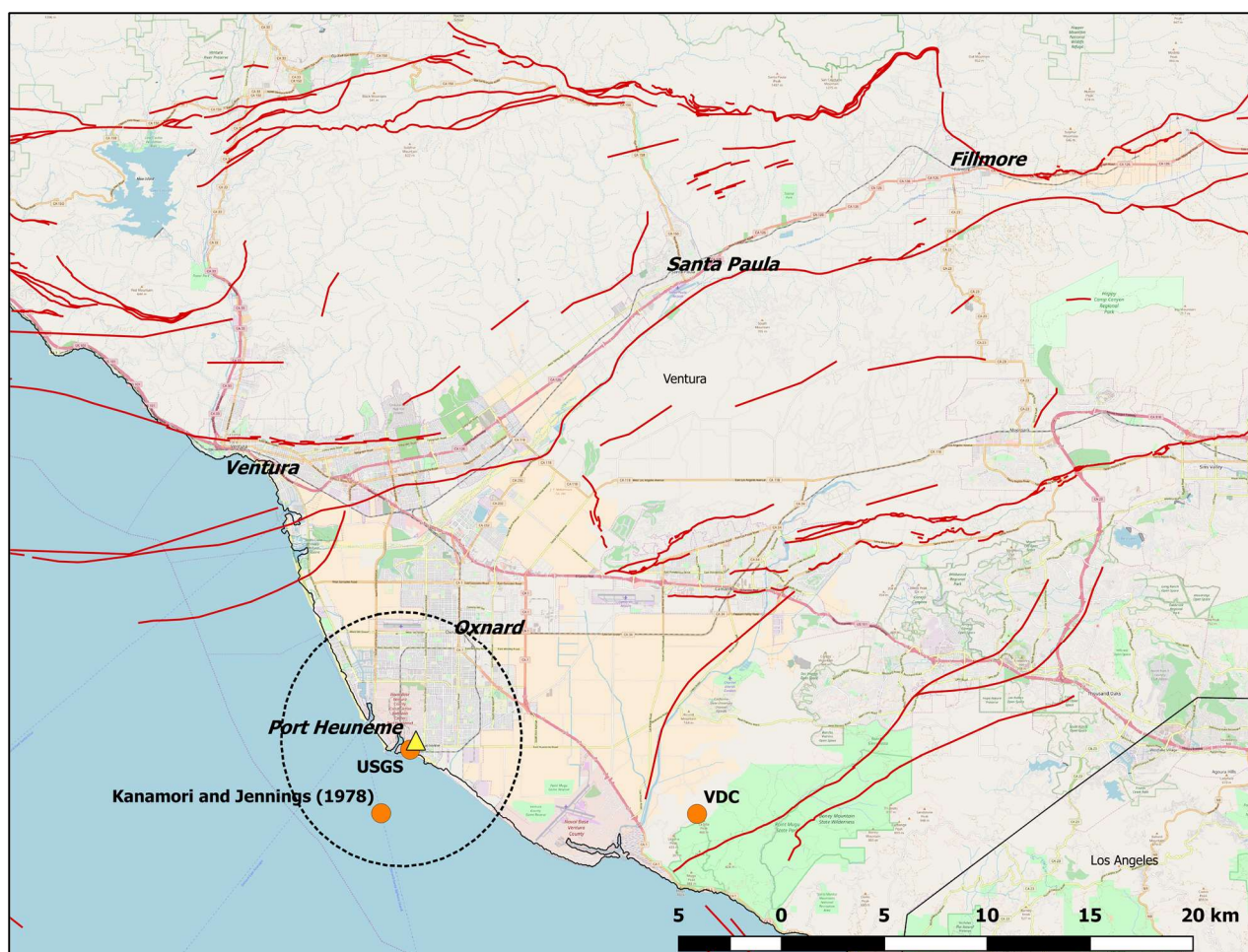


Figure A4.1.5. Epicentral coordinates as reported by different sources (orange circles). Yellow triangle depicts the location of CSMIP station 25281. Dashed circle indicates a 6-km distance from Port Hueneme. Red lines indicate fault traces according to the Quaternary Fault and Fold Database of the United States (data from USGS).

A4.1.2.2 Magnitude

The local magnitude M_L of this earthquake was around 4.7-4.8, as reported in Table A4.1.2. The value assigned to the California Institute of Technology is that reported in the ISC Bulletin (International Seismological Centre). Assuming a 1:1 relation between moment magnitude and local magnitude (e.g., Dost *et al.*, 2018), a value of **M4.8** is adopted herein to characterise this earthquake.

Kanamori & Jennings (1978) obtained a much larger value in the range 5.5-5.7 using a novel technique for the estimation of M_L . However, the authors acknowledge that said technique can yield different levels of accuracy, depending on additional factors.

Table A4.1.2. Estimations of moment magnitude (M), body-wave magnitude (m_b) and surface-wave magnitude (M_s).

Agency		M	m_b	M_L	M_s
NEIC	National Earthquake Information Center, USGS	-	-	4.8	-
PAS	California Institute of Technology	-	-	4.7	-

A4.1.2.3 Style-of-faulting

From the plot of the particle motion at CSMIP station 25281 (Figure A4.1.9), Housner & Hudson (1958) infer that the earthquake may have been generated along a fault oriented along the NW-SE direction (N37.5W, more precisely) and believe it can be assumed to have had a strike-slip mechanism with right-lateral movement, as the typical large Californian earthquakes generated along the San Andreas fault. However, it is noted that no such fault trace appears to exist close to the epicentral estimations given in Table A4.1.1 according to the Quaternary Fault and Fold Database of the United States (USGS) or the UCERF3 model, as shown in Figure A4.1.2 and Figure A4.1.5. The faults closest to the estimated epicentral coordinates are mostly WSW-ENE trending, to the north of Oxnard, and SW-NE trending, around the epicentre reported by the VDC.

A4.1.2.4 Stress drop

No information on the stress drop associated with this earthquake has been found.

A4.1.2.5 Foreshocks and aftershocks

According to the compendium of newspaper articles gathered by ICS (2006), an aftershock occurred around two minutes after the main shock, and another aftershock occurred on 21st March 1957 at 6.15 am (local time) but caused no damage and was so mild that was “barely recorded”, though reportedly felt. The magnitude of the latter appears to have been 2.2 on the Richter scale. The USGS catalogue does not contain this earthquake but does contain a M_L 3.2 that occurred on 22nd March 1957 at 9.50 am (UTC), with epicentre around 16 km south-east of the main shock. No further information has been found for any of these events or any other potential foreshocks/aftershocks.

A4.1.2.6 Nature of earthquake

No reference to this earthquake having an origin other than tectonic has been found. However, it is worth mentioning that Hough & Page (2016) conclude the possibility of significant earthquakes that occurred during the early 20th century in the greater Los Angeles area having been induced by activities related to oil and gas production cannot be discarded. Their study area did not cover that affected by the 1957 Port Hueneme earthquake, though, and the Human-Induced Earthquake Database does not have any indications of induced seismicity in Ventura county (Foulger *et al.*, 2016; Wilson *et al.*, 2017; Induced Earthquakes, 2017).

A4.1.3 Geology and ground conditions in the affected area

A4.1.3.1 Regional geology and topography

The cities affected by this earthquake lie within a small valley by the Californian western coast, as shown in Figure A4.1.6 (left), technically known as the Ventura basin, within the

Transverse Ranges geologic province (USGS, 2016). As a consequence, the topography is flat, particularly in Oxnard and Port Hueneme, but surrounded by mountain ranges such as the Topatopa, Santa Susana and the Santa Monica mountains. The Ventura basin is known for its vast oil field, which has been exploited since 1885 and contains Cretaceous- to Pleistocene-age, mostly marine, sediments (Davis *et al.*, 2015; California Resources Corporation, 2018).

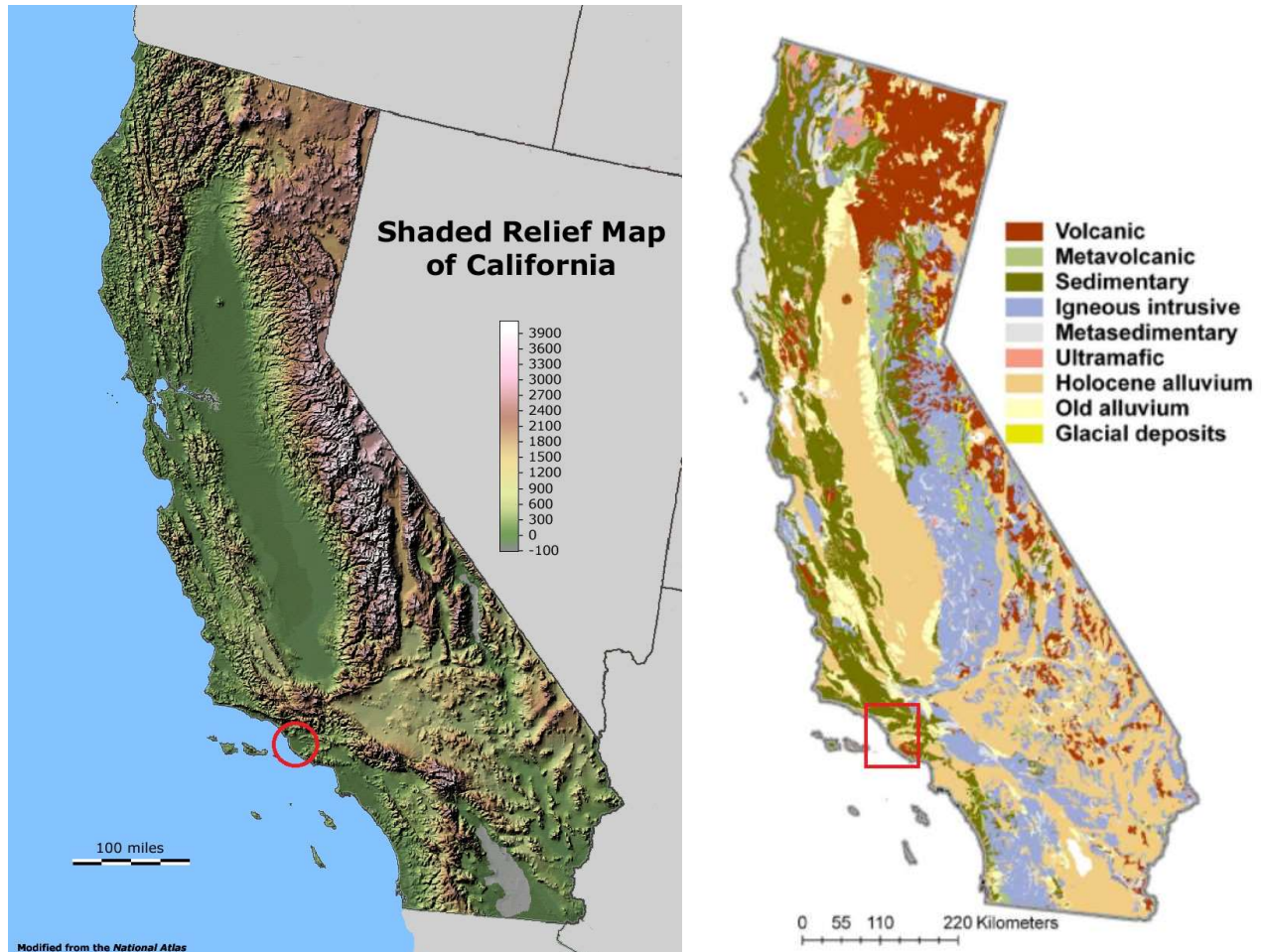


Figure A4.1.6. Topography (left; from GeologyCafe, 2017) and lithology of soil parent materials (right; from UCDavis) in California. Red circle and rectangle approximately enclose epicentral area.

A4.1.3.2 Site conditions in the affected area

According to the California Soil Resource Lab of the University of California, Davis (UCDavis), the epicentral area is dominated by sedimentary and Holocene alluvial soils, as shown in Figure A4.1.6 (right). Most of the area affected by the 1957 earthquake has been classified as having the weakest category of soils by Wills *et al.* (2011). According to the same authors, susceptibility to deep-seated landslides is null within the Ventura basin itself, but significantly high for several of the mountain ranges that surround it.

Figure A4.1.7 shows a series of V_{s30} values available for sites around the epicentral area, compiled by the USGS (Yong *et al.*, 2016). As can be observed, the cities of Oxnard, Ventura (officially, San Buenaventura) and Port Hueneme are dominated by soft soils with V_{s30}

values in the range 200-300 m/s. This is in agreement with the kind of soils shown in Figure A4.1.6 (right).

According to a document on earthquake risk by the City of Oxnard, the thick alluvial deposits that underlay said city and the high groundwater level lead to a high liquefaction potential in the area (City of Oxnard, 2016).

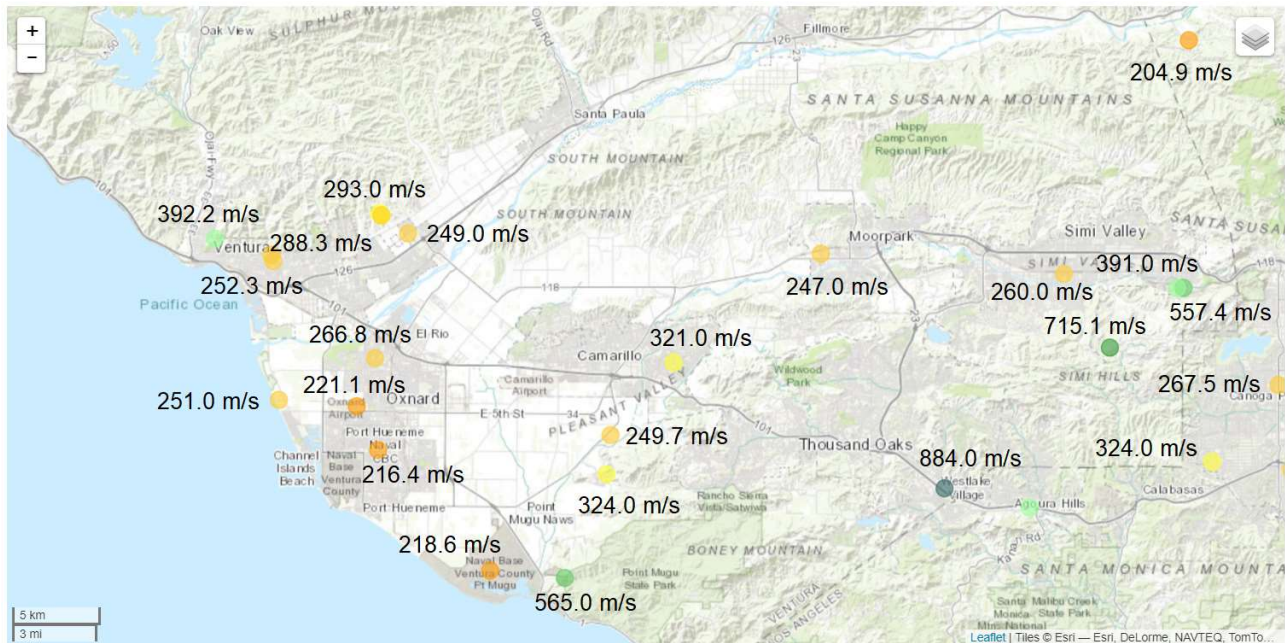


Figure A4.1.7. V_{s30} values around the epicentral area. Modified from Yong *et al.* (2016).

A4.1.4 Ground motions

A4.1.4.1 Intensity observations

The earthquake has been described in newspaper articles as of medium intensity (ICS, 2006). McGuire & Barnhard (1977) report a maximum Modified Mercalli Intensity (MMI) value of VI, and a 6-km epicentral distance to Port Hueneme, though they do not specify the epicentral coordinates. In terms of damage, a MMI of VI is described as causing a few instances of fallen plaster and slight damage (USGS).

The most affected cities were Port Hueneme, Oxnard and Ventura (officially, San Buenaventura). The shaking was also felt at Santa Barbara, Fillmore and Santa Paula, 55, 38 and 25 km away (respectively) from the epicentral coordinates reported by the USGS (see Figure A4.1.5), though no damage occurred at these sites (ICS, 2006). No further details regarding the spatial distribution of intensities have been found.

A4.1.4.2 Ground motion recordings

Anderson *et al.* (1999) report a maximum recorded peak ground acceleration of 0.08 g. Housner & Hudson (1958) mention 0.18 g instead, a value much closer to the 0.167 g reported by the Strong-Motion Virtual Data Center (VDC). It seems likely that the 0.08 g of Anderson *et al.* (1999) is actually a typo. According to the Strong-Motion Virtual Data Center, the hypocentral distance to the station to which this record belongs is 19.7 km (14 km epicentral distance), though a much shorter hypocentral distance of 6.0 km (0.5 km epicentral distance) is obtained when calculating the distance to the hypocentral coordinates reported by the USGS (Table A4.1.1; Figure A4.1.5). The station is located over more than 300 m-thick alluvium, at the ground level of a 1-storey warehouse.

However, the relevance of this earthquake is not due to the levels of ground acceleration that it generated but on the kind of motion. This moderate-magnitude earthquake was the first recorded strong motion for which a strong velocity pulse was observed, as shown in Figure A4.1.8 and Figure A4.1.9, and raised the question of whether engineering practices should be revised for buildings to be able to sustain single-pulse shocks from even larger-magnitude events (Housner & Hudson, 1958).

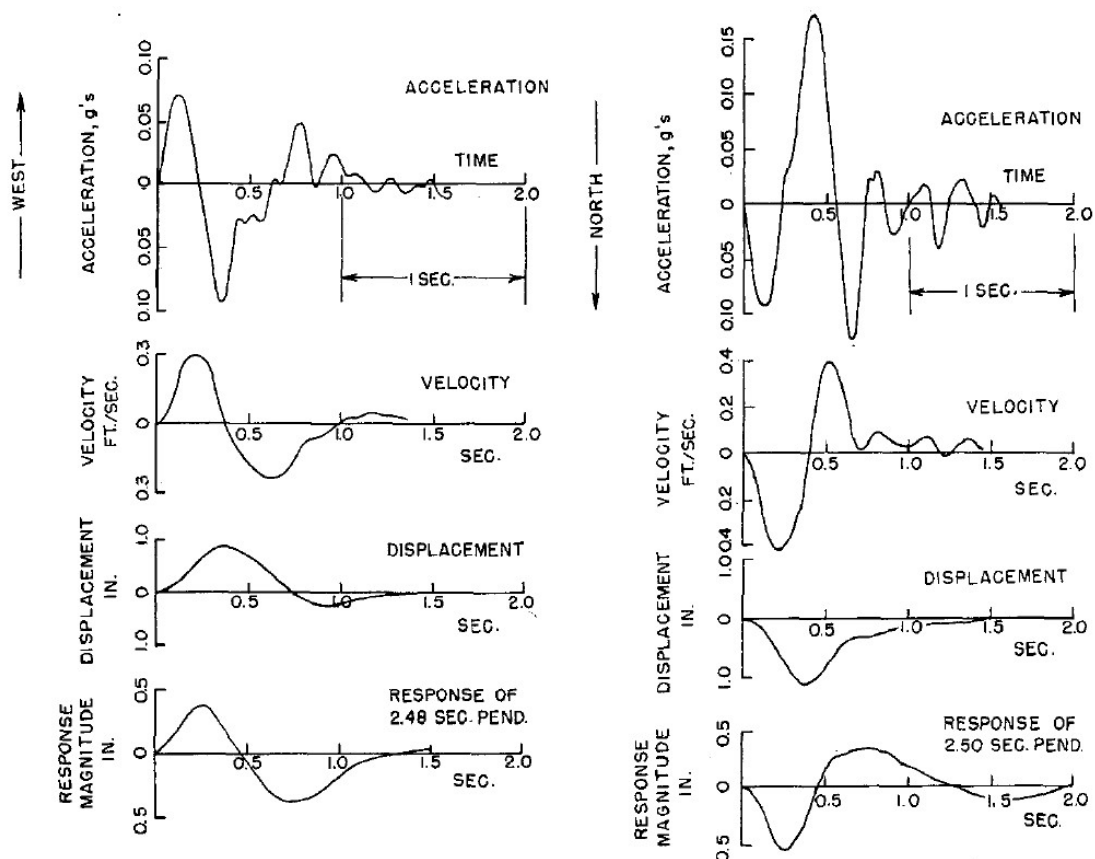


Figure A4.1.8. East-west (left) and north-south (right) components of ground motion, as recorded at CSMIP station 25281 (see location in Figure A4.1.5). From Housner & Hudson (1958).

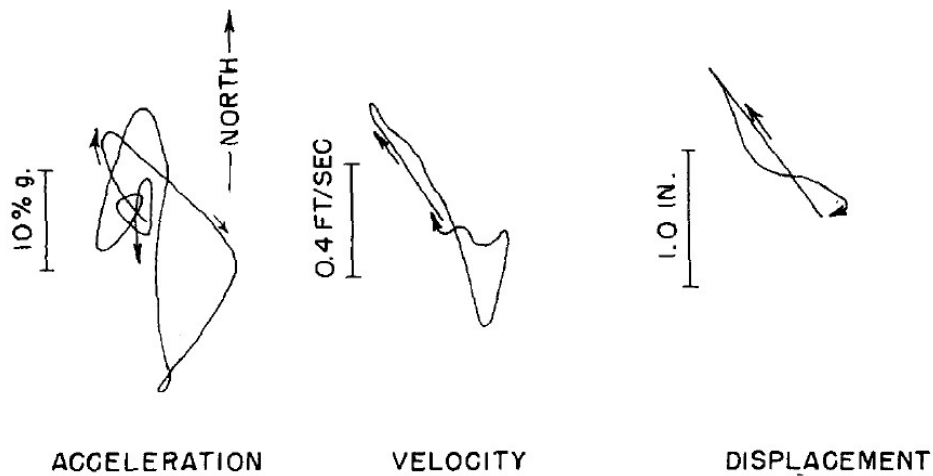


Figure A4.1.9. Particle motion at CSMIP station 25281 (see location in Figure A4.1.5). From Housner & Hudson (1958).

Being this a relatively old event, digital versions of the accelerograms recorded at CSMIP station 25281 are not of great quality. Two alternative versions were available to us. Those available from the Strong-Motion Virtual Data Center (VDC) are lacking the first tens of a second. An alternative version, digitised by Dr. S.K. Sarma from Imperial College and available to us courtesy of Dr. Julian J. Bommer, manages to reconstruct the missing accelerations, but is much shorter in total duration (less than 5.4 seconds against around 68 seconds for those from VDC). As a visual inspection of the two versions suggests that they are in overall agreement where they overlap, a new version was hereby generated by assembling together the first part of the reconstructed record and the remaining of the record downloaded from the Strong-Motion Virtual Data Center (VDC), with the purpose of recovering all the motion. The assemblage was carried out identifying the time shift that caused the smallest difference between the two versions, measured as the sum of the absolute differences at all time-steps within a range of 4.5 seconds in which the two signals overlapped. The reconstructed version was then used from time zero until the first occurrence of an almost null difference between the two versions, and the VDC version was used from that point onwards. Figure A4.1.10 shows the two versions (black and red lines), that from VDC with its corresponding time-shift, as well as the resulting version used in what follows (green lines), to which a cubic baseline correction was applied using SeismoSignal (Seismosoft, 2016) after inspection of the displacement time-histories indicated the need for it.

Figure A4.1.11, which depicts the resulting pseudo-acceleration response spectra, shows a pronounced peak in the spectrum for the north-south component of motion at around 0.4-0.5 seconds. A less prominent peak can be observed for the east-west component at around 0.3-0.4 seconds as well. Interestingly, this period range coincides with what is predicted by the model of Somerville (2003) to be the period at which the velocity pulse causes its largest impact for an earthquake of **M**4.8 and a site lying on soft soil, which is 0.44 seconds.

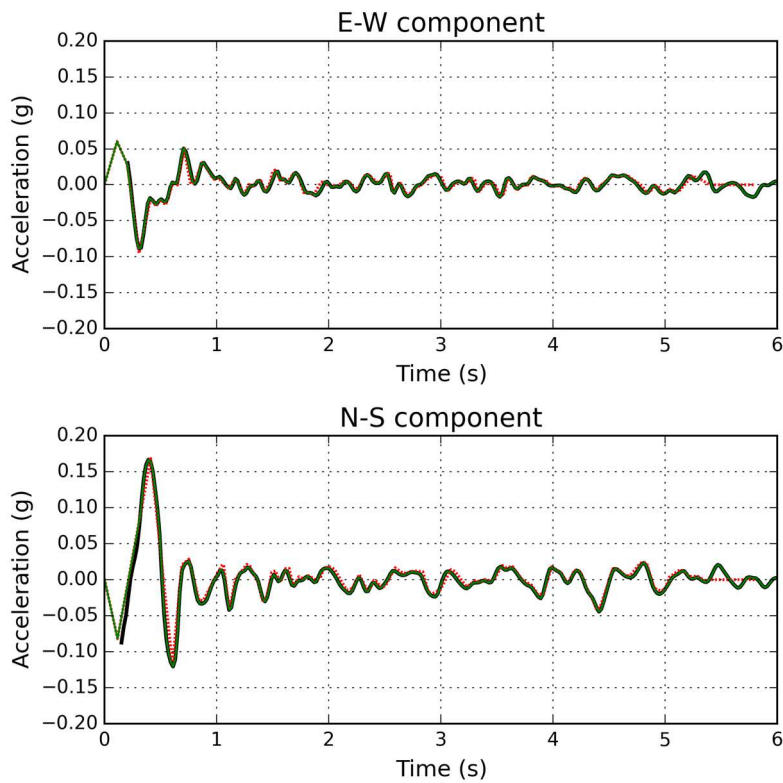


Figure A4.1.10. East-west (top) and north-south (bottom) components of ground motion, as recorded at CSMIP station 25281: version downloaded from the VDC (black), version digitised by Dr. S. K. Sarma (red), and version used herein stemming from a combination of the two (green).

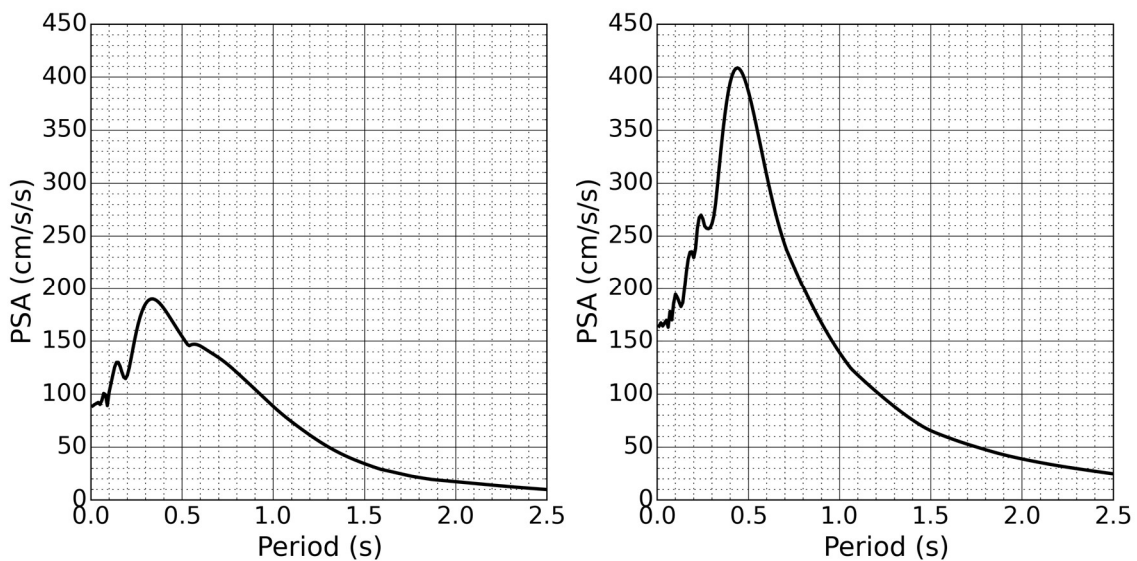


Figure A4.1.11. East-west (left) and north-south (right) pseudo-acceleration response spectra (cm/s^2) of the ground motion recorded at CSMIP station 25281.

Prompted by the statement of Housner & Hudson (1958) regarding the pulse-like characteristics of these earthquake, velocity histories of the available ground motions (obtained from their respective acceleration histories) were rotated at all non-redundant angles in order to visualise the behaviour of the pulse. The corresponding plots at three selected orientations are shown in Figure A4.1.12. If the N37.5W orientation of the causative fault inferred by Housner & Hudson (1958) were true, velocity pulses caused by directivity effects would be expected approximately at N52.5E (=N127.5W, the fault-parallel direction)

(Somerville *et al.*, 1997). However, pulses can be clearly observed in the reconstructed version of the record at directions between N100W and N30E, the one with the largest amplitude occurring at N20W, which would be forming an angle of 17.5° with the fault-normal direction. This can imply either that the orientation of the fault may be other than inferred by Housner & Hudson (1958), or that the scatter in the angle between the direction at which velocity pulses tend to be observed with respect to the fault causing the motion is large, as pointed out by Howard *et al.* (2005) and Shahi & Baker (2011). Moreover, a minimum angle of 22.5° exists between all orientations at which pulse-like velocity histories are observed and the fault-normal direction, which is within the margins observed by Howard *et al.* (2005).

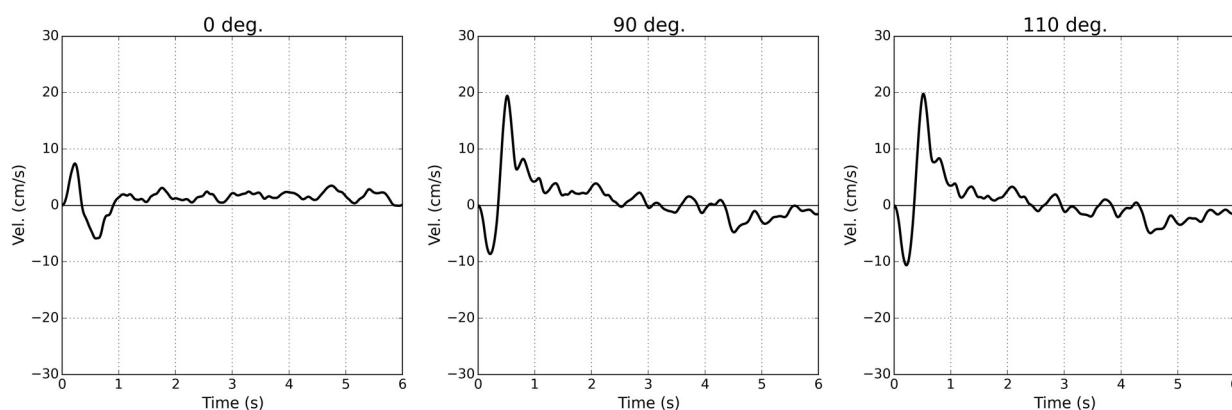


Figure A4.1.12. Velocity time-histories corresponding to CSMIP station 25281 integrated from acceleration histories in directions E-W (left), N-S (centre) and at 110° counter-clockwise from the E-W direction (N20W, right).

Being associated with the amplification of ground motions, it is interesting to observe the variation of the PGA and spectral demands at all possible orientations, as done in Figure A4.1.13, which shows the ratio between the demands at each angle and the maximum rotational demand, RotD100, for the reconstructed record. With the exception of $T=0.3$ seconds, the directions of maximum response (*i.e.*, directions at which the maximum rotational demand is observed) vary between N25W and N12E and are comprised within the range at which velocity pulses are observed. The plots corresponding to $T=0.4$ and $T=0.5$ seconds show substantially polarised motion. The plot corresponding to $T=0.3$ seconds is interesting because its direction of maximum response occurs at N32E, quite different from that of the other oscillator periods, but the spectral accelerations observed at N41W, 73° away from N32E, are almost as large (0.292 g vs. 0.283 g). It is also interesting to note that N32E is closer to the presumed fault-normal direction than the directions of maximum response at all other periods shown in Figure A4.1.13. In an attempt to explain this behaviour, spectrograms (*i.e.*, plots that show the variation in time of the frequency content of a waveform) were generated for this record at its as-recorded and fault-normal and fault-parallel directions, as well as at the direction of maximum response at $T=0.3$ s (N32E). However, no peculiarities came out of this exercise, except for the observation that the studied spectrograms are very similar, all but that at the N-S component, which seems to be rich in frequencies between 0.5 and 5.0 Hz (0.2-2.0 seconds). As shown in Figure A4.1.14, the E-W component appears to contain less of some of those frequencies in the same band, particularly at the beginning of the motion during which the peak demands occur.

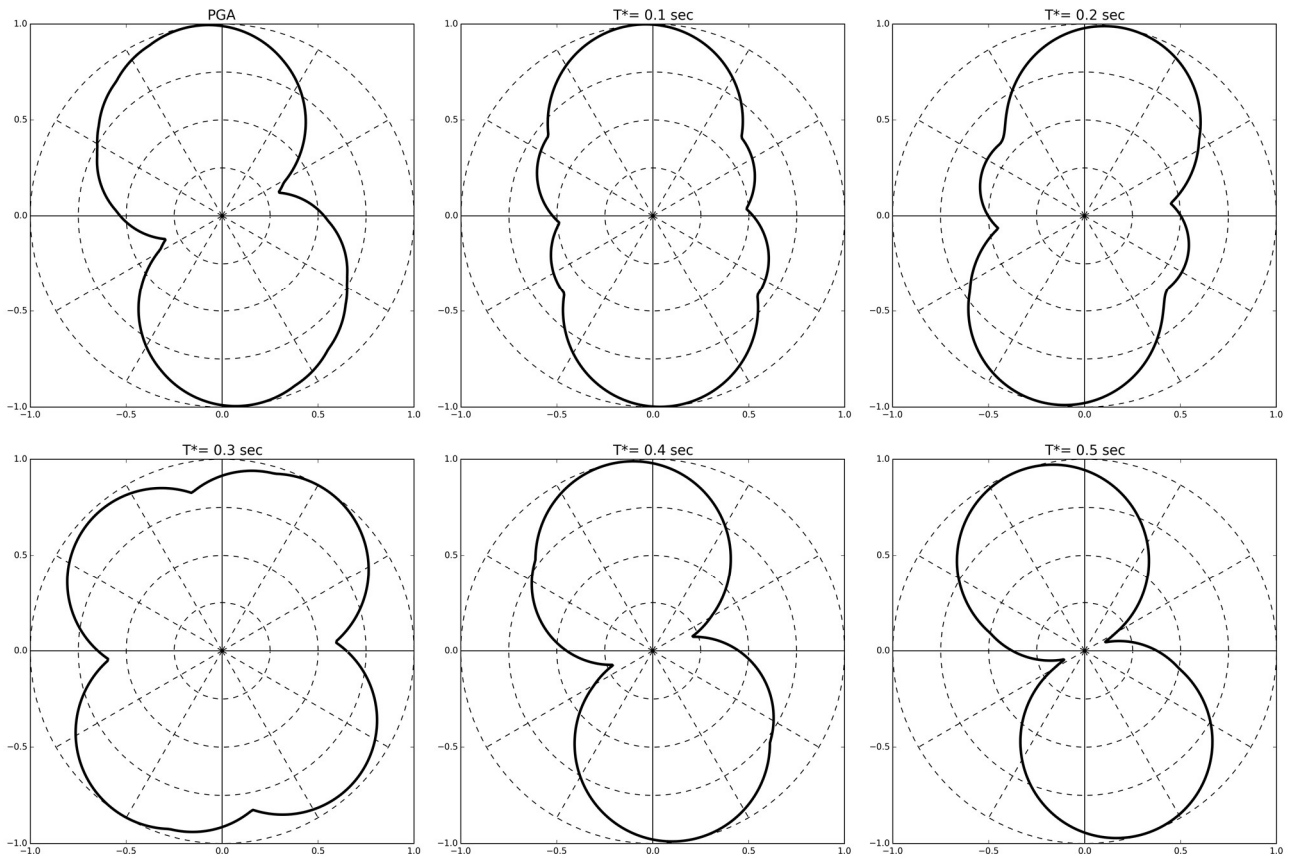


Figure A4.1.13. Ratio of PGA or pseudo-acceleration at all orientations with respect to the maximum rotational PGA or pseudo-acceleration (RotD100) for the record at CSMIP station 25281. Horizontal and vertical axes correspond to the E-W and N-S directions, respectively.

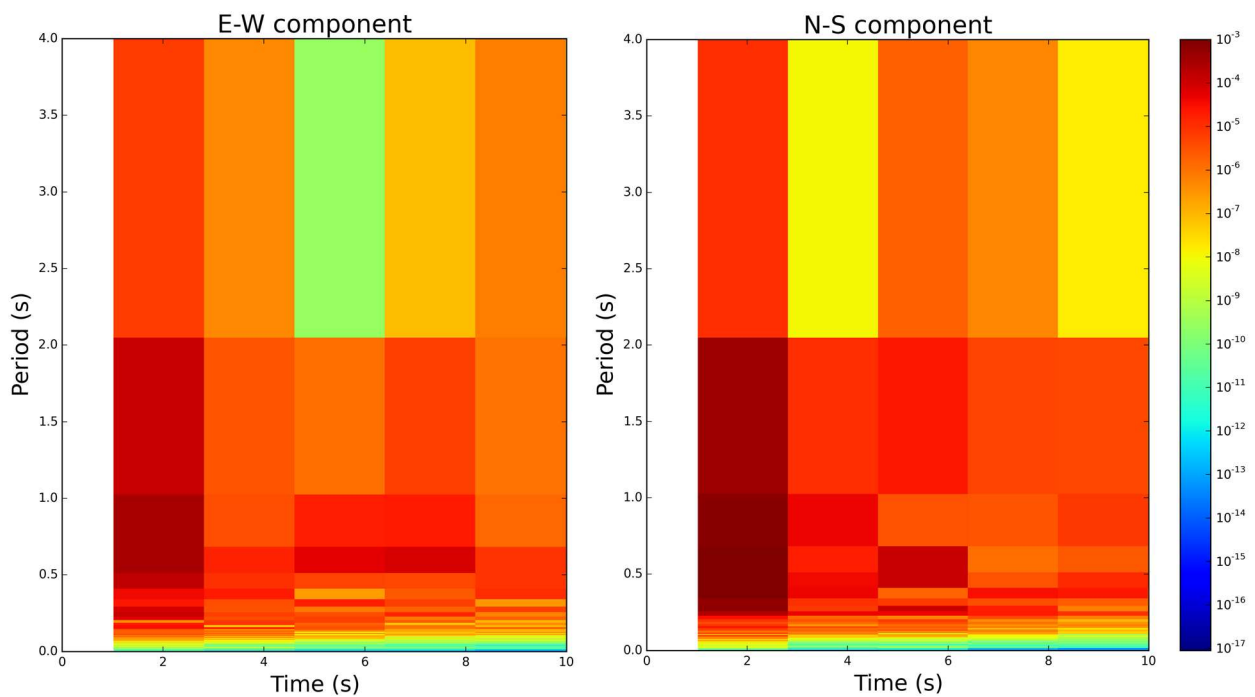


Figure A4.1.14. Spectrograms of the E-W (left) and N-S (right) components of the record at CSMIP station 25281.

The abundant uncertainties in this analysis (orientation of the causative fault, quality of the digitisation of the analogue records, epistemic and aleatoric variability of the models that describe directionality and directivity) do not allow for a strong conclusion to be drawn. However, it is of interest to have found a significant amplification of ground motions at a direction that could be considered close enough to the suspected fault-normal one, at a period relatively close to that predicted by the directivity model of Somerville (2003).

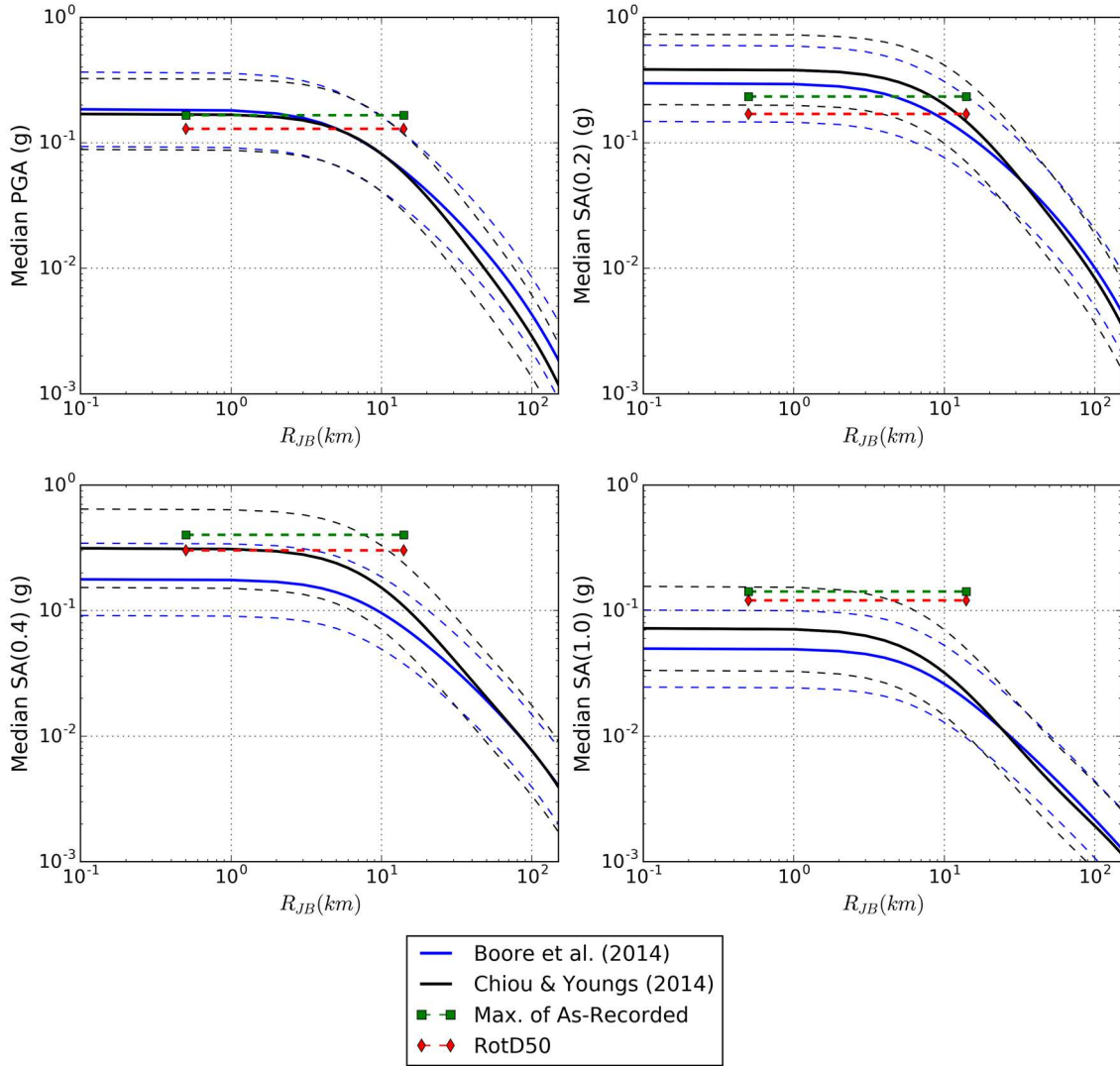


Figure A4.1.15. Trellis plots showing the ground motion prediction models of Boore *et al.* (2014; blue lines) and Chiou & Youngs (2014; black lines). Dashed lines indicate the plus/minus one standard deviation band. Magnitude **M**4.8, V_{s30} = 200 m/s, Z_{tor} =4.6 km, and 6.0 km hypocentral depth. Joyner-Boore distance assumed equal to epicentral distance. Green and red markers indicate values from accelerograms recorded at CSMIP station 25281.

With the purpose of understanding whether these recorded ground motions were or not typical for an earthquake like that of Port Hueneme, the series of Trellis plots shown in Figure A4.1.15 were generated using the OpenQuake Ground Motion Toolkit (Weatherill, 2014). Assuming a 1:1 relation between moment magnitude and local magnitude (e.g., Dost *et al.*, 2018), a value of **M**4.8 was used. A V_{s30} value of 200 m/s, a depth to the top of the rupture Z_{tor} of 4.6 km (calculated as explained later in Section A4.1.4.4) and a 6-km hypocentral depth were used as well. The ground motion models of Boore *et al.* (2014) and Chiou & Youngs (2014) were selected for their appropriateness for California. Figure A4.1.15 shows

as well the PGA and pseudo-acceleration (S_a) values obtained from the accelerograms for comparison. Green squares show the maximum of the two as-recorded components, while red triangles show the rotational median (*i.e.*, RotD50, the median PGA or S_a at all possible orientations), which is the metric resulting from the two ground motion models used. As the epicentral distance to the recording station is not known with precision, the plot shows these values at a range between 0.5 and 14.0 km, which are the possible values reported (Joyner-Boore distance assumed equal to epicentral distance herein, as no detailed information on the fault rupture is available). RotD50 values stemming from the records at CSMIP station 25281 lie around -0.51 to +1.13 standard deviations away from the medians predicted by the ground motion models for PGA, around -1.25 to +0.53 for $T=0.2$ s, around -0.04 to +2.14 for $T=0.4$ s and around +0.68 to +2.57 for $T=1.0$ s. If epicentral distances closer to the upper bound of 14 km were the correct ones, the observed ground motions would be above the median predicted ones in all cases. Better agreements can be observed at shorter epicentral distances. Overall, there is nothing particularly unusual or unexpected about the levels of ground motion observed for this earthquake.

A4.1.4.3 Inferred shaking levels

No inferences regarding shaking levels have been found in the literature. Being the epicentral location and the causative fault so uncertain, no attempt to infer shaking levels at locations other than CSMIP station 25281 are made herein.

A4.1.4.4 Duration of ground shaking

As can be observed in Figure A4.1.8, the duration of the ground motion recorded at CSMIP station 25281 0.5 to 14 km away from the epicentre appears to have been quite short, of less than a couple of seconds. This suspicion is confirmed when looking at the 5-75% of Arias definition of significant duration calculated directly from the waveforms recorded at CSMIP station 25281, as shown in Table A4.1.3. The 2.61 seconds obtained for the E-W component do not seem to be consistent with the acceleration time-histories plotted by Housner & Hudson (1958) (Figure A4.1.8). However, Figure A4.1.10 shows motion of a relatively stable amplitude continuing significantly beyond the 1.5 seconds shown in Figure A4.1.8. It is worth noting, once more, that these waveforms were recorded by an analogue station around six decades ago and are thus subject to significant technical limitations.

Table A4.1.3. 5-75% of Arias Intensity definition of significant duration calculated from the waveforms recorded at CSMIP station 25281.

Component	Duration (s)
E-W	2.61
N-S	0.49

Estimations of the 5-75% definition of the significant duration were obtained by means of the prediction equations of Bommer *et al.* (2009) and Afshari & Stewart (2016) as well. For the former, two alternative depths to the top of the rupture (Z_{tor}) were used, resulting from combining a 6-km or a 13.8-km hypocentral depth (Table A4.1.1) with a rupture area of

around 7.8 km² estimated by means of the empirical relations of Wells & Coppersmith (1994), and assuming a square rupture, a vertical fault and the hypocentre to be located at mid-depth. The two resulting values for Z_{tor} were 4.6 km and 12.4 km. For the model of Afshari & Stewart (2016), a strike-slip mechanism was assumed and the basin depth parameter z_1 was taken as equal to the median estimate from the relationship derived by Chiou & Youngs (2014), which leads to a sediment depth differential δz_1 of zero. Three values of V_{s30} (200, 400 and 600 m/s) were considered, based on the V_{s30} values reported in Figure A4.1.7 for the area. Results are shown in Figure A4.1.16 and Figure A4.1.17 for each of the two alternative hypocentral depths (6 and 13.8 km), together with the durations calculated from the waveforms, represented as covering epicentral distances from 0.5 to 14 km due to the uncertainty in the epicentral location. As can be observed, predictions obtained with the model of Afshari & Stewart (2016) for a 6-km hypocentral depth are in overall agreement with the observed duration of 2.61 seconds of the E-W component at CSMIP station 25281, but are all significantly larger than the observed 0.49 seconds of the N-S component. Predictions obtained for the same hypocentral depth with the model of Bommer *et al.* (2009) lie completely in between the values calculated for the two components. When a 13.8-km hypocentral depth is used, the 2.61 seconds of the E-W component lie between the predictions of the two models for 200 m/s, though not coinciding with either, and the 0.49 seconds of the N-S component are still smaller than all predictions. For a 6-km hypocentral depth and 200 m/s (at the station, Figure A4.1.7), the 2.61 seconds (E-W) lie within [+0.23,+1.48] and [-0.45,+0.23] standard deviations from the median predictions of the models of Bommer *et al.* (2009) and Afshari & Stewart (2016), respectively, while the 0.49 seconds (N-S) lie within [-2.79,-1.54] and [-3.22,-2.53] standard deviations of each model. For a 13.8-km hypocentral depth, the 2.61 seconds (E-W) lie within [+0.61,+1.10] and [-0.69,-0.37], while the 0.49 seconds (N-S) lie within [-2.41,-1.92] and [-3.46,-3.13] standard deviations of each model. These results suggest that a shallower hypocentral depth of 6 km is more likely than a deeper one of 13.8 km, and that the duration of the E-W component was relatively standard for the assumed characteristics of this earthquake, while that of the N-S component appears as particularly short. As it is the N-S component that presented the largest as-recorded PGA, this supports the observation that motion was mostly consisting of a strong pulse.

Oxnard, which was described as severely affected, lies right next to Port Hueneme, up to maximum epicentral distances of around 14-20 km, depending on the epicentral coordinates assumed to be correct. Ventura, which was also described as severely hit, lies at approximately at 20-35 km. According to Figure A4.1.16 and Figure A4.1.17, a maximum significant duration of around 6 seconds may have occurred in the most distant of these locations.

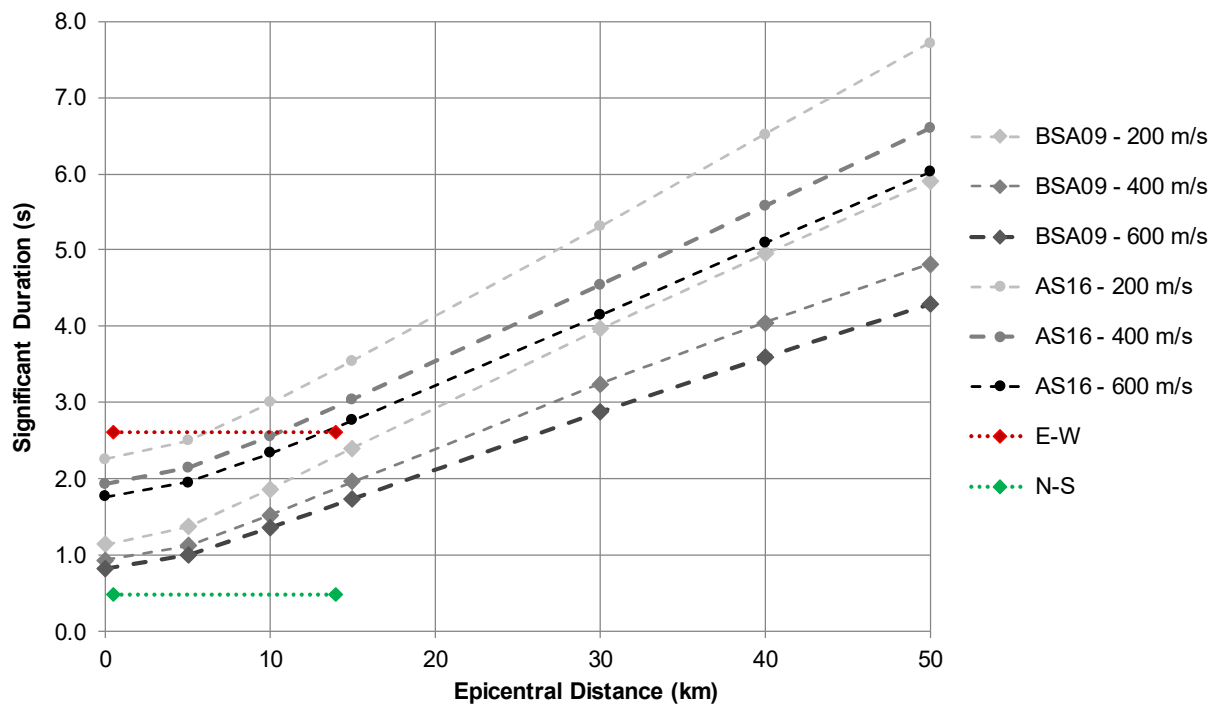


Figure A4.1.16. Estimation of the significant duration of the 1957 Port Hueneme earthquake, using prediction equations by Bommer *et al.* (2009, BSA) and Afshari & Stewart (2016, AS), with 6-km hypocentral depth and 4.6-km depth to the top of the rupture, and values calculated from the waveforms recorded at CSMIP station 25281.

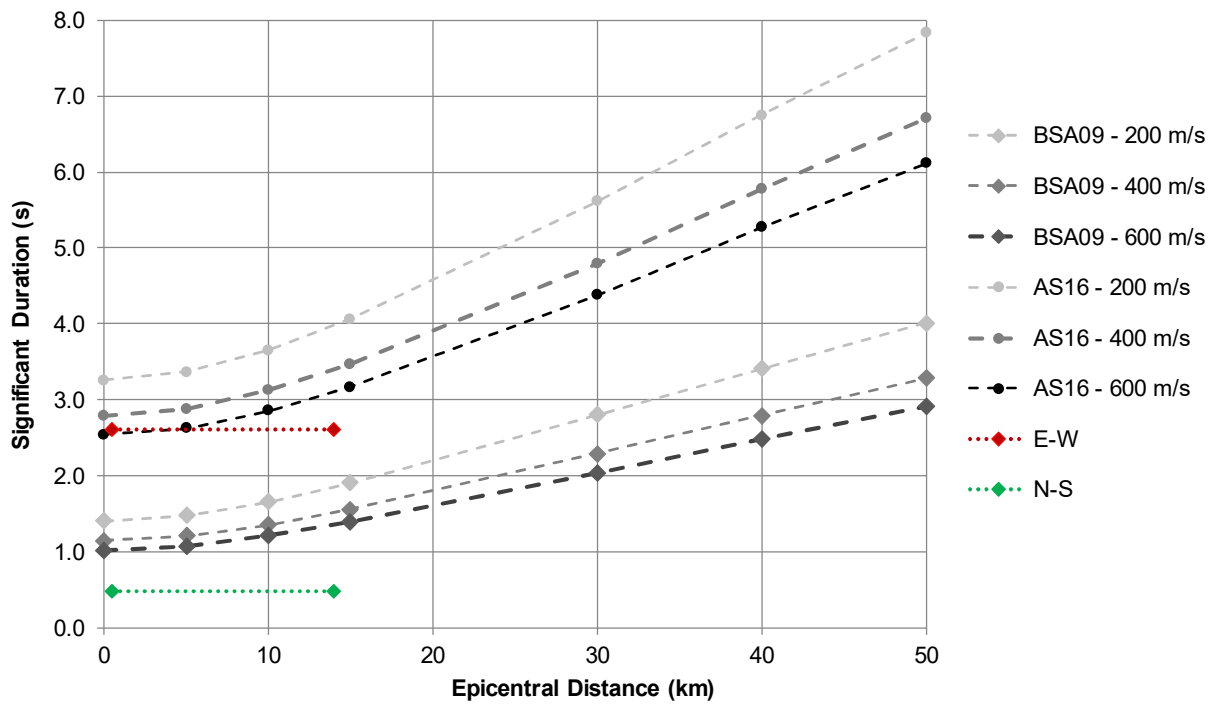


Figure A4.1.17. Same as Figure A4.1.16 but with 13.8-km hypocentral depth and 12.4-km depth to the top of the rupture.

A4.1.5 Collateral earthquake hazards

A4.1.5.1 Surface rupture

No reports of surface rupture have been found for this earthquake.

A4.1.5.2 Landslides

No reports of landslides have been found for this earthquake.

A4.1.5.3 Liquefaction

No reports of liquefaction have been found for this earthquake.

A4.1.5.4 Settlements

No reports of settlements have been found for this earthquake.

A4.1.6 Exposed population

A4.1.6.1 Socio-economic setting

According to the 2016 Human Development Report (United Nations, 2016), the Human Development Index (HDI) for the USA was 0.920 in 2015, ranking 10th in the world, while that of the Netherlands, which held the 7th position, was slightly larger. The difference in the inequality-adjusted HDI (IHDI) values is larger, that of the USA being 0.796, against 0.861 of the Netherlands. Table A4.1.4 compares the HDI and IHDI for both countries.

Table A4.1.4. Human Development Index and Inequality-adjusted Human Development Index for USA and the Netherlands. From United Nations (2016) and HDR-UNDP (2016).

Report	Data	USA			Netherlands		
		HDI	IHDI	Rank	HDI	IHDI	Rank
2016	2015	0.920	0.796	10	0.924	0.861	7

Figure A4.1.18 shows a comparison between the United States as a whole and the state of California in terms of household income percentiles. As can be observed, California is characterised by larger incomes. The county of Ventura, where the epicentral area of this earthquake was located, ranks 5th within the state in terms of median household income, with 76,500 US dollars, significantly higher than that of the whole state (Statistical Atlas, 2015). The production of oil had begun in the county as early as 1885 (Davis *et al.*, 2015), and the port of Hueneme was established at more or less around the same time (Weber & Kiessling, 1978).

The information presented in Table A4.1.4 and Figure A4.1.18 makes clear reference to recent times in history. While a detailed comparison of the economies of the United States and the Netherlands in 1957 is beyond the capabilities and scope of this work, it is worth noting that, after World War II, the United States was left in a relatively privileged position, as its territory had been mostly untouched, while Europe underwent a process of recovery (Jones, 2005). The Marshall Plan set by the USA was key in accelerating the latter, particularly in the Netherlands, which started a period of strong economic expansion at the beginning of the 1950s (Anderson, 2010). Meanwhile, the US dollar became the world's major reserve currency and the country adopted a leading position in the world's political and economic scene (Jones, 2005).

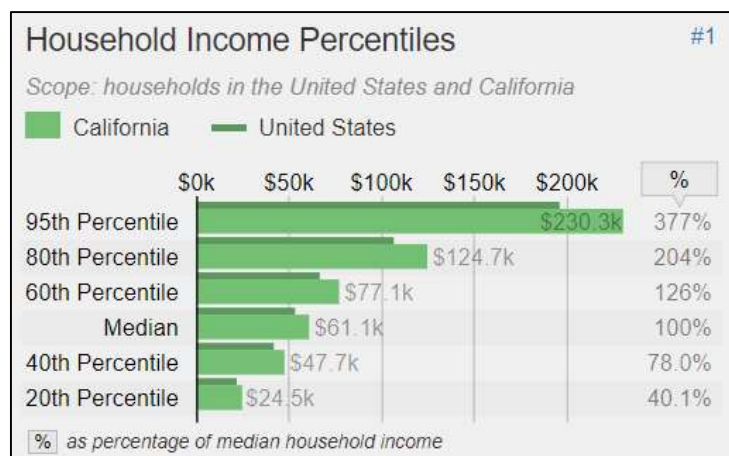


Figure A4.1.18. Comparison of household income percentiles for the United States and the state of California. From Statistical Atlas (2015).

A4.1.6.2 Population density and distribution

The whole of Ventura County, where the epicentral area of this earthquake was located, had a population of around 115,000 people in 1950 and 199,000 people in 1960. Table A4.1.5 shows the total population and population density of the three cities that were most affected by this earthquake.

Table A4.1.5. Total population and population density in the most affected cities. Data from Population.us (2016).

City	Population		Density (p/km ²)	
	1950	1960	1950	1960
Port Hueneme	3,024	11,067	249.9	914.6
Oxnard	21,567	40,265	212.5	396.7
Ventura	16,534	29,114	198.0	348.7

A4.1.6.3 Time of day of earthquake

This earthquake occurred on Monday 18th March 1957 at 10.56 am local time. Due to the scarce information on damage caused by this earthquake and the lack of casualties, it is not possible to make big inferences regarding the influence of the time of occurrence of the

earthquake over its consequences. It is noted, though, that one of the main buildings of a high school in Oxnard was deemed unusable after inspection, but there are no reports of injuries resulting from this damage, despite the earthquake occurring during school hours. Along the same lines, great losses in terms of products breaking when falling off shelves at stores are reported, but not injuries stemming from broken bottles or similar, despite the earthquake occurring during working hours.

A4.1.7 Characteristics of exposed building stock

A4.1.7.1 Seismic design codes

While Cutcliffe (2000) believes that it was the 1906 San Francisco earthquake which marked the start of a real interest in earthquake engineering and seismic design in the United States, Freeman (1932) stated a quarter of a century later that "the art of constructing earthquake-resisting buildings is still in the formative stage, that there are differences of opinions among experts and that there is much deficiency in important data". Further, he points at the 1925 Santa Barbara earthquake to have been more significant in raising awareness on the subject. It was this devastating event that prompted the first edition of the Uniform Building Code (UBC) in 1927, which contained the first written seismic design provisions for a regional level, but which did not become mandatory until 1961 (Beavers, 2002). Within California in particular, the 1933 Long Beach earthquake was of special importance, as it prompted the passing of the Field Act and Riley Act of 1933, which mandated the seismic design of schools and buildings, respectively (Beavers, 2002). However, the assessment and retrofitting of existing school buildings took many decades to occur, the final deadlines being set in 1967-1968 to 1970 and 1975 (FEMA, 2009).

As recapitulated by Beavers (2002), the origin of seismic design codes and building codes in general in the USA started in a fragmented fashion, by regions or states. For example, the Uniform Building Code (UBC) just mentioned above was typically used west of the Mississippi river. The National Building Code of the Building Officials and Code Administrators (BOCA) (known as the BOCA Code) was, instead, used in the upper midwest and northeast. It was first published in 1950, including seismic design provisions. In the south, the Standard Building Code (SBC) of the Southern Building Code Congress International (SBCCI) was used. Seismic design provisions were included in the SBC in 1976, by referencing ANSI A58.1, but "were not mandatory unless local authorities required seismic design, which was rarely the case", until 1988. The 1987 edition of the BOCA Code also incorporated the provisions of ANSI A58.1 and made them mandatory.

The ANSI A58.1 standard of the American National Standards Institute (ANSI) was first published in 1945 and was the first standard to consider earthquake loads (Beavers, 2002). However, seismic hazard did not have a role in ANSI A58.1, which only had a map showing the locations of destructive earthquakes of the past until its 1972 edition, in which a seismic hazard description similar to the 1949 USCGS (United States Coast and Geodetic Survey) map was incorporated. The 1972 edition of ANSI A58.1 was also the first one to outline

modern wind design provisions (Fratinardo & Schroeder, 2015; Ghosh, 2008), evolving from more basic guidelines developed in the 1950s (Huston, 2007).

The 1949 hazard map was the first one to encompass the whole of the contiguous USA, and it was based on "the premise that similar earthquakes will occur in the future where they have occurred in the past" (Beavers, 2002). For reasons that are not fully clear, this map was withdrawn in 1952, and replaced with a map that only showed the location of known past significant earthquakes. In the 1970s, the responsibility of producing hazard maps passed on to the USGS (United States Geological Survey), who published the first map developed in the form of probabilistic estimates of maximum acceleration contours on rock in 1976, and which, as highlighted by Beavers (2002), represented a significant paradigm shift. It should be noted, however, that the first edition of the ATC3-06, which in 1985 evolved into the National Earthquake Hazards Reduction Program (NEHRP) Recommended Provisions for Seismic Regulations for New Buildings and Other Structures, used a truncated version of this map in 1978, not allowing for values above 0.4g to be considered. This map was used for almost 20 years, given the inability to reach consensus on a different map that took place in between 1988 and 1994. It was finally updated by the USGS in 1997, after a four-year project called Project 97, during which large efforts were invested in giving a voice to all the professionals and sectors involved. Since then, the USGS hazard map has been updated in 2002, 2008 and 2014.

The way in which seismic loads were considered evolved significantly from the simple use of a 7.5%-10.0% of the building's weight as a lateral load (1927 edition of the UBC), with the progressive incorporation of significant factors such as soil type and capacity, seismic zonation, natural period of vibration of the structure, and importance of the building.

In 1988, ANSI combined with ASCE to update and re-designate ANSI A58.1-1982 to ASCE 7, which is now the most significantly recognised standard by all earthquake regulations, codes, standards, procedures and guidelines for basic seismic design in the USA (Beavers, 2002). Furthermore, ASCE 7 is also the "de facto" national wind design standard (Fratinardo & Schroeder, 2015). The International Building Code (IBC), whose first edition in 2000 was based in the NEHRP Provisions, makes reference to ASCE 7 for the definition of seismic and wind loads.

The Building Code Effectiveness Grading Schedule (BCEGS), developed by the Insurance Services Office (ISO), indicates that the overall level of code enforcement across the state of California is relatively high when compared to the country as a whole, as illustrated in Figure A4.1.19. Within the BCEGS classification schedule shown, classes 1-3 correspond to the maximum enforcement levels, while class 10 indicates no enforcement at all. These figures are expected for California, given its long history of seismic activity. However, the situation in 1957 was certainly different, considering that the 1927 edition of the UBC had been around only for three decades and that the Field Act and Riley Act of 1933 took many decades more to be enforced, going well into the 1970s.

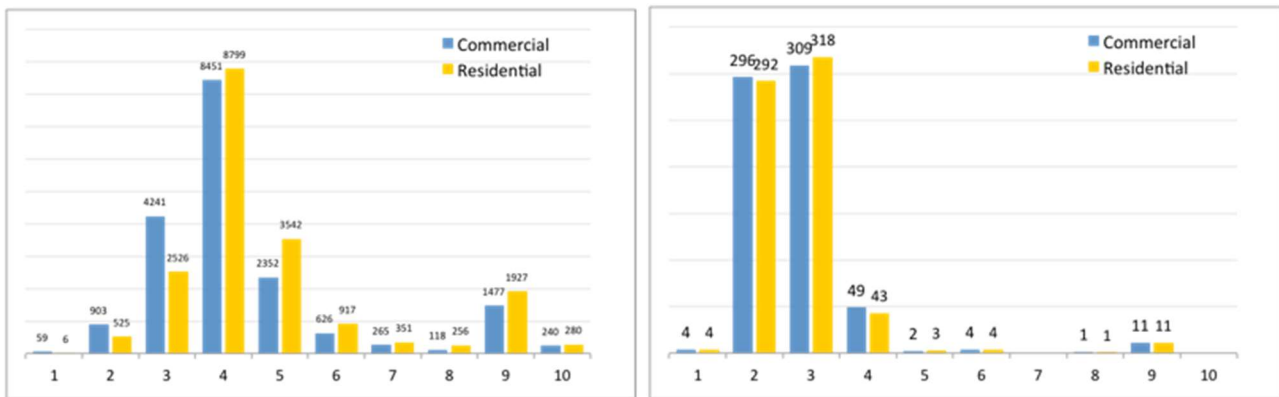


Figure A4.1.19. Distribution of communities by BCEGS class number for the whole of the United States (left) and the state of California (right). Personal lines include 1- and 2-family dwellings. Commercial lines include all other buildings. Classes 1-3: maximum enforcement. Class 10: no enforcement. From ISO Mitigation (2016).

A4.1.7.2 Building typologies

Data regarding typologies at the country level were collected from the PAGER Inventory Database v2.0 (Jaiswal & Wald, 2008). Figure A4.1.20 shows that the structure of most of the buildings in the USA consists of light wood frames (61.2%), and unreinforced brick masonry (19.3%) in a smaller proportion. The remaining 19.4% is mostly made up of heavy wood frames and mobile homes (Figure A4.1.21).

Figure A4.1.22 shows the proportion of Hazus (FEMA, 2012) building typologies in Ventura County, where this earthquake and the affected cities are located. According to this data, which is available from the OpenQuake Platform, 85% of the buildings in the county are light wood frames, a larger percentage than suggested by the PAGER Inventory Database v2.0 (Jaiswal & Wald, 2008) for the whole country. The remaining 15% is split among several other typologies, of which the most prominent are manufactured homes (a type of prefabricated building that is mostly constructed in a factory and then installed in site, 4.9%), low-rise reinforced masonry bearing walls with wood/metal deck diaphragms (2.7%), low-rise concrete shear walls (1.5%) and commercial and industrial wood structures (1.4%). Masonry bearing walls represent only a 3.5% of the total, much lower than the 19.3% suggested for the national level (Figure A4.1.20), of which 0.6% are unreinforced and 2.9% are reinforced. However, a document on earthquake risk by the City of Oxnard states that its Central Business District contains a large (unspecified) number of unreinforced masonry structures that could be particularly vulnerable to seismic action (City of Oxnard, 2016).

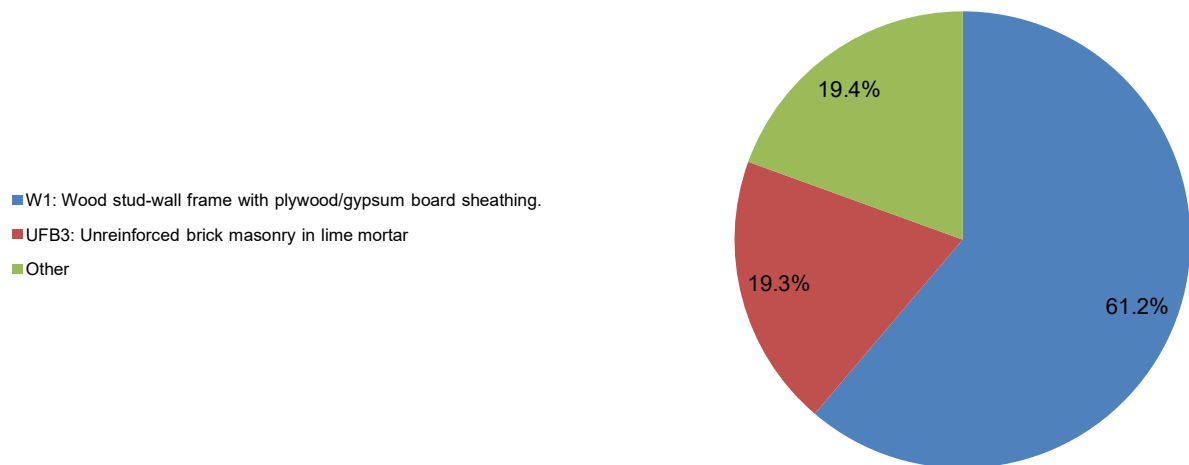


Figure A4.1.20. Proportion of buildings in the United States belonging to each typology. The subcategories within class "Other" are expanded upon in the figure below. Data from Jaiswal & Wald (2008).

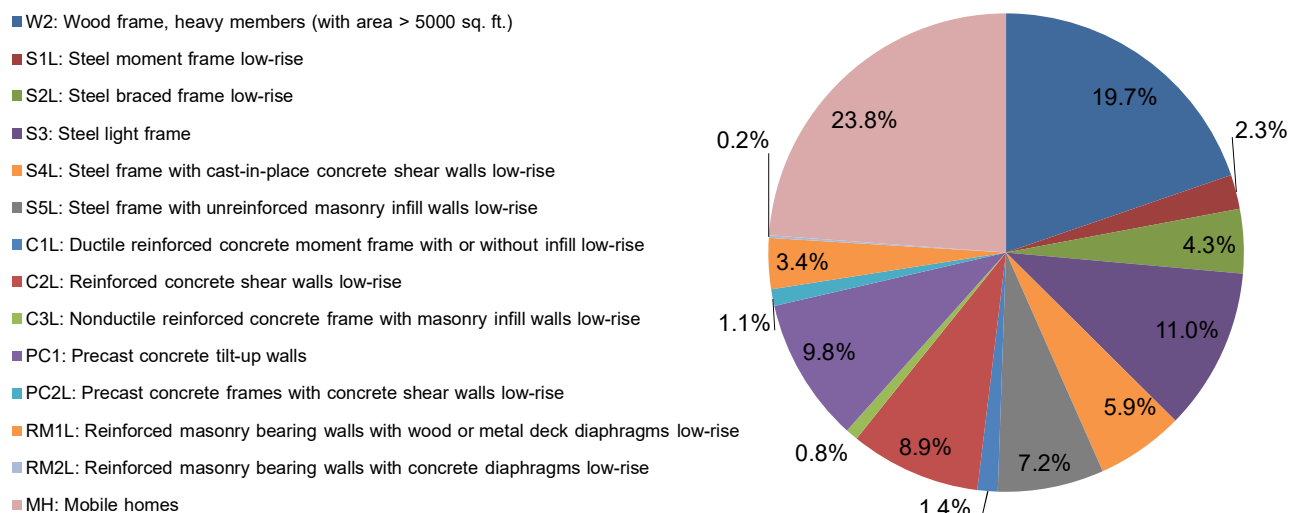


Figure A4.1.21. Breakdown of the "Other" class in the figure above. To determine the percentage that each of these sub-categories represents of the total in the USA, multiply the value in this figure by 0.194. Data from Jaiswal & Wald (2008).

While these proportions of building typologies are not likely to have been the same in 1957 when the Port Hueneme earthquake occurred, it is noted that the most popular typologies according to PAGER and Hazus already existed at the time. Light wood frames, for example, date back to the first half of the 19th century (Steve Allen Construction, 2014), and unreinforced brick masonry was forbidden for new constructions in California after 1933, though it continued to be present in the form of existing buildings (FEMA, 2009; Wikipedia). Reinforced masonry saw a rise in its popularity after the 1933 Long Beach earthquake destroyed a large number of unreinforced masonry structures 100 km to the south-east of Port Hueneme (Dickey, 1976; FEMA, 2009). Manufactured homes, an expression often mixed with mobile homes as the former can be considered an evolution of the latter, appeared in the early years of motorisation, which can be interpreted as being the first half of the 20th century (Wikipedia).

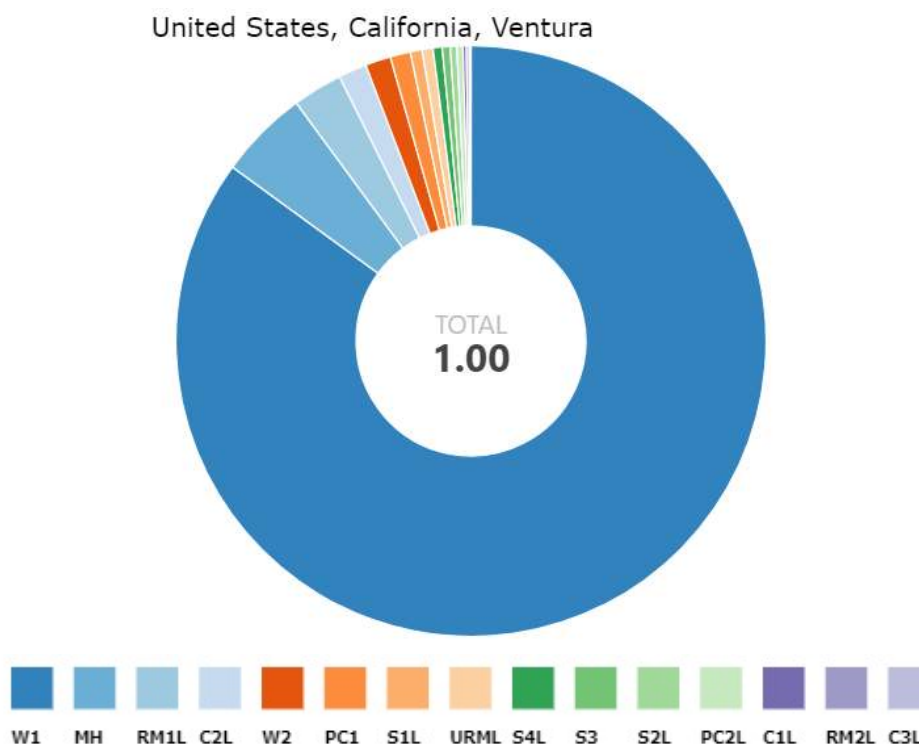


Figure A4.1.22. Hazus (FEMA, 2012) building fractions for Ventura County, California, USA. W1: light frame wood. MH: manufactured home. RM1L: low-rise reinforced masonry bearing walls with wood/metal deck diaphragms. C2L: low-rise concrete shear walls. W2: commercial and industrial wood. PC1: precast concrete tilt-up walls. S1L: low-rise steel moment frame. URML: low-rise unreinforced masonry bearing walls. S4L: low-rise steel frame with cast-in-place concrete shear walls. S3: steel light frame. S2L: low-rise steel braced frame. PC2L: low-rise precast concrete frames with concrete shear walls. C1L: low-rise concrete moment frame. RM2L: low-rise reinforced masonry bearing walls with precast concrete diaphragms. C3L: low-rise concrete frame with unreinforced masonry infill walls. From the OpenQuake Platform.

A4.1.7.3 Prior damage and retrofit

No details on prior damage or retrofit have been found.

A4.1.8 Damage observations

A4.1.8.1 Damage states

No statistics in terms of standardised damage scales have been found. The lack of photographs and detailed information on damage make it extremely difficult to infer the level of damage caused by this earthquake.

A4.1.8.2 Damage statistics and description

According to the newspaper articles gathered by ICS (2006), Port Heuneme, Oxnard and Ventura were the most severely hit. The small summary of the earthquake by Stover & Coffman (1993) supports this statement and describes the damage as minor, consisting of cracked walls, fallen plaster and the breaking of products knocked off shelves at stores.

Housner & Hudson (1958) mention that the number of reports of damage was relatively large for an earthquake of this magnitude. Weber & Kiessling (1978) describe the event as having caused “relatively great damage” for its magnitude.

The most complete description of damage caused by this earthquake was found in the compendium of newspaper articles gathered by ICS (2006), and can be summarised as follows:

Damage in Ventura (around 15 km away from the USGS epicentre, see Figure A4.1.5):

- cracked windows;
- cracked walls;
- stock knocked off shelves in stores;
- several schools evacuated (no details on final assessment);
- the new Shell office building at Ventura was evacuated (no details on final assessment).

Damage in Oxnard (right next to the epicentre, see Figure A4.1.5):

- broken windows in downtown buildings;
- cracked walls in several buildings;
- cornices jolted loose at two office buildings;
- widening of cracks;
- falling of plaster;
- damage described as “heavy” in markets, the detailed description only referring to damage to goods falling off shelves;
- bricks fell off Masonic Temple and a crack was reported in the building; intensive inspections were carried out (no details on final assessment);
- intensive inspections were carried out in the Santa Clara Catholic Church (no details on final assessment);
- a high school was evacuated and inspected; it appears to have suffered the heaviest damage, the main building deemed unusable;
- other schools in the area were evacuated.

A small fire occurred at Point Mugu, south-east of Port Hueneme, apparently caused by the snapping of two broken powerlines together, though it was quickly controlled (ICS, 2006).

One of the sources cited by ICS (2006) states that “except for widening of cracks, falling of plaster and scattered foodstuffs from the shelves of grocery stores, the rest of the county appeared to have ridden out the quake in fairly good shape”. This statement appears as contradictory when confronted against a high school building described as unusable. Unfortunately, no further details or photographs that could shed some light upon the matter have been found. However, it is worth of mention that the Long Beach, California, earthquake of 1933 had caused extensive damage to unreinforced masonry school buildings 100 km to the south-east of Port Hueneme and had led to the passing of the Field Act a

month later, which mandated the seismic design of schools in California (Dickey, 1976; Beavers, 2002; Cutcliffe, 2000). While the 1933 Long Beach earthquake did not result in the death of any children, this was simply due to it occurring outside of school hours (FEMA, 2009; Dickey, 1976). It is, thus, possible, that the decision to declare this high school building unusable after the 1957 Port Hueneme earthquake may have stemmed from a very cautious response over a sensitive matter such as the safety of school children. While no further details are available regarding this particular school building, it is noted that Cutcliffe (2000) estates that the behaviour of schools built or retrofitted after 1933 in subsequent earthquakes was much better than that of pre-1933 schools. It may be possible that the building damaged in 1957 had been built before 1933 and not retrofitted, and that any level of damage that it may have suffered was enough for the authorities to decide to take immediate action. While it is not possible to ascertain this for sure, it is noted that, according to FEMA (2009), retrofitting did not take place immediately after the Field Act, and it was only in 1967-1968 that a deadline for the assessment of pre-1933 school buildings was set to the year 1970, 13 years after the Port Hueneme earthquake.

In the quest for understanding the extent of damage caused by this earthquake, it is worth of notice that no photographs have been found to make a direct visual analysis. While it is possible that some photographs may have accompanied the original newspaper articles gathered by ICS (2006), one could also wonder if the lack of photographs may imply that what is described by extensive damage in some sources was not as extensive in more objective engineering terms and mostly consisting of damage to contents (e.g., products and objects falling off shelves) and non-structural components. In this sense, it is noted that FEMA P-774 (FEMA, 2009), a document dedicated to the behaviour of unreinforced masonry in earthquakes, contains references and photos of damage caused by many Californian events, such as the 1933 Long Beach or the 1925 Santa Barbara earthquakes, but none of the 1957 Port Hueneme one.

A4.1.8.3 Observed weaknesses

No information on systematic weaknesses has been found.

A4.1.8.4 Damage distribution

Other than the fact that Oxnard was more severely hit than Ventura, which is expectable, given their respective distances to the epicentre, no further details on damage distribution have been found.

A4.1.9 Casualties and losses

A4.1.9.1 Numbers of dead and injured

There were neither deaths nor injuries associated with this earthquake, though one woman was reportedly knocked off her chair in Ventura (ICS, 2006; Stover & Coffman, 1993).

A4.1.9.2 Causes of casualties

There were neither deaths nor injuries associated with this earthquake (ICS, 2006; Stover & Coffman, 1993).

A4.1.9.3 Estimates of economic losses

No information on economic losses in financial terms has been found. This earthquake is not listed in the NOAA or EM-DAT databases and, while it appears in the USGS catalogue and the ISC Bulletin, no comments on damage can be found in either source.

A4.1.10 Discussion and conclusions

This M_L 4.8 earthquake occurred on 18th March 1957, at 18.56 UTC (10.56 local time), in Port Hueneme, Ventura County, California. It reached a maximum Modified Mercalli Intensity of VI and affected mostly Port Hueneme, Oxnard and San Buenaventura (usually referred to as Ventura), all within Ventura County. It was the first earthquake for which a strong motion record consisting of a strong velocity pulse was recorded, previous ones having been limited to weak motion. A maximum PGA of 0.18 g was recorded at around 0.5 km (to 14 km, due to uncertainty) from the epicentre. No casualties were reported.

While damage has been described in some sources as relatively large, it appears to have consisted mostly of cracked windows, plaster and walls, the falling of pieces of plasters and bricks, and the loss of goods being knocked off shelves at stores. No details regarding the most affected structural typologies have been found, though light wood frames are predominant at present in the affected area.

There were reports of intensive inspections having been carried out for at least three buildings (a temple, a church and a school), but no details have been found on the final assessments except for the case of a high school, for which one of the main buildings was deemed unusable. No further details regarding the latter are known, and no photos of the damage in general have been found. Given the rise in awareness of the risk that unreinforced masonry buildings pose to children after the 1933 Long Beach earthquake, it is possible that damage that would nowadays be considered minor was deemed sufficient to decide not to use a certain building anymore at a time in which the assessment and retrofitting of old unreinforced masonry schools was still ongoing. While the lack of photographs may reflect the difficulties in accessing information from six decades ago, it may also suggest that the extent of damage was not as large as implied by certain verbal descriptions.

A4.1.11 References

A4.1.11.1 Bibliography

- Afshari, K. & J.P. Stewart (2016). Physically parametrised prediction equations for significant duration in active crustal regions. *Earthquake Spectra* **32**(4), 2057-2081.
- Anderson, M.W. (2010). The Dutch Economy: A History of the Dutch Economy since WWII. Available online at (last accessed 4th July 2018): <https://andersonmwa.wordpress.com/2010/02/01/the-dutch-economy-a-history-of-the-dutch-economy-since-wwii-2/>.
- Anderson, J.C., V.V. Bertero & R.D. Bertero (1999). *Performance improvement of long period building structures subjected to severe pulse-type ground motions*. Pacific Earthquake Engineering Research Center (PEER) Report 1999/09. Berkeley, California, USA.
- Beavers, J.E. (2002). A review of seismic hazard description in US design codes and procedures. *Progress in Structural Engineering and Materials* **4**, 46–63.
- Bommer, J.J., P.J. Stafford & J.E. Alarcón (2009). Empirical equations for the prediction of the significant, bracketed, and uniform duration of earthquake ground motion. *Bulletin of the Seismological Society of America* **99**(6), 3217-3233.
- Boore, D.M. & J.J. Bommer (2005). Processing of strong-motion accelerograms: needs, options and consequences. *Soil Dynamics and Earthquake Engineering* **25**, 93–115.
- Boore, D.M., J.P. Stewart, E. Seyhan & G.M. Atkinson (2014). NGA-West2 equations for predicting PGA, PGV, and 5% damped PSA for shallow crustal earthquakes. *Earthquake Spectra* **30**(3), 1057–1085.
- Chiou, B.S.-J. & R.R. Youngs (2014). Update of the Chiou and Youngs NGA model for the average horizontal component of peak ground motion and response spectra. *Earthquake Spectra* **30**(3), 1117–1153.
- Cutcliffe, S.H. (2000). Earthquake resistant building design codes and safety standards: The California experience. *GeoJournal* **51**, 259–262.
- Davis, T.L., J.S. Namson & S. Gordon (2015). *Ventura basin oil fields: structural setting and petroleum system*. Available online at: <http://www.thomasldavisgeologist.com/resources/Ventura-Basin-PS-AAPG-GdBk-May-2015.pdf>. Last accessed: 15th June 2018.
- Dickey, W.L. (1976). History and development of hollow brick for reinforcement. *Fourth International Brick and Block Masonry Conference, IB²MAC 1976*. Bruges, Belgium, April. Available online at: <http://www.hms.civil.uminho.pt/ibmac/1976/4c1.pdf>. Last accessed: 14th June 2018.
- Dost, B., B. Edwards & J.J. Bommer (2018). The relationship between M and ML: A review and application to induced seismicity in the Groningen gas field, the Netherlands. *Seismological Research Letters* **89**(3), 1062–1074.
- Federal Emergency Management Agency (FEMA) (2009). *Unreinforced masonry buildings and earthquakes – Developing successful risk reduction programs – FEMA P-774*. United States.
- Federal Emergency Management Agency (FEMA) (2012). *Hazus-MH 2.1 Technical Manual: Multihazard Loss Estimation Methodology: Earthquake Model*. Washington, DC, United States.
- Field, E.H., G.P. Biasi, P. Bird, T.E. Dawson, K.R. Felzer, D.D Jackson, K.M. Johnson, T.H. Jordan, C. Madden, A.J. Michael, K.R. Milner, M.T. Page, T. Parsons, P.M. Powers, B.E. Shaw, W.R.

Thatcher, R.J. Weldon II & Y. Zeng (2013). *Uniform California earthquake rupture forecast, version 3 (UCERF3)—The time-independent model*. U.S. Geological Survey Open-File Report 2013–1165, California Geological Survey Special Report 228, and Southern California Earthquake Center Publication 1792, 97 p. Available online at: <http://pubs.usgs.gov/of/2013/1165/>. Last accessed: 28th May 2018.

Foulger, G.R., M. Wilson, J. Gluyas & R. Davies (2016). *Human-induced earthquakes*. Report for the Nederlandse Aardolie Maatschappij BV (NAM), The Netherlands. Report available online at: <https://www.nam.nl/feiten-en-cijfers/onderzoeksrapporten.html#iframe=L2VtYmVkL2NvbXBvbmVudC8/aWQ9b25kZXJ6b2Vrc3JhcHBvcnRlbG>. Last accessed 28th November 2017.

Fratinaro, V.F. & S.A. Schroeder (2015). Historical study of the wind design provisions of ASCE 7. *Structures Congress 2015*, 829–839.

Freeman J.R. (1932). *Earthquake Damage and Earthquake Insurance*. 1st edition. New York: McGraw-Hill.

Hauksson, E. (1991). Seismotectonics. *Reviews of Geophysics* **29**(S2), 721–733

Housner, G.W. & D.E. Hudson (1958). The Port Hueneme earthquake of March 18, 1957. *Bulletin of the Seismological Society of America* **48**, 163–198.

Howard, J.K., C.A. Tracy & R.G. Burns (2005). Comparing observed and predicted directivity in near-source ground motion. *Earthquake Spectra* **21**(4), 1063–1092.

Hough, S.E. & M. Page (2016). Potentially induced earthquakes during the early twentieth century in the Los Angeles Basin. *Bulletin of the Seismological Society of America* **106**(6), 2419–2435.

Huston, E. (2007). SEAW's handbook of a rapid-solutions methodology for wind design. *Struct. Mag.*, 61–64.

Jaiswal, K. & D.J. Wald (2008). Creating a Global Building Inventory for Earthquake Loss Assessment and Risk Management. USGS Open File Report 2008-1160. Available electronically at <http://pubs.usgs.gov/of/2008/1160/>. Last accessed: 9th February 2017.

Jones, G. (2005). *Restoring a Global Economy, 1950–1980*. Available online at (last accessed 4th July 2018): <https://hbswk.hbs.edu/item/restoring-a-global-economy-19501980>.

Kanamori, H. & P.C. Jennings (1978). Determination of local magnitude, M_L , from strong-motion accelerograms. *Bulletin of the Seismological Society of America* **68**(2), 471–485.

McGuire, R.K. & J.A. Barnhard (1977). Magnitude, distance and intensity data for C.I.T. strong motion records. *Journal of Research of the United States Geological Survey* **5**(4), 437–443.

Petersen, M.D., M.P. Moschetti, P.M. Powers, C.S. Mueller, K.M. Haller, A.D. Frankel, Y. Zeng, S. Rezaeian, S.C. Harmsen, O.S. Boyd, N. Field, R. Chen, K.S. Rukstales, N. Luco, R.L. Wheeler, R.A. Williams & A.H. Olsen (2014). *Documentation for the 2014 update of the United States National Seismic Hazard Maps*. USGS Open-File Report 2014-1091, 243 pp.

Seismosoft (2016). *SeismoSignal 2016 – A computer program for signal processing of strong-motion data*. Available from <http://www.seismosoft.com>. Last accessed: 10th April 2017.

Shahi, S.K. & J.W. Baker (2011). An empirically calibrated framework for including the effects of near-fault directivity in Probabilistic Seismic Hazard Analysis. *Bulletin of the Seismological Society of America* **101**(2), 742–755.

Somerville, P.G., N.F. Smith, R.W. Graves & N.A. Abrahamson (1997). Modification of empirical ground motion attenuation relations to include the amplitude and duration effects of rupture directivity. *Seismological Research Letters* **68**(1), 199–222.

Somerville, P.G. (2003). Magnitude scaling of the near fault rupture directivity pulse. *Physics of the Earth and Planetary Interiors* **137**, 201–212.

Stierman, D.J. & W.L. Ellsworth (1976). Aftershocks of the February 21, 1973 Point Mugu, California earthquake. *Bulletin of the Seismological Society of America* **66**(6), 1931–1952.

Stover, C.W. & J.L. Coffman (1993). *Seismicity of the United States, 1568–1989 (Revised)*. United States Geological Survey Professional Paper 1527. Denver, Colorado, United States. Available online at: <https://pubs.er.usgs.gov/publication/pp1527>. Last accessed: 26th November 2018.

United Nations, ed. (2016). *Human Development Report 2016 - Human Development for everyone*. Report of the United Nations Development Program (UNDP), New York, United States.

Wallace, R.E. (1990). General features. In Wallace, R.E. (ed.): *The San Andreas fault system, California*. United States Geological Survey Professional Paper 1515, Washington, United States.

Weatherill, G.A. (2014). *OpenQuake Ground Motion Toolkit – User Guide*. Global Earthquake Model (GEM). Technical report.

Weber, F.H. Jr. & E.W. Kiessling (1978). General features of seismic hazards of Ventura County, California. In Weber, F.H. Jr., E.W. Kiessling, E.C. Sprotte, J.A. Johnson, R.W. Sherburne & G.B. Cleveland: *Seismic hazards study of Ventura County, California, 1975* (revised 1976), California Division of Mines and Geology Open-File Report 76-5 LA, USA. Available online at: <http://www.johnmartin.com/earthquakes/eqpapers/00000036.htm>. Last accessed 3rd July 2018.

Wells, D.L. & K.J. Coppersmith (1994). New empirical relationships among magnitude, rupture length, rupture width, rupture area, and surface displacement. *Bulletin of the Seismological Society of America* **84**(4), 974–1002.

Wills, C.J., F.G. Perez & C.I. Gutierrez (2011). Susceptibility to deep-seated landslides in California. United States Geological Survey Map Sheet 58. Available online at (last accessed 3rd July 2018): <http://www.sanandreasfault.org/MS58.pdf>.

Wilson, M.P., G.R. Foulger, J.G. Gluyas, R.J. Davies & B.R. Julian (2017). HiQuake: The human-induced earthquake database. *Seismological Research Letters* **88**(6), 1560–1565.

Winterer, E.L. & D.L. Durgam (1962). In Winterer, E.L. & D.L. Durgam (eds.): *Geology of Southeastern Ventura Basin, Los Angeles County, California – Shorter contributions to general geology*. Geological Survey Professional Paper 334-H. Geological Survey & United States Department of the Interior. Washington D.C., United States.

Yong, A., E.M. Thompson, D. Wald, K.L. Knudsen, J.K. Odum, W.J. Stephenson & S. Haefner (2016). *Compilation of V_{S30} Data for the United States*. U.S. Geological Survey Data Series 978, 8 p., <http://dx.doi.org/10.3133/ds978>. Data available at: <https://earthquake.usgs.gov/data/vs30/us/>. Last accessed: 29th May 2018.

A4.1.11.2 Web references

California Resources Corporation (2018): <http://www.crc.com/our-business/where-we-operate/ventura-basin>. Last accessed: 3rd July 2018.

City of Oxnard (2016) (last accessed 28th May 2018):
Earthquake Hazard in Oxnard: <https://www.oxnard.org/wp-content/uploads/2016/12/Earthquake.pdf>

EM-DAT – The Emergency Events Database (Université Catholique de Louvain, Brussels, Belgium; Cred. Prof. Dr. D. Guha-Sapir): <http://www.emdat.be/>. Last accessed: 22nd May 2018.

GeologyCafe (2017): <http://www.geologycafe.com/california/index.html>. Last accessed: 29th May 2018.

Induced Earthquakes (2017): <http://inducedearthquakes.org/>. Last download of the database: 24th October 2017.

Institute for Crustal Studies – University of California at Santa Barbara (ICS, 2006): Earthquake History 1951-1959 (last accessed 28th May 2018): https://projects.eri.ucsb.edu/sb_eqs/SBEQCatlog/SBEQdescrips/SBEQs1951-1959.html.

International Seismological Centre (ISC): <http://www.isc.ac.uk/>. Website for this earthquake (last accessed 28th May 2018): http://www.isc.ac.uk/cgi-bin/web-db-v4?event_id=886196&out_format=IMS1.0&request=COMPREHENSIVE. Website for the 1941 Santa Barbara earthquake (last accessed 3rd July 2018): http://www.isc.ac.uk/cgi-bin/web-db-v4?event_id=900879&out_format=IMS1.0&request=COMPREHENSIVE. Website for the 1973 Point Mugu earthquake (last accessed 3rd July 2018): http://www.isc.ac.uk/cgi-bin/web-db-v4?event_id=764165&out_format=IMS1.0&request=COMPREHENSIVE.

ISO Mitigation (2016): <https://www.isomitigation.com/bcegs/facts-and-figures.html>

National Geophysical Data Center / World Data Service (NGDC/WDS): Significant Earthquake Database. National Geophysical Data Center, National Oceanic and Atmospheric Administration (NOAA). DOI:10.7289/V5TD9V7K. <https://www.ngdc.noaa.gov/hazard/earthqk.shtml>. Last accessed: 22nd May 2018.

OpenQuake Platform: <https://platform.openquake.org>. Last accessed: 29th May 2018.

Statistical Atlas (2015): <https://statisticalatlas.com/state/California/Household-Income>. Last accessed: 30th May 2018.

Steve Allen Construction (2014) – History of light frame construction (last accessed 14th June 2018): <http://stevealleninc.com/2014/12/10/history-light-frame-construction/>.

Southern California Earthquake Data Center (SCEDC, 2012) – California Institute of Technology – Historical earthquakes and significant faults in southern CA: <http://scedc.caltech.edu/significant/index.html>. Last accessed: 15th June 2018.

1941 Santa Barbara earthquake: <http://scedc.caltech.edu/significant/santabarbara1941.html>. Last accessed: 3rd July 2018.

1973 Point Mugu earthquake: <http://scedc.caltech.edu/significant/pointmugu1973.html>. Last accessed: 3rd July 2018.

Strong-Motion Virtual Data Center (VDC): <http://www.strongmotioncenter.org/vdc/scripts/event.plx?evt=100>. Last accessed: 22nd May 2018.

United Nations Development Programme – Human Development Data (UNDP-HDD, 2016): <http://hdr.undp.org/en/data>. Last accessed: 6th September 2017.

University of California, Davis – California Soil Resource Lab (UCDavis): <https://casoilresource.lawr.ucdavis.edu/projects/pedology-and-soil-survey/gis-and-digital-soil-survey-projects/>. Last accessed: 29th May 2018.

United States Geological Survey (USGS):

Catalogue search: <https://earthquake.usgs.gov/earthquakes/search/>.

Earthquake facts (last accessed 15th June 2018): <https://earthquake.usgs.gov/learn/facts.php>.

Faults, earthquake geology and special earthquake study (last accessed 15th June 2018):

<https://earthquake.usgs.gov/research/faults/overview.php>.

Quaternary Fault and Fold Database of the United States (last accessed 28th May 2018):

<https://earthquake.usgs.gov/hazards/gfaults/>.

The Modified Mercalli Intensity scale (last accessed 28th May 2018):

<https://earthquake.usgs.gov/learn/topics/mercalli.php>.

Unified Hazard Tool (last accessed 28th May 2018):

<https://earthquake.usgs.gov/hazards/interactive/>.

Website for this earthquake (last accessed 28th May 2018):

<https://earthquake.usgs.gov/earthquakes/eventpage/ci3295906#executive>.

United States Geological Survey (USGS, 2016):

Geologic provinces of Southern California (last accessed 15th June 2018):

https://geomaps.wr.usgs.gov/archive/scamp/html/scg_prov.html.

Geologic Setting of the Transverse Ranges Province (last accessed 15th June 2018):

https://geomaps.wr.usgs.gov/archive/socal/geology/transverse_ranges/index.html.

Ventura Basin Study Group (VBSG) – Guide to Ventura Basin Maps & Cross sections:

<https://projects.eri.ucsb.edu/hopps/catframe.html>. Last accessed: 15th June 2018.

Wikipedia (last accessed 14th June 2018):

Manufactured housing: https://en.wikipedia.org/wiki/Manufactured_housing.

Mobile homes: https://en.wikipedia.org/wiki/Mobile_home.

Unreinforced masonry: https://en.wikipedia.org/wiki/Unreinforced_masonry_building.

A4.2. April 1966 M5.2 Tashkent Earthquake, Uzbekistan

This earthquake occurred on 25th April 1966, at 23.22 UTC (26th April, 05.22 local time), its epicentre reported to have been right below the densely populated Tashkent city centre. Considerable part of the city's building stock was destroyed, and the greatest damage was observed in the old adobe houses constructed without consideration of seismic design. A long sequence of aftershocks induced additional damage to buildings and, as a result, more than 300,000 people were left homeless. Consequences appear to have been extensive, both in terms of damage to the built environment and casualties, though the final figures are not clear, partly due to the culture of secrecy that was prevalent in the Soviet Union at the time of the earthquake.

A4.2.1 Tectonic and seismic setting

A4.2.1.1 Tectonic setting

The tectonic deformation of Central Asia, where Uzbekistan is located, is related to the collision between the Eurasian and Indian Plates that has been ongoing for the last 50 million years of the Cenozoic Era (Erdik *et al.*, 2005; Otajanov & Shibazaki, 2012; Zhang *et al.*, 1999). The collision has resulted, so far, in a total north-south shortening of about $2,600 \pm 900$ km in Central Asia. In the last 36 million years, the rate of northward movement of the Indian Plate has stabilised at approximately 5 cm per year, with a significant part being accommodated by the convergence of the mountain belts of Pamir and Tian Shan, both shown in Figure A4.2.1 (Rau, 2003; Ullah, 2016). Focal mechanisms of past earthquakes reflect the horizontal north-south compression to which the Central Asia and Tian Shan Ranges are subject, also in agreement with the general direction of the Indo-Eurasian convergence and its crustal shortening (Ullah, 2016; Umurzakov, 2010).

Tashkent is situated in the eastern part of Uzbekistan, on the foothills of the Middle Tian Shan mountain range (Figure A4.2.1), and its tectonic activity is influenced by the deformation of surrounding crustal blocks, namely, the Central Kazakhstan shield to the North, the Turan plate to the west, the Precambrian Indian platform to the south and the Tarim basin to the east (Artikov *et al.*, 2016).

Seismic activity of the western part of the Tian Shan Range that reaches eastern parts of Uzbekistan is related to the Cenozoic reactivation of older Mesozoic and Paleozoic faults (Rau, 2003; Thomas *et al.*, 1999). All three domains of the western Tian Shan (*i.e.* North, Middle and South) feature east-west trending active thrust faults (Rau, 2003; McCann *et al.*, 2013). The middle Tian Shan thrusts are terminated to the west by the largest active strike slip fault of Central Asia, known as the Talas Fergana fault. It is the NW-SE dextral strike-slip fault located north-east of Tashkent, as shown in Figure A4.2.1 (Ottajanov & Shibazaki, 2012; Rau, 2003).

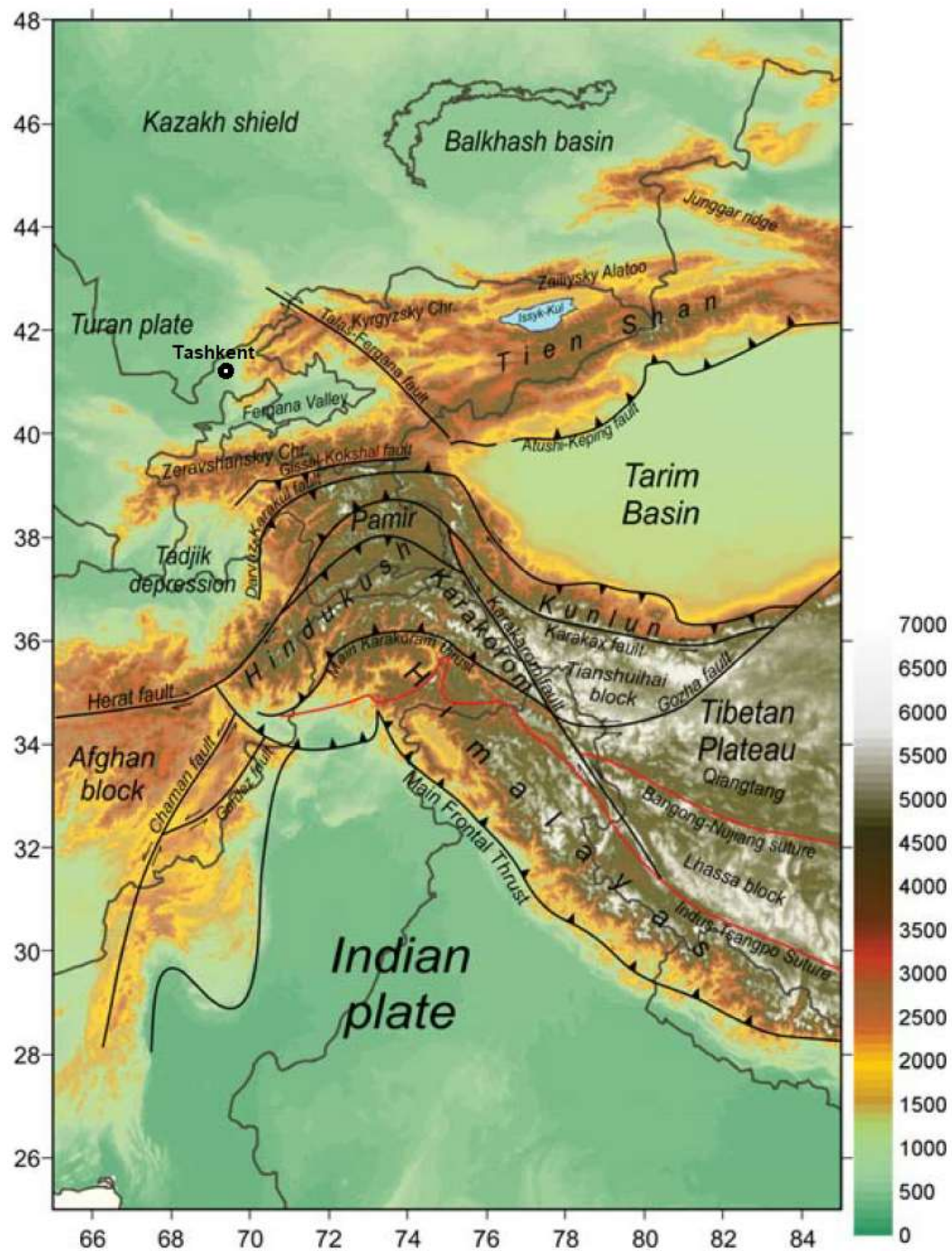


Figure A4.2.1. Relief and main tectonic features in Pamir – Hindukush and surrounding areas. Modified from Koulakov & Sobolev (2006).

According to Rau (2003), Tashkent is associated with N-S and NE-SW trending thrust faults, whose orientation might be the consequence of anti-clockwise Cenozoic rotation of the South Kazakh platform. Based on the information gathered from existing geologic studies and earthquake catalogs, Erdik *et al.* (2005) compiled a map of the active faults and their corresponding slip rates for the region of Tashkent, their results being shown in Figure A4.2.2. As observed from this map and that of Figure A4.2.1, the city of Tashkent is located on a plain, to which the spurs of the Tian Shan ridges are approaching from the northeast (Popular Geology, 1970). This includes the Karzhantau Ridge whose southern margin is followed by the NE-SW trending Karzhantau fault that passes underneath the city of Tashkent (Figure A4.2.2). The Karzhantau seismogenic zone is approximately 220

km long and 10-35 km wide, and is believed to be responsible for more than 20% of earthquakes in the region around Tashkent (King *et al.*, 1999; UNISDR, 1999; Shaw *et al.*, 2000). As will be shown later in Figure A4.2.11, the causative fault of the 1966 earthquake appears to be a branch of the Karzhantau system, perpendicular to the main NE-SW trending thrust.

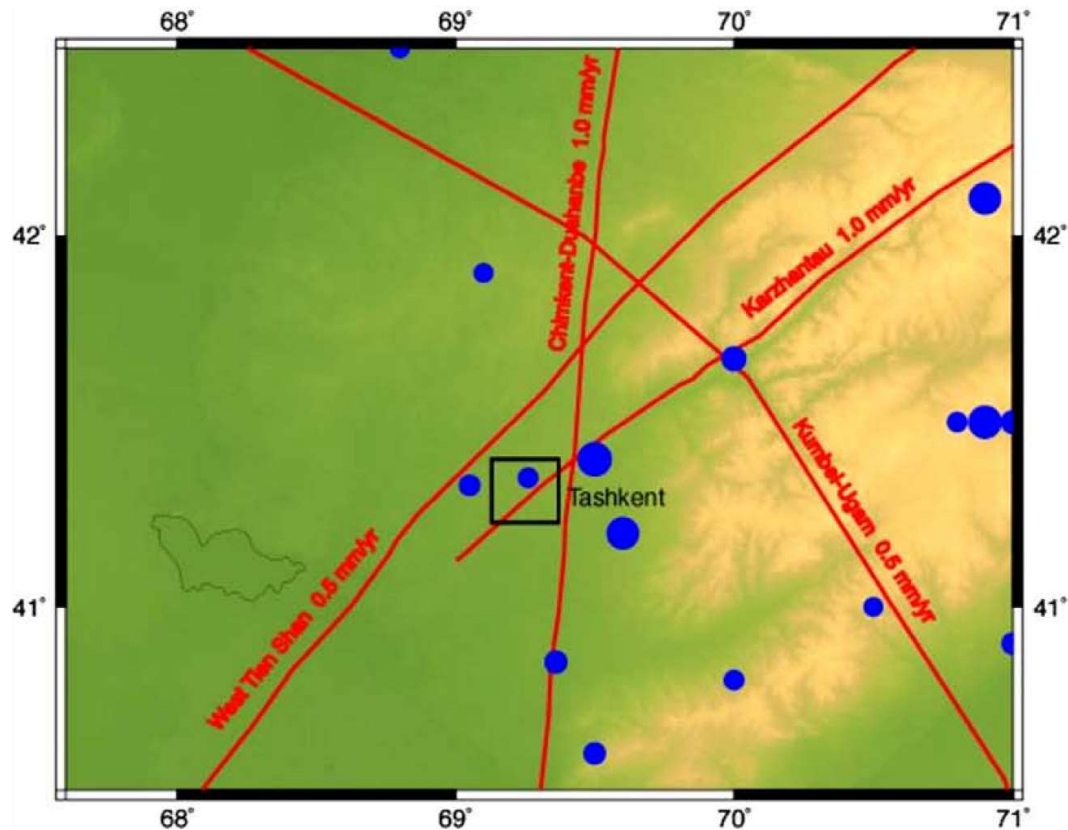


Figure A4.2.2. Major earthquakes and faults in the vicinity of Tashkent (city limits indicated with a square). From Erdik *et al.* (2005).

A4.2.1.2 Regional and local seismicity

Due to its location in the middle of Central Asia, Uzbekistan features high seismicity associated with the Eurasia-India continental collision (Erdik *et al.*, 2005; Mavlyanova *et al.*, 2004; Pilz *et al.*, 2015). Artikov *et al.* (2015) have identified several seismically active zones within the territory of Uzbekistan whose directions coincide with the strike lines of large tectonic deformations. The map of these internal seismic zones, capable of generating seismic events with magnitudes higher than five, is presented in Figure A4.2.3. It can be observed that the high level of seismic activity is especially prominent in the eastern mountainous part of the country, where the frequency and strength of the earthquakes significantly increases (Savarensky, 1966; Rau, 2003; Eurasia Travel, 2017). According to Tuychieva (2012), 330 population aggregates, including 121 cities, are situated in the seismically active areas, which corresponds to approximately 55% of the territory of Uzbekistan.

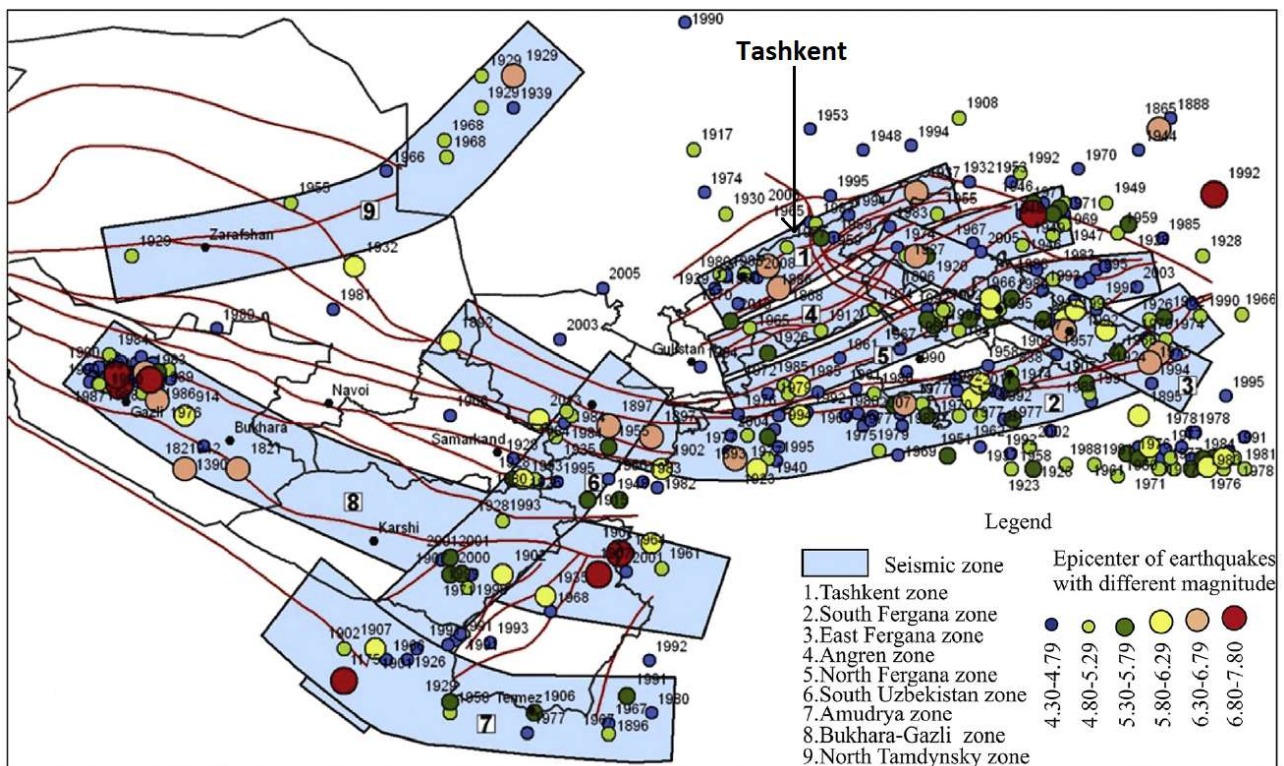


Figure A4.2.3. Map of seismogenic zones and epicentres of earthquakes within the territory of Uzbekistan and neighbouring areas since historical times. From Artikov *et al.* (2015).

Data about destructive earthquakes of Uzbekistan, which are mostly associated with the North-Fergana fault to the northeast of the country, are available from the year 1494 onward (King *et al.*, 1999; Rashidov, 2001). Historical manuscripts contain macroseismic data on more than 500 strong seismic events that occurred in Uzbekistan and had magnitude higher than 5.0 (Mavlyanova *et al.*, 2004). However, the collection of more accurate and reliable information about earthquakes started only much later, beginning with the 1868 Tashkent event (King *et al.*, 1999).

The instrumental seismicity period in Uzbekistan started with the installation of the first seismic station in Tashkent in 1901 (Mikhailova *et al.*, 2015; Mavlyanova *et al.*, 2004; Ullah, 2016). Full instrumental data exists for 8,630 seismic events recorded in the period 1955-2000 in Uzbekistan, whose distribution in time is depicted in Figure A4.2.4 (Mavlyanova *et al.*, 2004). Of these, 81 had magnitude equal to or higher than 5.0.

Throughout its long history of seismic activity, the city of Tashkent has been affected by many strong and devastating earthquakes (The World Bank, 2015; Erdik *et al.*, 2005; Mirjalilov *et al.*, 2000; Rashidov *et al.*, 2007). According to Pilz *et al.* (2015), the Tashkent region has been affected by more than 70 earthquakes with magnitude equal to or higher than 4.5, since 1868. Table A4.2.1 presents a chronological list of seismic events with an MSK intensity (Medvedev *et al.*, 1965) of VI or higher that affected Tashkent from 1868 until the beginning of the 21st century (UNISDR, 1999). Some of the listed earthquakes happened further away from the city, such as the 1946 Chatkal and the 1992 Susamyr events, located 230 km and 370 km north-east of Tashkent, respectively (Savarensky, 1966). As observed from the table, the maximum macroseismic intensity ever reached in

Tashkent was MSK VIII and corresponds to the 1966 seismic event, which was nucleated underneath the city centre (Sokolov & Chernov, 2001; Rashidov, 2001). Being the most destructive for the city of Tashkent, it resulted in large-scale redevelopment of the city (Erdik *et al.*, 2005; Eurasia Travel, 2017; King *et al.*, 1999; Rau, 2003; Mavlyanova *et al.*, 2004). A similar event struck Tashkent in 1868 (Eurasia Travel, 2017), and resulted in a considerable number of damaged buildings and several casualties (King *et al.*, 1999; IISSE NET, 2017).

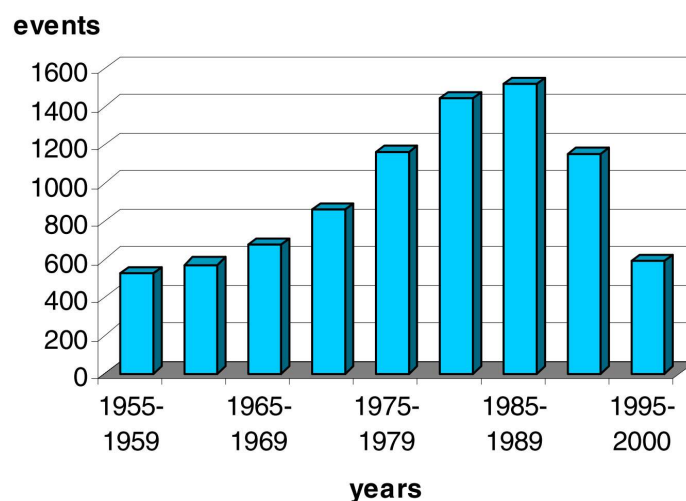


Figure A4.2.4. Earthquakes in Uzbekistan with magnitude in the range between 2.5 to 7.5 that happened in the period from 1955 to 2000. From Mavlyanova *et al.* (2004).

Table A4.2.1. Historical earthquakes and their effect in Tashkent. From UNISDR (1999).

Earthquake	Magnitude	Effect in Tashkent (MSK)
Tashkent, 1868	6.5	VII - VIII
Tashkent, 1886	6.7	VII
Kostakoz, 1888	6.4	VI - VII
Ura-Tyube, 1897	6.6	VI - VII
Tashkent, 1924	4.3	VII
Pskem, 1937	6.5	VI
Chatkal, 1946	7.5	VII - VIII
Tashkent, 1966	5.3	VIII
Tavaskay, 1977	5	VI
Nazarbek, 1980	5.1	VI - VII
Susamyr, 1992	7.3	VI

A4.2.1.3 Seismic hazard

Uzbekistan is situated in Central Asia, which is known as one of the most seismically active and hazardous regions of the world (Bindi *et al.*, 2012; Erdik *et al.*, 2005). Located in the north-eastern part of the country, the Uzbek capital, Tashkent, is associated with a high level of seismic hazard (Gupta, 2009; Think Hazard, 2017a; Pilz *et al.*, 2015).

The map of general seismic zoning for the territory of Uzbekistan, shown in Figure A4.2.5, is an integral part of the active seismic building code KMK 2.01.03-96 (1966) (Mavlyanova *et al.*, 2004). It is compiled for average ground conditions corresponding to soil class II according to the KMK 2.01.03-96 code. As defined in the code and observed from the map, the maximum expected intensity in Tashkent is MSK VIII and is associated with a recurrence period of 100 years. For an earthquake of intensity MSK VII in Tashkent, the estimated recurrence interval is 25 years (Mavlyanova *et al.*, 2004). For sites for which the map of Figure A4.2.5 specifies intensities equal to or larger than VI, seismicity is to be more precisely determined in accordance with additional seismic microzoning (SMZ) maps that take into account the influence of local ground conditions. In the case of Tashkent, the SMZ map of Figure A4.2.6 raises the maximum expected intensity to IX for the north-western areas of the city (Mavlyanova *et al.*, 2004; UNISDR, 1999).

At the time of the 1966 earthquake, the Uzbek Soviet Republic was using the official general seismic zoning (GSZ-57) map, which had been incorporated into the building code SN-8-57 (1958). This map was showing the areas in which intensities VI, VII, VIII and IX (on the GOST 6249-52 scale, see Section A4.2.8.1) were expected to occur (Lomnitz, 1974). The maximum expected intensity for the city of Tashkent was VIII (Wright, 1971), and was thus lower than the value assigned by current seismic provisions.

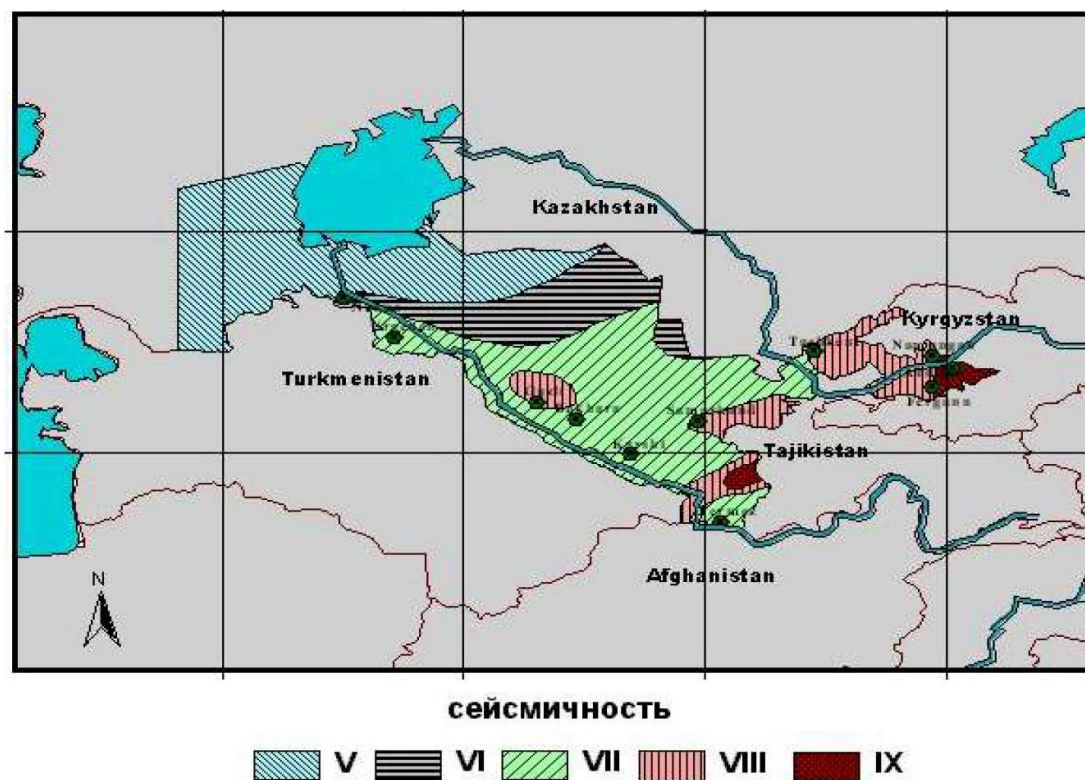


Figure A4.2.5. Map of general seismic zoning of the territory the Republic of Uzbekistan according to KMK 2.01.03-96 (1996). From Rashidov (2012).



Figure A4.2.6. Seismic microzoning (SMZ) map of Tashkent. Red star indicates epicentre of the 1966 earthquake according to Tamrazyan (1974). From Nurtaev (2005).

After the collapse of the Soviet Union, several probabilistic seismic hazard studies have been conducted by different authors for Central Asian cities, including Tashkent. Using the Site Approach of Magri *et al.* (1994), that allows for the use of ill-defined macroseismic data to carry out seismic hazard assessments, Bindi *et al.* (2012) studied the hazard of Central Asia and generated the hazard curve for the city of Tashkent shown in Figure A4.2.7. This curve expresses the probability of exceedance of a certain macroseismic intensity on the MSK-64 scale (Medvedev *et al.*, 1965) within a 50 years period. For the sake of comparison, the results of the seismic hazard study conducted by Negmatullaev *et al.* (1999) are also presented in Figure A4.2.7. As can be observed, intensity IX (MSK-64) is the maximum intensity with a probability of exceedance lower than 10% in 50 years, based on the findings of Bindi *et al.* (2012). Bindi *et al.* (2012) have also estimated that there is 14% probability for intensity VIII to be exceeded in 50 years, which is much lower than the 48% reported by Negmatullaev *et al.* (1999). Another seismic hazard study for Central Asia was done by Ullah (2016), who estimated a 10% probability of exceedance in 50 years for intensity VII in the city of Tashkent. This level of hazard is also supported by the study of Artikov *et al.* (2016).

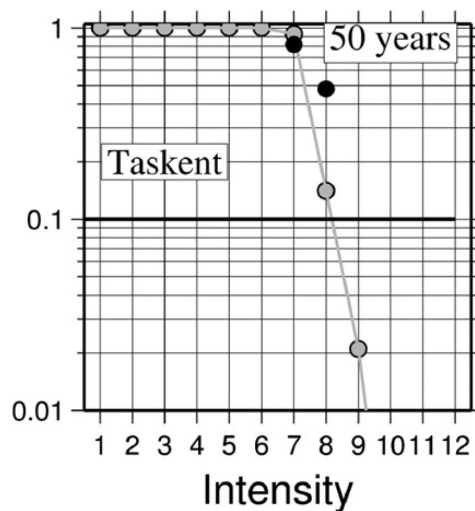


Figure A4.2.7. Hazard Curve in terms of MSK-64 Intensity computed for Tashkent by Bindi *et al.* (2012) (grey circles), and hazard estimates given by Negmatullaev *et al.* (1999) (black circles). From Bindi *et al.* (2012).

While the seismic hazard of Uzbekistan as a part of the U.S.S.R. was usually expressed by means of macroseismic intensity, some studies conducted after the collapse of the Soviet Union in the 1990s were conducted in terms of peak ground acceleration (PGA). According to the seismic hazard study performed by Rashidov *et al.* (2007), PGA on rock with an exceedance probability of 10% in 50 years (475-year return period) is in the range between 0.15 g and 0.17 g, depending on the specific part of the city. The PGA associated with an exceedance probability of 2% in 50 years are significantly higher and are in the range from 0.44 g to 0.59 g. The highest hazard, corresponding to the upper values of the PGA ranges, is associated with the northeastern part of the city, which is close to the intersection of several faults, as was shown in Figure A4.2.2. When considering surface soil instead of rock conditions, Rashidov *et al.* (2007) found that the PGA with an exceedance probability of 10% and 2% in 50 years lies in the range from 0.16 g to 0.41 g and from 0.44 g to 1.29 g, respectively. In this case, the most affected seem to be the northern part of the city, while the southern part indicates lower seismic hazard. This is in general agreement with the observations of Sokolov & Chernov (2001) who found that the seismic hazard (both in terms of seismic intensity and PGA) is lowest in the southeastern parts of the city overlaying thick gravel deposits. In addition, Sokolov & Chernov (2001) estimated that seismic hazard in terms of PGA is highest in the north-eastern parts of the city situated on shallow (<30 m) sandy loam deposits, while the highest hazard in terms of macroseismic intensity is associated with the northwestern parts lying on a thick (50-60 m) layer of sandy loam. These studies suggest that the seismic hazard of the Tashkent region is highly influenced by the local geological conditions.

The results from the Global Seismic Hazard Assessment Program (GSHAP; Giardini *et al.*, 1999) indicate a value of 0.42 g as the expected PGA on rock with a 10% of probability of exceedance in 50 years for the area of Tashkent (coordinates: 41.3 N 69.2 E). This value is much larger than those obtained by Rashidov *et al.* (2007) under the same conditions.

A4.2.2 Earthquake source characteristics

A4.2.2.1 Location, depth and time

The main shock occurred on 25th April 1966, at 23.22 UTC (26th April, 05.22 local time).

Estimates of the epicentral coordinates and hypocentral depth elaborated by the International Seismological Centre (ISC) and United States Coast and Geodetic Survey (USCGS), as reported in the website of the ISC, are summarized in Table A4.2.2. The epicentral coordinates and hypocentral depth reported by Tamrazyan (1974), as well as those included in the Earthquake Model Central Asia (EMCA) catalogue compiled by Mikhailova *et al.* (2015), are also given in the Table. Cells marked as (*f) correspond to parameters that were held fixed while inversion was carried out to retrieve those that remain. The map in Figure A4.2.8 shows the different estimations of epicentral coordinates enumerated in the table.

While the exact location of the epicentre for this event is not known, isoseismal maps, available in several publications and websites (e.g. Rasskazovsky, 1967; UNISDR, 1999; Attention! Earthquake! 2017; Savarensky, 1966), can help constrain it. According to these maps (one of which is shown in Figure A4.2.13), the epicentral area featuring the maximum level of macroseismic shaking intensity is associated with the central, urban part of Tashkent. Considering this, the estimation of Tamrazyan (1974) seems to be the most likely of the four shown in Figure A4.2.8.

Table A4.2.2. Epicentral coordinates and hypocentral depths from different sources.

Agency / Publication		Latitude	Longitude	Depth (km)
ISC	International Seismological Centre	41.3500 ° N	69.1700 °E	5.00 (*f)
USCGS ⁽¹⁾	United States Coast and Geodetic Survey	41.3000 ° N	69.2000 °E	5.00
Tamrazyan (1974)		41.3250 ° N	69.2830 °E	8.00
Mikhailova <i>et al.</i> (2015)		41.3500 ° N	69.2600 °E	8.00

(*f) fixed parameter used for inversion

(1) values reported in the ISC Bulletin citing USCGS as the source

Beside the ones listed in the table, many other authors (Mavlyanova *et al.*, 2004; Rau, 2003, Bubis, 1966; Savarensky, 1966; Utsu, 1990; Rasskazovsky, 1967) have also reported a hypocentral depth of 8 km. However, Savarensky (1966) believe that the depth of 8 km reported by the seismologists of the Uzbek SSR might be erroneous, as it was constrained using information from a single station (the seismological station of central Tashkent). According to RIA Novosti (2016), Earthquake-Report (2013) and Sputnik (2016a), the earthquake had a shallow focus and occurred at a depth between 3 km and 8 km.

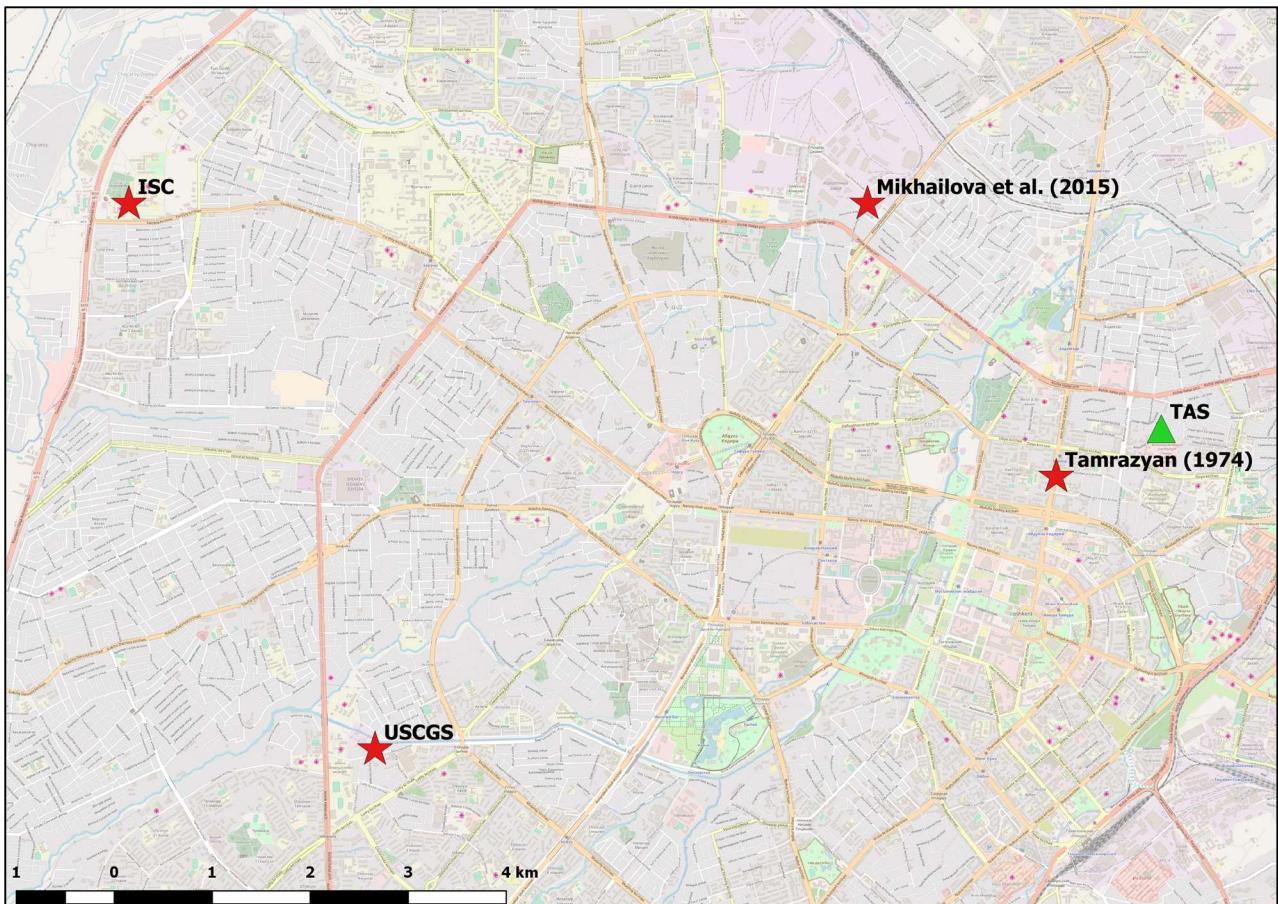


Figure A4.2.8. Estimations of epicentral coordinates according to different sources (red stars).

A4.2.2.2 Magnitude

Estimations of body-wave magnitude made by the International Seismological Centre (ISC) and the United States Coast and Geodetic Survey (USCGS) are reported in Table A4.2.3. The table also presents magnitudes reported by Leroy & Gracheva (2013) and by the EMCA catalogue of Mikhailova *et al.* (2015). Applying conversion models derived from world catalogues of the ISC, Weatherill *et al.* (2016) estimate a moment magnitude of **M5.06** with a standard deviation of 0.32, which is also included in the table.

Table A4.2.3. Estimations of moment magnitude (M), body-wave magnitude (mb) and surface-wave magnitude (MLH).

Agency		M	mb	MLH
ISC	International Seismological Centre		4.8	
USCGS ⁽¹⁾	United States Coast and Geodetic Survey		5.0	
Mikhailova <i>et al.</i> (2015)				5.2
Weatherill <i>et al.</i> (2016)		5.06		
Leroy & Gracheva (2013)		5.2		

(1) Values reported herein are those reported by the ISC citing USCGS as the source

In most publications this earthquake is associated with a magnitude of 5.3, though no information about the corresponding magnitude scale is provided (e.g., Ulomov, 1970; UNISDR, 1999; Mavlyanova *et al.*, 2004; Rashidov *et al.*, 2007; Popular Geology, 1970).

A4.2.2.3 Style-of-faulting

According to Scholz (1972), this earthquake displayed a reverse mechanism and was associated with a slip along a NW striking and sub-vertically dipping fault, as shown in Figure A4.2.9 and Figure A4.2.11 (Popular Geology, 1970; Mygeos, 2010). The rupture area of the fault stretched from 2-3 km to 8-9 km in depth and had a horizontal length of 4–5 km (Ulomov, 2016; RIA Novosti, 2016; Attention Earthquake! 2017). The north-eastern wall of the fault was deformed to a greater extent than the southwestern one, and up to 99% of the aftershock hypocentres were concentrated there. This resulted in a 3.5-cm uplift of the ground surface above the north-eastern block, as indicated in Figure A4.2.9 (Attention Earthquake! 2017; Mygeos, 2010; Ulomov, 2016; Popular Geology, 1970).

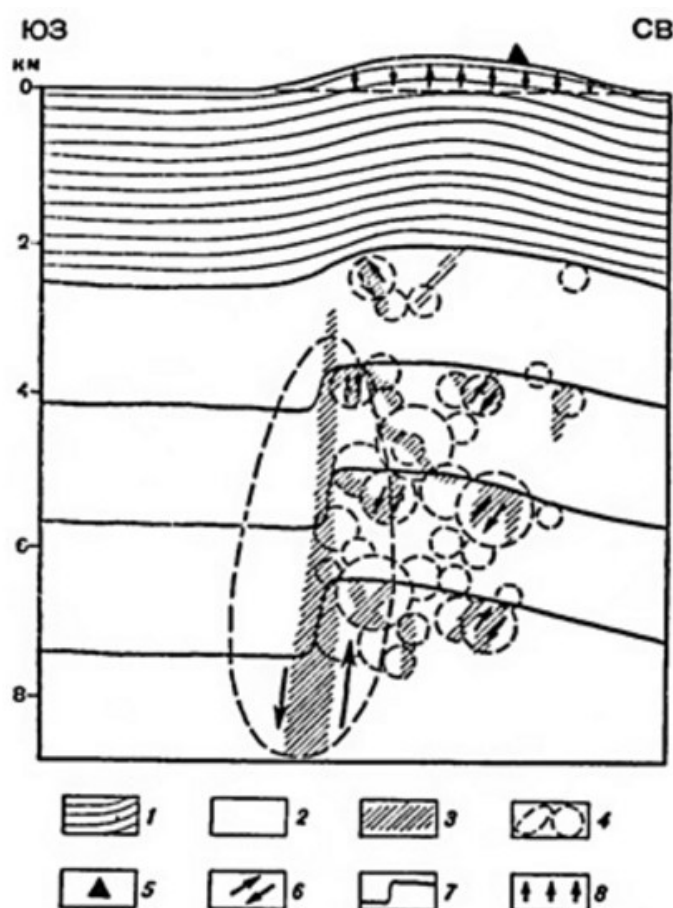


Figure A4.2.9. SW-NE section showing the mechanism of rock deformations during the Tashkent earthquake of 26th April 1966 and its aftershocks (according to Ulomov, V.I., 1967): 1 – Mesozoic + Cenozoic sediments; 2- Paleozoic base; 3 – zone of tectonic movements; 4 – hypocentral area of the main shock and its aftershocks; 5 – central Tashkent seismic station; 6 – direction of rock movements in the hypocentral area; 7 – conditional boundaries of rocks and the nature of their shear displacement; 8 – elevation of the Earth's surface according to geodetic data. CB: north-east; IO3: south-west. From Popular Geology (1970).

A4.2.2.4 Stress drop

No information could be found regarding the stress drop of this seismic event.

A4.2.2.5 Foreshocks and aftershocks

The main event was followed by a sequence of aftershocks, which lasted for several years and caused additional damage in the city (Ulomov, 2016; Attention! Earthquake! 2017). Kakhkharbek Abdullabekov, director of the Institute of Seismology of the Academy of Sciences of Uzbekistan, reported to Radio Ozodlik (2016) that 1,100 aftershocks occurred during the three years after the main shock. A similar quantitative description of aftershocks was also reported by RIA Novosti (2016) and Attention! Earthquake! (2017). Within the first days after the main seismic event, aftershocks happened one after another almost continuously and were accompanied by sharp geosounds resembling underground explosions and peals of thunder (RIA Novosti, 2016; Attention! Earthquake! 2017). After several months of strong repeated tremors, their energy and quantity gradually decreased (RIA Novosti, 2016; Attention! Earthquake! 2017).

The aftershocks occurred within a very limited area that does extend beyond the city limits (Gorshkov, 1966). The plan view of the aftershock distribution (Figure A4.2.10) reveals a general NW-SE direction, coinciding with the direction of the causative fault. From Figure A4.2.9 it is observed that most of the aftershock clusters were distributed subvertically, along the north-eastern section of the generating fault, in the depths ranging from 2 km to 8 km (Popular Geology, 1970; Shevchenko *et al.*, 2011; Mygeos, 2010). The energy class (K) of aftershocks and main shock, defined as the logarithm of the amount of energy (in Joules) released during these events, is specified in Figure A4.2.10 (Erdik *et al.*, 2005).

In the five-month period after the main shock, there were 15 aftershocks with intensities equal to or higher than V. Together with the mainshock, these 15 earthquakes released approximately 98.5% of the total amount of energy of Tashkent earthquakes in the year 1966 (Tamrazyan, 1974). Information about the date, origin time, magnitude and intensity of 14 out of 15 mentioned aftershocks, as well as of the mainshock, is shown in Table A4.2.4. As observed from the Table and indicated by many other web sources the strongest aftershocks reached intensity VII and occurred on 9th and 24th May, 4th and 29th June, 4th July 1966, and 24th March 1967 (RIA Novosti, 2016; Attention! Earthquake! 2017; Ulomov, 2016).

According to Rasskazovsky (1967), the local and central press have exaggerated when reporting the intensities of the aftershocks. The intensity of the strongest aftershocks could not have been higher than VI or VI-VII, since their impact was significantly smaller and thus not comparable with that of the main shock of intensity VIII. As Rasskazovsky (1967) emphasized, under the assumption that the five aforementioned strongest earthquakes had intensity VII, the main event would have had to be upgraded to IX on the GOST 6249-52 (1952) intensity scale.

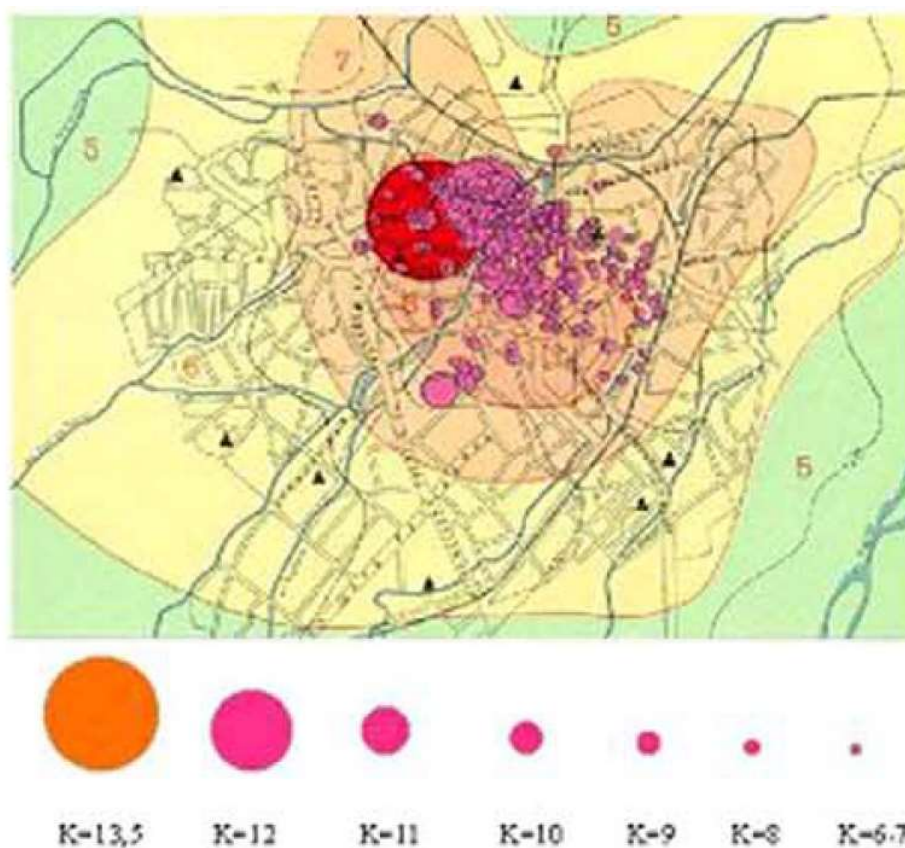


Figure A4.2.10. Epicentres of the main shock and its aftershocks and their energy classification (according to Russian seismologist Ulomov V.I.). From Erdik et al. (2005).

Table A4.2.4. Data for the 25th April 1966 Tashkent earthquake and its largest aftershocks. From Tamrazyan (1974).

#	Date (year 1966)	Origin time (GMT)	Magnitude	Intensity
1	25 April	23:23	5.3	VIII
2	07 May	21:10	3.9	VI - VII
3	09 May	17:27	3.5	V - VI
4	09 May	18:45	4.4	VII
5	09 May	18:50	4.1	VI
6	22 May	19:32		V - VI
7	24 May	7:49	3.7	VII
8	25 May	16:14		V - VI
9	04 June	21:11	3.7	VII
10	29 June	7:15		V - VI
11	29 June	9:00	3.6	VII
12	01 July	7:41		V - VI
13	04 July	14:22	4.0	VII
14	30 July	22:25		V - VI
15	15 August	23:07		V - VI

A4.2.2.6 Nature of earthquake

Several authors and sources (e.g. Popular Geology, 1970; Shaw *et al.*, 2000) associated this seismic event with the tectonic activity of the Karzhantau fault system crossing the city of Tashkent. The tectonic nature of this earthquake was also investigated in relation with the earthquake precursory signals that were manifested through variations of the subsurface water parameters. Significant rise in the groundwater level, its temperature and its Radon concentration were observed prior to the earthquake in the deep wells of the Tashkent region (Rau, 2003; Kumar *et al.*, 2013; Tomer, 2016; Hauksson, 1981; Sano *et al.*, 2016). Analyses of the fluctuations of the Radon gas concentration levels prior to the main shock and the aftershocks helped scientists to establish a correlation between the gas emissions and earthquake source zone deformation (Dubinchuk, 1993; Ulomov, 2007; Scholz, 1972).

A4.2.3 Geology and ground conditions in the affected area

A4.2.3.1 Regional geology and topography

Tashkent is situated within the Tashkent Oasis, on a hilly plain surrounded to the east and north-east by the Western Tian Shan mountain Ranges (*i.e.*, Karzhantau, Pskem, Ugam, Chatkal, and Kurama), and to the south by the Turkestan Range (Rashidov *et al.*, 1999; Juliev *et al.*, 2017; UNISDR, 1999). It lies on the 3rd, 4th and 5th terraces on the spacious right bank of the Chirchik River, which is the principal stream of the Tashkent Oasis and major right tributary of the Syr Darya River (Bubis, 1966; Rau, 2003; UNISDR, 1999). The Piedmont plain, on which Tashkent is located, is partitioned by the tributary streams of the Chirchik River into separate watershed areas. The largest (75%) area of the city lies within the Chirchik-Keles watershed divided by ravines and gorges, while the remaining southern part occupies the Chirchik River valley. The elevation of the Pritashkent depression in which the city is situated is, on average, 400 to 450 meters above sea level, while the elevation within the city itself is no more than 140 meters (Rashidov *et al.*, 1999).

Tashkent was a part of the Turan South Kazakh platform that was created in the late Paleozoic. As the Tashkent area underwent the extension during the Mesozoic, the back-arc basin was formed. The city lies on the Mesozoic sediments of this old basin that was later filled with Miocene-Pliocene deposits (Rau, 2003). The Paleozoic outcrops are evident north-east of Tashkent, on the spurs of the Karzhantau Ridge of the West Tian Shan, as observed from Figure A4.2.11. Paleozoic deposits of the Karzhantau Ridge and its associated thrust faults extend south-west towards Tashkent, into their buried position underneath the Mesozoic and Cenozoic strata, as depicted in Figure A4.2.11 (Rau, 2003; Popular Geology, 1970). The Cenozoic and Mesozoic cover in the epicentral area of the 1966 Tashkent event reaches depths of 2 km to 3 km, below which the Paleozoic deposits are placed (Figure A4.2.9). This earthquake is believed to have been generated on a NW-SE striking branch of the Karzhantau fault system (Popular Geology, 1970; Mygeos, 2010), though it is not clear in the literature how a reverse mechanism on such a branch relates to the broad NW-SE orientation of the compressive stresses.

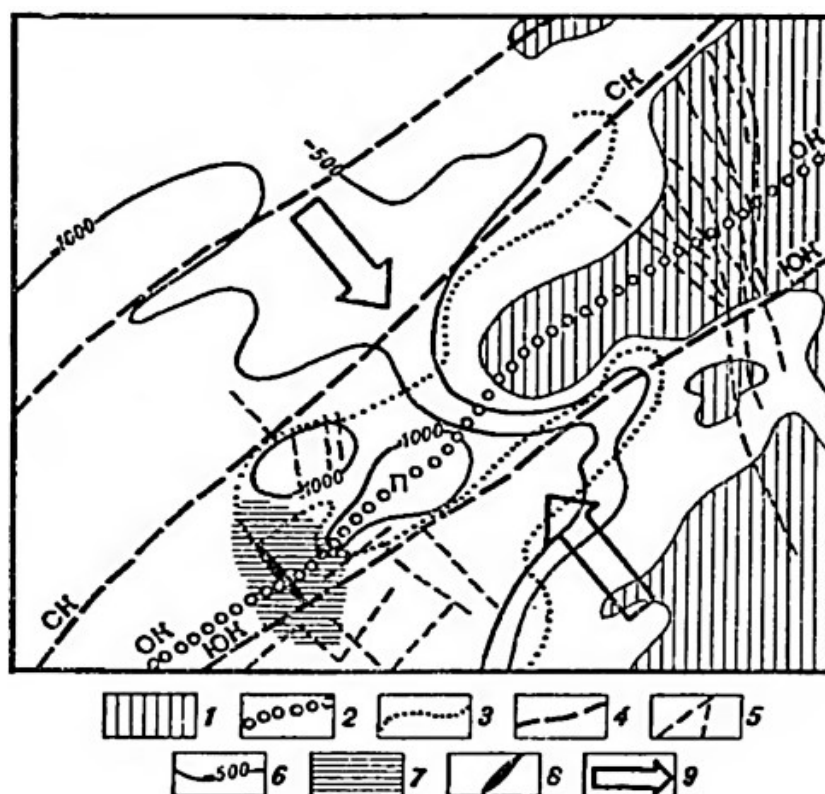


Figure A4.2.11. Tectonic setting of the Tashkent area affected by the earthquake on the 26th April 1966 (according to Gorshkov G.P.): 1 – exposed Paleozoic massifs; 2 – Karzhantau Range (in the east) and its continuation into buried state (in the west); 3 – border between outcrops of Cretaceous, Paleogene and Neogene deposits; 4 – the most significant, gently-sloping, longitudinal thrust faults: North Karzhantau (CK) and South Karzhantau (IOK); 5 – other tectonic rupture faults, usually steep; 6 – isohypses of the surface of the Paleozoic basement; 7 – epicentral area of the Tashkent earthquake and its aftershocks; 8 – causative fault rupture; 9 – compression stresses. From Popular Geology (1970).

A4.2.3.2 Site conditions in the affected area

The Pritashkent region, in which Tashkent is located, is characterized by alluvial and proluvial Quaternary deposits, including loess, loess-loamy soils, gravel, boulders and conglomerates (Rashidov *et al.*, 1999; Tuychieva, 2012). Within the city itself, dusty and macro porous loess soils are prevalent, together with loam and sandy loam soils overlying flood deposits of the Chirchik River (Rashidov, 2001; Pilz *et al.*, 2015; King *et al.*, 1999). These soils are inhomogeneous and feature moderate compressibility as well as hydro-consolidation properties (Pilz *et al.*, 2015; UNISDR, 1999). Their average bearing capacity is 1-1.5 kg/cm² in wet and 2-2.5 kg/cm² in dry state (King *et al.*, 1999). According to Rashidov *et al.* (2007), thickness of loess layers that are overlaying rocky basis can be up to 76 meters, and their bulk density is in the range between 1450-2300 kg/m³ and 250-1560 kg/m³ in natural and moistened condition, respectively.

According to Rau (2003), the eastern third of Tashkent is underlain by sands and gravels of Late Quaternary period. It can be distinguished between sands and gravels of Holocene age placed along the Chirchik River valley and those of Late Pleistocene age placed on the terraces of the Chirchik River and running parallel to it. These soils are coarse-grained and feature good hydraulic conductivity and continuity. Due to their hydraulic connection

with the Chirchik River, the change in the quality of the surface water has a direct impact on these sandy soils, which are found to be the most-polluted ones within the city (Rau, 2003). The 500-600 m thick Quaternary gravels of the eastern Tashkent grade westerly into loess soils of Middle Pleistocene age. The western two-thirds of Tashkent are covered by 30 to 40 meters of loess and loessic sediments and the water table in these parts of the city is shallow (1-3 meters below the surface), as reported by Rau (2003) and Rashidov (2001).

The results of seismic noise measurements described by Pilz *et al.* (2015) indicate three different H/V spectral ratio patterns. In the north and north-western parts of the city, H/V ratios indicate a fundamental soil frequency of around 3 Hz (0.33 s) associated with large amplifications (around 5), as well as a fundamental frequency of around 7 Hz (0.14 s) of the first higher mode. Loess deposits of 30 m to 40 m thickness overlaying layers of marlstone and a shallow groundwater level (3-25 m according to King *et al.*, 1999) are identified in this region. According to the SNiP II-7-81 (1982) seismic building code, this type of soil corresponds to category III. Based on the seismic microzoning (SMZ) map given by Kasymov (1984), the region covered by these soils has a maximum expected intensity of IX (Pilz *et al.*, 2015; King *et al.*, 1999). The south-eastern parts of Tashkent are characterized by 250 m to 300 m thick alluvial gravel terrace deposits with varying sand and water content, covered by a thin (approximately 5 m) layer of loess. A fundamental frequency of 2.5 Hz (0.40 s) is identified for compacted soils of this region. Based on the SNiP II-7-81 (1982) provisions, this soil is classified as type I and, according to the SMZ map, it is laying in the region with assigned intensity VIII (Kasymov, 1984). The third type of soil is identified on sites along the Chirchik River, for which H/V ratios indicate three resonant frequencies at approximately 3 Hz, 5 Hz and 7 Hz (0.33, 0.20 and 0.14 s). The soil consists of around 40 meters thick of loess lying over a layer of boulders, and a groundwater depth of 6 m to 20 m (King *et al.*, 1999; Pilz *et al.*, 2015). This type of soil is known as medium (type II) soil (SNiP II-7-81) and covers a region associated with seismic intensity VIII (Kasymov, 1984).

The loess deposits of Tashkent area are subject to many anthropogenic and exogenous geological processes that lead to soil erosion, landslides, mudslides, hydro-collapse, and subsidence, and the subsequent tilting and subsiding of structures (Tuychieva, 2012; Smalley *et al.*, 2006; Juliev *et al.*, 2017; Mavlyanova, 2004; Rau, 2003). The unstable and collapsible structures of loess soils in Tashkent have been created as a result of the rise of the groundwater level caused by uncontrolled water discharge of inefficient wastewater disposal systems and leaking of irrigation canals and sewage pipes. The areas of Tashkent covered by these soils are also susceptible to liquefaction (Pilz *et al.*, 2015; The World Bank, 2015; Rau, 2003).

The map of average shear wave velocity in the upper 30 m layer of the Earth's crust in the area of Tashkent, generated by the United States Geological Survey (USGS) V_{s30} Map Server using topographic slope as a proxy (Wald & Allen, 2007), is shown in Figure A4.2.12. According to this map, the V_{s30} velocities in the central area of Tashkent do not exceed 350 m/s, the epicentral area is associated with a V_{s30} value of approximately 280 m/s, and the central Tashkent seismological station (TAS) is placed in an area featuring

velocities in the range 270-300 m/s. While no information about the V_{s30} values are found in the available publications, some authors have reported the shear wave velocity associated with the specific soil conditions of Tashkent. According to Rashidov *et al.* (2007), shear wave velocities of the upper (up to 76 m thick) loess layers in the city of Tashkent are in the range between 250 - 1270 m/s, while for moistened soil conditions such velocity range is between 420-900 m/s. Sokolov & Chernov (2001) reported a shear wave velocity of 300 m/s for the (up to 60 m thick) loam and sandy loam deposits prevalent in the north-eastern parts and 400 m/s to the (0- to over 100-m thick) gravel deposits prevalent in the south-western parts of the city.

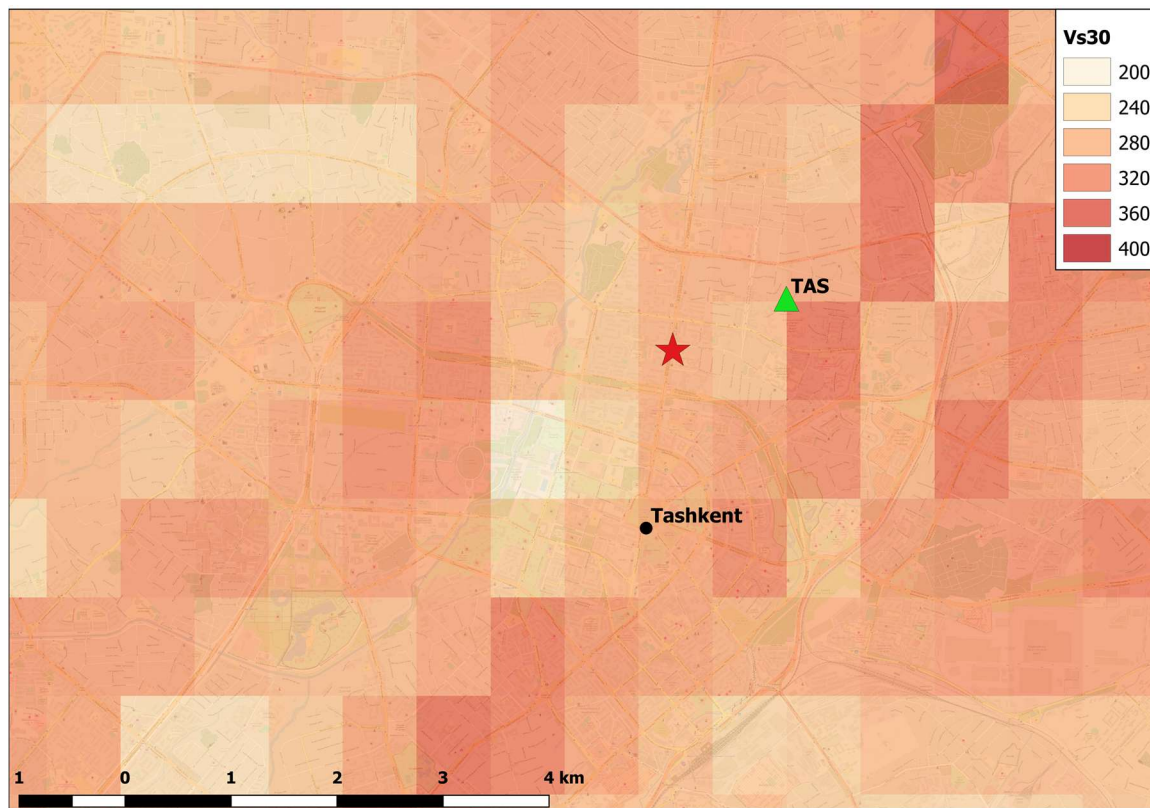


Figure A4.2.12. Estimation of V_{s30} in the area of Tashkent using topographic slope as a proxy. Data from the USGS V_{s30} map server (Wald & Allen, 2007). Red star indicates epicentre according to Tamrazyan (1974). Triangle indicates Central Tashkent Seismic Station.

A4.2.4 Ground motions

A4.2.4.1 Intensity observations

The macroseismic effects of this event have been widely studied by scientists from the Institute of Mechanics and Earthquake Resistance of Structures of the Academy of Sciences of the Uzbek SSR. According to Rasskazovsky (1967), an inspection of buildings in the damaged area was carried out in the period between 26th April and 1st October 1966. An isoseismal map, shown in Figure A4.2.13, was generated in accordance with the macroseismic data gathered within the first weeks of the survey (Rasskazovsky, 1967). The intensity was expressed in terms of the GOST 6249-52 (1952) seismic scale but

considering additional provisions and damage criteria in order to make a clear distinction between the areas ascribed with intensities VII and VIII. As pointed out by Rasskazovsky (1967) and indicated by Figure A4.2.13, the greatest seismic effects in terms of induced building damage have been observed within the city limits, in the densely populated areas enclosed by isoseismals VII and VIII. The maximum attributed seismic intensity VIII was experienced in an area covering approximately 10 to 15 km² (Raskazovsky, 1967; Rashidov *et al.*, 1974; RIA Novosti 2016; King *et al.*, 1999; Flyingnorth, 2012). On the outskirts of the city, the seismic effects did not exceed intensity VI (Geo-Storm, 2013; Rasskazovsky, 1967). As observed in Figure A4.2.13, maximum felt intensities are stretching in the north-west direction, coinciding with the strike of what many believe was the causative rupture and the alignment of the aftershocks (Attention! Earthquake!, 2017), though it is also observed that the isoseismal VII is stretching to the north-east.

Figure A4.2.13. Iseisismal map for the 1966 Tashkent earthquake. From Rasskazovsky (1967).

A4.2.4.2 Ground motion recordings

No ground motion recordings could be found for this seismic event in publicly-available databases. Information about the characteristics of the ground motions generated by this earthquake is scarce.

According to Khakimov & Nurtaev (2004), the earthquake was characterized by a high-frequency content. Strong soil oscillations with a frequency of 2-3 Hz have been reported in RIA Novosti (2016) and UZReport (2015). High-frequency vertical oscillations were prevalent during this seismic event, which resulted in the vertical component of ground motion being greater than the horizontal one (Savarensky, 1966; Mygeos, 2010; Bubis, 1966, Geo-Storm, 2013). According to Savarensky (1966), the amplitude of the horizontal ground motion was not less than 8 mm.

Though not clear in the sources, it is likely that these facts correspond to observations made at the Central Tashkent Seismic Station that was located at around 1-2 km of the epicentre (see Figure A4.2.12).

A4.2.4.3 Inferred shaking levels

This seismic event was of moderate magnitude but appears to have produced severe shaking, as indicated by the epicentral seismic intensity that was as high as VIII on the MSK-64 (Medvedev *et al.*, 1965) and GOST 6249-52 (1952) scales (Shaw *et al.*, 2000; Geo-Storm, 2013). At the same time, however, the severity of the shaking was very localized, an observation that several sources attribute to its shallow focus causing the vertical seismic waves to not spread far away and be quickly damped (Sputnik, 2016a; RIA Novosti, 2011, 2016; Radio Ozodlik, 2016; Attention! Earthquake!, 2017). Bubis (1966) emphasized that, given the shallow epicentral depth of this earthquake, the greatest force imposed on the buildings located within a radius of 1.5 km from the epicentre must have been generated by the vertical component of ground motion.

A4.2.4.4 Duration of ground shaking

Estimations of significant ground motion durations in terms of the 5-75% Arias Intensity definition were obtained using the prediction equations of Bommer *et al.* (2009) and Afshari & Stewart (2016), as shown in Figure A4.2.14. The depth to the top of the rupture used for the model of Bommer *et al.* (2009) was 3 meters, assigned in accordance with Figure A4.2.9. A range of distances to the rupture and velocities of 180 m/s, 360 m/s and 800 m/s, which correspond to the boundaries of the Eurocode 8 (CEN, 2004) definitions of soil types, were considered. The velocity of 280 m/s estimated from the USGS $V_{s,30}$ map server (USGS, 2017) for the epicentral area was also used with the predictive models.

As observed from the Figure A4.2.14, the estimated significant duration in the epicentre is rather short (0.56-0.92 seconds), and slightly higher values are obtained considering the model of Afshari & Stewart (2016) than that of Bommer *et al.* (2009). When moving further

from the epicentre, the estimated values of the significant duration based on the prediction model of Bommer *et al.* (2009) are found to be higher than those stemming from the model of Afshari & Stewart (2016), except for the case of $V_{s,30}=800$ m/s, for which a higher duration is indicated by the latter model. In all cases, the differences are very small.

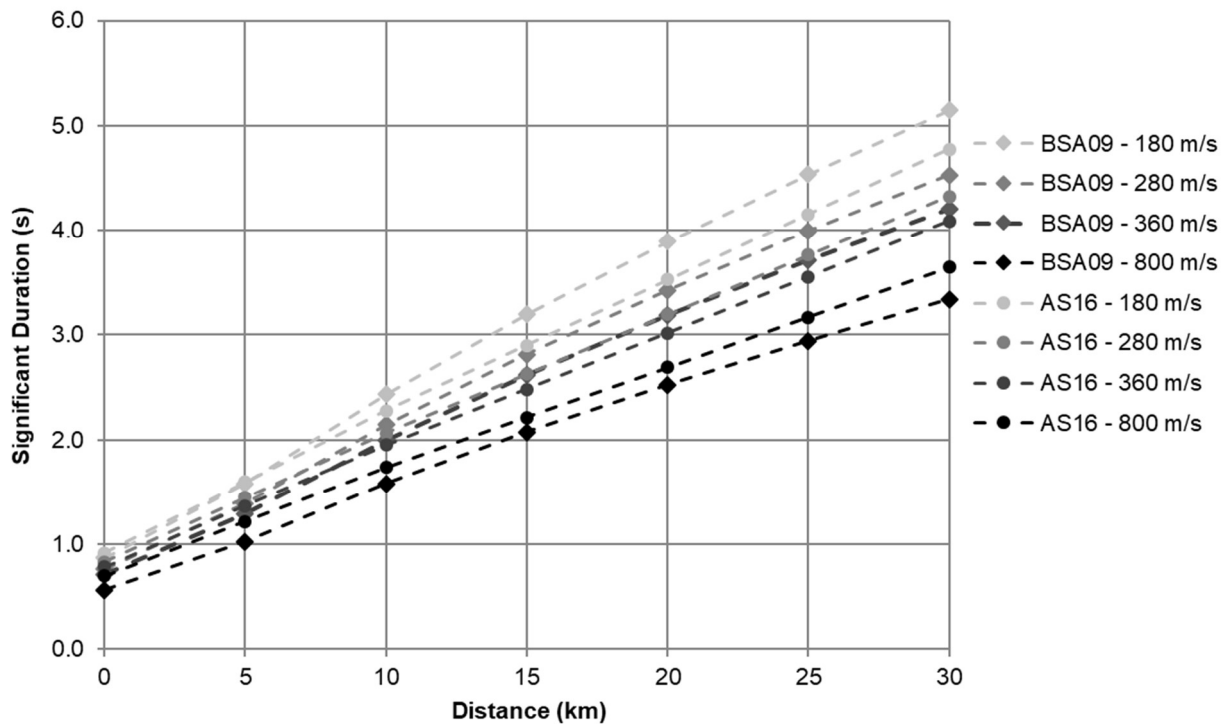


Figure A4.2.14. Estimation of the significant duration of the main shock, using prediction equations of Bommer *et al.* (2009, BSA) and Afshari & Stewart (2016, AS).

The earthquake duration indicated by the predictive models of Bommer *et al.* (2009) and Afshari & Stewart (2016) is much shorter than the value reported in several publications and websites. News agencies UZReport (2015) and RIA Novosti (2016) informed about the strong and high-frequency ground shaking that lasted for ten to twelve seconds. Similar shaking duration (12 seconds) was also reported by Geo-Storm (2013). According to Rashidov *et al.* (1974), the duration of the earthquake was much shorter and did not last more than six seconds, while Mygeos (2010) reported strong oscillations that lasted six to seven seconds. While none of these sources specified the definition of duration being reported nor the location, it could be expected that they were referring to the city of Tashkent.

A4.2.5 Collateral earthquake hazards

A4.2.5.1 Surface rupture

While no surface rupture has been documented for this seismic event, Gorshkov (1966) and Rasskazovsky (1967) reported that thin cracks appeared in dry soil after the earthquake. They were stretching mostly in the north-east direction coinciding with the

strike of the Karzhantau fault system, perpendicular to what is believed to be the causative fault (Figure A4.2.2).

A4.2.5.2 Landslides

No reports about landslide activity triggered by this earthquake have been found, in spite of landslide movements in the Tashkent area, generated mostly by rainfalls and seismic activity, being known to have occurred in the past (Juliev *et al.*, 2017). The susceptibility of this area to landslides is related to its position in a mountainous area and the presence of saturated loess, the highest hazard at the time being related to the activity of the Mingchukur landslide in the Bostanlik district northeast of Tashkent (GFDRR, 2017; Think Hazard, 2017b; Juliev *et al.*, 2017).

A4.2.5.3 Liquefaction

No reports on liquefaction effects have been found for this seismic event, despite the city of Tashkent being susceptible to this geotechnical phenomenon (Pilz *et al.*, 2015; The World Bank, 2015; Rau, 2003).

A4.2.5.4 Settlements

No settlements have been reported to have been caused by this earthquake. The mentioning of settlements in the different sources is generally associated with pre-existing conditions and the behaviour of the loess deposits present in the area, which leads to the tilting and subsiding of structures (Tuychieva, 2012; Smalley *et al.*, 2006; Juliev *et al.*, 2017; Mavlyanova, 2004; Rau, 2003).

A4.2.6 Exposed population

A4.2.6.1 Socio-economic setting

As a part of the Soviet Union in the period from 1925 to 1991, the Uzbek S.S.R. underwent significant changes in the economy, industry, education and many other spheres, which resulted in its shift from feudalism towards a socialist society. The U.S.S.R. made a special effort to improve the educational system and, by 1990, the literacy rate in Uzbekistan was as high as 98.7% (United Nations, 2004; Countries Quest, 2017; Alimova & Golovanov, 2005; Advantour, 2017). During the Soviet rule, Uzbekistan gained a considerable number of specialists and skilled workers that were trained for work in many industries, and particularly in the secondary industries. The specialized industries of the Uzbek S.S.R., such as the agro, chemical, silk, gold mining, natural gas and engineering industry contributed to the development of the Soviet Union's economy (Paramanov & Stokov, 2006; Alimova & Golovanov, 2005). Especially prosperous was the cotton industry that accounted for approximately 50% of the Uzbek S.S.R. agricultural output (Paramanov & Stokov, 2006). Even though Uzbekistan was a supplier of raw materials, some of which were high-value products like gold and rare metals, it did not benefit from their production

and sale (Alimova & Golovanov, 2005). The country did not have an opportunity to develop independently, as the entire economy of the Soviet Union was planned by the central government in Moscow (Paramanov & Strokov, 2006). As the development of the heavy and army industry was prioritized while consumer demands were neglected, the socio-economic conditions within the last few decades of the U.S.S.R. worsened (Alimova & Golovanov, 2005). The situation was aggravated by the fact that the second economy (*i.e.*, the informal sector) in the Soviet Union was growing rapidly (Trembl & Alexeev, 1993). The hardest living conditions were found in Uzbekistan, where in the year 1990 the total income of 70% of its population was below the subsistence level (Paramanov & Strokov, 2006). Following the break-up of the Soviet Union in 1991, Uzbekistan gained its independence and entered a period of larger economic, political and social instability (Paramanov & Strokov, 2006; Khalturin *et al.*, 2015; Bertelsmann Transformation Index (BTI), 2003), nevertheless subject to the fluctuations of the international markets and world recessions (Asian Development Bank, 2012).

According to the 2016 Human Development Report (United Nations, 2016), the Human Development Index (HDI) for Uzbekistan in 2015 was 0.701, while its Inequality-adjusted HDI (IHDI) was 0.590. This located Uzbekistan in the 105th place in the world's ranking, while the Netherlands ranks 7th. Table A4.2.5 compares the HDI and IHDI for both countries according to the Human Development Reports for a series of years (United Nations 1996; 2002; 2008; 2013; 2016). As values of HDI associated with the year of earthquake occurrence, *i.e.* year 1966, are not available, values from the oldest report that contains information about HDI for Uzbekistan are reported in the table. The column "Adj. HDI" provides the HDI values given in the 2016 report for previous years, adjusted for data consistency in time. While adjusted HDI values for Uzbekistan have steadily increased from the year 2000 till 2015, they are still systematically below those of the Netherlands.

Table A4.2.5. Human Development Index and Inequality-adjusted Human Development Index for Uzbekistan and the Netherlands.

Report	Data	Uzbekistan				Netherlands			
		HDI	IHDI	Rank	Adj. HDI	HDI	IHDI	Rank	Adj. HDI
1996	1993	0.679	N/A	94	N/A	0.970	N/A	9	N/A
2002	2000	0.727	N/A	95	0.594	0.935	N/A	8	0.878
2007/2008	2005	0.702	N/A	113	0.626	0.953	N/A	9	0.893
2013	2012	0.654	0.551	114	0.681	0.921	0.857	4	0.922
2016	2015	0.701	0.590	105	0.701	0.924	0.861	7	0.924

Table A4.2.6 presents a comparison between Uzbekistan and the Netherlands in terms of GDP, GDP per capita and unemployment rate. While the World Economic Outlook Database (WEO, 2017) does not report the unemployment rates for Uzbekistan, according to United Nations (2016) the unemployment rate was 10.1% in year 2015.

Table A4.2.6. Gross domestic product (GDP), GDP per capita and unemployment rate for Uzbekistan and the Netherlands, according to the World Economic Outlook Database (2017).

Indicator	Units	Uzbekistan		Netherlands	
		1992	2017	1992	2017
Gross domestic product, current prices	Billion USD	3.571	68.324	358.001	762.694
Gross domestic product per capita, current prices	USD	167.182	2,154.030	23,577.510	44,654.230
Unemployment rate	%	N/A	N/A	4.865	5.400

A4.2.6.2 Population density and distribution

Estimations of the population of Tashkent at the time of the 1966 earthquake vary between 1,092,000 and 1,500,000 people, spread over 140 km² (United Nations Statistics Division, UNSD, 1966; UNDP, 2016; Sputnik, 2016b; UNISDR, 1999; Erdik *et al.*, 2005). Erdik *et al.*, (2005) reported as well that, at the time of their writing, Tashkent had a population of approximately 2,200,000 people living in an area of 360 km². The State Committee of the Republic of Uzbekistan on Statistics (2017) and City Population (2017) report that 2,424,100 people are estimated to be residing in Tashkent at present time (2017).

A4.2.6.3 Time of day of earthquake

The earthquake struck at 05:22 am on a Tuesday, at a time in which most people are expected have been sleeping in their houses. This is likely to have had a negative impact on the number and severity of injuries, as well as the number of fatalities, considering that the greatest damage in both qualitative and quantitative terms was observed in residential buildings.

A4.2.7 Characteristics of exposed building stock

A4.2.7.1 Seismic design codes

Starting from the beginning of the 1950s, the former U.S.S.R. countries, including Uzbekistan, had a unified system of regulations for the construction industry defined by the SNiP standards. Accordingly, common standards for seismic hazard assessment and seismic design were also established (Bikhovsky *et al.*, 1960, King *et al.*, 1999; Tyagunov, 2012). While no information about the exact year associated with the introduction of seismic building design in Uzbekistan is available, it is expected that buildings in Uzbekistan followed no seismic design rules before the year 1940, when the first instructions for design of civil and industrial buildings and construction in seismic regions were established in the U.S.S.R as a whole (Bikhovsky *et al.*, 1960). The first normative document mandatory for all seismic-prone areas of the U.S.S.R. was the PSP 101-51 (1951) seismic code, whose basis on static theory led to a misconception of the actual seismic load distribution within a building. Implementation of dynamic theory in codes SN-8-57 (1958), SNiP II-A. 12-62 (1963) and SNiP II-A. 12-69 (1970) led to improvements in seismic design by introducing seismic and dynamic coefficients to reflect the intensity and

dynamic effects of an earthquake, respectively (King *et al.*, 1999). As knowledge on seismic resistant design further developed, methods for determining seismic loads changed, and were implemented with a number of new provisions in the SNiP II-7-81 (1982) seismic code.

One of the earliest seismic hazard assessments of Central Asia resulted in the compilation of seismic zoning maps of the former U.S.S.R. and adjacent territories in 1933 (Bindi *et al.*, 2012; Ullah, 2016). Developed by Mushketov (1933), these maps expressed seismicity levels by means of isoseismic lines for different intensities (Ullah, 2016). The general seismic zoning map of the U.S.S.R territories, named GSZ-37 and compiled by Gorshkov (1937), was the first prognostic map developed, as it described the hazard not only for the areas with known historical seismicity, but also for the five zones of “geological similarity” that extend from these areas (Shebalin, 1993; Pilz *et al.*, 2015; Ullah, 2016). The GSZ-37 map and the successive general seismic zoning maps (GSZ-57, GSZ-68, GSZ-78), compiled in 1957, 1968 and 1978, were all incorporated into the official seismic building codes (Ulomov, 1999; Pilz *et al.*, 2015; Shebalin, 1993). According to these maps (with the possible exception of the GSZ-37 map, for which no information is available), Tashkent was situated within a region whose maximum expected intensity was VIII. The design intensity for the buildings of Tashkent was increased from VIII to IX after the 1966 earthquake, though no changes were required in terms of structural detailing (Wright, 1971).

All the aforementioned maps were chiefly deterministic and primarily based on information from historical and instrumental seismicity (Ulomov, 1999; King *et al.*, 1999). The probability approach was introduced in an approximate manner with the GSZ-78 map (Bune & Gorshkov, 1980) that expressed the maximum shaking intensities with recurrence intervals of 100, 1,000 and 10,000 years (Bindi *et al.*, 2012; Shebalin, 1993; Ullah, 2016). This map was based on very heterogeneous data, the drawback attributed to the lack of adequate studies in the region (Ulomov, 1999). The influence of soft-soil conditions on the amplified response and seismicity of the site were not taken into account for the elaboration of this map (King *et al.*, 1999; Mavlyanova *et al.*, 2004; Thurman, 2011), which, according to Thurman (2011), led to underestimated levels of seismic hazard. The recurrence interval of the maximum expected MSK-64 intensity VIII in Tashkent is 1,000 years according to the GSZ-78 zonation map (Bindi *et al.*, 2012; Ullah, 2016; King *et al.*, 1999).

Compiled after the dissolution of the Soviet Union, the general seismic zoning (GSZ-97) map of Northern Eurasia (Ulomov, 1999) was the last seismic hazard map that covered the whole region of the former U.S.S.R. (Ullah, 2016). Originally, this map expressed seismic hazard in terms of probabilities of exceedance of macroseismic intensity levels in a 50-year period (Strakhov *et al.*, 1998). It was later converted into PGA values, and was as such included as a contribution to the Global Seismic Hazard Assessment Program (GSHAP; Giardini *et al.*, 1999) (Bindi *et al.*, 2012).

After gaining its independence in 1991, Uzbekistan established its own seismic code KMK 2.01.03-96 (1996), containing the map of general seismic zoning shown in Figure A4.2.5

(Mavlyanova *et al.*, 2004). For construction sites where intensity equal to or higher than VI is expected according to this code, seismicity is to be more precisely determined in accordance with seismic microzoning (SMZ) maps, where available. These SMZ maps account for influence of local site conditions on seismic intensity (Mavlyanova *et al.*, 2004).

MSK VIII is estimated to be the maximum expected seismic intensity for Tashkent according to the KMK 2.01.03-96 code, though it is recognized that a large part of the city has unfavourable soil conditions that could magnify the seismic effects (UNISDR, 1999; Mavlyanova *et al.*, 2004). UNISDR (1999) reported that the SMZ map for Tashkent, which accounts for the influence of these local site conditions on the seismic intensity, had been revised several times, and that the acting SMZ map at the time of their writing was that of Kasymov (1984), according to which the north-western part of the city lying on the thick unstable loess layers is associated with the maximum expected intensity IX, while the seismicity of the remaining (south-eastern) part is estimated as VIII (UNISDR, 1999; Mavlyanova *et al.*, 2004; Rashidov, 2001).

A4.2.7.2 Building typologies

Construction practices in Tashkent were largely driven by the different ideological and cultural influences to which the city was exposed throughout its history. By the time the Russian forces took over the rule of Tashkent in 1865, most of the buildings were loam (pakhsa-type) houses and wooden (synch-type) frames with adobe filler (Skjeggedal, 2012; IISEE NET, 2017; King *et al.*, 1999). The new Russian part of the city was built mostly of adobe (*i.e.* crude brick) houses whose wall-height and bay-width dimensions were greater than those observed in the old Asian part (IISEE NET, 2017; King *et al.*, 1999). By the beginning of the 20th century, a significant part of the Tashkent built-up area was composed of buildings made of one-storey air-dried materials (UNISDR, 1999; King *et al.*, 1999). After the Russian Revolution in 1917 and the subsequent rise of the Soviet Union, standardized architecture and construction practices controlled by the central Moscow authority were implemented throughout the U.S.S.R., including Tashkent (Skjeggedal, 2012; King *et al.*, 1999). Construction of one- to four-storey brick buildings started in 1932 and, by the year 1940, the dwelling area of Tashkent covered 2,800,000 m² with about 4% of multi-storey brick buildings with wooden ceilings that were constructed without consideration of any building design regulations (King *et al.*, 1999). Generally, the Soviet-era buildings constructed not only in Tashkent but throughout the Soviet Union featured high seismic vulnerability (Mavlyanova *et al.*, 2004; King *et al.*, 1999). Standards for seismic design and construction were implemented in the Soviet Union in the late 1940s and were updated several times during the U.S.S.R rule, but some authors (King *et al.*, 1999; Mavlyanova *et al.*, 2004; Thurman, 2011; Tyagunov, 2012) argue that the seismic hazard maps implemented in these standards were inadequate and had probably underestimated seismicity levels, in view of the several devastating earthquakes (*e.g.*, the 1976 and the 1984 Gazli, the 1988 Spitak, the 1995 Sakhalin and the 1991 Racha earthquake) that struck the Central Asian territories in the late 20th century (Tyagunov, 2012; King *et al.*, 1999). The workmanship was of poor-quality and there was a general absence of proper coordination of construction in Tashkent (Skjeggedal, 2012; Mavlyanova *et al.*, 2004). Even though the plan of the Soviet Union was the wide-spread

construction of multiple-storey apartment buildings, 85% percent of Tashkent people lived in one-storey buildings by the year 1958 (Skjeggedal, 2012). Later, in the 1960s and 1970s, construction of high-rise buildings was enabled and many large-panel as well as large-block frame structures were erected (King *et al.*, 1999).

Under the scope of the Risk Assessment Tools for Diagnosis of Urban Areas against Seismic Disaster project (UNISDR, 1999), information about the dwelling stock of Tashkent in terms of cost, space, number of inhabitants, number of floors and design system was collected and classified, as shown in Figure A4.2.15. At that time (year 1999) Tashkent had 36,740,000 m² of dwelling residential space inhabited by 2,120,000 people. As observed from Figure A4.2.15, the predominant construction systems were panel and masonry brick, while the least present were the monolithic reinforced concrete (RC) structures. Considerable part (around 20%) of urban housing denoted as 'other' in Figure A4.2.15 (left), consists of dwellings that were built using local weak materials, such as clay, loam, and straw. Around 50% of the dwelling stock are 1-5 storey buildings, as indicated in Figure A4.2.15 (right) (Ibragimov *et al.*, 2000; UNISDR, 1999).

The final report of the aforementioned project (UNISDR, 1999) includes the description of public buildings in Tashkent as well. Based on the report, 35% of public buildings were built before 1966 and their seismic design intensity levels range from VI to VIII. Those buildings were built mostly with brick bearing walls and walls of complex construction, while a smaller number consisted of frame buildings. After 1966, public buildings were constructed as brick buildings with complex walls, frame-panel and frame buildings with self-supporting brick walls. Most of the public buildings had 2-5 floors, although there were some structures with more than 5-stories (UNISDR, 1999).

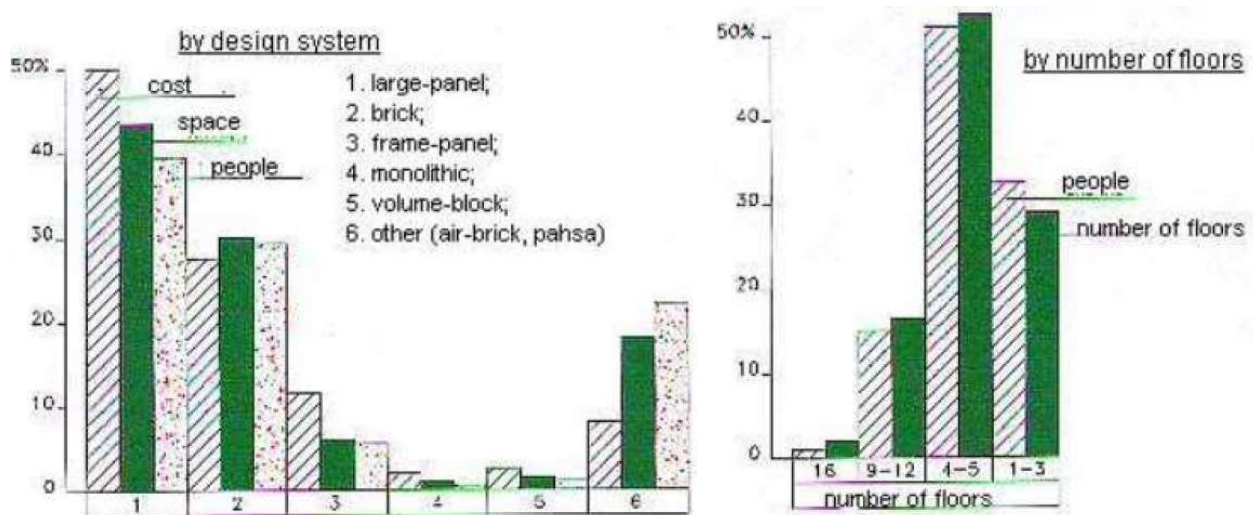


Figure A4.2.15. Characteristics of the dwelling stock of Tashkent by 1st January 1999. From UNISDR (1999).

With the purpose of carrying out a seismic hazard and risk assessment for the city of Tashkent, Erdik *et al.*, (2005) grouped residential buildings into eleven categories as per the Tashkent Zonal Scientific Research Institute of Typical and Experimental Design, according to the number of floors, structural system, material type and year of construction

(which should reflect the level of seismic design), as shown in Table A4.2.7. Their distribution within the city is shown on the map of Figure A4.2.16. As observed, prior to the 1966 earthquake, Tashkent dwelling stock consisted mostly of low-rise structures made of local materials, such as clay and sun-dried adobe houses, and brick buildings constructed without seismic considerations. At the time of the earthquake, the city had 7,206,000 m² of residential building space, a big part of which (2,970,000 m²) consisted of one-storey adobe brick houses. Large panel buildings accounted only for 4.9% of the residential area, as their construction started a few years prior to the earthquake (King *et al.*, 1999). There were no residential buildings with moment resisting frames before the 1966 earthquake, although the frame structural system had been already implemented in the buildings of public sector (IISSE NET, 2017; UNISDR, 1999).

Data available from the PAGER Inventory Database v2.0 (Jaiswal & Wald, 2008) for Uzbekistan was indirectly inferred from observations of Russian building typologies. In view of this, and given the lack of agreement with the more detailed information described above, the distribution of building typologies according to PAGER is not reproduced herein.

Table A4.2.7. Characteristics of the dwelling stock of Tashkent. Elaborated with data from Erdik *et al.* (2005), UNISDR (1999) and Foose (2005).

Group	Storeys	System/Material	Design ⁽¹⁾	Date
1-2DO66	1-2	Mostly adobe	Planned	Before 1966
1-2NEPL	1-2	Synch/pakhsa made of clay, loam, adobe	Not planned	Before 1948
1-2POS66	1-2	Fired brick	n/a ⁽³⁾	After 1966
16MONOL	16	RC monolithic	n/a ⁽³⁾	After 1980
2MNSEK	2	Multisectional/Apartments	Without seismic	Before 1966
4-5K_DO66	4-5	Brick	Without seismic	Before 1966
4-5K_SEYS	4-5	Brick	With seismic	After 1966
4-5P_POS66	4-5	Large panels	n/a ⁽³⁾	After 1966 ⁽²⁾
9-12KARK	9-12	Frame/Frame with panels	n/a ⁽³⁾	After 1980
9PAN	9	Large panels	n/a ⁽³⁾	After 1966
OBD	n/a	Volume block	n/a ⁽³⁾	After 1980

(1) The difference between Planned, Not planned, With and Without seismic design is not clearly stated in the sources.

(2) Erdik *et al.* (2005) say 1956, but this is likely to be a typo (note the name of the group saying 66, not 56).

(3) Not available in the sources. Likely to be "With seismic", based on the dates.

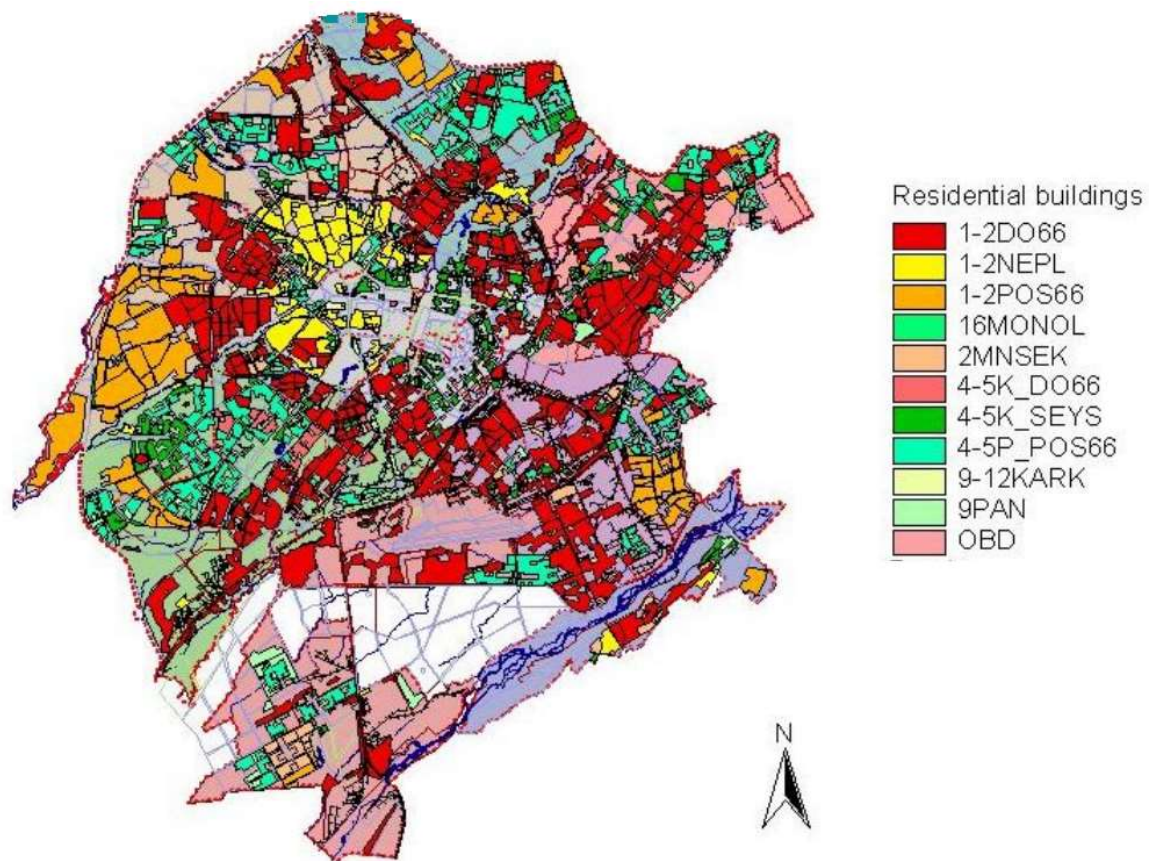


Figure A4.2.16. Map of different types of residential buildings in Tashkent. Description of typologies given in Table A4.2.7. Modified from Foose (2005).

A4.2.7.3 Prior damage and retrofit

As a large part of Tashkent is situated on thick loess soils with hydro-consolidation properties and a high level of underground water (see section A4.2.3.2), it is possible that some of its buildings located on such collapsible soils had already sustained some level of deformation and subsidence prior to the 1966 seismic event (Mavlyanova, 2004; Tuychieva, 2012; UNISDR, 1999). King *et al.* (1999) emphasized that many brick dwellings of Tashkent constructed before 1966 sustained damage due to foundation settlements. According to Mavlyanova *et al.* (2004) and King *et al.* (1999), many adobe buildings had already experienced deterioration before the 1966 seismic event.

Considering the number of earthquakes that had affected the city in the past, like those that struck in 1868, 1886 and 1946, it is probable that at the time of the 1966 seismic event some of the Tashkent buildings were already in a certain seismically-induced damaged state. In their publication, Rasskazovsky & Abdurashidov (1969) mention a few cases in which the damage induced on brick buildings by the Chatkal 1946 earthquake was aggravated by the later 1966 seismic event.

A4.2.8 Damage observations

A4.2.8.1 Damage states

Scientists of the Uzbek SSR Academy of Science made use of the GOST 6249-52 (1952) seismic scale for the description of damage levels observed on different building types of the surveyed area affected by the earthquake. However, as this seismic intensity scale does not cover the behaviour of structures designed according to seismic principles, additional criteria were adopted by the Uzbek scientists for the assessment of damage states and macroseismic intensities induced by this earthquake (Rasskazovsky, 1967).

GOST 6249-52 (1952) was the official seismic scale used in the Soviet Union until 1995 (Aptikaev & Erteleva, 2017). While its original documentation could not be found among the publicly available material, Gorshkov & Shenkareva (1960) describe it as stemming from macroseismic intensities VI through IX of the GEOFIAN seismic scale of Medvedev (1953). From this statement, it is inferred that the damage and vulnerability scales themselves are the same as for GEOFIAN. The latter is very simple and consists of three kinds of buildings: one-storey houses built in jagged stone, raw brick, adobe or similar (class A), buildings built in brick and/or stone (class B), and wooden houses (class C). The damage scale consists of four damage states:

- Light damage: fine cracks in plaster, whitewash and stoves.
- Considerable damage: cracks in plaster, stoves and partitions; splitting off of plaster fragments; fine cracks in walls; damaged chimneys, furnaces, etc.
- Destruction: large cracks in walls; breaking of masonry units; falling chimneys, cornices and parapets; partial local collapse of walls.
- Collapse: collapse of walls, ceilings and roofs in the entire building or of a considerable proportion of it; great deformation of walls.

The definition of the four seismic intensities that form the GOST 6249-52 macroseismic intensity scale as a function of the proportion of buildings of each vulnerability class that exhibit each damage state is shown in Table A4.2.8. Other additional criteria include:

- Intensity VI: formation of fine cracks (up to 1 cm) in roads and/or soils when the ground is wet; isolated cases of landslides in mountain regions.
- Intensity VII: fine cracks in dry ground; frequent cracks in wet ground; occasional landslides on steep road embankments and river banks; formation of cracks in roads in individual cases; isolated cases of dislocation of pipe joints; damage to stone fences; small landslides in mountain regions.
- Intensity VIII: cracks in the ground of several centimetres; numerous cracks on moist mountain slopes; small landslides on steep slopes; individual cases of broken pipe joints; shifting or overturning of monuments and statues; partial collapse of stone fences.
- Intensity IX: cracks in the ground up to 10 cm wide; cracks on river banks and slopes more than 10 cm wide; large number of landslides; damage to road

embankments in some cases; distortion of railroad tracks in individual cases; large number of cracks on roads and ground; frequent damage to pipes; overturning of monuments and statues; large proportion of chimneys and towers destroyed.

Table A4.2.8. GOST 6249-52 macroseismic intensities as a function of the proportion of buildings of each vulnerability class that exhibit each damage state. Elaborated from the description by Gorshkov & Shenkareva (1960). Text in grey and italics is inferred.

Int. VI	Vulnerability		
Damage	A	B	C
Light	Many	Many	-
Considerable	Individual cases	Individual cases	-
Destruction	-	-	-
Collapse	-	-	-

Int. VII	Vulnerability		
Damage	A	B	C
Light	<i>Most</i>	Most	Many
Considerable	Most	Many	Individual cases
Destruction	Individual cases	-	-
Collapse	-	-	-

Int. VIII	Vulnerability		
Damage	A	B	C
Light	<i>Most</i>	<i>Most</i>	Most
Considerable	<i>Most</i>	Most	Many
Destruction	Many	Individual cases	-
Collapse	Individual cases	-	-

Int. IX	Vulnerability		
Damage	A	B	C
Light	<i>Most</i>	<i>Most</i>	<i>Most</i>
Considerable	<i>Most</i>	<i>Most</i>	Many
Destruction	<i>Most</i>	Many	Individual cases
Collapse	<i>Many</i>	Individual cases	-

The (sub-)table corresponding to intensity VIII in Table A4.2.8 would describe the damage observed in Tashkent according to the reported maximum intensity.

A4.2.8.2 Damage statistics and description

As a result of the earthquake, the buildings located in the central and densely populated area of Tashkent sustained the greatest damage (Sputnik, 2016c). Most of these damaged buildings were made of crude brick and were not designed to withstand earthquake shaking (Mavlyanova *et al.*, 2004; King *et al.*, 1999; Bubis, 1966). Such buildings were mainly one-storey houses built in the period preceding the 1917 Russian Revolution and had either shallow (0.3 to 0.6 m) or no foundations at all (Sputnik, 2016a; King *et al.*, 1999; Bubis, 1966). Examples of crude brick houses that were severely damaged or destroyed during the 1966 earthquake are shown in Figure A4.2.17.

Considerable damage was also observed in fired brick multi-storey buildings that did not meet the rules of seismic design (Bubis, 1966), such as that shown in Figure A4.2.18. According to King *et al.* (1999) and IISSE NET (2017), there were 10 to 12 multi-storey brick buildings with wooden ceilings constructed in the 1940s and 1950s without consideration of seismic design that were damaged during the earthquake. Typical damage observed in buildings of this kind located in the epicentral area (seismic intensity VIII) include diagonal and horizontal cracking in single pier elements and staircases, as well as diagonal (x-type) cracking in bricks between apertures (King *et al.*, 1999; IISSE NET, 2017).



Figure A4.2.17. Damage to buildings made of crude brick. From Attention! Earthquake! (2017).



Figure A4.2.18. An example of damage induced on one of the fired brick buildings in Tashkent. From Bubis (1966).

According to Rasskazovsky (1967), large-panel buildings were located outside the area where the greatest damage was observed and the description of their response to the earthquake has not been found in the literature. At the time of the earthquake there were no residential frame buildings in Tashkent, but several public buildings with frame structural systems were damaged to a minor degree, mostly in the upper floors (IISSE NET, 2017; Rasskazovsky, 1967). Bubis (1966) reported that administrative and industrial buildings with RC frames and brick infills, or RC facing and finishing sustained the least damage. According to IISSE NET (2017), King *et al.* (1999) and Mavlyanova *et al.* (2004), buildings of modern construction did not collapse during this earthquake.

Qualitative and quantitative descriptions of building damage observed during the field survey of the damaged area of Tashkent were reported by Rasskazovsky (1967), according to whom buildings of GOST 6249-52 class A located in the zone of seismic

intensity VIII (Figure A4.2.13) were severely damaged during the earthquake and most of them were in need of either being repaired or demolished. Significantly less severe damage was observed on (mainly single-storey crude brick) class A buildings located within a zone of seismic intensity VII. It was also pointed out that damage to chimneys in zones of seismic intensity VII and VIII was almost identical and that around 50% of all the chimneys located in these zones were destroyed. Multi-storey fired-brick buildings located in the zone of assigned macroseismic intensity VIII were the main focus of the survey, which included the old buildings that did not meet seismic construction standards and were classified under GOST 6249-52 class B, as well as the buildings that were designed for seismicity VII and VIII.

Some examples of the building damage identified in the area of seismic intensity VIII are shown in Figure A4.2.19 through Figure A4.2.22. According to Rasskazovsky (1967), the type of cracking depicted in Figure A4.2.19 was observed in almost all residential buildings and was more often generated in the upper floors. Oblique and intersecting cracks, such as those on the wall of the building shown in Figure A4.2.20, were also more prominent in the upper floors, though they were observed in the lower floors as well. Figure A4.2.21 and Figure A4.2.22 depict the cracking that was observed on the external façades of buildings located in the area enclosed by isoseismal VIII. As Rasskazovsky (1967) pointed out, brick buildings that were built according to standards of earthquake-resistant construction sustained great damage, but such buildings were not covered by the GOST 6249-52 seismic scale. There were more than 30 brick buildings in the epicentral area which suffered severe damage even though they were designed for seismicity VIII in accordance with the seismic codes SN-8-57 and SNiP II-A. 12-62 (Rasskazovsky 1967).

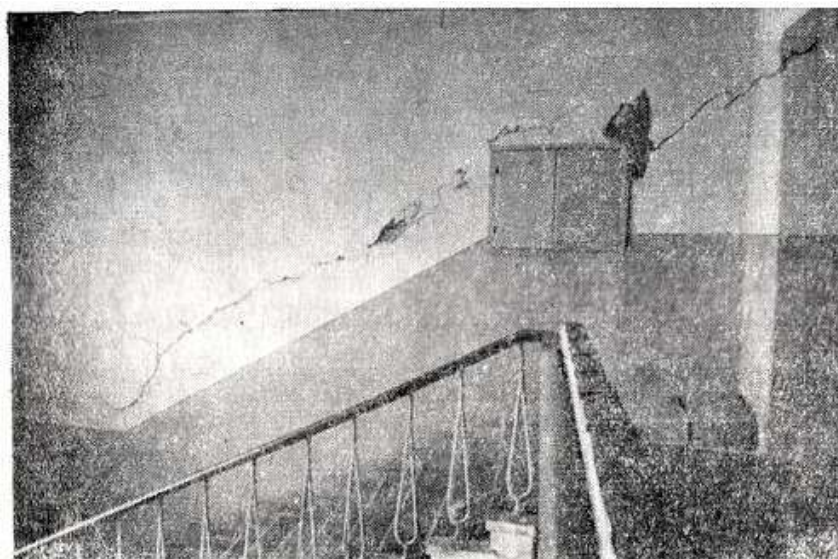


Figure A4.2.19. Cracking of walls next to staircases. Observed mostly in the upper floors of brick buildings located in the zone of seismic intensity VIII (GOST 6249-52). From Rasskazovsky (1967).



Figure A4.2.20. An example of wall cracking observed mostly in the upper floors of brick buildings located in the zone of seismic intensity VIII (GOST 6249-52). From Rasskazovsky (1967).



Figure A4.2.21. An example of masonry cracking commonly observed in buildings located in the zone of seismic intensity VIII (GOST 6249-52). From Rasskazovsky (1967).



Figure A4.2.22. An example of building located in the zone of seismic intensity VIII (GOST 6249-52) with a long horizontal crack induced below the attic floor. From Rasskazovsky (1967).

For the purposes of building restoration planning, Rasskazovsky & Abdurashidov (1969) classified observed instances of building damage into four different categories summarized in Table A4.2.9. Damage of the first category accounted for localized and easily repairable failures observed in masonry buildings. The second category of damage is associated with brick cracking that led to loss of bearing capacity of supporting construction, while bonds between the walls remained either intact or featured localized failures. According to Rasskazovsky & Abdurashidov (1969), such degree of damage was observed in most of the affected buildings. Damage categories three and four are both related to wall-to-wall connection failures, which in the former case negatively affected the integrity of building construction while in the latter case also resulted in considerable displacements of walls and consequently in the complete collapse of one-storey houses or the collapse of upper floors of multi-storey buildings. As indicated by Rasskazovsky & Abdurashidov (1969), as well as other authors (e.g. IISSE NET, 2017; Rashidov *et al.*, 1974), damage induced to multi-storey buildings was usually concentrated in the upper floors. According to Savarensky (1966) and Ulomov (2016), this is directly related to the high-frequency content of this earthquake.

Table A4.2.9. Categorization of damage sustained by Tashkent buildings during the 1966 seismic event. From Rasskazovsky & Abdurashidov (1969).

Category	Type of damage observed	Degree of damage	Type and quantity of affected buildings
1	Local failures in masonry concentrated in former doorways and embrasures that were later filled up with brick; collapse of architectural decorations, cornices, parapets, porticos, chimneys, plasters and relief ornaments of walls and ceilings	Slight	N/A
2	Type 1 damage + damage to supporting walls and piers due to cracking observed mainly at the joints of brickwork; type of cracks: diagonal (30 to 60 degrees inclined), intersecting and horizontal	Loss of bearing capacity of supporting walls and piers while keeping the general structural integrity intact	Observed in more than 50% of all the wrecked buildings; one-story and multi-story buildings of old and new construction were affected; damage to multistory buildings was mostly concentrated in the upper floors
3	Type 2 damage + failure of interconnections between perpendicular walls due to cracking along the wall junctions	Loss of bearing capacity of supporting walls and piers and loss of general structural integrity of building	Detected in ~ 25% of all the wrecked buildings; mostly observed in one-story buildings for which no anti-seismic construction measures have been carried out and in a number of multi-story buildings of old construction
4	Type 3 damage + considerable deflection of walls from the vertical plane and collapse of separate walls or their parts	Complete or partial collapse of building	Observed in one-story adobe buildings and in rare cases in upper stories of multistory buildings

When it comes to the total number of buildings affected by this earthquake, greatly diverging estimates have been reported by different authors. While Gangler *et al.* (2012) claim that 25% of all the buildings in Tashkent were destroyed by the earthquake and The New York Times mentions one fifth of the city having been “levelled”, the Deseret News (1984) reported that as much as 80% of the city was demolished. According to Lovell-Hoare & Lovell-Hoare (2013), the percentage of buildings damaged by this seismic event was approximately 70%. With respect to the residential area of Tashkent, Wright (1971) reported that one-third of the area was destroyed and that the buildings of another one-sixth of the area were damaged beyond repair. Mavlyanova *et al.* (2004) and IISEE NET (2017) reported that, as a consequence of the earthquake, the dwelling area of Tashkent reduced from 7.2 million m² to 2.8 million m², which would correspond to a 60% of the dwellings having been destroyed or demolished. They indicate a much larger demolished dwelling area than that reported by Sputnik (2016a) and UNISDR (1999), who estimated 2 million m² and 2.4 million m², respectively. According to UNISDR (1999) and as shown in Table A4.2.10, the dwelling area covered with one-storey adobe houses suffered the greatest damage.

In the cases in which the actual number of buildings is mentioned, the divergence is equally large. The estimation varies from 28,000 buildings reported by Earthquake-Report

(2013) and Von Hake & Cloud (1966) to approximately 96,000 apartments reported by Wright (1971). Sputnik (2016c) and Flyingnorth (2012) report that complete or partial destruction was sustained by more than 36,000 residential houses and public buildings. According to Skjeggedal (2012) the number of destroyed homes was 78,000, while according to Rasskazovsky & Abdurashidov (1969) the number of destroyed flats exceeds 84,000. Ruthven & Nanji (2004) reports 95,000 homes destroyed by this earthquake. Besides residential houses, the earthquake is also reported to have damaged/destroyed 245 industrial buildings, more than 236 administrative buildings, 700 trade and public catering objects, 181 educational institutions, 26 public utility buildings, 118-185 medical facilities, 36 cultural and community centres and 225 nurseries (RIA Novosti 2016; Sputnik, 2016a; Wright 1971).

Table A4.2.10. Comparison of Tashkent residential space before the 1966 earthquake (“total”) and residential space destroyed. From UNISDR (1999).

Building type	Dwelling space		
	Total	Destroyed	Destroyed
	(million m ²)		%
1-story, adobe	2.970	1.7	57.24
1-story, brick	1.880	0.4	21.28
2-story, brick	0.796	0.2	25.13
multistory (3-5 floors)	1.560	0.1	6.41
Total	7.210	2.4	33.29

Discrepancies in the number of instances of damage can be due to various reasons. First, the secrecy of the Soviet authorities to reveal the final figures of casualties highlighted by Gurenko & Dumitru (2009) is likely to have affected the reports on damage to buildings as well. Second, it is always hard to be certain of the meaning of the word “destroyed” in the context of post-earthquake assessment. While, according to the GOST 6249-52 scale, the damage state labelled as “destruction” would correspond to one degree less than that of complete collapse, it is not possible to be certain that the word has always been applied consistently. With respect to this, Rasskazovsky & Abdurashidov (1969) reported that there were actually no cases of completely destroyed buildings, although, according to their words, significant damage had been observed in all of the buildings located in the epicentral zone. Finally, there is the issue of translation, as a large proportion of the information is in Russian or has been derived from original data in Russian. The subtleties that make the difference between “destroyed” or “heavily damaged” can be lost in translation.

Not only buildings suffered the consequences of this earthquake. According to UNISDR (1999) and Rashidov *et al.* (1974), considerable damage was induced to underground structures and particularly to pipelines lying in saturated soft soils, though, on the contrary, RIA Novosti (2011) reports that water and power supply (systems) were not affected by the earthquake. According to Fergana (2006), the telecommunication system was completely damaged. There were as well some cases of road surface cracking induced by

the earthquake, while some parts of the roads located in the vicinity of damaged pipelines sustained subsidence (UNISDR, 1999).

As a final remark, it is relevant to note that the observed damage was the result of the cumulative effect of the main seismic event on 25th April 1966 and a large number of aftershocks that followed (Bommer *et al.*, 2001; Von Hake & Cloud, 1966).

A4.2.8.3 Observed weaknesses

At the time of the earthquake some of the main weaknesses of Tashkent buildings were related to the presence of buildings of old construction that were not built according to seismic-resistant design and to the poor quality of workmanship and construction materials.

The most damaged part of the building stock consisted of one-storey adobe houses that did not meet any seismic requirements and had either shallow or no foundations at all. Some of the weaknesses of multi-storey buildings made of fired brick and constructed without consideration of seismic design were: weak connections between floors and walls, unreinforced corners and joints of the walls and absence of seismic collars or flanges (Bubis, 1966).

According to King *et al.* (1999) and Mavlyanova *et al.* (2004), the occurrence of damage to the older brick buildings was highly related to complicated configurations in design, insufficient number of joints and belts, large basements located under parts of buildings, and irregular and asymmetrical configurations of walls. King *et al.* (1999) also point out that modern brick buildings that were designed according to SN-8-57 (1958) and SNiP II-A.12-62 (1963) seismic codes had generally performed well during the past earthquakes in Tashkent although they did have weaknesses associated with low quality of construction material and workmanship, mismatch between centre of rigidity and centre of mass, irregular configuration of load-bearing walls, and stiffness variations in the longitudinal and transverse directions. The brick dwelling stock built prior to the earthquake and of series 1-310 (Soviet designation for this particular kind of buildings) built from 1954-1963 did not have interior longitudinal walls or RC cores (King *et al.*, 1999; Mavlyanova *et al.*, 2004).

Damage induced to underground structures, including pipelines, occurred on places of rigid (flange and weld) connections, which feature higher seismic vulnerability compared to flexible joint connections (Rashidov *et al.*, 1974; UNISDR, 1999).

A4.2.8.4 Damage distribution

The greatest damage induced by this earthquake was sustained by the buildings situated in the centre of the city, on the fourth terrace of the Chirchik River. According to Bubis (1966), this area is located on more than 11 m thick loess soils, which are generally known to be capable of amplifying seismic ground motions (Wang *et al.*, 2017). However, neither Bubis (1966) nor any other author have made any inferences with respect to whether such soil conditions have influenced the spatial distribution of damage due to this earthquake.

Confrontation of the map of macroseismic intensity for the 1966 earthquake (Figure A4.2.13) and the seismic microzonation map of Figure A4.2.6, which represents the corollary of the descriptions of the soil conditions by Pilz *et al.* (2015), may explain the intensity VII isoseismal stretching slightly to the north-west, in relative terms with respect to its more moderate extension to the south-east, as smaller intensities are expected in the latter. Moreover, the shape of the VIII isoseismal on its north edge may be related to the concentration of one- to two-storey clay/loam/adobe buildings (1-2NEPL) in that area of the city, as depicted in Figure A4.2.16. However, the noticeable stretching of intensity VII towards the north-east cannot be easily explained with the available information.

The richness of the ground motion in the 2-3 Hz (0.33-0.50 s) range, as described by Khakimov & Nurtaev (2004), together with the fundamental frequencies of all soil types described by Pilz *et al.* (2015) for Tashkent lying in said range, are likely to have contributed to the low-rise buildings being the ones most affected by this earthquake.

A4.2.9 Casualties and losses

A4.2.9.1 Numbers of dead and injured

Most of the sources reported ten people killed by this seismic event (Lovell-Hoare & Lovell-Hoare, 2013; Earthquake-Report 2013; Gupta, 2009; Utsu, 1990; Von Hake & Cloud, 1966). On the other hand, the Central Asian and the Russian news agencies and websites reported that the number of fatalities was eight, which was adopted as the official death toll (Sputnik, 2016a; Sputnik, 2016c; RIA Novosti, 2011, 2016; Geo-Strom, 2013; Fergana, 2006). An article in The New York Times (1984) states that the official death toll was 15 people instead. The most extreme estimate rises up to 0.5% of the city's population (Sims, 2007), which would be equivalent to 5,500 to 7,500 people, but it is noted that these numbers appear to include at least hundreds of people who died from traumatic stress and heart attacks during the aftershock sequence (RIA Novosti 2011, 2016; Fergana, 2006, Attention! Earthquake! 2017), and it is not clear what the original source was. These large discrepancies and uncertainties in the number of reported deaths are related to the secrecy of the Soviet authorities who never actually revealed the real figures, as pointed out by Hutchings (1987) and Gurenko & Dumitru (2009).

According to the Public Library of Science (PLOS, 2013), four men died for every five women, while Sims (2007) reported that there were 20% more women than men affected by this earthquake.

It was reported by the Russian news agencies (Sputnik 2016a; RIA Novosti 2011, 2016; Geo-Storm, 2013) that around 200 people with various types of injuries were hospitalized. According to Von Hake & Cloud (1966), Earthquake-Report (2013) and Utsu (1990), the number of injured people was 1,000.

Sputnik (2016c), Flyingnorth (2012) and RIA Novosti (2016) report that more than 78,000 families, accounting for more than 300,000 people, were left homeless. Most of the remaining sources have also reported around 300,000 homeless people (Sputnik, 2016b; Sputnik, 2016a; Ruthven & Nanji, 2004; The New York Times, 1984; UNDP, 2016; Bommer *et al.*, 2001, Leroy & Gracheva, 2013; Pilz *et al.*, 2015). A different estimate was reported by Earthquake-Report (2013), Von Hake & Cloud (1966) and Gurenko & Dumitru (2009), who claim that around 100,000 people lost their homes. The number of people affected by this earthquake, according to Gupta (2009), Thurman (2011) and GFDRR (2017), was around 100,000.

The International Disaster Database (EM-DAT) reports 10 deaths and 100,000 people affected by this earthquake but does not report any case of injury.

A4.2.9.2 Causes of casualties

Even though the official death toll after the Tashkent 1966 earthquake was 8-15, it was reported by Geo-Storm (2013), Fergana (2006) and RIA Novosti (2016) that hundreds of people died from traumatic stress and especially from heart attacks in the period of aftershocks.

According to RIA Novosti (2016), 55% of injuries were the result of panic and fear which led to impulsive behaviour of people, some of whom jumped out of the upper floors of buildings. It was also reported that 35% of injuries were caused by falling debris (plaster, bricks, *etc.*) and falling of household items, while the rest (10%) of injuries were caused by wall and roof collapses (Ria Novosti, 2016).

A4.2.9.3 Estimates of economic losses

Based on what was reported in the International Disaster Database (EM-DAT), as well as Gupta (2009), Thurman (2011) and GFDRR (2017), this seismic event resulted in an economic loss of 300 million USD. Gurenko & Dumitru (2009) emphasize that the value of 300 million USD corresponds to economic losses estimated at the time of the event, while when adjusted for inflation to the year 2008 the loss would correspond to around 2 billion USD.

Thurman (2011) pointed out that devastating Central Asian earthquakes, such as the 1966 Tashkent event, induced not only direct but also considerable amount of indirect economic losses. The latter are related to the loss of manufacturing capacity, damaged distribution channels, reduced revenues, and unemployment, among others. Rasskazovsky & Abdurashidov (1969) reported that the earthquake interrupted the normal operation of governmental institutions.

A4.2.10 Discussion and conclusions

This **M5.2** earthquake occurred on 25th April 1966, at 23.22 UTC (26th April, 05.22 local time) and was one of the most destructive earthquakes known to have struck the Uzbek capital, Tashkent. It had moderate magnitude, but because of the shallow epicentral depth it provoked severe ground shaking. The most affected was the central Tashkent area covering 10-15 km², where the estimated macroseismic intensity was VIII. The earthquake had high-frequency content and the vertical component of ground motion was much stronger than the horizontal ones. The main shock was followed by a sequence of aftershocks that lasted for more than a year and were responsible for additional damage to buildings and an increased number of heart-attack and stress-related casualties.

As a result of the earthquake, a considerable part of the city was severely damaged or destroyed, with reported numbers of buildings affected ranging between 28,000 and 96,000. The greatest damage was observed on one-storey houses, built of local materials in the 19th century. Significant damage was also sustained by multi-storey brick buildings, mostly in the form of cracks on the upper floors. At the time of the earthquake most of the Tashkent building stock was constructed without consideration of seismic design, and this was one of the main reasons for the devastating consequences of this seismic event, together with many of the buildings having most likely been previously weakened by soil settlements and preceding seismic events.

The official death toll was 8-15 people, but the exact number of deaths is not known since Soviet officials kept it in secrecy. Estimates of unknown reliability rise up to 5,500-7,500 deaths, though these numbers are likely to include at least hundreds of elderly people who died from traumatic stress and heart attacks, particularly during the strongest phase of the aftershock series. Hundreds of people were injured, and the total number of affected people appears to have exceeded 300,000. The earthquake resulted in economic losses of approximately 300 million USD (in 1966 US dollars).

A4.2.11 References

A4.2.11.1 Bibliography

Afshari, K. & J. P. Stewart (2016). Physically parameterized prediction equations for significant duration in active crustal regions. *Earthquake Spectra* **32**(4), 2057-2081.

Alimova, D. A. & A. A. Golovanov (2005). Political changes and State formation: Uzbekistan. In Adle, C. (ed.): *History of civilizations of Central Asia (Towards contemporary civilization: from the mid-nineteenth century to the present time)*. UNESCO Publishing, Paris, France.

Aptikaev, F.F. & O.O. Erteleva (2017). A new generation Russian seismic scale. *Seismic Instruments* **53**(2), 146-154.

Artikov, T. U., R. S. Ibragimov, T. L. Ibragimova, M. A. Mirzaev & M. T. Artikov (2015). Revealing the seismicity increase in interrelationships in various seismic zones in Uzbekistan as a case study. *Geodesy and Geodynamics* **6**(5), 351-360.

Artikov, T. U., R. S. Ibragimov, T. L. Ibragimova & M. A. Mirzaev (2016). Study of modern seismic zoning maps' accuracy (case for Eastern Uzbekistan). *Geodesy and Geodynamics* **7**(6), 416–424.

Bikhovsky, V.A, J.I. Goldenblat & J.L. Korchynski (1960). Design of earthquake-proof building structures in the USSR. *Proceeding of the Second World Conference on Earthquake Engineering*, July 11-18, Tokyo and Kyoto, Japan. Available online at (last accessed 5th January 2018):
http://www.iitk.ac.in/nicee/wcee/article/vol.3_session4_1743.pdf

Bindi, D., K. Abdrakhmatov, S. Parolai, M. Mucciarelli, G. Grünthal, A. Ischuk, N. Mikhailova & J. Zschau (2012). Seismic hazard assessment in Central Asia: Outcomes from a site approach. *Soil Dynamics and Earthquake Engineering* **37**, 84–91.

Bommer, J.J., G. Georgallides & I.J. Tromans (2001). Is there a near-field for small-to-moderate magnitude earthquakes? *Journal of Earthquake Engineering* **5**(3), 395-423.

Bommer, J.J., P.J. Stafford & J.E. Alarcón (2009). Empirical equations for the prediction of the significant, bracketed, and uniform duration of earthquake ground motion. *Bulletin of the Seismological Society of America* **99**(6), 3217–3233.

Bubis, I.I. (1966). Engineering analysis of the aftereffects of the Tashkent earthquake, April 26, 1966. *Soil Mechanics and Foundation Engineering* **3**(5), 339-344.

Bune, V.I. & G.P. Gorshkov (1980). Seismic zonation of U.S.S.R. (in Russian). Nauka, Moscow, U.S.S.R., 307 pp.

Dubinchuk, V. T. (1993). Radon as a precursor of earthquakes. In: *Isotopic and geochemical precursors of earthquakes and volcanic eruptions. Proceedings of an Advisory Group Meeting. International Atomic Energy Agency (IAEA)*, 9-12 September 1991, Vienna, Austria. Available online at (Last accessed: 28th September 2017):
http://www-pub.iaea.org/MTCD/Publications/PDF/te_726_web.pdf

CEN (2004). *Eurocode 8: Design of Structures for Earthquake Resistance-Part1: General Rules, seismic actions and rules for buildings*. European Committee for Standardization, Brussels, Belgium.

Erdik, M., T. Rashidov, E. Safak & A. Turdukulov (2005). Assessment of seismic risk in Tashkent, Uzbekistan and Bishkek, Kyrgyz Republic. *Soil Dynamics and Earthquake Engineering* **25**(7-10), 473-486.

Foose, M. P. (2005). USGS Activities to evaluate and mitigate earthquake hazards. *Proceedings of the Second Gulf Seismic Forum (GSF II)*, Al Ain, United Arab Emirates. Available online at:
http://www.meseisforum.net/Docs/Cyber_Journals/Volume_4_2006/GSFII-%20Proceedings/FOOSE.pdf. Last accessed 28th September 2017.

Gangler, A., H. Nagler, F. Schwartze & E. Ribbeck (2012). *Tashkent in change - transformation of the urban structure*. University of Stuttgart. Available at (Last accessed 28th September 2017):
https://www.uni-stuttgart.de/si/stb/stb_forschung/taschkent/Taschkent%2008%2012%2002%20EN_s.pdf

Giardini, D., G. Grünthal, K. M. Shedlock & P. Zhang (1999). The GSHAP global seismic hazard map. *Annali di Geofisica* **42**(6), 1225–1228.

Gorshkov, G.P. (1937). The seismic map of the U.S.S.R (In Russian). In: *Bolshoy Soviety Atlas Mira*, 93, Moscow, U.S.S.R.

Gorshkov, G.P. (1966). Землетрясение в Ташкенте - геологические условия возникновения (Earthquake in Tashkent - geological conditions of its occurrence, in Russian). Journal of the Russian Academy of Sciences 'Priroda' (Nature, in Russian) № 9, 112-114. Available at: <http://neotec.ginllras.ru/comrus/gorshkov-g-p-1966-zemletryasenie-v-tashkente-geologicheskie-usloviya-vozniknoveniya.pdf>. Last assessed: 28th September 2017.

Gorshkov, G.P. & G.A. Shenkareva (1960). On the correlation of seismic scales – USSR. *Transactions of the Institute of Earth Physics of the Academy of Sciences USSR* 1(168), 44-64. Translation into English by the United States Joint Publications Research Service, New York, USA. Available online at: <http://www.dtic.mil/dtic/tr/fulltext/u2/a362451.pdf>. Last accessed: 20th February 2018.

GOST 6249-52 (1952). Шкала для определения силы землетрясения в пределах от 6 до 9 баллов (Scale for determining earthquake intensity from VI to IX, in Russian). Moscow, U.S.S.R.

Gupta, S. (2009). *Central Asia and Caucasus Disaster Risk Management Initiative (CAC DRMI)*. Risk Assessment for Central Asia and Caucasus Desk Study Review. Available at: http://www.unisdr.org/files/11641_CentralAsiaCaucasusDRManagementInit.pdf. Last assessed: 28th September 2017.

Gurenko, E. & D. Dumitru (2009) *Mitigating the adverse financial effects of natural hazards on the economies of Central Asia*. A Study of Catastrophe Risk Financing Options. Available at: http://siteresources.worldbank.org/FINANCIALSECTOR/Resources/CACDRM-Component2_CatRiskFinancingReport.pdf. Last assessed 28th September 2017.

Hauksson, E. (1981). Radon content of groundwater as an earthquake precursor: evaluation of worldwide data and physical basis. *Journal of Geophysical Research* 86(B10), 9397-9410.

Hutchings, R. (1987). *Soviet secrecy and non-secrecy*. Barnes & Noble Books, Totowa, New Jersey, USA.

Ibragimov, R.S., B. S. Nurtaev & S. A. Khakimov (2000). Methodology of assessment and mitigation of urban seismic risk, taking into account variability of seismic hazard parameters. *Proceeding of the 12th World Conference on Earthquake Engineering*, 30 January – 4 February, Auckland, New Zealand. Available at: <http://www.iitk.ac.in/nicee/wcee/article/2526.pdf>. Last accessed: 28th September 2017.

Jaiswal, K.S. & D.J. Wald (2008). *Creating a global building inventory for earthquake loss assessment and risk management*. U.S. Geological Survey, Open-File Report 2008-1160. Available online at: <https://pubs.usgs.gov/of/2008/1160/>. Last accessed: 7th July 2017.

Juliev, M., A. Pulatov & J. Hübl (2017). Natural hazards in mountain regions of Uzbekistan: A review of mass movement processes in Tashkent province. *International Journal of Scientific & Engineering Research* 8(2), 1102-1108.

Kasymov, S.M. (1984). Seismic microzonation map of Tashkent. Nauka, Moscow, USSR.

Khakimov, S.A. & B.S. Nurtaev (2004). Assessment of seismic hazard and vulnerability of different building types in central asia for antiseismic strengthening implementation. *Proceedings of the 13th World Conference on Earthquake Engineering*, August 1-6, Vancouver, Canada. Available online at: http://www.iitk.ac.in/nicee/wcee/article/13_396.pdf. Last assessed 28th September 2017.

Khalturin, V.I., P.G. Richards & W.-Y. Kim (2015). *Seismicity, recent seismic observations and seismological institutes in post-Soviet Central Asian Republics*. Lamont-Doherty Earth Observatory of Columbia University, Open Report, NY, USA. Available at (last assessed 28th September 2017): http://www.ideo.columbia.edu/~richards/my_papers/Central_Asia_report.pdf.

King, S.A., V.I. Khalturin & B.E. Tucker (eds.) (1999). *Seismic Hazard and Building Vulnerability in Post-Soviet Central Asian Republics*. Springer Science & Business Media, Dordrecht, the Netherlands. Parts of the book available online at (last accessed 28th December 2017): <https://docslide.net/documents/seismic-hazard-and-building-vulnerability-in-post-soviet-central-asian-republics.html>.

KMK 2.01.03-96 (1996). *Строительные нормы и правила. Строительство в сейсмических районах (Norms and regulations for construction in seismic regions, in Russian)*. Committee of the Republic of Uzbekistan on architecture and construction, Tashkent, 125 pp.

Koulakov, I. & S.V. Sobolev (2006). A tomographic image of Indian lithosphere break-off beneath the Pamir–Hindukush region. *Geophysical Journal International* **164**(2), 425–440.

Kumar, N., G. Rawat, V. M. Choubey & D. Hazarika (2013). Earthquake precursory research in western Himalaya based on the multi-parametric geophysical observatory data. *Acta Geophysica* **61**(4), 977–999.

Leroy, S.A.G. & R. Gracheva (2013). Historical Events. In: Bobrowsky, P. T. (Ed.): *Encyclopedia of Natural Hazards*. Springer, the Netherlands, 452–471.

Lomnitz, C. (1974). *Global tectonics and earthquake risk*. Elsevier Scientific Publishing Company, Amsterdam, the Netherlands.

Lovell-Hoare, S. & M. Lovell-Hoare (2013). Uzbekistan. Bradt Travel Guides LTD, UK.

Magri, L., M. Mucciarelli & D. Albarello (1994). Estimates of site seismicity rates using ill-defined macroseismic data. *Pure and Applied Geophysics* **143**, 618–632.

Mavlyanova, N., R. Inagamov, H. Rakhmatullaev & N. Tolipova (2004). Seismic code of Uzbekistan. *Proceedings of the 13th World Conference on Earthquake Engineering, August 1-6, Vancouver, Canada*. Available online at: http://www.iitk.ac.in/nicee/wcee/article/13_1611.pdf. Last accessed 28th September 2017.

Mavlyanova, N. (2004). Earthquake triggered collateral hazards on the territory of Uzbekistan. *Proceedings of the 13th World Conference on Earthquake Engineering, August 1-6, Vancouver, Canada*. Available online at: http://www.iitk.ac.in/nicee/wcee/article/13_1588.pdf. Last accessed 28th September 2017.

McCann, T., B. Nurtaev, V. Kharin & M. Valdivia-Manchego (2013). Ordovician-Carboniferous tectono-sedimentary evolution of the North Nuratau region, Uzbekistan (Westernmost Tien Shan). *Tectonophysics* **590**, 196–213.

Medvedev, S.V. (1953). A new seismic scale. *Transactions of the Institute of Earth Physics of the Academy of Sciences USSR* **21**, 110.

Medvedev, S., W. Sponheuer & V. Karnik (1965). *Seismic intensity scale, MSK 1964*. Academy of Sciences of the U.S.S.R., Soviet Geophysical Community, 13 pp.

Mikhailova, N.N., A.S. Mukambayev, I.L. Aristova, G. Kulikova, S. Ullah, M. Pilz & D. Bindi (2015). Central Asia earthquake catalogue from ancient time to 2009. *Annals of Geophysics* **58**(1), S0102.

Mirjalilov, A., K. Sudo, T. Rashidov, S. Khakimov, R. Shaw & S. Tyagunov (2000). UNISDR Project in Tashkent, Uzbekistan. *Proceedings of the 12th World Conference on Earthquake Engineering, 30 January – 4 February, Auckland, New Zealand*. Available at (Last accessed 28th September 2017): <http://www.iitk.ac.in/nicee/wcee/article/2540.pdf>.

Mushketov, D. I. (1933). *Опыт сейсмического районирования СССР (Experience with seismic zoning in the USSR, in Russian)*. Tr. Seismogeol. Inst. of Academy of Sciences of the U.S.S.R, 1-17.

Negmatullaev, S., A. Ischuk & Y. Potekhin (1999). Seismic hazard and building vulnerability in Tajikistan. In King, S. A., V. I. Khalturin & B. E. Tucker (eds.): *Seismic Hazard and Building Vulnerability in Post-Soviet Central Asian Republics*. NATO ASI Series (2. Environment), Springer, Dordrecht, **52**, 107-125.

Nurtaev, B. (2005). Earthquake and landslide hazard in Uzbekistan and countermeasures. *Proceedings of the 2nd Core Member Meeting (CMM2) for Asia-Pacific Region, Disaster Reduction Hyperbase (DRH) project, November 14-15, Kathmandu, Nepal*. Available online at: <http://drh.edm.bosai.go.jp/Project/Phase1/CMM2/CMM2-14%20Nurtaev.pdf>. Last accessed: 29th December 2017.

Otajanov, D. & B. Shibazaki (2012). Modelling earthquake cycles in thrust zones in Central Asia. *Proceedings of the International conference on Complexity in earthquake dynamics: From nonlinearity to earthquake prediction and seismic stability*, January 25-26, Tashkent, Uzbekistan. Available online at (last accessed 28th September 2017): https://www.researchgate.net/publication/308780652_Proceedings_of_the_international_conference_on_Complexity_in_earthquake_dynamics_From_nonlinearity_to_earthquake_prediction_and_seismic_stability.

Paramanov, V. & A. Stokov (2006). *Disintegration of the USSR and its consequences for Uzbekistan: economic and social spheres*. Conflict Studies Research Centre, Defence Academy of the United Kingdom. Available at https://www.files.ethz.ch/isn/92587/06_Apr.pdf. Last accessed: 28th September 2017.

Pilz, M., T. Abakanov, K. Abdrakhmatov, D. Bindi, T. Boxberger, B. Moldobekov, S. Orunbaev, N. Silacheva, S. Ullah, S. Usupaev & P. Yasunov (2015). An overview on the seismic microzonation and site effect studies in Central Asia. *Annals of Geophysics* **58**(1).

PSP 101-51 (1951). Положение по строительству в сейсмических районах (Regulations for construction in seismic regions, in Russian). The State Committee for construction of the Council of Ministers of the U.S.S.R.

Rashidov, T., V.T. Rasskazovsky & K. S. Abdurashidov (1974). Consequences of Tashkent earthquake 1966 and testing of restored brick walls. *Proceedings of the 5th World Conference on Earthquake Engineering*, June 25-29, Rome, Italy. Available at (Last accessed 28th September 2017): http://www.iitk.ac.in/nicee/wcee/article/5_vol1_508.pdf

Rashidov, T., L. Plotnikova & S. Khakimov (1999). Seismic hazard and building vulnerability in Uzbekistan. In King S.A., V.I. Khalturin & B.E. Tucker (eds.): *Seismic hazard and building vulnerability in post-Soviet Central Asian republics*. NATO ASI Series (2. Environment), Springer, Dordrecht **52**, 147-180.

Rashidov, T. (2001). Engineering and seismometric service in the buildings of Tashkent and Tashkent regions. In Erdik, M., M. Celebi, V. Mihailov & N. Apaydin (eds.): *Strong motion instrumentation for civil engineering structures*. Springer Science+Business Media, Dordrecht, the Netherlands.

Rashidov T., E. Kuzmina, A. Turdukulov, A. Khudaybergenov & I. Rashidov (2007). Seismic hazard assessment for the city of Tashkent. *Proceedings of the Natural cataclysms and global problems of the modern civilization workshop*, September 24-27, Baku, Azerbaijan. Available at (Last accessed 18th September 2017): <http://www.ias-icsd.org/resources/Symposium-Natural+Cataclysms+and+Global+Problems+of+the+Modern+Civilisation+-ICSD-IAS.pdf>

Rashidov, T. (2012). Problems and practical questions of decrease seismic safety in the conditions of Uzbekistan. *Proceedings of the International conference on Complexity in earthquake dynamics: From nonlinearity to earthquake prediction and seismic stability*, January 25-26, Tashkent, Uzbekistan. Available online at (Last accessed 28th September 2017): https://www.researchgate.net/publication/308780652_Proceedings_of_the_international_conference_on_Complexity_in_earthquake_dynamics_From_nonlinearity_to_earthquake_prediction_and_seismic_stability

Rasskazovsky, V.T. (1967). *Последствия ташкентского землетрясения (Consequences of the Tashkent earthquake*, in Russian). Institute of Mechanics and Earthquake Resistance of Structures, Academy of Sciences of the Uzbek SSR, Tashkent. Parts of the book available at: <http://mytashkent.uz/2010/10/30/posledstviya-tashkentskogo-zemletryaseniya/> . Last accessed 28th September 2017.

Rasskazovsky, V.T. & K. S. Abdurashidov (1969). Restoration of stone buildings after earthquake. *Proceedings of the Fourth World Conference on Earthquake Engineering*, January 13-18, Santiago de Chile. Available at: http://www.iitk.ac.in/nicee/wcee/article/4_vol3_B6-83.pdf. Last accessed 28th September 2017.

Rau, J. L. (2003). Environmental and urban geology of selected cities in central, south-west and south Asia. In United Nations Economic and Social Commission for Asia and the Pacific (ed.): *The Ground Beneath Our Feet: A factor in Urban Planning. Atlas of Urban Geology* **14**, 488 pp.

Ruthven, M. & A. Nanji (2004). *Historical Atlas of Islam*. Harvard University Press. Cambridge, Massachusetts, USA.

Sano, Y., N. Takahata, T. Kagoshima, T. Shibata, T. Onoue & D. Zhao (2016). Groundwater helium anomaly reflects strain change during the 2016 Kumamoto earthquake in Southwest Japan. *Scientific Reports* **6**, 1-7.

Savarensky, E. F. (1966) Ташкентское землетрясение и его возможные причины (Tashkent earthquake and its possible causes, in Russian). *Bulletin of the Russian Academy of Sciences*, Journal № 8, 34-43. Available at (Last accessed 28th September 2017): http://www.ras.ru/publishing/rasheald/rasheald_articleinfo.aspx?articleid=cee369d9-b7fe-4c77-9d46-afe940de7aec&print=1.

Scholz, C.H. (1972). Crustal movements in tectonic areas. *Tectonophysics* **14**(3–4), 201–217.

Shaw, R.K., F. Kaneko, S. Segawa & J. San (2000). Urban seismic risk mitigation in Asia: examples from UNISDR case studies. In Balasanian, S., A. Cisternas & M. Melkumyan (eds.): *Earthquake hazard and risk reduction*. Springer Science+Business Media, Dordrecht, the Netherlands.

Shebalin, N.V. (1993). Seismic hazard in the former U.S.S.R. In: McGuire, R. K. (ed.): *The practice of earthquake hazard assessment*. International Association of Seismology and Physics of the Earth's Interior (IASPEI).

Shevchenko, V.I., S.S. Aref'ev & A.A. Lukk (2011). Subvertical clusters of earthquake hypocenters unrelated to the tectonic structure of the Earth's crust. *Izvestiya, Physics of the Solid Earth* **47**(4), 276–298.

Sims, J. (2007). Natural disasters and the role of women. In Stoltman, J. P., J. Lidstone & L. M. DeChano (eds.): *International perspectives on natural disasters*. Springer, Dordrecht, The Netherlands.

Skjeggedal, S. (2012). Review of *Tashkent. Forging a Soviet City. 1930-1966* (by Stronski, P.). *Reviews in History*. Available online at: <http://www.history.ac.uk/reviews/review/1222>. Last accessed: 28th September 2017.

Smalley, I.J., N.G. Mavlyanova, K.L. Rakhmatullaev, M.S. Shermatov, B. Machalett, K. O'Hara Dhand & I.F. Jefferson (2006). The formation of loess deposits in the Tashkent region and parts of Central Asia; and problems with irrigation, hydrocollapse and soil erosion. *Quaternary International* **152-153**, 59-69.

SN-8-57 (1958). *Нормы и правила строительства в сейсмических районах* (Norms and regulations for construction in seismic regions, in Russian). The State Committee for construction of the Council of Ministers of the U.S.S.R. Available at (Last accessed 28th September 2017): <http://files.stroyinf.ru/Data2/1/4293793/4293793701.pdf>.

SNiP II-A. 12-62 (1963). *Строительство в сейсмических районах. Нормы проектирования* (Design standards and regulations for construction in seismic regions, in Russian). The State Committee for construction of the Council of Ministers of the U.S.S.R., Stroyizdat, Moscow.

SNiP II-A. 12-69 (1970). *Строительство в сейсмических районах. Нормы проектирования* (Design standards and regulations for construction in seismic regions, in Russian). The State Committee for construction of the Council of Ministers of the U.S.S.R., Stroyizdat, Moscow.

SNiP-II-7-81 (1982). *Строительство в сейсмических районах. Нормы проектирования* (Design standards and regulations for construction in seismic regions, in Russian). The State Committee for construction of the Council of Ministers of the U.S.S.R., Stroyizdat, Moscow. Available at: <http://www.stroyventmash.ru/download/SNiP-II-7-81.pdf>. Last accessed: 28th September 2017.

Sokolov, V.Y. & Y.K. Chernov (2001). Probabilistic microzonation of urban territories: a case of Tashkent city. *Pure and Applied Geophysics* **158**, 2295-2311.

Strakhov, V.N., V.I. Ulomov & L.S. Shumilina (1998). New maps of general seismic zoning of North Eurasia. *Izvestiya, Physics of the Solid Earth* **34**(10), 872–876.

Tamrazyan, G. P. (1974). Possible cosmic influences on the 1966 Tashkent earthquake and its largest aftershocks. *Geophysical Journal International* **38**, 423-429.

The World Bank (2015). *Central Asia – Earthquake risk reduction forum: forum proceedings*, October 27-28, Almaty, Kazakhstan. Available at (Last accessed 28th September 2017): <http://pubdocs.worldbank.org/en/451453873709673/Central-Asia-Earthquake-Risk-Reduction-Forum-Proceedings-2015-eng.pdf>

Thomas, J. C., J. R. Grasso, R. Bossu, J. Martinod & B. Nurtaev (1999). Recent deformation in the Turan and South Kazakh platforms, western central Asia, and its relation to Arabia-Asia and India-Asia collisions. *Tectonics* **18**(2), 201–214.

Thurman, M. (2011). *Natural disaster risk in Central Asia: A synthesis*. Bureau for Crisis Prevention and Recovery (BCRP), United Nations Development Program (UNDP) Study. Available at: <http://www.undp.org/content/dam/rbec/docs/Natural-disaster-risks-in-Central-Asia-A-synthesis.pdf>. Last accessed: 28th September 2017.

Tomer, A. (2016). Radon as an earthquake precursor: A Review. *International Journal of Science, Engineering and Technology* **4**(6), 815-822.

Treml, V.G. & M.V. Alexeev (1993). *The second economy and the destabilizing effect of its growth on the economy in the Soviet Union: 1965-1989*. Berkeley-Duke Occasional Papers on the second

economy in the USSR. Available at <https://www.ucis.pitt.edu/nceeer/1993-900-03-Treml.pdf>. Last accessed: 28th September 2017.

Tuychieva, M. (2012). Engineering-geological processes and phenomena in urban areas of seismically active regions of Uzbekistan and their role in assessing of seismic risk. *Proceedings of the International conference on Complexity in earthquake dynamics: From nonlinearity to earthquake prediction and seismic stability*, January 25-26, Tashkent, Uzbekistan. Available online at (Last accessed 28th September 2017):

https://www.researchgate.net/publication/308780652_Proceedings_of_the_international_conference_on_Complexity_in_earthquake_dynamics_From_nonlinearity_to_earthquake_prediction_and_seismic_stability

Tyagunov, S. (2012). Seismic risk assessment in the countries of Central Asia. *Proceedings of the International conference on Complexity in earthquake dynamics: From nonlinearity to earthquake prediction and seismic stability*, January 25-26, Tashkent, Uzbekistan. Available online at (Last accessed 28th September 2017):

https://www.researchgate.net/publication/267152572_SEISMIC_RISK_ASSESSMENT_IN_THE_COUNTRIES_OF_CENTRAL_ASIA

Ullah, S. (2016). *Seismic hazard assessment in Central Asia: combining site effects investigations and probabilistic seismic hazard*. Doctoral dissertation, Berlin, Germany. Available online at (Last accessed 28th September 2017):

http://gfzpublic.gfz-potsdam.de/pubman/item/escidoc:1498895:3/component/escidoc:1498894/Ullah_Shahid.pdf.

Ulomov, V.I. (1970). Деформация горных пород в области очага Ташкентского землетрясения 26 апреля 1966 г. (Deformation of rocks in the area of the Tashkent earthquake on 26 April 1966, in Russian). *Journal of the U.S.S.R. Academy of Sciences 'Физика Земли' (Physics of the Earth, in Russian)* № 9, 22-30. Available at [http://seismos-u.ifz.ru/p/ulomov_deformat_1970\(OCR\).pdf](http://seismos-u.ifz.ru/p/ulomov_deformat_1970(OCR).pdf). Last accessed 28th September 2017.

Ulomov, V.I. (1999). Seismic hazard of Northern Eurasia. *Annali di geofisica* **42**(6), 1023-1038.

Ulomov, V.I. (2007). Global changes in the seismic regime and water surface level of the Earth. *Izvestiya - Physics of the Solid Earth* **43**(9), 713–725.

Ulomov, V.I. (2016). Результаты исследований ташкентского 1966 г. и Газлийских землетрясений 1976 и 1984 гг. и их вклад в сейсмологию (Research results of the Tashkent 1966 and the Gazli Earthquakes of 1976 and 1984 and their contribution to Seismology, in Russian). *International Conference on Actual Problems in Modern Seismology*, October 12-14, Tashkent, Uzbekistan. Available at (Last accessed 28th September 2017):

http://seismos-u.ifz.ru/p/Ulomov_Tashkent_2016.pdf

Umurzakov, R. A. (2010). Structural and seismic indications of the elements of recent and present-day stress fields in several epicentral regions of Western Tien Shan. *Izvestiya-Physics of the Solid Earth* **46**(5), 379–386.

United Nations, ed. (1996). *Human Development Report 1996*. Report of the United Nations Development Programme (UNDP).

United Nations, ed. (2002). *Human Development Report 2002 – Deepening democracy in a fragmented world*. Report of the United Nations Development Programme (UNDP).

United Nations, ed. (2004). *Human Development Report 2004 – Cultural liberty in today's diverse world*. Report of the United Nations Development Programme (UNDP).

United Nations, ed. (2008). *Human Development Report 2007/2008 - Fighting climate change: human solidarity in a divided world*. Report of the United Nations Development Programme (UNDP).

United Nations, ed. (2013). *Human Development Report 2013 - The rise of the South: Human progress in a diverse world*. Report of the United Nations Development Programme (UNDP), New York, United States.

United Nations, ed. (2016). *Human Development Report 2016 – Human Development for Everyone*. Report of the United Nations Development Programme (UNDP), New York, United States.

United Nations International Strategy for Disaster Reduction (UNISDR) (1999). *Final report on the International Decade for Natural Disaster Reduction (IDNDR) project for the city of Tashkent*. Part of the Risk Assessment Tools for Diagnosis of Urban Areas against Seismic Disasters (UNISDR) initiative. 82 pp. Available Online at (Last accessed 28th September 2017):
<http://studylib.net/doc/7348597/final-report-on-the-idndr-UNISDR-project-for-the-city-of-Tashkent>

Utsu, T. (1990). *Catalog of damaging earthquakes in the world (through 1989)*. Utsu, Tokuji, Tokyo, 243 pp. Data available online at (Last accessed 28th September 2017):
http://iisee.kenken.go.jp/utsu/exworld_eng.html

Von Hake, C. A. & W. K. Cloud (1966) *United States earthquakes, 1966*. United States Geological Survey, Open-File Report 84-966. Available online at (Last accessed 28th September 2017):
<https://pubs.usgs.gov/of/1984/0966/report.pdf>

Wald, D.J. & T.I. Allen (2007). Topographic slope as a proxy for seismic site conditions and amplification. *Bulletin of the Seismological Society of America* **97**, 1379–1395. Slope-based online map viewer available at:
<http://usgs.maps.arcgis.com/apps/webappviewer/index.html?id=8ac19bc334f747e486550f32837578e1>. Data used herein downloaded from deprecated version last accessed on 28th September 2017.

Wang, L., Z. Wu & K. Xia (2017). Effects of site conditions on earthquake ground motion and their applications in seismic design in loess region. *Journal of Mountain Science* **14**(6), 1185-1193.

Weatherill, G.A., M. Pagani & J. García (2016). Exploring earthquake databases for the creation of magnitude-homogeneous catalogues: tools for application on a regional and global scale. *Geophysical Journal International* **206**, 1652-1676.

Wright, J. R. (1971). *Industrialized building in the Soviet Union*. Report of the U.S. Delegation to the U.S.S.R. National Bureau of Standards Special Publication 334, Washington D.C.

Zhang, P., Z. Yang, H. K. Gupta, S. C. Bhatia & K. M. Shedlock (1999). Global Seismic Hazard Assessment Program (GSHAP) in continental Asia. *Annali di Geofisica*, **42**(6), 1167-1190.

A4.2.11.2 Web references

Advantour (2017):
<http://www.advantour.com/uzbekistan/history/history-today.htm>
Last accessed: 28th September 2017

Asian Development Bank (2012):
<https://www.adb.org/sites/default/files/linked-documents/cps-uzb-2012-2016-ea.pdf>
Last accessed: 28th September 2017

Attention! Earthquake! (Внимание! Землетрясение!, in Russian) (2017):

<http://seismos-u.ifz.ru/personal/1966-1975.htm>

Last accessed: 28th September 2017

Bertelsmann Transformation Index (BTI, 2003):

<http://bti2003.bertelsmann-transformation-index.de/151.0.html?&L=1>

Last accessed: 28th September 2017

City Population (2017):

<http://www.citypopulation.de/Uzbekistan.html>. Last accessed: 28th September 2017.

Countries Quest (2017):

http://www.countriesquest.com/asia/uzbekistan/history/soviet_period.htm

Last accessed: 28th September 2017

Deseret News (1984):

https://news.google.com/newspapers?nid=336&dat=19840122&id=upg_AAAAlBAJ&sjid=EIMDAAAlBAJ&pg=7153,2221056. Last accessed: 28th September 2017

Earthquake-Report (2013):

<https://earthquake-report.com/2013/05/24/strong-earthquake-eastern-uzbekistan-on-may-24-2013/>

Last accessed: 28th September 2017

Eurasia Travel (2017):

http://eurasia.travel/uzbekistan/facts_about_uzbekistan/geography/

Last accessed: 28th September 2017

Fergana (Фергана, in Russian) (2006):

<http://www.fergananews.com/articles/4367>. Last accessed: 29th September 2017

Flyingnorth (2012):

<http://flyingnorth.net/2012/09/08/a-memorial-to-the-1966-tashkent-earthquake/>

Last accessed: 28th September 2017

Geo-Storm (in Russian) (2013):

<http://geo-storm.ru/priroda-i-klimat/stihii/tashkentskoe-zemletrjasenie-1966-goda/>

Last accessed: 28th September 2017

Global Facility for Disaster Reduction and Recovery (GFDRR, 2017):

<https://www.gfdr.org/uzbekistan>. Last accessed: 28th September 2017

International Institute of Seismology and Earthquake Engineering - Information network on earthquake disaster prevention technologies (IISEE NET, 2017):

<http://iisee.kenken.go.jp/net/hara/uzbekistan/DamageForBuildings.htm>

Last accessed: 28th September 2017

Mygeos (in Russian) (2010):

<http://www.mygeos.com/2010/02/20/zvuk-pri-zemletryasenyax>

Last accessed: 28th September 2017

Popular Geology (Популярная геология, in Russian) (1970):

http://popular.geo.web.ru/materials/library/yakush/capt_16.htm

Last accessed: 28th September 2017

Public Library of Science (PLOS, 2013):

<http://currents.plos.org/disasters/article/dis-12-0009-mortality-in-the-laquila-central-italy-earthquake-of-6-april-2009/>. Last accessed: 29th September 2017

Radio Ozodlik (Радио Озодлик, in Russian) (2016):
<https://rus.ozodlik.org/a/27699498.html>. Last accessed: 28th September 2017

RIA Novosti (РИА Новости, in Russian) (2011):
<https://ria.ru/eco/20110426/368030901.html>. Last accessed: 28th September 2017

RIA Novosti (РИА Новости, in Russian) (2016):
<https://ria.ru/spravka/20160426/1419855458.html>. Last accessed: 28th September 2017

Sputnik (in Russian) (2016a):
<http://ru.sputniknews-uz.com/infographics/20160420/2557397.html>
 Last accessed: 28th September 2017

Sputnik (in Russian) (2016b):
<http://ru.sputniknews-uz.com/society/20160423/2592721.html>
 Last accessed: 28th September 2017

Sputnik (in Russian) (2016c):
<http://ru.sputniknews-uz.com/culture/20160323/2265799.html>
 Last accessed: 28th September 2017

The Emergency Events Database (EM-DAT, Université Catholique de Louvain, Brussels, Belgium; Cred. Prof. Dr. D. Guha-Sapir): <http://www.emdat.be/>. Last accessed: 29th September 2017

The New York Times (1984):
<http://www.nytimes.com/1984/03/21/world/big-tremor-rocks-central-asia-area.html>
 Last accessed: 29th September 2017

The State Committee of the Republic of Uzbekistan on Statistics (2017): <http://stat.uz/en/>
 Last accessed: 15th September 2017

Think Hazard (2017a):
<http://thinkhazard.org/en/report/261-uzbekistan/EQ>. Last accessed: 28th September 2017

Think Hazard (2017b):
<http://thinkhazard.org/en/report/261-uzbekistan/LS>. Last accessed: 28th September 2017

United Nations Development Program (UNDP): <http://hdr.undp.org>
 UNDP (2016): 1966-2016: 50 years since the Tashkent Earthquake:
<http://www.uz.undp.org/content/uzbekistan/en/home/presscenter/articles/2016/04/30/1966-2016--50-years-since-the-tashkent-earthquake.html> (Last accessed: 28th September 2017)

United Nations Statistics Division (UNSD, 1966):
<https://unstats.un.org/unsd/demographic/products/dyb/dybsets/1965%20DYB.pdf>
 Last accessed: 28th September 2017

UZReport (2015):
http://society.uzreport.uz/news_e_131182.html. Last accessed: 28th September 2017

World Economic Outlook Database (WEO, 2017):
<https://www.imf.org/external/pubs/ft/weo/2017/01/weodata/index.aspx>
 Last accessed: 28th September 2017

A4.3. September 1978 M5.2 Albstadt and May 2014 M3.6 Darmstadt Earthquakes, Germany

The earthquakes studied in this report are the **M5.2 Albstadt** event that occurred on 3rd September 1978 (05.08 UTC) and the **M3.6 Darmstadt** event that occurred on 17th May 2014 (16.46 UTC).

The 1978 **M5.2 Albstadt** event occurred in the Baden-Württemberg state, in the south-west of Germany, and was the strongest earthquake in the country in the last 50 years. It caused damage to thousands of properties, mostly in the districts of Tailfingen, Onstmettingen and Ebingen of Albstadt, by the Swabian Alb mountains. It was followed by hundreds of aftershocks. Tens of people were injured and around 200 of them were left homeless as a consequence of this event.

The **M3.6 Darmstadt** event occurred in the Hesse state, in central Germany, and was the largest event of the 2014-2015 earthquake series that took place in the Odenwald mountains, in the vicinity of Ober-Ramstadt. It was followed by more than 300 earthquakes that kept on occurring for more than a year after the main shock. This earthquake caused slight-to-moderate damage to approximately 150 buildings, mostly in the Nieder-Beerbach district of Mühlthal, but produced no human casualties.

A4.3.1 Tectonic and seismic setting

A4.3.1.1 Tectonic setting

In Central Europe, where Germany is located, the earth crust was shaped mainly by Hercynian folding in the late Paleozoic and later, during the Tertiary period, by the continental collision between the European and African plates that resulted in the formation of the Alpine Orogenic belt (Bormann, 1994).

Both the Odenwald mountain range, associated with the epicentral region of the 2014 Darmstadt earthquake, and the Swabian Alps mountain range, associated with the 1978 Albstadt earthquake, are located on the eastern rim of the Upper Rhine Graben (URG), as shown in Figure A4.3.1. As a central part of the European Cenozoic Rift System, the URG was created through passive rifting in the Alpine foreland, in response to the E-W extension that was initiated during the Late Eocene collisional phase of the Alpine Orogeny (Peters, 2007; Homuth *et al.*, 2014). Being one of the most tectonically active areas of Germany and Central Europe, the NNE-SSW striking Upper Rhine Graben extends from Basel in the south to the Rhenish Massif close to Frankfurt in the north, covering a length of 320 km and a width of 40 km (Homuth & Rumpker, 2017; Homuth *et al.*, 2014).

The URG region is associated at present with a sinistral transtensional regime, resulting from the maximum horizontal compressive stress acting in the NW-SE direction (N150) not

only in the URG but also all over Central Europe (Peters, 2007; Homuth *et al.*, 2014). GPS measurements indicate a NW-SE push of 1 mm/year and an E-W opening of 0.5 mm/year in the URG area, which is in agreement with the results of seismological studies and fault slip analysis that revealed shortening and extension in the NW-SE and NE-SW direction, respectively (Peters, 2007). The fault plane solutions obtained for earthquakes in the Swabian Jura are in agreement with this orientation of the compressive stress (Fuchs, 2016; Ahorner *et al.*, 1972; Ahorner & Schneider, 1974; Schneider, 1980; Scherbaum & Stoll, 1983).

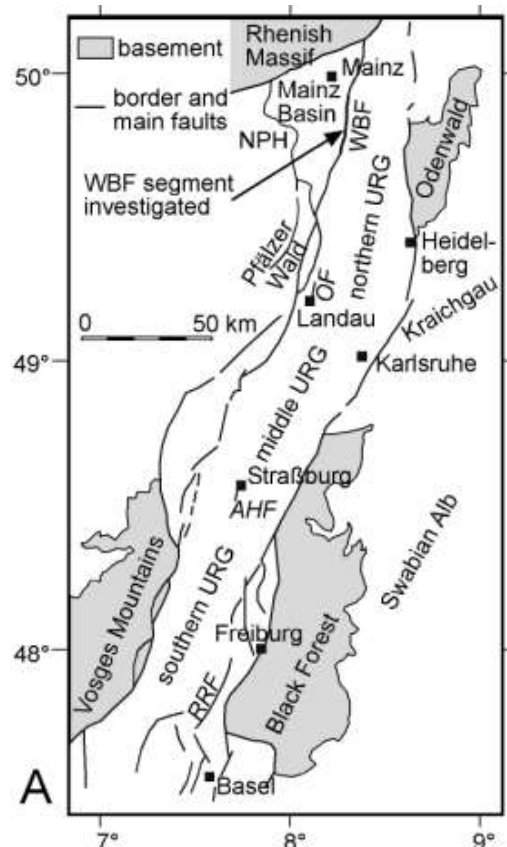


Figure A4.3.1. Structural map of the Upper Rhine Graben. NPH: Nordpfälzer Hügelland, AHF: Achenheim-Hangenbieten Fault, OF: Omega Fault, RRF: Rhine River Fault. From Peters (2007).

The northern part of the URG is limited to the east by the Odenwald mountains, which can be subclassified into a western crystalline and an eastern sedimentary (Buntsandstein) part, with the former being additionally subdivided by large systems of strike-slip faults into three subareas, as shown in Figure A4.3.2 (Homuth & Rumpker, 2017). The figure also depicts the two earthquake clusters that occurred in the crystalline Odenwald, south-east of Darmstadt, in the period from March 2014 to April 2015, including the main event of 17th May 2014. According to Homuth & Rumpker (2017), the concentration of earthquake epicentres within two spatially distinctive clusters suggests the existence of two different active fault zones, though they also point out that no clear connection could be established between the observed seismicity and specific fault structures, as detailed mapping of the latter is lacking in the region. These authors argue that a NE-SW striking normal fault (not shown herein), with outcrops stretching between Nieder-Ramstadt and Ober-Ramstadt, might be responsible for the earthquake cluster 1 and the 2014 Darmstadt earthquake (west of Ober-Ramstadt), while cluster 2 (between Ober-Ramstadt and Reinheim) could

be assigned either to a sinistral fault between Frankenstein Massif and the Flasergranitoid Zone (Figure A4.3.2 and Figure A4.3.3) or to some other unknown fault running parallel to it.

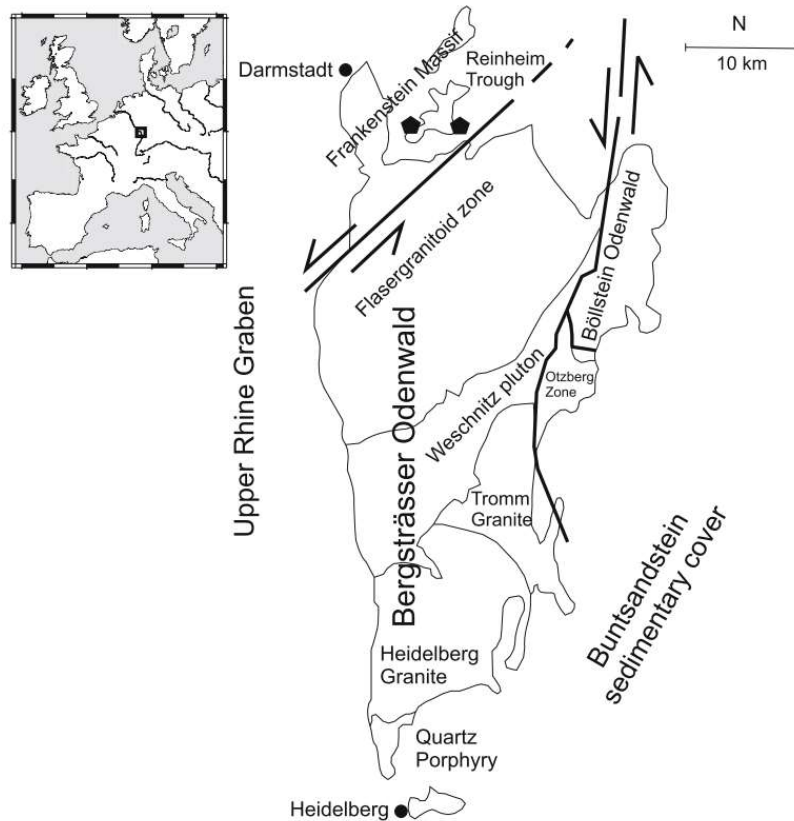


Figure A4.3.2. Tectonic map of the western (crystalline) Odenwald, associated with the 2014 Darmstadt earthquake. Thicker black lines represent faults in the region; black pentagons mark the locations of the two 2014-2015 earthquake clusters. From Homuth & Rumpker (2017).

The epicentral area of the 1978 Albstadt earthquake is placed within the Swabian Alps (also called Swabian Jura), a mountain range in south-western Germany that is bordered by the Black Forest mountains to the south-west (Figure A4.3.1), the Danube River to the south-east and the upper Neckar River to the north-west (Figure A4.3.4). A distinctive tectonic feature in the vicinity of the epicentral area is the NW-SE striking Hohenzollern Graben (HZGR) (Scherbaum & Stoll, 1983), created as a response to the pressure from the African plate and consequent folding of the Alps (Reutlinger, 2008). This 28-km long and 1.5-km wide geological ditch that sustained subsidence of ~100 m, consists of the Hercynian basement rocks overlaid by the Mesozoic strata with sedimentary cover of 1,200 m (Fuchs, 2016). Although seismic activity, including the 1978 event, has been observed in the region of the Hohenzollern Graben, Scherbaum & Stoll (1983) point out that the HZGR structure is not concordant with the location and orientation of the studied earthquake and its aftershocks.

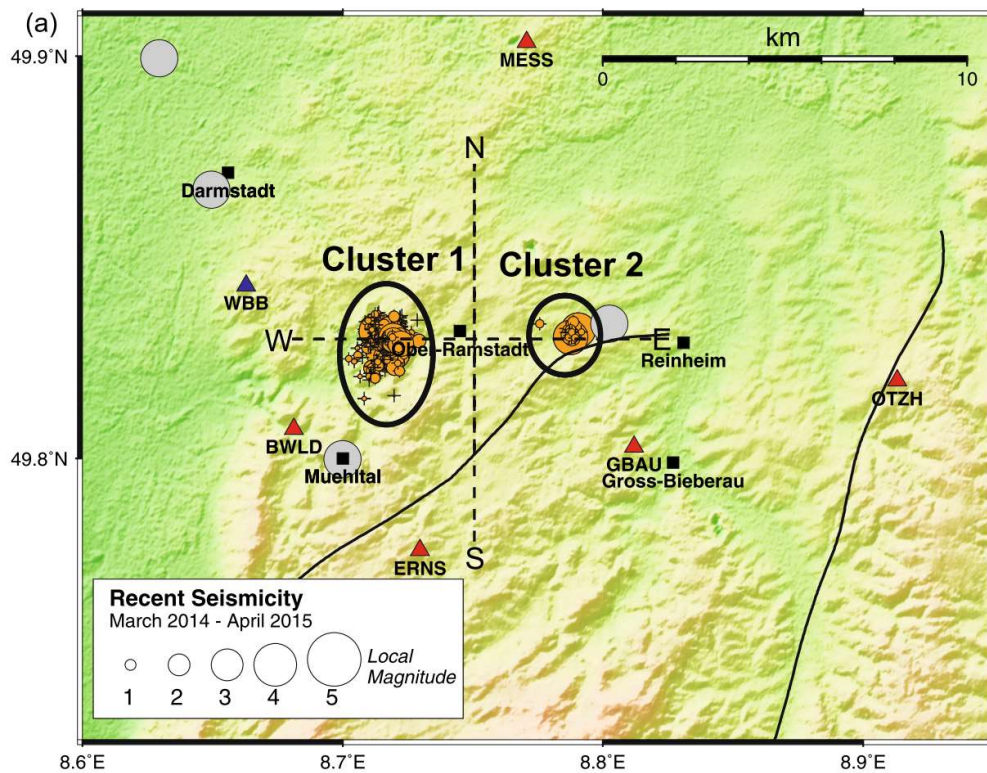


Figure A4.3.3. Map showing the relative locations (orange circles) of the March 2014 – April 2015 earthquake series near Ober-Ramstadt. Grey circles indicate the locations of swarm events in the 19th century. Continuous black lines show the course of the major faults introduced in Figure A.3.2.2. Main event of 17th May 2014 belongs to cluster 1. From Homuth & Rumpker (2017).

The focal mechanism of the 3rd September 1978 earthquake and its aftershocks, as well as the instrumental and macroseismic data of all major shocks in the Swabian Alps that happened since the beginning of the 20th century, are found to be consistent with sinistral strike-slip faulting in the NNE-SSW direction (Scherbaum & Stoll, 1983; Schneider, 1968; Haessler *et al.*, 1980; Turnovsky & Schneider, 1982). While the exact position of such fracture system responsible for the main 1978 event remains unclear, it is observed that a left-lateral fault, featuring the same (NNE-SSW) striking direction, was mapped as part of the SHARE project (Woessner *et al.*, 2015) in the immediate vicinity of the epicentral region (Figure A4.3.12).

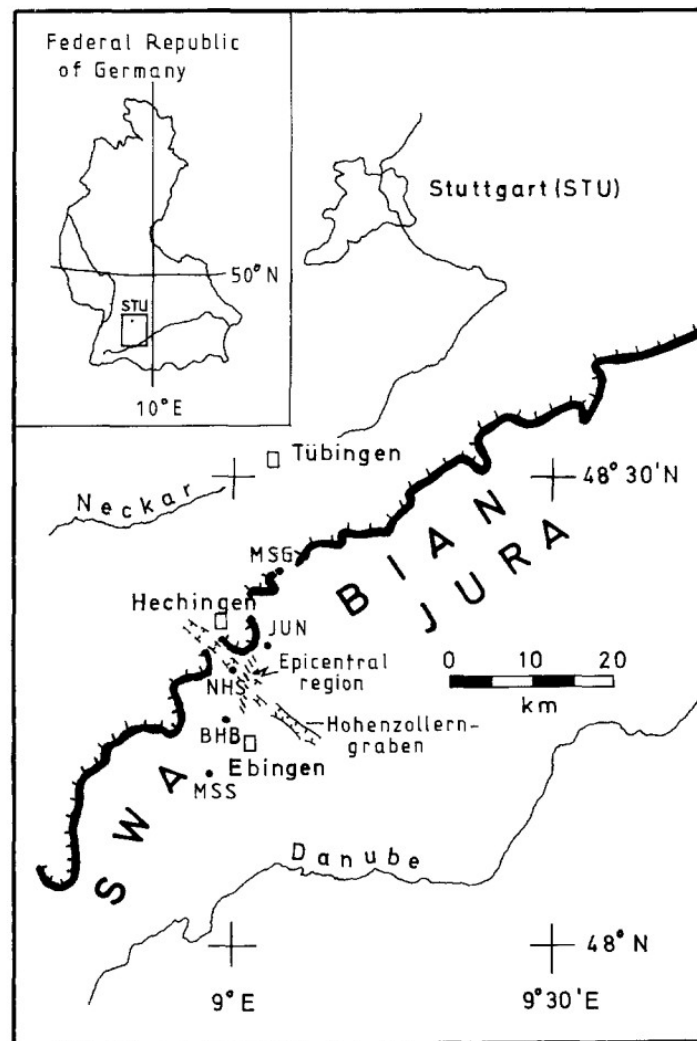


Figure A4.3.4. Geographic location of the Swabian Jura, associated to the 1978 Albstadt earthquake, within Germany. Ebingen (marked on the map) was one of the districts of Albstadt that was most affected. Seismic station codes: BHB (Braunhartsberg); JUN (Jungingen); MSG (Moessingen); MSS (Messtetten); NHS (Naeglelehaus). From Scherbaum & Stoll (1983).

A4.3.1.2 Regional and local seismicity

Being located within a seismically stable area of Central Europe (Bormann, 1994), faraway from plate tectonic boundaries, Germany is associated with low-to-medium intraplate seismicity within the context of Europe (Grünthal *et al.*, 2015), and low seismicity in a global context (Tyagunov *et al.*, 2006). Nevertheless, its seismic activity is found to be one of the highest in continental Europe north of the Alps (Tyagunov *et al.*, 2006; Grünthal, 2004; German Research Centre for Geosciences, GFZ, 2017c), with all parts of the country being considered capable of generating earthquakes (Grünthal *et al.*, 2015; Tyagunov *et al.*, 2006). Bormann (1994) points out that in consideration of the neotectonic crustal movements and deformations, as well as of the seismic activity of Germany, earthquakes of magnitude higher than 6 and epicentral MSK-64 (Medvedev *et al.*, 1965) intensity higher than 8.5 are not likely to happen. According to Grünthal (2004), in Germany, seismic events with magnitude M_L 5.1 and M_L 5.8 have an average recurrence period of 10 and 50 years, respectively, while earthquakes with the (up to date) highest observed magnitude (M_L 6.1) happen approximately every 100 years. Earthquakes in this

area are chiefly associated with shallow focal depth, in a range between 5 km to 20 km, with most of them taking place at a depth of around 10 km (GFZ, 2015; Grünthal, 2004).

The seismicity of Germany and neighbouring areas observed in the time-period between the years 1000 and 2001 is depicted on the map in Figure A4.3.5. Some of the most seismically active areas are recognized in the area along the River Rhine in west Germany, including the Upper Rhine Graben (from Basel to Frankfurt), the Middle Rhine area, and the Lower Rhine embayment that stretches up to Cologne (Köln) to the north and continues towards the Netherlands and north-east Belgium to the west (Tyagunov *et al.*, 2006; Grünthal, 2004; GFZ, 2015; Federal Institute for Geosciences and Natural Resources (BGR, 2017a). Besides the Rhine area, significant seismic activity occurs in the Swabian Alps, as well as in the eastern part of the country within the states of Saxony and Thuringia, and the region of Vogtland (Tyagunov *et al.*, 2006; Grünthal, 2004; GFZ, 2015). The earthquakes whose year of occurrence is specified on the map in Figure A4.3.5, and details of which are given in Table A4.3.1, are some of the strongest events whose shaking effects were felt in Germany and its border area since 1750. It is noticed that the maximum intensity of shaking observed during this period was VIII, and that several of the earthquakes listed in Table A4.3.1 were felt with this intensity in the area around Albstadt (Grünthal, 2004; GFZ, 2015). Though not depicted on the map in Figure A4.3.5, the **M**6.1 1692 Verviers (eastern Belgium) and the **M**6.3 1976 Friuli (northern Italy) earthquakes were also felt in Germany (Grünthal *et al.*, 2015).

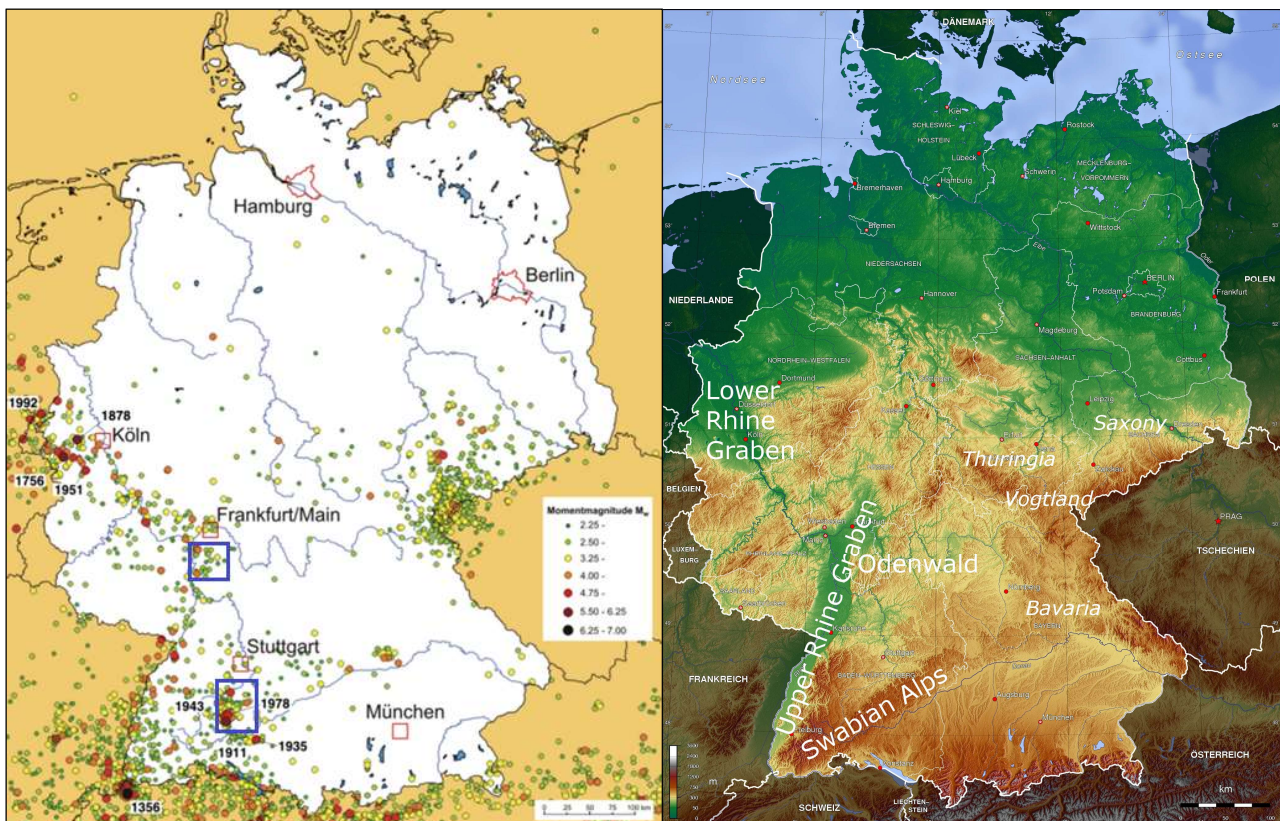


Figure A4.3.5. Epicentres and corresponding moment magnitude of earthquakes in Germany and neighbouring areas in the period 1000-2001 (left; from Grünthal, 2004). Blue rectangles indicate the epicentral areas of the 1978 $M_{5.2}$ Albstadt and the $M_{3.6}$ Darmstadt earthquakes. Topographic map of Germany with relevant features and regions (right; modified from World of Maps, 2018).

Within the Upper Rhine Graben, the highest seismic activity is observed in the Basel area and its adjacent regions, that is, the Vosges Mountains to the west and the Swabian Alps to the east (Figure A4.3.6; Peters, 2007). In the south-western part of the Swabian Alps, a confined area of considerable seismic activity is found around the Hohenzolern Graben, to the north of the city of Albstadt, where, according to Fuchs (2016), earthquakes with predominantly left-lateral strike slip mechanism took place from 1911 to 1978, with tendency to migrate towards north and, concurrently, to become shallower. According to Grünthal (2004), this area of the Swabian Alps is associated with the highest share of seismic energy released during the 20th century in Germany, while its corresponding federal state, Baden-Württemberg, has been recognized as the most seismically active state of Germany.

Unlike the southern part of the Upper Rhine Graben, its northern part and adjacent areas, where Darmstadt lies, are associated with comparable lower levels of seismicity (Peters, 2007). The strongest earthquake known to have hit the area was the 1952 ML 4.7 Worms event (Homuth & Rumpker, 2017). As shown in the map of Figure A4.3.7, the period between October 2010 and April 2015, in which the 2014 Darmstadt earthquake falls, saw an increase in seismic activity in the northern URG.

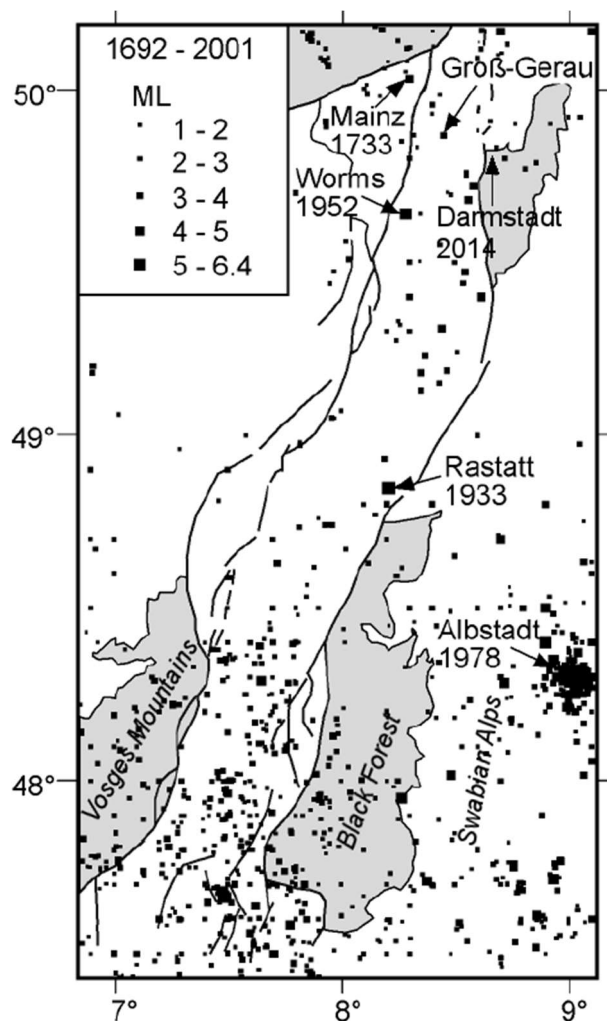


Figure A4.3.6. Distribution of earthquakes with magnitude ML >1 recorded in the Upper Rhine Graben and its surrounding area between 1692 and 2001. Location of the 2014 Darmstadt earthquake indicated by text, but no epicentres shown. Modified from Peters (2007).

Table A4.3.1. Selected strong earthquakes in Germany since 1750. From GFZ (2015) and Grünthal (2004).

Date	Location	Max. Intensity (I_0)	Magnitude M_L
18.11.1356	Basel (Switzerland)	IX	6.6
18.02.1756	Düren (east of Aachen)	VIII	6.1
26.08.1878	Tpollhausen (west of Cologne)	VIII	5.9
16.11.1911	Albstadt (south of Tübingen)	VIII	6.1
27.06.1935	Saulgau (northeast of Konstanz)	VII-VIII	5.8
28.05.1943	Albstadt	VIII	5.6
14.03.1951	Euskirchen (west of Bonn)	VII-VIII	5.7
03.09.1978	Albstadt	VII-VIII	5.7
13.04.1992	Heinsberg/Roermond (the Netherlands)	VII	5.9

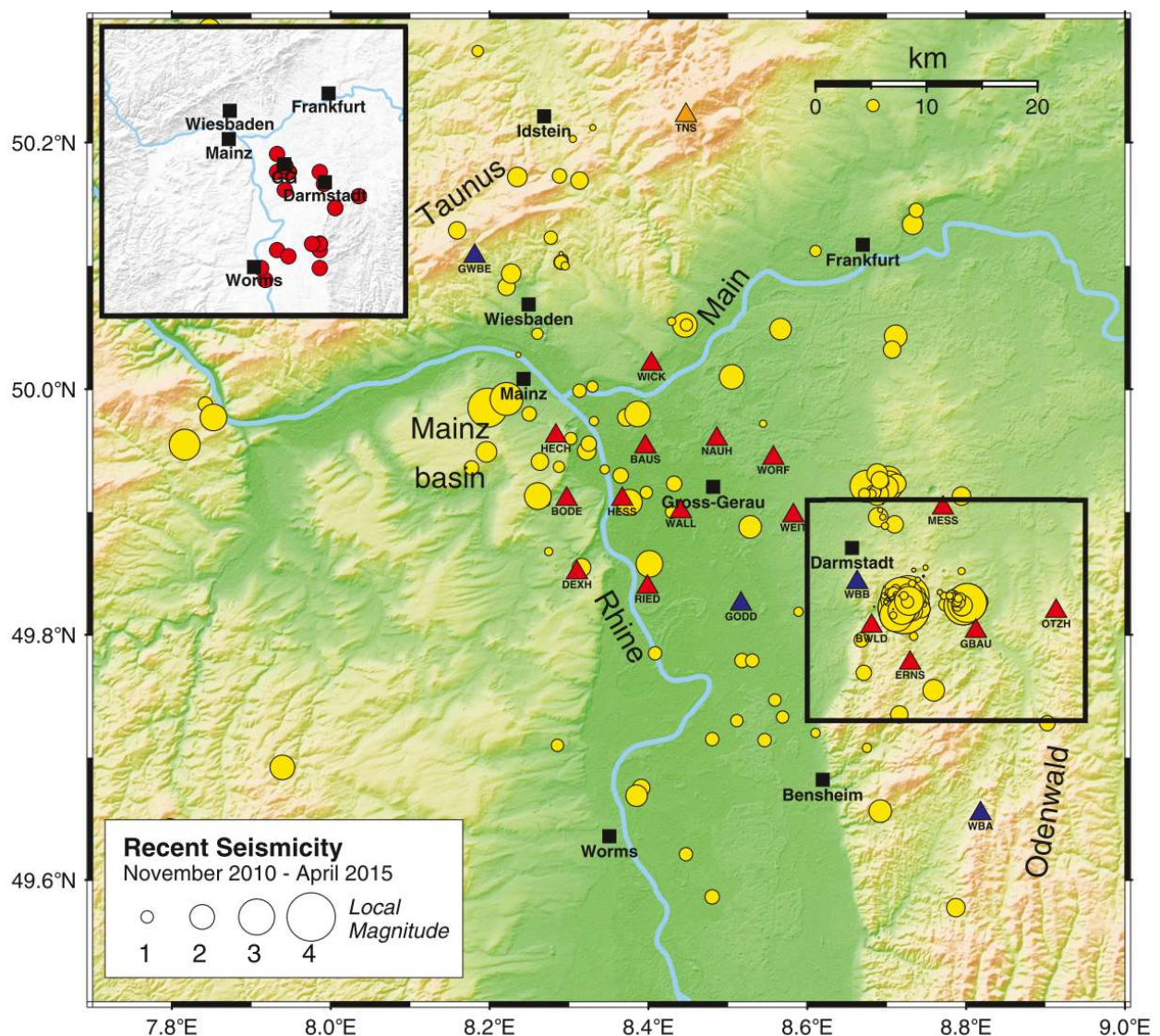


Figure A4.3.7. Recorded local seismicity (yellow circles) in the northern URG from November 2010 to April 2015. Triangles indicate the location of seismic stations. The inset shows the same area as the map, including the locations (in red) of the earthquake swarm of 1869 – 1871. Every red dot represents a cluster of events. The black rectangle in the eastern part of the investigation area indicates the position of the map in Figure A4.3.3., where clusters of the 2014-2015 earthquake series are depicted. From Homuth & Rumpker (2017).

A4.3.1.3 Seismic hazard

At the time of writing (December 2017), seismic hazard in Germany is characterised by the seismic zoning map shown in Figure A4.3.8, which was incorporated to the DIN 4149:2005-04 seismic code in 2005, as well as in the German National Annex to Eurocode 8, DIN EN 1998-1/NA:2011-01, and is based on the probabilistic seismic hazard assessment (PSHA) carried out by Grünthal & Bosse (1996), whose main outcome was the map depicted in Figure A4.3.9 (Grünthal *et al.*, 2015; García-Mayordomo *et al.*, 2004). The latter shows European Macroseismic Intensities (EMS-98; Grünthal, 1998) with a mean return period of 475 years (10% probability of exceedance in 50 years), while the former delineates earthquake prone zones that are capable of producing EMS-98 intensities higher than VI with the same mean return period. These seismic zones are associated with different levels of effective acceleration a_g , as shown in Table A4.3.2, which enable the implementation of acceleration-based seismic zoning in accordance with the Eurocode 8 provisions (Grünthal *et al.*, 2015).

The seismic hazard zones shown on the map of Figure A4.3.8 correspond chiefly to the German Federal States of Baden-Württemberg, Rhineland-Palatinate, North Rhine-Westphalia, Saxony and Thuringia, most of them being densely populated areas with highly developed industry and infrastructure (Tyagunov *et al.*, 2004; Tyagunov *et al.*, 2006; Grünthal *et al.*, 2015). According to Tyagunov *et al.* (2006), around 25% of the German territory, inhabited by approximately one third of the country's population, is located within seismic zones where EMS-98 intensities of shaking equal to or higher than VI are expected with a 10% probability of exceedance in 50 years. According to the seismic zoning map of Figure A4.3.8, Albstadt is located within seismic zone 3, where EMS-98 intensities higher than 7.5 and effective acceleration of 0.08 g are expected with a return period of 475 years, while Darmstadt, located in seismic zone 1, is associated with EMS-98 shaking intensities in the range between 6.5 and 7 and an effective acceleration of 0.04 g for the same return period.

Figure A4.3.10 presents the uniform hazard spectra (UHS) on rock with a 10% probability of exceedance in 50 years for coordinates corresponding approximately to the city of Albstadt and Darmstadt, according to the SHARE project (Woessner *et al.*, 2015). As observed on the plot, the values of expected PGA on rock with a 10% probability of exceedance in 50 years are 0.38 g for Albstadt and 0.065 g for Darmstadt. According to the results from the Global Seismic Hazard Assessment Program (GSHAP) (Giardini *et al.*, 1999) these values are 0.172 g for the Albstadt area (48.2N, 9.0E) and 0.08 g for the Darmstadt area (49.9N, 8.7E). All these PGA values are significantly higher than the values of effective acceleration indicated by the national seismic zoning map shown in Figure A4.3.8 and Table A4.3.2.

The new PSHA for Germany (Grünthal *et al.*, 2018) is still under publication at the time of writing (December 2017), but its results are readily available on the website of the German Research Centre for Geosciences (GFZ, 2017b). Figure A4.3.11 shows the acceleration response spectra with a 10% probability of exceedance in 50 years resulting from this study for Albstadt and Darmstadt. According to the plot, the expected PGA values are

0.149 g and 0.039 g for Albstadt and Darmstadt, respectively. While the latter is in good agreement with the value of effective acceleration assigned to the city of Darmstadt according to the German seismic zoning map shown in Figure A4.3.8 and Table A4.3.2, the former is significantly larger. It is not clear at this stage how the new values from Grünthal *et al.* (2018) will be adopted within the building code.

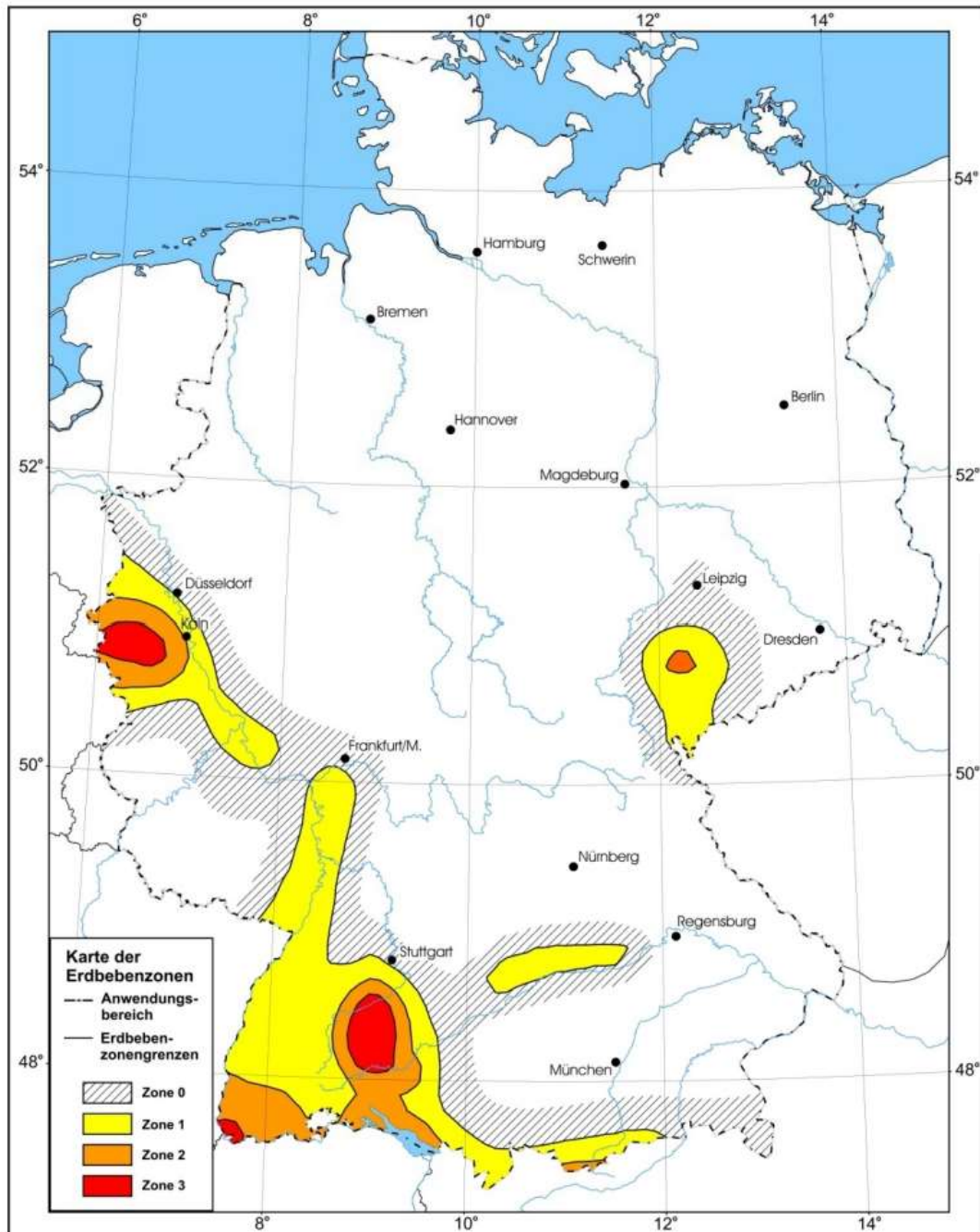


Figure A4.3.8. Seismic zoning map of the territory of Germany incorporated within the DIN 4149:2005-04 and DIN EN 1998-1/NA:2011-01. From Solomos *et al.* (2008).

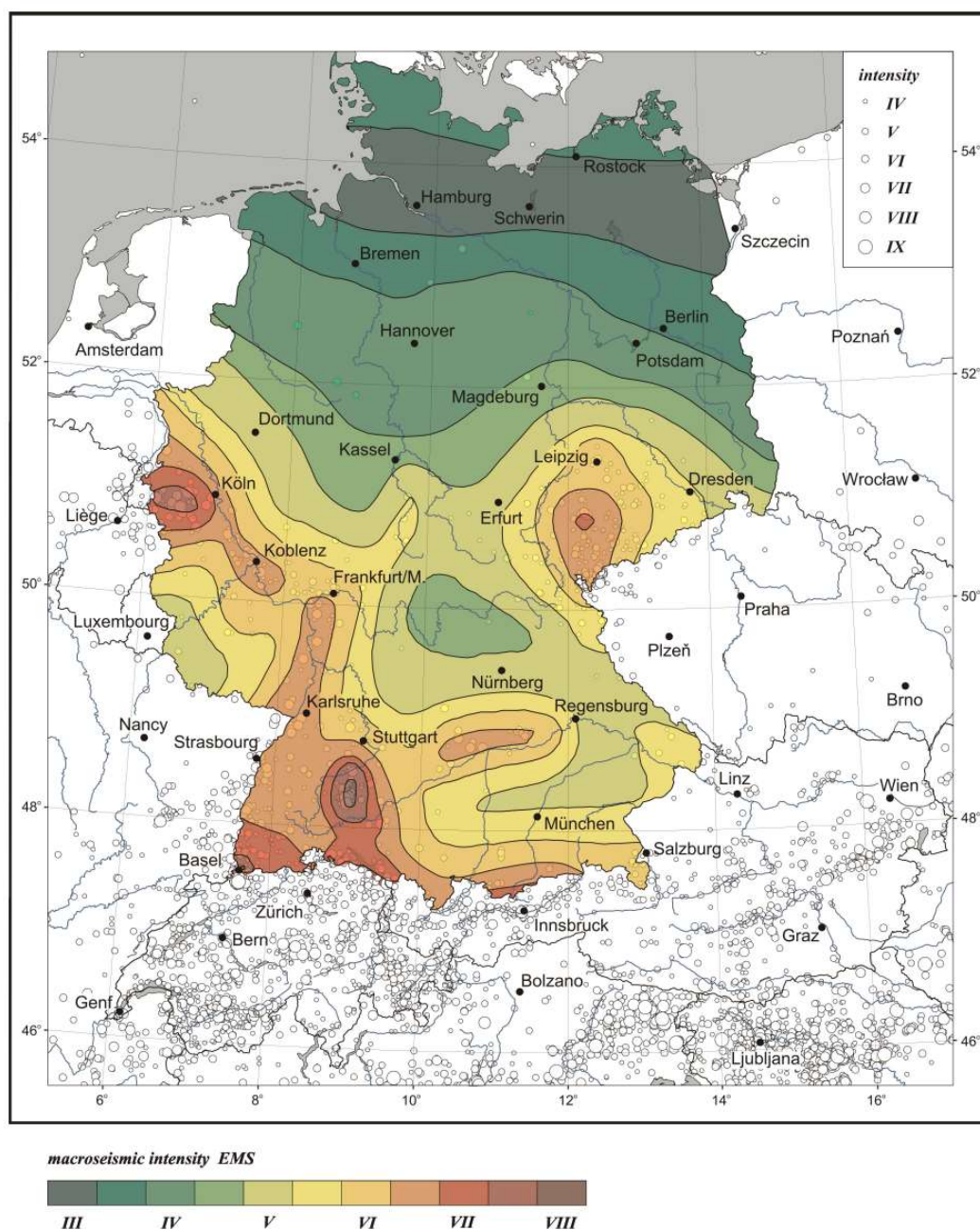


Figure A4.3.9. EMS-98 Intensity-based seismic hazard map of Germany (Grünthal & Bosse, 1996) for a 10% exceedance probability in 50 years. From Tyagunov et al. (2006) after Grünthal & Bosse, 1996.

Table A4.3.2. Allocation of intensity intervals and reference peak values of ground acceleration, i.e. effective acceleration, to earthquake zones shown in Figure A4.3.8. From DIN EN 1998-1/NA:2011-01.

Seismic zone	Intensity interval	Reference (effective) ground acceleration (m/s^2)
0	$6.0 \leq I < 6.5$	-
1	$6.5 \leq I < 7.0$	0.4
2	$7.0 \leq I < 7.5$	0.6
3	$I \leq 7.5$	0.8

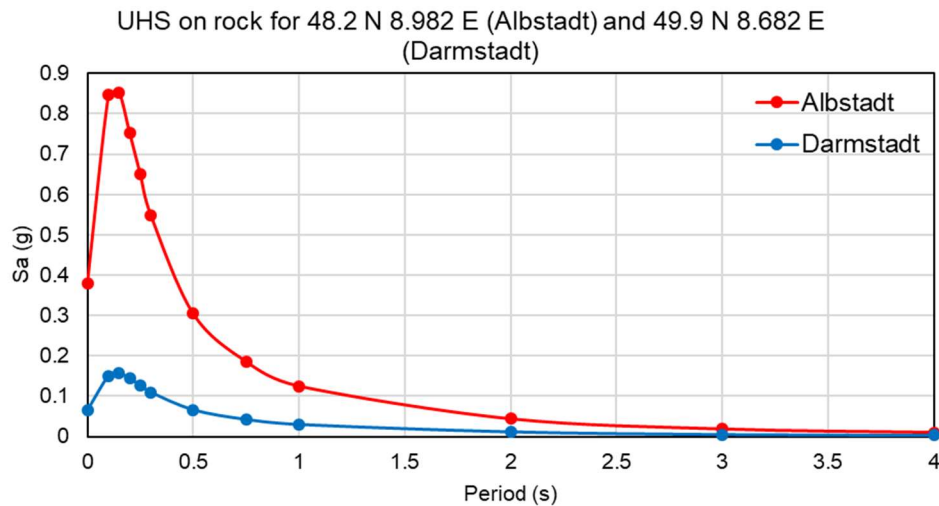


Figure A4.3.10. Uniform Hazard Spectra with a 10% probability of exceedance in 50 years for the closest available coordinates to the cities of Albstadt (red) and Darmstadt (blue) according to SHARE (Woessner et al., 2015).

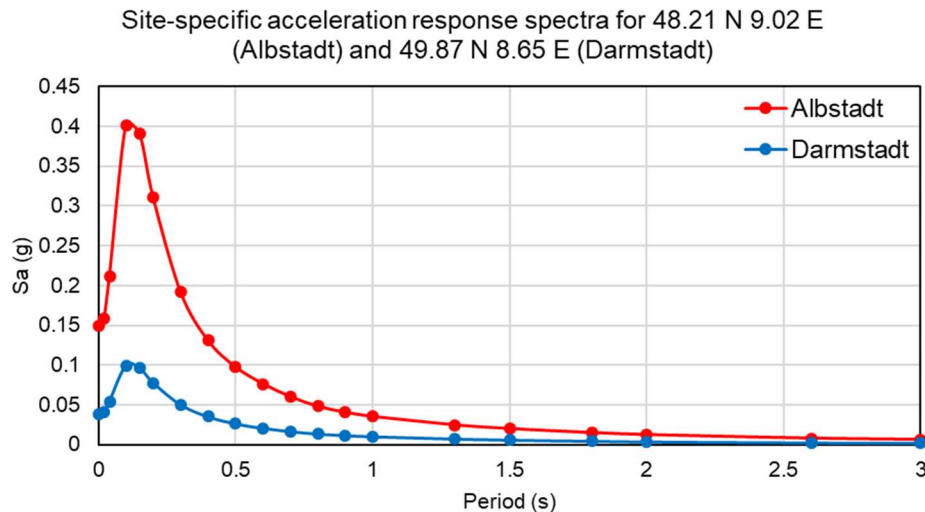


Figure A4.3.11. Site-specific acceleration response spectra with a 10% probability of exceedance in 50 years for the closest available coordinates to the cities of Albstadt (red) and Darmstadt (blue) according to GFZ (2017b),

A4.3.2 Earthquake source characteristics

A4.3.2.1 Location, depth and time

The Albstadt main shock occurred on 3rd September 1978, at 05.08 UTC (06.08 local time), while the Darmstadt main shock occurred on 17th May 2014, at 16.46 UTC (18.46 local time).

Several organizations and agencies report their own estimations of the epicentral coordinates and hypocentral depths. The information reported in the websites of the National Earthquake Information Center (NEIC) of the United States Geological Service (USGS), the International Seismological Centre (ISC), the German Federal Institute for

Geosciences and Natural Resources (BGR) and the German Research Centre for Geosciences (GFZ) is summarized in Table A4.3.3 and Table A4.3.4. Cells marked as (*f) correspond to parameters that were held fixed while inversion was carried out to retrieve those that remain. The epicentral coordinates and hypocentral depths calculated by Homuth & Rumpker (2017) and Müller *et al.* (2015), as well as those included in the catalogues of Germany and adjacent areas compiled by Schwarz *et al.* (2010b) and Leydecker (2011), are also presented in these tables. Figure A4.3.12 and Figure A4.3.13 show the different estimations of the epicentral locations enumerated above.

Table A4.3.3. Epicentral coordinates and hypocentral depths for the 1978 M5.2 Albstadt earthquake from different sources.

Agency / Publication		Latitude	Longitude	Depth (km)
NEIC	National Earthquake Information Center, USGS	48.2900 ° N	9.0080 °E	8.00
ISC	International Seismological Centre	48.2990 ° N	8.9285 °E	10.00 (*f)
BGR	Federal Institute for Geosciences and Natural Resources	48.2800 ° N	9.0200 °E	-
Schwarz <i>et al.</i> (2010b)		48.2900 ° N	9.0300 °E	6.50
Leydecker (2011)		48.2567 ° N	9.0267 °E	7.00 ± 2.00

(*f) fixed parameter used for inversion

Table A4.3.4. Epicentral coordinates and hypocentral depths for the 2014 M3.6 Darmstadt earthquake from different sources.

Agency / Publication		Latitude	Longitude	Depth (km)
NEIC	National Earthquake Information Center, USGS	49.7930 ° N	8.6320 °E	10.00
ISC	International Seismological Centre	49.8266 ° N	8.6356 °E	16.60
BGR	Federal Institute for Geosciences and Natural Resources	49.8100 ° N	8.7100 °E	-
GFZ	German Research Centre for Geosciences	49.8400 ° N	8.6500 °E	5.00
Homuth & Rumpker (2017)		49.8270 ° N	8.7180 °E	4.30 ± 1.50
Müller <i>et al.</i> (2015)		49.7960 ° N	8.6820 °E	5.00

The epicentral coordinates of the 1978 Albstadt event reported in the EK DAG German earthquake catalogue of Schwarz *et al.* (2010b) match those given by Fuchs (2016) and are also in good agreement with those implied by Figure A4.3.4 from Scherbaum & Stoll (1983). Haessler *et al.* (1980) calculated a hypocentral depth of 6.5 km for this event, which is consistent with the value reported in the EK DAG catalogue (Schwarz *et al.*, 2010b).

Homuth & Rumpker (2017), who located 356 earthquakes of the 2014-2015 series and identified two well-defined clusters (Figure A4.3.3), found that the epicentral area of the 2014 Darmstadt main shock did not spatially correlate with the most damaged area, which was the district of Nieder-Beerbach within the municipality of Mühlthal, and attributed this to the radiation pattern, the spatial variation of geological site conditions and the differences in the building stocks at different locations. On the contrary, the epicentre reported by

Müller *et al.* (2015) matches the observed damage distribution better but does not result from a relocation study of a large series, as in the case of Homuth & Rumpker (2017), which is more reliable.

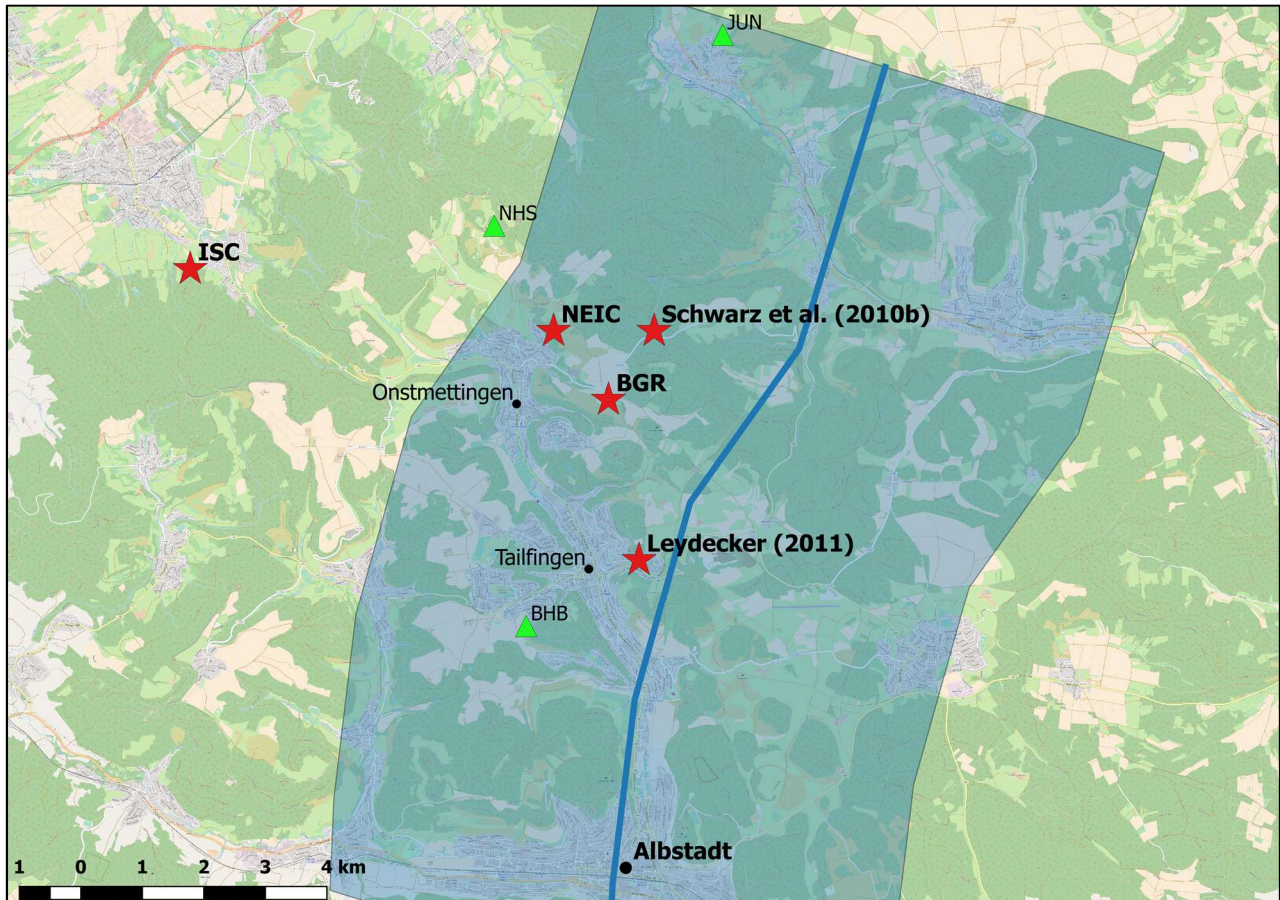


Figure A4.3.12. Estimations of epicentral coordinates (red stars) of the 1978 M5.2 Albstadt earthquake. The blue line represents the surface trace of the left-lateral, sub-vertically dipping strike-slip fault likely to have been the earthquake source, while the blue area represents the projection of the fault dipping plane to the ground surface, both according to SHARE (Woessner *et al.*, 2015). The surface projection should be to the side of the trace. The reasons for this not being the case are unknown, but it can be either an error in the database or a reflection of the uncertainty associated with the dip direction of the fault and/or its exact location, as properties of this fault have been inferred from the literature and by expert judgement, as explained in INGV-SHARE (2010).

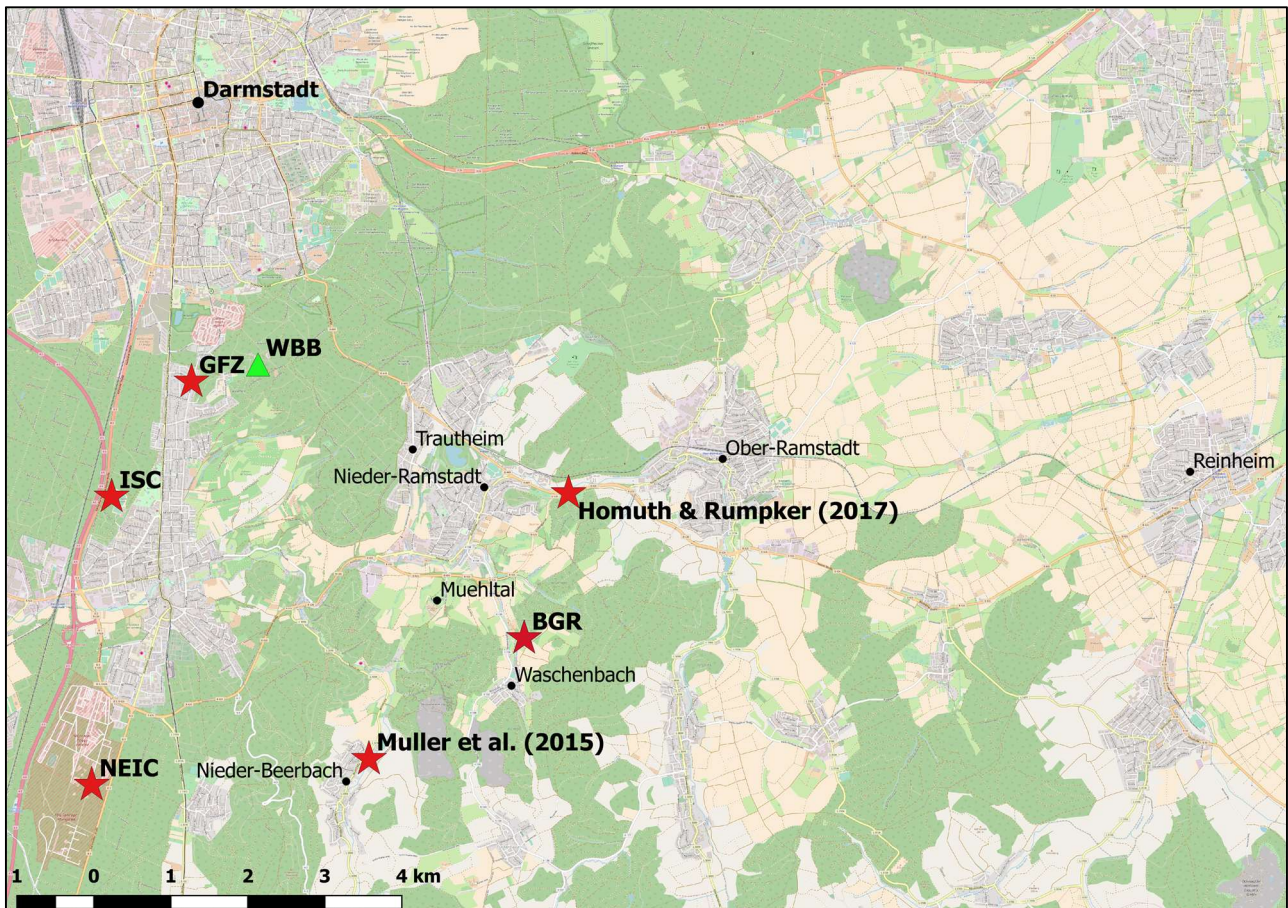


Figure A4.3.13. Estimations of epicentral coordinates (red stars) of the 2014 M3.6 Darmstadt earthquake.

A4.3.2.2 Magnitude

Estimations of magnitude reported on the websites of the National Earthquake Information Center (NEIC) of the United States Geological Service (USGS), the International Seismological Centre (ISC), the German Federal Institute for Geosciences and Natural Resources (BGR), the German Research Centre for Geosciences (GFZ), the Global Centroid Moment Tensor Project (GCMT; Dziewonski *et al.*, 1981; Ekström *et al.*, 2012), the Hessian State Office for Nature Conservation, Environment and Geology (HLNUG), as well as in the earthquake catalogues of Germany and adjacent areas compiled by Schwarz *et al.* (2010b) and Leydecker (2011), are summarized in Table A4.3.5 and Table A4.3.6. Magnitudes estimated by Haessler *et al.* (1980) and Homuth & Rumpker (2017) using the data from recordings of the seismic stations in the area of Albstadt and Darmstadt, respectively, are also included.

Table A4.3.5. Estimations of moment magnitude (M), body-wave magnitude (mb), local magnitude (M_L) and surface-wave magnitude (M_s) for the 1978 **M**5.2 Albstadt earthquake.

Agency		M	mb	M _L	M _s
NEIC	National Earthquake Information Center, USGS	-	-	-	5.3
ISC	International Seismological Centre	-	4.9	-	5.3
BGR	Federal Institute for Geosciences and Natural Resources	-	-	5.7	-
GCMT	Global Centroid Moment Tensor Project	5.2	4.9	-	5.3
Schwarz <i>et al.</i> (2010b)		5.1	-	5.7	-
Leydecker (2011)		-	-	5.7	-
Haessler <i>et al.</i> (1980)		-	4.9	5.7	5.1

Table A4.3.6. Estimations of moment magnitude (M), body-wave magnitude (mb), local magnitude (M_L) and surface-wave magnitude (M_s) depths for the 2014 **M**3.6 Darmstadt earthquake.

Agency		M	mb	M _L	M _s
NEIC	National Earthquake Information Center, USGS	3.6	3.6	-	-
ISC	International Seismological Centre	-	3.7	-	-
BGR	Federal Institute for Geosciences and Natural Resources	-	-	4.1	-
GFZ	German Research Centre for Geosciences	-	-	4.2	-
HLNUG	Hessian State Office for Nature Conservation, Environment and Geology	-	-	4.2	-
Homuth & Rumpker (2017)		-	-	4.2	-

A4.3.2.3 Style-of-faulting

The study of Haessler *et al.* (1980) revealed that the 1978 **M**5.2 Albstadt earthquake and its aftershocks were associated with dominant strike-slip faulting mechanism on a fault striking NNE. Focal mechanism solutions for the main shock determined by Turnovsky (1981) and the GCMT (Figure A4.3.14) also indicate strike-slip movement, with tensional axis in the NE direction. The fault plane solutions calculated by these two authors are summarized in Table A4.3.7. According to Turnovsky (1981), this event was a result of the left-lateral movement on the N20E striking and almost vertically dipping active fault plane (Fuchs, 2016).

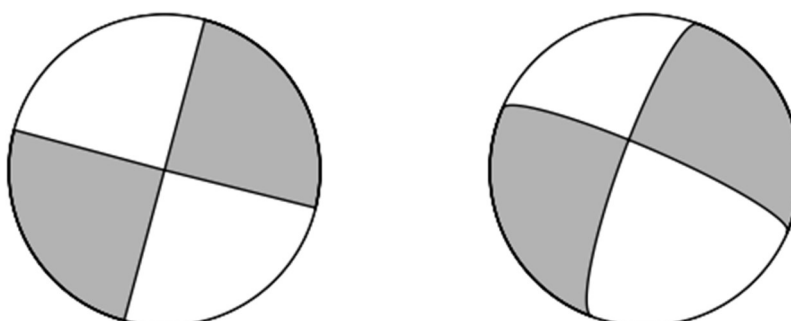


Figure A4.3.14. Focal mechanisms for the 1978 **M**5.2 Albstadt earthquake, according to GCMT (left) and Turnovsky (1981, right).

Table A4.3.7. Fault plane solutions and fault planes from different sources for the 1978 **M**5.2 Albstadt earthquake. Fault planes marked in grey are the preferred solution in each case.

Fault Plane 1			Fault Plane 2			Source
Strike	Dip	Rake	Strike	Dip	Rake	
285	90	180	15	90	0	GCMT
			200	75	-13	Turnovsky (1981)

The fault plane solution for the 2014 **M**3.6 Darmstadt earthquake, calculated by Homuth & Rümpker (2017) using data from more than 10 stations, indicates a strike-slip focal mechanism with a normal component, as shown in Figure A4.3.15 and Table A4.3.8. Considering that this event was part of the earthquake cluster (Figure A4.3.3 and Figure A4.3.17) whose fault plane solutions indicated predominantly left-lateral strike-slip mechanism with tension axis oriented NE-SW, and also considering the left-lateral transtensional regime to which this part of the Upper Rhine Graben is subject (see section A4.3.1.1), it is likely that the causative fault was the NE-SW oriented, sinistral strike-slip fault, *i.e.* the fault corresponding to plane 1 solution of Homuth & Rümpker (2017) from Table A4.3.8.

The focal mechanism for the 2014 **M**3.6 Darmstadt earthquake was also calculated by the USGS and GFZ, and their results are shown in Figure A4.3.15 and Table A4.3.8. The USGS fault plane solution indicates strike-slip movement with strong normal component, while the GFZ fault plane solution indicates an almost perfect strike-slip mechanism with a very small reverse component.

While different, all three focal mechanism solutions for the 2014 **M**3.6 Darmstadt earthquake enumerated above, show strong strike-slip components and are in overall general agreement with respect to the position of dilatational and compressional quadrants.

Table A4.3.8. Fault plane solutions and fault planes from different sources for the 2014 **M**3.6 Darmstadt earthquake. Fault planes marked in grey are the preferred solution in each case.

Fault Plane 1			Fault Plane 2			Source
Strike	Dip	Rake	Strike	Dip	Rake	
299	44	-177	207	88	-46	Regional Moment Tensor NEIC (USGS)
116	76	173	208	83	14	German Research Centre for Geosciences (GFZ)
34	51	-8	129	84	-140	Homuth & Rümpker (2017)

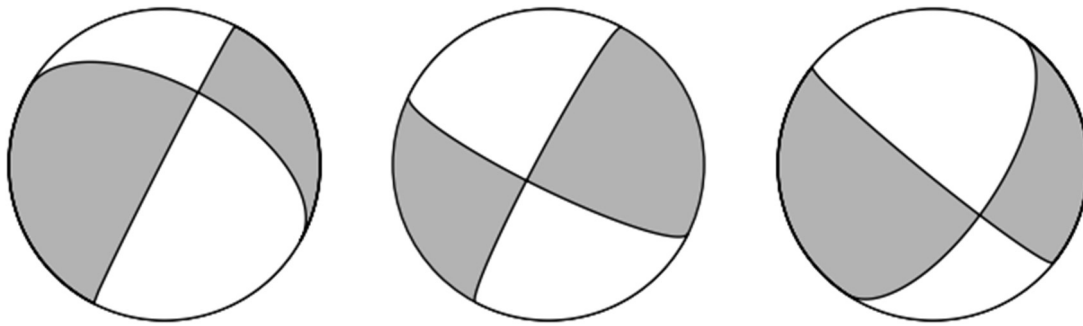


Figure A4.3.15. Focal mechanisms for the 2014 M3.6 Darmstadt earthquake, calculated by the USGS (left), GFZ (centre) and Homuth & Rumpker (2017, right).

A4.3.2.4 Stress drop

According to the results of the stochastic strong motion simulation for the 1978 **M**5.2 Albstadt earthquake performed by Langer (1990), the stress drop associated with this event is in the range between 1.8 MPa and 5.0 MPa. (18 bars and 50 bars). While not specifically addressing this seismic event, Fuchs (2016) report that spectral analyses indicate a stress drop of around 1 MPa (10 bars) for most of the earthquakes that happened in the Hohenzollern Graben (HZGR) region.

No information could be found regarding the stress drop for the 2014 **M**3.6 Darmstadt earthquake.

A4.3.2.5 Foreshocks and aftershocks

The 1978 **M**5.2 Albstadt earthquake was followed by a series of aftershocks. Reutlinger (2008) reported that seismic stations registered more than 60 aftershocks on 3rd September 1978, the day of the main shock, including three events of local magnitude M_L 4.1, 4.3 and 4.7 (USGS, 2017). More than 300 smaller events occurred until the end of 1978 (Scherbaum & Stoll, 1983). In the period from 4th September until 20th October, 67 aftershocks were registered by the network of 5 portable seismic stations (stations MSG, JUN, NHS, BHB and MSS, shown in Figure A4.3.4) installed in the epicentral area the day after the main shock. Their hypocentral coordinates were calculated by Haessler *et al.* (1980) and plotted by Scherbaum & Stoll (1983), as shown in Figure A4.3.16. From the plot on the left, it can be observed that the aftershocks were distributed within a confined area that stretches along the SW-NE direction. According to Scherbaum & Stoll (1983), their spatial distribution conforms with the strike and dip angles of the fault plane solution for the main event. They also point out that the focal mechanism of most of these events are concordant with a NNE-SSW striking sinistral strike-slip fault. It is observed that all these earthquakes occurred within a narrow vertical shallow zone with a width of only a few kilometers, which is also supported by the study of Turnovsky (1981). Most of the events had Wood-Anderson magnitudes (M_{WA} , expected to be similar to M_L) lower than 3 (Turnovsky, 1981; Fuchs, 2016).

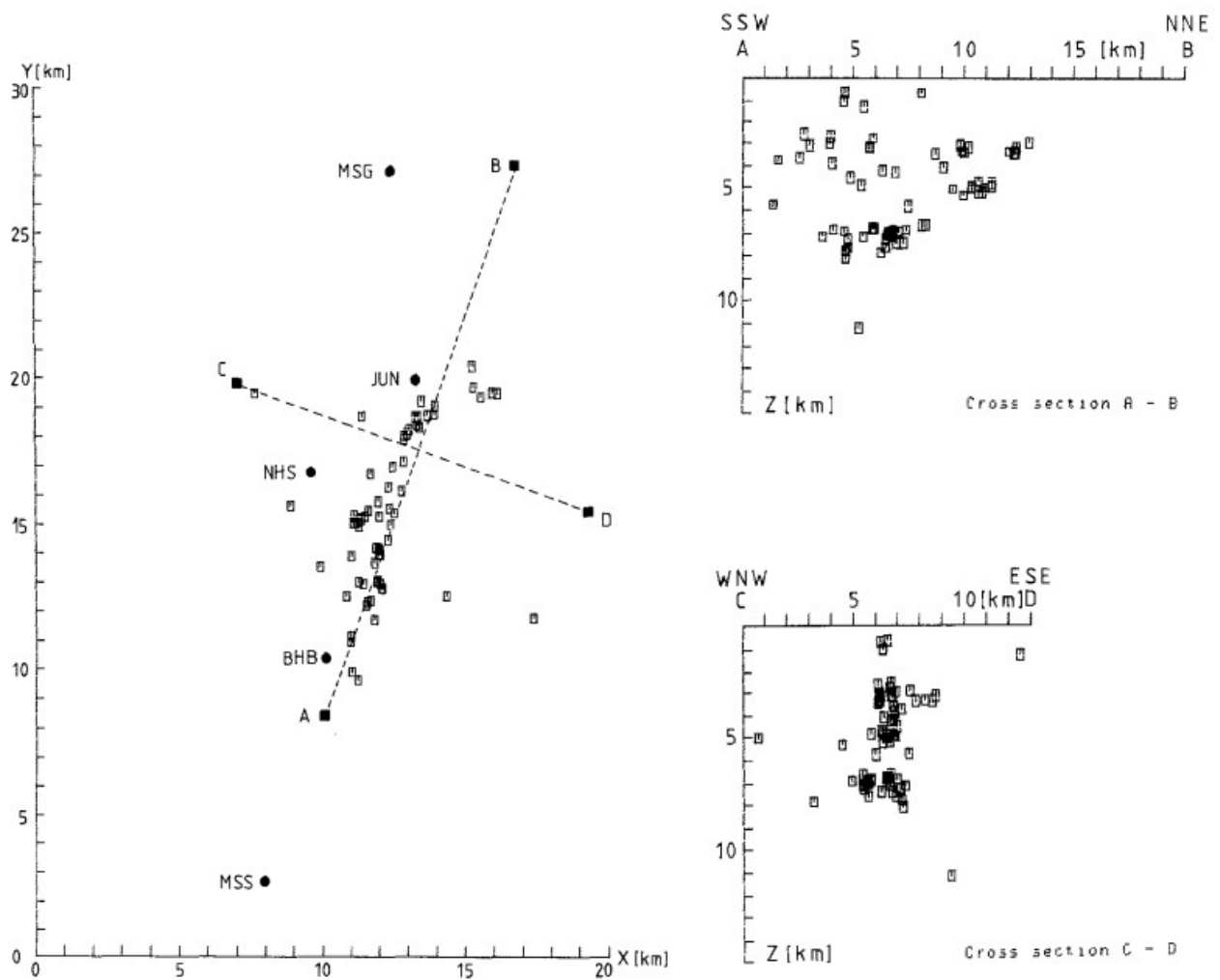


Figure A4.3.16. Hypocentres of the aftershocks of the 1978 M5.2 Albstadt earthquake, registered in the period from 4th September to 20th October: plan view (left) and cross-sections (right). From Scherbaum & Stoll (1983).

The 2014 **M**3.6 Darmstadt earthquake was the largest seismic event of the 2014-2015 earthquake series. From March 2014 to April 2015, 356 earthquakes, with local magnitudes in the range from -0.6 to 4.2, were recorded by the network of seismic stations shown in Figure A4.3.7 (Homuth & Rumpker, 2017). These seismic events were distributed within two distinctive clusters, located approximately 5 km from each other, as shown in Figure A4.3.3 and Figure A4.3.17. A sinistral strike-slip focal mechanism on steeply dipping fault planes was observed for most of these events (Homuth & Rumpker, 2017). Fault plane solutions for some of the earthquakes of cluster 1, including the event of 17th May 2014, indicate also the presence of a normal component of dip-slip movement (cf. Figure A4.3.15).

The distribution of hypocenters of the two clusters, projected onto N-S and E-W oriented vertical profiles, is shown in Figure A4.3.18. It is observed that these clusters are associated with shallow foci and narrow extent in the lateral, N-S direction. Seismic events of cluster 1 were mostly concentrated in depths between 1 and 6 km, while those of cluster 2 were located at depths from 5 to 6.5 km. Homuth & Rumpker (2017) point out that

earthquakes with local magnitudes as low as 1.5 were felt by the population, which is another indicator of shallow foci.

According to Homuth & Rumpker (2017), the earthquake time series shows neither the characteristics of a classic main shock – aftershock sequence, nor those of a swarm, and presents three easily identifiable main shocks: 17th May 2017 (M_L 4.2), 29th October 2014 (M_L 3.5) and 15th March 2015 (M_L 3.5). The authors also mention that the events that could be associated with the first two may represent a mixture of aftershock activity and a short-lasting swarm.

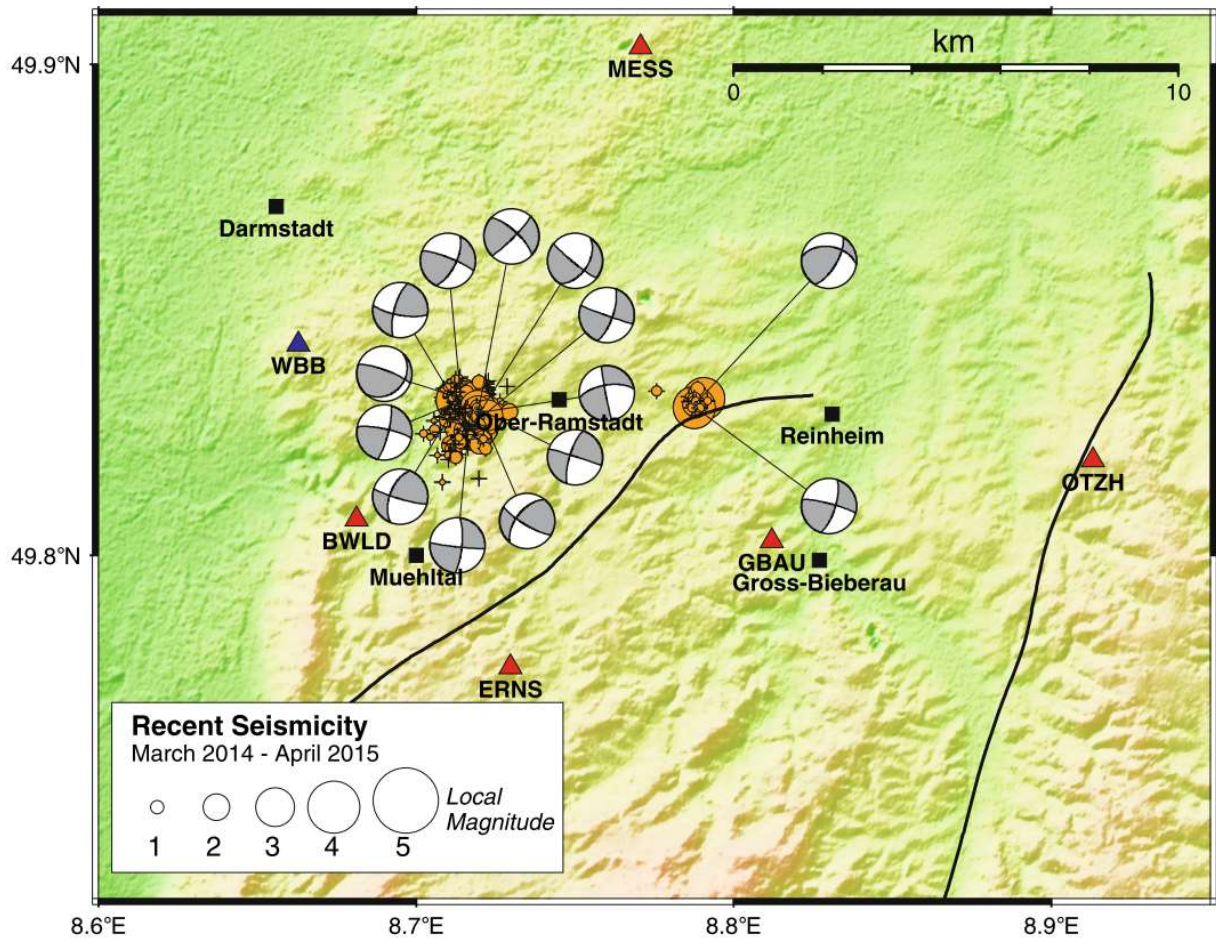


Figure A4.3.17. Determined focal mechanisms (grey symbols) mapped together with the relative locations (orange circles) of the 2014 – 2015 earthquake series near Ober-Ramstadt. Main event of 17th May 2014 belongs to cluster 1 (to the left). Continuous black lines show the course of the major faults introduced in Figure A4.3.2. From Homuth & Rumpker (2017).

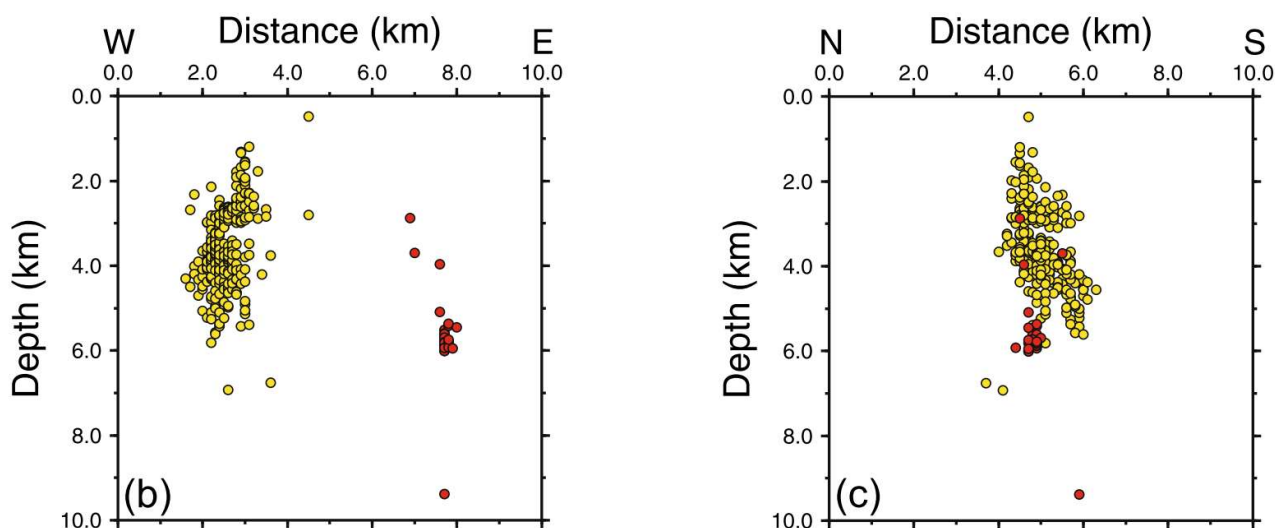


Figure A4.3.18. The distribution of hypocentres along a W-E and a N-S profile for the 2014-2015 earthquake series near Ober-Ramstadt. Yellow and red circles represent earthquakes belonging to cluster 1 and cluster 2, respectively (see Figure A4.3.3). From Homuth & Rümpker (2017).

A4.3.2.6 Nature of earthquake

No evidence of these earthquakes having an origin other than tectonic has been found.

Many authors (Haessler *et al.*, 1980; Turnovsky & Schneider, 1982) related the 1978 **M**5.2 Albstadt earthquake to the tectonic movements on a NNE striking fault, though information about the exact position of such fault did not exist at the time. Fuchs (2016) argue that the seismic activity in the Hohenzollern Graben region, in which this event occurred, is a response to the stress concentrations that are induced by the thinning of the brittle shallower part of the earth crust, which are believed to be due to local lateral crustal heterogeneities and the Urach thermal anomaly. It is noted, however, that exploitation of the latter for energy production only started in 2002, many years after the 1978 Albstadt earthquake (Foulger *et al.*, 2016; Wilson *et al.*, 2017).

According to Earthquake Report (2014a), seismologists agree that all the earthquakes of the 2014-2015 earthquake series (including the 17th May 2014 event) were of tectonic origin. They also report that the shallow hypocentral foci, as well as some other characteristics of these events, coincide with those of earthquakes induced by fracking and mining anthropogenic activity, but add that no such activity has ever been carried out around the epicentral area.

A4.3.3 Geology and ground conditions in the affected area

A4.3.3.1 Regional geology and topography

The city of Darmstadt lies along the Eastern Border Fault (EBF), which is on the boundary between the northern part of the Upper Rhine Graben (URG) to the west and the Odenwald mountain range to the east. The northern URG is a 40-km wide and 150-km

long extensional basin filled with Cenozoic sediments up to 3.5-km thick, underlain by Mesozoic and Palaeozoic sedimentary rocks (Figure A4.3.19) (Przyrowski & Schäfer, 2014; Homuth *et al.*, 2014). The Cenozoic basin fill of the URG consists mostly of marine to nearshore continental sediments of the Tertiary period, while its Quaternary sediments are of fluvial origin (Przyrowski & Schäfer, 2014). According to Peters (2007), the Cenozoic graben fill reaches its minimum thickness of 400 m in Darmstadt, with its Pleistocene part being evident in Figure A4.3.20, where a more detailed geological map of the epicentral region of the 2014 Darmstadt earthquake and its surrounding area is depicted. According to this map, the epicentral and the most affected area (between Nieder-Beerbach and Ober-Ramstadt) is bordered by the URG to the west, the Sprendlinger Horst to the north, the Flasegranitoid zone to the south and Reinheim Bay to the east (Schwarz *et al.*, 2015). The Frankenstein massif, on which most of the affected area is settled, represents the northern part of the crystalline Odenwald (Figure A4.3.2), and features a dominant presence of magmatic (e.g. Gabbro and Diorite) rocks.

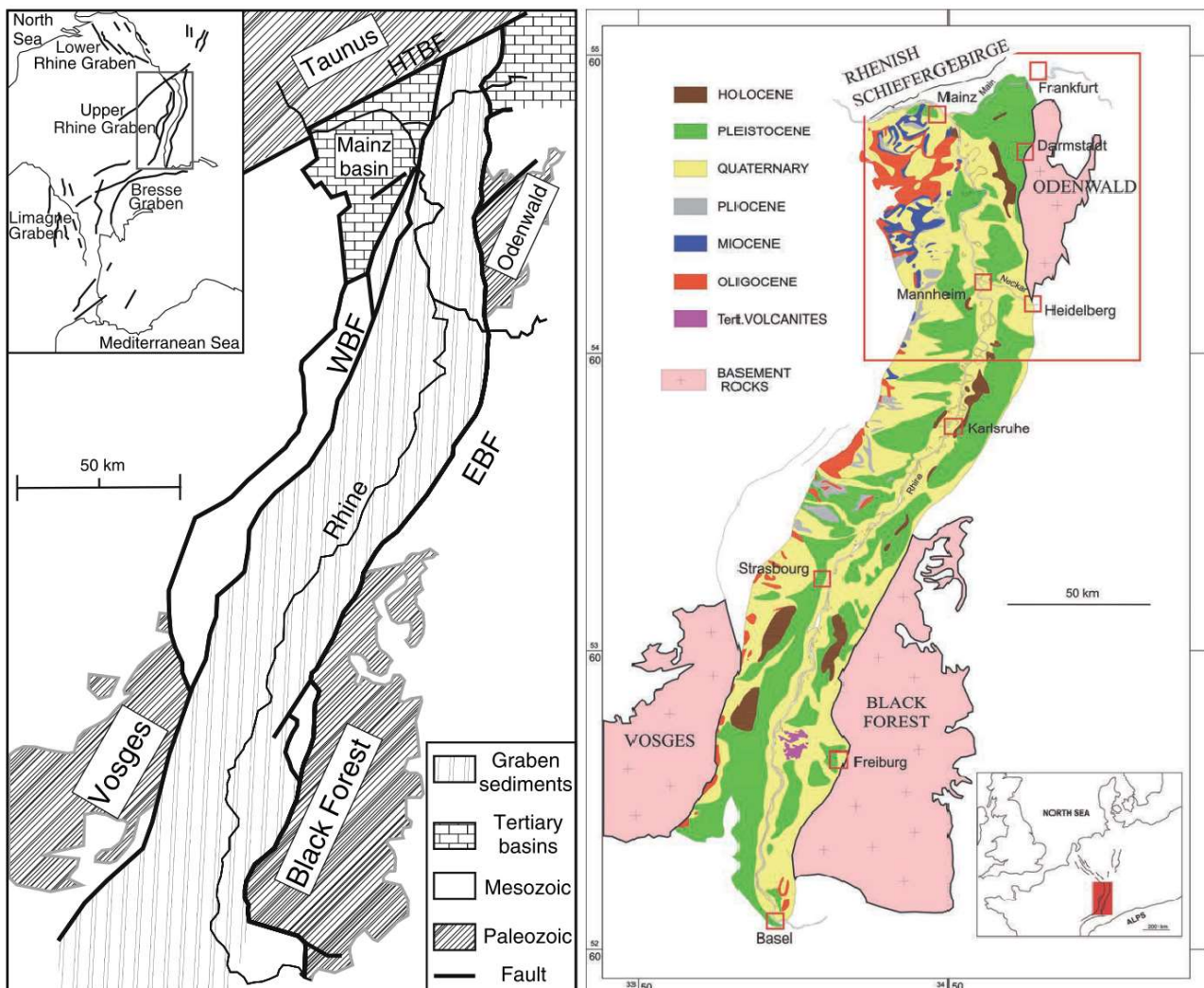


Figure A4.3.19. Maps of the Upper Rhine Graben containing major faults and bordering areas (left; from Homuth *et al.*, 2014) and generalised geology (right; from Przyrowski & Schäfer, 2014). HTBF: Hunsrück Taunus Border Fault; WBF: Western Border Fault; EBF: Eastern Border Fault. Upper left corner: Sketch map showing the Cenozoic rift system of western and central Europe.

Located in the Swabian Alps, the epicentral area of the 1978 Albstadt earthquake is characterized by a Paleozoic granitic and metamorphic basement overlain by an approximately 1-km-thick layer of horizontally stratified sediments of the Mesozoic era (Scherbaum & Stoll, 1983). During the Jurassic period of the Mesozoic era, a seabed of limestones was formed in the Swabian Jura. Limestones of the White Jurassic lithostratigraphic unit of the Southern German Jurassic super group can be observed in Figure A4.3.21, where a geological map of Tailfingen, the area most affected by the 1978 Swabian Jura earthquake, is shown.

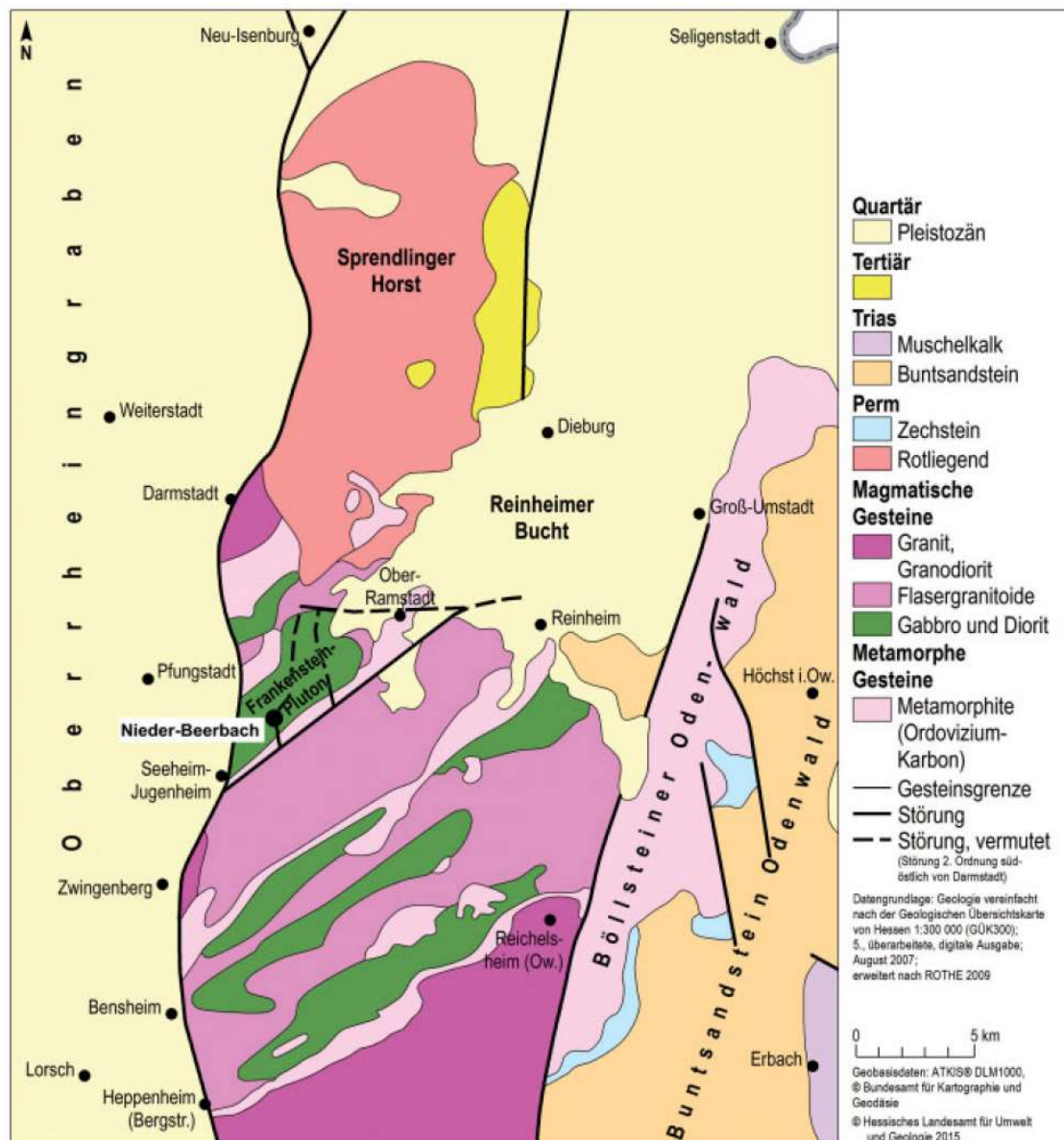


Figure A4.3.20. Large-scale geological situation around the region of the 17 May 2014 Darmstadt earthquake. Quartär (Quaternary period); Pleistozän (Pleistocene epoch); Tertiär (Tertiary period); Trias (Triassic period); Muschelkalk (Muschelkalk - lithostratigraphic unit); Buntsandstein (Buntsandstein - lithostratigraphic unit); Perm (Permian period); Zechstein (Zechstein – unit of a sedimentary rock); Rotliegend (Rotliegend - lithostratigraphic unit); Magmatische Gesteine (magmatic rocks); Granit, Granodiorit (Granit, Granodiorite); Flasergranitoide (Flasergranitoide – the crystalline western part of the Odenwald Mountains); Gabbro und Diorit (Gabbro and Diorite); Metamorphe Gesteine (metamorphic rocks); Metamorphite, Ordovizium-Karbon (Ordovician-carbon); Gesteinsgrenze (full line: rock border); Störung (Thick full line: fault); Störung, vermutet (Dashed line: suspected fault). From Schwarz et al. (2015).

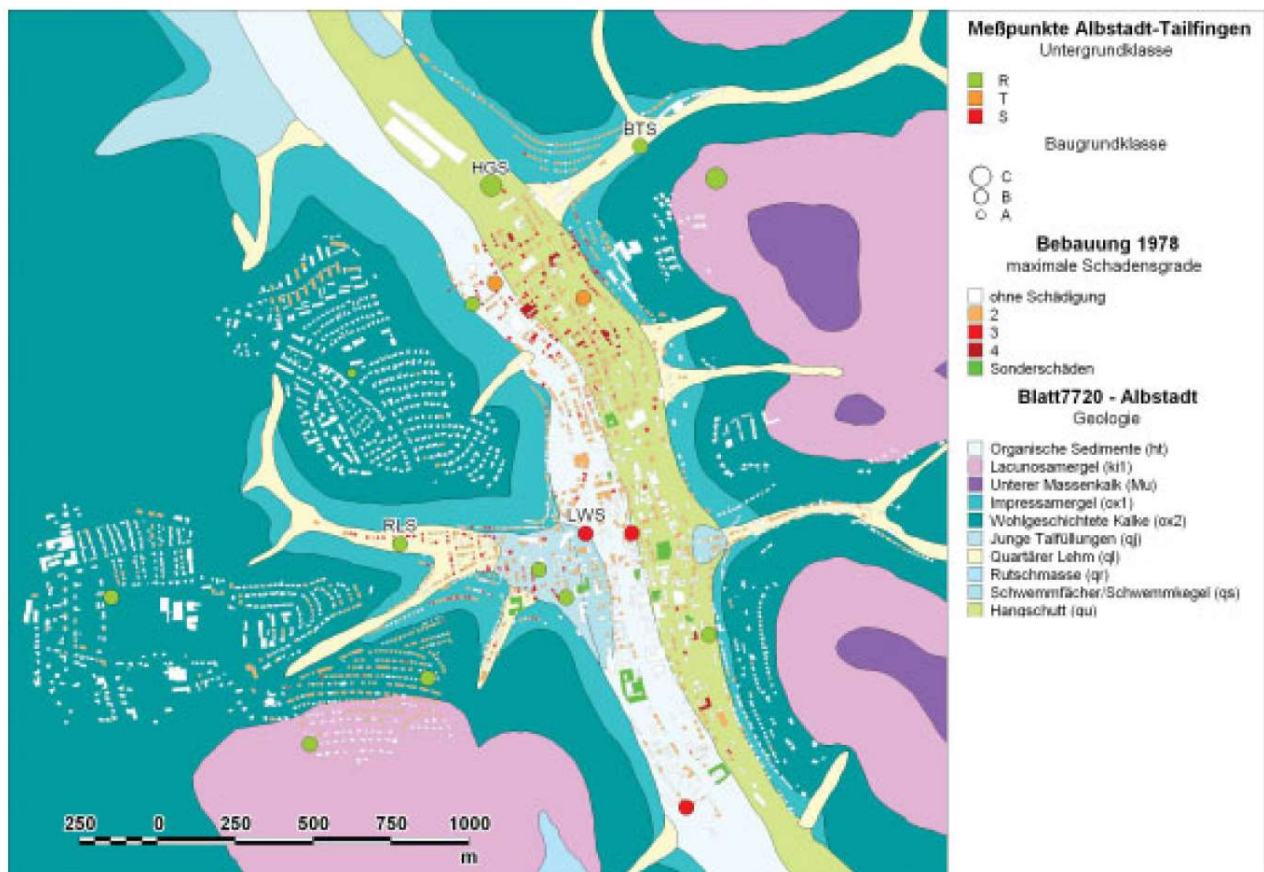


Figure A4.3.21. Geological situation of Albstadt-Tailfingen with building stock of 1978 and sites of instrumental investigations. R, T and S: geological subsoil classes; A, B and C: soil condition classes (see section A4.3.3.2). Maximum damage grades (EMS-98): ranging from "no damage" (white square) to damage grade IV. Special damage (e.g. damage to industrial chimneys) shown with green squares. Organische Sedimente (Organic Sediments); Quartärer Lehm (Quaternary Clay); Rutschmasse (sliding mass); Hangschutt (slope debris); geologic formations of White Jurassic lithostratigraphic unit of the Southern German Jurassic supergroup: Unterer Massenkalk (The Lower Massenkalk Formation), Impressamergel (Impressamergel Formation), Wohlgeschichtete (Wohlgeschichtete Kalk Formation), Lacunosamergel (Lacunosamergel Formation). From Amstein et al. (2005).

A4.3.3.2 Site conditions in the affected area

For the design of buildings according to German codes DIN 4149:2005-04 and DIN EN 1998-1/NA:2011-01, the influence of site conditions on seismic design loads is taken into account in accordance with the site classification scheme shown in Table A4.3.9. Soil condition classes (A, B, C) are characterized by the $V_{s,25}$ parameter, which is used for differentiation between soil types in the upper 25 meters (Lang & Schwarz, 2006). It can be distinguished between three geological subsoil classes (R, T, S) that vary in total thickness of sediments overlaying the geological bedrock, ranging from zero to more than 100 km. The schematic representation of the geological subsoil cases for Germany shown on the map in Figure A4.3.22 indicates that the areas affected by both the 1978 and 2014 earthquakes are located over soil classified as R.

Table A4.3.9. Possible combinations of site-specific subsoil classes of the German earthquake code DIN 4149:2005-04 and DIN EN 1998-1/NA:2011-01. From Lang & Schwarz (2006).

Geological subsoil class: Soil condition class:		R: areas predominantly characterized by rocks $H_{TOT} < 25$ m	T: transition zones between R and S $H_{TOT} < 100$ m	S: sediment basins $H_{TOT} > 100$ m
A: firm to medium-firm soil	$V_{s,25}^* > 800$ m/s	A-R	-	-
B: loose soil (gravel to coarse sands, marls)	$350 \text{ m/s} < V_{s,25}^* < 800$ m/s	B-R	B-T	(B-S)**
C: fine-grained soil (fine sands, loesses)	$150 \text{ m/s} < V_{s,25}^* < 350$ m/s	C-R	C-T	C-S

* Average shear-wave velocity of the uppermost 25 m of subsoil materials (m/s)

** As proposed by Lang et al. (2004). Combination B-S is not considered in DIN 4149:2005.

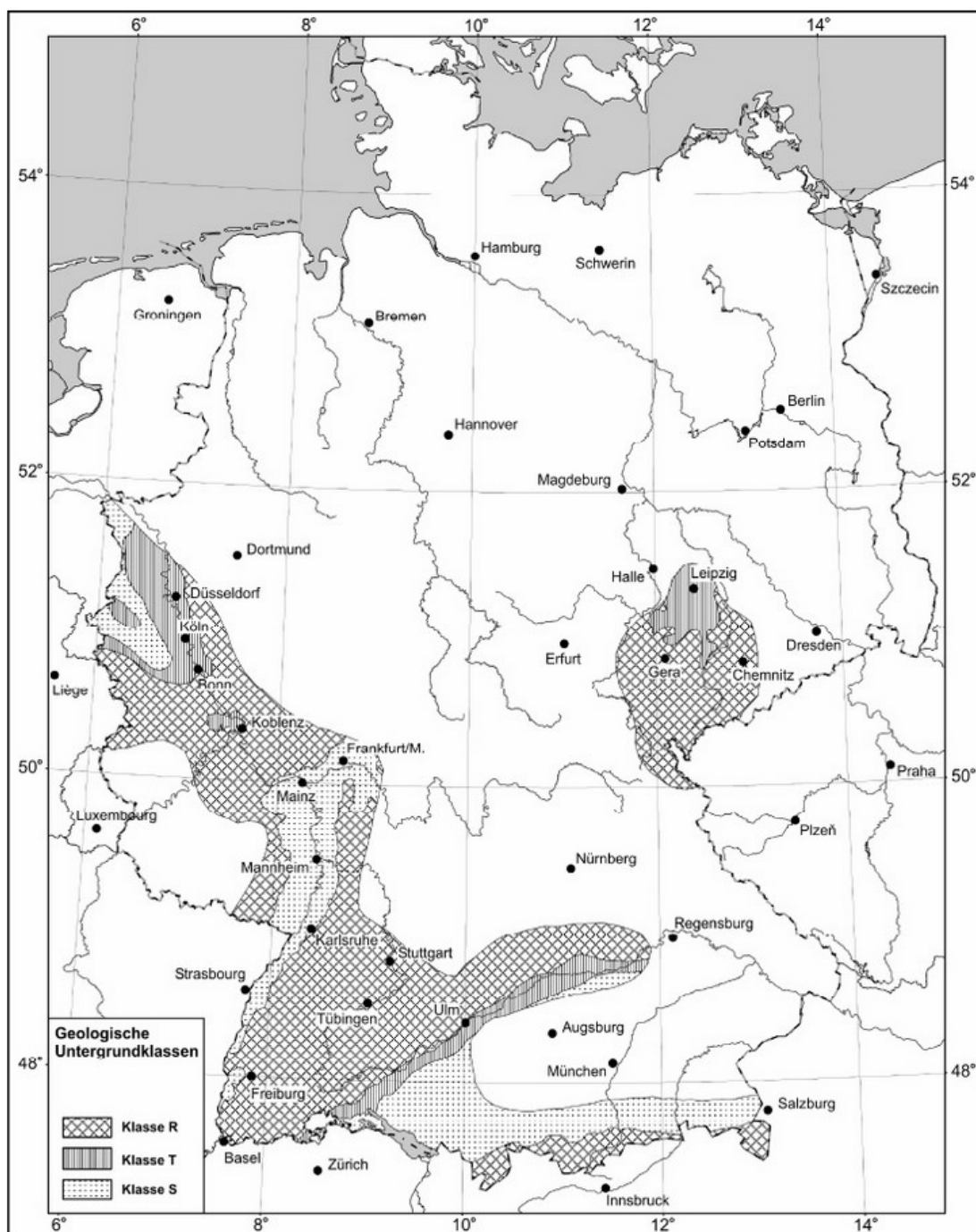


Figure A4.3.22. Schematic representation of the geological subsurface classes in the earthquake zones of the Federal Republic of Germany. From DIN EN 1998-1/NA:2011-01.

Lang & Schwarz (2006) presented the classification of site-conditions shown in Table A4.3.9 in a frequency-amplification domain, using combinations between boundary values of velocity ($V_{s,25}$) and total sedimentary layer thickness (H_{TOT}), as shown in Figure A4.3.23. This plot can be used to define the ground conditions at a specific site according to the provisions of the DIN EN 1998-1/NA:2011-01 code by plotting the results of the instrumental site response studies (e.g. H/V spectral ratio) and comparing the position of their peak values with respect to the theoretically defined one-dimensional site classification scheme. Such procedure was used for the assessment of subsoil classes in Tailfingen, the urban district of Albstadt that was most affected by the 1978 earthquake, and the results, reported by Schwarz *et al.* (2008), are shown in Figure A4.3.24. As observed from the figure, the predominant geological subsoil class in Tailfingen is class R, in accordance with the DIN EN 1998-1/NA:2011-01 map shown in Figure A4.3.22. Presence of geological subsoil class T and class S is observed in the middle of Tailfingen valley, where sediments are thicker than in the surrounding slope areas. It can be also observed in Figure A4.3.24 that the soil condition class B is dominant in the Tailfingen area.

In the Onstmettingen district of the city of Albstadt, which was also affected by the 1978 Albstadt earthquake and is located north of Tailfingen (Figure A4.3.12), alluvial deposits are found within the valley and Jurassic chalk and marl rocks are found in the high-lying areas surrounding the valley, while the transition slope area is characterized with slope debris, bolder and clay (Porro & Schraft, 1989; Figure A4.3.64, Section A4.3.8.4).

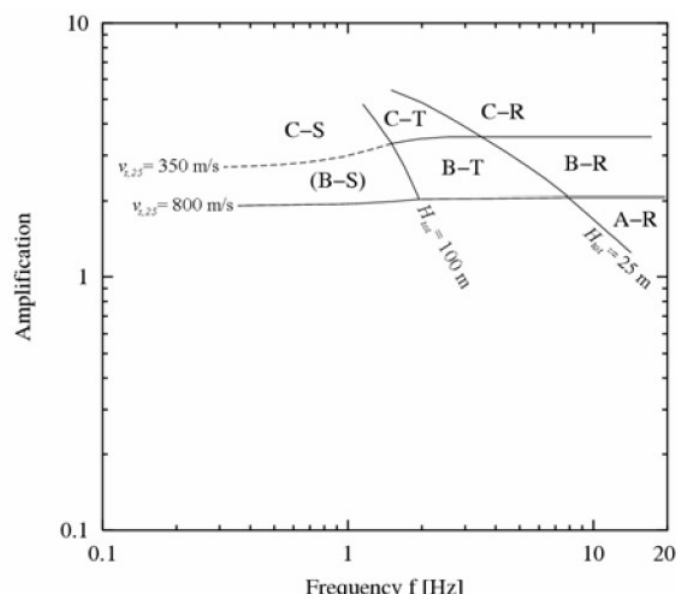


Figure A4.3.23. Representation of possible combinations of site-specific subsoil classes, defined by DIN EN 1998-1/NA:2011-01, in a frequency-amplification domain. From Lang & Schwarz (2006).

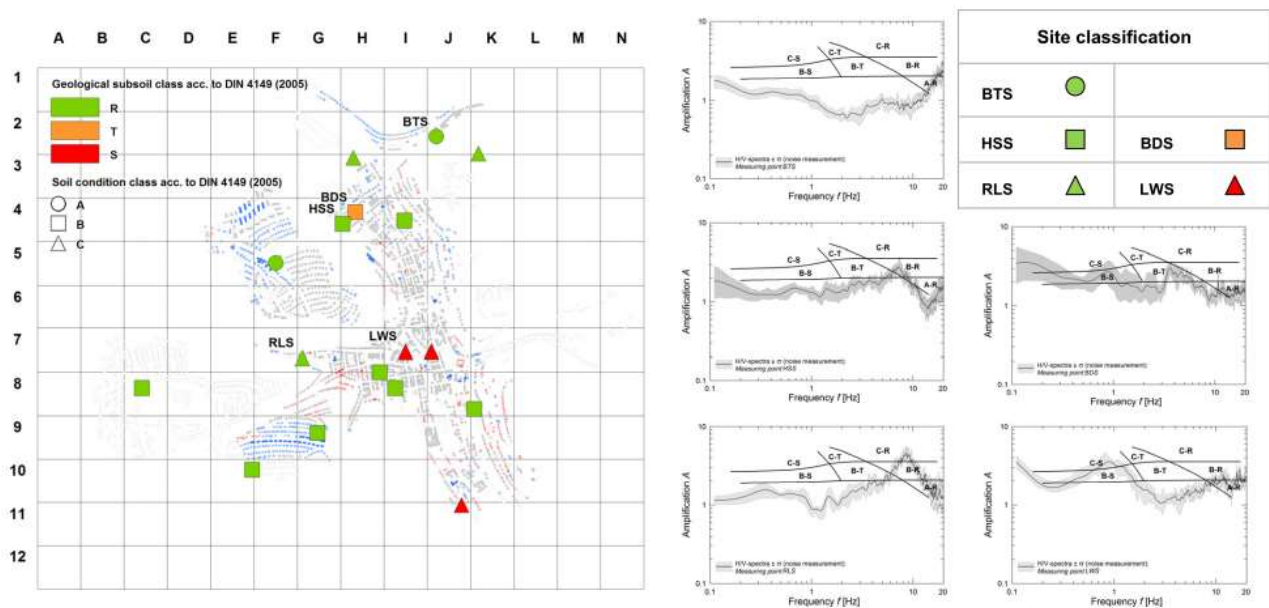


Figure A4.3.24. Classification of ground conditions in Tailfingen (Albstadt) within subsoil classes defined by DIN EN 1998-1/NA:2011-01 (left), based on the results of instrumental site response studies (right). From Schwarz *et al.* (2008).

Figure A4.3.25 depicts the soil map of Nieder-Beerbach, the area most affected by the 2014 **M3.6** Darmstadt earthquake. This map shows that the area is mostly covered by alluvial deposits, aeolian loose sediments (loess) and loose deposits with a high-water table that can flow even on low gradients, as well as by magmatic (diorite and gabbro) rocks and in smaller amount metamorphic (seprpentinite and amphibolite) rocks. Schwarz *et al.* (2015) point out that the soil map in Figure A4.3.25 indicates the presence of subsoil classes B-R and C-R according to DIN EN 1998-1/NA:2011-01 soil classification, which present the highest amplification potential.

According to the online soil map viewer of the Federal Institute for Geosciences and Natural Resources (BGR, 2017b), the epicentral area of the 1978 **M5.2** Albstadt earthquake is covered by limestones, marlstones and dolostones. This soil map also indicates that the epicentral area of the 2014 **M3.6** Darmstadt earthquake according to Homuth & Rümpker (2017) lies on brown loess soils including sand loess and loess-like deposits, while the epicentral area according to Müller *et al.* (2015), which is also the area most affected by this seismic event (Nieder-Beerbach), lies on acid to intermediate acid magmatic and metamorphic rocks. To the west and north-west of these areas, towards Darmstadt, soils of the river terraces and flood sediments can be found.

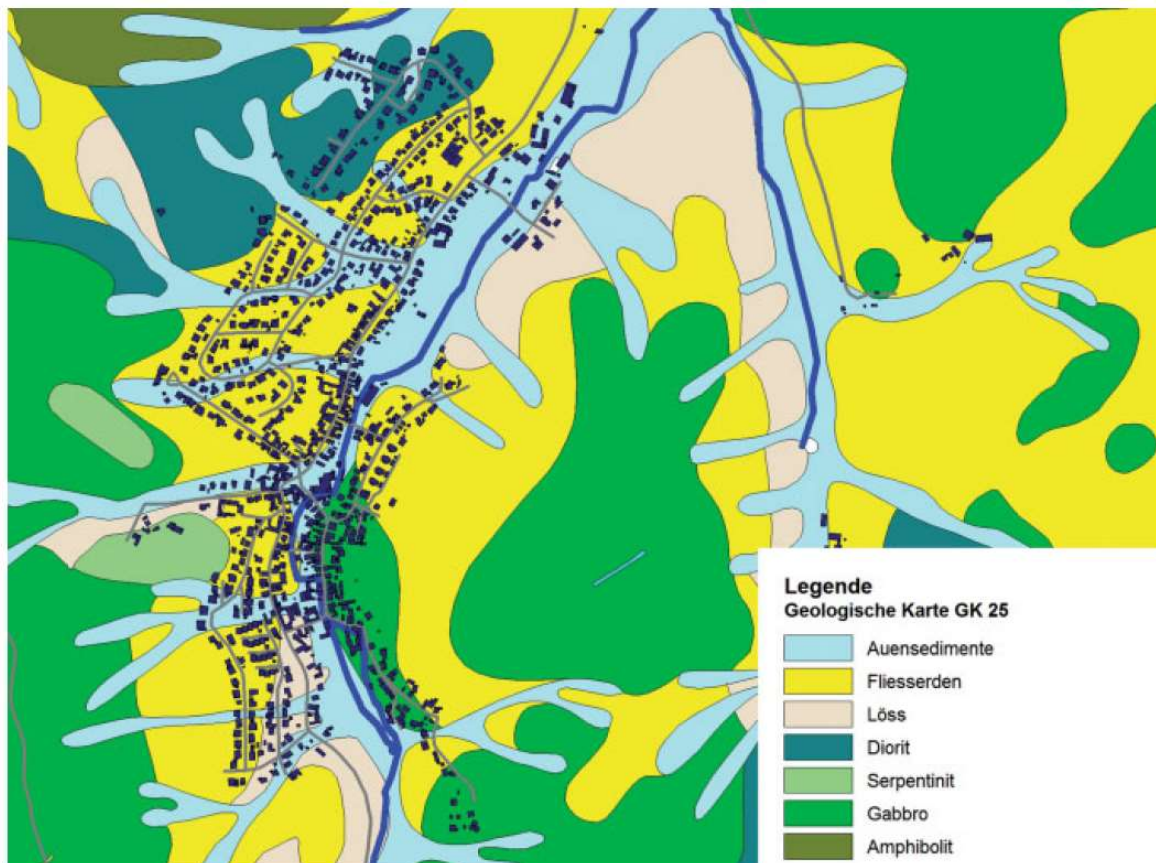


Figure A4.3.25. Soil map (GK 25) of the affected area around Nieder-Beerbach. Auensedimente (alluvial deposits); fließerden (loose deposits with a high water-table that can flow even on low gradients); löss (loess); diorit (diorite); serpentinit (serpentine); gabbro (gabbro); amphibolit (amphibolite). From Schwarz *et al.* (2015).

Figure A4.3.26 and Figure A4.3.27 depict the average shear wave velocity to a depth of 30 meters (V_{s30}) for the area of Albstadt and Darmstadt, respectively, as calculated by the United States Geological Survey (USGS, 2017a; Wald & Allen, 2007) V_{s30} Map Server using topographic slope as a proxy. As observed from Figure A4.3.26, the epicentre of the 1978 Albstadt earthquake (according to Schwarz *et al.*, 2010b) and the seismological station JUN lie over soils with a value of V_{s30} of approximately 900 m/s. According to the RESORCE database (Akkar *et al.*, 2014), the value of V_{s30} at station JUN is 1,000 m/s, which is slightly higher than the value obtained from the USGS Map Server. Figure A4.3.27 reveals that the $V_{s,30}$ value corresponding to the epicentre of the 2014 Darmstadt earthquake (according to both Homuth & Rümpker, 2017, and Müller *et al.*, 2015) is also 900 m/s. Seismological station WBB, located in the vicinity of the epicentre, is associated with $V_{s,30}$ values in the range between 800 and 900 m/s.

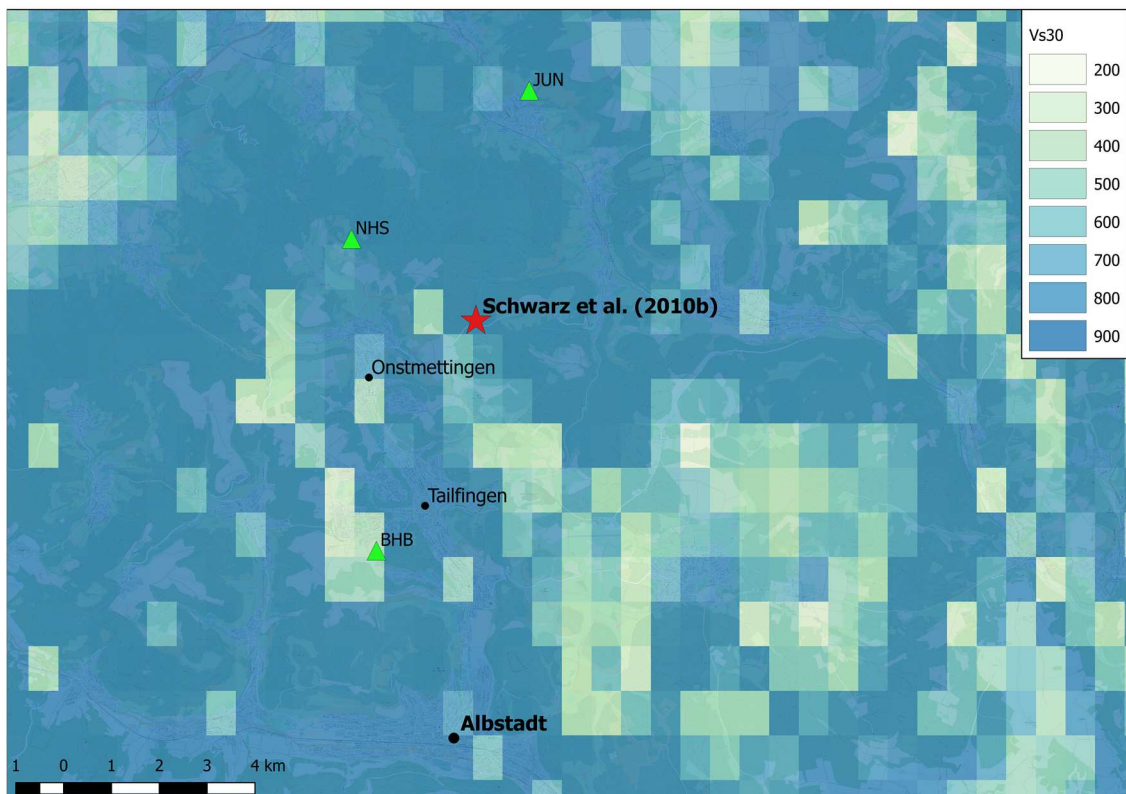


Figure A4.3.26. Estimation of Vs30 in the area of Albstadt using topographic slope as a proxy. Data from the USGS Vs30 map server (USGS, 2017a; Wald & Allen, 2007). Red star indicates epicentre (according to Schwarz et al., 2010b); green triangles indicate seismic stations.

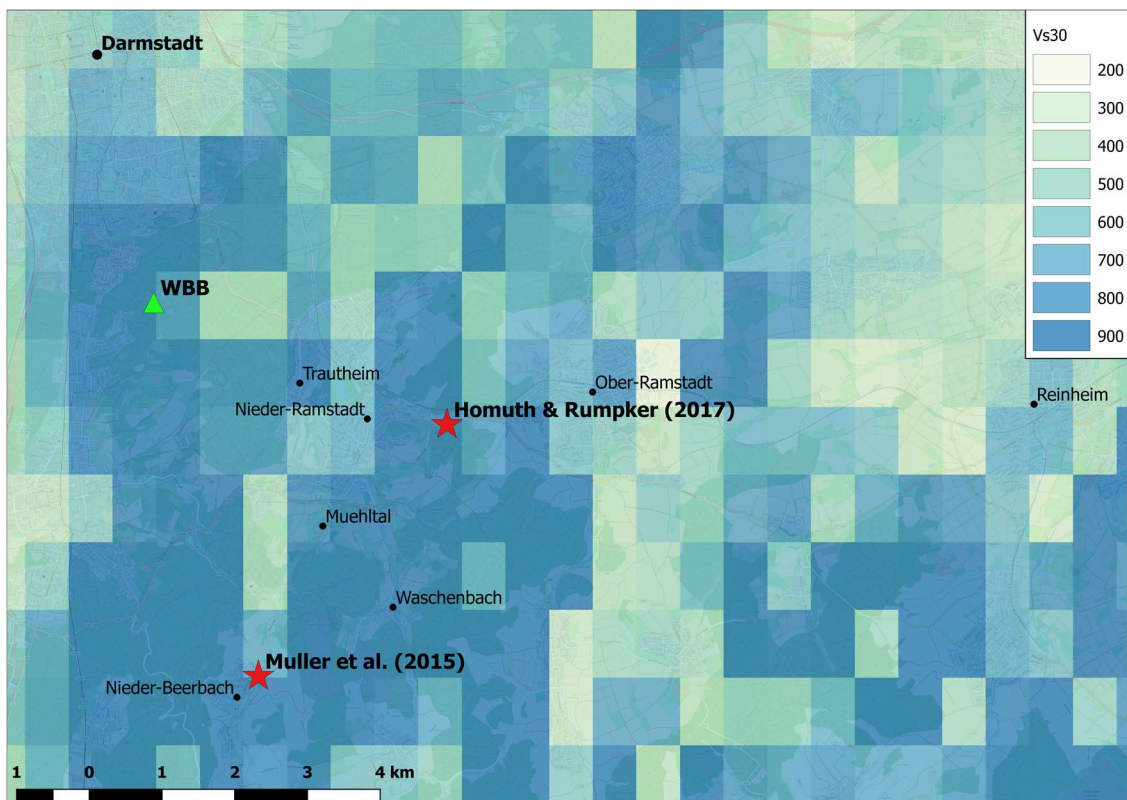


Figure A4.3.27. Estimation of Vs30 in the area of Darmstadt using topographic slope as a proxy. Data from the USGS Vs30 map server (USGS, 2017a; Wald & Allen, 2007). Red stars indicate epicentre (according to Homuth & Rumpker, 2017 and Müller et al., 2015); green triangle indicates WBB station.

A4.3.4 Ground motions

A4.3.4.1 Intensity observations

The 1978 **M5.2** Albstadt earthquake was felt within a radius of 400 km (Schwarzwaelder Messenger, 2013; Stuttgart News, 2011), and produced the greatest effects in the Tailfingen, Ebingen and Onstmettingen districts of Albstadt, which is the largest city in the Zollernalbkreis district of the German State of Baden-Württemberg (Blauß, 1980). Figure A4.3.28 depicts the macroseismic intensity map and macroseismic observations of the 3rd September 1978 Albstadt earthquake that were plotted by Beinersdorf & Schwarz (2014), combining data from Hiller (1985) and Meidow (2008). As observed in the figure, this seismic event is associated with a maximum EMS-98 intensity of shaking of VII-VIII (7.5). This is in agreement with the maximum intensity level indicated by the macroseismic shaking map of Procházková *et al.* (1979), shown in Figure A4.3.29, reproduced by Schwarz *et al.* (2010b) and included in the EKDAG earthquake catalogue for Germany and its adjacent areas. According to the EKDAG catalogue (Schwarz *et al.*, 2010b), both the epicentral and maximum observed EMS-98 intensity were VII-VIII (7.5). Beinersdorf *et al.* (2013) reported an EMS-98 intensity of VII-VIII for this seismic event as well, backed by the damage grades that were assigned to buildings located in the most affected districts of Albstadt, as will be later shown in Figure A4.3.52.

The earthquake catalogues of Leydecker (2011) and Van Gils & Leydecker (1991), which are available from the BGR website, report an MSK-64 intensity of 7.5 for the 1978 Albstadt seismic event. The catalogue of Van Gils & Leydecker (1991) also reports a radius of perceptibility of 330 km. The National Center for Environmental Information (NOAA) reports a Modified Mercalli intensity (MMI) of VIII, while Blauß (1980) reports intensities in the VII-VIII range on the Mercalli - Sieberg intensity scale. According to the catalogue of Grünthal & Wahlström (2003), this earthquake was felt over an area of 340,000 km², which is in agreement with the 330-km radius mentioned by Van Gils & Leydecker (1991).

Figure A4.3.30 depicts the USGS ShakeMap (Worden *et al.*, 2017) in terms of Modified Mercalli Intensities (MMI) for the 1978 Albstadt event, elaborated using intensity information from Haessler *et al.* (1980). According to this map, the maximum reached intensity of shaking was 6.9 MMI, which is lower than the values reported by NOAA for the same scale.

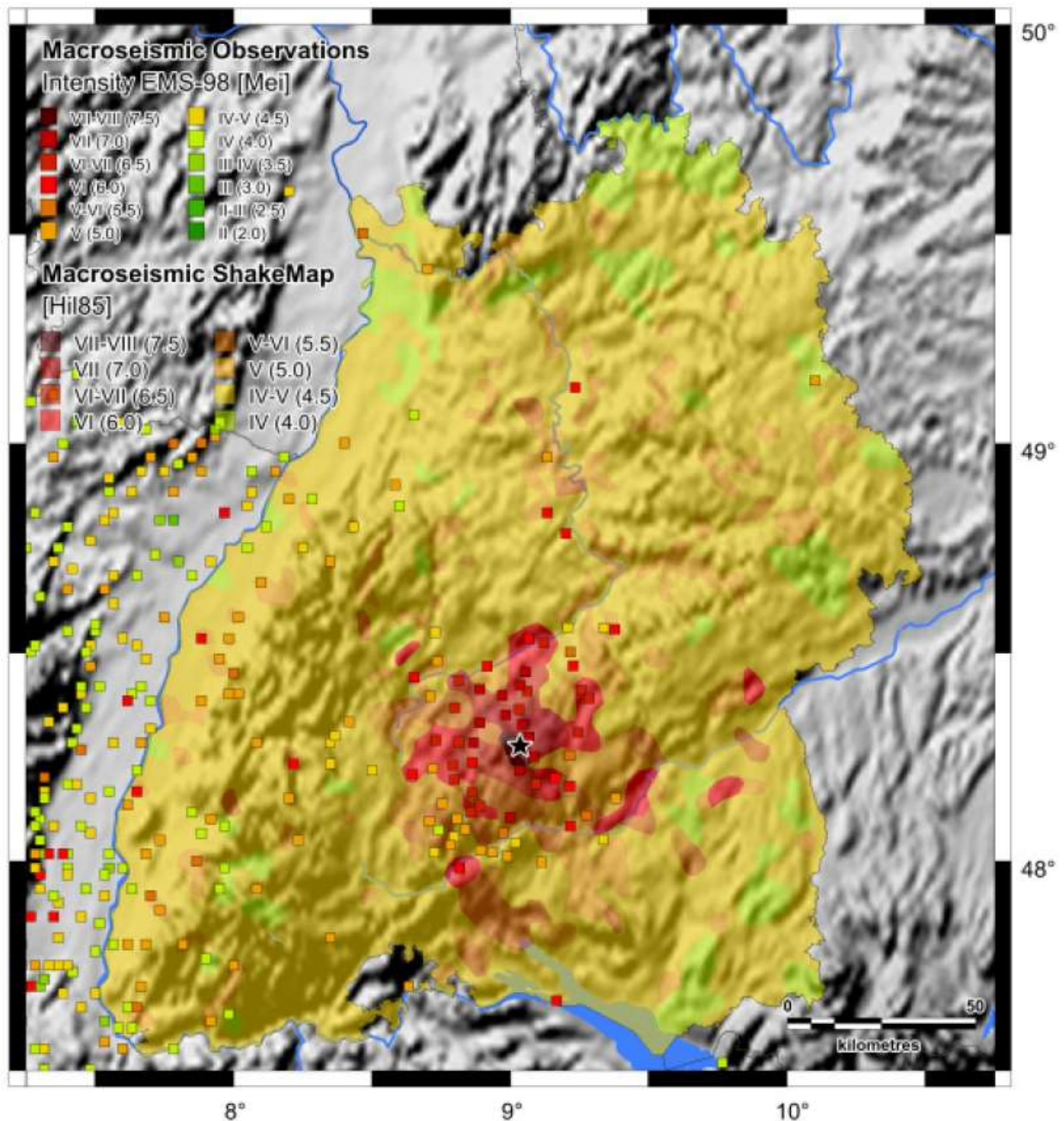


Figure A4.3.28. Macroseismic intensity map of the Albstadt earthquake on 3rd September 1978 according to Hiller (1985) and macroseismic observations according to Meidow (2008). From Beinersdorf & Schwarz (2014).

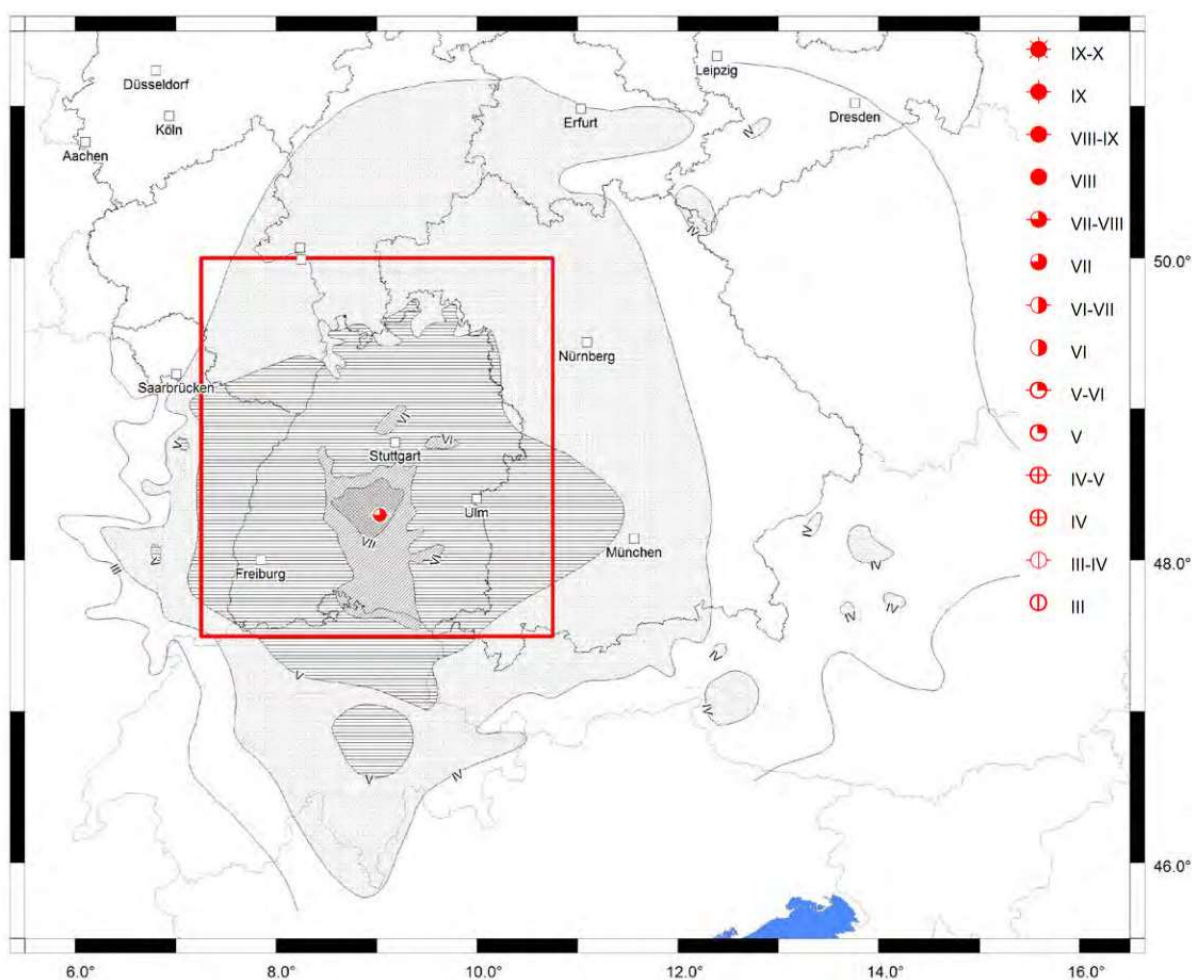


Figure A4.3.29. Macroseismic intensity map for the 1978 Albstadt earthquake, after Procházková *et al.* (1979). From Schwarz *et al.* (2010b).

The 2014 **M**3.6 Darmstadt earthquake produced shaking across almost all of the entire Rhine-Main area, including Frankfurt, and induced the greatest effects in the Nieder-Beerbach district of Mühlthal municipality, that belongs to the Darmstadt-Dieburg district of the Hesse German State (Juskus Earthquake News, 2014; Schwarz *et al.*, 2015). The earthquake was felt as far as Taunus to the north, Rhenish Hesse region of State Rhineland-Palatinate to the west, Aschaffenburg town of Bavaria State to the east and Stuttgart city of Baden-Württemberg State to the south (Juskus Earthquake News, 2014; Earthquake Report, 2014b).

The Hessian State Office for Nature Conservation, Environment and Geology (HLNUG, 2017) received more than 520 answers in response to their online macroseismic questionnaire. The EMS-98 intensities that were assigned in accordance to these and the corresponding macroseismic map are shown in Table A4.3.10 and Figure A4.3.31. As can be observed in Figure A4.3.31, the greatest number of answers came from densely populated areas, located north-west of the epicentre reported by Müller *et al.* (2015; Figure A4.3.13), that is, north-west of Nieder-Beerbach. However, the qualitatively most severe damage, associated with intensity of shaking EMS-98 VII (yellow triangles on the map), was reported for the area around the epicentre, *i.e.* in Nieder-Beerbach itself. An EMS-98 intensity of VII was assigned to cases of severe damage to chimneys. However, Schwarz

et al. (2015) argue that, according to the EMS-98 scale, this intensity level relates to complete destruction of chimneys, *i.e.* collapse of chimney stacks above the roof line, while a partial chimney collapse, observed on many properties (e.g., Figure A4.3.54), would be an indicator of intensity VI. Schwarz *et al.* (2015) emphasize that interpretation of chimney damage as an indicator of EMS-98 intensity VI instead of VII is in agreement as well with the results of a field survey of the affected building stock, which, apart from damage to chimneys, revealed either no damage or only instances of minor structural damage.

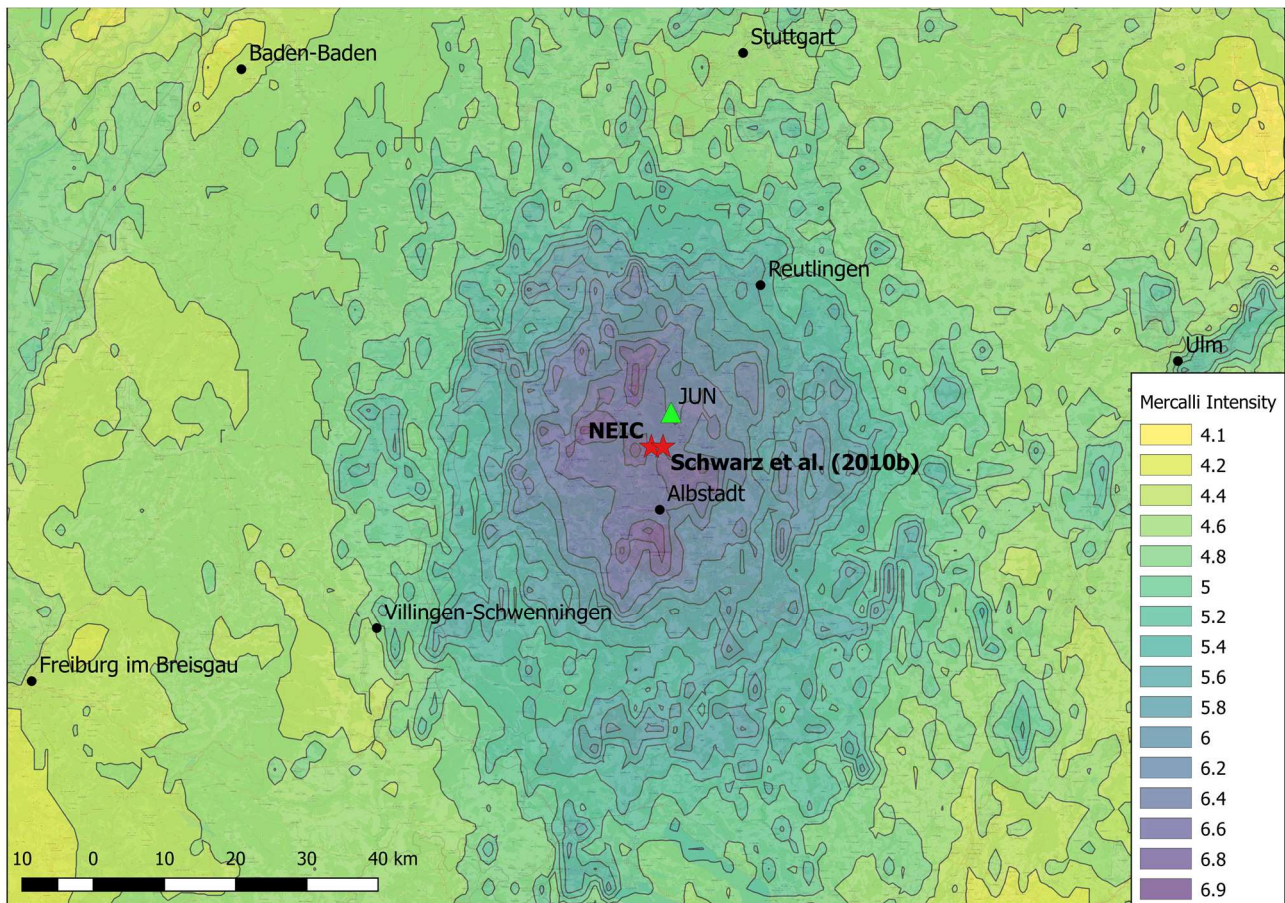


Figure A4.3.30. USGS ShakeMap (2017b) in terms of Modified Mercalli Intensities (MMI) for the 1978 M5.2 Albstadt earthquake. Red stars indicate the epicentres according to the USGS (NEIC) and Schwarz *et al.* (2010b).

The very few results of the “Did You Feel it?” questionnaire, available on the USGS website (USGS, 2017c), indicated a MMI value of 4.0 associated with the 2014 Darmstadt event, which is much lower than the value reported by Schwarz *et al.* (2015). This discrepancy might be related to the fact that none of the answers to the USGS questionnaire came from the most-affected Nieder-Beerbach area, where, according to Schwarz *et al.* (2015), site effects contributed to increased levels of damage.

Table A4.3.10. Assignment of EMS-98 intensities for the 2014 Darmstadt earthquake, according to answers to the questionnaires at HLNUG website. From Schwarz et al. (2015).

Intensity (EMS-98)	III	IV	V	VI	VII
Number of answers	42	163	258	47	12

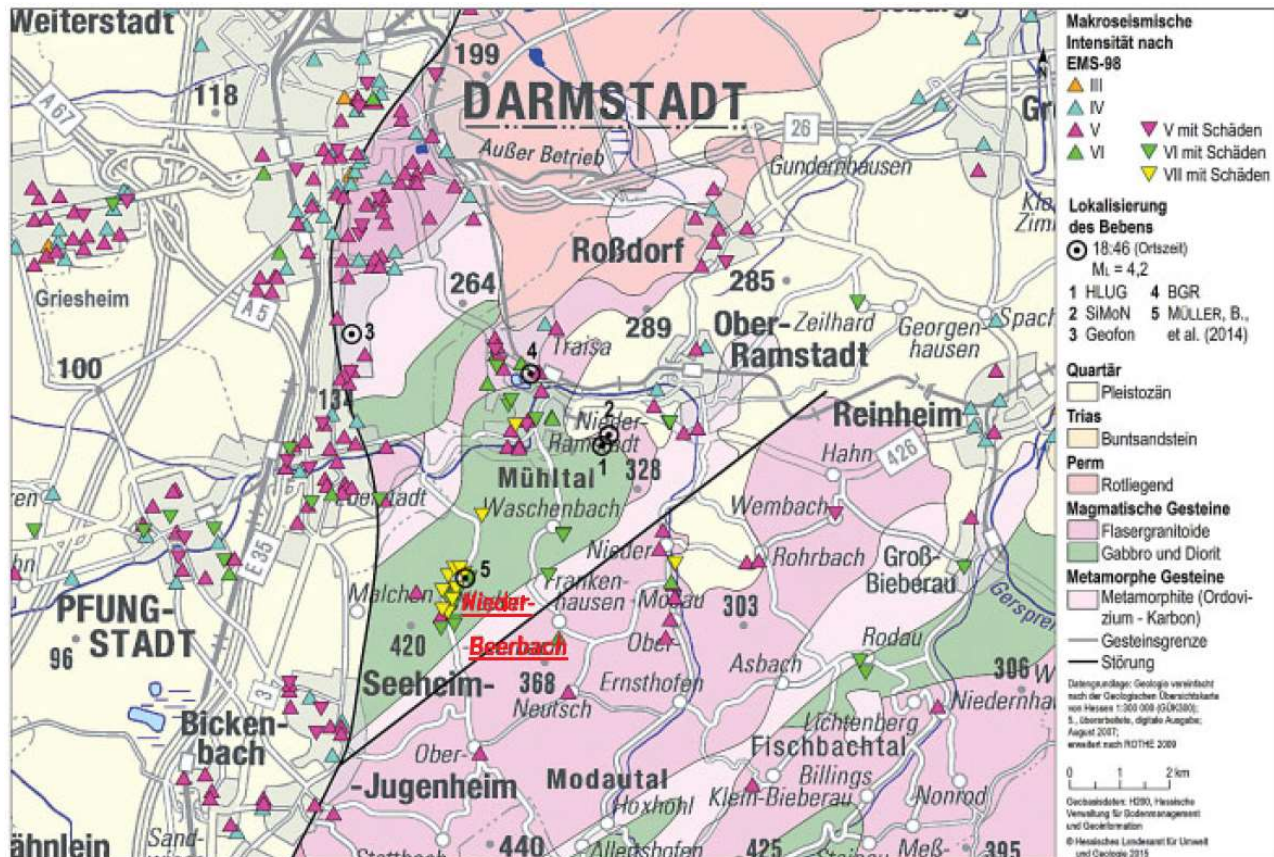


Figure A4.3.31. Macroseismic map of the 2014 Darmstadt earthquake according to answers to the questionnaires from the HLNUG website. Triangles indicate location of properties for which the questionnaires were answered on the HLNUG website. Down-facing triangles indicate the location of properties for which damage was reported. From Schwarz et al. (2015).

A4.3.4.2 Ground motion recordings

The 1978 $M_{5.2}$ Albstadt earthquake was recorded on a free-field site at the Jungingen (JUN) station that is located approximately 5 km from the epicenter coordinates reported by Schwarz *et al.* (2010b). The accelerogram shown in Figure A4.3.32 corresponds to its vertical component of ground motion (the only one available), which was retrieved from the RESORCE database (Akkar *et al.*, 2014) and has a PGA of 122 cm/s^2 . The main characteristics of this waveform are summarized in Table A4.3.11. The Fourier amplitude spectrum in Figure A4.3.33 and the pseudo-acceleration response spectrum in Figure A4.3.34 reveal that the fundamental frequency of this record is around 4.6 Hz ($T=0.22$ seconds), while a second relevant peak can be observed at around 3 Hz ($T=0.33$ seconds). The displacement response spectra for this accelerogram is presented in Figure A4.3.35.

From the publicly available literature it has not been possible to understand why only the vertical component of the record at JUN station is available, or why Schwarz *et al.* (2005) indicate that information derived from the records at said station should be interpreted with caution. Based on data from Wieck & Schneider (1980), which we could not access, Beinersdorf & Schwarz (2014) report PGA values of 0.11-0.13 g for the 1978 Albstadt earthquake, which appear to be consistent with the 122 cm/s² of the vertical component. Schwarz *et al.* (2005) also report that, based on the ground motion levels associated to the aftershocks, Wieck & Schneider (1980) concluded that PGA values between 0.2 and 0.3 g are likely to have occurred in the epicentral area, though it is not clear how they arrived to this conclusion.

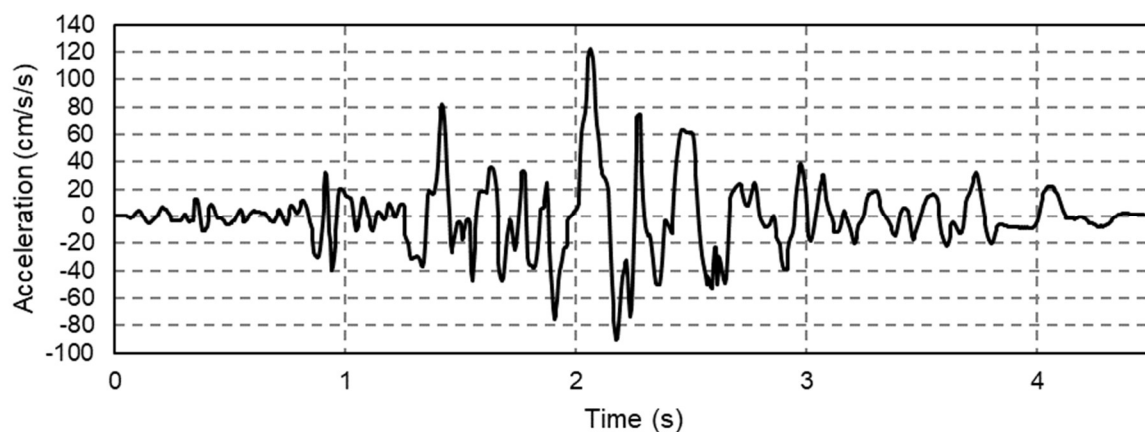


Figure A4.3.32. Vertical acceleration time-history recorded for the 1978 M5.2 Albstadt earthquake at station JUN, 5 km away from the epicentre reported by Schwarz *et al.* (2010b). Waveform data from RESORCE database (Akkar *et al.*, 2014).

Table A4.3.11. Main characteristics of one waveform of the 1978 M5.2 Albstadt earthquake available from the RESORCE database, processed with SeismoSignal (Seismosoft, 2016).

Station	Station Name	Latitude	Longitude	Repi (km)	PGA (cm/s ²)	PGV (cm/s)	PGD (cm)
JUN	Jungingen	48.3330 ° N	9.0450 ° E	5.0	122.000	4.701	0.397

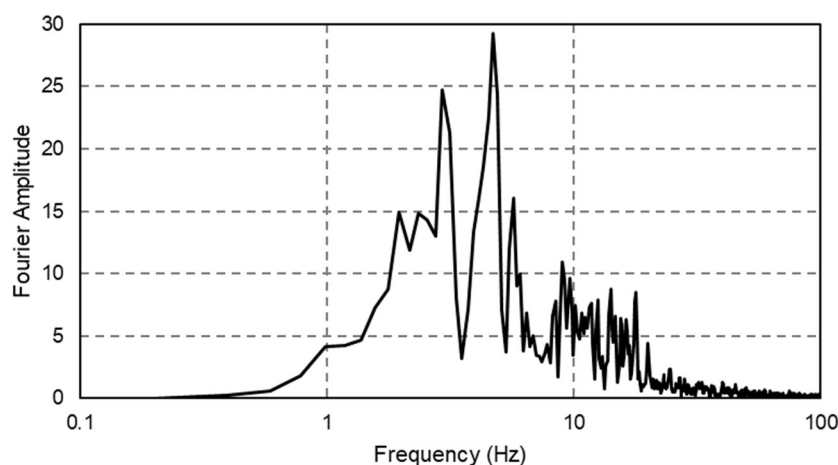


Figure A4.3.33. Fourier Amplitude for the vertical component of the acceleration time-history recorded for 1978 M5.2 Albstadt earthquake at station JUN, 5 km away from the epicentre. Obtained with SeismoSignal (Seismosoft, 2016).

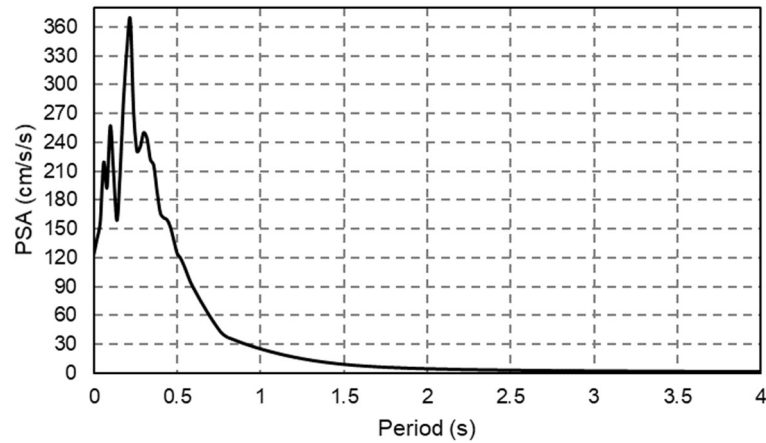


Figure A4.3.34. Pseudo-acceleration response spectra (5% of critical damping) for the vertical component of the acceleration time-history recorded for 1978 M5.2 Albstadt earthquake at station JUN, 5 km away from the epicentre. Obtained with SeismoSignal (Seismosoft, 2016).

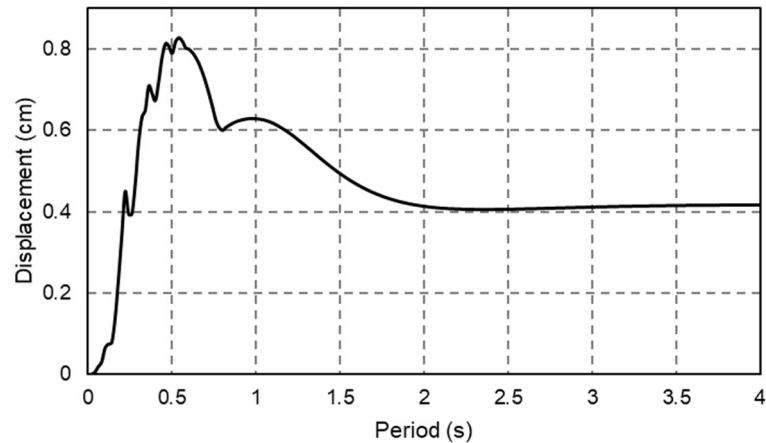


Figure A4.3.35. Displacement response spectra (5% of critical damping) for the vertical component of the record of the 1978 M5.2 Albstadt earthquake at station JUN, 5 km away from the epicentre. Obtained with SeismoSignal (Seismosoft, 2016).

During the 2014 **M**3.6 Darmstadt earthquake, a velocity of 12.9 mm/s was recorded by the WBB (Darmstadt-Eberstadt) seismic station that is located approximately 4.4 km and 5.3 km from the epicentral coordinates estimated by Homuth & Rümpker (2017) and Müller *et al.* (2015), respectively (Schwarz *et al.*, 2015; see Figure A4.3.13).

Table A4.3.12 presents the characteristics of the velocity records obtained at stations Waldmühle (north of Nieder-Beerbach) and Frankenhausen (around 2 km south-east of Nieder-Beerbach) for the 2014 **M**3.6 Darmstadt earthquake, as reported by Müller *et al.* (2015). According to the table, the maximum velocity recorded during this event corresponds to the x-component of ground motion and is equal to 104.77 mm/s at the station Waldmühle, and 25.114 mm/s at the station Frankenhausen. The corresponding predominant frequency is 7 Hz (0.14 s) for the record of the former station and 4.88 Hz (0.20 s) for the record of the latter station. According to Müller *et al.* (2015), an elongation of the velocity isolines in the NNE-SSW direction can be observed.

Table A4.3.12. Results of the velocity recordings for the 2014 M3.6 Darmstadt earthquake at the station Waldmühle and Frankenhausen. Recording times are not correct. From Müller et al. (2015).

Station	Date and hour	PGV (mm/s)			Frequency (Hz)		
		horizontal component		vertical component			
		x	y	z	x	y	z
Waldmühle	17.05.2014 19:02:20	104.77	104.56	23.28	7	6	11
Frankenhausen	17.05.2014 18:45:58	25.114	20.9092	16.3738	4.88	4.98	6.35

A4.3.4.3 Inferred shaking levels

The PGA ShakeMap (Worden *et al.*, 2017) for the 1978 M5.2 Albstadt earthquake, available from the USGS website, is shown in Figure A4.3.36. The ShakeMap was compiled using the Ground Motion Prediction Equation (GMPE) of Campbell (2003), the ground motion-intensity conversion equation of Atkinson & Kaka (2007) and intensity information from Haessler *et al.* (1980). The spatial pattern of the map is consistent with the epicentre location defined by the USGS (NEIC) and Schwarz *et al.* (2010b). The highest resulting PGA indicated on this map is 0.26 g, which lies in the range between 0.2 and 0.3 g estimated by Wieck & Schneider (1980), as reported by Schwarz *et al.* (2005), while that at JUN station is around 0.2 g. The maximum Peak Ground Velocity (PGV) estimated from the velocity ShakeMap is 17.1 cm/s and is much higher than the PGV value recorded at the JUN station. The maximum estimated Spectral Acceleration (SA) takes value of 0.35 g at a period of 0.3 s, 0.17 g at 1 s and 0.04 g at 3 s.

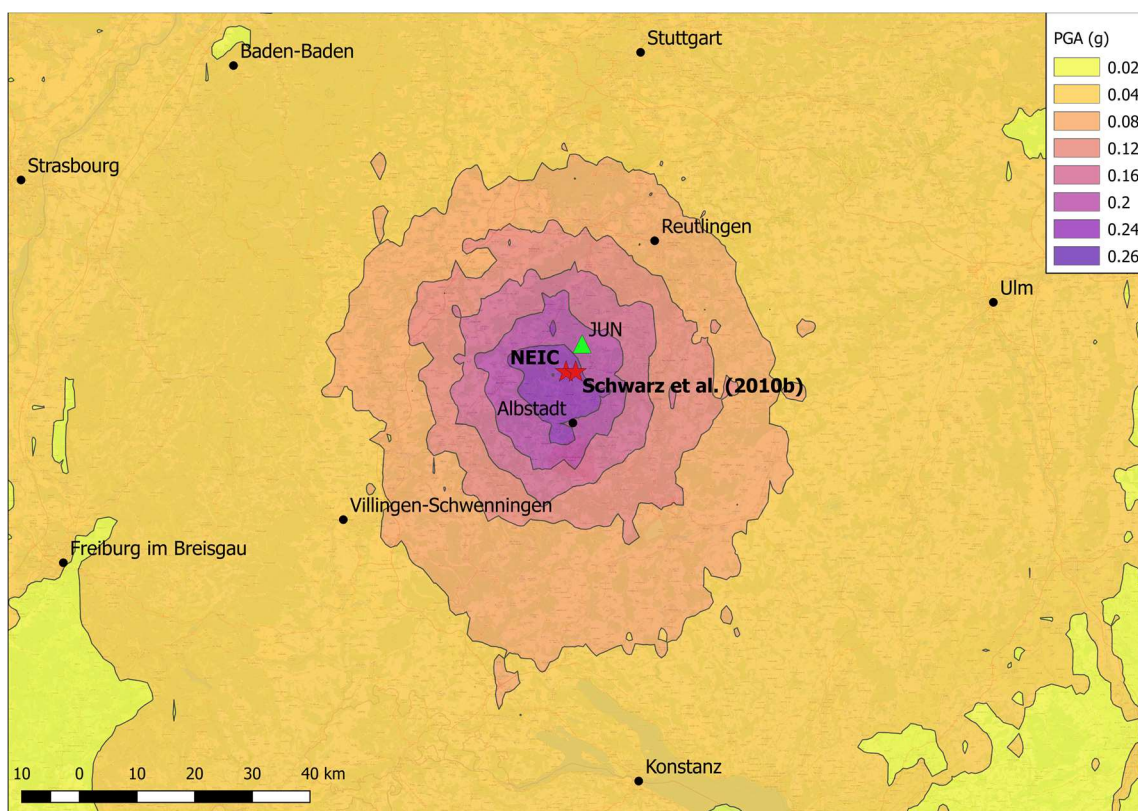


Figure A4.3.36. USGS ShakeMap (2017b) in terms of PGA for the 1978 M5.2 Albstadt earthquake. Red stars indicate the epicentres according to the USGS (NEIC) and Schwarz et al. (2010b).

No PGA ShakeMap is available for the 2014 **M3.6** Darmstadt earthquake.

A4.3.4.4 Duration of ground shaking

The 5%-75% definition of the significant duration of the ground motion record of the 1978 **M5.2** Albstadt earthquake available from the RESORCE database was calculated for vertical component using the SeismoSignal software (Seismosoft, 2016). Results are shown in Table A4.3.13.

Table A4.3.13. Significant duration (5%-75% of Arias Intensity, in seconds) of the ground motion of the 1978 **M5.2** Albstadt earthquake recorded at JUN station (available from the RESORCE database, Akkar et al., 2014).

Station	Station Name	Latitude	Longitude	Repi (km)	V component
JUN	Jungingen	48.3330 ° N	9.0450 ° E	5.0	1.145

Estimations of earthquake significant durations of the 1978 **M5.2** Albstadt earthquake were carried out using the models of Bommer *et al.* (2009) and Afshari & Stewart (2016) based on the 5%-75% Arias Intensity definition, as shown in Figure A4.3.37. Haessler *et al.* (1980) estimated a rupture area of 14 km², rupture length of 4.5 km and a hypocentral depth of 6.5 km for this event. Considering these values, the depth to the top of the rupture used for the model of Bommer *et al.* (2009) is approximated as 4.95 km. A series of distances were considered, including the epicentral distance from the fault rupture to the station JUN (approximately 5 km). Velocities of 180 m/s, 360 m/s and 800 m/s, which correspond to the boundaries of the Eurocode 8 (CEN, 2004) definitions of soil types, were considered. The velocity of 900 m/s, estimated from the USGS $V_{s,30}$ map server (USGS, 2017a) for the epicentral area and for the station JUN, was also used.

As observed in Figure A4.3.37, higher values are obtained using the model of Afshari & Stewart (2016) than that of Bommer *et al.* (2009). The significant duration calculated for Station JUN (Table A4.3.13) matches very well the curve obtained using $V_{s,30}$ =800 m/s and the prediction model of Bommer *et al.* (2009). Applying the predictive models using the epicentral distance to Station JUN (5 km), a 4.95 km depth to the top of the rupture and $V_{s,30}$ of 900 m/s as estimated from the $V_{s,30}$ USGS Map (Figure A4.3.26), observed duration for the vertical component (Table A4.3.13) is 0.44 standard deviations above the prediction of the model of Bommer *et al.* (2009) and -0.62 standard deviations below the prediction of Afshari & Stewart (2016) model.

The aforementioned values are in good agreement with the duration of 2 seconds reported by Blauß (1980). On the other hand, the local newspaper Reutlinger (2008) reported that the shaking lasted for almost 30 seconds, at an unspecified location that can be suspected to be Reutlingen, given the source, around 30 km to the north-east of the epicenter. Stuttgart News (2011) reports that, depending on the location, the duration of the 1978 **M5.2** Albstadt earthquake was between 10 to 12 seconds.

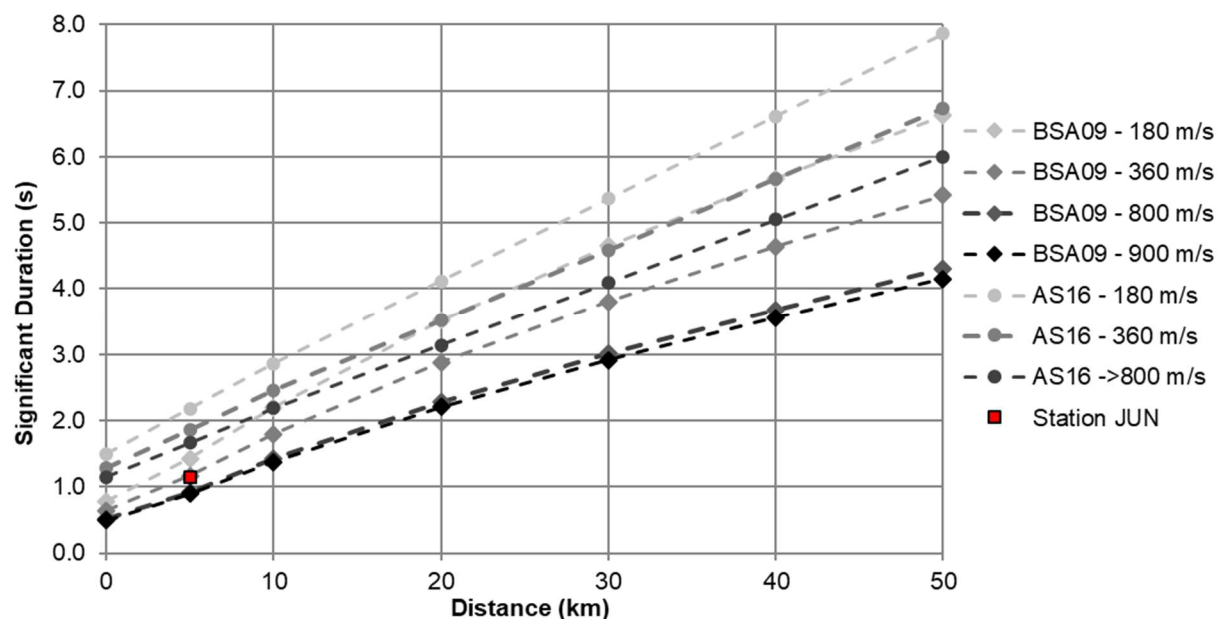


Figure A4.3.37. Estimation of the significant duration of the 1978 M5.2 Albstadt earthquake, using prediction equations by Bommer *et al.* (2009, BSA) and Afhsari & Stewart (2016, AS), and significant duration calculated for the vertical component of the accelerogram recorded at the JUN station.

Estimations of earthquake significant duration of the 2014 **M**3.6 Darmstadt earthquake were also obtained by means of the same prediction models, as shown in Figure A4.3.38. As no information about the depth to the top of the rupture is available for this event, the epicentral depth of 4.3 km estimated by Homuth & Rümpler (2017) was used for the model of Bommer *et al.* (2009). A range of distances to the fault rupture and velocities of 180 m/s, 360 m/s and 800 m/s, which correspond to the boundaries of the Eurocode 8 (CEN, 2004) definitions of soil types, were considered. The value of $V_{s,30} = 900$ m/s (see Figure A4.3.27), estimated from the USGS $V_{s,30}$ Map Server (USGS, 2017a) for the epicentre defined by Homuth & Rümpler (2017) and Müller *et al.* (2015), was also considered herein.

As observed from Figure A4.3.38, higher values are obtained using the model of Afshari & Stewart (2016) than that of Bommer *et al.* (2009). Both models indicate a very short significant duration at the epicentre, which does not exceed 1.5 seconds. It is noted, however, that the model of Bommer *et al.* (2009) was derived using data from earthquakes with magnitudes in the range **M**4.8-7.9, and it is being applied herein for a much smaller magnitude of **M**3.6.

Earthquake Report (2014b) gathers reports from residents regarding the duration of shaking of the 2014 Darmstadt earthquake. While those reports came from many different locations of the felt area, most of them make reference to a duration between 2 to 5 seconds. A longer duration was reported by Spiegel (2017), who inform that the shaking lasted up to 10 seconds, though they do not specify the corresponding location.

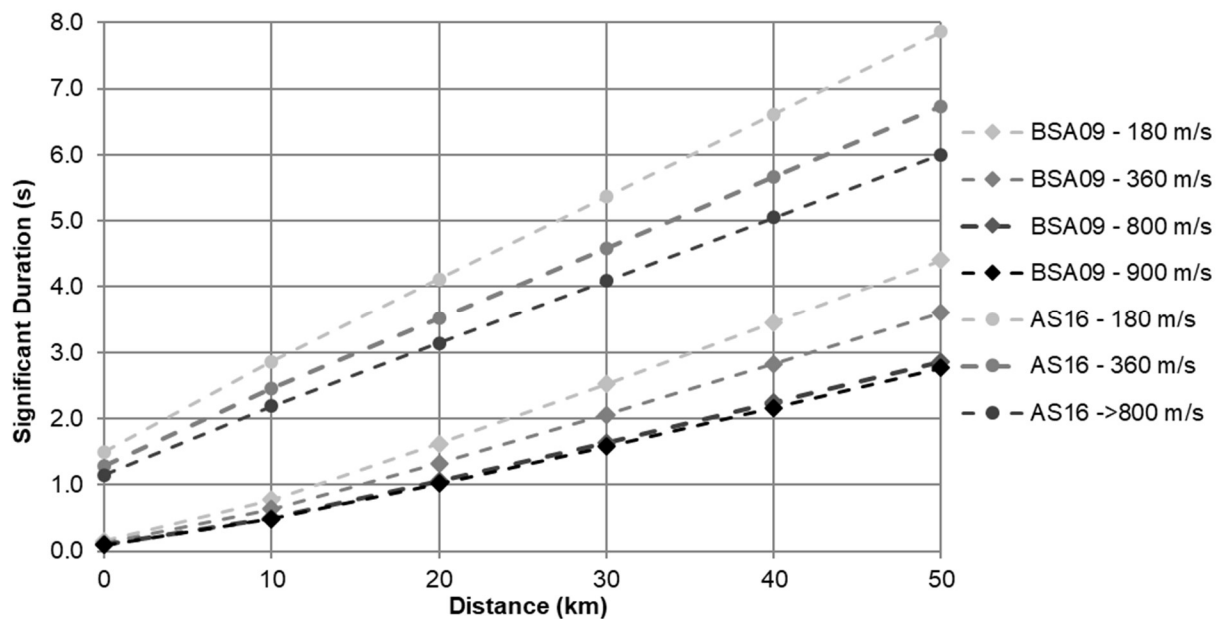


Figure A4.3.38. Estimation of the significant duration of the 2014 M3.6 Darmstadt earthquake, using prediction equations by Bommer et al. (2009, BSA) and Afhsari & Stewart (2016, AS).

A4.3.5 Collateral earthquake hazards

A4.3.5.1 Surface rupture

No surface rupture has been documented neither for the 1978 **M**5.2 Albstadt nor for the 2014 **M**3.6 Darmstadt earthquake. Peters (2007) reports that earthquakes documented in the area of the Upper Rhine Graben up to that date had not produced surface ruptures.

Haessler *et al.* (1980) calculated source parameters for the 1978 seismic event and their results indicate a length of rupture of 4.5 km, a rupture area of 14 km², and an associated average dislocation of 0.1 m. The same value of the average displacement on fault associated with this event was also reported by Langer (1990) and Beinersdorf & Schwarz (2014). Assuming a rectangular rupture area, the dimension down dip would be around 3.1 m. This, together with hypocentral depths of the order of those shown in Table A4.3.3, support the lack of observation of surface rupture for this earthquake.

A4.3.5.2 Landslides

No reports of landslides associated with the 1978 **M**5.2 Albstadt earthquake and the 2014 **M**3.6 Darmstadt earthquake have been found.

A4.3.5.3 Liquefaction

No liquefaction phenomena have been reported for the 1978 **M**5.2 Albstadt or the 2014 **M**3.6 Darmstadt earthquake.

A4.3.5.4 Settlements

No settlements have been reported for the 1978 M5.2 Albstadt or the 2014 M3.6 Darmstadt earthquake.

A4.3.6 Exposed population

A4.3.6.1 Socio-economic setting

According to the 2016 Human Development Report (United Nations, 2016), the Human Development Index (HDI) for Germany in 2015 was 0.926, while its Inequality-adjusted HDI (IHDI) was 0.859. This located Germany in the 4th place in the world's ranking, while the Netherlands ranks 7th. Based on the data reported in Country Economy (2017), in the year 1980, the HDI of the Federal Republic of Germany (West Germany) was 0.739, which located it in the 16th place in world ranking, while the Netherlands ranked 7th with an HDI value of 0.783. Table A4.3.14 compares the HDI and IHDI for both countries from the last two Human Development Reports (United Nations, 2015; United Nations, 2016) and from the data reported in Country Economy (2017). The column "Adj. HDI" provides the HDI values given in the 2016 report for previous years, adjusted for data consistency in time. According to Table A4.3.14, HDI values observed during the recent years are very similar in Germany and the Netherlands.

Table A4.3.14. Human Development Index and Inequality-adjusted Human Development Index for Germany and the Netherlands.

Report/ Source	Data	Germany				Netherlands			
		HDI	IHDI	Rank	Adj. HDI	HDI	IHDI	Rank	Adj. HDI
Country Economy	1980	0.739	-	16	-	0.783	-	7	-
2016	1990	-	-	-	0.801	-	-	-	0.83
2015	2014	0.916	0.853	6	0.924	0.922	0.861	5	0.923
2016	2015	0.926	0.859	4	0.926	0.924	0.861	7	0.924

Both the states of Hessen and Baden-Württemberg lie in what became West Germany, controlled by the United States, France and the United Kingdom, after the Second World War. The first years after the war were extremely difficult for the West German population, as big percentages of the built land had been destroyed and food was scarce. However, thanks to the Marshall Plan, the country experienced an unprecedented growth rate in the 1950s, during which the importance of the agricultural sector was dramatically reduced and manufacturing became the driver of the economy (Solsten, 1995; Heidenreich & Krauss, 1998). By the 1960s the growth rate slowed down, and it was faced with a serious crisis in 1973-1974 with the global upsurge in oil prices, which reflected in a peak in unemployment rates around 1977 (Heidenreich & Krauss, 1998). However, by 1976 growth had resumed, though it was only by mid-1978, the year in which the Albstadt

earthquake occurred, that the economy was considered to be back in balance (Solsten, 1995).

With a low corruption level (Transparency International, 2017) and very skilled labour force (The World Factbook, 2017a), the economy of Germany ranked 4th in the world in GDP terms and 5th in terms of Purchasing Power Parity (PPP) in 2016 (The World Bank, 2017a; 2017b). The contribution of the service sector to the total GDP amounts to 69.3%, while industry and agriculture contribute with 30.1% and 0.6%, respectively (The World Factbook, 2017a). Especially developed is the technology industry sector, such as mechanical, automotive, electronical and chemical industries, whose products are some of the main German exports (Legislative Council of the Hong Kong, 2015; The World Factbook, 2017a). In the world's ranking, Germany was the 3rd largest exporter of goods in 2016 (The World Factbook, 2017b). Of all the European Union (EU) countries, Germany features the lowest youth unemployment rate and one of the lowest total unemployment rates (Eurostat, 2017). A minimum wage was introduced by the German government in 2015, and it amounted to 9.79 USD (€8.84) in January 2017 (The World Factbook, 2017a).

Table A4.3.15 presents a comparison between Germany and the Netherlands in terms of GDP, GDP per capita and unemployment rate for years 1980, 2014 and 2017.

Table A4.3.15. Gross domestic product (GDP), GDP per capita and unemployment rate for Germany and the Netherlands, according to the World Economic Outlook Database (WEO, 2017).

Indicator	Units	Germany			Netherlands		
		1980	2014	2017	1980	2014	2017
Gross domestic product, current prices	Billion USD	850.642	3,885.440	3,423.290	189.524	881.033	762.694
Gross domestic product per capita, current prices	USD	11,069.880	47,978.610	41,243.880	13,393.890	52,240.300	44,654.230
Unemployment rate	%	3.359	5.008	4.161	3.354	7.434	5.400

A4.3.6.2 Population density and distribution

According to City Population (2016), the number of people residing in Albstadt was 46,369 in the year 1987 and 44,431 in the year 2015. The website of the city of Albstadt (Albstadt, 2018) reports 45,544 inhabitants for the year 2017, distributed among the different districts as shown in Table A4.3.16. The districts of Tailfingen, Onstmettingen and Ebingen, which were the most affected by the 1978 Albstad earthquake, amount to 35,628 people.

According to the Statistical Office of Hesse (2014), Nieder-Beerbach, the district most affected by the 2014 Darmstadt earthquake, had a population of 5,286 people distributed in 2,355 households in 2011. Table A4.3.17 shows the corresponding values for a series of districts, whose location and EMS-98 intensities can be observed in Figure A4.3.31.

Table A4.3.16. Population of the districts of Albstadt in December 2017. Data from Albstadt (2018).

	People
Albstadt	45,544
Ebingen	19,402
Tailfingen	11,284
Truchteltingen	3,141
Onstmettingen	4,942
Laufen	1,707
Lautlingen	1,785
Margrethausen	965
Pfeffingen	2,019
Burgfelden	299

Table A4.3.17. Population and number of households of the districts of Mühlital, Ober-Ramstadt and Darmstadt in May 2011. Data from the Statistical Office of Hesse (2014).

	People	Households
Mühlital	13,404	5,976
Frankenhausen	654	261
Nieder-Beerbach	1,920	867
Nieder-Ramstadt	5,286	2,355
Traisa	2,811	1,263
Trautheim	2,118	951
Waschenbach	615	279
Ober-Ramstadt	14,547	6,414
Modau	2,580	1,095
Ober-Ramstadt	9,633	4,302
Rohrbach	1,323	591
Wembach	1,011	426
Darmstadt	143,499	72,342
Arheilgen	16,902	7,560
Eberstadt	22,077	10,218
Kern	87,960	47,550
Kranichstein	10,863	4,476
Wixhausen	5,697	2,538

Figure A4.3.39 depicts the population density in the areas affected by both earthquakes, according to Gridded Population of the World (GPW v4.0; CIESIN, 2016).

The USGS EXPO-CAT database (Allen *et al.*, 2009) estimates that during the 1978 M5.2 Albstadt earthquake around 11,607,374 people were exposed to intensity MMI 4, of which 62.25% was urban and 37.75% was rural population, respectively (Figure A4.3.40). Around 8,379,228 people were exposed to intensities higher than MMI 4, of which approximately 2,354 people were exposed to the highest observed MMI intensity of 7.5.

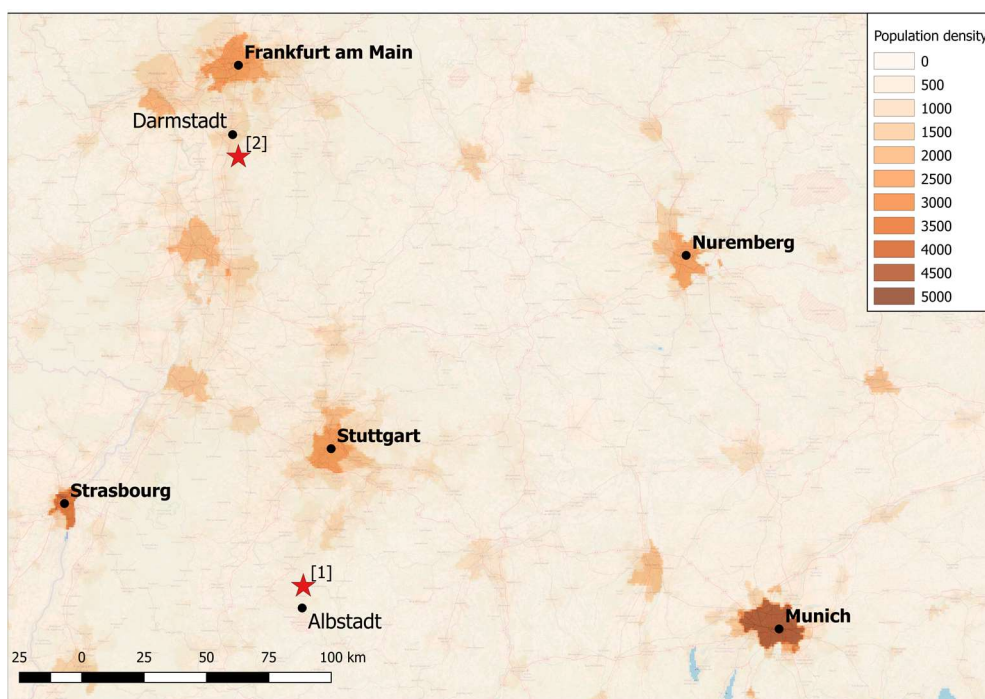


Figure A4.3.39. Population density (people/km²) in the affected areas as of 2015, according to Gridded Population of the World (GPW v4.0, CIESIN, 2016). Red star [1] marks the epicentre of the 1978 M5.2 Albstadt earthquake (according to Schwarz et al., 2010b), red star [2] marks that of the 2014 M3.6 Darmstadt earthquake (according to Müller et al., 2015).

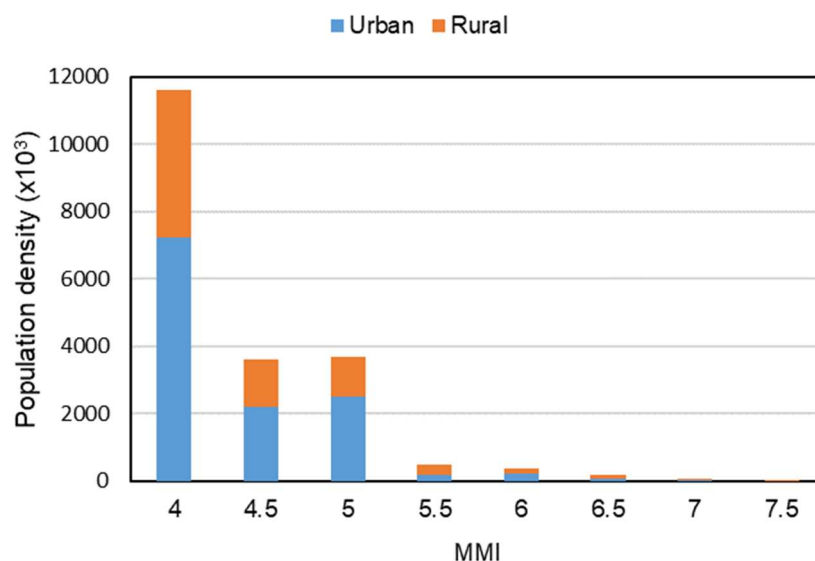


Figure A4.3.40. Disaggregation of estimated urban and rural population exposed to MMI 4 to MMI 7.5 shaking intensities during the 1978 M5.2 Albstadt earthquake. Data from USGS EXPO-CAT database (Allen et al., 2009).

A4.3.6.3 Time of day of earthquake

The 1978 M5.2 Albstadt earthquake struck on Sunday morning at 06.08 local time. Considering that this event induced extensive damage to chimneys and roof tiles, which in many cases have fallen from the roofs onto the streets, it is possible that the number of

casualties could have been much higher had the earthquake struck during the day time, when more people are outside of their houses.

The 2014 **M**3.6 Darmstadt earthquake struck on Saturday evening at 18.46 local time. As this earthquake induced mostly localized and limited damage to buildings and did not pose a threat to human life, the time of the day of this event did not play a significant role in terms of human casualties.

A4.3.7 Characteristics of exposed building stock

A4.3.7.1 Seismic design codes

Regulations for earthquake resistant design and construction were first introduced in Germany in 1957, when the DIN 4149 (1957-07) seismic code was published. However, its application was not compulsory, and was only first enforced as such in 1971 in the state of Baden-Württemberg, where Albstadt is located (Schwarz *et al.*, 2015). The seismic zoning map incorporated in this code was based on maximum intensities observed from past earthquakes throughout the country (Grünthal *et al.*, 2015). This deterministic approach for seismic zoning was integrated as well in the subsequent seismic code DIN 4149-1 (1981-04), issued in 1981, where maximum (MSK) intensities associated with past damaging earthquakes of the Federal Republic of Germany (West Germany) were used as a base for map compilation (Grünthal *et al.*, 2015). These maps were based solely on historical seismicity (Grünthal *et al.*, 2015), without consideration of neotectonic setting of the region (García-Mayordomo *et al.*, 2004). It was only in the 1981 version that the German state of Hesse, where Darmstadt is located, started to be included among those to consider seismic loading for the design and construction of buildings (Schwarz *et al.*, 2015).

In the German Democratic Republic (GDR, East Germany), probabilistic seismic hazard zoning was officially implemented in seismic building standards in 1989 by the construction supervision agency of the East Germany state (Grünthal *et al.*, 2015; García-Mayordomo *et al.*, 2004). After German reunification, the seismic zoning map of the 1981 version of DIN 4149 seismic code was updated to account for the *Länders* (*i.e.* German political divisions) of the GDR, and became an integral part of the revised version of the code, *i.e.* DIN 4149-1/A1 (1992-12), in 1992 (Grünthal *et al.*, 2015).

The probabilistic approach for seismic hazard zoning was first introduced in Germany in the 1990s through the PSHA study of Grünthal & Bosse (1996), which resulted in the seismic hazard map shown in Figure A4.3.9, expressed in terms of EMS-98 intensities with a 475-year return period (Grünthal *et al.*, 2015; García-Mayordomo *et al.*, 2004; Tyagunov *et al.*, 2006). This map was used for the compilation of the official seismic zoning map of Germany (Figure A4.3.8), which was integrated within the DIN 4149:2005-04 code, and within the currently used German National Annex to Eurocode 8 (DIN EN 1998-1/NA:2011-01) (GFZ, 2017a; Grünthal *et al.*, 2015). This seismic zoning map is accompanied with a map of geological subsoil classes and soil condition classes, details of which can be found in section A4.3.3.2. Site-specific conditions of the seismic-prone zones

in Germany are taken into account through the soil factor (S), which is used as a parameter influencing the response spectra defined by the 2005 version of the DIN 4149 seismic code and by the currently enforced Eurocode 8 provisions (Ringhofer, 2010).

The DIN 4149 code specifies a maximum number of storeys below which seismic loads need not be considered for the design of residential buildings (Daniell *et al.*, 2014; Daniell, 2015). This means that not all buildings built at a site that falls within a seismic zone after the implementation of the code is designed to sustain earthquake loads. Moreover, each German state has to ratify the code for it to be used in its territory. According to Daniell (2015), the 2005 version of DIN 4149 was ratified by most states, but by mid-2013, the new Eurocodes had only been ratified by the state of Baden-Württemberg, where Albstadt is located.

Existing wind maps for Germany and Europe show that the states of Hesse and Baden-Württemberg are subject to weaker long-term average wind speeds than northern areas of Germany and the Netherlands and, in general, to some of the lowest in Europe (Troen & Lundtang Petersen, 1989; Kasperski, 2002). While it has not been possible to access information regarding the wind design of the building stock exposed to the 1978 and 2014 earthquakes, it is possible that their overall lateral resistance may be lower than those of buildings further north in Europe, assuming wind to be a more significant load than seismic action, for buildings that might be exempted from being designed for the latter, or that may have been designed before the introduction of seismic regulations.

A4.3.7.2 Building typologies

According to the PAGER Inventory Database v2.0 (Jaiswal & Wald, 2008), 20% of the German building stock consists of unreinforced brick masonry in lime mortar, as shown in Figure A4.3.41. Ductile reinforced concrete moment frames with or without infill are present in the same percentage (20%), except in case of rural residential buildings, among which they present a 6% of total. Other common building typologies in Germany are concrete block unreinforced masonry with lime or cement mortar, reinforced masonry bearing walls with concrete diaphragms, and, to a lesser extent, rectangular cut stone masonry block with lime mortar. It is noted that half of the building stock is not accounted for in these percentages.

According to Daniell (2015), less than one third of the building stock of Germany to date has been built after 1981, a statement that is supported by Tyagunov *et al.* (2006), though the latter do not specify numbers. However, Tyagunov *et al.* (2006) also point out that, due to a good quality of workmanship, only a small part of the other two thirds is found to be seismically vulnerable to the seismic hazard levels of the country. The residential building stock of Germany is characterized with vulnerability classes A to D on the EMS-98 seismic scale, with classes B and C being the most prevalent ones (Tyagunov *et al.*, 2006; Tyagunov *et al.*, 2004). Daniell (2015) expresses, nevertheless, concern that even within the zones classified as seismic, large percentages of the buildings do not need to comply with seismic requirements due to the number of storeys threshold. Daniell (2015) estimates these percentages to be 89%, 75% and 48% for zones 1, 2 and 3, respectively.

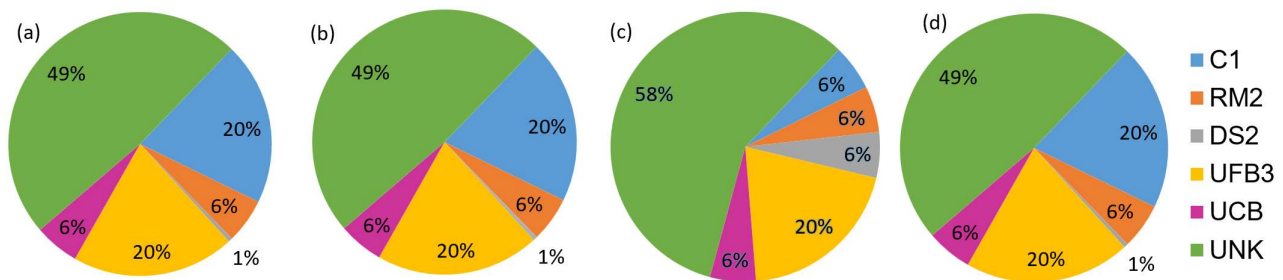


Figure A4.3.41. Proportion of buildings in Germany belonging to each typology: (a) rural and non-residential, (b) urban and non-residential, (c) rural and residential, and (d) urban and residential. C1: ductile reinforced concrete moment frame with or without infill. DS2: rectangular cut stone masonry block with lime mortar. RM2: reinforced masonry bearing walls with concrete diaphragms. UFB3: unreinforced brick masonry in lime mortar. UCB: concrete block unreinforced masonry with lime or cement mortar. UNK: not specified (unknown/default). Data from Jaiswal & Wald (2008).

A variety of building typologies can be found in the city of Albstadt, most of them dating from the 20th century (Beinersdorf *et al.*, 2013; Schwarz *et al.*, 2008). For the Tailfingen and Onstmettingen districts of Albstadt, which were largely affected by the 1978 earthquake, detailed information about the building stock was gathered during a building survey conducted in the year 2003, when approximately 5,200 buildings were investigated and classified according to parameters such as geometry, regularity, number of storeys, year of construction and vulnerability (Beinersdorf *et al.*, 2013). Results of the survey (Table A4.3.18, Figure A4.3.42) reveal that masonry constructions are predominant in Albstadt, including a large variety of mixed types of masonry with timber and reinforced concrete (RC) elements. Masonry buildings with wood floor construction, built during the 1920-1930 period, are made of stones extracted from local quarries or of full clay bricks, laid with weak mortar (Beinersdorf *et al.*, 2013; Schwarz *et al.*, 2008; Schwarz *et al.*, 2010a).

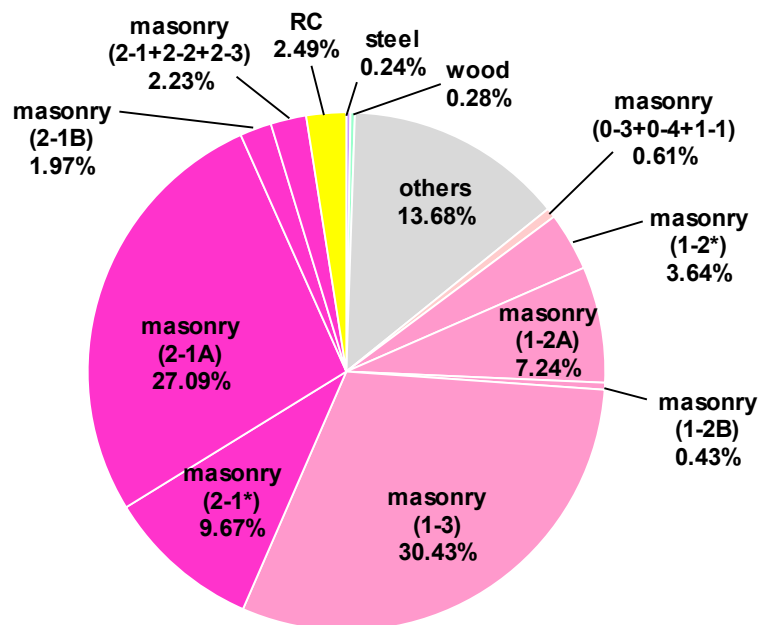


Figure A4.3.42. Proportion of different building typologies in Albstadt-Tailfingen and Albstadt-Onstmettingen. Data from Beinersdorf *et al.* (2013).

Table A4.3.18. Building typologies in Albstadt-Tailfingen and Albstadt-Onstmettingen. ERD = earthquake resistant design. Data from Beinersdorf et al. (2013).

MAIN TYPE	CODE	DESCRIPTION	NUMBER	%
Others	others	Non-specified (e.g. garages etc.)	631	13.68
Masonry	0-1	Rubble stone, fieldstone	-	-
	0-2	Adobe (earth brick)	-	-
	0-3	Simple stone	6	0.13
	0-4	Massive stone	4	0.09
	1-1	Unreinforced, with manufactured stone units	18	0.39
	1-2*	Unreinforced masonry with wooden floors	168	3.64
	1-2A	2-storey, year of construction 1920-1940	334	7.24
	1-2B	3-storey, year of construction 1920-1930	20	0.43
	1-3	Unreinforced masonry/timber mixed	1403	30.42
	2-1*	Unreinforced, with RC floors	446	9.67
	2-1A	2-storey, year of construction 1950-1965	1249	27.08
	2-1B	3-storey, year of construction 1955-1965	91	1.97
	2-1	Unreinforced with RC frame elements	1	0.02
	2-2		77	1.67
	2-3	Reinforced or confined	25	0.54
Reinforced Concrete (RC)	3-1	Frame without ERD	28	0.61
	3-2	Walls without ERD	26	0.56
	4-1	Frame with moderate level of ERD	36	0.78
	4-2	Walls with moderate of ERD	24	0.52
	5-1	Frame with high level of ERD	1	0.02
	5-2	Walls with high level of ERD	-	-
Steel	6	Steel structures	11	0.24
Wood	7	Timber structures	13	0.28

Figure A4.3.43 shows the EMS-98 vulnerability classes of the investigated building stock, as assigned by Beinersdorf *et al.* (2013), adapted to account for local building typologies that are typical of Albstadt and other south German cities. The distribution of vulnerability classes reveals that classes BC to C are dominant in the investigated area. Table A4.3.19 and Figure A4.3.44 give a more detailed characterization of some of the most relevant building typologies enumerated in Table A4.3.18, namely masonry buildings with timber framework (type 1-3), unreinforced masonry with wooden floors (type 1-2) and masonry with RC floors (type 2-1), according to Beinersdorf *et al.* (2013) and Schwarz *et al.* (2010a). To account for the variation in number of storeys and year of construction, the subtypes (A and B) of building types 1-2 and 2-1 were considered. In Table A4.3.19, bold symbols indicate the most likely vulnerability class (VC), symbols in parenthesis indicate probable vulnerability classes while those in italic refer to vulnerability classes of exceptional cases. Vulnerability classes assigned in accordance with the original (unadapted for local building types, indicated as “general”) EMS-98 seismic scale are also presented in the table. As can be observed, vulnerability class B is typical for building types 1-2A and 1-2B, while types 2-1A and type 2-1B tend to belong to the less-vulnerable

class C. Building type 1-3 is characterized with class BC with tendency to C (Beinersdorf *et al.*, 2013). The median (VC_{median}) and the mean (VC_{mean}) vulnerability classes corresponding to each of these building typologies are specified in Figure A4.3.44.

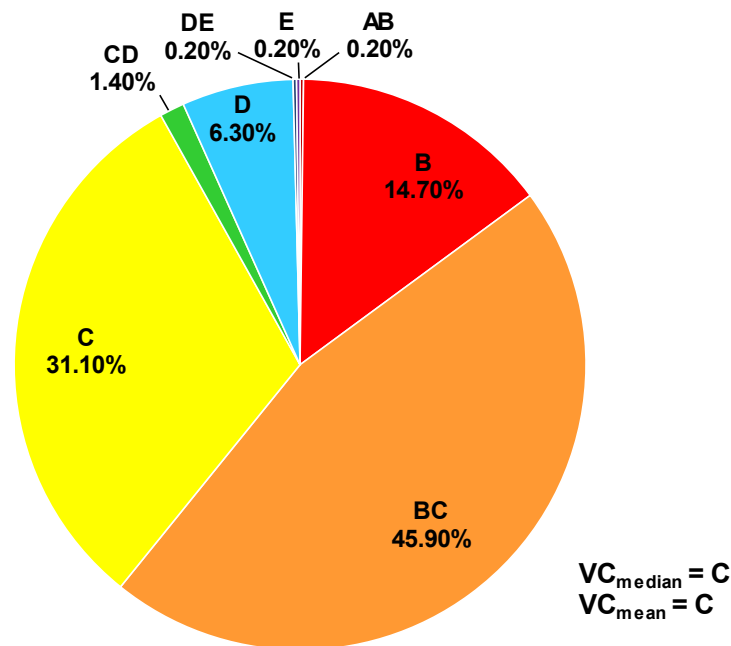


Figure A4.3.43. Vulnerability classes of the investigated building stock in Albstadt-Tailfingen and Albstadt-Onstmettingen according to EMS-98. Data from Beinersdorf *et al.* (2013).

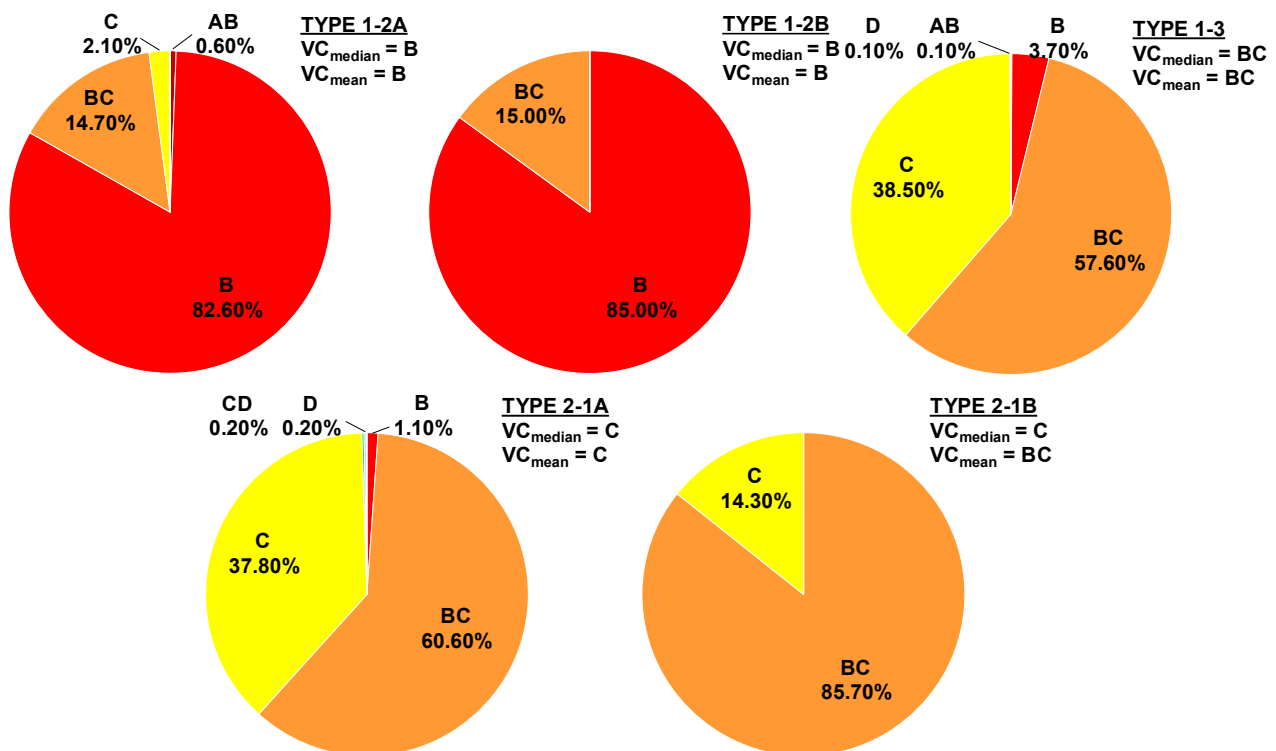





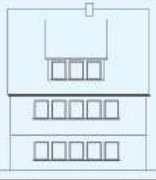

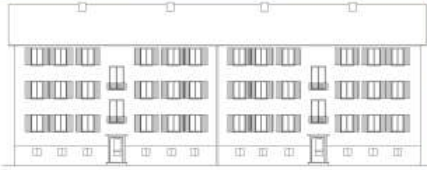



Figure A4.3.44. Vulnerability classes (VC) of representative masonry building types (type: 1-2A, 1-2B, 1-3, 2-1A, 2-1B, as in Table A4.3.18) in Albstadt-Tailfingen and Albstadt-Onstmettingen. Data from Beinersdorf *et al.* (2013).

The number of masonry houses (type 1-2A, 1-2B, 2-1A and 2-1B) investigated in the Tailfingen district of Albstadt is shown in Figure A4.3.45 (right) and their distribution is presented on the map in Figure A4.3.45 (left).

Table A4.3.19. Representative masonry building types (1-2A, 1-2B, 1-3, 2-1A, 2-1B, as in Table A4.3.18) in Albstadt-Tailfingen (T) and Albstadt-Onstmettingen (O), and their corresponding vulnerability classes (VC) according to the EMS-98 scale. From Schwarz et al. (2010a).

Type	Representative building	Example	Parameter	Data sets*	VC
unreinforced masonry with wooden floors		EMS-98			general (A) B (BC)
1-2 A			n = 2 stories 1920 – 1939	179 ds (T) 151 ds (O)	(AB) B (BC)
1-2 B			n = 3 stories 1920 – 1930	18 ds (T) 2 ds (O)	(AB) B (BC)
unreinforced masonry/timber mixed		EMS-98			no definition
1-3			n = 2 stories 1910 – 1930	933 ds (T) 469 ds (O)	(B) BC (C)
unreinforced masonry with RC floors		EMS-98			general (B) C (D)
2-1 A			n = 2 stories 1949 – 1965	393 ds (T) 846 ds (O)	(BC) C (CD)
2-1 B			n = 3 stories 1955 – 1965	65 ds (T) 26 ds (O)	(BC) C (CD)

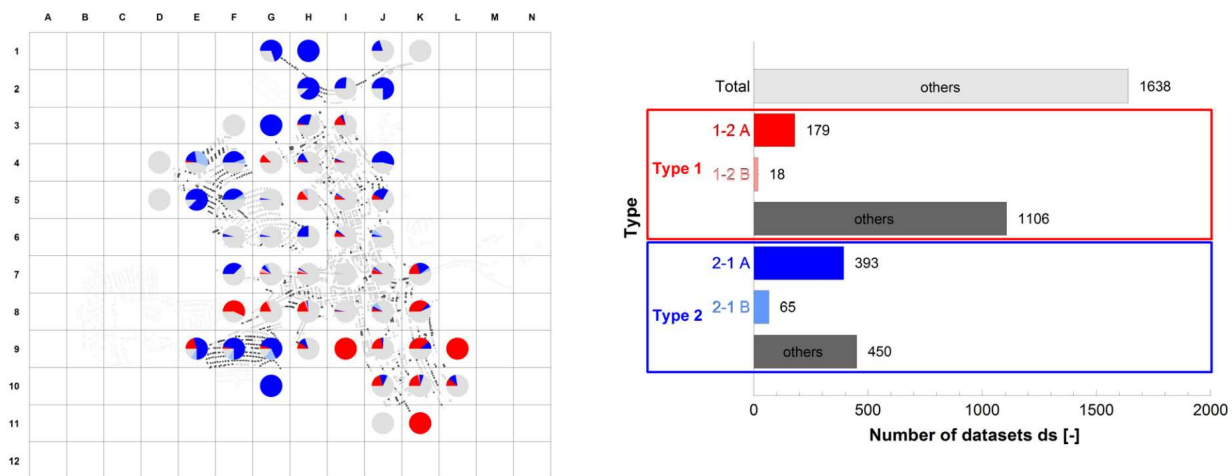


Figure A4.3.45. Distribution of building types 1-2A, 1-2B, 2-1B and 2-1B (left) and their total number (right) in Albstadt-Tailfingen. Map on the left depicts percentage of different types of masonry buildings within a mesh of raster elements. From Schwarz *et al.* (2008).

Information regarding the building stock exposed to the 2014 **M3.6** Darmstadt earthquake is significantly scarcer than for the 1978 Albstadt case. The Nieder Beerbach district of Mühlthal municipality, which was the most affected area, consists mostly of one- and two-family houses that were built in the period from the late 19th century to the 1920s. These are mostly masonry houses that fall under vulnerability class B of the EMS-98 scale (Schwarz *et al.*, 2015; Earthquake Damage Analysis Center (EDAC), 2014). According to Schwarz *et al.* (2015), there are also a few houses of mixed masonry and timber construction that could be assigned to EMS-98 vulnerability class C. Masonry buildings of more modern construction, built after 1960, can be found in the western part of Nieder-Beerbach. They are characterized by better quality rigid diaphragms and fall under vulnerability class C on the EMS-98 scale (EDAC, 2014; Schwarz *et al.*, 2015). The distribution of vulnerability classes corresponding to the existing building stock of Nieder-Beerbach in the year 2014 is shown in Figure A4.3.46.

According to the data presented herein, masonry constructions seem to be typical of both Albstadt and Darmstadt, and, according to Schwarz *et al.* (2008), it is also the predominant building type in most of the cities and villages in Germany. It is, however, observed that a large variety of masonry construction (depending on their age, number of storeys, building material) can be found in the areas affected by these two earthquakes, and that mixed types of masonry and timber, associated with less-vulnerable class BC, represent a considerable part of the investigated building stock.

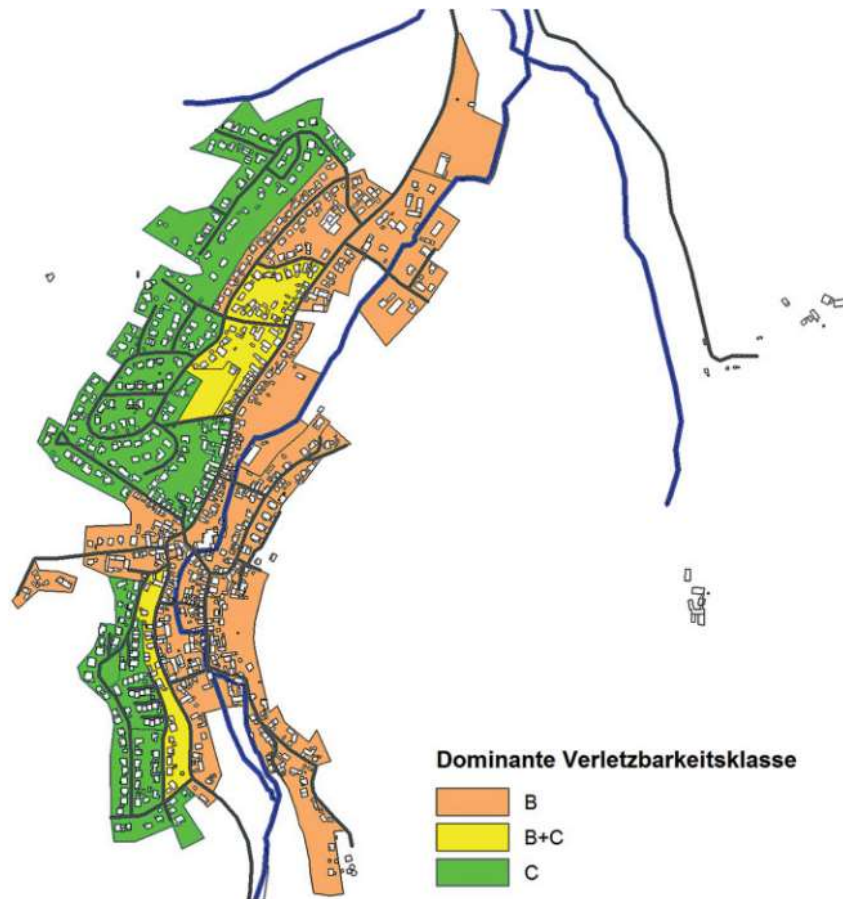


Figure A4.3.46. Distribution of vulnerability classes of the existing building stock in Nieder-Beerbach, the area most affected by the 2014 Darmstadt earthquake, assigned on the basis of the results of a building and damage survey. From Schwarz et al. (2015).

A4.3.7.3 Prior damage and retrofit

No explicit indication of prior damage or retrofit could be found for the buildings exposed to the 1978 Albstadt earthquake.

Considering the bombing of Darmstadt during the Second World War, as well as the relatively old building stock of Nieder-Beerbach, it is possible that some dwellings in this area presented some level of damage before the 2014 Darmstadt earthquake.

A4.3.8 Damage observations

A4.3.8.1 Damage states

All sources found make use of the European Macroseismic Scale (EMS-98; Grünthal, 1998) for the description of the damage states of buildings associated with the 1978 Albstadt and 2014 Darmstadt seismic events. Details of this seismic scale can be found in Section 3.8.1 of Chapter 3 and Appendix II.

A4.3.8.2 Damage statistics and description

The areas most affected by the 1978 **M**5.2 Albstadt earthquake were the Tailfingen, Onstmettingen and Ebingen districts of Albstadt, while other parts of the Zollernalbkreis district of Baden-Württemberg State (Killer, Starzeln, Hausen, Jungingen) were damaged to a smaller extent. Instances of damage were observed as well in other districts of Baden-Württemberg state, such as peripheral areas of Reutlingen (Figure A4.3.30) and Tübingen. Given the significant aftershock activity, it is likely that the consequences reported in the literature be not only of the main shock but of several earthquakes of the series.

Estimates of the number of buildings damaged by the 1978 **M**5.2 Albstadt earthquake differ depending on the author and vary between 5,000 and 11,500. According to Bostenaru (2003), damage was observed on 5,000 buildings, while collapse was recorded for 60 buildings. Stuttgart News (2011) reports that hundreds of buildings were severely damaged within a range of 50 km from the epicentre. Grünthal (2004) and GFZ (2017c) mention 6,850 damaged homes, while Swiss Re (2017) reports about more than 7,000 damage cases. Reutlinger (2008) reports that the number of heavily damaged buildings was around 11,500. According to Blauß (1980), 8,000 damaged buildings were found in Albstadt, while damage to additional 3,000 buildings was observed in surrounding communities.

The earthquake catalogue of Schwarz *et al.* (2010b) reports 7,840 damaged buildings, of which 3,120 were in Tailfingen, 1,510 in Onstmettingen, 2,630 in Ebingen and 580 in other Albstadt communities. According to said report, 23 factory chimneys and 2,200 chimneys of residential buildings were demolished, 324 buildings were shored up, and 69 partial and one full demolition were carried out. A somewhat different number of affected house chimneys was reported by Blauß (1980) who mentions about 1,300 cases of partial chimney collapse and fallen chimney pots, and another 2,200 cases of cracking of chimney stacks. Broken chimney pots and bricks and their falling from the roof were also reported by Schwarz *et al.* (2010b). According to Blauß (1980), the great extent of chimney damage in otherwise less-damaged buildings was due to their dynamic properties being different from those of buildings to which they are attached. Dislodgment of roof tiles from rafters and their falling onto the streets was also observed, as shown in Figure A4.3.47. Blauß (1980) points out that steeply-pitched roofs and those lacking sufficient stiffness in their skeletons were damaged to a greater extent.



Figure A4.3.47. Falling of roof tiles induced by the 1978 Albstadt earthquake. From Blauß (1980).

Cracking and falling of plaster was observed on the interior and exterior of many properties (Schwarz *et al.*, 2010b). Examples of plaster fractures and extensive cracking of inner walls are shown in Figure A4.3.48. Many buildings sustained considerable cracking at the corners of doors and window openings, examples of which are shown in Figure A4.3.49 (Schwarz *et al.*, 2010b; Blauß, 1980). Damaged gable ends were also commonly observed and, in some cases, like in the one shown in Figure A4.3.50, they fully collapsed. According to Blauß (1980), significant damage was sustained by buildings whose foundations were shallow and did not reach depths below the frost line (~80 cm).

There were 23 (Schwarz *et al.*, 2010b) to 25 (Blauß, 1980) damaged factory chimneys, which, according to Blauß (1980), were damaged to such extent that the upper third of the chimney structure had to be removed in most of the cases (Figure A4.3.51).

Outside the area of Albstadt, damage was observed in the town of Mössingen, within the Tübingen district of Baden-Württemberg, where roof tiles fell from dozens of buildings onto the streets and the tower of the Church of Peter and Paul was damaged. One case of a collapsed bedroom ceiling was observed in the Öschingen district of Mössingen, while in the Talheim district of Mössingen some roads were closed in order to prevent possible losses induced by chimney collapse and their falling from the roof (Reutlinger, 2008). Reutlinger (2008) reports that a similar situation was observed as well in the Reutlingen district of Baden-Württemberg. In Killer, locality in the town of Burladingen in the Zollernalbkreis district, the gable wall of one church sustained considerable damage (Schwarz *et al.*, 2010b). The Hohenzollern Castle, located approximately 15 km north-east of Albstadt was also damaged by this earthquake (Castle Hohenzollern, 2010).

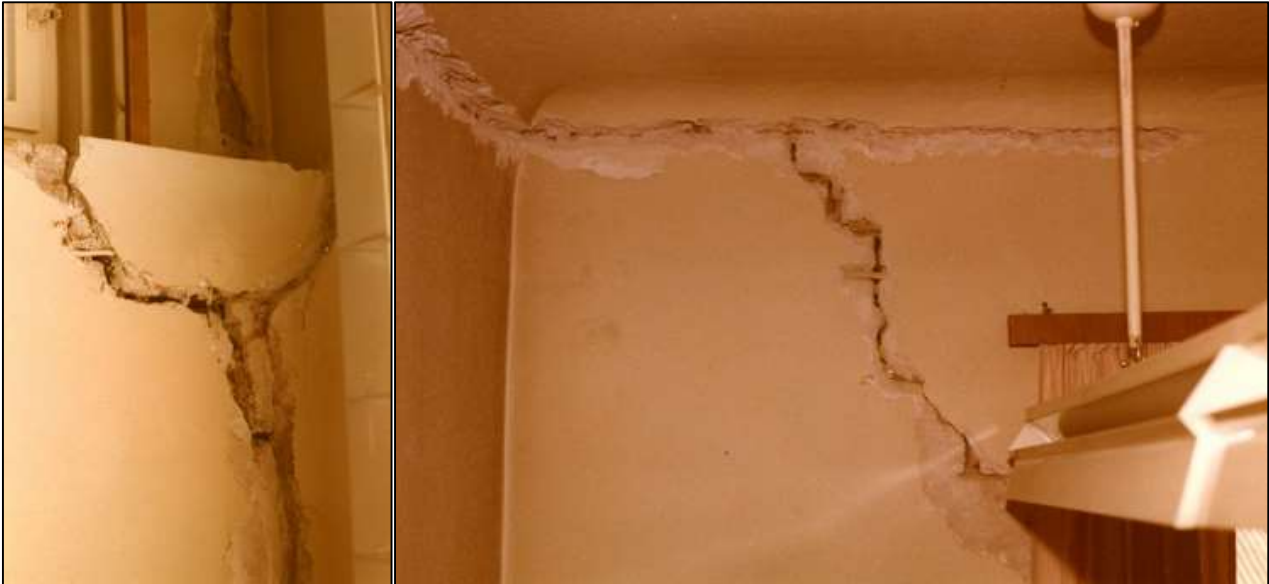


Figure A4.3.48. Falling of plaster and extensive cracking of inner building walls induced by the 1978 Albstadt earthquake. From Schwarzwaelder Messenger (2013).



Figure A4.3.49. Extensive cracking observed at the corners of windows and doors due to the 1978 Albstadt earthquake. From Schwarz et al. (2010b).

According to Schwarz *et al.* (2010b), around 75% of the buildings damaged by the 1978 Albstadt earthquake had been constructed shortly after the Second World War. Buildings erected closer to the time of the earthquake that were designed and constructed in accordance with building regulations behaved well during the shaking. In particular, well-constructed timber-frame buildings and RC buildings, as well as masonry buildings with cement mortar of good quality, sustained only minor damage (Blauß, 1980; Schwarz *et al.*, 2010b).

According to Daniell *et al.* (2012), 44% of all damage to residential buildings induced by the 1978 Albstadt event was non-structural, while Porro & Schraft (1989) report that

around 50% of damage could be attributed to non-structural elements such as heating, electrical installations, sanitary installation.

The 1978 Albstadt event interrupted the normal functioning of the telephone network, as well as water and power supplies (Schwarz *et al.*, 2010b; Reutlinger, 2008).



Figure A4.3.50. Damage to the gable end of a masonry building observed during the 1978 Albstadt earthquake. From Schwarz *et al.* (2010b)



Figure A4.3.51. Damage to factory chimneys observed during the 1978 Albstadt earthquake. From Schwarzwälder Messenger (2013).

In 2003-2004, scientists made a great effort to re-interpret the building damage that was induced by the 1978 Albstadt event. For 1,850 buildings (1,000 in Tailfingen and 850 in Onstmettingen) that were damaged by this event, the damage state was re-evaluated and classified in terms of the EMS-98 scale, the outcome being reported by Schwarz *et al.* (2010a) and Beinersdorf *et al.* (2013). Detailed information about the building stock of Tailfingen and Onstmettingen, obtained by means of a building survey (as described in Section A4.3.7.2) enabled scientists to classify the damage observed according to the different building typologies that sustained it (Beinersdorf *et al.*, 2013). Figure A4.3.52 depicts EMS-98 damage grades induced by this event on the whole building stock that was existing at the time of the earthquake in the investigated area. As observed in the plot, around 60% of the building stock of Tailfingen and Onstmettingen did not sustain any damage (DG0), while damage grade 4 (DG4) was observed only in a few cases. The mean damage grade was DG1 while the median was DG0. Schwarz *et al.* (2010a) report that most of the buildings sustained a moderate level of damage associated with diagonal cracks between the openings (*i.e.*, doors and windows) and the out-of-plane collapse of non-anchored gable walls. Masonry buildings sustained the greatest damage, according to Beinersdorf *et al.* (2013). The spatial distribution of damage is explained in section A4.3.8.4.

Beinersdorf *et al.* (2013) report as well the EMS-98 damage grades for each of the representative types of masonry buildings shown in Figure A4.3.44 and Table A4.3.19 (type 1-2A, 1-2B, 1-3, 2-1A, 2-1B), as shown in Figure A4.3.53. As can be observed, many buildings of type 1-2, with predominant vulnerability class B, are associated with damage grade 1 (DG1) and few-to-many with damage grade 2 (DG2). Building type 1-3, whose dominant vulnerability class is BC, shows damage grade 1 in many cases, while damage grade 2 and damage grade 3 are observed only for a small percentage of this type of buildings. Finally, buildings of the type 2-1, characterized with vulnerability class C, are related in large number with DG1, and in few cases with DG2 and DG3, while DG4 was observed in a single case. While median damage grades ($D_{m,Med}$) vary across these five building types, mean damage grade D1 is common to all of them. These observations are in agreement with the findings of Porro & Schraft (1989), who report that buildings constructed before the 1950s appeared to have been more severely affected than those constructed afterwards (further details provided in section A4.3.8.4).

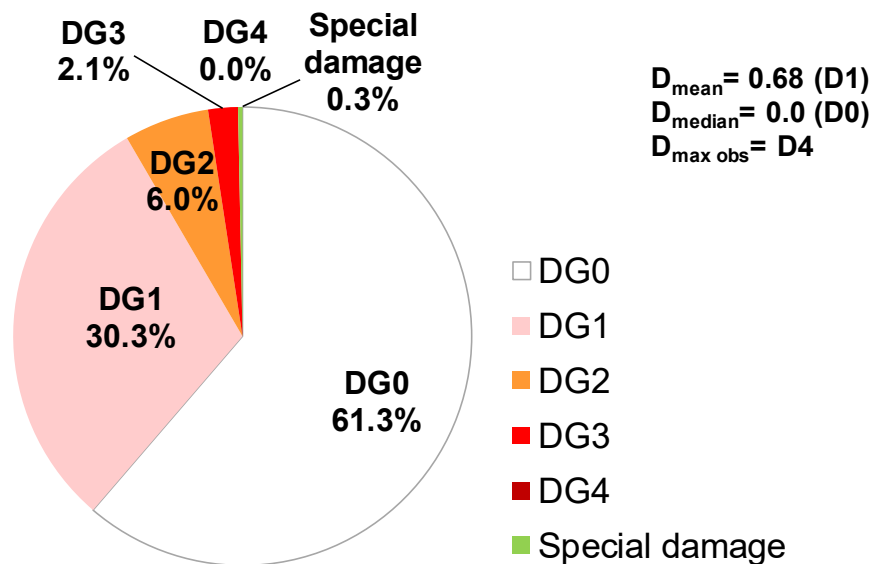


Figure A4.3.52. Observed damage grades (DG) after the 1978 Albstadt earthquake for the total building stock of 1978 in the study area of Albstadt-Tailfingen and Albstadt-Onstmettingen. Data from Beinersdorf et al. (2013).

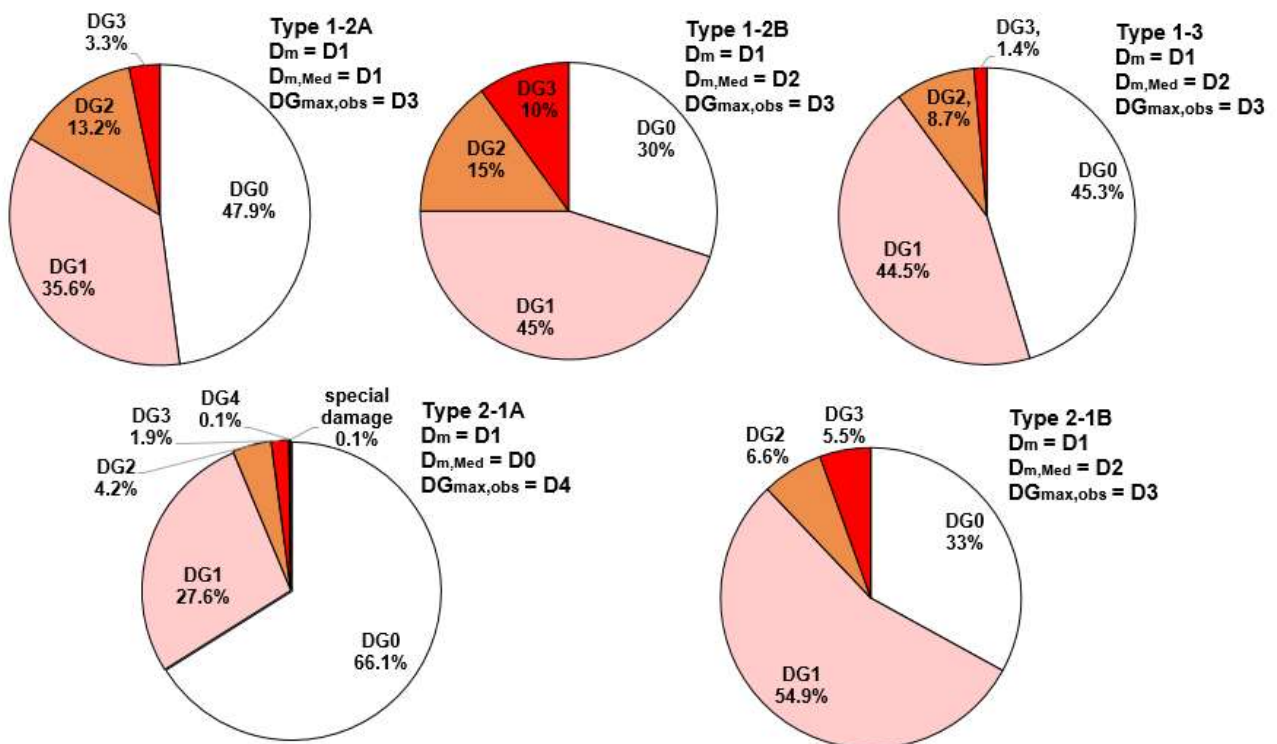


Figure A4.3.53. Observed damage grades (DG) after the 1978 Albstadt earthquake for the predominant building types of masonry construction of the building stock at the time of the earthquake. From Beinersdorf et al. (2013).

The 2014 **M3.6** Darmstadt earthquake caused damage on approximately 150 buildings, mainly in the Nieder-Beerbach district of the municipality Mühlthal, though instances of damage were also observed in other districts of this municipality, such as Trautheim, Waschbach and Nieder-Ramstadt (Schwarz *et al.*, 2015). According to Schwarz *et al.* (2015), many of the damaged buildings had been built before 1980, that is, before DIN 4149 was enforced in the state of Hesse, where the affected areas are located.

Non-structural damage associated with the dislodgment and overturning of chimneys and damage to roof tiles was observed on many properties (Figure A4.3.54). According to HLNUG (2017), 36 chimneys were damaged by this event. Other free-standing building elements and structures, like the fountain shown in Figure A4.3.55, also sustained damage, mostly in the form of residual displacements and rotations. Small horizontal and diagonal cracks were observed on most of the affected properties (Schwarz *et al.*, 2015; Müller *et al.*, 2015). Damage to gable walls was mostly limited to cracks around window openings (Figure A4.3.56), as is common for earthquakes of this intensity level. More significant cracks, such as those shown in Figure A4.3.57, were in many cases generated as a result of inadequate connections between different parts of masonry constructions (Schwarz *et al.*, 2015). Vertical cracking was common in the external walls that were not designed to withstand earthquake loads. Cracking was also observed in some of the buildings presumed to correspond to EMS-98 vulnerability class C, particularly due to inadequate construction and design. An example shown in Figure A4.3.58 (left) depicts cracking observed in a building with an irregular base and a heavy reinforced concrete roof (Schwarz *et al.*, 2015). The upper parts of buildings in Nieder-Beerbach were usually found to be more damaged compared to the lower ones (Schwarz *et al.*, 2015; Müller *et al.*, 2015). The Protestant church located in this area was also significantly damaged (EDAC, 2014).



Figure A4.3.54. Cracking of a chimney stack (left) and damage to roof tiles (right) induced by the 2014 Darmstadt earthquake. From Schwarz *et al.* (2015).

Damage grades assigned by Schwarz *et al.* (2015) to residential buildings in Nieder-Beerbach that were exposed to the 2014 Darmstadt earthquake are shown in Table A4.3.20. While it is not clear in the source whether these represent all the buildings in the area or a smaller sample, an overview of the area by means of Google Maps suggests that they are likely to be, if not all, the majority of the buildings in Nieder-Beerbach. Smaller

cracking, which was observed in the majority of the affected buildings, was used by Schwarz *et al.* (2015) as an indicator of damage grade D1, while more extensive cracks, like those shown in Figure A4.3.57, were considered to be an indicator of damage grade D2.

Schwarz *et al.* (2015) report that the damage observed after the 2014 Darmstadt earthquake is typical for earthquakes of this magnitude (M_L 4.2).



Figure A4.3.55. Rotation of the fountain up to 2.5 cm at the joint (a process which also affected many chimneys) during the 2014 Darmstadt earthquake. From Schwarz *et al.* (2015).

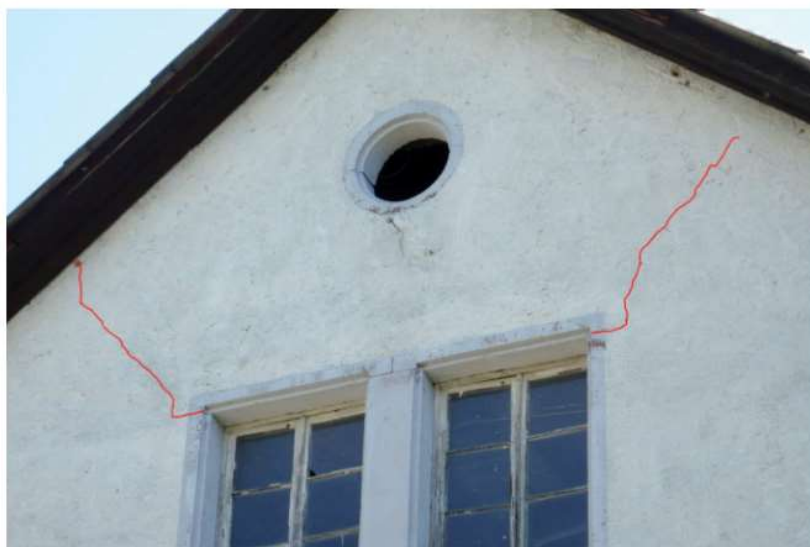


Figure A4.3.56. Diagonal cracks in the gable of the attic floor observed after the 2014 Darmstadt earthquake. From Schwarz *et al.* (2015).



Figure A4.3.57. Cracking observed at connections between different building elements(left) and balustrade crack (right) caused by the 2014 Darmstadt earthquake. From Schwarz et al. (2015).



Figure A4.3.58. Thick diagonal shear crack in a modern masonry building (left); horizontal shear crack in a newer masonry building (right) induced by the 2014 Darmstadt earthquake. From Schwarz et al. (2015).

Table A4.3.20. Number of residential buildings per vulnerability class and EMS-98 damage grade caused by the 2014 Darmstadt earthquake. Data from Schwarz et al. (2015).

Damage Grade (EMS-98)	Vulnerability Class (EMS-98)			
	A-B	B	C	Total
D0	ca. 330			
D1	1	95	37	133
D2	1	18	2	21

A4.3.8.3 Observed weaknesses

According to Blauß (1980), considerable damage associated with the 1978 Albstadt earthquake was sustained by buildings that were constructed soon after the end of the Second World War, when the quality of building materials and the overall quality of construction was rather low. The author also adds that significant damage was observed in houses with shallow foundations, which were founded up to the depth of frost-line. Significant cracking of walls was observed in properties with load bearing walls made of hollow block masonry (Schwarz *et al.*, 2010b; Blauß, 1980). Beinersdorf *et al.* (2013) highlights the use of weak mortar in masonry houses built during the 1920s and 1930s. Blauß (1980) reports that in the areas where intensity of shaking equal to or lower than V was felt, some of the affected buildings had significant defects and weaknesses before the earthquake.

According to Schwarz *et al.* (2015), many buildings in Nieder-Beerbach that were damaged by the 2014 Darmstadt earthquake were constructed before the 1980s, and were, therefore, not designed in accordance with any seismic regulations, as the first regulations of such type were introduced in the German state of Hesse with the DIN4149-1:1981-04 seismic code in 1981. With respect to the observed weaknesses associated with more recent constructions in Nieder-Beerbach, Schwarz *et al.* (2015) report that many such buildings had inadequate structural design and construction, and that inadequate and weak connections between different parts of masonry buildings resulted in extensive cracking during the 2014 earthquake.

A4.3.8.4 Damage distribution

The distribution of damage induced in the districts of Tailfingen and Onstmettingen by the 1978 Albstadt earthquake is shown in terms of damage grades of the EMS-98 scale in Figure A4.3.59 and Figure A4.3.60, respectively. Schwarz *et al.* (2010a) and Beinersdorf *et al.* (2013) argue that extensive damage was confined within a narrow zone that coincides with the projection of the fault rupture to the ground surface according to Hiller (1985), as observed from Figure A4.3.59 and Figure A4.3.60.

Figure A4.3.61 depicts the ratio between the number of buildings in Tailfingen that were damaged to some extent by the 1978 Albstadt event and the total number of buildings existing at that time, plotted on a mesh map of 100x100m² grid elements by Schwarz *et al.* (2005). As this map does not differentiate across different levels of damage severity (*i.e.* different damage grades), it is complemented by that of Figure A4.3.62, which shows the mean damage ratio (D_m) using the same mesh of grid elements. As observed from this figure, the northern and the south-western parts of Tailfingen were the most severely damaged, and their associated level of mean damage grade exceeded DG2 on the EMS-98 scale.

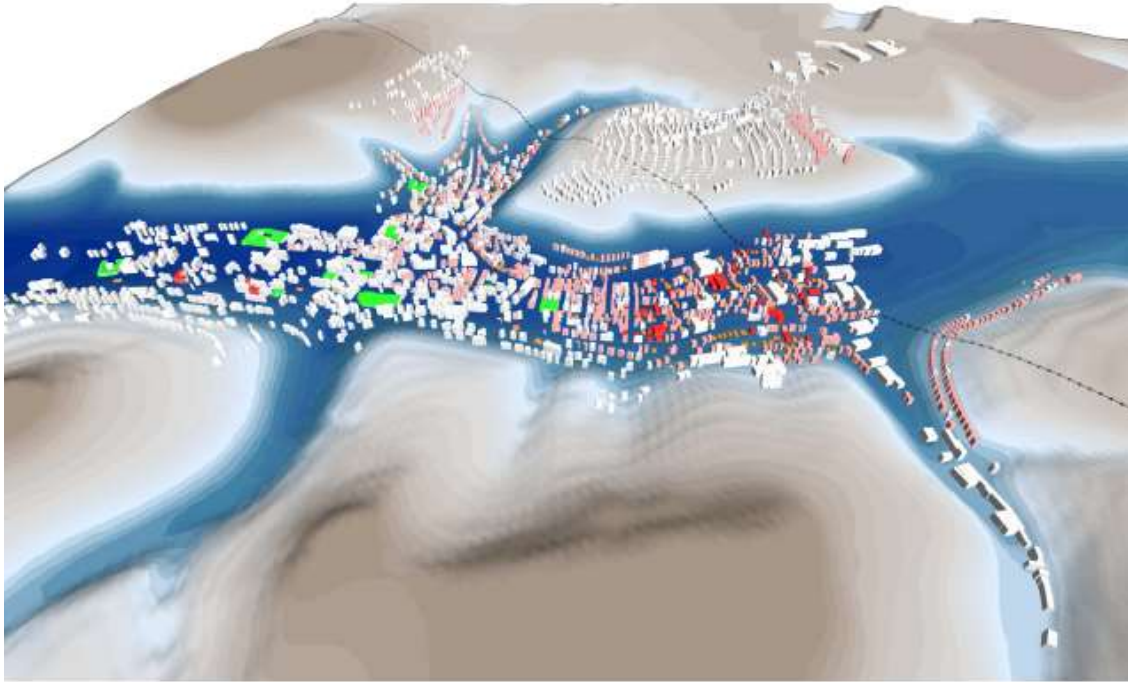


Figure A4.3.59. View of the investigated buildings in Albstadt-Tailfingen with observed damage (same colour-coding as in Figure A4.3.52) and exceptional damage (green). Projection of the rupture of the 1978 Albstadt earthquake onto the surface (black line) according to Hiller (1985).
From Schwarz et al. (2010a).

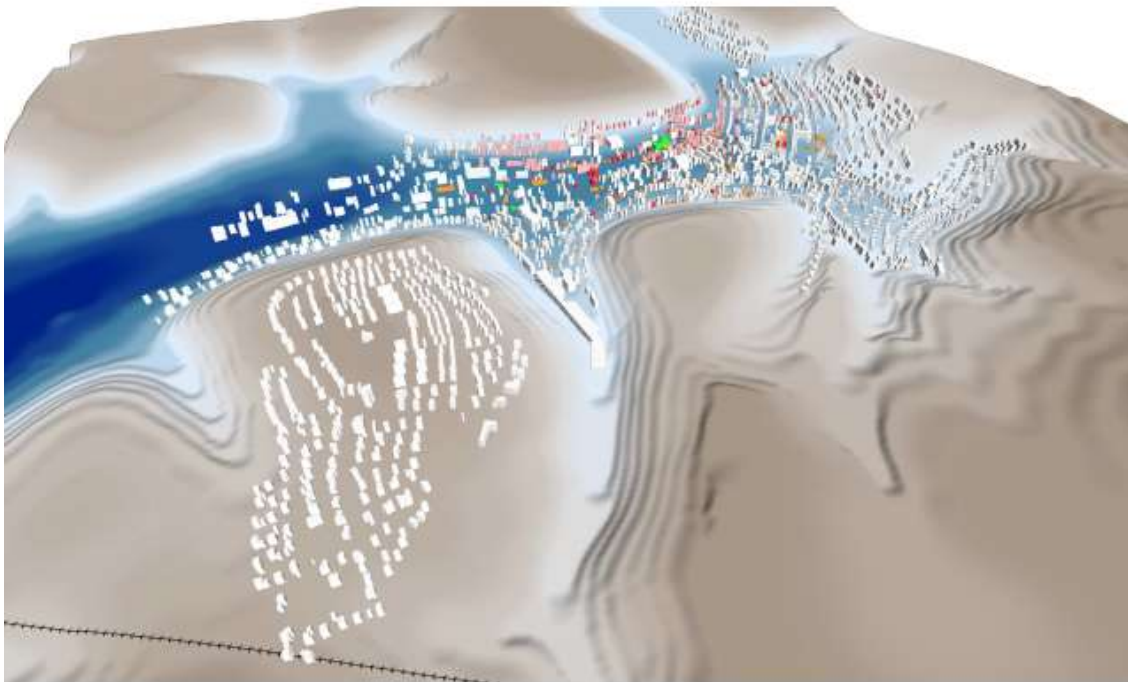


Figure A4.3.60. View of the investigated buildings in Albstadt-Onstmettingen with observed damage (same colour-coding as in Figure A4.3.52) and exceptional damage (green). Projection of the rupture of the 1978 Albstadt earthquake onto the surface (black line) according to Hiller (1985).
From Schwarz et al. (2010a).

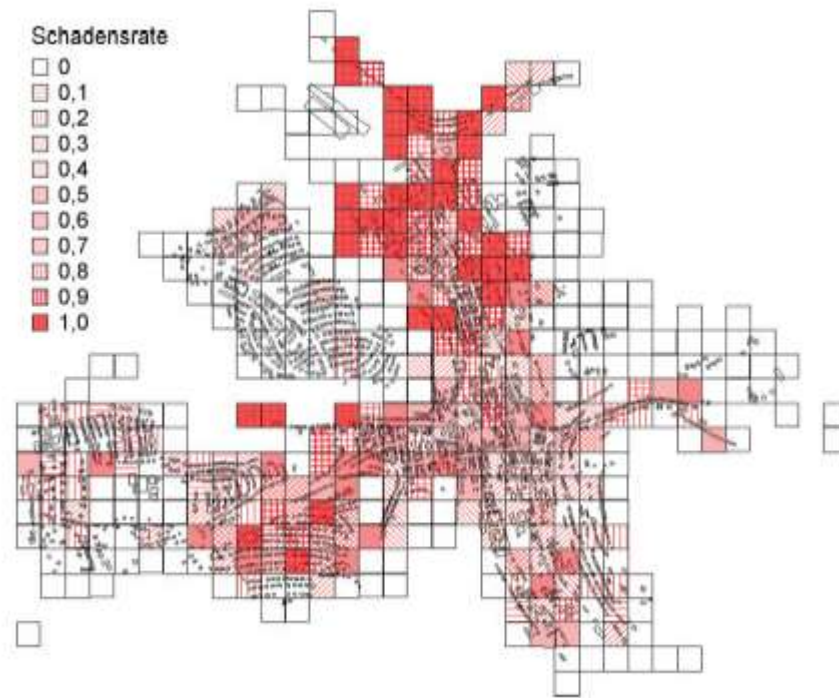


Figure A4.3.61. Reconstruction of the damage survey of Albstadt-Tailfingen using a mesh of 100×100 m² grid elements. Loss ratio (number of damaged buildings, irrespective of the degree of damage, over total number of buildings) shown in colour scale (0, white: no buildings damaged; 1, red: all buildings damaged). From Schwarz et al. (2005).

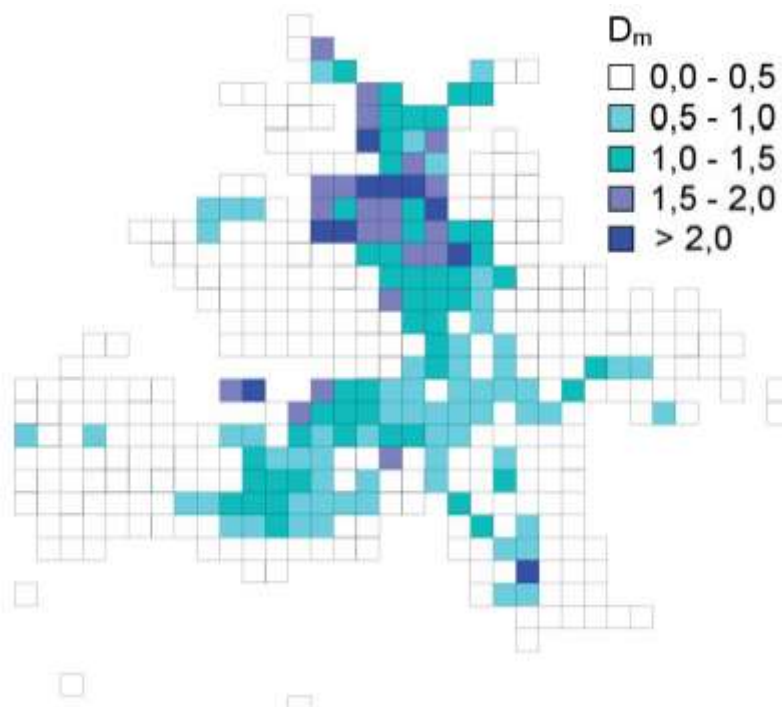


Figure A4.3.62. Mean EMS-98 damage grades (D_m , colour scale) for 100×100 m² grid elements in Albstadt-Tailfingen. From Schwarz et al. (2005).

To study the influence of subsoil conditions on the distribution of damage observed during the 1978 Albstadt earthquake, Beinersdorf *et al.* (2013) plotted the observed damage grades with respect to the soil-classification of damaged sites in Tailfingen and Onstmettingen according to the DIN EN 1998-1/NA:2011-01 building code (Table A4.3.9).

Their results, shown in Figure A4.3.63 (left) correspond to the investigated building stock that consists of 4,612 buildings shown in Table A4.3.18 and Figure A4.3.42. Their findings indicate that higher damage grades (*i.e.*, DG3 and DG4) were observed mostly in areas with subsoil classes B-R and C-R, which, according to Beinersdorf *et al.* (2013), are capable of generating amplification of ground motions at a building site. These authors also calculated the local intensity increments (ΔI_s), that is, the difference between the seismic intensity at the ground surface and the intensity that would have occurred on bedrock, which represents the effects of the local conditions found at a specific site, including deep geology, subsoil and topography. As shown in Figure A4.3.63 (right), positive local intensity increments, that imply an amplification of ground motions due to site effects, prevail in all the damage cases observed.

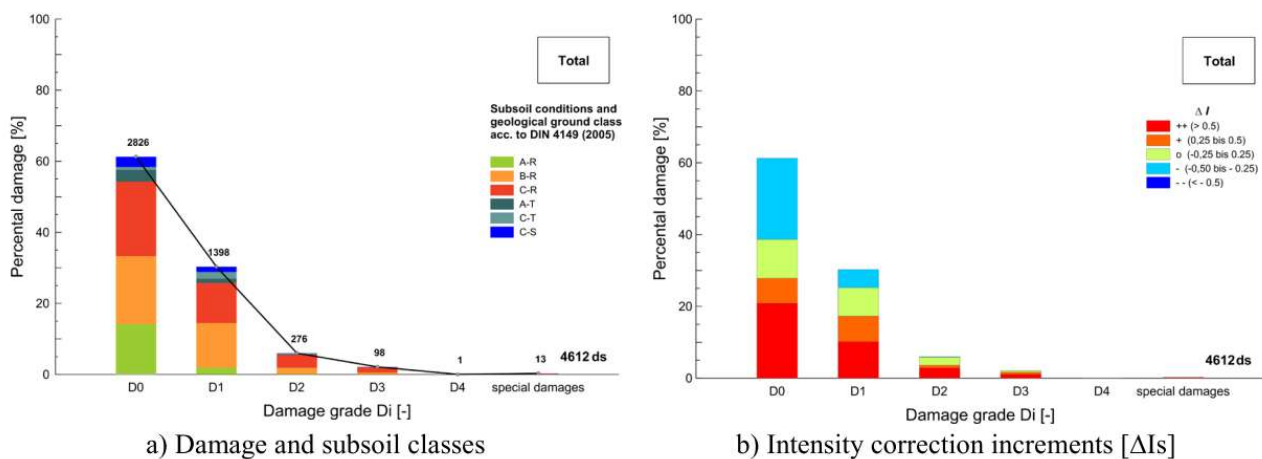


Figure A4.3.63. Distribution of damage grades and assigned subsoil class according to DIN EN 1998-1/NA:2011-01 and its effects on the observed damage associated with the 1978 Albstadt earthquake. From Beinersdorf *et al.* (2013).

For the Onstmettingen district of Albstadt, affected by the 1978 Albstadt seismic event, Porro & Schraft (1989) observed a certain degree of correlation between the distribution of mean damage ratios, expressed as the ratio between loss amount and the value of all affected (not all exposed) buildings, and soil conditions found at the site, as shown in Figure A4.3.64. The earthquake catalogue of Schwarz *et al.* (2010b) supports this, as it reports that the area most damaged by this earthquake was limited to valley settlements, while higher-laying regions were left undamaged. Porro & Schraft (1989) also report the agreement of their results with those of Bossenmayer (1985), who investigated the influence of both subsoil conditions and the year of building construction on the mean damage ratio, as shown in Table A4.3.21. The findings of these authors indicate that buildings constructed in Onstmettingen before the 1950s show higher mean damage ratios than those of later construction. Also, buildings located on loose soils (alluvial sites and slope debris) sustained more damage compared to those located on rock site conditions, but this difference was observed only in the case of buildings constructed before the 1950s, while in all other cases, the subsoil conditions do not appear to have had a significant effect on the mean damage ratio. According to the authors, such observations could be explained by the fact that seismic building regulations had not been established in Germany before the 1950s.

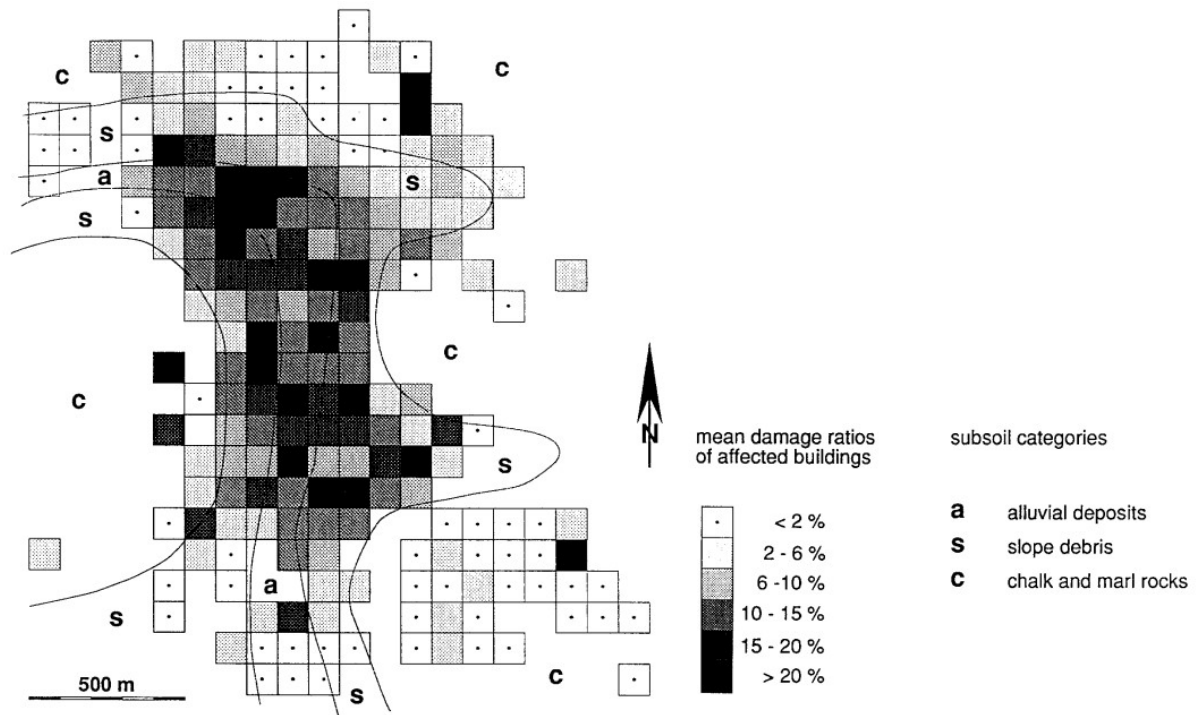


Figure A4.3.64. Geographic distribution of subsoil categories and mean damage ratios in Albstadt-Onstmettingen for the 1978 Albstadt earthquake. Damage ratios were calculated with respect to the total value of affected buildings, not the total of all exposed buildings. From Porro & Schraft (1989).

Table A4.3.21. Effect of subsoil and age of buildings on the mean damage ratio (Albstadt earthquake of 3.9.1978). From Porro & Schraft (1989).

subsoil	year of construction	number of buildings	MDR
Alluvial soil	pre-1900	175	13.7
	1900-1950	172	15.9
	post 1950	46	4.6
Slope debris	pre-1900	141	14.8
	1900-1950	310	13.5
	post-1950	275	4.9
chalk and marl	pre-1900	5	8.9
	1900-1950	41	4.3
	post-1950	257	3.1

Amstein *et al.* (2005) reported that industrial chimney damage (referred to as special damage indicated by green colour in Figure A4.3.21, Figure A4.3.52, Figure A4.3.59 and Figure A4.3.60) observed during the 1978 Albstadt earthquake was concentrated mostly in the middle of the Tailfngen valley. According to Amstein *et al.* (2005), this could be explained by the fact that geological subsoil classes T and S (according to DIN EN 1998-1/NA:2011-01) that correspond to deep sediment basins covered with thick deposits and lower values of $V_{s,25}$ (see section A4.3.3.2) are found in the middle of Tailfngen valley (see Figure A4.3.21, orange and red circles), and are associated with a lower fundamental

frequency of oscillation (see Figure A4.3.23), *i.e.* a higher predominant period of oscillation, which matches the high period of oscillation typical of tall factory chimneys.

The distribution of mean damage grades assigned by Schwarz *et al.* (2015) to residential buildings in Nieder-Beerbach exposed to the 2014 Darmstadt earthquake is shown in Figure A4.3.65 (left), while areas where damage claims associated with this event were recorded are shown in Figure A4.3.65 (right). The distribution of damage induced by this earthquake according to Müller *et al.* (2015) is presented in Figure A4.3.66. As observed from these figures, damage was concentrated along the valley in an area running parallel to the Beerbach river. According to Schwarz *et al.* (2015), concentration of damage within this confined area was due to its vicinity to the epicentre as well as due to the local site effects that have contributed to the amplified response of ground motion. When compared against Figure A4.3.25, it can be observed that the areas with higher concentration of damage correspond roughly to those covered by alluvial and mobilised deposits.

Schwarz *et al.* (2015) and Müller *et al.* (2015) believe that the lack of uniformity in the distribution of damage among the building stock of Nieder-Beerbach may be related as well to the differences in building age, type of material and construction methods used, as well as by extensions and rebuilding that had taken place in some of the properties.

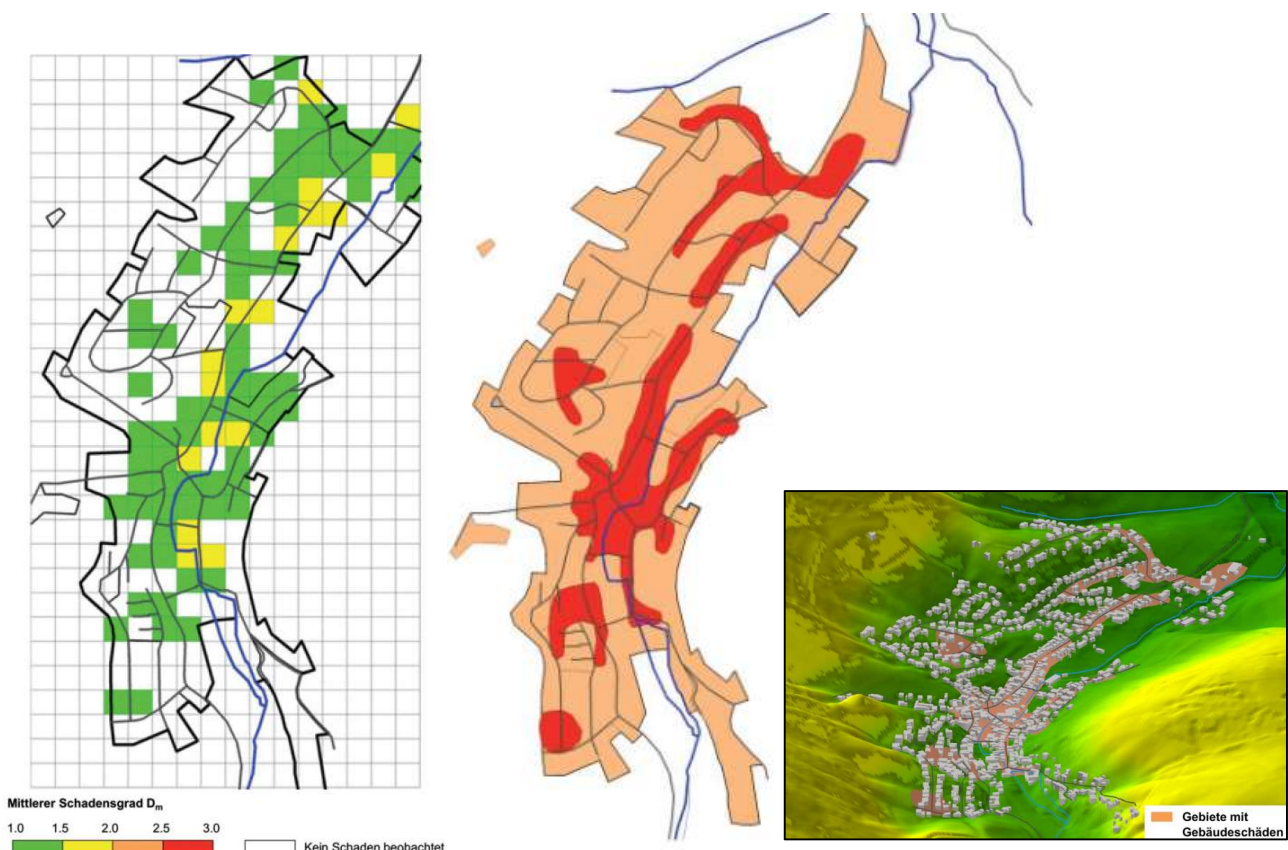


Figure A4.3.65. Mean EMS-98 damage grades (colour scale) associated with buildings in Nieder-Beerbach that were damaged by the 2014 Darmstadt earthquake. White colour indicates no observed damage (left). Areas of Nieder-Beerbach where damage claims due to the 2014 Darmstadt earthquake were recorded (red; right). Inset: 3D representation of the topographical setting and identification of damaged areas (orange). All from Schwarz *et al.* (2015).

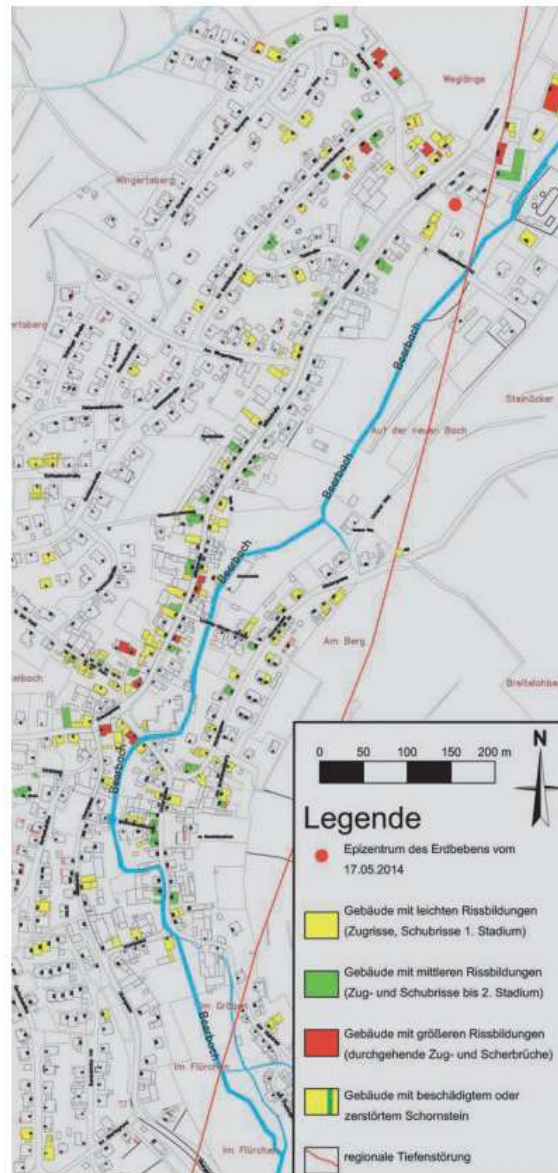


Figure A4.3.66. Damage distribution: buildings with slight (yellow), middle (green) and thick (red) cracks, and with damaged or destroyed chimneys (yellow with green). Right red circle and red line represent the epicentre and regional faults, respectively. From Müller et al. (2015).

A4.3.9 Casualties and losses

A4.3.9.1 Numbers of dead and injured

No cases of fatalities have been reported for the 1978 Albstadt earthquake. The number of injured people was 23 according to Bostenaru (2003) and 35 according to the data reported in the EM-DAT database. This seismic event left between 100 (Bostenaru, 2003) and 200 (EM-DAT) homeless people. The number of evacuated people ranges from 200 people (Reutlinger, 2008) to 300 homes (Bostenaru, 2003). Spiegel (1992) reports that 20 people were trapped under the rubble and had to be dug out of it. While the EM-DAT database reports a total of 235 people affected by this earthquake, Bostenaru (2003)

indicates that this number is as high as 20,000, though it is noted that in neither case the meaning of “affected” is specified.

No human casualties are associated with the 2014 **M3.6** Darmstadt earthquake.

A4.3.9.2 Causes of casualties

According to Reutlinger (2008), two dozen people were injured due to the collapse of walls induced by the aftershock that happened a couple of hours after the main shock of the 1978 Albstadt earthquake.

A4.3.9.3 Estimates of economic losses

For the **M5.2** 1978 Albstadt earthquake the EM-DAT database and the NOAA report a total loss of 150 million USD, while Grünthal (2004) reports losses of 140 million USD (estimated at the time of the earthquake). According to Tyagunov *et al.* (2006), the total damage was estimated to be €140 million. Bostenaru (2003), Stuttgart News (2011) and Grünthal (2004) report a total economic loss of 275 million Deutsche Marks (roughly 170 million USD) and, according to the former author, 120 million Deutsche Marks (roughly 74 million USD) of these losses were insured. According to Porro & Schraft (1989), the total damage in the Onstmettingen district of Albstadt amounted to 50 million USD, of which 35 million USD were insured.

The damage induced by the 2014 **M3.6** Darmstadt earthquake amounts to €1 million according to Juskus Earthquake News (2014) and The Local (2014). The NOAA reports losses of 1.36 million USD associated with this event, while according to Earthquake Report (2014a) these losses exceeded 1 million USD.

A4.3.10 Discussion and conclusions

With intensity VII-VIII on the EMS-98 scale, the **M5.2** Albstadt seismic event of 3rd September 1978 (05.08 UTC) was one of the most damaging earthquakes to have occurred in Germany. It caused damage to around 5,000 to 11,500 properties located mostly in the Tailfingen, Onstmettingen and Ebingen districts of Albstadt. Around 50% of all the damage induced by this event was associated with non-structural elements. Particularly extensive damage was sustained by chimneys and roof tiles, which in many cases collapsed onto the streets, while other common types of damage were the cracking and falling of plaster, cracking of masonry walls and the collapse of gable ends. Buildings that were located in the valleys on alluvial soil deposits sustained higher degrees of damage than those located on rocky ground conditions in higher-laying regions. Around 75% of the damaged buildings had been constructed shortly after the end of the Second World War, while newer constructions performed significantly better. Dozens of people were reported injured as a consequence of this earthquake, though it appears that most injuries are, in fact, associated with one of its largest aftershocks, which occurred only 5 hours after the main shock. Approximately 200 people were left homeless. Losses induced by this event range between 140 and 170 million USD.

The M3.6 Darmstadt earthquake of 17th May 2014 (16.46 UTC) was the strongest of a series of events that occurred from April 2014 to March 2015 in the area south-east of Darmstadt. The intensity estimated for this event is VI-VII on the EMS-98 scale, and it produced much milder damage than the 1978 Albstadt earthquake, as could be reasonably expected given the difference in magnitude and the similar depths and epicentral distances, notwithstanding uncertainties. It caused slight-to-moderate damage to around 150 buildings, most of which were located in the Nieder-Beerbach district of Mühlthal municipality. It is possible that local site effects played a role in the concentration of damage within this confined area of the Nieder-Beerbach valley. Many of the affected properties were built without consideration of seismic regulations. Cracks were observed on most of the buildings in the affected area, though their severity varied across different properties. Considerable damage was also sustained by chimneys. This event did not cause any casualties but is estimated to have generated economic losses of around 1 to 1.4 million USD.

A4.3.11 References

A4.3.11.1 Bibliography

Afshari, K. & J. P. Stewart (2016). Physically parameterized prediction equations for significant duration in active crustal regions. *Earthquake Spectra* **32**(4), 2057-2081.

Ahorner, L., H. Murawski & G. Schneider (1972). Seismotektonische traverse von der Nordsee bis zum Apennin (Seismo-tectonic traverse from the North Sea to the Apennines, in German). *Geologische Rundschau* **61**, 915-942.

Ahorner, L. & G. Schneider (1974). Herdmechanismen von erdbeben im Oberrheingraben und in seinen randgebirgen (Focal mechanisms of earthquakes in the Upper Rhine Graben and in its border mountains). In Fuchs, K. & H. Illies (eds.): *Approaches to Taphrogenesis*. Schweizerbart, Stuttgart, Germany.

Akkar, S., M. A. Sandikkaya, M. Senyurt, A. A. Sisi, B. Ö. Ay, P. Traversa, J. Douglas, F. Cotton, L. Luzi, B. Hernandez & S. Godey (2014). Reference database for seismic ground-motion in Europe (RESORCE). *Bulletin of Earthquake Engineering* **12**(1), 311–339.

Allen, T. I., D. J. Wald, P. S. Earle, K. D. Marano, A. J. Hotovec, K. Lin & M. G. Hearne (2009). An Atlas of ShakeMaps and population exposure catalog for earthquake loss modeling. *Bulletin of Earthquake Engineering* **7**(3), 701-718.

Amstein, S., D.H. Lang & J. Schwarz (2005). Schütterwirkungen historischer erdbeben und aktuelle anwendungsgebiete für das erdbebeningenieurwesen (Shaking effects of historical earthquakes and current applications for earthquake engineering, in German). *Bautechnik* **82**(9), 641-656.

Atkinson, G.M. & S.I. Kaka (2007). Relationships between felt Intensity and instrumental ground motion in the central United States and California. *Bulletin of the Seismological Society of America* **97**, 497-510.

Beinersdorf, S., J. Schwarz & T. Langhammer (2013). Vulnerability assessment of a building stock and reliability considerations on the basis of observed damage grades: reconstruction of the

September 3, 1978 Albstadt earthquake. *Proceedings of the Vienna Congress on Recent Advances in Earthquake Engineering and Structural Dynamics (VEESD)*, August 28-30, Vienna Austria. Available online at (last accessed 28th December 2017):

[https://www.academia.edu/22416074/Vulnerability assessment of a building stock and reliability considerations on the basis of observed damage grades Reconstruction of the September 3 1978 Albstadt earthquake?auto=download](https://www.academia.edu/22416074/Vulnerability_assessment_of_a_building_stock_and_reliability_considerations_on_the_basis_of_observed_damage_grades_Reconstruction_of_the_September_3_1978_Albstadt_earthquake?auto=download)

Beinersdorf, S. & J. Schwarz (2014). ShakeMaps for Central Europe implementing macroseismic observations. *Proceedings of the 2nd European Conference on Earthquake Engineering and Seismology*, August 25-29, Istanbul, Turkey. Available online at (last accessed 28th December 2017): http://www.eaee.org/Media/Default/2ECCES/2ecces_eaee/238.pdf

Blauß, H. (1980). Erdbeben am 3. September 1978 auf der Schwäbischen Alb (Earthquake on 3rd September 1978 in the Swabian Alps, in German). *Schadenprisma-Journal for loss prevention and damage research of public-law insurance companies* **1**, 1-6.

Bommer, J. J., P. J. Stafford & J. E. Alarcón (2009). Empirical equations for the prediction of the significant, bracketed, and uniform duration of earthquake ground motion. *Bulletin of the Seismological Society of America* **99**(6), 3217–3233.

Bormann, P. (1994). Seismotectonics and seismic hazard of Germany in the European context. *Bulletin of the Indian Society of Earthquake Technology* **31**(2), 55—89.

Bossenmayer, H. (1985). *Analyse von erdbebenschäden in Baden-Württemberg und folgerungen (Analysis of earthquake damage in Baden-Württemberg and conclusions*, in German). Lecture of the Baden-Württemberg Ministry of Home Affairs on 15 April 1985 on bases and application of Eurocode 8.

Bostenaru, M.D. (2003). *Prefabricated metal construction of the modern movement*. Report of the World Housing Encyclopedia (WHE) - an encyclopedia of housing construction in seismically active areas of the world. Available online at: <http://www.world-housing.net/WHEReports/wh100100.pdf>. Last accessed: 28th December 2017.

CEN (2004). *Eurocode 8: Design of structures for earthquake resistance - Part1: General rules, seismic actions and rules for buildings*. European Committee for Standardization, Brussels, Belgium.

Center for International Earth Science Information Network - CIESIN - Columbia University (2016). Gridded Population of the World, Version 4 (GPWv4). Palisades, NY: NASA Socioeconomic Data and Applications Center. <http://dx.doi.org/10.7927/H4NP22DQ>.

Daniell, J.E. (2015). Global view of seismic code and building practice factors. In Beer, M., I.A. Kougiumtzoglou, E. Patelli & S.-K. Au (eds.): *Encyclopedia of Earthquake Engineering*. Springer Berlin Heidelberg, 1109-1119.

Daniell, J.E., B. Khazai, F. Wenzel & A Vervaeck (2012). The worldwide economic impact of historic earthquakes. *Proceedings of the 15th World Conference on Earthquake Engineering*, September 24-28, Lisboa, Portugal. Available online at (last accessed 28th December 2017): https://www.researchgate.net/publication/258434390_The_Worldwide_Economic_Impact_of_Earthquakes_Paper_No_2038.

Daniell, J. E., F. Wenzel, B. Khazai, J.G. Santiago & A. Schaefer (2014). A worldwide seismic code index, country-by-country global building practice factor and socioeconomic vulnerability indices for use in earthquake loss estimation. *Proceedings of the 2nd European Conference on Earthquake Engineering and Seismology*, August 25-29, Istanbul, Turkey. Available online at: http://www.eaee.org/Media/Default/2ECCES/2ecces_eaee/1400.pdf. Last accessed: 28th December 2017.

DIN 4149:1957-07 (1957). *Bauten in deutschen erdbebengebieten. Richtlinien für bemessung und ausführung (Buildings in German earthquake zones; design loads, guidelines for design and construction, in German)*. German Institute for Standardization (DIN), Berlin, Germany.

DIN 4149-1:1981-04 (1981). *Bauten in deutschen erdbebengebieten; lastannahmen, bemessung und ausführung üblicher hochbauten (Buildings in German earthquake zones; design loads, dimensioning, design and construction of conventional buildings, in German)*. German Institute for Standardization (DIN), Berlin, Germany.

DIN 4149-1/A1 (1992-12) (1992). *Bauten in deutschen erdbebengebieten; lastannahmen, bemessung und ausführung üblicher hochbauten (Buildings in German earthquake zones; design loads, dimensioning, design and construction of conventional buildings, in German)*. German Institute for Standardization (DIN), Berlin, Germany.

DIN 4149:2005-04 (2005). *Bauten in deutschen erdbebengebieten - Lastannahmen, bemessung und ausführung üblicher hochbauten (Buildings in German earthquake areas - Design loads, analysis and structural design of buildings, in German)*. Standards committee building and civil engineering (NABau) of German Institute for Standardization (DIN), Berlin, Germany.

DIN EN 1998-1/NA:2011-01 (2011). *Nationaler Anhang - National festgelegte Parameter - Eurocode 8: Auslegung von Bauwerken gegen Erdbeben - Teil 1: Grundlagen, Erdbebeneinwirkungen und Regeln für Hochbau (National Annex - Nationally determined parameters - Eurocode 8: Design of structures for earthquake resistance - Part 1: General rules, Seismic actions and rules for buildings, in German)*. German Institute for Standardization (DIN), Berlin, Germany.

Dziewonski, A.M., T.-A. Chou & J. H. Woodhouse (1981). Determination of earthquake source parameters from waveform data for studies of global and regional seismicity. *Journal of Geophysical Research* **86**, 2825-2852.

Ekström, G., M. Nettles & A. M. Dziewonski (2012). The global CMT project 2004-2010: Centroid-moment tensors for 13,017 earthquakes. *Physics of the Earth and Planetary Interiors* **200-201**, 1-9.

Foulger, G.R., M. Wilson, J. Gluyas & R. Davies (2016). *Human-induced earthquakes*. Report for the Nederlandse Aardolie Maatschappij BV (NAM), The Netherlands. Report available online at: <https://www.nam.nl/feiten-en-cijfers/onderzoeksrapporten.html#iframe=L2VtYmVvL2NvbXBvbmVudC8/aWQ9b25kZXJ6b2Vrc3JhcHBvcnRlbG>. Last accessed 28th November 2017.

Fuchs, K. (2016). Intraplate seismicity induced by stress concentration at crustal heterogeneities - the Hohenzollern Graben, a case history. In Dawson, J.B., D.A. Carswell, J. Hall & K.H. Wedepohl (eds.): *The nature of the lower continental crust*. Blackwell Scientific Publication, Osney Mead, Oxford, United Kingdom.

García-Mayordomo, J., E. Faccioli & R. Paolucci (2004). Comparative study of the seismic hazard assessments in European national seismic codes. *Bulletin of Earthquake Engineering* **3**, 51-73.

Giardini, D., G. Grünthal, K. M. Shedlock & P. Zhang (1999). The GSHAP global seismic hazard map. *Annali di Geofisica* **42**(6), 1225–1228.

Grünthal, G. (1998). European Macroseismic Scale 1998 (EMS-1998). Cahiers du Centre Europeen de Geodynamique et de Seismologie 15, Centre Europeen de Geodynamique et de Seismologie, Luxembourg. Available online at (last accessed 28th December 2017): http://www.franceseisme.fr/EMS98_Original_english.pdf.

Grünthal, G. (2004). Erdbeben und erdbebengefährdung in Deutschland sowie im Europäischen Context (Earthquake and earthquake hazard in Germany in the European context, in German). *Geographie und Schule* **151**, 14-23.

Grünthal, G. & C. Bosse (1996). *Probabilistische karte der erdbebengefährdung der Bundesrepublik Deutschland – Erdbebenzonierungskarte für das nationale anwendungsdokument zum Eurocode 8 (Probabilistic map of the seismic hazard of the Federal Republic of Germany Republic of Germany - Earthquake zoning card for the national application document for Eurocode 8, in German)*. Scientific Technical Report 96/10, German Research Centre for Geosciences (GFZ), Potsdam, Germany.

Grünthal, G. & R. Wahlström (2003). An Mw based earthquake catalogue for central, northern and northwestern Europe using a hierarchy of magnitude conversions. *Journal of Seismology* **7**, 507-531.

Grünthal, G., C. Bosse & D. Stromeyer (2015). Building-code related seismic hazard analyses of Germany and their relation to SHARE. In Butenweg, C. & D. Kaiser (eds.): *Seismic Hazard Harmonization in Europe (SHARE): DGEB-Workshop in Frankfurt a.M., Germany, 27. May 2014*. DGEB, Aachen, Germany. Available online at (last accessed 28th December 2017):

<http://gfzpublic.gfz->

potsdam.de/pubman/item/escidoc:916888:5/component/escidoc:989908/916888.pdf

Grünthal, G., D. Stromeyer, C. Bosse, F. Cotton & D. Bindi (2018). The Probabilistic Seismic Hazard Assessment of Germany – Version 2016, considering the range of epistemic uncertainties and aleatory variability. *Bulletin of Earthquake Engineering*, in press. DOI: 10.1007/s10518-018-0315-y

Haessler, H., P. Hoangtrong, R. Schick & K. Strobach (1980). The September 3, 1978, Swabian Jura earthquake, Germany. *Tectonophysics* **68**(1-2), 1-14.

Heidenreich, M. & G. Krauss (1998). Chapter 7 – The Baden-Württemberg production and innovation regime – Past successes and new challenges. In Braczyk, H.-J., P.N. Cooke & M. Heidenreich (eds.): *Regional innovation systems: the role of governances in a globalized world*. UCL Press – Routledge, Taylor & Francis. Available online at: http://www.sozialstruktur.uni-oldenburg.de/dokumente/ris_bawue.pdf. Last accessed: 8th February 2018.

Hiller, D. (1985). *Makroseismische Wirkungen des Albstadt-Bebens vom 3. September 1978 in Baden-Württemberg (Macroseismic effects of the Albstadt quake of September 3, 1978 in Baden-Württemberg, in German)*. Doctoral thesis, Institute for Geophysics at the University of Stuttgart, Germany.

Homuth, B., G. Rümpker, H. Deckert & M. Kracht (2014). Seismicity of the northern Upper Rhine Graben — Constraints on the present-day stress field from focal mechanisms. *Tectonophysics* **632**, 8-20.

Homuth, B. & G. Rümpker (2017). The 2014–2015 earthquake series in the northern Upper Rhine Graben, Central Europe. *Journal of Seismology* **21**(1), 83-98.

Jaiswal, K. S. & D. J. Wald (2008). *Creating a global building inventory for earthquake loss assessment and risk management*. U.S. Geological Survey, Open-File Report 2008-1160. Available online at: <https://pubs.usgs.gov/of/2008/1160/>. Last accessed: 7th July 2017.

Kasperski, M. (2002). A new wind zone map for Germany. *Journal of Wind Engineering and Industrial Aerodynamics* **90**, 1271-1287.

Lang, D.H. & J. Schwarz (2006). Instrumental subsoil classification of Californian strong motion sites based on single-station measurements. *Proceedings of the 8th U.S. National Conference on Earthquake Engineering (NCEE)*, April 22-26, San Francisco, Unites States. Available online at: https://www.researchgate.net/publication/268176792_Instrumental_subsoil_classification_of_Californian_strong_motion_sites_based_on_single-station_measurements.

Last accessed: 28th December 2017.

Langer, H. (1990). Input parameters for estimating seismic loading. *Natural Hazards* **3**, 125-139.

Leydecker, G. (2011). Earthquake catalogue for Germany and adjacent areas (800-2008 AD). Federal Institute for Geosciences and Natural Resources (BGR), Hannover, Germany. Available online at (last accessed 28th December 2017):

https://www.bgr.bund.de/EN/Themen/Seismologie/Erdbebenauswertung_en/Kataloge_en/historisch/germany_en.html?nn=1569354

Medvedev, S., W. Sponheuer & V. Karnik (1965). *Seismic intensity scale, MSK 1964*. Academy of Sciences of the U.S.S.R., Soviet Geophysical Community, 13 pp.

Meidow, H. (2008). Beobachtungen makroseismischer schütterwirkungen historischer erdbeben (Observations of macroseismic shaking effects of historical earthquakes, in German). Data file.

Müller, B., B. Litschko & U. Pippig (2015). Auswirkungen des Erdbebens vom 17. Mai 2014 in Nieder-Beerbach (Hessen) und Ableitung realistischer Anhaltswerte bei Erschütterungen (Impact of the earthquake of May 17, 2014 in Nieder-Beerbach (Hesse) and derivation of realistic reference values in case of shocks, in German). *GeoResources: Journal for Resources, Mining, Tunnelling, Geotechnics and Equipment*, issue 1-2015. Available online at (last accessed 28th December 2017): <http://www.georesources.net/download/GeoResources-Zeitschrift-1-2015.pdf>

Peters, G. (2007). *Active tectonics in the Upper Rhine Graben. Integration of paleoseismology, geomorphology and geomechanical modeling*. Doctoral dissertation at Faculty of Earth and Life Sciences - Vrije Universiteit, Amsterdam, the Netherlands. Available online at (last accessed 28th December 2017): <https://research.vu.nl/ws/portalfiles/portal/42176131>

Porro, B. & A. Schraft (1989). Investigation of insured earthquake damage. *Natural Hazards* **2**, 173-184.

Przyrowski, R. & A. Schäfer (2014). Quaternary fluvial basin of northern Upper Rhine Graben. *Zeitschrift der Deutschen Gesellschaft für Geowissenschaften - Journal of the German Society for Geosciences* **166**(1), 71-98.

Ringhofer, A. (2010). *Erdbebennormung in Europa und deren Anwendung auf Wohnbauten in Holz-Massivbauweise (Earthquake standardization in Europe and its application to residential buildings erected in solid timber construction, in German)*. Master thesis, Graz University of Technology, Austria. Available online at (last accessed 28th December 2017): <http://diglib.tugraz.at/download.php?id=576a714629a01&location=browse>

Seismosoft (2016). SeismoSignal - A computer programme for signal processing of strong-motion data. <http://www.seismosoft.com/seismosignal>.

Scherbaum, F. & D. Stoll (1983). Source parameters and scaling laws of the 1978 Swabian Jura (southwest Germany) aftershocks. *Bulletin of the Seismological Society of America* **73**(5), 1321-1343.

Schneider, G. (1968). Erbeben und tektonik in Suedwestdeutschland (Earthquakes and tectonics in southwestern Germany, in German). *Tectonophysics* **5**(6), 459-511.

Schneider, G. (1980). Seismic stresses in southern Germany. In Scheidegger A.E. (eds.): *Tectonic stresses in the Alpine-Mediterranean region*. Rock Mechanics / Felsmechanik / Mécanique des Roches. Springer, Vienna, Austria.

Schwarz, J., T. Langhammer & C. Kaufmann (2005). Quantifizierung der schadenspotentiale infolge erdbeben- Teil 1: Rekonstruktion des Bebens in der Schwäbischen Alb vom 03. September 1978 (Quantification of damage potential due to earthquakes - Part 1: Reconstruction of the quake in the Swabian Alps from September 03, 1978, in German). *Bautechnik* **82**(8), 520-532.

Schwarz, J., S. Beinersdorf, T. Swain, T. Langhammer, M. Leipold, C. Kaufmann & T. Wenk (2008). Realistic vulnerability and displacement functions for masonry structures derived from damaging earthquakes in Central Europe. *Proceedings of the 14th World Conference on Earthquake Engineering, October 12-17, Beijing, China*. Available online at: <https://www.research-collection.ethz.ch/bitstream/handle/20.500.11850/152648/eth-2665-01.pdf>. Last accessed: 28th December 2017.

Schwarz, J., S. Beinersdorf, T. Langhammer, C. Kaufmann & M. Leipold (2010a). Vulnerability functions for masonry structures derived from recent earthquakes in Germany. *Proceedings of the 14th European Conference on Earthquake Engineering, 30th August – 3rd September, Ohrid, Macedonia*. Available online at (last accessed 28th December 2017): https://www.academia.edu/21393089/Vulnerability_functions_for_masonry_structures_derived_from_recent_earthquakes_in_Germany?auto=download

Schwarz, J., S. Beinersdorf, H. Meidow & L. Ahorner (2010b). *Magnitudenorientierter erdbebenkatalog für Deutsche und angrenzende gebiete (EKDAG) – erweiterter Ahorner-Katalog (version 1.0) (Earthquake catalogue for Germany and adjacent areas (EKGAD), in German)*. Bauhaus University, Weimar, Germany.

Schwarz, J., H. Maiwald, M. Leipold, T. Langhammer, M. Kracht & B. Müller (2015). Das erdbeben vom 17. Mai 2014 in Südhessen – ingenieuranalyse der Erdbebenschäden (The earthquake of 17 May 2014 in southern Hesse - engineering analysis of earthquake damage, in German). *Bautechnik* **92**(9), 647-659.

Solomos, G., A. Pinto & S. Dimova (2008). *A review of the seismic hazard zonation in national building codes in the context of Eurocode 8. Support to the implementation, harmonization and further development of the Eurocodes*. Joint Research Centre, European Commission. Available online at: <http://eurocodes.jrc.ec.europa.eu/doc/EUR23563EN.pdf>. Last accessed: 8th February 2018.

Solsten, E. (ed.) (1995). *Germany: a country study*. Federal Research Division, Library of Congress, Washington, USA. Available online at: <http://countrystudies.us/germany/>. Last accessed: 8th February 2018.

Troen, I. & E. Lundtang Petersen (1989). *European wind atlas*. Riso National Laboratory, Roskilde, Denmark, for the Commission of the European Communities. Available online at (last accessed 8th February 2018): http://orbit.dtu.dk/files/112135732/European_Wind_Atlas.pdf.

Turnovsky, J. (1981). *Herdmechanismus und Herdparameter der Erdbebenseerie 1978 auf der Schwäbischen Alb (Focal mechanism and source parameters of the earthquake series 1978 in the Swabian Alps, in German)*. Dissertation, University of Stuttgart, Germany.

Turnovsky, J. & G. Schneider (1982). The seismotectonic character of the September 3, 1978, Swabian Jura earthquake series. *Tectonophysics* **83**(3-4), 151-162.

Tyagunov, S., L. Stempniewski, G. Grünthal, R. Wahlström & J. Zschau (2004). Vulnerability and risk assessment for earthquake prone cities. *Proceedings of the 13th World Conference on*

Earthquake Engineering (WCEE), August 1-6, Vancouver, Canada. Available online at: http://www.iitk.ac.in/nicee/wcee/article/13_868.pdf. Last accessed: 28th December 2017.

Tyagunov, S., G. Grünthal, R. Wöhlstorm, L. Stempniewski & J. Zschau (2006). Seismic risk mapping for Germany. *Natural Hazards and Earth System Sciences* **6**, 573-586.

United Nations, ed. (2015). *Human Development Report 2015 – Work for Human Development*. Report of the United Nations Development Programme (UNDP), New York, United States.

United Nations, ed. (2016). *Human Development Report 2016 – Human Development for Everyone*. Report of the United Nations Development Programme (UNDP), New York, United States.

Van Gils, J.M. & G. Leydecker (1991). Catalogue of European earthquakes with intensities higher than 4. Commission of the European Communities (CEC) - nuclear science and technology, Report EUR 13406 EN, Brussels, Belgium. Available online at (last accessed 28th December 2017): https://www.bgr.bund.de/EN/Themen/Seismologie/Erdbebenauswertung_en/Kataloge_en/historisch/EU_Oe_Schw_en.html?nn=1558132.

Wald, D.J. & T.I. Allen (2007). Topographic slope as a proxy for seismic site conditions and amplification. *Bulletin of the Seismological Society of America* **97**, 1379–1395. Slope-based online map viewer available at: <http://usgs.maps.arcgis.com/apps/webappviewer/index.html?id=8ac19bc334f747e486550f32837578e1>. Data used herein downloaded from deprecated version last accessed on 6th November 2015.

Wilson, M.P., G.R. Foulger, J.G. Gluyas, R.J. Davies & B.R. Julian (2017). HiQuake: The human-induced earthquake database. *Seismological Research Letters* **88**(6), 1560-1565. Database available at: <http://inducedearthquakes.org/>. Last accessed: 5th February 2018.

Woessner, J., D. Giardini, H. Crowley, F. Cotton, G. Grünthal, G. Valensise, R. Arvidsson, R. Basili, M. B. Demircioglu, S. Hiemer, C. Meletti, R. W. Musson, A. N. Rovida, K. Sesetyan, M. Stucchi & The SHARE Consortium (2015). The 2013 European Seismic Hazard Model: Key Components and Results. *Bulletin of Earthquake Engineering* **13**(12), 3553–3596. Online data source: <http://www.efehr.org/en/home/>. Last accessed: 28th December 2017.

Worden, C.B., E.M. Thompson, M. Hearne & D.J. Wald (2017). *ShakeMap V4 Manual: technical manual, user's guide, and software guide*. United States Geological Survey. Available online at: <http://usgs.github.io/shakemap/>.

A4.3.11.2 Web references

Albstadt (2018): <https://www.albstadt.de/Einwohnerzahlen>. Last accessed: 7th February 2018.

Castle Hohenzollern (Burg Hohenzollern, in German) (2010): <http://www.burg-hohenzollern.com/castle-history.html>. Last accessed: 28th December 2017.

City Population (2016): <https://citypopulation.de/>. Last accessed: 28th December 2017.

Country Economy (2017): <https://countryeconomy.com/HDI>. Last accessed: 28th December 2017.

Earthquake Damage Analysis Center (EDAC, 2014): <https://www.edac.biz/forschung/erdbeben/feldeinsaetze/nieder-beerbach-2014/>. Last accessed: 28th December 2017.

Earthquake Report (2014a): <https://earthquake-report.com/2014/11/05/continuous-earthquake-swarm-near-darmstadt-germany/>. Last accessed: 28th December 2017.

Earthquake Report (2014b): <https://earthquake-report.com/2014/05/17/moderate-earthquake-germany-on-may-17-2014/>. Last accessed: 28th December 2017.

Eurostat (2017):
<http://ec.europa.eu/eurostat/documents/2995521/8357265/3-31102017-CP-EN.pdf/cc23432e-f918-4f93-9fe7-0c03badb9792>. Last accessed: 28th December 2017.

Federal Institute for Geosciences and Natural Resources (BGR): <https://www.bgr.bund.de/DE>
 BGR (2017a):
https://www.bgr.bund.de/EN/Themen/Seismologie/Erdbebenauswertung_en/Kataloge_en/historisc/h/germany_en.html?nn=1559752. Last accessed: 28th December 2017.
 BGR (2017b):
<https://geoviewer.bgr.de/mapapps/resources/apps/geoviewer/index.html?lang=en&serviceURL=https://services.bgr.de/wms/boden/buek5000/>. Last accessed: 28th December 2017.

Global Centroid Moment Tensor Project (GCMT): <http://www.globalcmt.org/>. Last accessed: 28th December 2017.

German Research Centre for Geosciences (GFZ): <http://gfzpublic.gfz-potsdam.de>
 GFZ (2015), last accessed 10th November 2017:
<http://www.gfz-potsdam.de/en/section/seismic-hazard-and-stress-field/topics/where-in-germany-does-the-earth-quake/seismicity-in-germany-in-global-context/>.
 GFZ (2017a), last accessed 28th December 2017:
http://www.gfz-potsdam.de/de/din4149_erdbebenzonenabfrage/.
 GFZ (2017b), last accessed 28th December 2017:
<http://www-app5.gfz-potsdam.de/d-eq haz16/index.html>. Last accessed: 28th December 2017.
 GFZ (2017c) , last accessed 28th December 2017:
<https://www.gfz-potsdam.de/en/section/seismic-hazard-and-stress-field/topics/where-in-germany-does-the-earth-quake/seismicity-in-germany-in-european-context/>

Hessian State Office for Nature Conservation, Environment and Geology (HLNUG):
<https://www.hlnug.de/start.html>
 HLNUG (2017), last accessed 28th December 2017:
<https://www.hlnug.de/themen/geologie/erdbeben/in-hessen-gespuerte-erdbeben.html>

International Seismological Centre (ISC): <http://www.isc.ac.uk/>

INGV-SHARE – The European Database of Seismogenic Faults (2010): <http://diss.rm.ingv.it/share-edsf/sharedata/SHHTML/DECS009INF.html> (fault nearby Albstadt). Last accessed: 5th February 2018.

Juskus Earthquake News (Juskis Erdbebennews, in German) (2014):
<http://juskis-erdbebennews.de/2014/05/erneutes-erdbeben-im-suedlichen-hessen-veraengstigt-die-menschen-dutzende-haeuser-beschaedigt-staerkstes-erdbeben-seit-jahren/>.
 Last accessed: 28th December 2017.

Legislative Council of the Hong Kong, 2015 (last accessed 28th December 2017):
<http://www.legco.gov.hk/research-publications/english/1415fsc13-development-of-innovation-and-technology-in-germany-20150225-e.pdf>

National Geophysical Data Center / World Data Service (NGDC/WDS): Significant Earthquake Database. National Geophysical Data Center, National Oceanic and Atmospheric Administration (NOAA). DOI:10.7289/V5TD9V7K.: <https://www.ngdc.noaa.gov/hazard/earthqk.shtml>

Reutlinger (in German) (2008):
<http://www.gea.de/region+reutlingen/tuebingen/zu+tausenden+auf+die+strasse+gerannt.464039.htm>. Last accessed: 28th December 2017.

Schwarzwaelder Messenger (schwarzwaelder-bote, in German) (2013): [http://www.schwarzwaelder-bote.de/inhalt.zollernalbkreis-erdbeben-zwischen-albstadt-und-killertal-
weckt-erinnerungen-an-1978.092cfb02-0f75-409d-bb88-a50d03ccd668.html](http://www.schwarzwaelder-bote.de/inhalt.zollernalbkreis-erdbeben-zwischen-albstadt-und-killertal-weckt-erinnerungen-an-1978.092cfb02-0f75-409d-bb88-a50d03ccd668.html).
Last accessed: 28th December 2017.

Spiegel (in German) (1992): <http://www.spiegel.de/spiegel/print/d-13688075.html>

Spiegel (in German) (2017): [http://www.spiegel.de/wissenschaft/natur/darmstadt-erdbeben-
erschuettert-hessen-a-1170278.html](http://www.spiegel.de/wissenschaft/natur/darmstadt-erdbeben-erschuettert-hessen-a-1170278.html). Last accessed: 28th December 2017.

Statistical Office of Hesse – Hessisches Statistisches Landesamt (2014): [https://www.destatis.de/GPStatistik/servlets/MCRFileNodeServlet/HEHeft_derivate_00004268/Teil
%201_Regierungsbezirk%20Darmstadt.pdf;jsessionid=160769FE99D46FFC702A35928AA6221E](https://www.destatis.de/GPStatistik/servlets/MCRFileNodeServlet/HEHeft_derivate_00004268/Teil%201_Regierungsbezirk%20Darmstadt.pdf;jsessionid=160769FE99D46FFC702A35928AA6221E)
(in German). Last accessed: 7th February 2018.

Stuttgart News (Stuttgarter Nachrichten, in German) (2011): [http://www.stuttgarter-
nachrichten.de/inhalt.alb-beben-1978-der-naechste-sechser-kommt-bestimmt.690a1e0b-a6b9-
4afb-8dc6-234bbc63d239.html](http://www.stuttgarter-nachrichten.de/inhalt.alb-beben-1978-der-naechste-sechser-kommt-bestimmt.690a1e0b-a6b9-4afb-8dc6-234bbc63d239.html). Last accessed: 28th December 2017.

Swiss Re (2017): <https://openminds.swissre.com/stories/983/>.
Last accessed: 28th December 2017.

The International Disaster Database (EM-DAT): <http://www.emdat.be/database>

The Local (2014): <https://www.thelocal.de/20140519/earthquake-damages-70-homes-in-hesse-germany>
Last accessed: 28th December 2017.

The World Bank (2017a): <http://databank.worldbank.org/data/download/GDP.pdf>. Last accessed:
28th December 2017.

The World Bank (2017b): http://databank.worldbank.org/data/download/GDP_PPP.pdf. Last
accessed: 28th December 2017.

The World Factbook (2017a) (last accessed 28th December 2017):
<https://www.cia.gov/library/publications/the-world-factbook/geos/gm.html>.

The World Factbook (2017b) (last accessed 28th December 2017):
<https://www.cia.gov/library/publications/the-world-factbook/rankorder/2078rank.html>

Transparency International (2017) (last accessed 28th December 2017):
https://www.transparency.org/news/feature/corruption_perceptions_index_2016.

United States Geological Survey (USGS): <https://www.usgs.gov/>
USGS (2017a): <https://earthquake.usgs.gov/data/vs30/>. Last accessed: 28th December 2017.
USGS (2017b) – 3rd September 1978 Albstadt earthquake (last accessed 28th December 2017):
<https://earthquake.usgs.gov/earthquakes/eventpage/usp0000wbj#executive>.
USGS (2017c) – 17th May 2014 Darmstadt earthquake (last accessed 28th December 2017):
<https://earthquake.usgs.gov/earthquakes/eventpage/usb000qsmq#executive>.

World Economic Outlook Database (WEO, 2017):
<https://www.imf.org/external/pubs/ft/weo/2017/02/weodata/index.aspx>.
Last accessed: 28th December 2017.

World of Maps (2018): <https://www.weltkarte.com/typo3temp/images/deutschland-topographie.jpg>.
Last accessed: 5th February 2018.

A4.4. November 1983 M4.8 Liège Earthquake, Belgium

This earthquake occurred on 8th November 1983, at 00.49 UTC (01.49 local time), to the west of the city of Liège, eastern Belgium, a region that had undergone extensive mining exploitation for several hundreds of years until shortly before the occurrence of this seismic event. The earthquake was the strongest to occur in the area since the beginning of the 20th century and led to significant damage. This is attributed, firstly, to the vulnerability of the building stock, possibly already weakened by the ground settlement triggered by the local mining activity, and, secondly, to a combination of tectonic and site effects such as the shallowness of the epicentre, the potential amplification of the ground motion due to the presence of soft soils, and the collapse of underground coal mines.

A4.4.1 Tectonic and seismic setting

A4.4.1.1 Tectonic setting

Belgium is situated within the stable Eurasian plate in Central Europe, the geological evolution of which is closely related to the spreading history of the Atlantic Ocean and the drift of the African plate relative to the Eurasian plate. Three major tectonic cycles are generally recognized: the Caledonian, the Variscan (or Hercynian) and the Alpine cycle (*e.g.*, Plant *et al.*, 2003).

The distribution of faults in Central Europe proves the existence of large-scale stable tectonic stress in the upper crust for long periods of time. According to the World Stress Map project (WSM, Heidbach *et al.*, 2016; Figure A4.4.1), the mean direction of the maximum horizontal compressive stress in the area between the Alps and the North Sea is around N145° (*e.g.*, Ahorner, 1985). Large scale plate tectonics is the controlling factor for both the principal orientation of stress and the seismotectonic activity of Central Europe. This produces the motion of post-Hercynian, deep rooted, conjugate strike-slip fault zones, which are arranged SSW-NNE and WNW-ESE, parallel to the direction of the maximum shear stress of the present-day stress field (Ahorner, 1985), thus leading to pull-apart NNW-SSE normal faulting in areas situated between conjugate strike-slip fault planes.

This is the case for Liège, situated in a joint position between two active seismotectonic zones of the Lower Rhine Graben and the Brabant Massif (Camelbeeck & De Becker, 1985). The area activated in 1983 is located at the transition between the two mutually orthogonal geological systems, delineated by the NE-SW Meuse (Maas) River stream east of Liège, crosscutting with NNW-SSE extensional structures at an angle of ~45°, as shown in Figure A4.4.2. Given the scarcity of available stress data, the authors of this report believe that no safe conclusion can be drawn on the local stress type and orientation at the epicentral area of the 1983 earthquake included in the red rectangle of Figure A4.4.1.

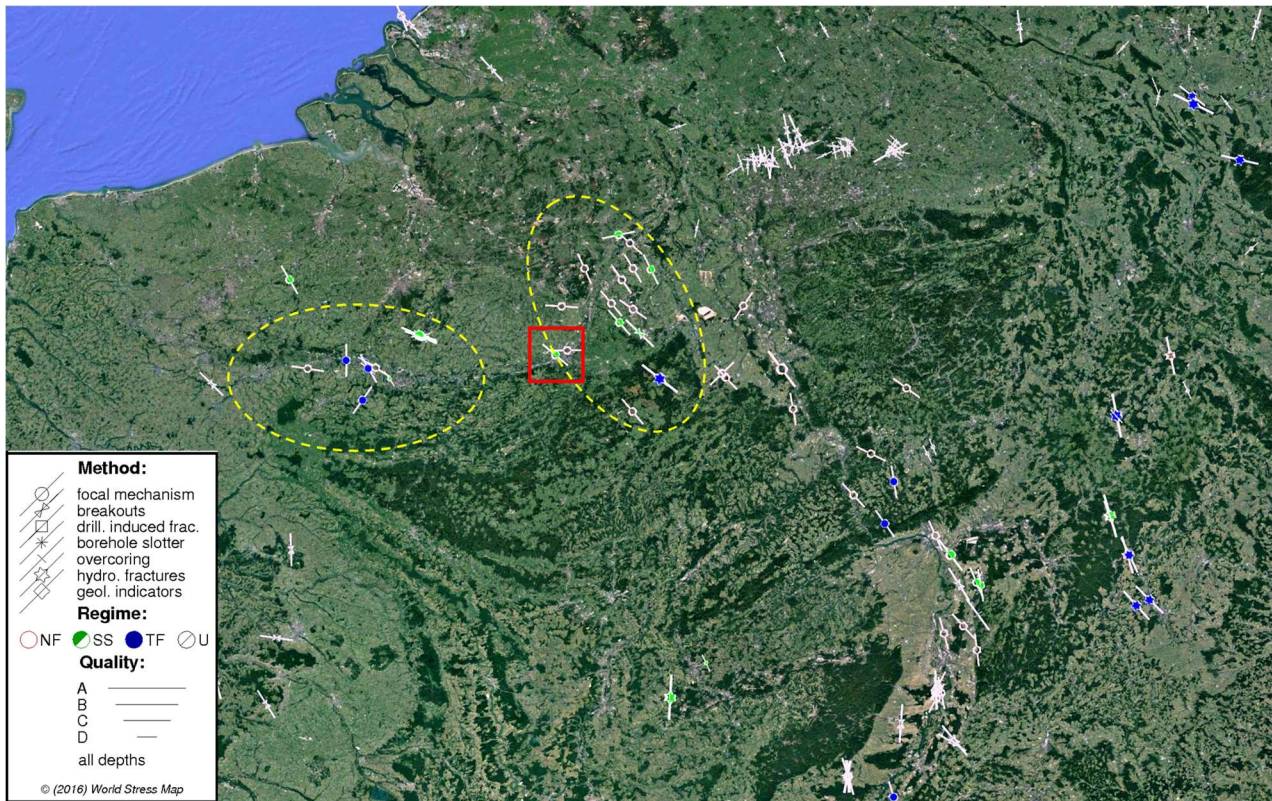


Figure A4.4.1. Stress state in the broader region. The red box encloses the 1983 epicentral area. White bars and colour solid circles represent the preferred direction and style of faulting, respectively. Dashed yellow ellipses enclose two distinct fault clusters in the region. From WSM (Heidbach *et al.*, 2016).

The area hit by the 1983 earthquake is a coal zone. It is located in an almond-shape multi-fractured basin, with fractures divided into three categories (Liégeois, 1985): (a) shallow-dipping dislocations arranged conformably to the coal seams, related to thrust faulting, (b) high-angle, south-dipping dislocations, presenting an important lateral component of motion, and (c) N-S oriented dislocations, cutting and displacing the dislocations of the first category. The Seraing, Marie and St-Gilles faults belong to the second category of structures, striking in a general ESE-WNW direction ($\sim N70^\circ E$), dipping to the NNW, and presenting a strong dextral strike-slip motion component (Liégeois, 1985) (Figure A4.4.3, left). According to Camelbeeck & De Becker (1985), the St-Gilles fault is considered as the causative fault of the 1983 Liège earthquake, whereas Camelbeeck (2013), based on relocated hypocenters of the 1983 sequence (Figure A4.4.3, right), suggests that the earthquake occurred on the Marie fault instead.

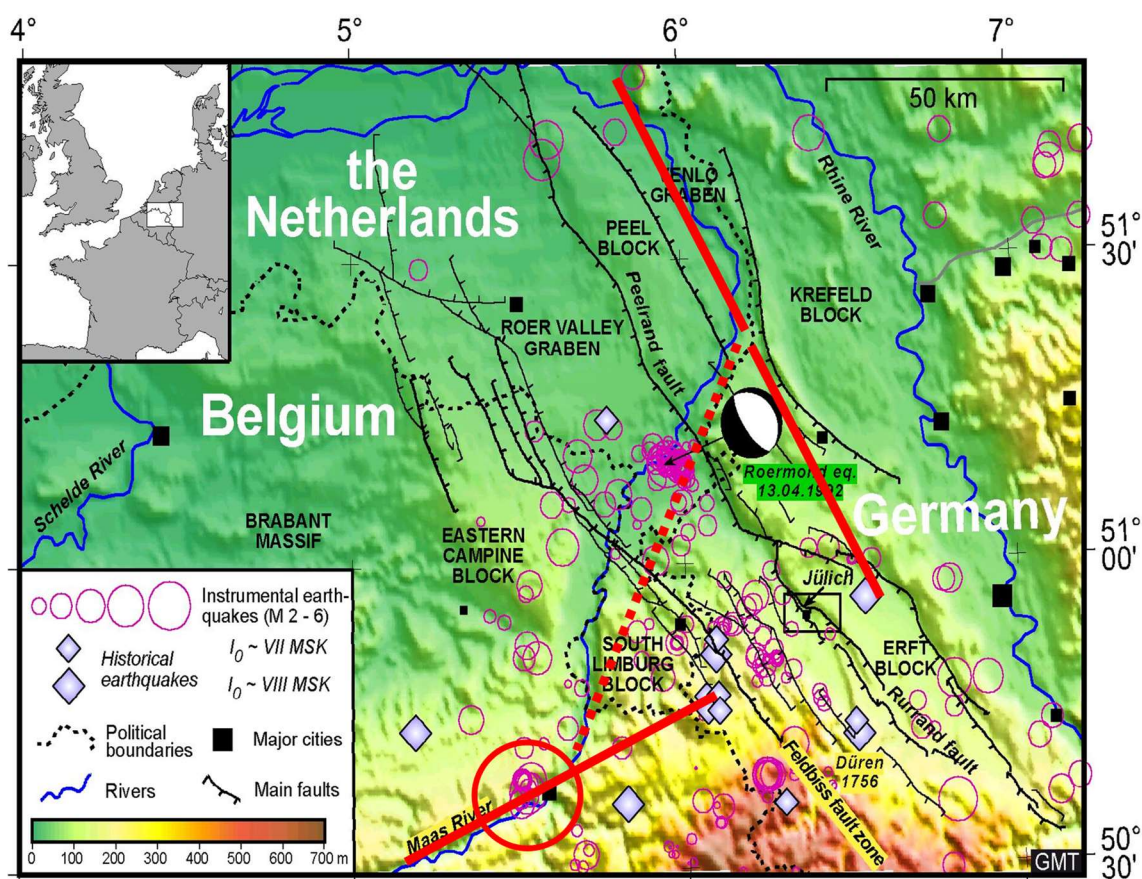


Figure A4.4.2. Seismotectonic map of the Lower Rhine graben system in the border area of Belgium, Germany and the Netherlands. Continuous red lines indicate the direction of main tectonic structures. Dashed red line indicates a possible tectonic lineament inferred by the stream of the Meuse (Maas) River. Modified from Royal Observatory of Belgium (2017).

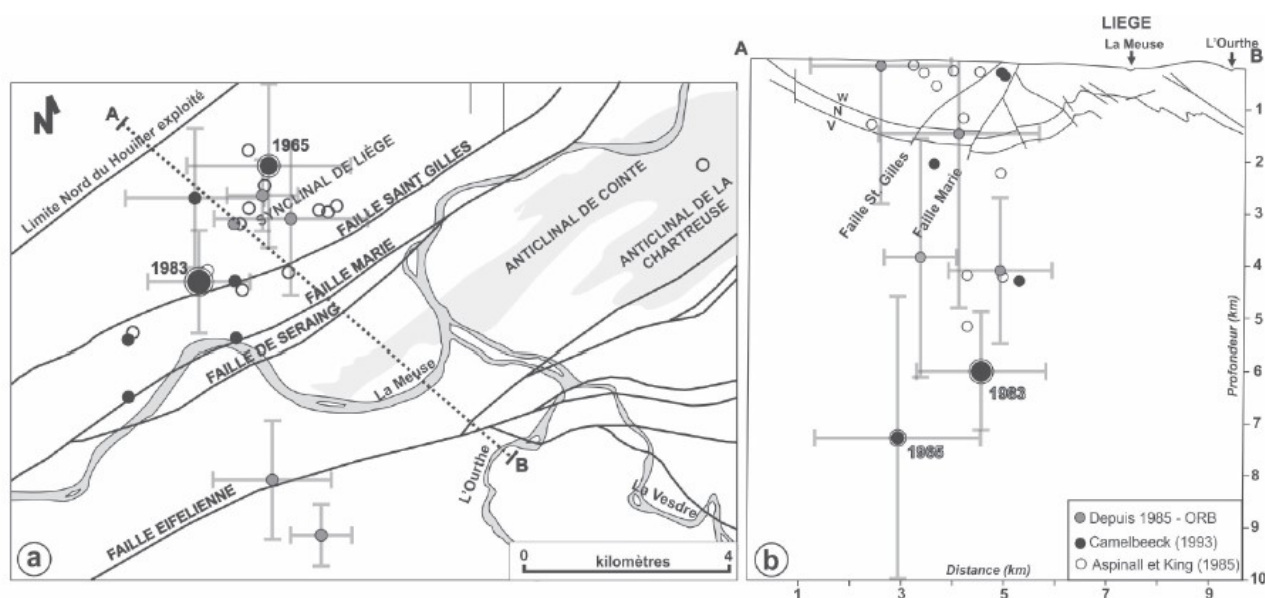


Figure A4.4.3. Seismic activity in the region of Liège. Localisation of the epicentres of earthquake that occurred between 1965 and 2013 throughout Liège basin (left); distribution of the epicentres along the section A-B, indicating their depth (right). From Camelbeek *et al.* (2013).

A4.4.1.2 Regional and local seismicity

Seismic activity in the European plate decreases from south to north. Figure A4.4.4 (left) presents the seismic activity in the broader region around Liège with $M_L \geq 3.0$, extracted from the United States Geological Survey (USGS) earthquake catalogue for the period 1900-2017. Leaving aside the uncertainties in the catalogue, especially in the period prior to the establishment of the digital era in the 1980s, one can conclude that seismicity is located within the crust and no sub-crustal activity is evidenced. There are areas with diffuse seismicity, but some spatial clusters can also be observed, with seemingly aseismic regions identified in northern Belgium, northern France, the Netherlands and Germany.

Historical research has revealed that the region under study has never been seismically inactive. Since the 14th century, at least three earthquakes with magnitude larger than 6.0 have occurred in the region between the Rhine valley and the North Sea (Plumier *et al.*, 2006). In particular, the macroseismic epicentres of two relevant historical earthquakes that occurred on 18th September 1692 (**M**5.8) and 3rd December 1828 (**M**5.0) lie near the epicentral area of the 1983 event. The former produced intensities of the order of VIII.

When focusing on the local seismic activity (Figure A4.4.4, right), it can be observed that the majority of foci are aligned in a general NNW-SSE direction, compatible with the orientation of extensional Neogene structures occupying north Belgium and cross-cutting the Paleozoic formations of the Variscan orogeny in the south (Figure A4.4.2), the activation of which cannot be excluded (De Becker *et al.* 1985).

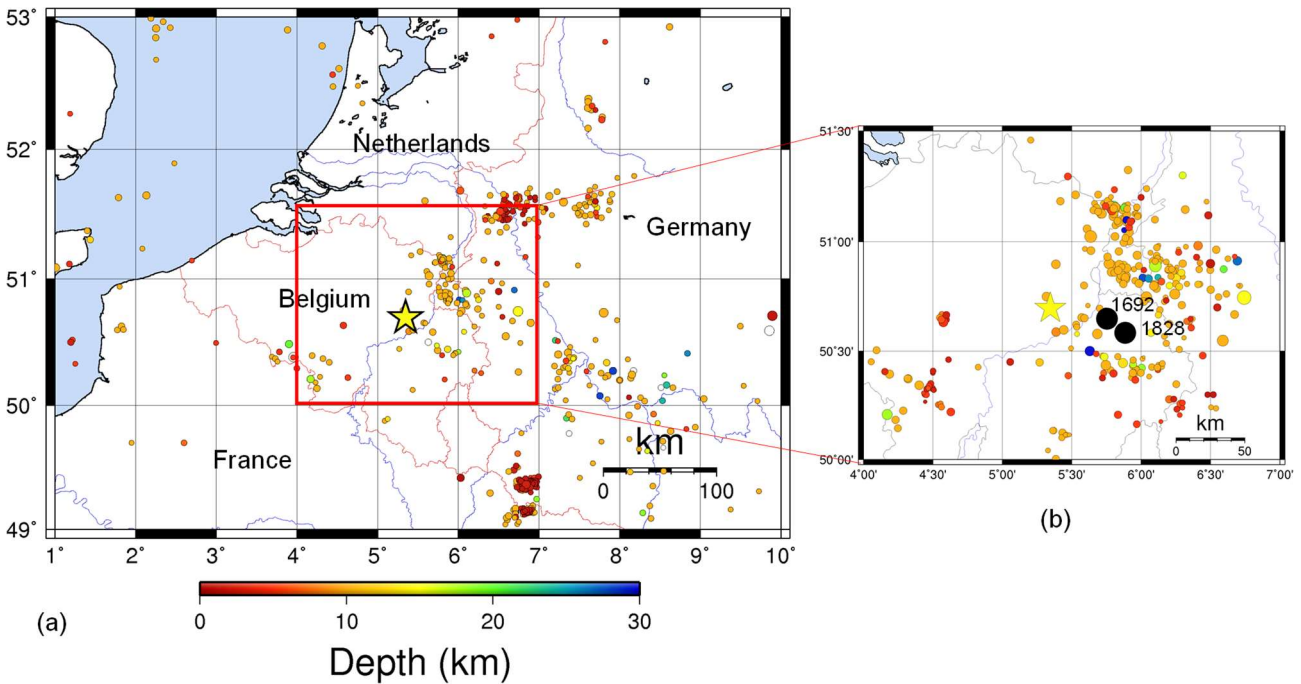


Figure A4.4.4. Seismic activity of the broader region with $M_L \geq 3.0$ since 1900 (left); seismic activity with $M_L \geq 2.0$ in the region of Liège, corresponding to the red rectangle of panel (a) (right). Earthquake data extracted from USGS catalogue. Yellow star and black solid circles represent the epicentre of the 1983 earthquake and two historical earthquakes, respectively.

A4.4.1.3 Seismic hazard

Figure A4.4.5 shows the official seismic hazard map for Belgium, which is the result of a probabilistic seismic hazard assessment carried out by Leynaud *et al.* (2000). As can be observed, the seismic hazard is highest in Hainaut, to the south-west of the country, and in the province of Liège, on the eastern side. For the area affected by the 1983 Liège earthquake, peak ground accelerations on rock with a 10% probability of exceedance in 50 years range between 0.12 and 0.14 g. This seismic hazard map has been the basis for the division of Belgium into five different zones for the elaboration of the Belgian National Annex to Eurocode 8 (NBN, 2011), as shown in Figure A4.4.6. The reference PGA values on rock, indicated for each zone from 0 (lowest hazard) to 4 (highest hazard) in the map of Figure A4.4.6, determine the design spectrum to be used for structural design and assessment purposes. As can be observed, the province of Liège is located within the highest seismic zone 4.

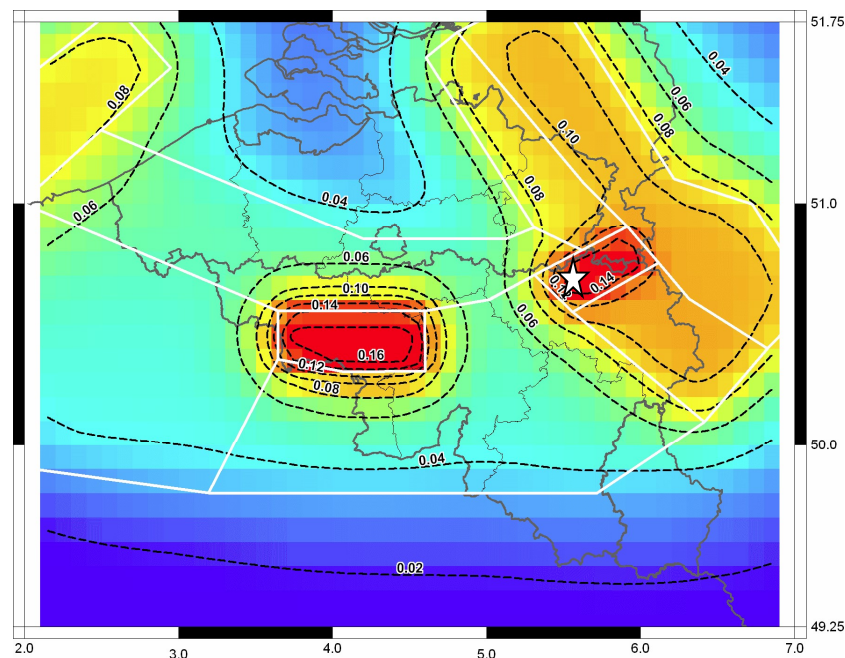


Figure A4.4.5. Peak Ground Acceleration (g) on rock for a return period of 475 years (10% probability of exceedance in 50 years), according to the Royal Observatory of Belgium (ROB, 2016). The white lines represent zones of seismic sources as defined by Leynaud *et al.* (2000).

According to the Global Seismic Hazard Assessment Program (GSHAP; Giardini *et al.*, 1999), Belgium and, particularly, the areas of Hainaut and Liège, exhibit the highest level of seismic hazard across northern Europe. PGA values on rock with a 10% probability of exceedance in 50 years for the closest coordinates to the 1983 earthquake's epicentre are around 0.092 g (Figure A4.4.7). These values range between 0.1 and 0.175 g according to the more recent SHARE project (Woessner *et al.*, 2015; Figure A4.4.8, left), a range that is relatively in good agreement with that of GSHAP and NBN (2011). The spectral acceleration for period $T=0.15$ s, mean representative eigenperiod for the majority of the local building stock (see A4.4.7.2), is also depicted in Figure A4.4.8 (right) with values of interest in the range 0.3-0.35 g.

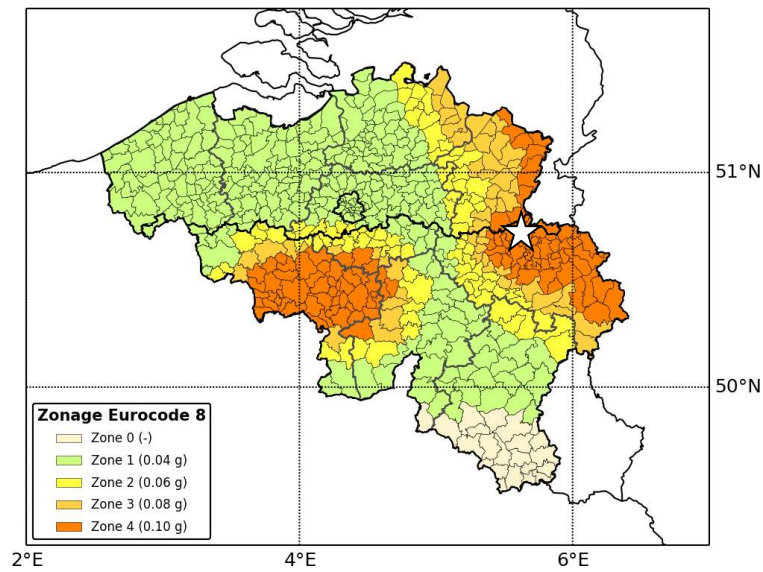


Figure A4.4.6. Seismic zones of Belgium according to the Belgian National Annex to Eurocode 8. From ROB (2016). The white star indicates the approximate location of the epicentre of the 1983 Liège earthquake.

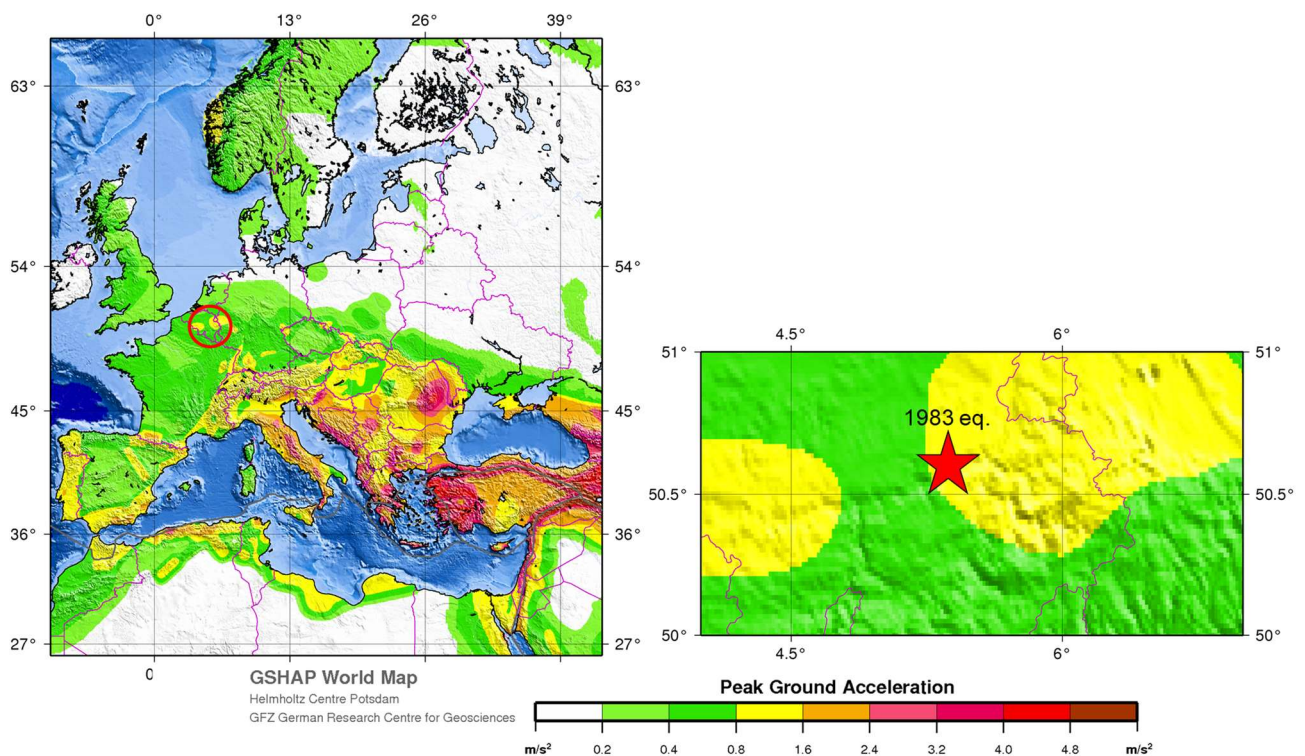


Figure A4.4.7. Peak ground acceleration (PGA, m/s^2) values on rock with a 10% probability of exceedance in 50 years according to results from GSHAP in Europe (left); enlarged area around the epicentre of the 1983 Liège earthquake indicated by the red circle on the left panel (right).

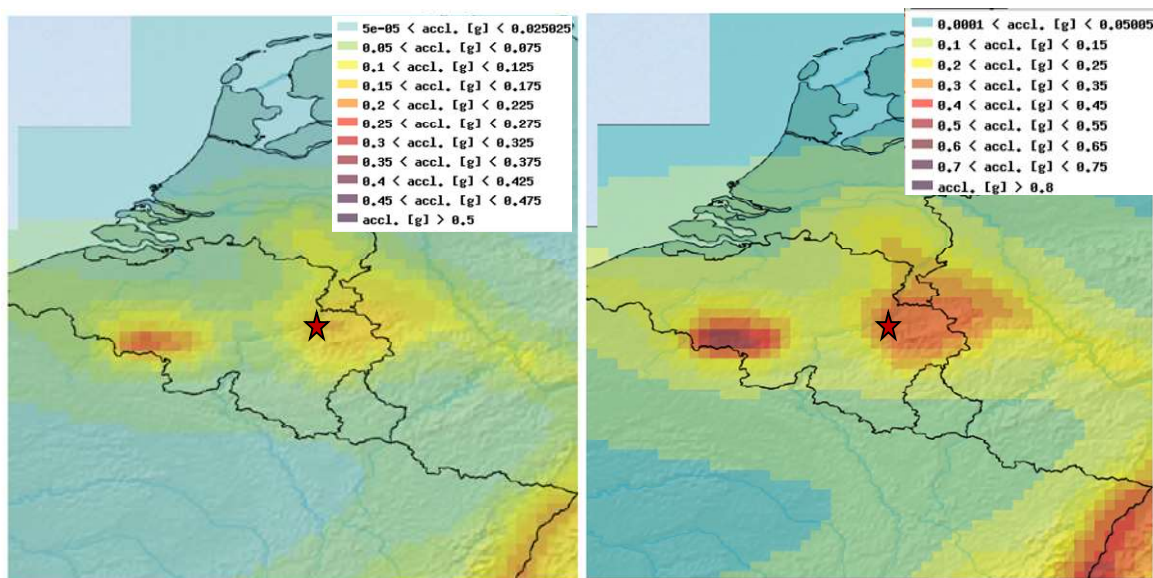


Figure A4.4.8. Mean hazard map for Belgium, according to SHARE: PGA on rock (left) and pseudo-spectral acceleration for $T=0.15$ s (right) with 10% probability of exceedance in 50 years.

Table A4.4.1 summarizes the values of PGA on rock with 10% probability of exceedance in 50 years from the different sources mentioned above, while Figure A4.4.9 presents a comparison between the corresponding 5%-damped mean uniform hazard spectrum from SHARE for the closest available coordinates to the city of Liège and the Eurocode 8 Type (II) design spectrum for an input PGA of 0.1 g. The overall match is adequate, except at the short period range, where SHARE predicts larger values than those of the design spectrum.

Table A4.4.1. Peak ground acceleration (PGA, g) values on rock with a 10% probability of exceedance in 50 years (475 years of return period) according to results from Leynaud *et al.* (2000), GSHAP, SHARE and NBN (2011) for Eurocode 8.

CITY	Leynaud <i>et al.</i> (2000)	NBN (EC8)	GSHAP	SHARE
Liège	0.120 -0.140 g	0.100 g (Zone 4)	0.092 g	0.166 g

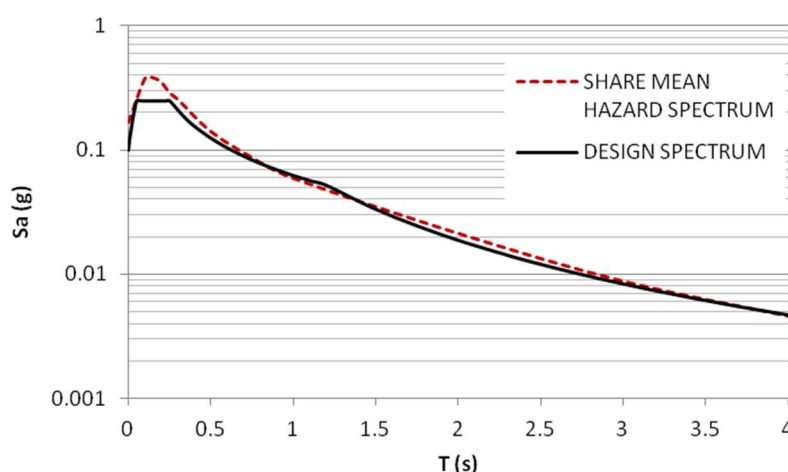


Figure A4.4.9. Uniform Hazard Spectra for the closest available coordinates to the city of Liège, according to SHARE mean hazard model, vs Type II Eurocode 8 Design spectrum on the rock for input $PGA=0.10$ g.

A4.4.2 Earthquake source characteristics

A4.4.2.1 Location, depth and time

The main shock occurred on 8th November 1983, at 00.49 UTC (01.49 local time).

Several organizations and agencies report their own estimations of the epicentral coordinates and hypocentral depth. The information reported in the websites of the Royal Observatory of Belgium (ROB), the National Earthquake Information Center (NEIC) of the United States Geological Service (USGS), and the International Seismological Centre (ISC) is summarised in Table A4.4.2 and Figure A4.4.10. The estimate of Ahorner & Pelzing (1985), whose epicentral coordinates have an uncertainty of around 2km, has also been included. Cells marked as (*f) correspond to parameters that were held fixed while inversion was carried out to retrieve those that remain.

Table A4.4.2. Epicentral coordinates and hypocentral depths from different sources.

Agency / Publication		Latitude	Longitude	Depth (km)
NEIC	National Earthquake Information Center, USGS	50.696 °N	5.346 °E	10.00 (*f)
ROB	Royal Observatory of Belgium	50.628 °N	5.515 °E	5.80
ISC	International Seismological Centre	50.728 °N	5.306 °E	5.20
Ahornor & Pelzing (1985)		50.630 °N	5.523 °E	6.00

(*f) fixed parameter used for inversion

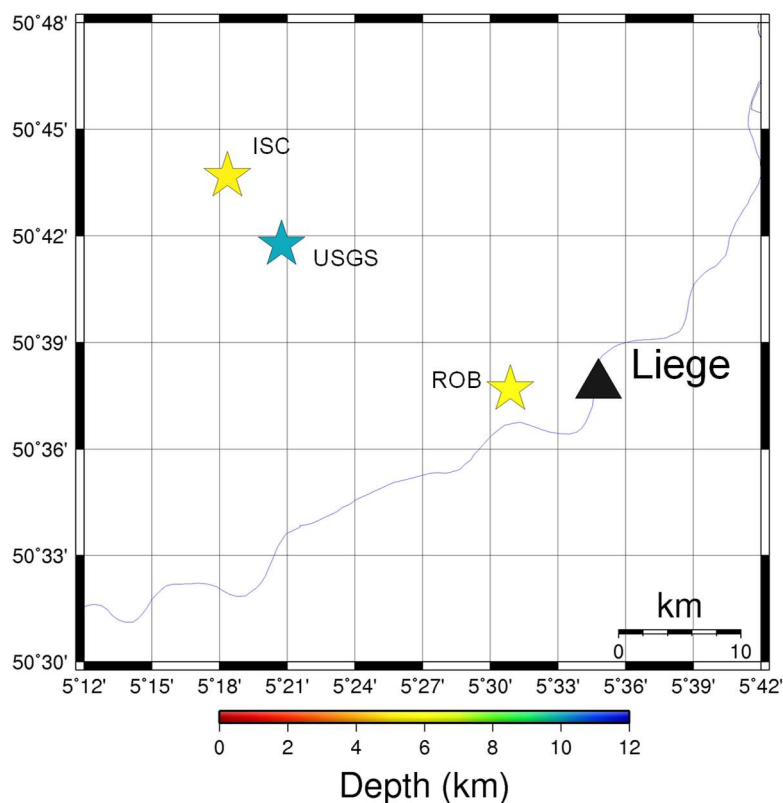


Figure A4.4.10. Estimation of epicentral coordinates of the 1983 earthquake by each agency listed in Table A4.4.2.

A4.4.2.2 Magnitude

Estimations of magnitude reported by various sources are presented in Table A4.4.3. As no information on moment magnitude appears to be available in the literature, the seismic moments (M_0) reported by Camelbeeck & De Becker (1985) and Ahorner & Pelzing (1985) were used to calculate it as (Hanks & Kanamori, 1979):

$$M_w = \frac{2}{3} \log_{10}(M_0 [\text{dyn}\cdot\text{cm}]) - 10.7$$

Ahorner & Pelzing (1985) report an expected value of $\log_{10}(M_0)$ of 23.21, with a standard deviation of 0.33, while Camelbeeck & DeBecker (1985) report a seismic moment M_0 of $1.5 \cdot 10^{23}$ dyn·cm, that is, an expected value of $\log_{10}(M_0)$ of 23.18. Considering the two estimates, the expected moment magnitude is **M4.8**, though values ranging between **M4.5** and **M5.0** would fall within one standard deviation of Ahorner & Pelzing (1985).

Table A4.4.3. Estimations of moment magnitude (**M**), body-wave magnitude (**mb**), surface-wave magnitude (**Ms**), and local magnitude (**M_L**).

Agency / Publication		M	mb	ML	Ms
NEIC	National Earthquake Information Center, USGS	-	5.0	4.9	4.3
ROB	Royal Observatory of Belgium	-	-	5.0	4.6
ISC	International Seismological Centre	-	4.6	-	-
EMSC	European Mediterranean Seismological Centre	-	-	5.1	-
Ahorner & Pelzing (1985)		-	-	5.1	-
Calculated from seismic moment M_0		4.8	-	-	-



A4.4.2.3 Style-of-faulting

Two different fault plane solutions have been proposed for the 1983 Liège earthquake from the analysis of P-wave first motion data, as presented in Table A4.4.4 (Faber & Bonjer, 1985; Ahorner & Pelzing, 1985). The first one, by Ahorner & Pelzing (1985), is a predominating strike-slip dislocation combined with a small thrust component, while the second one, by Faber & Bonjer (1985), indicates almost purely normal, dip-slip faulting. In both cases, the fault plane that strikes roughly east-west and dips 45 to 80 degrees in a northerly direction is consistent with the Marie-St. Gilles fault geometry (Ahorner & Pelzing, 1985; Jongmans & Campillo, 1990). By means of numerical modelling, Jongmans & Campillo (1989) observed that the ground motions generated by the strike-slip solution fit better the observed damage pattern, though no strong conclusion seems to be made in the literature.

In an attempt to define which one of the two nodal planes would correspond to the fault plane, Ahorner and Pelzing (1985) compared the corner frequencies observed for recordings of one of the aftershocks to theoretical values calculated for both fault planes of their strike-slip solution. They concluded that while the NNW-SSE trending fault plane

generates corner frequencies closer to those observed for the aftershock, the WSW-ENE fault plane relates better to the geological situation in the region.

Table A4.4.4. Focal mechanism solutions from two different sources. Nodal planes marked in grey are the preferred fault plane in each case. The beachballs on the right display the graphical representation of the available solutions.

Nodal Plane 1			Nodal Plane 2			Source	Beachball
Strike	Dip	Rake	Strike	Dip	Rake		
250	80	160	347	60	20	Ahorner & Pelzing (1985)	
280	45	-70	100	45	-110	Faber & Bonjer (1985)	

A4.4.2.4 Stress drop

Camelbeeck & De Becker (1985) calculated the stress drop of the Liège main shock by means of an empirical relation between the latter, local magnitude and source radius, and estimated it to be 4 MPa (40 bars). An unusually high stress drop of approximately 15.6 MPa (156 bars) was estimated by Ahorner & Pelzing (1985) from S wave spectra, suggesting the existence of high crustal stresses at shallow depth. This value is significantly higher than those previously calculated for other earthquakes in the Lower Rhine Embayment and in the Rhenish Massif (Ahorner, 1985; Ahorner & Pelzing, 1985). However, it is in agreement with the results of a hydraulic fracturing experiment carried out in a research borehole 50 km south-east of Liège, where a maximum shear stress of 3.8 MPa (38 bars) was observed at 400 m below the surface, with a tendency to increase with depth (Ahorner, 1985).

A4.4.2.5 Foreshocks and aftershocks

According to Philips (1985) the earthquake was not preceded by any foreshocks. However, Camelbeeck & De Becker (1985) report four small events of low magnitude preceding the main shock, recorded by one station between 20th October 1983 and the date of the main shock, but not enough information was available for their study.

The mainshock was followed by three aftershocks, the largest of which had a local magnitude M_L of 3.4-3.6, as shown in Table A4.4.5 (Camelbeeck & De Becker, 1985). Only data regarding the second and the third aftershocks are given by Camelbeeck & De Becker (1985) and the USGS. However, it is worth noting that the poor coverage of the area by seismological stations does not allow for an accurate identification of all the foreshocks and aftershocks that may have potentially occurred. A short field study using an array of 8 temporary stations in and around Liège was conducted, through which 14 local events were recorded between 12th and 15th November 1983, seven of which were conjectured to be aftershocks of the 8th November 1983 earthquake while the other seven

were probably induced by mining, as discussed by Aspinall & King (1985). Figure A4.4.11 presents the location of the aftershocks listed in Table A4.4.5, as well as the events recorded by the local array deployed for the field study.

Table A4.4.5. Source parameters of the aftershocks of the 1983 event.

Date	Time	USGS				ROB (in Camelbeeck & De Becker, 1985)			
		Lat.	Lon.	Depth (km)	M _L	Lat.	Lon.	Depth (km)	M _L
1983-11-08	00:55	-	-	-	2.7	-	-	-	2.7
1983-11-08	01:24:54.52	50.622	5.532	10.0	2.9	50.65	5.55	0 – 4.0	2.9
1983-11-08	02:13:21.46	50.587	5.387	8.4	3.6	50.65	5.48	4.0 ± 2.0	3.4

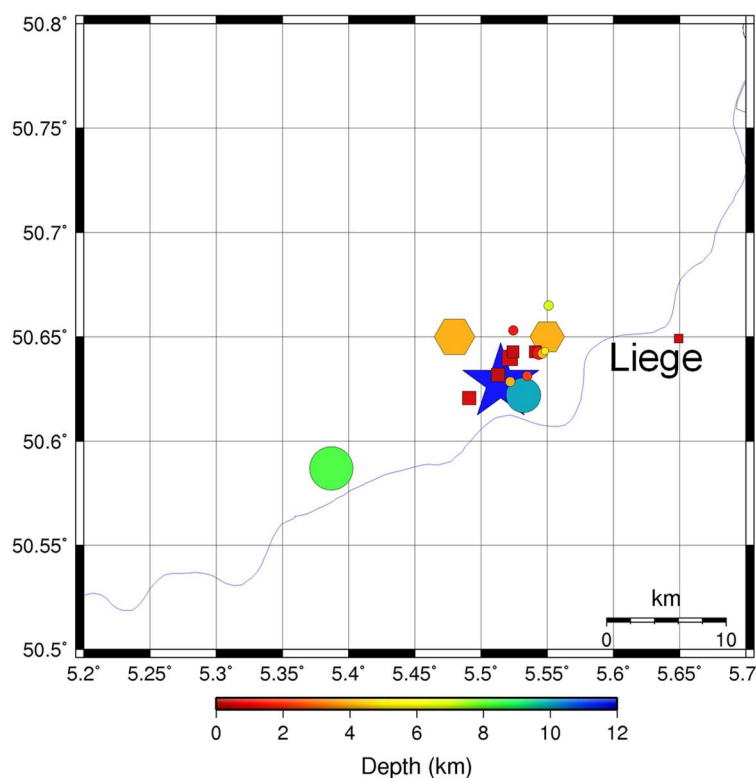


Figure A4.4.11. Map of the activated area presenting the location of the epicentres of the aftershocks. The blue star denotes the ROB location of the main shock. Large solid circles and hexagons represent USGS and ROB locations of the two largest aftershocks, respectively (see Table A4.4.5). Small solid circles and squares represent aftershocks and mining events, respectively, recorded by a local field study (Aspinall & King, 1985).

A4.4.2.6 Nature of earthquake

According to Camelbeeck & de Becker (1985), the earthquake of 8th November 1983 was not an unexpected event, since it was related to the active seismotectonic zones of the Lower Rhine Graben and the Brabant Massif, which are highly capable of generating tectonic earthquakes (Ahorner, 1985).

While it appears that the tectonic setting in the area is capable of naturally producing earthquakes like the one of 8th November 1983, an explanation by Camelbeeck *et al.*

(2013) for the mechanisms that generate earthquakes may pose an alternative view. Camelbeeck *et al.* (2013) suggest that earthquakes may be originated by the stresses generated in the lithosphere and the Earth's crust due to horizontal variations of the gravitational potential energy, associated with the topography and the density of the lithosphere. From this perspective, a possible causative factor for some intra-plate earthquakes may be a local decrease of the coefficient of static friction at the eventual focal point, which may occur due to variations of the fluid circulation in the earth's crust caused by natural or man-made reasons. From this point of view, the role of the interruption of the coal exploitation at the Liège basin around the time of the earthquake may be responsible as a possible trigger of this kind of mechanism. The area struck by this earthquake is a coal zone that had been abundantly exploited for over some hundreds of years. Several hundreds of millions of tons of coal had been excavated from the Liège underground, resulting in a local weight reduction of the earth's crust and strain release by the mining works. Moreover, coal mining affected the underground water tables due to the need for drainage in the deep galleries. The dewatering procedure resulted in the shutdown of certain springs and the drying of certain grounds. With the closing of the coal mines, reactivation of certain water springs occurred, which may have affected the rock stresses by reducing the internal friction (Liégeois, 1985). Although it is certain that variations of the water content and consequently of the stresses at the upper layers of the Earth's crust took place at that time, no direct research has been conducted to confirm a clear association between this variation and the 1983 Liège earthquake.

A4.4.3 Geology and ground conditions in the affected area

A4.4.3.1 Regional geology and topography

As summarised by Pirson *et al.* (2008), the geological setting of Belgium chronologically extends from Lower Palaeozoic to Quaternary. Excepting the Quaternary cover, rocks outcropping in Belgium can be divided into two large geographic areas, roughly coinciding with the northern and southern regions of the country (Fourmarier, 1954; Boulvain & Pingot, 2002). In southern Belgium, where Liège is located, consolidated Palaeozoic rocks subjected to strong deformation at the end of Carboniferous dominate over large areas, and sparse Cenozoic deposits are also found. Almost all these rocks are of sedimentary origin (Bultynck & Dejonghe, 2001), while exhibits of magmatic rocks are rare (André, 1983).

Liège is built on the alluvial plain of the river Meuse, at its junction with the river Ourthe (Figure A4.4.12), with its suburbs extending on the nearby hills. As shown in Figure A4.4.13, it lies on Devonian and Carboniferous formations belonging to a tectonic unit called Namur synclinorium (Olive *et al.*, 2015), which presents a discontinuity on the Cambro-Silurian basement (Brabant massif) to the north and is limited by the Eifel thrust fault to the south (Figure A4.4.12). According to Jongmans & Campillo (1990) and (Liégeois, 1985), the Namur synclinorium comprises the following Paleozoic rocks:

- Westphalian shales and sandstones of about 1300 m thickness containing worked coal layers that outcrop in the town.
- Namurian shales and sandstones of around 300 m in thickness.
- Visean limestone 150 to 200 m thick.
- Some thin layers of Frasnian, Givetian and Famennian ages.

These formations are folded in a NE-SW direction (Figure A4.4.12). In the north, the layers form the northern limb of an 8-km wide syncline that underlies the town. The southern limb is composed of frequently over-folded small synclines and anticlines. In the south, the Chartreuse anticline and another syncline follow, which are cut by the Eifel fault.

The whole Carboniferous basin is affected by NE-SW trending faults, which dip at angles between 45° and 90°, and present significant right-lateral horizontal displacements ranging to up to one kilometre (Figure A4.4.12). The Paleozoic rocks are overlain by flat-layered Mesozoic and Cenozoic sediments. Quaternary formations are composed of alluvial and slope deposits. These layers are mainly exposed north of Liège (Figure A4.4.13).

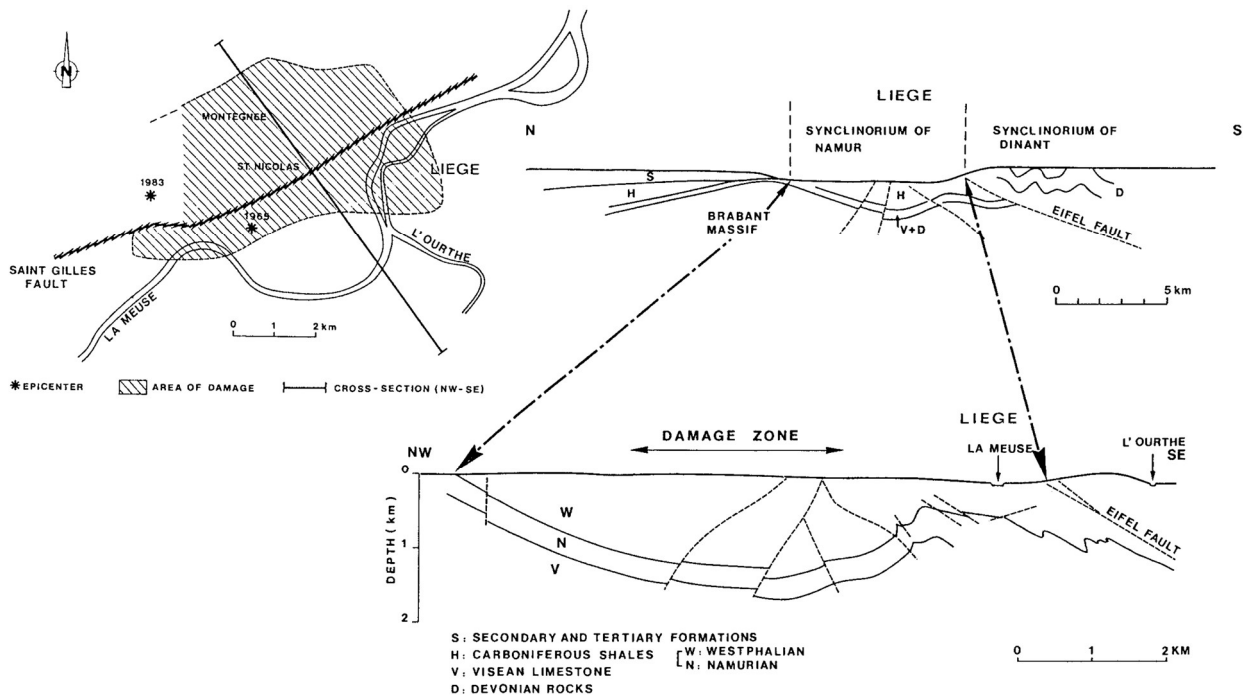


Figure A4.4.12. Structural sketch-map of the Liège basin (left) and geological cross section of the Liège area (right). From Jongmans & Campillo (1990).

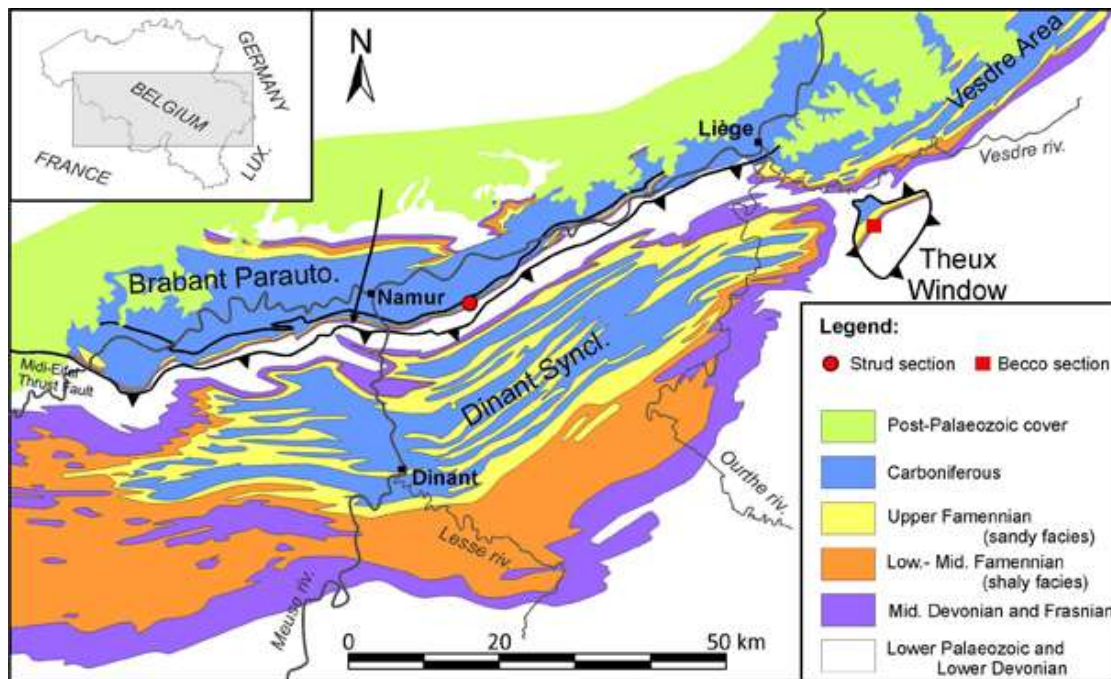


Figure A4.4.13. Geological map of Southern Belgium. From Olive *et al.* (2015).

A4.4.3.2 Site conditions in the affected area

Liège is mostly built over alluvial deposits of the valley of the Meuse River and on soil accumulating around and over the hills (De Becker & Camelbeeck, 1985). Due to mining, a good knowledge of the geological configuration and of the mechanical properties of soils and rocks exists for the affected area. The cross-section of Figure A4.4.14 (bottom) illustrates in detail the geotechnical profile of the area of Figure A4.4.14 (top). According to Jongmans & Campillo (1990), the different formations are divided into three main groups, for which velocities of P-waves (V_p), S-waves (V_s) and density values (ρ) are available, and the average V_s in the top 30 m of the soil column (V_{s30}) was approximately estimated from the available information in each case:

1. **Carboniferous bedrock:** It is composed of shales and sandstones including coal layers. Long term mining has caused local surface subsidence and fracturing of the rocks surrounding the mine galleries. Velocity of P- (V_p), S-waves (V_s) and density values (ρ) in the Carboniferous massif are the following:
 - In the upper layer (10 m thick), $V_p = 800$ m/s, $V_s = 400$ m/s and $\rho = 1.8$ gr/cm³.
 - Between 10 m and 15 m, $V_p = 2500$ m/s, $V_s = 1250$ m/s and $\rho = 2.5$ gr/cm³.
 - Deeper than 100 m, $V_p = 3500$ m/s, $V_s = 1750$ m/s and $\rho = 2.65$ gr/cm³.
 Average velocity for the upper 15 m of this formation is estimated to be ~520 m/s.
2. **Secondary and Tertiary sediments:** They consist of a lay of greenish marly clay underlying a thick layer of chalk. Typical velocity of P- (V_p), S-waves (V_s) and density values (ρ) for the secondary and Tertiary sediments are the following:

- In the marly clay (up to 10 m thick), $V_p = 600-1000$ m/s, $V_s = 300-400$ m/s, $\rho = 1.8-2.0$ gr/cm³.
- In the chalk, having a maximum thickness of 30 m, $V_p = 1000-2500$ m/s, $V_s = 500-750$ m/s, $\rho=1.9$ gr/cm³. At the top of the layer, caverns generated due to chalk solution by meteoric waters are likely to cause damage to superstructures.

Assuming a 10-metre thickness for the top layer, V_{s30} in this formation is estimated to range between 410 and 580 m/s.

3. **Recent deposits:** They consist of (a) alluvial deposits of the Meuse (Maas) river, whose width varies between a few hundred metres and one km, (b) slope deposits found at the western hillside, (c) mining fillings, whose location is generally not well known, and (d) other fillings, each with the following characteristics:

- a) Alluvial plain: It consists mainly of a 5- to 10-metre thick layer of gravel underlying silty sand. Total thickness is between 12 and 15 m. $V_p = 300-2000$ m/s, $V_s = 100-400$ m/s. The water table level is generally found at the top of the layer.
- b) Slope deposits: They consist of silts, clay sands, sandy gravels and pebbles, with an extension of a few hundred metres and a maximum thickness of 30 to 40 m. $V_p = 400-500$ m/s, $V_s = 200$ m/s, $\rho = 1.6-2.0$. These deposits are likely to amplify ground motions significantly.
- c) Mining rock filling deposits: At one location, $V_p = 300-500$ m/s and $V_s = 200$ m/s have been obtained.
- d) Fillings of construction materials remnants and earth can be observed mainly along the alluvial plain.

V_{s30} in this formation is estimated to vary between 150 and 240 m/s.

The potential for liquefaction of the foundation soil is expected to have increased after the rearrangement of the water table in the area, after the interruption of the mining works discussed in A4.4.2.6 (Liégeois, 1985).

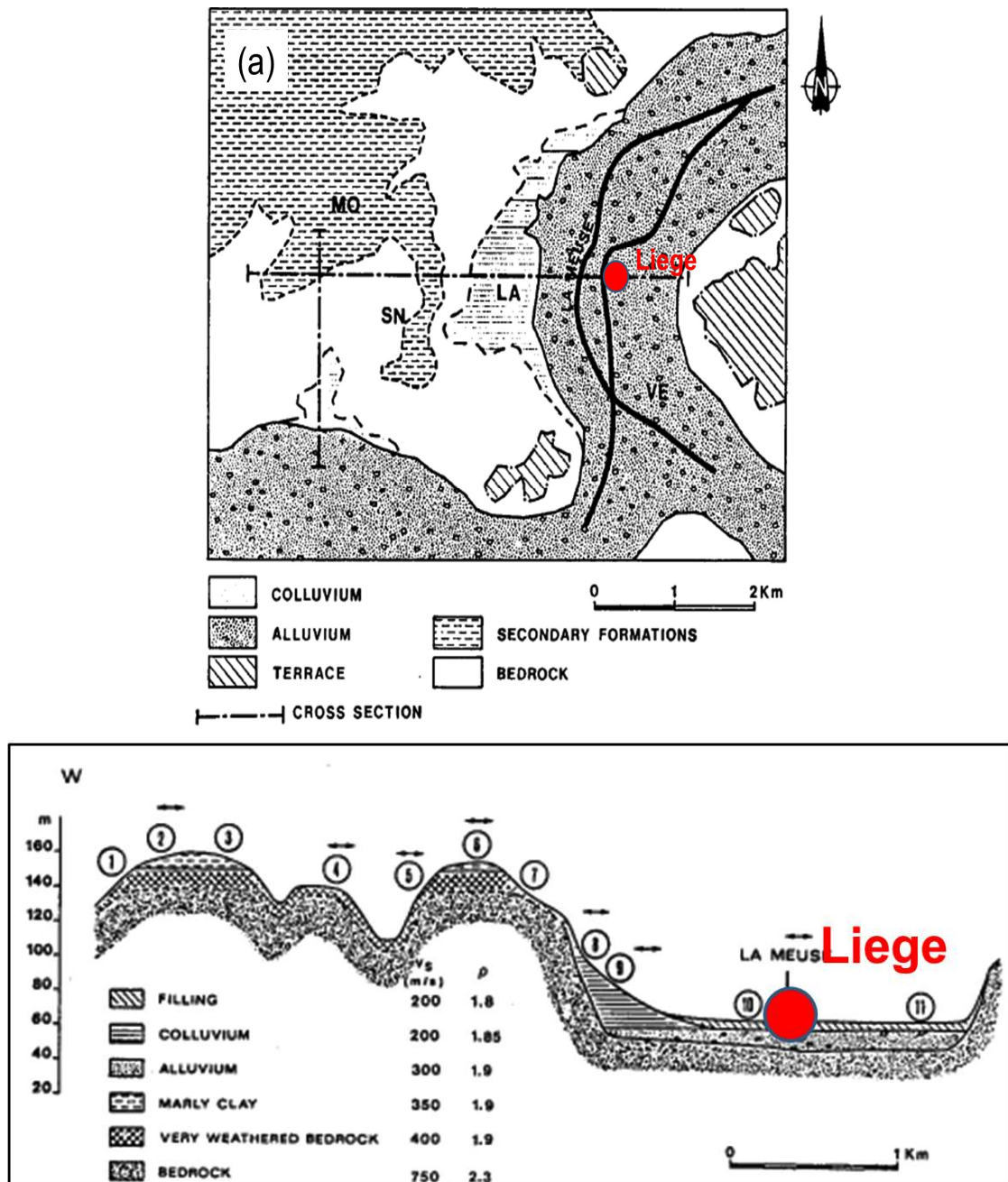


Figure A4.4.14. Geotechnical map of the meizoseismal area (top); Cross-section along the E-W line shown on panel (bottom). From Jongmans & Campillo (1990).

A4.4.4 Ground motions

A4.4.4.1 Intensity observations

There are two alternative macroseismic intensity maps available in the literature for this earthquake. The first was elaborated by ROB at the time of the earthquake, after the interpretation of questionnaires sent to different Belgian municipalities for this purpose. Originally, the macroseismic intensity map was reported in the MSK-64 intensity scale. García Moreno & Camelbeeck (2013) re-elaborated it in terms of the European Macroseismic Scale (EMS-98, Grünthal, 1998), as shown in Figure A4.4.15, which suggests that the localities closer to the epicentre attained a maximum intensity of VII (“damaging”). Camelbeeck *et al.* (2013) extended the map for it to cover not only Belgium but also the neighbouring countries, as shown in Figure A4.4.16. It is remarkable how the earthquake was felt up to a 2000-km radius: to the north until Amsterdam, to the east up to Frankfurt, to the south close to Metz, and it seems to have reached the western Belgian borders as well. The intensity of the map ranges from II (“scarcely felt”) to VII (“damaging”), identified in the epicentral area around Liège.

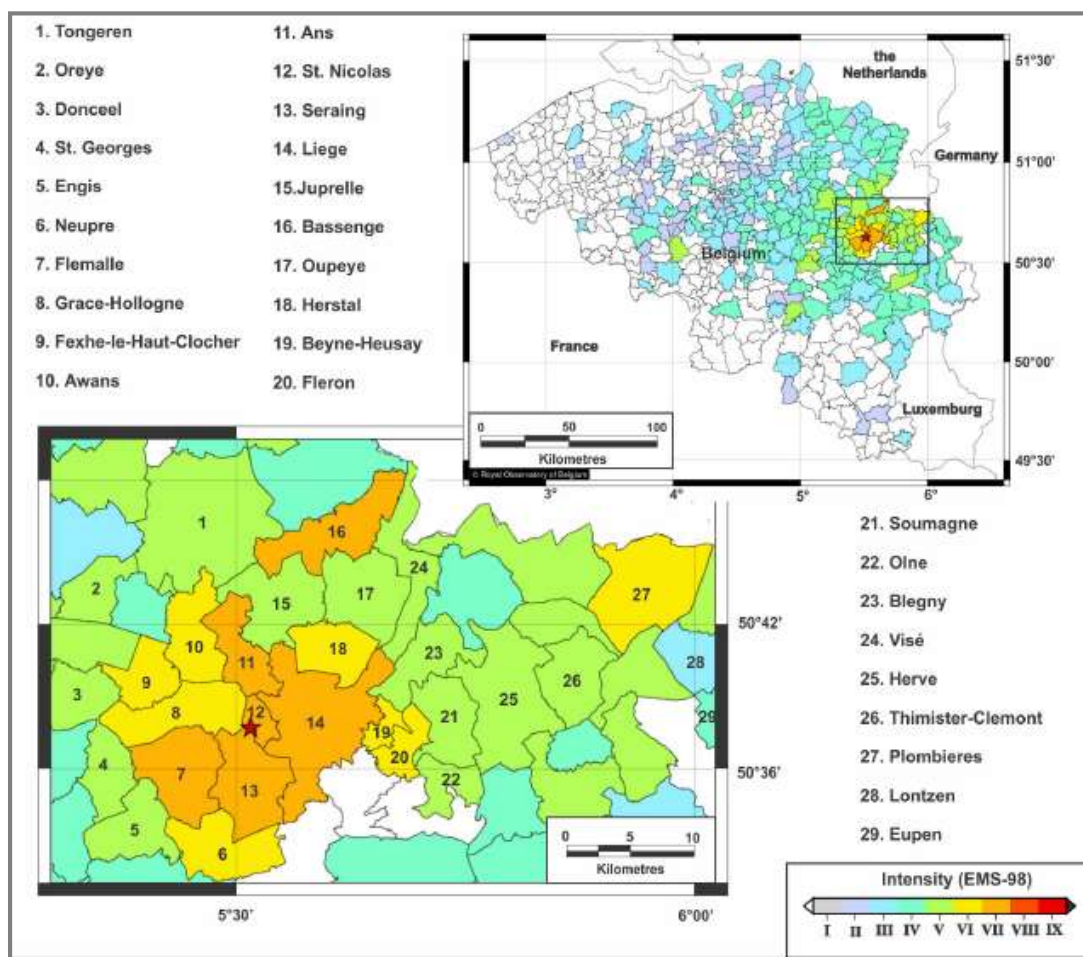


Figure A4.4.15. Macroseismic map of the 1983 Liège earthquake in terms of the EMS-98 scale, from García Moreno & Camelbeeck (2013). The black rectangle indicates the region with the most affected localities. Red star denotes the earthquake’s epicentre.

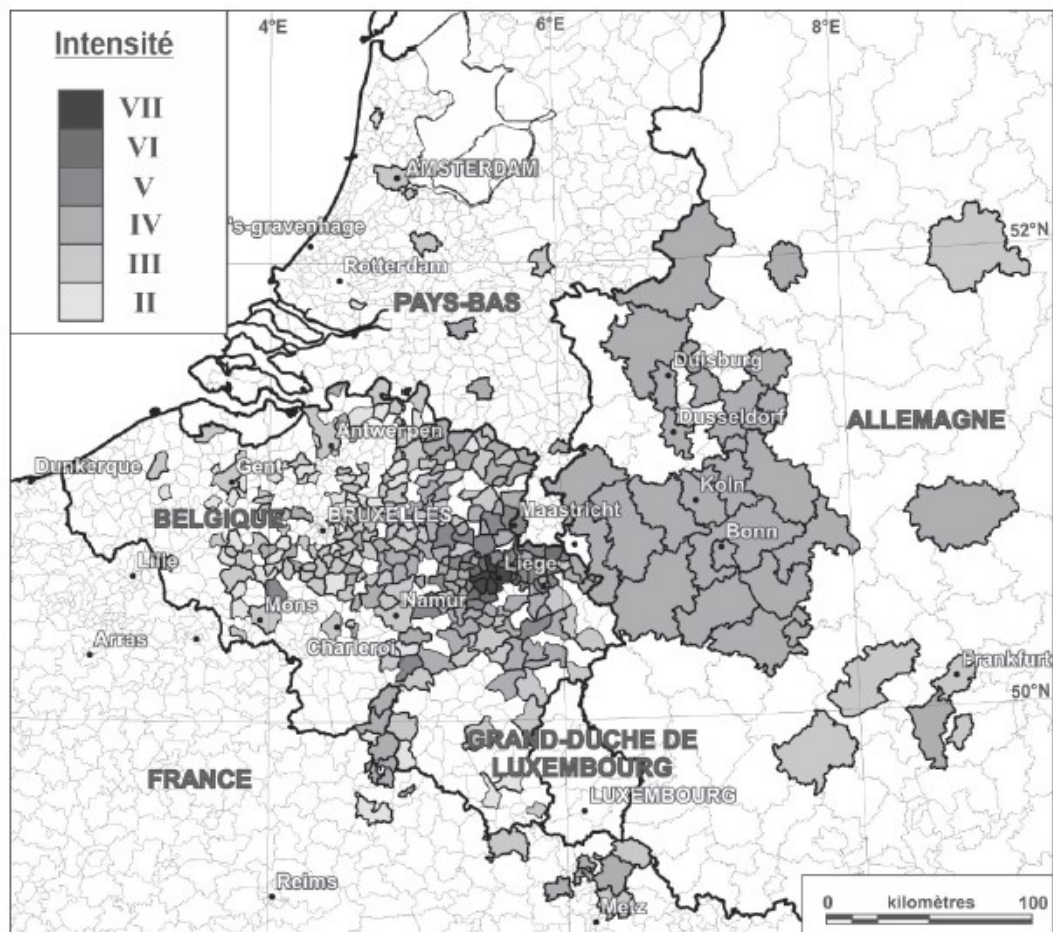


Figure A4.4.16. Macroseismic map of the 1983 Liège earthquake in terms of the EMS-98 intensity scale. From Camelbeeck *et al.* (2013).

The second macroseismic intensity map, shown in Figure A4.4.17, was elaborated by François *et al.* (1987) in terms of the Modified Mercalli Intensity (MMI) scale, on the basis of 1663 answers to earthquake perception questionnaires (“macroseismic inquiries”) that were irregularly collected throughout the affected area. Highest intensity VIII (“severe”) is reached at very concentrated locations. It is remarkable that intensities above VI are mostly located to the western part of the studied area. It is worth noting the irregular configuration of the VI isoseismal contour, the progressive reduction of intensity towards the north and the rapid decrease towards the south, as well as the drop of intensity at the city centre. The authors sustain that the latter is by no means explained by the absence of responses, but is related to the absence of mining activities in the city centre (“zone non concédée”, *i.e.*, area non-conceded for exploitation, in Figure A4.4.17). More specifically, they observe that the maxima of the intensities seem to coincide with the spatial field of coal mining activity, which makes them assume that mining works might have deconsolidated or destabilised the exploited zone. They refer, as well, to alternative explanations of the high intensities related to the deterioration of structures due to the continuous soil movement from the coal mining works. For this reason, macroseismic maps for different building typologies, discretized per construction date, were developed. However, this information is not publicly available.

The maximum intensities observed in the aforementioned maps are in agreement with the epicentral intensities of VI to VII in the MSK scale and VII to slightly above VII in the MMI scale reported by the EEFIT survey team, based on their visual inspection of the damage (EEFIT, 1984).

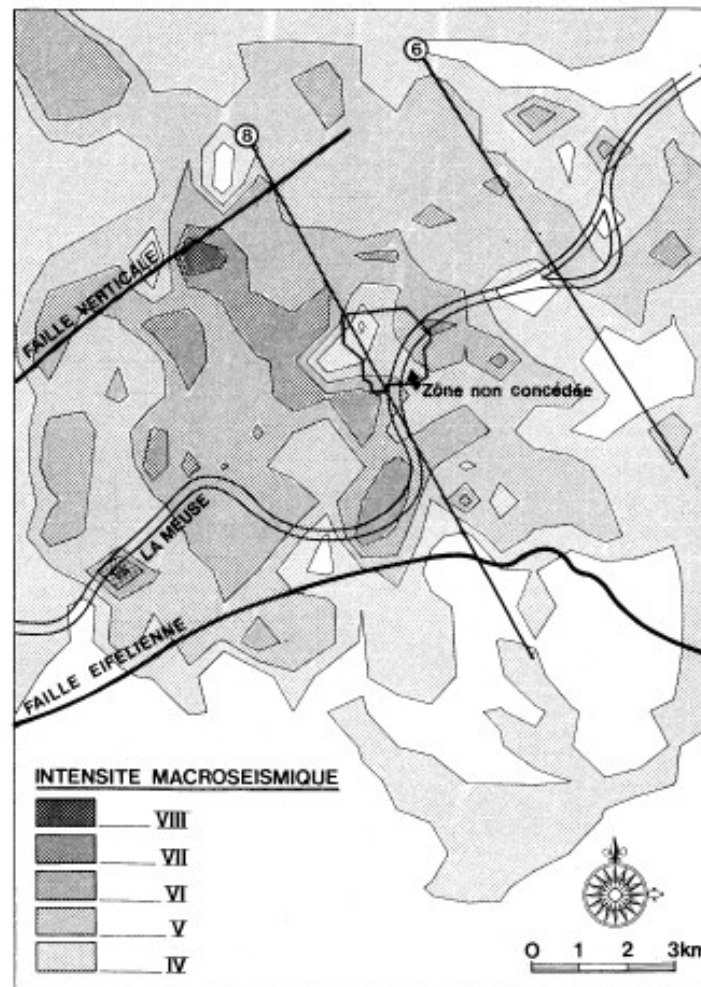


Figure A4.4.17. Macroseismic map in terms of Modified Mercalli Intensity scale based on macroseismic inquiries questionnaires. From François *et al.* (1987).

De Becker & Camelbeeck (1985) estimated the maximum MSK intensity I_0 to have been 7.44, based on the macroseismic relationship of Kövesligethy (Sponheuer, 1960), assuming a hypocentral depth ranging from 2 to 5 km, the macroseismic radii of isoseismals available from the macroseismic map of the ROB, and a constant attenuation factor k of 0.033 km^{-1} . This estimation is in good agreement with instrumentally measured values and the maximum MSK intensity estimate of VII. The attenuation curve of De Becker & Camelbeeck (1985) for the main shock indicates a drop to MSK VI at around 10 km and MSK V at 20 km from the epicentre.

Figure A4.4.18 displays the ShakeMap (Worden *et al.*, 2017) for the 1983 Liège earthquake in terms of MMI instrumental intensity, elaborated by the USGS using 545 macroseismic intensity data points from Hinzen & Oemisch (2001) and the Intensity Prediction Equation (IPE) of Atkinson & Wald (2007). The maximum instrumental MMI computed is 5.72, smaller than the macroseismic MSK and EMS-98 intensities of VII

based on observed damage (De Becker & Camelbeeck, 1985; García Moreno & Camelbeeck, 2013), or the maximum intensity $I_0=7.44$ calculated by De Becker & Camelbeeck (1985).

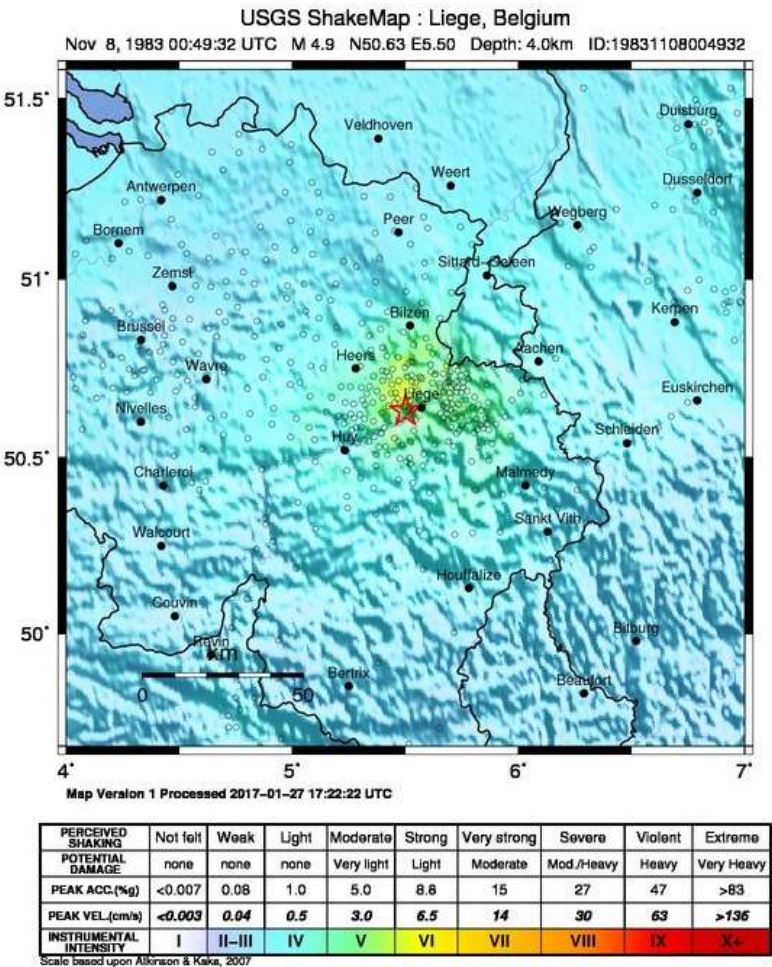


Figure A4.4.18. USGS ShakeMap (2017) in terms of Modified Mercalli Intensity (MMI). The red star is the epicentre of the main shock.

A4.4.4.2 Ground motion recordings

There are no near-field records of the ground motions generated by this earthquake (García Moreno & Camelbeeck, 2013). The nearest available recording of the mainshock is at an epicentral distance of 35 km (Jongmans & Campillo, 1990). A very limited amount of information on ground motions generated by the mainshock and the largest aftershock (M_L 3.6, Table A4.4.5) at 21 seismic stations in Germany in the distance range up to 144 km is available through the work of Ahorner & Pelzing (1985), though none of these waveforms are available to the authors of the present report.

In their observations, Ahorner & Pelzing (1985) highlight a long signal duration at station JUE (74 km away from the epicentre) due to the underground conditions (1000 m thick soft soil) and a good signal-to-noise-ratio at BNS, which is situated on hard rock, 124 km away from the epicentre.

A4.4.4.3 Inferred shaking levels

As no strong motion recordings are available for this earthquake, estimations of the ground motion shaking levels from the earthquake characteristics and/or the distribution of damage acquire particular relevance. With the aim of estimating the peak ground accelerations that the epicentral area might have experienced, Plumier (1985) investigated a series of tombs that were knocked down or moved during the earthquake in a cemetery located nearby the epicentre and concluded that acceleration values in the range 0.15-0.20 g probably occurred. Similar PGA values were estimated for the epicentral area by Camelbeeck (1985) from the dynamic parameters of the 1983 earthquake (0.13 g).

In the absence of instrumentally measured accelerations, García Moreno & Camelbeeck (2013) approximated the spatial distribution of spectral accelerations using both fragility curves and the vulnerability index method of Faccioli *et al.* (1999), in combination with information on damage observed after the earthquake from five different sources. In the first case, they used the fragility curves of HAZUS (FEMA, 2003) and Lang & Bachmann (2004) (Bsl) to calculate mean response spectral accelerations (MRSA) at $T=0.3$ seconds for Flémalle and Saint Nicolas, knowing the ratio of each vulnerability class presenting a given degree of damage, under the assumption that all damaged buildings were classified as low unreinforced masonry structures (URML). Where the number of buildings falling under the categories of moderate (MD) and extensive (ED) damage was larger than that of slight damage (SD), the MRSA was obtained as the average of the MSRA from the two former, while that calculated using the SD fragility curves was used otherwise. As the data for the locality of Liège was insufficient, the MRSA in this area was estimated using the correlation observed between the values of MRSA calculated for Flémalle and Saint Nicolas and their total damage indices (TDI) from an unpublished report of the University of Liège. Figure A4.4.19 shows the results obtained for each of the two sets of fragility functions used. Similarly, García Moreno & Camelbeeck (2013) applied the relationship between damage, PGA and vulnerability index, I_v , proposed by Faccioli *et al.* (1999) and obtained an estimation of mean PGA, which was subsequently converted into MRSA values using the equations recommended by Plumier *et al.* (2005) for natural periods around 0.3 s and soil type E.

García Moreno & Camelbeeck (2013) found that the results of all methods were generally in good agreement with each other, but dispersion was important. For the epicentral area (0-3 km), the HAZUS fragility curves suggest MRSA at $T=0.3$ s ranging from 0.02 to 0.35 g, while the Bsl curves and the vulnerability index method suggest a range between 0.004 and 0.39 g. However, most of the values lie within 0.10-0.30 g and 0.13-0.34 g, respectively. 84th-percentile spectral accelerations in the same area reach 0.45 to 0.60 g which, using the equations recommended by Plumier *et al.* (2005), translate into PGA values between 0.13 and 0.20 g, which are in agreement with the values estimated by Plumier (1985) and Camelbeeck (1985). These maxima seem to be concentrated to the north and east of the epicentre.

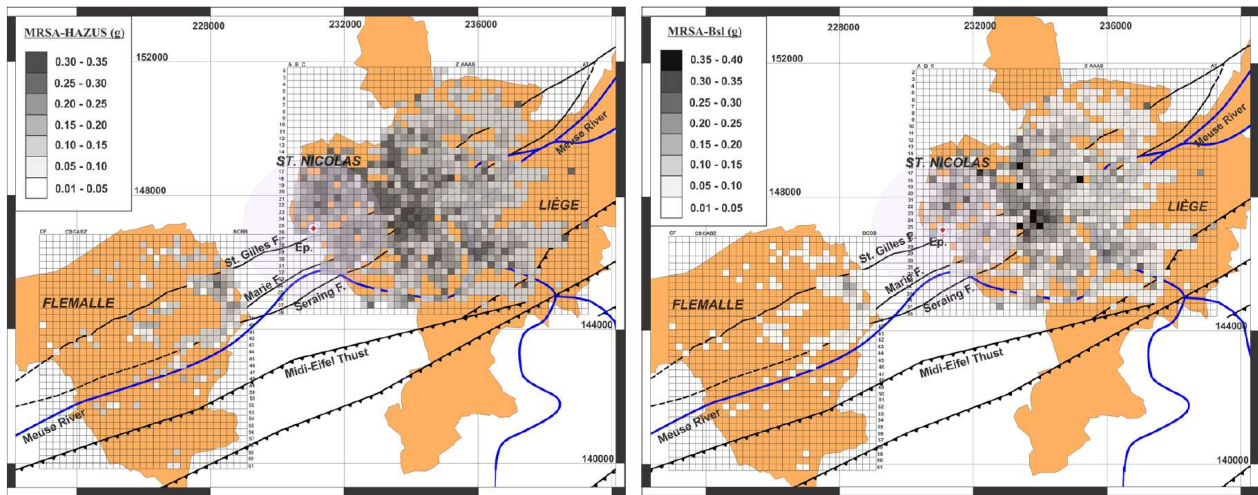


Figure A4.4.19. Spatial distribution of MRSA (T~0.3 s) applying Bsl (left) and HAZUS (right) fragility curves for URML buildings. From García Moreno & Camelbeeck (2013).

Figure A4.4.20 shows the ShakeMap (Worden *et al.*, 2017) for the 1983 Liège earthquake in terms of PGA and spectral acceleration at T=0.3 seconds, elaborated by the USGS using 545 macroseismic intensity data points from Hinzen & Oemisch (2001), the Ground Motion/Intensity Conversion Equation (GMICE) of Atkinson & Kaka (2007), the Ground Motion Prediction Equation of Atkinson & Boore (2006), and the Intensity Prediction Equation (IPE) of Atkinson & Wald (2007). The derived PGA equals 0.32 g (Figure A4.4.20, left) and the PGV (Peak Ground Velocity) equals 17.5 cm/sec. Maximum spectral accelerations at periods of 0.3 (Figure A4.4.20, right), 1.0 and 3.0 seconds are estimated to be 0.46 g, 0.14 g and 0.03 g, respectively. It is noted that the spectral acceleration value for a period of 0.3 s, which is the closest natural period to that expected for most of the local structural typologies, is higher than the ones estimated by García Moreno & Camelbeeck (2013) through the aforementioned methods, and those of the NBN (EC8) design spectrum as well as the SHARE mean spectrum (Figure A4.4.9) for a 10% probability of exceedance in 50 years.

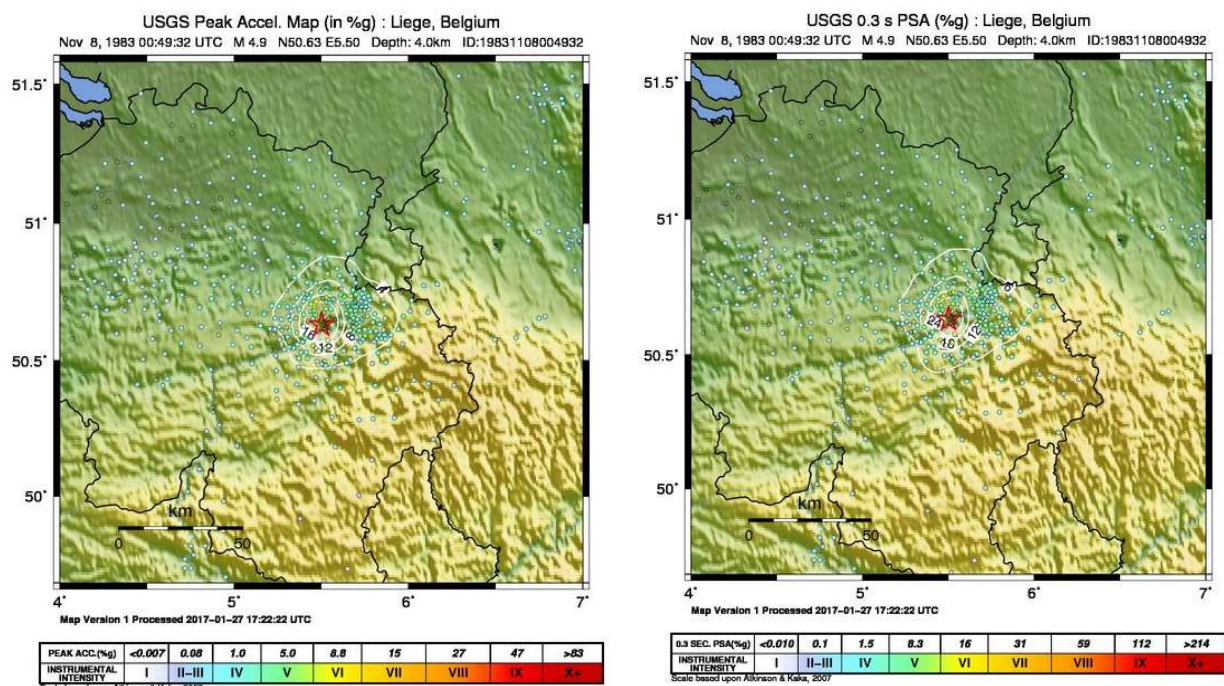


Figure A4.4.20. Peak Ground Acceleration map (left) and Spectral acceleration map for 0.3 s from USGS (2017). The red star is the epicentre of the main shock.

A4.4.4.4 Duration of ground shaking

Since near field strong motion recordings do not exist and the authors have not had access to existing far field recordings, the duration of ground shaking can only be inferred through observed macroseismic effects or by means of duration prediction models. Phillips (1985) reports an estimation of the duration at the epicentre of 2 to 5 seconds, while Liégeois (1985) provides an estimate of 4 seconds, pointing out a significant number of cycles of the ground excitations.

Estimations of earthquake significant durations were obtained using the empirical relations proposed by Bommer *et al.* (2009) and Afshari & Stewart (2016), in terms of 5-75% of Arias intensity (Figure A4.4.21). The upper edge of the seismogenic fault was set to 5.13 km, based on the hypocentral solution provided by Ahorner & Pelzing (1985), who estimated a depth of 6 km and a source radius of 0.87 km. Given that no details are available with respect to the locations at which the 2-5 seconds shaking was observed, a range of distances to the rupture for the two extreme values of V_{s30} present in the area (see section A4.4.3.2) are considered. For an epicentral distance of 0-15 km, which is believed to correspond to the epicentral area where the duration of the earthquake is reported to have been between 2 and 5 seconds (Phillips, 1985; Liégeois, 1985), the estimates obtained by means of the equation of Afshari & Stewart (2016) seem to match the lower bound of the values reported for all the range of site conditions considered, while only the estimations carried out with the softer soils lie in this range when using the model of Bommer *et al.* (2009).

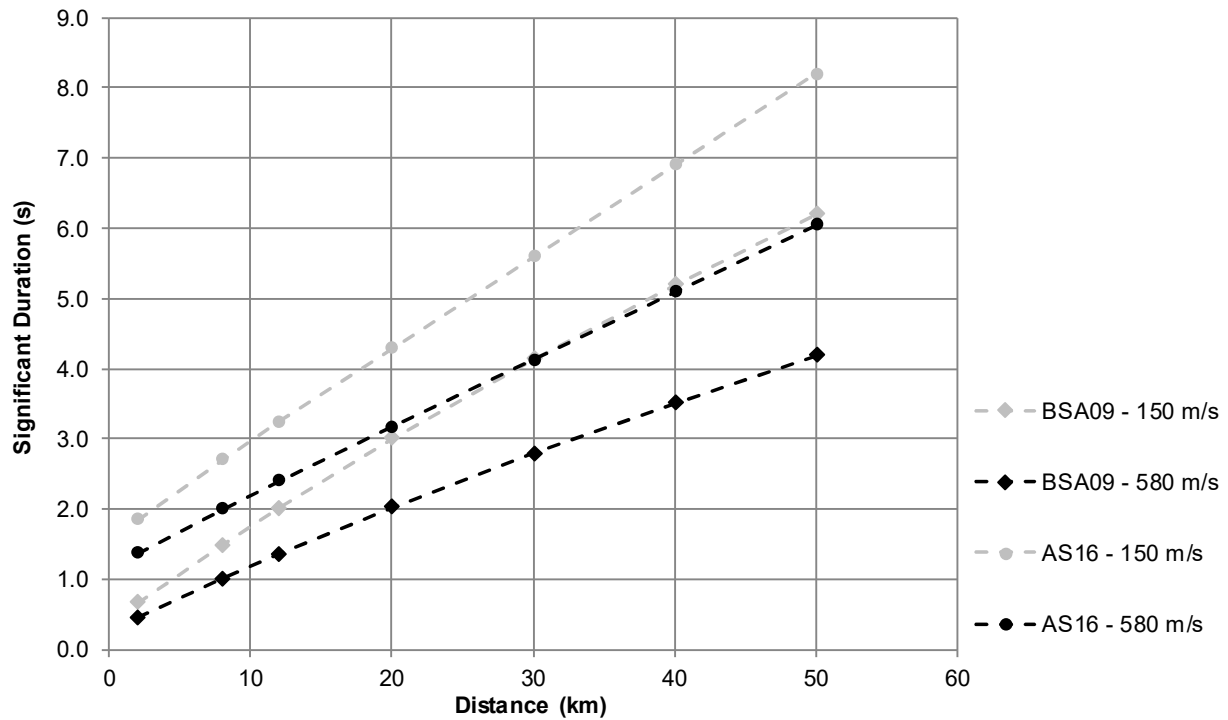


Figure A4.4.21. Estimation of the significant duration of the 1983 mainshock in Liège, using prediction equations by Bommer et al. (2009, BSA) and Afshari & Stewart (2016, AS).

A4.4.5 Collateral earthquake hazards

A4.4.5.1 Surface rupture

No surface rupture has been documented for this event. As Ahorner & Pelzing (1985) estimate a source radius of 0.87 km and an average dislocation of 0.27 m using S-wave displacement spectra, and the Royal Observatory of Belgium have calculated a hypocentral depth of 5.8 km, it is clear that the rupture due to an event of this size could not have reached the surface.

A4.4.5.2 Landslides

No land sliding has been documented for this event.

A4.4.5.3 Liquefaction

No liquefaction effects have been documented, even though the conditions due to increased inflow of water that occurred after the interruption of the mining works, together with the long duration of the strong motion, may have produced dynamics capable enough to affect the overburdened soils and the superstructures.

A4.4.5.4 Settlements

Indications of settlements reported for this earthquake appear to be associated to the existence of coal mines below part or all of the epicentral area. According to the investigators of EEFIT (EEFIT, 1984), settlement of buildings was still ongoing nine days after the earthquake. They also observed that some graves had settled unevenly in the cemetery. In their report, they seem to suggest a potential connection between these settlements and extensive chimney damage.

A4.4.6 Exposed population

A4.4.6.1 Socio-economic setting

According to the 2016 Human Development Data (UNDP-HDD, 2016), the Human Development Index (HDI) for Belgium was 0.755 in 1980 and 0.896 in 2015, while its Inequality-adjusted HDI (IHDI) was 0.821 in the 2016 Human Development Report (United Nations, 2016). According to the 2015 world's ranking reported in 2016, Belgium is located in the 22nd place, while the Netherlands ranks 7th. Table A4.4.6 compares the HDI and IHDI for both countries for data between 1980 and 2015. The column "Adj. HDI" provides the HDI values given online (UNDP-HDD, 2016) for the years mentioned above, adjusted for data consistency in time.

Table A4.4.6. Human Development Index and Inequality-adjusted Human Development Index for Belgium and the Netherlands. HDD: Human Development Data (UNDP-HDD, 2016). HDR: Human Development Report (United Nations, 2016).

Report	Data	Belgium				Netherlands			
		HDI	IHDI	Rank	Adj. HDI	HDI	IHDI	Rank	Adj. HDI
HDD 2016	1980	-	-	-	0.755	-	-	-	0.787
HDD 2016	1985	-	-	-	0.774	-	-	-	0.799
HDR 2016	2015	0.896	0.821	22	-	0.924	0.861	7	-

By the beginning of the 1980s a recession in the world economy started and lasted for about five years, as Figure A4.4.22 (left) illustrates. The recession initiated in the United States and quickly spread to other industrialized countries, mainly due to governmental policies on local economies and the increase in oil price that followed the 1979 Iranian Revolution (WDR, 1983; Oral History Center, 2011). Both Belgium and the Netherlands experienced a drop in their GDP with respect to the previous years, a fact that was reflected in the GDP per capita as well as the increased unemployment rate. It is also evident from Figure A4.4.22 (right) that after 1995 the economy of Netherlands has followed a rather faster growth rate with respect to that of Belgium, despite all the fluctuations after the new world recession period after 2010.

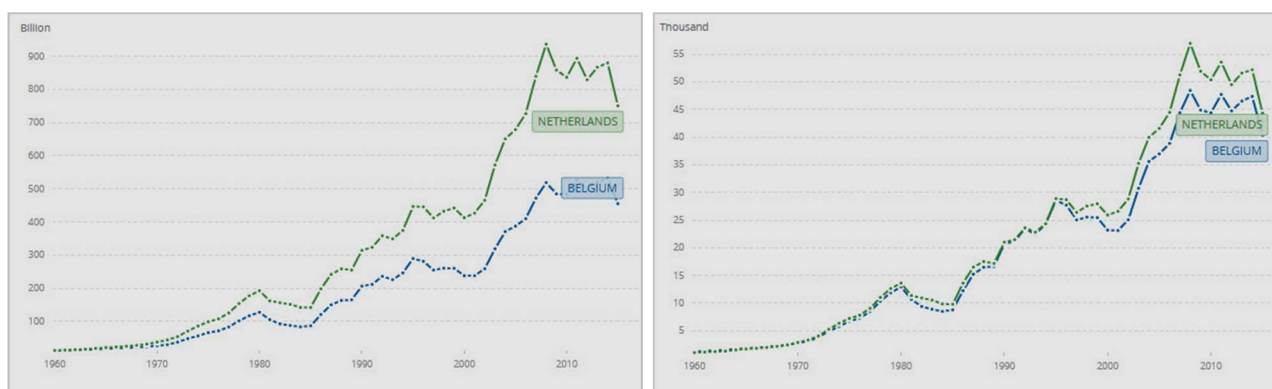


Figure A4.4.22. GDP (left) and GDP per capita (right) fluctuation for Belgium and Netherlands for the last 65 years according to World Bank national accounts data and the Organization for Economic Cooperation and Development (OECD) National Accounts data files (The World Bank, 2017).

Table A4.4.7 presents a comparison between Belgium and the Netherlands in terms of gross domestic product (GDP), GDP per capita and unemployment rate for 1980 and 1984, to represent the situation during the 1983 earthquake, and 2015, for the current picture. According to the Statistical Authority of Belgium (Statistics Belgium), the net income per person for the province of Liège was about 5% lower than the national average income per person in 2014 (latest available data). More particularly the city of Liège is part of the “sillon industriel”, that is, the former industrial backbone of Belgium, which was the first fully industrialized area of Europe. The industrial expansion of Liège in the 19th century, based on coal mines and steel industry, led to important urbanization (Jongmans & Campillo, 1990). It also provided much wealth, which is reflected in some of the city’s architecture. Currently, the iron and steel industry is no longer the core of Liège’s economy, which has been shifted mainly towards other kinds of manufacturing, commerce, real estate, construction and services.

Table A4.4.7. Gross domestic product (GDP), GDP per capita and unemployment rate for the Belgium and the Netherlands, according to International Monetary Fund (2017).

Indicator	Units	Belgium			Netherlands		
		1980	1984	2015	1980	1984	2015
Gross domestic product, current prices	Billions of US dollars	124.137	81.69	454.288	189.524	149.824	750.696
Gross domestic product per capita, current prices	US dollars	12,596.23	8,290.87	40,528.93	13,393.89	10,428.36	44,322.83
Unemployment rate	% of total labor force	8.300	10.825	8.500	3.354	8.254	6.891

A4.4.6.2 Population density and distribution

The province of Liège is composed by four arrondissements (administrative counties), of which the arrondissement of Liège is the most densely populated and consists of 24 municipalities, one of which is called Liège as well (Figure A4.4.23). The official estimate

of 1990 for the administrative arrondissement of Liège, which includes the affected localities, is a total of 590,000 inhabitants (City Population, 2009).

Details for the population of affected municipalities are given in Table A4.4.8. It may be observed that in the early 1980s Liège had around 215,000 inhabitants with approximately 3,000 inhabitants per km², being the most densely populated municipality of the county, together with Saint Nicolas. As a matter of fact, the maps of Figure A4.4.24 and Figure A4.4.25 confirm that Liège and its surrounding municipalities are some of the most densely populated localities of Belgium. The epicentre of the 1983 earthquake was located in the municipality of Saint Nicolas and primarily affected the city of Liège and the localities of Saint Nicolas, Seraing and Flémalle.

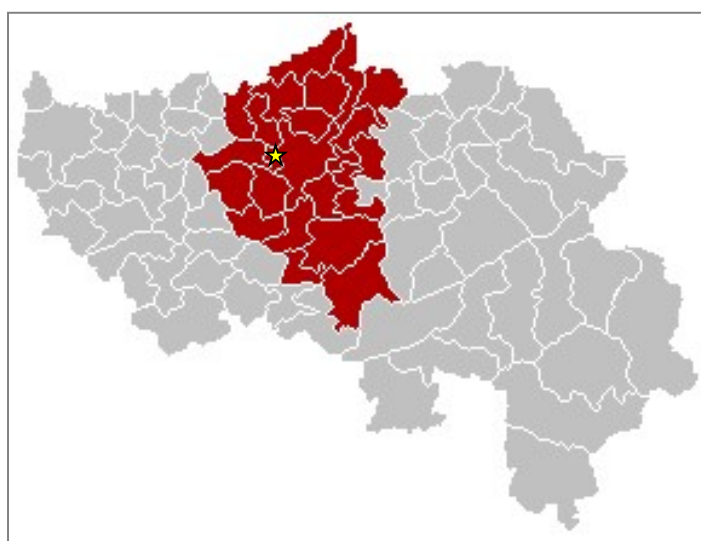


Figure A4.4.23. In red, location of the county of Liège with 24 distinct municipalities (source: Wikipedia). The yellow star denotes the epicentre of the 1983 earthquake located in the municipality of Saint Nicolas.

Table A4.4.8. Population and population density for most affected municipalities (intensities of VI, VII) as indicated in Figure A4.4.15 (source: Statplanet and Census 2011 – Statistics Belgium).

Municipality	Population (1981)	Population density (1981)	Population (2011)	Population density (2011)
Neupre	8,009	253	38,770	1,647
Flemalle	28,217	769	25,351	691
Grace-Hollogne	21,848	638	21,937	641
Fexhe-le-Haut-Clocher	2,540	132	3,183	165
Awans	7,242	253	8,859	326
Ans	26,016	1,114	27,652	1,184
Saint Nicolas	25,755	3,764	23,227	3,395
Seraing	64,543	1,827	63,363	1,793
Liège	214,119	3,086	195,965	2,824
Herstal	38,592	1,639	38,770	1,647
Beyne-Heusay	11,590	1,583	12,036	1,644
Fleron	15,602	1,137	16,250	1,184

According to the USGS EXPO-CAT database (Allen *et al.*, 2009; USGS-PAGER), over 800,000 people are estimated to have been exposed to an MMI intensity of V or more (intensity level that indicates that the earthquake is felt, and vulnerable structures may start to exhibit low damage). Over 90% of this population was at an urban environment. Disaggregating the above figures, a total of 505,000 is estimated to have been exposed to MMI V to VI and around 180,000 to VI and VI+0.5.

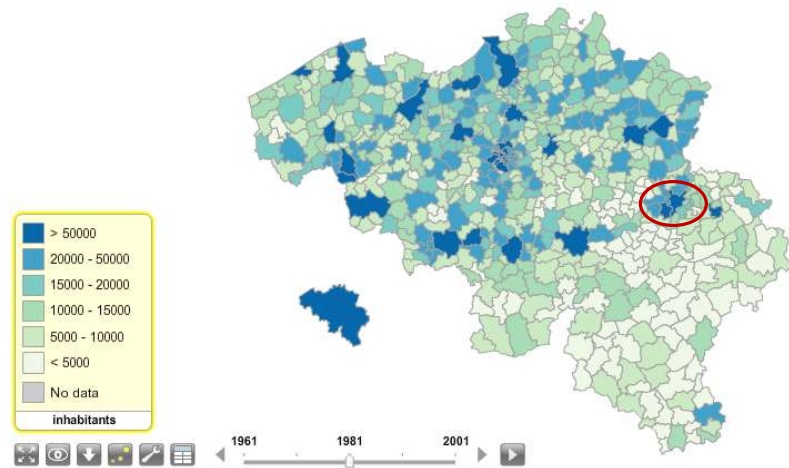


Figure A4.4.24. Population distribution in the municipalities of Belgium during 1981. The red circle approximately indicates the area affected by the 1983 Liège earthquake. From Statplanet (2005).

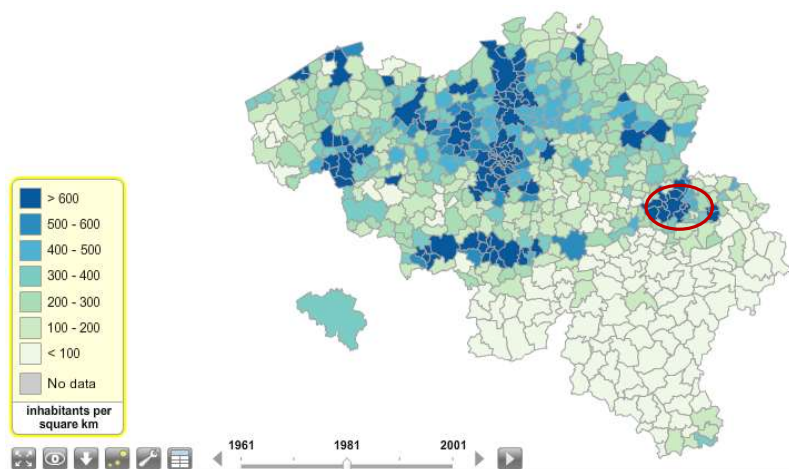


Figure A4.4.25. Population density distribution in the municipalities of Belgium during 1981. The red circle approximately indicates the area affected by the 1983 Liège earthquake. From Statplanet (2005).

A4.4.6.3 Time of day of earthquake

The earthquake hit the region of Liège on a Tuesday at 00:49 UTC (01:49 local time), awakening the population in a radius of more than 30 km. Being the fall of innumerable chimneys, chimney covers and decorative stone pediments (which caused severe damage to roof covers and cars parked in front of the houses) the most visible impact of the earthquake, it is likely that more casualties would have resulted from the fall of these objects had the earthquake struck during the daytime (Plumier *et al.*, 2006).

A4.4.7 Characteristics of exposed building stock

A4.4.7.1 Seismic design codes

In Belgium, the first investigations aimed at estimating ground motion levels for the safety of new buildings date from the 1970s and were motivated by the construction of the first nuclear reactors in the country (Vanneste *et al.*, 2014). The first study encompassing the country as a whole was that of Van Gils & Zaczek (1978). Investment in seismic hazard assessments and the development of a seismic network in Belgium, which had been very limited in the past, increased after the 1983 Liège earthquake. The GSHAP project (Giardini *et al.*, 1999) allowed for an update, but it was not until the year 2000 that a new seismic hazard map (Leynaud *et al.*, 2000) was elaborated thanks to a cooperation between the Liège University and the Royal Observatory of Belgium (ROB). This map has served as the basis for the seismic zonation map included in the Belgian National Annex of Eurocode 8 (NBN, 2011), which became in force on 1st January 2012 as the NBN-ENV 1998 standard, replacing the previous NBN ISO 3010:1993. The latter was a Belgian application of the ISO 3010 norm from the International Organization for Standardization, which contained guidelines for the design of structures taking into consideration seismic loads. Both standards had coexisted in the period between 2002, when the first version of the National Annex was published, and 2012. A technical document (Doneux *et al.*, 2003) was also published with practical guidelines regarding the construction in seismic zones, being a state of the art for Belgium and northern European construction.

While the implementation of seismic design codes can certainly have an impact on the vulnerability of new structures, policies to urge the seismic assessment and retrofitting of existing old buildings do not seem to exist in Belgium (Plumier *et al.*, 2006).

A4.4.7.2 Building typologies

Data regarding typologies at the country level collected from the PAGER Inventory Database v2.0 (Jaiswal & Wald, 2008) for Belgium are summarized in Figure A4.4.26. As can be observed, no differences are made in the database between urban/rural and residential/non-residential. According to this data, around 80% of the dwellings of Belgium are unreinforced masonry (of either brick or rubble stone). Reinforced concrete frames represent only a small percentage (12%) of all the dwellings, and no information regarding their ductility capacities is available in the database.

García Moreno & Camelbeeck (2013) mention that the main construction typology in the region of Liège is that of low rise (1-3 story), unreinforced masonry buildings with timber floors, sharing one or two walls, and dates mostly from the end of the 19th to the beginning of the 20th century. In effect, the data obtained from the 2011 Census reveals an important predominance of buildings constructed prior to 1919 in the region of Liège, as shown in Figure A4.4.27. Table A4.4.9 describes the main type of buildings found in the region of Liège, being often representative of the kind of construction typically built in Central and Northern Europe.

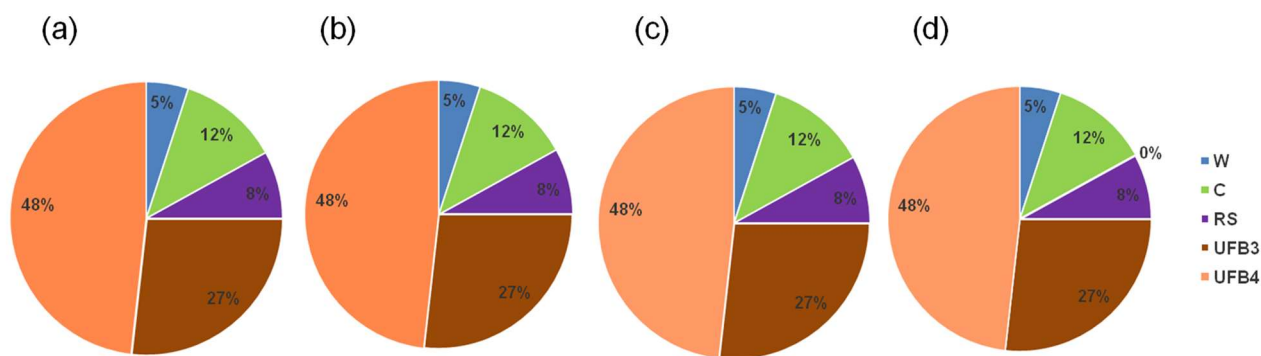


Figure A4.4.26. Proportion of building main typologies in Belgium for (a) rural residential, (b) urban residential, (c) rural non-residential, (d) urban non-residential typologies: W: wood, C: reinforced concrete, RS: Rubble stone (field stone) masonry, UFB3: Unreinforced brick masonry in lime mortar, UFB4: Unreinforced fired brick masonry, cement mortar. 2013 Data from USGS-PAGER (Jaiswal & Wald, 2008).

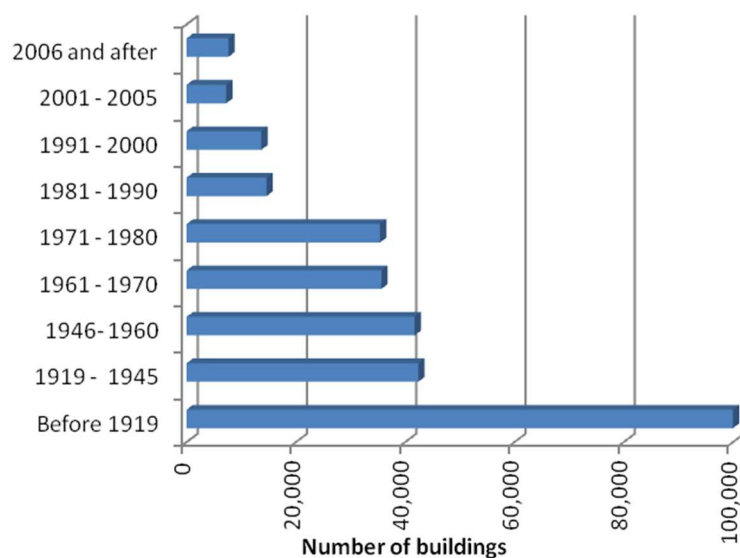


Figure A4.4.27. Distribution of the building stock the region of Liège according to their construction period. From Census 2011 data.

In their search for fragility functions to represent the low-rise unreinforced masonry building stock of Liège in 1983, García Moreno & Camelbeeck (2013) select the pre- and low-code low-rise unreinforced masonry (URML) vulnerability category of the HAZUS programme (Kircher *et al.*, 1997a), with natural periods assumed to lie in the range 0.1-0.3 seconds, and the class 1 fragility curve of Lang & Bachmann (2004). The latter was derived for low-rise (1-3 storeys) unreinforced masonry buildings with timber floors constructed before 1940 in the region of Basel, Switzerland, with natural periods between 0.2 and 0.8 seconds.

Moreover, with respect to the European Macroseismic scale EMS-98 vulnerability classification (Grünthal, 1998), Camelbeeck *et al.* (2013) consider the low-rise unreinforced masonry buildings of Liège within A and B classes, on a scale ranging from A to F, where A is the most vulnerable.

Table A4.4.9. Buildings typically found in the region of Liège according to Jongmans & Plumier (2000), as reported in García Moreno & Camelbeeck (2013).

Type of House	Age	Description
Modest house	Mid-19th–beginning 20th century	~40m ² per floor brick-masonry house aligned with the street in groups of buildings sharing one or two walls, usually presenting two levels (one storey), and two-sided steeply pitched tile roof. Presence of elongated doors and windows and sometimes ornamental motives on the facade.
Average house	End 19th–beginning 20th century	60–80m ² per floor brick-masonry house aligned with the street in groups of buildings sharing one or two walls, usually presenting 3–4 levels (2–3 storeys), two-sided pitched tile roof, large doors and windows, presence of balconies and others ornamental motives on the facade (projecting cornice, etc.).
Maison de Maître (Elegant townhouse)	End 19th–beginning 20th century	80–120m ² per floor brick-masonry building aligned with the street and sharing one or two walls, usually presenting 3–5 high ceiling levels (2–4 floors), tile roofs with two or more sloping sides, very large doors and windows, projecting cornice, presence of balconies and facade built in bricks covered with ornamental rocks or other decorative materials.
Historic house	18th–19th century	40–100m ² per floor brick-masonry building usually located in the historical centre, sharing one or two walls. Three to four levels (2–3 floors) slate roofs, presence of ornamental rocks on the facade, high narrow windows and doors.
Modern house	1930–present day	60–100m ² brick-masonry building with garage or/and ground floor semi-underground (sub-basement). Usually located outside the city centre sharing one or two walls. Three to four levels (2–3 floors), presence of flat roofs, wide windows and mix brick–rough stone facades.
Rural house	19th–beginning 20th century	~100m ² isolated brick-masonry building presenting tiles or slate two-sided steeply pitched roofs. Two levels (1 floor), windows and doors generally embedded in rocks and facade in bricks or rough stones.
Apartments	1940–present day	Large mix brick–reinforced concrete building with ~5 floors (individual apartments), wide windows and flat roof.

In addition, Plumier *et al.* (2006) report a seismic risk study of Jongmans & Plumier (2000) in the region of Wallonia, which comprises the municipality of Liège. The latter used the method of the vulnerability index of Faccioli *et al.* (1999), which is calibrated on the basis of real damage observed in Italy, to assess the vulnerability of the Belgian building stock in an empirical way, as a function of a series of structural characteristics such as regularity in plan and in elevation, openings, bearing material and structural system. The basic index (I_v) and the modifiers for different building descriptive elements are summarized in Table A4.4.10 for the main typologies. The more vulnerable the structure (e.g. old masonry at the end of a row of terraced houses) the higher the index is.

Table A4.4.10. Vulnerability index defined for the different types of buildings located in the region of Liège according to Jongmans & Plumier (2000) and Plumier *et al.* (2006), as reported in García Moreno & Camelbeeck (2013).

Type of building	Basic lv	High % of open space	Low resistance ground floor	Heavy balconies	Slenderness	Irregular Structure	Risk of hammering	Additional Reinforcements
LR brick masonry built before 1940								
Isolated or sharing two walls	+42	+5	+5	+5	+5	+5	+5	-15
End of a row or in a corner	+52	+5	+5	+5	+5	+5	+5	-15
LR brick masonry built after 1940								
Isolated or sharing two walls	+17	+4	+4	+4	+4	+4	+5	-10
End of a row or in a corner	+28	+4	+4	+4	+4	+4	+5	-10
Buildings with more than five storeys								
Mix masonry–reinforced concrete	-5	+10	+5	+20	+10	+20	+5	
Modern reinforced concrete	-20	+10	+5	+20	+10	+20	+5	

A4.4.7.3 Prior damage and retrofit

The Earthquake Engineering Field Investigation Team (EEFIT, 1984) who inspected the affected area 9 days after the earthquake, explicitly refer to the poor state of repair and maintenance of the damaged buildings prior to the earthquake, the weathering damage, and the poor nature of the ground and foundations, which had, in their opinion, experienced settlements before the earthquake. Moreover, a quick inspection at the centre of Liège revealed cases of recent cracked masonry but, most probably, unrelated to the earthquake. Both François *et al.* (1987) and Camelbeeck *et al.* (2013) refer, as well, to the pre-existence of vertical cracks in bearing walls due to the ground settlement from the mining activity of the area. Finally, De Becker & Camelbeeck (1985) make reference to the potential alterations of the bearing capacity of the pre-First World War brick constructions due to improper repairs, air pollution from the industrial environment as well as collapse of the underground coal mines.

A4.4.8 Damage observations

A4.4.8.1 Damage states

In order to quantify the damage due to the 1983 Liège earthquake, García Moreno & Camelbeeck (2013) use the damage scale defined by FEMA for the HAZUS programme (Kircher *et al.*, 1997a) and its equivalence with the European Macroseismic Scale EMS-98 (Grünthal, 1998) according to the recommendations of Hill & Rossetto (2008), which are described in Table A4.4.11. For details regarding EMS-98 please refer to Section 3.8.1 of

Chapter 3 and Appendix II. Crossing data from five different sources, they also estimated the repair costs associated to each damage state, as shown in the table. They believe that the reason for these values to be relatively higher than others in the literature (Kircher *et al.*, 1997b; Vacareanu *et al.*, 2004) is that the Belgian authorities superimposed the structural and the non-structural damage in the data they released.

Table A4.4.11. Damage states equivalence as per Hill & Rossetto (2008) and corresponding repair cost ratio as per García Moreno & Camelbeeck (2013).

	Damage states			
HAZUS (FEMA, Kircher <i>et al.</i> , 1997)	Slight Damage (SD)	Moderate Damage (MD)	Extensive Damage (ED)	Complete Damage (CD)
EMS-98 (Grünthal, 1998)	Slight Damage (D1)	Moderate Damage (D2)	Substantial to Heavy Damage (D3)	Very Heavy Damage (D4) + Destruction (D5)
Repair cost (% of building's value) (García Moreno & Camelbeeck, 2013)	>3% (& no damaged chimney)	<21% (& repairs needed at the chimney)	<50%	>50% ("uninhabitable")

Among other sources, García Moreno & Camelbeeck (2013) make use of data from the unpublished report of the University of Liège (PSE-UL, in what follows), in which the intensity of damage is quantified using a damage index consisting of a weighted sum of the gravity indexes that represent the state of damage of a series of features of each building, as described in Table A4.4.12.

Table A4.4.12. Codes defined for the calculation of damage index (I_d) by the authors of the PSE-UL report to evaluate the damage of the buildings affected by the 1983 earthquake (Jongmans & Campillo, 1990).

Damaged feature	No damage	Slight damage		Heavy damage	
		Index	Description	Index	Description
Chimney	0	1	Chimney broken	1	Chimney broken
Roof	0	2	- replacement of less than 50 tiles - shoring in the storehouse on an area less than 15m ² - battens to repair - dormer-window broken	3	- replacement of more than 50 tiles - shoring in the storehouse on an area more than 15m ²
Internal walls	0	1	- cracked plaster - less than 1.5m ³ masonry to repair	3	- more than 1.5m ³ masonry to repair
External walls	0	2	- cracks - mortar joints to repair - replacement of less than 50 bricks - less than 5m ³ to repair - shoring less than 20 m ²	4	- replacement of more than 50 bricks - more than 5m ³ to repair - shoring more than 20m ² - setting reinforced concrete
Floor and ceiling	0	1	- replacement of pavement - ceiling cracks	3	- demolition and reconstruction of flooring - shoring of ceiling
Decorative and brittle elements	0	1	- windows broken - doors, windows, building-stones, chimney pieces to take down and remount	2	- replacement of stone window-frames - replacement of chimney pieces, lintels, etc.

A4.4.8.2 Damage statistics and description

Different reports exist regarding the figures and extension of damage, and these differ according to the authority and investigation team in charge of the damage registration.

According to Jongmans & Campillo (1990), about 13,000 buildings were damaged to some extent in the region of Liège and its districts, with a larger concentration of damage in the western part of the town of Liège and in the suburbs of Saint Nicolas and Montegnée, as will be discussed below. Of these, 25 buildings are reported by Jongmans & Campillo (1990) to have been partially or totally destroyed. García Moreno & Camelbeeck (2013) refer to 16,000 houses damaged at different grades, based on the findings of De Becker (1985) and Plumier *et al.* (2006).

Being the original reports for the 16,000 houses only available in paper format and, consequently, virtually impossible to re-process, García Moreno & Camelbeeck (2013) have gathered damage data coming from five different sources: (i) ROB questionnaires to assess macroseismic intensity, whose answers provide information regarding the percentage of damaged chimneys per locality; (ii) a report by the fire brigade that contains a list of 1750 surveyed buildings, of which 168 (9.6%) were declared uninhabitable and 37 (2.1%) were marked to be demolished due to the intense damage on their structure; (iii) a document by the authorities of the locality of Flémalle containing brief damage descriptions for 686 buildings; (iv) an unpublished report by D. Jongmans, from the University of Liège, based on data from the Belgian Calamity Centre regarding damage in Saint Nicolas and Liège (the “PSE-UL” report), in the form of detailed information for 3461 buildings in Saint Nicolas and damage distribution for both Saint Nicolas and Liège (detailed information for individual buildings in Liège has been lost); and (v) several paper files from the Belgian Calamity Centre containing a brief description of damaged features and repair costs of 113 buildings .

Jongmans & Campillo (1990), as well as the survey team of EEFIT (EEFIT, 1984), state that the majority of the buildings in the affected area are one- or two-story old masonry houses (Figure A4.4.28, right), typically between 80 and 100 years old at the time of the earthquake and, in general, poorly built, some of which are likely to have presented previous damage as described in Section A4.4.7.3. This observation is confirmed by the pie charts of Figure A4.4.28, which depict the age distribution and the number of storeys of the damaged buildings, as reported by Jongmans & Campillo (1990). It is noted that the relatively small contribution of buildings older than 110 years to the total number of damaged buildings is due to less buildings of this age existing in the first place, not to them being more resistant than newer structures.

Modern reinforced concrete buildings and well-constructed brick-built dwellings were generally found undamaged by the surveyors of EEFIT (EEFIT, 1984). Their report enumerates examples of four well-built modern brick clad structures in the epicentral area that appeared undamaged by the earthquake. Additionally, a modern concrete elevated highway in Laven carefully inspected by the team, including its abutment bearings, gave

no sign of damage. As a matter of fact, Jongmans & Campillo (1990) report that, among the damaged buildings, only 7% were less than 20 years old (Figure A4.4.28, left).

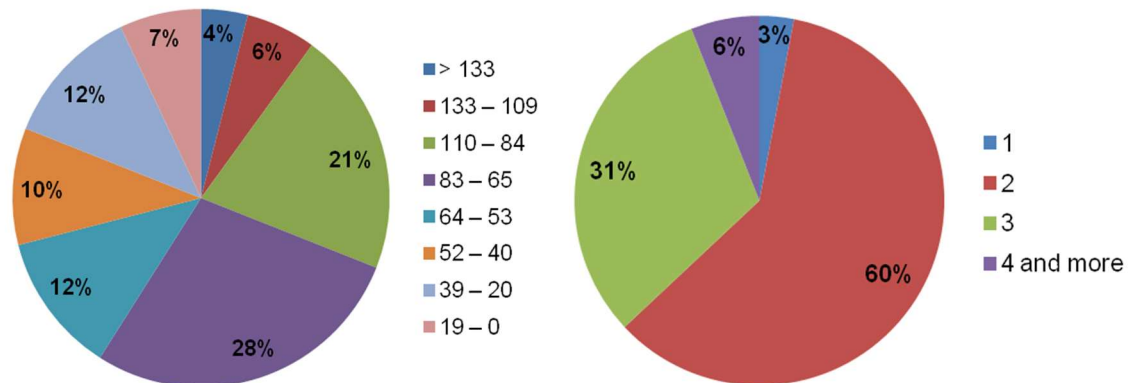


Figure A4.4.28. Age distribution of damaged buildings (years; left) and distribution per number of storeys of damaged buildings (right). From the data of Jongmans & Campillo (1990).

According to the detailed data made available in the electronic supplement to the publication of García Moreno & Camelbeeck (2013), the total percentage of damaged buildings for the most affected localities is herein summarized. Saint Nicolas presented damage in 36.2% of its building stock, which corresponds to a sum of 3554 buildings. As shown in Figure A4.4.29 (left), 29.5% of the buildings suffered either moderate or extensive damage (D2-D3). In Flémalle, damage to 613 buildings (10.6% of the building stock of the area) was reported. The distribution per damage state in Flémalle is illustrated in Figure A4.4.29 (right). At the agglomeration of Liège an average of 32.0% of damaged buildings can be inferred from the data, assuming a uniform number of buildings per reported cell, with the percentage of buildings presenting Moderate Damage being 28.7% of the total building stock, under the same assumption.

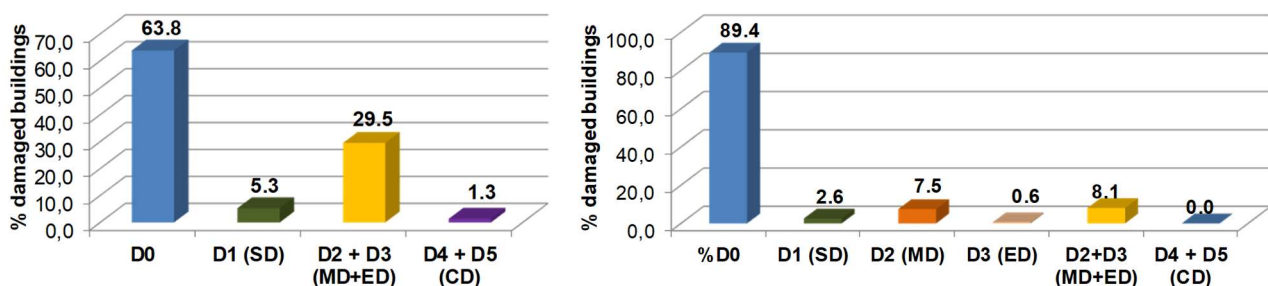


Figure A4.4.29. Percentage distribution of damaged buildings per damage state for the locality of Saint Nicolas (left) and Flémalle (right), according to data from García Moreno & Camelbeeck (2013).

In their recent study based on past data collection, ARUP (2016) have estimated that around 1% of houses in the most affected area (Saint Nicolas) sustained Grade 4 (very heavy) damage, and about 0.2% Grade 5 (destruction).

In Table A4.4.13 damage details are summarized for the most affected and, consequently, investigated localities of Liège, Saint Nicolas and Flémalle, as reported by DeBecker & Camelbeeck (1985).

Table A4.4.13. Quantitative outcome of damage of the most affected localities. Data from De Becker & Camelbeeck (1985).

	Liège	Saint Nicolas	Flémalle
Data of Status	14 March 1984	29 December 1983	15 November 1983
Demolitions	22	15	N/A
Uninhabitable Houses	36	93	N/A
Chimneys	N/A	817 interventions	339 in danger of collapse 34 destroyed
Façades	N/A	356 stanchions	163 with important cracks
Roof Covers	N/A	100 interventions	N/A
Other	2 unusable churches 235 families to be rehoused	-	247 houses with important interior damage

In the map of Figure A4.4.30 the total number of buildings and the percentage of damaged chimneys reported in the electronic supplement to the publication of García Moreno & Camelbeeck (2013) are depicted for the localities of the province of Liège and the neighbouring Limburg for which no further detailed damage information is available. García Moreno & Camelbeeck (2013) suggest that the proportion of damaged chimneys can be considered a proxy for the proportion of buildings representing moderate and extensive damage, considering that chimneys begin to fail from degree of damage D2 ($D2 \leq D \leq D3$) in the EMS-98 damage scale (Grünthal, 1998). As shown in Figure A4.4.30, many of these localities appear to have been less affected than Liège, Saint Nicolas and Flémalle, as many of them have had only less than 10% of their building stock affected. Overall, the total number of presumably damaged buildings at these locations sums up to 4,335 out of a total of 49,673.

Due to the small impact of Liège earthquake when compared to global disasters, no extensive reports are available within global losses databases. The USGS vaguely reports hundreds of damaged buildings, which, from the local studies, appears as a severe underestimation.

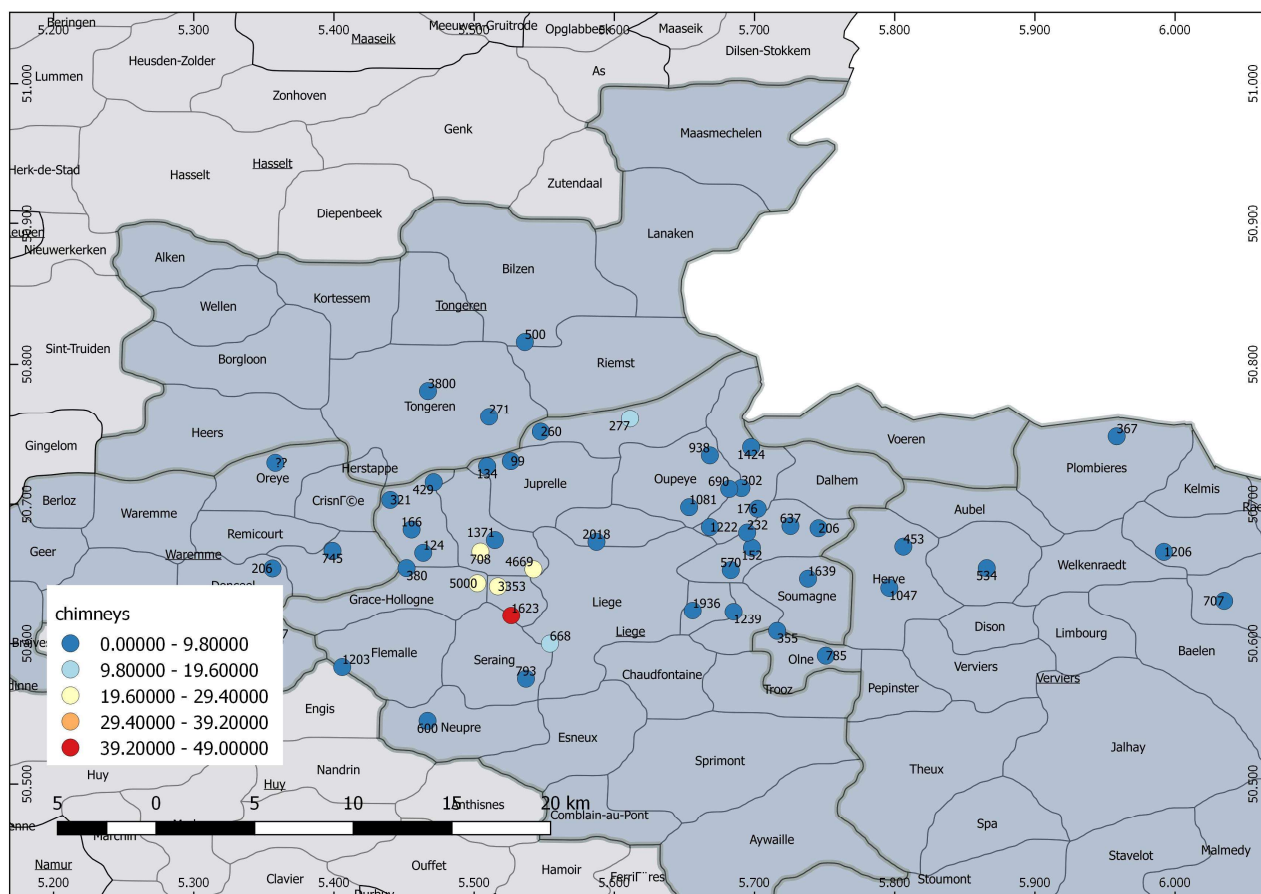


Figure A4.4.30. Percentage of damaged chimneys (as per the colour scale) in the localities of the province of Liège and few of the province of Limburg. Total number of buildings (damaged and not damaged) marked on the map. Elaborated with data from García Moreno & Camelbeeck (2013).

The principal types of damage observed, which correspond mostly to Grade 3 (Substantial to Heavy damage D3) in the EMS-98 scale (Camelbeeck *at al.*, 2013), were the following (EEFIT, 1984; Jongmans & Campillo, 1990; Doneux et al., 2003; ARUP, 2016):

- failure of chimneys;
- fall of unstable or poorly constructed parts, such as parapets, cut stone pediments, chimney covers or various toppings;
- vertical cracks between façade and cross-wall;
- shear cracking of walls, often starting from openings, doors and windows;
- collapse of roofs;
- fall of ceilings.

Chimneys are slender elements with little resistance to bending, especially when the corrosion of the mortar no longer provides a real bond to the bricks (Figure A4.4.31). According to Jongmans & Campillo (1990), about 10,000 chimney failures were observed. From the analysis of damage data and photographs, ARUP (2016) concluded that about 80% of the chimneys in Saint Nicolas, the worst affected area (EMS-98 VII), had failed, while the EEFIT survey team estimate 90% (EEFIT, 1984). This percentage quickly drops down to 2-15% in other areas subject to lower EMS-98 intensities of VI-VII and to less than 1% to 10% in areas subject to EMS-98 intensity V. From the same analysis, ARUP (2016)

estimated that failure proportions of parapets ranged up to about 10% in the worst affected areas, and the volume of masonry falling was substantial, typically 10% of the parapet volume.



Figure A4.4.31. Chimney of good quality damaged (left); fall of chimney over a car (centre); fall of massive stone in a central road (right). From Doneux *et al.* (2003).

A common damaging effect, although not often very visible from the outside of the building, involves vertical cracks, more or less continuous, between the façade and the partition wall, as illustrated in Figure A4.4.32. This effect is favoured by several causes, as explained by Doneux *et al.* (2003): absence of horizontal diaphragms or connections between them and the structural walls, a weak linkage of new façades to previously constructed walls, and the notch for the water system required by municipal law. The insufficient interlock of the masonry walls in the corners was also an observed reason of out-of-plane overturning. This effect was exacerbated when these cracks existed prior to the earthquake, notably due to mining settlements, which are widespread in the region.

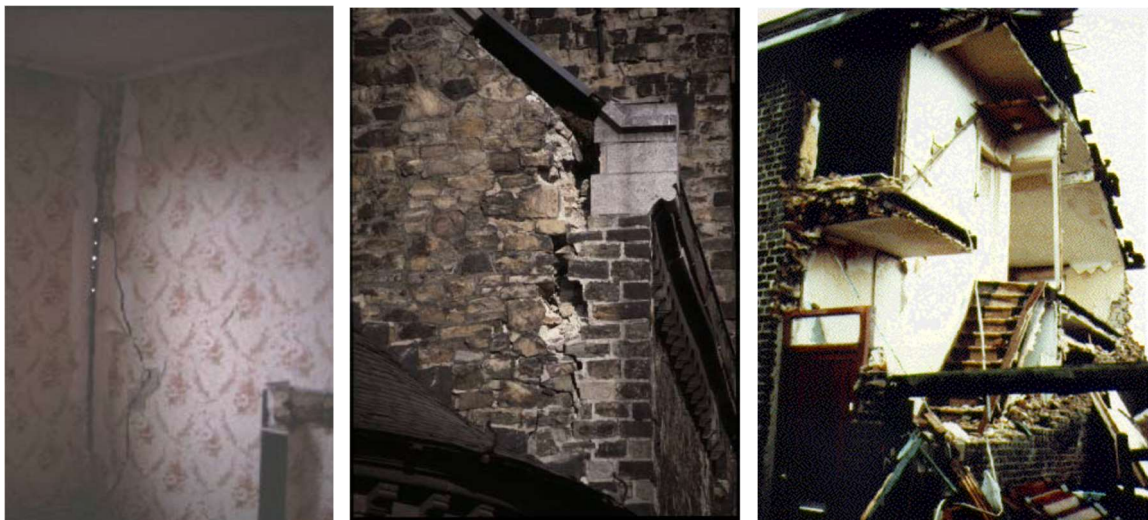


Figure A4.4.32. Crack at the angle of the walls (left), severe cracking between two walls at the church St Gilles (centre), and collapse of the external wall façade (right). From Doneux *et al.* (2003).

ARUP (2016) estimate that large-scale out-of-plane wall failures were observed in 1% of the older unreinforced masonry buildings considered to be in the “worst condition”, while smaller failures involving around 1m² or less of area, particularly of gables, appear to have occurred more frequently, in around 5 to 10% of these buildings, when subject to EMS-98 intensity VII.

Partial or total collapse of the roof was observed in a more limited extent (Figure A4.4.33, left). This may be attributed to significant out-of-plane deformation of the walls and/or poor connection between the walls and the roof, heavy roofing material, or poor in-plane resistance of the horizontal roofing system (Doneux *et al.*, 2003).

The investigators of EEFIT (EEFIT, 1984) point out at buckled pavement tiles observed in a district of Liège with extensive chimney damage as strong indicators of ground movements. Finally, a survey conducted in the cemeteries allowed for the observation that approximately 10% of the gravestones were damaged and some graves had settled unevenly, possibly indicating poor ground conditions (Figure A4.4.33, right). The same work highlights as well the potential influence of the coal mine located under part or all of the epicentral area on the damage extent, as they observed that 9 days after the earthquake settlement of the buildings was still ongoing. This is also clearly stated by Camelbeeck in CSENPC *et al.* (2009), who clarifies that, although the collapse of mining cavities cannot trigger an earthquake, it may lead to a worsening of the consequences of a seismic event that can occur of its own accord.



Figure A4.4.33. Roof collapse due to walls displacement, from Doneux *et al.* (2003) (left); cemetery of St Gilles, from EEFIT (1984) (right).

A local newspaper (RTBF, 2013) makes reference to extensive damage to contents and non-structural elements of houses and stores at the city centre, what has, however, not been further analysed by scientific reports and papers.

A4.4.8.3 Observed weaknesses

As described above, more than 10,000 buildings in the epicentral and surrounding area exhibited partial or total collapse of their brick-made chimneys. As said, these are slender elements with poor connection with the rest of the structure and are the first to oscillate

and subsequently collapse during a dynamic shaking. Similarly, several hanging elements, pediments, covers of chimneys, radiators, and heavy cladding with insufficient connections to the main structure failed as well. All the above-mentioned features are parts of the typical construction and architectural technique of the traditional Belgian (and central European) buildings, which are the most vulnerable as well as numerous.

Doneux *et al.* (2003) draw attention to the common case of poor connections of the structural walls with one another and to the flexible diaphragm, as well as of the new façades of certain buildings to their pre-existing perpendicular walls, often aggravated by pre-existing vertical cracks believed to be due to the notch created for the water sewage system. EEFIT (1984) highlight as well the general lack of maintenance of many of the affected buildings and the poor nature of the foundations and the ground beneath them. It is likely that these weaknesses may have negatively affected the lateral response of the buildings during the earthquake (Camelbeeck *et al.*, 2013; François *et al.*, 1987).

A4.4.8.4 Damage distribution

On a small scale, the 1983 earthquake main damage concentrations can be correlated with local superficial deposits which tend to amplify ground motions in the frequency range of the exposed buildings (Jongmans & Campillo, 1990). Figure A4.4.34 illustrates in juxtaposition the geotechnical map of the area (right) and the damage distribution (left). Damage appears to be more concentrated on the western side of the map, where secondary formations can be found (marked MO on Figure A4.4.34, right), at the foot of the western hill-side (marked LA on Figure A4.4.34, right) and in some specific locations within the alluvial plain (marked VE on Figure A4.4.34, right), particularly at the junction of the Meuse and the Ourthe rivers, an area characterised by very heterogeneous alluvial deposits. Of all these, the correlation between damage and soft deposits is particularly strong at the foot of the western-hill side, where the deposits may reach a thickness of 30-40 m. At the same time, damage seems to be more scattered in the areas where the bedrock outcrops.

García Moreno & Camelbeeck (2013) carried out a similar comparison by making use of the total damage indices available in the PSE-UL report (see Table A4.4.12) for the city of Liège and its suburb Saint Nicolas, and observed the same correlation as Jongmans & Campillo (1990). Their map showing the percentage of buildings presenting moderate damage or greater in Liège, Saint Nicolas and Flémalle, elaborated through the combination of different data sources and shown in Figure A4.4.35, shows patterns similar to those of Figure A4.4.34 (left), but covering a larger area that includes Flémalle and showing how the damage is concentrated around 3 km to the east of the epicentre. Jongmans & Campillo (1990) believe that the damage pattern observed is strongly influenced by the presence of the NE-SW orientated syncline (Section A4.4.3.1), which is likely to have played a relevant role in the amplification of ground motions. García Moreno & Camelbeeck (2013) mention that 60% of the buildings situated in this zone likely presented some extent of moderate-to-high damage.

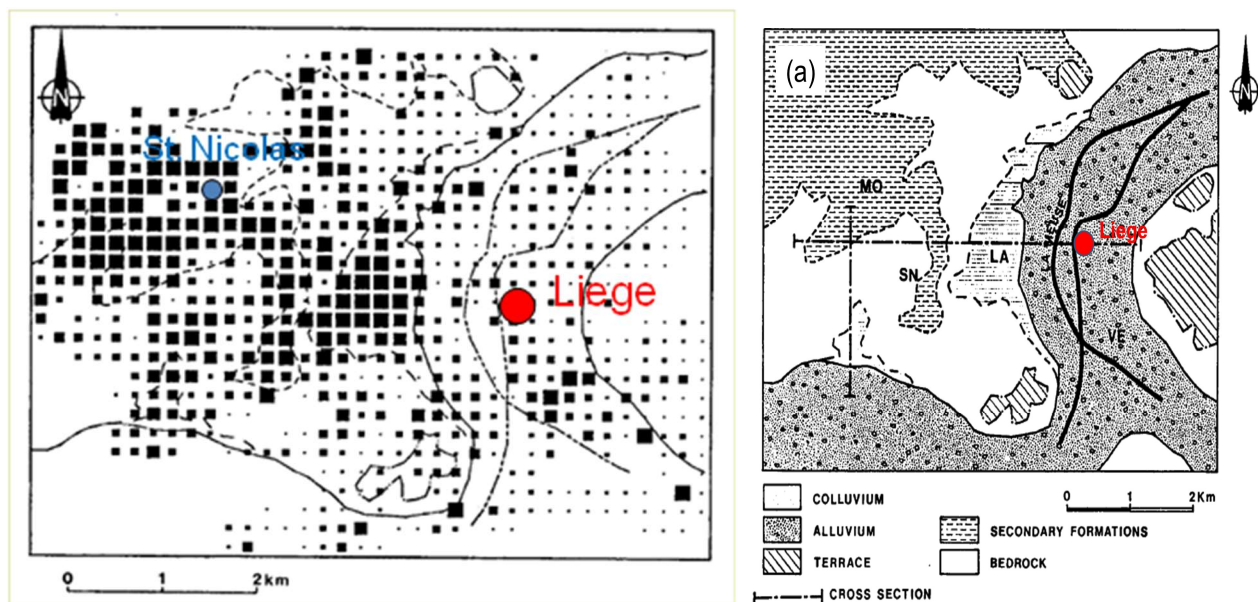


Figure A4.4.34. Damage map, black squares are proportional to the extent of the buildings damage (left); geotechnical map of the same area (right). From Jongmans & Campillo (1990).

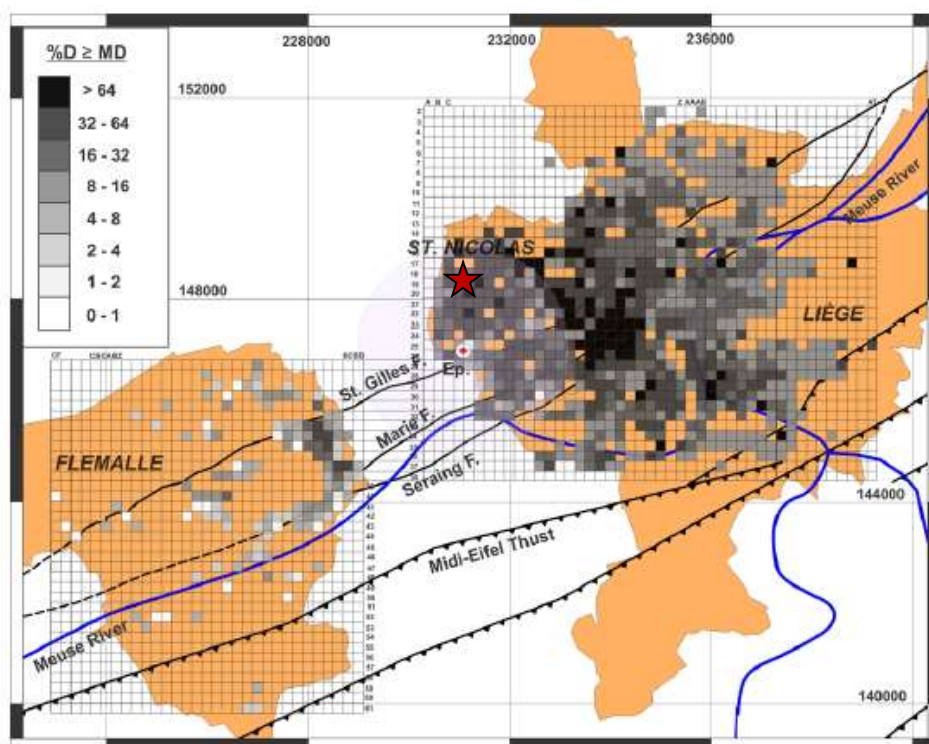


Figure A4.4.35. Percentage of buildings presenting moderate or greater damage (%D ≥ MD) after the 1983 Liège earthquake calculated for square areas of 0.040 km² over the localities of Saint Nicolas, Liège and Flémalle. Red star indicates epicentre. From García Moreno & Camelbeeck (2013).

A4.4.9 Casualties and losses

A4.4.9.1 Numbers of dead and injured

Reports indicate the occurrence of two immediate deaths and four additional ones in the days following the earthquake (e.g., EEFIT, 1984; Jongmans & Campillo, 1990).

There do not seem to be records of the exact number of injured people, but several sources suggest a number of around 30: USGS PAGER-CAT reports 30, The New York Times (1983) says about 26, EEFIT (1984) mentions several dozens, while De Becker & Camelbeeck (1985) mention that 20 people were transferred to the hospital.

In spite of the relative low magnitude of the earthquake, its consequences were unusually important. On top of the dead and injured, around one thousand people were left homeless and in need of immediate shelter (García Moreno & Camelbeeck, 1985).

A4.4.9.2 Causes of casualties

One of the immediate deaths was due to either the collapse of the ceiling of the adjacent house (DH, 2013) or of her own bedroom (The New York Times, 1983), while the other was that of an 80-year old person who suffered from a heart attack caused by the shock (The New York Times, 1983).

The four indirect deaths that are included in the disaster outcome (La Meuse, 2013; EEFIT, 1984; Jongmans & Campillo, 1990) are related to intoxication by carbon monoxide from gas heaters trapped into the house due to the ignored collapse of their chimney. In fact, in the winter months after the earthquake, a significantly higher than usual number of poisoning by carbon monoxide was reported (Camelbeeck *et al.*, 2006; CSENPC *et al.*, 2009). This increase is attributed by the authors of the aforementioned references to the cracking of the chimneys as a consequence of the earthquake.

Most of the injuries were linked to falling elements (stones, chimneys, parapets) on the roads and to falling debris while running out of the buildings (Plumier *et al.*, 2006).

A4.4.9.3 Estimates of economic losses

On the anniversary for the 30 years of the Liège earthquake of 1983, local newspapers (Liège fan, 2013; La Dernière Heure, DH, 2013) reported that the overall cost of the earthquake was around two billion French francs, which would correspond to around 50 million euros, without accounting for the inflation over the years. De Becker & Camelbeeck (1985) mention a similar number of 60 million US dollars, while 50 million US dollars are reported in the International Disaster Database (EM-DAT, 2018) and the Significant Earthquake Database of the National Centers for Environmental Information of the National Oceanic and Atmospheric Administration (NOAA) of the United States. Around 16,000 home owners were financially supported by the Belgian Calamity Centre due to their houses being affected by different extents of damage.

Jongmans & Campillo (1990) mention a much larger figure of 80 million US dollars lost in total repair costs, and highlight that the real economic loss was much higher. Assuming inflation for the dollar of 2.69% per year between 1983 and 2016, the 80 million US dollars are equivalent to around 192 million US dollars (or 182 million euro) in 2016, according to online conversion calculators. On the other extreme, EEFIT (1984) estimated a much lower value of 5 million British pounds.

While García Moreno & Camelbeeck (2013) studied the spatial distribution of the mean value of total repair cost (TRC) per building over a 200 m x 200 m grid covering Liège and Saint Nicolas, elaborated from the data available in the PSE-UL report, they do not provide an estimation of the overall economic loss. From the electronic supplement to their paper, a total repair cost of 7,291,000 euros is computed for the grids of Saint Nicolas with available information, while the average TRC for all grids of Liège amounts to 1,366 euro per building.

A4.4.10 Discussion and conclusions

This **M4.8** (**M_L 5.0**) earthquake occurred on 8th November 1983, at 00.49 UTC (01.49 local time), to the west of the densely-populated city of Liège, within the locality of Saint Nicolas, in eastern Belgium. The main shock reached a maximum EMS-98 intensity of VII. Damage was reported for about 13,000-16,000 buildings, of which an estimate of 25-205 were destroyed, and most economic loss estimates exceed 50 million US dollars. Two immediate deaths, around 30 injuries and four indirect deaths that occurred because of intoxications with carbon monoxide trapped inside the houses after the collapse of thousands of chimneys were registered. The main reasons for the high losses were:

- the proximity of the epicentre to a highly populated region;
- the shallowness of the hypocentre;
- site amplification effects;
- the high amplitudes of motion estimated to have occurred at frequencies close to the natural ones of the exposed structures;
- the influence of past coal mining activities on the weakening of foundation soils;
- the poor state of maintenance, pre-existing weaknesses and inherent vulnerability of the building stock.

The latter played an important role in the aftermath of the event, given that the building stock was composed mainly of unreinforced masonry structures with almost null earthquake resistance, some of which are understood to have presented pre-existing vertical cracks, potentially due to vibrations and settlement from the mining activity in the area, as well as the notch of the piping system running parallel to the walls. Moreover, several architectural elements that were improperly constructed and linked to the bearing structure, such as chimneys, parapets, pediments, heavy wall toppings, severely jeopardized the safety of the population.

Though a reference to the possible role of the interruption of coal exploitation in the area and the consequent variation of local stresses on the triggering of this event has been found in the literature, no study appears to have been undertaken to the present time to verify this hypothesis. Due to this and the tectonic environment being clearly capable of producing earthquakes of these characteristics, this is not considered an induced event, although its effects are likely to have been aggravated by the man-induced rearrangement of the water table and mining-derived soil instabilities.

A4.4.11 References

A4.4.11.1 Bibliography

Afshari, K. & J. Stewart (2016). Physically parametrized prediction equations for significant duration in active crustal regions. *Earthquake Spectra* **32**(4), 2057–2081.

Ahorner, L. (1985). The general pattern of seismotectonic dislocations in central Europe as the background for the Liège. In Melchior, P.D. (ed.): *Seismic activity in Western Europe*. NATO ASI Series, Reidel Publishing Company, pp. 41–56.

Ahorner, L. & R. Pelzing (1985). The source characteristics of the Liège earthquake on November 8, 1983, from digital recordings in West Germany. In Melchior, P.D. (ed.): *Seismic activity in Western Europe*. NATO ASI Series, Reidel Publishing Company, pp. 263–289.

Allen, T.I., D.J. Wald, P.S. Earle, K.D. Marano, A.J. Hotovec, K. Lin & M.G. Hearne (2009). An Atlas of ShakeMaps and population exposure catalog for earthquake loss modelling. *Bulletin of Earthquake Engineering* **7**, 701–718.

Ambraseys, N. N., K. A. Simpson & J.J. Bommer (1996). Prediction of horizontal response spectra in Europe. *Journal of Earthquake Engineering and Structural Dynamics* **25**, 371–400.

André, L. (1983). *Origine et évolution des roches éruptives du Massif du Brabant (Belgique) (Origin and evolution of the eruptive rocks of the Massif du Brabant (Belgium), in French)*. Thèse de doctorat inédite (unpublished doctoral thesis, cited by Pirson *et al.*, 2008), Université libre de Bruxelles, Faculté des Sciences, 2 vol., 299 & 123 pp., Bruxelles.

ARUP (2016). *Risk assessment of falling hazards in earthquakes in the Groningen region: Appendices 1-4*. ARUP report 229746_032.0_REP1008 for Nederlandse Aardolie Maatschappij.

Aspinall W.P. & G.C.P. King (1985). A temporary array search for aftershocks of the 1983 November 8, Liège, Belgium, earthquake. In Melchior, P.D. (ed.): *Seismic activity in Western Europe*. NATO ASI Series, Reidel Publishing Company, pp. 319–328.

Atkinson, G.M. & D.M. Boore (2006). Earthquake ground-motion prediction equations for Eastern North America. *Bulletin of the Seismological Society of America* **96**(6), 2181–2205.

Atkinson, G.M. & S.I. Kaka (2007). Relationships between felt intensity and instrumental ground motion in the Central United States and California. *Bulletin of the Seismological Society of America* **97**, 497–510.

Atkinson, G.M. & D.J. Wald (2007). “Did You Feel It?” intensity data: A surprisingly good measure of earthquake ground motion. *Seismological Research Letters* **78**, 362–368.

Bommer, J.J., P.J. Stafford & J.E. Alarcón (2009). Empirical equations for the prediction of the significant, bracketed, and uniform duration of earthquake ground motion. *Bulletin of the Seismological Society of America* **99**(6), 3217-3233.

Boulvain, F. & J.-L. Pingot (2002). *Une introduction à la géologie de la Wallonie (An introduction to the geology of Wallonia, in French)*. Université de Liège, Faculté des Sciences, Département de Géologie, Unité de pétrologie sédimentaire. Online course: <http://www.ulg.ac.be/geolsed/geolwal/geolwal.htm>. Last accessed: 10th October 2017.

Bultynck, P. & L. Dejonghe (ed.) (2001). Guide to a revised lithostratigraphic scale of Belgium, *Geologica Belgica*, 4/1-2, 168 pp.

Camelbeeck, T. (1985). Etude Microsismique du séisme de Liège du 8 Novembre 1983, Estimation du "strong ground motion". In Breesch, L., T. Camelbeeck, M. De Becker, A. Gurbinar, A. Monjoie, A. Plumier & J.M. Van Gils (eds.): *Le séisme de Liège et ses implications pratiques*, Annales des travaux publics de Belgique, **4**.

Camelbeeck T. & M. De Becker (1985). The earthquakes of Liège, of November 8, 1983 and December 21, 1965. In Melchior, P. D. (ed.): *Seismic activity in Western Europe*. NATO ASI Series, Reidel Publishing Company, pp. 233-248.

Camelbeeck T., Alexandre P. & Kusman D. (2006). Les séismes en Belgique et leurs effets sur le bâti, le patrimoine architectural et l'environnement (Earthquakes in Belgium and their effects on buildings, architectural heritage and the environment, in French). *Conference : Evaluation et prévention du risque sismique en Région wallonne*, October 2016, Moulins de Beez, Namur, Wallonia, Belgium, pp. 87-99.

Camelbeeck, T., A. Plumier & D. García-Moreno (2013). Le tremblement de terre de Liège du 8 Novembre 1983 (The earthquake of Liège of 8th November 1983, in French). *Ciel et terre* **129**(5), 99 - 104

Conseil Scientifique de l'Environnement du Nord-Pas-de-Calais (CSENPC), Parc Naturel Régional Scarpe-Escaut, Région Nord Pas-de-Calais, Conseil Général Pas-de-Calais (2009). Sismicité et risques (Seismicity and risk, in French). *Actes de la journée du 3 Avril 2009*, Pas-de-Calais, France, pp. 12-16. Available online at: www.enrx.fr/content/download/3847/14652/file. Last accessed: 9th October 2017.

De Becker, M. (1985). L'enquête macrosismique du séisme de Liège du 8 novembre 1983 (Macroseismic survey of the 8th november 1983 Liège earthquake, in French). In Breesch, L., T., Camelbeeck, M., De Becker, A. Gurbinar, A., Monjoie, A., Plumier & J.M. Van Gils. (eds.): *Le séisme de Liège et ses implications pratiques (The earthquake of Liège and its practical implications, in French)*, Annales des travaux publics de Belgique **4**.

De Becker, M. & Camelbeeck, T. (1985). Macroseismic inquiry of the Liège earthquake of November 8, 1983. In Melchior, P. D. (ed.): *Seismic activity in Western Europe*. NATO ASI Series, Reidel Publishing Company, pp. 301-309.

De Becker, M., T. Camelbeeck, C. Poitevin (1985). Clustering of seismicity in the regions of Brabant and Ardennes massives before the Liège earthquake of Nov. 8, 1983. In Melchior, P. D. (ed.): *Seismic activity in Western Europe*. NATO ASI Series, Reidel Publishing Company, pp. 175-187.

Doneux, C., A. Plumier, V. Caporaletti, F. Ferrario, D., Stoica (2003). *Guide technique parasismique belge pour maisons individuelles (Belgian earthquake-proofing guide for single-family homes, in French)*, Université de Liège, Belgique. Available online at: <https://orbi.ulg.ac.be/bitstream/2268/9079/1/GuidePSB-compl.pdf>. Last accessed: 20th April 2017.

- Earthquake Engineering Investigation Team (EEFIT, 1984). *The Liège earthquake 8th November 1983, Damage inspection report Volume I*. Ove Arup & Partners, London, United Kingdom, 76pp.
- Faber, S. & K.-P. Bonjer (1985). Phase recognition and interpretation at regional distances from the Liège event of November 8, 1983. In Melchior, P. D (ed.): *Seismic activity in Western Europe*. NATO ASI Series, Reidel Publishing Company, pp. 249–262.
- Faccioli, E., V. Pessina, G.M. Calvi & B. Borzi (1999). A study on damage scenarios for residential buildings in Catania city. *Journal of Seismology* **3**, 327–343.
- Federal Emergency Management Agency (FEMA) (2003). *Multi-hazard Loss estimation methodology – Earthquake model*, HAZUS MR4 Technical manual, Washington D.C.
- Fourmarier, P. (éd.) (1954). Prodrôme d'une description géologique de la Belgique (Prodrôme of a geological description of Belgium, in French). *Société Géologique de Belgique*, 826pp.
- François M., A. Pissart & J.-P. Donnay (1987). Analyse macroseismique du tremblement de terre survenu à Liège le 8 Novembre 1983 (Macroseismic analysis of the 8th november 1983 Liège earthquake, in French), *Annales de la Société géologique de Belgique*, T.109-1986, 529-538.
- García Moreno, D. & T. Camelbeeck (2013). Comparison of ground motions estimated from prediction equations and from observed damage during the M=4.6 1983 Liège earthquake (Belgium). *Natural Hazards and Earth System Sciences* **13**, 1983–1997.
- Giardini, D., G. Grünthal, K.M. Shedlock & P. Zhang (1999). The GSHAP global seismic hazard map. *Annali di Geofisica* **42**(6), 1225-1228. On-line data source: a service of Helmholtz Centre Potsdam <http://gmo.gfz-potsdam.de>.
- Grünthal G. (ed.) (1998). *European Macroseismic Scale 1998*, Cahiers du Centre Européen de Géodynamique et de Séismologie: Vol. 15. Europ. Center for Geodyn. and Seism, Luxembourg
- Hanks, T. & H. Kanamori (1979). A magnitude moment scale. *Journal of Geophysical Research* **84**, 2348-2351.
- Heidbach, O., M. Rajabi, K. Reiter, M. Ziegler & the WSM Team (2016). *World Stress Map Database Release 2016*. GFZ Data Services. Available online at: www.world-stress-map.org. Last accessed: 20th April 2017.
- Hill, M. & T. Rossetto (2008). Comparison of building damage scales and damage descriptions for use in earthquake loss modelling in Europe. *Bulletin of Earthquake Engineering* **6**, 335–365.
- Hinzen K.-G. & M. Oemisch (2001). Location and magnitude from seismic intensity data of recent and historic earthquakes in the Northern Rhine area, central Europe. *Bulletin of the Seismological Society of America* **91**(1), 40-56.
- Jaiswal, K. & D.J. Wald (2008). Creating a global building inventory for earthquake loss assessment and risk management. USGS Open File Report 2008-1160. Available online at: <http://pubs.usgs.gov/of/2008/1160/>. Last accessed: 15th June 2017.
- Jongmans, D. & M. Campillo (1989). Influence de la source et de la structure géologique sur la répartition des dégâts lors du tremblement de terre de Liège du novembre 1983 (Influence of the source and the geological structure on the distribution of damage during the Liège earthquake of November 1983, in French). *Bulletin de la Société Géologique de France* **8**(4), 849-857.
- Jongmans, D. & M. Campillo (1990). The 1983 Liège earthquake: damage distribution and site effects. *Earthquake Spectra* **6**(4), 713-737.

Jongmans, D. & A. Plumier (2000). *Etude pilote du risque sismique sur une partie de la ville de Liège (4 km²) (Pilot study on the seismic risk in a part of the city of Liège (4km²), in French)*. Internal Report, Faculté des Sciences Appliquées, Université de Liège.

Kircher, C.A., A.A. Nassar, O. Kustu & W.T. Holmes (1997a). Development of building damage functions for earthquake loss estimation. *Earthquake Spectra* **13**, 663–682.

Kircher, C. A., R.K. Reitherman, R.V. Whitman & C. Arnold (1997b). Estimation of earthquake losses to buildings. *Earthquake Spectra* **13**, 703–720.

Lang, K. & H. Bachmann (2004). On the seismic vulnerability of existing buildings: a case study of the city of Basel. *Earthquake Spectra* **20**, 43–66.

Leynaud, D., D. Jongmans, H. Teerlynck & T. Camelbeeck (2000). Seismic Hazard Assessment in Belgium. *Geologica Belgica* **3**(1-2), 67-86.

Liégeois, R.M.G.L. (1985). Geological and mining aspects of the Liège area. In Melchior, P. D. (ed.): *Seismic activity in Western Europe*. NATO ASI Series, Reidel Publishing Company, pp. 347–368.

NBN EN 1998-1 ANB (2011). Eurocode 8 – Calcul des structures pour leur résistance aux séismes - Partie 1: Règles générales, actions sismiques et règles pour les bâtiments - Annexe nationale (Eurocode 8: Design of structures for earthquake resistance - Part 1: General rules, seismic actions and rules for buildings – National Annex, in french).

Olive, S., G. Clement, J. Denayer, C. Derycke, V. Dupret, P. Gerrienne, P. Gueriau, J.-M. Marion, B. Mottequin & C. Prestianni (2015). Flora and fauna from a new Famennian (Upper Devonian) locality at Becco, eastern Belgium. *Geologica Belgica* **18**(2-4), 92-101.

Phillips D.W. (1985). Macroseismic effects of the Liège earthquake with particular reference to industrial installations. In Melchior, P. D. (ed.): *Seismic activity in Western Europe*. NATO ASI Series, Reidel Publishing Company, pp. 369-384.

Pirson, S., P. Spagna, J.-M. Baele, F. Damblon, P. Gerrienne, Y. Vanbrabant & J. Yans (2008). An overview of the geology of Belgium. *Memoirs of the Geological Survey of Belgium* **55**, 71pp.

Plant, J.A., S. Reeder, R. Salminen, D.B. Smith, T. Tarvainen, B. De Vivo & M.G. Petterson (2003). The distribution of uranium over Europe: geological and environmental significance. *Applied Earth Science (Transactions of the Institution of Mining and Metallurgy Section B)*, **112**(3), 221-238.

Plumier, A. (1985). Les effets sur les constructions, Les réparations. (The impact on the constructions, the repairs, in French) In Breesch, L., T. Camelbeeck, M. De Becker, A. Gurpinar, A. Monjoie, A. Plumier & J.M. Van Gils: *Le séisme de Liège et ses implications pratiques (The earthquake of Liège and its practical implications, in French)*, Annales des travaux publics de Belgique **4**.

Plumier, A., C. Doneux, T. Camelbeeck, G. Van Rompaey, D. Jongmans, M. Wathelet, H. Teerlynck & F. Nguyen (2005). *Seismic risk assessment and mitigation for Belgium in the frame of EUROCODE 8: final report*. Brussels, Federal Science Policy (SP1481).

Plumier, A., T. Camelbeeck, & A.-M. Barszez (2006). Le risque sismique et sa prévention en région Wallonne (The seismic risk and its prevention on The Wallone region, in French). In: *Les risques majeurs en Région Wallonne (Major risks in Wallone region, in French)*. Prévenir en aménageant, Aménagement et Urbanisme, vol. 7 – Direction générale de l'Aménagement du territoire du logement et du patrimoine (DGATLP), 240–273.

Sponheuer, W. (1960). Methoden zur Herdtiefenbestimmung in der Makroseismik. (Methods for depths estimation in macroseismic, in German). *Freiberger Forschungs-Hefte C 88*, Akademie Verlag Berlin, 117 pp.

United Nations, ed. (2016). *Human Development Report 2016 - Human Development for everyone*. Report of the United Nations Development Program (UNDP), New York, United States.

Vacareanu, R., D. Lungu, A. Aldea & C. Arion (2004). *An advanced approach to earthquake risk scenarios with applications to different European towns (RiskUE), Report WP7: Seismic Risk Scenarios Handbook*. European Commission, Brussels.

Van Gils J.M. & Y. Zaczek (1978). La séismicité de la Belgique et son application en génie parasismique (The seismicity in Belgium and its application in seismic design, in French). *Annales des Travaux Publics de Belgique* **6**, 1-38.

Vanneste, K., B. Vleminckx, K. Verbeeck & T. Camelbeeck (2014). *Development of seismic hazard maps for Belgium*. Workshop: Results of the European Project SHARE: Seismic Hazard Harmonization in Europe, DGEB, e.V.

WDR (1983). *World Development Report 1983*. The World Bank Oxford University Press, New York, USA.

Woessner, J., D. Giardini, H. Crowley, F. Cotton, G. Grünthal, G. Valensise, R. Arvidsson, R. Basili, M. B. Demircioglu, S. Hiemer, C. Meletti, R. W. Musson, A. N. Rovida, K. Sesetyan, M. Stucchi & The SHARE Consortium (2015). The 2013 European Seismic Hazard Model: Key Components and Results. *Bulletin of Earthquake Engineering* **13**(12), 3553–3596.
Available online at: <http://www.efehr.org/en/home/>. Last accessed: 17th October 2017.

Worden, C.B., E.M. Thompson, M. Hearne & D.J. Wald (2017). *ShakeMap V4 Manual: technical manual, user's guide, and software guide*. United States Geological Survey. Available online at: <http://usgs.github.io/shakemap/>.

A4.4.11.2 Web references

Census 2011 Belgique - Statistics Belgium: http://www.census2011.be/download/statsect_fr.html. Last accessed: 10th October 2017.

City Population - Population Statistics for Countries, Administrative Areas, Cities and Agglomerations – Interactive Maps and Charts (2009):
<https://www.citypopulation.de/php/belgium-Liège.php>. Last accessed: 12th May 2017.

EM-DAT – The Emergency Events Database (Université Catholique de Louvain, Brussels, Belgium; Cred. Prof. Dr. D. Guha-Sapir): <http://www.emdat.be/>. Last accessed: 4th April 2018.

International Monetary Fund (2017). World Economic Outlook Database 2017 (16th January 2017): <https://www.imf.org/external/pubs/ft/weo/2016/02/weodata/index.aspx>. Last accessed: 15th June 2017.

International Seismological Centre (ISC): <http://www.isc.ac.uk>.

La Dernière Heure (DH, 2013): <http://www.dhnet.be/regions/Liège/il-y-a-juste-30-ans-un-seisme-frappait-Liège-527c6af3357099b117a35485>. Last accessed: 7th May 2017.

La Meuse – local online newspaper (2013):
<http://www.lameuse.be/852766/article/regions/liege/actualite/2013-11-06/le-seisme-de-1983-n-avait-pas-fait-qu-une-victime-a-liege-deux-jeunes-sont-mor>. Last accessed: 9th March 2017.

Liège fan – local online newspaper (2013): <http://liegefan.be/?p=89662>. Last accessed: 9th March 2017.

National Geophysical Data Center / World Data Service (NGDC/WDS): Significant Earthquake Database. National Geophysical Data Center, National Oceanic and Atmospheric Administration (NOAA). DOI:10.7289/V5TD9V7K. <https://www.ngdc.noaa.gov/hazard/earthqk.shtml>. Last accessed: 4th April 2018.

Oral History Center – The Bancroft Library, University of California at Berkeley (2011): <http://bancroft.berkeley.edu/ROHO/projects/debt/1980srecession.html>. Last accessed: 9th October 2017.

Radio-télévision belge de la Fédération Wallonie-Bruxelles (RTBF, 2013): https://www.rtbf.be/info/regions/detail_il-y-a-30-ans-la-terre-tremblait-a-liege?id=8129550
Last accessed: 7th of May 2017

Royal Observatory of Belgium:

Main website: <http://seismologie.be/en>.

Belgian seismic hazard map (ROB, 2016): http://seismologie.be/fr/recherche/seismologie/aleas-et-risques-sismiques/eurocode-8?station_id=uccb&date=20170420. Last accessed: 22nd May 2017.

Seismotectonic map of the Lower Rhine Graben (ROB, 2017) (last accessed 9th March 2017): <http://seismologie.be/SAFE/Rotem/safe2.html>.

Statistics Belgium: <https://bestat.economie.fgov.be/>. Last accessed: 9th March 2017.

Statplanet – Interactive Maps and Visualizations (2005):

<http://www.vub.ac.be/SOCO/belcens/en/belcens.html>. Last accessed: 7th May 2017.

The World Bank Group (2017) - World Bank Open Data: <http://data.worldbank.org>. Last accessed: 11th May 2017.

The New York Times (1983): <http://www.nytimes.com/1983/11/09/world/around-the-world-earthquake-in-belgium-kills-2-and-injures-26.html>. Last accessed: 16th February 2017.

United States Geological Survey (USGS, PAGER):

<https://earthquake.usgs.gov/data/pager/references.php>

United States Geological Survey (USGS): <https://earthquake.usgs.gov/>

Website for this event (last accessed 19th February 2017):

<https://earthquake.usgs.gov/earthquakes/eventpage/usp0001zn0#executive>

United Nations Development Programme – Human Development Data (UNDP-HDD, 2016): <http://hdr.undp.org/en/data>. Last accessed: 16th February 2017.

A4.5. December 1989 M5.4 Newcastle Earthquake, Australia

This earthquake occurred on 27th December 1989, at 23.27 UTC (28th December 1989, 10.27 local time), and is believed to have had its epicentre around Boolaroo, a suburb of the Lake Macquarie-Newcastle area. It caused severe widespread damage, particularly to older load-bearing masonry buildings in the districts of Hamilton and The Junction, as well as Newcastle Central Business District, the main reasons being the complete lack of seismic design of the building stock and its deterioration due to lack of maintenance, as well as site effects. It also caused thirteen deaths and hundreds of injuries, though it is believed that the casualties would have been many more had the earthquake occurred at a different time of the year and of the day. There is no consensus regarding its possible triggering by mining activities in the area.

A4.5.1 Tectonic and seismic setting

A4.5.1.1 Tectonic setting

This earthquake occurred in the vicinity of the city of Newcastle, in New South Wales, south-eastern Australia. The Australian continent is usually regarded as a stable continental region with low-to-medium seismic hazard, due to its location in the middle of one of the World's largest tectonic plates, quite distant from all major plate boundaries (Leonard *et al.*, 2007; McCue *et al.*, 1990a; Rajabi *et al.*, 2016), as shown in Figure A4.5.1. Nevertheless, it is believed to be subject to deformations caused by far-field stresses generated at the boundaries and buoyancy forces originated by the dynamics of the mantle (Quigley *et al.*, 2010), though it is generally recognised that the exact conditions that lead to the occurrence of large intraplate earthquakes within it are not fully understood (Clark & Leonard, 2003).

Newcastle and its coalfields lie on the north-east tip of the Sydney Basin, which forms, together with the Gunnedah Basin to the north, an approximately 1500-km long basin system, as shown in Figure A4.5.2 (Quinn *et al.*, 2008). The basin is separated at surface from the New England Orogen by the shallowly ENE-dipping Hunter-Mooki thrust system (Korsch *et al.*, 1997; Leaman, 1990; Quinn *et al.*, 2008). The basin system was initiated as a rift but evolved first into a foreland-basin and finally into a foreland fold-thrust belt (Glen, 2005). Due to this, NW-SE to NNW-SSE trending structures dipping between 55 and 75 degrees that originated as normal faults during the extensional phase and now act as a thrust system dominate the region (Crapp & Nolan, 1975; Lohe & Dean-Jones, 1995). Both the Lachlan Orogen and the New England Orogen form part of the Tasman orogenic system, or Tasmanides, and exhibit evidence of fault mechanics involving both shallow thrust faults sliding over an inferred basal detachment surface, or décollement, as well as deeper-rooted faults that penetrate the basement (Gray *et al.*, 2006; Quinn *et al.*, 2008; Rajabi *et al.*, 2016).

The present-day stress field acting on the Sydney Basin is characterised by an overall NE-SW orientation of the maximum compressive stress, at least at a large scale (Clark & Leonard, 2003; Quinn *et al.*, 2008; Reynolds *et al.*, 2003). However, Clark & Leonard (2003)

refer to the work of Hillis & Reynolds (2000) to point out that the orientation of the stress field is actually variable, as the basin lies in an area of transition between the stress trajectories observed to the north and south of Eastern Australia. The work Rajabi *et al.* (2016) supports this idea, as it highlights that the maximum horizontal stress is highly variable across New South Wales, and that it rotates from approximately NE-SW in the basins of South Sydney and Bloucester to ENE-WSW in the basins of North Sydney, Clarence-Moreton and Gunnedah. Rajabi *et al.* (2016) believe that, while the large-scale orientation of the maximum horizontal stress is mostly controlled by plate boundary forces, local perturbations are likely due to the influence of basement topography, basin geometry, lithological contrasts, igneous intrusions, faults and fractures.

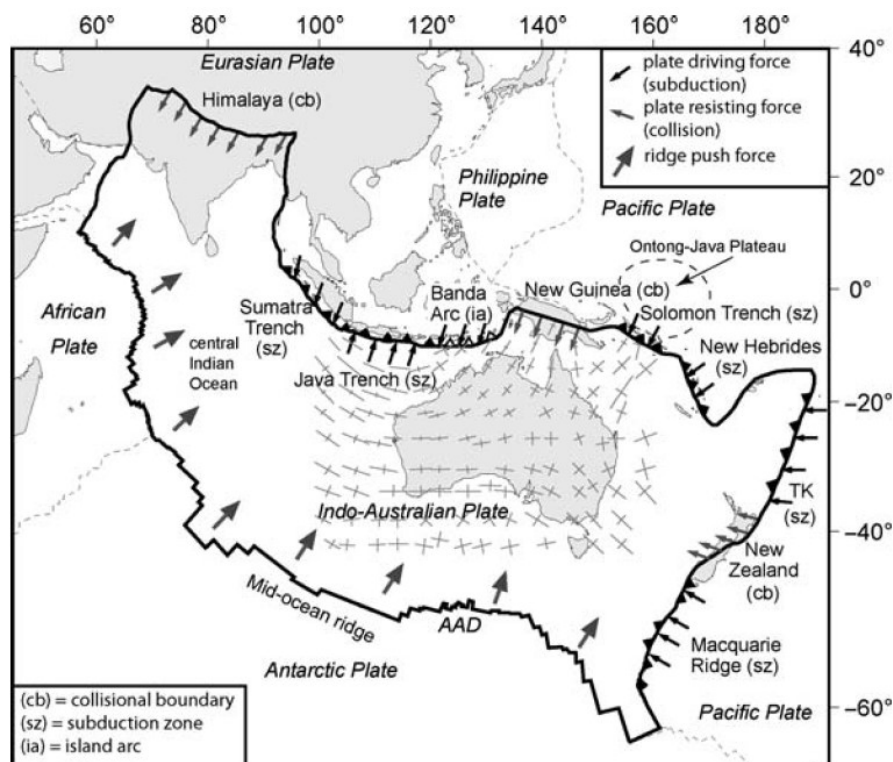


Figure A4.5.1. Plate boundary forces (black arrows) and orientation of maximum and minimum horizontal stresses (grey crosses, according to the model of Reynolds *et al.*, 2003). From Quigley *et al.* (2010).

Knowledge on faults in New South Wales is characterised as moderate to low by Clark *et al.* (2012), who point out that most intra-plate regions of the world are similarly under-explored in this respect, mainly due to the low perception of hazard associated to them and a relatively low rate of occurrence of large earthquakes that produce surface ruptures. For this reason, attribution of the 1989 Newcastle earthquake to a particular fault is not a trivial task. Klose (2007) suggests that this earthquake originated in the Newcastle fault, a reverse fault striking 330N, located in the interior of the crust beneath the Newcastle coal field and believed by the author to be the tip of an eastward extension of the Hunter-Mooki thrust zone. Geomorphic features such as the submerged Lake Macquarie and the hills of suburban Newcastle, the observed damage pattern and the location of an aftershock support the idea of such an orientation of the causative fault (Gibson *et al.*, 1990).

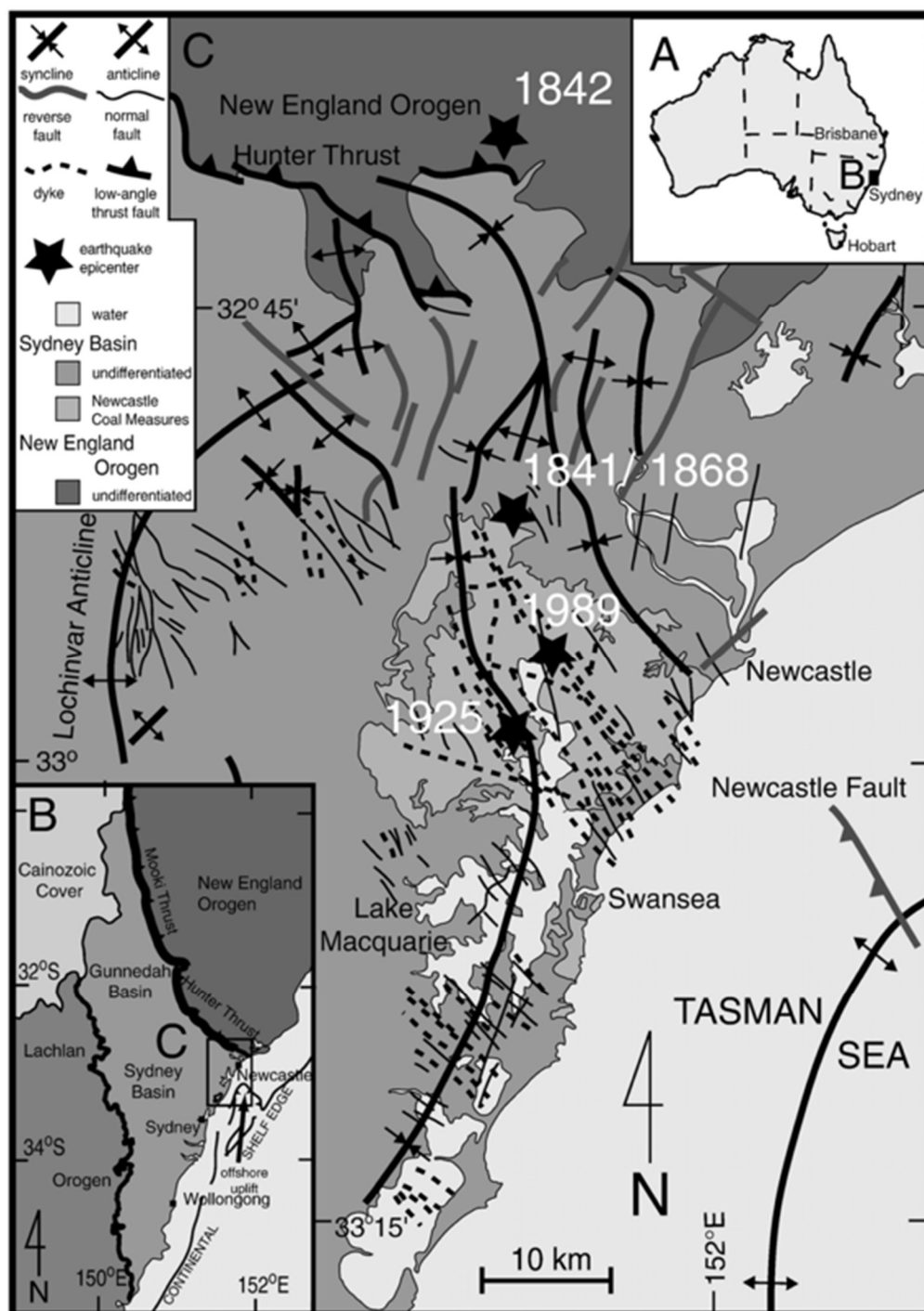


Figure A4.5.2. Geological setting of the 1989 Newcastle earthquake. A (top right corner): location of inset B in Australia. B (bottom left corner): Sydney and Gunnedah basins, Lachlan and New England Orogens, and Hunter-Mooki thrust. C: Key structural and geological features of the Newcastle Coalfield. The Newcastle fault depicted here is not likely to be the one originating the earthquake, according to Klose (2007) and Gibson *et al.* (1990). From Quinn *et al.* (2008).

A4.5.1.2 Regional and local seismicity

As a consequence of its location well within one of the largest tectonic plates of the Earth, Australia is characterised by low-to-medium seismic hazard that occurs in relatively well defined temporal clusters (Clark *et al.*, 2012; Gibson & Dimas, 2009; Leonard *et al.*, 2007; McCue *et al.*, 1990a; Rajabi *et al.*, 2016). Nevertheless, seismic activity is relatively high for an intraplate region (Quigley *et al.*, 2010; Rajabi *et al.*, 2016) and, as of 2007, the catalogue of Australian earthquakes contained around 27,000 events that allow to delineate four regions of sustained seismicity, as marked by the purple polygons in Figure A4.5.3 below (Leonard *et al.*, 2007). Newcastle is located within the southwest region, which hosts, on average, an earthquake of magnitude equal to or larger than 5 every four and a half years, while Australia as a whole has an average of 1.3 earthquakes of this size per year (Leonard *et al.*, 2007).

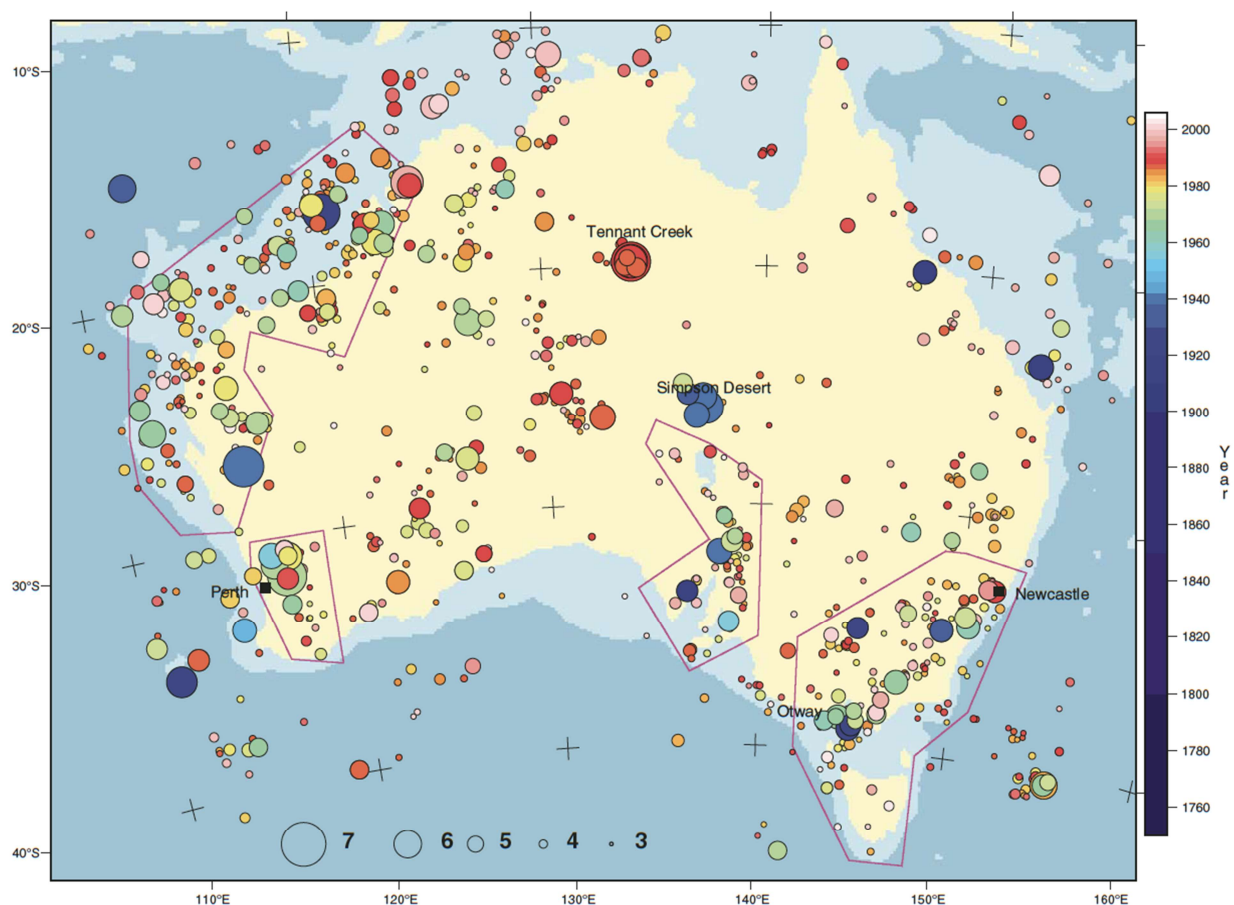


Figure A4.5.3. Earthquakes in Australia of magnitude equal to or larger than 3.5 since 1974 and equal to or larger than 5.5 since 1909. From Leonard *et al.* (2007).

Figure A4.5.4 depicts the significant earthquakes that have occurred in the Hunter Valley – which comprises New Castle – since European settlement in 1804 until 2002, according to Sinadinovsky *et al.* (2002). Most of them were felt in Newcastle, but (minor) damage was only reported for the 18th June 1868 and 18th December 1925 ones, apart from the 1989 Newcastle earthquake under study (McCue *et al.*, 1990b; Sinadinovsky *et al.*, 2002).

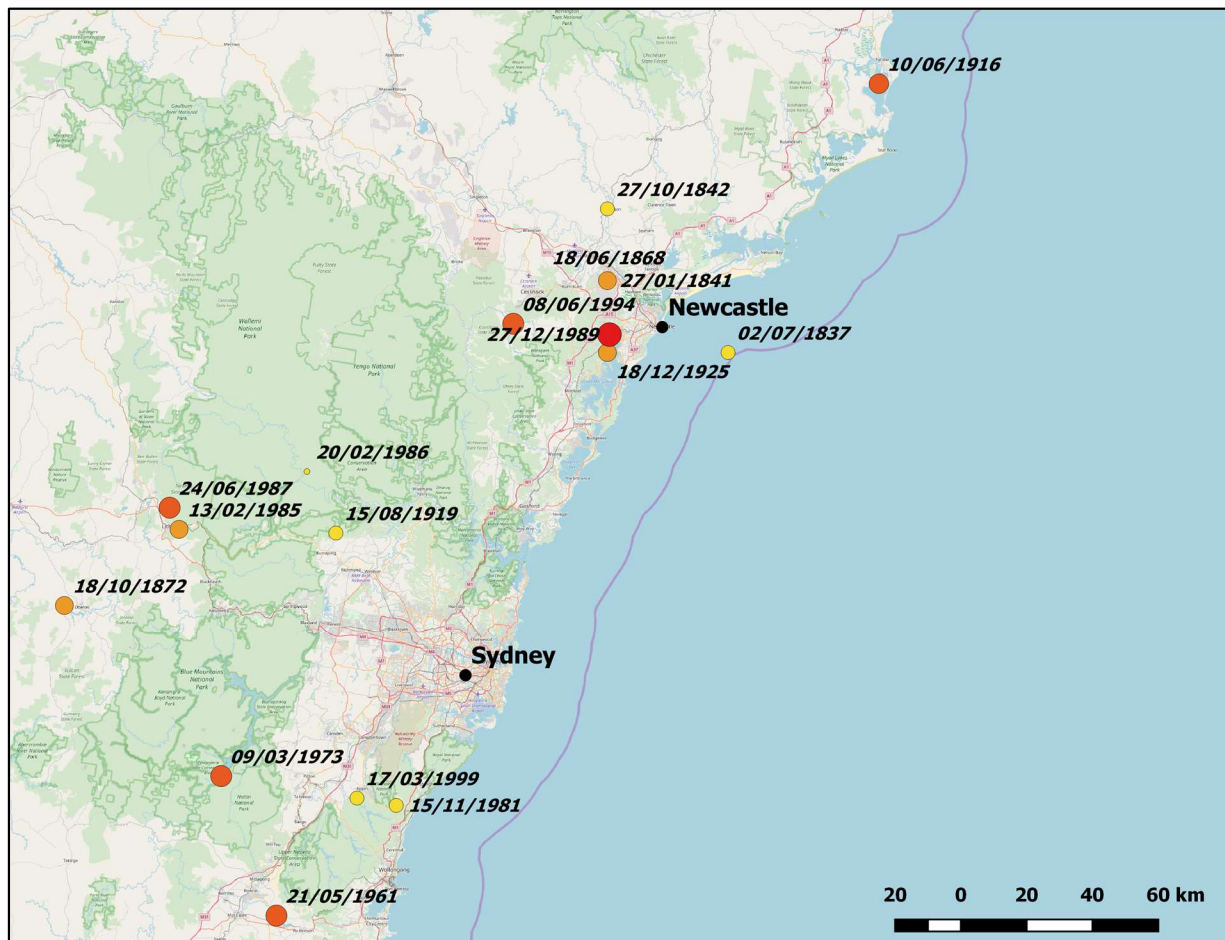


Figure A4.5.4. Significant earthquakes in the Hunter Valley between 1804 and 2002, according to data from Sinadinovsky *et al.* (2002). Colour scale and circle size indicate maximum macroseismic intensity, from IV (yellow, smaller) to VIII (red, larger).

A4.5.1.3 Seismic hazard

Figure A4.5.5 and Figure A4.5.6 show the 1991 and 2012 official seismic hazard maps for Australia, respectively, in terms of PGA on rock with 10% probability of exceedance in 50 years (Gaull *et al.*, 1990; Burbidge, 2012). The first map, which was published shortly after the 1989 Newcastle earthquake despite having been elaborated and accepted for publication before (Gibson & Dimas, 2009), indicates PGA values ranging between 0.10 and 0.12 g for the area around Newcastle, while the second shows significantly lower values between 0.05 and 0.06 g. This discrepancy is not surprising for this part of the world, given the uncertainties associated to active faults and seismicity in the region and the time lapse in between the two. Moreover, before the publication of the 1991 hazard map and before the 1989 earthquake, the area around Newcastle was classified as not requiring seismic design at all (Donaldson, 1990; Wilson *et al.*, 2008).

A recent local study carried out by Geoscience Australia for the area of Newcastle and Lake Macquarie shows much larger PGA values of 0.20-0.25 g on rock and 0.25-0.45 g on regolith for the same recurrence period (Dhu *et al.*, 2002). According to Gibson & Dimas (2009), the reason for these high values may lie in the earthquake recurrence model being based on

historical seismic activity extremely concentrated around the area, and the ground motion model used having been derived for continental shield regions, while Newcastle lies over much younger crust.

Table A4.5.1 summarises the values of PGA on rock with 10% probability of exceedance in 50 years according to different sources, including the Global Seismic Hazard Assessment Program (GSHAP) (Giardini *et al.*, 1999).

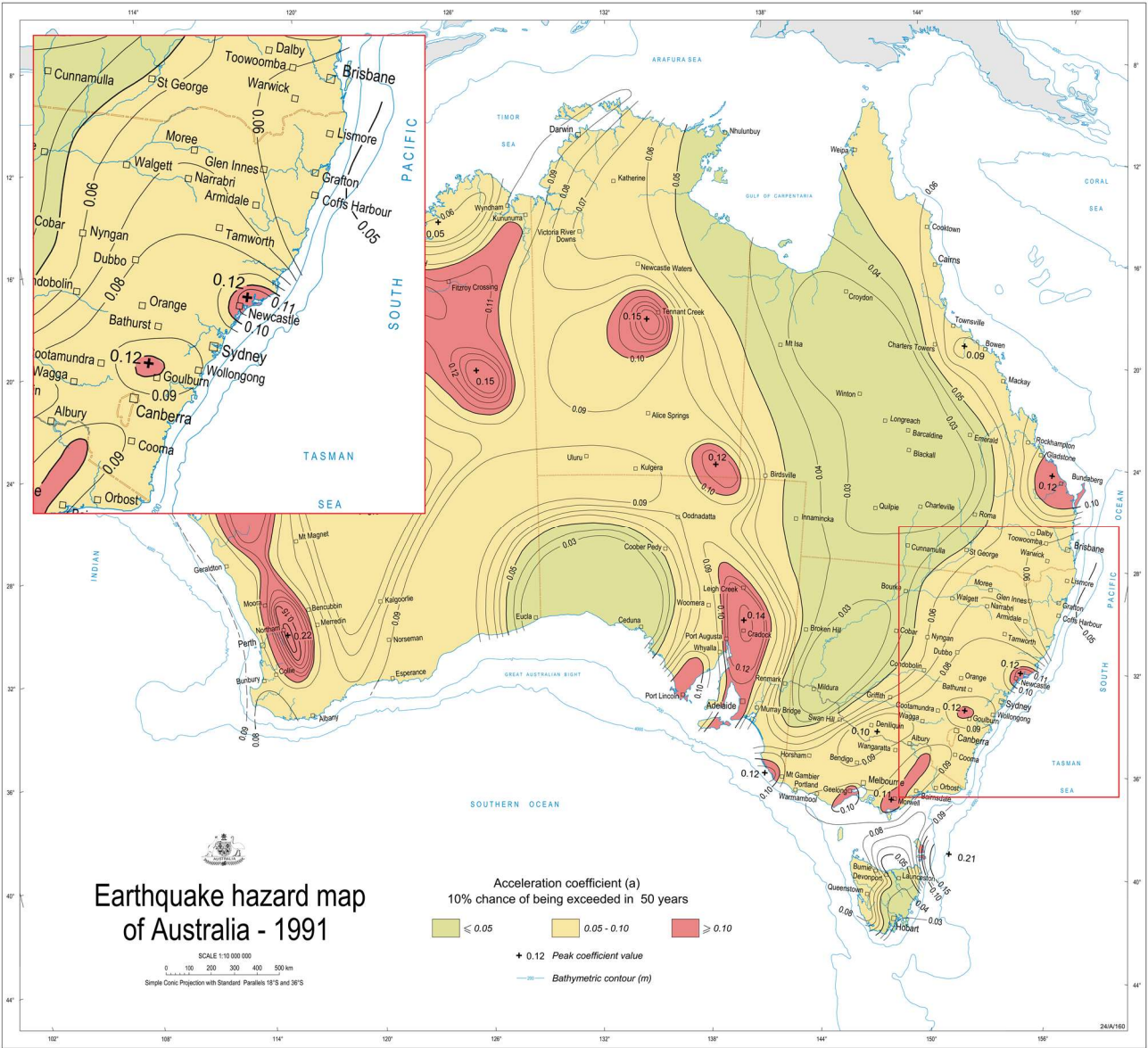


Figure A4.5.5. 1991 seismic hazard map for Australia (Gaull *et al.*, 1990) in terms of PGA on rock with a 10% probability of exceedance in 50 years. Inset on the top left shows a detail of the Newcastle area. Modified from Australian Government.

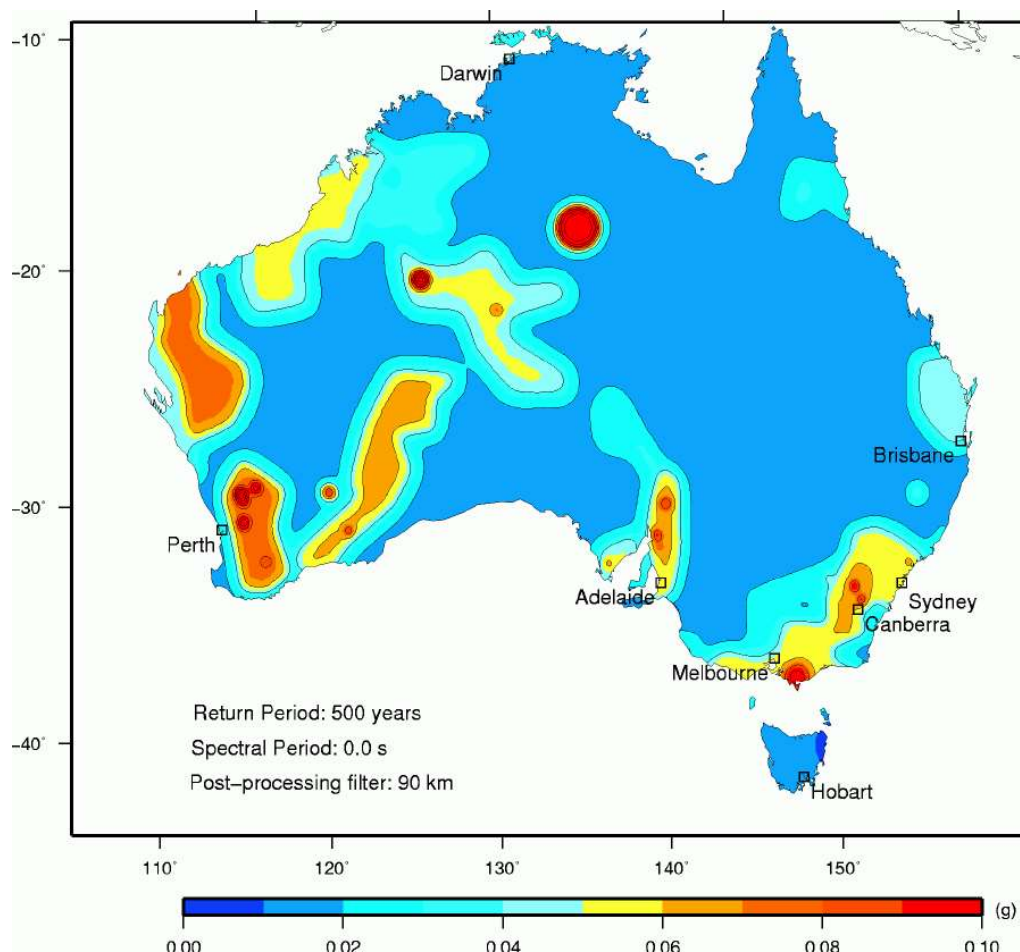


Figure A4.5.6. 2012 seismic hazard map for Australia (Burbidge, 2012) in terms of PGA on rock with a 500-year return period (approximately 10% probability of exceedance in 50 years). From Australian Government.

Table A4.5.1. PGA on rock with 10% probability of exceedance in 50 years in Newcastle according to different sources.

Place	Geoscience Australia		Dhu <i>et al.</i> (2002)	GSHAP
	1991	2012		
Newcastle	0.10-0.12	0.05-0.06	0.20-0.25	0.095

A4.5.2 Earthquake source characteristics

A4.5.2.1 Location, depth and time

The main shock occurred on 27th December 1989, at 23.27 UTC (28th December 1989, 10.27 local time).

Several organizations and agencies report their own estimations of the epicentral coordinates and hypocentral depth. The information reported in the websites of Geoscience Australia (GA), the National Earthquake Information Center (NEIC) of the United States Geological Service (USGS), and the International Seismological Centre (ISC) is summarized

in Table A4.5.2. Epicentral coordinates estimated by McCue *et al.* (1990) are also shown and the corresponding locations are shown on the map in Figure A4.5.7.

Table A4.5.2. Epicentral coordinates and hypocentral depths from different sources.

Agency / Publication		Latitude	Longitude	Depth (km)
GA	Geoscience Australia	32.946 °S	151.607 °E	11.0
NEIC	National Earthquake Information Center, USGS	32.967 °S	151.619 °E	10.0
ISC	International Seismological Centre	32.940 °S	151.562 °E	3.7
McCue <i>et al.</i> (1990a, 1990b)		32.950 °S	151.61 °E	11.5

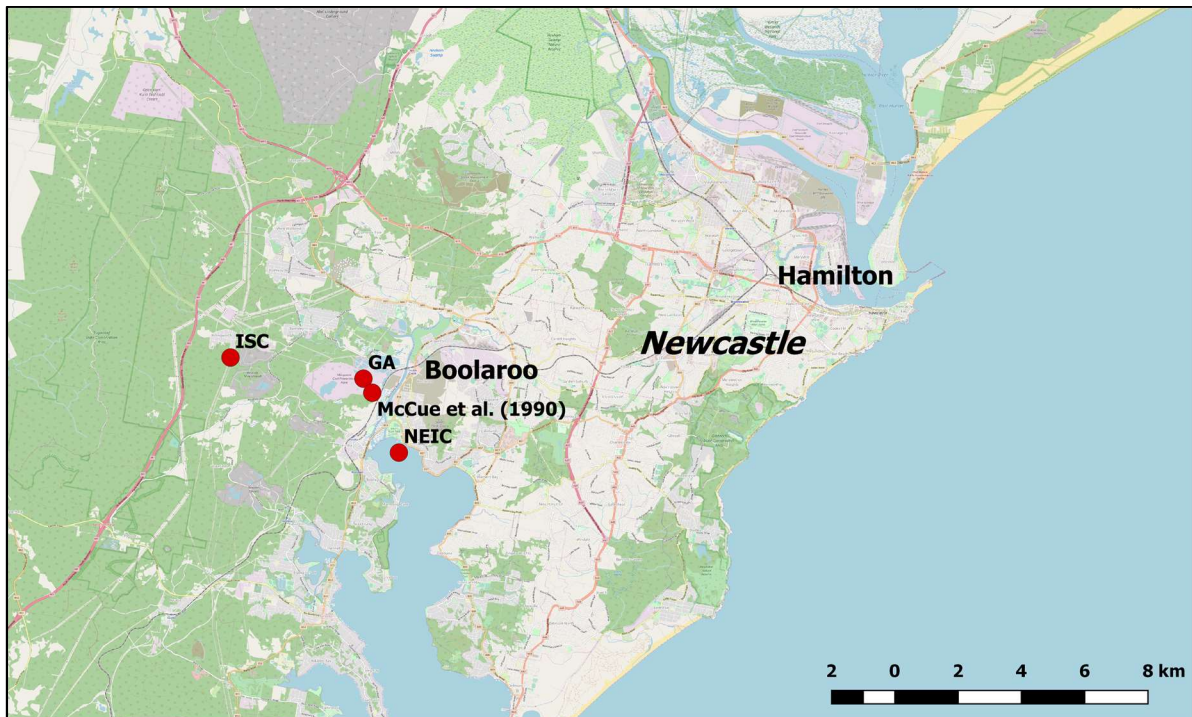


Figure A4.5.7. Estimation of epicentral coordinates.

Given the low coverage of the seismographic network in south-west Australia at the time, the closest seismograph being located 105 to the south of Newcastle, the epicentral coordinates reported in Table A4.5.2 entail large uncertainties. McCue *et al.* (1990a, 1990b) highlight that a 12- to 15-km uncertainty is associated to their estimate of latitude and longitude, while the depth carries a 0.5-km uncertainty as well. Nevertheless, the main shock is believed to have been located close to Boolaroo, as this location is close to a well-located aftershock, the mechanisms and depths of the two events are consistent, and the aftershock was felt in the area that was most damaged by the main shock (Gibson *et al.* 1990).

First believed to have been located within the inner-city suburb of Hamilton, the constraining of the hypocentral depth to 11.5 ± 0.5 km by means of teleseismic observations at the Eskdalemuir array in Scotland and the similarities between the depths calculated for the main shock and an aftershock played an important role in the relocation of the epicentre within Boolaroo (Sinadinovski *et al.*, 2002). Of the hypocentral parameters, the depth is the only one that can be considered to be relatively well constrained.

A4.5.2.2 Magnitude

Estimations of magnitude made by the same agencies and authors are reported in Table A4.5.3.

Table A4.5.3. Estimations of moment magnitude (**M**), body-wave magnitude (**mb**), surface-wave magnitude (**Ms**), and local magnitude (**M_L**).

Agency / Publication		M	mb	ML	Ms
GA	Geoscience Australia	5.4	5.7	5.5	4.6
NEIC	National Earthquake Information Center, USGS	-	5.4	-	-
ISC	International Seismological Centre	-	5.4	-	4.1
McCue <i>et al.</i> (1990a, 1990b)		-	-	5.6	-

A4.5.2.3 Style-of-faulting

This earthquake had a reverse mechanism (McCue *et al.* 1990a, 1990b), as shown in Figure A4.5.8 and Table A4.5.4. While the lack of surface faulting and a well-defined series of aftershocks do not allow to unequivocally define the fault plane, geomorphological considerations lead Gibson *et al.* (1990) to believe that the plane striking N150E and dipping steeply north-east corresponds to that of the fault, as its possible outcrop is consistent with the hills of suburban Newcastle and the submerged Lake Macquarie. The other plane would instead outcrop in an area with swamps and flat topography.

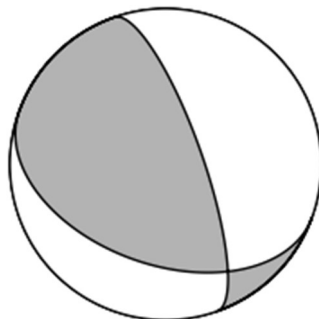


Figure A4.5.8. Focal mechanism of the main shock according to McCue *et al.* (1990a, 1990b).

Table A4.5.4. Focal mechanism solution. Nodal plane marked in grey is the preferred fault plane.

Nodal Plane 1			Nodal Plane 2			Source
Strike	Dip	Rake	Strike	Dip	Rake	
150	75	44	110	32	-	McCue <i>et al.</i> (1990a, 1990b)

A4.5.2.4 Stress drop

Based on studies of intraplate scaling for earthquakes of the central and eastern United States, Rynn *et al.* (1992) report that the stress drop may have probably ranged between 2.4 and 9.9 MPa.

A4.5.2.5 Foreshocks and aftershocks

According to McCue *et al.* (1990a, 1990b), there were almost no aftershocks to this earthquake, and the only one large enough in magnitude to be located was an M_L 2.1 that occurred on 29th December 1989 at 09.08 UTC at 13.6 km depth. According to Rynn *et al.* (1992), however, an additional M_L 2.9 took place on 23rd February 1990 west-south-west of the main shock, though they state that it was not strictly an aftershock. While they do not provide further explanation for their statement, it is likely to be due to it being located around 20 km away from the presumed NW-SE trending causative fault (*i.e.*, from the epicentres of the main shock and the 29th December aftershock), as shown in Figure A4.5.9. Nevertheless, Klose (2007) talks about two aftershocks, and the 23rd February event is briefly mentioned by Melchers (1990). Both of the shocks were felt (Rynn *et al.*, 1992). It is noted that the shock of 23rd February 1990 occurred six days after the end of the conference about the Newcastle earthquake in which McCue *et al.* (1990b) and many other authors presented their findings, rendering it impossible for it to be mentioned in the conference proceedings.

Rynn *et al.* (1992) mention the population having reported further tremors in the six months after the main shock, but none of these having been recorded by the local temporary seismograph.

No reference to any foreshocks has been found in the literature.



Figure A4.5.9. Location of earthquakes occurring after the main shock (orange circles). Red star indicates epicentre of main shock according to Geoscience Australia.

A4.5.2.6 Nature of earthquake

Based on a numerical simulation, Klose (2007) proposed that the Newcastle earthquake was the result of the dewatering of deep coal mines in the region that had been exploited for around 200 years. Quinn *et al.* (2008) challenge their view and argue that his idea is supported by neither the available geological and seismic data nor the numerical model, and that, in view of the regional seismic activity, the 1989 Newcastle earthquake was not an anomalous event. In particular, they believe that the areas surrounding the Hunter and Newcastle coal fields show no particular increase in seismic density or decrease in depth with respect to the rest of the region.

At the time in which the study by Klose (2007) was published, The Australian (2007) and ABC (2007) published the response of several Australian scientists who believed that the study cannot be considered conclusive, as the earthquake was not unusual for the seismicity of the area and it occurred farther away from the mines than is common for mining-induced earthquakes. Nevertheless, they do not discard the possibility of it having been induced but warn against considering it certain.

As the investigation of Klose (2007) has not been corroborated by other sources, this earthquake is classified herein as tectonic in origin.

A4.5.3 Geology and ground conditions in the affected area

A4.5.3.1 Regional geology and topography

The Sydney Basin, within which Newcastle is located (Figure A4.5.2), has a depth of approximately 5 to 6 km or 4 to 8 km (depending on the source) and lies over the continental crust of the Palaeozoic Lachlan Orogen, which is exposed to its west and south, and that of the Devonian-Triassic New England Orogen, which is exposed to its north, and from which it is separated at surface by the shallowly ENE-dipping Hunter-Mooki thrust system (Korsch *et al.*, 1997; Leaman, 1990; McCue *et al.*, 1990a; Quinn *et al.*, 2008). The region is dominated by a thrust system conformed by NW-SE to NNW-SSE trending structures.

The north-east corner of the Sydney Basin is a structural subdivision called the Hunter Valley Dome Belt and is bounded by the Hunter thrust to the north-east and a basement fault to the south-west whose projection at the surface marks the southern boundary of the Hunter Valley (McCue *et al.*, 1990a).

According to Gibson *et al.* (1990), the most relevant geomorphological structures in the immediate surrounding of the epicentre are the submerged valley of Lake Macquarie, which is located to the south-west of the city (to the south of Boolaroo in Figure A4.5.9), and the hills of the suburban areas of Newcastle to the east and south-east. Swamps dominate the terrain to the north-north-east, in the areas surrounding the course of the Hunter River (to the north and east of Hamilton in Figure A4.5.9).

A4.5.3.2 Site conditions in the affected area

According to Rynn *et al.* (1992), most of the city of Newcastle lies on alluvium deposited in the basin during the Pleistocene ice age that began 110,000 years ago and is still ongoing. These deposits consist of a combination of well-sorted and classified marine sands and poorly sorted fluvial sands, silts and muds, all Holocene (Quaternary) in age. In the broader area, marine sands and fluvial sediments (both Holocene as well) predominate along the coastal areas and inland, respectively. McCue *et al.* (1990a) make further reference to several meters of estuarine alluvial silt and sand covering a former course of the Hunter River and a swamp.

Based on results from a series of around 100 cone penetration tests (CPT) carried out by the University of Newcastle, Dhu *et al.* (2002) classified the area of Newcastle into six regolith site classes, as shown in Figure A4.5.10 and enumerated below (V_{s30} values obtained in an approximate fashion from a series of plots of idealised soil profiles by Dhu *et al.*, 2002):

- Class C: Weathered rock.
 - Maximum thickness 15 m.
 - V_{s30} around 1500 m/s.
- Class D: Silt and clay.
 - Maximum thickness 16.5 m.
 - V_{s30} around 235 m/s.
- Class E: Sand overlying silt and clay.
 - Maximum thickness 30 m.
 - V_{s30} around 300 m/s.
- Class F: Sand with interbedded silt and clay.
 - Maximum thickness 39 m.
 - V_{s30} around 180 m/s.
- Class G: Silt and clay with interbedded sand.
 - Maximum thickness 30 m.
 - V_{s30} around 350 m/s.
- Class H: Barrier sand.
 - Maximum thickness 30 m.
 - V_{s30} around 250 m/s.

Classes D through H overlay up to 15 metres of weathered rock.

By means of a series of equivalent linear analyses using different earthquake magnitudes and values of peak ground acceleration on bedrock, Dhu *et al.* (2002) calculated the amplification factors to be expected for the soil classes enumerated above. Their results, shown in Table A4.5.5, show amplifications of up to 1.5 for sites lying on weathered rock, and between 1.85 and 3.60 for those lying over all the rest of the soil classes.

Table A4.5.5. Peak median amplification factors for the soil site classes in Newcastle and Lake Macquarie and the periods at which they occur, for different input motions. From Dhu *et al.* (2002).

Rock Motion		Class C		Class D		Class E		Class F		Class G		Class H	
M	PGA (g)	T (s)	Max. Amp.	T (s)	Max. Amp.	T (s)	Max. Amp.	T (s)	Max. Amp.	T (s)	Max. Amp.	T (s)	Max. Amp.
4.5	0.05	0.06	1.50	0.25	2.95	0.67	3.17	0.91	3.32	0.40	3.17	0.67	3.60
4.5	0.10	0.06	1.50	0.26	2.81	0.67	3.02	0.91	3.20	0.40	3.06	0.71	3.38
5.5	0.05	0.06	1.50	0.25	2.61	0.71	2.87	0.91	3.03	0.40	2.81	0.71	3.23
5.5	0.10	0.06	1.50	0.26	2.49	0.71	2.74	1.00	2.90	0.42	2.69	0.77	3.00
5.5	0.25	0.06	1.50	0.28	2.30	0.83	2.58	1.11	2.67	0.45	2.51	0.91	2.70
6.5	0.05	0.06	1.49	0.25	2.59	0.67	2.52	0.83	2.59	0.40	2.74	0.71	2.72
6.5	0.10	0.06	1.50	0.26	2.47	0.71	2.40	1.00	2.41	0.42	2.62	0.77	2.48
6.5	0.25	0.06	1.50	0.28	2.29	0.83	2.17	1.25	2.12	0.45	2.39	1.00	2.15
6.5	0.50	0.06	1.50	0.30	2.09	1.00	1.95	1.67	1.90	0.53	2.13	1.25	1.85

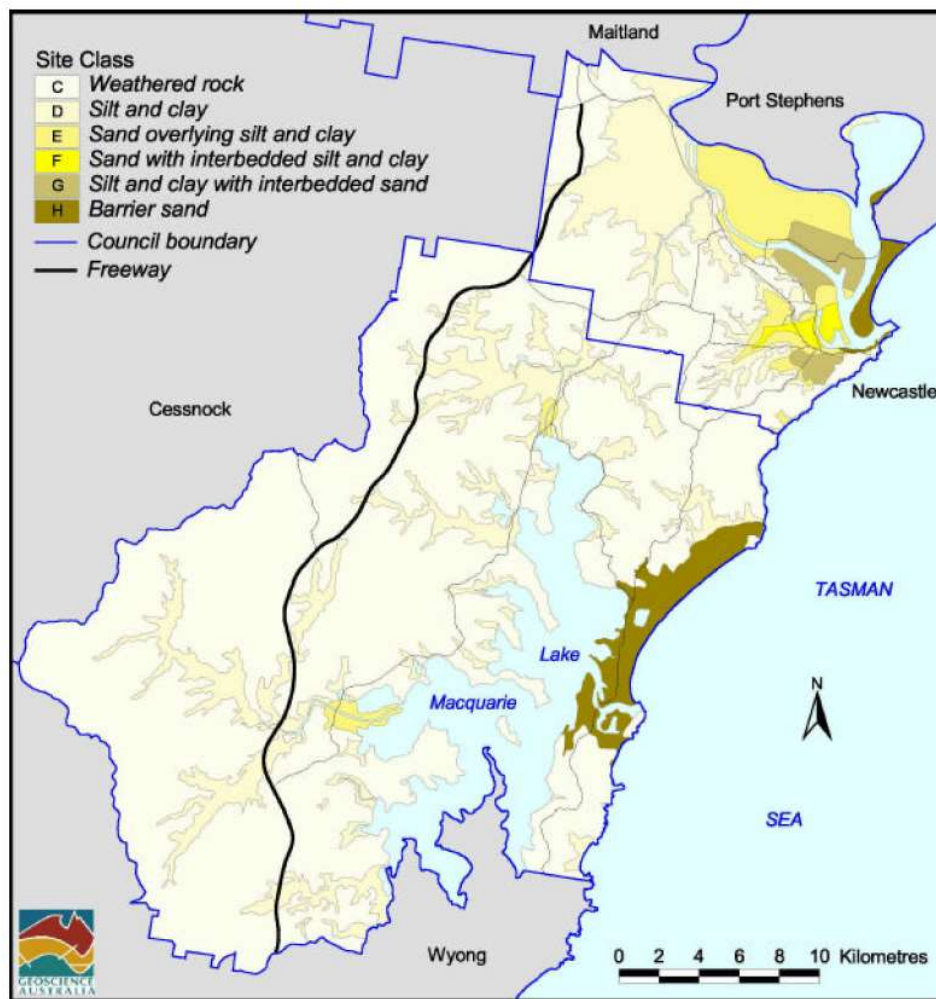


Figure A4.5.10. Soil classification of the Newcastle-Lake Macquarie area. From Dhu *et al.* (2002).

According to Rynn *et al.* (1992), the water table lies only within a metre of the surface. In view of this and the high contents of sand within the sediments of the area, it is concluded that liquefaction susceptibility in the area is high. Based on empirical relations between epicentral distance, PGA, Modified Mercalli Intensity, earthquake magnitude and liquefaction susceptibility, Rynn *et al.* (1992) suggests that liquefaction may have been possible in sites within 50 km from the epicentre, an affirmation that is supported by Melchers (1990).

A4.5.4 Ground motions

A4.5.4.1 Intensity observations

According to Sinadinovsky *et al.* (2002), the 1989 Newcastle earthquake was felt from Albury, Cooma and Bermagui, in the south, to Temora and Narromine in the west, and Coonabarabran, Inverell, Armidale, and Coffs Harbour in the north, up to 550 km from Newcastle. The area sustaining structural damage extended from Newcastle to Liverpool (Sydney) in the south (138 km), Scone in the north-west (145 km), and Gladstone (near Kempsey) in the north (320 km). The radius of perceptibility was about 310 km (Sinadinovsky *et al.*, 2002). The Modified Mercalli Intensity map elaborated by Rynn *et al.* (1992) and redrawn by Sinadinovski *et al.* (2002), which is shown in Figure A4.5.11, reaches values of MMI up to VIII in the Central Business District (CBD) of Newcastle and ranges generally between VI and VIII in all of the epicentral area.

Figure A4.5.12 shows the USGS ShakeMap (Worden *et al.*, 2017) in terms of Modified Mercalli Intensity for this event elaborated using 184 intensity points from the Geoscience Australia Isoleismal Atlas. Given that the ultimate source is Geoscience Australia, it is not clear why the maximum MMI reached is slightly below 7.4 instead of reaching 8 (VIII) as in Figure A4.5.11

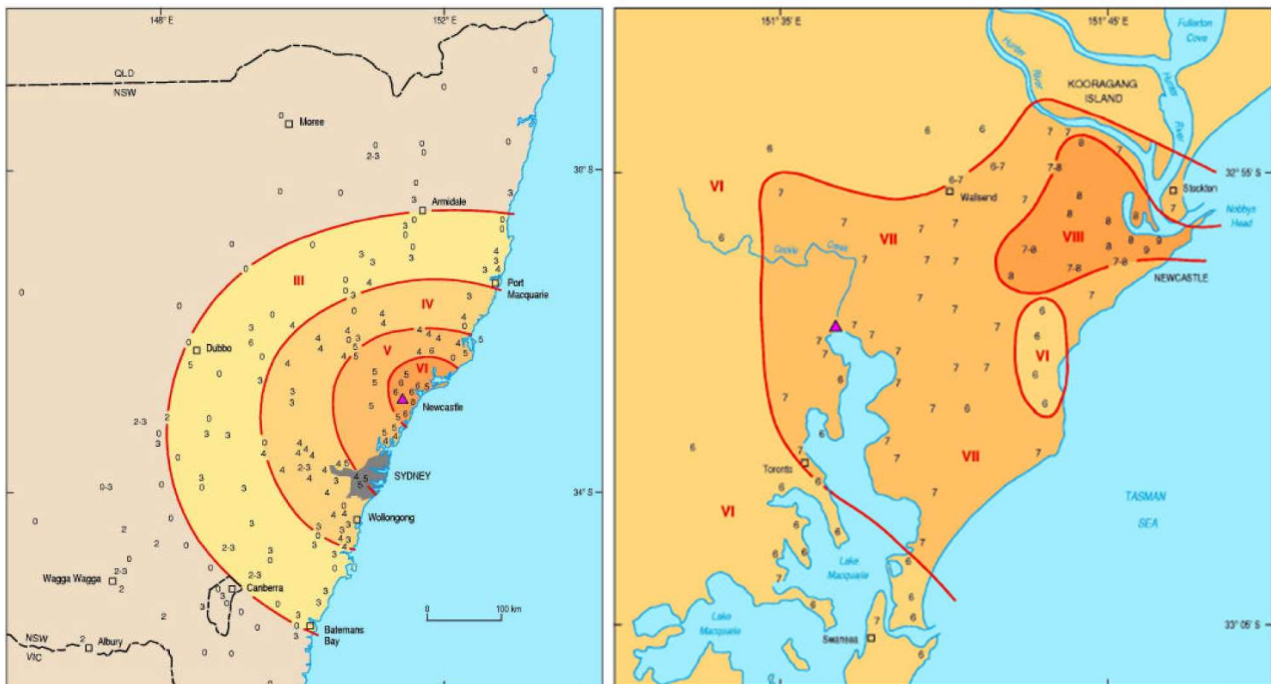


Figure A4.5.11. Modified Mercalli Intensity map for the 1989 Newcastle main shock: broader area (left) and epicentral area (right). From Sinadinovsky *et al.* (2002).

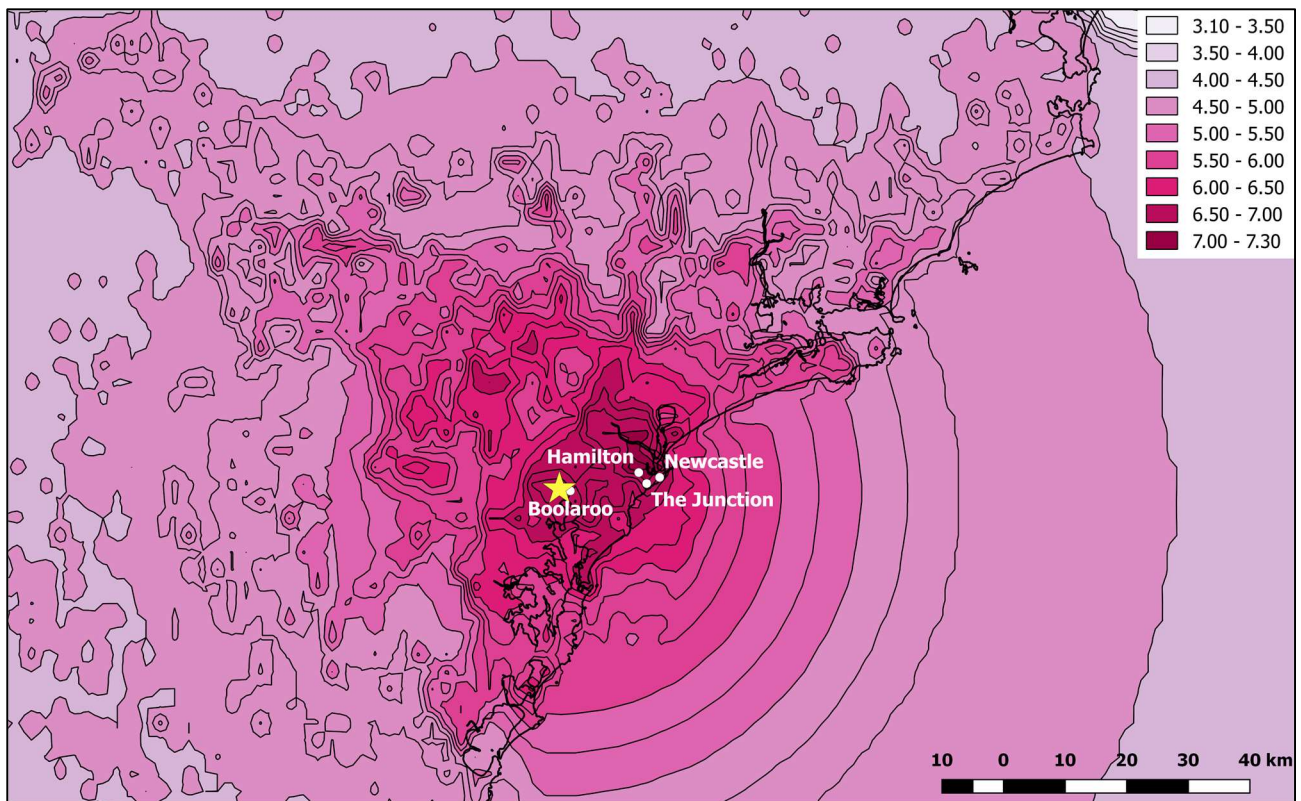


Figure A4.5.12. USGS ShakeMap in terms of Modified Mercalli Intensity. Yellow star indicates epicentre according to Geoscience Australia.

A4.5.4.2 Ground motion recordings

Information on ground motion recordings for this earthquake is scarce, as there were no strong motion recorders near Newcastle at that time (McCue *et al.*, 1990a). The nearest station consisted of a triaxial vibration recorder installed at Ellalong, approximately 30 km to the west of the epicentre, but that only recorded the first 3.6 seconds of shaking and missed the strongest ground motions (McCue *et al.*, 1990a).

A4.5.4.3 Inferred shaking levels

Sinadinovsky *et al.* (2000) generated synthetic accelerograms for the 1989 Newcastle main shock using the Green's function method and an accelerogram of the 29th December aftershock recorded on rock at an epicentral distance of around 20 km, which reached PGA values of only 0.01 g. As shown in Figure A4.5.13, the resulting ground motions reach a horizontal PGA of around 0.25 g in the N-S direction, which Sinadinovsky *et al.* (2000) regard as realistic, highlighting that this value was most likely further amplified by site effects. The E-W horizontal component and the vertical component reach 0.08 and 0.03 g, respectively. According to the corresponding 5% damped response spectra, values of up to 0.75 g could have been expected in the 0.2-0.45 seconds period range, without accounting for site amplification.

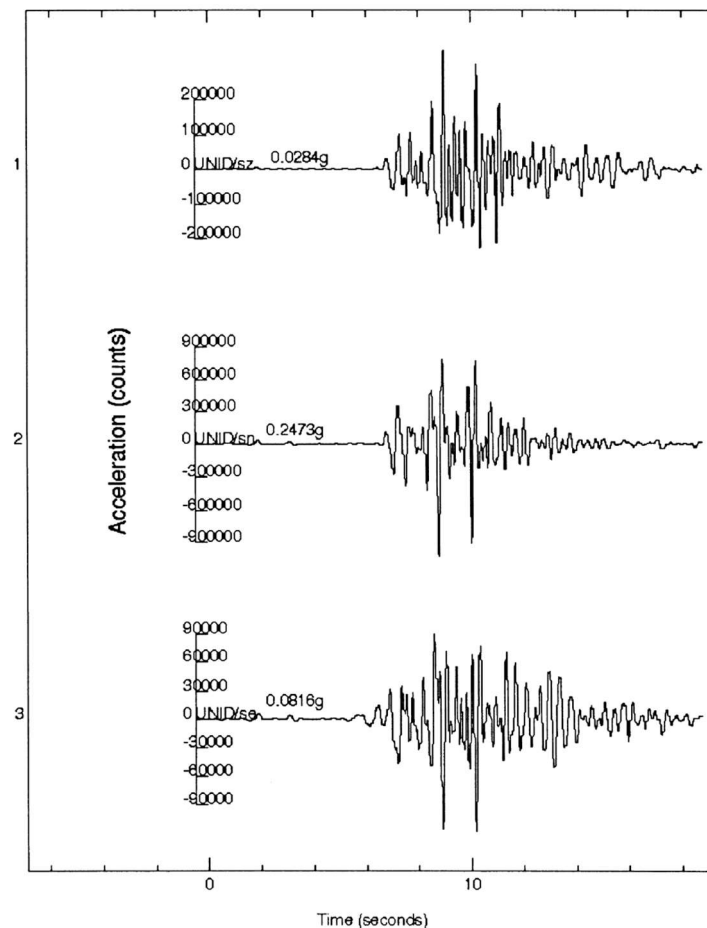


Figure A4.5.13. Synthetic accelerograms for the 1989 Newcastle main shock: vertical (top), N-S (centre) and E-W (bottom) components. From Sinadinovsky *et al.* (2000).

Figure A4.5.14 shows the USGS ShakeMap (Worden *et al.*, 2017) in terms of PGA, elaborated using the ground motion prediction equation of Campbell (2003) and converting MMI data points using the model of Atkinson & Kaka (2007). While the metadata summary of the USGS reports a maximum PGA of 0.29 g, the map itself only shows values up to 0.26 g. As these values already account for soil conditions, they may appear as low against the 0.25 g on rock obtained by Sinadinovsky *et al.* (2000). However, it is noted that the ground motion model of Campbell (2003) (and possibly the conversion equation of Atkinson & Kaka, 2007) predicts the geometric mean of two as-recorded horizontal components, while the geometric mean of the accelerograms generated by Sinadinovsky *et al.* (2000) is not known but would be 0.14 g in the most extreme scenario. Then, the amplification due to soil conditions would be $0.26 / 0.14 = 1.86$ for PGA.

From their extended series of ShakeMaps, the USGS reports predicted maximum spectral accelerations of 0.50, 0.31 and 0.07 g at periods of 0.3, 1.0 and 3.0 seconds.

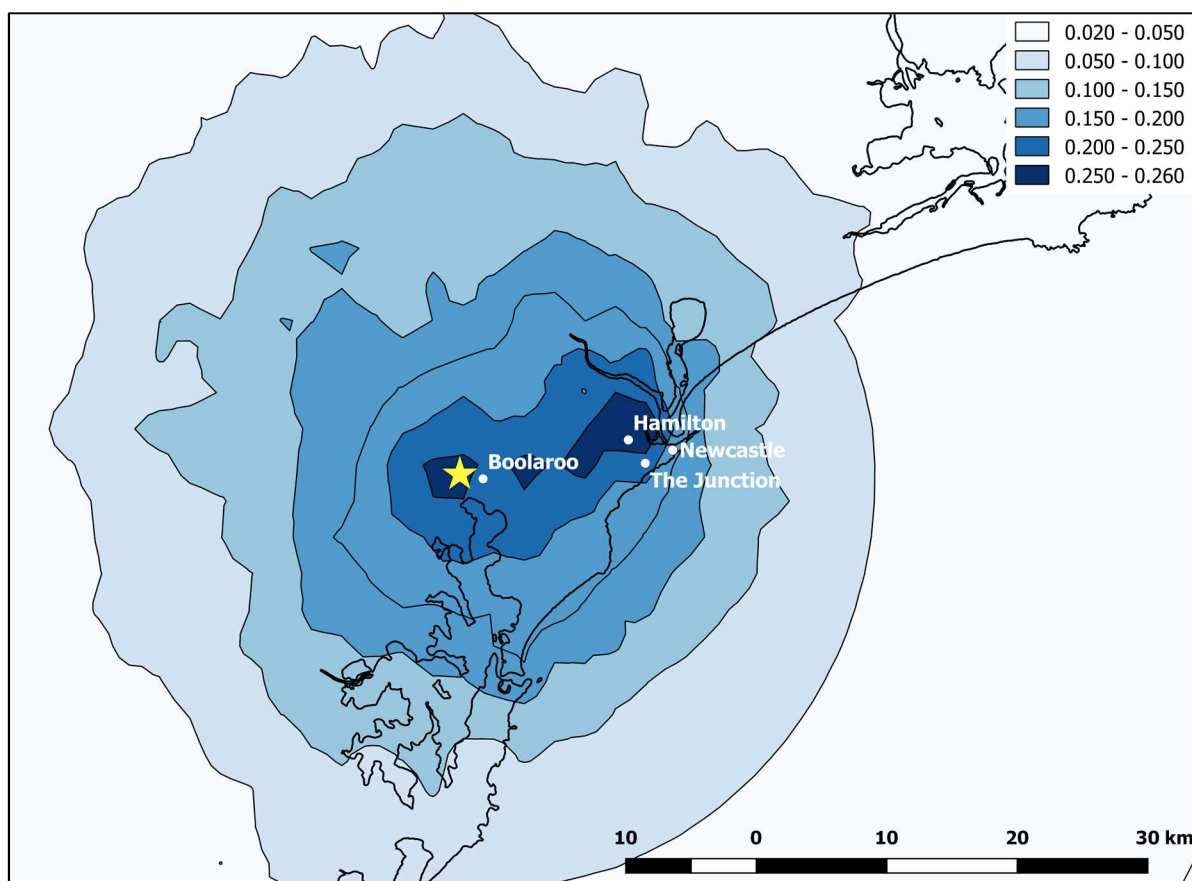


Figure A4.5.14. USGS ShakeMap in terms of Peak Ground Acceleration (PGA, g). Yellow star indicates epicentre according to Geoscience Australia.

A4.5.4.4 Duration of ground shaking

Collins & Jordan (1997) and Donaldson (1990) describe the earthquake as having a 10- to 12-second duration, while McCue (1990a) mentions that most observers in Newcastle describe the event more as an explosion rather than as an earthquake, with a duration of around 2-3 seconds. None of the three specifies the location. According to Sinadinovsky *et al.* (2002), the shaking was felt in Newcastle for around 5 to 6 seconds. Commenting on the possibility of occurrence of liquefaction, Walker (1991) points out that it was unlikely because of the short duration of the ground motion.

Estimations of earthquake significant durations can be obtained by means of prediction equations such as those of Bommer *et al.* (2009) and Afshari & Stewart (2016), whose results for the 5-75% of Arias intensity definition of significant duration are shown in Figure A4.5.15. As there is no precise information concerning the distances to which the durations reported above make reference to, a range of distances to the rupture are considered. For the model of Bommer *et al.* (2009), a depth to the top of the rupture of 9.1 km, resulting from a hypocentral depth of 11 km (Geoscience Australia) and a source radius of 1.86 km (Rynn *et al.*, 1992) was used. In view of the soil classes described in Section A4.5.3.2, three values of V_{s30} were considered: 180 m/s (lower bound, Class F), 1500 m/s (upper bound, Class C), and 350 m/s (intermediate value, class G). It is noted that the model of Afshari & Stewart (2016) does not change with V_{s30} values above 600 m/s. As can be observed in Figure A4.5.15, the duration of the ground motion within 20 km of the source is estimated to have

ranged between less than a second and 3.5 seconds, values that lie along the lines of those reported by McCue (1990a). In order to understand if larger values could have been expected, a much shallower depth to the top of the rupture of 1.8 km, resulting from considering a hypocentral depth of 3.7 km instead (ISC, see Table A4.5.2), was used together with the lower-bound V_{s30} value of 180 m/s in the model of Bommer *et al.* (2009). In this more extreme case, durations of up to 8.2 seconds are predicted at a distance of 50 km, but the prediction at around 20 km only rises up to 4.6 seconds. In any case, both the durations obtained by means of the two prediction models and those vaguely reported in the literature point at a short duration.

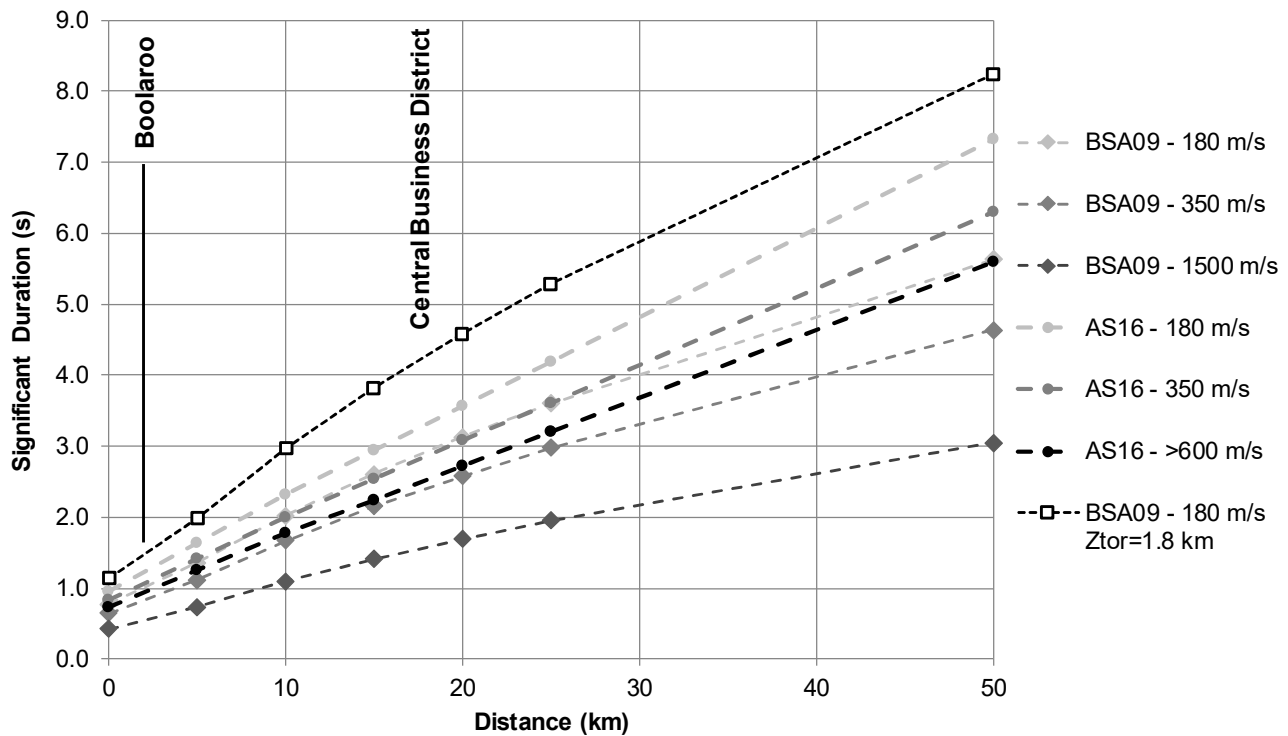


Figure A4.5.15. Estimation of significant duration of the main shock, using prediction equations by Bommer *et al.* (2009, BSA) and Afshari & Stewart (2016, AS). Depth to the top of the rupture (Z_{tor}) of 9.1 km except when noted otherwise.

A4.5.5 Collateral earthquake hazards

A4.5.5.1 Surface rupture

No evidence of surface rupture was found for this earthquake (e.g., Brunsdon, 1990; Clark *et al.*, 2012; Gibson *et al.*, 1990; McCue *et al.*, 1990a; Rynn *et al.*, 1992; Sinadinovsky *et al.*, 2002). As pointed out by the authors, this is consistent with any of the hypocentral depths reported in Table A4.5.2 and the estimation of Rynn *et al.* (1992) of a source radius of 1.86 km.

A4.5.5.2 Landslides

Landfill slumping and escarpment movements were observed in the period following the weekend of 2nd-3rd February 1990, which was characterized by a near-record deluge of rain. According to Brunsdon (1990) and Melchers (1990), these phenomena were not considered to be a direct consequence of the Newcastle earthquake. However, Melchers (1990) mention the occurrence of one landslide on the western side of a hill in Speers Point that caused some building damage, though no major details are provided.

A4.5.5.3 Liquefaction

Brunsdon (1990), McCue *et al.* (1990a) and Melchers (1990) reported that liquefaction was not observed in the form of sand boils or mud volcanoes, though Harkness & Hassanain (2002) attribute the differential settlements to which houses near the epicentre were subject to the loss of bearing capacity of the foundations due to the liquefaction of the soil beneath them. According to these authors, these houses had been built on landfill over a former swamp and, consequently, the water table was particularly high in the area. The affected houses presented cracks in masonry and bathroom tiles, and lack of appropriate alignment of doors, windows and floors. Melchers (1990) further mention the observation of surface settlements in Mayfield, relatively close to the main downtown area of Newcastle, and suggest these may be due to incipient liquefaction.

A4.5.5.4 Settlements

While McCue *et al.* (1990a) highlight the “almost complete lack of ground deformation” for this earthquake as surprising, Brundson (1990) mentions several reports of movement of damaged buildings for several weeks after the occurrence of the earthquake. However, according to McCue *et al.* (1990a), assessment of these cases reported by homeowners do not support this statement.

McCue *et al.* (1990a) and Melchers (1990) acknowledge, however, the occurrence of 5 cm of coseismic subsidence on the southern abutment of a bridge located 10 km north of Newcastle during the earthquake itself. Brundson (1990) make further reference to some instances of building damage having been originated or exacerbated by the collapse or settlement of underground workings from former mines that are currently filled with water. Melchers (1990) highlights that any instances of settlement that may have occurred were not considered a major problem.

A4.5.6 Exposed population

A4.5.6.1 Socio-economic setting

According to the 2016 Human Development Data (UNDP-HDD, 2016), the Human Development Index (HDI) for Australia was 0.866 in 1990 and 0.939 in 2015, while its Inequality-adjusted HDI (IHDI) was 0.861 in the 2016 Human Development Report (United

Nations, 2016). According to the 2015 world's ranking reported in 2016, Australia is located in the 2nd place, while the Netherlands ranks 7th. Table A4.5.6 compares the HDI and IHDI for both countries in 1990 and 2015. The columns "Adj. HDI" provides the HDI values given online (UNDP-HDD, 2016) for 1990, adjusted for data consistency in time.

Table A4.5.6. Human Development Index and Inequality-adjusted Human Development Index for Australia and the Netherlands. HDD: Human Development Data (UNDP-HDD, 2016). HDR: Human Development Report (United Nations, 2016).

Report	Data	Australia				Netherlands			
		HDI	IHDI	Rank	Adj. HDI	HDI	IHDI	Rank	Adj. HDI
HDD 2016	1990	-	-	-	0.866	-	-	-	0.830
HDR 2016	2015	0.939	0.861	2	-	0.924	0.861	7	-

The Newcastle region, or Hunter Valley region, was first settled in 1804 (Rynn *et al.*, 1992). During the 19th century, the main industries in the area were coal mining, sheep and cattle grazing, and wine production (Wilkinson, 2011). At the beginning of the 20th century, the government encouraged the development of steel and aluminium in the region, and at least six power plants were established between 1957 and 1985, making use of the extensive coal deposits in the area (Wilkinson, 2011). The region has experienced a shift from the primary and secondary industries towards the services sector since the mid-20th century (Wilkinson, 2011). The port is a fundamental part of the economy of the city of Newcastle and the region in general.

Table A4.5.7 presents a comparison between Australia and the Netherlands in terms of GDP, GDP per capita and unemployment rate. According to Wilkinson (2011), the gross regional product (GRP) of the Hunter region was 28.4 billion Australian dollars in 2006-2007 (around 22.7 billion USD), which represented 8% of the gross State product of New South Wales.

Table A4.5.7. Gross domestic product (GDP), GDP per capita and unemployment rate for Australia and the Netherlands, according to the World Economic Outlook Database (IMF, 2017).

Indicator	Units	Australia		Netherlands	
		1989	2015	1989	2015
Gross domestic product, current prices	Billions USD	308.28	2,420.16	254.54	750.70
Gross domestic product per capita, current prices	USD	18,201.62	37,653.28	17,141.77	44,322.83
Unemployment rate	%	6.18	10.38	5.67	6.89

A4.5.6.2 Population density and distribution

Figure A4.5.16 shows the distribution of the population in the Newcastle-Lake Macquarie region in 1996 (left) and 2015 (right). According to the Australian Bureau of Statistics, the total population for the Lake Macquarie local government area, *i.e.*, the region marked in Figure A4.5.16 (left), was 197,371 people in 2016 and 177,185 people in 2001, the oldest year for which data is available on their website. Harkness & Hassanain (2002) describe

Newcastle as a low density city. However, according to the EXPO-CAT database (Allen *et al.*, 2009), around 3 million people are estimated to have been exposed to Modified Mercalli Intensities of IV or larger, as shown in Figure A4.5.17. However, taking into consideration the macroseismic intensity maps of Figure A4.5.11, the total population values just reported and the offset in time of these, it can be inferred that the numbers in Figure A4.5.17 might be slightly overestimated, as a total of over 206,000 people are estimated to have been exposed to MMI VII or higher by the latter.

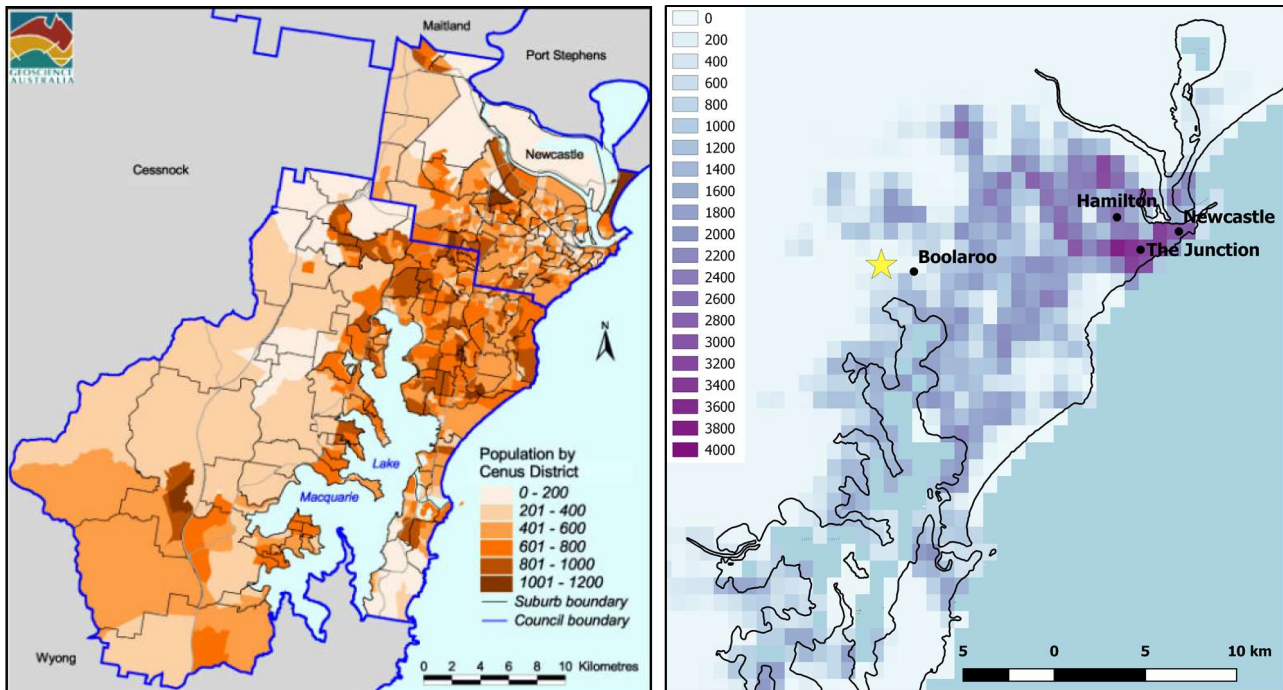


Figure A4.5.16. Population distribution in the Newcastle-Lake Macquarie by census collection district in 1996, from Stehle *et al.* (2002; left). Population density in 2015 in the same area (people/km²), according to data from Gridded Population of the World v4.0 (CIESIN, 2016).

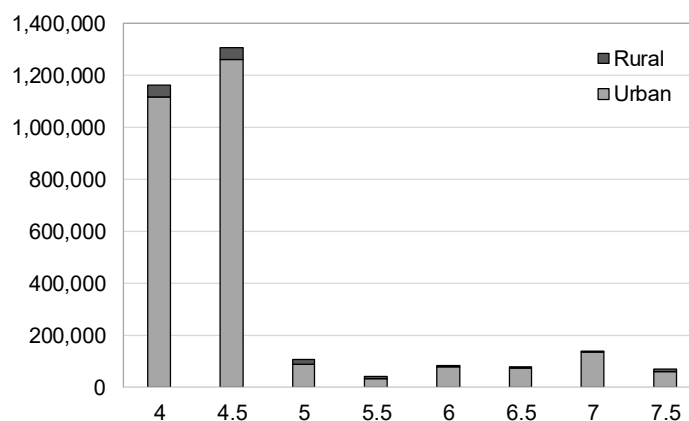


Figure A4.5.17. Estimation of total population exposed to different Modified Mercalli Intensities (MMI). Data from EXPO-CAT database (Allen *et al.*, 2009).

A4.5.6.3 Time of day of earthquake

This earthquake occurred on the morning of 28th December 1989, local time. Although it was a Thursday, in those days all schools, colleges and tertiary institutions (80-85% of the

workforce usually employed) were closed due to the holiday period between Christmas and New Year's Day. Moreover, Woodside & McCue (2016) report that there was an ongoing bus strike that day. Rynn *et al.* (1992) estimated that about 165,000 people (43% of the population) were away from their normal place of work or residence during the earthquake in the Hunter Valley region. Compared to the 13 deaths and around 100 injuries that resulted from this earthquake, the authors estimated 700-900 total deaths and between 6,800 and 10,000 people injured if the earthquake had occurred at the same time in the morning of a normal working day (Rynn *et al.*, 1992). Melchers (1990) highlights that many cases of masonry from parapets and façades falling onto school playgrounds, and that the consequences would have been devastating had there been children playing in them.

Harkness & Hassanain (2002) point out that the fact that the earthquake occurred during the morning was fortunate with regards to the consequences of the collapse of the Workers Club, as the auditorium would have had an audience present had the earthquake occurred at night. Daniell & Love (2010) report that a concert was scheduled for the night of 28th December (local time; *i.e.*, the night of the same day of the earthquake) at said auditorium, with an expected attendance of 2,000 people.

A4.5.7 Characteristics of exposed building stock

A4.5.7.1 Seismic design codes

According to Woodside & McCue (2016), it was only after the Second World War that the design of structures for seismic loads started in Australia, but only in areas such as the Territory of Papua New Guinea, where the Commonwealth Department of Works was designing buildings, dams, roads, airports and bridges at the time. It is believed that the first Australian document addressing seismic design was the Comworks Technical Instruction 5-A-21, which was published in 1961 but did not apply to Australia itself, even though a magnitude 5.6 earthquake had caused extensive damage and three injuries in Adelaide in 1954.

It was only after the 1968 magnitude 6.8 Meckering earthquake that awareness regarding the need for seismic design in Australia started to grow and the Australian National Committee for Earthquake Engineering (ANCEE) was formed with the purpose of working on the development of a code (Woodside & McCue, 2016; Wilson *et al.*, 2008). Though facing large resistance from the structural engineering community, the first Australian Earthquake Standard AS 2121 was finally published in 1979 (Woodside & McCue, 2016; Wilson *et al.*, 2008). Woodside & McCue (2016) describe AS 2121-1979 as a self-sufficient code, as it concerned both loading and design. It was applicable to common general-purpose structures but did not include bridges or special buildings or houses.

Dividing the country into a series of seismic zones (Figure A4.5.18), the area around Newcastle belonged to Zone 0, the lowest of all (Donaldson, 1990; Wilson *et al.*, 2008). This implied that structural design in Newcastle did not need to follow AS 2121-1979. Besides the seismic zonation introduced by the code, each Australian state or territory set up its own

regulations regarding the way in which structural design was controlled. According to Loveridge (1990), in the state of New South Wales (to which Newcastle belongs) there was at the time an ordinance (Ordinance 70) which stated that buildings erected in areas subject to seismic activity must be designed in accordance with the requirements of the Council, though it provided no specifications regarding how these requirements would be specified. In practice, the Council referred to AS 2121-1979 (Loveridge, 1990). However, AS 2121-1979 appears to have been generally ignored in the country as a whole (Woodside & McCue, 2016).

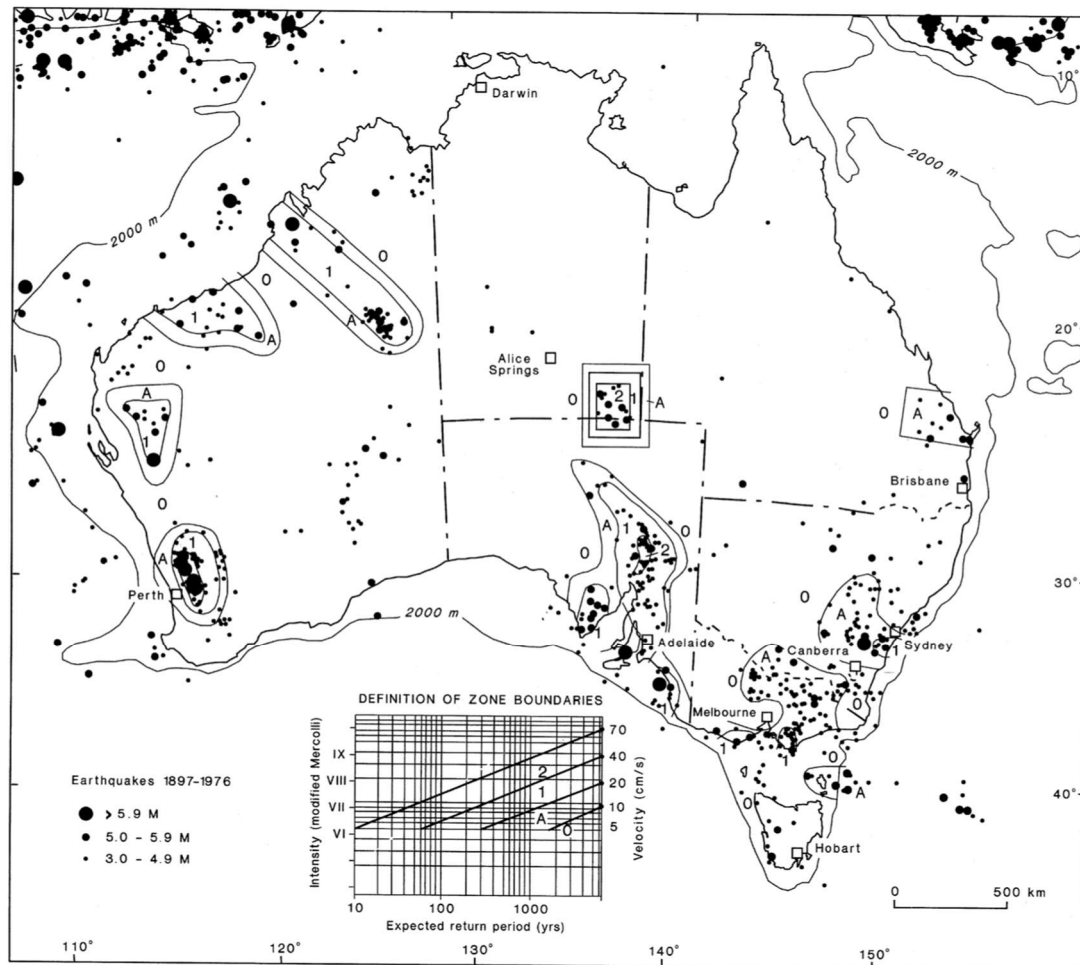


Figure A4.5.18. Seismic zonation map from AS 2121-1979. Zones marked with letters 0, A, 1 and 2, with increasing requirements for seismic design in that order. From Woodside & McCue (2016).

In 1988, Standards Australia decided to revise AS 2121. The new subcommittee met for the first time on 12th December 1989, around two weeks before the 1989 Newcastle earthquake, which became key in changing the perception of seismic risk in Australia (Woodside & McCue, 2016), to the point of having a specific chapter on recommendations for the revision of regulations in one of the main reports on the earthquake, edited by Melchers (1990). The new AS 1170.4 code, based largely on the American ATC-3-06 provisions (CITE), was first issued for public review in 1991 and was finally published in 1993 and adopted by the Building Code of Australia in 1994 (Woodside & McCue, 2016; Wilson *et al.*, 2008). Since then, the Australian Earthquake Loading Standard is updated roughly every 10 years, while the National Earthquake Hazard Map is updated every five (Burbidge, 2012).

A4.5.7.2 Building typologies

According to Stehle *et al.* (2002), many different typologies of buildings are present in the core of the old city of Newcastle, most of them dating back to the late 19th century, and fewer to the 20th. Not only are their construction types varied, including brick, timber, concrete, some stone and steel, but so too are their administrative, commercial, retail, cultural, residential, industrial and transportation functions. As a consequence of the lack of seismic design regulations for Newcastle before the 1989 earthquake (see Section A4.5.7.1), most of these buildings had not been designed for seismic loading (Bubb, 1990).

An extensive field survey of the building stock of the Newcastle and Lake Macquarie areas was carried out around the year 2001 within the context of the Australian Cities Project, to be used for the risk assessment study presented by Dhu & Jones (2002). One in every ten and twenty buildings were surveyed in inner and outer Newcastle, respectively, while a smaller rate was used for Lake Macquarie, with an overall 6,000 sites having been assessed in terms of position, use, age, stories, height, distance to nearest neighbouring building (important in terms of the potential for pounding in earthquakes between adjacent structures), plan regularity, vertical regularity, foundations, walls, roof, windows, window protections, awnings, brick chimneys, brick parapets, brick fences, gable roof with brick ends, soffit, water tank, ventilator, and the material and geometry of secondary structures (Stehle *et al.*, 2002). Figure A4.5.19 and Figure A4.5.20 depict the spatial distribution of surveyed buildings, classified according to the material of their external walls. As can be observed, brick and timber appear to be the most common categories, with the former being more popular to the East of the Newcastle area and the latter gaining relevance towards the West. From the observation of similar maps of Stehle *et al.* (2002) related to the material of the roofs, it appears that tiles and metal are the most common in all areas.

Stehle *et al.* (2002) further mapped the distribution of vulnerable buildings and building components in the area. From the resulting maps it can be observed that gable roofs, buildings with vertical irregularities, and suspending awnings seem to be quite common in the downtown areas of Newcastle, while brick chimneys taller than 2 metres seem to dominate the scene to the south-west of the urban area, north-east of Lake Macquarie. Brick pier foundations are very common in all areas.

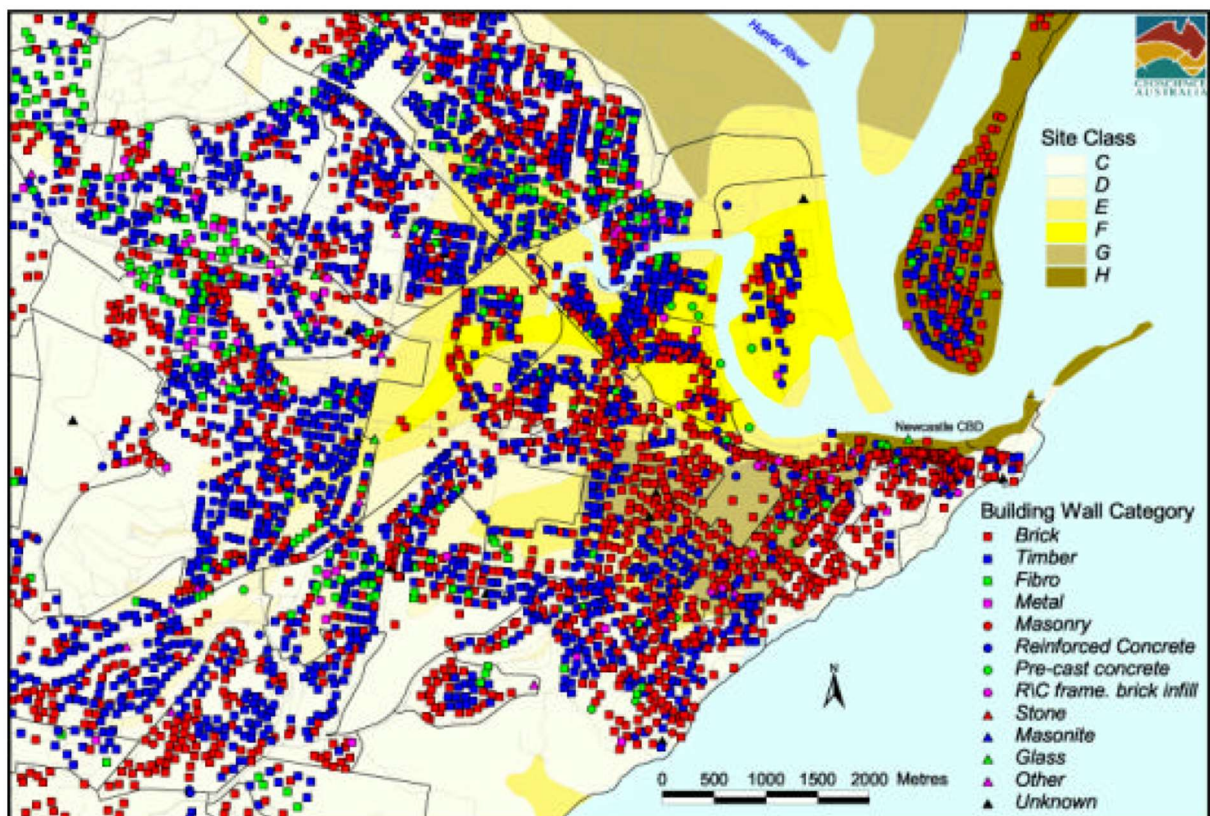


Figure A4.5.19. Distribution of buildings in the Newcastle area according to external wall type. From Stehle et al.(2002).

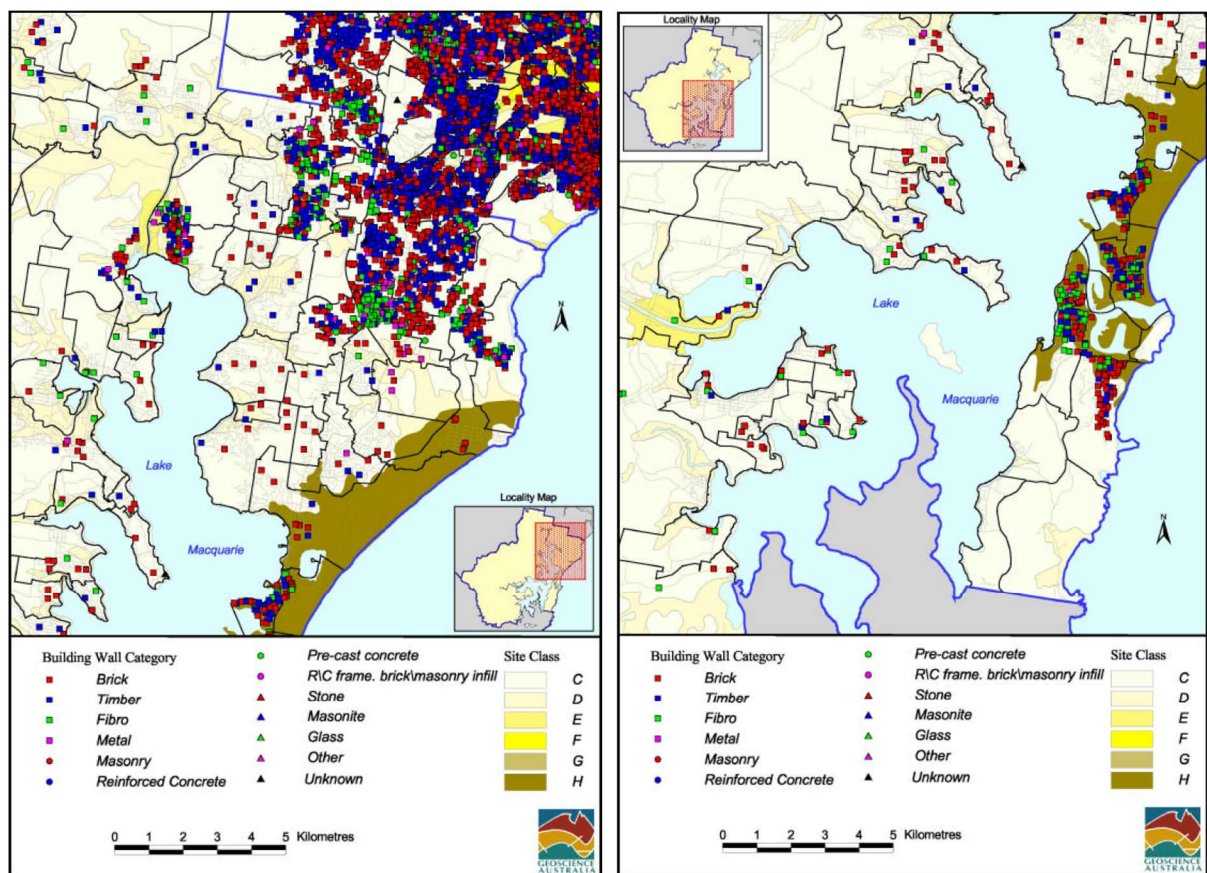


Figure A4.5.20. Distribution of buildings in the northern (left) and southern (right) Lake Macquarie area according to external wall type. From Stehle et al.(2002).

Based on the information that could be gathered from the exterior of these buildings, such as external cladding and estimation of its construction date, Stehle *et al.* (2002) classified the surveyed buildings according to HAZUS structural class definitions. The opinion of experts and knowledge on the evolution of construction techniques in time were used to compensate for the uncertainties associated with inferring structural typologies from such scarce information, an outstanding example of which is that of determining whether the structure of a building with a brick façade is unreinforced masonry, a timber frame or a reinforced concrete frame. Table A4.5.8 shows the assumptions made by Stehle *et al.* (2002) for this particular case.

Table A4.5.8. Classification of building type given an exterior brick skin.

Age	Unreinforced Masonry	Timber Frame (Brick Veneer)	Reinforced concrete frame with masonry infill (if above 2 storeys)
Up to 1900	100%	0%	0%
1901 up to 1939	100%	0%	0%
1931 up to 1950	90%	10%	0%
1951 up to 1960	80%	20%	100%
1961 up to 1970	10%	90%	100%
1971 up to 1980	1%	99%	100%
1981 up to 1990	1%	99%	100%
1991 up to 2000	1%	99%	100%
Under Construction	1%	99%	100%

The typologies existing in the Newcastle and Lake Macquarie areas, together with their corresponding number of building counts, are summarised in Table A4.5.9 and Figure A4.5.21 (left). In order to ease visualization, the plot on the right of Figure A4.5.21 shows the proportion of categories other than wood frames and unreinforced masonry for a total of 297 surveyed buildings. Figure A4.5.22 through Figure A4.5.24 show the resulting spatial distribution of the buildings per HAZUS structural typology. According to Melchers (1990), 2- and 3-storey buildings are mainly concentrated in the Central Business District (Figure A4.5.23) and some of the surrounding suburban shopping districts. As Stehle *et al.* (2002) checked the quality of the sampling of the building survey against census data from 1996 and concluded that the level of agreement was sufficiently reasonable, it is believed that these proportions and distributions could be considered representative of the overall building stock in 2001. It is clearly noted, however, that the situation in 1989 is not expected to have been exactly the same.

According to these statistics, the most common construction types in Newcastle are low-rise (*i.e.* one- to three-storey) timber frames (around 75% of the total), followed by low-rise unreinforced masonry (URM) (around 19% of the total), examples of which are shown in Figure A4.5.25 and Figure A4.5.26. Timber frames can be cladded with more timber, fibreboard or brick veneer, being the latter usually difficult to distinguish from load-bearing masonry constructions (Maqsood *et al.*, 2016). Cavity brick masonry appears to be the most common form of unreinforced masonry residential structure and typically consist of an external masonry wythe that can be load-bearing or not, an internal load-bearing masonry

wythe, and a tiled or metal roof, in many cases with discontinuous stone or brick footings (e.g., Melchers, 1990). Both brick veneers and brick cavity walls were usually bonded with lime mortar.

Table A4.5.9. Classification of the surveyed buildings according to HAZUS structural types (RC: reinforced concrete). From Stehle *et al.* (2002).

HAZUS Structural Type	Description	Storeys	External wall	N° of Buildings
W1	Wood, Light Frame	1 - 2	Timber, Fibro, Masonite, Brick, Metal	4711
S1L	Steel Moment Frame	1 - 3	Metal	6
S1M	Steel Moment Frame	4 - 7	Metal	1
S1H	Steel Moment Frame	>7	Metal	1
S3	Steel Light Frame	1	Metal	28
C1L	RC Moment Resisting Frame	1 - 3	Glass. Reinforced concrete.	64
C1M	RC Moment Resisting Frame	4 - 7	Glass. Reinforced concrete.	13
C1H	RC Moment Resisting Frame	>7	Glass. Reinforced concrete.	6
C2L	Concrete Shear Walls	1 - 3	Glass. Reinforced concrete.	19
C2M	Concrete Shear Walls	4 - 7	Glass. Reinforced concrete.	5
C2H	Concrete Shear Walls	>7	Glass. Reinforced concrete.	4
C3L	Concrete Frame Buildings with Unreinforced Masonry Infill Walls	1 - 3	RC Frame with Brick/Masonry Infills, Brick	83
C3M	Concrete Frame Buildings with Unreinforced Masonry Infill Walls	4 - 7	RC Frame with Brick/Masonry Infills, Brick	21
C3H	Concrete Frame Buildings with Unreinforced Masonry Infill Walls	>7	RC Frame with Brick/Masonry Infills, Brick	16
PC1	Precast Concrete Tilt-Up Walls	Any	Pre- Cast Concrete	30
URML	Unreinforced Masonry Bearing Walls	1 - 2	Masonry, Stone and Brick	1218
URMM	Unreinforced Masonry Bearing Walls	>3	Masonry, Stone and Brick	89

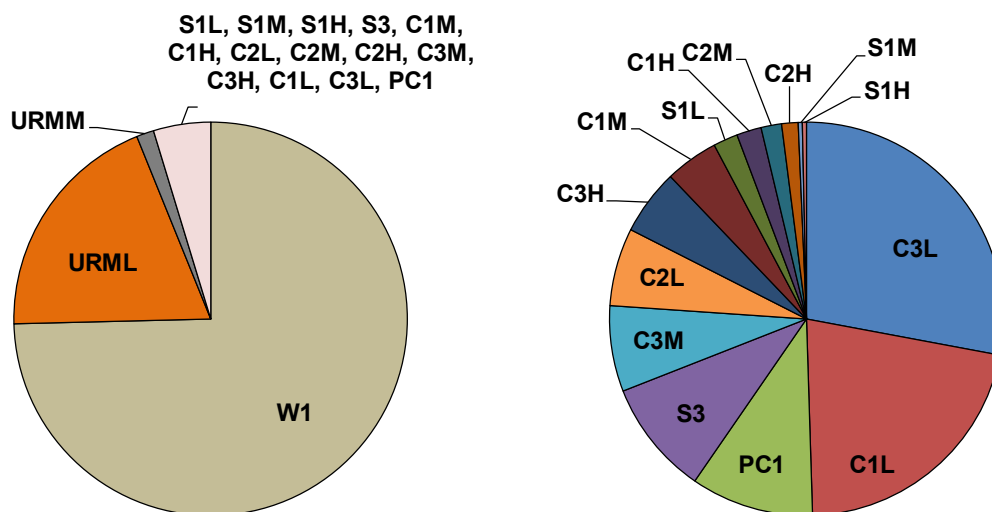


Figure A4.5.21. Distribution of surveyed buildings according to HAZUS structural typologies: all typologies (left) and typologies other than wood frames and unreinforced masonry (right).

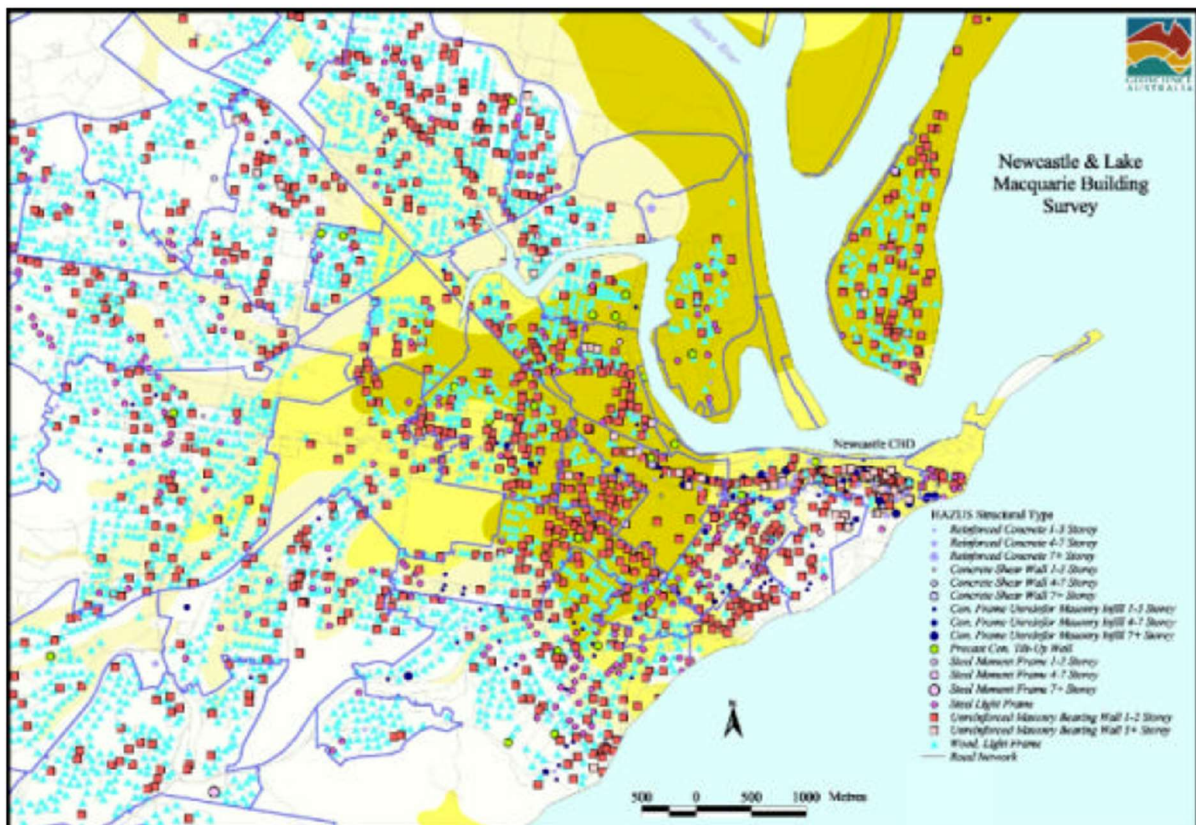


Figure A4.5.22. Distribution of HAZUS building structural types in Newcastle area. Cyan triangles: wood light frame; red squares: 1- and 2-storey unreinforced masonry. From Stehle et al. (2002).

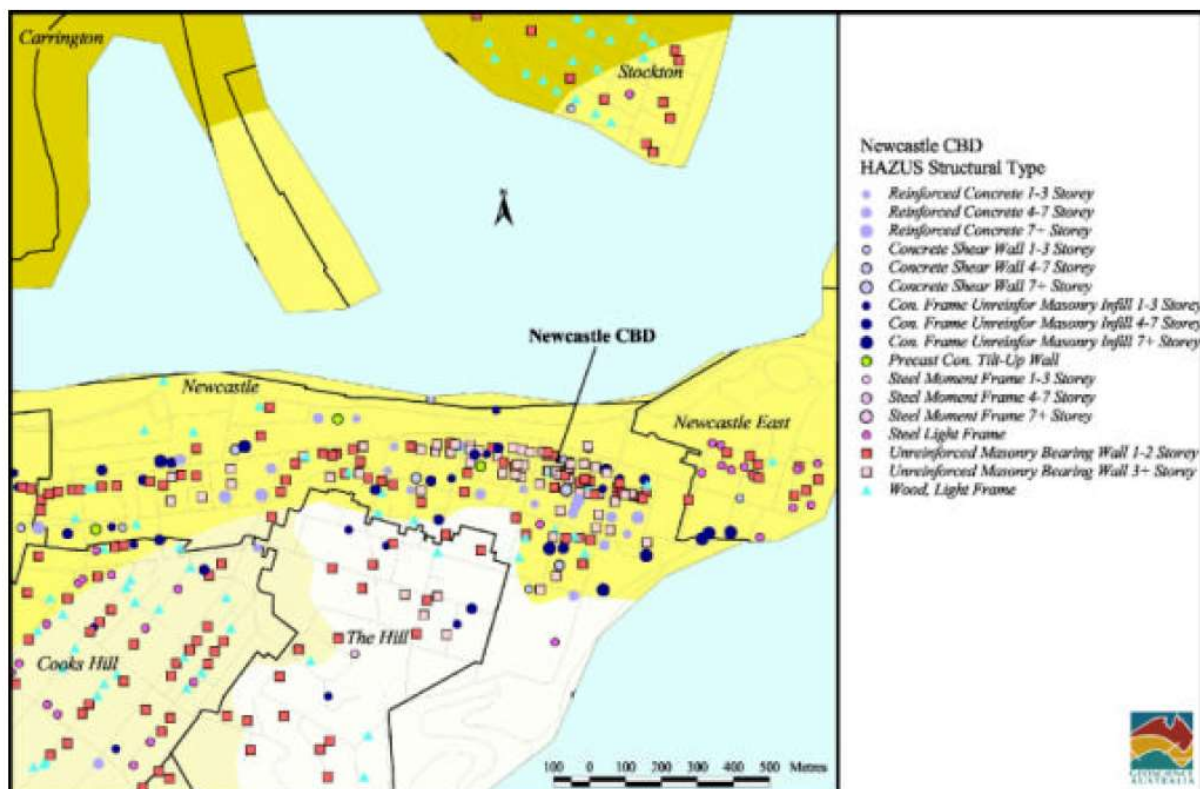


Figure A4.5.23. Distribution of HAZUS building structural types in the Newcastle Central Business District (CBD). From Stehle et al. (2002).

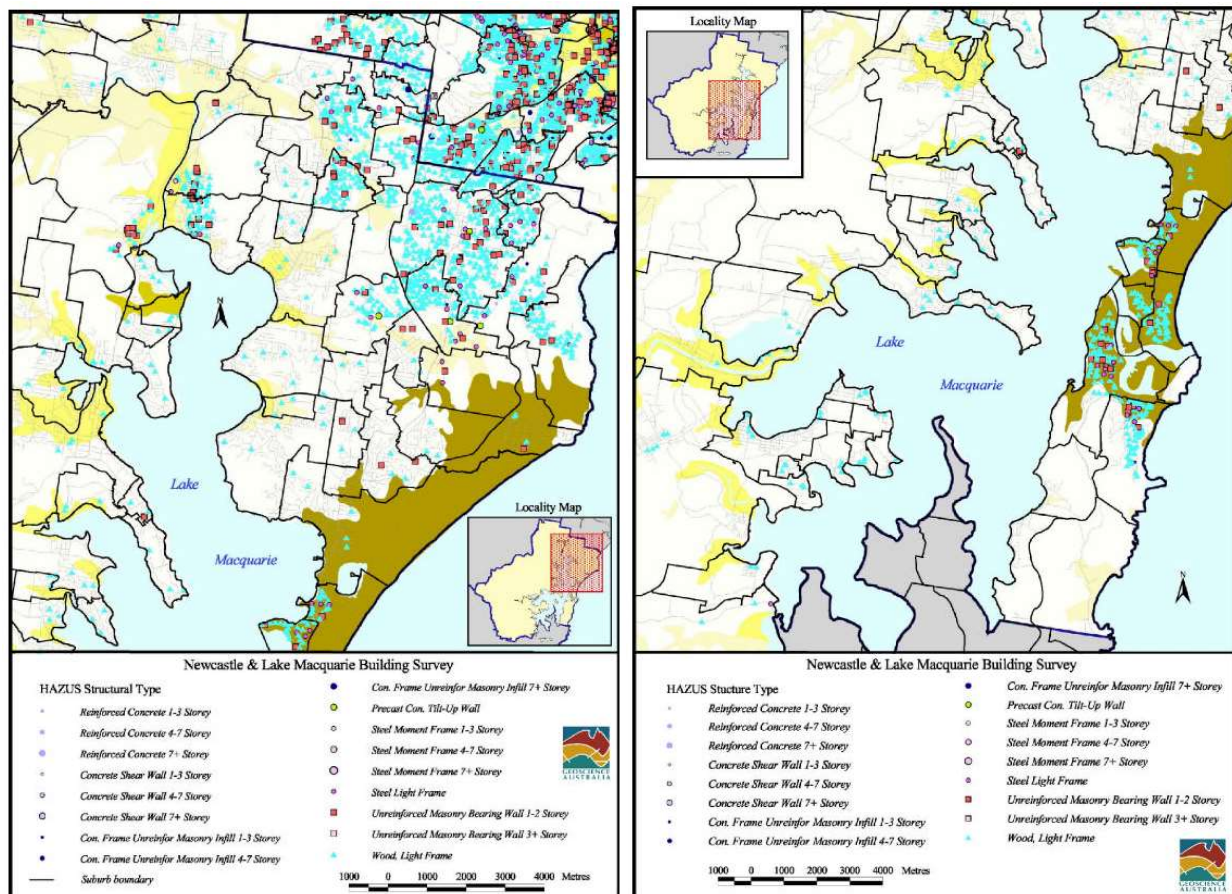


Figure A4.5.24. Distribution of HAZUS building structural types in the northern (left) and southern (right) Lake Macquarie area. Cyan triangles: wood light frame; red squares: 1- and 2-storey unreinforced masonry. From Stehle *et al.* (2002).



Figure A4.5.25. Examples of unreinforced masonry structures: (a) pre-1945 brick commercial building, (b) post-1945. From Maqsood *et al.* (2016).

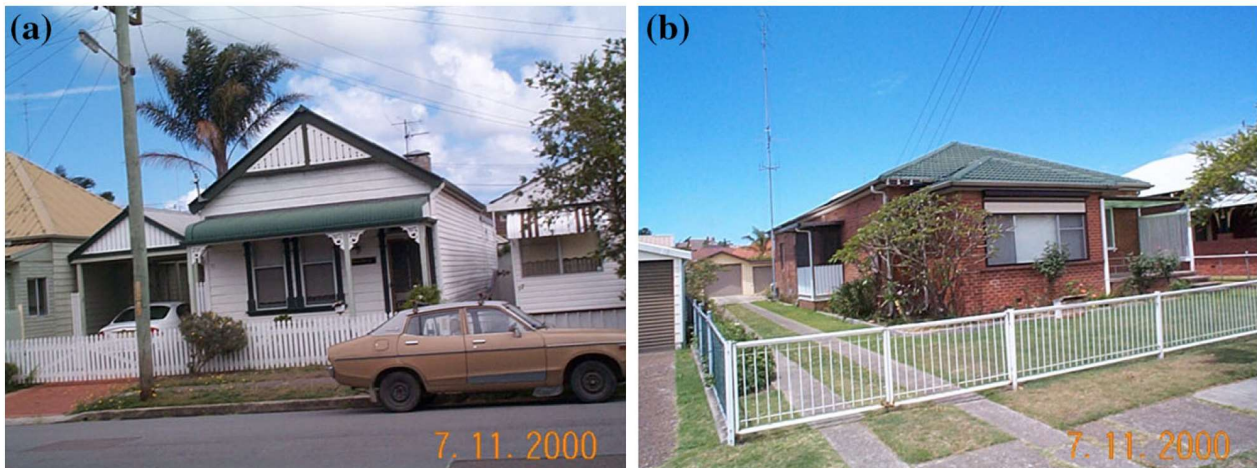


Figure A4.5.26. Examples of timber structures: (a) pre-1945 timber frame building, (b) post-1945 timber frame building (brick veneer). From Maqsood et al. (2016).

A4.5.7.3 Prior damage and retrofit

Donaldson (1990) states that many old homes in the inner suburbs of the city of Newcastle as well as the Christ Church Cathedral presented, in 1989, defects and repairs directly attributable to the 1925 Boolaroo earthquake (M_L 5.0). Similarly, Harkness & Hassanain (2002) report to have found evidence of “what appeared to be repairs” from this same earthquake in several old buildings during the participation of one of the authors in a post-disaster survey. None of the two sources provide any further details.

Ties linking external masonry wythes with either their internal counterparts (cavity brick walls) or timber frames (brick veneers) were found to be largely corroded, and lime mortar to be weathered (e.g., Melchers, 1990). This aspect is further discussed in Section A4.5.8.3.

A4.5.8 Damage observations

A4.5.8.1 Damage states

Most of the information on the damage caused by the 1989 Newcastle earthquake to around 5,000 buildings was collected by the Newcastle City Council following the colour classification shown in Table A4.5.10.

Table A4.5.10. Damage coding system. From Stuart (1990) and Melchers (1990).

Building Classification	Description
Red	Immediate public danger
Amber	Severe damage, possible danger, access required
Blue	Damaged but habitable
Green	Minor damage

Based on the relationship between Modified Mercalli Intensity and damage to masonry structures described in Table A2.3.2 of Appendix II, the reported maximum MMI values of VIII would imply damage to the two lowest quality masonry classes in the scale, even getting to partial collapses, no damage to the highest quality masonry (reinforced, well designed and constructed), and some damage to reinforced masonry with good workmanship and mortar, but not designed to resist earthquake loading.

A4.5.8.2 Damage statistics and description

Revisiting the 1989 Newcastle earthquake after 13 years, Harkness & Hassanain (2002) provide the following very synthetic statistics on damage:

- 50,000 buildings damaged, including 147 schools and 3,000 commercial buildings.
- 300 buildings were demolished, more than one third of them were homes.
- 1,000 homeless people.

These figures agree with what is reported on the Earthquake Collection website of the Newcastle Region Library, which adds that approximately 40,000 of the 50,000 buildings were homes. Woodside & McCue (2016) appear to agree with Harkness & Hassanain (2002) in the 147 schools and 3,000 commercial and other buildings but report overall damage to more than 35,000 homes, a number slightly below that reported by the Newcastle Region Library. According to Woodside & McCue (2016), between 300 and 400 people were housed in temporary accommodation at the peak of the post-earthquake crisis.

In what follows, the report edited by Melchers (1990) is taken as the main guideline for the description of the observed damage, as it collects the efforts of all the teams and people involved in the post-earthquake assessment. It is, however, noted, that a large part of what is reported by Melchers (1990) is contained as well in smaller papers presented at the Conference on the Newcastle Earthquake held in February 1990, the most relevant of which are those of Stuart (1990, general statistics), Pedersen (1990, commercial buildings), Bubb (1990, Council buildings), Loke (1990, institutional buildings), Nichols (1990, churches), Page (1990, patterns of failure), and Donaldson (1990, residential buildings).

According to Melchers (1990), at least 10,000 buildings within the district of Newcastle itself (which appears to include only the Central Business District and additional areas of comparable size, e.g. Figure A4.5.23) sustained moderate to substantial damage, but highlight that not all buildings were seriously damaged. Moreover, many other buildings appear to have been undamaged, though a number is not specified and they describe the overall damage as widespread, but mostly non-structural. Table A4.5.11 shows the number of properties classified according to the codes presented in Table A4.5.10 for around 5,000 buildings within the jurisdiction of the Newcastle City Council, not including government buildings. It is noted that different administration and census divisions exist under the name of Newcastle and their areas vary in how much of the extended metropolitan area they cover. From the information found, the expression “Newcastle City Council” is interpreted to be the Local Government Area, as defined by the Australian Bureau of Statistics and shown in the

inset of Figure A4.5.27. However, the map contained in the report edited by Melchers (1990) covers a smaller area, as shown in the broader Figure A4.5.27. According to Table A4.5.11, around 61% of the buildings assessed only sustained minor damage, while the remaining 15%, 14% and 10% were classified as blue, amber and red, respectively. Both Melchers (1990) and Stuart (1990) note that these numbers are not necessarily the final ones, as the works on data collection and interpretation had not been concluded at their time of writing. Figure A4.5.28 is a more modern version of Figure A4.5.27, showing the location of the damaged residential buildings (3,504 in total), using the same colour classification.

According to Melchers (1990) and Stuart (1990) of all the buildings assessed (Table A4.5.11), between 78 and 90 had been approved for complete demolition, while 173 to 200 had been approved for partial demolition.

Table A4.5.11. Classification of the surveyed buildings according to their damage state. From Stuart (1990) and Melchers (1990).

Properties \ Coding	Red	Amber	Blue	Green	Total
Residential	228	419	513	2344	3504
Commercial	222	255	227	673	1377
Other	36	1	27	28	92
Total	486	675	767	3045	4973

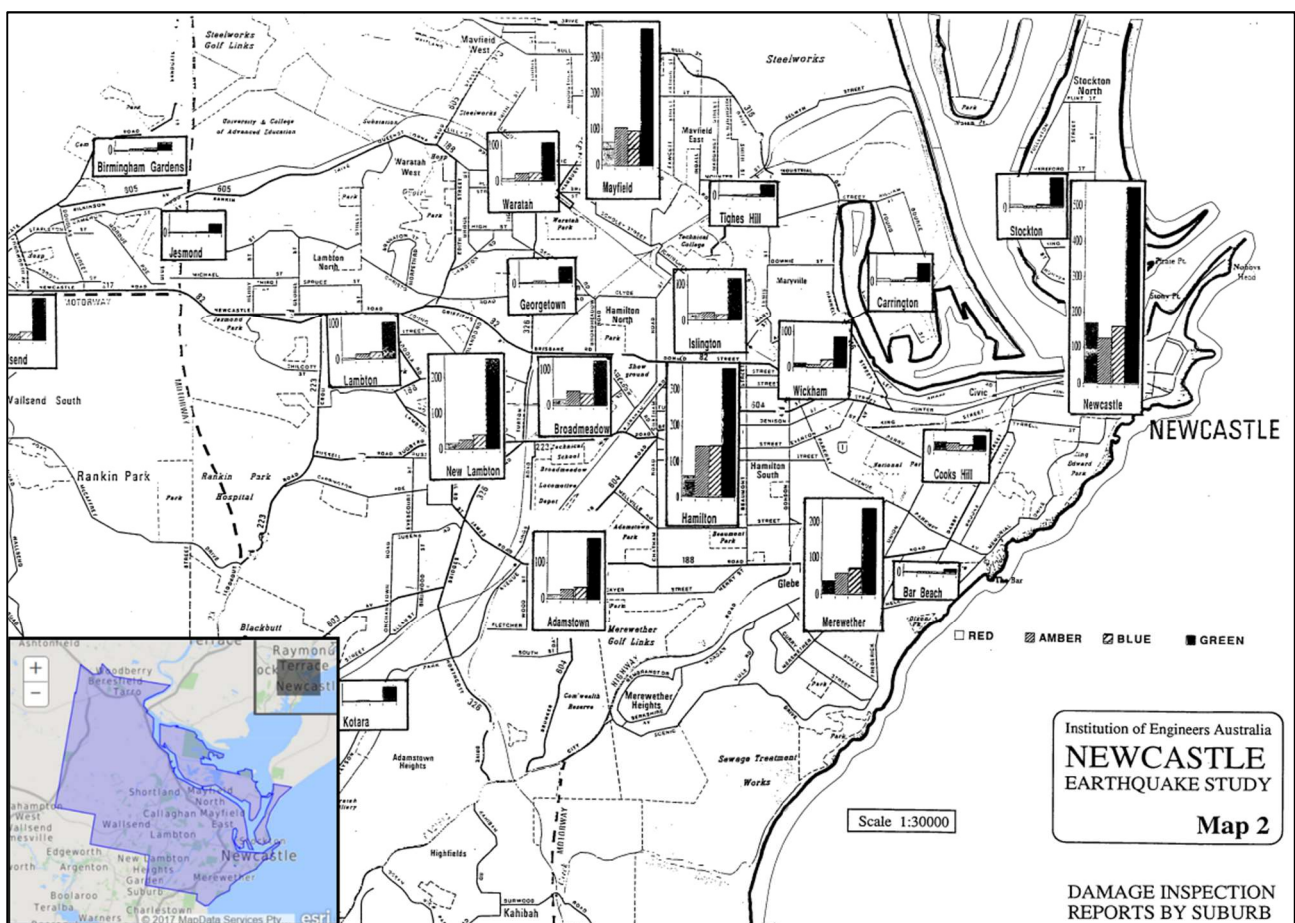


Figure A4.5.27. Distribution of damage in Newcastle. From Melchers (1990). Inset shows the extent as Newcastle as a Local Government Area (from the Australian Bureau of Statistics).

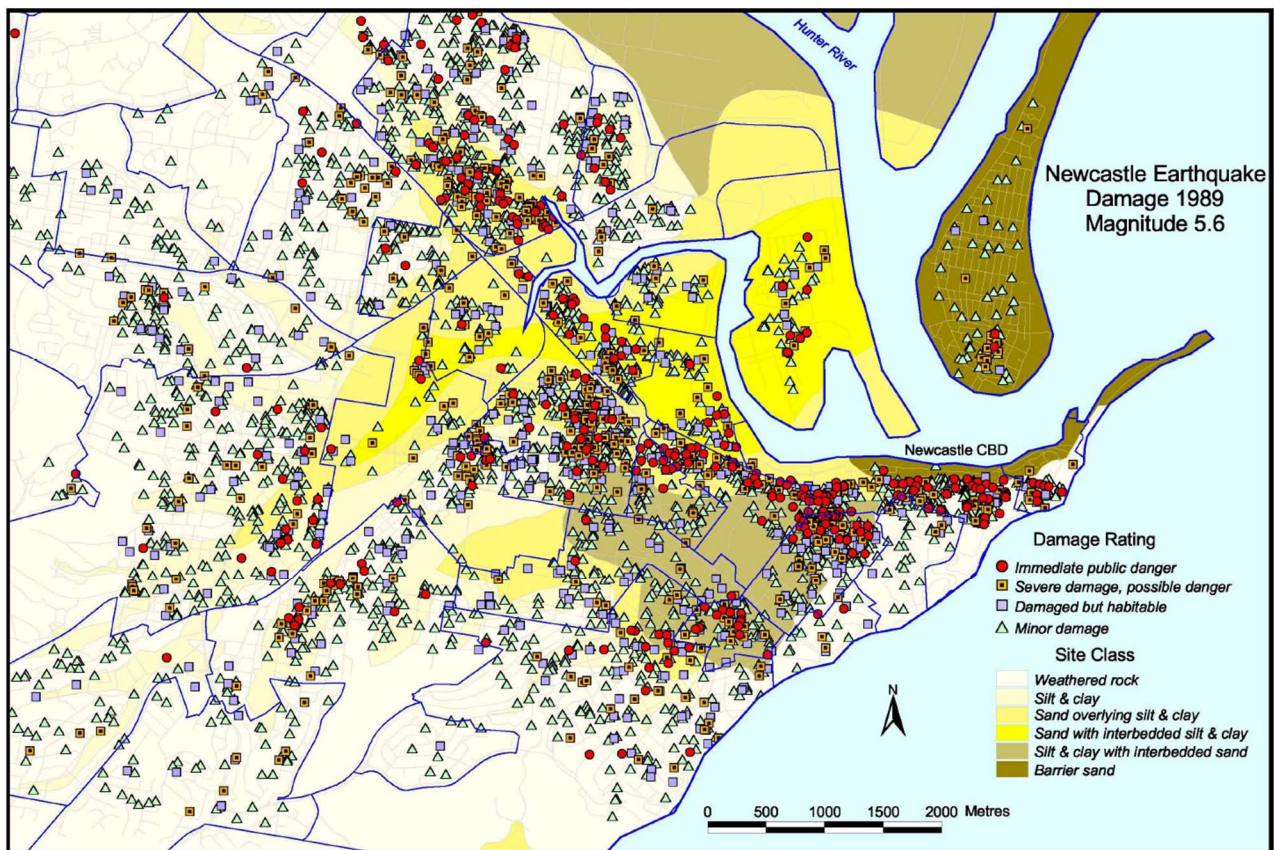


Figure A4.5.28. Distribution of damage to residential buildings in Newcastle. From Edwards *et al.* (2004).

Melchers (1990) summarises the kind of damage observed as follows:

- Structural failure, understood as the partial or total collapse of floors and/or roofs of buildings was not common. This statement is supported by Pedersen (1990).
- Parapet failure was widespread and represented a hazard not only during the earthquake but afterwards as well.
- Gable end failure was also widespread and affected both newer and older buildings.
- Corner failure, understood as vertical cracking of the masonry near corners or returns in walls and which may affect the stability of the adjacent perpendicular masonry panel, was widespread in all buildings that contained brittle unreinforced masonry.
- Transverse panel failure, understood as the failure of a wall in bending, was common. The occurrence of this type of failure was influenced by the corrosion of ties between non-structural outer wythes and their structural inner counterparts.
- Shear failure, which does not usually result in wall collapse.

- Torsional failure, understood not as the failure of structural elements under torsion but as the increase of forces in individual elements due to eccentricities of the centres of mass and stiffness, was observed in a number of cases.
- Consequential failure, understood as a failure that occurs as a consequence of a previous different failure, occurred in limited numbers. Examples of this include the collapse of a suspended awning due to the overload generated by masonry falling over it, the damage caused to contents of the Art Gallery of the City Library due to falling masonry from a parapet damaging the roof, or the damage to electrical transformers and mechanical equipment due to similar causes.
- Settlement in time of foundations lying over alluvium was observed in the weeks following the earthquake and affected both previously damaged and undamaged buildings. This appears to be particularly true of a series of churches and religious buildings assessed by Nichols (1990).

According to Melchers (1990) and Pedersen (1990), post-1950 non-residential buildings, which consist mostly of steel or concrete frames with brick infill panels, performed well during the earthquake and only suffered from minor damage to their infills, ceilings, parapets and façades. Only three buildings of this kind are known to have been damaged: the 2-storey Junction Motor Lodge, a 3-storey apartment block at The Junction, and the Newcastle Workers Club. The first saw severe damage to its reinforced concrete columns on the ground floor due to a soft storey effect, though it did not collapse. The unreinforced load-bearing brick masonry of the second were severely cracked (widths up to 70-80 mm) in the ground floor due to excessive torsional eccentricity, but did not collapse either. Both buildings were practically undamaged in the above floors. The Newcastle Workers Club was a more complex building that had been extended during the years, with older sections relying on load-bearing masonry and newer sections having been built in reinforced concrete. A whole section of this building, a 3-storey frame with a double-storey height at the top built in 1972, collapsed completely. According to an independent investigation carried out by Melchers (2010), this was likely due to one or two reinforced concrete columns being significantly under-strength and failing in compression, leading to progressive failure of neighbouring columns and a wall due to overloading, subsequently causing the collapse of part of a slab and, finally, two more beneath it, as shown in Figure A4.5.29.

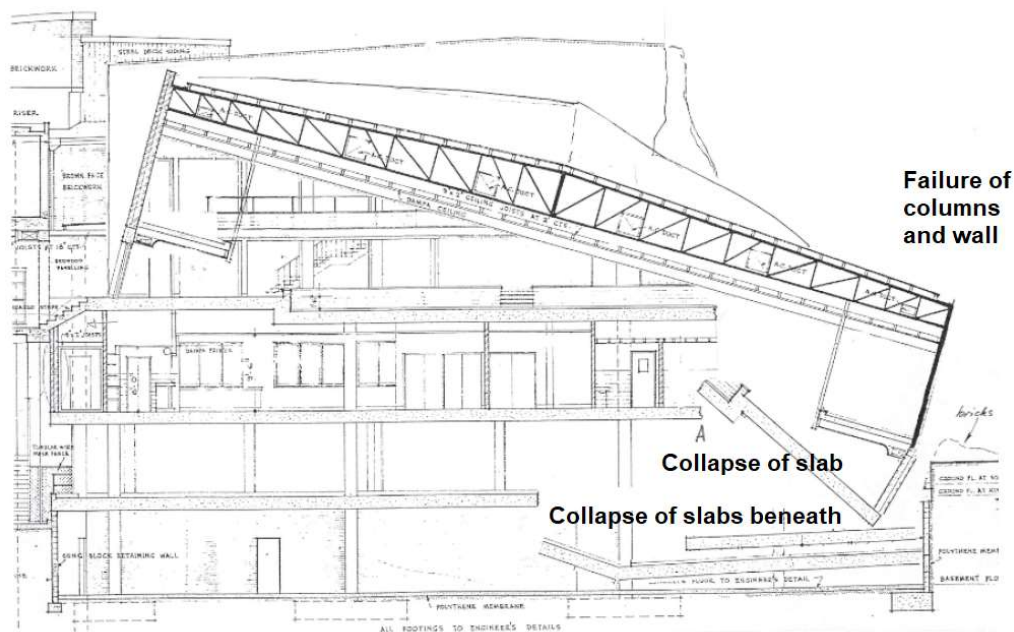


Figure A4.5.29. Reconstruction of the cross-section through the Newcastle Workers Club showing collapsed wall, rotation of the steel structure of the roof and collapse of concrete slabs beneath. Modified from Melchers (2010).

Pre-1950 non-residential buildings performed worse than post-1950 ones, as most of them were constructed in brick masonry and exhibited the typical failure modes associated to this kind of structures (Melchers, 1990; Pedersen, 1990). According to Melchers (1990), the two main reasons for this were the complete corrosion or lack of cavity ties linking the external and internal wythes of cavity masonry walls and the weathering of lime mortar with time, both of which lead to decreased out-of-plane resistance of masonry. Another very common form of damage was the failure of suspended awnings, particularly in the commercial centre of Hamilton. Around the 1950s, the timber posts that had traditionally supported awnings were removed and replaced by steel tie rods as a safety measure against traffic. Failure of these structures was subsequently due to the failure of the anchor rod to the façade, the complete out-of-plane failure of the façade, and/or the overloading generated by masonry falling onto the awning, as illustrated in Figure A4.5.30 (left) (Melchers, 1990; Harkness & Hassanain, 2002). Taller 5- to 6-storey loadbearing masonry non-residential buildings performed in various ways during the earthquake, some suffering only from minor damage and some others having ended substantially damaged to the point of requiring demolition.

Several institutional and heritage buildings fall under the pre-1950-built category and, as such, suffered from significant damage (Melchers, 1990; Loke, 1990). These include schools, colleges, churches, hospitals, a fire station, and an ambulance station. According to Melchers (1990), 70 out of the 151 heritage buildings of the Newcastle Central Business District and surround areas suffered from some kind of damage, mostly related to masonry failures. The Christ Church Cathedral was severely damaged, mostly in the form of cracking and dislodgement of the brick flying buttresses (though none fell completely), dislodgement and falling of ornamentations, shear cracking and out-of-plane movements of walls (Collins & Jordan, 1997; Melchers, 1990).



Figure A4.5.30. Awning collapse due to parapet falling onto it (left), typical damage in masonry walls (centre) and failure of both inner and outer masonry wythes of top storey and gable (right).
Photos by M. Maloy, from McCue (1990a).

According to Melchers (1990), residential buildings (and those with similar structural characteristics) suffered from widespread damage, ranging from minor cracking to significant partial collapses that required subsequent demolition, affecting mostly cavity brick masonry constructions, followed by brick veneer construction (light timber frames with masonry cladding) and, finally, timber houses, which were the least affected. Though in some cases the damage was minor, cavity brick houses generally suffered from severe in-plane shear cracking, tilting of both load-bearing and non-load-bearing wythes due to out-of-plane action, partial loss of roof support due to the displacement of the walls beneath, cracking of walls in flexure under out-of-plane action, collapse of the external wythe due to corroded, inadequate or non-existent wall ties, and collapse of gable ends and parapets. Examples of typical damage to masonry are shown in Figure A4.5.30 (centre and right). As brick veneer constructions were more modern, their wall ties were more adequate and, consequently, failure of the veneer due to out-of-plane shaking was rare in this typology, though there were cases of collapse of gable ends, displaced or tilted veneers, minor damage to tiled roofs and minor cracking of plaster. Finally, being timber houses flexible and low in mass, their performance was good overall, though the main cause of damage to this kind of structure was the relative movement between the flexible timber frame and other more rigid elements, such as chimneys, and with respect to its foundation, mostly due to sliding. However, damage to the timber frame was rare even in the last cases. The dislodgement and overturning of chimneys was also observed in older structures (newer structures did not tend to have chimneys).

Regarding the impact on industry, Melchers (1990) highlights that most losses were related to the failure of the electrical supply or to the inadequate anchoring of non-structural elements and components, such as light fittings.

Melchers (1990) describes the following damage (or lack of) to lifelines:

- There was no significant damage to roads, bridges, water and sewage systems (except for some minor leaks on previously-corroded pipes), gas pipelines (except for minor leaks that were easily repaired).
- The petroleum supply pipeline between Sydney and Newcastle appeared as undamaged at first but suffered from a leak several days later during a safety test.
- The electrical supply was lost right after the earthquake due to the tripping off of transformers, which were easily reset, the damage suffered by several porcelain insulators, and minor damage to equipment, but there were no reports of damage to transmission lines or towers. Most of the supply was restored after two and a half hours and full restoration took three weeks, but the fully normal reliability of the supply was recovered only after months (Caldwell, 2010).
- The telephone network operated with some difficulty after the earthquake, at worst reduced by 87% of its capacity, due to the displacement of equipment racks and the subsequent damage to cables. All problems were solved within seven hours.

A4.5.8.3 Observed weaknesses

The main weakness was, undoubtedly, the complete lack of design of most buildings (including non-structural components such as infills, parapets and chimneys) to sustain lateral loads, which was a direct consequence of the lack of awareness on seismic hazard of engineers in New South Wales (e.g., Donaldson, 1990; Woodside & McCue, 2016).

Several authors (e.g., Bubb, 1990; Donaldson, 1990; Melchers, 1990; Page, 1990; Pedersen, 1990) highlight the significant role played by aging and general deterioration and lack of maintenance in the performance of structures subject to this earthquake. In particular, rusting of wall cavity ties (linking internal and external wythes of masonry) and weathered mortar joints have been pointed out as a frequent cause of failure. In the transcript of one of the discussions of the Conference on the Newcastle Earthquake (Bubb, 1990), John Nichols mentioned that a significant number of the walls he had looked at and that had failed due to the corrosion of the cavity ties were facing south and consequently exposed to winds coming from that direction.

The lack of articulation joints in infill masonry also comes up in the discussion transcribed by Bubb (1990) as the reason for masonry panels being unable to accommodate displacement without rapidly incurring in failure.

Melchers (1990) highlight as well the negative effect of unsupervised building alterations executed over the years, in particular those involving the removal of internal walls, the insertion of beam supports into masonry and the lack of bonding between new and old masonry members.

According to Melchers (1990) and Harkness & Hassanain (2002), the widespread failure of awnings was largely due to the badly-designed anchoring systems that supported them. Timber posts that traditionally served as columns were removed in the 1950s and replaced by steel tie rods as a safety measure against traffic. However, these were often simply anchored to the façade by means of a bolt and a bearing plate, which means that it was the out-of-plane capacity of the façade which dictated the stability of the awning.

Pedersen (1990) makes reference as well to problems of subsidence due to the presence of underground coal mines, highly plastic clay foundations and areas of potential landslip as having affected pre-1950 commercial buildings.

A4.5.8.4 Damage distribution

According to Gibson *et al.* (1990), serious damage was observed only within a relatively limited area, as can be observed in Figure A4.5.28.

Several authors have pointed out the significant influence of the geology of the area and, in particular, the location of the alluvial deposits, on the spatial pattern of damage (*e.g.*, Brunston, 1990; McCue *et al.*, 1990a, 1990b; Melchers, 1990; Poulos, 1991; Rynn *et al.*, 1992). Melchers (1990) mentions that, while damage to residential buildings was widespread, it was particularly severe in the inner areas of the city where foundations lie on alluvial deposits. With the purpose of showing this correlation, Brunston (1990) plotted the location of the latter together with the macroseismic isoseismals, the correspondence between the largest intensities and the alluvial deposits being evident, as shown in Figure A4.5.31 (compare as well Figure A4.5.28 against Figure A4.5.10). The two areas where the worst damage was observed, Hamilton and The Junction (see Figure A4.5.31) are located over 10 to 20 m of these alluvial desposits (Brunston, 1990). According to Rynn *et al.* (1992), very few exceptions to this close relationship between damage and alluvial deposits were observed, one of them being that of buildings located on basement rock in the immediate epicentral area.

One of the most heavily-damaged area was the Newcastle Central Business District (CBD), which is located within the alluvial deposits, as shown in Figure A4.5.31 (Stuart, 1990). Rynn *et al.* (1992) believes that this area was also influenced by the effects of creeping of the sediments at the interface with the basement rock, due to the slope of the latter.

Though it is believed that the epicentre was located around Boolaroo and not in the very downtown area of Newcastle, Melchers (1990) noted that the degree of damage to residential buildings decreased with distance from the central area, as more distant suburbs consisted mostly of newer timber or brick veneer constructions (see Figure A4.5.19 and Figure A4.5.22). It is not clear if the suburbs being mentioned lie within the alluvial deposits or not. However, the influence of the spatial distribution of building typologies with different levels of vulnerability must not be overlooked.

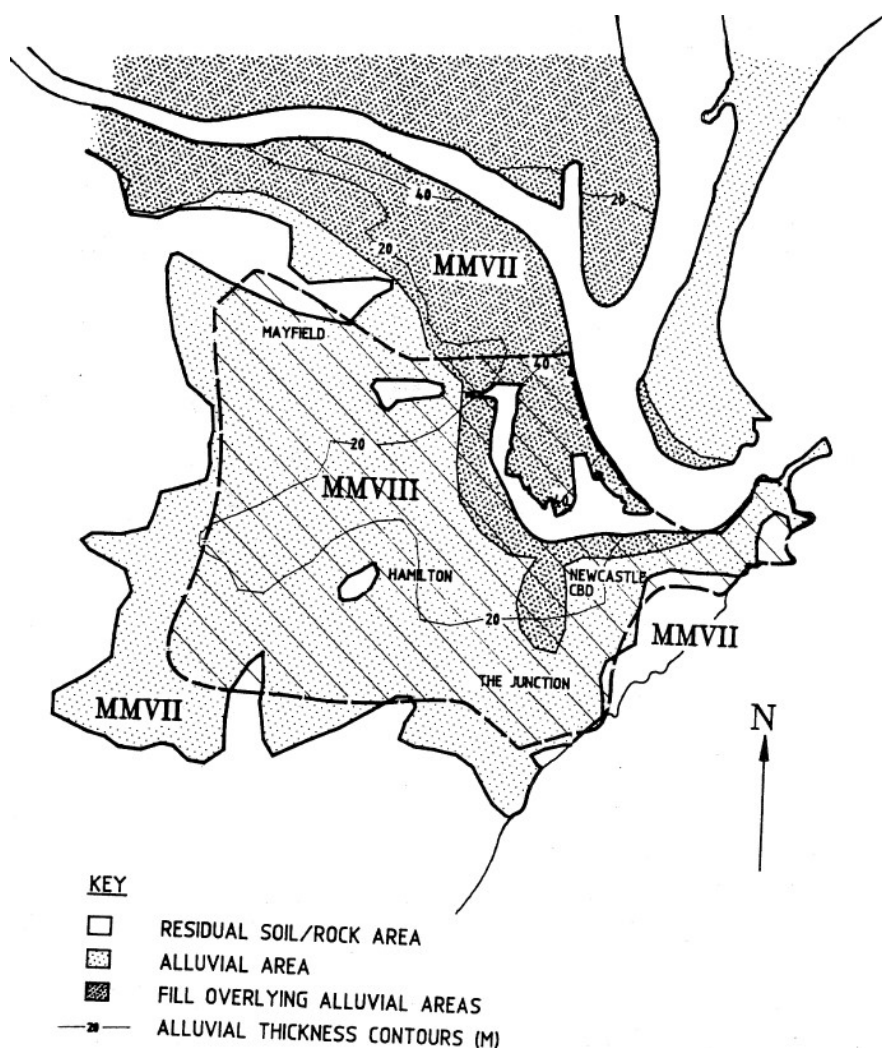


Figure A4.5.31. Relationship between observed macroseismic intensities (MMI) and alluvial region. From Brunsdon (1990).

A4.5.9 Casualties and losses

A4.5.9.1 Numbers of dead and injured

Thirteen people died as a result of this earthquake (Melchers, 1990; Harkness & Hassanain, 2002; Newcastle Region Library). It is believed that some sources mention only twelve (e.g., USGS; EM-DAT database; NOAA database; McCue *et al.*, 1990b) because one of them was a heart attack.

The exact number of injured people is not known, but fluctuates around 100 to 200 people. Melchers (1990) refer to an estimation of 100 to 120 people being severely injured, and many more having suffered from minor injuries. Harkness & Hassanain (2002) speak of 120 officially-recorded injuries but highlight that 162 were hospitalised and that no records of other minor injuries exist. The Earthquake Collection website of the Newcastle Region Library speaks of 160 being hospitalised as well. The EM-DAT database mentions 115 injured, while the NOAA database only reports 100 and the USGS says “more than 100”.

A4.5.9.2 Causes of casualties

According to Melchers (1990), the 100-120 estimated serious injuries were due to collapsing awnings and falling masonry, while 9 people died in the collapse of the Newcastle Workers Club, 3 people died due to awning or parapet collapses, and at least one person died of a heart attack.

A4.5.9.3 Estimates of economic losses

According to the USGS, the NOAA database and the EM-DAT database, economic losses due to this earthquake amounted to around 1,000-1,100 million US dollars (USD). Melchers (1990) reports a value of 1,000 million dollars, without specifying whether they are USD or Australian dollars (AUD) though, given that the report edited by Melchers (1990) is Australian, it is assumed that Australian dollars are implied. According to online conversion data for December 1989 – January 1990, this would be around 780 million USD (Investing.com, 2018). Stuart (1990) reports 1,100 million AUD, while Donaldson reports 2,000 AUD instead.

Harkness & Hassanain (2002) speak of the total damage exceeding 1,500 million AUD. However, they then mention that total insurance payout amounted to 1,020 million, in terms of AUD of 1996, which would be equivalent to 820 million USD of 1989, according to the Inflation Calculator of the Reserve Bank of Australia. Finally, they say that the total financial cost is estimated to have been 4,000 million, without specifying currency. Given that this is stated right after talking in terms of 1996 AUD, it is assumed that this is the case, and this would be equivalent to around 3,200 million AUD in 1989 (around 2,500 USD in 1989). They do not specify what is included in these total losses either. It appears that the source might be the same as for Woodside & McCue (2016), who briefly speak of the damage having been estimated at 4,000 million AUD, including an insured loss of around 1,000 million AUD. The Earthquake Collection website of the Newcastle Region Library also mentions 4,000 million, assumed to be AUD.

According to Melchers (1990), 800 million AUD of the total 1,000 million was direct property losses, while the remainder covered contents losses, loss of business, etc. The author warns about the possibility of these numbers being an overestimation, given that his time of writing was so close to the time of occurrence of the earthquake. The figures given in recent years by Harkness & Hassanain (2002) and Woodside & McCue (2016) appear to support these large initial loss estimates, but it is not clear what the ultimate sources of said figures are.

For their work on the vulnerability of Australian buildings, Maqsood *et al.* (2016) obtained data of insurance claims settled by the Insurance Australia Group (IAG). They report a total of around 14,000 insurance claims for building damage, including contents, for a total of approximately 86 million USD of 1989. These 14,000 insurance claims seem to be the same as those reported by Fulford *et al.* (2002) for a total of 97 million AUD dollars of 1989, as IAG is a parent company of NRMA insurance, cited by Fulford *et al.* (2002). According to Fulford *et al.* (2002), these claims are estimated to be only 50% of the residential building claims in the region of Newcastle and Lake Macquarie. However, Harkness & Hassanain

(2002) speak of a total of 70,000 insurance claims made. This discrepancy might be explained when considering that Walker (1991) reports that losses related to commercial and public buildings were much larger than those related to residential buildings, the latter amounting to only 200 million (likely AUD of 1989-1991) while the former sum up to 600 million dollars (likely AUD of 1989-1991), one third of which seems to be related to business interruption. According to Harkness & Hassanain (2002), the impact on economic activities was large, as they say that the retail sector in Newcastle had not fully recovered, even after eleven years.

A4.5.10 Discussion and conclusions

This **M5.4** earthquake occurred on 27th December 1989, at 23.27 UTC (28th December 1989, 10.27 local time), and had its epicentre around Boolaroo, in the broader area of Newcastle, Australia. Estimated losses range between 1,000 and 2,500 million US dollars (of 1989), though there is large uncertainty in the figures reported.

Severe widespread damage was observed (MMI VIII), particularly to older load-bearing masonry buildings, while more modern structures performed better, their damage being usually limited to their non-structural components. Some exceptions to this were observed, nevertheless, the most prominent being the full collapse of a section of the Newcastle Workers Club, apparently due to two reinforced columns being severely under-strength, and which resulted in the death of nine people. The overall casualty toll (13 dead, 100-162 injured) was relatively low in comparison with the damage caused, and was positively influenced by the fact that the earthquake occurred during the Christmas-New Year holiday period, on the day of a bus strike, and during the morning, the latter being of relevance because the collapsed Workers Club was meant to host an event in its auditorium that same night.

The most prominent reasons for the damage observed were:

- the complete lack of seismic design of the exposed building stock, including non-structural components such as parapets, chimneys and awnings,
- the amplification of ground motions due to the effects of alluvial deposits,
- the lack of maintenance of the building stock, expressed mainly in the form of extremely corroded wall ties and weathered lime mortar, and
- the weakening of structures due to unsupervised structural alterations.

A study published in 2007 asserting that this earthquake was triggered by the dewatering of mines in the area was challenged by another paper published the following year and by several Australian scientists in the media.

A4.5.11 References

A4.5.11.1 Bibliography

- Afshari, K. & J. Stewart (2016). Physically parametrized prediction equations for significant duration in Active Crustal Regions. *Earthquake Spectra* **32**(4), 2057-2081.
- Allen, T. I., D. J. Wald, P. S. Earle, K. D. Marano, A. J. Hotovec, K. Lin & M. G. Hearne (2009). An Atlas of ShakeMaps and population exposure catalog for earthquake loss modeling. *Bulletin of Earthquake Engineering* **7**(3), 701-718.
- Atkinson, G.M. & S.I. Kaka (2007). Relationships between felt intensity and instrumental ground motion in the Central United States and California. *Bulletin of the Seismological Society of America* **97**, 497-510.
- Bommer, J.J., P.J. Stafford & J.E. Alarcón (2009). Empirical equations for the prediction of the significant, bracketed, and uniform duration of earthquake ground motion. *Bulletin of the Seismological Society of America* **99**(6), 3217-3233.
- Brunsdon, D.R. (1990). The December 28, 1989 Newcastle, Australia Earthquake. *Bulletin of the New Zealand National Society for Earthquake Engineering*, **23**(2), 102-120. Available at [http://www.nzsee.org.nz/db/Bulletin/Archive/23\(2\)0102.pdf](http://www.nzsee.org.nz/db/Bulletin/Archive/23(2)0102.pdf). Last accessed: 24th April 2018.
- Bubb, G. (1990). Behaviour of structures – Council buildings. *Conference on the Newcastle Earthquake: Conference Proceedings*, February 15-17, Newcastle, New South Wales, Australia, 26-27.
- Burbridge, D.R. (ed.) (2012). *The 2012 Australian earthquake hazard map*. Record 2012/71, GeoCat 74811. Geoscience Australia, Canberra, Australia.
- Caldwell, R. (2010) Effects of the Newcastle earthquake of 1989 on the New South Wales high voltage transmission system. *Australian Journal of Structural Engineering* **11**(3), 253-265.
- Campbell, K.W. (2003). Prediction of strong ground motion using the hybrid empirical method and its use in the development of ground-motion (attenuation) relations in Eastern North America. *Bulletin of the Seismological Society of America* **93**(3), 1012-1033.
- Center for International Earth Science Information Network - CIESIN - Columbia University (2016). *Gridded Population of the World, Version 4 (GPWv4)*. Palisades, NY: NASA Socioeconomic Data and Applications Center. <http://dx.doi.org/10.7927/H4NP22DQ>.
- Clark, D. & M. Leonard (2003). Principal stress orientations from multiple focal-plane solutions: new insight into the Australian intraplate stress field. *Geological Society of America Special Papers* **372**, 91-105.
- Clark, D., A. McPherson & R. Van Dissen (2012). Long-term behaviour of Australian stable continental region (SCR) faults. *Tectonophysics* **566**, 1-30.
- Collins, B.B., & J.B. Jordan (1997). Earthquake damage repair and strengthening of Christ Church Cathedral, Newcastle NSW. *Seventh International Conference on Structural Faults & Repair*, July 1997, Edinburgh, Scotland. Available online at (last accessed 24th April 2018): <http://www.newcastlecathedral.org.au/common/download/Earthquakerepairs.pdf>.
- Crapp, C.E. & R.C. Nolan (1975). Newcastle District. In Traves, D. M. & D. King (eds.): *Economic Geology of Australia and Papua New Guinea – Vol. 2 Coal*, Australian Institute of Mining and Metallurgy.

- Daniell, J.E. & D. Love (2010). The socio-economic impact of historic Australian earthquakes. *Australian Earthquake Engineering Society 2010 Conference*, Perth, Western Australia.
- Dhu, T. & T. Jones (eds.) (2002). *Earthquake Risk in Newcastle and Lake Macquarie*. Geoscience Australia Record 2002/15, Geoscience Australia, Canberra.
- Dhu, T., D. Robinson, C. Sinadinovski, T. Jones, N. Corby, A. Jones & J. Schneider (2002). Earthquake hazard. In Dhu, T. & T. Jones (eds.): *Earthquake Risk in Newcastle and Lake Macquarie*. Geoscience Australia Record 2002/15, Geoscience Australia, Canberra.
- Donaldson, R.J. (1990). Behaviour of structures – Patterns of failure in domestic buildings after the 1989 Newcastle earthquake. *Conference on the Newcastle Earthquake: Conference Proceedings*, February 15-17, Newcastle, New South Wales, Australia, 44-48.
- Fulford, G., T. Jones, J. Stehle, N. Corby, D. Robinson, J. Schneider & T. Dhu (2002). Earthquake Risk. In Dhu, T. & T. Jones (eds.): *Earthquake Risk in Newcastle and Lake Macquarie*. Geoscience Australia Record 2002/15, Geoscience Australia, Canberra.
- Gaull B.A., M.O. Michael-Leiba & J.M.W. Rynn (1990). Probabilistic earthquake risk maps of Australia. *Australian Journal of Earth Sciences* **37**, 169-187.
- Giardini, D., G. Grünthal, K.M. Shedlock & P. Zhang (1999). The GSHAP global seismic hazard map. *Annali di Geofisica* **42**(6), 1225-1228.
- Gibson, G. & V.A. Dimas (2009). Earthquake hazard at Newcastle. *Australian Earthquake Engineering Society 2009 Conference*, Newcastle, New South Wales, Australia.
- Gibson G., V. Wesson & K. McCue (1990). The Newcastle Earthquake aftershock and its implications. *Conference on the Newcastle Earthquake: Conference Proceedings*, February 15-17, Newcastle, New South Wales, Australia, 14-18.
- Glen, R.A. (2005) The Tasmanides of eastern Australia. In Vaughan, A.P.M., P.T. Leat & R.J. Pankhurst (eds.): *Terrane processes at the margins of Gondwana*. Special Publications, vol. 246. Geological Society, London, pp. 23–96.
- Gray, D.R., D.A. Foster, R.J. Korsch & C.V. Spaggiari (2006). Structural style and crustal architecture of the Tasmanides of eastern Australia: Example of a composite accretionary orogen. *Geological Society of America Special Papers* **414**, 119-132.
- Harkness, E.L. & M.A. Hassanain (2002). Seismic Damage in NSW, Australia: Construction Insurance, Social, and Economic Consequences. *Journal of Performance of Constructed Facilities* **16**(2), 75-84.
- Hillis, R.R. & S.D. Reynolds (2000). The Australian stress map. *Journal of the Geological Society of London* **157**, 915-921.
- Klose, C.D. (2007). Geomechanical modeling of the nucleation process of the 1989 Newcastle earthquake in Australia. *Earth and Planetary Science Letters* **256**, 547–553.
- Korsch, R.J., D.W. Johnstone & K.D. Wake-Dyster (1997). Crustal architecture of the New England Orogen based on deep seismic reflection profiling. Tectonic and Metallogenesis of the New England Orogen. *Geological Society of Australia Special Publication* **19**, 29–51.
- Leaman, D.E. (1990). Geological note: the Sydney Basin: composition of basement. *Australian Journal of Earth Sciences* **37**, 107–108.

- Leonard, M., D. Robinson, T. Allen, J. Schneider, D. Clark, T. Dhu & D. Burbidge (2007). Toward a better model of earthquake hazard in Australia. *GSA Special Papers 2007* **425**, 263-283.
- Lohe, E.M. & G.L. Dean-Jones (1995). Structural Geology of the Newcastle-Gosford Region. In Sloan, S.W. & M.A. Allman (eds.): *Engineering geology of the Newcastle-Gosford region*, Australian Geomechanics Society, 14-39.
- Loke, J.Y.O. (1990). Behaviour of structures – Institutional. *Conference on the Newcastle Earthquake: Conference Proceedings*, February 15-17, Newcastle, New South Wales, Australia, 28-31.
- Loveridge, R. (1990). Building regulations. *Conference on the Newcastle Earthquake: Conference Proceedings*, February 15-17, Newcastle, New South Wales, Australia, 88-89.
- Maqsood, T., M. Edwards, I. Ioannou, I. Kosmidis, T. Rossetto & N. Corby (2016). Seismic vulnerability functions for Australian buildings by using GEM empirical vulnerability assessment guidelines. *Natural Hazards* **80**(3), 1625–1650.
- McCue, K., V. Wesson & G. Gibson (1990a). The Newcastle, New South Wales, earthquake of 28 December 1989. *BMR Journal of Australian Geology & Geophysics* **11**, 559- 567.
- McCue, K., V. Wesson & G. Gibson (1990b). Seismological aspects of the Newcastle NSW earthquake of 28 December 1989. *Conference on the Newcastle Earthquake: Conference Proceedings*, February 15-17, Newcastle, New South Wales, Australia, 9-12.
- Melchers, R.E. (ed.) (1990). *Newcastle earthquake study*. Report of The Institution of Engineers, Australia.
- Melchers, R.E. (2010). Investigation of the failure of the Newcastle Workers Club. *Australian Journal of Structural Engineering* **11**(3), 163-176.
- Nichols, J. (1990). Behaviour of structures – Churches. *Conference on the Newcastle Earthquake: Conference Proceedings*, February 15-17, Newcastle, New South Wales, Australia, 35-38.
- Page, A.W. (1990). Behaviour of structures – Patterns of failure. *Conference on the Newcastle Earthquake: Conference Proceedings*, February 15-17, Newcastle, New South Wales, Australia, 39-43.
- Pedersen, I. (1990). Behaviour of structures – Major commercial buildings. *Conference on the Newcastle Earthquake: Conference Proceedings*, February 15-17, Newcastle, New South Wales, Australia, 21-25.
- Poulos, H.G. (1991). Relationship between local soil conditions and structural damage in the 1989 Newcastle earthquake. *Transactions of the Institution of Engineers, Australia. Civil engineering* **33**(3), 181-188.
- Quigley, M.C., D. Clark, & M. Sandiford (2010). Tectonic geomorphology of Australia. *Geological Society, London, Special Publications* **346**(1), 243-265.
- Quinn, C.D., R.A. Glen & C.F.K. Diessel (2008). Discussion of “Geomechanical modeling of the nucleation process of Australia's 1989 M5.6 Newcastle earthquake” by C.D. Klose [Earth Planet. Sci. Lett. 256 (2007) 547–553], *Earth and Planetary Science Letters* **269**(1–2), 296-302.
- Rajabi, M., M. Tingay & O. Heidbach (2016). The present-day stress field of New South Wales, Australia. *Australian Journal of Earth Sciences* **63**(1), 1-21.

Reynolds, S. D., D. Coblenz & R.R. Hillis (2003). Influences of plate-boundary forces on the regional intraplate stress field of continental Australia. In Hillis, R.R. & R.D. Muller (eds.): *Evolution and dynamics of the Australian Plate*. Geological Society of Australia Special Publication 22, 59–70.

Rynn, J.M.W., E. Brennan, P.R. Hughes, I.S. Pedersen & H.J. Stuart (1992). The 1989 Newcastle, Australia, earthquake: the facts and the misconceptions. *Bulletin of the New Zealand National Society for Earthquake Engineering* **25**(2), 77–145.

Sinadinovski, C., K.F. McCue & M. Somerville (2000). Characteristics of strong ground motion for typical Australian intra-plate earthquakes and their relationship with the recommended response spectra. *Soil Dynamics and Earthquake Engineering* **20**, 101–110.

Sinadinovski, C., T. Jones, D. Stewart & N. Corby (2002). Earthquake history, regional seismicity and the 1989 Newcastle earthquake. In Dhu, T. & T. Jones (eds.): *Earthquake Risk in Newcastle and Lake Macquarie*. Geoscience Australia Record 2002/15, Geoscience Australia, Canberra.

Stehle, J., N. Corby, D. Stewart & I. Hartig (2002). The elements at risk in Newcastle and Lake Macquarie. In Dhu, T. & T. Jones (eds.): *Earthquake Risk in Newcastle and Lake Macquarie*. Geoscience Australia Record 2002/15, Geoscience Australia, Canberra.

Stuart, H. (1990). Post earthquake assessment of building damage. *Conference on the Newcastle Earthquake: Conference Proceedings*, February 15–17, Newcastle, New South Wales, Australia, 52–58.

United Nations, ed. (2016). *Human Development Report 2016 - Human Development for everyone*. Report of the United Nations Development Program (UNDP), New York, United States.

Walker, G. (1991). Lessons from the 1989 Newcastle earthquake. In Rynn, J.M.W. (ed.): *Proceedings: what we have learnt from the Newcastle earthquake: lessons in building design, regulation, disaster management, earth science and the legal and insurance implications*, October 24–25, The University of Queensland, Australia.

Wilkinson, J. (2011). *The Hunter region: an economic profile*. NSW Parliamentary Library Research Service e-brief 16/2011. Available online at (last accessed 25th April 2018): <https://www.parliament.nsw.gov.au/researchpapers/Documents/the-hunter-region-an-economic-profile/Newcastle%20and%20the%20Hunter%20GG%202.pdf>.

Wilson, J.L., N.T. Lam & L. Pham (2008) Development of the new Australian earthquake loading standard. *Earthquake Engineering in the low and moderate seismic regions of Southeast Asia and Australia* **8**, 25–30.

Woodside, J. & K. McCue (2016). Early history of seismic design and codes in Australia. In *Australasian Structural Engineering Conference: ASEC 2016*. Barton, ACT: Engineers Australia, 2016: 194–207. Available at: <http://www.aees.org.au/wp-content/uploads/2017/02/History-of-Seismic-Codes-in-Australia-Rev.pdf>. Last accessed: 25th April 2018.

Worden, C.B., E.M. Thompson, M. Hearne & D.J. Wald (2017). *ShakeMap V4 Manual: technical manual, user's guide, and software guide*. United States Geological Survey. Available online at: <http://usgs.github.io/shakemap/>.

A4.5.11.2 Web references

ABC (2007): <http://www.abc.net.au/news/2007-01-09/australian-experts-reject-newcastle-quake-claims/2168560>. Last accessed: 24th April 2018.

Australian Bureau of Statistics – Census Data:

<http://www.abs.gov.au/websitedbs/D3310114.nsf/Home/Census>. Last accessed: 25th April 2018.

Australian Government – Website for data dissemination (last accessed 23th April 2018):

1991 Australian seismic hazard map: <https://data.gov.au/dataset/earthquake-hazard-map-of-australia-1991/resource/f85d0f4f-0845-4624-b7d1-4671e630206c>.

2012 Australian seismic hazard map: [https://data.gov.au/dataset/the-2012-australian-earthquake-hazard-map/resource/208b62c9-2dda-4e72-8c74-8ce7b0a833a2?inner span=True](https://data.gov.au/dataset/the-2012-australian-earthquake-hazard-map/resource/208b62c9-2dda-4e72-8c74-8ce7b0a833a2?inner_span=True).

EM-DAT – The Emergency Events Database (Université Catholique de Louvain, Brussels, Belgium; Cred. Prof. Dr. D. Guha-Sapir): <http://www.emdat.be/>. Last accessed: 4th April 2018.

Geoscience Australia: <http://www.ga.gov.au>

Geoscience Australia Earthquake Page:

(Mainshock)

<http://www.ga.gov.au/earthquakes/getQuakeTechController.do?orid=620500&quakeld=314918>

(Aftershock)

<http://www.ga.gov.au/earthquakes/getQuakeTechController.do?orid=1177418&quakeld=314708>

Inflation Calculator of the Reserve Bank of Australia (last accessed 26th April 2018):

<https://www.rba.gov.au/calculator/annualDecimal.html>.

International Monetary Fund (2017). World Economic Outlook Database 2017 (16th January 2017):

<https://www.imf.org/external/pubs/ft/weo/2016/02/weodata/index.aspx>. Last accessed: 15th July 2017.

Investing.com (2018): <https://www.investing.com/currencies/aud-usd-historical-data>. Last accessed: 26th April 2018.

National Geophysical Data Center / World Data Service (NGDC/WDS): Significant Earthquake Database. National Geophysical Data Center, National Oceanic and Atmospheric Administration (NOAA). DOI:10.7289/V5TD9V7K. <https://www.ngdc.noaa.gov/hazard/earthqk.shtml>. Last accessed: 4th April 2018.

The Australian (2007):

<https://www.theaustralian.com.au/news/nation/newcastle-earthquake-study-far-fetched/news-story/02d6a56f61d786138e89c3c4a12be18a?sv=baa861a5700bee5c1591447829885645>.

Last accessed: 24th April 2018.

The Newcastle Region Library – Earthquake Collection (last accessed 27th April 2018):

<http://www.newcastle.nsw.gov.au/Library/Heritage-History/Search-the-Collection/Earthquake-Collection>.

The World Bank: <http://www.worldbank.org>

The World Bank. World Development Indicators (last accessed 28th April 2017):

<http://databank.worldbank.org/data/reports.aspx?source=2&country=AUS>

United Nations Development Programme – Human Development Data (UNDP-HDD, 2016):

<http://hdr.undp.org/en/data>. Last accessed: 24th April 2018.

United States Geological Survey (USGS): <https://earthquake.usgs.gov/>

Website for this event (last accessed 26th April 2018):

<https://earthquake.usgs.gov/earthquakes/eventpage/usp00043na#executive>.

A4.6 April 1992 M5.4 Roermond Earthquake, The Netherlands

This earthquake occurred on 13th April 1992, at 01.20 UTC (03.20 local time), very close to the city of Roermond, in the south of the Netherlands. Apart from a smaller event reported to have occurred 0.2 seconds earlier, no other foreshock activity had been observed. It is the strongest earthquake to have been recorded in the Netherlands and north-western Europe to date, though its size and statistical probability of occurrence are in clear agreement with the tectonics of the region. It was felt over a large area extending to places located over 500 km away from the epicentre. Significant losses were registered in the Netherlands and Germany, mainly associated to masonry buildings. Landslides and liquefaction phenomena were observed, though they did not contribute to the damage to the building stock. One death and 45 injured people were reported.

A4.6.1 Tectonic and seismic setting

A4.6.1.1 Tectonic setting

The 1992 Roermond earthquake originated from the rupture at the depth continuation of the Peel Boundary (or Peelrand) fault, which defines the northeast border of the Roer Valley Graben, whose southwest limit is the Feldbiss Fault Zone (Ahorner, 1994; Camelbeeck & Meghraoui, 1996; Vanneste *et al.*, 2013). To the northwest, the Roer Valley Graben widens into the West Netherlands Basin, while to the southeast it narrows and finally disappears, extending for around 145 km overall. The Roer Valley Graben is the central graben of the Lower Rhine Graben (or Lower Rhine Embayment), a system of grabens and horsts separated by NW-SE trending normal faults (Figure A4.6.1) located in the triple frontier comprising the Netherlands, Germany, and Belgium (Vanneste *et al.*, 2013). The direction of the regional maximum compressive stress is parallel to these faults, causing the Roer Valley Graben to be subject to extensional tension forces perpendicular to its axis and to give place to thick sedimentary basins (Braunmiller *et al.*, 1994; Camelbeeck & van Eck, 1994; Ewald *et al.*, 2006). It is believed that this intraplate stress field is a consequence of the interaction between the Eurasian and the African tectonic plates (Ahorner, 1994).

Figure A4.6.2 presents a simplified cross-section through the Roer Valley Graben near the area of Roermond. During the 1992 earthquake, the western block moved down with respect to the eastern one (Ahorner, 1994).

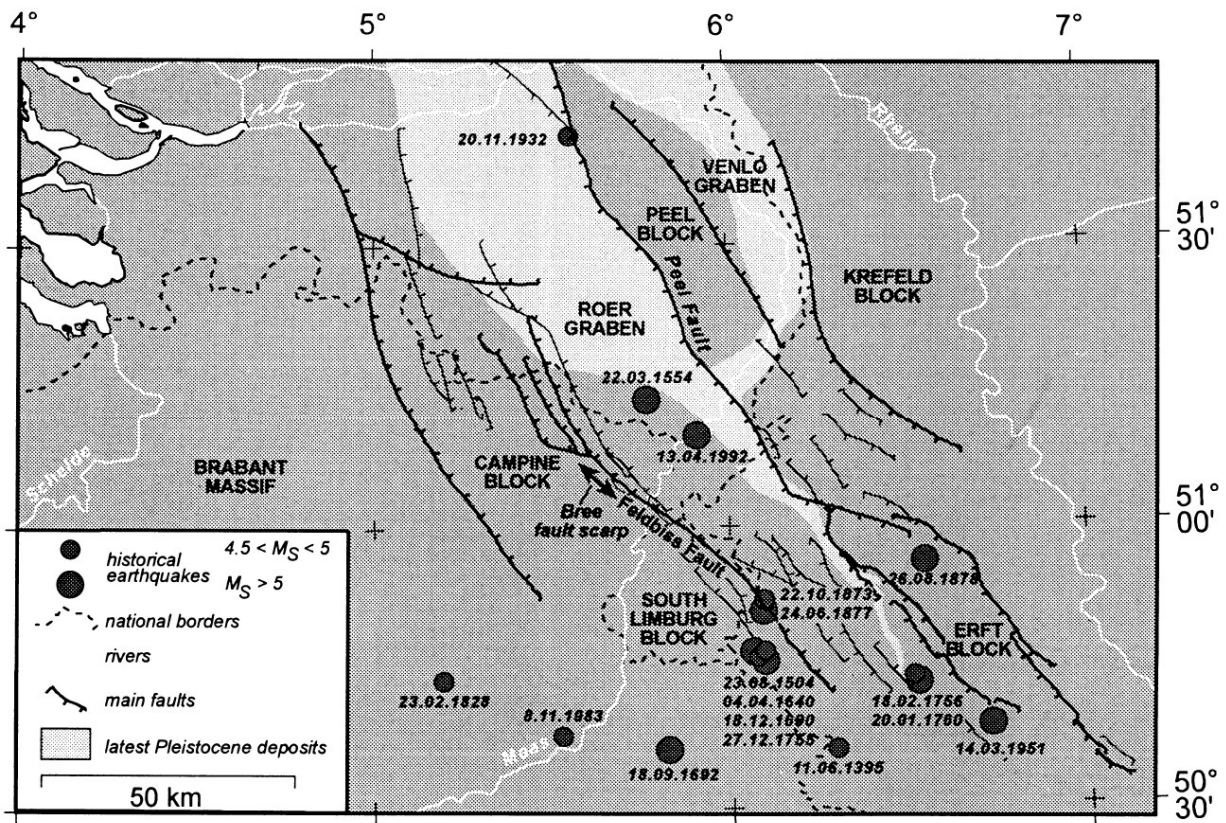


Figure A4.6.1. Quaternary faults along the Roer Valley. Main historical earthquakes with magnitude M larger than 4.5 shown. From Camelbeeck & Meghraoui (1998).

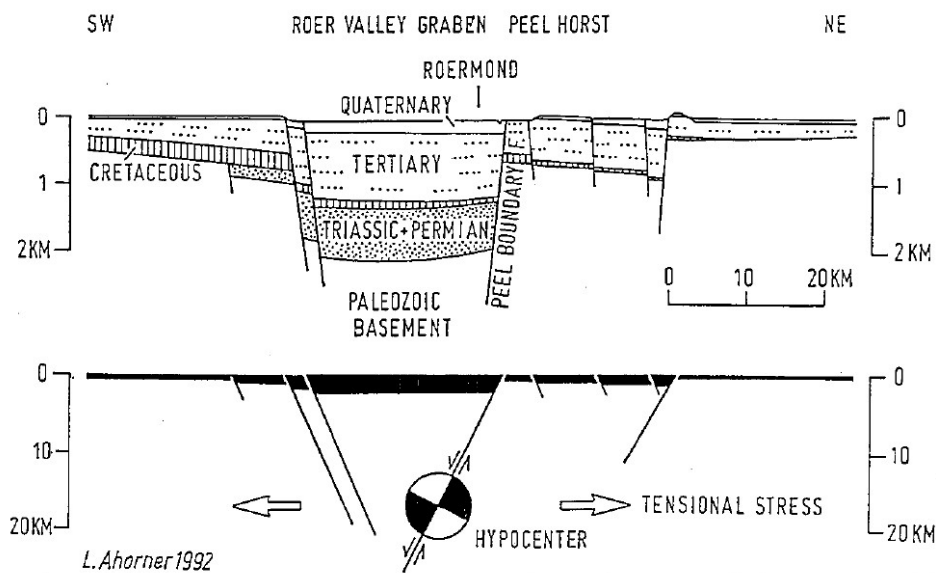


Figure A4.6.2. Simplified cross-section through the Roer Valley Graben near Roermond. From Ahorner (1994).

A4.6.1.2 Regional and local seismicity

Though being the most active tectonic region in north-western Europe and presenting a rather continuous seismic activity, the Roer Valley Graben is characterized by low deformation rates and long recurrence times for large seismic events (Camelbeeck *et al.*, 1994; Ewald *et al.*, 2006; Vanneste *et al.*, 2013).

According to Vanneste *et al.* (2013), and as shown in Figure A4.6.3, seven earthquakes with surface-wave magnitude M_s larger than or equal to 5.0 and epicentres within the Roer Valley Graben have been recorded since 1350, including the 1992 Roermond one. Before the latter, the last equally damaging earthquake was that of 18th February 1756 near Düren (Germany) which, with an estimated magnitude of M_s 5.7 and a maximum epicentral intensity of VIII MSK, was the most important event of a seismic series that lasted almost four years (Braunmiller *et al.*, 1994; Vanneste *et al.*, 2013). Most of the observed events are concentrated around certain areas, especially to the south, and very few events have been recorded in the northern Roer Valley Graben.

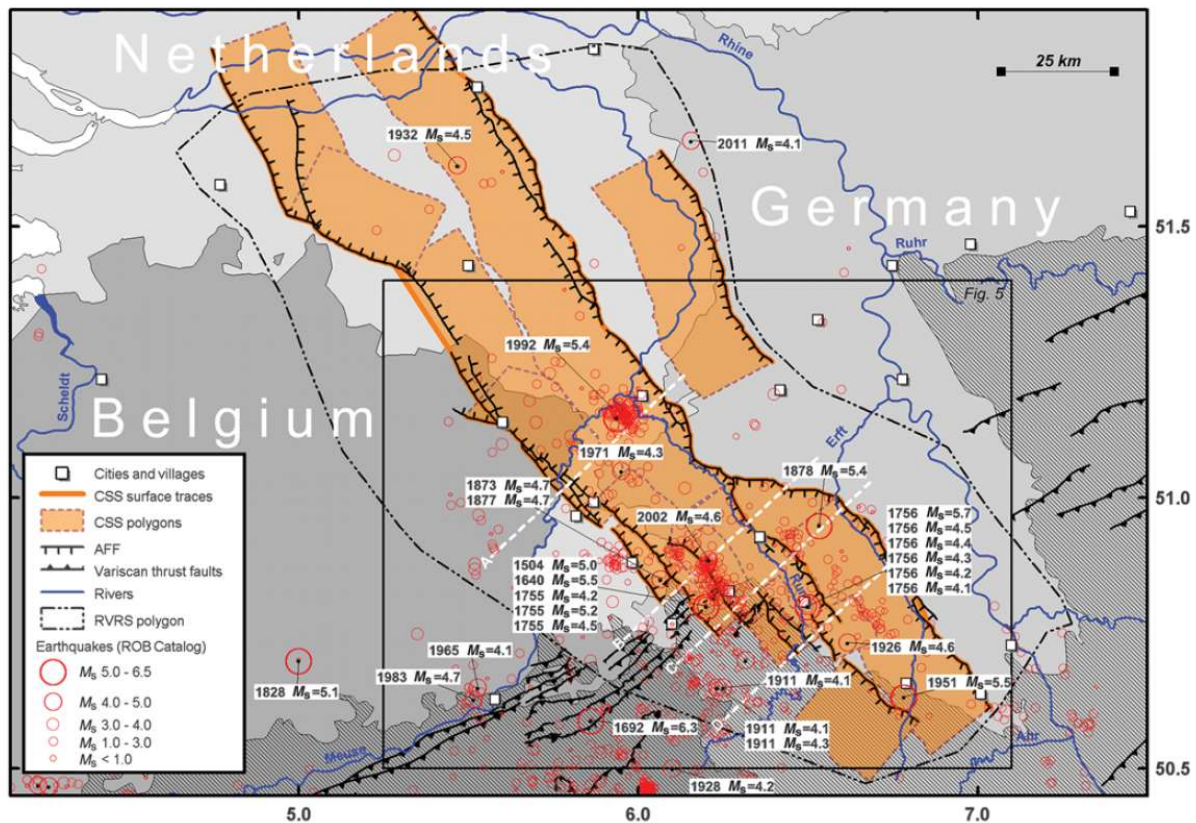


Figure A4.6.3. Historical and instrumental seismicity (1350-2011) in the Lower Rhine Graben according to the catalog of the Royal Observatory of Belgium, overlying the seismogenic sources defined by Vanneste *et al.*, (2013). From Vanneste *et al.*, (2013).

Atakan *et al.* (2000) draw attention to the importance of taking into consideration paleoseismic studies when defining recurrence periods of seismic events. While addressing the question of whether the faults along the Roer Valley Graben are capable of producing an earthquake larger than the 1992 Roermond one, Camelbeeck & Meghraoui (1996) concluded that the return period of a $M_{6.5}$ event estimated only from historical and instrumental seismicity data (40,000 years) is significantly longer than if determined taking into consideration palaeoseismic data (two or three possible occurrences during the last 12,000 years).

A4.6.1.3 Seismic hazard

Information regarding the seismic hazard in the Roer Valley Graben can be found spread amongst national hazard maps of each of the countries involved and regional studies.

In 1984, Ahorner & Rosenhauer (1986) generated a seismic hazard map for Germany and adjacent regions in which it can be seen that the macroseismic intensity expected for Roermond and a series of cities in between the latter and Koblenz is around 7.25-7.50 in the MSK scale (MSK-81; Medvedev *et al.*, 1981) for a return period of 10,000 years (Figure A4.6.4). According to Rosenhauer & Ahorner (1994), it became clear at that time that the Lower Rhine Embayment belonged to the most active seismic zone in western and central Europe. When incorporating the 1992 Roermond earthquake to the seismic catalogue, Rosenhauer & Ahorner (1994) observed an increase in the annual probability of experiencing a VII MSK intensity at Roermond from 0.00049 to 0.00024, and concluded that the inclusion of the 1992 earthquake had moderate effects on the overall seismic hazard. At the same time, de Crook (1994) stated that the influence is, actually, negligible. However, the current seismic hazard map for Germany (Grünthal *et al.*, 1998, Figure A4.6.5) presents similar values of EMS-98 intensity expected in a much shorter return period of 475 years (10% probability of exceedance in 50 years).

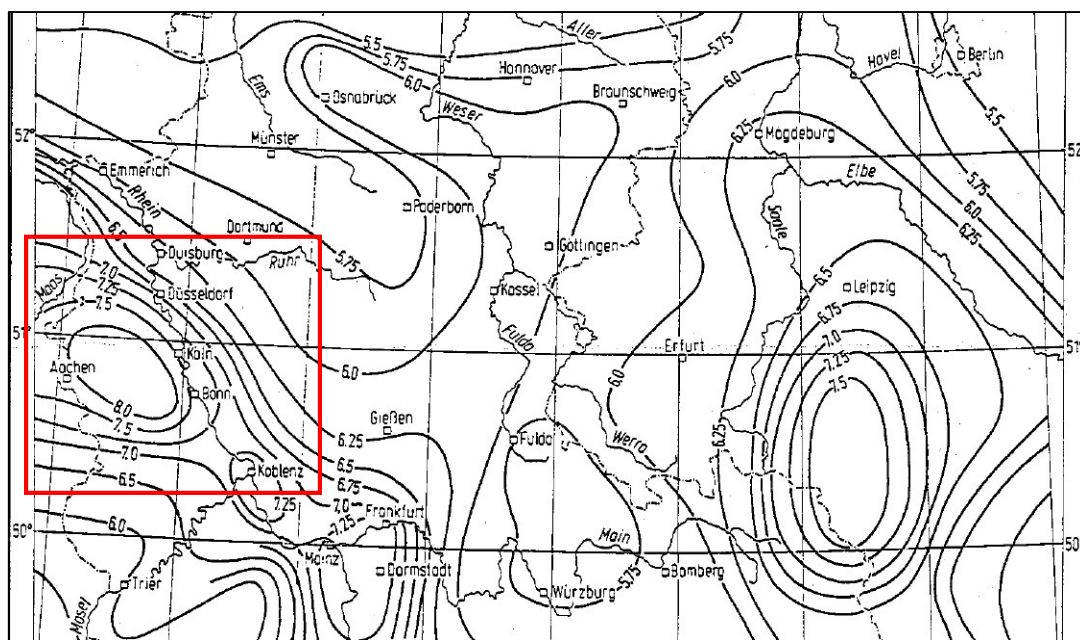


Figure A4.6.4. Extract of the hazard map of Ahorner & Rosenhauer (1986), from Rosenhauer & Ahorner (1994). Isolines correspond to MSK intensity values with a 10,000 years return period. The red rectangle frames the area most affected by the 1992 earthquake.

Figure A4.6.6 shows the outcome of a probabilistic seismic hazard analysis carried out by de Vos (2010) for the southern Netherlands. The expected PGA on rock with a 10% probability of exceedance in 50 years according to this study is around 100 cm/s^2 (0.102 g) for Roermond and most of the area affected by the 1992 earthquake. This value is in relatively good agreement with those of the official seismic hazard map for Belgium, on which the microzonation for Eurocode 8 for this country is based (Figure A4.6.7, Leynaud *et al.*, 2000).

Within the seismic hazard zonation map of the Netherlands (de Crook, 1996, Figure A4.6.8), it is not clear whether Roermond falls in zone C or D, being the corresponding design PGA in rock (10% probability of exceedance in 50 years) 0.05 g and 0.10 g, respectively. The Royal Netherlands Meteorological Institute (KNMI) is preparing an update of this map (Brouwer *et al.*, 2010).

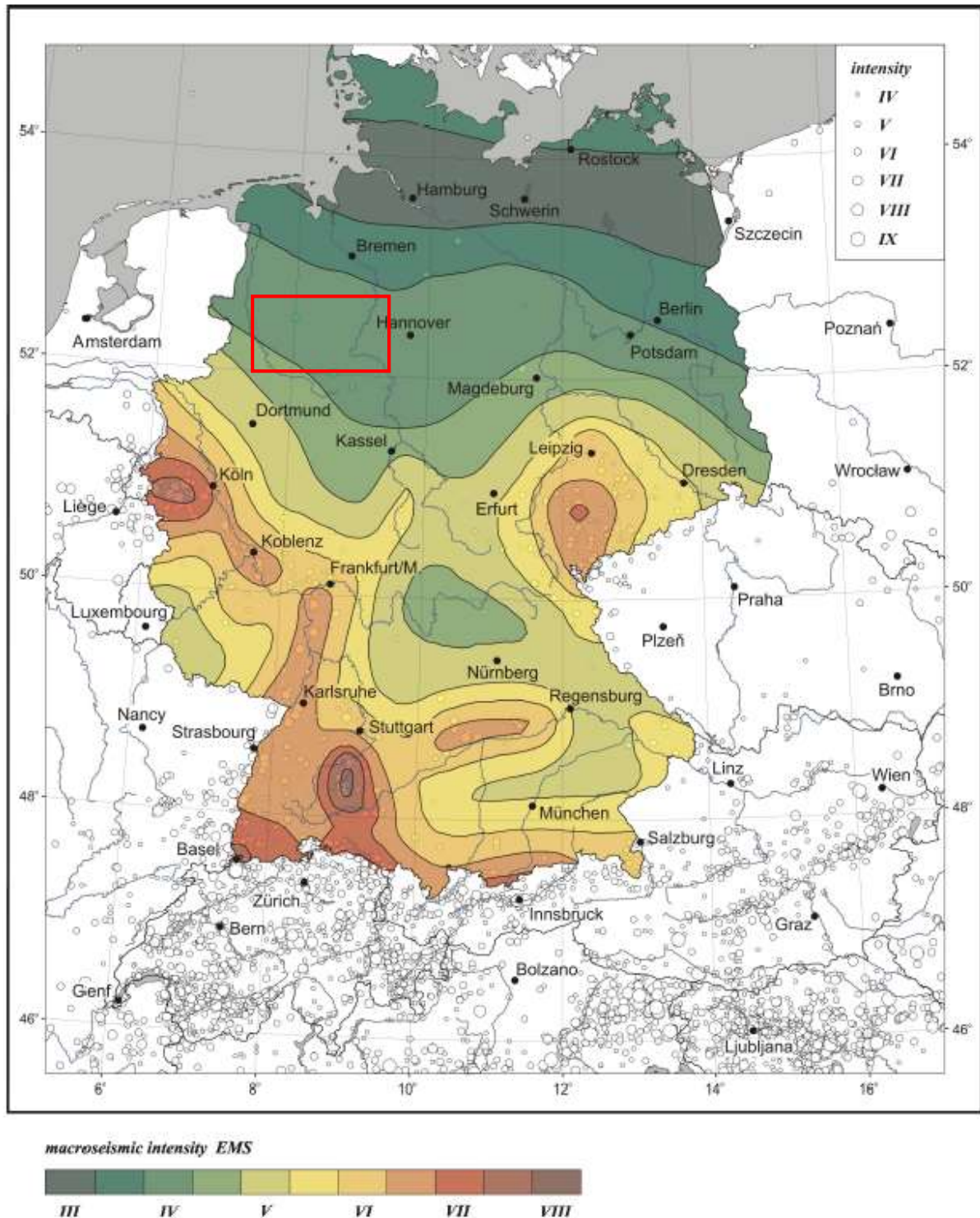


Figure A4.6.5. Seismic hazard in Germany in terms of European Macroseismic Scale (EMS-98) intensities for a 10% probability of exceedance in 50 years. From Grünthal *et al.* (1998). The red rectangle frames the area most affected by the 1992 earthquake.

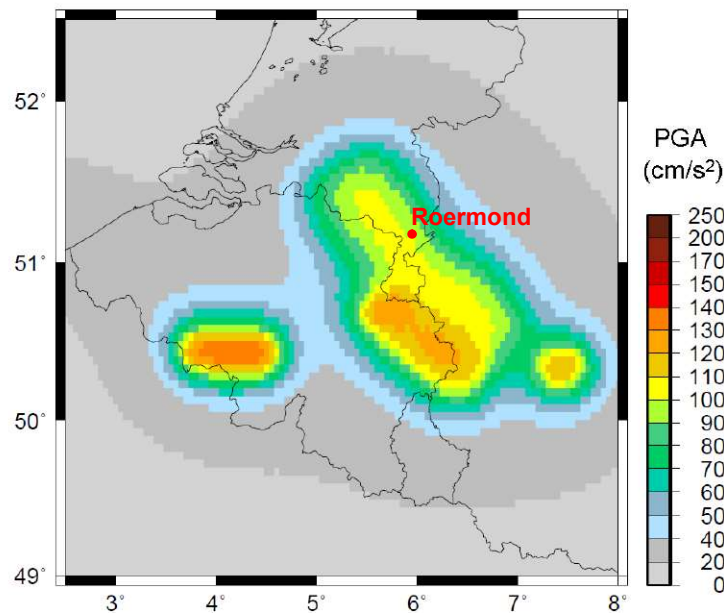


Figure A4.6.6. PGA on rock with 10% probability of exceedance in 50 years (475 years return period) for the southern Netherlands. From de Vos (2010).

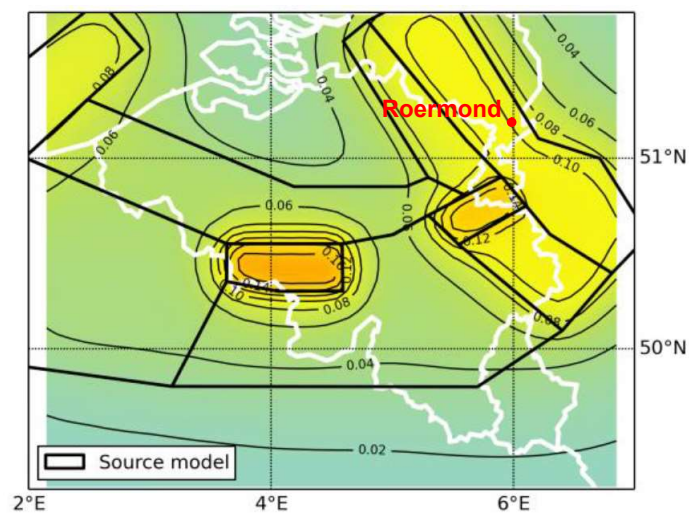


Figure A4.6.7. Official hazard map for Belgium (Leynaud *et al.*, 2000): PGA on rock with 10% probability of exceedance in 50 years (475 years return period) for Belgium. Image from Vanneste *et al.* (2014).

Figure A4.6.9 shows the 5% damped uniform hazard spectra on rock from the SHARE (Seismic Hazard Harmonization in Europe) project (Woessner *et al.*, 2015) for the closest available coordinates to some of the cities which suffered relevant damage: Roermond and Herkenbosch, in the Netherlands, and Heinsberg and Cologne, in Germany. The corresponding PGA values on rock with a 10% probability of exceedance in 50 years are, in order, 0.113 g, 0.105 g, 0.121 g, and 0.089 g. The Global Seismic Hazard Assessment Program (GSHAP) yields significantly lower values of 0.070 g, 0.071 g, 0.084 g and 0.085 g, respectively (Giardini *et al.*, 1999).

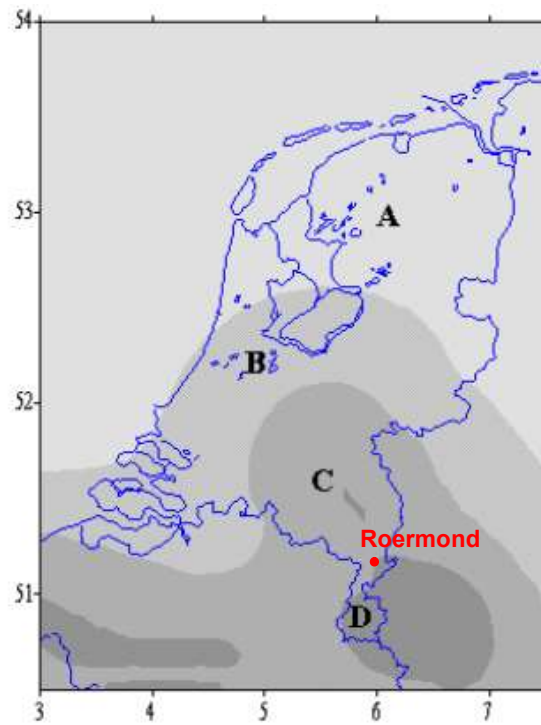


Figure A4.6.8. Hazard zonation in the Netherlands, from the work of de Crook (1996). For a 10% probability of exceedance in 50 years, the design PGA values on rock are 0.010 g (zone A), 0.022 g (zone B), 0.050 g (zone C) and 0.100 g (zone D). Image from Brouwer *et al.* (2010).

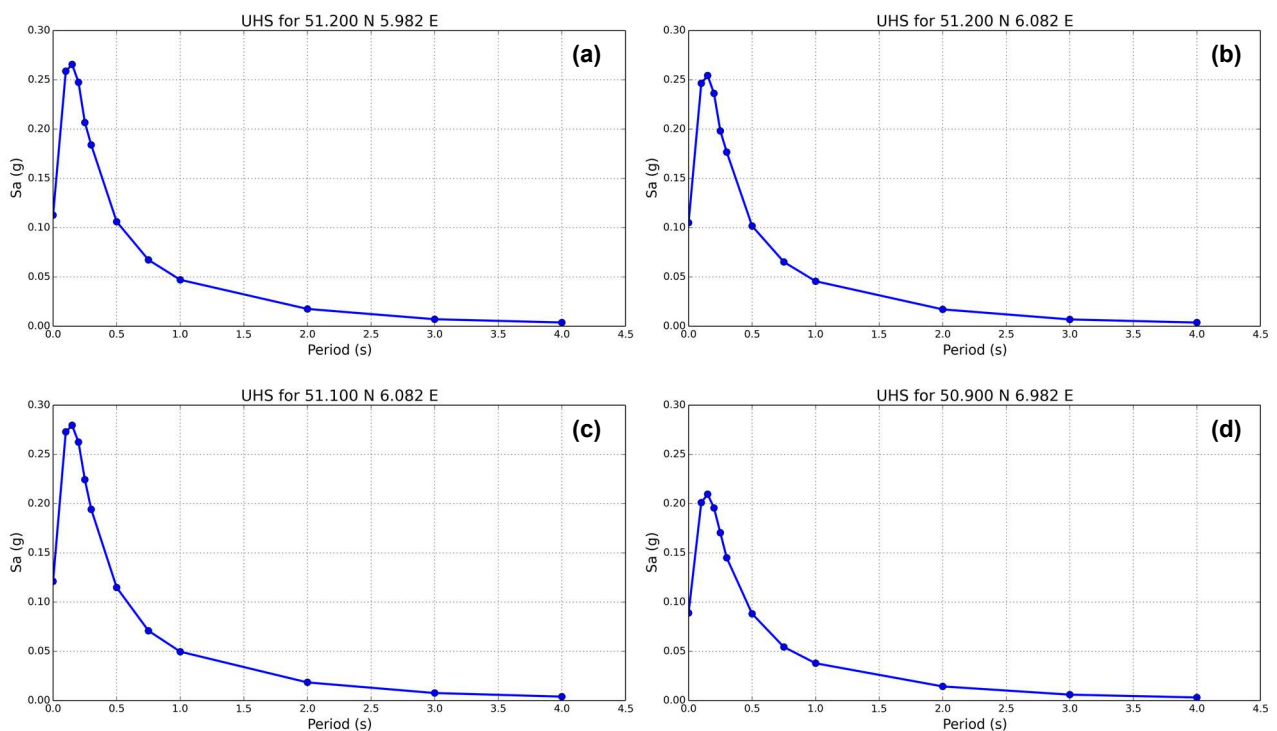


Figure A4.6.9. Uniform Hazard Spectra for the closest available coordinates to the cities of (a) Roermond (Netherlands), (b) Herkenbosch (Netherlands), (c) Heinsberg (Germany) and (d) Cologne (Germany), according to SHARE (5% critical damping). Values correspond to PGA and spectral acceleration on rock with a 10% probability of exceedance in 50 years (mean).

The Worldwide Seismic Design Tool of the United States Geological Survey (USGS) make use of the results from GSHAP to estimate the spectral accelerations at 0.2 and 1.0 seconds with a 2% probability of exceedance in 50 years shown in Table A4.6.1. It should be noted that these values result from significant approximations and are therefore classified within the lowest reliability category of the USGS database.

Table A4.6.1. Spectral accelerations at 0.2 and 1.0 seconds with a 2% probability of exceedance in 50 years, according to GSHAP. "UFC+GSHAP" and "EUCode+GSHAP" make reference to different estimation methods

Location	Latitude	Longitude	Case	Sa(0.2) (g)	Sa(1.0) (g)
Roermond	51.200	5.982	UFC+GSHAP	0.350	0.140
			EUCode+GSHAP	0.370	0.150
Herkenbosch	51.200	6.082	UFC+GSHAP	0.360	0.140
			EUCode+GSHAP	0.370	0.150
Heinsberg	51.100	6.082	UFC+GSHAP	0.420	0.17
			EUCode+GSHAP	0.430	0.170
Cologne	50.900	6.982	UFC+GSHAP	0.430	0.170
			EUCode+GSHAP	0.450	0.180

A4.6.2. Earthquake source characteristics

A4.6.2.1 Location, depth and time

The main shock occurred on 13th April 1992, at 01.20 UTC (03.20 local time).

Several organizations and agencies report their own estimations of the epicentral coordinates and hypocentral depth. The information reported in the websites of the Royal Netherlands Meteorological Institute (KNMI), the Royal Observatory of Belgium (ROB), the National Earthquake Information Center (NEIC) of the United States Geological Service (USGS), the Global Centroid Moment Tensor Project (GCMT; Dziewonski *et al.*, 1981; Ekström *et al.*, 2012), the International Seismological Centre (ISC) and the GEM Earthquake Consequences Catalogue is summarized in Table A4.6.2. Cells marked as (*f) correspond to parameters that were held fixed while inversion was carried out to retrieve those that remain. Table A4.6.2 also includes the epicentral coordinates and hypocentral depths calculated by Ahorner (1994) and Camelbeeck *et al.* (1994). Note that in some cases it is not clear whether the reported coordinates correspond to the epicentre or to the centroid of the moment tensor solution.

There appears to be no agreement with respect to the hypocentral depth. Scherbaum (1994) carried out a series of stochastic simulations of the strong ground motion of this earthquake considering three different hypocentral depths (13, 21 and 25 km) and concluded that the shallow source is the most inconsistent with the observations. Meidow & Ahorner (1994) recognize the difficulties of justifying a maximum observed epicentral intensity of VII with a shallow hypocentre, but believe the reduced intensity levels are due to the influence of the sedimentary graben fill on the attenuation of the seismic waves. By

adjusting the epicentral intensity to account for this influence, Meidow & Ahorner (1994) calculate a depth of 17 km, which they find more accurate than the 26 km they would obtain without said adjustment. Braunmiller *et al.* (1994) estimated the source mechanism of the earthquake considering a hypocentral depth of 18 km and 13 km and observed a slightly better fit with the former than with the latter. It should be noted that Ahorner (1994) and Camelbeeck *et al.* (1994) provide their estimations with a variability of ± 3 km and ± 1 km, respectively, therefore overlapping in the range 16.4-17.6 km.

Table A4.6.2. Epicentral coordinates and hypocentral depths from different sources

Agency / Publication		Latitude	Longitude	Depth (km)
KNMI	Royal Netherlands Meteorological Institute	51.1620 ° N	5.9330 ° E	15.40
ROB	Royal Observatory of Belgium	51.1480 ° N	5.9370 ° E	19.00
NEIC	National Earthquake Information Center, USGS	51.1530 ° N	5.7980 ° E	21.20
GCMT	Global Centroid Moment Tensor Project	51.5600 ° N	5.6300 ° E	15.00
ISC	International Seismological Centre (inversion)	51.1391 ° N	5.7587 ° E	21.20 (*f)
GEM	GEM Earthquake Consequences Database	51.1500 ° N	5.9300 ° E	15.00
Ahorner (1994)		51.1700 ° N	5.9250 ° E	14.60
Camelbeeck <i>et al.</i> (1994)		51.1633 ° N	5.9533 ° E	17.40

(*f) fixed parameter used for inversion

The map in Figure A4.6.10 shows the different estimations of the epicentral coordinates enumerated above. Note the good agreement amongst the positions reported by KNMI, ROB, GEM, Ahorner (1994) and Camelbeeck *et al.* (1994), in contraposition with those of GCMT, ISC and NEIC.

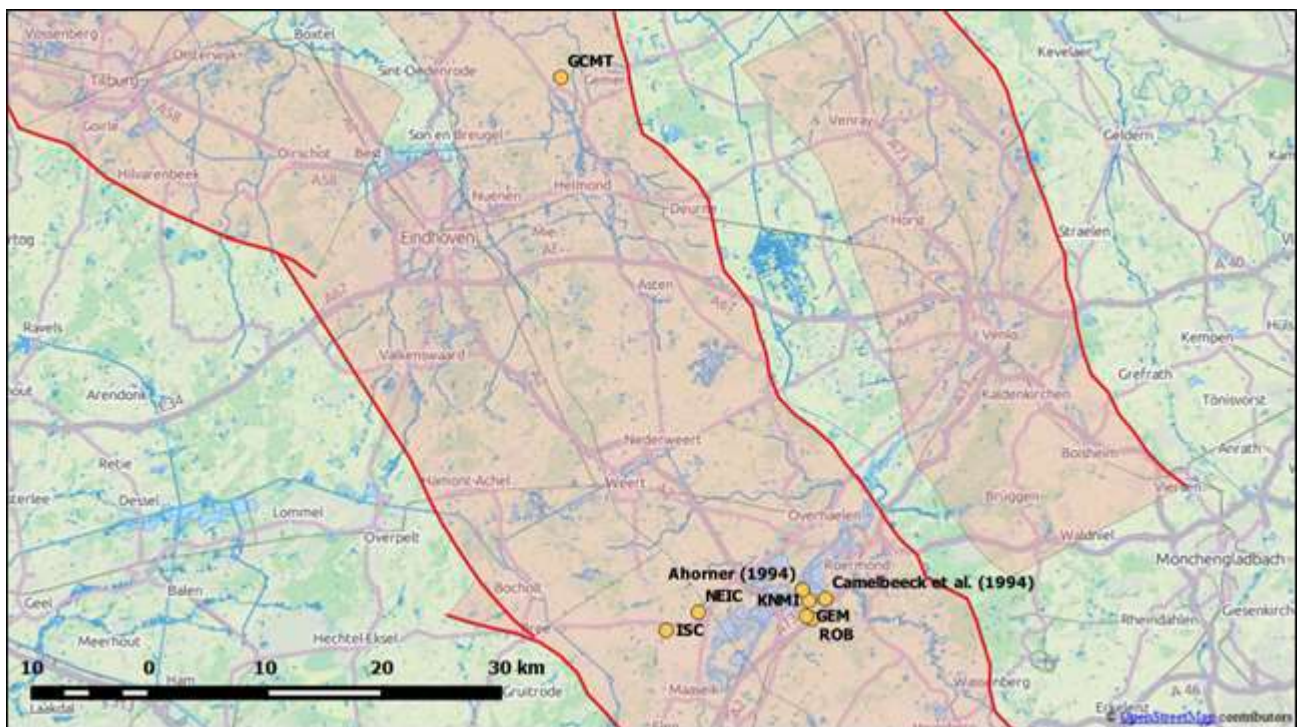


Figure A4.6.10. Estimation of epicentral coordinates (yellow circles). Red lines represent the surface traces of the main faults in the area. Red areas represent the projection of the faults planes. Faults position from SHARE (Basili *et al.*, 2013).

A4.6.2.2 Magnitude

Estimations of magnitude made by the same agencies and studies are reported in Table A4.6.3.

Table A4.6.3. Estimations of moment magnitude (**M**), body-wave magnitude (**mb**), local magnitude (**M_L**) and surface-wave magnitude (**M_s**)

Agency		M	mb	M _L	M _s
KNMI	Royal Netherlands Meteorological Institute	-	-	5.8	-
ROB	Royal Observatory of Belgium	5.3	-	5.8	5.4
NEIC	National Earthquake Information Center, USGS	5.4	5.5	5.9	5.2
GCMT	Global Centroid Moment Tensor Project	5.3	5.4	-	5.0
ISC	International Seismological Centre (inversion)	-	5.3	-	5.6
GEM	GEM Earthquake Consequences Database	5.4	-	-	-
Ahorner (1994)		5.3	-	5.9	-
Camelbeeck <i>et al.</i> (1994)		5.4	-	5.8	-

A4.6.2.3 Style-of-faulting

All sources agree in the focal mechanism being almost purely normal, and identify the Peel Boundary Fault as the responsible for this earthquake. However, the strike of the preferred nodal plane varies between 124° and 143° for different authors. Camelbeeck & van Eck (1994) believe this variation is due to different local velocity models being used and different focal depths being assumed. The estimation of the strike by Ahorner (1994) is 124° (Figure A4.6.11). The author recognizes that there is a slight misalignment between this value and the 145° of the near-surface trace of the Peel Boundary fault, but believes that a change of orientation is taking place at depth.

Table A4.6.4 and Figure A4.6.11 summarize the focal mechanisms calculated by different authors. In many cases, only the fault plane is reported.

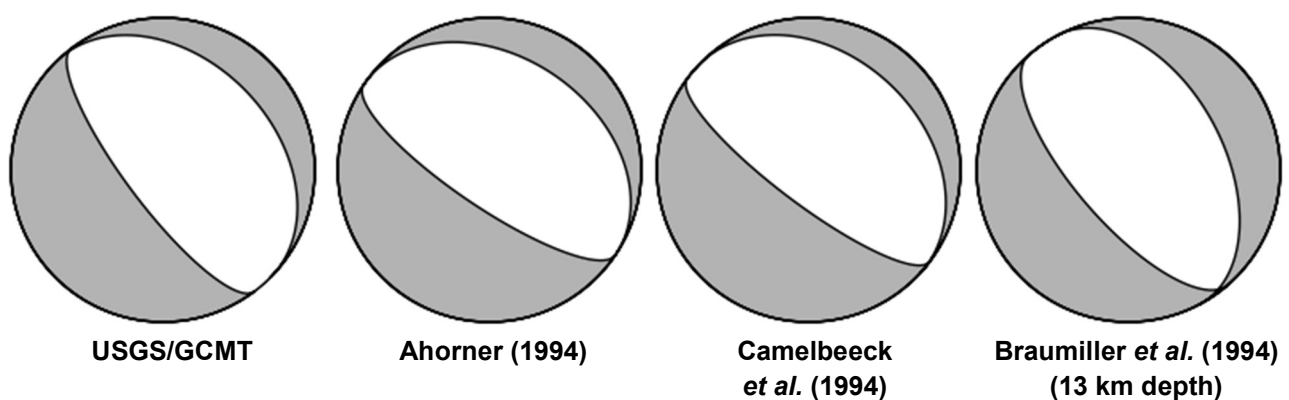


Figure A4.6.11. Fault plane solutions for the main shock according to different sources.

Table A4.6.4. Fault plane solutions and fault planes from different sources. Fault planes marked in gray are the preferred solution in each case.

Fault Plane 1			Fault Plane 2			Source
Strike	Dip	Rake	Strike	Dip	Rake	
143	68	-87	314	22	-98	NEIC (USGS) / GCMT
124	68	-90	124	22	-90	Ahorner (1994)
127	70	-92	<i>n/a</i>	<i>n/a</i>	<i>n/a</i>	Camelbeeck <i>et al.</i> (1994)
139	58	263	<i>n/a</i>	<i>n/a</i>	<i>n/a</i>	Braunmiller <i>et al.</i> (1994) - 13 km depth assumed
138	58	262	<i>n/a</i>	<i>n/a</i>	<i>n/a</i>	Braunmiller <i>et al.</i> (1994) - 18 km depth assumed

A4.6.2.4 Stress drop

Ahorner (1994) reports a stress drop of 4.4 MPa. Camelbeeck *et al.* (1994) estimate a significantly larger value of 9.7 MPa, with a variation of ± 6.4 MPa. The 4.4 MPa of Ahorner (1994) fall within the lower bound of the latter, while the 12 MPa resported by Pelzing (1994) fall within the upper bound. Grünthal & Grosser (1992) estimate it to be between 1 and 7 MPa.

A4.6.2.5 Foreshocks and aftershocks

The main shock was preceded by a smaller event that occurred 0.2 seconds earlier. According to Ahorner (1994), its magnitude was M_L 4.8, while for Oncescu *et al.* (1994) it was closer to M_L 4.0, "approximately two units smaller than the main shock". Ahorner (1994) estimated their hypocentral locations being 51.168°N 5.927°E 14.0 km deep and 51.170°N 5.925°E 14.6 km deep for the foreshock and main shock, respectively, and concluded that they were significantly close to each other. Apart from this one previous event, no other foreshock activity had been observed (Camelbeeck *et al.*, 1994).

Over 200 aftershocks were detected (Oncescu *et al.*, 1994b), but the seismic activity decreased rapidly, with 50 events being detected during the first four hours and another 50 events during the next twenty (Camelbeeck & van Eck, 1994). Twenty-nine aftershocks with M_L equal to or larger than 2.0 were detected until 17th May 1992, with four of them being larger than 3.0 (Ahorner, 1994). The plot in Figure A4.6.12 shows the number of events observed per day during the first month after the main shock. As shown in the map of Figure A4.6.13, this activity was observed both in the direct vicinity of the epicentre and within a localized area 40 km south-east of the main shock, along the axis of the Roer Valley Graben (Camelbeeck & van Eck, 1994).

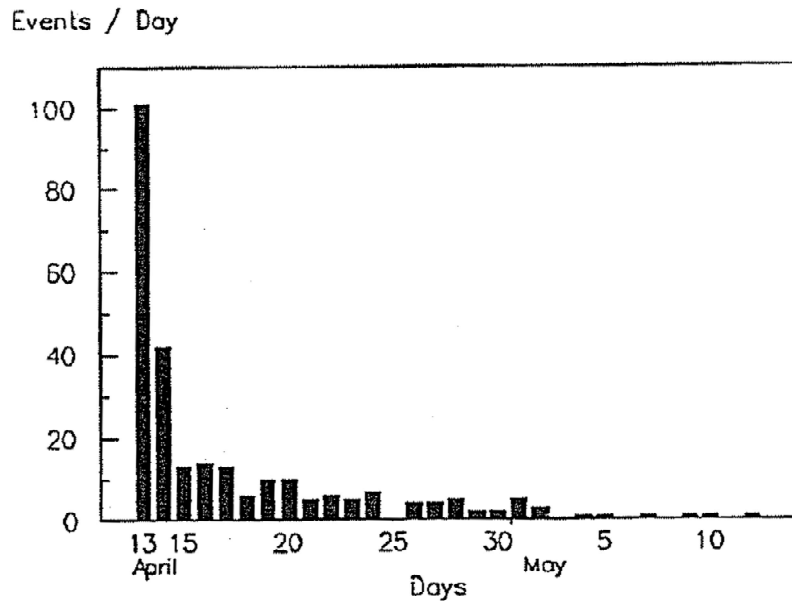


Figure A4.6.12. Number of events observed per day during the first month after the main shock. From Camelbeeck *et al.* (1994).

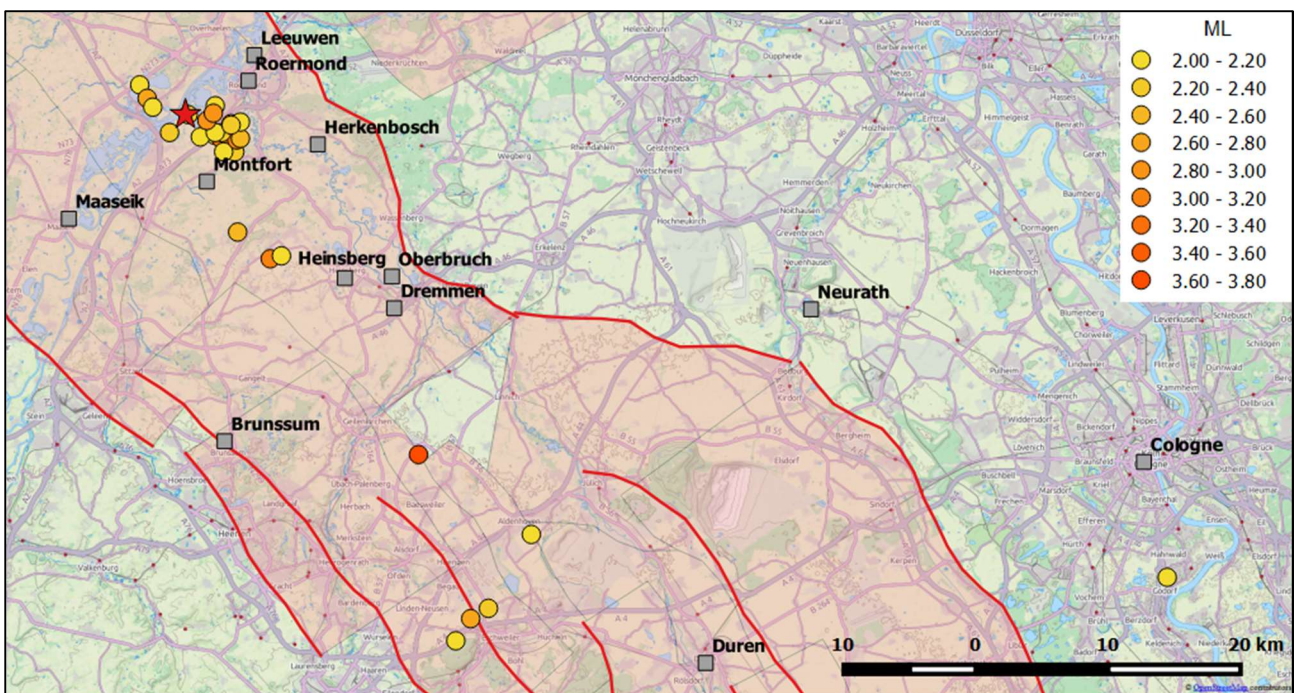


Figure A4.6.13. Location of aftershocks with ML equal to or larger than 2.0, according to Ahorner (1994). The red star marks the epicentre of the main shock, according to the same author.

A4.6.2.6 Nature of earthquake

This is a tectonic earthquake. According to Camelbeeck & van Eck (1994), although this event is one of the largest observed in western Europe in the 20th century, its size and location are in fully agreement with state-of-the-art knowledge of seismic hazard in the region.

A4.6.3 Geology and ground conditions in the affected area

A4.6.3.1 Regional geology and topography

The city of Roermond and most of the cities that suffered significant damage during the 1992 Roermond earthquake are located within the Roer Valley Graben, the central graben of the Lower Rhine Graben, located in the triple frontier comprising the Netherlands, Germany, and Belgium. The area lacks relevant topographic features, with the exception of a few isolated fault scarps (Evers, 2000).

The Lower Rhine Graben forms part of the European Cenozoic Rift System. It originated in the Early Tertiary (Oligocene) and was later filled with different layers of sediments of variable depth (Vanneste *et al.*, 2013). In the central Roer Valley Graben, the thickness of Neogene deposits can vary between 500 m and 900 m from west to east, while outside of the central area the depth of the deposits is generally less than 200 m. The largest thickness of Neogene sediments is located in the northwest sector, where they can reach to up to 1200 m. In the southeast, thicknesses progressively decrease. Younger Quaternary deposits are generally more than 100 m thick in all the graben, with the largest thickness being over 200 m in the northern areas. According to Ewald *et al.* (2006), the basin reaches a maximum overall depth of 1900 m. Figure A4.6.14 shows the general topography of the area and the depth of the sedimentary basin of the Roer Valley Graben, to the south of Roermond.

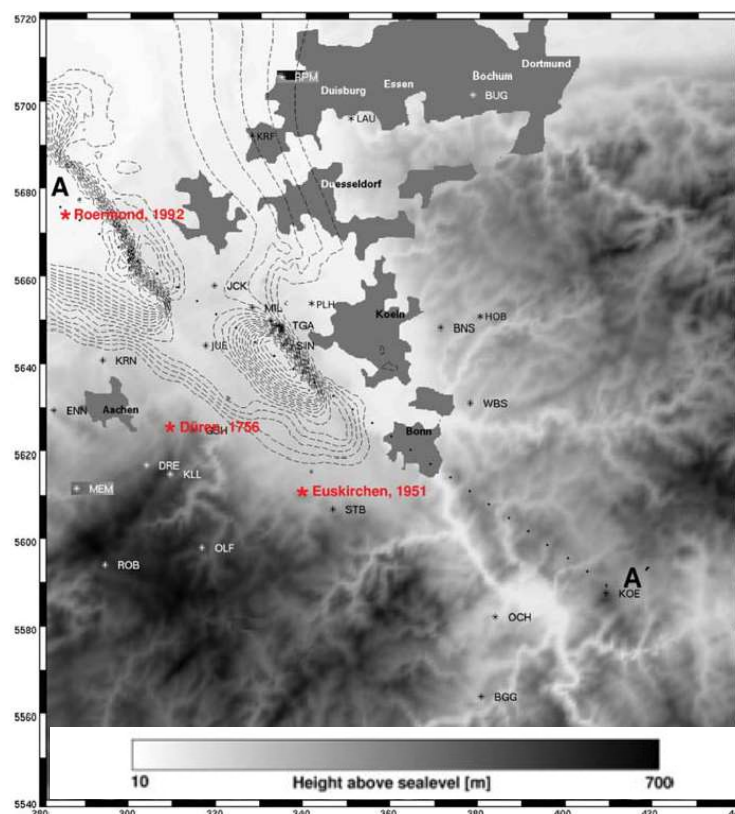


Figure A4.6.14. Topography (grey scale) and sedimentary basin depths of the Roer Valley Graben, to the south of Roermond. The sedimentary basin depth is indicated by dashed isolines in 100 m intervals. Epicentres of the 1992 Roermond earthquake and other two relevant events marked with red stars. Relevant urban settlements marked in gray (Ewald *et al.*, 2006).

A4.6.3.2 Site conditions in the affected area

As mentioned above, the Roer Valley Graben is filled with different layers of sediment. According to Schokker & Koster (2004), the oldest are an alternation of marine, coastal and fluvial materials deposited during the Tertiary and Early Quaternary. The withdrawal of the sea from the area left medium- to coarse-grained sediments from the Rhine-Meuse river depositional system. After this system disappeared in the second half of the Middle Pleistocene, the graben has been filled with local fine-grained sand, silt and peat. Figure A4.6.15 shows simplified geological cross sections of the Roer Valley Graben. Site effects are likely to be observed in this kind of geological structure (Ewald *et al.*, 2006; Horrent *et al.*, 1994).

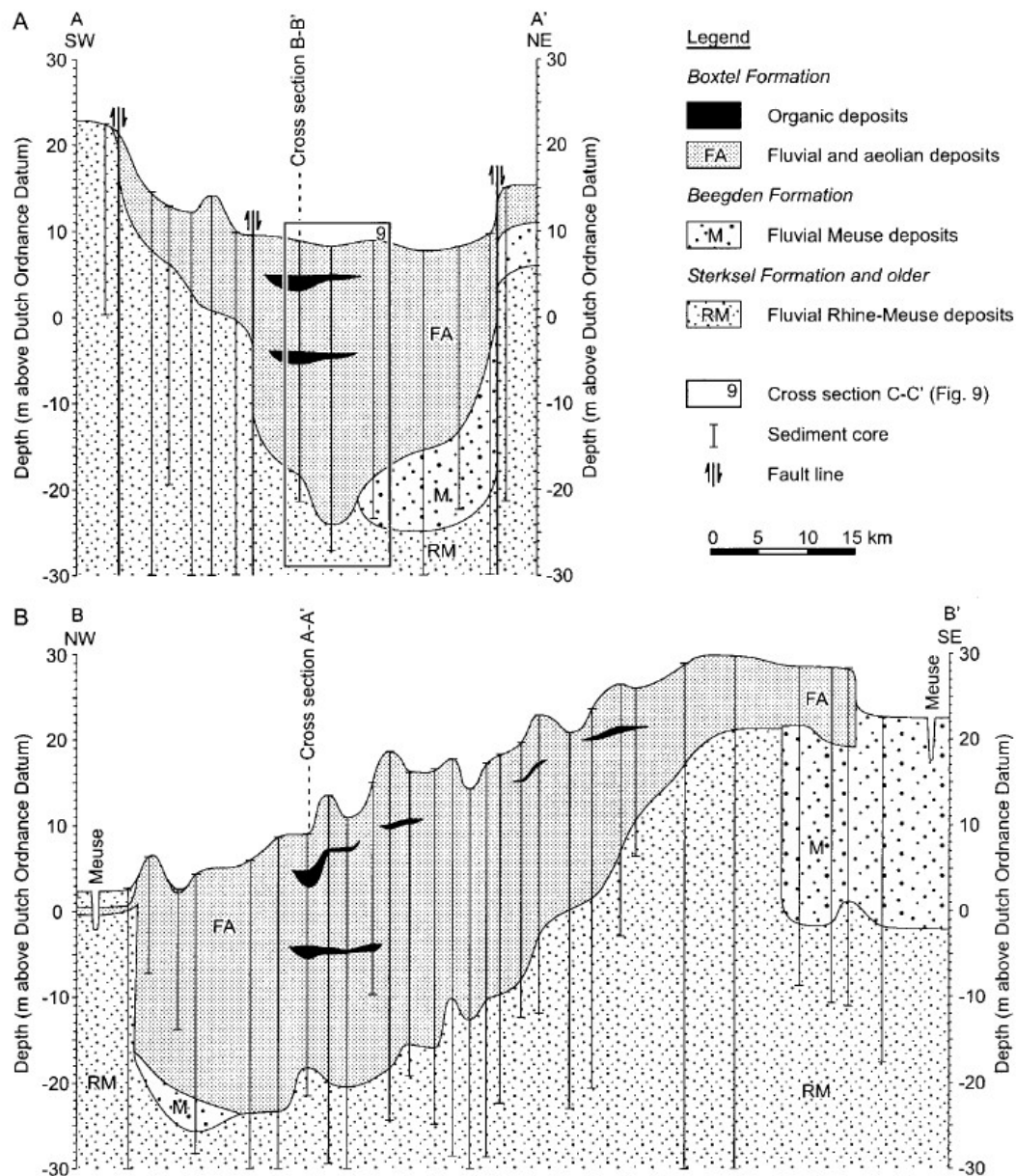


Figure A4.6.15. Simplified SW-NE (top) and NW-SE (bottom) geological cross sections showing the Middle and Upper-Pleistocene deposits in the Roer Valley Graben. FA: fluvial and aeolian fine-grained deposits. M: coarse-grained fluvial Meuse deposits. RM: medium- to coarse-grained fluvial Rhine-Meuse deposits (Schokker & Koster, 2004).

Davenport *et al.* (1994) and Nieuwenhuis (1994) report very shallow groundwater table levels in some areas of the Roer Valley Graben, of around 2.0 m and 3.5 m, respectively. The combination of loose sands and a water table at shallow depth suggests a significant likelihood of susceptibility to the occurrence of liquefaction. A study carried out by Lap (1987) concluded that the area around and to the south of Roermond presents a significant liquefaction potential, as shown in the map of Figure A4.6.16. This study also concluded that no liquefaction was to be expected in the area of Brunssum (25 km south of the epicentre) but, according to Maurenbrecher *et al.* (1994), the fact that the soil in the area has been reworked should suggest otherwise.

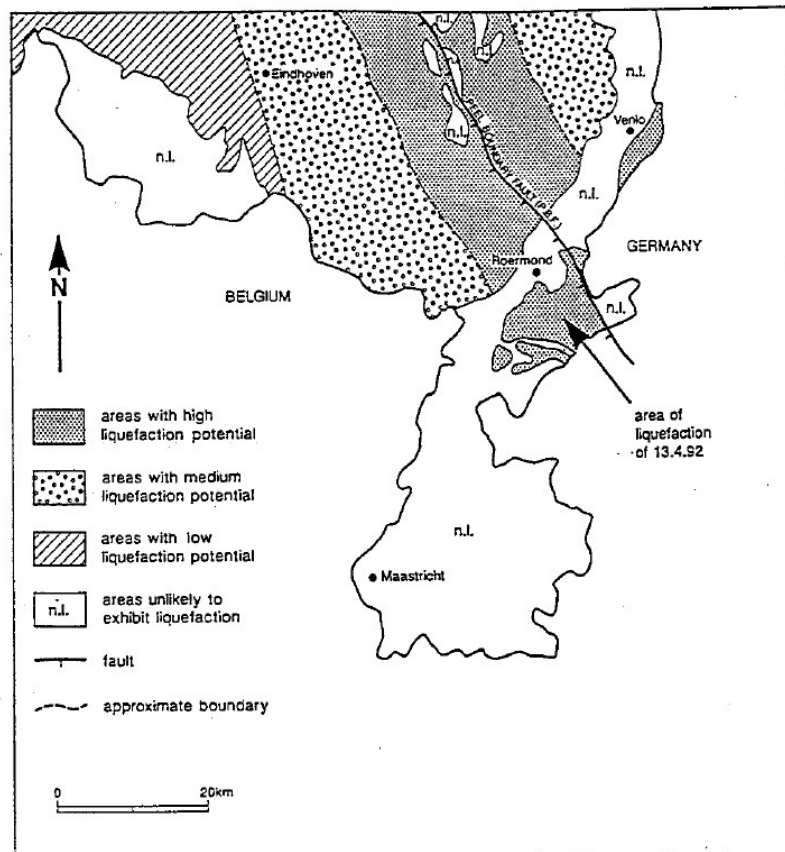


Figure A4.6.16. Susceptibility to liquefaction under a **M6** earthquake along the Peel Boundary Fault. From Davenport *et al.* (1994), after Lap (1987).

A4.6.4 Ground motions

A4.6.4.1 Intensity observations

Haak *et al.* (1994) carried out a significant effort to gather personal and community reports of macroseismic intensity from Belgium, Czech Republic, France, Germany, the Netherlands and the United Kingdom and homogenise them with the aim of elaborating the macroseismic intensity map of the 1992 Roermond earthquake. Different countries had used different intensity scales (MSK-64; Medvedev *et al.*, 1965; EMS-92, Grünthal, 1993; MSK-81, Medvedev *et al.*, 1981), and the final map was produced in terms of MSK-81 (Medvedev *et al.*, 1981), whose equivalence with the European Macroseismic Scale EMS-

98 is, roughly, one to one (Musson *et al.*, 2010). Low intensity areas were difficult to delimitate as a consequence of most people being asleep and not woken up by the shaking. Interpolation was needed for the intensity III isoline for areas such as the North Sea and the English Channel. The maximum observed intensity was VII ("damaging"), but the authors estimated a theoretical epicentral intensity of 7.4 (between "damaging" and "heavily damaging"), based on the average isoseismal radii. According to Meidow & Ahorner (1994), these were 6 km for intensity VII ("damaging"), 42 km for VI ("slightly damaging"), 102 km for V ("strong"), 179 km for IV ("largely observed"), 322 km for III ("weak") and 440 km for II ("scarcely felt"). Figure A4.6.17 shows the resulting map, which was adopted as well by the Royal Netherlands Meteorological Institute (KNMI). The inner isoseismals show an elongation in the southeast direction.

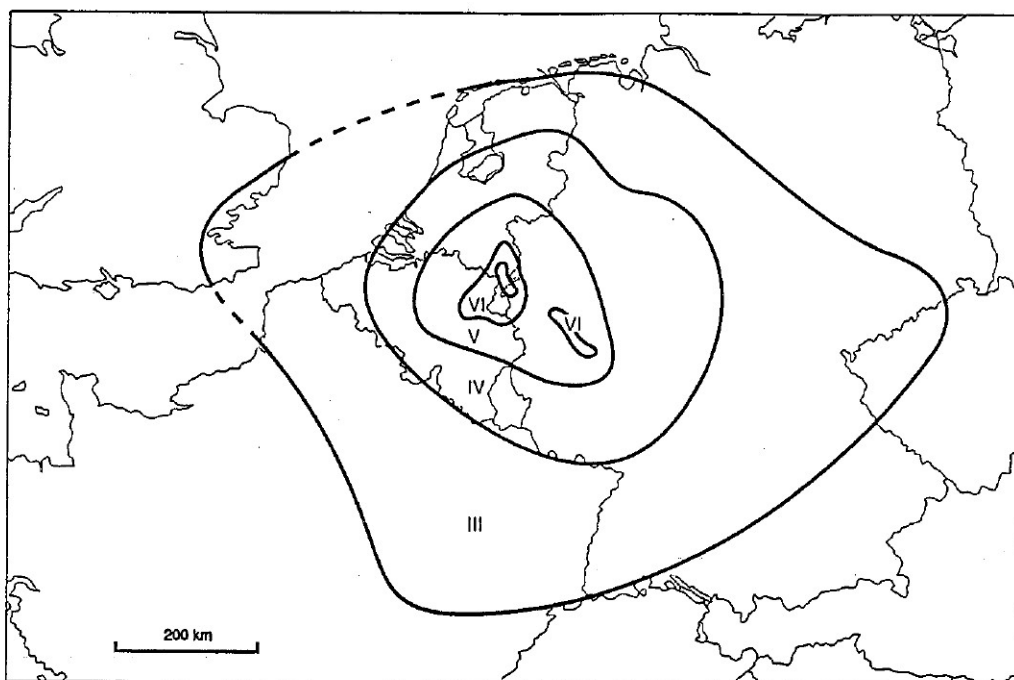


Figure A4.6.17. Isoseismal map of the 1992 Roermond earthquake. Intensities expressed in the MSK-81 scale. From Haak *et al.* (1994).

According to Meidow & Ahorner (1994), a maximum observed magnitude of VII MSK is "unusually low" when compared to other large seismic events in the Lower Rhine Embayment, and believe this is due to the absorption effect of the very thick sedimentary layers in the area, which reach a 1.5 km thickness near the epicentre.

Macroseismic reports were received from places located more than 500 km away from the epicentre, such as Berlin, Munich, Zürich and south-east England (Ahorner, 1994; Meidow & Ahorner, 1994). The event was felt over an area of approximately 600,000 km² (Ahorner, 1994). Islands of intensity V that can be explained by local site conditions were observed.

A4.6.4.2 Ground motion recordings

Due to the limited range of the instruments at the permanent stations around the Roermond area, most of them saturated and, consequently, there are no near-field records available for the 1992 Roermond main shock. The exact limit epicentral distance from which records are available is somewhere between 50 and 100 km, depending on the source (Camelbeeck *et al.*, 1994; Gariel *et al.*, 1994; Scherbaum, 1994). For this report, it was possible to have access to three records from the German network by means of the RESORCE European ground motion database (Akkar *et al.*, 2014). Figures A3.1.18 to 20 show plots of their corresponding acceleration time-histories.

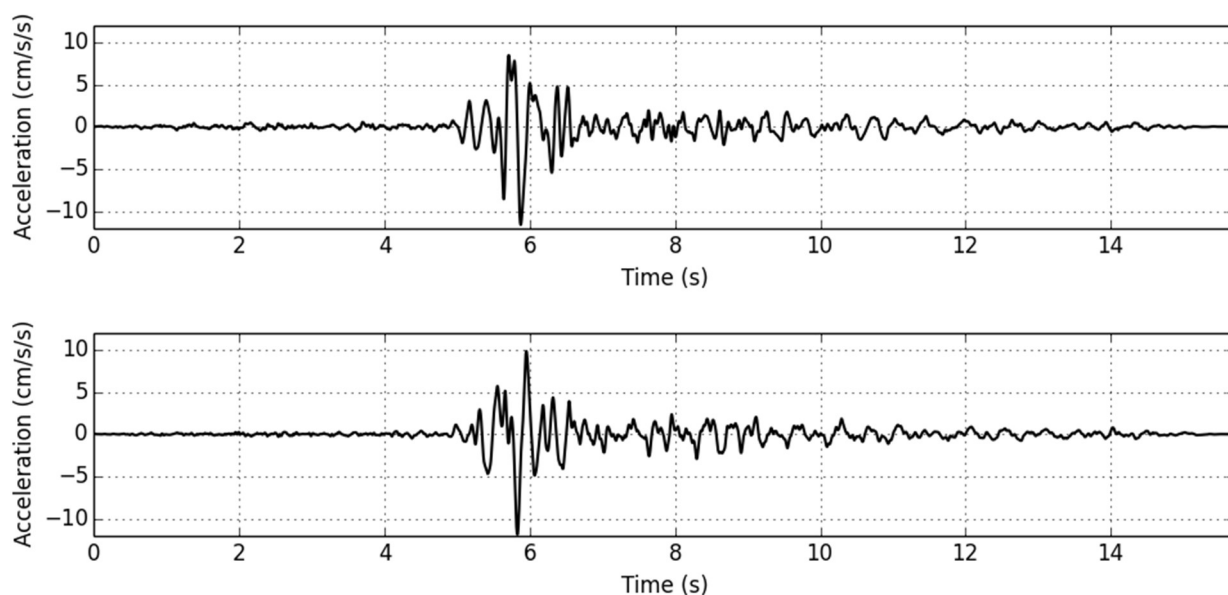


Figure A4.6.18. Horizontal acceleration time-histories recorded for the main shock at station GSH, in Germany. Waveform data from RESORCE database (Akkar *et al.*, 2014).

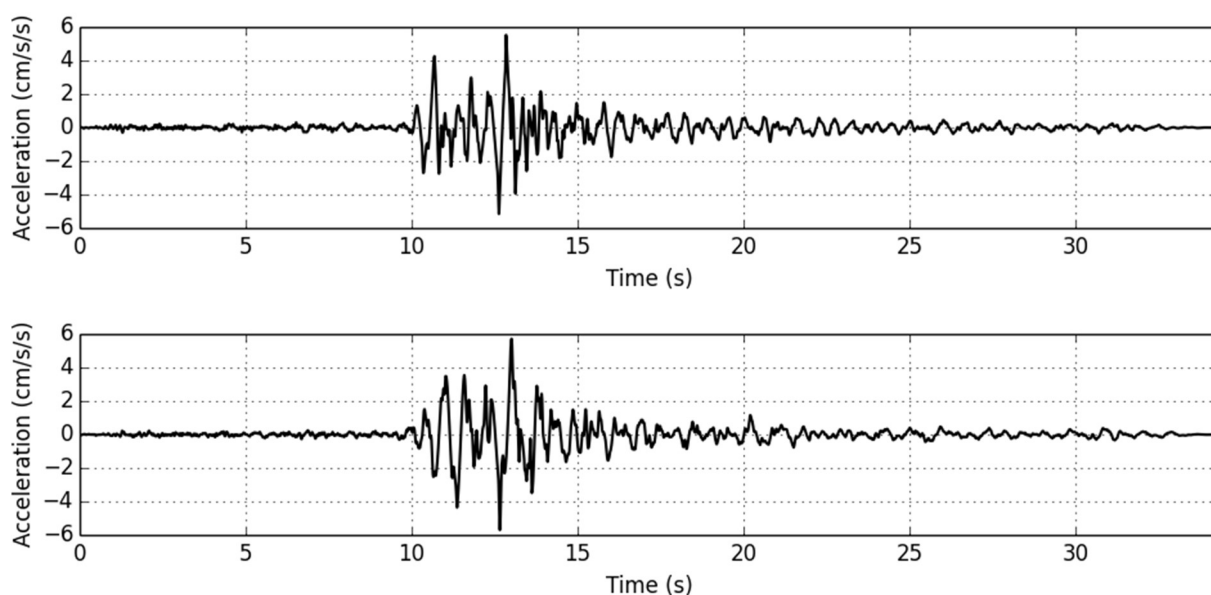


Figure A4.6.19. Horizontal acceleration time-histories recorded for the main shock at station OLF, in Germany. Waveform data from RESORCE database (Akkar *et al.*, 2014).

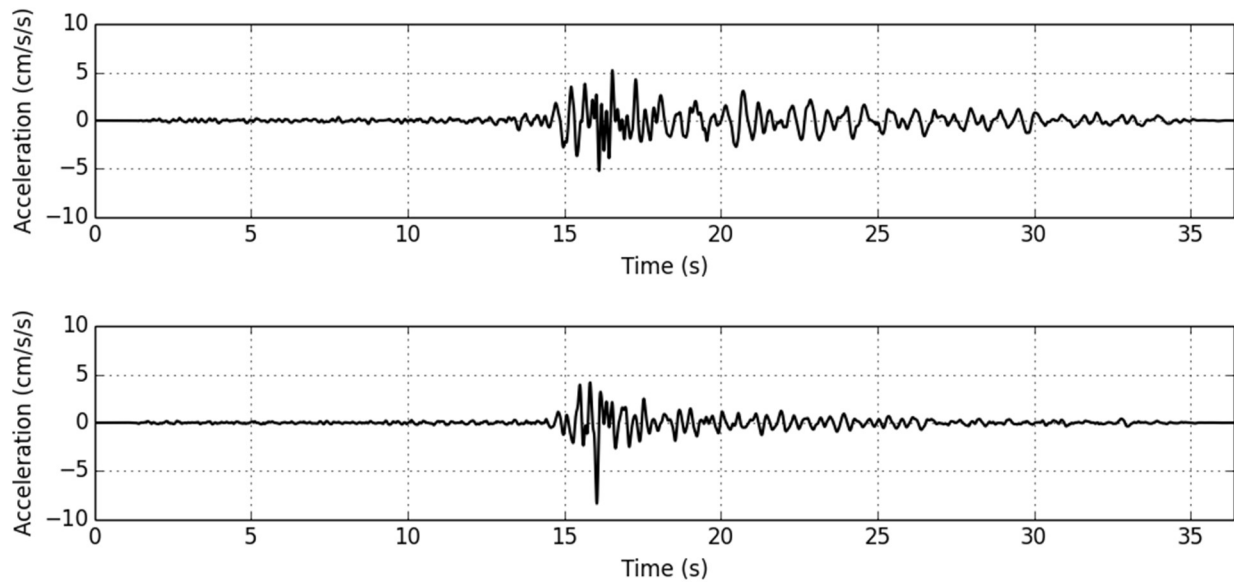


Figure A4.6.20. Horizontal acceleration time-histories recorded for the main shock at station WBS, in Germany. Waveform data from RESORCE database (Akkar *et al.*, 2014).

The pseudo-acceleration and displacement response spectra shown in Figure A4.6.21 were obtained using the OpenQuake ground motion toolkit (Weatherill, 2014). Table A4.6.5 summarizes some of the main characteristics of the waveforms and the recording stations of these 3 records and other 5 that could be collected from the literature (Helm *et al.*, 1994; Meidow & Ahorner, 1994). Indicated epicentral distances are calculated with respect to the epicentral coordinates of Ahorner (1994).

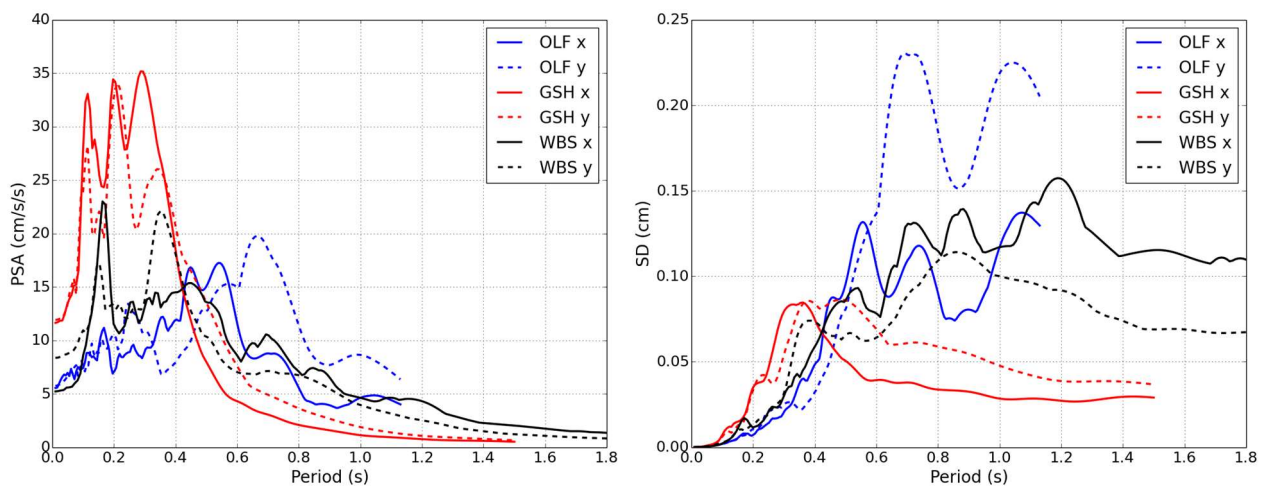


Figure A4.6.21. Pseudo-acceleration (left) and displacement (right) response spectra (5% of critical damping) for each of the two horizontal components (x, y) of the three records available from the RESORCE database (Akkar *et al.*, 2014).

By comparing records from stations KKW, BGG and KOE shown in the table above, all of which correspond to, approximately, the same epicentral distance, Meidow & Ahorner (1994) highlight the influence of site amplification. Stations BGG and KOE are located on firm rock outside the Middle Rhine Valley, while station KKW is located on soft soil within the basin. The maximum recorded peak ground acceleration is clearly larger on the latter.

Table A4.6.5. Main characteristics of waveforms and recording stations for 8 records of the main shock. Sources: RESORCE database (R, Akkar *et al.*, 2014), Meidow & Ahorner (MA, 1994), and Helm *et al.* (Hea, 1994). Note: the exact location of station KKW (Mülhem-Kärlich) is not available, and the coordinates corresponding to the Mülhem-Kärlich power station are reported.

Station	Country	Latitude	Longitude	Repi (km)	Soil	PGA X (cm/s ²)	PGA Y (cm/s ²)	Source
GSH	Germany	50.737	6.377	58.0	B, $V_{s30}=660$ m/s	11.603	11.874	R
OLF	Germany	50.496	6.421	83.0	B, $V_{s30}=660$ m/s	5.524	5.715	R
WBS	Germany	50.808	7.286	103.0	B, $V_{s30}=660$ m/s	5.202	8.348	R
KKW	Germany	50.408	7.490	138.9	soft	44.000	-	MA
BGG	Germany	50.206	7.337	146.2	rock	22.000	-	MA
KOE	Germany	50.425	7.732	151.6	rock	8.000	-	MA
Surbourg	France	48.915	7.852	286.0	loess, quaternary	9.100	10.000	Hea
Hoffen	France	48.942	7.964	287.3	loess, quaternary	3.400	3.800	Hea

On a similar line, Braunmiller *et al.* (1994) comment that stations located within the sedimentary basin of northern Germany show large low-frequency oscillating signals, and, in a more general observation, that attenuation of high frequency signals differs significantly for different source-receiver paths. Furthermore, they observe a relatively high complexity in the body-wave part of the seismograms at distances between 100 and 1,500 km, which they claim is due to the different heterogeneous crustal structures along the travel paths.

A4.6.4.3 Inferred shaking levels

In view of the lack of records in the epicentral area for the main shock, Gariel *et al.* (1994) used the accelerograms of the aftershocks recorded by the temporary stations deployed after the main event to generate synthetic horizontal accelerograms of the former by means of the empirical Green's function method. Table A3.1.6 presents the peak ground acceleration values calculated by the authors for each of the six stations they studied. A particularly high value of 0.35 g for station HLN strikes the eye as surprising. The authors say that, while it is possible that the assumption of linearity adopted when using the empirical Green's function method may be responsible for an unrealistically high result, this value is somehow supported by the fact that the town of Haelen, where the station is located, suffered from significant damage. Furthermore, one of the turbines of the local power plant moved during the main shock. Nevertheless, it is possible that the actual acceleration values may have been slightly smaller, especially because of possible non-linear effects caused by the alluvial soils in the area. Peak ground accelerations calculated for the other stations range from 0.06 to 0.18 g, which the authors claim is in agreement with what could be expected for this event. Figure A3.1.22, in which observed and computed acceleration values are compared with those predicted by the Boore & Joyner (1982) attenuation model, supports this statement.

Given that no records are available for the area around Brunssum, where significant earthquake-triggered landslides were observed, Alkema *et al.* (1994) carried out estimates

of the peak ground acceleration based on different ground motion prediction equations, as shown in Table A4.6.7.

Table A3.1.6. Peak ground acceleration values calculated by Gariel *et al.* (1994) using the empirical Green's function method. $Repi_1$ and $Repi_2$ are the epicentral distances with respect to the epicentral coordinates defined by Ahorner (1994) and provided by Gariel *et al.* (1994), respectively.

Station	Country	Latitude	Longitude	$Repi_1$ (km)	$Repi_2$ (km)	PGA X (cm/s ²)	PGA Y (cm/s ²)
ODL	Netherlands	51.146	6.000	5.9	5.0	150.0	175.0
HLN	Netherlands	51.236	5.957	7.7	6.2	174.0	350.0
THN	Netherlands	51.160	5.845	5.7	8.6	60.0	72.0
KIN	Belgium	51.146	5.776	10.7	13.4	110.0	130.0
STP	Netherlands	51.194	5.728	14.0	14.8	-	120.0
MAS	Belgium	51.097	5.712	16.9	15.1	80.0	57.0

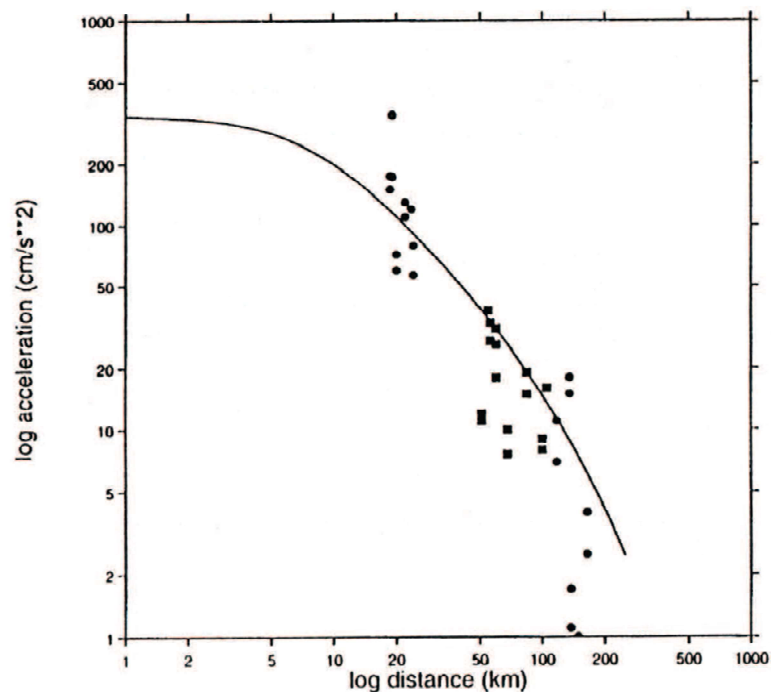


Figure A3.1.22. Comparison between observed and computed peak ground acceleration values in Belgium (dots) and Germany (squares) and values predicted by the Boore & Joyner (1982) attenuation model. From Gariel *et al.* (1994).

Table A4.6.7. Peak horizontal accelerations at the location of the landslides in Brunssum, 25 km away from the epicentre, estimated from different ground motion prediction equations (GMPEs). From Alkema *et al.* (1994).

GMPE	PGA (g)
Ambraseys (1990)	0.07
Chiaruttini & Siro (1981)	0.14
Campbell (1981)	0.05
Campbell (1985)	0.05
Joyner & Boore (1981)	0.07
Joyner & Boore (1988)	0.07

The website of the United States Geological Service (USGS) provides two different ShakeMaps for the 1992 Roermond earthquake. ShakeMaps (Worden *et al.*, 2017) present estimations of the ground shaking based on the magnitude, location, fault dimensions, style of faulting, site conditions and, where available, observations from recording stations and/or macroseismic intensity observations. Due to the lack of availability of these data, the map shown in Figure A4.6.23 was generated using the Californian ground-motion prediction equation of Boore *et al.* (1997), which is based on as-recorded horizontal components. As can be observed, the maximum PGA predicted is 0.22 g, which is significantly below the 0.35 g calculated by Gariel *et al.* (1994) for station HLN. Estimations for stations KIN, ODL, STP match relatively well the contour lines, while values calculated by Gariel *et al.* (1994) for THN and MAS are significantly lower than those of the ShakeMap.

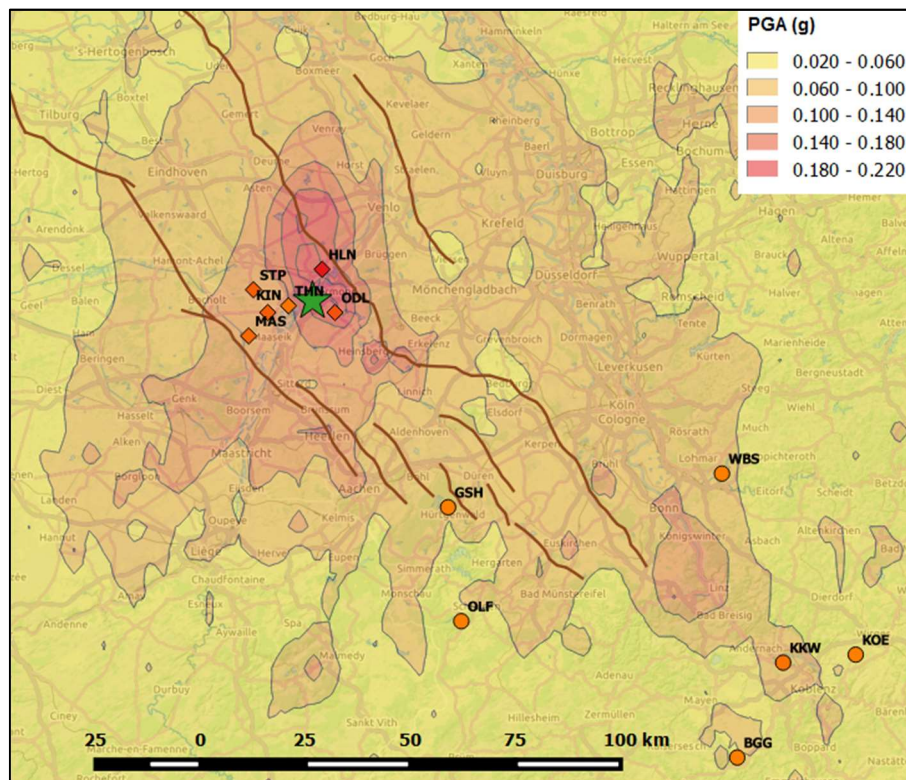


Figure A4.6.23. USGS ShakeMap (option 1, outdated website) in terms of peak ground acceleration. The green star marks the epicentre of the main shock, according to Ahorner (1994). Circles indicate stations for which records are available (see Table A4.6.5). Rhombuses correspond to stations for which estimations are available (see Table A4.6.6 (USGS, 2015).

The map shown in Figure A4.6.24 is an alternative to the previous one, and it constitutes an estimation generated based on the macroseismic intensity map of Haak *et al.* (1994), combined with intensity to ground motion conversion models as well as ground motion prediction equations. This ShakeMap presents higher peak ground acceleration values around the epicentral area, which support the 0.35 g calculated by Gariel *et al.* (1994). Estimations from these authors for stations KIN and STP match relatively well the contour lines, while those for stations ODL, THN and MAS are significantly lower than those of the ShakeMap.

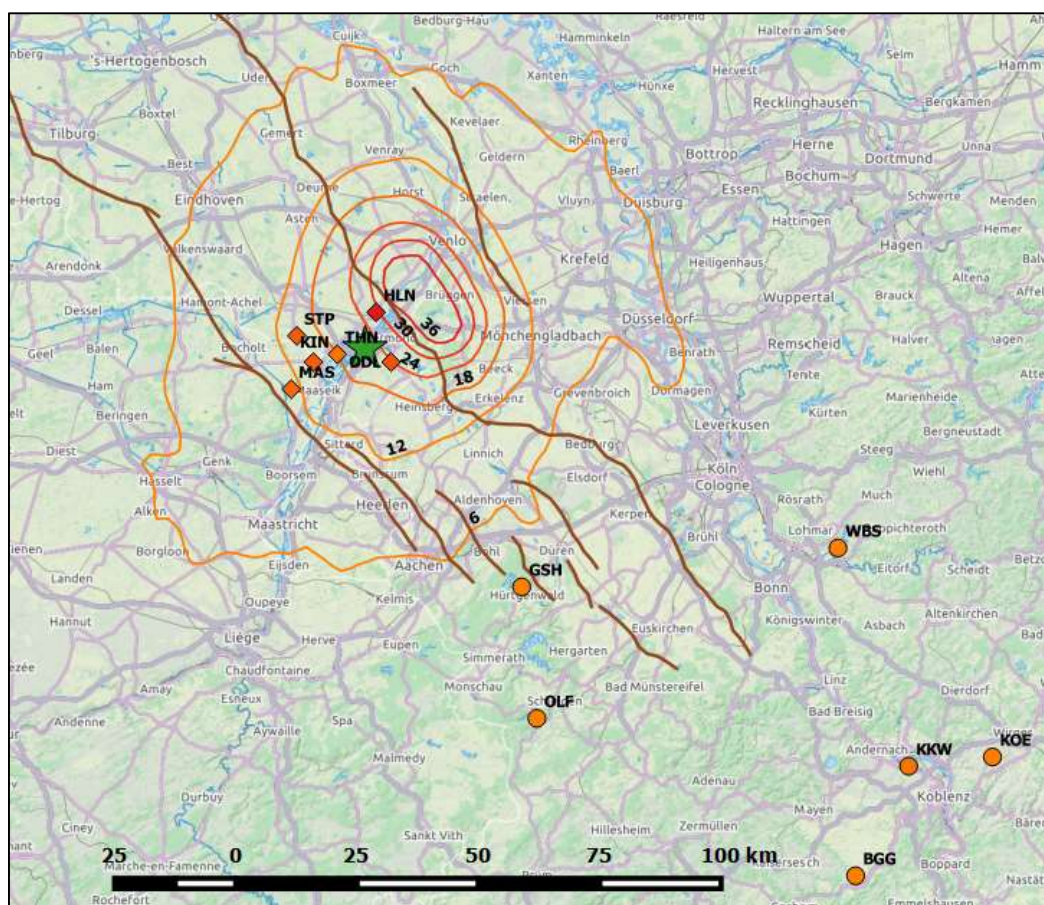


Figure A4.6.24. USGS ShakeMap (option 2, renovated website) in terms of peak ground acceleration. Values of the contour lines correspond to percentages of g . The green star marks the epicentre of the main shock, according to Ahorner (1994). Circles indicate stations for which records are available (see Table A4.6.5). Rhombuses correspond to stations for which estimations are available (see Table A4.6.6).

A4.6.4.4 Duration of ground shaking

The 5%-75% definition of the significant duration of the three records from the RESORCE database (Akkar *et al.*, 2014) was calculated for each as-recorded horizontal component using the OpenQuake ground motion toolkit (Weatherill, 2014). Results are shown in Table A4.6.8.

Table A4.6.8. Significant duration (5%-75% of Arias intensity, in seconds) of the ground motions available from the RESORCE database (Akkar *et al.*, 2014).

Station	Repi (km)	X component	Y component
GSH	58.0	0.88	0.90
OLF	83.0	3.04	2.74
WBS	103.0	6.84	2.06

Gariel *et al.* (1994) highlight that the duration of strong accelerations observed in their synthetic records is "only a few seconds", but do not provide values. In contrast, The New

York Times (1992) reports that the earthquake lasted for more than 20 seconds, though no specification with respect to the location they are referring to is given.

Ewald *et al.* (2006) carried out 3D modelling simulations of wave propagation during the 1992 Roermond earthquake in the Lower Rhine Embayment, and concluded that there is a strong correlation between the duration of shaking and the depth of the basin. Figure A4.6.25 shows the shaking durations they calculated. No details with respect to the definition of duration being used are provided.

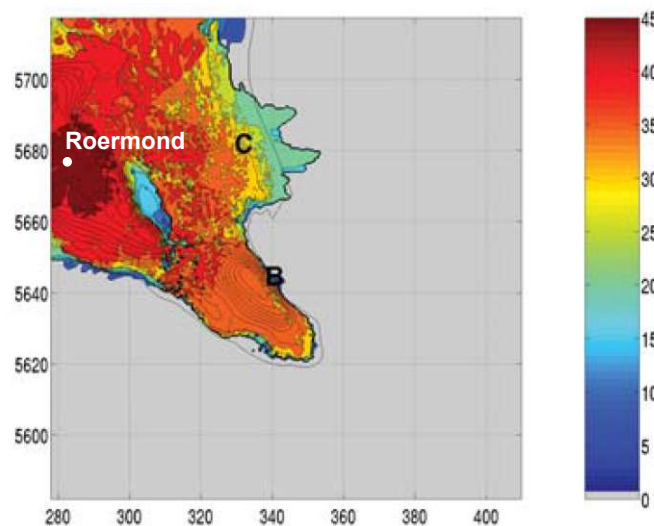


Figure A4.6.25. Shaking duration for the 3D simulation of the 1992 Roermond earthquake by Ewald *et al.* (2006).

Estimations of earthquake significant durations can be obtained by means of prediction equations such as those of Bommer *et al.* (2009) and Afshari & Stewart (2016). For the former, two alternative depths to the top of the rupture were used, based on estimations of fault rupture parameters by Ahorner (1994) and Camelbeeck *et al.* (1994). A series of distances were considered, covering the three stations for which records are available. The RESORCE database (Akkar *et al.*, 2014) metadata file indicates a value of V_{s30} at these three stations of 659.6 m/s, so this value and an extreme alternative of 180 m/s are used. General results obtained are plotted in Figure A4.6.26, while Table A4.6.9 contains the specific values obtained at the locations of the available recorded ground motions. Both models predict longer durations than those observed, except for the case of the as recorded X component of station WBS, for which the estimations of the model of Bommer *et al.* (2009) are smaller, though that of Afshari & Stewart (2016) is still larger. Observed durations are within $[-2.52, +0.49]$ and $[-2.22, +0.79]$ standard deviations of the model of Bommer *et al.* (2009), when using the depths to the top of the rupture of Ahorner (1994) and Camelbeeck *et al.* (1994), respectively, and within $[-3.55, -0.55]$ standard deviations of the model of Afshari & Stewart (2016).

Values of V_{s30} are not known for the area around the epicentre. The same range as above was combined with a null distance to the fault rupture, and the resulting values lie between 0.38 and 0.66 seconds, for the model of Bommer *et al.* (2009), and between 1.45 and 1.91 seconds, for that of Afshari & Stewart (2016). These are significantly smaller than those

shown in Figure A4.6.25, a fact that may support the observation of Ewald *et al.* (2006) regarding the relevance of the influence of the basin geometry on the duration of the shaking.

Table A4.6.9. Estimation of significant duration (5%-75% of Arias intensity, in seconds) of the ground motions available from the RESORCE database (Akkar *et al.*, 2014) using prediction equations by Bommer *et al.* (2009, BSA09) and Afshari & Stewart (2016, AS). For BSA09, two alternative estimations of fault rupture parameters by Ahorner (1994, A94) and Camelbeeck *et al.* (1994, C94) were used.

Station	Repi (km)	FROM WAVEFORMS		FROM PREDICTION EQUATIONS		
		X component	Y component	BSA09-A94	BSA09-C94	AS16
GSH	58.0	0.88	0.90	3.59	3.04	6.80
OLF	83.0	3.04	2.74	4.53	3.83	8.33
WBS	103.0	6.84	2.06	5.20	4.40	9.55

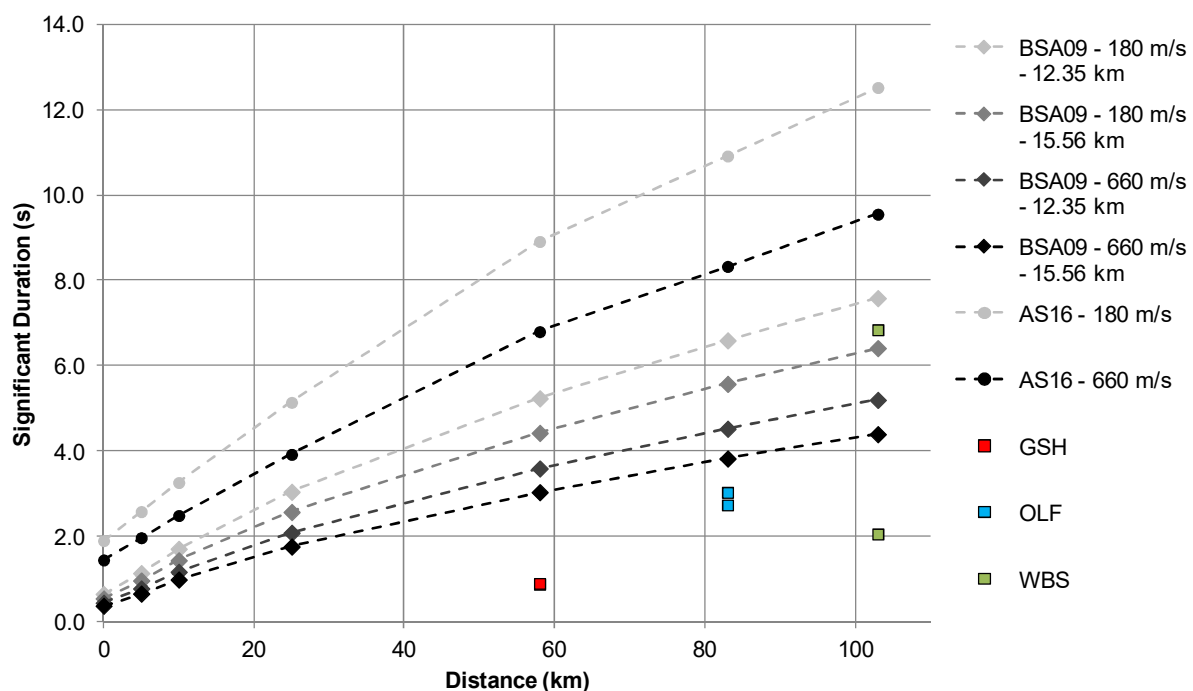


Figure A4.6.26. Estimation of the significant duration of the main shock, using prediction equations by Bommer *et al.* (2009, BSA) and Afshari & Stewart (2016, AS), and significant duration calculated for the two as-recorded horizontal components of the three available accelerograms.

A4.6.5 Collateral earthquake hazards

A4.6.5.1 Surface rupture

No surface rupture observed (Vanneste *et al.*, 1999).

A4.6.5.2 Landslides

While Davenport *et al.* (1994) state that the only reported landslides induced by the 1992 Roermond earthquake in the Netherlands occurred at Brunssum, Meidow & Ahorner (1994) report the occurrence of landslides in Leeuwen as well (Figure A4.6.27). According to the latter study, those that occurred in Germany were only small, mostly from shore lines of artificial lakes. No damage to buildings or infrastructure due to landslides was reported.

The most significant landslides observed were those of Brunssum, 25 km to the south of the epicentre. The largest of those was 200 m wide and 25 m long, and occurred 300 m away from the smaller one (Alkema *et al.*, 1994). The area had suffered from a previous slide in 1955, which occurred without any seismic trigger (Maurenbrecher *et al.*, 1994). The overall slope in the area is gentle, of around 1 in 5, but locally stepped, and it consists of loose, reworked, uniformly graded, fine quartz sands. No ground-motion records are available for this area, but Alkema *et al.* (1994) estimate it to have been between 0.05 g and 0.14 g, from empirical attenuation relationships. According to the authors, these values are significantly smaller than those that would be necessary to destabilize these slopes. This, in combination with the groundwater table being almost at the surface at the foot of the slope, and taking into consideration the locally reworked nature of the ground, leads Alkema *et al.* (1994) and Maurenbrecher *et al.* (1994) to believe that liquefaction at the foot of the slope may have been the cause of the landslides in Brunssum. Hack *et al.* (2007) point out that no clear indications of liquefaction were observed in their vicinity, though remains of sand volcanoes were found several kilometres away, possibly indicating that liquefaction phenomena may have occurred, at least in some points. The liquefaction study of Lap (1987) had concluded years earlier that no liquefaction was to be expected in the area of Brunssum.

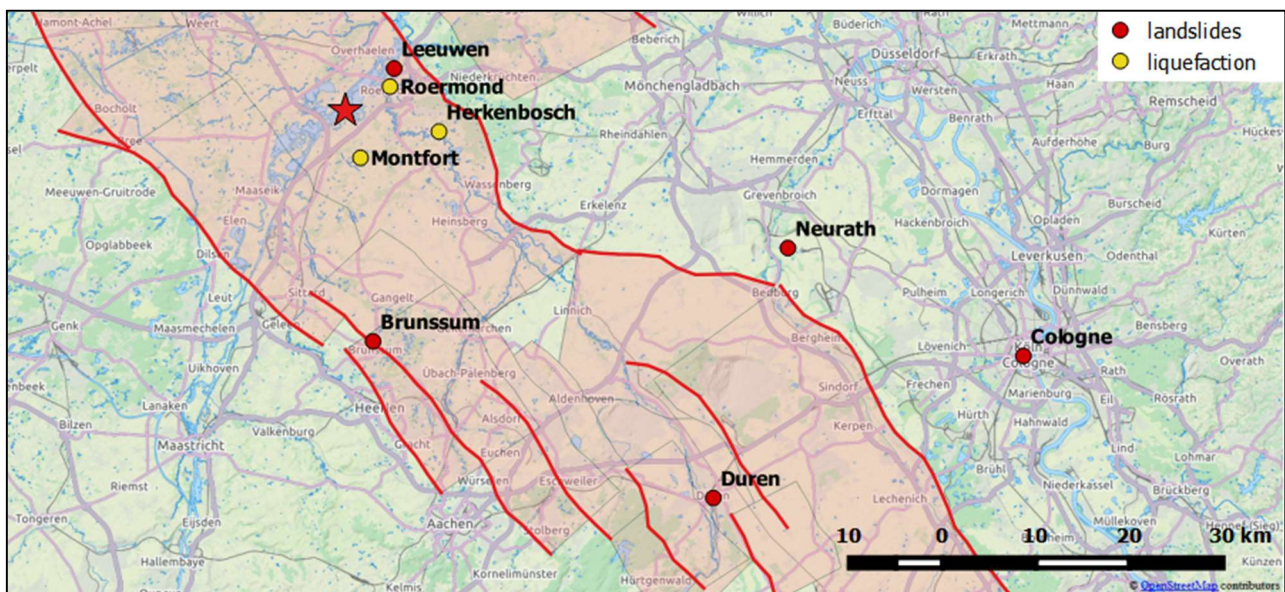


Figure A4.6.27. Map of geotechnical effects triggered by the 1992 Roermond earthquake. Data from Meidow & Ahorner (1994) and Nieuwenhuis (1994). The red star marks the epicentre of the main shock, according to Ahorner (1994).

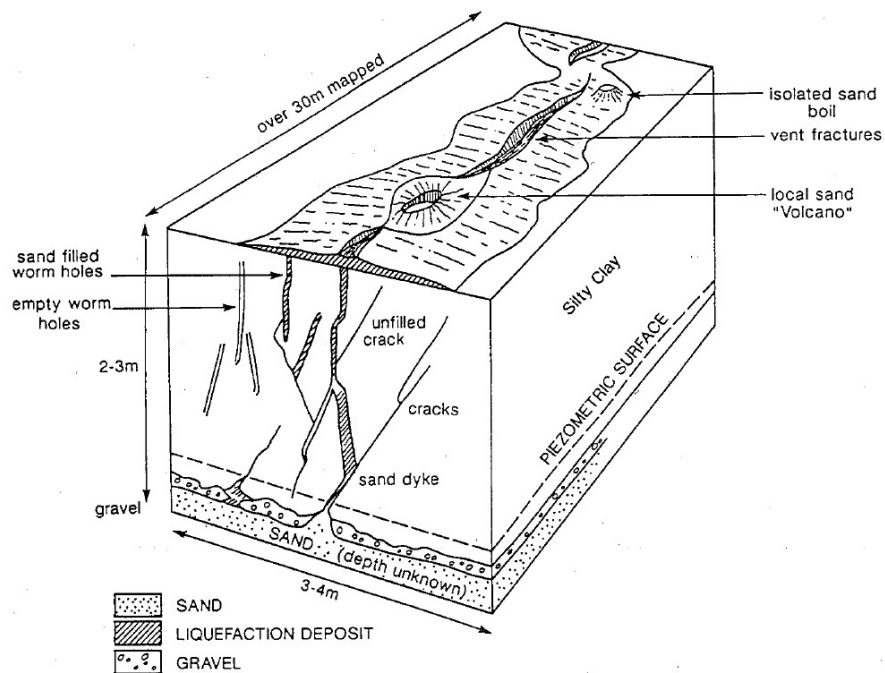


Figure A4.6.28. Liquefaction structures observed at Herkenbosch. From Davenport *et al.* (1994).

A4.6.5.3 Liquefaction

According to Nieuwenhuis (1994), evidence of liquefaction in the form of fracture vents and sand boils was observed at three places within a 10 km radius from the epicentre: near Herkenbosch, near Montfort, and to the north of Roermond (Figure A4.6.27). As can be observed in Figure A4.6.16, all these areas had been identified as being susceptible to liquefaction. However, no liquefaction was observed in areas further north also marked as highly or moderately susceptible. Hack *et al.* (2007) mention that remains of sand volcanoes were found "several kilometres" away from the landslides in Brunssum.

None of the farms located around Herkenbosch suffered from damage due to liquefaction, but Nieuwenhuis (1994) believes that significant damage would have occurred, had the liquefied area exceeded 1% of the total area. No comments regarding damage to buildings due to liquefaction in other areas have been found.

Figure A4.6.28 shows a diagram of the kind of effects observed at Herkenbosch. Groundwater levels at the time of the earthquake were close to the surface (Davenport *et al.*, 1994).

A4.6.5.4 Settlements

No reports of settlements have been found for this earthquake.

A4.6.6 Exposed population

A4.6.6.1 Socio-economic setting

According to the 2014 Human Development Report (United Nations, 2014), the Human Development Index (HDI) for the Netherlands, Germany and Belgium was 0.915, 0.911 and 0.881, respectively, placing these countries 4th, 6th and 21st in the world's ranking. Their Inequality-adjusted HDIs (IHDI) were 0.854, 0.846 and 0.806, respectively as well. Tables A4.6.10-11 compare the HDI and IHDI for the three countries for the years 1993 (around the time of the earthquake) and 2013. IHDI values are not available for reports generated before 2010. The column "Adj. HDI" provides the HDI values given in the 2014 report for 1993, adjusted for data consistency in time. As can be observed, the Netherlands and Germany present a relatively similar level of human development, while that of Belgium seems to be smaller (Tables A4.6.10-11).

Table A4.6.10. Human Development Index and Inequality-adjusted Human Development Index for Germany and the Netherlands.

Report	Germany				Netherlands			
	HDI	IHDI	Rank	Adj. HDI	HDI	IHDI	Rank	Adj. HDI
1993	0.957	-	12	0.782	0.970	-	9	0.826
2014	0.911	0.846	6	-	0.915	0.854	4	-

Table A4.6.11. Human Development Index and Inequality-adjusted Human Development Index for Belgium and the Netherlands.

Report	Belgium				Netherlands			
	HDI	IHDI	Rank	Adj. HDI	HDI	IHDI	Rank	Adj. HDI
1993	0.952	-	16	0.805	0.970	-	9	0.826
2014	0.881	0.806	21	-	0.915	0.854	4	-

In 1992, the European Monetary System suffered a significant crisis. The effects of this crisis over the gross domestic product (GDP) of the Netherlands, Germany and Belgium becomes apparent in Table A4.6.12, which shows the GDP annual percent change before and after 1992. In the case of Germany and Belgium, this percentage became negative, while for the Netherlands it decreased significantly, though staying positive. The GDP per capita, estimated from the combination of the total GDP (data from the World Economic Outlook Database 2015) and the 1990 population (United Nations data, as reported in Gridded Population of the World v.3.0; CIESIN, 2005), is very similar for the three countries in 1992.

In spite of the financial crisis, Gariel *et al.* (1994) describe the area affected by the 1992 Roermond earthquake as highly urbanized and industrialized. Twelve years later, Ewald *et*

al. (2006) describe the whole Lower Rhine Embayment as being "densely populated and highly industrialized with large petrochemical and chemical plants".

Table A4.6.12. Gross domestic product (GDP), GDP per capita, annual percent change and population of Germany, Belgium and the Netherlands.

Indicator	Units	Germany		Netherlands		Belgium	
		1992	2014	1992	2014	1992	2014
GDP, current prices	Billions of US dollars	1,971.377	3,859.547	321.928	866.354	224.842	534.672
GDP, annual percent change	%, before year	2.200	1.607	2.030	0.875	1.490	1.043
	%, after year	-1.180	1.620	0.760	1.559	-1.460	1.341
GDP, current prices	US dollars	24,818.115	47,589.972	21,530.785	51,372.963	22,558.664	47,721.586
Population (*)	1000 People	79,433	81,100	14,952	16,864	9,967	11,204

(*) Population data:

For 1992: 1990 UN data, as reported in the Gridded Population of the World (GPW v.3.0) website.

For 2014: 2014 data, from the World Economic Outlook Database 2015.

A4.6.6.2 Population density and distribution

Given the proximity of the epicentre to several urban agglomerations and the extent to which the earthquake was felt, defining the exact number of people exposed to significant shaking during the 1992 Roermond seismic event is not simple. Nevertheless, it is clear that the area is (and was) densely populated (Ewald *et al.*, 2006), as can be observed in Figure A4.6.29, which shows the population density in 1990 according to data from Gridded Population of the World v.3.0 (CIESIN, 2005).

Figure A4.6.29 also shows the cities and districts that observed either the largest damage or some kind of geotechnical issue. The most damaged locations were Roermond (57,000 people, 2015), Herkenbosch (4,000 people in 2015, a district within Roerdalen, with 20,000 people), Heinsberg (41,000 people in 2015), whose most affected districts were Oberbruch and Dremmen, and Bonn (311,000 people in 2015). Damage was also reported in Cologne (1 million people in 2015) and Maaseik (25,000 people in 2015). It should be noted that Cologne and Bonn are part of a large metropolitan area with a population of around 10 million people.

The USGS EXPO-CAT database (Allen *et al.*, 2009) estimates that around 91,000 people were exposed to a MMI intensity of VII, of which around 65% (59,000) was urban population. The plot on the left of Figure A4.6.30 shows the total (urban plus rural) estimations for different intensity levels while the plot on the right shows in detail the exposure to MMI VI and larger.

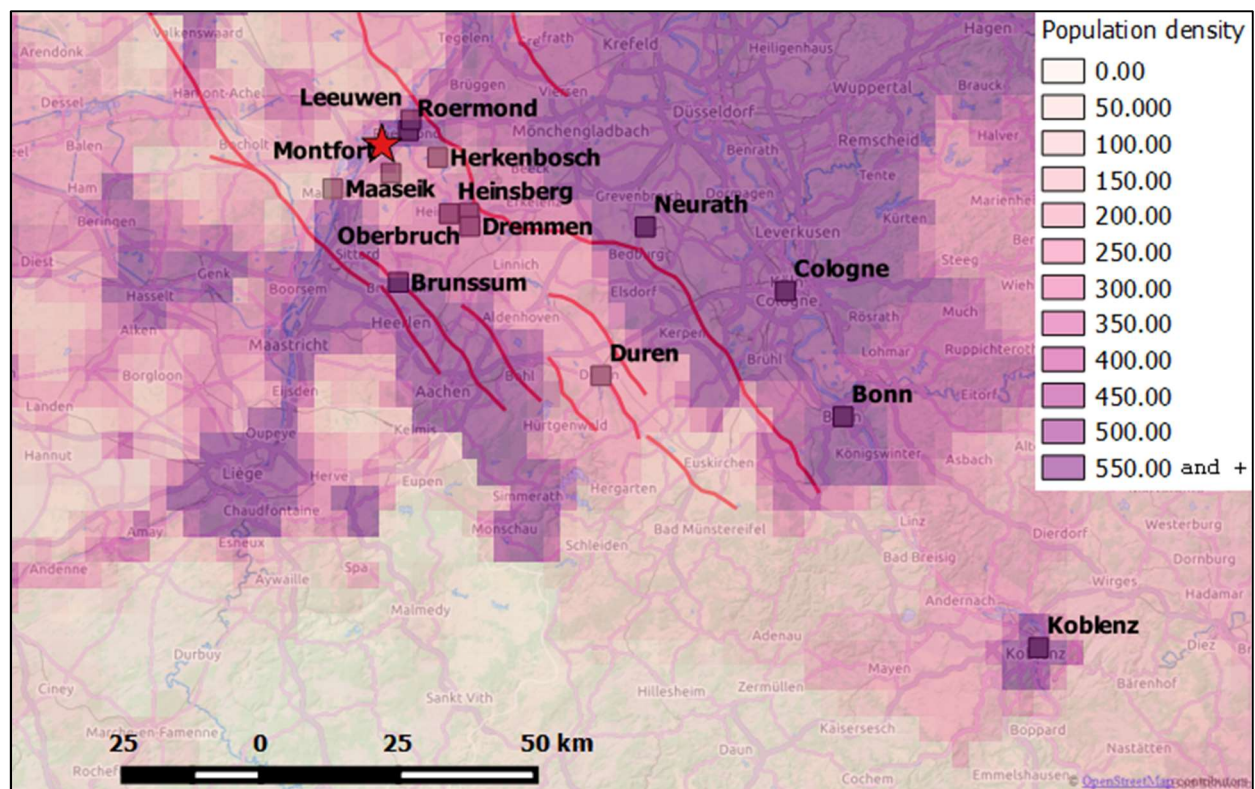


Figure A4.6.29. Population density (persons/km²) around the Roermond area in 1990. Data from Gridded Population of the World (GPW v.3.0; CIESIN, 2005). The red star marks the epicentre of the main shock, according to Ahorner (1994).

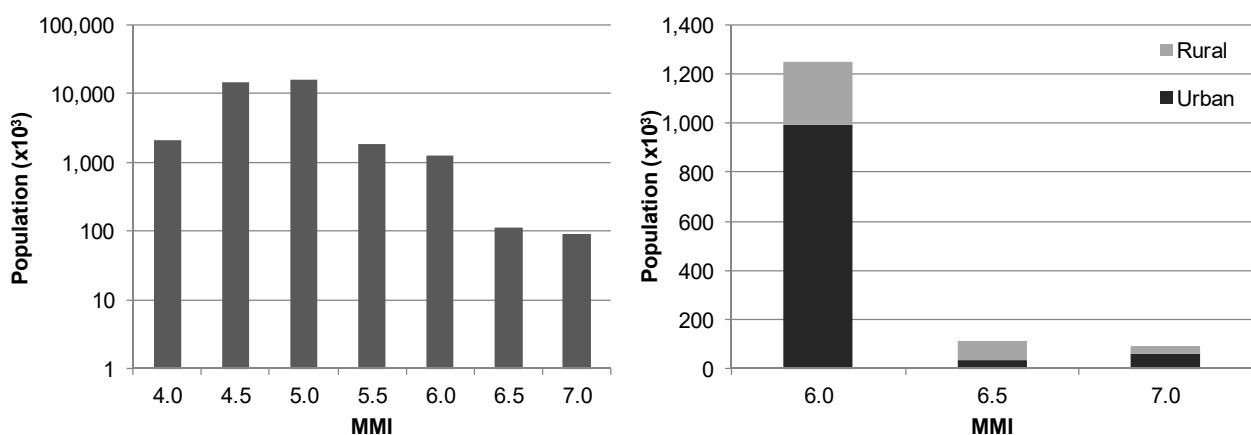


Figure A4.6.30. Left: estimation of total (urban plus rural) population exposed to different Modified Mercalli Intensities (MMI). Right: disaggregation of rural and urban population exposed to MMI VI and larger. Data from the USGS EXPO-CAT database (Allen *et al.*, 2009).

A4.6.6.3 Time of day of earthquake

According to the website of the Royal Netherlands Meteorological Institute and the GEM Earthquake Consequences Database, the number of casualties would have been significantly larger had the earthquake taken place during the day-time and not in the middle of the night, as it did. This is due to the fact that very few people were on the streets, and most injuries were caused by debris falling over those who were evacuating buildings.

A4.6.7 Characteristics of exposed building stock

A4.6.7.1 Seismic design codes

In the Netherlands, the first Building Act or Decree ("Bouwbesluit") came into force in 1992, and contained all the technical requirements applicable for the whole country. It was updated in 2003 and in 2012, when it stopped making reference to the old Dutch TGB NEN 6700 series of building regulations and adopted the Eurocodes instead. The TGB series of standards first appeared in 1972 and were updated in 1990, changing their previous deterministic perspective into a probabilistic one. In particular, the 6700 series specified the requirements to ensure the safety and serviceability of structures, both during their construction and in their subsequent use. However, the NEN 6702 code, which refers to loadings and deformations, did not specify seismic load values in the text itself, and only contained a reference to a zonation map elaborated in terms of modified Mercalli intensities and Eurocode 8 (in its latest version) in its comments regarding special projects (Brouwer *et al.*, 2010).

The current hazard zonation map for the Netherlands was elaborated by de Crook (1996), is based on an earthquake catalogue compiled up to 1993. The study was carried out in terms of macroseismic intensities, which were then translated into design peak ground accelerations. The Royal Netherlands Meteorological Institute (KNMI) is preparing an update of this map (Brouwer *et al.*, 2010).

According to Brouwer *et al.* (2010), in the Netherlands there is no legal obligation to take into consideration seismic actions in the design of buildings and, in general, Dutch engineers believe that wind loading is always governing the design of standard structures, over earthquake loading.

The first seismic code of the Federal Republic of Germany was the DIN 4149, introduced in 1981, and then revised in 1992 to be applied to the reunified country. Its latest version dates from 2005 (DIN, 2005), and follows the Eurocode 8 (CEN, 2004) text (Brouwer *et al.*, 2010), though it does not pretend to be its implementation, which is DIN EN 1998 (DIN, 2010) instead. In spite of having been withdrawn, DIN 4149:2005-04 is still being applied, since DIN EN 1998 is not in the lists of the Technical Building Regulations of the country. Brouwer *et al.* (2010) highlight that, as opposed to the case of the Netherlands, taking into account seismic loads is mandatory in Germany, especially in the area around the Lower Rhine Embayment, which is one of the most seismically active areas of the country.

In Belgium, the first investigations aimed at estimating ground motion levels for the safety of new buildings date from the 1970s and were motivated by the construction of the first nuclear reactors in the country (Vanneste *et al.*, 2014). The first study encompassing the country as a whole was that of van Gils & Zaczek (1978). Investment in seismic hazard assessments and the development of a seismic network in Belgium increased after the 1983 Liège earthquake, which caused two deaths, several injuries and considerable damage. In the 1990s, the GSHAP project (Giardini *et al.*, 1999; Giardini *et al.*, 2003) allowed for an update, but it was not until the year 2000 that a new seismic hazard map

(Leynaud *et al.*, 2000) was elaborated thanks to a cooperation between the Liège University and the Royal Observatory of Belgium (ROB). This map has served as the basis for the seismic zonation map included in the Belgian national annex (BIN, 2002) to Eurocode 8 (CEN, 2004), which became in force in 2012 as the NBN-ENV 1998 standard, which replaced the previous NBN ISO 3010:1993. The latter was a Belgian application of the ISO 3010 norm from the International Organization for Standardization, which contains guidelines for the design of structures taking into consideration seismic loads.

A4.6.7.2 Building typologies

Information regarding building typologies in the Roer Valley Graben is scarce to null. For this reason, data regarding typologies at the country level were collected from the PAGER Inventory Database v2.0 (Jaiswal & Wald, 2008) for the Netherlands, Belgium and Germany, and summarized in Figures A4.6.31-33. As can be observed, unreinforced brick masonry is the most common typology in the Netherlands and Belgium for urban, rural, residential and non-residential buildings (statistics for Belgium are not differentiated in this sense). In the Netherlands, reinforced concrete frames with low ductility capacities represent only a small percentage of the urban residential buildings, but are more frequent for non-residential buildings, for which steel is also an alternative. In Belgium, the remaining 25% is split across reinforced concrete with unspecified ductility characteristics, rubble stone masonry and wood, in decreasing order of importance. Unreinforced masonry is very common in Germany, but a larger proportion of ductile reinforced concrete frames and reinforced masonry walls with concrete diaphragms can be observed. Unfortunately, the typology of around 50% of the building stock has not been identified and is marked as "unknown" in Figure A4.6.33.

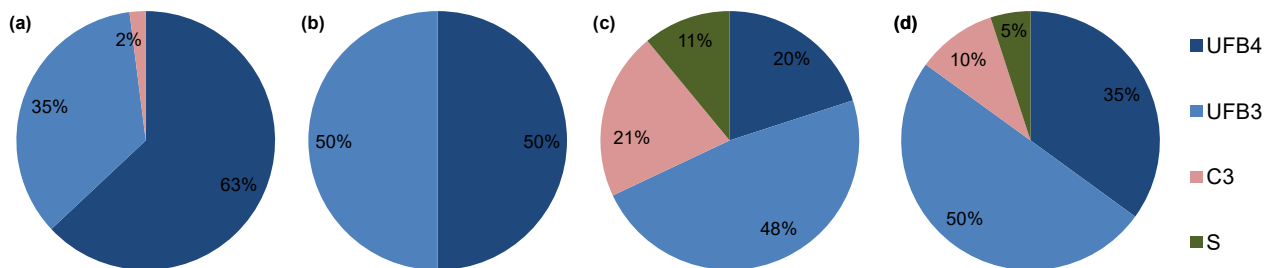


Figure A4.6.31. Proportion of buildings in the Netherlands belonging to each typology: (a) urban and residential, (b) rural and residential, (c) urban and non-residential, and (d) rural and non-residential. UFB4: unreinforced fired brick masonry, cement mortar. UFB3: unreinforced brick masonry in lime mortar. C3: non-ductile reinforced concrete frame with masonry infill walls. S: steel. Data from Jaiswal & Wald (2008).

According to the Dutch Census 2011 (Schulte Nordholt *et al.*, 2014), by 1990 approximately 9.7%, 30.6% and 59.7% of the dwellings had been constructed before 1920, between 1920 and 1960, and after 1960, respectively (Figure A4.6.34). This distinction is relevant for future reference to damage statistics reported in Pappin *et al.* (1994).

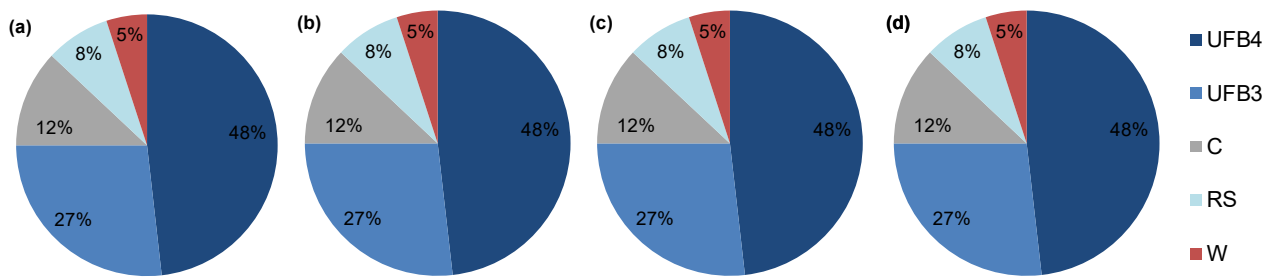


Figure A4.6.32. Proportion of buildings in Belgium belonging to each typology: (a) urban and residential, (b) rural and residential, (c) urban and non-residential, and (d) rural and non-residential. UFB4: unreinforced fired brick masonry, cement mortar. UFB3: unreinforced brick masonry in lime mortar. C: Reinforced concrete. RS: Rubble stone (field stone) masonry. W: Wood. Data from Jaiswal & Wald (2008).

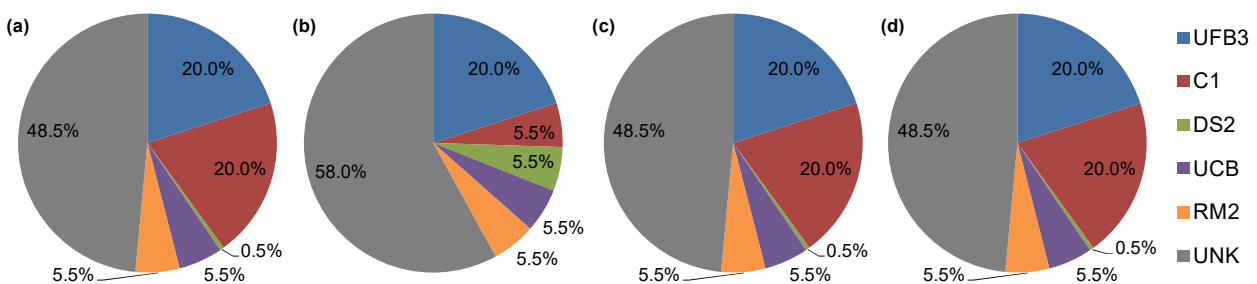


Figure A4.6.33. Proportion of buildings in Germany belonging to each typology: (a) urban and residential, (b) rural and residential, (c) urban and non-residential, and (d) rural and non-residential. UFB3: unreinforced brick masonry in lime mortar. C1: ductile reinforced concrete moment frame with or without infill. DS2: rectangular cut stone masonry block with lime mortar. UCB: concrete block unreinforced masonry with lime or cement mortar. RM2: reinforced masonry bearing walls with concrete diaphragms. UNK: not specified (unknown). Data from Jaiswal & Wald (2008).

Residential single- and multi- family houses built in the Netherlands between the beginning of the 18th century and the mid-20th century usually consist of timber diaphragms and solid or cavity walls. RC diaphragms with cavity walls became more common only after the end of the Second World War. Mixed floor systems consisting on timber ground floor and attic and concrete first floor can also be found in residential terraced houses. From the 1960s onwards, the use of timber or steel frames with timber shear panels for single-family houses spread, though this typology always represented a very small percentage of the buildings built each year.

According to Koopman (2007), houses dating to the first two decades after the Second World War were usually 3 to 4 storey multi-family buildings, 70% of which were built with brick masonry load bearing walls, and 30% of which were built with large concrete blocks, or panel building systems, or using in-situ concrete. Floors and horizontal roofs were usually made of a combination of prefabricated non-reinforced concrete elements and in-situ concrete, with the reinforcement placed in the latter. Sloped roofs were constructed in timber and covered in tiles. Façades were usually made of brickwork.

Since the mid-1960s, higher-rise buildings up to 10-storeys high became more common (Koopman, 2007). Most structures built in the late 1960s and 1970s were carried out with

in-situ concrete. Light blocks were used for non-bearing partition walls. Floors were either casted in-situ using steel tunnel moulds as well, or were made of a combination of 50 mm thick prefabricated concrete slab flooring elements over which in-situ concrete was placed. Most façades were prefabricated, either in timber or in masonry, the latter usually consisting of an inner layer of gas concrete blocks and an outer layer of brick. The use of precast structural reinforced concrete walls gained more popularity in the 1980s.

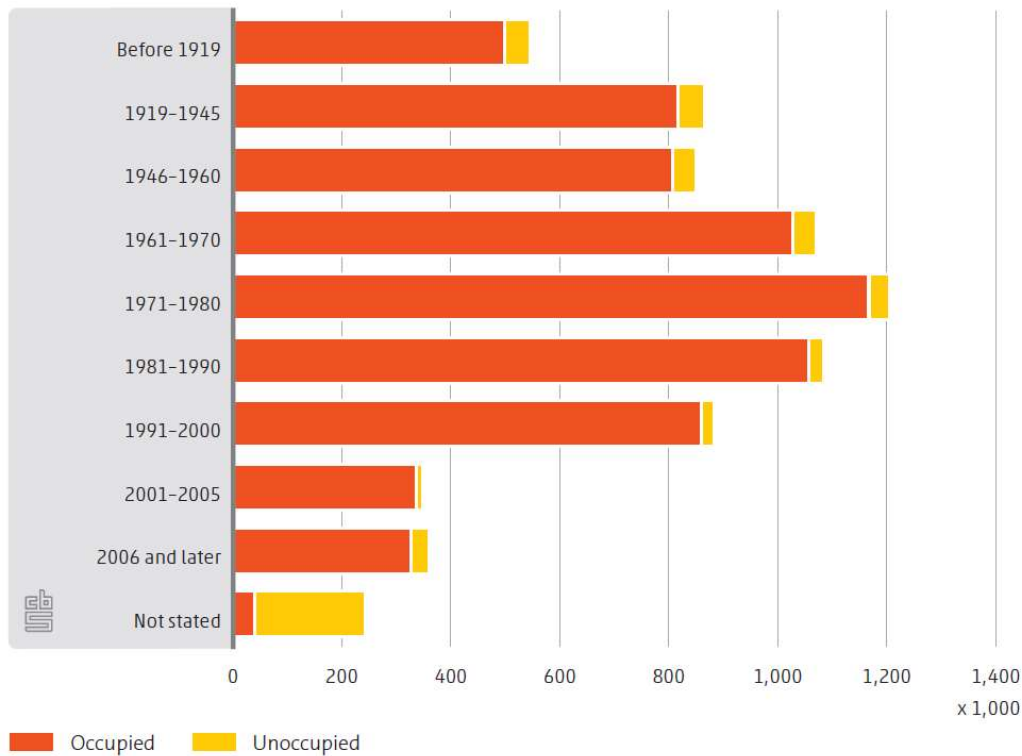


Figure A4.6.34. Dwellings in the Netherlands by period of construction and occupancy status. From the Dutch Census 2011 (Schulte Nordholt *et al.*, 2014).

Mixed residential-commercial buildings in the Netherlands usually consist of solid walls or calcium silicate unreinforced masonry walls in the upper floors, with many of the walls replaced at ground floor with steel frames or precast reinforced concrete columns. Hollow block slabs, with cast-in-place structural walls, replaced with reinforced concrete frames at the ground floor became more common after the Second World War, while their precast walls and columns alternative spread from the 1970s onwards.

Regarding the situation of Germany, Tyagunov *et al.* (2006) say that, though pre-code buildings are dominant in quantity, the generally good workmanship with which they were built prevents them from being as vulnerable as could be expected. In their multi-risk assessment of the city of Cologne, Germany, Grünthal *et al.* (2006) highlight that the largest part of its building stock is not more than 50 years old, as the city was severely damaged during the Second World War. As a consequence, around 80% of the structures can be assigned to a C vulnerability class within the EMS-98 scale, in which A and F correspond to the most and least vulnerable classes, respectively. Figure A4.6.35 shows the proportions of the total building stock that can be assigned to each typology (on the left) and each EMS-98 vulnerability class (on the right). As can be observed, masonry is

the most common structural type in Cologne, an observation which matches the information of Jaiswal & Wald (2008, Figure A4.6.33).

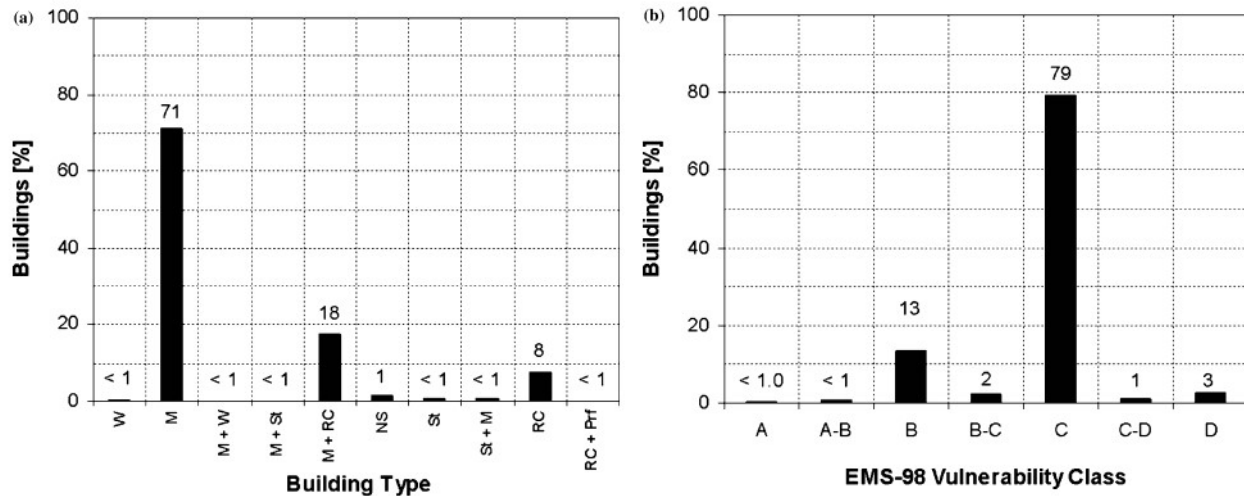


Figure A3.1.35. Proportion of buildings in Cologne, Germany, belonging to each typology (a) and to each EMS-98 vulnerability class (b). W: wooden. M: masonry. St: steel. RC: reinforced concrete. NS: natural stone. Prf: Prefabricated (Grünthal *et al.*, 2006).

A4.6.7.3 Prior damage and retrofit

No details on prior damage or retrofit available.

A4.6.8 Damage observations

A4.6.8.1 Damage states

The most comprehensive statistics regarding the damage caused by the 1992 Roermond earthquake can be found in the work by Pappin *et al.* (1994), who used a damage scale very similar to that of the MSK intensity scale (MSK-64; Medvedev *et al.*, 1965; see Appendix II). This damage scale is described in Table A3.1.13.

Table A3.1.13. Definition of damage levels used in the study of Pappin *et al.* (1994).

Damage Level		Definition for load-bearing masonry
D0	Undamaged	No visible damage
D1	Slight damage	Hairline cracks
D2	Moderate damage	Cracks 5-20 mm
D3	Heavy damage	Cracks 20 mm or wall material dislodged
D4	Partial destruction	Complete collapse of individual wall or individual roof support
D5	Collapse	More than one wall collapsed or more than half of roof

A4.6.8.2 Damage statistics and description

According to Camelbeeck & van Eck (1994), the level of damage caused by the main shock was relatively low if compared to that observed due to other seismic events in the region. Braunmiller *et al.* (1994) state that no fatal building collapses occurred. In the epicentral area, numerous walls and roofs collapsed, and chimneys and Church towers cracked (Davenport *et al.*, 1994). Small cracks formed in walls and plaster, and pieces of plaster fell down (Meidow & Ahorner, 1994). According to The New York Times (1992), telephone lines were cut, electricity supplies were interrupted and water mains were damaged in some areas. The GEM Earthquake Consequences Database reports 1400 buildings damaged by shaking, out of which 100 were believed to have been damaged beyond repair. Several vehicles were damaged due to falling objects.

Meidow & Ahorner (1994) mention Roermond (Netherlands), Herkenbosch (Netherlands) and Heinsberg (Germany) as the most affected places. In the latter, Oberbruch and Dremmen saw more than 100 and about 30 significantly damaged buildings, respectively, making them the most affected districts. Furthermore, about 50 buildings in the surrounding villages suffered extensive damage as well. Around this area, many uppermost part of gables fell down and large cracks opened in walls. Three houses had to be torn down due to the large likelihood of an imminent collapse, while other eight buildings had to be temporarily evacuated. Many other walls and chimneys were in risk of imminent collapse as well. Meidow & Ahorner (1994) point out that the most vulnerable buildings suffered the most significant damage. In Dremmen, the roof of the Marienklöster chapel partially collapsed.

Around 500 buildings were damaged in Herkenbosch. As can be observed in Figure A4.6.36, a large proportion of buildings suffered from a combination of types of damage (Maurenbrecher & de Vries, 1995).

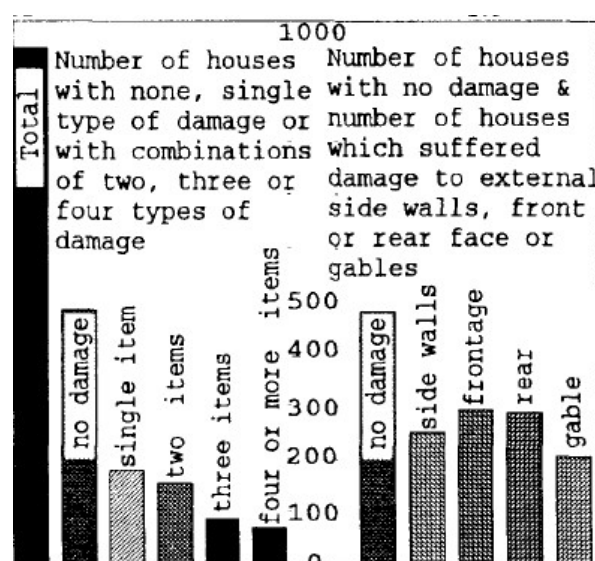


Figure A3.1.36. Damage observed in Herkenbosch, the Netherlands, according to questionnaires filled out by the population. From Maurenbrecher & de Vries (1995).

According to Davenport *et al.* (1994), many historic buildings in the city of Roermond were seriously damaged. These include the Munsterkerk and Minderbroederskerk churches, some ornate roofs near the railway station, and brickwork of the Vroom & Dreesmann department store. Damage to building foundations was also documented.

More than 150 churches were damaged in Germany, many of them around Heinsberg, but also in regions as distant as Cologne, Bonn and Koblenz, located at approximately 75 km, 95 km and 150 km away from the epicentre, respectively (Meidow & Ahorner, 1994). Six finials broke out off their embeddings in the 13th century cathedral in Cologne, and one stone weighting around 500 kg fell from the top of a 60 m tower, striking a whole in the roof of the transept. In Bonn, more than 60 private and public buildings suffered from damages including the collapse of chimneys and cracking of walls. Damage to plaster was widespread all over the town. Figure A4.6.37 shows examples of damage observed in Bonn.

Meidow & Ahorner (1994) point out that most of the damage observed at distances larger than 20 km consisted on small cracks in chimneys and walls, as well as plaster falling off walls and ceilings, though islands of higher damage like those mentioned above occurred at more distant locations.

The most systematised statistics regarding damage caused by this earthquake have been gathered by Pappin *et al.* (1994), who report on the damage ratios observed during a three-day visit to the affected area by the UK-based Earthquake Engineering Field Investigation Team (EEFIT). This group of experts rapidly found that the only building typology to regularly occur in sufficient numbers for statistics to be relevant was residential masonry, and, therefore, decided to focus on it. They subdivided the full typology into those built before 1920, those built between 1920 and 1960, and those built after 1960, and observed that the first were the only ones who had systematically experienced high levels of damage. For this reason, information regarding the three groups was collected during the initial stages of the survey, while later stages only focused on buildings built before 1920.

Figures A4.6.38-39 show the damage ratios obtained for this category, using the damage scale defined in Table A4.6.13, in the first case, and simply grouping results into "no damage" and "some level of damage" categories, in the second. As can be observed, the largest proportion of damaged buildings was observed in Oberbruch, Germany. It should be noted that Herkenbosch, a town which clearly experienced severe damage, was not part of the survey. From the plots in Figure A4.6.40, which present the corresponding results for residential masonry buildings built after 1920, it becomes apparent that, in general, these buildings suffered far less damage than those built before 1920.



Figure A4.6.37. Damage to a residential house (left) and a car (right) in the city of Bonn (Germany). Photos copyright of Seismic Workgroup, St.-Michael-Gymnasium Monschau (2005)

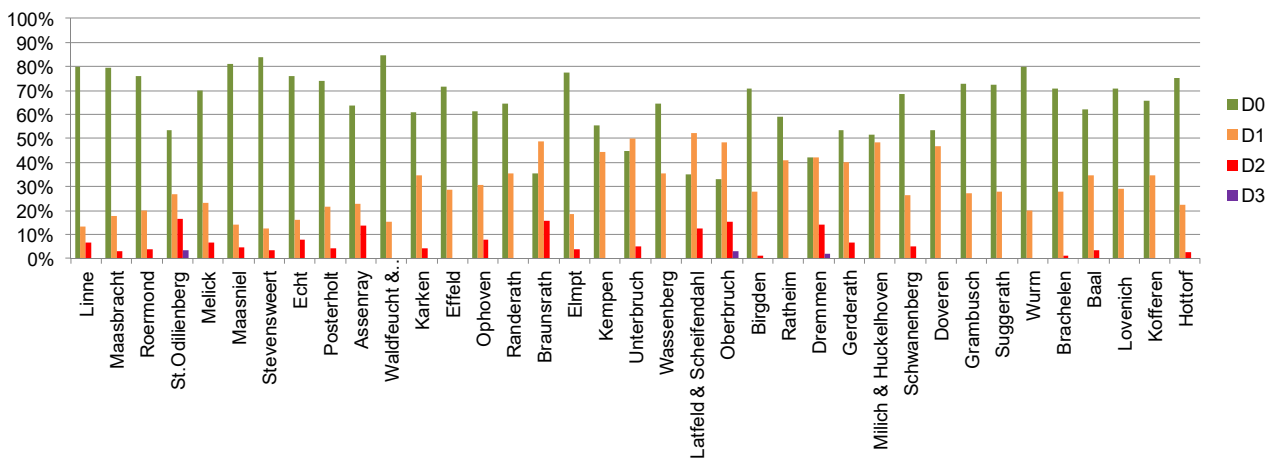


Figure A4.6.38. Damage ratios observed by the Earthquake Engineering Field Investigation Team (EEFIT, Pappin *et al.*, 1994) for residential masonry buildings built before 1920. Locations ordered from closest to most distant from the epicentre, as defined by Ahorner (1994).

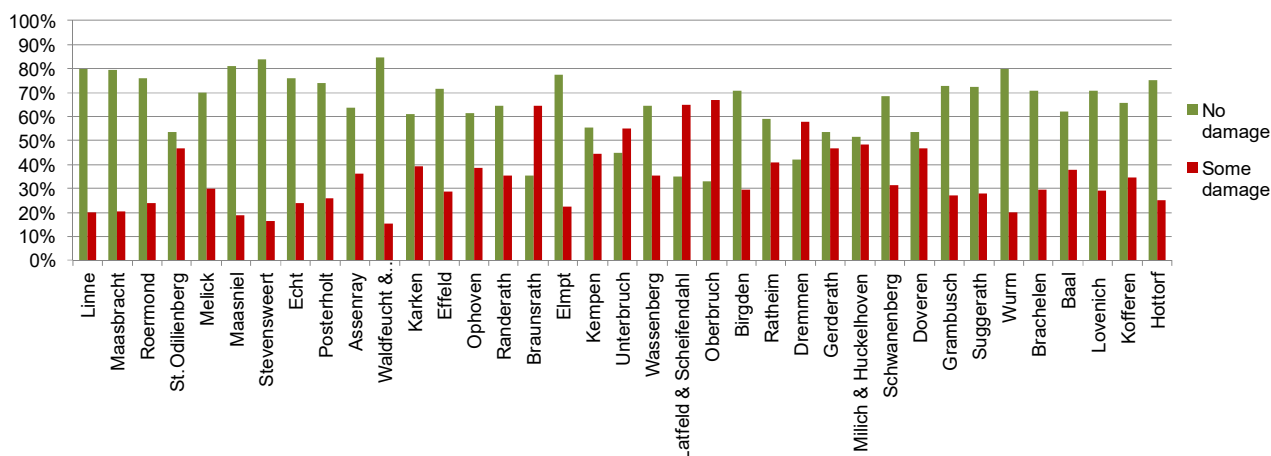


Figure A4.6.39. Damage ratios observed by the Earthquake Engineering Field Investigation Team (EEFIT, Pappin *et al.*, 1994) for residential masonry buildings built before 1920. Locations ordered from closest to most distant from the epicentre, as defined by Ahorner (1994).

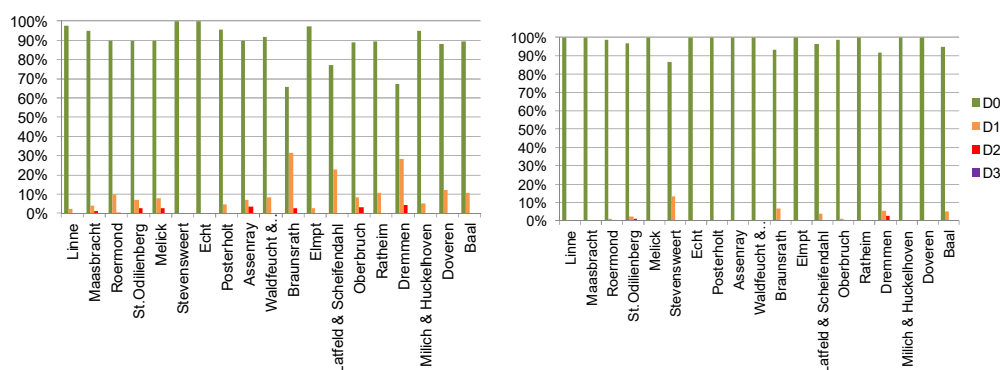


Figure A4.6.40. Damage ratios observed by the Earthquake Engineering Field Investigation Team (EEFIT, Pappin *et al.*, 1994) for residential masonry buildings built between 1920 and 1960 (left), and after 1960 (right). Locations ordered from closest to most distant from the epicentre, as defined by Ahorner (1994).

A4.6.8.3 Observed weaknesses

No details regarding systematic causes of failure and damage were found in the literature. However, from the results of Pappin *et al.* (1994) it becomes clear that older masonry buildings were significantly more vulnerable than more modern ones. Furthermore, and as observed during other small-to-moderate magnitude earthquakes (e.g., Sargeant *et al.*, 2008), the frequency with which damage to chimneys was observed is also a sign of an increased vulnerability of these structures (Figure A4.6.41).



Figure A4.6.41. D2 (left) and D3 (right) damage to chimneys (Schwarz *et al.*, 2010).

A4.6.8.4 Damage distribution

The 1992 Roermond earthquake was felt in places located over 500 km away from the epicentre, such as Berlin, Munich, Zürich and southeast England (Ahorner, 1994). Intensity V effects (e.g., people waking up, some frightened people, hanging objects swinging considerably, china and glasses clattering, etc.) were observed in locations as far as Luxemburg, Frankfurt, Siegen and Kassel, at 174 km, 227 km, 150 km and 248 km from the epicentre, respectively. According to Meidow & Ahorner (1994), these islands of intensity V are due to local site conditions.

Significant damage was observed in the Netherlands and Germany, but not so much in Belgium (Horrent *et al.*, 1994). Figure A4.6.42 shows the location of the cities and towns which suffered significant damage, as described above. The location of the cities studied by the Earthquake Engineering Field Investigation Team (EEFIT; Pappin *et al.*, 1994) are also included, though a detail of the area is presented in Figure A4.6.43. Some degree of correlation can be observed between the results of Pappin *et al.* (1994) and the estimated PGA values from the USGS ShakeMap. Meidow & Ahorner (1994) report local observations of MSK intensities VI to VII from Bonn to Koblenz. As can be observed, the trend of damage seems to be elongated to the south-east and shifted eastwards with respect to the instrumental epicentre. According to Meidow & Ahorner (1994), this can be explained both through soil amplification and the specific geometry and dynamics of the earthquake source.

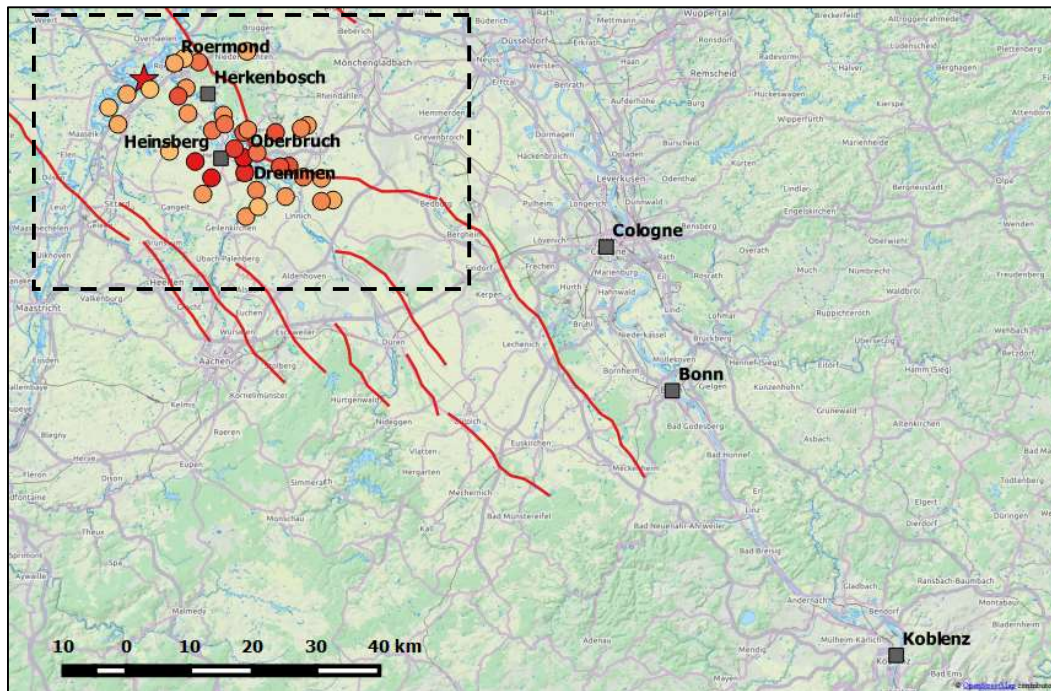


Figure A4.6.42. Location of cities and towns which suffered significant damage. Orange-to-red dots corresponds to the cities studied by the EEFIT (Pappin *et al.*, 1994).

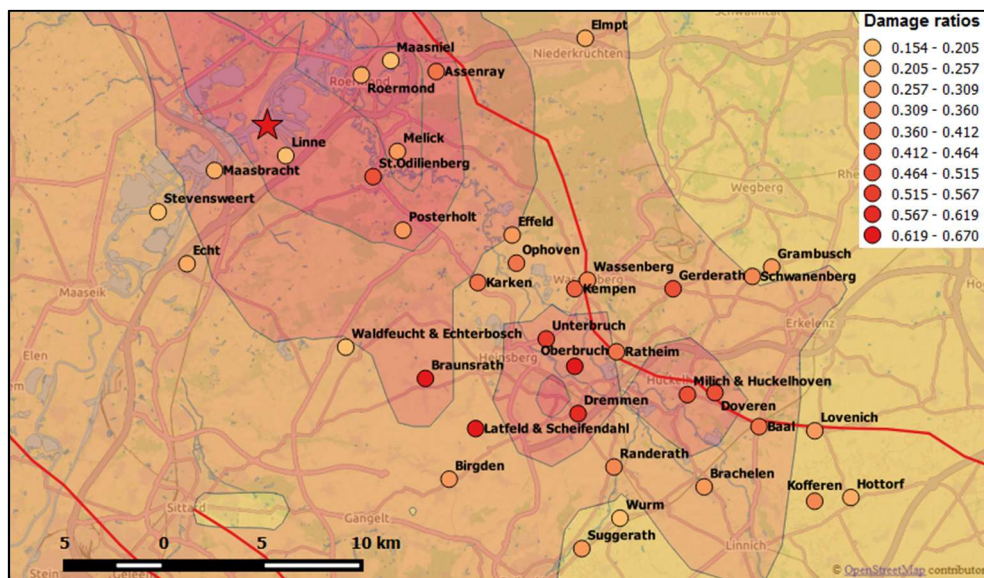


Figure A4.6.43. Location of cities studied by the EEFIT (Pappin *et al.*, 1994) over PGA ShakeMap from the USGS (see Inferred shaking levels section). Colour of dots represents the extent of damage to residential masonry buildings built before 1920 according to the specified scale (ratio makes reference to any kind of damage, *i.e.*, the summation of D1, D2 and D3 damage ratios).

Figure A4.6.44 shows the locations of damaged churches, as reported by Meidow & Ahorner (1994). Slight and moderate damage occurred in regions with MSK macroseismic intensities of V-VI and VI, respectively, while heavy damage took place in regions with intensity larger than VI.

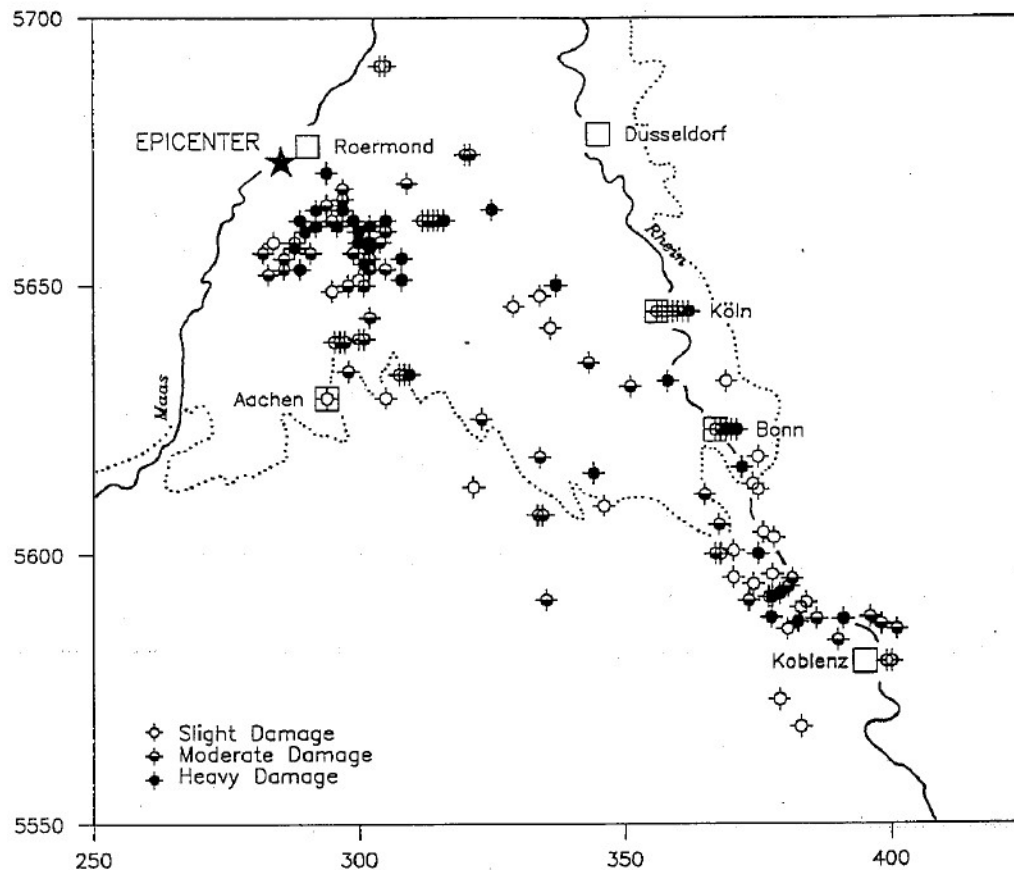


Figure A4.6.44. Location of churches damaged by the earthquake. Slight damage: fine cracks in plaster, fall of small pieces of plaster, and loosening of pinnacles or similar construction parts. Moderate damage: small cracks in walls and vaults, cracks between church tower and nave, and falling of pinnacles. Heavy damage: large and deep cracks in walls and vaults, and damage to load-bearing parts. From Meidow & Ahorner (1994).

Ewald *et al.* (2006) carried out 3D modelling simulations of wave propagation during the 1992 Roermond earthquake in the Lower Rhine Embayment, and concluded that there is a strong correlation between the high observed macroseismic intensities and the contours of the sedimentary basin. Meidow & Ahorner (1994) point out that the thick sediments (over 500 m) in the area close to the epicentre acted decreasing the ground motions in the epicentral area, while relatively larger macroseismic intensities can be observed where sedimentary layers have thicknesses of up to 100 m. They also conclude that the shape of the isoseismals is strongly influenced by local site conditions. Ahorner (1994) also observed that stations located on layers of unconsolidated sediments suffered from amplification effects, but give no indication with respect to the location of these stations. Through the analysis of a series of aftershocks, Horrent *et al.* (1994) concluded that site effects were significant because systematic amplifications were observed at the same stations for events varying in location and source mechanism. They observed particularly high amplifications at station HLN, which is located north of Roermond, quite close to the Peel Boundary Fault trace, the same station for which (Gariel *et al.*, 1994) computed large accelerations (0.35 g).

A4.6.9 Casualties and losses

A4.6.9.1 Numbers of dead and injured

Only one death was reported for this earthquake, and it corresponds to a 79-year-old woman in Bonn who died of a heart attack apparently triggered by the tremor (USGS, GEM Earthquake Consequences Database).

Twenty and twenty-five people were reported injured in Roermond and Heinsberg, respectively. Of the latter, four were in serious condition (USGS, GEM Earthquake Consequences Database). Meidow & Ahorner (1994) also mention some minor injuries being reported at distant towns such as Euskirchen (82 km) and Langenfeld (71 km), but provide no further details.

According to the GEM Earthquake Consequences Database, 200 people were left homeless. This number was estimated based on damage statistics of the building stock.

A4.6.9.2 Causes of casualties

As mentioned earlier, the registered death was due to a medical condition triggered by fear resulting from the ground shaking.

Several sources (e.g., Meidow & Ahorner, 1994; GEM Earthquake Consequences Database; The New York Times, 1992) point out that the registered injuries were caused by falling parts of chimneys, masonry and roofing tiles. Meidow & Ahorner (1994) also mention that some people were slightly injured due to shattering of window glasses.

A4.6.9.3 Estimates of economic losses

According to the GEM Earthquake Consequences Database, Munich Re estimated the total direct losses to be 206 million US\$, of which 120 million correspond to Germany, 50 million correspond to the Netherlands, and 6 million correspond to Belgium. The remaining 30 million correspond to insured losses in Germany. Insured losses in the Netherlands and Belgium are not known.

The Royal Netherlands Meteorological Institute (KNMI) reports a total loss of 275 million guilders, of which 170 million correspond to damage in the Netherlands. With the official conversion rate of 1999, these values are approximately 125 and 77 million Euros, respectively.

Braunmiller *et al.* (1994) report an estimated damage in the epicentral region (Roermond, Herkenbosch and Heinsberg) of around 130 to 200 million US\$. Hinzen & Oemisch (2001) report an overall value of 125 US\$, which is on the lower bound of the estimation by Braunmiller *et al.* (1994) for the epicentral area alone.

Meidow & Ahorner (1994) report that first estimates of damage to public buildings in the district of Heinsberg reached approximately 500,000 DM (around 256 thousand Euros, with the official conversion rate of 1999). Further, they report the repair costs for the cathedral in Cologne to be around 50,000 DM (around 25.6 thousand Euros)

A4.6.10 Discussion and conclusions

This **M5.4** earthquake occurred on 13th April 1992, at 01.20 UTC (03.20 local time), very close to the city of Roermond, in the south of the Netherlands. Apart from a smaller event reported to have occurred 0.2 seconds earlier, no other foreshock activity had been observed, but over 200 small aftershocks were detected. It is the strongest earthquake to have been recorded in the Netherlands and north-western Europe to date, though its size and statistical probability of occurrence are in clear agreement with the tectonics of the region.

It was felt over a large area extending to places located over 500 km away from the epicentre, and reached a maximum MSK-81 (very similar to EMS-98) intensity of VII. Significant losses were registered in the Netherlands and Germany, and in a much lesser extent in Belgium. Residential masonry buildings built before 1920 and churches were the most affected constructions. No damage reports were found for buildings designed to modern codes. Overall, around 1,400 buildings were reported to have been damaged, of which 100 are believed to have been affected beyond repair. Instances of damage included cracks of various widths to masonry, collapse of numerous walls, gables and roofs, and the cracking and collapsing of chimneys, which were the non-structural elements most frequently damaged.

Landslides and liquefaction phenomena were observed, though they did not contribute to the damage to the building stock.

The characteristics of the basin of the Roer Valley seem to have played a significant role in the ground motion levels, as well as in the duration of the shaking.

One death was reported, albeit this being attributed to a medical condition triggered by fear resulting from the ground shaking. An additional 45 injuries were also reported, which were caused by falling parts of chimneys, masonry and roofing tiles.

A4.6.11 References

A4.6.11.1 Bibliography

Afshari, K. & J.P. Stewart (2016). Physically parametrised prediction equations for significant duration in active crustal regions. *Earthquake Spectra* **32**(4), 2057-2081.

Ahorner, L. (1994). Fault-plane solutions and source parameters of the 1992 Roermond, the Netherlands, mainshock and its stronger aftershocks from regional seismic data. *Geol. En Mijnb.* **73**, 199–214.

Ahorner, L. & W. Rosenhauer (1986). Regionale erdbebengefährdung (Regional earthquake hazard, in German). In: Realistische seismische lastannahmen für bauwerke. Abschlußbericht an das Institut für Bautechnik Berlin - König und Heunisch, Bratende Ingenieure, Frankfurt/Erdbebenstation Bensberg der Universität Köln / Institut für Geophysik der Universität Stuttgart. 334 pp.

Akkar, S., M.A. Sandikkaya, M. Senyurt, A. Azari Sisi, B.Ö. Ay, P. Traversa, J. Douglas, F. Cotton, L. Luzi, B. Hernandez & S. Godey (2014). Reference database for seismic ground-motion in Europe (RESORCE). *Bulletin of Earthquake Engineering* **12**(1), 311–339.

Alkema, D., M. Mosselman & I. Paulussen (1994). Earthquake-triggered landslides at the Brunssummerheide, Limburg, the Netherlands: preliminary studies following the 1992 Roermond earthquake. *Geol. En Mijnb.* **73**, 387–391.

Allen, T.I., D.J. Wald, P.S. Earle, K.D. Marano, A.J. Hotovec, K. Lin & M.G. Hearne (2009). An Atlas of ShakeMaps and population exposure catalog for earthquake loss modeling. *Bull. Earthq. Eng.* **7**, 701–718. Database available online at (last accessed 9th February 2017): <https://earthquake.usgs.gov/data/pager/references.php>.

Atakan, K., V. Midzi, B.M. Toiran, K. Vanneste, T. Camelbeeck & M. Meghraoui (2000). Seismic hazard in regions of present day low seismic activity: uncertainties in the paleoseismic investigations along the Bree Fault Scarp (Roer Graben, Belgium). *Soil Dynamics and Earthquake Engineering* **20**, 415–427.

Basili, R., V. Kastelic, M. B. Demircioglu, D. Garcia Moreno, E.S. Nemser, P. Petricca, S.P. Sboras, G.M. Besana-Ostman, J. Cabral, T. Camelbeeck, R. Caputo, L. Danciu, H. Domac, J. Fonseca, J. Garcia-Mayordomo, D. Giardini, B. Glavatovic, L. Gulen, Y. Ince, S. Pavlides, K. Sesetyan, G. Tarabusi, M.M. Tiberti, M. Utkucu, G. Valensise, K. Vanneste, S. Vilanova & J. Wössner (2013). The European Database of Seismogenic Faults (EDSF) compiled in the framework of the Project SHARE. <http://diss.rm.ingv.it/share-edsf/> (last accessed: 22nd May 2015), doi: 10.6092/INGV.IT-SHARE-EDSF.

BIN (2002). *NBN-ENV 1998-1-1: 2002 NAD-E/N/F, Belgische toepassingsrichtlijn Eurocode 8: Ontwerp en dimensionering van aardschokbestendige structuren – Deel 1-1: Algemene regels – Aardschokken en algemene richtlijnen voor structuren. (Belgian application guideline Eurocode 8: Design and dimensioning of earthquake-resistant structures - Part 1-1: General rules - Earth shocks and general guidelines for structures).*

Bommer, J.J., P.J. Stafford & J.E. Alarcón (2009). Empirical equations for the prediction of the significant, bracketed, and uniform duration of earthquake ground motion. *Bulletin of the Seismological Society of America* **99**(6), 3217–3233.

Boore, D.M. & W.B. Joyner (1982). The empirical prediction of ground motion. *Bulletin of the Seismological Society of America* **72**, S43–S60.

Boore, D.M., W.B. Joyner & T.E. Fumal (1997). Equations for estimating horizontal response spectra and peak acceleration from western North American earthquakes: a summary of recent work. *Seismological Research Letters* **68**(1), 128–153.

Braunmiller, J., T. Dahm & K.-P. Bonjer (1994). Source mechanism of the 1992 Roermond earthquake from surface-wave inversion of regional data. *Geophysical Journal International* **116**, 663–672.

- Brouwer, J.W.R., T. Van Eck, F.H. Goutbeek & A.C.W.M. Vrouwenvelder (2010). The meaning of Eurocode 8 and induced seismicity for earthquake engineering in the Netherlands. *Fifth International Conference on Recent Advances in Geotechnical Earthquake Engineering and Soil Dynamics and Symposium in Honor of Professor I. M. Idriss*, San Diego, California, May 24-29.
- Camelbeeck, T. & T. van Eck (1994). The Roer Valley Graben earthquake of 13 April 1992 and its seismotectonic setting. *Terra Nova* **6**, 291–300.
- Camelbeeck, T. & M. Meghraoui (1996). Large earthquakes in Northern Europe more likely than once thought. *EOS* **77**, 405–409.
- Camelbeeck, T. & M. Meghraoui (1998). Geological and geophysical evidence for large palaeo-earthquakes with surface faulting in the Roer Graben (northwest Europe). *Geophysical Journal International* **132**, 347–362.
- Camelbeeck, T., T. van Eck, R. Pelzing, L. Ahorner, J. Loohuis & H.W. Haak (1994). The 1992 Roermond earthquake, the Netherlands, and its aftershocks. *Geol. En Mijnb.* **73**, 181–197.
- CEN (2004). Eurocode 8: Design of Structures for Earthquake Resistance - Part 1: General rules, seismic actions and rules for buildings.
- Center for International Earth Science Information Network - CIESIN - Columbia University, United Nations Food and Agriculture Programme - FAO, and Centro Internacional de Agricultura Tropical - CIAT (2005). *Gridded Population of the World, Version 3 (GPWv3)*. Palisades, NY: NASA Socioeconomic Data and Applications Center (SEDAC). <http://dx.doi.org/10.7927/H4639MPP>.
- Davenport, C.A., J.M.J. Lap, P.M. Maurenbrecher & D.G. Price (1994). Liquefaction potential and dewatering injection structures at Herkenbosch: field investigations of the effect of the 1992 Roermond earthquake, the Netherlands. *Geol. En Mijnb.* **73**, 365–374.
- De Crook, T. (1994). Earthquake hazard for Roermond, the Netherlands. *Geol. En Mijnb.* **73**, 425–429.
- De Crook, T. (1996). A seismic zoning map conforming to Eurocode 8, and practical earthquake parameter relations for the Netherlands. *Geol. En Mijnb.* **75**, 11–18.
- De Vos, D. (2010). *Probabilistic Seismic Hazard Assessment for the Southern part of the Netherlands*. MSc. thesis. Utrecht University.
- DIN (2005). *DIN 4149:2005-04: Bauten in deutschen Erdbebengebieten - Lastannahmen, Bemessung und Ausführung üblicher Hochbauten (Buildings in German earthquake areas - load assumptions, design and execution of conventional buildings, in German)*. Germany.
- DIN (2010). *DIN EN 1998-1:2010-12: Eurocode 8: Auslegung von Bauwerken gegen Erdbeben - Teil 1: Grundlagen, Erdbebeneinwirkungen und Regeln für Hochbauten. (Eurocode 8: Design of structures against earthquakes - Part 1: Fundamentals, earthquake effects and rules for buildings, in German)*. Germany.
- Dziewonski, A.M., T.-A. Chou & J. H. Woodhouse (1981). Determination of earthquake source parameters from waveform data for studies of global and regional seismicity. *Journal of Geophysical Research* **86**, 2825–2852.
- Ekström, G., M. Nettles & A. M. Dziewonski (2012). The global CMT project 2004-2010: Centroid-moment tensors for 13,017 earthquakes. *Physics of the Earth and Planetary Interiors* **200-201**, 1-9.
- Evers, L. (2000). *An extended abstract on geophysical investigations for fault identification in paleoseismology*. Royal Netherlands Meteorological Institute. Available online at <http://www.knmi.nl/~evers/paleoseismology/paleoseis.html>. Last accessed: 9th June 2015.

Ewald, M., H. Igel, K.-G. Hinzen & F. Scherbaum (2006). Basin-related effects on ground motion for earthquake scenarios in the Lower Rhine Embayment. *Geophysical Journal International* **166**, 197–212.

Gariel, J.C., C. Horrent, D. Jongmans & T. Camelbeeck (1994). Strong ground motion computation of the 1992 Roermond earthquake, the Netherlands, from linear methods using locally recorded aftershocks. *Geol. En Mijnb.* **73**, 315–321.

Giardini, D., G. Grünthal, K.M. Shedlock & P. Zhang (1999). The GSHAP global seismic hazard map. *Annali di Geofisica* **42**(6), 1225–1228.

Grünthal, G. (ed.) (1993). *European Macroseismic Scale 1992 (updated MSK scale)*. European Seismological Commission, Subcommittee on Engineering Seismology, Working Group Macroseismic scale.

Grünthal, G. & H. Grosser (1992). Roermond erdbeben vom 13 April 1992: Zu physikalischen herddparametern und zur makroseismischen herdtiefenschätzung (Roermond earthquake of 13 April 1992, in German). In: *Report by the Arbeitsgruppe Wisstechn. Task force und Erdebebenkatastrophenforschung*. Hannover: 2/1–2/4.

Grünthal, G., D. Mayer-Rosa & W.A. Lenhardt (1998). Abschätzung der Erdbebengefährdung für die D-A-CH-Staaten-Deutschland, Österreich, Schweiz (Estimate of earthquake hazard for the D-A-CH countries: Germany, Austria, Switzerland, in German). *Bautechnik* **75**, 753–767.

Grünthal, G., A.H. Thieken, J. Schwarz, K.S. Radtke, A. Smolka & B. Merz (2006). Comparative Risk Assessments for the City of Cologne – Storms, Floods, Earthquakes. *Natural Hazards* **38**, 21–44.

Haak, H.W., J.A. van Bodegraven, R. Sleeman, R. Verbeiren, L. Ahorner, H. Meidow, G. Grünthal, P. Hoang-Trong, R.M.W. Musson, P. Henni, Z. Schenková & R. Zimová (1994). The macroseismic map of the 1992 Roermond earthquake, the Netherlands. *Geol. En Mijnb.* **73**, 265–270.

Hack, R., D. Alkema, G.A.M. Kruse, N. Leenders & L. Luzi (2007). Influence of earthquakes on the stability of slopes. *Engineering Geology* **91**, 4–15.

Helm, J.A., M. Bour & P. Hoang-Trong (1994). Accelerometer recordings of the 1992 Roermond earthquake, the Netherlands, and ground motion simulations using the empirical Green's function method. *Geol. En Mijnb.* **73**, 331–337.

Hinzen, K.-G. & M. Oemisch (2001). Location and magnitude from seismic intensity data of recent and historic earthquakes in the northern Rhine area, Central Europe. *Bulletin of the Seismological Society of America* **91**, 40–56.

Horrent, C., D. Jongmans & T. Camelbeeck (1994). Local ground motion variations observed in the region of Roermond, the Netherlands, from aftershocks of the April 1992 earthquake. *Geol. En Mijnb.* **73**, 323–330.

Jaiswal, K. & D.J. Wald (2008). *Creating a Global Building Inventory for Earthquake Loss Assessment and Risk Management*. USGS Open File Report 2008-1160. Available electronically at: <http://pubs.usgs.gov/of/2008/1160/>.

Koopman, F.W.A. (2007). General Overview of the Problems, Needs and Solutions in the Dutch Urban Building Envelopes. In Melgaard, E., G. Hadjimichael, M. Almeida & L.G.W. Verhoef (eds.): *COST C16 Improving the Quality of Existing Urban Building Envelopes*, IOS Press.

- Lap, J.M.J. (1987). Earthquake-induced liquefaction potential in the area south of Eindhoven, the Netherlands. *Mem. Centre Eng. Geol. Netherlands* **47**, 40 pp.
- Leynaud, D., D. Jongmans, H. Teerlynck & T. Cambelbeeck (2000). Seismic hazard assessment in Belgium. *Geologica Belgica* **3**, 67–86.
- Maurenbrecher, P.M. & G. de Vries (1995). Assessing damage for Herkenbosch, The Netherlands, due to the Roermond earthquake of April 13, 1992. *WIT Transactions on the Built Environment* **14**, 397–404.
- Maurenbrecher, P.M., D.G. Price & W. Verwaal (1994). Technical note on the 1992 Brunssummerheide landslide in Limburg, the Netherlands. *Geol. En Mijnb.* **73**, 393–398.
- Medvedev, S., W. Sponheuer & V. Karnik (1965). *Seismic intensity scale, MSK 1964*. Academy of Sciences of the U.S.S.R., Soviet Geophysical Community, 13 pp.
- Medvedev, S., W. Sponheuer & V. Karnik (1981). Report of the ad-hoc panel meeting of experts on the updating of the MSK-64 seismic intensity scale. *Gerlands Beiträge zur Geophysik* **90**, 261–268.
- Meidow, H. & L. Ahorner (1994). Macroseismic effects in Germany of the 1992 Roermond earthquake and their interpretation. *Geol. En Mijnb.* **73**, 271–279.
- Musson, R.M., G. Grünthal & M. Stucchi (2010). The comparison of macroseismic intensity scales. *J. Seismol.* **14**, 413–428.
- Nieuwenhuis, J.D. (1994). Liquefaction and the 1992 Roermond earthquake, the Netherlands. *Geol. En Mijnb.* **73**, 357–364.
- Oncescu, M.-C., T. Cambelbeeck & H. Martin (1994a). A note on the foreshock of the 1992 Roermond earthquake, the Netherlands. *Geol. En Mijnb.* **73**, 229–233.
- Oncescu, M.-C., T. Camelbeeck & H. Martin (1994b). Source parameters for the Roermond aftershocks of 1992 April 13–May 2 and site spectra for P and S waves at the Belgian seismic network. *Geophysical Journal International* **116**, 673–682.
- Pappin, J.W., A.R. Coburn & C.R. Pratt (1994). Observations of damage ratios to buildings in the epicentral region of the 1992 Roermond earthquake, the Netherlands (extended abstract). *Geol. En Mijnb.* **73**, 299–302.
- Pelzing, R. (1994). Source parameters of the 1992 Roermond earthquake, the Netherlands, and some of its aftershocks recorded at the stations of the Geological Survey of NorthRhine-Westphalia. *Geol. En Mijnb.* **73**, 215–223.
- Rosenhauer, W. & L. Ahorner (1994). Seismic hazard assessment for the Lower Rhine Embayment before and after the 1992 Roermond earthquake. *Geol. En Mijnb.* **73**, 415–424.
- Sargeant, S.L., P.J. Stafford, R. Lawley, G. Weatherill, A.-J.S. Weston, J.J. Bommer, P.W. Burton, M. Free, R.M.W. Musson, T. Kuuyuor & T. Rossetto (2008). Observations from the Folkestone, U.K., Earthquake of 28 April 2007. *Seismological Research Letters* **79**, 672–687.
- Scherbaum, F. (1994). Modelling the Roermond earthquake of 1992 April 13 by stochastic simulation of its high-frequency strong ground motion. *Geophysical Journal International* **119**, 31–3.
- Schokker, J. & E.A. Koster (2004). Sedimentology and facies distribution of Pleistocene cold-climate aeolian and fluvial deposits in the Roer Valley Graben (southeastern Netherlands). *Permafrost and Periglacial Processes* **15**, 1–20.

Schulte Nordholt, E., J. van Zeijl, L. Hoeksma & Centraal Bureau voor de Statistiek (2014). *Dutch census 2011: analysis and methodology*. Statistics Netherlands, The Hague. Available online at: <https://www.cbs.nl/NR/rdonlyres/5FDCE1B4-0654-45DA-8D7E-807A0213DE66/0/2014b57pub.pdf>. Last accessed: 9th February 2017.

Schwarz, J., S. Beinersdorf, H. Meidow & L. Ahorner (2010). *Magnitudenorientierter Erdbebenkatalog für deutsche und angrenzende Gebiete - EK DAG - erweiterter Ahorner-Katalog - Version 1.0 (Magnitude-oriented earthquake catalog for Germany and adjacent areas - EK DAG - extended Ahorner catalog - Version 1.0, in German)*. SeismoGeologisches Büro Dr. Meidow & Earthquake Damage Analysis Center (Bauhaus-Universität, Weimar).

Tyagunov, S., G. Grünthal, R. Wahlström, L. Stempniewski & J. Zschau (2006). Seismic risk mapping for Germany. *Natural Hazards and Earth System Sciences* **6**, 573–586.

United Nations, ed. (2014). *Human Development Report 2014 - Sustaining human progress: Reducing vulnerabilities and building resilience*. Report of the United Nations Development Programme (UNDP), New York, United States.

Van Gils J.M. & Zaczek, Y. (1978). La séismicité de la Belgique et son application en génie parasismique (The seismicity of Belgium and its application in earthquake engineering, in French). *Annales des Travaux Publics de Belgique* **6**, 1-38.

Vanneste, K., M. Meghraoui & T. Camelbeeck (1999). Late Quaternary earthquake-related soft-sediment deformation along the Belgian portion of the Feldbiss Fault, Lower Rhine Graben system. *Tectonophysics* **309**, 57–79.

Vanneste, K., T. Camelbeeck & K. Verbeeck (2013). A Model of Composite Seismic Sources for the Lower Rhine Graben, Northwest Europe. *Bulletin of the Seismological Society of America* **103**, 984–1007.

Vanneste, K., B. Vlemminckx, K. Verbeeck & T. Camelbeeck (2014). Development of seismic hazard maps for Belgium. *Workshop: Results of the European Project SHARE: Seismic Hazard Harmonization in Europe*.

Weatherill, G. A. (2014). *OpenQuake ground motion toolkit - User guide*. Global Earthquake Model (GEM). Technical Report.

Woessner, J., D. Giardini, H. Crowley, F. Cotton, G. Grünthal, G. Valensise, R. Arvidsson, R. Basili, M. B. Demircioglu, S. Hiemer, C. Meletti, R. W. Musson, A. N. Rovida, K. Sesetyan, M. Stucchi & The SHARE Consortium (2015). The 2013 European Seismic Hazard Model: Key Components and Results. *Bulletin of Earthquake Engineering* **13**(12), 3553–3596. Online data source: <http://www.efehr.org/en/home/>. Last accessed: 3rd December 2017.

Worden, C.B., E.M. Thompson, M. Hearne & D.J. Wald (2017). *ShakeMap V4 Manual: technical manual, user's guide, and software guide*. United States Geological Survey. Available online at: <http://usgs.github.io/shakemap/>.

A4.6.11.2 Web references

GEM Earthquake Consequences Database (2015): <http://gemecd.org/>. Last accessed: 6th September 2015.

Global Centroid Moment Tensor Project (CMT): <http://www.globalcmt.org/>. Last accessed: 6th September 2015.

International Seismological Centre (ISC): <http://www.isc.ac.uk/>. Last accessed: 6th September 2015.

Royal Netherlands Meteorological Institute (KNMI): http://www.knmi.nl/index_en.html.
Last accessed: 6th September 2015.

Royal Observatory of Belgium (ROB): <http://seismologie.oma.be/>.

Website for this event (last accessed 6th September 2015):

<http://seismologie.oma.be/en/seismology/earthquakes-in-belgium/xq187gr23>.

Seismic Workgroup, St.-Michael-Gymnasium Monschau, (2005):

http://seismic.mgm-monschau.de/english/artikel/artikel_1_3.php.

Last accessed: 6th September 2015.

Statistics Netherlands: <http://statline.cbs.nl/>. Last accessed: 6th September 2015.

The New York Times (1992): <https://www.nytimes.com/1992/04/14/world/rare-quake-hits-north-europe-hurting-40.html>. Last accessed: 28th March 2019.

United States Geological Service (USGS): <http://earthquake.usgs.gov/earthquakes/>.

Outdated ShakeMap website for this event (last accessed 6th September 2015):

<http://earthquake.usgs.gov/earthquakes/shakemap/atlas/shake/199204130120/>.

Renovated website for this event (last accessed 6th September 2015):

<http://earthquake.usgs.gov/earthquakes/eventpage/usp00055q3#executive>.

World Economic Outlook Database 2015 (2015):

<http://www.imf.org/external/pubs/ft/weo/2015/01/weodata/index.aspx>.

Last accessed: 6th September 2015.

A4.7. March 1993 M5.4 Pyrgos Earthquake, Greece

This earthquake occurred on 26th March 1993, at 11.58 UTC (14.58 local time) in the western Peloponnese. It was widely felt in the latter and in the island of Zakynthos, and affected several localities in the prefecture of Ilia. In Pyrgos city centre, its capital, about 50% of the masonry buildings suffered moderate damage and several public buildings had to be evacuated. An extended foreshock activity that started at the end of 1992 preceded the main shock, which was then followed by a series of shallow aftershocks that lasted for a few months. Few injuries and an important amount of financial aid to the affected population was the aftermath of the moderate, yet damaging earthquake of 1993 in a historically active seismic area.

A4.7.1 Tectonic and seismic setting

A4.7.1.1 Tectonic setting

The area affected by this earthquake is situated in the Kyparissiakos Gulf, around 50 km to the east of the northwesternmost end of the western Hellenic Arc, as shown in Figure A4.7.1, along which orthogonal convergence between the African and the European plate occurs (McKenzie, 1972; Jackson, 1994; Koukouvelas *et al.*, 1996). According to Sachpazi *et al.* (2016), the large variations observed in the rate of convergence of the western Hellenic Arc is due to the westward extrusion of Anatolia driven by the collision of Arabia (McKenzie, 1972) and the southwestward pull exerted by slab rollback (Royden, 1993). The subduction of the African oceanic domain beneath the Aegean lithosphere is believed to have initiated in the Late Cretaceous and is still active at present (Jolivet & Brun, 2010). The high deformation rate of the Aegean domain has been demonstrated by GPS studies (*e.g.*, McClusky *et al.*, 2000; Kahle *et al.*, 2000; Chousianitis *et al.*, 2015).

The 1993 Pyrgos earthquake occurred beneath the northern edge of Kyparissiakos Gulf, a 45 km long segment of the Ionian coast of western Peloponnese, trending NNW-SSE, almost parallel to the Hellenic Trench (Figure A4.7.1), and generally following the geometry of the fold-and-thrust belt of the External Hellenides (*e.g.*, Philippson, 1898; Aubouin, 1977; Jacobshagen, 1979) and of the modern Hellenic arc (McKenzie, 1972; LePichon & Angelier, 1979; Fountoulis *et al.*, 2014). According to Papanikolaou *et al.* (2007), a NNW–SSE offshore longitudinal fault parallel to the shelf with slip rate around 3 mm/year represents the physical division of the structure between the uplifted coastal area and the present-day Gulf. The region is a transition zone, as to the north lie the highly seismogenic and rapidly deforming areas of north-west Peloponnese and the Corinth Rift while, to the southwest, deformation is mainly related to the active subduction and thrust faulting (Figure A4.7.2).

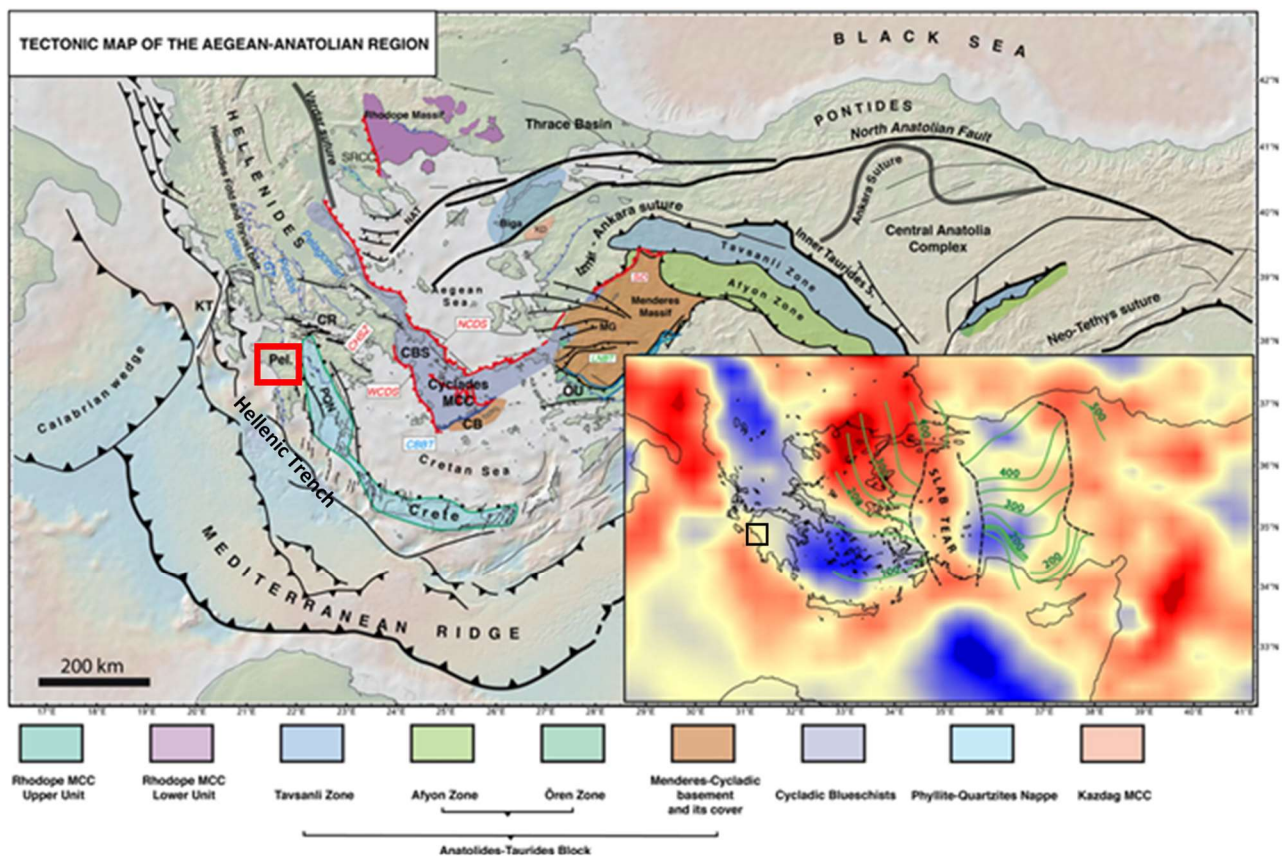


Figure A4.7.1. Geological and geodynamic context in the Aegean Sea and Anatolia and (inset) P-wave seismic tomography model of the upper mantle (average between 100 and 250 km) with isobaths of the slab (green lines). Rectangle surrounds the study area. From Jolivet *et al.* (2015).

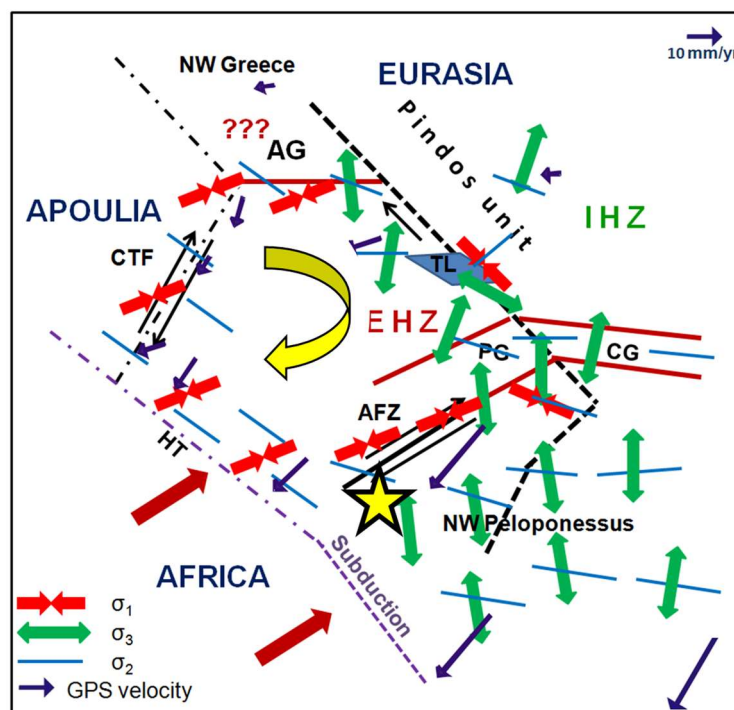


Figure A4.7.2. Sketch map of western Greece which summarizes seismological and CGPS data for the area of study. AFZ-Andravida Fault Zone; AG-Amvrakikos Gulf; CTF-Cephalonia Transform Fault; CG-Corinth Gulf; EHZ-External Hellenides Zone; HT-Hellenic Trench; IHZ-Internal Hellenides Zone; PG-Patras Gulf; TL-Trichonis Lake. The yellow star denotes the location of the 1993 earthquake. Modified from Kassaras *et al.* (2012).

Figure A4.7.3 shows that the Pyrgos basin is affected by Pliocene synsedimentary faults, striking both parallel (NW) and perpendicular (NE) to the Hellenides. According to Koukouvelas *et al.* (1996), the direction of the maximum compression is NE-SW, as indicated by the slickenside lineations on the fault planes of the two systems. In contrast, a WNW-trending younger fault system formed in the area during the Quaternary is subject to compression along the WNW-ESE direction instead (Koukouvelas *et al.*, 1996).

Melis *et al.* (1994) describe three main orientations of normal faulting systems that can be identified in the region: (i) a NW-SE trending set, located to the south-south-east, south-east, east and north of the city, (ii) two E-W trending fault zones to the west and east of Pyrgos, and (iii) a NE-SW trend which is characteristic of faults to the north of the city. Strike-slip motion has only been reported for the E-W trending fault zones (Melis *et al.*, 1994). All these three trends seem to converge at the city of Pyrgos, with the NW-SE one being considered as the dominant one. The complexity of the fault systems in the area makes it difficult to identify the causative fault of the 1993 earthquake, as will be discussed in Section A4.7.2.3.

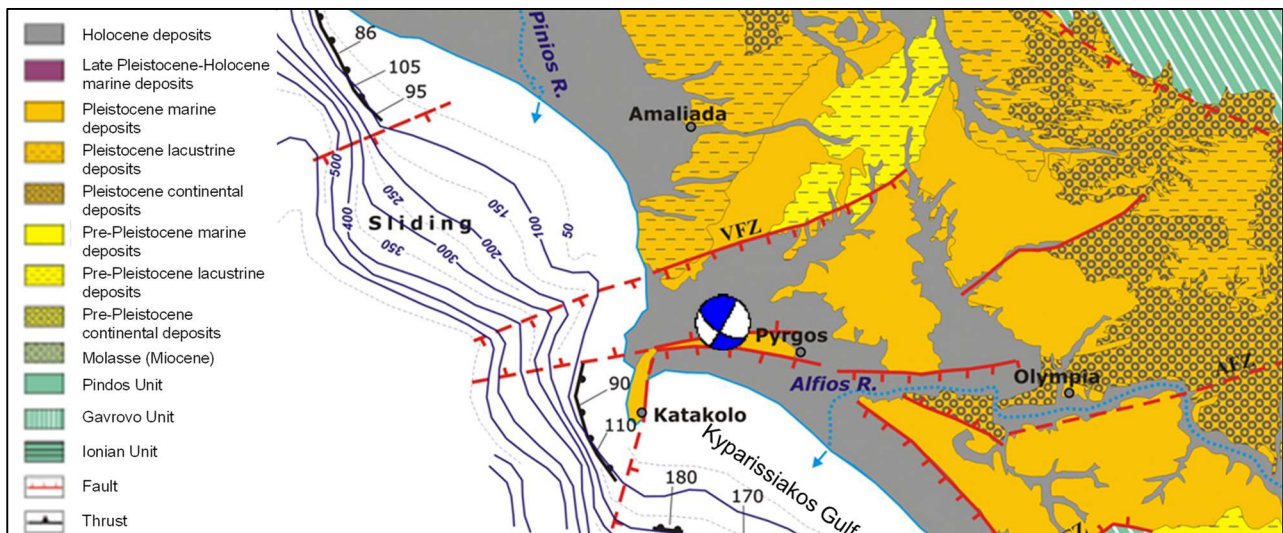


Figure A4.7.3. Top: Simplified geological map of the study area showing onshore and offshore faults. LaFZ: Lapithas fault zone, AFZ: Alfios fault zone, EFZ: Epitalio fault zone, VFZ: Vounargo fault zone, and Pyrgos–Tropaea. The beach-ball is the GCMT solution of the 1993 earthquake. From Papanikolaou *et al.* (2007).

A4.7.1.2 Regional and local seismicity

The study area is notable for its historical paucity of large earthquakes (Ambraseys & Jackson, 1990). The typical magnitude of the onshore seismicity in the Peloponnese is $M_L \sim 5.2$ (Ambraseys & Jackson, 1990), with a maximum magnitude of $M 6.4$ observed during the earthquake of 8th June 2008. During the last 30 years, the Western Peloponnese has been affected by 8 earthquakes that caused human casualties and damage, as shown in Table A4.7.1 and Figure A4.7.4.

Table A4.7.1. Damaging earthquakes in Western Peloponnesus since 1986. Source parameters from catalogue courtesy of Dr. Kassaras (Kassaras *et al.*, 2016).

ID	Year	Month	Day	Hour	Min	Lat	Lon	Depth	Mw	Affected area
1	1986	9	13	17	24	37.070	22.180	23.0	5.2	Kalamata
2	1988	10	16	12	34	37.930	20.920	25.0	5.7	Kyllini
3	1993	3	26	11	58	37.684	21.437	15.0	5.4	Pyrgos
4	1993	7	14	12	31	38.170	21.770	19.0	5.5	Patra
5	1995	6	15	0	15	38.360	22.200	7.0	6.2	Aigio
6	2002	12	2	4	58	37.809	21.150	12.5	5.5	Vartholomio
7	2008	2	14	10	9	36.549	21.772	25.0	6.7	Koroni
8	2008	6	8	12	25	37.964	21.505	25.8	6.4	Achaia-Ilia

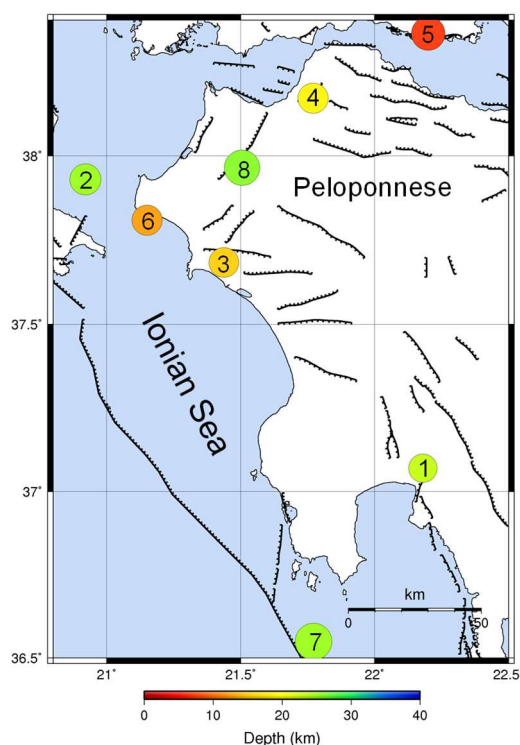


Figure A4.7.4. Damaging earthquakes in Western Peloponnesus since 1986. Numbers correspond to their chronological order (column labelled “ID” in Table A4.7.1).

The 8th June 2008 **M**6.4 Movri Mountain earthquake was the first modern, strong strike-slip earthquake occurring in the Greek mainland (Papadopoulos *et al.*, 2010). It occurred on a high-angle dextral strike-slip blind fault (Koukouvelas *et al.*, 2009) striking NE–SW, dipping NW with a small reverse component, similar to one of the possible fault plane solutions of the 1993 Pyrgos earthquake. Historical seismicity showed no evidence that the causative fault of the 2008 event had ruptured in the last 300 years (Papadopoulos *et al.*, 2010).

Kassaras *et al.* (2016) carried out an extensive effort to compile a reliable catalogue of earthquakes for the western Hellenic Arc, relocating a large number of hypocentres and gathering focal mechanism solutions available from the literature. The resulting catalogue contains 11,544 earthquakes (not all of which have been relocated) and covers the period

between 1986 and 2012, though it is noted that the quality of the data increases significantly after 2008, when the Hellenic Unified Seismological Network (HUSN) was implemented. Around 75% of the events have local magnitudes equal to or larger than 2.0. From Figure A4.7.5 and Figure A4.7.6, which present the spatial distribution of these relocated events, the following observations are made:

- The area north-east of the 1993 epicentre is dominated by seismicity aligned in a NE-SW direction, most of which is related to the **M**6.4 2008 Andravida (Movri) aftershock sequence.
- Earthquakes east of Zakynthos (left side of white rectangle in Figure A4.7.5) are deeper, indicating active subduction beneath Peloponnesus.
- The crustal block including Zakynthos, Cephalonia, Lefkada, NW Peloponnesus, Patras Gulf and Aitolokarnania (indicated by a white rectangle in Figure A4.7.5) is characterized by high marginal activity and almost no internal seismic deformation. The marginal faults of this block have produced several moderate to strong earthquakes during the last decade (*e.g.*, Kassaras *et al.*, 2016).

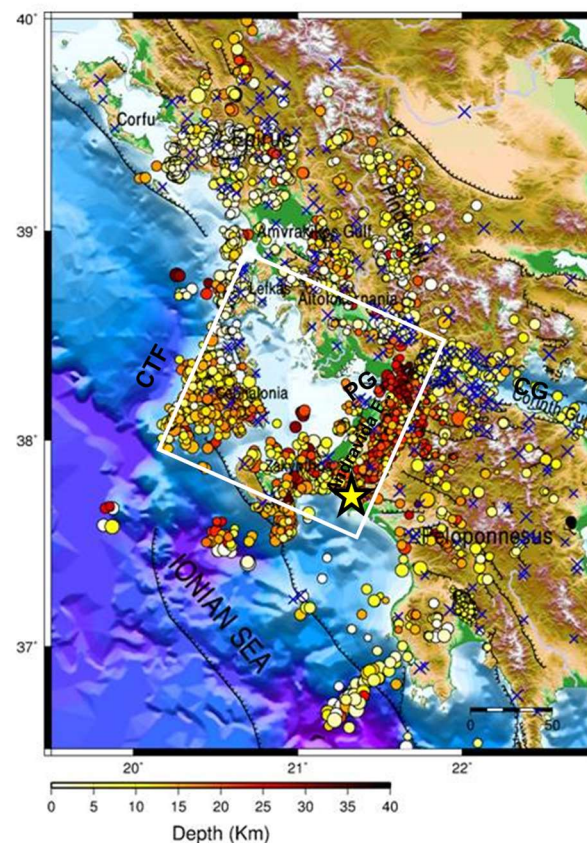


Figure A4.7.5. 7500 relocated earthquakes with $M_L \geq 2.0$ in western Greece. CTF: Cephalonia Transform Fault; PG: Patras Gulf. Yellow star denotes the epicentre of the 1993 event. Modified from Kassaras *et al.* (2013).

Figure A4.7.6(b) focuses on selected relocated seismicity with $M_L \geq 2.0$ around the 1993 epicentral area since 2008, when the detectability of the Greek network was improved by the installation of HUSN, with an average of over 1600 earthquakes with $M_L \geq 2.0$ being detected per year. The pattern is complex, since crustal and sub-crustal seismicity coexist within a small area. Reliable fault plane solutions of crustal earthquakes for the area of

Figure A4.7.6(c) indicate extensive dextral strike-slip motion along NE-SW and steep SE dipping fault planes, parallel to the strike of the Cephalonia Transform Fault (CTF).

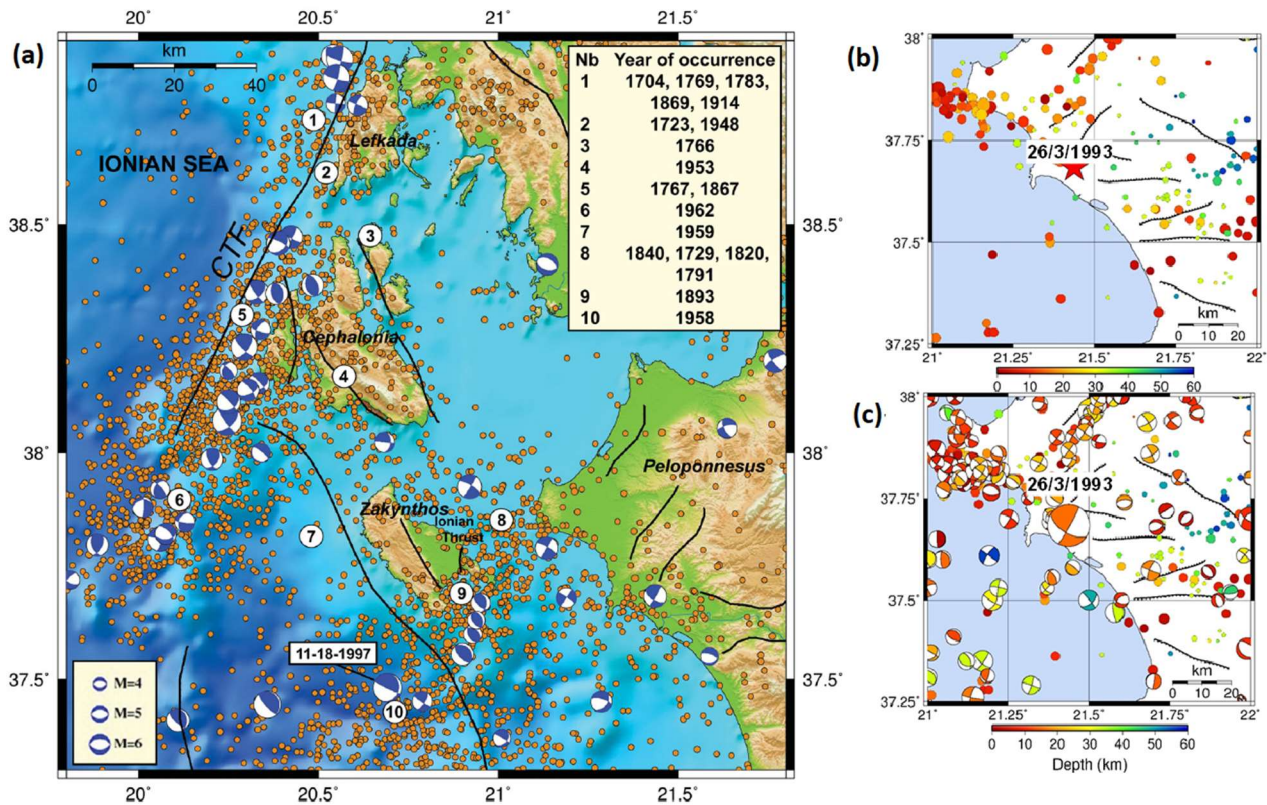


Figure A4.7.6. (a) Seismotectonic map presenting 1964-2005 earthquakes with $M > 3.6$ (orange circles) and $M > 6.0$ events before 1964 (white circles with numbers). Fault plane solutions of 1964-2005 earthquakes with $M > 4.5$ shown. From Papadimitriou *et al.* (2012). (b) Hypocentral locations for earthquakes with $M_L \geq 2.0$ in the period 2008-2012 for the area around Pyrgos (data from catalogue compiled by the Seismological Laboratory of the Department of Geophysics-Geothermics of the National and Kapodistrian University of Athens, DGSSL-NKUA, and used by Kassaras *et al.*, 2013). (c) Hypocentral locations like in panel (c) for 2008-2012 plus focal mechanisms for the period 1860-2015 from the catalogue of Kassaras *et al.* (2016).

A4.7.1.3 Seismic hazard

Greece is the most earthquake prone country in Europe. Several studies on the seismic hazard of Greece are available, and they constitute the basis of the Greek Earthquake Resistant Design Code (EAK 2000, 2004). According to the latter and since 1994, the expected PGA value on rock with a 10% probability of exceedance in 50 years (return period ~ 475 years) for the area of study is 0.24 g. However, a great majority of the Pyrgos and surroundings building stock has been erected with a seismic coefficient between 0.04 g - 0.12 g, depending on the soil conditions, according to the seismic codes in force until 1994 (Karantoni & Bouckovalas, 1997) (see Section A4.7.7.1).

The design PGA on rock with a 10% probability of exceedance in 50 years (EAK 2000, 2004) is significantly smaller than that estimated by the Global Seismic Hazard Assessment Program (GSHAP, Giardini *et al.*, 1999) and the SHARE Project (Woessner *et al.*, 2015) for the city of Pyrgos, all of which are summarised in Table A4.7.2. As shown in Figure A4.7.7 (left), SHARE assigns PGA values ranging between 0.35 and 0.40 g to

the whole region. The SHARE spectral acceleration for a period of 0.30 seconds, mean representative period of the majority of the local building stock (mid-rise reinforced concrete buildings), is also depicted in Figure A4.7.7 (right) with values of interest ranging between 0.50 and 0.65 g.

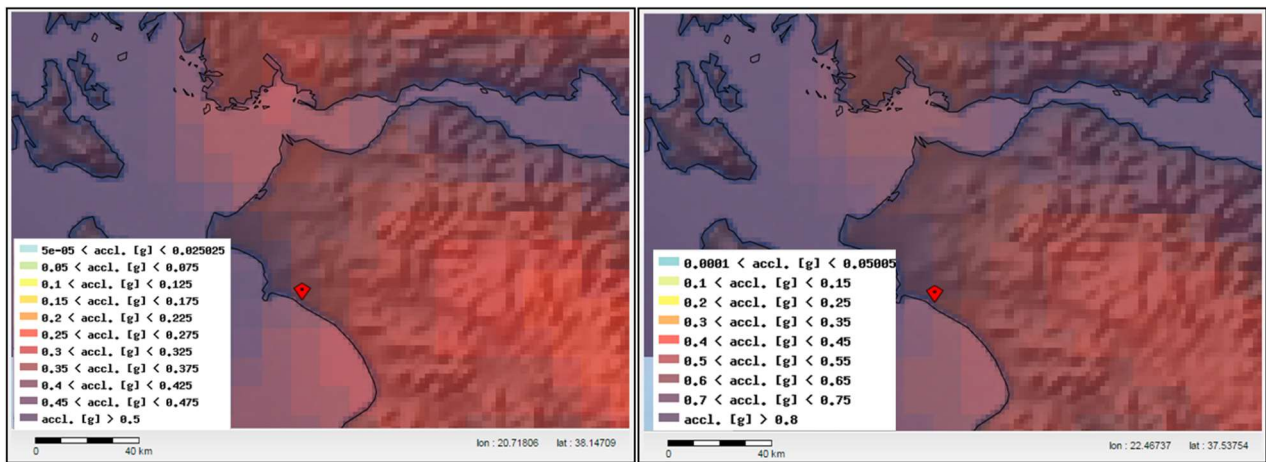


Figure A4.7.7. Mean hazard map from the SHARE project for Peloponnesus in terms of PGA (left) and spectral acceleration at T=0.30 s (right) for rock site conditions.

Table A4.7.2. Peak ground acceleration (PGA, g) values on rock with a 10% probability of exceedance in 50 years (475-year return period) according to GSHAP, SHARE and EAK 2000 (2008; to be used in agreement with Eurocode 8).

CITY	EAK 2000 (EC8)	GSHAP	SHARE
Pyrgos	0.24 g (Zone II)	0.308 g	0.389 g

Figure A4.7.8 presents a comparison between the uniform hazard spectrum resulting from SHARE and the Eurocode 8 (CEN, 2004) Type I design spectrum for a PGA value of 0.24 g, as per EAK 2000 (2004). Results from SHARE suggest relatively increased peak and spectral accelerations in the short period range compared to the code provisions, while a relatively good correspondence is observed for periods higher than 0.5 s.

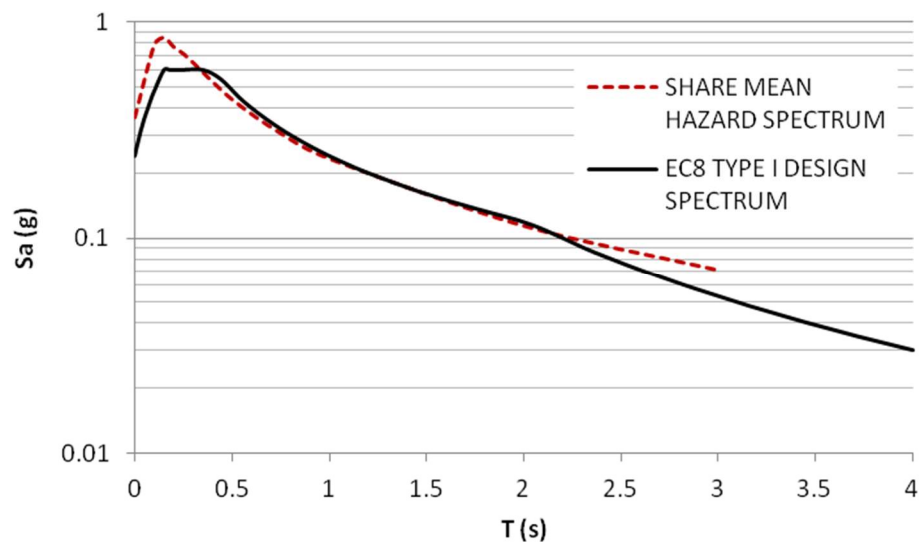


Figure A4.7.8. SHARE mean uniform hazard spectrum for the area of Pyrgos (10% probability of exceedance in 50 years) vs. Eurocode 8 Type I Design spectrum for input PGA=0.24 g.

A3.7.2 Earthquake source characteristics

A4.7.2.1 Location, depth and time

The main shock occurred on 26th March 1993, at 11.58 UTC (14.58 local time).

Several organizations and agencies report their estimations of the epicentral coordinates and hypocentral depth. The information reported for the main shock of the sequence in the websites of the Geodynamics Institute of the National Observatory of Athens (GI-NOA), the Aristotle University of Thessaloniki (THE), the International Seismological Centre (ISC), the EHB Bulletin, the United States Geological Survey (USGS) and the Global Centroid Moment Tensor Project (GCMT; Dziewonski *et al.*, 1981; Ekström *et al.*, 2012) is summarized in Table A4.7.3, while the different epicentral coordinates are mapped in Figure A4.7.9.

Table A4.7.3. Epicentral coordinates and hypocentral depths from different sources.

Agency/Publication		Latitude	Longitude	Depth (km)
GI-NOA	Geodynamics Institute, National Observatory of Athens	37.650 °N	21.440 °E	5.00
THE	Aristotle University of Thessaloniki	37.680 °N	21.310 °E	16.00
ISC/EHB	International Seismological Centre / EHB Bulletin	37.611 °N	21.522 °E	15.00 (*f)
ISC	International Seismological Centre	37.684 °N	21.437 °E	45.20
NEIC	National Earthquake Information Center, USGS	37.589 °N	21.391 °E	10.00
GCMT	Global Centroid Moment Tensor Project (**)	37.610 °N	21.180 °E	15.00

(*f) fixed parameter used for inversion

(**) centroid (not hypocentral) location

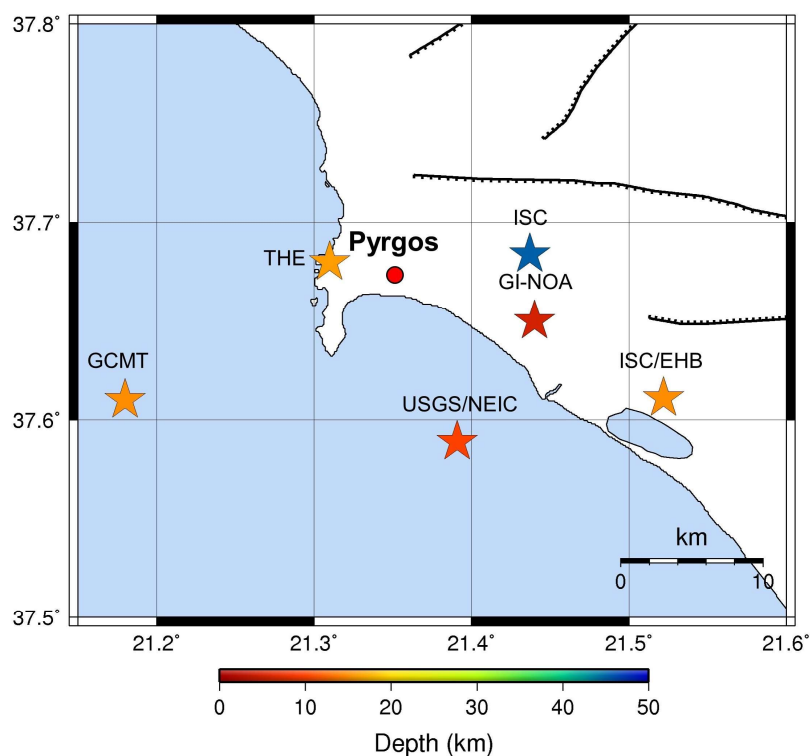


Figure A4.7.9. Epicentral location as per the agencies listed in Table A4.7.3.

A4.7.2.2 Magnitude

Estimations of magnitude reported by the same sources are presented in Table A4.7.4.


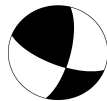
Table A4.7.4. Estimations of moment magnitude (**M**), body-wave magnitude (**mb**), surface-wave magnitude (**Ms**), and local magnitude (**M_L**).

Agency/Publication		M	mb	ML	Ms
GI-NOA	Geodynamics Institute, National Observatory of Athens	-	-	5.0	-
THE	Aristotle University of Thessaloniki	-	-	4.8	-
ISC	International Seismological Centre		5.2		5.1
NEIC	National Earthquake Information Center, USGS	5.4	5.2	4.8	5.2
GCMT	Global Centroid Moment Tensor Project	5.4	5.1	-	5.2

A4.7.2.3 Style-of-faulting

According to Papanastassiou *et al.* (1994), Stavrakakis (1996) and the GCMT Project, the main-shock displays a dextral strike-slip mechanism with a thrust component on a nodal plane striking NE-SW and dipping SE, as shown in Table A4.7.5. On the contrary, Melis *et al.* (1994) interpret the 1993 event as occurring on a sinistral strike-slip fault-plane striking NW-SE, due to its epicentral location falling to the south-east of the city of Pyrgos, where this orientation represents the dominant trend of faulting (strike, dip and rake not available for this author). These contrasting views result from the complexity of the fault systems in the area around Pyrgos, as discussed in Section A4.7.1.1, which is also reflected in the fact that foreshocks with epicentres to the southwest of Pyrgos appear to have occurred on planes with a NW-SE strike and NE dip, while those with epicentres to the north, as well as the majority of the aftershocks, were generated on planes with a NE-SW strike and dipping SE instead (Stavrakakis, 1996). The mechanisms of these events are equally variable, as can be appreciated in Figure A4.7.10, which presents fault plane solutions of the mainshock and the three largest foreshocks determined by first motion P-waves polarities (Papanastassiou *et al.*, 1994).

Table A4.7.5. Fault plane solutions available for the 1993 mainshock. Fault planes marked in grey are the preferred solutions.

Nodal Plane 1			Nodal Plane 2			Source	Beachball
Strike	Dip	Rake	Strike	Dip	Rake		
30	86	150	122	60	5	GCMT	
14	70	158	112	69	21	Papanastassiou <i>et al.</i> (1994)	

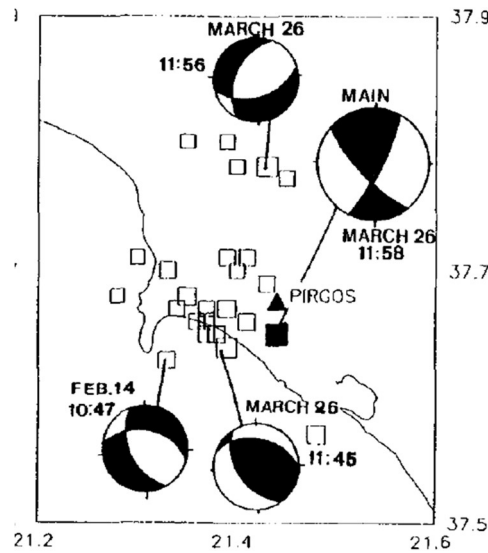


Figure A4.7.10. Focal mechanisms of the main shock and the largest foreshocks derived from P-wave first motion polarities. From Stavrakakis (1996).

A4.7.2.4 Stress drop

Since no information on the stress drop of this event was found in the literature, an estimate is given herein by employing the empirical relations of Wells & Coppersmith (1994). The scalar moment M_0 of the mainshock has been reported to be $1.61 \cdot 10^{24}$ dyn.cm, corresponding to a moment magnitude **M**5.4 (GCMT). By assuming the relation connecting moment release and rupture surface (SR) of strike-slip faults (Wells & Coppersmith, 1994):

$$M = 3.98 + 1.02 \cdot \log(SR) \quad (1)$$

and by applying Brune's (1970) formula:

$$\Delta\sigma = 7M_0/16r^3 \quad (2)$$

where $r=2.8$ km is the radius of an assumed circular source, the stress drop for this earthquake is estimated at around 3.2 MPa.

A4.7.2.5 Foreshocks and aftershocks

The main shock was preceded by significant foreshock activity that started on 10th February 1993 on a fault plane striking NW-SE and dipping SE, with a normal mechanism with a small strike-slip component (Stavrakakis & Papanastassiou, 1995; Stavrakakis, 1996). There is considerable disagreement in the literature with respect to which were the most relevant events, probably stemming from some of them being poorly determined, as reported in the ISC Bulletin. What most sources seem to agree on are on the two foreshocks that occurred on 26th March 1993 at 11.45 and 11.56 UTC, 13 and 2 minutes before the main shock, the first with reported magnitudes m_b 4.6 (USGS), M_s 5.0 (Stavrakakis, 1996) and M_L 4.8 (Koukouvelas *et al.*, 1996), and the second m_b 4.6 (USGS), M_s 5.1 (Stavrakakis, 1996) and M_L 4.0 (Koukouvelas *et al.*, 1996). According to Stavrakakis & Papanastassiou (1995) and Stavrakakis (1996), the 11.45 foreshock

occurred in the offshore area southwest of the city of Pyrgos, on a fault plane striking NW-SE and dipping SE, as the 14th February M_s 4.6 one, but with thrust faulting, while the 11.56 foreshock occurred to the north of the city of Pyrgos on a NE-SW striking fault with a normal mechanism. The map on the left of Figure A4.7.11 shows the location and main characteristics of the foreshocks according to the USGS.

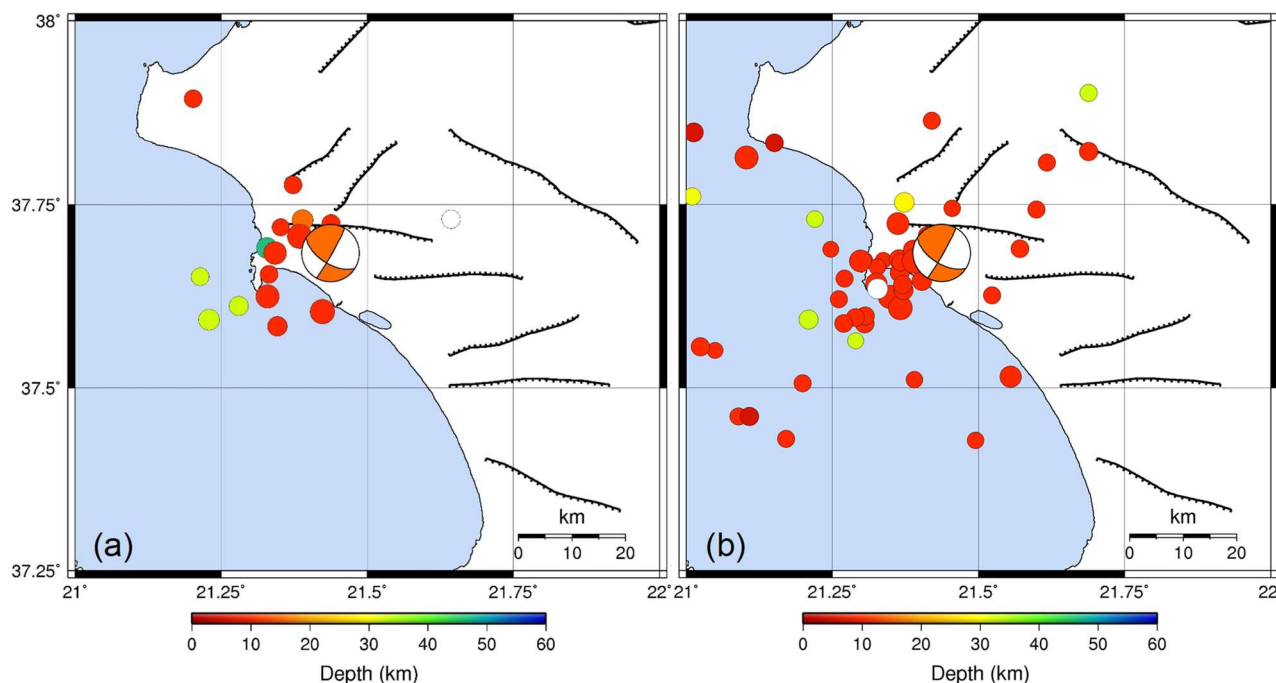


Figure A4.7.11. Map of the activated area presenting the location of the foreshocks (left) and aftershocks (right) according to data from the USGS. The beach ball represents the focal mechanism of the 1993 mainshock according to GI-NOA.

Although the main shock was of moderate magnitude, it produced a rich aftershock sequence with magnitudes up to 4.7 and focal depths smaller than 20 km that lasted for a few months (Lekkas *et al.*, 2000) (Figure A4.7.11, right). Stavrakakis (1996) reports that more than 900 aftershocks were recorded by a temporary seismological network installed by the Institute of Geodynamics of the National Observatory of Athens during the first ten days after the main shock, and that over 1,300 events with M_s between 2.5 and 4.7 occurred until 30th April 1993. Melis *et al.* (1994) highlight that events with M_L up to 4.0 occurred for over two weeks.

A4.7.2.6 Nature of the earthquake

An issue of debate among scientists is whether hydrocarbon exploration works are capable of triggering seismic activity in the already seismic area of Pyrgos. A possible causative mechanism is thought to be deep on- and off-shore drilling perturbing neighboring faults. The matter has never been published in scientific literature but has been reported in the local media (e.g., The Best, 2017). However, the lack of a direct proven correlation between the more than 10 drillings that have been carried out in the region of Ilia since the 1980s and the seismicity in the area, as well the years that passed between the last activity on a drilling site and the last two major earthquakes in Ilia (Pyrgos

1993, Vartholomio 1999), do not allow to draw conclusions in this regard for the 1993 Pyrgos earthquake, and the tectonic origin is still the prevailing hypothesis.

A4.7.3 Geology and ground conditions in the affected area

A4.7.3.1 Regional geology and topography

The area of Ilia, where Pyrgos is located, is characterized by a complex lithostratigraphy and deformation pattern. Intense geodynamical processes associated to the Post-Alpine cycle, which continued during the Holocene, produced the main graben of Ilia. Later on, E-W trending active normal faults with several meters of throw corresponding to rates of 0.4–0.6 mm/yr were formed, producing a series of smaller horsts and grabens within the main Ilia graben itself (Lekkas, 1996; Lekkas *et al.*, 2000).

The city of Pyrgos is built over an outcropping horst of marly bedrock (Group III in Figure A4.7.13) and the sediments overlying the surrounding grabens (Groups I and II in Figure A4.7.13). These are all marked as Pleistocene marine deposits on the map of Figure A4.7.3, which, by showing their existence along the coastal zone up to 15–20 km distance from the coastline and at altitudes of several hundred meters (Fountoulis, 1994; Mariolakos *et al.*, 1998), demonstrates the occurrence of significant vertical tectonic movements during the Quaternary (Papanikolaou *et al.*, 2007). In spite of this, the topography of the city is relatively flat.

In the area most affected by the 1993 Pyrgos earthquake, neotectonic structures are covered by recent Post-Alpine geological formations. According to Lekkas (1996) and Lekkas *et al.* (2000), and as shown in Figure A4.7.12, the ones that outcrop are the following (from recent to older):

- **Marsh deposits.** Alternations of clay, clayey silt and silty sand with total thickness of approximately 5 to 10 m.
- **Alluvium.** Loose soft clay with silt and sand intercalations, as well as isolated instances of gravel and pebbles. The formation is less than 12 m thick, highly inhomogeneous and anisotropic.
- **Erymanthos formation.** Complex, terrigenous conglomerate of Pleistocene age. It overlays the paleo-relief and is 2-8 m thick. Within Pyrgos, it consists of clays and sandy clays, loose horizontal sandy conglomerates and microconglomerates.
- **Vounargos formation.** Clay, silt, sand, sandstone and marl from the Plio-Pleistocene, alternating continuously both in lateral and vertical directions.

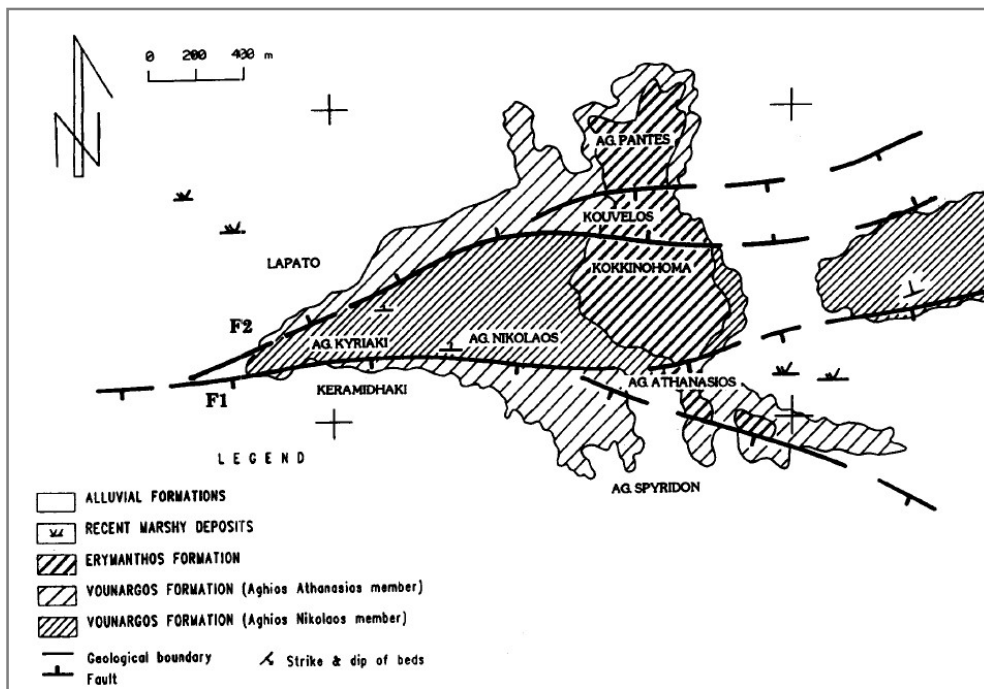


Figure A4.7.12. Geological-tectonic map of the urban complex of Pyrgos. From Lekkas (1996).

A4.7.3.2 Site conditions in the affected area

The basic soil formations found in the area may be divided into three groups (Figure A4.7.13; Bouckovalas *et al.*, 1995):

- **Group I, alluvial deposits:** This formation is found at the lowland of Pyrgos. It consists of soft clays, silty sands and silts. Its thickness varies from less than 5 m at the southern and eastern parts of the city, reaching 20 m at its northern and western parts.
- **Group II, Pleistocene deposits:** They are extensively found in the city of Pyrgos. They consist of clays or silty sands with some fine gravels, clayey sands alternating with sandy clays or sandy silts. Locally, loose conglomerates are also observed. Their thickness varies between 5 and 20 m.
- **Group III, marly bedrock:** It outcrops at the central part of the city. It consists mainly of silty or sandy marls, thinly bedded in places and including interlayers of sands or sandy silts, sandstones and lignite with a maximum thickness of about 2 m. The total thickness of this formation in the area is above 50 m.

Alluvial and Pleistocene deposits (soil groups I and II, respectively) are known to be susceptible to liquefaction when submerged below the water table (e.g., Sachpazis, 2011). According to data from boreholes reported by Bouckovalas *et al.* (1996), the water-table can be found at around 2 m depth at several locations, as indicated in Figure A4.7.13. As a consequence, susceptibility to liquefaction is quite high for most of the city of Pyrgos.

Figure A4.7.14 shows the shear wave velocities measured at the three crossholes shown in Figure A4.7.13 (Bouckovalas *et al.*, 1996). According to these plots, rough average V_{s30} estimates for each soil formation are as follows:

- Group I: $V_{s30} \approx 200$ m/s
- Group II: $V_{s30} \approx 300$ m/s
- Group III: $V_{s30} \approx 500$ m/s

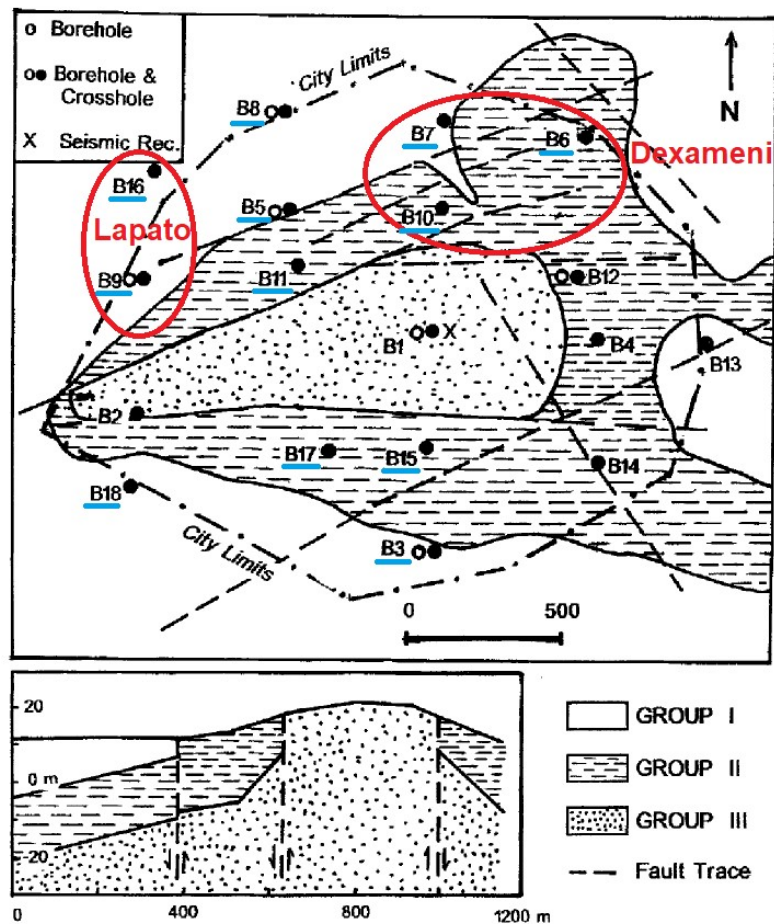


Figure A4.7.13. Geological map of the city of Pyrgos and (bottom) cross-section along boreholes B8-B17. In red, indication of zones with most damaged RC buildings (explained in A4.7.8.4). Boreholes underlined in light blue have water-table at around 2 m depth. Modified from Bouckovalas *et al.* (1996).

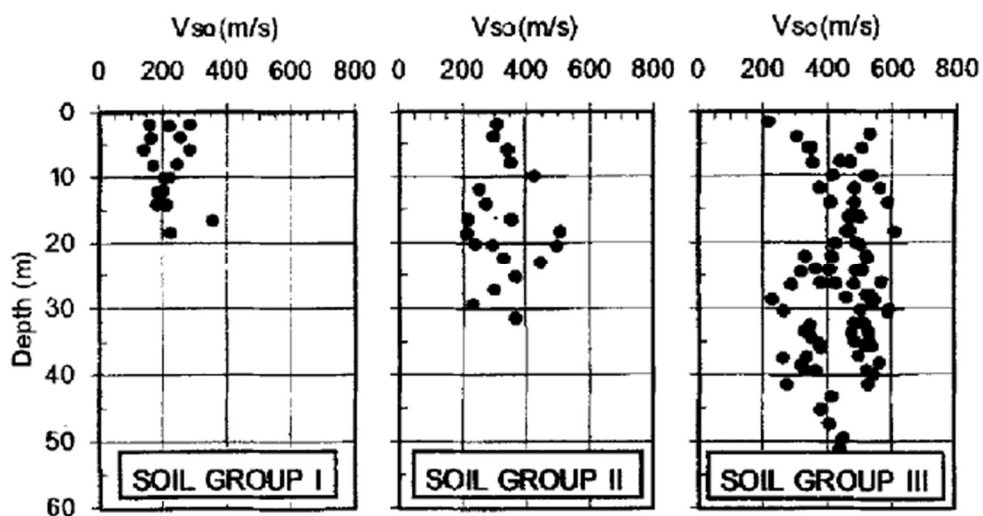


Figure A4.7.14. Summary of crosshole measurements of shear wave velocity (m/s). From Bouckovalas *et al.* (1996).

According to the microzonation study of Bouckovalas *et al.* (1996), the city of Pyrgos can be divided into three zones with distinctly different seismic response characteristics, as depicted in Figure A4.7.15:

- **Zone A**, with fundamental site periods between 0.06 and 0.19 s, peak ground velocity amplification (PGV) ratio of 1.00-1.10, and a maximum spectral acceleration amplification ratio of 1.57.
- **Zone B**, with fundamental site periods between 0.29 and 0.45 s, PGV amplification ratio of 1.13-1.34 and maximum spectral acceleration amplification ratio of 1.90.
- **Zone C**, with fundamental site periods between 0.65 and 0.95 s, PGV amplification ratio of 1.22-2.04 and maximum spectral acceleration amplification ratio of 2.80.

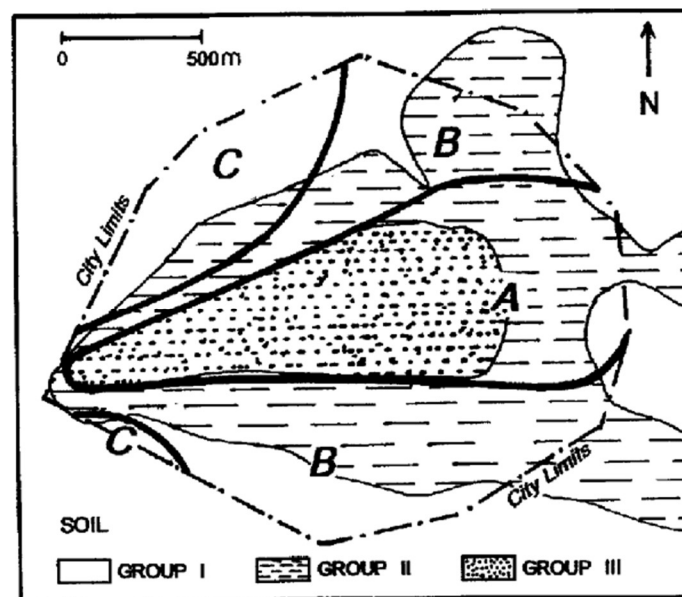


Figure A4.7.15. Seismic zones defined in Pyrgos. From Bouckovalas *et al.* (1996).

A4.7.4 Ground motions

A4.7.4.1 Intensity observations

The earthquake was felt within a wide area of western Peloponnesus and Zakynthos Island. Lekkas *et al.* (2000) assessed the macroseismic field in terms of the 1992 European Macroseismic Scale (EMS-92; Grünthal, 1993), taking into account the building typologies and their vulnerability in combination with the observed damage. Figure A4.7.16 presents the intensity distribution per district in the area where the most damage was observed. Maximum EMS-92 intensities of VIII were observed in areas of Pyrgos and Lasteika (located 2 km NW of the city) where ground fractures were identified (see Section A4.7.5.1). EMS-92 intensities of VII occurred in the villages of Lambeti, Agios Georgios, Varvasena, Vitineika, Koliri, and others located in the vicinity, 4–6 km away from Pyrgos. Considerably lower EMS-92 intensities of IV were observed in the area of the localities of Amaladia, Kardama and Douneika, only 8 to 15 km north of Pyrgos, and along a SW–NE

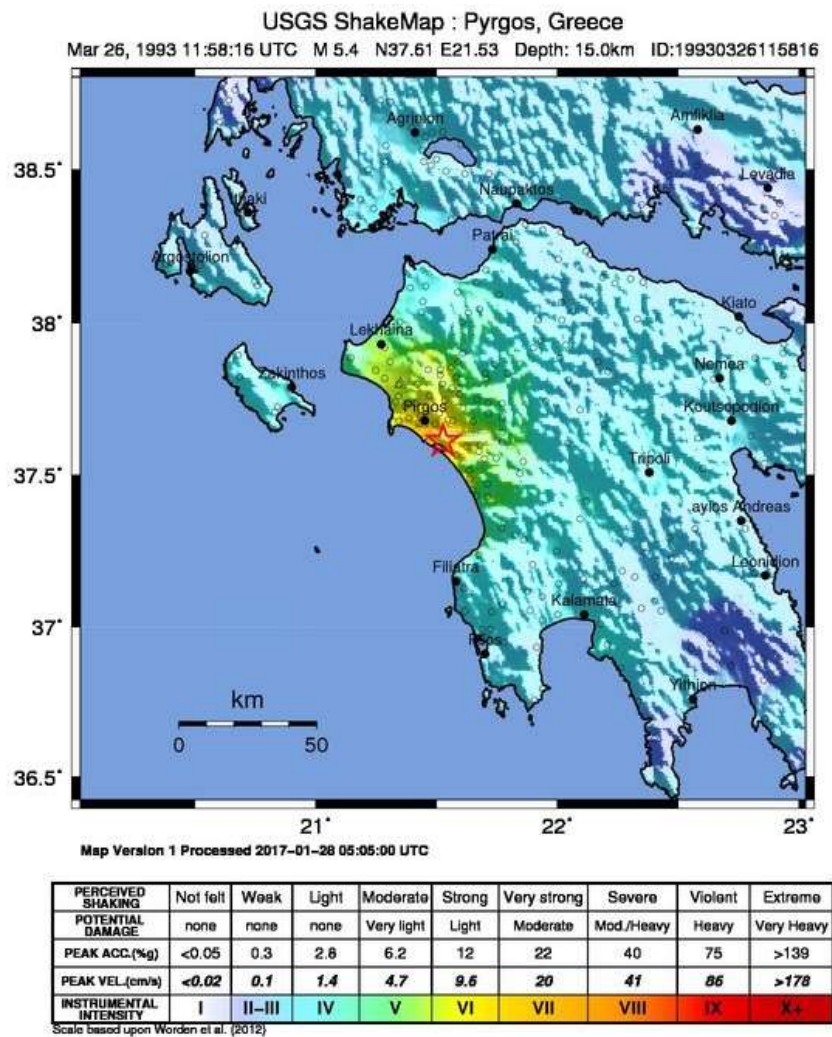


Figure A4.7.17. ShakeMap (2017) in terms of Modified Mercalli Intensity (MMI). The red star indicates the epicentre of the main shock.

A4.7.4.2 Ground motion recordings

Strong motion records have been obtained for the main shock, three foreshocks, and four aftershocks from the Engineering Strong Motion Database (ESM, Luzi *et al.*, 2016). Records have been obtained for AMAL and PYR1 stations (SMA-1 instruments with a ~N80° and N215° orientation, respectively), which are located in the cities of Amaliás (AMAL) and Pyrgos (PYR1), approximately 18 and 3 km away from the epicentre, respectively, as shown in Figure A4.7.18. Peak parameters of the Pyrgos mainshock derived using the SeismoSignal software (Seismosoft, 2016) are presented in Table A4.7.6 (in the time domain) and in Table A4.7.7 (in the frequency domain). The acceleration time histories recorded at station PYR1 during the main shock are plotted in Figure A4.7.19.

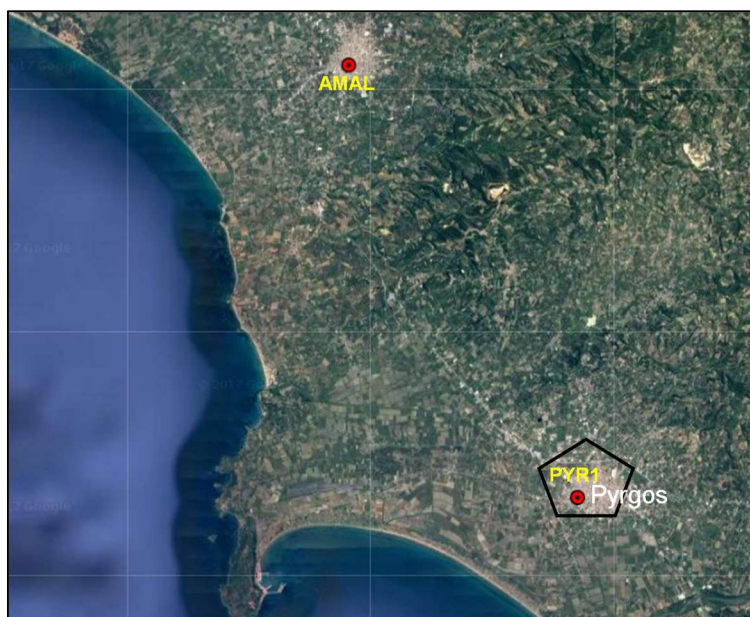


Figure A4.7.18. Accelerometric stations for which recordings of the 1993 sequence are available. The black polygon surrounds the affected area of Pyrgos.

Table A4.7.6. Summary of the peak ground motion parameters of the three components (L: longitudinal, T: transversal, V: vertical) available for the 1993 sequence (waveforms from ESM, Luzi *et al*, 2016). A: AMAL, P: PYR1. Light blue highlights the mainshock.

Day	Time	Component									Station
		L (x)			T (y)			V (z)			
		PGA cm/sec ²	PGV cm/sec	PGD cm	PGA cm/sec ²	PGV cm/sec	PGD cm	PGA cm/sec ²	PGV cm/sec	PGD cm	
14-Mar	11:44	7.2	8.0	0.5	8.0	0.5	0.1	8.8	0.5	0.10	A
26-Mar	11:45	107.0	4.3	0.4	219.0	6.3	0.6	70.0	1.4	0.15	P
26-Mar	11:45	30.0	0.9	0.05	56.0	1.8	0.15	22.0	0.4	0.03	A
26-Mar	11:56	99.0	4.0	0.3	117.0	5.0	0.45	53.0	0.9	0.11	P
26-Mar	11:56	45.0	1.4	1.8	46.0	1.8	0.11	34.0	0.7	0.04	A
26-Mar	11:58	165.0	11.4	1.2	432.0	21.2	2.3	150.0	3.0	0.40	P
26-Mar	11:58	113.0	5.1	0.9	89.0	5.0	0.89	43.0	1.3	0.16	A
26-Mar	12:26	27.0	1.2	0.09	42.0	1.9	0.16	8.4	0.25	0.02	P
26-Mar	12:26	32.1	0.7	0.08	22.1	1.0	0.15	11.9	0.5	0.07	A
26-Mar	12:49	31.0	1.0	0.1	36.0	1.6	0.16	16.0	0.3	0.03	P
26-Mar	12:49	38.2	1.5	0.07	62.8	2.5	0.16	19.8	0.5	0.08	A
27-Mar	02:51	11.7	25.4	0.7	25.4	0.7	0.08	10.7	0.4	0.09	A
30-Mar	19:08	5.5	14.5	0.6	14.5	0.6	0.08	5.9	0.2	0.06	A

Table A4.7.7. Predominant frequency content of the mainshock. Waveforms from ESM (Luzi *et al*., 2016), computations by SeismoSignal (Seismosoft, 2016).

Day	Time	Fundamental Period (sec)			Station
		L	T	V	
26-Mar	11:58	0.12	0.26	0.08	PYR1
26-Mar	11:58	0.14	0.16	0.14	AMAL

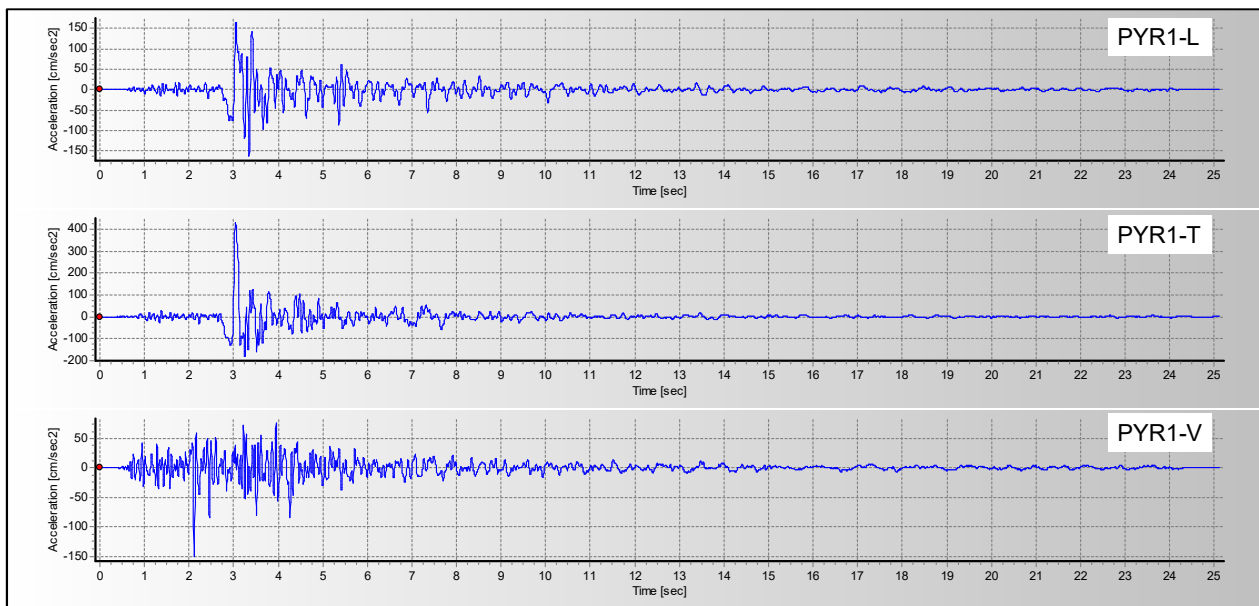


Figure A4.7.19. Acceleration time series of the 1993 mainshock recorded at PYR1, located ~3 km away from the epicentre. Waveforms obtained from the ESM (Luzi *et al.*, 2016), representation by SeismoSignal (Seismosoft, 2016).

Station PYR1 is located in the basement of a one-storey reinforced concrete building in the city centre, with shallow footings lying over 3.5 m of fill that cover the marly bedrock, and a relatively large plan (18 x 19 m, approximately). These characteristics allow to consider soil amplification effects and soil-structure effects to be relatively minimal, and the ground motions therein recorded as closely representing those of the free-field bedrock (Bouckovalas *et al.*, 1996). Considering the orientation of the instrument (N215°) allows to determine that the maximum as-recorded acceleration coincides with the NW-SE direction, parallel to the principal extensional axis of the GCMT solution, and perpendicular to the NE-SW major strike-slip structure that produced the 2008 **M**6.4 earthquake, suggested to be the causative fault zone.

Figure A4.7.20 depicts the pseudo-acceleration response spectra for the PYR1 and AMAL records available for the main shock. The highest pseudo-acceleration values occur in the ~0.15-0.30 s period range, which corresponds to the response characteristics of the majority of the local buildings. When comparing Figure A4.7.20 against Figure A4.7.8, it is noted that the transverse component recorded at PYR1 attains similar levels of spectral acceleration at the plateau to those of the SHARE uniform hazard spectrum with a 10% probability of exceedance in 50 years (slightly above 0.8 g), while the longitudinal component lies, in general, below both the SHARE and EC8 spectra, except for the peak at around 0.12 seconds (~0.7 g).

The pseudo-acceleration spectra of the foreshocks (Figure A4.7.21) and the most important aftershocks (Figure A4.7.22) are illustrated with reference to the time and the recording station. Interestingly, it is again the transverse component at station PYR1 for the 11.45 UTC foreshock that produces the largest spectral accelerations of the set, with values comparable to those of the EC8 spectrum in Figure A4.7.8 in the short period range up to around 0.25 seconds.

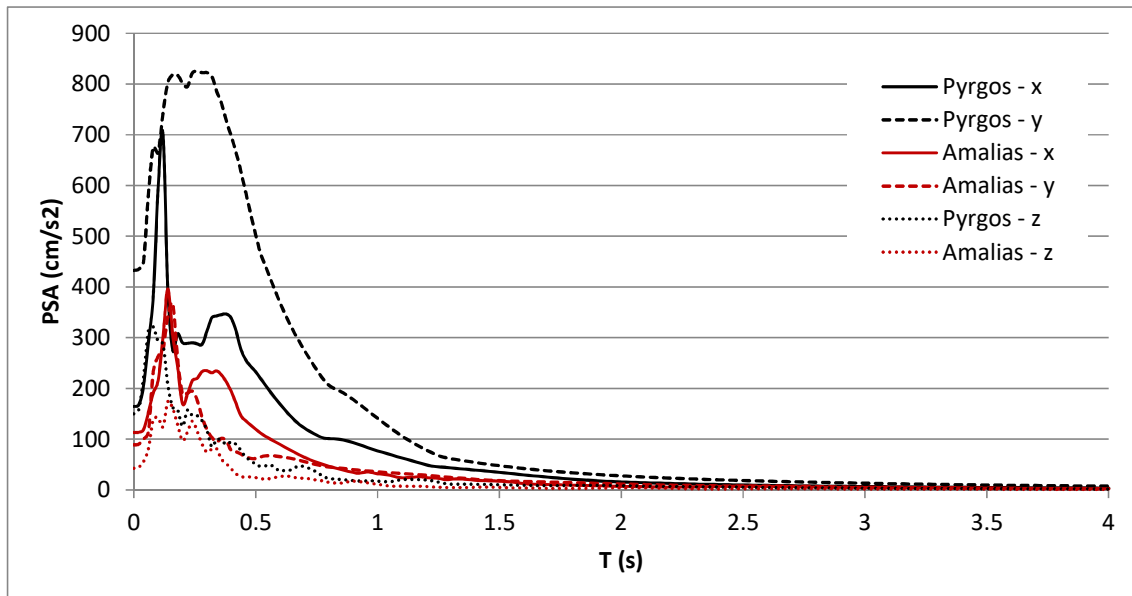


Figure A4.7.20. Pseudo-acceleration response spectra for the time-series of the main shock recorded at stations PYR1 and AMAL (x: longitudinal, y: transverse, z: vertical), calculated with SeismoSignal (Seismosoft, 2016).

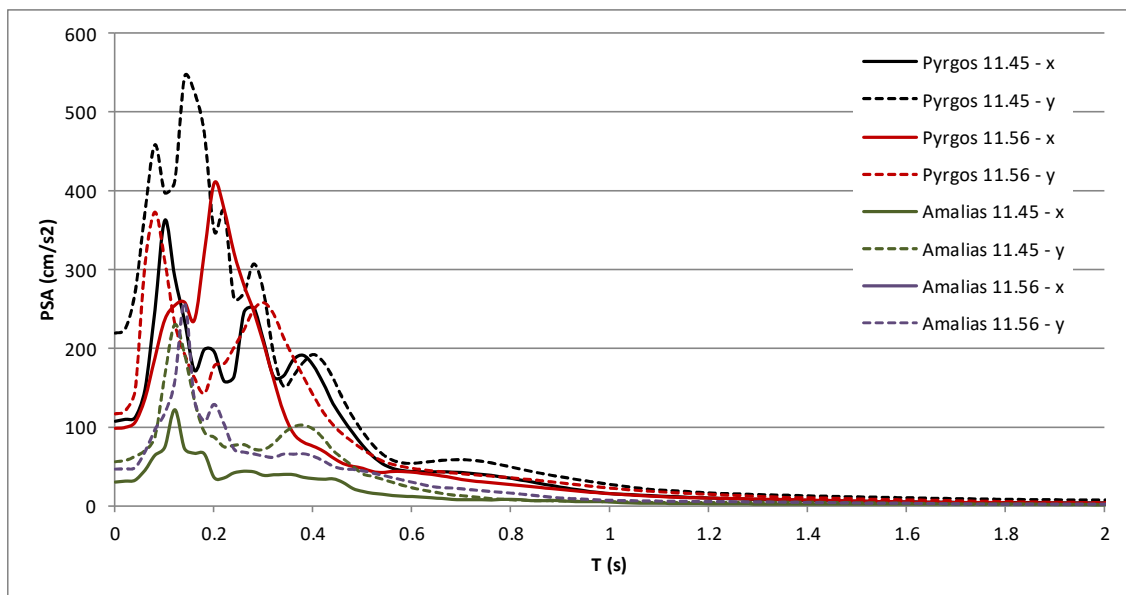


Figure A4.7.21. Pseudo-acceleration response spectra for the time-histories of the foreshocks (x: longitudinal, y: transverse), calculated with SeismoSignal (Seismosoft, 2016). Waveform data available from the ESM (Luzi *et al.*, 2016)

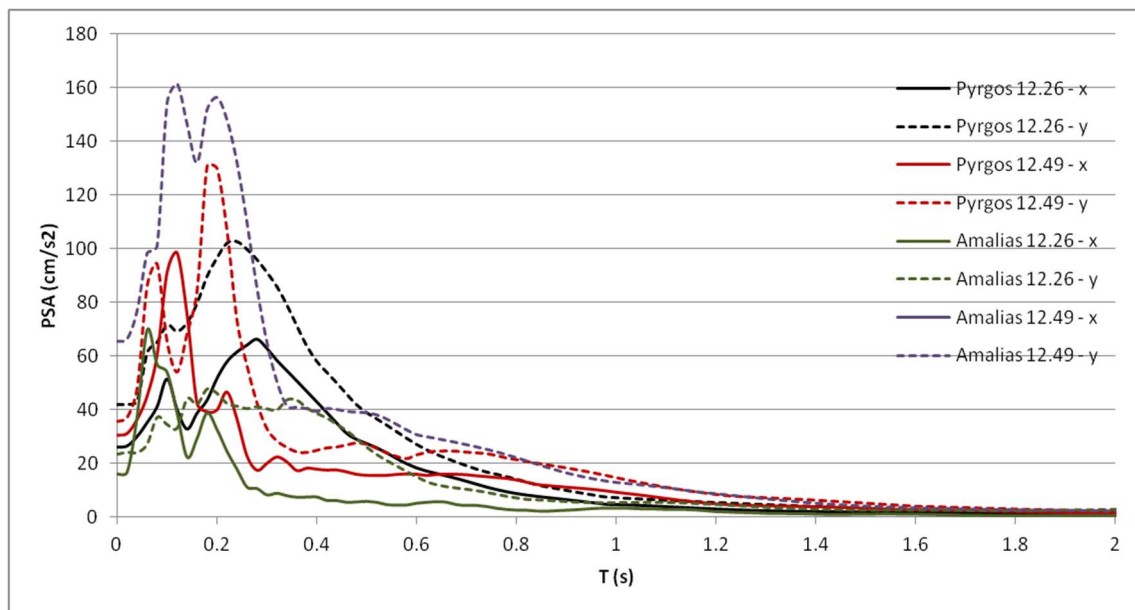


Figure A4.7.22. Pseudo-acceleration response spectra for the time-histories of the aftershocks (x: longitudinal, y: transverse), calculated with SeismoSignal (Seismosoft, 2016). Waveform data available from the ESM (Luzi *et al.*, 2016).

A4.7.4.3 Inferred shaking levels

The USGS generates ShakeMaps (Worden *et al.*, 2017) of inferred Peak Ground Acceleration (PGA), Peak Ground Velocity (PGV) and Peak Spectral Acceleration (PSA) combining information from seismic instrumentation and reported intensity, as explained in A4.7.4.1, and considering the Ground Motion Prediction Equation of Chiou & Youngs (2008). The maximum derived PGA is equal to 0.35 g (Figure A4.7.23, left) and the maximum PGV is equal to 25 cm/sec (Figure A4.7.23, right). Maximum spectral accelerations at periods 0.3s, 1.0s and 3.0s were estimated equal to 0.58 g, 0.19 g and 0.04 g, respectively. It is noted that the value for $T=0.3$ s, which was already identified as relevant for the local structural typologies (Section A4.7.4.2), lies within those stemming from SHARE (Woessner *et al.*, 2015) for a 10% probability of exceedance in 50 years for the region.

With the purpose of studying the spatial distribution of damage, Bouckovalas *et al.* (1996) and Karantoni & Bouckovalas (1997) carried out site-specific response analyses using data from 18 soil profiles from Pyrgos, the accelerograms recorded at station PYR1, and one-dimensional wave propagation techniques. Figure A4.7.24 shows their results for four oscillator periods, each of them representative of a particular building typology (0.05 s for 1-storey brick masonry, 0.10 s for 1-storey stone and 2-storey brick masonry, 0.20 s for 2-storey stone, and 0.35 s for reinforced concrete 2- to 7-storey structures). As can be observed and will be discussed in Section A4.7.8.4, site effects are expected to have been relevant in modifying the ground motions across the affected area, both in terms of amplification and deamplification.

A4.7.4.4 Duration of ground shaking

The 5-75% of Arias Intensity definition of significant duration was calculated using the SeismoSignal software (Seismosoft, 2016) for the two records of the main shock. Results are presented in Table A4.7.8.

Table A4.7.8. Significant duration (seconds) of the three components (L: longitudinal, T: transversal, V: vertical) for the two recordings of the mainshock (waveforms from ESM database, Luzi *et al.*, 2016).

Day	Time	Significant duration (sec)			Station
		L	T	V	
26-Mar-93	11:58	1.7	0.62	2.9	PYR1
26-Mar-93	11:58	4.6	4.4	7.7	AMAL

Estimations of earthquake significant duration were also obtained using the empirical relations proposed by Bommer *et al.* (2009) and Afshari & Stewart (2016), in terms of 5-75% of Arias intensity, for a range of epicentral distances and V_{s30} values corresponding to the ranges reported for the area (see Section A4.7.3.2). The upper edge of the rupture was set to 2.2 km, given the most unfavourable hypocentral solution at 5 km depth from all available sources (see Table A4.7.3) minus the source radius estimate of 2.8 km calculated by means of the models of Wells & Coppersmith (1994) in Section A4.7.2.4.

Figure A4.7.25 shows the resulting durations obtained, as well as those calculated for the horizontal components of the records at PYR1 and AMAL stations. As can be observed, values computed for PYR1 lie around the curves for the upper V_{s30} values considered. This is expected, as said station is located over the marly bedrock, for which an upper bound V_{s30} value of 600 m/s is expected (soil group III in Figure A4.7.14). Assuming the latter, the calculated values lie within [-0.53,1.29] and [-1.46,0.20] standard deviations of the models of Bommer *et al.* (2009) and Afshari & Stewart (2016), respectively.

While detailed information regarding the soil conditions at the location of station AMAL has not been found, a V_{s30} value of around 350 m/s can be estimated from data from the United States Geological Survey (USGS) V_{s30} Map Server, calculated using topographic slope as a proxy (Wald & Allen, 2007). Assuming this value, the calculated durations lie within [0.90,0.98] and [0.43,0.50] standard deviations of the models of Bommer *et al.* (2009) and Afshari & Stewart (2016), respectively.

It is noted that estimations from both models are quite in good agreement for V_{s30} values of 300 and 600 m/s, particularly at distances above 10 km. If the depth to the top of rupture is increased (that is, if a deeper hypocentre is adopted for the calculation), the model of Bommer *et al.* (2009) then predicts durations around 0.5 to 1 seconds shorter in said distance range.

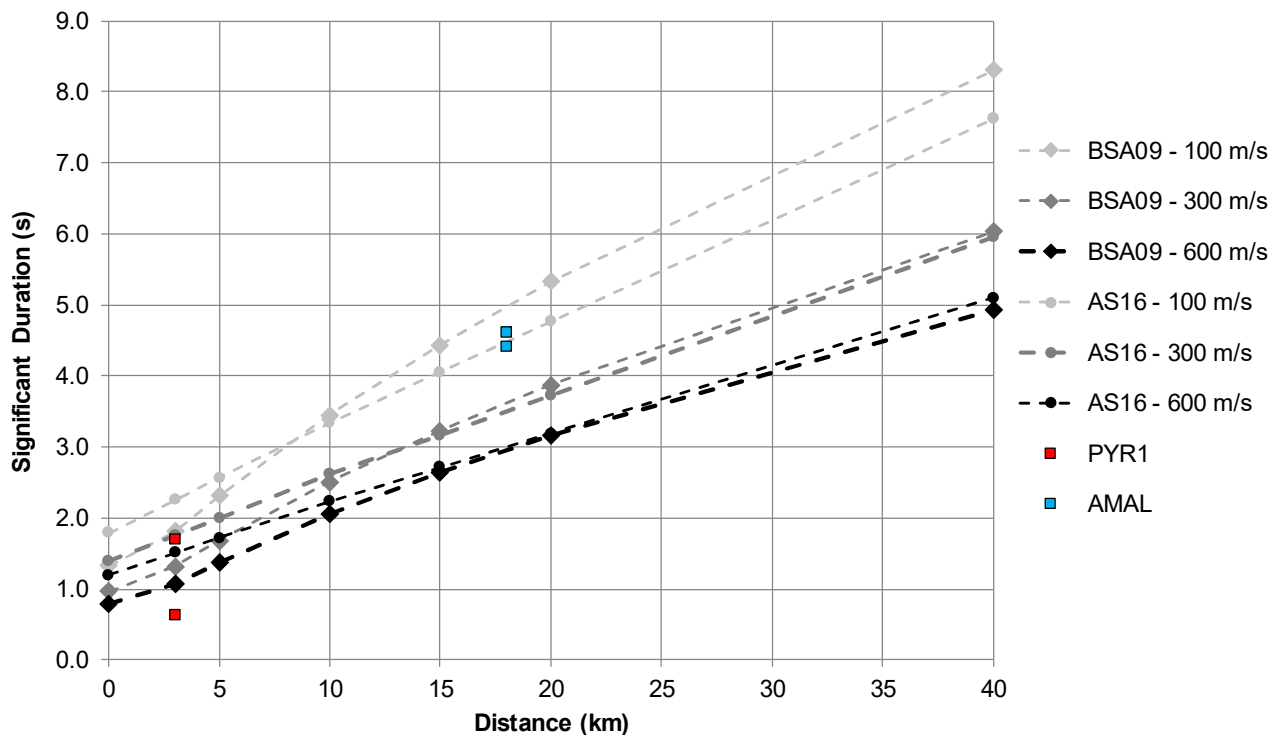


Figure A4.7.25. Estimation of the significant duration of the main shock, using prediction equations by Bommer *et al.* (2009, BSA) and Afshari & Stewart (2016, AS), and significant duration calculated for the two horizontal components of the records from stations PYR1 and AMAL.

A4.7.5 Collateral earthquake hazards

As a consequence of the many collateral effects observed, the environmental effects-based macroseismic intensity is estimated to have been of the order of VII in the Environmental Seismic Intensity (ESI 2007) scale (Papanikolaou *et al.*, 2009). Figure A4.7.26 summarizes the secondary effects caused by the 1993 earthquake.

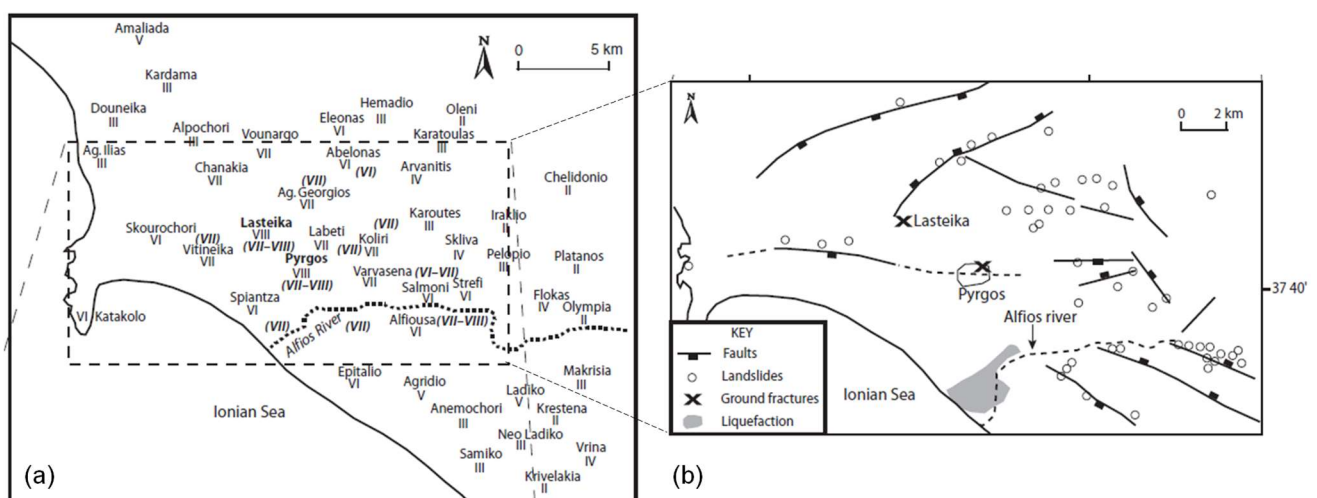


Figure A4.7.26. (a) ESI 2007 distribution for the 1993 Pyrgos earthquake (according to Papanikolaou *et al.*, 2009, bold italics in parentheses). (b) Map of the observed environmental effects: ground fractures and liquefaction from Lekkas (1994) and Lekkas *et al.* (2000), landslide locations from Koukouvelas *et al.* (1996). Modified from Papanikolaou *et al.* (2009).

A4.7.5.1 Surface rupture

While the Pyrgos earthquake and the accompanying aftershock sequence caused a number of secondary effects, such as ground failures of some tens of metres arranged partly en-echelon at the northeastern part of Pyrgos (Figure A4.7.26, b) and Lasteika village, cutting both paved roads and cultivated land (Lekkas *et al.*, 2000), no surface rupture directly associated to the earthquake source has been documented. This is expected, considering the moderate magnitude of the mainshock and its hypocentral depth. According to Lekkas *et al.* (2000), ground fractures could be related to reactivated faults at two sites, and to liquefaction, landslides, lateral mass instability or differential ground settlement in all other cases.

A4.7.5.2 Landslides

This event triggered 47 small-scale landslides and 7 instances of soil lateral spreading within an onshore area of 145 km² (Figure A4.7.26, b). These failures were soil falls at 23 sites, soil block slides at 18 sites and soil slides at 6 sites (Koukouvelas *et al.*, 1996). Their vast majority occurred along fault scarps and steep slopes in the Alfios southern river bank, with faces oriented perpendicular to active faults, which indicates structural rather than climatic driving factors (Koukouvelas *et al.*, 1996). Several land failures were observed in the region of Vounargo, north of Pyrgos (Lekkas *et al.*, 2010), an area which has been recently monitored as an active landslide (Nikolakopoulos *et al.*, 2017).

A4.7.5.3 Liquefaction

Liquefaction phenomena at seven localities within an area of 145 km² were reported (Figure A4.7.26, b) (Koukouvelas *et al.*, 1996), as well as changes in the water table of the area (Lekkas, 1994; Lekkas, 2000; Lekkas *et al.*, 2000). Sand boils up to 50 cm in diameter were observed (Lekkas, 1994). Subsidence was also observed in alluvial unconsolidated deposits within Pyrgos (Lekkas, 1994) possibly affecting the extent of damage. Liquefaction together with subsidence was observed at deltaic silty sand deposits in the coastal area (5 km²), at Alfios river banks, and south-west of the city in an uninhabited area (Bouckovalas, 1994). In view of the high water-table observed in most of the city and the presence of alluvial and Pleistocene deposits at these locations, the occurrence of liquefaction and subsidence was not a surprise. The latter was one of the most important factors affecting the extent of damage.

A4.7.5.4 Settlements

As reported in Section A4.7.5.3.

A4.7.6 Exposed population

A4.7.6.1 Socio-economic setting

According to the 2016 Human Development Report (United Nations, 2016), the Human Development Index (HDI) for Greece was 0.874 in the early 1990s, and 0.866 in 2015, while its Inequality-adjusted HDI (IHDI) in 2015 was 0.758. According to the world's ranking, Greece is currently located in the 29th place with a drop from the 25th place held in 1993, while the Netherlands has moved up from 9th to 6th place. Table A4.7.9 compares the HDI and IHDI for both countries for Human Development Data between 1990 and 2016. The column "Adj. HDI" provides the HDI values given in the 2016 report for previous years, adjusted for data consistency in time. It is noted that between 1990 and 1994 significant changes in the HDI values are observed globally as a consequence of modifications introduced in 1993 to the way in which the index is calculated.

Table A4.7.9. Human Development Index and Inequality-adjusted Human Development Index for Greece and the Netherlands. HDR: Human Development Report (United Nations, 1994; 2016)

Report	Data	Greece				Netherlands			
		HDI	IHDI	Rank	Adj. HDI	HDI	IHDI	Rank	Adj. HDI
HDR 1990	1980s	0.949	-	-	0.760	0.984	-	-	0.830
HDR 1994	1993	0.874	-	25	0.769	0.923	-	9	0.840
HDR 2016	2015	0.866	0.758	29	-	0.924	0.861	6	-

Table A4.7.10 presents a comparison between Greece and the Netherlands in terms of gross domestic product (GDP), GDP per capita and unemployment rate for 1993 and 2015. The economy of the Netherlands underwent an important growth especially after 1985 and again after the year 2000, when the gap with Greece's economy increased even more. The latter presented a more moderate growth until 2008 when it steadily started to drop (Figure A4.7.27). In 1993, when the earthquake occurred, the country's economy was rising.

Table A4.7.10. Gross domestic product (GDP), GDP per capita and unemployment rate for Greece and the Netherlands, according to the World Economic Outlook Database (2016)

Indicator	Units	Greece		Netherlands	
		1993	2015	1993	2015
Gross domestic product, current prices	Billions USD	109.01	195.32	348.10	750.67
Gross domestic product per capita, current prices	USD	10,450.67	17,988.51	22,766.61	44,322.83
Unemployment rate	%	9.70	25.03	5.53	6.89

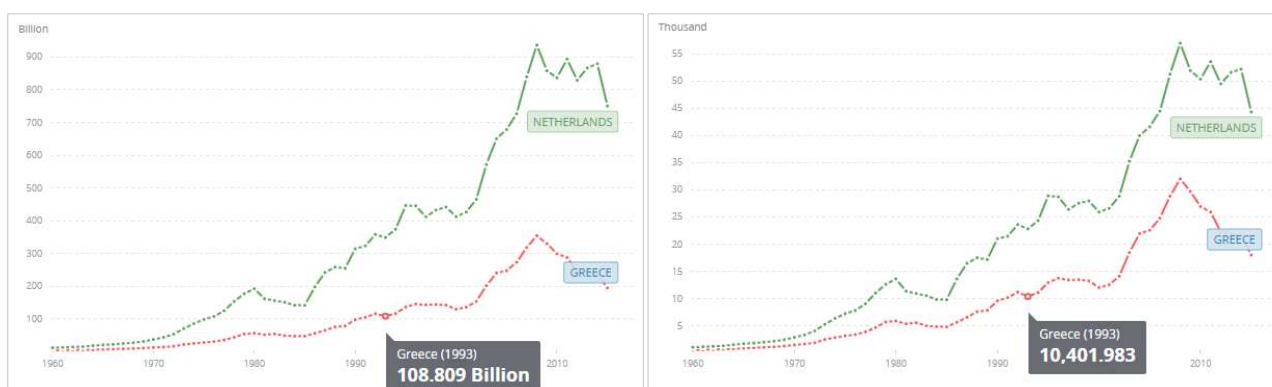


Figure A4.7.27. (a) GDP and (b) GDP per capita fluctuation for Belgium and Netherlands for the last 65 years according to World Bank national accounts data and the Organization for Economic Cooperation and Development (OECD) National Accounts data files (The World Bank, 2017).

According to the Statistical Authority of Greece (EL.STAT., 2011), the net average income per person in 2000 (earliest available data) was about 34% lower for the Prefecture of Ilia than for the whole of the country. The economy of the Prefecture of Ilia, of which Pyrgos is the capital, has always been based, especially in past times, on the agricultural and farming sector, and on the industrial elaboration and exportation of agricultural products. Katakolo (see Figure A4.7.28) is the port of the prefecture, which thanks to the vicinity with Ancient Olympia, it receives a relevant number of ships and cruise ferries. The latter, in combination with the long coastline, contributes positively to the tourism in the area.

A4.7.6.2 Population density and distribution

Details for the population of the most affected districts, according to the EMS-92 intensity mapping of Figure A4.7.16, are given in Table A4.7.11 according to the 1991 census (EL.STAT. Census, 1991). As can be observed, in the early 1990s the city of Pyrgos had around 29,000 inhabitants, with an average density of 600 inhabitants per km². Pyrgos is the most densely populated municipality of the Prefecture of Ilia (Figure A4.7.28) and was the only urban district affected by the 1993 earthquake. Among the 52 prefectures of the country, Ilia is the 42nd in population and 43rd in population density. In Figure A4.7.28 the spatial extent of the population per affected location is illustrated.

Table A4.7.11. Population and population density in 1991 for the most affected districts (EMS-92 intensity V – VIII) (Data from EL.STAT., 1991)

District	Population	Population density (people/km ²)
City of Pyrgos	28,660	630.13
Agios Georgios	788	125.64
Abelonas	807	64.07
Varvasena	1,243	116.78
Vitineika	284	63.85
Eleonas	468	49.40
Koliri	1,069	77.63
Lasteika	493	137.94

Paleo-Varvasena	445	90.36
Salmoni	725	61.83
Skourochori	703	85.00
Strefi	875	108.02

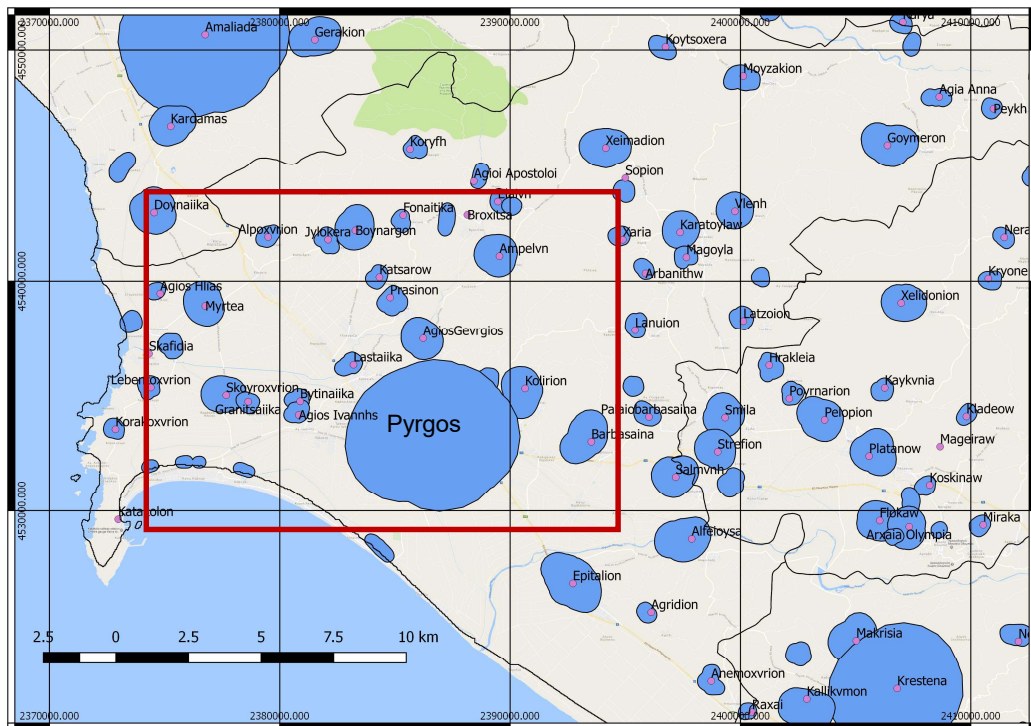


Figure A4.7.28. Illustration of spatial extent of population in the prefecture of Ilia. Most affected area is enclosed by the red square. Data from GEODATA (2015).

According to the USGS EXPO-CAT database (Allen *et al.*, 2009; USGS-PAGER), over 185,000 people were exposed to an MMI intensity equal to or larger than V (intensity at which the earthquake is strongly felt and vulnerable structures may start to exhibit low damage). Around 75% of this population corresponded to an urban environment. Disaggregating the above figure, a total of 122,000 is estimated to have been exposed to MMI values larger than V but smaller than VI, and around 65,000 to MMI larger than VI, mainly concentrated in the city of Pyrgos. An estimated 1.5 million people largely felt the earthquake (MMI>IV), although observed no damage.

A4.7.6.3 Time of day of earthquake

The earthquake hit the region of Pyrgos on a Friday at 14.58 local time. Two strong foreshocks preceded at 14.45 ($M_s 5.0$) and 14.56 ($M_s 5.1$), and awakened the population. Given the extent of damage and the low number of casualties and injuries, the time of occurrence of the event could be considered to have had a positive impact over its consequences. Considering that most of the damage was observed in old masonry, mainly residential buildings, it may be assumed that the majority of the population was out of their homes, leading to a more positive aftermath.

A4.7.7 Characteristics of exposed building stock

A4.7.7.1 Seismic design codes

The first official Earthquake Resistant Design (ERD) code was established in Greece with the Royal Decree of 1959 after the destructive earthquakes in the Ionian Islands in 1954. Until then, few codes with limited force existed (e.g., “About Seismic Code of Loutraki-Korinthos”, 1928; Regulation on structural design and seismic code, 1939) and foreign building codes, mainly German codes such as DIN1045, were of application for the analysis and dimensioning with the method of allowable stresses only for vertical loading. In a premature seismic code of 1939, a Greek seismic hazard map was proposed with five hazard zones, following the approach of the American 1937 one, proposing constant seismic coefficients based on the seismicity and the ground conditions (Figure A4.7.29, left). Pyrgos’s coefficient was ranging between 0.04 and 0.12 g (from rock to soft soil) with a maximum coefficient in the whole of the Greek territory of 0.12 g. Reinforced concrete buildings prior to 1959 were strictly frame structures in a dense grid of beams and columns, slabs of small thickness (8-12cm), shallow foundations and infill walls carefully built, providing an important overstrength to the flexible frame. With respect to load-bearing masonry structures of the same period, these rarely followed any structural or seismic design regulation, but often empirical construction techniques of high quality were of application, including practices to stand lateral loading.

The ERD code of 1959 introduced, as a state’s law, the pseudostatic analysis and the uniform distribution of lateral seismic loads. The latter were defined as a fraction of the building’s weight, based on the seismic coefficient (ε) of the area. The country was, thus, divided into three hazard zones to which a coefficient was attributed, according to similar criteria as of 1939. Pyrgos was then located in a moderate to high seismic zone with design coefficient $\varepsilon=0.06$ g to 0.12 g (from rock to soft soil), the maximum coefficient in the whole of the Greek territory being 0.16 g. Shear walls started being included in the buildings’ design and, provided that these exceeded a ratio of the surface area of the plan, lateral loading was allowed to be discarded. The 1959 ERD code was in force at least until 1984 when Additional Articles were proposed, after the destructive earthquakes of Thessaloniki (1978) and Athens (1981). The decades of the 1960s and 1970s saw the greatest urbanization of Greece’s modern history and, thus, an important amount of building stock may be claimed to have followed the premature seismic provisions.

The Additional Articles of 1984 opened the way to the modernization of the seismic design conception. The use of 3D modelling for the design of multi-storey buildings was imposed and detailed specifications on construction detailing were introduced so as to provide bearing elements with ductility capacity. The seismic coefficient according to the seismic hazard map of 1959 remained, but the triangular lateral load distribution was introduced along with the control of the horizontal deformations. Other important additions included the capacity check of reinforced concrete joints and the characterization of importance as a function of the building use.

The New Greek Earthquake Resistant Design Code (NEAK) was put in force in 1994. This, in combination with the New Greek Reinforced Concrete Design Code (NEKOS) in force since 1991, completely changed the design philosophy of buildings in the country. One of the main revolutionary modifications was the introduction of the probabilistic seismic acceleration design spectrum, which replaced the use of the constant seismic coefficient. This was accompanied by a new seismic hazard map which divided the country in four zones (Figure A4.7.29, top right). Significantly increased coefficients were proposed, based on the latest seismological findings, which by then were expressed in terms of peak ground acceleration (PGA). Pyrgos was located again in a moderate to high seismic zone with design PGA=0.24g (maximum value for Greece is 0.36g). Other important new aspects were the establishment of the dynamic spectral method as the main design methodology, the introduction of the behavior factor q to represent the effects of ductility, and the incorporation of the collapse prevention approach, through the capacity design of strategic elements.

With the modification of 2004, the Greek Earthquake Resistant Design Code (EAK 2000, 2004) was finalized, recognizing three seismic zones (Figure A4.7.29, bottom right) in the new seismic hazard map of the country. This latest map has served as the basis for the seismic zonation map included in the Greek National Annex of Eurocode 8 (CEN, 2004) whose application is in parallel use with the National Codes (EAK 2000, 2004 and EKOS 2000, 2001) since 2011. Moreover, the Greek retrofiting Code (KANEPE, 2012), compatible with the relevant articles of the Eurocodes, is in force since 2011.

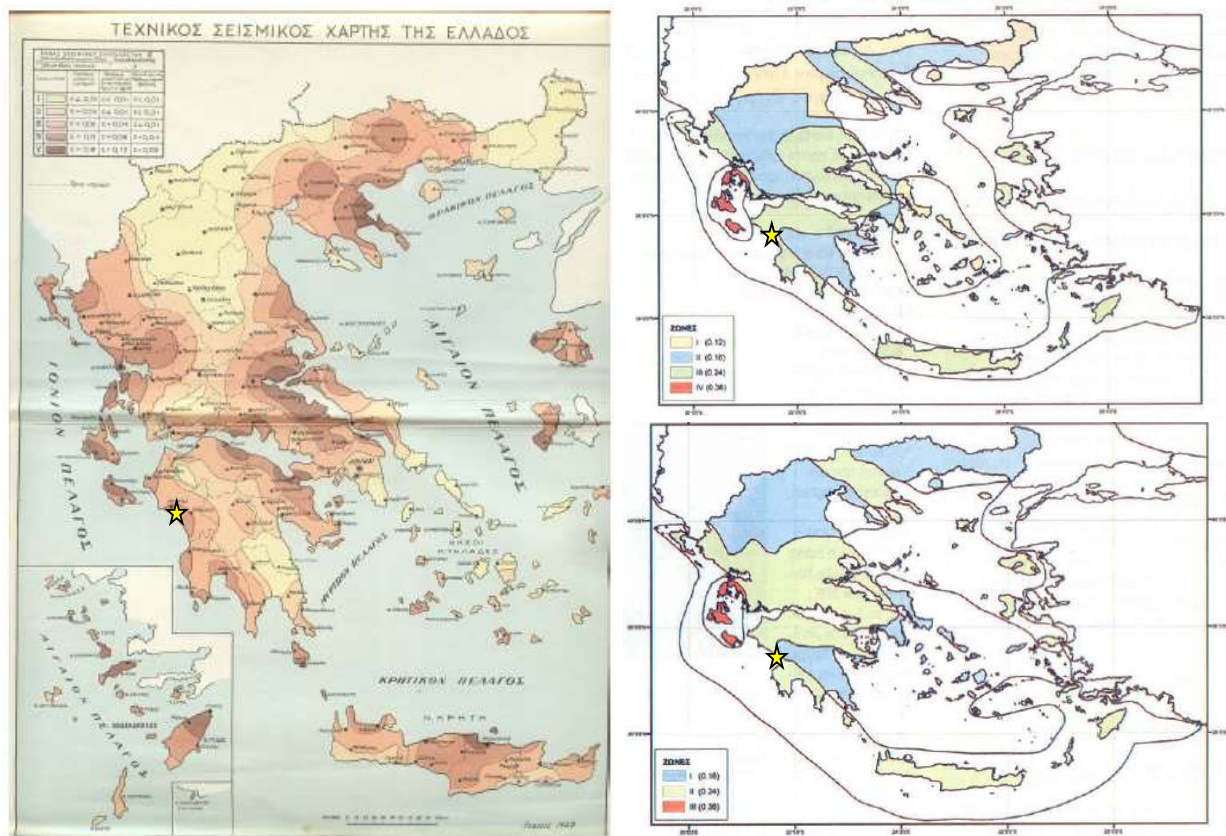


Figure A4.7.29. Seismic hazard map of the 1930s with five zones (Rousopoulou, 1949; left); NEAK 1995, EAK 2000 with four zones (top right); EAK 2000 (2004) with three zones (bottom right). With yellow star the location of Pyrgos, laying always on a seismic prone area, yet not the highest one.

The chronological review of the seismic design codes in Greece presented above was based on Anastasiadis (2008), personal knowledge and academic notes of one of the authors.

A4.7.7.2 Building typologies

Data regarding typologies at the country level were collected from the PAGER Inventory Database v2.0 (Jaiswal & Wald, 2008) for Greece and are summarized in Figure A4.7.30. It is observed that the vast majority of residential and non-residential buildings of the urban environment in Greece are non-ductile reinforced concrete (RC) frames and only in the rural environment an important ratio (~40%) of stone or brick masonry appears.

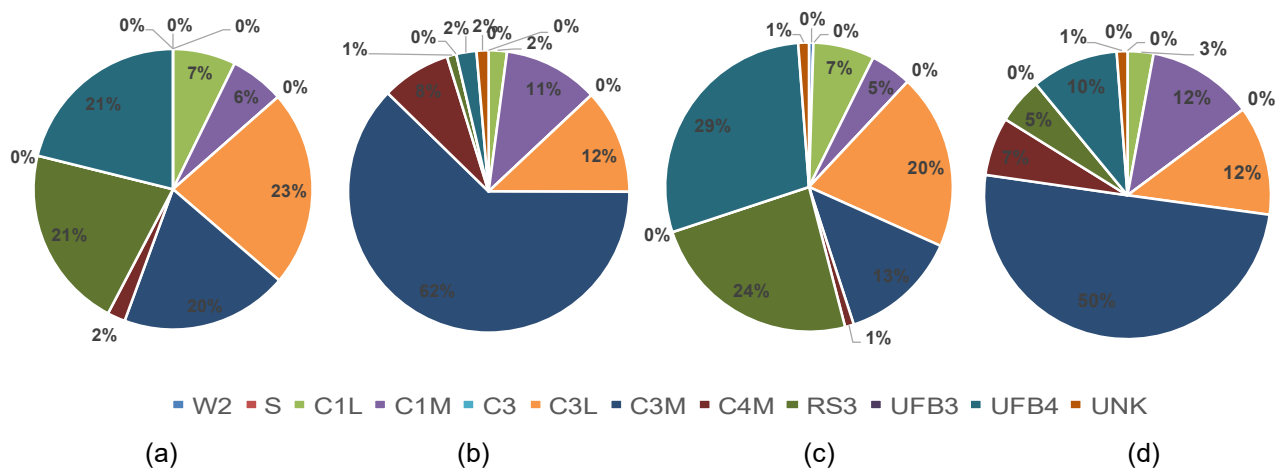


Figure A4.7.30. Proportion of building main typologies in Greece for (a) rural residential, (b) urban residential, (c) rural non-residential, (d) urban non-residential typologies: C1L: Ductile reinforced concrete moment frame with or without infill low-rise, C1M: Ductile reinforced concrete moment frame with or without infill mid-rise, C3: Non-ductile reinforced concrete frame with masonry infill walls, C3L: Nonductile reinforced concrete frame with masonry infill walls low-rise, C3M: Nonductile reinforced concrete frame with masonry infill walls mid-rise, C4M: Nonductile reinforced concrete frame without masonry infill walls mid-rise, RS3: Local field stones with lime mortar, UFB3: Unreinforced brick masonry in lime mortar, UFB4: Unreinforced fired brick masonry, cement mortar; UNK: Not specified. Data from Jaiswal & Wald (2008)

The distribution of building typologies within the municipality of Pyrgos is very close to that of residential buildings in rural environments at the country level shown in Figure A4.7.30. During the Greek national project EPANTYK (2009), data regarding the building stock of the main municipalities was collected and digitised from the 2001 Buildings Census. Table A4.7.12 and Figure A4.7.31 summarise this information for the area of interest. According to these, the prevailing material for the building stock of Pyrgos is reinforced concrete (5,693, 58% of the total). The number of buildings with bearing masonry of concrete or clay bricks is 3,389 (35% of the total), mainly distributed along the periphery of the city. A small number of stone buildings were registered (402, 4% of total) at the most central city blocks, mainly erected before 1946 (Figure A4.7.32; Pomonis *et al.*, 2014). According to Pomonis *et al.* (2014), 46.5% were old load bearing masonry structures and 52.2% were RC frames with unreinforced clay brick infill panels. Moreover, they mention that 66% of the building stock is ground-floor buildings, which can be also confirmed from Figure A4.7.33.

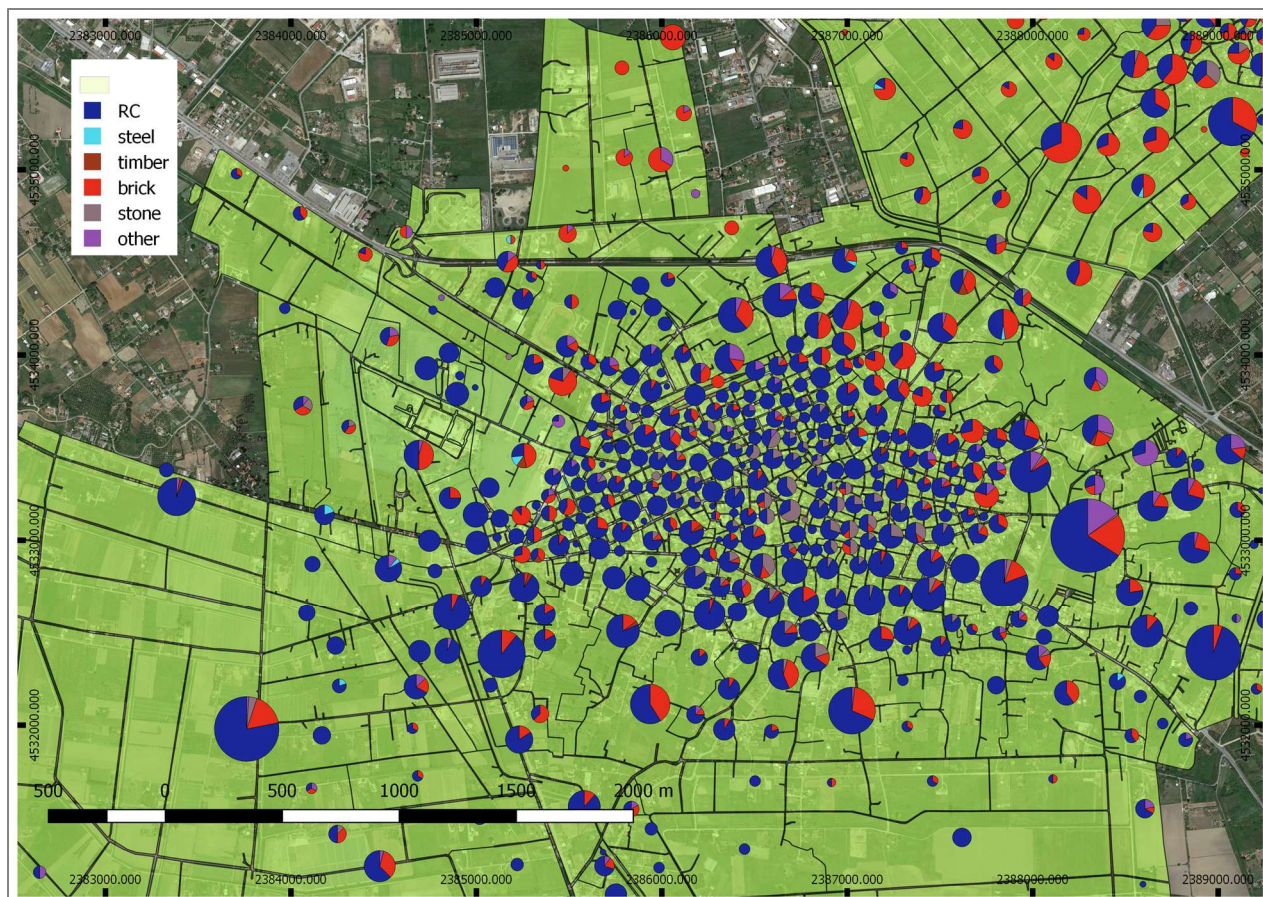


Figure A4.7.31. Distribution of construction material per building within each building block of Pyrgos (Data from EPANTYK, 2009).

In Figure A4.7.32, which depicts the construction period of the main building typologies, a peak in the number of brick masonry structures is observed in the early 1980s, while the significant boost of RC construction coincides with the urbanization era after the 1970s. According to Karantoni & Bouckovalas (1997), the largest proportion of the Greek building stock erected after the 1960s is reinforced concrete frames with brick infills, a fact that has been proved, to the authors' knowledge, to have created confusion in the bearing material characterization during the census and thus, a large amount of the buildings counted as brick actually corresponds to reinforced concrete structures. These buildings have followed the 1959 National Seismic code with seismic design coefficients in the range 0.04–0.12 g, updated to 0.24 g only after the introduction of the New Seismic Code in 1995. Figure A4.7.33 shows a disaggregation of the building stock by material and number of storeys, according to the data from EPANTYK (2009).

Table A4.7.12. Number of buildings per material for the municipality of Pyrgos. Data from EPANTYK (2009).

Material	Number of buildings	Ratio (%) of buildings
Reinforced Concrete	5,693	58
Steel	39	0
Timber	14	0
Brick	3,389	35
Stone	402	4
Other	216	2
Total	9,753	100

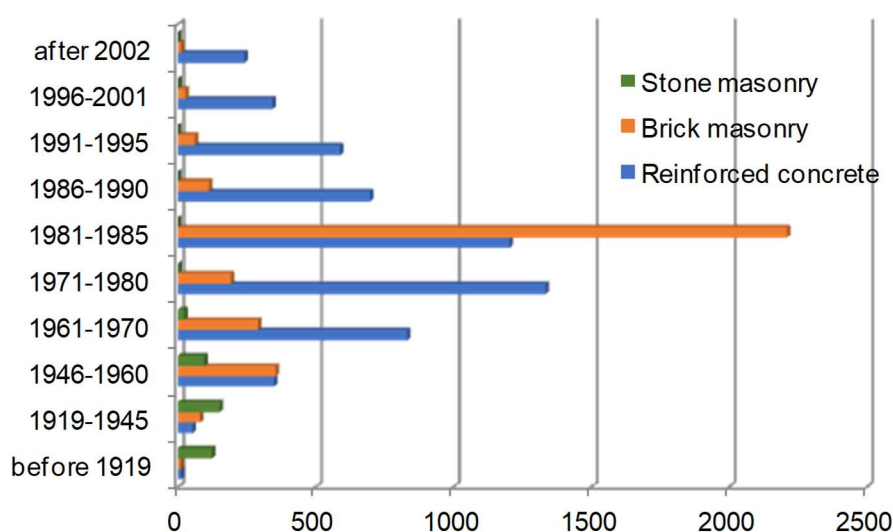


Figure A4.7.32. Distribution of the building stock in the municipality of Pyrgos according to their construction period for reinforced concrete and brick or stone masonry buildings (Data from EPANTYK, 2009).

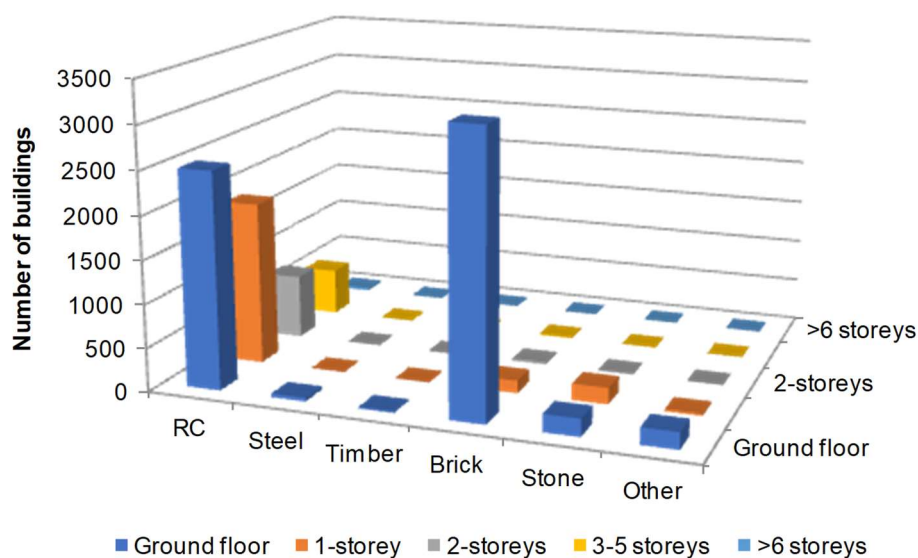


Figure A4.7.33. Distribution of the building stock in the municipality of Pyrgos according to their construction material and height (Data from EPANTYK, 2009).

Karantoni & Bouckovalas (1997) carried out a post-earthquake survey of a sample of 1,023 masonry buildings in Pyrgos, their disaggregation per material and height being summarized in Table A4.7.13. The authors report that “almost all plain masonry buildings of the city of Pyrgos” were analysed in their study but it is clear, as Pomonis *et al.* (2014) also confirm, that the 1,023 surveyed buildings were located in the city centre, which contains approximately a quarter of the masonry buildings of the municipality, as can be observed in Figure A4.7.31. Acknowledging that the date of construction of masonry buildings is an important factor, as it determines not only the material but also the structural form of the building and its seismic performance, Karantoni & Bouckovalas (1997) distinguished a series of relevant construction periods, as summarized in Table A4.7.14.

Table A4.7.13. Number of masonry buildings with different construction materials and number of storeys examined by Karantoni & Bouckovalas (1997).

Material	1-storey	2-storey	3-storey	Total
Adobe	131	22	0	153
Stone masonry	222	447	15	684
Brick masonry	87	21	1	109
Mixed masonry	23	51	3	77
Total	463	541	19	1023

Table A4.7.14. Characteristics of masonry buildings in downtown Pyrgos per construction time, according to Karantoni & Bouckovalas (1997).

Period	Characteristics
1800-1850	Adobe material (hand-made, air-dried blocks of clay (30-40%) and earth reinforced with hay or straw (60-70%); 1-2 storeys of ~3m height; timber roofs and floors
1850-1900	Stone masonry walls of 0.55-1.00m thickness; 1-3 storeys; storey height>5m; the spandrel extends up to the sills of the upper storey which are integral with the adjacent piers; timber roofs and floors
1900-1940	Stone masonry or solid brick (few); 1-3 storeys; relatively smaller height of storeys; different way of sill construction. The 0.15thick sills are unbonded to the 0.55-0.80m thick adjacent piers, so they are considered as infill. The height of the spandrel is formed by the head of the windows or doors up to the next storey floor, it is not that strong and is easily distinguished from the walls.
1940-today	Stone or brick (solid or hollow); 1-2 storeys; RC floor and timber roof; high variability
	Stone or brick (solid or hollow); 1-2 storeys; RC floor and RC roof and tie-beams; high variability

Finally, based on the evolution of the seismic design codes in Greece (see Section A4.7.7.1) and engineering judgment studying the seismic performance of existing structures, the assumptions of Table A4.7.15 have been made in the context of the national study ASPIDA (2015) for the attribution of a vulnerability class according to the EMS-98 scale (Grünthal, 1998) and a building typology according to the macroseismic vulnerability method (Giovinazzi & Lagomarsino, 2004) to the reinforced concrete building stock, based on their year of construction.

Table A4.7.15. Building typologies and EMS-98 vulnerability classes assigned to RC buildings in Greece as a function of their year of construction according to ASPIDA (2015).

Construction Time Period	Seismic Design	Building Typology (Giovinazzi & Lagomarsino, 2004)	Most Probable EMS-98 Vulnerability class
Before 1919	Without	Frame in RC without seismic design	C
1919 – 1945			
1946 – 1960			
1961 – 1970	Moderate	Frame in RC with moderate seismic design	D
1971 – 1980			
1981 – 1985			
1986 – 1990			
1991 – 1995	High	Frame in RC with moderate seismic design	E
1996 – 2001			
After 2002			

A4.7.7.3 Prior damage and retrofit

No indications about prior damage or retrofit are given. However, from the personal experience of one of the authors, it appears that the lack of maintenance and general deterioration of abandoned buildings or houses used as secondary homes may have played a relevant role in the capacity of the buildings to withstand the ground shaking.

A4.7.8 Damage observations

A4.7.8.1 Damage states

For their analysis of the damage caused by the 1993 Pyrgos earthquake, Karantoni & Bouckovalas (1997) rated the degree of damage of the masonry buildings in Pyrgos city centre built before 1950, according to the 5-degree scale defined in Table A4.7.16. A damage index was first assigned to each floor in the building, and an average index was calculated for each building as a whole. Table A4.7.17 establishes the equivalence between the final average degree of damage and a broader verbal description of the level of damage sustained, as per the same authors. The correspondence with the scale proposed by the Earthquake Planning and Protection Organization of Greece (EPPO) for the post-seismic habitability survey according to Anagnostopoulos & Moretti (2008) is also shown in the table.

Pomonis *et al.* (2014) re-classified the damage reported by Karantoni & Bouckovalas (1997) for the masonry building according to the EMS-98 damage scale (Grünthal, 1998). For details regarding the latter, please refer to Section 3.8.1 of Chapter 3 and Appendix II.

Table A4.7.16. Rating of damage to old masonry structures (Karantoni & Bouckovalas, 1997)

Degree of damage (D.D.)	Description of damage
0	No damage
1	A few fissures of 1mm average width
2	A number of cracks with 5mm average width or isolated cracks of 10mm average width, without disintegration of masonry walls
3	Intense cracking, masonry walls beginning to disintegrate
4	Disintegration of masonry walls, total or partial collapse

Table A4.7.17. Rating of damage for all masonry structures per Karantoni & Bouckovalas (1997). Correspondence with habitability scale per Anagnostopoulos & Moretti (2008).

Degree of Damage (D.D.)	Rate of damage	Habitability color tagging (EPPO)
0-0.5	Almost undamaged	Green – Safe for use
1-1.5	Light damage	Yellow – Not dangerous / Repairable
2	Moderate damage	
2.5-3	Heavy damage	Red – Dangerous / Not repairable
3.5-4	Very heavy damage	

A4.7.8.2 Damage statistics and description

The main shock of Pyrgos earthquake has been reported to have caused extensive damage within a radius of 15-20km. The damage was particularly severe to masonry buildings, which represent almost 50% of the building stock at the city centre. At least 580 masonry buildings in the city centre sustained some kind of damage. A large unspecified number of these buildings had to be demolished following the earthquake. According to Lekkas (2000), at least 50% of the buildings in Pyrgos were damaged. The International Disaster Database (EM-DAT, 2018) reports a total of 1,516 affected people.

Karantoni & Bouckovalas (1997) examined a total of 1,023 masonry buildings (almost a quarter of the masonry buildings in the Pyrgos municipality inventory) after the earthquake, with the characteristics (material, number of storeys) enumerated in Table A4.7.13 and Table A4.7.14. The number of damaged buildings per degree of damage and their percentage with respect to the total masonry building stock examined is illustrated in Figure A4.7.34. The disaggregation of damaged buildings is presented per masonry material and assessed EMS-98 damage grade in Table A4.7.18 (the summation of the individual percentages is slightly different from the total shown, as a consequence of the results of Pomonis *et al.* (2014) only including 1,004 1- to 2-storey buildings, and neglecting 19 3-storey masonry buildings).

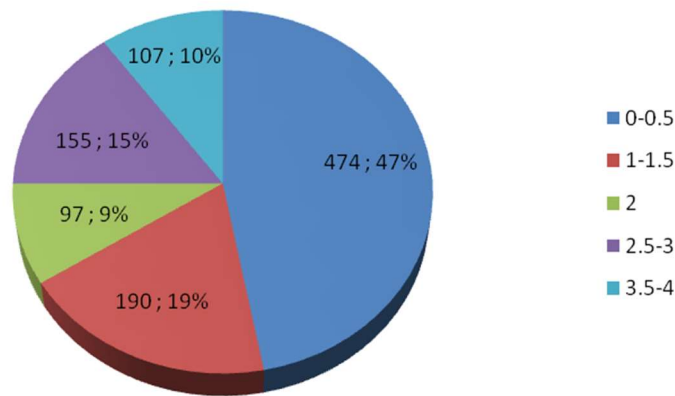


Figure A4.7.34. Number and percentage of damaged masonry buildings according to data from Karantoni & Bouckovalas (1997). Damage grades as in Table A4.7.17.

Table A4.7.18. Number and ratio of damaged buildings per masonry typology (Karantoni & Bouckovalas, 1997) and disaggregation per EMS-98 damage grades (Pomonis *et al.*, 2014).

Construction material	Total number	Damaged		EMS-98 Damage Grades (%)				
		Number	%	D1	D2	D3	D4	D5
Adobe	153	128	83%	0.7%	10.7%	9.3%	23.3%	40.0%
Stone masonry	684	351	51%	3.9%	22.0%	13.5%	8.6%	3.0%
Brick masonry	109	38	35%	0%	9.1%	10.9%	9.1%	6.4%
Mixed masonry	77	63	82%	5.6%	16.7%	20.8%	30.6%	6.9%
Total	1023	580	57%	3.1%	18.5%	13.1%	12.5%	9.2%

In order to assess the effects of construction materials and the number of storeys, Figure A4.7.35 summarizes the total number of recorded damaged buildings, their ratio and average degree of damage (D.D.) according to the data collected and analysed by Karantoni & Bouckovalas (1997). Both Figure A4.7.35 and Table A4.7.18 show that adobe masonry buildings exhibit higher damage than the other masonry types, due to their poor material properties. Karantoni & Bouckovalas (1997) attribute the higher mean D.D. of 1-storey adobe and brick buildings with respect to their 2-storey counterparts to the high percentage of particularly poor-quality adobe structures within the sample of 1-storey buildings. Taking this into consideration, they believe that the degree of damage index increases with increasing number of storeys, and that this trend may be related to the increase of the fundamental period of the structures with the number of storeys and the consequent resonance with the large spectral acceleration values observed in the period range between 0.20 and 0.30 s (Figure A4.7.20). In general, the authors also observed larger degree of damage indices in the upper than in the lower storeys of 2- and 3-storey masonry buildings, the main cause of which appears to have been out-of-plane failure. They did observe as well in-plane failures in the form of wide diagonal cracks in 19 out of the 541 2-storey buildings they studied. The damage pattern and the mean degree of damage index per masonry type and period of construction (as per Table A4.7.14), are summarized in Table A4.7.19.

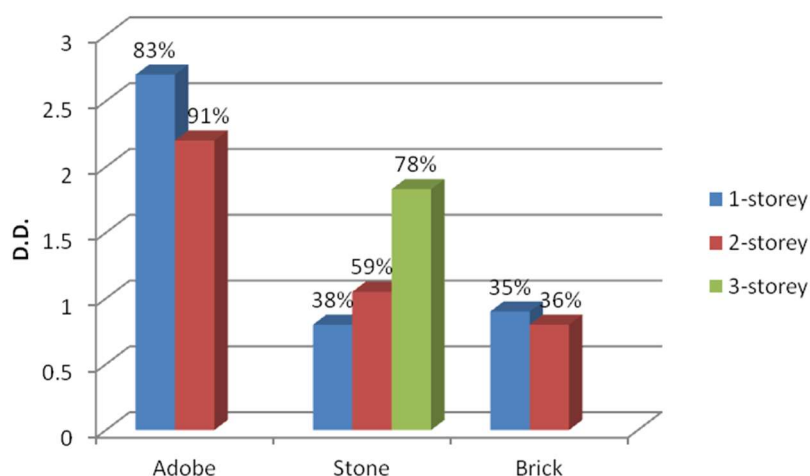


Figure A4.7.35. Relation between masonry material, mean degree of damage (D.D.) and percentage of damaged buildings. Data from Karantoni & Bouckovalas (1997).

Table A4.7.19. Damage patterns per masonry typology after Karantoni & Bouckovalas (1997)

Period	Material	Mean D.D. of all	Mean D.D. of damaged ones	Damage observed
1800-1850	Adobe; 1-2 storeys (Figure A4.7.36)	2.6 (heavy)	3.0 (very heavy)	<ul style="list-style-type: none"> - Vertical cracking of spandrel (more severe in 2nd storey) - Turnover of external whyth at the top of the walls due to out-of-plane action (especially at the 2nd storey) - Local buckling of the lower parts of the walls
1850-1900	Stone masonry walls; 1-3 storeys; (Figure A4.7.37)	1.0 (light)	1.9 (moderate)	<ul style="list-style-type: none"> - Vertical cracking of the spandrel of the upper floor and of the corners due to separation of orthogonal walls - Diagonal cracking of the piers (usually starts from the 1st storey and extends even to the roof level strong lintels)
1900-1940	Stone masonry or solid brick (few); 1-3 storeys;			<ul style="list-style-type: none"> - Vertical cracking of spandrels in the upper floors - Separation of sills from adjacent walls due to the lack of bonding - Diagonal cracking of the piers (without extension to upper walls weak lintels)
1940-1997	Brick (solid or hollow); 1-2 storeys; RC floor and timber roof	0.85 (very light)	2.5 (moderate to heavy)	<ul style="list-style-type: none"> - Concentration of damage in one of two storeys - If damage to upper storey: RC slab distributes inertial forces to the walls, damage due to out-of-plane action; damage is light for low tensile stresses - If first storey is damaged: wide diagonal cracking, with decomposition of masonry; damage due to in-plane action to buildings with low % of walls or piers parallel to the direction of seismic action
	Brick (solid or hollow); 1-2 storeys; RC floor and RC roof and tie-beams			<ul style="list-style-type: none"> - Very good seismic performance - Light horizontal cracking separating tie beams and masonry



Figure A4.7.36. Adobe masonry buildings with damage from partial or total collapse (source: EPPO; left); “Motsaiko”, erected in the 19th century, was the only building that collapsed almost completely (source: Vitinaika, 2008; right).



Figure A4.7.37. Severe damage to stone buildings: (left) diagonal cracking at piers (source: EPPO); (right) vertical cracking of spandrels of upper floor (source: Tempo24, 2016).

Damage to RC buildings was limited, despite the contrasting difference between the seismic design coefficients of 0.06-0.12 g for which most of the building stock of Pyrgos was designed (1959 ERD Code) and the 0.45 g maximum PGA recorded during the main shock (Karantoni & Bouckovalas, 1997). 22 buildings with 2 to 7 storeys developed cracks in the RC frame itself (Figure A4.7.38). Most of these were located within the districts of Dexameni and Lapato. The buildings located at Dexameni developed very light diagonal cracking at the top of the first storey columns and shear walls, while those in Lapato presented much more serious instances of damage, such as the disintegration of the concrete of the first storey columns (Karantoni & Bouckovalas, 1997). Apart from these localised cases, most of the RC buildings in the city presented damage to the infill masonry. The latter is usually constructed in Pyrgos and Greece with hollow clay bricks and cement-lime mortar. Karantoni & Bouckovalas (1997) describe the typical damage pattern to infill panels being diagonal cracking due to in-plane seismic action, with cracks developed within the mortar joints as well as the bricks themselves. In addition, the different displacement capacity of the RC frame and the more fragile infill panels led to small-width repairable cracks at the joints of the RC elements with the infill walls.



Figure A4.7.38. Example of severely damaged RC building with severe cracking and concrete spalling at the node and column and diagonal cracking of the infill panels (source: EPPO).

Pomonis *et al.* (2014) mention as well that two wings of the state's hospital were severely damaged. Although no further details are given about its structural typology, according to the authors' experience, it was probably erected at the end of the 20th century. Iliia Oikonomia (2017) newspaper makes also reference to damage to churches, neoclassical buildings of the 19th-20th century, schools and to the hospital which has to be partially evacuated.

The sources described above are not completely clear regarding whether the statistics presented for the masonry buildings cover all of the buildings of the city of Pyrgos or only a part of them and, if the latter, whether the proportions of different damage levels could be extrapolated to the totality of the building stock. Due to this lack of definitive numbers of affected buildings, ranges were estimated based on the descriptions and numbers presented above, resulting in an estimate of 378-1,800 damaged and 107-222 destroyed buildings. The lower bounds result from considering the 356 masonry buildings classified as EMS-98 damage grades 1 through 3 by Pomonis *et al.* (2014) plus 22 RC buildings reported as having suffered from structural damage (Karantoni & Bouckovalas, 1997; Pomonis *et al.*, 2014) as the number of damaged, and the 107 cases of "very heavy" damage reported by Karantoni & Bouckovalas (1997). The upper bound of destroyed buildings stems from the 222 masonry buildings classified as EMS-98 damage grades 4 and 5 by Pomonis *et al.* (2014). It is noted that the buildings analysed by Karantoni & Bouckovalas (1997) and Pomonis *et al.* (2014) are the same ones, and what changes is their distribution across different damage categories. Moreover, it is noted as well that these buildings represent a quarter of those existing in Pyrgos, which might imply that many others were damaged but not included in the statistics. The upper bound of 1,800 damaged buildings is an unspecific number that results from the comment of Pomonis *et al.* (2014) regarding most of the RC buildings having exhibited non-structural damage to their infill masonry walls and on there being around 1,800 RC buildings constructed after

1984 in the city of Pyrgos. It thus cannot be overemphasised that these numbers are estimates and cannot be deemed conclusive.

Due to the small impact of Pyrgos earthquake when compared to global disasters, no extensive reports are available within global loss databases.

A4.7.8.3 Observed weaknesses

No reports of systematic weaknesses were found in the literature. However, from the damage statistics it may be inferred that the main reasons of severe damage to masonry buildings were the material quality, the construction technique and the seismic design philosophy, or lack of it (Bouckovalas *et al.*, 1996).

A4.7.8.4 Damage distribution

The spatial distribution of damage was not uniform across the city of Pyrgos, despite its extension being only an area of about 4 km² (Bouckovalas *et al.*, 1996; Lekkas, 1996). Studies aiming at identifying the factors that may have influenced this distribution have focused on two different aspects: the neotectonic macrostructure of the area (Lekkas *et al.*, 2000) and the geological/geotechnical conditions (Bouckovalas *et al.*, 1996; Karantoni & Bouckovalas, 1997).

According to Lekkas *et al.* (2000), spatial distribution patterns could be observed both on a microscale (within a single inhabited area) as well as on a macroscale, within the broader region. Their findings are summarized in Figure A4.7.39, which shows how the areas with EMS-92 intensities equal to or larger than V are limited to the north by the Katakolo-Vounargo fault zone and, to the east, by the Hemadio-Pelopio-Olympia graben. Unlike the gradual attenuation of intensities that takes place to the south, Lekkas *et al.* (2000) observe an abrupt drop in intensity values along these major neotectonic features. The highest intensities occurred within the block defined by the latter, in the suburbs of Pyrgos and in Lasteika village (2 km NW of Pyrgos), where ground fractures were identified, in spite of the seismic behavior of the foundation grounds having been relatively satisfactory (Zone A in the city centre, Figure A4.7.15). Lekkas *et al.* (2000) refer as well to the significant damage sustained even by some structures designed with the modern ERD Codes of the era in these areas.

Some more details regarding damage to modern structures are given by Karantoni & Bouckovalas (1997), who noted that the RC damaged buildings are concentrated in two parts of the city, Dexameni and Lapato (marked in Figure A4.7.13), the latter associated to much more serious instances of damage than the former. Based on seismic ground response computations performed for 18 soil profiles (Figure A4.7.24) using the ground motion record from station PYR1 as the input at bedrock, Karantoni & Bouckovalas (1997) estimated that spectral accelerations for $T=0.35$ s (fundamental period for medium-height RC buildings) at these locations may have ranged between 1.07 and 1.28 g, values that are among the highest ones of all sites considered, and that fundamental periods of vibration of the soil columns ranged between 0.33 and 0.71 seconds. The authors, thus,

suggest that the proximity of the natural periods of the buildings, the soil sediments and the frequency content of the earthquake may have caused these buildings to experience particularly high demands. They point out, however, that the fact that only a small proportion of this kind of building suffered from damage indicates that other factors may have had an influence as well.

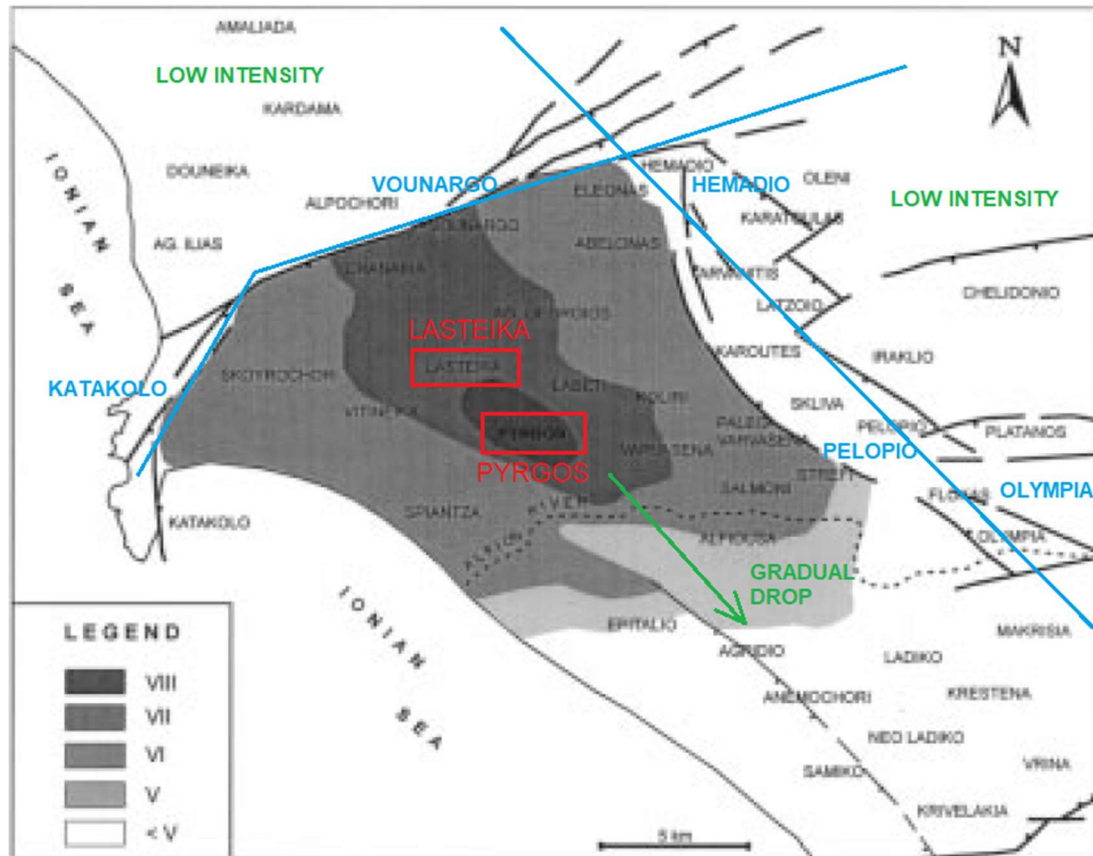


Figure A4.7.39. Intensity distribution in EMS-1992 scale in the major area of Pyrgos and relation with neotectonic macrostructures. Modified from Lekkas *et al.* (2000).

The backbone of the study of Karantoni & Bouckovalas (1997) is the same as that of Bouckovalas *et al.* (1996), who investigated the correlation between damage to masonry buildings of Pyrgos and the spectral accelerations computed for the same 18 soil profiles for three periods of interest that represented the corresponding building stock (Figure A4.7.24). In a first plot (Figure A4.7.40, top), the average degree of damage per city cell (see Section A4.7.8.1) was plotted against the spectral acceleration of the main building typologies computed from the response spectrum of the accelerograms recorded at station PYR1. In a second plot (Figure A4.7.40, bottom), the local response spectra calculated for the 18 borehole positions (Figure A4.7.13) and the average degree of damage of the corresponding locations were compared instead. This second plot, which represents the conditions when considering site effects, shows a clearer tendency for damage to increase with the spectral accelerations, suggesting that the distribution of damage to masonry structures may have been influenced by the amplification and/or deamplification of ground motion under different soil conditions. Bouckovalas *et al.* (1996) acknowledge, however, that other factors may contribute to the scatter in Figure A4.7.40 (bottom), such as directivity and construction technique or quality. When mentioning directivity, Bouckovalas

et al. (1996) highlight that indications of directivity were not obtained as a strong conclusion from waveform analyses but were inferred only by the observation of NE-oriented ruptures of relevant aftershocks (Stavrakakis & Papanastassiou, 1995), the shape of the mainshock intensity contours and the resulting distribution damage (Stavrakakis, 1996), and are, thus, not conclusive.

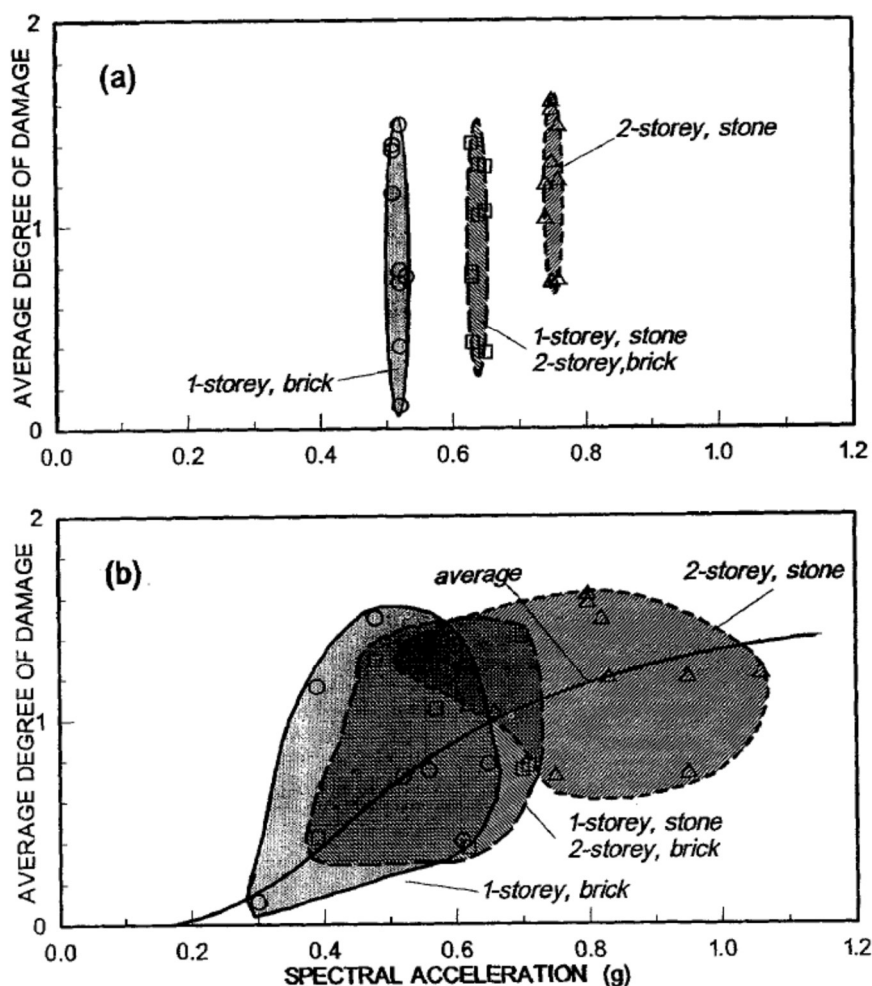


Figure A4.7.40. Correlation between average degree of damage and spectral acceleration without (top) and with (bottom) effect of soil conditions (Bouckovalas *et al.*, 1996)

A4.7.9 Casualties and losses

A4.7.9.1 Numbers of dead and injured

The International Disaster Database (EM-DAT, 2018) and Iliia Oikonomia (2017) report 16 injuries and 1 dead woman. However, Bouckovalas *et al.* (1996) state that this earthquake did not cause any deaths, and the USGS catalogue only mentions two slight injuries.

A4.7.9.2 Causes of casualties

No details are given for the causes of casualties but, in view of the extensive damage observed, it is likely that they might be a direct consequence of structural and non-

structural damage. Only Pomonis *et al.* (2014) report that an elderly woman lost her life while trying to flee from a building during the earthquake shock. If this were true and the cause of death was an accident occurred during the act of fleeing itself and not due to the failure of the structure, this could explain why Bouckovalas *et al.* (1996) did not consider this as a death caused by the earthquake.

A4.7.9.3 Estimates of economic losses

Despite occurring in a region of high seismicity, the consequences of the earthquake were rather severe. At least 50% of the structures of Pyrgos city suffered damage to some extent and the direct cost is estimated by Lekkas (2000) to have been 160 million US\$. Assuming an inflation for the dollar of 2.22% per year between 1993 and 2017, on-line conversion calculators provide an estimate of equivalence of 160 million US dollars (in 1993) with around 271 million US dollars (or 230 million euro) in 2017.

Ilia Oikonomia (2017) local newspaper reports that the earthquake, with its extensive damage on private and public buildings, had an important impact on the social fabric and the economy of the area. The total estimated cost reached 60 billion drachmas (~176 million euro) according to local testimonies, figures in accordance with the above-mentioned ones.

Karantoni & Bouckovalas (1997) remark that a large number of masonry buildings had to be demolished following the earthquake, whereas RC structures were repaired and retrofitted. It is noteworthy that the anticipated cost for infill repairs was much higher than that for repairing the cracks of the RC frames. Although repair and rehabilitation works took place in a large extent in Pyrgos boosting the local economy, local newspapers (Ilia Oikonomia, 2017; Vitinaika, 2008) mention that the authorities did not take advantage of these interventions for significant structural, architectural or urban upgrade of the city.

According to the personal experience of one of the authors, there is no compulsory earthquake insurance in Greece and, in case of a disaster, only the state is responsible to provide financial subsidies to the affected residents. This is given in the form of rent subsidy and/or financing repair/reconstruction works.

A4.7.10 Discussion and conclusions

This moderate-size **M5.4** earthquake occurred on 26th March 1993, at 11.58 UTC, with epicentre near the city of Pyrgos, capital of the prefecture of Ilia. The main shock was widely felt and was preceded by significant foreshock activity and followed by numerous aftershocks. Recorded ground motions and their resulting spectral accelerations were particularly high, especially in contrast with the seismic coefficients with which large proportions of the building stock had been designed, based on their erection period. A maximum EMS-92 intensity of VIII was reached at the city of Pyrgos, where almost 50% of the masonry building stock was reported damaged to some extent. One death (due to

trying to flee from a building during the shock) and 16 injuries were registered, and the direct economic loss was estimated to be around 160 million US dollars at the time.

Despite being designed with relatively outdated seismic provisions, only 22 reinforced concrete buildings suffered from structural damage, though all of them are reported to have suffered non-structural damage to their infill walls. It was masonry structures that suffered most of the damage reported due to the absence of earthquake resistant configurations, poor material quality as well as deterioration over the years. The most affected typology was adobe constructions, followed by stone masonry and by brick masonry, though those built in brick masonry appear to have generally suffered the heaviest damage. While final numbers of affected buildings are not conclusive, an estimate of 378-1,800 damaged and 107-222 destroyed buildings (including both masonry and RC structures) can be made based on the available information, the 1,800 upper bound including a large proportion of non-structural damage.

Site effects and the resonance of buildings with soil sediments with similar dynamic characteristics have been identified as possible factors influencing the widespread damage observed and its spatial distribution, which was not even, whereas indications of directivity effects have been mentioned but not studied in detail.

The 1993 event triggered 47 small landslides, caused soil liquefaction and subsidence at the coastal area and the river's bank, as well as several ground fractures, though only liquefaction and subsidence appear to have had a relevant impact on the extent of the losses.

While a debate has been recently initiated in Greece regarding the possible connection between the observed seismicity and hydrocarbon exploration and extraction in the already seismically active area of Pyrgos and western Greece, the lack of scientific publications to support it, the inherent high levels of tectonic seismicity in the area, and the lack of reference to the 1993 earthquake within the Human-Induced Earthquake Database (Foulger et al., 2016; Wilson et al., 2017; Induced Earthquakes, 2017) suggest that a natural origin is the most likely.

A4.7.11 References

A4.7.11.1 Bibliography

Afshari, K. & J. Stewart (2016). Physically parametrized prediction equations for significant duration in active crustal regions. *Earthquake Spectra* **32**(4), 2057-2081.

Allen, T. I., D. J. Wald, P. S. Earle, K. D. Marano, A. J. Hotovec, K. Lin & M. G. Hearne (2009). An Atlas of ShakeMaps and population exposure catalog for earthquake loss modeling. *Bulletin of Earthquake Engineering* **7**(3), 701-718.

Ambraseys, N. & J. A. Jackson (1990). Seismicity and associated strain of central Greece between 1890 and 1988. *Geophysical Journal* **101**, 663-708.

Anagnostopoulos, S. & M. Moretti (2008). Post-earthquake emergency assessment of building damage, safety and usability—Part 1: Technical issues. *Soil Dynamics and Earthquake Engineering* **28**, 223–232.

Anastasiadis, K. (2008). Η εξέλιξη των αντισεισμικών κανονισμών (The evolution of the seismic design codes, in Greek). In Mousiopoulos, N., G. Penelis, I. Avramidis, K. Stilianidis, N. Kalogirou & D. Aravantinos (eds.): *30 χρόνια μετά το σεισμό της Θεσσαλονίκης – Μνήμες και προοπτική (30 years after Thessaloniki's earthquake – Memories and prospective, in Greek)*, Aristotle University of Thessaloniki, Anniversary tribute.

ASPIDA (2015). Infrastructures upgrade for seismic protection of the country and strengthen service excellence through Action, project MIS-448326, implemented under the *Action, Development Proposals for Research Bodies-ASPIS-KRIPIS* (in Greek).

Aubouin J. (1977). Méditerranée orientale et Méditerranée occidentale: esquisse d'une comparaison du cadre alpin. *Bulletin de la Société Géologique de France* **S7-XIX**(3), 421-435.

Bommer, J.J., P.J. Stafford & J.E. Alarcón (2009). Empirical equations for the prediction of the significant, bracketed, and uniform duration of earthquake ground motion. *Bulletin of Seismological Society of America* **99**(6), 3217-3233.

Bouckovalas, G. (1994) *Microzonation of Pyrgos: Local soil effects and liquefaction analyses*. Research Report, National Technical University of Athens, Geotechnical Division.

Bouckovalas, G., P. Marinos, G. Tsiambaos & N. Sabatakakis (1995). Geology effects in the seismic microzonation of Pyrgos, Greece. *Proceedings of the XI European conference on Soil mechanics and Foundation engineering*, Copenhagen, 28 May-1 June, vol. 4, 31-6.

Bouckovalas, G., A. Anagnostopoulos, A. Kapenis & F. Karantoni (1996). Analysis of soil effects and distribution of damage from the Pyrgos 1993 (Greece) earthquake. *Geotechnical and Geological Engineering* **14**, 111-128.

Brune, J.N. (1970). Tectonic stress and the spectra of seismic shear waves from earthquakes. *Journal of Geophysical Research* **75**(26), 4997-5009.

CEN (2004). *Eurocode 8: Design of structures for earthquake resistance - Part1: General rules, seismic actions and rules for buildings*. European Committee for Standardization, Brussels, Belgium.

Chiou, B.S.J. & R.R. Youngs (2008). An NGA model for the average horizontal component of peak ground motion and response spectra. *Earthquake Spectra* **24**(1), 173-215.

Chousianitis, K., A. Ganas & C.P. Evangelidis (2015). Strain and rotation rate patterns of mainland Greece from continuous GPS data and comparison between seismic and geodetic moment release. *Journal of Geophysical Research: Solid Earth* **120**, 3909-3931.

Dziewonski, A.M., T.-A. Chou & J.H. Woodhouse (1981). Determination of earthquake source parameters from waveform data for studies of global and regional seismicity. *Journal of Geophysical Research* **86**, 2825-2852.

EAK 2000 (2004). *Greek Seismic Code* (with additional articles). Earthquake Planning and Protection Organization, Athens, Greece.

EKOS 2000 (2001). *Greek Code for the Design of Reinforced Concrete Structures*. Earthquake Planning and Protection Organization, Athens, Greece.

- Ekström, G., M. Nettles & A.M. Dziewonski (2012). The global CMT project 2004-2010: Centroid-moment tensors for 13,017 earthquakes. *Physics of the Earth and Planetary Interiors* **200-201**, 1-9.
- EPANTYK (2009). *Αναπτυξη λογισμικού ΣΓΠ για την αναπαράσταση του δομικού πλούτου των ΟΤΑ της χώρας και της σεισμικής του τρωτοτητας σε επιπεδο οικοδομικών τετραγώνων (Development of GIS software for the representation of the structural wealth of the municipalities of the country and of its structural vulnerability in buildings block level, in Greek)*, YP.ES.A & H.D., KEDKE & TEE.
- Foulger, G.R., M. Wilson, J. Gluyas & R. Davies (2016). *Human-induced earthquakes*. Report for the Nederlandse Aardolie Maatschappij BV (NAM), The Netherlands. Report available online at: <https://www.nam.nl/feiten-en-cijfers/onderzoeksrapporten.html#iframe=L2VtYmVkl2NvbXBvbmVudC8/aWQ9b25kZXJ6b2Vrc3JhcHBvcnRlbG>. Last accessed 28th November 2017.
- Fountoulis, I. (1994). *Neo-tectonic evolution of the Central-Western Peloponnese*. Ph.D. Thesis, Faculty of Geology, National and Kapodistrian University of Athens, GAIA 7, 386pp. (in Greek, abridged English version).
- Fountoulis, I., I. Mariolakos & I. Ladas (2014). Quaternary basin sedimentation and geodynamics in SW Peloponnese (Greece) and late stage uplift of Taygetos Mt. *Bollettino di Geofisica Teorica ed Applicata* **55**(2), 303-324.
- Giardini, D., G. Grünthal, K.M. Shedlock & P. Zhang (1999). The GSHAP global seismic hazard map. *Annali di Geofisica* **42**(6), 1225-1228. On line data source: a service of Helmholtz Centre Potsdam <http://gmo.gfz-potsdam.de>.
- Giovinazzi, S. & S. Lagomarsino (2004). A macroseismic method for the vulnerability assessment of buildings. *Proceedings of the 13th World Conference on Earthquake Engineering*, Vancouver, Canada, August 1-6.
- Grünthal, G. (ed.) (1993). *European macroseismic scale 1992: updated MSK scale*. Vol. 7. European Seismological Commission, Subcommission on Engineering Seismology, Working Group Macroseismic scale.
- Grünthal, G. (1998). *European Macroseismic Scale 1998 (EMS-1998)*. Cahiers du Centre Europeen de Geodynamique et de Seismologie 15, Centre Europeen de Geodynamique et de Seismologie, Luxembourg. Available online at (last accessed 28th December 2017): http://www.franceseisme.fr/EMS98_Original_english.pdf.
- Jackson, J.A. (1994). Active Tectonics of the Aegean Region, Annual Review. *Earth and Planetary Science Letters* **22**, 239-271.
- Jacobshagen, V. (1979). Structure and geotectonic evolution of the Hellenides. *Proceedings of the VI Colloquium on the Geology of the Aegean Region*, Athens, Greece, 1977, **3**, pp. 1355–1367.
- Jaiswal, K. & D.J. Wald (2008). Creating a global building inventory for earthquake loss assessment and risk management. *USGS Open File Report 2008-1160*. Available online at: <https://pubs.usgs.gov/of/2008/1160/>. Last accessed: 5th April 2017.
- Jolivet, L. & J.P. Brun (2010). Cenozoic geodynamic evolution of the Aegean. *International Journal of Earth Sciences* **99**, 109-138.
- Jolivet, L., A. Menanta, P. Sternaia, A. Rabillard, L. Arbaret, R. Augier, V. Laurent, A. Beaudoin, B. Grasemanne, B. Huet, L. Labroussef & L. Le Pourhiet (2015). The geological signature of a slab tear below the Aegean. *Tectonophysics* **659**, 166–182.

Kahle, H.G., M. Cocard, Y. Peter, A. Geiger, R. Reilinger, A. Barka & G. Veis (2000). GPS-derived strain rate field within the boundary zones of the Eurasian, African, and Arabian plates. *Journal of Geophysical Research* **105** (23).

KANEPE (2012). *Regulation of Repair and Strengthening of Buildings*. Earthquake Planning and Protection Organization, Athens, Greece.

Karantoni, F. & G. Bouckovalas (1997). Description and analysis of building damage due to Pyrgos, Greece earthquake. *Soil Dynamics and Earthquake Engineering* **16**, 141-150.

Kassarar, I., A. Karakonstantis, K. Vlachou, V. Kapetanidis, G. Kaviris, P. Papadimitriou, N. Voulgaris, E. Lagios & K. Makropoulos (2012). *Study of the geodynamics in Aitolokarnania (W. Greece) based on joint seismological and GPS Data*. Poster for the 33rd General Assembly of the European Seismological Commission, Moscow, Russia, 2 pp. Available online at: https://www.researchgate.net/publication/259339406_study_of_the_geodynamics_in_aitoloakarnania_w_greece_based_on_joint_seismological_and_gps_data. Last accessed: 28th February 2018.

Kassarar, I., A. Karakonstantis, K. Vlachou, V. Kapetanidis, G. Kaviris, K. Vlachou, P. Papadimitriou, N. Voulgaris & K. Makropoulos (2013). *On the geodynamics of western Greece deduced by massive seismological observations*. Poster for the IAHS/IAPSO/IASPEI Joint Assembly, Gothenburg, Sweden, 22-26 July. Available online at: http://www.academia.edu/20932820/On_the_geodynamics_of_western_Greece_deduced_from_massive_seismological_observations. Last accessed 28th February 2018.

Kassarar, I., V. Kapetanidis & A. Karakonstantis (2016). On the spatial distribution of seismicity and the 3D tectonic stress field in western Greece. *Physics and Chemistry of the Earth* **95**, 50-72. Catalogue data courtesy of Dr. I. Kassarar.

Koukouvelas, I., A. Mpresiakas, E. Sokos & T. Doutsos (1996). The tectonic setting and earthquake ground hazards of the 1993 Pyrgos earthquake, Peloponnese, Greece. *Journal of the Geological Society London* **153**, 39-49.

Koukouvelas, I., S. Kokkalas & P. Xypolias (2009). Surface deformation during the Mw 6.4 (8 June 2008) Movri Mountain earthquake in the Peloponnese, and its implications for the seismotectonics of western Greece. *International Geology Review* **52**(2), 249-268.

Lekkas, E. (1994). Liquefaction – Risk zonation and urban development in Western Peloponnese (Greece). *Proceedings 7th International Congress, International Association of Engineering Geology*, 5-9 September, Lisbon, Portugal, 2095-2102.

Lekkas, E. (1996). Pyrgos earthquake damages (based on E.M.S.-1992) in relation with geological and geotechnical conditions. *Soil Dynamics and Earthquake Engineering* **15**, 61-68.

Lekkas, E. (2000). A multidisciplinary project for urban and emergency planning in seismic regions: the case of Pyrgos city (w. Peloponnese Greece). *6th International Conference on Seismic Zonation (6ICSZ)*, EERI, California, USA, November 12-15, 1017-1022.

Lekkas, E., I. Fountoulis & D. Papanikolaou (2000). Intensity distribution and neotectonic macrostructure Pyrgos earthquake data (26 March 1993, Greece), *Natural Hazards* **21**, 19-33

Lekkas, E. (ed.), M. Fournelis M., M. Diakakis, L. Gouliotis, E. Kotsi & I. Delakourides (2010). *Επιχειρησιακή οργάνωση των δήμων του ΑΣΔΑ για την Πολιτική Προστασία & αντιμετώπιση φυσικών & περιβαλλοντικών κινδύνων Β' φάση: δράσεις μείωσης σεισμικών γεωδυναμικών κινδύνων (Operational organization of the Municipalities of the Development Association of Western Attica for Civil Protection & treatment of natural and environmental Risks, B phase: actions for reduction of seismic geodynamic hazards, in Greek)*. Development Association of Western Attica, National Kapodestrian University of Athens, Athens, Greece. Available online at:

https://home.asda.gr/PdfFiles/Publications/FysikoiKindynoi/02_Draseis_meiosis_seismikon_geodinamikon_kindinon_2010.pdf. Last Accessed: 1st June 2017.

LePichon, X. & J. Angelier (1979). The Hellenic arc and trench system: a key to the neotectonic evolution of the Eastern Mediterranean area. *Tectonophysics* **60**, 1–42.

Luzi L, R. Puglia, E. Russo & ORFEUS WG5 (2016). Engineering Strong Motion Database. Istituto Nazionale di Geofisica e Vulcanologia, Observatories & Research Facilities for European Seismology. Available online at (last accessed 26th October 2017): http://esm.mi.ingv.it/DYNASTAGE/CadmoDriver?action=prepare&find_div=1&page=ACC_Events_Stations_Waveform_progressive&rock=INVALID&state=find_progressive_div&tabber=1&token=NULLNULLNULLNULL.

Mariolakos, I., V. Sabot, I. Fountoulis, A. Markopoulou-Diakantoni, R. Mirkou (1998). Filiatra. Neotectonic Map of Greece at scale 1/100,000. *Earthquake Planning & Protection Organization*, Athens.

McClusky, S., S. Balassanian, A. Barka, C. Demir, S. Ergintav, I. Georgiev, O. Gurkan, M. Hamburger, K. Hurst, H. Kahle, K. Kastens, G. Kekelidze, R. King, V. Kotzev, O. Lenk, S. Mahmoud, A. Mishin, M. Nadariya, A. Ouzounis, D. Paradissis, Y. Peter, M. Prilepin, R. Reilinger, I. Sanli, H. Seeger, A. Tealeb, M.N. Toksöz & G. Veis (2000). Global Positioning System constraints on plate kinematics and dynamics in the eastern Mediterranean and Caucasus. *Journal of Geophysical Research* **105**, 5695–5719.

McKenzie, D.P. (1972). Active tectonics of the Mediterranean region. *Royal Astronomical Society Geophysical Journal* **30**, 109-182.

Melis, N., G. Tselentis & E. Sokos (1994). The Pyrgos (March 26, 1993; Ms = 5.2) earthquake sequence as it was recorded by the Patras seismic network. *Bulletin of Geological Society of Greece* **30**(5), 175-180.

Nikolakopoulos, K., K. Kavoura, N. Depountis, A. Kyriou, N. Argyropoulos, I. Koukouvelas & N. Sabatakakis (2017). Preliminary results from active landslide monitoring using multidisciplinary surveys. *European Journal of Remote Sensing* **50**(1), 280-299.

Papadimitriou, P., K. Chousianitis, A. Agalos, A. Moshou, E. Lagios & K. Makropoulos (2012). The spatially extended 2006 April Zakynthos (Ionian Islands, Greece) seismic sequence and evidence for stress transfer. *Geophysical Journal International* **190**(2), 1025–1040.

Papadopoulos, G.A., V. Karastathis, C. Kontoes, M. Charalampakis, A. Fokaefs, I. & Papoutsis (2010). Crustal deformation associated with east Mediterranean strike-slip earthquakes: The 8 June 2008 Movri (NW Peloponnese), Greece, earthquake (Mw6.4). *Tectonophysics* **492**, 201–212.

Papanikolaou, D., I. Fountoulis & Ch. Metaxas (2007). Active faults, deformation rates and Quaternary paleogeography at Kyparissiakos Gulf (SW Greece) deduced from onshore and offshore data. *Quaternary International* **171-172**, 14-30.

Papanikolaou, I.D., D.I. Papanikolaou & E.L. Lekkas (2009). Advances and limitations of the Environmental Seismic Intensity scale (ESI 2007) regarding near-field and far-field effects from recent earthquakes in Greece: implications for the seismic hazard assessment. In: K. Reicherter, A.M. Michetti & P.G. Silva (eds.): *Palaeoseismology: Historical and Prehistorical records of earthquake ground effects for seismic hazard assessment*. The Geological Society, London, Special Publications 316, 11–30.

Philippon, A. (1898). La tectonique de l' Egeide. *Annales de Geographie*, 112–141.

Pomonis, A., M. Gaspari & F.S. Karababa (2014). Seismic vulnerability assessment for buildings in Greece based on observed damage data sets. *Bollettino di Geofisica Teorica ed Applicata* **55**(2), 501-534.

- Rousopoulou, A. (1949). Αντισεισμικοί Κατασκευαί (Earthquake Resistant Structures, in Greek) ed. T.E.E.
- Royden, L.H. (1993). The tectonic expression of slab pull at continental convergent boundaries. *Tectonics* **12**, 303–325.
- Sachpazi, M., M. Laigle, M. Charalampakis, J. Diaz, E. Kissling, A. Gesret, A. Becel, E. Flueh, P. Miles & A. Hirn (2016). Segmented Hellenic slab rollback driving Aegean deformation and seismicity. *Geophysical Research Letters* **43**(2), 651-658.
- Sachpazis, C. (2011). Soil liquefaction potential assessment of a coastal foundation ground and its suitability for a CCGT Power Plant construction in Greece. *Electronic Journal of Geotechnical Engineering* **16**, 679-708
- Seismosoft (2016). *SeismoSignal 2016 – A computer program for signal processing of strong-motion data*. Available from <http://www.seismosoft.com>. Last accessed: 10th April 2017.
- Stavrakakis, G. N. (1996). Strong motion records and synthetic isoseismals of the Pyrgos, Peloponnisos, southern Greece, earthquake sequence of March 26, 1993. *Pure and Applied Geophysics* **146**, 147–161.
- Stavrakakis, G.N. & D. Papanastassiou (1995). Spatial-temporal analysis of the Pyrgos, Peloponnisos, Southern Greece, earthquake sequence of 1993. *Proceedings of the 5th International Conference on Seismic Zonation*, October 17-19, Nice, France, 1141-1148.
- United Nations, ed. (1994). *Human Development Report 1994*. United Nations Development Program (UNDP), New York, United States.
- United Nations, ed. (2016). *Human Development Report 2016 - Human Development for everyone*. Report of the United Nations Development Program (UNDP), New York, United States.
- Wald, D.J. & T.I. Allen (2007). Topographic slope as a proxy for seismic site conditions and amplification. *Bulletin of the Seismological Society of America* **97**, 1379–1395. Slope-based online map viewer available at: <http://usgs.maps.arcgis.com/apps/webappviewer/index.html?id=8ac19bc334f747e486550f32837578e1>. Data used herein downloaded from deprecated version last accessed on 7th September 2016.
- Wells, D.L. & K.J. Coppersmith (1994). New empirical relationships among magnitude, rupture length, rupture width, rupture area, and surface displacement. *Bulletin of the Seismological Society of America* **84**(4), 974-1002.
- Wilson, M.P., G.R. Foulger, J.G. Gluyas, R.J. Davies & B.R. Julian (2017). HiQuake: The human-induced earthquake database. *Seismological Research Letters* **88**(6), 1560-1565.
- Worden, C.B., M.C. Gerstenberger, D.A. Rhoades & D.J. Wald (2012). Probabilistic relationships between ground-motion parameters and Modified Mercalli intensity in California. *Bulletin of the Seismological Society of America* **102**(1), 204-221.
- Woessner, J., D. Giardini, H. Crowley, F. Cotton, G. Grünthal, G. Valensise, R. Arvidsson, R. Basili, M. B. Demircioglu, S. Hiemer, C. Meletti, R. W. Musson, A. N. Rovida, K. Sesetyan, M. Stucchi & The SHARE Consortium (2015). The 2013 European Seismic Hazard Model: Key Components and Results. *Bulletin of Earthquake Engineering* **13**(12), 3553–3596. Online data source: <http://www.efehr.org/en/home/>. Last accessed: 3rd December 2017.

Worden, C.B., E.M. Thompson, M. Hearne & D.J. Wald (2017). *ShakeMap V4 Manual: technical manual, user's guide, and software guide*. United States Geological Survey. Available online at: <http://usgs.github.io/shakemap/>.

A4.7.11.2 Web references

Earthquake Planning and Protection Organization (EPPO):
<http://www.oasp.gr/node/2053>. Last accessed: 3rd April 2017.

EM-DAT – The Emergency Events Database (Université Catholique de Louvain, Brussels, Belgium; Cred. Prof. Dr. D. Guha-Sapir): <http://www.emdat.be/>. Last accessed: 28th February 2018.

Global Centroid Moment Tensor Project (GCMT): <http://www.globalcmt.org>.
Last accessed: 15th October 2017.

Geodynamics Institute-National Observatory of Athens (GI-NOA): <http://www.gein.noa.gr/en/>.
Last accessed: 23rd March 2017.

Hellenic Statistical Authority (EL.STAT.): Gross domestic product per capita by Nuts II/III: <http://www.statistics.gr/el/statistics/-/publication/SEL57/> (in Greek). Last accessed: 23rd March 2017.

Hellenic Statistical Authority (EL.STAT. Census, 1991): Demographic characteristics 1991 <http://www.statistics.gr/el/statistics/-/publication/SAM03/1991> (in Greek). Last accessed: 23rd March 2017.

Hellenic Unified Seismic Network (HUSN): <http://www.gein.noa.gr/en/networks/husn>.

Ilia Oikonomia Local newspaper (2017): <http://www.iliaoikonomia.gr/content/26-martioy-1993-oi-seismoi-poy-katestrepsan-ton-pyrgo>. Last accessed: 14th June 2017.

Induced Earthquakes (2017): <http://inducedearthquakes.org/>. Last accessed: 28th November 2017.

International Seismological Centre, On-line Bulletin (ISC): <http://www.isc.ac.uk>, International Seismological Centre, Thatcham, United Kingdom.

International Seismological Centre, EHB Bulletin (ISC/EHB): <http://www.isc.ac.uk/isc-ehb/search/catalogue/>. International Seismological Centre, Thatcham, United Kingdom.

Open Geospatial data for Greece (GEODATA, 2015): <http://geodata.gov.gr/>. Last accessed: 23rd March 2017.

Permanent Regional Seismological Network operated by the Aristotle University of Thessaloniki (THE): http://geophysics.geo.auth.gr/ss/station_index_en.html.

Seismological Laboratory of the Department of Geophysics-Geothermics of the National and Kapodistrian University of Athens (DGSSL-NKUA): <http://dgssl.geol.uoa.gr>.

Tempo24 local newspaper (2016): <http://www.tempo24.gr/eidisi/65568/o-pyrgos-23-hronia-prin-oi-seismoi-poy-katestrepsan-tin-poli-deite-fotografies>. Last accessed: 27th March 2017.

The Best local news portal (2017): <http://www.thebest.gr/news/index/viewStory/433405>.
Last accessed: 27th March 2017.

The World Bank Group (2017), World Bank Open Data: <http://data.worldbank.org>. Last accessed: 20th March 2017.

United States Geological Survey (USGS): <https://earthquake.usgs.gov/earthquakes/>
Website for this event (last accessed 1st June 2017):
<https://earthquake.usgs.gov/earthquakes/eventpage/usp0005q5f#executive>
PAGER data, products and references: <https://earthquake.usgs.gov/data/pager/references.php>.

Vitinaiika local blog (2008): http://vytinaiika.blogspot.gr/2008/03/blog-post_26.html. Last accessed: 23rd March 2017.

World Economic Outlook Database (2016):
<https://www.imf.org/external/pubs/ft/weo/2016/02/weodata/download.aspx>. Last accessed: 23rd March 2017.

A4.8. July 1996 M4.8 Épagny-Annecy Earthquake, France

This earthquake occurred on 15th July 1996, at 00.13 UTC (02.13 local time), near the city of Épagny, about 30 km south-south-west of Geneva and 4 km north-west of Annecy, both of which are part of the Community of Greater Annecy. The earthquake was the strongest event to occur in the department of Haute-Savoie (Auvergne-Rhône-Alpes region, south-east France) since the Chamonix earthquake of 29 April 1905. Nearly one thousand aftershocks were recorded, lasting for many months, with the strongest one (M_L 4.2-4.3) occurring 8 days after the mainshock, but foreshock activity was nearly negligible. The earthquake was felt up to a 100-km distance and caused damage to 180 communities around the epicentre, but no serious casualties. The total monetary loss was estimated to have been one of the highest in France due to earthquakes.

A4.8.1 Tectonic and seismic setting

A4.8.1.1 Tectonic setting

The Vuache fault, which generated the earthquake of 15th July 1996 in Épagny, is a 30-km long, NW-SE trending structure (Schardt, 1981) that runs through the Molasse basin and connects the southern Jura Mountains to the northern Subalpine chains across the Geneva-Rumilly molasse basin (Figure A4.8.1). The regional tectonic context is dominated by the ongoing convergence between the European and Adriatic plates which causes crustal thickening along the northern Subalpine chains and the Jura Mountains, with shortening being accommodated by NNE trending Plio-Quaternary thrust faults and folds (Thouvenot *et al.*, 1998; Baize *et al.*, 2011). These structures are being cut by a series of NW-SE to N-S trending tear faults, among which the left-lateral strike-slip Vuache fault, which is considered to have been reactivated during the Cretaceous, is the most prominent one (Dufumier, 2002). Its geometry suggests that it constitutes a lateral thrust ramp that accommodates differential shortening between the Jura and the northern Subalpine chains (Thouvenot *et al.*, 1998).

Towards the northwest, the Vuache fault is split into several branches (Baize *et al.* 2011), along the southwest flank of the Mandallaz Mountain. The trace in the middle part of the fault is elusive due to the extensive reshaping of surface geology and morphological features under glacial/periglacial conditions during/after the last glacial maximum (Thouvenot *et al.*, 1998). To the southeast, the fault cuts through the substrata of the perialpine Annecy Lake, the third largest lake in France. Morphological features, such as the left-lateral curvature of folds and faults south of Annecy, suggest that the fault likely continues beneath the Alpine nappes (Baize *et al.*, 2011; Doudoux *et al.*, 1992). There is also hard evidence that the fault extends at depth into the basement, as revealed by seismic lines analysis (Baize *et al.*, 2011). The above remarks imply that the true length of the fault may reach about 80 km instead of the known 30 km described earlier, a fact that would have a relevant impact on earthquake hazard.

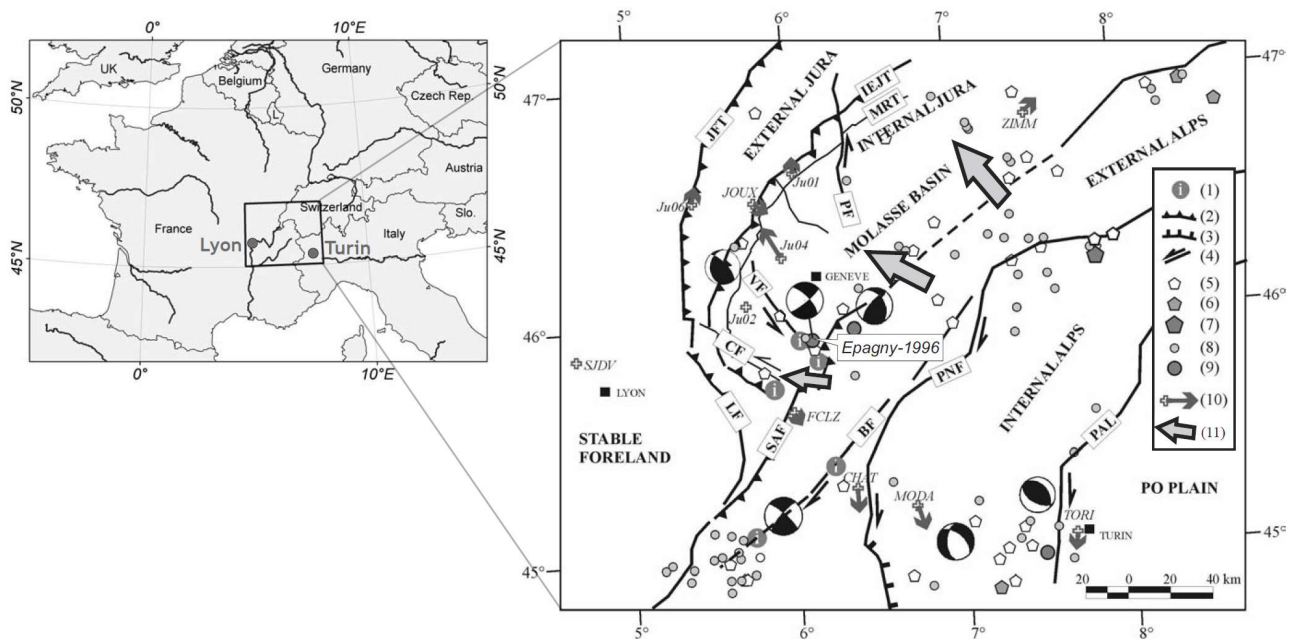


Figure A4.8.1. Location of the broader area around the Haute-Savoie department in France (left), Seismotectonic map in the broader area of the Vuache fault (VF) at the southern Jura and Molasse basin (right). Barbed lines with triangles (2) or hatchings (3) represent reverse/thrust or normal faults, respectively. Pentagons (5-7) or circles (8-9) represent epicentres of historical earthquakes or events recorded in the instrumental era. Velocity vectors (10) with respect to stable foreland as derived by GPS, the arrow in the legend corresponds to 1 mm/a; JFT: Jura frontal thrust; IEJT: Internal-External Jura thrust; MRT: Mont-Risoux thrust; PF: Pontarlier fault; CF: Culoz fault; LF: Lagnieu fault; SAF: Sub-alpine front; BF: Belledonne fault; PNF: Penninic front; PAL: Peri-Adriatic line. From Baize *et al.* (2011).

The ground displacement field around the Vuache fault, as determined by a GPS network that was installed in 2000, revealed sinistral kinematics in a NW-SE direction at a rate of 1.0 ± 0.2 mm per year (Walpersdorf *et al.*, 2006). At a larger scale in this part of western Europe, Tesauro *et al.* (2005) observed relatively large compressional strain rates in south-west Switzerland, reaching up to 12 ns/year. In the region of the Vuache fault, the strain rates are slightly extensional but low, at ~ 1 ns/yr, as shown in Figure A4.8.2. The strain orientation appears to facilitate left-lateral slip on NW-SE to N-S trending faults, but the strain field is very different to the south (N-S extension) and to the north of Annecy (SW-NE compression), which is indicative of the complexity of the regional stress field. The low strain rate is also reflected on the slip rate on the Vuache fault. Estimates on the accumulated horizontal displacement on the fault over the last 5-12 Myr range between 1 and 15 km (Charollais *et al.*, 1983), roughly equivalent to an average slip of 0.08 to 3 mm/yr (Thouvenot *et al.*, 1998).

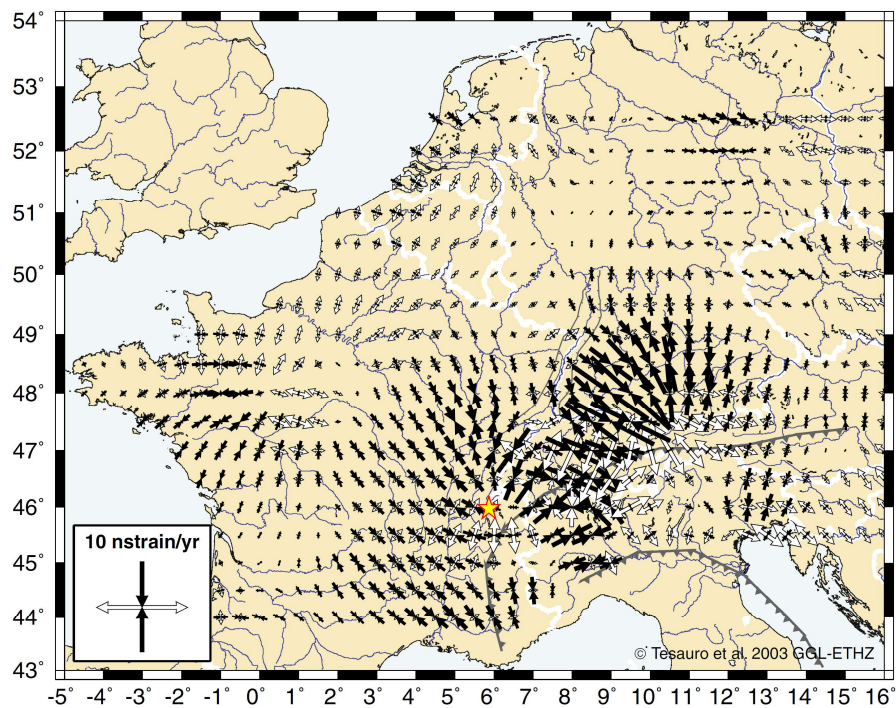


Figure A4.8.2. Principal axes and values of strain rates in Western Europe. The star at [$\sim 46^{\circ}\text{N}, \sim 6^{\circ}\text{E}$] marks the epicentre of the 15th July 1996 earthquake in Épagny. From Tesauro *et al.* (2005).

A4.8.1.2 Regional and local seismicity

The seismicity in the region of south-east France and the western Alps is considered as moderate, with daily observed low-magnitude events ($M_L < 1.5$) but with only a few $M_L > 3.0$ events occurring each year, and likely one or two **M6** or larger events per century (Thouvenot *et al.*, 1998), mostly along the French-Italian border, as depicted in Figure A4.8.3. Several earthquakes have been reportedly felt in the department of Haute-Savoie since the 19th century, with the strongest ones having intensities in the meizoseismal area between VII and VIII on the MSK64 scale (Table A4.8.1). The **M5.8** earthquake of Valais (Switzerland) on 25th January 1946 had an epicentral intensity of VII-VIII that was reduced to IV-V in Annecy, which was about 120 km away. The most significant recorded earthquake that shook the region before 1996 has been the Chamonix event of 29th April 1905, with an estimated magnitude of **M5.3** (Cara *et al.*, 2017), epicentral intensity between VII and VIII, and an average of VI in Annecy (SisFrance, 1996). Other significant earthquakes include the **M5.3** Correncon event of 1962, 110 km south-west of Annecy, and the M_L 5.1 Entremont (Le Grand-Bornard) event of 14th December 1994, 25 km east-north-east of Annecy (MSK64 intensity V), on a hidden right-lateral strike-slip fault (Frechet *et al.*, 1996; Dufumier, 2002).

In Annecy itself, one of the largest historic earthquakes has been the 11th August 1839 event ($I_0 = \text{VII}$), which is shown in Figure A4.8.4 together with other relevant historic events on a local scale. As can be observed, the Vuache fault has given some signs of activity during the 20th century. The 1936 Frangy event is considered as unambiguously ascribed to the Vuache fault, at the south-east end of the homonymous mountain. About the same

region was ruptured on 29th May 1975 by a M_L 4.2 earthquake, while in 1983 a couple of $M_L \approx 3.0$ events were recorded near the north-west part of Vuache mountain (Figure A4.8.4). Other than that, the Vuache fault has been rather quiet since the 17th century, which can be attributed to the low strain rates in the area. Even after the installation of the regional Sismalp network of 44 seismological stations by the Observatoire de Grenoble in 1994, which lowered the detection threshold down to events with magnitude 1.5, only two events were recorded on the Vuache fault in August 1995 (Table A4.8.1) with M_L slightly less than 2.0 (Thouvenot *et al.*, 1998). At the time of its occurrence, the 15th July 1996 Épagny earthquake was considered as the most significant event to have been recorded in the Alps during the digital instrumentation era (Courboulex *et al.*, 1999). The Vuache fault is believed to have a recurrence time of 200-600 years for earthquakes up to M_6 (Thouvenot *et al.*, 1998).

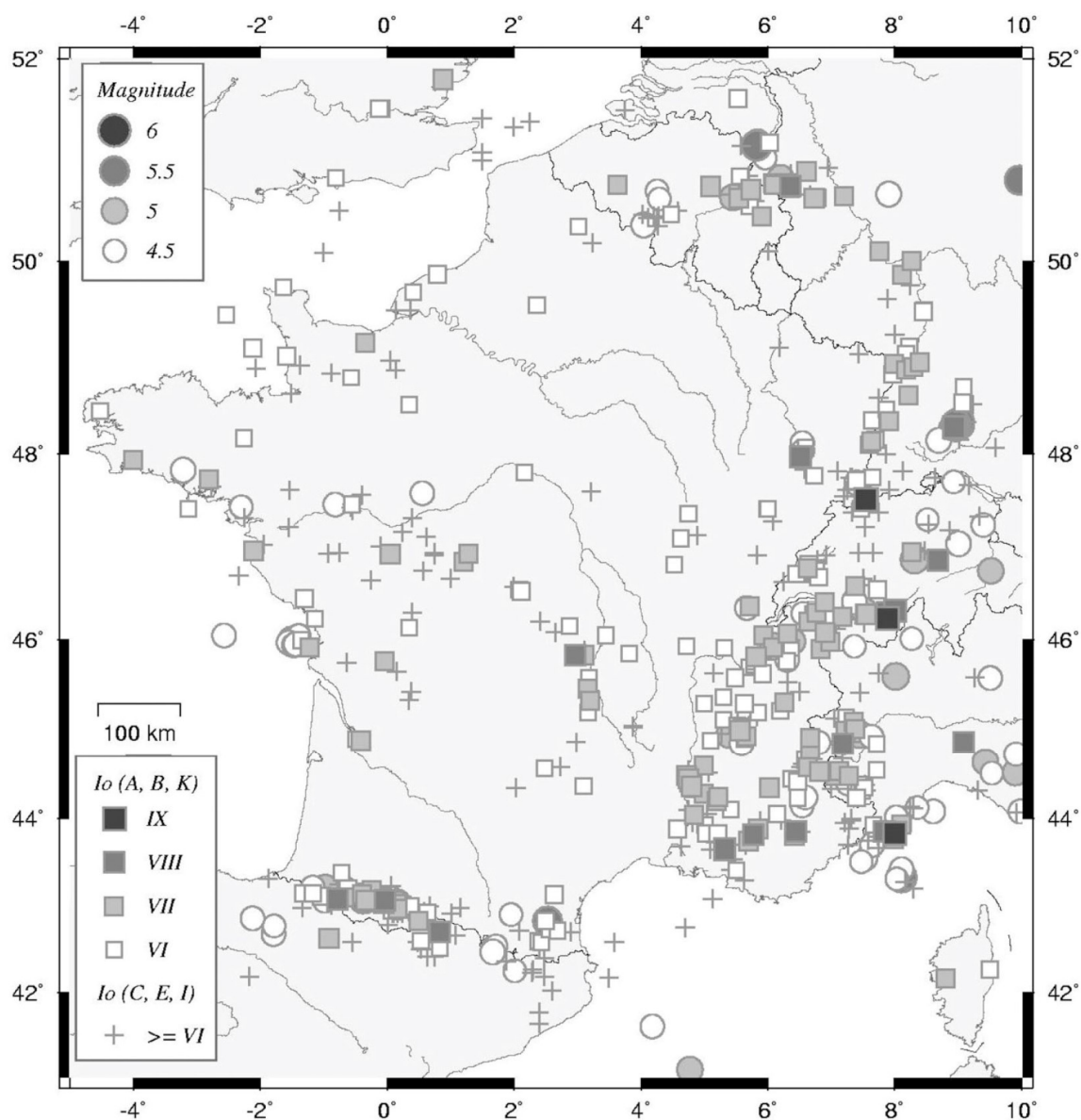


Figure A4.8.3. Historic (squares/crosses for certain/uncertain, extracted from the SisFrance database, up to 2001) and instrumental seismicity (circles) recorded in French catalogues for the whole of France (CEA/LDG 1962-2002). From Scotti *et al.* (2004).

Table A4.8.1. Earthquakes felt in the Haute-Savoie department of France. List compiled using information from Dominique *et al.* (1996), Thouvenot *et al.* (1998), SisFrance, Cara *et al.* (2017), QuakeBulletin, SEHS (2015), NEIC-USGS and the Swiss Seismological Service (SED). The magnitudes are M_L , unless otherwise stated.

Origin time (UTC after 1960)	Location	Magnitude	I ₀ (MSK)
11/03/1817 21:25	Saint-Gervais-les-Bains		VII
13/05/1833 02:00	Annecy		III
11/08/1839 20:00	Annecy		VII
02/12/1841 19:53	Albanais (Rumilly)		VI
05/03/1847 23:22	Annecy		IV
25/07/1855 12:50	Valais (Switzerland)		IX
29/04/1905 01:59	Chamonix (Mont Blanc)	M5.3	VIII
17/04/1936 03:19	Frangy (SE Vuache f.)		VII
25/01/1946 17:32	Valais (Switzerland)	5.8	VII-VIII
25/04/1962 04:44	Corrençon	5.3	VII-VIII
29/05/1975 00:32	SE Vuache f.	4.2	V-VI
16/11/1983 00:28	Chaumont	3.0	
11/06/1988 22:44	Chamonix	4.0	V
14/12/1994 08:56	Entremont	5.1	VI
19/08/2000 08:37	Faucigny	3.6	IV-V
23/02/2001 22:19	Martigny (Switzerland)	3.4	V
22/02/2003 20:41	Saint Die (Vosges)	5.4	VI-VII
23/02/2004 17:31	Besançon (Doubs)	5.1	V-VI
12/06/2004 04:44	Albertville (Savoie)	3.5	IV-V
08/09/2005 11:27	Chamonix and Martigny	4.5	V

Figure A4.8.4 shows a significant seismic gap in the central segment of the Vuache fault between the 1975 and the 1996 events. According to Dufumier (2002), the gap has lasted at least 200 years and indicates the potential for a future **M5** to **M6** event.

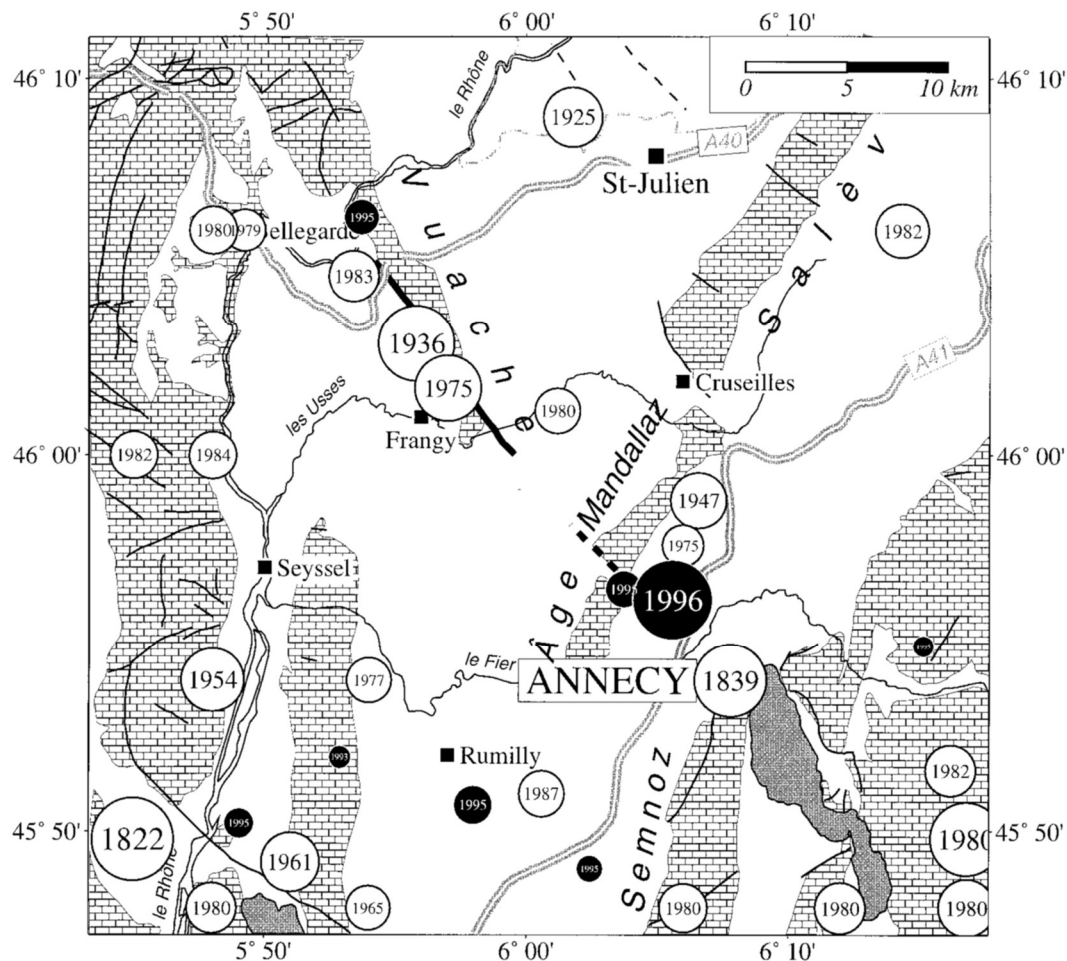


Figure A4.8.4. Historic seismicity in the region of Annecy. The brick pattern indicates calcareous Subalpine chains (east) and Jura folds (west) while the thick line is the trace of the Vuache Fault. After Thouvenot *et al.* (1998).

A4.8.1.3 Seismic hazard

The first seismic zonation was developed in France in the 1980s and became official in 1991. It was based on the analysis of limited historical seismic data and qualitative expertise. The established map (Figure A4.8.5, left) was strongly influenced by political decisions regarding construction regulations (Terrier *et al.*, 2006). According to this obsolete zonation, 5 zones of increasing seismicity are recognized (0, Ia, Ib, II and III) with the majority of the metropolitan country being located in low seismicity zones. In particular, the department of Haute-Savoie (#74) is mostly in Zone IB, with its northern third in the less hazardous Zone IA.

With the development of Eurocode 8 (EC8; CEN, 2004) and seismic research taking place at European level, the seismic zonation was reassessed, based on probabilistic seismic hazard analysis. Taking into account geological and seismological data, as registered for 40 years, it was possible to divide the country in five different zones with homogeneous seismic hazard (Figure A4.8.5, right), with no null seismicity zone, according to their peak ground acceleration with 10% probability of exceedance in 50 years: 1 (very low seismicity, 0.04 g), 2 (low seismicity, 0.07 g), 3 (moderate seismicity, 0.11 g), 4 (average seismicity, 0.16 g), and 5 (strong seismicity, 0.30 g). Contrary to the previous division, the

seismic hazard characterization was made at the municipality level (Géorisques, 2017) and seismic design regulations are now applicable to more than 21,000 communities, instead of the previous 5,000.

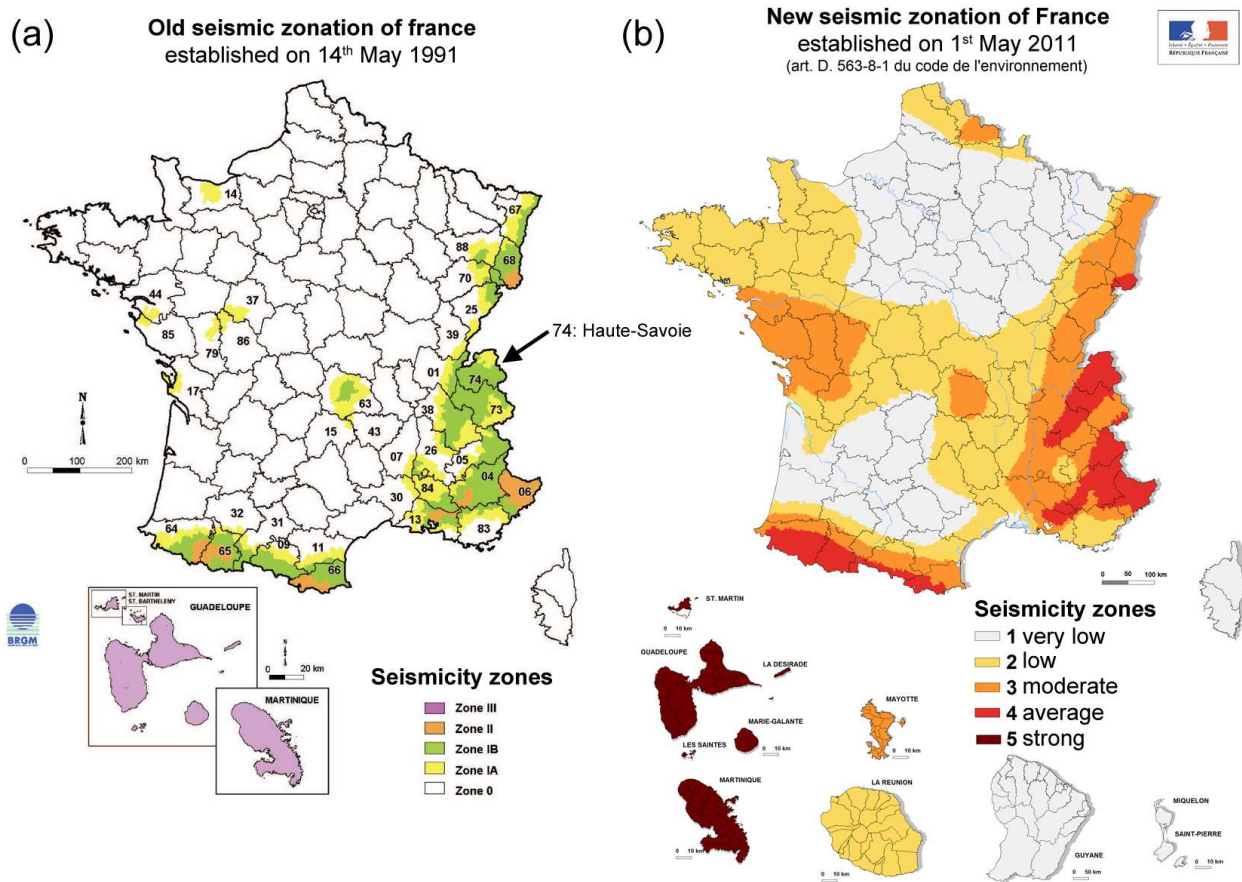


Figure A4.8.5. Old seismic zonation map for France established on 14th May 1991 (left); new seismic zonation map, established on 1st May 2011 (right). Figure modified after Fabriol & Garry (2002) and Plan séisme (2017).

At the time of the 1996 Épagny earthquake, the affected area was in zone IB, corresponding to “weak seismicity” of the old zonation regulations, which comprised areas where no shocks equal or greater than IX had been observed while the return period of earthquakes that cause epicentral intensities of VIII and VII exceeded 250 and 75 years, respectively (Solomos *et al.*, 2008). For the Community of Greater Annecy, Zone IB translated to a nominal rock PGA value of 0.150 g, with 10% probability of exceedance in 50 years (or a return period of 475 years; Table A4.8.2). This value was that corresponding to the design of structures of Class B (Solomos *et al.*, 2008).

Figure A4.8.6 shows how some differences in the broader area of Rhône-Alpes between the old and new hazard maps are significant, as there is now a narrow zone 4 running from Lake Geneva towards the south-west. The hazard level has increased in most of the region while there are no communes in the lowest hazard zone (a large part of the region was in negligible seismic zone before). Almost the entire Haute-Savoie department is now in zone 4, except for its western end, which is in zone 3. The Community of Greater Annecy has been upgraded to zone 4, corresponding to “average risk” in the new seismic

zonation, with the north-west part of the Vuache fault (including Frangy) being classified as zone 3 (moderate risk). Some adjustments were made to the new seismic zonation on 6th January 2015, lowering the class by one degree in two communities (Veynes and Saintes-Maries-de-la-Mer) (Plan séisme, 2017).

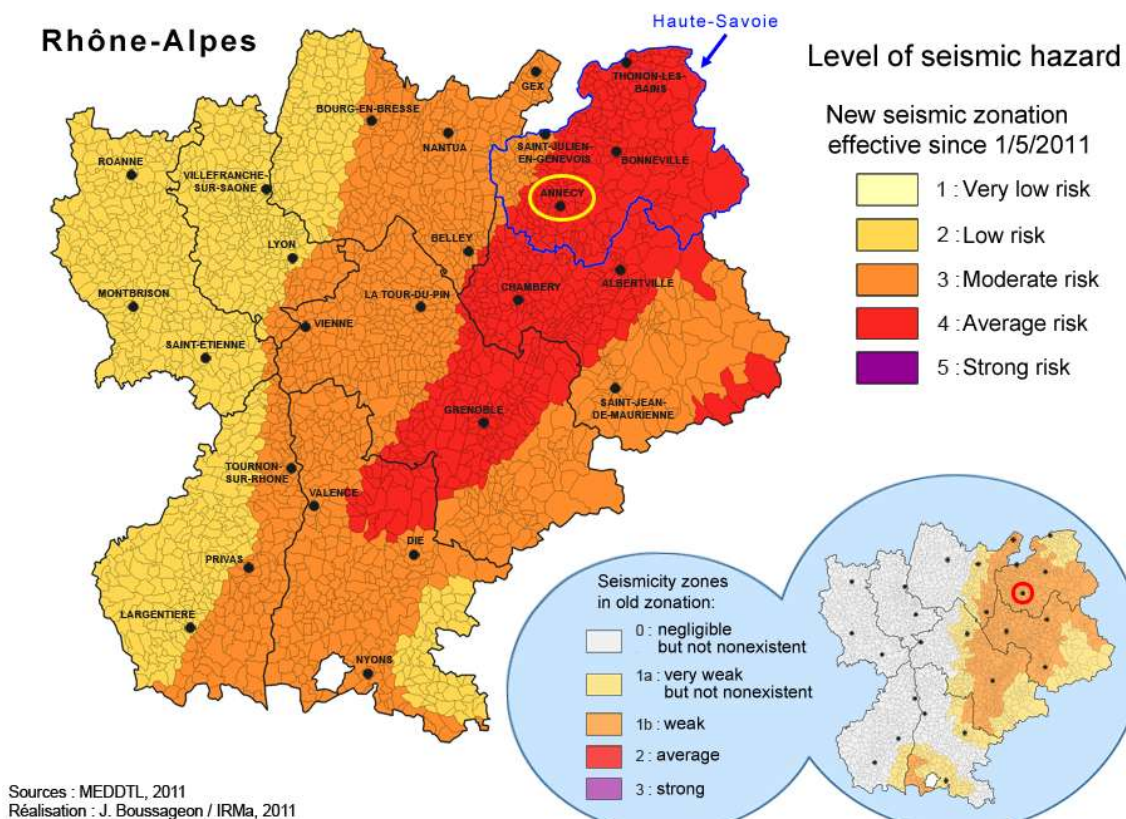


Figure A4.8.6. New (large, top-left) and former (lower-right) seismic zonation of the Rhône-Alpes region, with the area of Annecy marked with a yellow ellipse and a red circle, respectively. Figure modified after Institut des Risques majeurs (IRMA, 2011).

According to the results of the Global Seismic Hazard Assessment Program (GSHAP) (Giardini *et al.*, 1999), the area of Annecy exhibits PGA values with a 10% probability of exceedance in 50 years of around 0.133 g. In the updated hazard maps of the SHARE project (Woessner *et al.*, 2015), the estimated PGA in the broader area of Annecy is between 0.100 g and 0.125 g (Figure A4.8.7).

Table A4.8.2 summarizes the values of PGA on rock with 10% probability of exceedance in 50 years from the different sources mentioned above, while Figure A4.8.8 presents a comparison between the corresponding 5%-damped mean uniform hazard spectrum from SHARE for the closest available coordinates to the city of Annecy and the Eurocode 8 Type (II) design spectrum for an input PGA of 0.16 g.

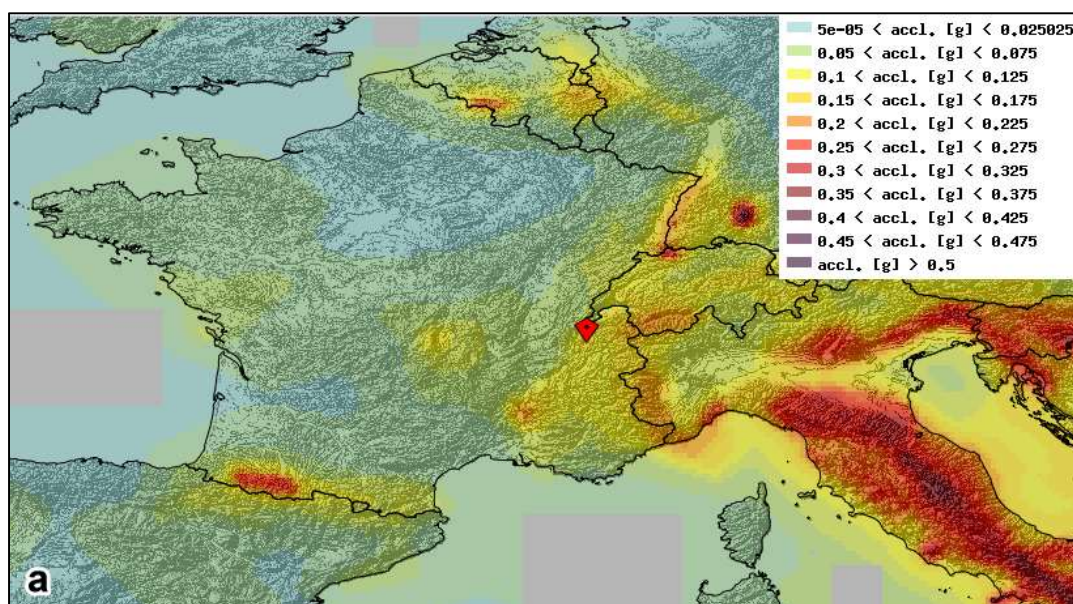


Figure A4.8.7. Mean Hazard map from the SHARE project for the broader area of France in terms of PGA for rock site conditions with a 10% probability of exceedance in 50 years (or 475 years of return period). The red diamond marks the epicentre of the 15th July 1996 earthquake in Épagny.

Table A4.8.2. Peak ground acceleration (PGA, g) values on rock with a 10% probability of exceedance in 50 years (475 years of return period) according to the French National Annex to Eurocode 8, GSHAP and SHARE. “Old zone Ib” refers to the nominal acceleration of the old seismic zonation in France (14th May 1991).

AREA	Old Zone Ib	French Annex to Eurocode 8	GSHAP	SHARE
Annecy	0.150 g	0.160 g	0.133 g	0.125 g

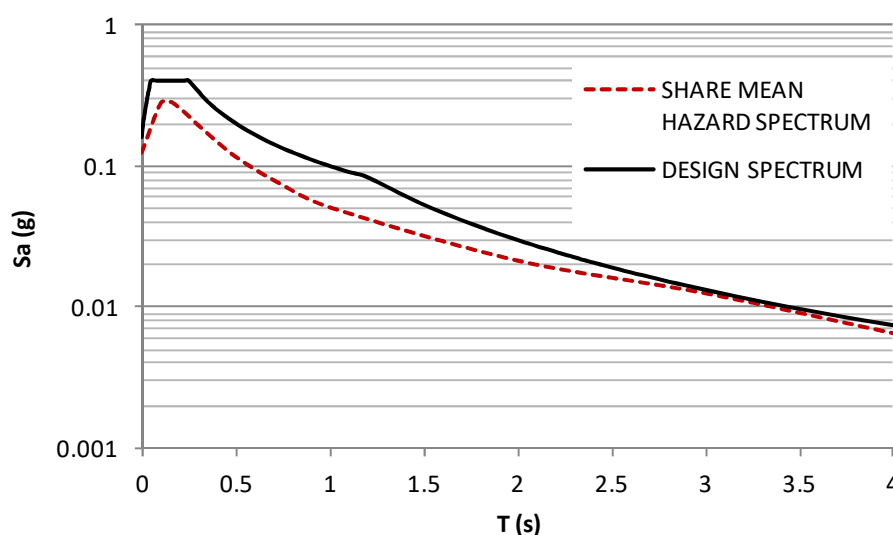


Figure A4.8.8. Uniform Hazard Spectra for the closest available coordinates to the city of Annecy, according to SHARE mean hazard model, vs Type II Eurocode 8 Design spectrum on the rock for input PGA=0.160 g.

A4.8.2 Earthquake source characteristics

A4.8.2.1 Location, depth and time

The main shock occurred on 15th July 1996, at 00.13 UTC (02.13 local time). Table A4.8.3 and Figure A4.8.9 show the estimations of the epicentral coordinates and hypocentral depth from several organizations and agencies. No solution for the location or the focal mechanism of this event is available from the Global Centroid Moment Tensor (GCMT; Dziewonski *et al.*, 1981; Ekström *et al.*, 2012) catalogue. Cells marked as (*f) correspond to parameters that were held fixed while inversion was carried out to retrieve those that remain.

The epicentre was located at the city of Épagny, at the south-east segment of the Vuache fault. Many different estimates concur that the focal depth was very shallow, at about 3-5 km. Dufumier (2002) mentions that the macroseismic depth of 3-5 km deduced by macroseismic observations of Scotti *et al.* (1999) is compatible to the most thorough work of Thouvenot *et al.* (1998) who suggest a focal depth of 2-3 km. Similarly, Dominique *et al.* (1996) report that the 3 km depth for the main shock is common for strike-slip faults. However, Dufumier (2002), who performed moment tensor inversion using regional surface waves, with the best fit detected at 10 km, considered unlikely that the hypocentre was located at a depth of less than 5 km. Fixing the depth at 3 km is hypothesised to be the reason for the incompatibility between the normal faulting focal mechanism solution of Bock (1997) and the local tectonics (see Section A4.8.2.3). Based on their comparison between macroseismic intensity data and their model for the prediction of macroseismic intensity, Marin *et al.* (2004) also support the idea of a deeper hypocentre.

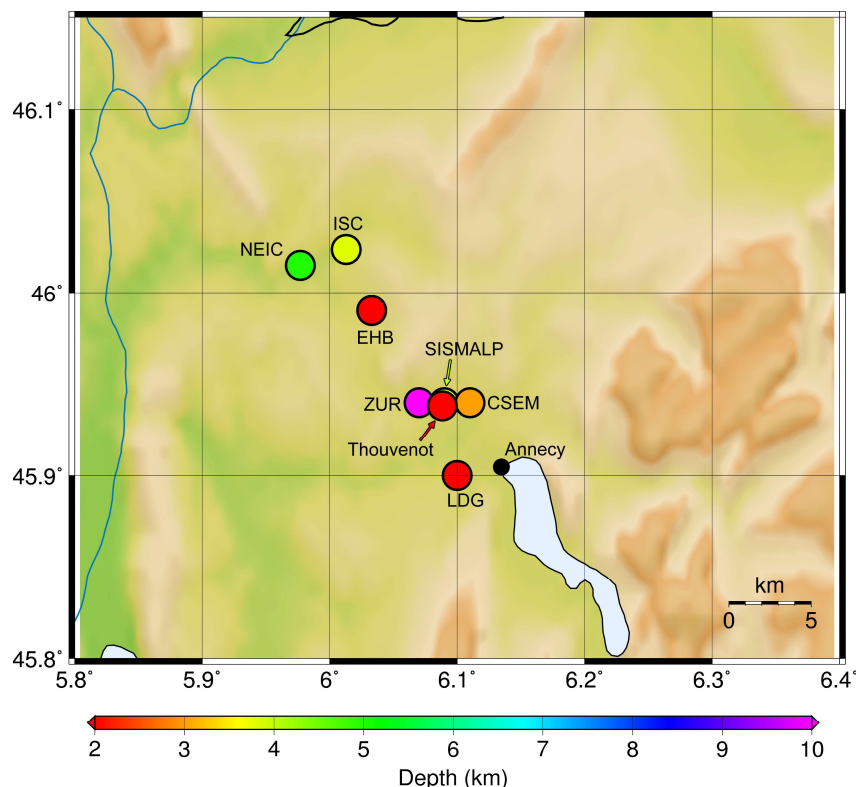


Figure A4.8.9. Estimation of epicentral coordinates by each source listed in Table A4.8.3.

Table A4.8.3. Epicentral coordinates and hypocentral depths from different sources.

Agency / Publication		Latitude	Longitude	Depth (km)
ISC	International Seismological Centre	46.0236 °N	6.0129 °E	3.8
EHB	ISC-EHB Bulletin (Engdahl <i>et al.</i> , 1998)	45.9900 °N	6.0330 °E	2.0 (*f)
SISMALP	Laboratoire de Géophysique Interne et Tectonophysique de l'Observatoire de Grenoble	45.9400 °N	6.0900 °E	4.0
NEIC	National Earthquake Information Center (USGS)	46.0150 °N	5.9770 °E	5.0
ZUR	Swiss Seismological Service (SED)	45.9400 °N	6.0700 °E	10.0
LDG	Laboratoire de Détection et de Géophysique/CEA	45.9000 °N	6.1000 °E	2.0
EMSC	European-Mediterranean Seismological Centre	45.9400 °N	6.1100 °E	3.0
Thouvenot <i>et al.</i> (1998) (relocated)		45.9383 °N	6.0883 °E	2.0 (*f)

(*f) fixed parameter used for inversion

A4.8.2.2 Magnitude

Estimations of magnitude made by various agencies and authors are reported in Table A4.8.4. The **M**5.3 value reported by the EMSC and obtained through moment tensor inversion (Bock, 1997) has been considered as an overestimation by Dufumier (2002) due to the very low, fixed focal depth of 3 km. Others (Cornou, 1997; Courboux *et al.*, 1999; Dufumier, 1999) report more conservative values of moment magnitude. A final value of **M**4.8, the average calculated by Dufumier (2002) from different sources, is adopted herein.

Table A4.8.4. Estimations of moment magnitude (**M**), local magnitude (M_L), body-wave magnitude (m_b) and surface-wave magnitude (M_s).

Agency / Publication		M	M_L	m_b	M_s
NEIC	National Earthquake Information Center (USGS)	-	-	4.5	-
ISC	International Seismological Centre - GEM catalogue	-	-	4.3	4.2
EMSC	European-Mediterranean Seismological Centre/Bock (1997)	5.3	-	-	-
LDG	Laboratoire de Détection et de Géophysique/CEA	-	5.3	-	-
ZUR	Swiss Seismological Service (SED)	-	5.4	-	-
IDC	International Data Center	-	-	4.17	-
ReNaSS	Reseau National de Surveillance Sismique, Strasbourg	-	5.2	-	-
Scotti <i>et al.</i> (1999)		-	4.65	-	-
Dufumier (1999), as reported in Dufumier (2002)		4.2	-	-	-
Cornou (1997)		4.7	-	-	-
Courboux <i>et al.</i> (1999)		4.8	-	-	-

A4.8.2.3 Style-of-faulting

The first focal mechanism solution of the 15th July 1996 Épagny earthquake was determined by the rapid moment tensor inversion scheme of the EMSC, using regional recordings of long period (20-50 s) waveforms (Bock, 1997). However, this solution suggested oblique-normal to normal faulting (Figure A4.8.10, right), which is incompatible with the Vuache fault, which is a well-established left-lateral, strike-slip structure, and is also incompatible with the polarities of the P-wave onsets (Dufumier, 2002). A more

adequate faulting style was determined using first motion polarities by Thouvenot *et al.* (1998) in a most comprehensive study of the 1996 Épagny earthquake, with one of the two nodal planes indicating NW-SE trending, sinistral strike-slip faulting, with a steep dip (80°) towards the northeast, as shown in Figure A4.8.10 (left). A similar solution was verified by Dufumier (2002) using moment tensor inversion. Table A4.8.5 summarises these last three solutions.

Table A4.8.5. Fault plane solutions and fault planes from different sources. Fault planes marked in grey are the preferred solution in each case.

Fault Plane 1			Fault Plane 2			Source
Strike	Dip	Rake	Strike	Dip	Rake	
59	80	-160	316	70	-11	Thouvenot <i>et al.</i> (1998)
65	46	-124	289	53	-60	Bock (1997)
53	72	-174	321	84	-18	Dufumier (2002)

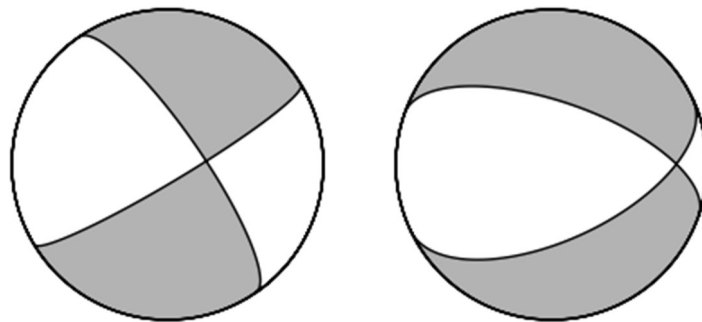


Figure A4.8.10. Two different types of focal mechanisms for the 15th July 1996 Épagny mainshock, one indicating mainly NW-SE strike-slip faulting (Thouvenot *et al.*, 1998; left) and another suggesting a nearly E-W trending fault with a significant normal component (Bock, 1997; right).

According to Thouvenot *et al.* (1998), Bock (1997) provided two possible explanations for the observed discrepancy of the EMSC solution. The first was that it could be due to a change of the mechanism during the rupture, beginning as strike-slip but evolving to oblique-normal, causing contradiction between the results of first motion polarities and moment tensor inversion. However, Thouvenot *et al.* (1998) believes that this explanation is unlikely for events of moderate magnitude and short rupture time, and that the most probable scenario is that a tenfold amplification of Rayleigh waves occurred towards the north, due to strong lateral inhomogeneities, which could also explain the overestimated values of seismic moment (**M**5.3).

Despite the moderate magnitude of the 15th July 1996 Épagny earthquake, Courboux *et al.* (1999) detected directivity effects. Using the seismograms of two aftershocks as empirical Green's functions, they observed that the rupture was composed of two sub-events that can be linked to two distinct spatial clusters that were discriminated in the aftershock sequence. The larger one, which includes the best estimate of the mainshock's hypocentre, lied 500 to 800 m northeast of the Vuache fault, while the smaller one occurred closer to the fault trace, to the south of the former (Thouvenot *et al.*, 1998). While proposing three alternative rupture propagation scenarios, Courboux *et al.* (1999) favour

one in which the entire rupture took place within the southern segment, with a very short propagation to the northwest and a longer one to the south east. They believe that the epicentral coordinates that would result for the main shock from this scenario would still be within the uncertainty associated to those of Thouvenot *et al.* (1998). Thouvenot *et al.* (1998), however, suggested that the south-east-directed propagation started at the mainshock's hypocentre on the northern cluster and broke the two distinct segments in cascade. They believe that the dense concentration of aftershocks along the north-western edge indicates that the Mandallaz mountain might have acted as a barrier, restricting the rupture to the south-east part of the Vuache fault.

A4.8.2.4 Stress drop

Courboux *et al.* (1999) calculated a seismic moment of $1.9 \cdot 10^{16}$ N·m (**M4.8**) from the recordings of station SGEM in Geneva, located approximately 30 km away from the epicentre. Through their analysis, they estimated a stress drop value of 5.5 MPa, assuming a rupture velocity of 3 km/s and an approximate rupture area of 2.5 km².

A4.8.2.5 Foreshocks and aftershocks

Although the Vuache fault has been seismically active in the past, only two events reportedly occurred within the one year before the mainshock of 15th July 1996, with a magnitude slightly less than 2.0 (see Table A4.8.6). Thouvenot *et al.* (1998) considers the possibility that the second of these two events, which occurred on 2nd August 1995 with an epicentre close to the northwest part of the area that was activated in 1996, as shown in Figure A4.8.11, could be a foreshock of the 1996 earthquake in Épagny because the unusually long duration of the aftershock sequence could justify an unusually early precursory event.

Table A4.8.6. Foreshocks, mainshock and aftershocks of the 15th July 1996 earthquake in Épagny.

Origin time (UTC after 1960)	Location	Magnitude	I _o (MSK)
02/08/1995 03:05	Sillingy (Vuache f.)	2.0	IV
21/08/1995 19:32	Sillingy (Vuache f.)	2.0	III
15/07/1996 00:13	Epagny (Vuache f.)	M4.8	VII-VIII
23/07/1996 04:08	Epagny (Vuache f.)	4.3	V
16/04/1998 12:35	Annecy (Vuache f.)	3.1	

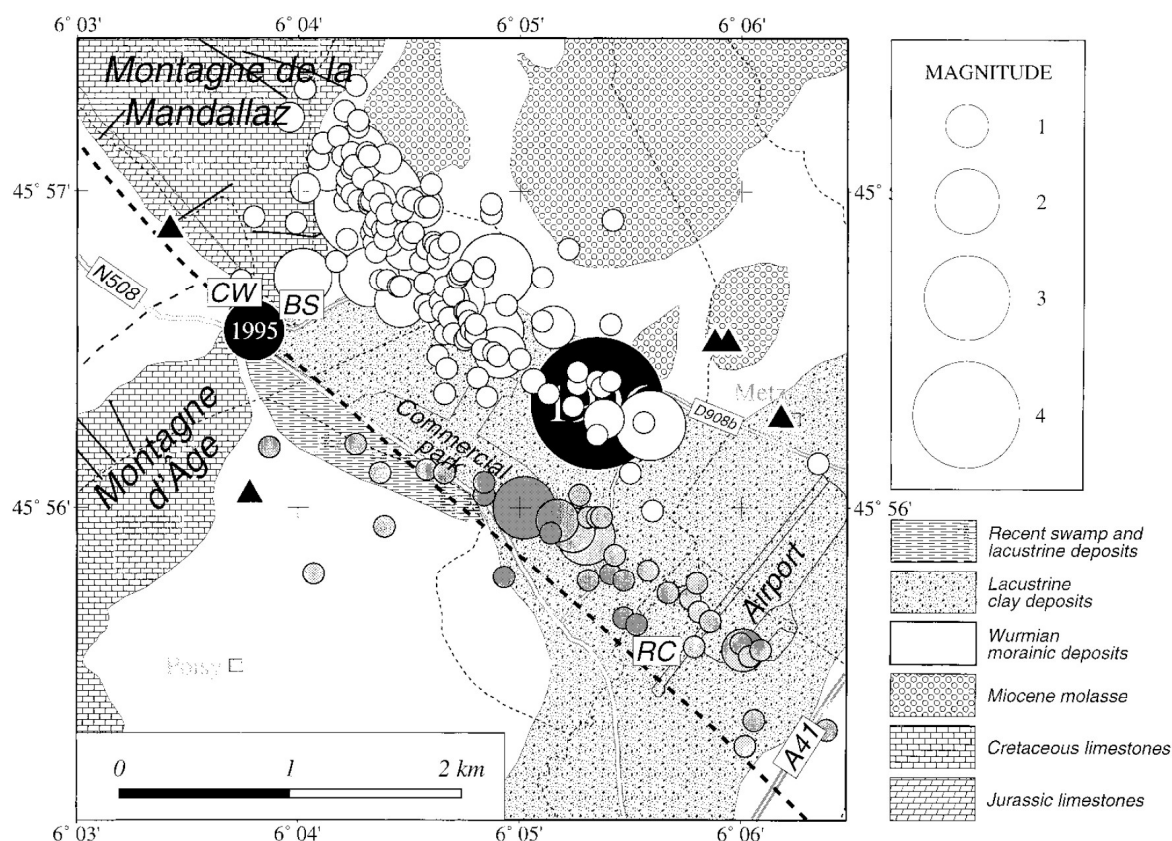


Figure A4.8.11. Map of the aftershock sequence of the 15th July 1996 earthquake in Épagny (large black circle). White and shaded circles denote the major and minor distinct spatial clusters. The smaller black circle represents the foreshock of 2nd August 1995. The thick dashed line represents the inferred extension of the Vuache Fault. From Thouvenot *et al.* (1998).

Several hundreds of aftershocks were recorded by a temporary seismological network of ten single-component stations that was installed by the Observatoire de Grenoble on the same day as the mainshock, within 4 km of the epicentre, complemented by four 3-component and two single-component stations two days later (Thouvenot *et al.*, 1998). The largest aftershock, of M_L 4.3, occurred 8 days later on 23rd July, near the north-west edge of the aftershocks distribution. Thouvenot *et al.* (1998) reports that the duration of the aftershock sequence was unusually long, with events of $1 \leq M_L \leq 2$ being recorded and felt in the area even two years after the mainshock. The aftershocks distribution, which is shown in Figure A4.8.11, is 5 km long, spread in the NW-SE direction (N310E), and is compatible with the left-lateral Vuache fault, as is also indicated by the focal mechanism of the mainshock (strike N316E). The hypocentres are constrained at depths shallower than 4.7 km, with 96% of them having occurred inside a limestone layer corresponding to the Upper Jurassic (Tithonian) and Lower Cretaceous (Urgonian) series, as shown in Figure A4.8.12 (Thouvenot *et al.*, 1998). The focal mechanisms of most aftershocks are similar to that of the main event, with a few, however, having a more significant normal component.

As mentioned in Section A4.8.2.3 and shown in Figure A4.8.11, two clusters of aftershocks can be identified. The mainshock was located by Thouvenot *et al.* (1998) at the southeast end of the larger and deeper northern cluster, while the less populated and shallower southern cluster, offset from the former by around 500 to 800 m, apparently hosted the 1995 foreshock at its NW extension. The steep dip (N73E) of the main (northern) structure

is in agreement with the focal mechanism while the latter structure is considered to have acted as an up-stepping splay of the main fault (Thouvenot *et al.*, 1998).

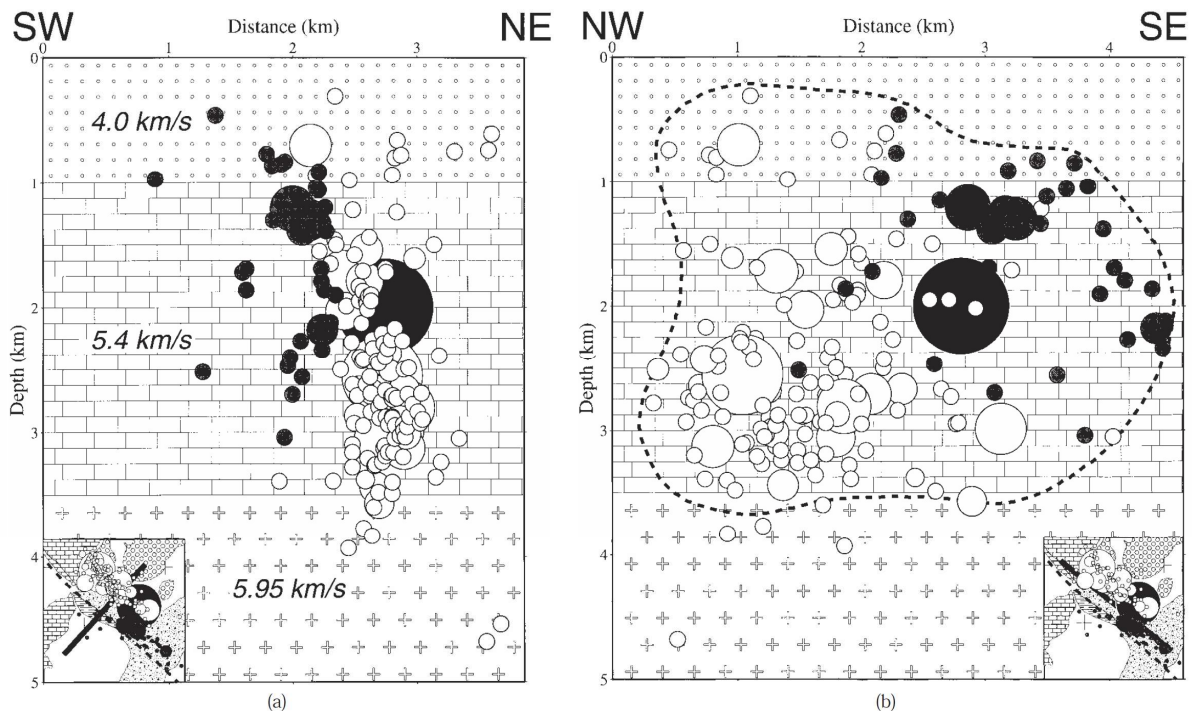


Figure A4.8.12. Cross-sections of the aftershocks distribution perpendicular (left) to the Vuache fault and along strike (right). White circles correspond to the main (northern) cluster and dark circles to the southern cluster. The mainshock is depicted by a large black circle. The thick dashed line is the inferred extension of the 10 km² rupture surface. From Thouvenot *et al.* (1998).

A4.8.2.6 Nature of earthquake

There is no evidence to suggest that the mainshock of 15th July 1996 was either induced or triggered by anthropogenic activity. It is considered a tectonic earthquake, a result of the slow accumulation of stress due to a deformation rate of ~1mm/yr on the Vuache fault (Thouvenot *et al.*, 1998).

A4.8.3 Geology and ground conditions in the affected area

A4.8.3.1 Regional geology and topography

The Community of Greater Annecy is located between the Jura mountains and the external Alps, at the boundary between the subalpine massif of Bornes and Bauges, in the east and south-east, respectively, and the molassic plain in the north-west (Dominique *et al.*, 1996). The latter formations are of lower Miocene age (23 – 16 Ma) and are constituted of limestone, marls and conglomerates. They overlay carbonate formations of Mesozoic age (Jurassic and Cretaceous).

Folded structures (Jura folds) are present in the northwest of Annecy, forming the mountains (from north to south) of Saleve, Mandallaz and Age, all of them located to the

north-north-west of Annecy (Figure A4.8.11, Figure A4.8.13). These folds and reverse faults/thrusts are cross-cut by the almost perpendicular Vuache sinistral strike-slip fault. In the late Quaternary, glaciers contributed to the development of depressions which are now filled with glacial, fluvial and lacustrine deposits of Upper Pleistocene and Holocene age, during or after the Würm glaciation, the last glacial period in the Alpine region (Dominique *et al.*, 1996). As shown in Figure A4.8.13, the urban settlement of Annecy is located along the valley of the mountain ranges that surround it.

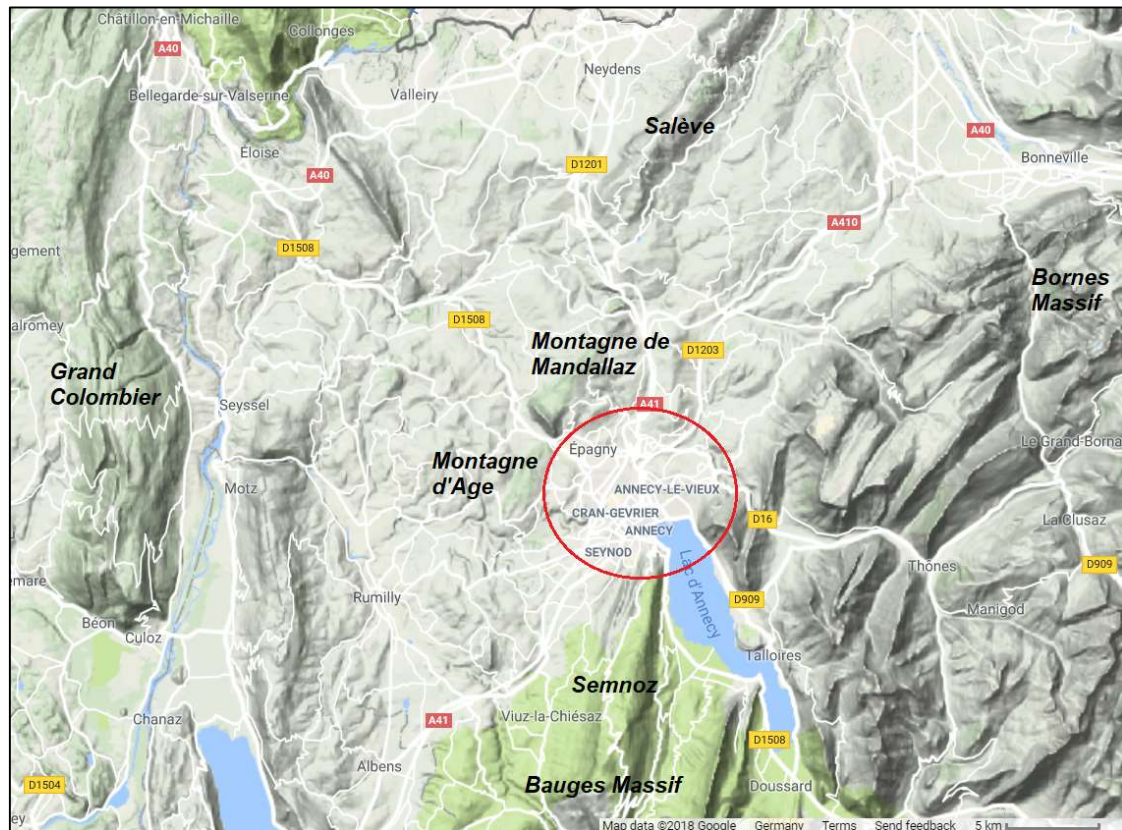


Figure A4.8.13. Topography of Annecy (enclosed in red circle) and its surroundings. Mountains indicated in bold italics. From Google Maps.

According to Dominique *et al.* (2008), the bedrock in the area of the Community of Greater Annecy can be divided into three zones:

- 1) the mountains of Ages and Mandallaz in the northwest, mainly composed of limestones and marls of Jurassic and Cretaceous age;
- 2) the Bornes and Bauges massifs in the south, mainly composed of limestone and marls of Cretaceous age;
- 3) peri-Alpine molassic formations between the abovementioned zones.

Most of the landscape in the area is covered by Cretaceous terrains, with a series of limestone cliffs and of embankments composed of softer rocks (sandstone or marls). Tertiary formations, consisting of sandy limestones, sandstone and marls outcrop locally on the sides of the hills. During Aquitanian-Chattien, lacustrine red molasses were deposited, forming the peri-Alpine molassic furrow, composed of a succession of coarse sandstones and marls up to 1000 m thick. In the Quaternary, during the Würm glaciation,

the glaciers from Mont Blanc and the Rhone eroded the molassic furrow and deposited most of the ground moraine, usually covered by regressional moraine, composed of boulders and pebbles in a sandy-clay melange. Lacustrine deposits composed of silt and clay (distal ones, north-west of Epagny and south of Annecy) or gravels and sands (proximal ones), created by the filling of lakes after the glacial retreat, are found in the areas of Epagny, Metz-Tessy, Cran-Gevrier, Meythet, Annecy and Pringy. Modern fluvial deposits, consisting of coarse gravels in a sand-clay formation, are only present on the banks of the main rivers such as Fier and Thiou, while a system of two nested fill terraces is formed at Cran-Gevrier (Dominique *et al.*, 2008).

A4.8.3.2 Site conditions in the affected area

According to the USGS Global V_{s30} model (Wald & Allen, 2007), an extract of which is shown in Figure A4.8.14, the broader area of the Community of Greater Annecy is generally described by values around 750 m/s, relatively larger than those of many other regions in France, with the mountainous regions reaching up to 900 m/s while the alluvial plains exhibit smaller values, around 500 m/s and down to 350 m/s in Annecy. The USGS ShakeMap for Epagny event uses a reference rock V_{s30} of 686 m/s for the mainshock.

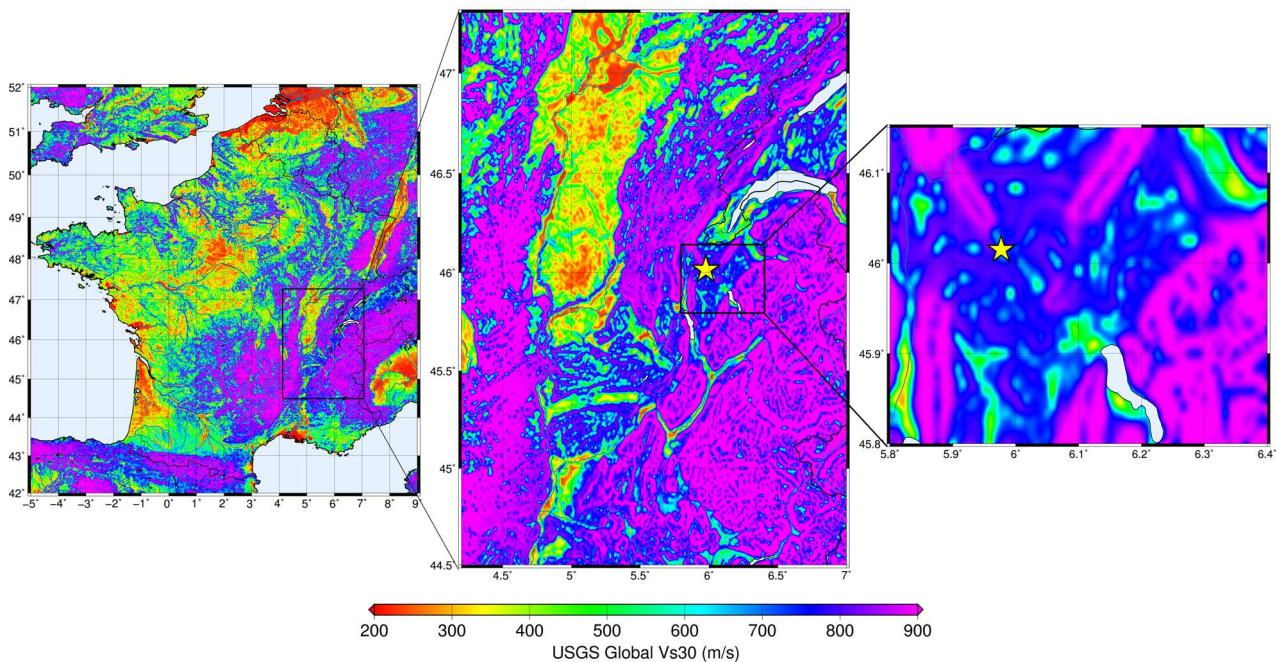


Figure A4.8.14. Map of V_{s30} (m/s) for France (left), the broader area of the Haute-Savoie department (middle), and the broader area of Annecy (right). The star denotes the epicentre of the 15th July 1996 mainshock. Maps generated using data from the USGS Global V_{s30} model (Wald & Allen, 2007).

The town of Épagny is located on thick alluvial gravels, with a thickness of 30 m, over 150 m of very thick lacustrine clays (Baize *et al.*, 2011). The topography of the Annecy basin is generally low, with several areas below 500 m (shaded parts of Figure A4.8.15), but there are also hills of bedrock, such as Annecy-le-Vieux, and the Mandallaz mountain. Soon after the mainshock, Thouvenot *et al.* (1998) installed four accelerometric stations on the alluvial plain and one station (VIEU) on the hill of Annecy-le-Vieux and inverted the signals

of 30 aftershocks to obtain the site response function at each station. Their results, which are depicted in Figure A4.8.15, showed that station VIEU had a spectral ratio close to 1, thus no site amplification, while the other stations exhibited amplification up to 8 in the range between 1 and 10 Hz (0.1-1.0 second periods), with buildings in the area having a resonant frequency within this range (between 1 and 5 Hz, *i.e.*, 0.2-1.0 seconds) (Thouvenot *et al.*, 1998).

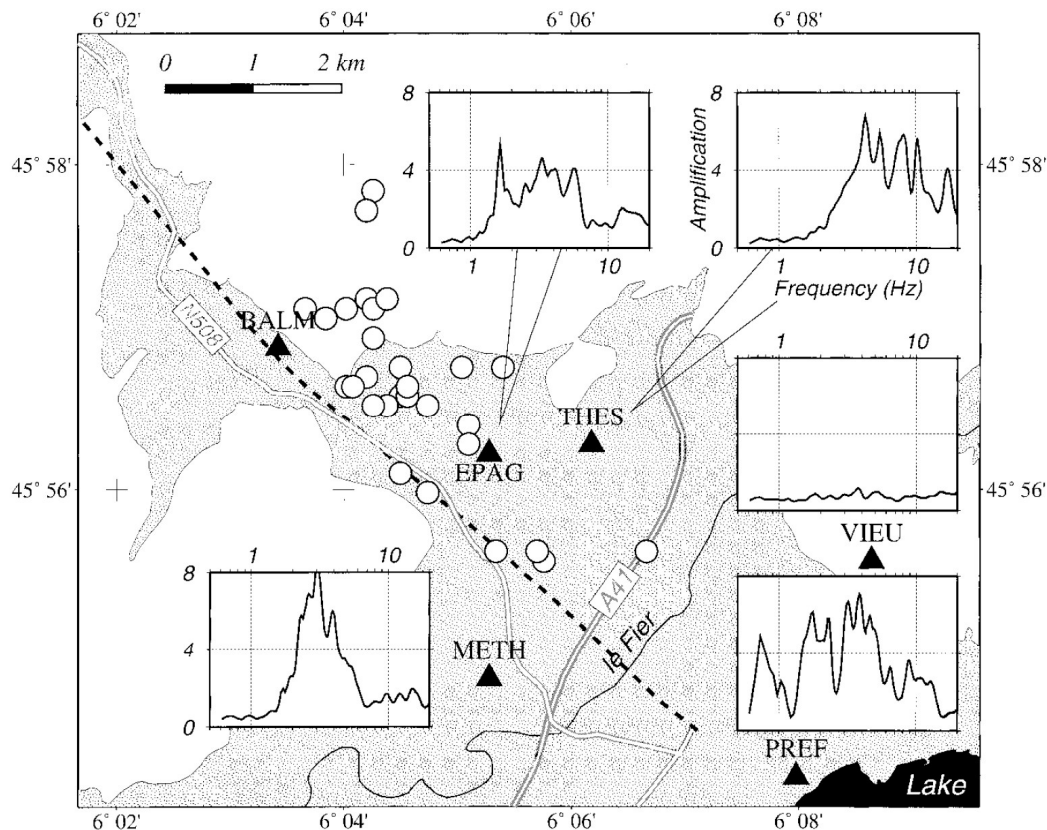


Figure A4.8.15. Site response functions for five stations (triangles) in the area of Annecy. Shaded parts of the map denote where topography is lower than 500 m, which broadly coincides with the urban settlements. White circles denote the aftershocks that were used for the measurements. From Thouvenot *et al.* (1998).

The more recent official microzonation of the Annecy basin shown in Figure A4.8.16 was elaborated by the French Geological Survey (Bureau des recherches Géologiques et Minières, BRGM) and divides the area into five zones for soils (Z1 through Z5) and one for rock (Z0). For each of these areas, a reference acceleration spectrum to be used for buildings of EC8 Class B is defined. All of them start at a PGA between 2.0 to 2.9 m/s² but differ substantially in their corner periods and the spectral acceleration at the plateau, as shown in Table A4.8.7. The largest amplification is expected for zone Z2, followed by Z3. According to the map of Figure A4.8.16, both Épagny and the town of Annecy are located in zones Z3 to Z4. Metz-Tessy, which was severely damaged during the earthquake, is located in zone Z2.

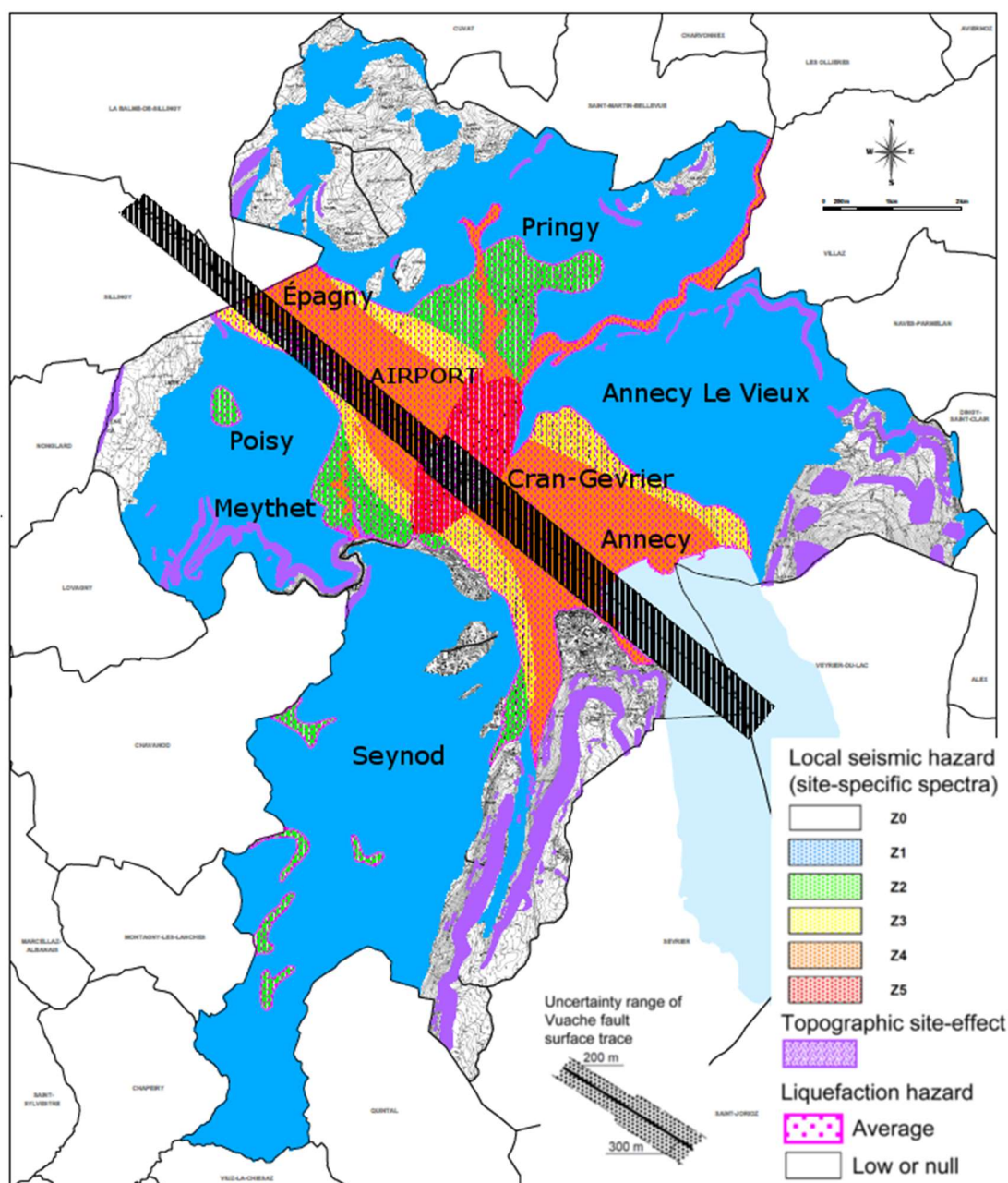


Figure A4.8.16. Seismic microzonation of the Community of Greater Annecy. Figure modified after BRGM (2008b).

Table A4.8.7. PGA, spectral acceleration at the plateau and corner periods of the plateau for the spectra of zones Z0 through Z5 buildings of Class B and for bridges of category I (EC8). Data from BRGM (2008a).

ZONES	T _B (s)	T _C (s)	PGA (m/s ²)	Plateau (m/s ²)
Zone 0	0.10	0.18	2.0	5.0
Zone 1	0.08	0.14	2.3	9.0
Zone 2	0.15	0.23	2.9	15.35
Zone 3	0.15	0.30	2.6	10.0
Zone 4	0.16	0.28	2.3	7.0
Zone 5	0.16	0.25	2.3	7.0

The microzonation map of Figure A4.8.16 delineates as well the areas susceptible to topographic site effects and liquefaction. All the areas affected by the 1996 earthquake are characterized by average liquefaction hazard (BRGM, 2008b). Peripheral areas lying on moraines, molasses, limestones and old alluvial deposits are classified as having low to no liquefaction hazard. Areas indicated as having a potential for topographic site effects lie in the mountainous surrounding the main urban settlements. Susceptibility to landslides and rockfalls is high in those areas as well (BRGM, 2008c).

Finally, it is interesting to mention that local newspapers of neighbouring localities of Haute-Savoie (Le messager, 2016) make reference to the concern of the locals that a potential earthquake may cause fluctuations in the rich underground water table (Evian sources are located there) and lead to landslides and rockfalls. The destabilization itself of Evian water sources would be very damaging for the local economy.

A4.8.4 Ground motions

A4.8.4.1 Intensity observations

The maximum reported macroseismic intensity for the 15th July 1996 main shock in Épagny was about VIII on the MSK64 scale (Medvedev & Sponheuer, 1969) in the vicinity of Annecy (Bisch, 1996). The radii of the MSK64 VII (“very strong”, *i.e.*, causing fear to people, shifting and overturning furniture, causing objects to fall from shelves, serious damage to old buildings, collapse of masonry chimneys and small landslides) and MSK64 VIII (“damaging”, *i.e.*, causing people to feel unstable even outdoors, partial collapse of older structures, opening of cracks and fissures) isoseismals were around 7 and 3 km, respectively, as depicted in Figure A4.8.17 (Thouvenot *et al.*, 1998). The distribution of isoseismals shows an internal ellipsoid of higher intensity (MSK64 V) spreading towards the northeast to Geneva (30 km from epicentre), while an outer ellipsoid of lower intensity (MSK64 III and IV) spreads towards the southwest to Grenoble (87 km from epicentre) and Lyon (98 km from epicentre), though intensities of II and III have also been reported towards the north-west. The map of Figure A4.8.17 was created from the processing of 3,283 answers to questionnaires distributed to the public on request of the Bureau Central Sismologique Française (BSCF, 1996).

The high intensity of this earthquake has been mainly attributed to its shallow hypocentral depth and to site amplification effects due to the lacustrine deposits in the Annecy basin, which may have been able to amplify the strong ground motion up to 8 times, as measured for a subset of 30 aftershocks by Thouvenot et al., 1998 (Figure A4.8.15).

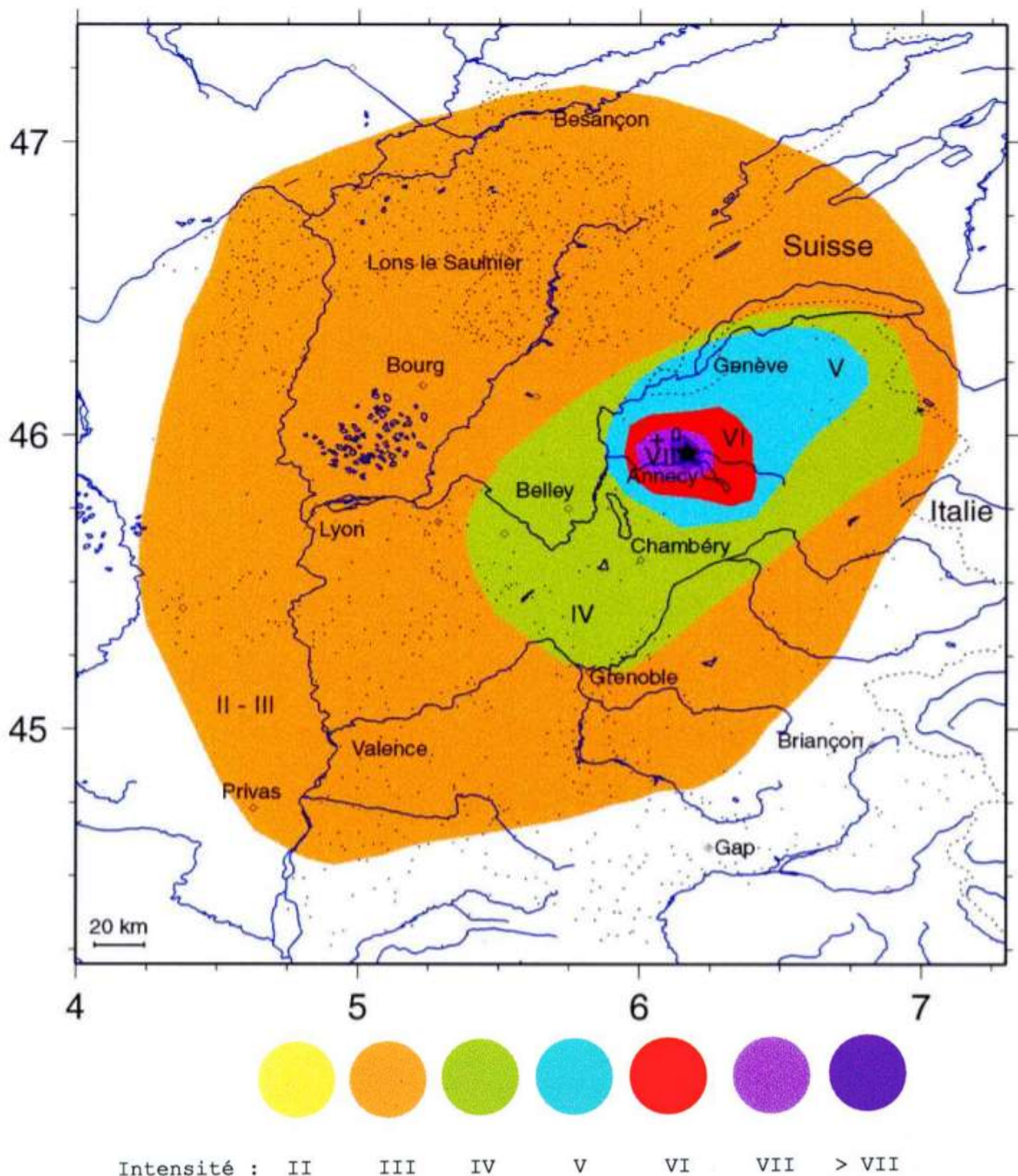


Figure A4.8.17. Isoseismal curves for macroseismic intensities in the MSK64 scale for the earthquake of 15th July 1996 in Épagny. Macroseismic epicentre indicated with star. Instrumental epicentres according to the National Seismic Surveillance Network (ReNaSS) and the local network indicated with a plus symbol and a circle. From BCSF (1998).

For unknown reasons, the macroseismic intensity map available from SisFrance (1996) for this earthquake is different from that shown in Figure A4.8.17 in terms of the shape of the isoseismals. Figure A4.8.18 (left) displays the macroseismic observation points per locality as reported by SisFrance (1996) in MSK-64 scale and Figure A4.8.18 (right) illustrates the isoseismals generated using these points, which indicate a maximum MSK-64 intensity of 7-7.5, which agrees with the VII-VIII of Figure A4.8.17.

The ShakeMap (Worden *et al.*, 2017) for the 1996 Epagny earthquake in terms of MMI instrumental intensity elaborated by the USGS shown in Figure A4.8.19 makes use of data from 3 seismic stations and the 782 points of macroseismic intensity from SisFrance (1996). The Ground-Motion/Intensity Conversion Equation (GMICE) of Worden *et al.* (2012) and Intensity Prediction Equations (IPE) as developed by USGS have been applied. The maximum instrumental MMI Intensity computed is 7.4, compatible with the macroseismic MSK64 intensity of VIII of Figure A4.8.17 based on observed damage. Interestingly, USGS EXPO-CAT database (Allen *et al.*, 2009; USGS-PAGER) only enumerates population exposed up to MMI values of 5.5.

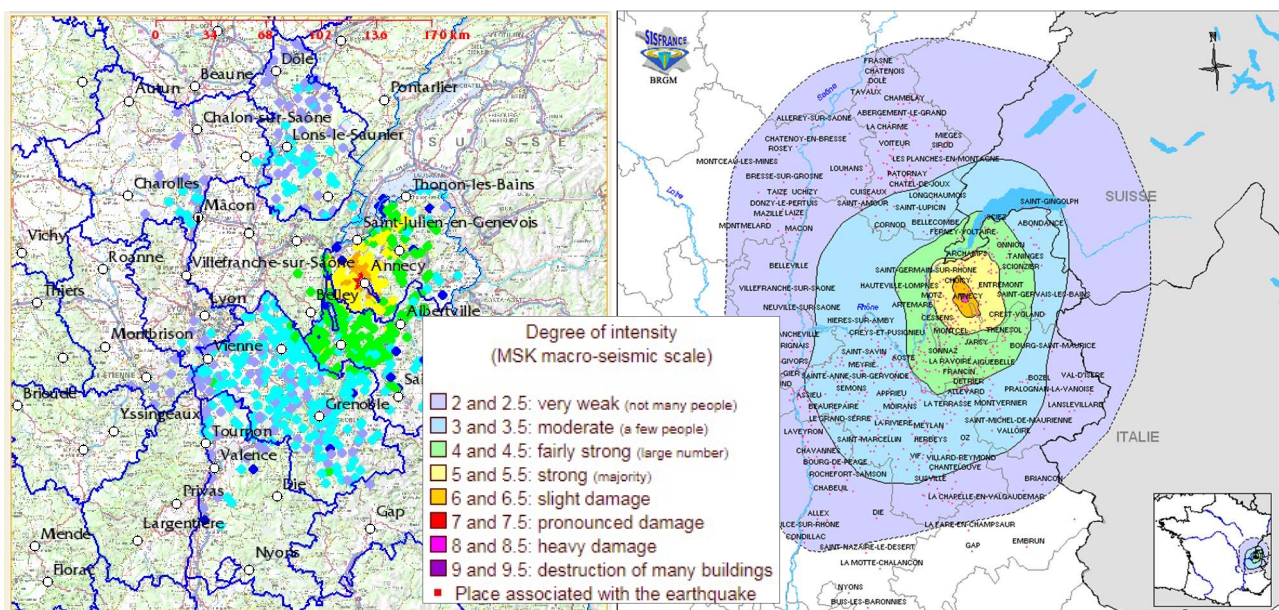


Figure A4.8.18. Macroseismic MSK-64 intensity observations per prefecture (left); map of isoseismals according to abovementioned recordings (right). Maps from SisFrance (1996).

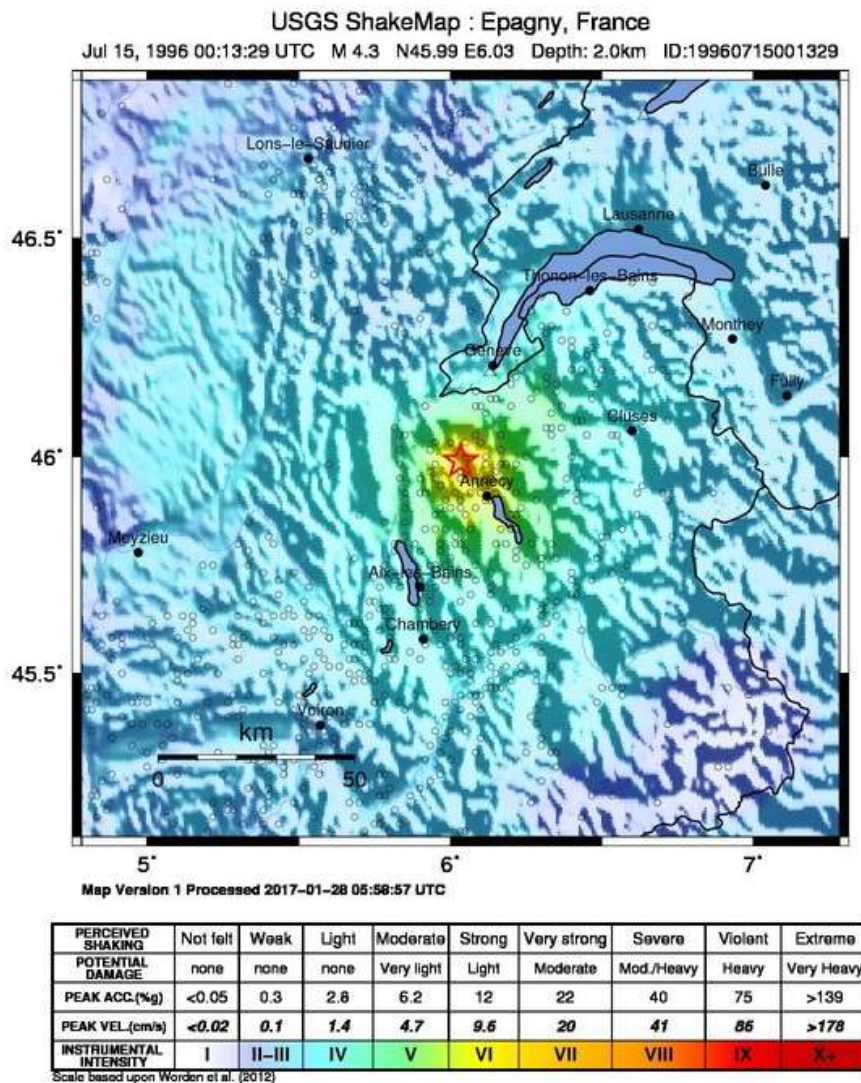


Figure A4.8.19. USGS Shakemap (2017) in terms of Modified Mercalli Intensity (MMI). The red star is the epicentre of the main shock.

A4.8.4.2 Ground motion recordings

No local accelerometric stations were operational at the time that the main shock occurred. The closest station was SGEM in Geneva at an epicentral distance of 31 km, which recorded a maximum acceleration of 8 cm/s² (0.008 g). Station OGSi (Sixt-Fer-a-Cheval) of the French Accelerometric Network (RAP), at a distance of 55 km ENE of the epicentre and lying over EC8 soil type A (rock) according to the Engineering Strong Motion (ESM) Database, recorded a maximum acceleration value of around 1 cm/s² (0.001 g) (Dominique *et al.*, 1996; acceleration time series displayed in Figure A4.8.20). Data from the three stations whose location is shown in Figure A4.8.21 is available from the Engineering Strong Motion (ESM) Database (Luzi *et al.*, 2016), and can be also found in Dominique *et al.* (1996) and VCE (2013). Table A4.8.8 summarises the information from all the ground motion recordings available with increasing epicentral distance.

Figure A4.8.22 presents the pseudo-acceleration response spectra for the OGAG, OGSi and OGGM records available for the main shock. The highest pseudo-acceleration (S_a) value corresponds to a natural period of 0.08 s and is observed at the N-S component of

OGSI station. The peak spectral parameters are listed for the available accelerograms in Table A4.8.9.

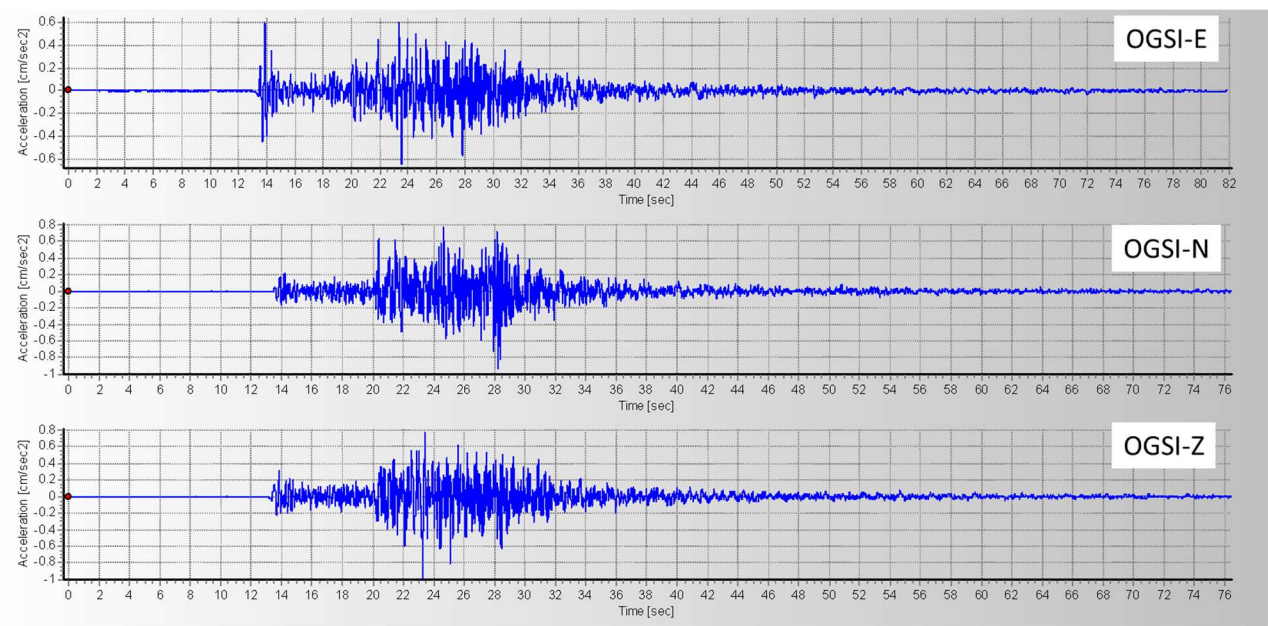


Figure A4.8.20. Acceleration time series of the 1996 mainshock recorded at OGS, located 55 km away from the epicentre over EC8 soil type A. Waveforms obtained from the ESM database (Luzi *et al.*, 2016), plots elaborated with Seismosignal (Seismosoft, 2016).

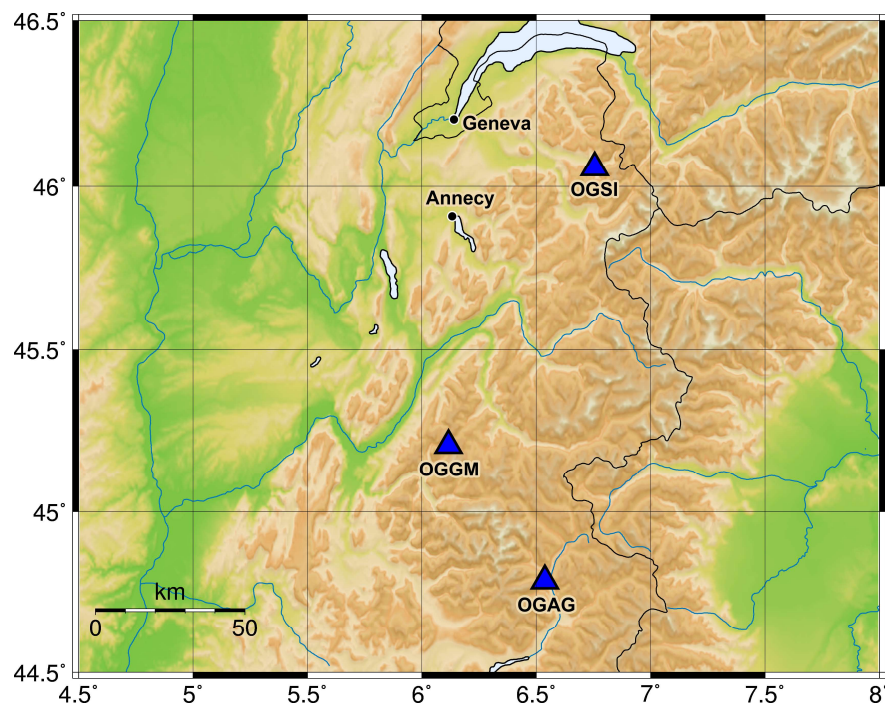


Figure A4.8.21. Accelerometric stations for which recordings of the 1996 earthquake are available in the ESM database.

Table A4.8.8. Peak ground acceleration (PGA), peak ground velocity (PGV) and epicentral distances for five records of the 15th July 1996 Épagny earthquake.

Network	Station	R _{epi} (km)	Component	PGA (cm/s ²)	PGV (cm/s)	Source
CH	SGEM	31.4	E-W	7.600	0.300	Dominique <i>et al.</i> (1996); VCE (2013)
			N-S	8.000		
			Z	7.400		
RA	OGSI	57.6	E-W	0.632	0.040	ESM database
			N-S	0.930	0.042	
			Z	1.054	0.047	
FR	OGGM	91.3	E-W	0.667	0.024	ESM database
			N-S	0.558	0.019	
			Z	0.666	0.024	
CH	SYVJ	102.0	-	4.000	0.120	VCE (2013)
FR	OGAG	143.6	E-W	0.077	0.005	ESM database
			N-S	0.085	0.004	
			Z	0.084	0.002	

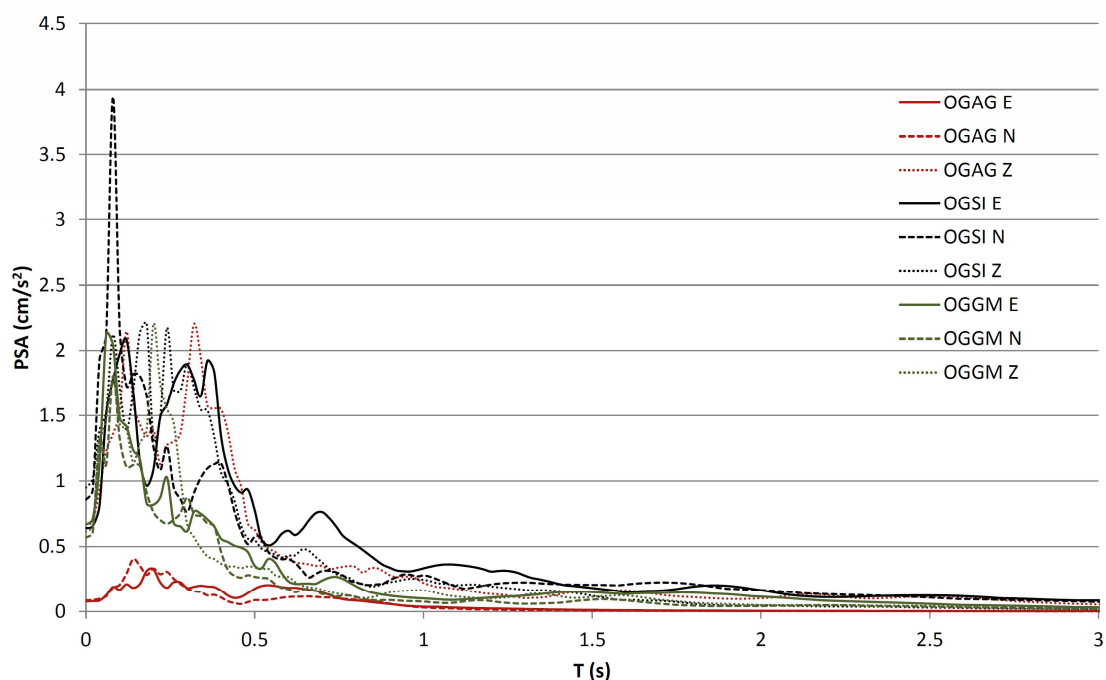


Figure A4.8.22. Pseudo-acceleration (Sa) response spectra obtained with Seismosignal (Seismosoft, 2016) for the time-series of the main shock available from the ESM Database.

Table A4.8.9. Summary of the peak spectral parameters of the mainshock. Data from the ESM Database, computations done with Seismosignal (Seismosoft, 2016).

Day	Time	Fundamental Period (sec)			Max Sa (cm/sec ²)			Station
		E	N	Z	E	N	Z	
15-Jul-96 00:13		0.12	0.08	0.18	2.1	3.9	2.3	OGSI
		0.06	0.08	0.2	2.1	1.8	2.3	OGGM
		0.2	0.14	0.32	0.3	0.4	2.2	OGAG

A4.8.4.3 Inferred shaking levels

Since no acceleration records are available for the mainshock at distances closer than 30 km, only theoretical estimates can be assumed for the shaking level in the meizoseismal area. Figure A4.8.23 shows the inferred PGA and the respective regression curves as reported by the USGS ShakeMap (Worden *et al.*, 2017), converted from macroseismic intensity values using the model of Worden *et al.* (2012) and combined with ground motion prediction models. At the nearest distance of around 3 km from the epicentre, the inferred PGA values are about 0.20 g, while a maximum value of 0.35 g may have been reached at a distance of ~8km, as may be seen from the inferred PGA points of Figure A4.8.23 (right). For reference, the PGA values of the proposed spectra for buildings of Class B in Annecy (see Section A4.8.3.2 and Table A4.8.7) are about 0.2 g for rock and up to 0.3 g for Zone 2, while the plateau reaches up to 1.56 g in Zone 2 and the respective SHARE estimate for PGA in Annecy is about 0.125 g with a 10% probability of exceedance in 50 years.

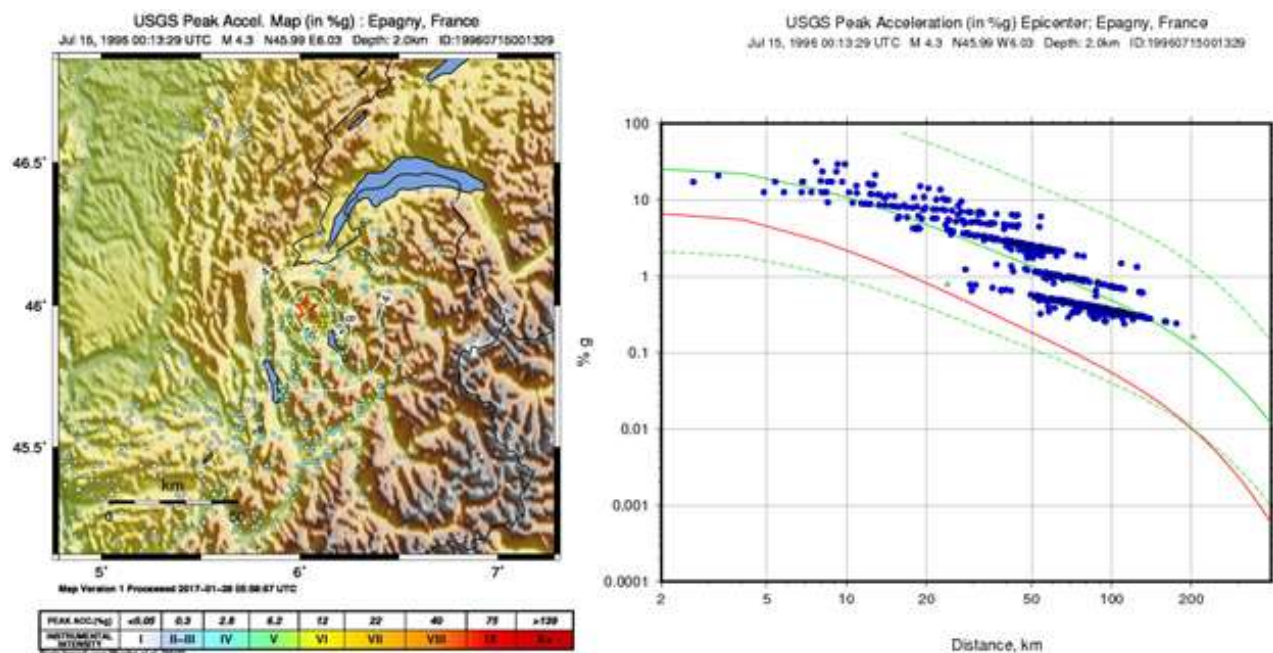


Figure A4.8.23. ShakeMap of inferred PGA (isolines) in the broader area of Annecy for the 15th July 1996 earthquake in Épagny (left); regression of inferred PGA relative to epicentral distance, with blue dots representing MMI observations (SisFrance, 1996) converted to PGA using the model of Worden *et al.* (2012) while red and green lines show the unbiased and biased Ground Motion Prediction Equations (GMPE) of Chiou and Youngs (2008), respectively (right). Dashed green lines show the GMPE $\pm 3\sigma$ bounds. Figures after USGS.

A4.8.4.4 Duration of ground shaking

As shown in Table A4.8.10, strong motion total and T90 effective durations in the range of 20-30 seconds have been reported for seismic records at epicentral distances larger than 30 km, (VCE, 2013; ESM). While no explanations are provided in either source, these are likely to refer to the complete accelerogram durations and the 5-95% of Arias definition of significant duration. The closest station, SGEM, at 31 km, installed on an alluvial flat plain, has the highest reported total duration of 29 sec (VCE, 2013), while other stations present a smooth raise in duration with increasing distance. Significant durations in terms of the 5-

75% of Arias intensity definition were also calculated using Seismosignal (Seismosoft, 2016) for three stations with available waveform data (ESM).

Estimations of earthquake significant durations in terms of 5-75% of Arias Intensity were calculated using the empirical models of Bommer *et al.* (2009) and Afshari & Stewart (2016) for a set of V_{s30} values: 260 m/s and 900 m/s, being the lowest and highest USGS V_{s30} value for Annecy, respectively (Figure A4.8.24), and 350 m/s and 573 m/s being the reported V_{s30} values for stations SYVJ (at 102 km) and SGEM, respectively. The models assume **M**4.8 and depth 1.0 km to the top of the rupture, assuming it reached the uppermost boundary of the limestone layer (Figure A4.8.12). The measured significant duration values for the closest available station, OGSJ, at a distance of around 58 km, are slightly higher than those estimated through both models for the lower V_{s30} values (260 m/s), in spite of lying over EC8 soil type A, which corresponds to V_{s30} values larger than 800 m/s. On the other hand, values for the E-W component at stations OGGM and OGAG are more compatible with harder soils (V_{s30} in the range 573-900 m/s), as expected, given that both of them are believed to lie over EC8 soil type A as well (ESM), while their respective significant duration for the N-S components is higher.

Table A4.8.10. Duration of strong motion for the 15th July 1996 earthquake in Épagny as reported by VCE (2013) and ESM, and 5-75% of Arias intensity definition of significant duration calculated from the waveforms available from ESM.

Network	Station	V_{s30} (m/s)	R_{epi} (km)	Significant Duration* (s)		Reported Duration (s)
				NS	EW	
CH	SGEM	573	31.4	-	-	29.0**
RA	OGSJ	1500	57.6	8.0	9.2	21.8***
FR	OGGM	3000	91.3	10.7	8.2	24.5***
CH	SYVJ	260	102	-	-	25.3**
FR	OGAG	1500	143.6	19.7	12.6	28.6***

* calculated from the waveforms available from the ESM database.

** "Total duration" reported by VCE (2013), likely referring to the complete accelerogram duration

*** T_{90} effective duration, reported by ESM, likely referring to the 5-95% of Arias definition of significant duration

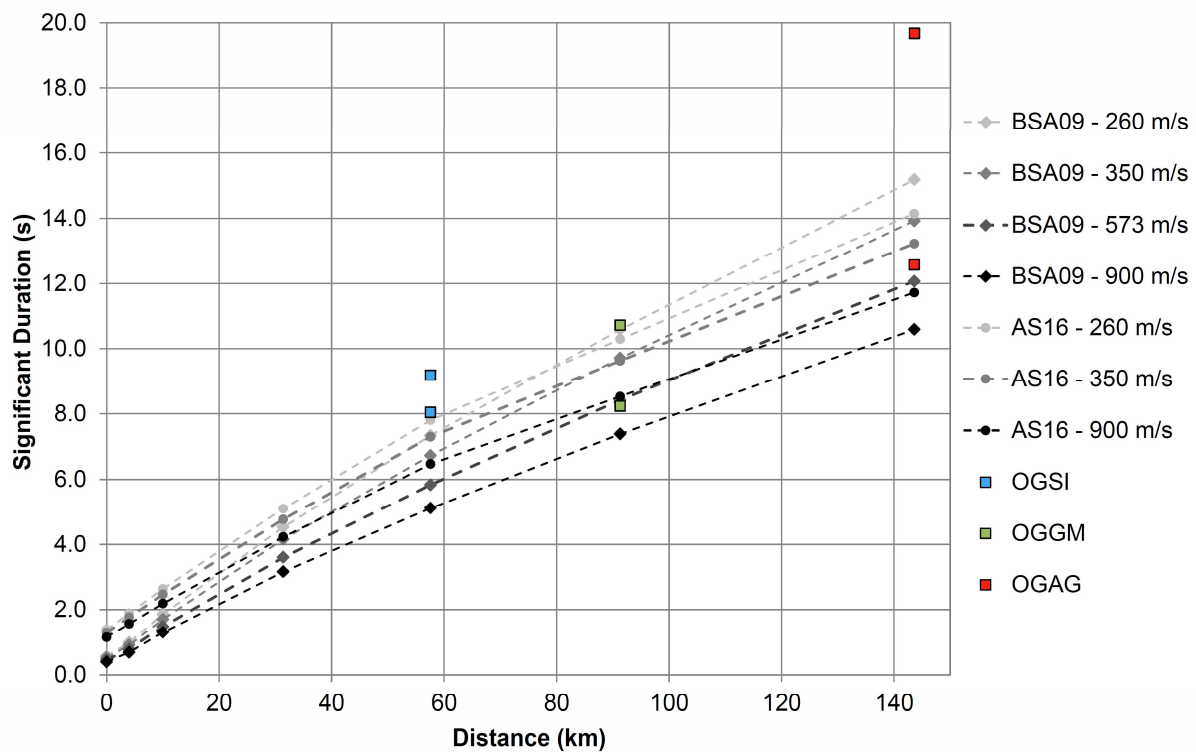


Figure A4.8.24. Observed durations (squares) and estimated significant durations (dashed lines) for a range of epicentral distances and V_{s30} values, predicted by the models of Bommer *et al.* (2009, BSA) and Afshari & Stewart (2016, AS), for the Épagny mainshock of 15th July 1996.

A4.8.5 Collateral earthquake hazards

A4.8.5.1 Surface rupture

Despite the moderate magnitude of the 15th July 1996 earthquake, Thouvenot *et al.* (1998) believe that the rupture may have reached the surface because of its shallow focal depth. However, the Institut des Risques Majeurs (IRMA, 2015) estimates that a **M**6.0 event would be required for the rupture to appear clearly on the surface.

Thouvenot *et al.* (1998) estimated an average slip of around 12 cm on the fault, considering the surface area of the aftershocks and the released seismic moment. The rupture did indeed disrupt the overlying cover of soft, shallow sediments, as there have been observations of co-seismic cracks appearing at several places. Thouvenot *et al.* (1998) report NW-SE oriented cracks observed two days after the mainshock, with an opening of 2 to 3 cm and a length of 200 m parallel to the Vuache fault, near the southwest tip of the Annecy-Meythet airport's runway, 1.7 km south-south-east of the epicentre, at the extrapolation of the aftershocks plane to the surface and near the epicentres of the minor southern cluster. A horizontal, left-lateral east-west displacement of 1 cm, including a vertical offset of 1 cm, was also observed at a warehouse in Chaumontet, 2km northwest of the epicentre, near the inferred trace of the Vuache fault (Thouvenot *et al.*, 1998).

A4.8.5.2 Landslides

This earthquake reportedly caused only minor landslides along the shoreline of Annecy Lake (Dominique *et al.*, 2008). No rockfalls caused by the mainshock have been recorded other than some testimonies of “pebble noise” by the occupants of a night club, at the southeast end of a cliff in Chaumontet (Dominique *et al.*, 1996). On the other hand, on 21st July 1996, a significant collapse occurred in a former limestone (*pierre à ciment*) quarry, 6 hours after an M_L 3.4 aftershock, in Chamaz (Savoie), about 25 km SW of its epicentre. According to Dominique *et al.* (1996), it is likely that said aftershock accelerated the process of collapse of an already weakened structure, though no further connection with the main shock is implied.

A4.8.5.3 Liquefaction

No significant liquefaction effects were observed in the Annecy basin, in spite of liquefaction hazard existing all the way from Annecy to Épagny, as discussed above. Only some hints of liquefaction were reported at the southwest end of the Annecy-Meythet airport's runways (see Figure A4.8.16 for location), in the form of small cones of sand. There are also unconfirmed suspicions that some of the small landslides along the shores of Annecy Lake could have been caused by liquefaction (Dominique *et al.*, 2008).

A4.8.5.4 Settlements

No reports of settlements have been found for this earthquake.

A4.8.6 Exposed population

A4.8.6.1 Socio-economic setting

According to the 2016 Human Development Report (UNDP-HDR, 2016), the Human Development Index (HDI) for France was 0.830 in 1996 and 0.897 in 2015, while its Inequality-adjusted HDI (IHDI) was 0.813 in UNDP (2016). According to the 2015 world's ranking reported in 2016, France is located in the 21st place, while the Netherlands ranks 7th. Table A4.8.11 compares the HDI and IHDI for both countries for Human Development Data between 1996 and 2015. The column "Adj. HDI" provides the HDI values given online (UNDP-HDD, 2016) for the years mentioned above, adjusted for data consistency in time.

Table A4.8.11. Human Development Index and Inequality-adjusted Human Development Index for France and the Netherlands. HDD: Human Development Data (UNDP-HDD, 2016). HDR: Human Development Report (United Nations, 2016).

Report	Data	France				Netherlands			
		HDI	IHDI	Rank	Adj. HDI	HDI	IHDI	Rank	Adj. HDI
HDD 2016	1996	- (*)	-	-	0.830	-	-	-	0.867
HDR 2016	2015	0.897	0.813	21	-	0.924	0.861	7	-

(*) Given the revision of data and methodology of HDI definition in the 1999 HDI report, which includes the 1996 data, the non-adjusted HDI value has not been included.

Observing the GDP per capita of both countries (Figure A4.8.25, right), it is evident that although the French economy is bigger, being as well a much bigger country (Figure A4.8.25, left), both economies have followed the same growth rate per capita until 1995, shortly before the Épagny earthquake, when that of the Dutch started to increase with respect to the French one, thanks to a more stable economy. However, both countries have maintained similar growth rates and experienced fluctuations after 2008.

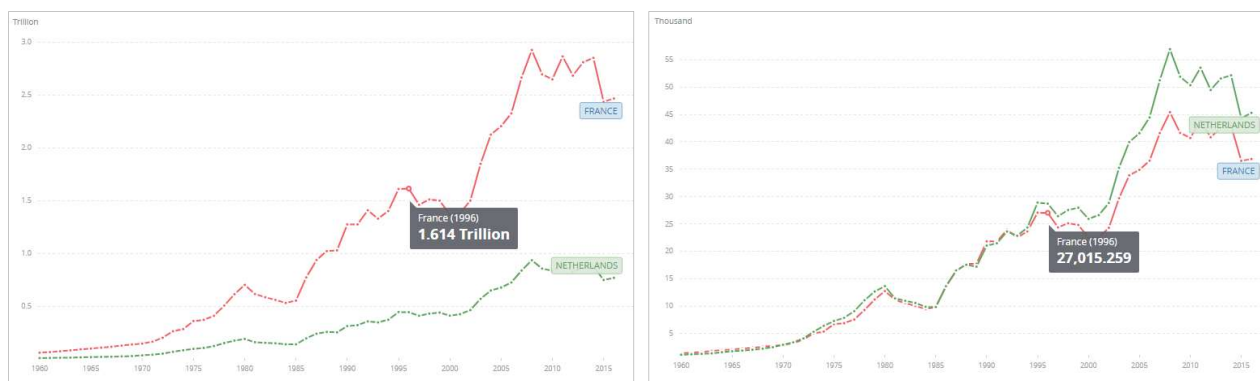


Figure A4.8.25. GDP (in US\$) (left) and GDP per capita (in US\$) (right) fluctuation for France and Netherlands for the last 65 years according to World Bank national accounts data and the Organization for Economic Cooperation and Development (OECD) National Accounts data files (The World Bank, 2017).

Table A4.8.12 presents a comparison between France and the Netherlands in terms of gross domestic product (GDP), GDP per capita and unemployment rate for 1996 and 2015, the latter for the current picture. According to the National Institute of Statistics and Economic Studies (INSEE), the net income per person for the region of Auvergne-Rhône-Alpes was almost equal to the national average income per person in 2011 (latest available data). More particularly, Annecy was placed among the wealthiest cities of France, despite the diversity of the economic status of its different districts/localities. According to Arnal *et al.* (2000), many districts of the Community of Greater Annecy classify as being “high-income”, including Annecy and Épagny. However, a series of districts in between these two along a NW-SE line classify as low to intermediate. The unemployment rate as well was below the country’s average, according to the data used by Arnal *et al.* (2000).

Table A4.8.12. Gross domestic product (GDP), GDP per capita and unemployment rate for France and the Netherlands, according to the World Economic Outlook Database (IMF, 2017).

Indicator	Units	France		Netherlands	
		1996	2015	1996	2015
Gross domestic product, current prices	Billions USD	1,614.71	2,420.16	445.85	750.70
Gross domestic product per capita, current prices	USD	27,870.57	37,653.28	28,708.64	44,322.83
Unemployment rate	%	10.83	10.38	6.44	6.89

The economy of the Community of Greater Annecy is based on the industry and the tertiary sector, including mechanical and electronic production, textile, alimentary and tourism industry (Arnal *et al.*, 2000). The industrial development dates back to the 19th century and reached a peak during the 1960s with the decentralization of important industrial chains. It is characteristic that, currently, 40% of the total local employees work in activities related to exportation (Carnet Photographique, 2017). Meanwhile, 35% of the employees are highly qualified, against the national rate of 17%, placing Annecy among the most developed centres of the alpine regions (Carnet Photographique, 2017). These are mainly concentrated in Annecy and Annecy-le-Vieux (Arnal *et al.*, 2000). Dominique *et al.* (2008) mention a total working power of 2,500 employees for the years 1990-1999, with at least 265 registered enterprises. A nuclear power plant is located as well within the borders of Greater Annecy.

A4.8.6.2 Population density and distribution

According to Arnal *et al.* (2000), the epicentre of the earthquake was located in the Marais of Epagny, 4 km to the northwest of Annecy, in the locality of Epagny, which is part of the Community of Greater Annecy of Annecy. The latter was composed until 2002 by the ten communities marked in red in Figure A4.8.26, to which the communities of Chavanod, Quintal and Montagny-les-Lanches were then annexed. Currently, 34 localities have been merged under the Community of Greater Annecy, whose capital is the city of Annecy and belongs to the Prefecture of Haute-Savoie, located in the region of Auvergne-Rhône-Alpes. In 1999, the total population of Greater Annecy, with 10 communities, was 128,087 inhabitants (Wikipedia, 2017, after INSEE).

Details for the population of the most affected localities, as investigated in Dominique *et al.* (1996; 2004), are given in Table A4.8.13. Dominique *et al.* (2008) mention an increasing trend of the population during the years 1990-1999.

According to the USGS EXPO-CAT database (Allen *et al.*, 2009; USGS-PAGER), over 325,295 people were exposed to an MMI intensity of over IV (intensity level that indicates that the earthquake is felt with moderate vibration). Over 68% of this population was at an urban environment. A total of 25,249 people is estimated to have been exposed to MMI V and V+0.5.

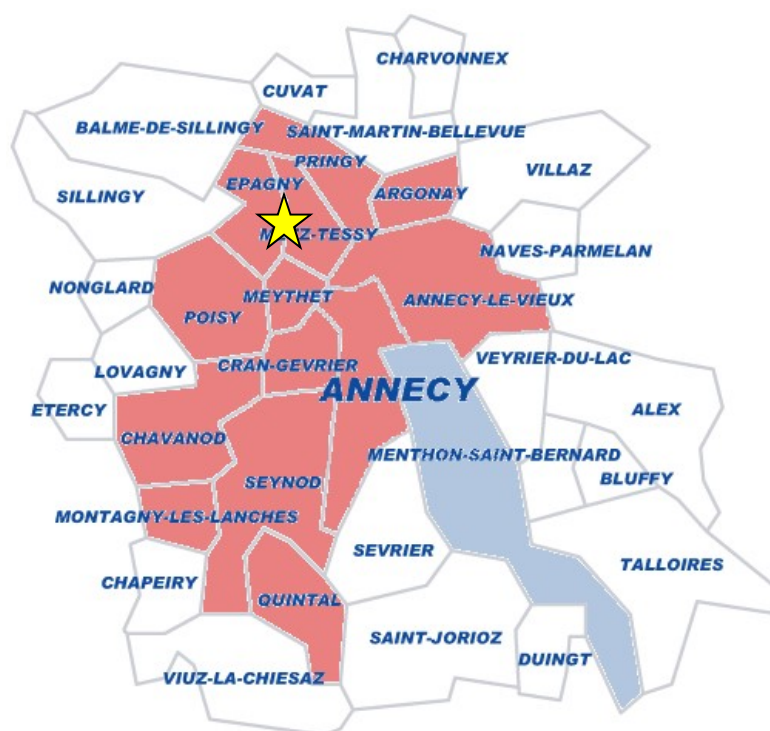


Figure A4.8.26. In red, localities composing the Community of Greater Annecy in 2015 (Wikipedia, 2017). The yellow star denotes the epicentre of the 1996 earthquake according to Arnal *et al.* (2000) located between the localities of Epagny and Metz-Tessy.

Table A4.8.13. Population and population density in 1999 for most affected municipalities according to Dominique *et al.* (1996; 2004) after INSEE (1999).

Municipality	Population	Surface (m ²)	Population density (people/km ²)
Annecy	50,319	66.94	751.70
Annecy-Le-Vieux	18,867	17.01	1,109.17
Argonay	1,904	5.16	368.99
Balme-de-Sillingy	3,716	16.51	225.08
Charvonnex	744	4.71	157.96
Chavanod	1,852	13.36	138.62
Choisy	1,336	16	83.50
Cuvat	756	4.72	160.17
Cran-Gevrier	16,382	4.8	3,412.92
Epagny	2,352	12.06	195.02
Metz-Tessy			
Meythet	7,696	3.24	2,375.31
Montagny-les-Lanches	374	4.38	85.39
Nonglard	472	4.12	114.56
Poisy	5,496	11.33	485.08
Pringy	424	9.06	46.80
Seynod	16,498	19.17	860.62
Quintal	943	9.13	103.29

A4.8.6.3 Time of day of earthquake

The earthquake hit the area at 02:13 local time, awakening the population in a radius of more than 30 km. Being the fall of chimneys, chimney covers, decorative stone elements and glass panels (which caused damage to roof covers and cars parked in front of the houses) the most visible impact of the earthquake, it is likely that more casualties would have resulted from the fall of these objects had the earthquake struck a few hours earlier, considering in particular the crowded streets of the old districts of Annecy during the celebrations of Bastille day, which finished soon before the earthquake struck (e.g., Libération, 1996; Thouvenot *et al.*, 1998).

A4.8.7 Characteristics of exposed building stock

A4.8.7.1 Seismic design codes

The first seismic guidelines in France were published in 1955 under the name “Recommandations AS 55” after the **M6.8** 1954 earthquake in Algeria. In this document, the seismic action was taken into account as a percentage of the mass of the structure homogeneously distributed along the height. The catastrophic earthquake in Morocco in 1960 led to the elaboration of the first seismic code PS65/64, which was transformed into a Unified Technical Document (Document Technique Unifié) in 1969 (PS69) after negotiations between the professional world and the public administration. The application of the seismic provisions became compulsory in 1977 for tall buildings, in 1980 for public buildings, and in 1981 for residential buildings only in the highly hazardous Guadeloupe and Martinique. The last version of PS69 was further completed with lessons learnt after the next disastrous earthquake of Algeria in 1980 and the code PS69/82 (DTU P 06-003) was issued.

A decree of 14th May 1991 separated the structures into two categories: “of normal risk” and “of special risk”. In the first category were included all structures whose damage is important to their occupants, while in the second category even the minor damage could have impact to a large number of people. In 1997, PS92 (“Règles de construction parasismique, règles applicables aux bâtiments”) replaced the previous version and, in parallel, the simplified code PS-MI 89/92, applicable to individual houses, was published. This was the first time that nominal values of ground acceleration were introduced per seismic zone and building class. The building classification of the 1991 decree was further discretized into four classes according to their occupancy and height. In 1998, the application of the seismic provisions became compulsory for all new buildings and the ones undergoing structural transformations.

Finally, the decree of 22nd October 2010 imposed Eurocode 8 as a law in France, allowing for the harmonization of the seismic design with the most modern developments at European level. In parallel, the new seismic zonation was introduced, as discussed in Section A4.8.1.3.

Moreover, the municipalities of France have the possibility to establish plans customized on their territory for the prevention and management of the risk concerning their communities (“Plans de Prévention des Risques”). These may have a regulatory force and they often include seismic microzonation studies, structural and social vulnerability mapping, land use regulations, prevention and emergency planning. Multiple hazards (seismic, landslides, flood) are often combined. For the communities of Annecy and Epagny regions, the plan for risk prevention was proposed by Dominique *et al.* (2004) and Dominique *et al.* (2008), respectively, under request of the Prefecture of Haute-Savoie. The microzonation map of Figure A4.8.16 was elaborated within the context of this plan.

The information for the historical review above was taken from Fabriol & Garry (2002), Plan séisme-historique (2013) and Terrier *et al.* (2006).

A4.8.7.2 Building typologies

The data regarding building typologies for France contained in the PAGER Inventory Database v2.0 (Jaiswal & Wald, 2008) was not directly compiled from information from the country but assumes that the typologies are the same as those that can be found in Italy. Under this assumption, and as can be observed in Figure A4.8.27, unreinforced masonry (with a variety of types of mortar) represents around 50% of the building stock in France for urban, rural, residential and non-residential buildings. Around 10% of the dwellings belong to ductile reinforced concrete (RC) frames with or without infill walls, while 32% are nonductile RC frames.

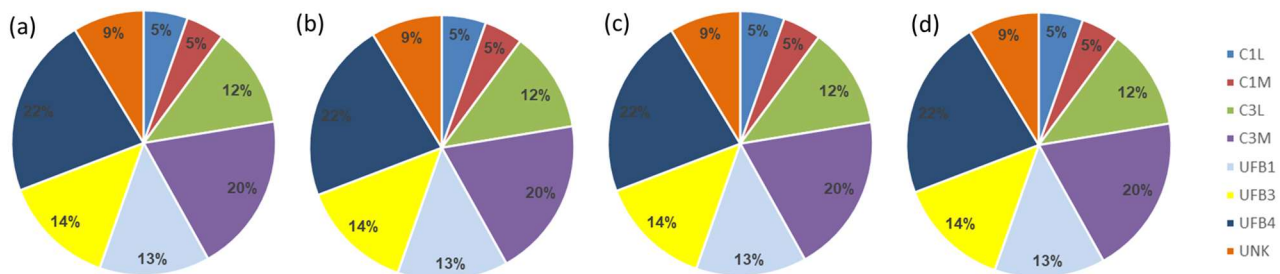


Figure A4.8.27. Proportion of building main typologies in France (assumed to be the same as for Italy) for (a) rural residential, (b) urban residential, (c) rural non-residential, (d) urban non-residential typologies: C1: ductile reinforced concrete moment frame with or without infill (L: low-rise; M: mid-rise); C3: nonductile reinforced concrete frame with masonry infill walls (L: low-rise; M: mid-rise); UFB1: unreinforced brick masonry in mud mortar without timber posts; UFB3: unreinforced brick masonry in lime mortar; UFB4: unreinforced fired brick masonry, cement mortar; UNK: not specified. 2007 data from USGS-PAGER, Jaiswal & Wald (2008).

Table A4.8.14 enumerates the main building typologies in France according to the World Housing Encyclopaedia, which incorporates official inventory data extracted from INSEE, and classifies buildings based on their construction material and subtype. The respective probability of collapse for different seismic intensities is shown as well (Thibault, 2009).

Table A4.8.14. Summary of construction types and vulnerability in France according to the World Housing Encyclopaedia. Data from Thibault (2009).

Construction material	Construction subtype	Probability of collapse (%) of building type when subjected to the specified shaking intensity			
		IX (~0.65 - 1.24 g)	VIII (~0.34 - 0.65 g)	VII (~0.18 - 0.34 g)	VI (0.092 - 0.18 g)
Masonry	Rubble stone in mud or lime mortar or without mortar	18-70	5-24	3-8	0.5
	Massive stone (in lime/cement mortar)	16-54	4-19	2-5	0-3
	Unreinforced brick masonry in cement mortar with reinforced concrete floor/roof slabs	14-47	3-17	0-4	0-2
	Confined brick/block masonry with concrete posts/tie columns and beams	10-38	0-12	0-2	0
	Unreinforced concrete block masonry in lime/cement mortar	15-50	4-18	2-5	0-3
	Reinforced concrete block masonry in cement mortar	13-45	3-16	0-4	0-2
Structural concrete	Concrete moment resisting frames designed for gravity loads only	10-55	4-20	0-5	0-3
	Concrete moment resisting frames designed with seismic features	6-40	0-12	0-2	0
	Concrete moment resisting frames with unreinforced masonry infill walls	12-45	3-14	0-3	0-2
	Concrete shear walls cast in-situ	8-36	0-10	0-2	0

Regarding the built environment of Annecy and the surrounding affected localities, not much specific information is available. Historical and touristic presentations of the city (e.g., Carnet Photographique, 2017) make reference to a historical city centre around the medieval castle, which was preserved when the city expanded after the 19th century. The city underwent as well an era of significant erection of modern buildings during the Thirty Glorious years (1945-1973) (Musées – Patrimoine, 2017).

Dominique *et al.* (2008) have mapped the exposed assets with respect to their occupancy type. They report that buildings related to tourism and public administration (*i.e.*, historical buildings, monuments, buildings of strategic importance) are located in the old town of Annecy and in the vicinity of the lake. On the other hand, the economic and commercial centre of the area, with more modern buildings, is situated in the localities of Seynod, Cran-Gevrier, Meythet, Metz-Tessy, Argonay, Annecy-le-Vieux and Épagny. Several industries, including one regulated by a European Law related to the safety of sites where hazardous substances are handled (also known as the Seveso directive, Wikipedia), are located in the surroundings of Annecy.

Given the lack of further information available in the literature on the historical and most vulnerable stone structures of the city centre of Annecy, the authors will try to make inferences based on the urban heritage of the neighbouring cities of the canton of Valais, in Switzerland, as buildings in both sites are of similar architectural configuration and materials, and date from approximately the same period of construction, around the 19th century. According to Kazantzidou-Firtinidou *et al.* (2015), most of these buildings are composed by an arched ground floor and flexible timber floors. Often, due to occupancy

changes during the years, they have undergone structural modifications, such as walls demolitions or replacement of timber floors with solid reinforced concrete slabs. The vulnerability study of Kazantzidou-Firtinidou *et al.* (2015) for Sion, a valaisan city with comparable seismic hazard (design PGA 0.15 g), revealed high probabilities of severe damage to the stone masonry buildings, with the most privileged collapse mechanism being that of façade overturning.

Finally, from the description of damage in Dominique *et al.* (1996), a large concentration of 1- to 2-storey masonry buildings may be observed, especially in the rural area in the surroundings of Annecy. Few evidences are given also of reinforced concrete frame buildings. To the author's experience (Kazantzidou-Firtinidou, 2015), multi-storey buildings of both concrete block bearing masonry and reinforced concrete shear walls are the most common modern typology.

A4.8.7.3 Prior damage and retrofit

Not much information is available regarding prior damage and retrofit of the buildings prior to the earthquake. However, Dominique *et al.* (1996) highlight that the surveyors experienced some difficulty in determining whether all the cracks identified during the post-seismic assessment were due to the ground shaking or existed prior to it.

A4.8.8 Damage observations

A4.8.8.1 Damage states

Information on damage has only been found in descriptive terms based on the outcome of site investigations (*e.g.*, Dominique *et al.*, 1996).

As discussed in Section A4.8.4.1, the maximum intensity estimated in the epicentral area is VIII in MSK-64 scale (Medvedev & Sponheuer, 1969) and VII has been attributed to a radius up to 7 km from the epicentre. The MSK-64 scale defines an intensity magnitude according to the degrees of damage that buildings of different typologies experience, as explained in Section 3.8.1 of Chapter 3 and Appendix II. An MSK-64 intensity of VIII implies that:

- many buildings of type C (reinforced buildings, well-built wooden structures) suffered damage of grade 2, and a few suffered damage of grade 3;
- many buildings of type B (ordinary brick buildings, load-bearing timber frames with infills, *etc.*) suffered damage of grade 3 and a few suffered damage of grade 4;
- many buildings of type A (buildings in field stone, adobe, *etc.*) suffered damage of grade 4 and a few suffered damage of grade 5.

A4.8.8.2 *Damage statistics and description*

Based on local publications, Arnal *et al.* (2000) mention that the main shock caused significant damage in 180 communities. 11,800 damage claims were registered, among which 11,080 corresponded to buildings situated in the community of Annecy.

Around 600 chimneys exhibited some degree of damage (cracking, displacement, rotation) or collapsed damaging the roofs as well as the cars parked underneath, as shown in Figure A4.8.28 (Arnal *et al.*, 2000). Chimneys made of brick, being the most vulnerable, suffered most of the damage, while reinforced concrete chimneys performed quite well, with only their covering plates being displaced (Dominique *et al.*, 1996). The slippage and detachment of roof tiles, especially from the ridge flashing, was also common. Damage to the old buildings' dormers (*i.e.*, rooftop windows that come out of the plane of the roof, Figure A4.8.29, left) was observed, as well, with the fall of that of a renovated ancient building hosting a nursery school (Figure A4.8.29, right) being the most severe one (Dominique *et al.*, 1996).

The most common type of structural damage observed in masonry buildings was cracking of the façade wall or in its connection to perpendicular bearing walls or slabs, an example of which is shown in Figure A4.8.30 (left) (Le moniteur, 1997). Cracks of different width appeared also on the façades and the vaults of numerous churches, as those shown in Figure A4.8.30 (centre and right) (Dominique *et al.*, 1996). In some cases, the extensive fall of plaster revealed cracks on the internal walls of residential buildings and churches as well (Dominique *et al.*, 1996). Severe cracks and partial falls of the pediments (*i.e.*, ornamental gable-like structures usually placed over façades) were attributed to the movement of the ridge board of the roof (Dominique *et al.*, 1996).



Figure A4.8.28. Damaged roof from chimney fall in Metz Tessy (left). Rotated chimney in Chaumontet (right). From Dominique *et al.* (1996).



Figure A4.8.29. Confined dormer of Rumilly hospital severely cracked (left); fall of stone dormer at the nursery school of Metz-Tessy (right). From Dominique *et al.* (1996).

It is noticeable that a 15 m-high brick chimney in the locality of Lovagny was destabilized especially at its upper part but did not collapse. Similarly, the performance of Montrottier's castle (13th-15th centuries) was outstanding, as it developed only a couple of cracks in its interior but no further damage, in spite of its complex architecture and its location on top of a hill (Dominique *et al.*, 1996).

On the other extreme, the main church and the Town Hall of Épagny were damaged beyond repair and had to be demolished (Thouvenot *et al.*, 1998). These were the only two buildings that did not survive the earthquake, while a building in Chanaz, severely damaged by the mainshock, collapsed during the aftershock of 21st July.



Figure A4.8.30. Deep cracks on the angle of a building in Pont-Verre (left), from Dominique *et al.* (1996). Large cracks on the severely damaged church of Epagny (centre) and cracks at the vault of the church in Poisy (right), both from Davidovici (N/A).

Regarding the newer structures, a four-storey building presented X-cracks of large width in the masonry walls of the ground floor and its 50 residents had to be evacuated (Thouvenot *et al.*, 1998) (Figure A4.8.31). This was marked as a unique case of construction/design failure, considering that the surrounding buildings were not particularly affected (Dominique *et al.*, 1996). A couple of reinforced concrete staircases developed cracks, one of which was due to pounding between adjacent buildings and led to the breaking of windows.

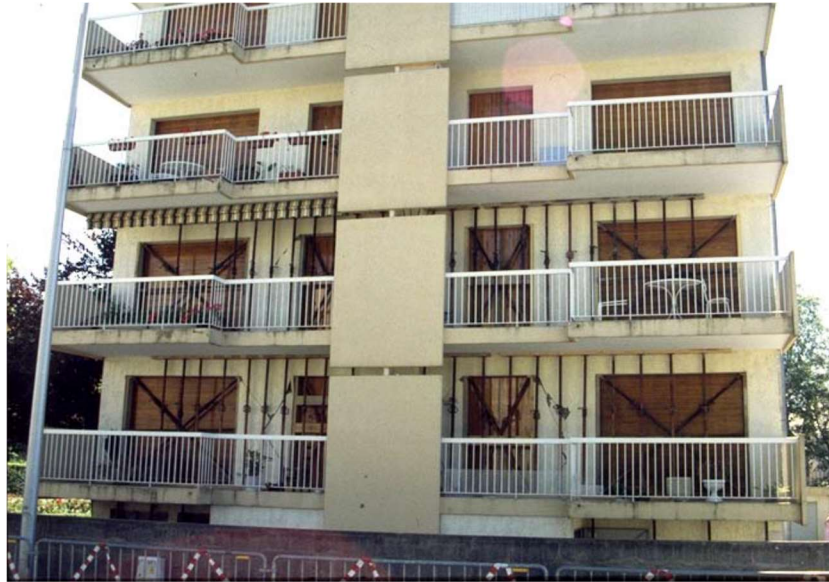


Figure A4.8.31. Wide X-cracks on masonry walls of apartments block in Meythet and subsequent shoring of the building. From Davidovici (2008).

Arnal *et al.* (2000) mentions the occurrence of a power outage (disruption at 3 power poles) and highlights the difficulties experienced in the communication among the disaster managers and towards the public.

Finally, due to the small impact of this earthquake when compared to global disasters, no extensive reports are available within global losses databases. The USGS catalogue vaguely reports minor damage. In this respect, it is relevant to highlight that, as mentioned in Section A4.8.7.3, it was not always clear to the surveyors (Dominique *et al.*, 1996) whether all the cracks identified during the post-seismic assessment were due to the ground shaking and did not exist prior to it.

A4.8.8.3 Observed weaknesses

Not much information is available regarding the state of the buildings prior to the earthquake. However, and as described above, for the similar case of the old town of Sion (Kazantzidou-Firtinidou *et al.*, 2015) and as further confirmed by Le moniteur (1997), the multiple structural modifications the buildings of the historical centre of Annecy have undergone during the years, without accounting for their seismic performance, is likely to have been a significant aggravating parameter.

The technical magazine *Cahier Technique du Bâtiment* (CTB, 1996) tried to provide an explanation for the damage observed, separating it into two large categories, as reported by Le moniteur (1997). Damage to the older buildings was attributed to the absence of proper anchoring of the walls and the bad quality of the support of the timber beams, as well as to the poor maintenance and the multiple structural modifications the buildings had undergone during the years, as mentioned before. Newer constructions are believed to have suffered mainly due to poor seismic design or construction errors.

A4.8.8.4 Damage distribution

According to Thouvenot *et al.* (1998), most of the damage was concentrated in the older districts of the city of Annecy and the communities located NW of the city, namely, Epagny, Metz-Tessy, Meythet, Poisy, Pringy, while the city of Annecy and Annecy-le-Vieux, a suburb, exhibited, comparatively, less damage. These are located in the proximity of the epicentre at the southern edge of the Vuache fault, and are marked in blue in the map of Figure A4.8.32.

The ratio of damage claims to number of residences per locality, reported by Fabriol & Garry (2002) (after CETE de Lyon and Méditerranée) and illustrated in red in Figure A4.8.32, quantitatively confirms these observations. According to this data, 87% of the dwellings in Epagny and 80% of those in Metz-Tessy, both of them located within a radius of around 1 km from the epicentre, appear to have suffered some degree of damage. Some differences between the communities reported by Thouvenot *et al.* (1998) and Fabriol & Garry (2002) are observed: Poisy is not mentioned by the latter, while Pringy seems to have a relatively low damage ratio. Sillingy, which was not enumerated by Thouvenot *et al.* (1998), appears as one of the most affected localities in the data reported by Fabriol & Garry (2002). These small discrepancies may be due to the percentages of Fabriol & Garry (2002) condensing all types of damage together, as well as to the criteria to define the most affected localities not being clear. For example, it is possible that Sillingy not be listed by Thouvenot *et al.* (1998) because its 30% damage ratio may refer to lighter instances of damage than that of other localities. It is noted that these potential explanations are hypothetical.

Most of the damage observed during the post-seismic survey of Dominique *et al.* (1996) is reported to be oriented perpendicular to the NW-SE direction, along which the causative fault strikes. Out-of-plane façade cracks and the fall of chimney elements and objects were observed in the NE-SW direction while objects (bottles) were noted to have followed the NW-SE excitation movement.

According to Thouvenot *et al.* (1998), site effects clearly played a role in the distribution of damage throughout the localities of the Community of Greater Annecy. They make explicit reference to the small amount of damage Annecy-le-Vieux suffered overall, despite having the same epicentral distance with the city of Annecy. Their explanation is based on the moraine and Tertiary molasse the municipality of Annecy-le-Vieux is mainly built on, which led to a low amplification of waves, while structures of Annecy, built on lacustrine clays deposits, suffered greater damage. Similarly, they associate the damage concentration in

Épagny and Meythet (Figure A4.8.32) with the amplified site functions of Figure A4.8.15 in a frequency range close to the eigenfrequencies of the buildings (see Section A4.8.3.2).

The relatively important damage reported in Rumilly in spite of being more than 15 km southwest of the epicentre (see Figure A4.8.32), is also attributed to local site effects induced by the blocks of clay till enclosed within the sandstone (Molasse Burdigalen) on which the municipality is built (Dominique *et al.*, 1996).

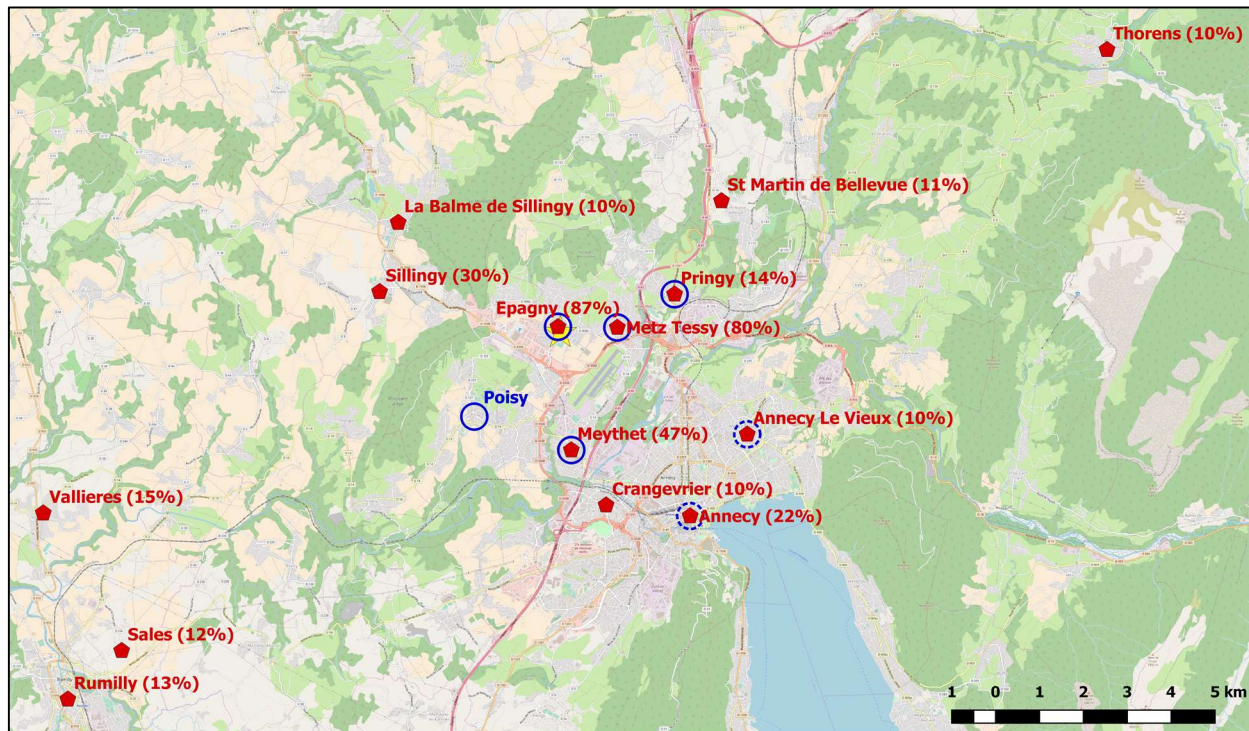


Figure A4.8.32. Ratio of damage insurance claims to number of residences (red pentagons and text, as reported by Fabriol & Garry, 2002). Most damaged (solid line blue circles) and comparatively less damaged (dashed blue circles) enumerated by Thouvenot *et al.* (1998). Yellow star (behind Épagny) denotes epicentre by Thouvenot *et al.* (1998).

A4.8.9 Casualties and losses

A4.8.9.1 Numbers of dead and injured

No serious casualties have been reported. Only one person was slightly injured (Arnal *et al.*, 2000; USGS).

A significant (though unknown) number of people panicked and needed psychological support, particularly those who initially thought the shock was related to an explosion, due to the very low seismic risk awareness of the locals (Arnal *et al.*, 2000; Mémoires des catastrophes, 2012; mayor's interview at IRMA, 2008).

A4.8.9.2 Causes of casualties

Only one light injury from broken glass has been reported (Arnal *et al.*, 2000).

A4.8.9.3 Estimates of economic losses

The Institut des Risques majeurs (IRMA, 2015) mentions that 590 damage claims have been registered in total for any type and level of damage. In comparison with the percentages of claims reported by Fabriol & Garry (2002), this number seems small, though the reason for this discrepancy is not known. The total amount spent in repair works has been estimated in the order of 60 million euro (IRMA, 2015). A larger amount of 500 to 600 million French francs (76 to 92 million euro) for 11,600 damage claims is reported by Arnal *et al.* (2000) citing local newspapers of the time. Assuming 1.72% average inflation rate for euro between 1996 and 2017, the current equivalent amount would be between 110 and 132 million euro. Arnal *et al.* (2000) report that around 400 million French francs (or 61 million euro; with inflation 87 million euro) were compensated by insurances. L'Argus de l'Assurance (2016) reports that the earthquake of Épagny led to the highest economic loss from seismic disasters in metropolitan France since 1982. This corresponds to 110 million euros, being the most recent estimate, based on the earthquake's aftermath.

Arnal *et al.* (2000) report that company-owned buildings were subject to post-earthquake usability assessments before allowing to resume business operations. No information has been found regarding the amount of time this process took and the financial losses that derived from it.

A4.8.10 Discussion and conclusions

This **M4.8** tectonic earthquake occurred on 15th July 1996 at 00:13 UTC on the well-known Vuache fault, a NW-SE left-lateral strike-slip structure in the vicinity of the Community of Greater Annecy, with its hypocentre estimated at a depth between 3 and 10 km. The relatively large maximum MSK-64 intensity of VIII observed was primarily due to the very shallow focal depth of the mainshock, the small epicentral distances and site effects. The extent of the damage and its spatial distribution were likely influenced by the high site amplification (up to a factor of 8 in the 1–10 Hz frequency range) that could be inferred from observations made in the Annecy basin during the aftershock sequence.

Although only secondary surface cracks were observed, the main rupture is believed to have roughly reached up to 1 km below the surface, breaching the limestone layer and disturbing the overlying cover of softer sediments. Some minor liquefaction effects at the runway of the Annecy-Meythet airport and a possible minor rockfall were reported due to the mainshock in areas of known susceptibility to these phenomena.

With a total estimated financial loss of around 70-100 million euros affecting 180 localities, this earthquake illustrates that even seismic events of moderate magnitude can cause significant economic impact when they occur in densely populated areas. Damage claims for 11,800 buildings were registered, while two buildings were damaged beyond repair and had to be demolished, and one building collapsed during an aftershock. Damage reported consisted mainly on the cracking/displacement/rotation of chimneys (around 600 cases),

the slippage and detachment of roof tiles, failure of pediments and dormers, and the cracking of load-bearing walls and Church vaults. In general, damage to older buildings is believed to have been associated with deficiencies such as lack of proper anchoring of walls, poor support of timber beams, poor maintenance and the several modifications carried out on the structures along their lives, while poor seismic design and construction errors are believed to have affected newer buildings.

While only one person with a minor superficial injury due to broken windows was reported, more casualties could have occurred as a consequence of falling chimneys and roof elements had the earthquake happened two hours earlier, as large crowds had been in the streets of Annecy and its suburbs celebrating a national festivity.

A4.8.11 References

A4.8.11.1 Bibliography

Afshari, K. & J. Stewart (2016). Physically parametrized prediction equations for significant duration in Active Crustal Regions. *Earthquake Spectra* **32**(4), 2057-2081.

Allen, T.I., D.J. Wald, P.S. Earle, K.D. Marano, A.J. Hotovec, K. Lin & M.G. Hearne (2009). An Atlas of ShakeMaps and population exposure catalog for earthquake loss modelling (USGS-EXPO-CAT, PAGER-CAT). *Bulletin of Earthquake Engineering* **7**, 701–718.

Arnal, C., R. Fillod, R. Nifle, R. d'Ercole, P. Pigeon, O. Baussart, V. Cambot, L. Gnemmi & J. Wattez (2000). *Mise au point d'un outil d'aide à la décision dans le domaine du risque sismique. Demarche experimentale d'appropriation de la problématique des risques par les acteurs d'une collectivite urbaine (Development of a decision support tool in the field of seismic risk. Experimental approach to the appropriation of the problem of risks by the actors of an urban community, in French)*. Bureau des recherches Géologiques et Minières (BRGM), RP-50020-FR.

Baize, S., M. Cushing, F. Lemeille, C. Gelis, D. Texier, G. Nicoud & J.-L. Schwenninger (2011). Contribution to the seismic hazard assessment of a slow active fault, the Vuache fault in the southern Molasse basin (France). *Bulletin de la Société Géologique de France* **182**, 347–365.

Bisch, P. (1996). *Le séisme d'Épagny du 15 juillet 1996 – Préambule (The Épagny earthquake of 15th July 1996 – Preamble, in French)*. In: *Le Séisme d'Épagny (Haute-Savoie. France) du 15 Juillet 1996*. Report of the AFPS mission. Associé Française du Génie Parasismique, Paris.

Bock, G. (1997). *A Rapid Warning System for Earthquakes in the European-Mediterranean region*, GeoForschungsZentrum (GFZ) 1st Year Progress report, European Commission, DG XIII, 54-60.

Bommer, J.J., P.J. Stafford & J.E. Alarcón (2009). Empirical equations for the prediction of the significant, bracketed, and uniform duration of earthquake ground motion. *Bulletin of the Seismological Society of America* **99**(6), 3217-3233.

Bureau Central Sismologique Français (BCSF) (1998). *Observations sismologiques – Séismicité de la France en 1993 – 1994 – 1995 – 1996 (Seismological observations – French seismicity in 1993 – 1994 – 1995 – 1996, in French)*. Institut de Physique du Globe, Université Louis Pasteur, Strasbourg, France. Available online at (last accessed 10th April 2018): http://www.seisme.prd.fr/donnees/publi/1993-1996/obs_sismo_1993-96.pdf.

Bureau de Recherches Géologiques et Minières (BRGM, 2008a). *Plan de Prévention des Risques naturels prévisibles, PPR de la commune d'Annecy – Second Livret: Annexes Techniques (Plan for the prevention of foreseeable natural hazards, PPR of the Commune of Annecy – Second book: technical annexes, in French)*. BRGM, Prefecture de la Haute Savoie. Available online at: <http://www.haute-savoie.gouv.fr/Politiques-publiques/Environnement-risques-naturels-et-technologiques/Prevention-des-risques-naturels/Donnees-communales-plans-de-prevention-des-risques-naturels/Annecy>. Last accessed: 10th April 2018.

Bureau de Recherches Géologiques et Minières (BRGM, 2008b). *Plan de Prévention des Risques naturels prévisibles, Aléa sismique local (Spectres spécifiques) Aléa liquéfaction, Effet de site topographique – Planche 2 (Plan for the prevention of foreseeable natural hazards, local seismic hazard (specific spectra), liquefaction hazard, topographic site effects - Image 2, in French)*. BRGM, Prefecture de la Haute Savoie. Available at (last accessed 25th July 2017): http://www.haute-savoie.gouv.fr/content/download/5642/29313/file/Planche_2_cle08773b-10.pdf.

Bureau de Recherches Géologiques et Minières (BRGM, 2008c). *Plan de prévention des risques naturels prévisibles, Aléa mouvement des terrains – Planche 3 (Plan for the prevention of foreseeable natural hazards, land movement hazard – Image 3, in French)*. BRGM, Prefecture de la Haute Savoie. Available at (last accessed 25th July 2017): http://www.haute-savoie.gouv.fr/content/download/5643/29317/file/Planche_3_cle0148be-10.pdf.

Cara, M., J. Van der Woerd, P.-J. Alasset, J. Benjumea & A.S. Mériaux (2017). The 1905 Chamonix earthquakes: active tectonics in the Mont Blanc and Aiguilles Rouges massifs. *Swiss Journal of Geosciences* **110**(2), 631-651.

CEN (2004). *Eurocode 8: Design of structures for earthquake resistance - Part 1: General rules, seismic actions and rules for buildings*. European Committee for Standardization, Brussels, Belgium.

Charollais, J., B. Clavel, E. Amato, A. Escher, R. Busnardo, N. Steinhauser, O. Macsotay & P. Donse (1983). Etude préliminaire de la faille du Vuache (Jura meridional) (Preliminary study of the Vuache fault (Meridional Jura), in French). *Bulletin de la Société Vaudoise des Sciences Naturelles* **76**, 217-256.

Chiou, B.S.J. & R.R. Youngs (2008). An NGA model for the average horizontal component of peak ground motion and response spectra. *Earthquake Spectra* **24**(1), 173-215.

Cornou, C. (1997). *Etude des premières données du Réseau Accélérométrique Permanent*, DEA Physique et Chimie de la Terre, Université Louis Pasteur, Strasbourg, 30 p.

Courboux, F., N. Deichmann & J.-C. Gariel. (1999). Rupture complexity of a moderate intraplate earthquake in the Alps: the 1996 M5 Épagny-Annecy earthquake. *Geophysical Journal International* **139**, 152–160.

Davidovici, V. (2008). Annecy 15 juillet 1996 – Renforcement après séisme Bâtiment d'habitations in: *Problématique et Technique de construction*, Journées Techniques Ministère de l'Ecologie, du Développement et de l'Aménagement Durables / Plan séisme, 5-6 February, Paris, France. Available online at (last accessed 10th April 2018): <http://docplayer.fr/31829887-Problematique-et-techniques-de-renforcement.html>.

Davidovici, V. (N/A). *Edifices religieux: diagnostic et renforcement (Religious buildings: diagnosis and retrofit, in French)*. Presentation. Plan Séisme, France. Available online at (last accessed 10th April 2018): http://www.planseisme.fr/IMG/pdf/24_Edifices_religieux.pdf.

Dominique, P., J.L. Bles, F. Deverly, F. Berthier & P. Rosset (1996). *Le séisme d'Annecy (Haute-Savoie, France) du 15 Juillet 1996: rapport de mission (The Annecy earthquake of 15th July 1996:*

report of the mission, in French). Bureau des recherches Géologiques et Minières (BRGM), R 39029, 55 pp.

Dominique, P., B. Le Brun, J.L. Nédellec, Th. Winter & N. Zornette (2004). *Plan de prévention des risques naturels prévisibles des communes du bassin annecien: rapport d'avancement (Natural risk prevention plan for the communes of the Annecian basin: progress report, in French)*, Bureau des recherches Géologiques et Minières (BRGM), RP-52664-FR, 22pp.

Dominique, P., A. Evans, B. Le Brun, J.L. Nédellec, Th. Winter, N. Zornette, C. Mirgon & M. Imbault (2008). *Plan de prévention des risques naturels prévisibles - PPR de la commune d'Épagny - Premier livret: Présentation (Natural risk prevention plan for the communes of Epagny – PPR of the Commune of Épagny – First book: Presentation, in French)*, Bureau des recherches Géologiques et Minières (BRGM), 84 pp.

Dufumier, H. (1999). Synthèse des calculs de magnitudes et de mécanisme au foyer pour le séisme d'Épagny (Synthesis of magnitude and focal mechanism computations for the Épagny earthquake, in French). *Proceedings of the 5th AFPS meeting, Octobre 1999*, ENS Cachan, Paris.

Dufumier, H. (2002). Synthesis of magnitude and focal mechanism computations for the $M \geq 4.5$ earthquakes in France for the period 1995-2000. *Journal of Seismology* **6**, 163–181.

Doudoux, B., J.-C. Barféty, J.-C. Carfantan, M. Tardy & G. Nicoud (1992). Carte géologique de la France à 1/50 000, feuille 702: Annecy-Ugine, BRGM, Orléans – Notice explicative 144 p., feuille couleur par Donzeau M., R. Wernli, J. Charollais, G. Montjuvent (1997).

Dziewonski, A.M., T.-A. Chou & J. H. Woodhouse (1981). Determination of earthquake source parameters from waveform data for studies of global and regional seismicity. *Journal of Geophysical Research* **86**, 2825-2852.

Ekström, G., M. Nettles & A. M. Dziewonski (2012). The global CMT project 2004-2010: Centroid-moment tensors for 13,017 earthquakes. *Physics of the Earth and Planetary Interiors* **200-201**, 1-9.

Engdahl, E.R., R. van der Hilst, & R. Buland (1998). Global teleseismic earthquake relocation with improved travel times and procedures for depth determination. *Bulletin of the Seismological Society of America* **88**, 722-743. Online data available at: <http://www.isc.ac.uk/ehbbulletin/>.

Fabriol, H. & G. Garry (eds.) (2002). *Plans de prévention des risques naturels (PPR) – Risques sismiques – Guide méthodologique (Natural risks prevention plan (PPR) – Seismic risk – Methodological guide, in French)*. Ministère de L'Ecologie et du Développement Durable, Ministère de l'Équipement, des Transports, du Logement, du Tourisme et de la Mer, Paris, France. Available online at: http://www.planseisme.fr/IMG/pdf/guide_ppr_sismique_2002.pdf. Last accessed: 11th April 2018.

Frechet, J., F. Thouvenot, L. Jenatton, P. Hoang-Trong & M. Frogneux (1996). Le séisme du Grand-Bornand (Haute-Savoie) du 14 Décembre 1994: un coulissage dextre dans le socle subalpin (The Grand-Bornand (Haute-Savoie) earthquake of 14 December 1994: a dextral sliding in the subalpine basement, in French). *Comptes rendus de l'Académie des Sciences* **323**, 517-524.

Giardini, D., G. Grünthal, K.M. Shedlock & P. Zhang (1999). The GSHAP global seismic hazard map. *Annali di Geofisica* **42**(6), 1225-1228.

Jaiswal, K. & D.J. Wald (2008). *Creating a global building inventory for earthquake loss assessment and risk management*. USGS Open File Report 2008-1160. Available online at: <http://pubs.usgs.gov/of/2008/1160/>. Last accessed: 15th June 2017.

Kazantzidou-Firtinidou, D., C. Bozzano, C. Luchini, P. Lestuzzi & S. Podestà (2015). *Etude de la vulnérabilité sismique des bâtiments existants des villes de Sion et de Martigny - Méthodologie et Résultats*. (Study of the seismic vulnerability of existing buildings in the towns of Sion and Martigny - Methodology and Results, in French) Centre de Recherche sur l' Environnement Alpin (CREALP), Sion, Switzerland (not published).

Luzi, L., R. Puglia, E. Russo & ORFEUS WG5 (2016). *Engineering Strong Motion Database*. Istituto Nazionale di Geofisica e Vulcanologia, Observatories & Research Facilities for European Seismology. Available online at (last accessed 3th December 2017): http://esm.mi.ingv.it/DYNASTAGE/CadmoDriver?_action=prepare_find_div=1&_page=ACC_Events_Stations_Waveform_progressive&_rock=INVALID&_state=find_progressive_div&_tabber=1&_token=NULLNULLNULLNULL.

Marin, S., J.P. Avouac, M. Nicolas & A. Schlupp (2004). A probabilistic approach to seismic hazard in metropolitan France. *Bulletin of the Seismological Society of America* **94**, 2137–2163.

Medvedev, S., W. Sponheuer & V. Karnik (1965). *Seismic intensity scale, MSK 1964*. Academy of Sciences of the U.S.S.R., Soviet Geophysical Community, 13 pp.

Seismosoft (2016). SeismoSignal 2016 – A computer program for signal processing of strong-motion data, available from <http://www.seismosoft.com>. Last accessed: 10th July 2017.

Scotti, O., D. Baumont, G. Quenet & A. Levret (2004). The French macroseismic database SISFRANCE: Objectives, results and perspectives. *Annals of Geophysics* **47**, 571–581.

Solomos, G., A. Pinto & S. Dimova. (2008). *A review of the seismic hazard zonation in national building codes in the context of Eurocode 8*. European Commission Joint Research Centre (JRC), Scientific and Technical Reports, Luxembourg. Available online at (last accessed: 25th July 2017): <http://eurocodes.jrc.ec.europa.eu/doc/EUR23563EN.pdf>.

Terrier M., G. Bertrand & A. Roullé (2006). *Risque sismique, évolution du cadre réglementaire (Seismic risk, evolution of the regulatory framework, in French)*. Bureau des recherches Géologiques et Minières (BRGM). Available online at: http://www.irma-grenoble.com/PDF/mallettes/sismique/DOC_fiche09.pdf. Last accessed: 16th July 2017.

Tesauro, M., C. Hollenstein, R. Egli, A. Geiger & H.G. Kahle (2005). Continuous GPS and broad-scale deformation across the Rhine Graben and the Alps. *International Journal of Earth Science* **94**, 525–537.

Thibault C. (2009). *Building construction vulnerability and inventory for France, WHE-PAGER Project*. Available online at (last accessed 21st November 2017): <http://www.world-housing.net/wp-content/uploads/pager/2009/08/France1.pdf>

Thouvenot, F., J. Fréchet, P. Tapponnier, J.-C. Thomas, B. Le Brun, G. Ménard, R. Lacassin, L. Jenatton, J.-R. Grasso, O. Coutant, A. Paul & D. Hatzfeld (1998). The M_L 5.3 Épagny (French Alps) earthquake of 1996 July 15: a long-awaited event on the Vuache Fault. *Geophysical Journal International* **135**, 876–892.

United Nations, ed. (2016). *Human Development Report 2016 – Human Development for Everyone*. Report of the United Nations Development Programme (UNDP), New York, United States.

Vienna Consulting Engineers (VCE, 2013). *Structural fragility assessment using field monitoring data*. Network of European Research Infrastructures for Earthquake Risk Assessment and Mitigation, NERA-D15.4. Available online at (last accessed 28th July 2017): ftp://www.orfeus-eu.org/pub/NERA/Deliverables/NERA_D15.4.pdf.

Wald, D.J. & T.I. Allen (2007). Topographic slope as a proxy for seismic site conditions and amplification. *Bulletin of the Seismological Society of America* **97**, 1379–1395. Slope-based online map viewer available at: <http://usgs.maps.arcgis.com/apps/webappviewer/index.html?id=8ac19bc334f747e486550f32837578e1>.

Walpersdorf, A., S. Baize, E. Calais, P. Tregoning & J.M. Nocquet (2006). Deformation in the Jura Mountains (France): First results from semi-permanent GPS measurements. *Earth and Planetary Science Letters* **245**, 365–372.

Woessner, J., D. Giardini, H. Crowley, F. Cotton, G. Grünthal, G. Valensise, R. Arvidsson, R. Basili, M. B. Demircioglu, S. Hiemer, C. Meletti, R. W. Musson, A. N. Rovida, K. Sesetyan, M. Stucchi & The SHARE Consortium (2015). The 2013 European Seismic Hazard Model: Key Components and Results. *Bulletin of Earthquake Engineering* **13**(12), 3553–3596. Available online at: <http://www.efehr.org/en/hazard-data-access/hazard-maps/>. Last accessed: 16th November 2017.

Worden, C.B., M.C. Gerstenberger, D.A. Rhoades & D.J. Wald (2012). Probabilistic relationships between ground-motion parameters and Modified Mercalli Intensity in California. *Bulletin of the Seismological Society of America* **102**(1), 204–221.

Worden, C.B., E.M. Thompson, M. Hearne & D.J. Wald (2017). *ShakeMap V4 Manual: technical manual, user's guide, and software guide*. United States Geological Survey. Available online at: <http://usgs.github.io/shakemap/>.

A4.8.11.2 Web references

Bureau Central Sismologique Français – Fiche séisme Annecy (BCSF, 1996): http://www.franceseisme.fr/donnees/intensites/1996/960715_0013/Fiche_960715.php. Last accessed: 16th July 2017.

Bureau de Recherches Géologiques et Minières (BRGM): <http://www.brgm.fr/>

Cahier Technique du Bâtiment (CTB, 1996) No 179: <https://www.cahiers-techniques-batiment.fr/>

Carnet photographique – Economie d'Annecy (2017): http://www.voyagesphotosmanu.com/economie_annecy.html. Last accessed: 16th July 2017.

Centre d'Etudes Techniques de l'équipement (CETE) – current Centre d'études et d'expertise sur les risques, l'environnement, la mobilité et l'aménagement (CEREMA): <http://www.cerema.fr/>. Last accessed: 1st December 2017.

Centre Sismologique Euro-Méditerranéen (CSEM/EMSC): <http://www.emsc-csem.org/>.

ESM - Engineering Strong Motion Database:
Website for this event (last accessed 19th July 2017):
http://esm.mi.ingv.it/DYNA-stage/CadmoDriver?_action_do_single=1&_criteria=CZ001%3d%20AZ014itaca_event_idIAZ012FR-1996-0020%27&_page=ACC_Events_D&_rock=INVALID&_state=find&_tabber=3&_token=NULLNULLNULL.

Géorisques (2017): <http://www.georisques.gouv.fr/>. Last accessed: 18th July 2017.

Global Centroid Moment Tensor Project (GCMT): <http://www.globalcmt.org>. Last accessed: 9th May 2018.

Institut des Risques majeurs – Interview with the mayor (IRMA, 2008): http://www.irma-grenoble.com/05documentation/04dossiers_videos_afficher.php?id_DT=5&id_DTvideo=31. Last accessed: 11th April 2018.

Institut des Risques majeurs – Aléa et zonage sismique en Rhône-Alpes (IRMA, 2011): http://www.irma-grenoble.com/05documentation/04dossiers_PJ.php?id_PJ=91&id_DT=5. Last accessed: 11th April 2018.

Institut des Risques majeurs – Epagny 96 (IRMA, 2015): http://www.irma-grenoble.com/05documentation/04dossiers_articles.php?id_DTart=51&id_DT=5. Last accessed: 11th April 2018.

International Data Center (IDC): <https://www.ctbto.org/>.

International Monetary Fund (2017). World Economic Outlook Database 2017 (16th January 2017): <https://www.imf.org/external/pubs/ft/weo/2016/02/weodata/index.aspx>. Last accessed: 15th July 2017.

International Seismological Centre (ISC): <http://www.isc.ac.uk>. Last accessed: 28th June 2017.

Laboratoire de Détection et de Géophysique/CEA (LDG): <http://www-dase.cea.fr/>. Last accessed: 28th June 2017.

Laboratoire de Géophysique Interne et Tectonophysique de l'Observatoire de Grenoble (SISMALP): <https://sismalp.osug.fr/sismalp.html>. Last accessed: 28th June 2017.

L'Argus de l'assurance (2016): <http://www.argusdelassurance.com/gestion-des-risques/risques-sismiques-en-france-jusqu-a-8-md-de-dommages-assures-rien-que-pour-les-batiments-residentiels.113409>. Last accessed: 11th April 2018.

Le messager (2016): <http://www.lemessager.fr/chablais/les-chablaisiens-doivent-ils-craindre-un-seisme-de-grande-ia923b0n168624>. Last accessed: 26th July 2017.

Le moniteur (1997): <http://www.lemoniteur.fr/articles/parasismique-un-premier-bilan-apres-le-seisme-d-annecy-483825>. Last accessed: 17th July 2017.

Libération (1996): http://www.liberation.fr/france-archive/1996/07/16/annecy-tremble-la-faute-a-la-faille-le-seisme-n-a-fait-qu-un-blese-leger-mais-de-nombreux-degats_176906. Last accessed: 15th July 2017.

Mémoires des catastrophes (2012): <http://memoiresdescatastrophes.org/temoignage/s32ym2nsw4g/view>. Last accessed: 25th July 2017.

Musées – Patrimoine (2017): <http://musees.agglo-annecy.fr/Patrimoines/Decouvrez-nos-patrimoines/Annecy>. Last accessed: 11th April 2018.

National Earthquake Information Center (NEIC): <http://neic.usgs.gov/>. Last accessed: 28th June 2017.

National Institute of Statistics and Economic Studies (INSEE): <https://www.insee.fr/en/accueil>.

National Institute of Statistics and Economic Studies (INSEE, 1999). The results of 1999 Census: <https://www.insee.fr/fr/statistiques/2118516?sommaire=2118522&q=1999#titre-bloc-77>. Last accessed: 15th July 2017.

Plan Séisme (2017): <http://www.planseisme.fr/>. Last accessed: 11th April 2018.

Plan séisme-historique (2013): <http://www.planseisme.fr/Historique.25.html>. Last accessed: 20th July 2017.

QuakeBulletin:

<http://www.quakebulletin.com/quake/st/major-quakes-FRB9>. Last accessed: 28th June 2017.

Reseau National de Surveillance Sismique, Strasbourg (ReNass): <http://renass.unistra.fr/>. Last accessed: 28th June 2017.

Swiss Seismological Service (SED): <http://proto-seismo.ethz.ch/en/home/>. Last accessed: 28th June 2017.

Services de l'Etat en Haute-Savoie (SEHS, 2015):

<http://www.haute-savoie.gouv.fr/Politiques-publiques/Securite-et-protection-de-la-population/Protection-civile/Risques-majeurs/Risque-sismique/Definition-du-risque-sismique>. Last Accessed: 28th June 2017.

SisFrance - Sismicite historique de la France-Metropole:

http://www.sisfrance.net/donnees_seisme.asp?DPT=92. Last accessed: 28th June 2017.

Website for this earthquake (1996):

http://www.sisfrance.net/fiche_SIG.asp?action=init&NUM EVT=740153&LAT=45%B0%2055%27%20N&LONG=6%B0%2005%27%20E&IEPC=7. Last accessed: 3th December 2017.

The World Bank Group (2017). World Bank Open Data: <http://data.worldbank.org>. Last accessed: 11th of July 2017.

United Nations Development Programme – Human Development Data (UNDP-HDD, 2016):

<http://hdr.undp.org/en/data>. Last accessed: 16th July 2017.

United States Geological Survey (USGS): <https://earthquake.usgs.gov/>

Website for this event (last accessed 19th July 2017):

<https://earthquake.usgs.gov/earthquakes/eventpage/usp0007m27#executive>

United States Geological Survey (USGS, PAGER):

<https://earthquake.usgs.gov/data/pager/references.php>

Wikipedia (2017):

Community of Greater Annecy: https://en.wikipedia.org/wiki/Community_of_Greater_Annecy. Last accessed: 20th July 2017.

Seveso Directive: https://en.wikipedia.org/wiki/Directive_96/82/EC. Last accessed: 18th December 2017.

World Housing Encyclopedia (WHE): <http://www.world-housing.net/>.

A4.9. April 2002 M5.1 Au Sable Forks (New York) Earthquake, USA

This earthquake occurred on 20th April 2002, at 10.50 UTC (6.50 local time), near the town of Au Sable Forks, New York, located on the border between Clinton and Essex counties, in an area to the north-eastern flank of the Adirondack Mountains. With a moment magnitude of 5.1, it was the strongest event to have occurred in Eastern North America since 1988 and the largest one recorded by modern regional broadband networks, until the 2011 M5.8 Mineral Virginia earthquake. The earthquake caused moderate-to-light damage to roads, bridges, buildings, and chimneys, and was felt at a distance of several hundred kilometres. While not having caused any casualties, it was responsible for the highest monetary losses ever registered in the state of New York due to an earthquake, half of which were attributed to the reparation cost of infrastructures.

A4.9.1 Tectonic and seismic setting

A4.9.1.1 Tectonic setting

The area which hosted the Au Sable Forks earthquake of 20th April 2002 is situated in the Eastern North America (ENA) craton of Grenville at the north-eastern flank of the Adirondack massif, in the state of New York (Figure A4.9.1, top). Tectonic features in the area were formed over a long time interval, from 2.8 Ga to 115 Ma during (a) the activity of the Great Meteor hotspot (Crough, 1981), (b) the major Grenvillian orogeny associated with the collision of Laurentia (Eastern North America) with Amazonia (Western South America), and (c) the subsequent formation of the Rodinia supercontinent (Levin, 2006) that transects this region (Faill, 1997). Similarity between the tectonic setting of the Grenville orogen and the modern Alpine-Himalayan orogen suggests that they both formed as a consequence of similar continent-to-continent collisional processes (Carr *et al.*, 2000).

The area that was seismically activated in 2002 lies west of the Lake Champlain, which represents a boundary zone between the Grenville craton to the west and the Palaeozoic (400 Ma) Appalachian thrust belt to the east (Figure A4.9.2), that over-thrusts the Grenville basement (Seeber *et al.*, 2002; Viegas *et al.*, 2010a). This boundary zone strikes approximately NNE-SSW (Wheeler, 1995) and is expressed as a 20 km deep, east-dipping thrust fault (Musacchio *et al.*, 1997), the surface expression of which is the Champlain Thrust (Viegas *et al.*, 2010a). The area is dominated by N-S normal faults associated with post-Grenville opening of the Iapetus Ocean and, later on, with thrust/reverse faults of the same direction related to the lower Paleozoic closing of the ocean (Seeber *et al.*, 2002). Available focal mechanisms of contemporary earthquakes in this area are compliant with thrust/reverse faulting in a predominant NW-SE direction, whereas N-S and NE-SW thrust/reverse faulting is also evidenced (Asgharzadeh-Sadegh, 2012).



Figure A4.9.1. USGS map showing the location of the 2002 Au Sable Forks earthquake (yellow star) within the region of Eastern North America (ENA) (top). Map presenting the tectonic stress direction and the style of faulting in the broader region, created in Google earth using data from the World Stress Map Database (Heidbach *et al.*, 2016) (bottom). Blue solid circles indicate reverse faulting and white bars denote the direction of the principal compressional component of the tectonic stress tensor (σ_1).

Horizontal velocities at continuous GPS measuring sites in the Central and Eastern U.S. (CEUS) with respect to a rigid North America, appear to follow a random pattern. However, spatial filtering reveals a spatially coherent N-S strain pattern, most likely resulting from post-glacial rebound (Calais, 2005) and/or large-scale plate kinematics (Du *et al.*, 2003). The 2002 Au Sable Forks earthquake occurred in a transition zone between crustal uplift

to the north and crustal subsidence to the south. This area was also active prehistorically, as indicated by lake disturbances and landslides (Lamontagne *et al.*, 2004).

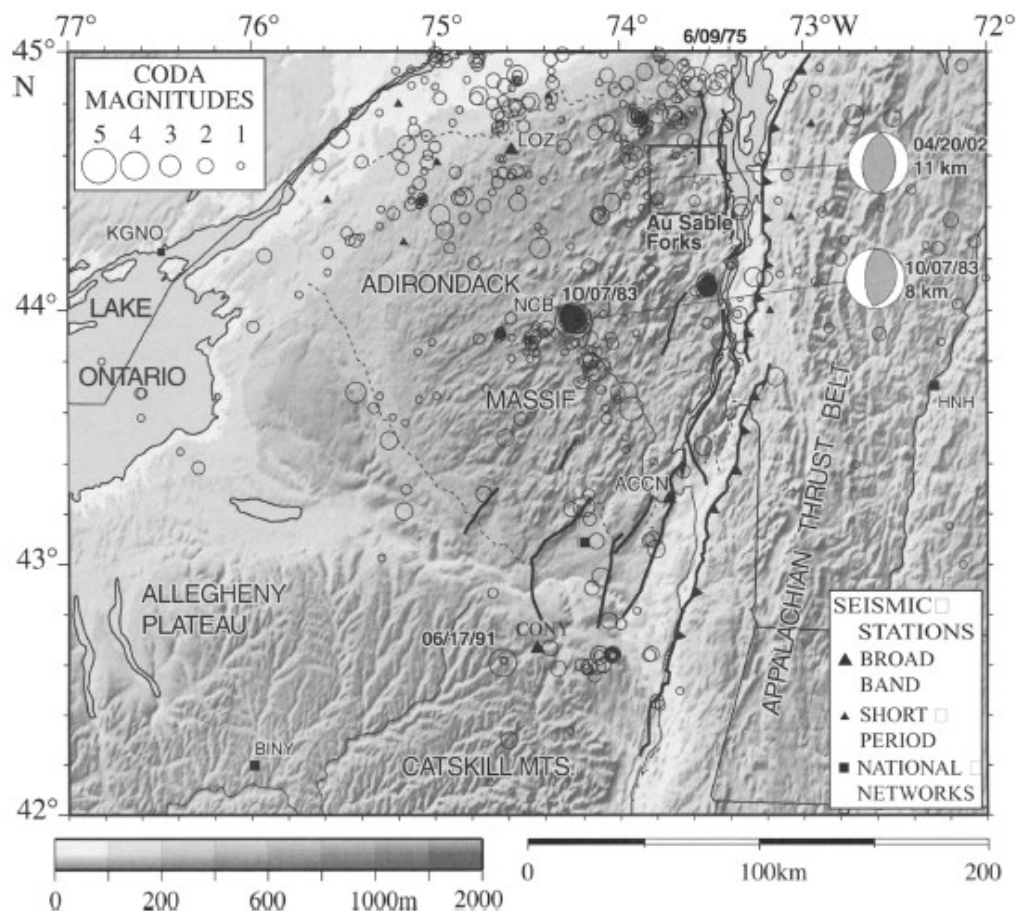


Figure A4.9.2. Map showing the topography of Adirondacks region, the 2002 Au Sable Forks epicentral area with a rectangle and its focal mechanism, other important earthquakes marked by dates. Thick lines are major post-Grenville faults. Seismic stations are also marked. From Seeber *et al.* (2002).

Despite the Grenville-age structure striking predominantly E-W in this area, the 2002 earthquake is related to sub-vertical fracture zones trending NNE similarly to earthquakes in the Grenville Provinces. These zones are traced for hundreds of kilometers across the entire massif (Isachsen *et al.*, 1983), but nevertheless exhibit very little accumulated displacement (Seeber *et al.*, 2002). As shown in Figure A4.9.1 (bottom), the maximum compressive stress in the region is near-horizontal and has an average ENE trend (Du *et al.*, 2003) compatible with large scale plate kinematics, *i.e.*, the expansion of the Atlantic that pushes the North American plate westward, thus reactivating zones of weakness (Inland Marine Underwriters Association, 2001).

A4.9.1.2 Regional and local seismicity

The North-Eastern United States (NEUS) is characterized by low to moderate seismic activity, which is typical of stable continental regions. Seismicity studies indicate that earthquakes occur at greater depths to the west of the epicentral area, in the Grenville Province, than to the east (*e.g.*, Ma & Atkinson, 2006). Although Eastern North America

(ENA) is generally much less seismically active than the western plate boundary regions, there are some areas of substantial seismicity and earthquake hazard. However, the factors that lead to the occurrence of strong earthquakes in ENA remain, in general, poorly known (Lamontagne *et al.*, 2004), due to the difficulties associated with the large error in the routinely calculated epicentres (Asgharzadeh-Sadegh, 2012) and very small displacements observed along the surface trace of tectonic lineaments (Seeber *et al.*, 2002), which do not ease the elaboration of realistic models of the seismogenic structures in the area.

Seismic activity in ENA is associated to a wide range of magnitudes and comprises very active as well as almost aseismic regions (Atkinson, 1989). According to Adams & Basham (1989) and as shown in Figure A4.9.3, it can be spatially grouped into four zones:

- the Western Quebec Seismic Zone (WQSZ) (northeast of Ottawa River),
- the Lower St. Lawrence Seismic Zone (LSZ),
- the Charlevoix Seismic Zone (CSZ), and
- the Southern Ontario Seismic Zone (SOSZ).

As indicated by the yellow star in Figure A4.9.3, Au Sable Forks is located at the southern part of the Western Quebec Seismic Zone (WQSZ), east of St. Lawrence River, characterized as moderately active (Viegas *et al.*, 2010a). The WQSZ, a 160-km wide zone, is situated over the Mesozoic Great Meteor hotspot track. Kimberlite intrusions and other igneous rocks striations (Heaman & Kjarsgaard, 2000) cross the whole WQSZ in a SE-NW direction consistently with seismicity (Sykes, 1980; Ma & Atkinson, 2006).

The epicentral area is characterized by moderate seismic activity (Viegas *et al.*, 2010a). Earthquakes in this zone are mainly thrust, or a combination of thrust and strike-slip events (Lamontagne, 1999; Asgharzadeh-Sadegh, 2012), while seismicity seems to be clustered mostly along the St. Lawrence rift (Figure A4.9.4).

A significant number of earthquakes is recorded each year in the WQSZ with magnitudes equal to or larger than 1 (Lamontagne *et al.*, 2004) and depths from about 5 to 25 km. Around 65% of events are located between 7 and 15 km depth, with the shallower aligned parallel to St. Lawrence Rift in a SW-NE direction, bisecting almost perpendicularly the deeper seismicity that is aligned in a NNW-SSE direction. The 2002 Au Sable Forks epicentre was located at the intersection of the two arrangements.

Several historical and instrumental damaging earthquakes occurred in this area before the 2002 Au Sable Forks event, as illustrated by Table A4.9.1 and Figure A4.9.4. A common characteristic of the stronger events is the large area in which shaking was felt, which could be as far as hundreds of kilometres away and could trigger landslides, in addition to structural damage (Lamontagne *et al.*, 2004).

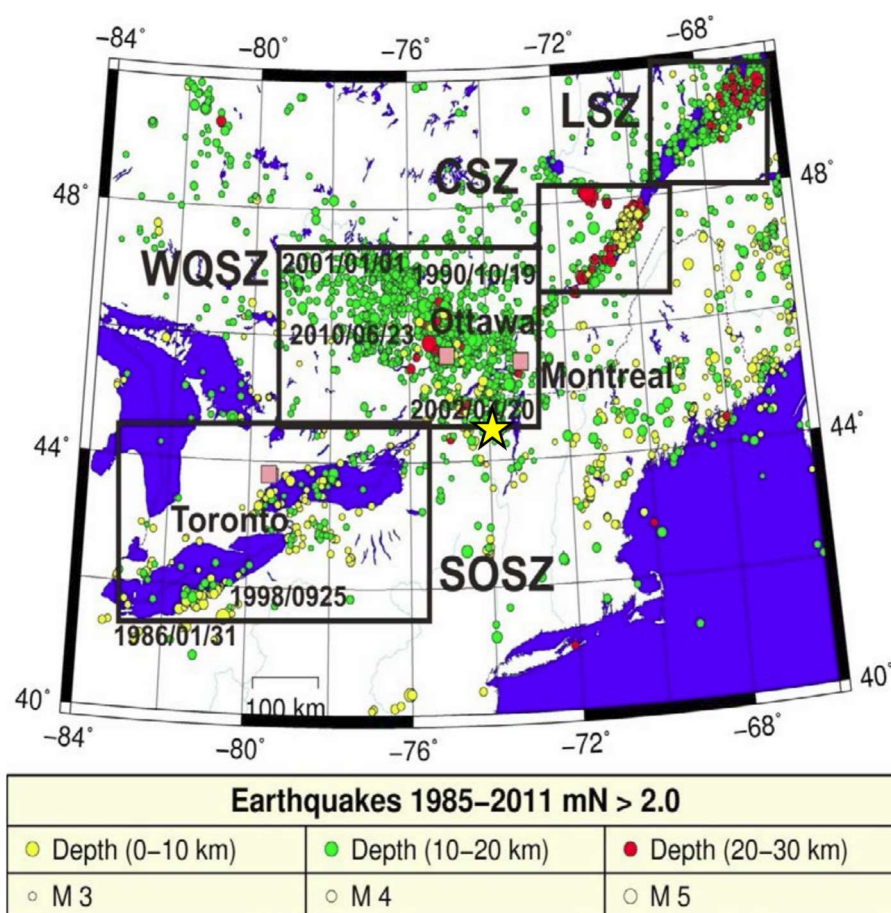


Figure A4.9.3. Seismicity in Eastern North America (ENA): Lower St. Lawrence Zone (LSZ); Charlevoix Seismic Zone (CSZ); Western Quebec Seismic Zone (WQSZ); Southern Ontario Seismic Zone (SOSZ). From Asgharzadeh-Sadegh (2012).

Table A4.9.1. Damaging earthquakes in ENA. Data from Inland Marine Underwriters Association (2001).

Date	Mag.	Comments
05/02/1663	7.0	Charlevoix region, Québec. Widely felt. Reports of vast landslides in the St. Lawrence, Batiscan and Saint-Maurice valleys.
16/09/1732	5.8	Near Montréal, Québec. Widely felt. About 300 houses damaged in the city of Montréal. No injuries.
15/12/1791	6.0	Charlevoix region, Québec. Widely felt. Some damage at Baie-Saint-Paul and Les Éboulements.
17/10/1860	6.0	Charlevoix region, Québec. Widely felt. Minor damage at Rivière-Ouelle.
20/10/1870	6.5	Charlevoix region, Québec. Widely felt. Minor damage at Baie-Saint-Paul.
01/03/1925	6.7	Charlevoix region, Quebec. Widely felt. Considerable damage along the St. Lawrence River near the epicentre.
01/11/1935	6.2	Québec-Ontario border. Felt over much of eastern Canada.
04/09/1944	5.6	Ontario-New York border. Widely felt.
25/11/1988	6.0	Region of Quebec. Felt in a 1,000-km radius from the epicentre.

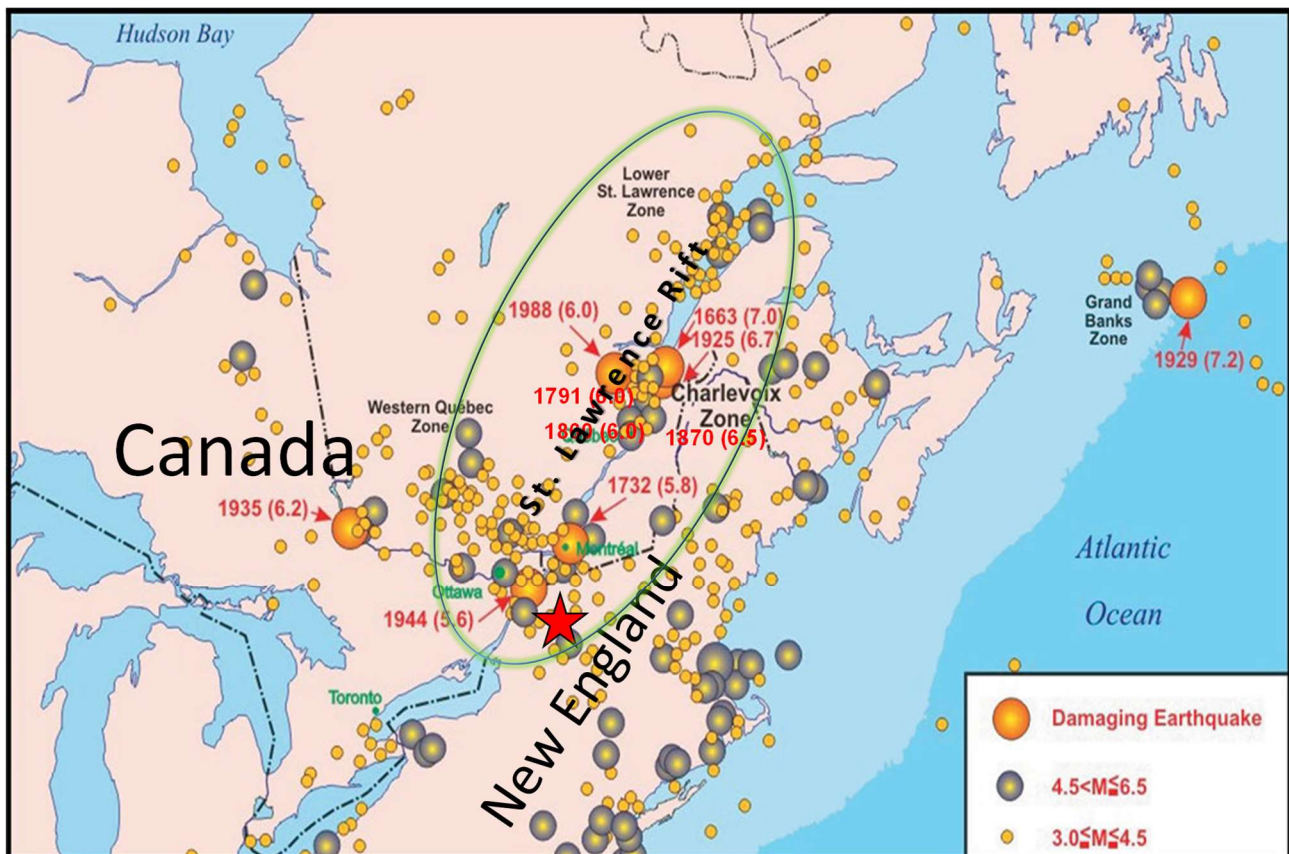


Figure A4.9.4. Historical and instrumental seismicity of ENA. The ellipse highlights the St. Lawrence Rift. The red star indicates the 2002 Au Sable Forks earthquake. Modified after Lamontagne *et al.* (2004).

A4.9.1.3 Seismic hazard

The U.S. Geological Survey (USGS) National Seismic Hazard Maps (NSHM) provide the estimate of the probability of earthquakes expressed in terms of Peak Ground Acceleration (PGA) and Spectral Acceleration (Sa) covering the entire United States. According to both the 2008 and 2014 maps (Petersen *et al.*, 2008; 2014), Au Sable Forks exhibits PGA values with a 10% probability of exceedance in 50 years (475-year return period) of 0.07 – 0.1 g, as shown in Figure A4.9.5.

In addition, the website of the New York State Standard Multi-Hazard Mitigation Plan (NYSHMP, 2014a) published hazard maps for New York State, in terms of peak ground acceleration (PGA) (Figure A4.9.6) and spectral acceleration (Sa) at 0.2 s and 1 s period, based on the USGS 2008 national seismic hazard map and using a more localised scale. As it is evident that the north-eastern part of the state, where the 2002 earthquake occurred, exhibits higher seismic hazard. According to the same source, one damaging earthquake is expected in New York State (NYS) every 22 years on average. As can be observed on the map of Figure A4.9.6, PGA values with a 10% probability of exceedance in 50 years for Au Sable Forks range between 0.07 and 0.09 g.

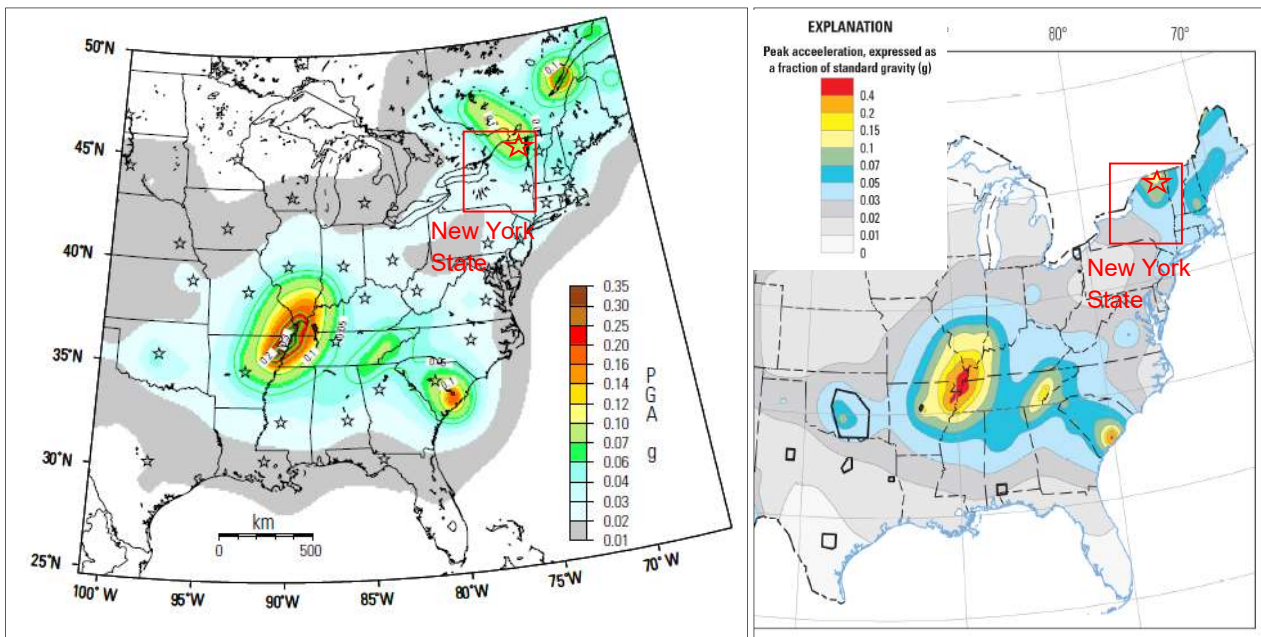


Figure A4.9.5. Extract of the 2008 (left) and 2014 (right) hazard maps for the Eastern United States, elaborated by the USGS (2017). Values correspond to peak ground acceleration (g) on rock with a 10% probability of exceedance in 50 years. From Petersen *et al.* (2008; 2014).

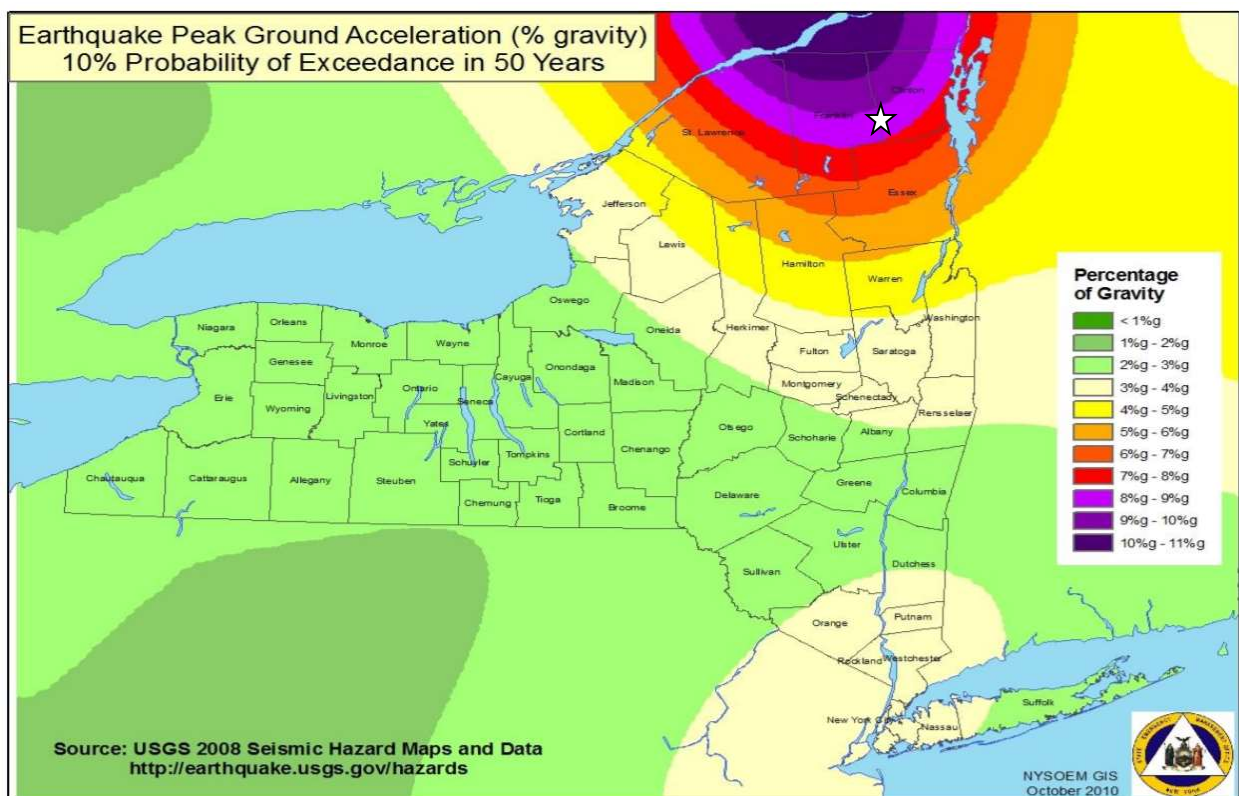


Figure A4.9.6. Seismic Hazard map in PGA with 10% probability of exceedance in 50 years for New York State, released in 2008 (republished in NYSHMP, 2014b). White star indicates epicentre of the 2002 earthquake according to the USGS. Au Sable Forks located slightly south of it.

According to the map of the Global Seismic Hazard Assessment Program (GSHAP) (Giardini *et al.*, 1999), the epicentral area of the Au Sable Forks earthquake exhibits expected PGA values on rock of around 0.097 g with a 10% probability of exceedance in an exposure time of 50 years, quite in agreement with the values from the US hazard

maps (Figure A4.9.7). In Table A4.9.2, the expected PGA values per different publications are summarised.

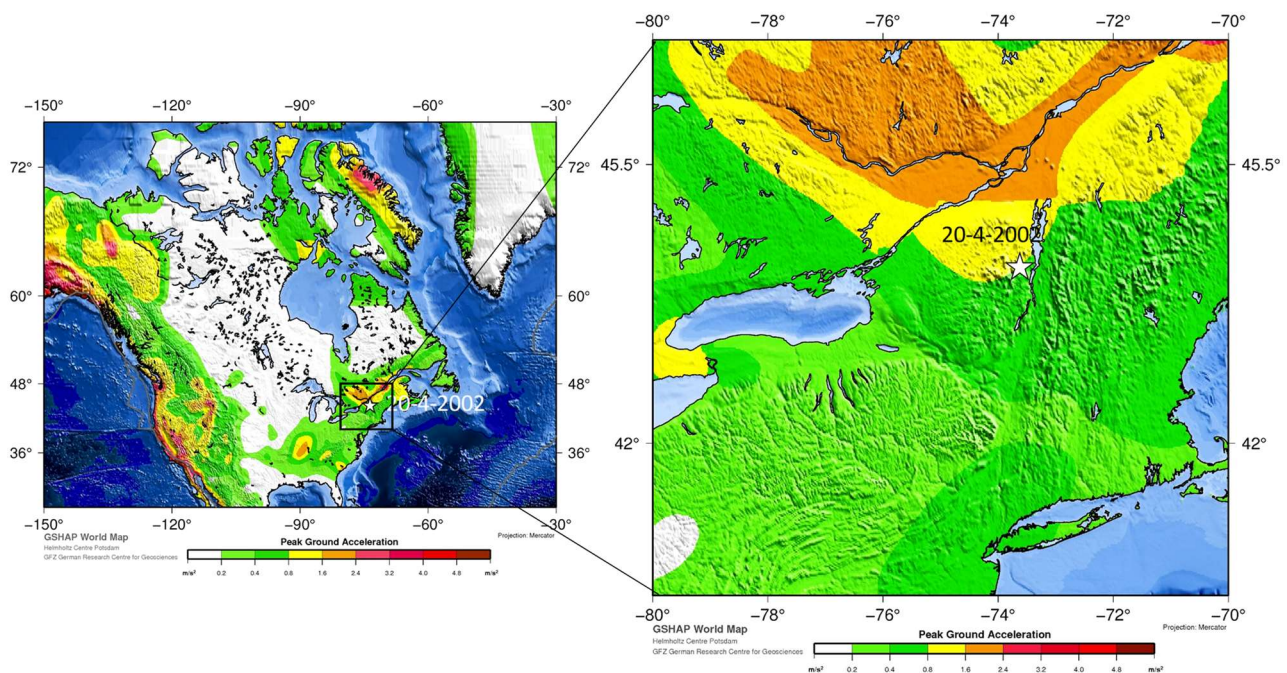


Figure A4.9.7. GSHAP map of PGA (m/s^2), with a 10% probability of exceedance in 50 years (or 475 years of return period), for North America (left) and for the broader area of the CSZ in ENA (right). The star denotes the epicentre of the 20th April 2002 Au Sable Forks mainshock.

Table A4.9.2. Peak ground acceleration (PGA, g) values on rock with a 10% probability of exceedance in 50 years according to results from USGS (2008; 2014) as published in Petersen (2008; 2014), NYSHMP (2014) and GSHAP.

AREA	USGS 2008	USGS 2014	NYSHMP 2014 as per USGS 2008	GSHAP
Au Sable Forks	0.070 – 0.100 g	0.070 – 0.100 g	0.070 - 0.080 g	0.097 g

A4.9.2 Earthquake source characteristics

A4.9.2.1 Location, depth and time

The main shock occurred on 20th April 2002, at 10.50 UTC (06.50 local time). Table A4.9.3 and Figure A4.9.8 summarise the estimations of epicentral coordinates and hypocentral depth from several organizations and agencies.

The epicentre was located in the vicinity of the town of Au Sable Forks. Different estimates concur that the focal depth was between 5 and 15 km. Kim *et al.* (2002) relocated the mainshock using a master event technique at 11 km depth, a solution also confirmed by Viegas *et al.* (2010a) as being consistent with the aftershocks distribution (Seeber *et al.*, 2002) and with the depth of the regional seismicity (Ma & Atkinson, 2006).

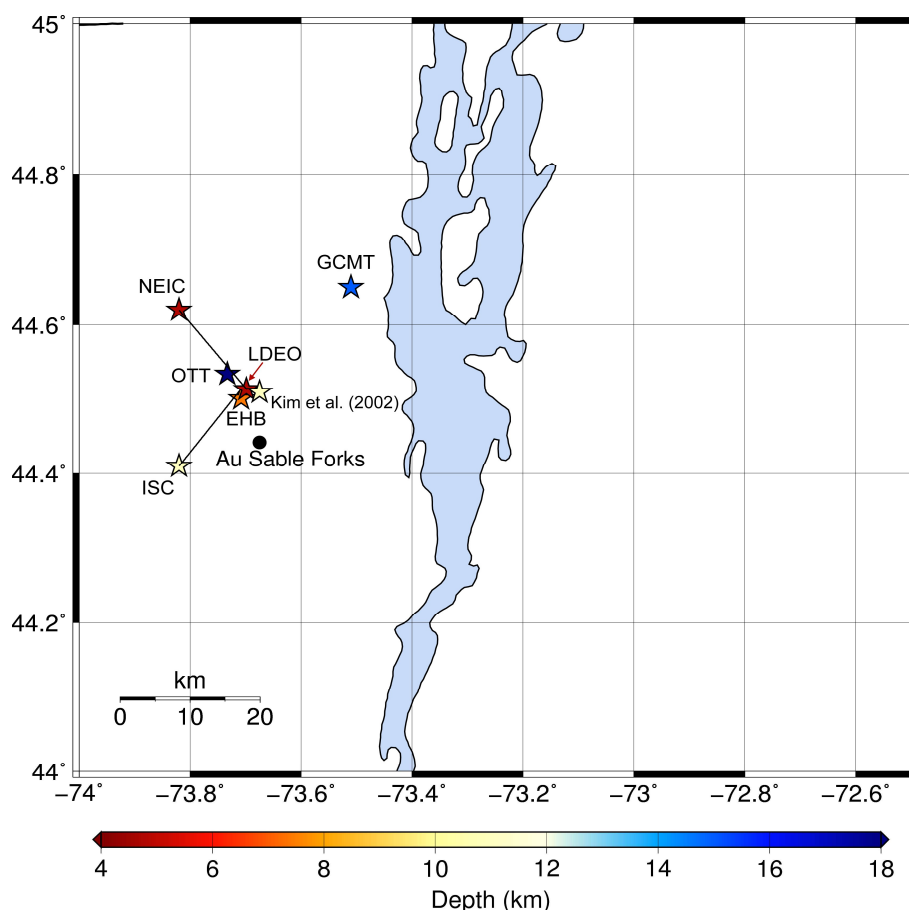


Figure A4.9.8. Estimation of epicentral coordinates of the 2002 Au Sable Forks earthquake by each agency listed in Table A4.9.3.

Table A4.9.3. Epicentral coordinates and hypocentral depths from different sources.

Agency / Publication		Latitude	Longitude	Depth (km)
NEIC	National Earthquake Information Center, USGS	44.5120 °N	73.6970 °W	4.8
ISC	International Seismological Centre	44.5100 °N	73.7110 °W	11.0 (*f)
EHB	ISC-EHB Bulletin (Engdahl <i>et al.</i> , 1998)	44.5000 °N	73.7080 °W	7.4
LDEO	Lamont-Doherty Earth Observatory	44.5125 °N	73.6987°W	4.8
GCMT	Global CMT Project	44.6500 °N	73.5100 °W	15.0 (*f)
OTT	Canadian Hazards Information Service	44.5335 °N	73.7329 °W	18.0 (*f)
Kim <i>et al.</i> (2002)		44.5090 °N	73.6750 °W	11.0

(*f) fixed parameter used for inversion

A4.9.2.2 Magnitude

Estimations of the magnitude of the 2002 mainshock made by various agencies and authors are reported in Table A4.9.4.

Table A4.9.4. Estimations of moment magnitude (**M**), body-wave magnitude (m_b), surface-wave magnitude (M_s), and local magnitude (M_L).

Agency / Publication		M	m_b	M_s	M_L
NEIC	National Earthquake Information Center, USGS	-	5.2	4.2	5.3
ISC	International Seismological Centre	-	5.3	4.2	-
LDEO	Lamont-Doherty Earth Observatory	-	-	-	5.3
GCMT	Global CMT Project	5.1	-	-	-
OTT	Canadian Hazards Information Service	5.0	-	-	-
Atkinson & Sonley (2003)		5.0	-	-	-
Seeber <i>et al.</i> (2002)		5.0	-	-	-

A4.9.2.3 Style-of-faulting

Table A4.9.5 and Figure A4.9.9 summarize the focal mechanisms of the 2002 Au Sable Forks main shock from various sources. All three alternatives imply dip-slip reverse faulting striking N-S or NNW-SSE, consistent with the general trend of faulting in the region (Viegas *et al.*, 2010a; Lamontagne, 1999) (Figure A4.9.2). However, the exact geometry of the causative fault has not been clearly defined.

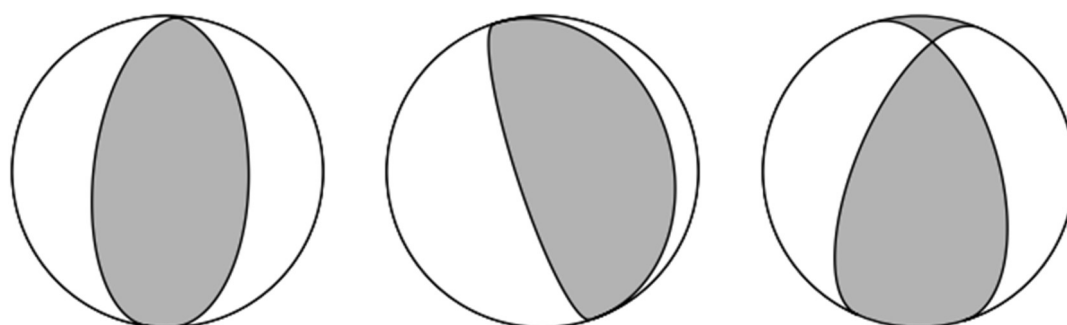


Figure A4.9.9. Focal mechanisms of the 20 April Au Sable Forks mainshock determined by LDEO (left), GCMT (centre) and SLU (right).

Table A4.9.5. Fault plane solutions and fault planes from different sources.

Fault Plane 1			Fault Plane 2			Source
Strike	Dip	Rake	Strike	Dip	Rake	
359	43	84	188	47	96	Lamont-Doherty Earth Observatory (LDEO)
341	15	89	162	75	90	GCMT
343	44	59	203	53	116	Saint Louis University (SLU)

A4.9.2.4 Stress drop

Based on the available observations and a non-constant scaling relationship proposed for ENA by Shi *et al.* (1998), Atkinson & Sonley (2003) determined that a Brune's stress drop of 15.1 MPa best correlates with the source spectra identified by using the spectral ratios of the main shock and six aftershocks to remove the effects of path attenuation and site modulation. A very similar Brune's stress drop estimate of 130 ± 14 bars (~ 13 MPa) was obtained by Boatwright & Seekins (2011) through the analysis of 36 broadband and

accelerograph recordings within 550 km of the epicentre. Viegas *et al.* (2010b) determined a relatively higher average Brune's stress drop value of 19 MPa.

A4.9.2.5 Foreshocks and aftershocks

No foreshock activity was reported in the epicentral area, though it may have occurred but passed undetected by the existing regional seismological network (Seeber *et al.*, 2002). The Au Sable Forks sequence does include, however, nine aftershocks that were recorded by regional broadband networks, the largest of which with a local magnitude M_L of 3.7 (Viegas *et al.*, 2010a). A temporary local network of 12 portable stations deployed two days after the mainshock by the LDEO recorded 74 aftershocks with magnitudes ≤ 3.1 in the 8 subsequent months.

Preliminary hypocentres derived from the Au Sable Forks local network recordings are aligned along a west-dipping plane, consistently with aftershocks of an earthquake with magnitude 5.2 occurred in 1983 in the central Adirondacks for which a similar fault plane solution is inferred (Seeber *et al.*, 2002).

The epicentres of the largest aftershocks, which occurred before the installation of the local network, exhibit a systematic westward bias with respect to the later, locally recorded events. Most of the latter are located within a $1 \times 2 \times 3$ km rock volume at 10-13 km depth, consistent with the depth of the mainshock at 11 km derived by Seeber *et al.* (2002), Kim *et al.* (2002) and Viegas *et al.* (2010a). The same bias is also visible in the depths determined for locally and regionally recorded aftershocks, the latter being significantly shallower (Seeber *et al.*, 2002), as shown in Figure A4.9.10. A double difference method applied to the locally recorded aftershocks (Viegas *et al.*, 2010b) shifted the epicentres to the east, reducing the location uncertainties which were likely due to the wave-paths being affected by the lateral velocity contrasts between the Appalachian and Grenvillian geological provinces.

A4.9.2.6 Nature of earthquake

There is no evidence to suggest that the mainshock of 20th April 2002 was triggered by anthropogenic activity. It is considered as a tectonic earthquake whose inferred focal mechanism and distribution of aftershocks are explained by the activation of pre-existing tectonic features created during the complex geological history of ENA. However, the ambiguity of the identification of the fault plane combined with the lack of detailed information of the background seismicity of the area fed rumours among the locals that related the cause of this earthquake to a potential underground explosion part of what they believe are unofficial activities in the Plattsburgh Air Force Base (AFB), located 15 km to the north of the epicentre and closed in 1995, and other various causes (Cyberspaceorbit, 2002; Great dreams, 2002). It cannot be overemphasised that these are speculative rumours and none of these claims are scientifically supported.

It is noted that Hough (2014), who studied a set of injection-induced earthquakes in the Central and Eastern United States explicitly mentions the 2002 Au Sable Forks earthquake as a tectonic one.

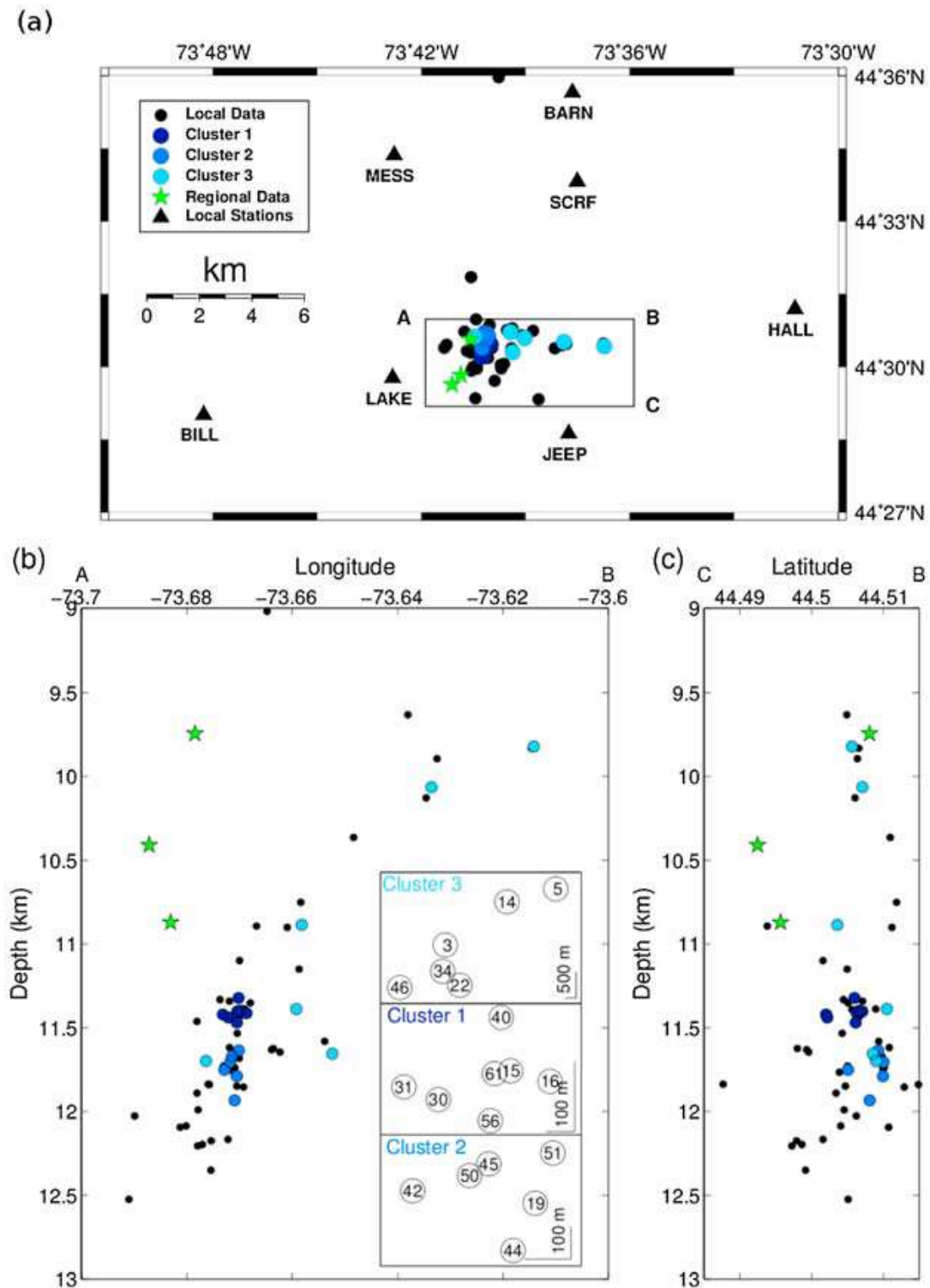


Figure A4.9.10. Top: Map of the stations of the local network (black triangles) and epicentres of the aftershocks recorded locally (solid circles). Bottom: Cross sections along dip (left) and along strike (right) of the inferred fault plane. Black dots are initial hypocentral locations. Blue dots are relocated aftershocks. Green stars are earthquakes recorded regionally. From Viegas *et al.* (2010b).

A4.9.3 Geology and ground conditions in the affected area

A4.9.3.1 Regional geology and topography

Au Sable Forks is located at the juncture of the west and east branches of the Au Sable River, which then flow into Au Sable Chasm and, finally, into Lake Champlain on the east. This region is the boundary between the North American craton of Grenville to the west and the Palaeozoic (400 Ma) Appalachian thrust belt to the east, as mentioned above (Seeber *et al.*, 2002; Viegas *et al.*, 2010a). As described by Pierre & Lamontagne (2004), the topography of the epicentral region varies greatly from mostly flat land around Lake Champlain to very steep mountainous areas closer to the epicentre.

According to Hughes & Luetgert (1991), the Appalachians region is characterized by a series of tectonostratigraphic terranes accreted to North America during multiple orogenic events. Three major terranes are identified, a western terrane consisting of Grenvillian formations, a central terrane mainly of volcanic rocks, and an Avalonian terrane with distinctive Precambrian and mid-Paleozoic faunas. Au Sable Forks is situated on the western terrane consisting of crystalline rocks, specifically Middle Proterozoic granulite and meta-anorthosite (Figure A4.9.11).

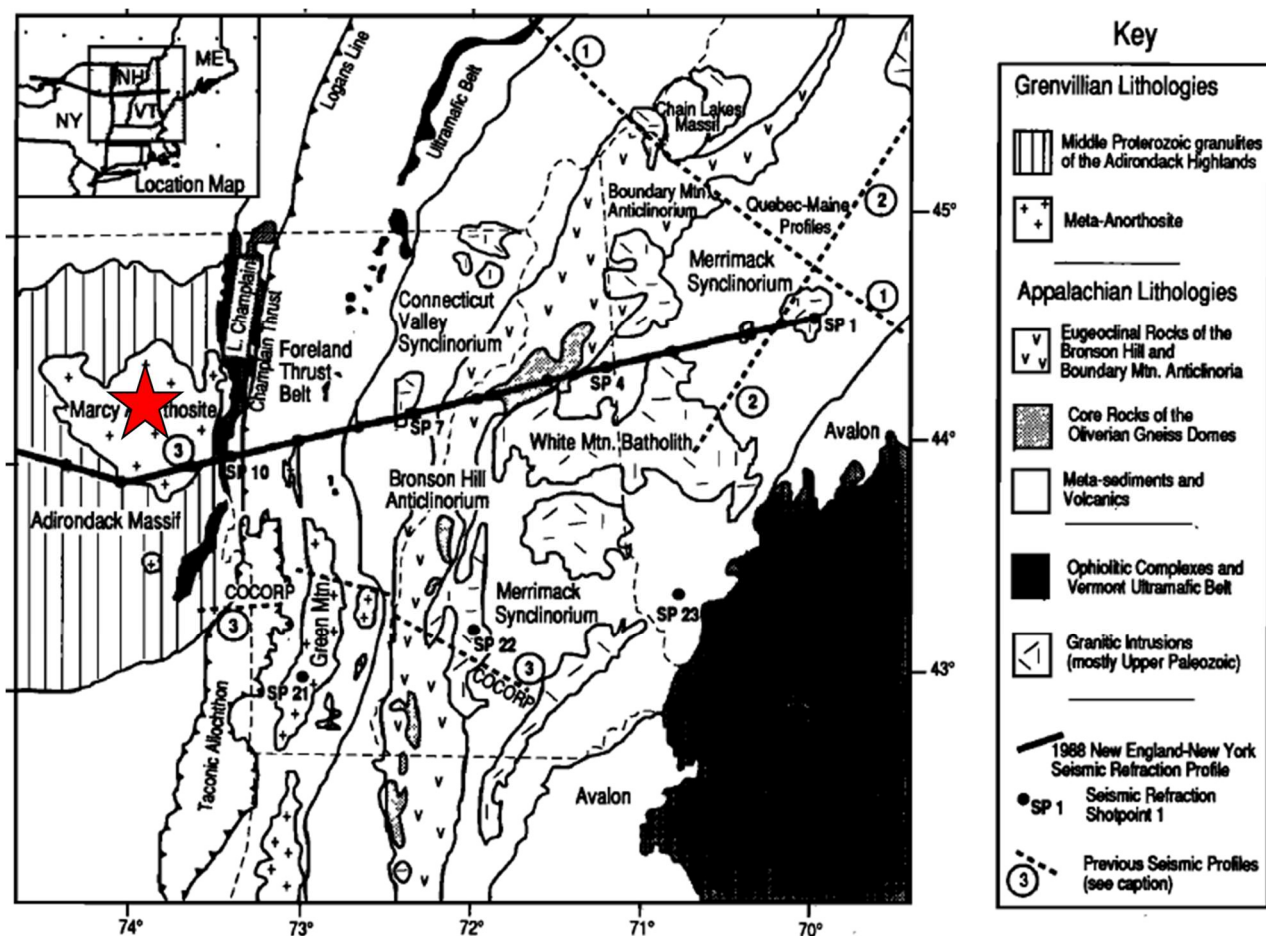


Figure A4.9.11. Simplified geological map of the Adirondack and Appalachian region. From Hughes and Luetgert (1991).

A4.9.3.2 Site conditions in the affected area

Three different kinds of site conditions can be found in the epicentral region (Seeber *et al.*, 2002; Pierre & Lamontagne, 2004): (1) hard rock - hard glacially polished rock, (2) stiff soil - glacially consolidated sediment, and (3) weak postglacial unconsolidated sediment - weak soil between 6 and 10 metres thick. According to Pierre & Lamontagne (2004), the bedrock is exposed in the mountainous areas, while thick glacial outwash and lake sediments fill the valley along the Au Sable River.

Figure A4.9.12 presents the V_{s30} distribution in the area of Lake Champlain from the global USGS V_{s30} model based on topographic slope (Wald & Allen, 2007), which indicates overall stiff soil conditions ($V_{s30} \sim 900$ m/s) but a much lower value of 400 m/s at Au Sable Forks and other human settlements. V_{s30} measured in two positions near the epicentre has been determined at more than 700 m/s by Multichannel Analysis of Surface Waves (MASW) (Yong *et al.*, 2016). These values correspond to NEHRP (2014) soil category “B” (hard rock, $762 < V_{s30} \leq 1524$ m/s), whereas most of the Adirondack Mountains have soil type “A” (very hard rock, such as granite, gneisses, $V_{s30} > 1524$ m/s) (NYSHMP, 2014b).

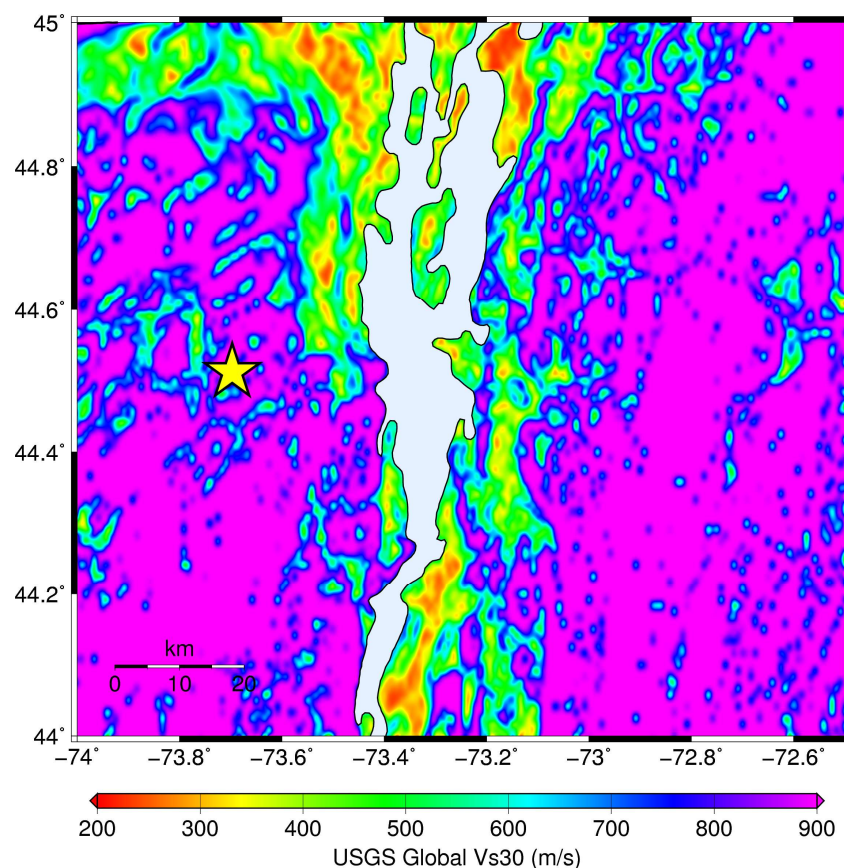


Figure A4.9.12. Map of V_{s30} (m/s) for the broader area of Lake Champlain. The star denotes the epicentre of the 20th April 2002 mainshock. Map drawn using data from the USGS Global V_{s30} model (Wald & Allen, 2007).

According to the ground movement hazard map of the State of New York (NYSHMP, 2014c), concerning the susceptibility to landslides and rockfall, Au Sable Forks is located in an area of low landslide susceptibility, despite having experienced nine events in the

past. The mountainous area to its south-west, however, is categorised as having high susceptibility and moderate incidence.

No information was found about the liquefaction susceptibility of the area, though it is noted that the soil conditions described above are not likely to be prone to liquefaction. It is noted that liquefaction was observed during this earthquake, but it occurred in geotechnical fillings and not in the natural soil formations.

A4.9.4 Ground motions

A4.9.4.1 Intensity observations

In the absence of seismic stations in the immediate vicinity of the epicentre as well as a clear register of the distributed damage, most of the available intensity maps are based on the public's experience and observation of effects. Hence, the ShakeMap (Worden *et al.*, 2017) of Figure A4.9.13 displays the distribution of the estimated Modified Mercalli Intensity according to the almost three thousand Did You Feel It (DYFI) responses of the public, complemented with the Intensity Prediction Equation (IPE) of Atkinson & Wald (2007). The maximum estimated Intensity is 6.4 and it seems to attenuate faster to the west of the epicentre than to the east towards Lake Champlain. This could, however, be an artefact of the distribution of the population around the topography of the area, which is reflected in a larger number of DYFI responses received from the areas to the east of the epicentre than from the west.

The maximum intensity registered, based on inferences from the DYFI responses, is VII, indicating very strong shaking, and is located in both Redford and Keeseville, around 30 km away from the epicentre. In Figure A4.9.14, the DYFI-based attenuation of the intensity with the distance is illustrated against the values predicted by the model of Atkinson & Wald (2007). As can be observed, the median intensities tend to follow relatively well the prediction of the model at distances larger than 100 km. Between 40 and 100 km, however, the model seems to predict higher values than those observed, while closer to the epicentre the observed values seem to be larger instead. It is noted, however, that the amount of data is significantly smaller in the epicentral area than at larger distances.

Interestingly, USGS EXPO-CAT database (Allen *et al.*, 2009; USGS-PAGER) enumerates population exposed up to a much higher intensity of VIII+0.5.

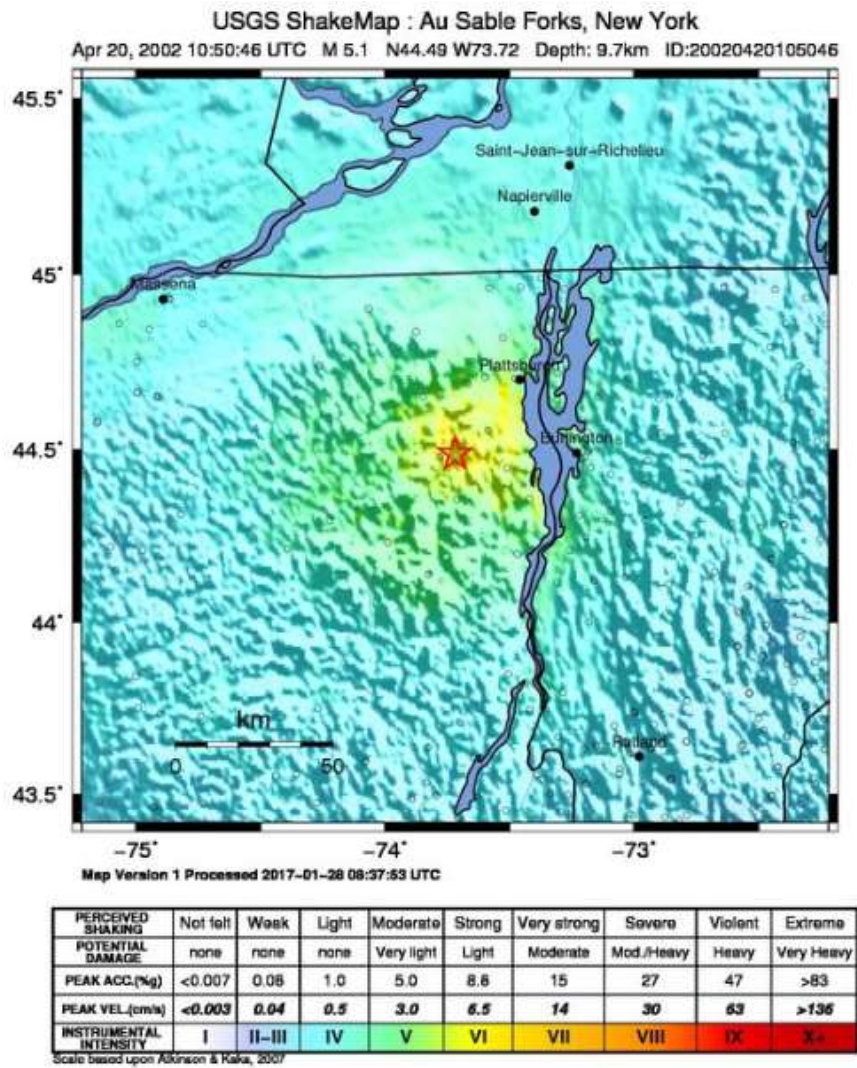


Figure A4.9.13. USGS Shakemap (2017) in terms of Modified Mercalli Intensity (MMI). The red star is the epicentre of the main shock.

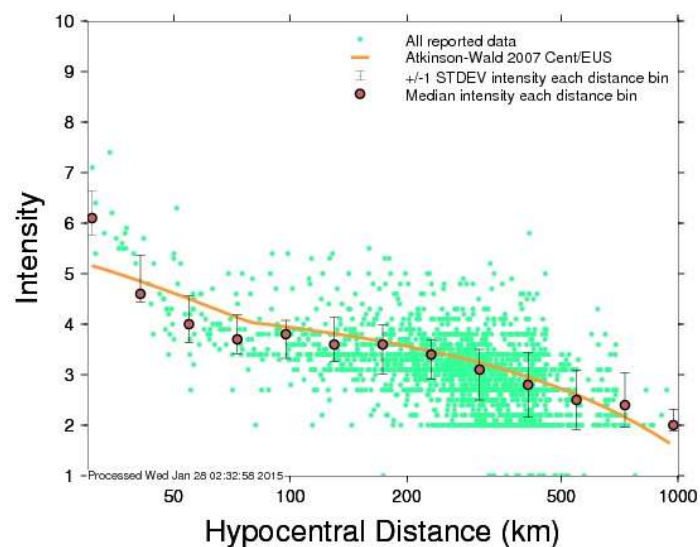


Figure A4.9.14. Intensity attenuation with distance from the epicentre (USGS, 2017). Green dots indicate the actual answers per distance, red points the median intensity per distance bin with a standard deviation interval and orange curve the values of the intensity prediction equation of Atkinson & Wald (2007).

A4.9.4.2 Ground motion recordings

The 2002 earthquake of Au Sable Forks was the first moderate event in the ENA to be well recorded by regional broadband stations located all over the United States and Canada. More than 50 broadband three-component records are available for the mainshock from regional stations over distance ranges from 70 to 4000 km, examples of which are shown in Figure A4.9.15 (Seeber *et al.*, 2002).

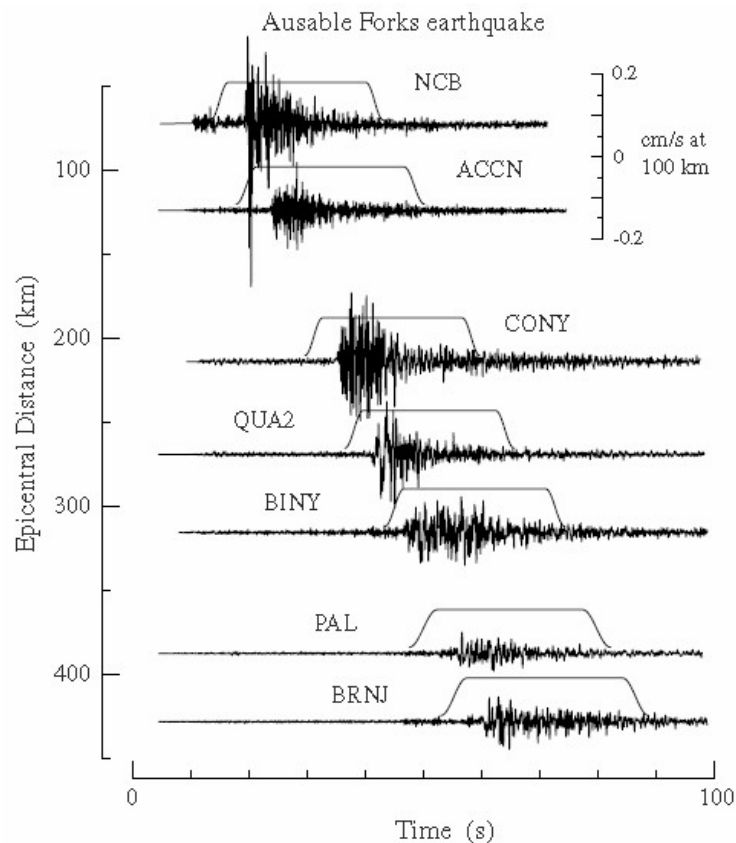


Figure A4.9.15. E–W component record section of ground velocity for the Au Sable Forks earthquake at seven broadband stations. From Boatwright & Seekins (2011).

The high signal-to-noise ratio of the available earthquake records over a broad frequency range enabled their spectral analysis, which yielded a pronounced sag at a frequency near 2 Hz, suggestive of significant source complexity (Atkinson & Sonley, 2003).

Atkinson & Sonley (2003) compared the peak spectral accelerations of the Au Sable Forks event at different frequencies to those of other ENA earthquakes of **M**5.0 (± 0.2) and against a range of ground motion attenuation relations used for ENA for moderate-size events, and came to the conclusion that the propagation of energy for the Au Sable Forks earthquake is typical for the region of ENA. As shown in Figure A4.9.16, the largest values observed were of the order of 0.6 cm/s² at 0.5 Hz (2 seconds), 10 cm/s² at 1 Hz (1 second), 200 cm/s² at 5 Hz (0.2 seconds) and 300 cm/s² at 10 Hz (0.1 seconds). The same conclusion was drawn by Boore *et al.* (2010), who carried out analogous comparisons.

M=5.0 (± 0.2): Observed PSA vs. ground motion relations

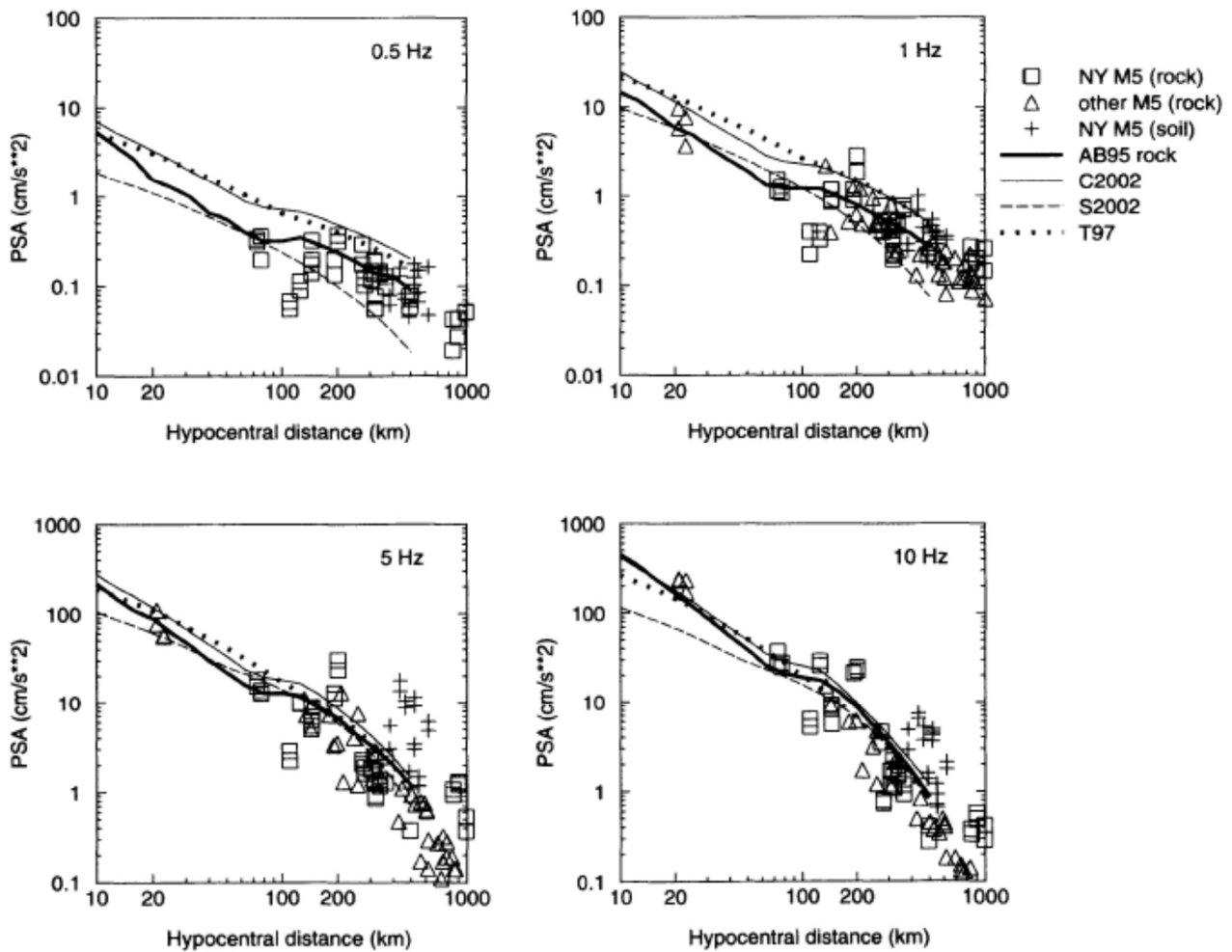


Figure A4.9.16. Response spectral amplitudes vs hypocentral distance for the for **M5.0 (± 0.2)** earthquakes on rock (squares for Au Sable Forks, triangles for other events) and soil for the Au Sable Forks event (crosses) compared to various ground-motion prediction equations (GMPEs) for rock sites in the ENA. From Atkinson & Sonley (2003).

A4.9.4.3 Inferred shaking levels

Since strong motion recordings for this earthquake are only available at distances larger than 70 km, the peak ground acceleration values expected to have been observed during the earthquake, estimated by the USGS based on information from reports of felt intensity (Did You Feel It?, DIYF), the ground motion prediction equation of Campbell (2003) and the Inverse Ground motion intensity conversion equation of Atkinson & Kaka (2007), are of particular interest. The peak ground acceleration (PGA) contours are illustrated in the ShakeMap of Figure A4.9.17 (left) and the peak spectral acceleration (PSA) contours for 0.3 s period, being the closest fundamental period to the majority of the exposed building stock, are mapped in Figure A4.9.17 (right). The maximum estimated PGA and PSA at 0.3 s are around 0.20 g and 0.30 g, respectively.

In view of the relatively good agreement observed between the spectral accelerations of the recorded ground motions of the 2002 Au Sable Forks earthquake and the prediction

models against which Atkinson & Sonley (2003) compared them, maximum spectral accelerations at 0.2 and 0.1 seconds in the ranges 0.10-0.30 g and 0.10-0.40 g at a hypocentral distance of 10 km can be inferred from Figure A4.9.16.

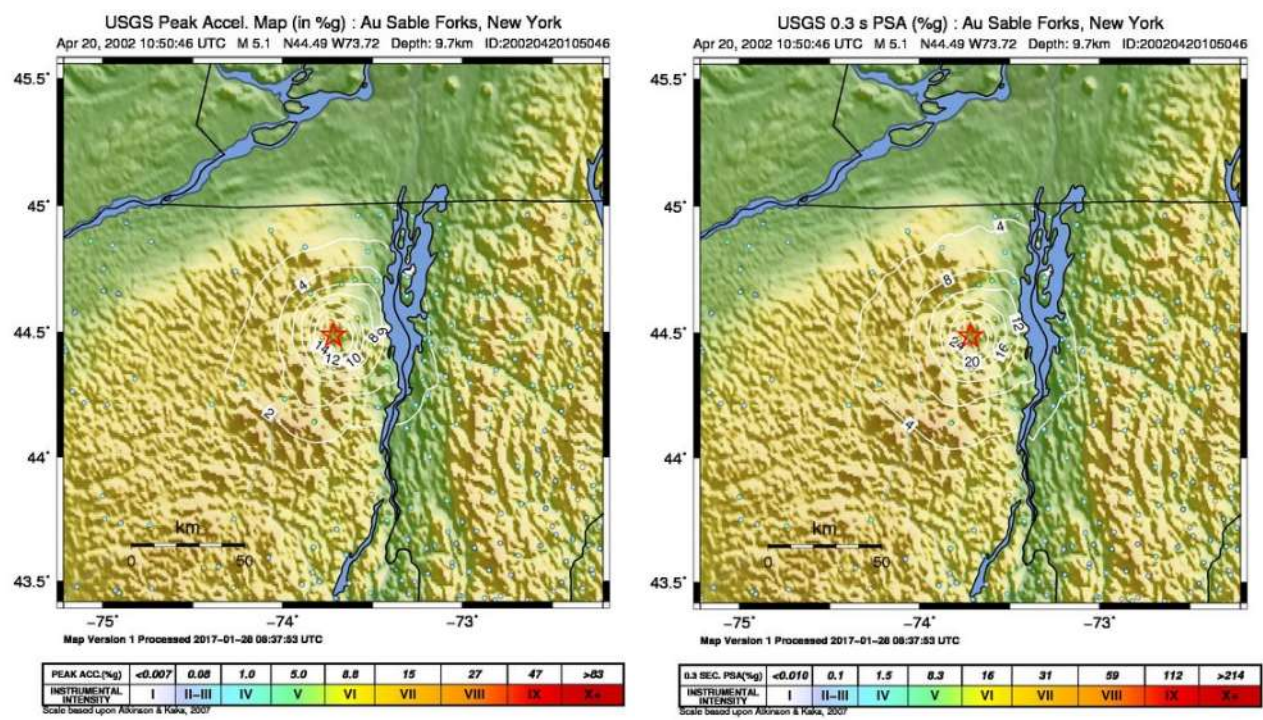


Figure A4.9.17. Peak Ground Acceleration (left) and Peak Spectral Acceleration at 0.3 s period for Au Sable Forks 2002 earthquake (USGS, 2017).

A4.9.4.4 Duration of ground shaking

As near field strong motion recordings do not exist and no access to existing far field recordings was possible, the duration of ground shaking can only be inferred by means of duration prediction models. Estimations of earthquake significant durations in terms of 5-75% of Arias intensity were obtained using the empirical relations proposed by Bommer *et al.* (2009) and Afshari & Stewart (2016), and the results are shown in Figure A4.9.18¹. Based on the hypocentral solution provided by LDEO, the hypocentral depth equals 4.8 km and the source radius approximately 1 km, and thus the upper edge of the seismogenic fault was set at 3.8 km. A range of distances to the rupture and soil types present in the area (see Section A4.9.3.2) were considered, together with an extreme value of 200 m/s to provide an idea of an upper bound.

Residents of New London, New Hampshire, around 170 km south-east of Au Sable Forks, reported that shaking lasted between 15 and 20 seconds (CNN, 2002). This is consistent with the values shown in Figure A4.9.18 at large distances for soft soils, though it is noted that the model of Bommer *et al.* (2009) is being applied out of the distance range for which it was derived.

¹ Calculated as per a previous version of this report with M5.0 instead of the finally adopted M5.1.

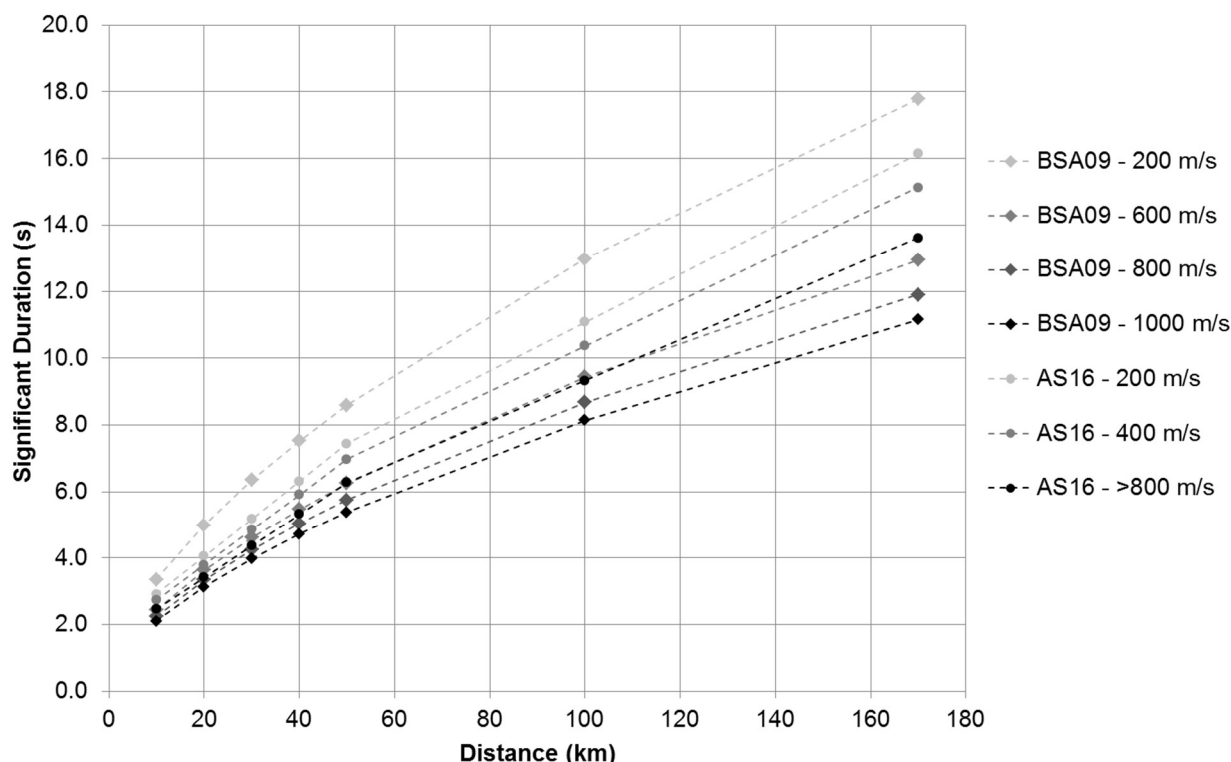


Figure A4.9.18. Observed durations (squares) and inferred significant durations (dashed lines) for a range of epicentral distances and V_{s30} values, predicted by the models of Bommer *et al.* (2009, BSA09; diamonds; valid up to a distance of 150km) and Afshari & Stewart (2016, AS16; circles), for the mainshock of 20th April 2002 in Au Sable Forks.

A4.9.5 Collateral earthquake hazards

A4.9.5.1 Surface rupture

Viegas *et al.* (2010a) report that no surface rupture occurred for this event. This is compatible with the small source radius reported by LDEO and the depth of the mainshock reported between 5 and 15 km.

A4.9.5.2 Landslides

A violent rockslide was triggered by the seismic ground motion on a mountainous area with 60°-slopes around 34 km to the south of the epicentre, as Pierre & Lamontagne (2004) explain. Blocks of rocks and soil drifted as far as 400 to 600 m. Landslides of such extent are rare for earthquakes of moderate size (Pierre & Lamontagne, 2004).

A4.9.5.3 Liquefaction

According to Pierre & Lamontagne (2004), evidence of liquefaction was found at the steep fill slope (34°-45°) of the embankment of a road located on the hillside of a river basin in the most affected area. The material of the fill was silt to fine sand with high moisture, thus

susceptible to liquefaction and instability under seismic cyclic excitation. It is suspected that a flood that occurred in the summer of 1998 may have had an influence on the saturation of the material. The increase in the internal pore pressures of the saturated fine-grained material due to the 2002 earthquake led to the failure of the soil's cohesion from the top to the bottom of the slope and, eventually, failure of the fill's stability.

A4.9.5.4 Settlements

Only one explicit reference to ground settlement has been found for this earthquake, and it corresponds to a case of subsidence at the end supports of a small masonry arch bridge built in 1936 (Pierre & Lamontagne, 2004). Its sidewalks, parapets and stonework were damaged as a consequence.

A4.9.6 Exposed population

A4.9.6.1 Socio-economic setting

According to the 2004 Human Development Report (United Nations, 2004), the Human Development Index (HDI) for the USA was 0.939 in 2002. According to the 2002 world's ranking reported in 2004, the USA are located in the 8th place, while the Netherlands ranked 5th. Inequality-adjusted HDI (IHDI) values only started being calculated in 2010, and thus are not available for 2002. In 2015, the IHDI of the USA was 0.796, while that of the Netherlands was 0.861 (United Nations, 2016). Table A4.9.6 compares the HDI and IHDI for both countries. The column "Adj. HDI" provides the HDI values given online (UNDP-HDD, 2016) for 2002, adjusted for data consistency in time.

Table A4.9.6. Human Development Index and Inequality-adjusted Human Development Index for USA and the Netherlands. From United Nations (2016) and HDR-UNDP (2016).

Report	Data	USA				Netherlands			
		HDI	IHDI	Rank	Adj. HDI	HDI	IHDI	Rank	Adj. HDI
2004	2002	0.939	-	8	0.889	0.942	-	5	0.881
2016	2015	0.920	0.796	10	-	0.924	0.861	7	-

It is evident, as Figure A4.9.19 indicates, that the United States follow, in general, a stable and growing economic course, which was slightly destabilized in 2008 during the world's economic recession. Considering the size of the USA compared to the Netherlands, its GDP is several times higher (Figure A4.9.19, left). However, the GDP per capita of the two countries are comparable in magnitude, with that of the USA exceeding that of the Netherlands most of the time (Figure A4.9.19, right). However, the IHDI ranking suggests that wealth is more evenly distributed in the latter than in the former.



Figure A4.9.19. GDP (left) and GDP per capita (right) fluctuation for the USA and the Netherlands for the last 65 years according to World Bank national accounts data and the Organization for Economic Cooperation and Development (OECD) National Accounts data files (The World Bank, 2017).

Table A4.9.7 presents a comparison between the United States and the Netherlands in terms of gross domestic product (GDP), GDP per capita and unemployment rate for 2002, to represent the situation during the 2002 earthquake, and 2015, for the current picture. According to the Department of Numbers (2016), the GDP per capita of the State of New York was higher than the US average by 23% in 2002 and by 26% in 2016. However, in particular for the counties of Clinton and Essex, on the boundary of which Au Sable Forks town is located, the per capita income is lower than the respective figure of New York State (33,236\$) in 2015 (US Census Bureau, 2015) by 50% and 25% respectively. This is expected, as the whole of the state of New York includes the wealth concentrated around New York City, which does not necessarily represent the conditions elsewhere in the state. The economy of the area around Au Sable Forks is based on services provision (educational, healthcare, social), retail trade, manufacturing and agriculture, according to the US Census Bureau (2009-2013). US Beacon (2000) gives some more details regarding the economy of the town of Au Sable Forks, where on top of the aforementioned employment categories it is mentioned that an important percentage of the locals was occupied in the construction sector, according to 2000 census data.

Table A4.9.7. Gross domestic product (GDP), GDP per capita and unemployment rate for the USA and the Netherlands, according to International Monetary Fund (2017).

Indicator	Units	USA		Netherlands	
		2002	2015	2002	2015
Gross domestic product, current prices	Billions USD	10,977.53	18,036.65	467.016	750.70
Gross domestic product per capita, current prices	USD	38,113.89	56,083.97	28,919.20	44,322.83
Unemployment rate	%	5.78	5.28	3.67	6.89

A4.9.6.2 Population density and distribution

Au Sable Forks is a town of the state of New York that is located on the boundary between Clinton and Essex counties (Figure A4.9.20, right), with the northern part of the community, within Clinton county, being the most inhabited one.

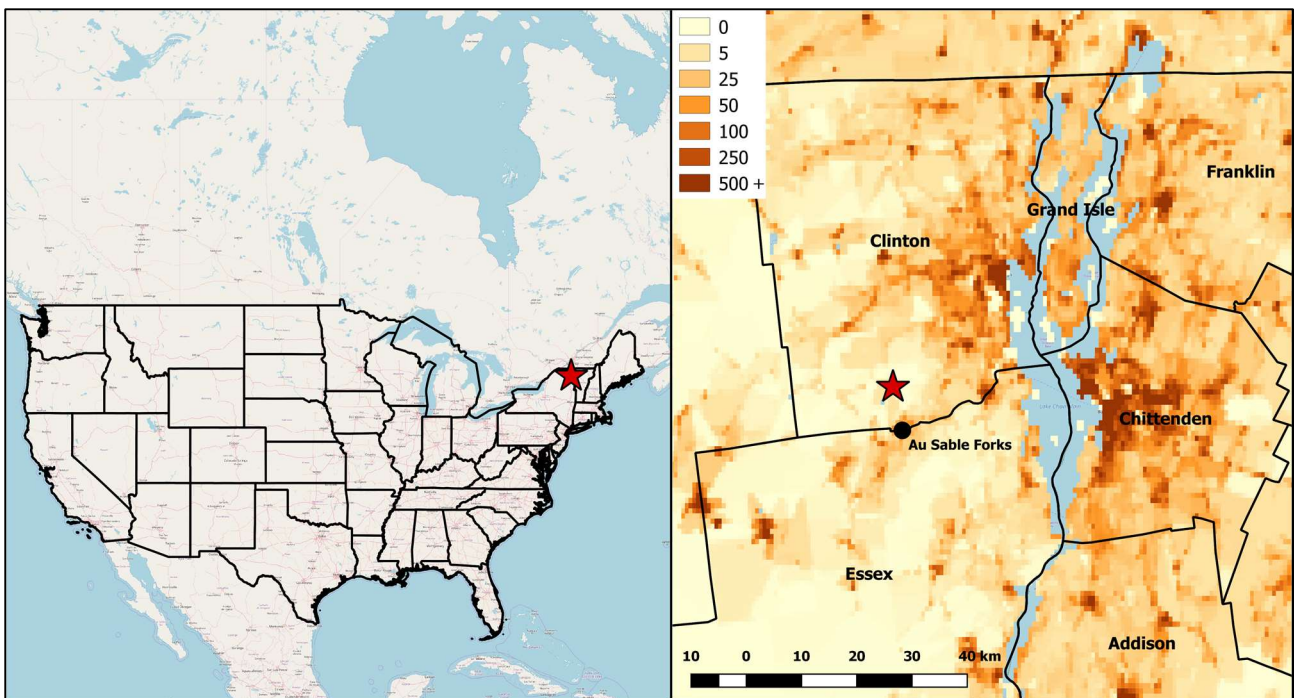


Figure A4.9.20. Location of Au Sable Forks town within the United States (left) and population density (people/km²) in the year 2005 around the epicentral area, according to data from Gridded Population of the World GPW v4.0 (CIESIN, 2016). Red star denotes the epicentre.

The area hit by the 2002 earthquake is scarcely populated, as Figure A4.9.20 (right) illustrates, yet located in the highly populated State of New York. In Table A4.9.8 the population of the most affected communities (MMI \geq VI), as inferred from a zoom-into the isoseismal contours of the USGS ShakeMap (Figure A4.9.13), is listed for the year 2000. Moreover in Table A4.9.9 the population of the six New York counties affected by the earthquake and thus eligible for federal assistance (Pierre & Lamontagne, 2004) is also given. According to the New York State Hazard Mitigation Plan (NYSHMP, 2008; 2014b), the Presidential Disaster Declaration issued in 2002 concerned the counties of Clinton, Essex, Franklin, Hamilton, Warren and Washington, although it is clear that not all of their entire population was directly affected.

According to the USGS EXPO-CAT database (Allen *et al.*, 2009; USGS-PAGER), over 428,445 people were exposed to an MMI intensity of over V (intensity level that indicates that the earthquake is felt and vulnerable structures may start to exhibit low damage). Around 50% of this population was at an urban environment. Disaggregating the above figures, a total of 8,738 people is estimated to have been exposed to MMI over VII (VII to VIII+0.5) with a 70% being at rural environment. The latter may be considered as an overestimation given that no other scientific sources provide MMI intensity over VII.

Table A4.9.8. Population in 2000 of most affected communities (MMI \geq VI inferred from the USGS ShakeMap, Figure A4.9.13). Data from US Beacon (2000).

Community	Population (2000)
Keesville	1,834
Peru	1,514
Au Sable Forks	670
Redford	512
Schuyler Falls	1,187
Jay	1,429

Table A4.9.9. Total population in 2000 of affected counties, eligible for federal assistance (Pierre & Lamontagne, 2004). Data from US Census Bureau (2017).

County	Population (2000)
Clinton	80,525
Essex	38,717
Franklin	50,558
Hamilton	5,252
Warren	63,979
Washington	61,022

A4.9.6.3 Time of day of earthquake

The earthquake hit the area of the North-eastern Adirondack mountains at 6:50:45 am local time (10:50:45 UTC) on a Saturday. This may have had a positive impact on the casualty aftermath, as the roads may have been busier at a later hour or a weekday, though no reference to this has been found in the literature. Moreover, having occurred at the start of the day, the failure of the electrical supply that lasted up to 10 hours in certain areas likely had a milder impact than if it had occurred at night time.

A4.9.7 Characteristics of exposed building stock

A4.9.7.1 Seismic design codes

While Cutcliffe (2000) believes that it was the 1906 San Francisco earthquake which marked the start of a real interest in earthquake engineering and seismic design in the United States. Freeman (1932) stated, a quarter of a century later, that "the art of constructing earthquake-resisting buildings is still in the formative stage, that there are differences of opinions among experts and that there is much deficiency in important data". Further, he points at the 1925 Santa Barbara earthquake to have been more significant in raising awareness on the subject. It was this devastating event that prompted the first edition of the Uniform Building Code (UBC) in 1927, which contained the first written seismic design provisions for a regional level, but which did not become mandatory until 1961 (Beavers, 2002).

As recapitulated by Beavers (2002), the origin of seismic design codes and building codes in general in the USA started in a fragmented fashion, by regions or states. For example, the Uniform Building Code (UBC) mentioned above was typically used west of the Mississippi river. The National Building Code of the Building Officials and Code Administrators (known as the BOCA Code) was, instead, used in the upper midwest and northeast. It was first published in 1950, including seismic design provisions. In the south, the Standard Building Code (SBC) of the Southern Building Code Congress International (SBCCI) was used. Seismic design provisions were included in the SBC in 1976, by referencing ANSI A58.1 (1982), but "were not mandatory unless local authorities required seismic design, which was rarely the case", until 1988. The 1987 edition of the BOCA Code also incorporated the provisions of ANSI A58.1, and made them mandatory.

The ANSI A58.1 standard of the American National Standards Institute (ANSI) was first published in 1945 and was the first standard to consider earthquake loads (Beavers, 2002). However, seismic hazard did not have a role in ANSI A58.1, which only had a map showing the locations of destructive earthquakes of the past until its 1972 edition, in which a seismic hazard description similar to the 1949 USCGS (United States Coast and Geodetic Survey) map was incorporated. The 1972 edition of ANSI A58.1 was also the first one to outline modern wind design provisions (Fratinaro & Schroeder, 2015; Ghosh, 2008), evolving from more basic guidelines developed in the 1950s (Huston, 2007).

The 1949 hazard map was the first one to encompass the whole of the contiguous USA and it was based on "the premise that similar earthquakes will occur in the future where they have occurred in the past" (Beavers, 2002). For reasons that are not fully clear, this map was withdrawn in 1952 and replaced with a map that only showed the location of known past significant earthquakes. In the 1970s, the responsibility of producing hazard maps passed on to the USGS (United States Geological Survey), who published the first map developed in the form of probabilistic estimates of maximum acceleration contours on rock in 1976 and which, as highlighted by Beavers (2002), represented a significant paradigm shift. It should be noted, however, that the first edition of the ATC3-06, which in 1985 evolved into the National Earthquake Hazards Reduction Program (NEHRP) Recommended Provisions for Seismic Regulations for New Buildings and Other Structures, used a truncated version of this map in 1978, not allowing for values above 0.4g to be considered. This map was used for almost 20 years, given the inability to reach consensus on a different map that took place in between 1988 and 1994. It was finally updated by the USGS in 1997, after a four-year project called Project 97, during which large efforts were invested in giving a voice to all the professionals and sectors involved. Since then, the USGS hazard map has been updated in 2002, 2008 and 2014.

The way in which seismic loads were considered evolved significantly from the simple use of a 7.5%-10.0% of the building's weight as a lateral load (1927 edition of the UBC) with the progressive incorporation of significant factors such as soil type and capacity, seismic zonation, natural period of vibration of the structure and importance of the building.

In 1988, ANSI combined with ASCE to update and re-designate ANSI A58.1-1982 to ASCE 7, which is now the most significantly recognised standard by all earthquake

regulations, codes, standards, procedures and guidelines for basic seismic design in the USA (Beavers, 2002). Furthermore, ASCE 7 is also the "de facto" national wind design standard (Fratinardo & Schroeder, 2015). In addition, in its 2012 revision (ASCE 7-10) it incorporated seismic requirements for non-structural elements based on the NEHRP Provisions. The International Building Code (IBC), whose first edition in 2000 was also based in the NEHRP Provisions, makes reference to ASCE 7 for the definition of seismic and wind loads, incorporating seismic analysis requirements with reference to ASCE 7-05. Currently the 2015 IBC is in force and the regional and local codes are based on the IBC with specific amendments (Anderson & Naeim, 2012).

According to the Division of Building Standards and Codes of New York State (2017), an integrated building and fire code was introduced by law in 1981, ensuring that all the communities of the state apply the same standards. Prior to this date, the decision of codes enforcement was left upon the local governments. Hence, on 1st January 1984, the Uniform Fire Prevention and Building Code (Uniform Code) was enforced for all municipalities except the city of New York, which kept its own Code. In 2003, the Uniform Code was updated according to the most modern national models included into the International Code Council (ICC) with the latest update to take place in 2010. It is underlined that local governments (cities, towns, villages and counties) are responsible for enforcing the Uniform Code.

The Building Code Effectiveness Grading Schedule (BCEGS), developed by the Insurance Services Office (ISO), indicates that the overall level of code enforcement across the state of New York is relatively low when compared to the country as a whole and to states like California, in which awareness with respect to seismic risk is much greater (ISO Mitigation, 2016). Figure A4.9.21 shows the distribution of communities by BCEGS class number for the United States as a whole and for the state of New York. Within this classification schedule, classes 1-3 correspond to the maximum enforcement levels, while class 10 indicates no enforcement at all. These figures agree with statements of Beavers (2002) and Cutcliffe (2000) who highlight that, due to their relative lack of seismic activity, the effort to incorporate good seismic design practices in building codes has been more challenging in the central and eastern USA, when compared to other areas of the country. In fact, New York State scores in average 7, which is a rather unfavourable score in the 1 to 10 scale (ISO Report, 2016). Interestingly, as the 2005-2015 trends of ISO Mitigation (2016) reveal, a drop is observed in the average BCEGS class of New York state for both residential and commercial buildings, from class 6 in 2005 to class 7 in 2015, what indicates a leniency in code adoption and enforcement.

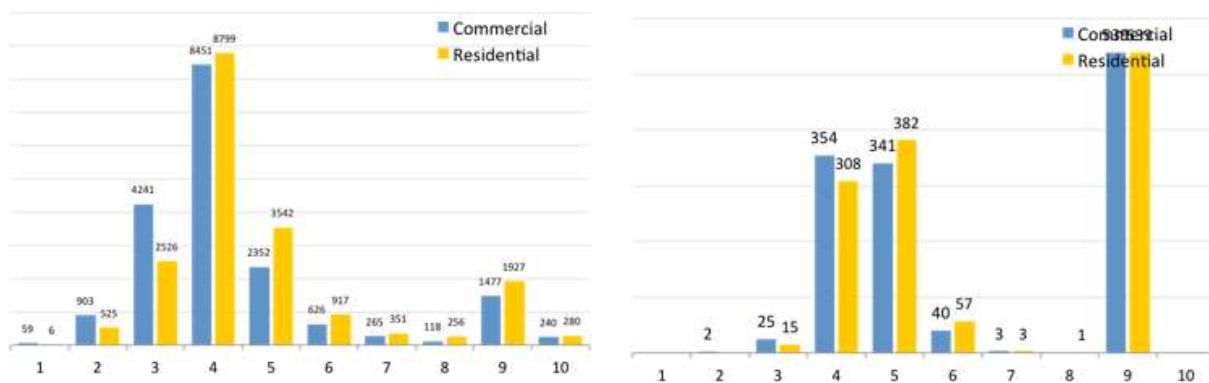


Figure A4.9.21. Distribution of communities by BCEGS class number for the whole of the United States (left) and the state of New York (right). Personal lines include 1- and 2-family dwellings. Commercial lines include all other buildings. Classes 1-3: maximum enforcement. Class 10: no enforcement (ISO Mitigation, 2016).

A4.9.7.2 Building typologies

Data regarding typologies at the country level collected from the PAGER Inventory Database v2.0 (Jaiswal & Wald, 2008) for the United States are summarized in Figure A4.9.22. As can be observed, wood stud-wall frames with board sheathing is the most common typology in the USA for urban, rural, residential and non-residential buildings. Around 20% of the dwellings of USA are unreinforced brick masonry while a 5% of mobile homes is registered. The supremacy of the aforementioned typology in the area of interest is also confirmed from visual inspection by means of Google Street View.

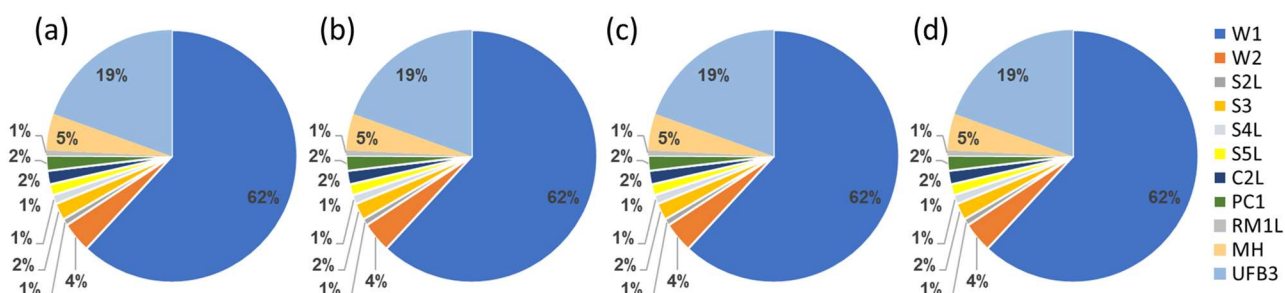


Figure A4.9.22. Proportion of building main typologies in USA for (a) rural residential, (b) urban residential, (c) rural non-residential, (d) urban non-residential typologies: W1: Wood stud-wall frame with plywood/gypsum board sheathing, W2: Wood frame, heavy members (with area > 5000 sq. ft.); S2L: Steel braced frame low-rise; S3: Steel light frame; S4L: Steel frame with cast-in-place concrete shear walls low-rise; S5L: Steel frame with unreinforced masonry infill walls mid-rise; C2L: Reinforced concrete shear walls low-rise; PC1: Precast concrete tilt-up walls; RM1L: Reinforced masonry bearing walls with wood or metal deck diaphragms low-rise; MH: Mobile homes; UFB3: Unreinforced brick masonry in lime mortar. 2002 Data from USGS-PAGER Jaiswal & Wald (2008).

From the information available from the US Census Bureau (2009-2013) and presented in Figure A4.9.23, it is evident that a large number of the buildings of the most affected municipalities were built prior to 1939 and most probably with low or no seismic provisions (Bruneau & Lamontagne, 1994). According to the same source, the main building typology is 1-unit house detached (Figure A4.9.24), a typical configuration for the U.S. rural areas.

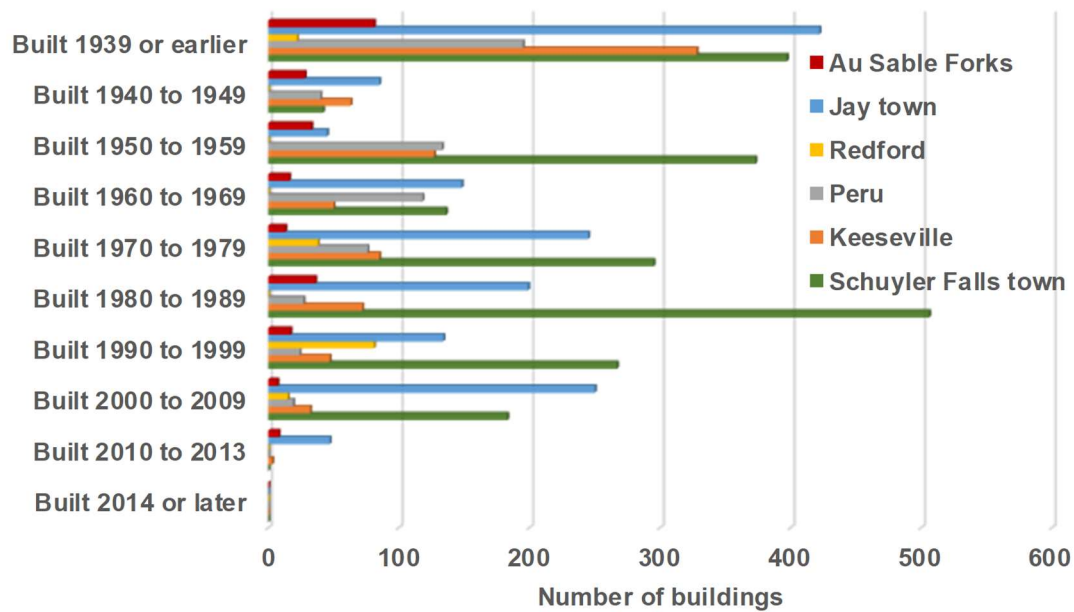


Figure A4.9.23. Distribution of the building stock of the affected communities according to their construction period. Data of 2015 from US Census Bureau (2009-2013).

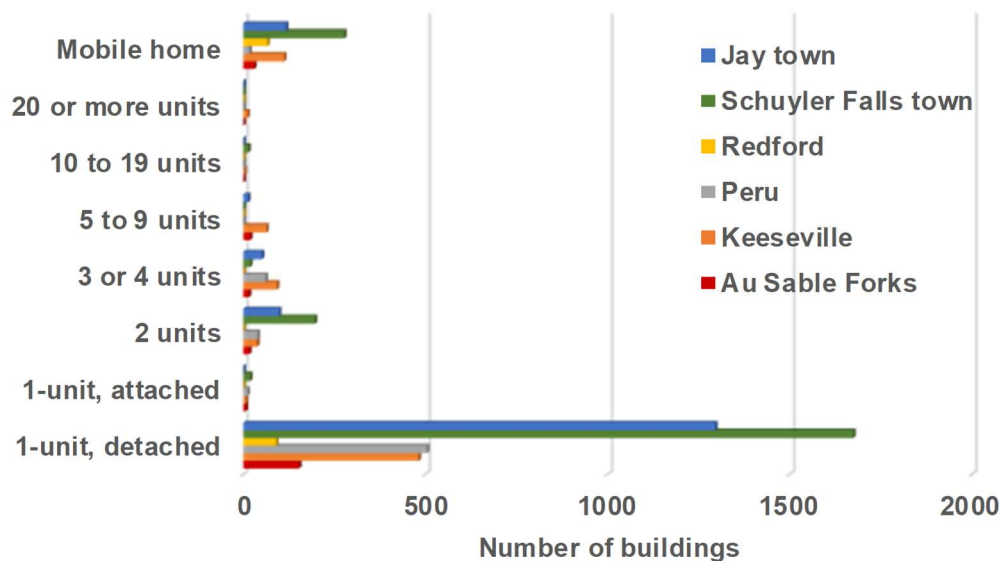


Figure A4.9.24. Distribution of buildings per number of units for the most affected municipalities. Data of 2015 from US Census Bureau (2009-2013).

A4.9.7.3 Prior damage and retrofit

No details on prior damage or retrofit of the built environment are available. Reference is only made to the potential weakening of the road between Keeseville and Clintonville due to a flood during the summer of 1998 (Pierre & Lamontagne, 2004). This part of the road exhibited damage to its filled slopes at several locations.

A4.9.8 Damage observations

A4.9.8.1 Damage states

Given the relatively low level of structural damage observed, there are no reports making use of standardised damage scales for this earthquake. The damage is only given in descriptive terms based on the outcome of site investigations (Pierre & Lamontagne, 2004).

As discussed in Section A4.9.4.1, Modified Mercalli intensities (MMI) between VI and VII have been estimated in an extended area around the epicentre. As explained in Appendix II, the MMI scale defines an intensity value according to the degrees of damage masonry buildings experience. The maximum estimated intensities correspond to damage to the lowest quality masonry and some cracks to ordinary masonry with neither special reinforcement nor extreme weaknesses, as Table A2.3.2 (Appendix II) describes.

A4.9.8.2 Damage statistics and description

The consequences of the 2002 Au Sable Forks earthquake appear to have been minor to moderate but spread over a large region and thus affecting around 900 residential and professional buildings to some extent (Pierre & Lamontagne, 2004). Seeber *et al.* (2002) indicate damage to the buildings content as the most widespread (compatible with intensity VI of Figure A4.9.13), but highlight as well that many chimneys fell or were damaged, and that structural damage to buildings was also observed in areas close to the epicentre, where VII intensities were reported, as described in Section A4.9.4.1. Damage and malfunction of infrastructures, in particular the road and electrical networks, was widely reported as well (Revetta & Harradine, 2013; CNN, 2002; Pierre & Lamontagne, 2004). It is noticeable that Clinton and Essex counties were declared in a state of emergency due to the numerous instances of damage (ranging from minor, *e.g.*, shattered glass, to more significant, *e.g.*, cracking of buildings) reported by the locals (CNN, 2002; New York Times, 2002).

According to several sources (Pierre & Lamontagne, 2004; New York Times, 2002; USGS, 2002), damage to buildings consisted mostly of:

- cracking and toppling of chimneys (*e.g.*, Figure A4.9.25, left),
- damage to wooden cornices (*e.g.*, Figure A4.9.25, right),
- cracking of non-structural heavy cladding of unreinforced masonry,
- damage to cladding of structural timber buildings (*e.g.*, Figure A4.9.26),
- damage to foundations of older buildings located over alluvial deposits, attributed by Pierre & Lamontagne (2004) to the tendency of the latter to amplify ground motions.



Figure A4.9.25. Rotation and partial destruction of a chimney in Au Sable Forks (left); deformed cornices at a residential building in Au Sable Forks (right). From Pierre & Lamontagne (2004).

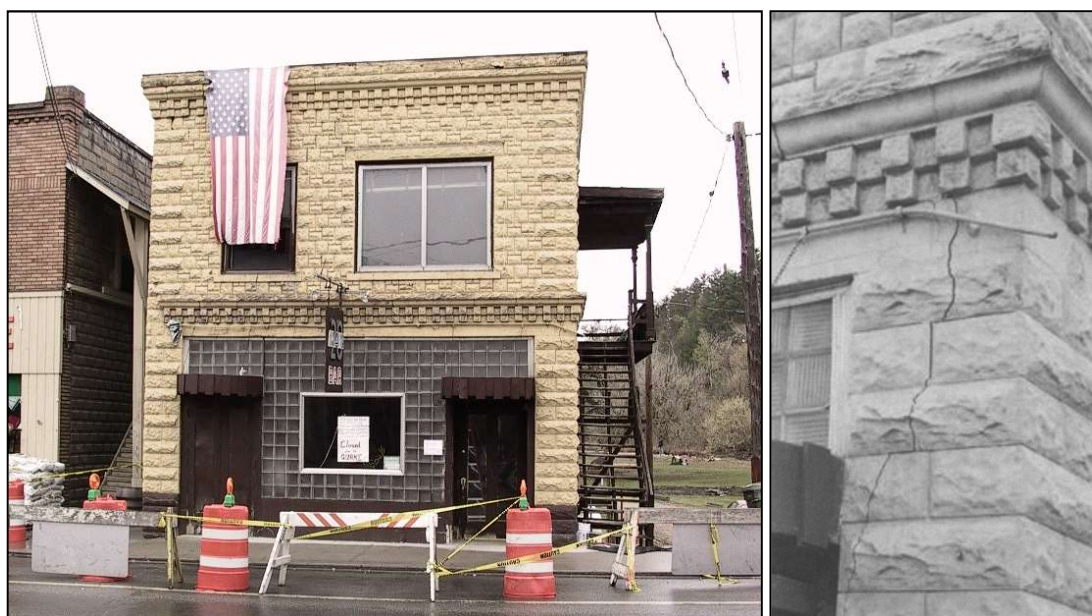


Figure A4.9.26. Damage to architectural unreinforced masonry front wall. From M. Withers, CERL, Univ. Memphis (LDEO) (left) and Pierre & Lamontagne (2004) (right).

A major impact of the earthquake was the damage to the road network and in particular to a part of State Route 9 between Keeseville and Clintonville, as explained by Pierre & Lamontagne (2004) and depicted in Figure A4.9.27. As discussed in Section A4.9.5.3, the fill of the steepened slope liquefied, leading to the collapse of some sections of the road at a length of around 60 metres (ABC News, 2011). Vague reference is also made to other local failures of the road network by Pierre & Lamontagne (2004). ABC News (2011) briefly state that County Road 39 was also damaged. CNN (2002) mentions that the New York Department of Transportation immediately started the inspections for the adequacy of bridges, the outcome of which does not appear to have been made publicly available. Only damage to a small masonry arch bridge from 1936 has been reported by Pierre & Lamontagne (2004). The bridge was cracked at its sidewalks, parapets and stonework of

its arch, mainly due to settlement at its end supports. Finally, a shallow crack of unconfirmed origin was observed at the support of the small Fern Lake Dam. Temporary measures were taken to prevent possible leaks.



Figure A4.9.27. Damage on State Route 9 (Photo Courtesy of Frank Revetta and Eric Therm at APN Magazine, 2003).

As thoroughly described by Pierre & Lamontagne (2004), the electricity supply was interrupted following the earthquake for periods lasting between 15 minutes and 10 hours, as a consequence of secondary effects and several malfunctions of the equipment including:

- the partial or complete damage of three transmission towers by a severe rockslide that occurred in a mountainous location between Raven Hill and Green Hill, between Elizabethtown and Westport (Section A4.9.5.2),
- the breaking of a fuse due to the amplification of motion at the top of a 13-metre tall pole of a secondary electric line feeding the Peru area,
- the false tripping of the protection system of a generator of the power plant located on the Saranac River near Plattsburgh,
- a serious short circuit at Jay substation caused by damaged inflicted to a ceramic post insulator.

Finally, the New York Times (2002) reports the occurrence of water main breaks, though no further details about the extent or the location of the damage is provided. Pierre & Lamontagne (2004) mention that the water and sewer systems of Peru town were affected by cracks that appeared on pre-cast blocks and the surfacing of a pre-existing leak of a water line.

Because of the small impact of Au Sable Forks earthquake compared to global disasters, no extensive reports are available within global losses databases.

A4.9.8.3 Observed weaknesses

Three kinds of weaknesses may be highlighted for this earthquake. First, the steep slopes of the mountainous zones, combined with the use of a silt to fine sand fill for geotechnical works, which led to numerous rockslides and soil failures (Pierre & Lamontagne, 2004). Second, the vulnerability of the electric equipment to seismic accelerations. Third, and finally, the vulnerability of non-structural elements such as false front walls of unreinforced masonry, timber cornices and chimneys (Pierre & Lamontagne, 2004; Bruneau & Lamontagne, 1994).

A4.9.8.4 Damage distribution

The damage described in Section A4.9.8.2 may be localized in Figure A4.9.28. Au Sable Forks is the closest inhabited district to the epicentre (#1 in Figure A4.9.28), where Pierre & Lamontagne (2004) confirm damage to the foundation of a church, cracks to the unreinforced masonry front walls and cornices of buildings, and damage to several chimneys. MCEER (2002) refer also to a chimney at Lake Placid.

As mentioned, the road network presented slope failure at some sections of the State Route 9 between Keeseville and Clintonville (#2 in Figure A4.9.28). The dam which was slightly cracked is sited a few kilometres to the south of the epicentre (#3 in Figure A4.9.28). The severe rockslide which damaged the transmission towers, as described, occurred close to the State Route 9, at a mountainous location between Elizabethtown and Westport, around 34km to the south of the epicentre (#4 in Figure A4.9.28). The hydrogenerator plant that went offline is located northerly of the map's margins on the Saranac River, near Plattsburgh. The substation that caused the severe power problem is located at Jay (#5 in Figure A4.9.28), same as the damaged arched bridge, according to MCEER (2002).

Although from Figure A4.9.28 it may appear that the damage was concentrated within a few kilometres of the epicentre, this map concerns mainly the infrastructures affected, while the 900 damaged buildings reported by Pierre & Lamontagne (2004) are spread over a much larger region comprising six counties (see Table A4.9.9), with the most affected being Clinton and Essex.

While the role of the topography on the distribution of damage resulting from rockslides or geotechnical failures is apparent, Seeber *et al.* (2002) and Pierre & Lamontagne (2004) highlight as well that the unconsolidated sediments are likely to have played a fundamental role in amplifying ground motions in the alluvial valleys, along which most of the damage to buildings appears to have been located (shaded areas of Figure A4.9.28). In addition, there appears to have been a larger concentration of older buildings in these areas, due to their suitability as farmland (Seeber *et al.*, 2002).

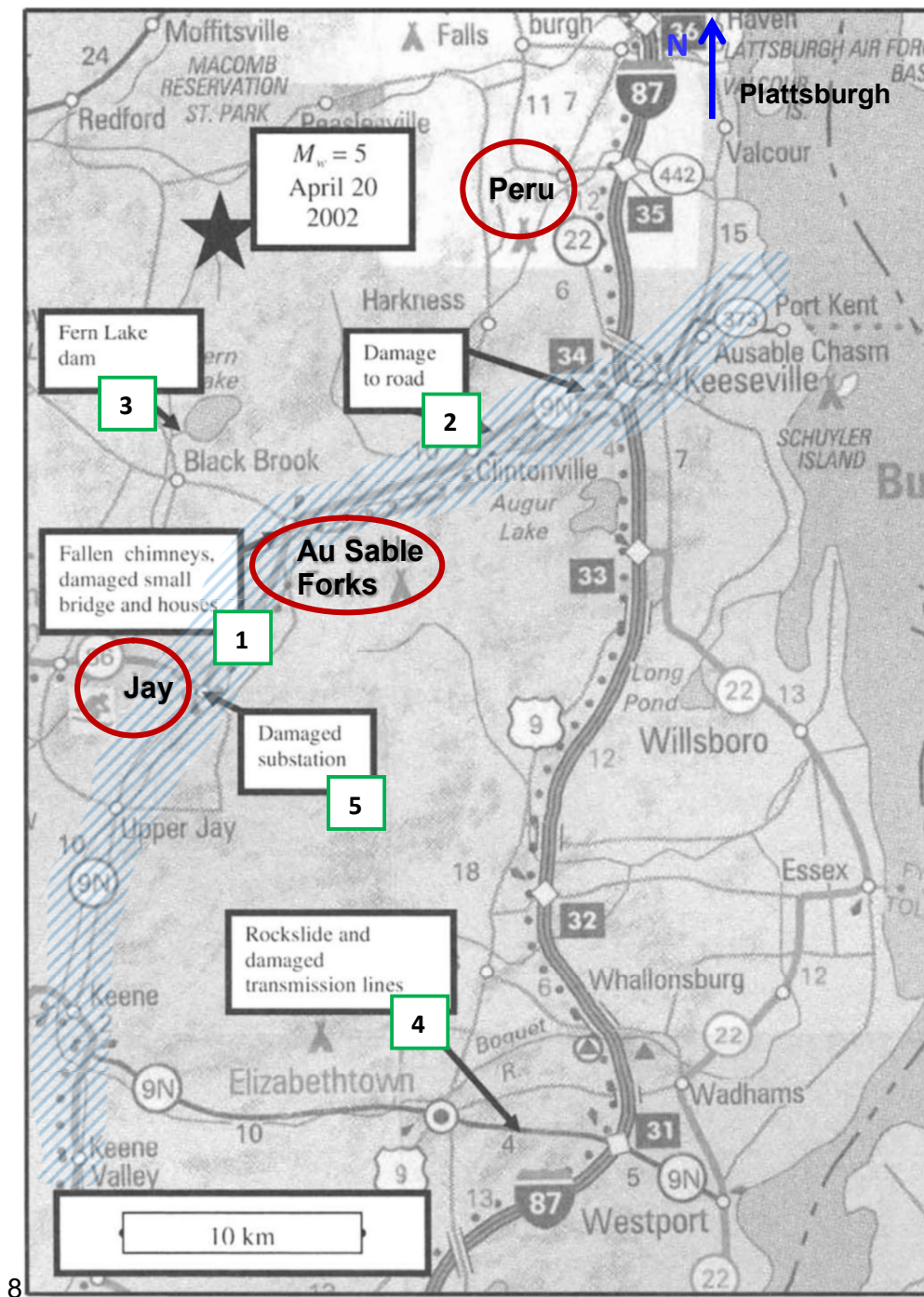


Figure A4.9.28. Location of damage sites. Areas shaded in blue approximately indicate the location of the alluvial valleys. Modified from Pierre & Lamontagne (2004), who adapted it from AAA New York State Map.

A4.9.9 Casualties and losses

A4.9.9.1 Numbers of dead and injured

No injuries or deaths are reported by the scientific or media sources (e.g., Pierre & Lamontagne, 2004; New York Times, 2002). Similarly, USGS PAGER-CAT (Allen *et al.*, 2009) reports no injuries or homeless due to the earthquake.

A4.9.9.2 Causes of casualties

No casualties are reported.

A4.9.9.3 Estimates of economic losses

Despite the moderate size of the earthquake, the economic loss due to the damage to homes, businesses and state infrastructures has been recently estimated at over 16 million US dollars for the counties of Clinton and Essex (Revetta & Harradine, 2013).

Seeber *et al.* (2002) remark that, after the earthquake, the counties of Clinton and Essex were assigned a “Federal Disaster Area” status, and that an estimate of financial losses exceeding 10 million US dollars was announced. Pierre & Lamontagne (2004) highlight that about half of the 10 million US dollars initial estimate for damage repair was directed to the rehabilitation of infrastructures.

Considering that, according to NYSHMP (2014b), the total building inventory value for the affected counties is around 17 million US dollars (around 8.5 million dollars for Clinton and Essex, Table A4.9.10) and that damage was not reported for the entire building stock, it may be inferred that the loss most recently estimated at over 16 million US dollars for the two most affected counties, is greatly attributed to infrastructures rehabilitation and/or downtime losses. Otherwise, damage to the building stock would have been substantial to the point of almost requiring its complete replacement.

Table A4.9.10. Building inventory value for the counties affected by the 2002 earthquake, in thousands of US dollars. Data from NYSHMP (2014b).

County	Residential	Non-residential	Total
Clinton	3,862	1,555	5,417
Essex	2,512	659	3,171
Franklin	2,511	784	3,295
Hamilton	777	120	897
Warren	4,410	1,550	596
Washington	3,048	821	3,869
Total	17,120	5,489	17,245

On 16th May 2002 a Major Presidential Disaster Declaration was issued for the State of New York (DR-1415), unique for earthquake episodes throughout the state’s history (FEMA Disasters, 2004). Unfortunately, no official information regarding individual and public financial assistance appears to be available, other than a rough estimate of more than 2 million US dollars of “eligible damage”, as described in the New York State Hazard Mitigation Plan (NYSHMP, 2014a).

A4.9.10 Discussion and conclusions

The M5.1 Au Sable Forks earthquake on 20th April 2002 occurred within the north-eastern part of the North American continental plate, west of Lake Champlain, and was the first moderate seismic event in Eastern North America to be recorded by broadband instruments. Due to the overall low seismic risk awareness of the region, the earthquake was unexpected for local communities, although damaging earthquakes are known to occur in the area every 22 years on average. Large epicentral distances to recording instruments did not allow for the precise determination of its source parameters as well as those of its largest aftershocks, whereas smaller aftershocks were likely undetected/unresolved.

Although the epicentral area is not densely inhabited, minor to moderate damage to around 900 buildings was observed over a large area. The false front walls of unreinforced masonry and chimneys were some of the most vulnerable elements and, consequently, the most commonly damaged. More severe was the impact of the secondary effects, such as the rockslides and liquefaction that occurred, and the vulnerability of the components of the electrical network, all of which led to the interruption of road access and electricity supply for several hours. Topography and the amplification of ground motions due to site effects were identified as having had a large influence over the damage observed.

Six counties of New York State were, for the first time, declared in a state of emergency due to earthquake disaster and the economic impact was as high as 16 million US dollars, mainly directed to the rehabilitation of infrastructures. No casualties were reported.

A4.9.11 References

A3.9.11.1 Bibliography

- Adams, J. & P. Basham, (1989). The seismicity and seismotectonics of Canada east of the Cordillera. *Journal of the Geological Association of Canada* **16**, 3-16.
- Afshari, K. & J. Stewart (2016). Physically parametrized prediction equations for significant duration in Active Crustal Regions. *Earthquake Spectra*, **32**(4), 2057-2081.
- Allen, T. I., D. J. Wald, P. S. Earle, K. D. Marano, A. J. Hotovec, K. Lin & M. G. Hearne (2009). An Atlas of ShakeMaps and population exposure catalog for earthquake loss modeling. *Bulletin of Earthquake Engineering* **7**(3), 701-718.
- Anderson J. & F. Naeim (2012). Historical development of building code seismic provisions – Appendix. In Anderson J. & F. Naeim (2012): *Basic Structural Dynamics*, John Wiley & Sons, Inc.
- American National Standards Institute (ANSI) (1982). ANSI A58.1, Minimum Design Loads for Buildings and other Structures, Washington, U.S.A.
- Asgharzadeh-Sadegh P. (2012). *Focal mechanisms and variations in tectonic stress fields in eastern Canada (western Quebec and southern Ontario)*, MSc Thesis, Queen's University, Kingston, Ontario, Canada, 188pp. Available online at (last accessed 12th April 2018):

https://qspace.library.queensu.ca/bitstream/handle/1974/7280/Asgharzadeh%20Sadegh_Parisa_20120614_MSC.pdf?sequence=1.

Atkinson, G.M. (1989). Implications of eastern ground-motion characteristics for seismic hazard assessment in eastern North America. *Annals of the New York Academy of Sciences* **558**, 128–135.

Atkinson, G.M. & E. Sonley (2003). Ground motions from the 2002 Au Sable Forks, New York earthquake of M 5.0. *Seismological Research Letters* **74** (3), 339–349.

Atkinson, G.M. & D.J. Wald (2007). “Did You Feel It?” intensity data: A surprisingly good measure of earthquake ground motion. *Seismological Research Letters* **78**, 362–368.

Atkinson, G.M. & S.I. Kaka (2007). Relationships between felt intensity and instrumental ground motion in the Central United States and California. *Bulletin of the Seismological Society of America* **97**, 497–510.

Beavers, J.E. (2002). A review of seismic hazard description in US design codes and procedures. *Progress in Structural Engineering and Material* **4**, 46–63.

Boatwright, J., and L. Seekins (2011). Regional spectral analysis of three moderate earthquakes in Northeastern North America. *Bulletin of Seismological Society of America* **101**, 1769–1782.

Bommer, J.J., P.J. Stafford & J.E. Alarcón (2009). Empirical equations for the prediction of the significant, bracketed, and uniform duration of earthquake ground motion. *Bulletin of the Seismological Society of America* **99**(6), 3217–3233.

Boore, D.M., K.W. Campbell & G.M. Atkinson (2010). Determination of stress parameters for eight well-recorded earthquakes in Eastern North America. *Bulletin of the Seismological Society of America* **100**(4), 1632–1645.

Bruneau, M. & M. Lamontagne (1994). Damage from 20th century earthquakes in eastern Canada and seismic vulnerability of unreinforced masonry buildings. *Canadian Journal of Civil Engineering* **21**, 643–662.

Calais, E. (2005). *Geodetic velocity field for stable North America*. Available online at: <http://web.ics.purdue.edu/~ecalais/projects/noam/noam/>. Last accessed: 27th April 2018.

Campbell K.W. (2003). Prediction of strong ground motion using the hybrid empirical method and its use in the development of ground-motion (attenuation) relations in eastern North America. *Bulletin of the Seismological Society of America* **93**(3), 1012–1033.

Carr, S.D., R.M. Easton, R.A. Jamieson & N.G. Culshaw (2000). Geologic transect across the Grenville orogen of Ontario and New York. *Canadian Journal of Earth Sciences* **37**(2-3), 193–216.

Center for International Earth Science Information Network - CIESIN - Columbia University (2016). *Gridded Population of the World, Version 4 (GPWv4)*. Palisades, NY: NASA Socioeconomic Data and Applications Center. <http://dx.doi.org/10.7927/H4NP22DQ>.

Crough, S. T. (1981). Mesozoic hotspot epeirogeny in eastern North America. *Geology* **9**, 2–6.

Cutcliffe, S.H. (2000). Earthquake resistant building design codes and safety standards: The California experience. *GeoJournal* **51**, 259–262.

Du, W.-X., W.-Y. Kim & L.R. Sykes (2003). Earthquake source parameters and state of stress for the northeastern United States and southeastern Canada from analysis of regional seismograms. *Bulletin of the Seismological Society of America* **93**(4), 1633–1648.

- Engdahl, E.R., R. van der Hilst, & R. Buland (1998). Global teleseismic earthquake relocation with improved travel times and procedures for depth determination. *Bulletin of the Seismological Society of America* **88**, 722-743. Online data available at: <http://www.isc.ac.uk/ehbbulletin/>.
- Faill, R. T. (1997). A geologic history of the north-central Appalachians; Part 1, Orogenesis from the Mesoproterozoic through the Taconic Orogeny. *American Journal of Science* **297**, 551-619.
- Fratinaro, V.F. & S.A. Schroeder (2015). Historical study of the wind design provisions of ASCE 7. *Structures Congress 2015*, ASCE Library, 829–839.
- Freeman J.R. (1932). *Earthquake Damage and Earthquake Insurance*. 1st edition. McGraw-Hill Co, New York, USA.
- Ghosh, S.K. (2008). Searching for simplicity: The evolution of wind provisions in standards and codes in the United States. *RCI Interface*, 13–21.
- Giardini, D., G. Grünthal, K.M. Shedlock & P. Zhang (1999). The GSHAP global seismic hazard map. *Annali di Geofisica* **42**(6), 1225-1228.
- Grünthal, G. (ed.) (1998). European Macroseismic Scale 1998 (EMS-98). *Cahiers du Centre Européen de Géodynamique et de Séismologie* **15**, Centre Européen de Géodynamique et de Séismologie, Luxembourg, 99 pp.
- Heaman, L. M. & B.A. Kjarsgaard (2000). Timing of eastern North American kimberlite magmatism: continental extension of the Great Meteor hotspot track? *Earth Planetary Science Letters* **178**, 253-268.
- Heidbach, O., M. Rajabi, K. Reiter, M. Ziegler & the WSM Team (2016). World Stress Map Database Release 2016. GFZ Data Services. Available online at www.world-stress-map.org.
- Hough, S.E. (2014). Shaking from injection-induced earthquakes in the Central and Eastern United States. *Bulletin of the Seismological Society of America* **104**(5), 2619–2626.
- Hughes, S. & J. H. Luetgert (1991). Crustal structure of the western New England Appalachians and the Adirondack Mountains. *Journal of Geophysical Research* **96**, 16471–16494.
- Huston, E. (2007). SEAW's handbook of a rapid-solutions methodology for wind design. *STRUCTURE Magazine*, 61–64.
- Isachsen, Y.W., E.P. Geraghty & R.W. Wiener (1983). Fracture domains associated with a neotectonic basement-cored dome: The Adirondack Mountains, New York. In Gabrielsen, R.H., I.B. Ramberg, D. Roberts & O.A. Steinlein (eds.): *Proceedings of the 4th International Conference on Basement Tectonics*, International Basement Tectonics Association, Salt Lake City, Utah, 287-305.
- ISO Report, A Verisk Analytics Business (2016). *National Building Code Assessment Report ISO's Building Code Effectiveness Grading Schedule 2015*, Insurance Services Office, Inc. Jersey city, NJ, U.S.A. Available online at: https://www.isomitigation.com/downloads/ISO-BCEGS-State-Report_web.pdf.
- Jaiswal, K. & D.J. Wald (2008). *Creating a Global Building Inventory for Earthquake Loss Assessment and Risk Management*. Open File Report 2008-1160. U.S. Geological Survey, 110p. Available online at: <http://pubs.usgs.gov/of/2008/1160/>.

Kim, W.-Y., L. Seeber, & J. G. Armbruster (2002). Source process of the Mw 5.0 Au Sable Forks, New York earthquake from local aftershock monitoring network data. *Eos Transactions American Geophysical Union* **83**(47), Fall Meeting, Abstract S22D-01.

Lamontagne, M. (1999). *Rheological and Geological Constraints on the Earthquake Distribution in the Charlevoix Seismic Zone*, Open File Report D-3778, Ph.D. Thesis, Carleton University, Geological Survey of Canada. Available on CD-ROM.

Lamontagne, M., M. Beauchemin, T. Toutin (2004). Earthquakes of the Charlevoix Seismic Zone, Québec. *CSEG Recorder Online*, Natural Resources Canada **29**(8), Ottawa, Ontario. Available online at: <https://csegrecorder.com/articles/view/earthquakes-of-the-charlevoix-seismic-zone-quebec>. Last accessed: 27th April 2018.

Levin, H. L. (2006) *The Earth through Time*, 8th ed. John Wiley & Sons, Inc, New York, 560 pp.

Ma, S. & G. M. Atkinson (2006). Focal depths for small to moderate earthquakes ($mN \geq 2.8$) in western Quebec, southern Ontario, and northern New York. *Bulletin of the Seismological Society of America* **96**(2), 609–623.

Musacchio, G., W.D. Mooney, J.H. Luetgert & N.I. Christensen (1997). Composition of the crust in the Grenville and Appalachian Provinces of North America inferred from VP=VS ratios. *Journal of Geophysical Research* **102**, 15225–15242.

Musson R., G. Grünthal & M. Stucchi (2010). The comparison of macroseismic intensity scales. *Journal of Seismology* **14**(2), 413-428.

National Earthquake Hazards Reduction Program (NEHRP, 2004). *NEHRP Recommended provisions for seismic regulations for new buildings and other structures – FEMA 450*. Building Seismic Safety Council, National Institute of Building Sciences, Washington D.C., U.S.A.

Petersen, M.D., A.D. Frankel, S.C. Harmsen, C.S. Mueller, K.M. Haller, R.L. Wheeler, R.L. Wesson, Y. Zeng, O.S. Boyd, D.M. Perkins, N. Luco, E.H. Field, C.J. Wills, & K.S. Rukstales (2008). *Documentation for the 2008 update of the United States National Seismic Hazard maps*. Open-File Report 2008–1128, U.S. Geological Survey, 128 p. Available online at: https://pubs.usgs.gov/of/2008/1128/pdf/OF08-1128_v1.1.pdf.

Petersen, M.D., M.P. Moschetti, P.M. Powers, C.S. Mueller, K.M. Haller, A.D. Frankel, Y. Zeng, S. Rezaeian, S.C. Harmsen, O.S. Boyd, N. Field, R. Chen, K.S. Rukstales, N. Luco, R.L. Wheeler, R.A. Williams & A.H. Olsen (2014). *Documentation for the 2014 update of the United States National Seismic Hazard maps*. Open-File Report 2014–1091, U.S. Geological Survey, 243 p. Available online at: <https://pubs.usgs.gov/of/2014/1091/>.

Pierre J.-R. & M. Lamontagne (2004). The 20 April 2002, Mw5.0 Au Sable Forks, New York, earthquake: A supplementary source of knowledge on earthquake damage to lifelines and buildings in Eastern North America. *Seismological Research Letters* **75**(5), 626-636.

Revetta F. & K. Harradine (2013). Northern New York – Western Quebec Seismic Zone, Paper No.51-1. *Northeastern Section – 48th Annual Meeting*, The Geological Society of America. Available online at: https://gsa.confex.com/gsa/2013NE/finalprogram/abstract_214718.htm.

Richter C.F. (1958). *Elementary seismology*. W.H. Freeman and Co., San Francisco, USA.

Seeber, L., W.-Y. Kim, J. G. Armbruster, W.-X. Du & A. Lerner-Lam (2002). The 20 April 2002 Mw 5.0 earthquake near Au Sable Forks, Adirondacks, New York: A first glance at a new sequence. *Seismological Research Letters* **73**, 480–489.

Shi, J., W.-Y. Kim, and P. Richards (1998). The corner frequency and stress drops of intraplate earthquakes in the northeastern United States. *Bulletin of the Seismological Society of America* **88**, 531–542.

Sykes, L.R. (1980). Earthquakes and other processes within lithospheric plates and the reactivation of pre-existing zones of weakness. In D.W. Strangway (ed.): *The Continental Crust and Its Mineral Deposits*. Geological Association of Canada, Special Paper **20**, 215–237.

United Nations, ed. (2004). *Human Development Report 2004 – Cultural liberty in today's diverse world*. Report of the United Nations Development Programme (UNDP), New York, United States.

United Nations, ed. (2016). *Human Development Report 2016 - Human Development for everyone*. Report of the United Nations Development Program (UNDP), New York, United States.

Viegas, G., L.G. Baise & R.E. Abercrombie (2010a). Regional wave propagation in New England and New York. *Bulletin of the Seismological Society of America* **100**(5A), 2196–2218.

Viegas, G., R.E. Abercrombie & W.-Y. Kim (2010b). The 2002 M5 Au Sable Forks, NY, earthquake sequence: Source scaling relationships and energy budget. *Journal of Geophysical Research* **115** (B7), doi 10.1029/2009JB006799.

Wald, D.J. & T.I. Allen (2007). Topographic slope as a proxy for seismic site conditions and amplification. *Bulletin of the Seismological Society of America* **97**, 1379–1395. Slope-based online map viewer available at: <http://usgs.maps.arcgis.com/apps/webappviewer/index.html?id=8ac19bc334f747e486550f32837578e1>.

Wheeler, R.L. (1995). Earthquakes and the cratonward limit of Iapetan faulting in eastern North America. *Geology* **23**, 105–108.

Worden, C.B., E.M. Thompson, M. Hearne & D.J. Wald (2017). *ShakeMap V4 Manual: technical manual, user's guide, and software guide*. United States Geological Survey. Available online at: <http://usgs.github.io/shakemap/>.

Yong, A., E.M. Thompson, D. Wald, K.L. Knudsen, J.K. Odum, W.J. Stephenson & S. Haefner (2016). Compilation of V_{S30} Data for the United States. *U.S. Geological Survey Data Series* **978**, <http://dx.doi.org/10.3133/ds978>.

A3.9.11.2 Web references

ABC News (2011) (last accessed 6th September 2017): <http://abcnews.go.com/US/major-east-coast-earthquakes/story?id=14365156#1>.

APN Magazine (2003) (last accessed 5th September 2017): <http://www.apnmag.com/natural%20selections/spring03/earthquake.htm>.

Inland Marine Underwriters Association (IMUA) (2001) (last accessed 7th September 2017): <http://www.imua.org/Files/reports/Natural%20Disasters%20-%20Country%20Profile%20Series%20-%20Canada.html>.

Canadian Hazards Information Service, Natural Resources Canada (OTT): <http://www.earthquakescanada.nrcan.gc.ca/index-en.php>. Last accessed: 7th January 2018.

City – Data (2016): <http://www.city-data.com/city/Au-Sable-Forks-New-York.html>. Last accessed: 6th January 2018.

CNN (2002): <http://edition.cnn.com/2002/US/04/20/new.english.tremors/>. Last accessed: 5th September 2017.

Cyberspaceorbit (2002): <http://www.cyberspaceorbit.com/quin.html>. Last accessed: 12th September 2017.

Department of Numbers (2016): <http://www.deptofnumbers.com/gdp/new-york/>. Last accessed: 10th September 2017.

Division of Building Standards and Codes, New York State (2017): <https://www.dos.ny.gov/dcea/>. Last accessed: 10th September 2017.

Earth & Atmospheric Sciences, Saint Louis University (SLU, 2004): http://www.eas.slu.edu/eqc/eqc_mt/MECH.NA/20020420105044/index.html. Last accessed: 10th September 2017

Earthquake Engineering to Extreme Events, University of Buffalo (MCEER, 2002): <http://mceer.buffalo.edu/research/Reconnaissance/Plattsburgh4-20-02/>. Last accessed: 6th September 2017.

FEMA Disasters (2004): <https://www.fema.gov/disaster/1415>. Last accessed: 9th September 2017.

Global Centroid Moment Tensor Project (GCMT): <http://www.globalcmt.org/>. Last accessed: 8th September 2017.

Great Dreams (2002): http://www.greatdreams.com/ny/newyork_quakes.htm. Last accessed: 10th September 2017.

International Seismological Centre (ISC): <http://www.isc.ac.uk>. Last accessed: 8th September 2017

International Monetary Fund (2017) - World Economic Outlook Database 2017 (16th January 2017): <https://www.imf.org/external/pubs/ft/weo/2016/02/weodata/index.aspx>. Last accessed: 5th September 2017.

ISO Mitigation (2016): <https://www.isomitigation.com/bcegs/facts-and-figures.html>

Lamont-Doherty Cooperative Seismographic Network Earth Observatory (LDEO):
 Websites for this event:
 Mainshock Location, Depth & Source Mechanism:
http://www.ldeo.columbia.edu/LCSN/NYQuake_2002/20020420_nyquake.html. Last accessed: 7th January 2018.
 Local Seismographic Network: http://www.ldeo.columbia.edu/LCSN/NYQuake_2002/RAMPS.html. Last accessed: 8th September 2017.
 Earthquake damage: http://www.ldeo.columbia.edu/LCSN/NYQuake_2002/damage.html. Last accessed: 5th September 2017.
 Did You Feel It (Community Internet Intensity Map):
http://www.ldeo.columbia.edu/LCSN/eq/20020420_AuSable/Intensity_Map.html. Last accessed: 8th September 2017.

New York State Standard Multi-Hazard Mitigation Plan in Homeland Security and Emergency Services Website (NYSHMP, 2014a): <http://www.dhSES.ny.gov/recovery/mitigation/plan.cfm>. Last accessed: 9th September 2017.

New York State Hazard Mitigation Plan – Earthquake (NYSHMP, 2008): <http://www.dhSES.ny.gov/recovery/mitigation/archive/hm-plan-2008.cfm>. Last accessed: 9th September 2017.

New York State Hazard Mitigation Plan – Earthquake (NYSHMP, 2014b): Available online at: <http://www.dhSES.ny.gov/recovery/mitigation/documents/2014-shmp/Section-3-7-Earthquake.pdf>. Last accessed: 9th September 2017.

New York State Hazard Mitigation Plan - Landslide (NYSHMP, 2014c):
<http://www.dhSES.ny.gov/recovery/mitigation/documents/2014-shmp/Section-3-14-Landslide.pdf>.
Last accessed: 10th September 2017.

New York Times (2002): <http://www.nytimes.com/2002/04/21/nyregion/quake-is-felt-from-boston-to-baltimore.html?mcubz=0>. Last accessed: 6th September 2017.

The World Bank Group (2017). World Bank Open Data: <http://data.worldbank.org>. Last accessed: 6th September 2017.

United Nations Development Programme – Human Development Data (UNDP-HDD, 2016):
<http://hdr.undp.org/en/data>. Last accessed: 6th September 2017.

United States Geological Survey (USGS): <https://earthquake.usgs.gov/>
Website for this event (last accessed 10th September 2017):
<https://earthquake.usgs.gov/earthquakes/eventpage/ld2002042000#executive>.
Unified Hazard Tool (UHT): <https://earthquake.usgs.gov/hazards/interactive/>.

US Beacon (2000): <http://www.usbeacon.com/economic/New-York/Au-Sable-Forks.html>. Last
accessed: 6th September 2017.

US Census Bureau (2009-2013). Selected economic characteristics – American Community
Survey 5-Year Estimates:
https://factfinder.census.gov/faces/tableservices/jsf/pages/productview.xhtml?pid=ACS_13_5YR_D_P03&prodType=table. Last accessed: 6th September 2017.

US Census Bureau (2017): <https://www.census.gov/>. Last accessed: 6th September 2017.

A4.10. April 2002 M4.8 Tbilisi Earthquake, Georgia

This earthquake occurred on 25th April 2002, at 17:41 UTC (22:41 local time) and is, to date, the strongest instrumentally recorded seismic event in the region. It caused extensive damage to low-rise, brick and stone buildings in the old part of Tbilisi, mostly due to their vulnerability but also as a consequence of the shallowness of the epicentre and site effects. The main shock was accompanied by a series of aftershocks that caused additional damage. According to most sources, six people died and many more were injured. The lack of funds and a risk preparedness plan resulted in a severe social and economic situation in the country.

A4.10.1 Tectonic and seismic setting

A4.10.1.1 Tectonic setting

Georgia is situated in the Caucasus region, an active part of the Alpine-Himalayan collision belt (Chelidze *et al.*, 2002; Javakhishvili *et al.*, 2004; Philip *et al.*, 1989; Cisternas & Philip, 1997). The geodynamics and seismotectonics of this region are defined by the present convergence between the Eurasian and Afro-Arabian plates, which is happening at a rate of about 20-30 mm/year (DeMets *et al.*, 1990; Allen *et al.*, 2004; Varazanashvili *et al.*, 2012). The northward movement of the Arabian plate is inducing a compressional stress field with a dominant N-S orientation (Tsereteli *et al.*, 2014a; Varazanashvili *et al.*, 2012).

Located between the Greater and Lesser Caucasus mountain ranges, the area around Tbilisi features a complex tectonic structure (Shengelia *et al.*, 2011). Tbilisi city lies at the eastern end of the W-E oriented Achara-Trialeti fold-thrust belt, which is bounded by the North Achara-Trialeti thrust to the north and by the South Achara-Trialeti thrust to the south, marked as ATN and ATS in Figure A4.10.1, respectively. These two thrusts are connected by the Tbilisi-Mtkvari fault (TM in the figure) which runs through Tbilisi (Tsereteli *et al.*, 2014b; Rastsvetaev, 1989; Adamia *et al.*, 2005; Varazanashvili *et al.*, 2008). According to Varazanashvili *et al.* (2008) and Gamkrelidze *et al.* (2008), this NW-SE oriented, right-lateral strike-slip fault is responsible for the Tbilisi earthquake that struck on 25th April 2002.

With the exception of these regional thrusts, the majority of fault structures in Georgia are located at large depths and are hidden by sediments of various thicknesses, their only manifestation at surface being flexures, en echelon folds and clusters of regional faults, and their existence being confirmed by clusters of earthquake epicentres occurring in the area (Gamkrelidze *et al.*, 1998).

Of all these active structures, those that are longitudinally oriented (W-E or WNW-ESE) are compressional and consist mainly of reverse fault thrusts (like the Achara-Trialeti thrusts), tectonic nappes and fault-propagation folds. Transverse faults (submeridional, NE-SW and NW-SE) are of both compressional and extensional nature, predominantly exhibiting strike-

slip behaviour (Trifonov *et al.*, 1999; Varazanashvili *et al.*, 2008; Karakhanian *et al.*, 2004; Chelidze *et al.*, 2002; Varazanashvili *et al.*, 2012).

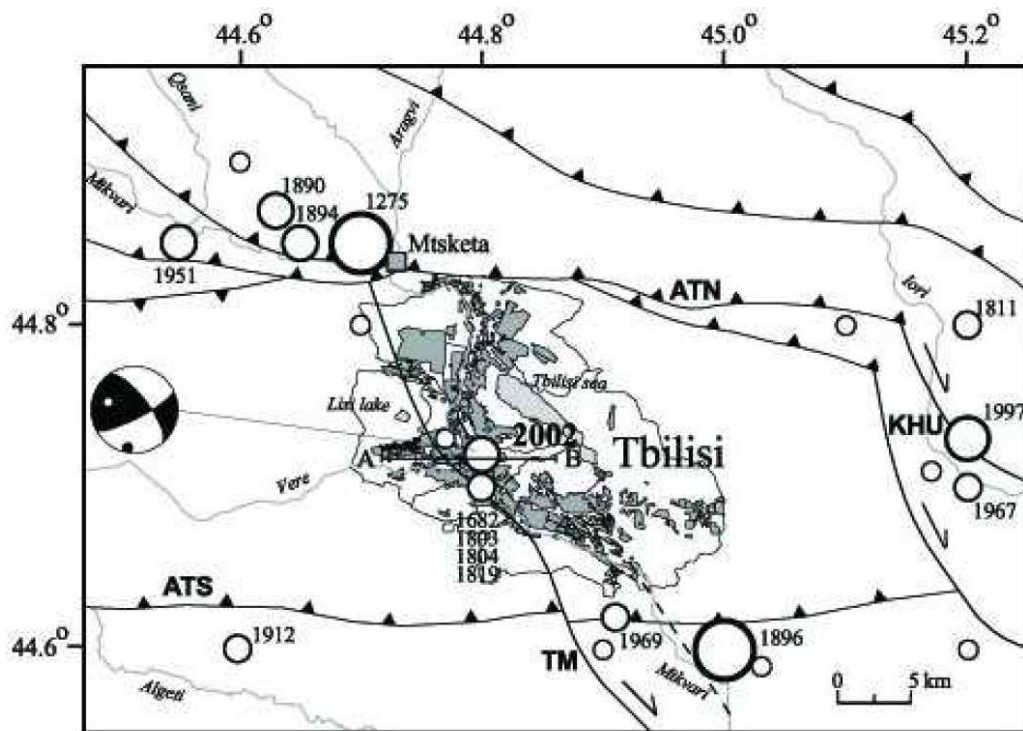


Figure A4.10.1. Tectonic setting of the Tbilisi area. From Varazanashvili *et al.* (2008).

A4.10.1.2 Regional and local seismicity

Georgia is located in a region of moderate seismicity (Chelidze *et al.*, 2002; Javakhishvili *et al.*, 2004; Shengelia *et al.*, 2011). Nevertheless, earthquakes with magnitude (M_s) up to 7.0 and macroseismic intensity (MSK-64) up to IX have occurred in the country, as shown in the map of Figure A4.10.2. Seismic events like these have a recurrence period of around 10^3 to 10^4 years (United Nations Development Program, UNDP, 2014; Chelidze *et al.*, 2002).

The seismicity observed in Georgia is mostly associated with the active faults of the Greater and Lesser Caucasus, though the Tbilisi area, which lies in the intermountain depression, features lower levels of seismicity than the two (Javakhishvili *et al.*, 2004; Shengelia *et al.*, 2011; Tsereteli *et al.*, 2014b). However, as Javakhishvili *et al.* (2004) point out, historical data shows that the capital was affected several times by strong earthquakes. The recurrence period of earthquakes with MSK intensity VII in the region was, approximately, 85 years during the historical period, and could be related to either strong regional earthquakes with magnitudes larger than 6.0, or moderate local earthquakes with magnitudes in the range 4.0-5.0 (Varazanashvili *et al.*, 2008).

Varazanashvili *et al.* (2008) point out the existence of two clusters of strong historical earthquakes, one of which lies at the intersection between the North Achara-Trialeti thrust (ATN) and the Tbilisi-Mtkvari fault, around 15 km north of Tbilisi, while the other is that observed immediately beneath the Tbilisi area, associated with the activity of Tbilisi-Mtkvari fault, as shown in Figure A4.10.1. The latter includes the seismic events of 1682, 1803,

1804, and 1819, with surface wave magnitudes in the range 3.5–4.5 and macroseismic effects of V–VI MSK in Tbilisi (Godoladze *et al.*, 2005; Javakhishvili *et al.*, 2004; Varazanashvili *et al.*, 2008). The South Achara-Trialeti thrust (ATS) represents, as well, a source of strong historical seismic events, the most important of which is the Ms 6.3 1896 earthquake, which caused the strongest macroseismic effects in the Tbilisi area during historical times (25 km south-east of the city of Tbilisi) (Javakhishvili *et al.*, 2004; Varazanashvili *et al.*, 2008).

The data about earthquakes that happened in this region during the Middle Ages appears to be less accurate and reliable. In this regard Javakhishvili *et al.* (2004) argues that the macroseismic intensities of the earthquakes of 1193, 1688 and 1742 (larger than or equal to VII MSK, at an epicentral distance of about 50–100 km) given in the report of Gotsadze *et al.* (1990) are overestimated.

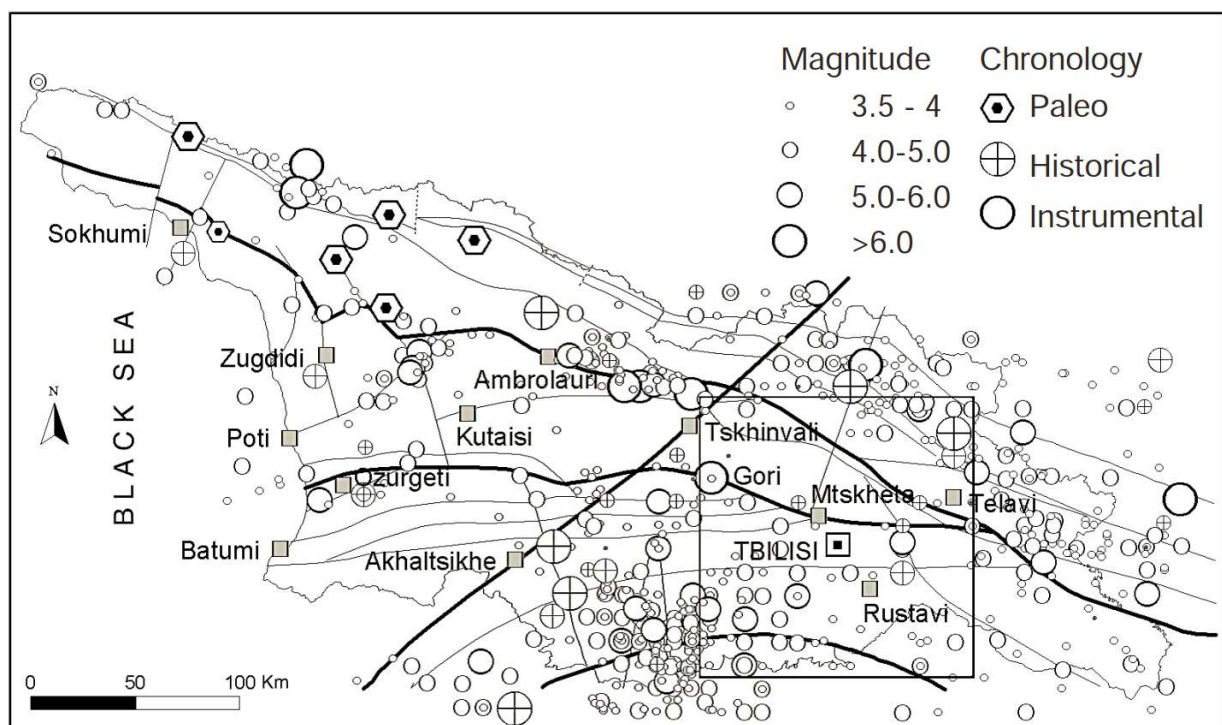


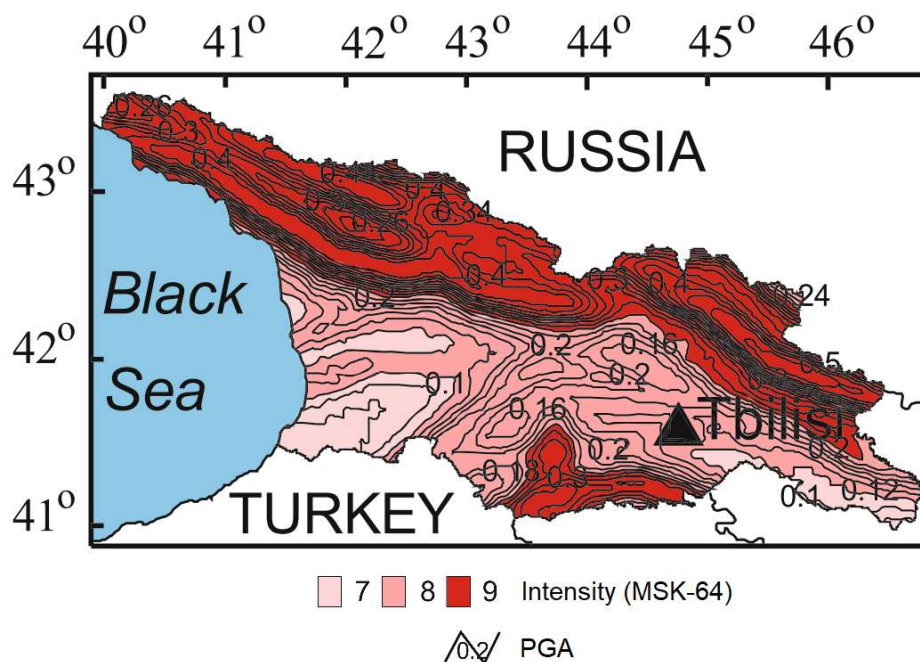
Figure A4.10.2. Paleo, historical (before 1900) and instrumental (after 1900) seismicity of Georgia. Thick and thin lines indicate main and minor faults, respectively. From Javakhishvili *et al.* (2004).

The installation of the first seismological station in Tbilisi in 1899 marked the beginning of the instrumental seismicity period. However, the data quality was rather low until 1930 (Chelidze *et al.*, 2002; Javakhishvili *et al.*, 2004). The strong earthquakes recorded in the vicinity of Tbilisi during this early instrumental period were the 1912, 1913 and 1920 events, with macroseismic intensities of V–VI MSK in the city (Javakhishvili *et al.*, 2004). Since 1930 Tbilisi was affected by around 12 moderate to strong seismic events with intensity MSK V (Javakhishvili *et al.*, 2004). The Ms 4.2 1969 and the 2002 earthquakes were the strongest events that have struck the city in the modern instrumental period (Javakhishvili *et al.*, 2004; Shengelia *et al.*, 2011), which can be said to have started in 1962 when the network was equipped with high-gain seismic instruments (Chelidze *et al.*, 2002; Javakhishvili *et al.*, 2004).

A4.10.1.3 Seismic hazard

The probabilistic seismic hazard map of Georgia, adopted as a normative map in the PN 01.01-09 building code in 2009, is shown in Figure A4.10.3. This map shows expected peak ground accelerations (PGA) and MSK-64 intensities with a 2% probability of exceedance in 50 years (return period of 2,500 years), and for the area of Tbilisi their corresponding values are 0.17 g and VIII, respectively. The Georgian seismic code (PN 01.01-09, 2009) expresses that intensities and peak accelerations depicted on this map are corresponding to soils of category II, with shear-wave velocities in the range 300-800 m/s.

As Georgia had its own seismic code established only in 2009, the normative seismic hazard map at the time of the 2002 earthquake was probably the one incorporated in the SNiP II-7-81 (1982) seismic code, namely, the general seismic zoning (GSZ-78) map compiled for the territories of the Soviet Union. According to this map, the maximum MSK-64 intensity to be expected in the area of Tbilisi for its corresponding average ground conditions (category II soil, as per SNiP II-7-81 code), was VII, with a recurrence interval of 100 years.



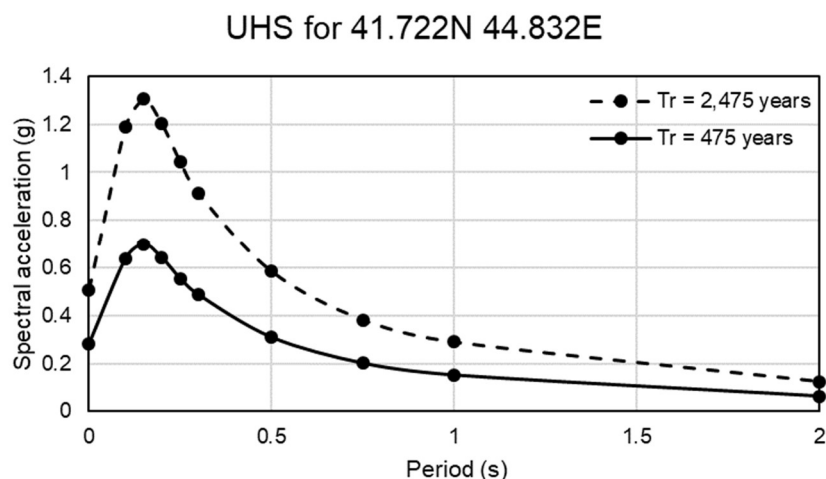


Figure A4.10.4. Uniform Hazard Spectra for the Tbilisi area according to SHARE, representing spectral acceleration values on rock with a 10% and 2% probability of exceedance in 50 years corresponding to a return period of 475 and 2,475 years, respectively.

Hazard curves for the area of Tbilisi calculated by Slejko *et al.* (2008) indicate values of expected PGA on rock with a 10% and 2% probability of exceedance in 50 years of approximately 0.2 g and 0.38 g, respectively, which are smaller than those of the SHARE project (Figure A4.10.4). However, the PGA of 0.17 g that has a 2% probability of exceedance in 50 years according to the 2009 seismic hazard map in Figure A4.10.3 is significantly lower than the value of ~0.38 g indicated by Slejko *et al.* (2008) and even more so than that of SHARE (*i.e.* 0.51 g).

Results from the Global Seismic Hazard Assessment Program (GSHAP; Giardini *et al.*, 1999) indicate a value of 0.24 g as the expected PGA on rock with a 10% of probability of exceedance in 50 years for the Tbilisi area (41.7 N, 44.8 E). This value lies in between ~0.2 g and 0.28 g, which correspond to the assessments of Slejko *et al.* (2008) and the SHARE project, respectively.

Seismic hazard maps for the region of Georgia, or parts of it, have been compiled by several other authors (*e.g.*, Javakhishvili *et al.*, 2004; Slejko *et al.*, 2008; Tsereteli *et al.*, 2014a). As the seismic maps compiled by Slejko *et al.* (2008) indicate higher levels of hazard than the normative map, Tsereteli *et al.* (2014a) and Varazanashvili *et al.* (2012) argue that there is a need for a substantial revision and recalculation of the normative hazard map and acting seismic codes.

Table A4.10.1 compares the values of PGA and MSK-64 Intensity with 1%, 2%, 5% and 10% probability of exceedance in 50 years in Tbilisi, according to hazard maps elaborated by different authors (Balassanian *et al.*, 1999; Chelidze *et al.*, 2002; Javakhishvili *et al.*, 2004; Slejko *et al.*, 2008; PN 01.01-09, 2009; Tsereteli *et al.*, 2014a). The hazard maps of Slejko *et al.* (2008) take into account the soil conditions of Tbilisi, which consist mostly of rock and stiff soil ($V_{s30} > 360$ m/s). Tsereteli *et al.* (2014a) generated hazard maps representing probabilities of exceedance of 2% and 10% in 50 years, for soil conditions corresponding to $V_{s,30} = 300$ m/s and $V_{s30} = 760$ m/s. As not all maps are available in said source, the values shown in Table A4.10.1 correspond to $V_{s30} = 300$ m/s in the case of a 2%

probability, and to $V_{s30}=760$ m/s in the case of a 10% probability. As mentioned previously, the values shown for the Georgian building code (PN 01.01-09, 2009) correspond to $V_s=300-800$ m/s. Finally, Javakhisvili *et al.* (2004) did not take into consideration soil properties, while Balassannian *et al.* (1999) and Chelidze *et al.* (2002) do not mention explicitly what soil conditions their results make reference to.

Table A4.10.1. Seismic hazard of Tbilisi assessed by various authors.

PoE in 50 years		Balassanian <i>et al.</i> (1999)	Chelidze <i>et al.</i> (2002)	Javakhisvili <i>et al.</i> (2004)	Slejko <i>et al.</i> (2008)	Tsereteli <i>et al.</i> (2014)	PN 01.01-09 (2009)	SHARE	GSHAP
PGA (g)	1%		0.1-0.3	0.15-0.2					
	2%		0.1-0.2	0.1-0.15	0.24-0.56	0.3-0.4	0.17	0.51	
	5%		0.1-0.2	0.05-0.1					
	10%				0.16-0.32	0.2-0.25		0.28	0.24
MSK-64	1%	0.1-0.3	VIII	VIII					
	2%		VII-VIII	VII-VIII			VIII		
	5%		VII	VII					
	10%	VII-VIII							

A4.10.2 Earthquake source characteristics

A4.10.2.1 Location, depth and time

The main shock occurred on 25th April 2002, at 17.41 UTC (22.41 local time).

Several organizations and agencies report their own estimations of the epicentral coordinates and hypocentral depth. The information reported in the websites of the National Earthquake Information Center (NEIC) of the United States Geological Service (USGS), the International Seismological Centre (ISC), the European-Mediterranean Seismological Centre (EMSC), the Swiss Seismological Service at ETH Zurich, as well as the Earthquake Catalogue of Georgia by the M. Nodia Georgian Institute of Geophysics, is summarized in Table A4.10.2. The epicentral coordinates and hypocentral depth calculated by Varazanashvili *et al.* (2008) using data from 47 stations, including the seismic network of Georgia and adjacent countries, are also included in the table. Cells marked as (*f) correspond to parameters that were held fixed while inversion was carried out to retrieve those that remain. The different estimations of epicentral locations enumerated above are depicted on the map in Figure A4.10.5.

Table A4.10.2. Epicentral coordinates and hypocentral depths from different sources.

Agency / Publication		Latitude	Longitude	Depth (km)
NEIC	National Earthquake Information Center, USGS	41.7650 ° N	44.9600 °E	10.00 (*f)
ISC	International Seismological Centre	41.7630 ° N	44.8230 °E	10.00 (*f)
EMSC	European-Mediterranean Seismological Centre	41.7492 ° N	44.9113 °E	40.00
ZUR_RMT ⁽¹⁾	Swiss Seismological Service	41.7650 ° N	44.9600 °E (*f)	12.00
M.Nodia Institute of Geophysics of Georgian Academy of Science		41.7350 ° N	44.8360 °E	6.00
Varazanashvili <i>et al.</i> (2008)		41.7500 ° N	44.8200 °E	6.89

(*f) fixed parameter used for inversion

(1) Values reported herein are those reported by the ISC citing ZUR_RMT as the source

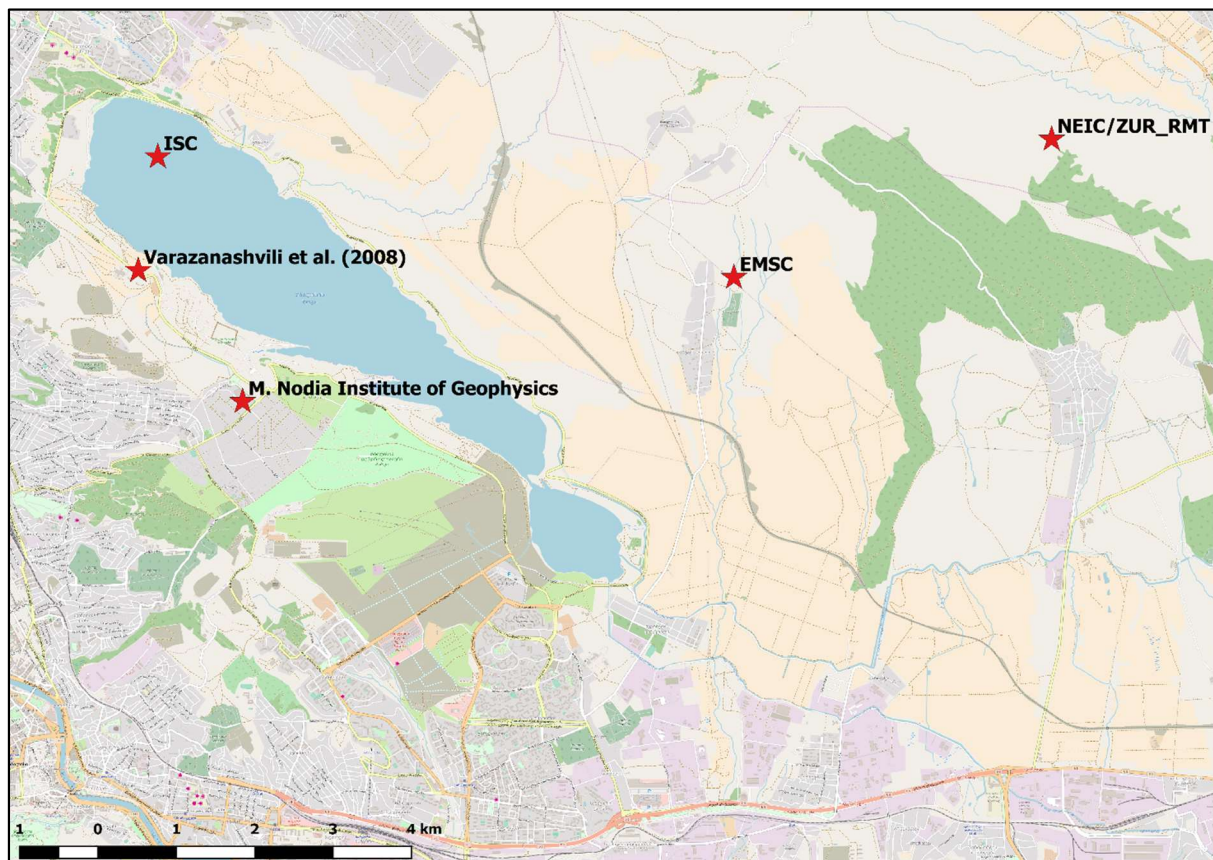


Figure A4.10.5. Estimations of epicentral coordinates (red stars).

According to Varazanashvili *et al.* (2008), the root mean square (RMS) error of their estimation is 0.17, while that of the USGS is 1.13. This suggests that the hypocentre location is potentially better constrained by Varazanashvili *et al.* (2008), which would imply that the earthquake most probably occurred in the Nadzaladevi district of Tbilisi, in the immediate vicinity of an artificial water reservoir. Varazanashvili *et al.* (2008) also found that hypocentral depths estimated as a function of hypocentral intensity by means of two empirical relations are similar to those calculated from instrumental data, though slightly smaller (5 ± 1 km and 4 ± 1 km).

A4.10.2.2 Magnitude

Estimations of magnitude reported on the websites of the National Earthquake Information Center (NEIC) of the United States Geological Service (USGS), the International Seismological Centre (ISC), the European-Mediterranean Seismological Centre (EMSC), the Swiss Seismological Service at ETH Zurich, and the Earthquake Catalogue of Georgia by the M. Nodia Georgian Institute of Geophysics are presented in Table A4.10.3. The table also includes the magnitude reported by the study of Varazanashvili *et al.* (2008).

For this seismic event the Earthquake Model of the Middle East (EMME) catalogue (Zare *et al.*, 2014) reports a moment magnitude **M**5.1 that was found through conversion from surface-wave magnitude $M_s=4.5$ reported by the Seismic Monitoring Centre of Georgia (SMCG). A magnitude of **M**5.0, converted from M_s 4.3, is reported in the earthquake catalogue of Weatherill *et al.* (2016).

Table A4.10.3. Estimations of moment magnitude (M), body-wave magnitude (mb), local magnitude (M_L) and surface wave magnitude (M_s).

Agency/Publication		M	mb	M_L	M_s
NEIC	National Earthquake Information Center, USGS	-	4.8	-	4.3
ISC	International Seismological Centre	-	4.7	-	4.3
EMSC	European-Mediterranean Seismological Centre	-	4.6	-	4.1
ZUR_RMT ⁽¹⁾	Swiss Seismological Service	4.8	-	-	-
M.Nodia Institute of Geophysics of Georgian Academy of Science		5.15	-	-	4.6
Varazanshili <i>et al.</i> (2008)		-	-	-	4.6

(1) Values reported herein are those reported by the ISC citing ZUR_RMT as the source

A4.10.2.3 Style-of-faulting

Based on the P wave polarity data from 32 stations, Varazanashvili *et al.* (2008) determined the focal mechanism solution for this earthquake to be mostly strike-slip (Figure A4.10.6). As shown in Table A4.10.4, one nodal plane corresponds to right-lateral movement on a fault striking NW-SE and dipping to the NE direction, while the other indicates a fault plane striking in the WSW-ENE direction and dipping sub-vertically to the south-southeast. Since the isoseismals for this earthquake (section A4.10.4.1) are spreading mostly in the NW-SE direction, the causative fault is most probably the one corresponding to the fault plane 1 solution. The observation by Gamkrelidze *et al.* (2008) of a steep fault with an average strike azimuth of 335° likely going through the city of Tbilisi supports this preference for the first fault plane.

Table A4.10.4. Fault plane solutions and fault planes from Varazanashvili *et al.* (2008). Fault plane marked in grey is the preferred solution.

Fault Plane 1			Fault Plane 2			Source
Strike	Dip	Rake	Strike	Dip	Rake	
322	61	159	63	72	31	Varazanashvili <i>et al.</i> (2008)

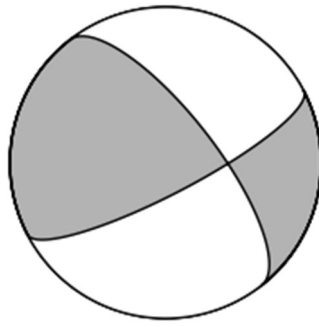


Figure A4.10.6. Focal mechanism according to Varazanashvili *et al.* (2008).

A4.10.2.4 Stress drop

No information could be found regarding the stress drop of this event.

A4.10.2.5 Foreshocks and aftershocks

The main shock was accompanied by a sequence of foreshocks and aftershocks (Gabrichidze *et al.*, 2004; Javakhishvili *et al.*, 2004; Varazanashvili *et al.*, 2008). Out of five foreshocks that preceded the earthquake, two were felt by the population of Tbilisi. They occurred on the 11th and the 21st of April 2002, and had surface wave magnitudes M_s of 3.7 and 2.0, respectively (Varazanashvili *et al.*, 2008).

In the first week following the main shock, the temporary seismic network that was installed immediately after the earthquake (Gabrichidze *et al.*, 2004; Godoladze *et al.*, 2005) detected 368 seismic events with magnitude M_s equal to or lower than 3.0, of which ten were felt by the population. By 22nd December, 1122 aftershocks had been recorded by the Tbilisi seismology observatory stations (Akhaldedashvili *et al.*, 2004). Some of these aftershocks caused macroseismic intensities as high as III on the MSK-64 scale (Javakhishvili *et al.*, 2004). The poor distribution of seismic stations in Georgia at that time did not allow for an accurate estimation of the aftershock distribution (Varazanashvili *et al.*, 2008).

A4.10.2.6 Nature of earthquake

No reference to this earthquake having an origin other than tectonic has been found. Gamkrelidze *et al.* (2008) and Varazanashvili *et al.* (2008) have reported that the earthquake was the manifestation of the activity of the Tbilisi-Mtkvari fault that stretches along the Mtkvari River in the area of Tbilisi. This fault is thought to be the generator of the 1682, 1803, 1804, 1819 and 2002 Tbilisi earthquakes. Moreover, Jimsheladze *et al.* (2008) have observed, by means of a field study, microtemperature anomalies in the ground in the weeks before the earthquake which, in their opinion, was the evidence of the active movement of the earth crust.

A4.10.3 Geology and ground conditions in the affected area

A4.10.3.1 Regional geology and topography

Tbilisi lies in the Transcaucasian intermountain depression of the Eastern part of Georgia. The altitude of the city is between 380 and 770 m above sea level. It is surrounded by mountains on three sides: the Saguramo Range to the north, the Iori Plain to the east and south-east, and various Trialeti sub-ranges to the south and west. The city lies on terraces of the Mtkvari River and stretches around 30 km along it (Adeishvili *et al.*, 2011; Gabrichidze *et al.*, 2004). Part of the city situated on the right bank of the Mtkvari River is built on the foothills of the Trialeti Range. This unfavourable mountainous environment resulted in restricted urban development and uneven population density in that part of the city. Throughout its history, the complex relief of the Tbilisi area has been remodelled by natural processes such as landslides, mudflows, floods and erosion, usually heavily influenced by the anthropogenic activities therein carried out (Adeishvili *et al.*, 2011).

In Figure A4.10.7, a geologic map of the Tbilisi area is presented, together with a vertical section of the shallow crust. The latter is oriented along latitude (line A-B) and intersects the Tbilisi fault, whose activity generated the 2002 Tbilisi earthquake (Gamkrelidze *et al.*, 2008). In their study, Gamkrelidze *et al.* (2008) took into consideration several indicators that prove the existence of the Tbilisi fault and its relation to this particular seismic event. Through the analysis of satellite imagery of Tbilisi city, they identified the presence of a rectilinear scarp in the relief. They then corroborated this observation by means of analyses of the temperature field of the Tbilisi area, the abrupt change in the direction of the Mtkvari River from sub-latitudinal to sub-meridional, and consideration of previous studies of the hydrogeological and hydrodynamic characteristics of the Middle Eocene deposits on which Tbilisi is laying (Bardzishvili, 1976; Gamkrelidze *et al.*, 2008). All this data supports the idea of the existence of a young fault stretching along the Mtkvari River from Mtskheta to the NW towards Rustavi to the SE and dipping NE, as shown in Figure A4.10.7. Gamkrelidze *et al.* (2008) believe that this fault most probably rejuvenated from an old hidden deep fault that strikes parallel to it, as can be observed in Figure A4.10.7.

Much of the Tbilisi area is covered by alluvial Quaternary sediments, with outcrops of Tertiary period deposits along the Mtkvari River (see Figure A4.10.7). The thickness of the Quaternary alluvial deposits overlaying the footwall of the Tbilisi fault is 35-40 m (Gamkrelidze *et al.*, 2008). According to Varazanashvili *et al.* (2008), the 2002 earthquake generated by this fault occurred at the boundary between sedimentary and granitic layers, at around 5-8 km depth.

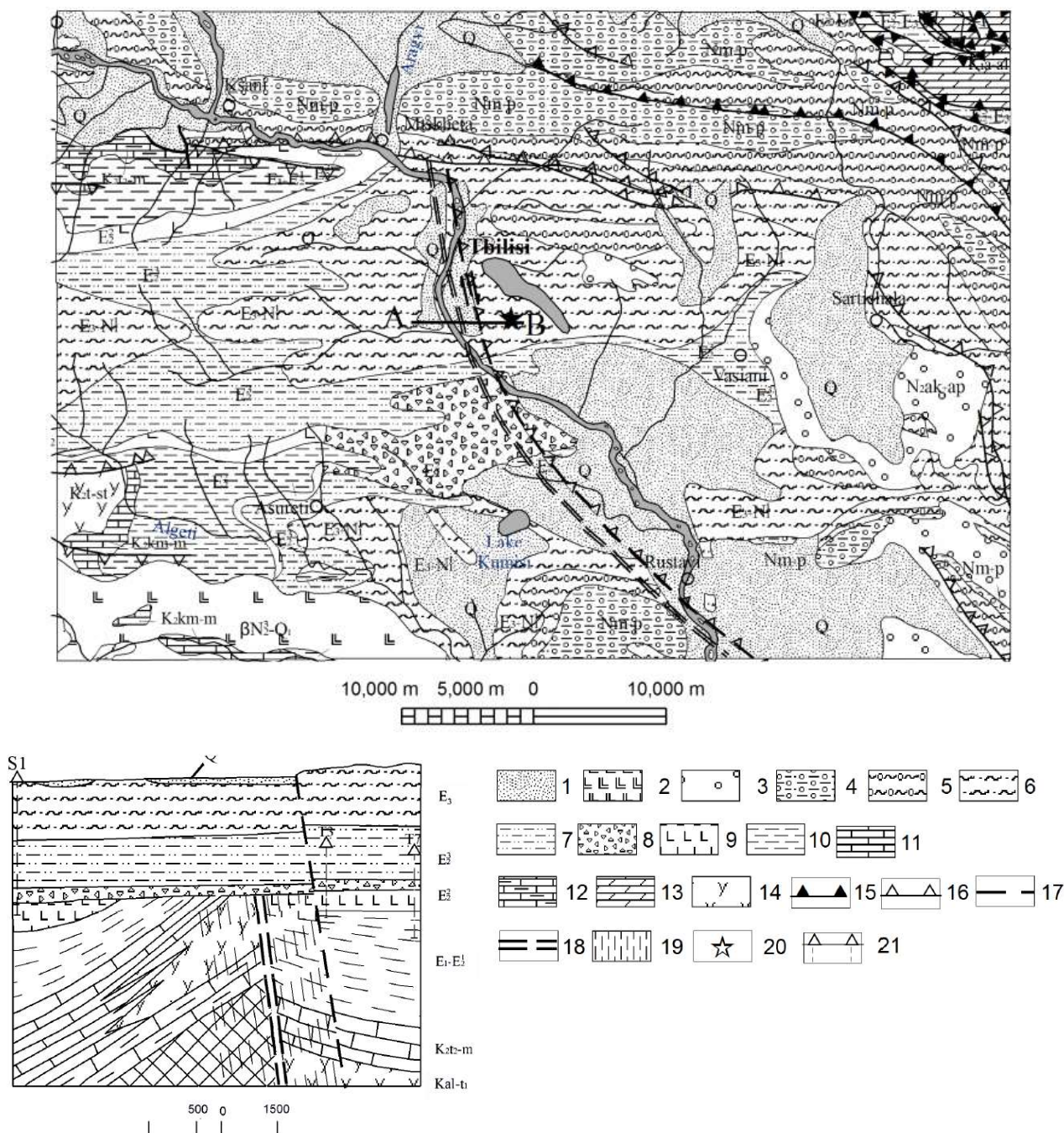


Figure A4.10.7. Geologic map of eastern termination of Adjara-Trialeti zone and adjacent areas. 1 – Quaternary alluvial-proluvial and talus deposits, 2 – Upper Pliocene-Lower Quaternary continental subalkalic basalts, andesite-basalts, andesites, 3 – Upper Pliocene (Aghchagil and Apsheron stages) continental and marine molasse, 4 – Neogene (Meotian and Pontian stages) marine and continental molasse, 5 – Middle and Upper Miocene (Sarmatian) marine and continental molasse, 6 – Oligocene and Lower Miocene marine molasse, 7 – Upper Eocene terrigenous deposits, 8 – Exposure of Middle Eocene olistostrome stratum, 9 – Middle Eocene volcanogenic suite (subalkaline basalts, dacites and their tuffs), 10 – Palaeocene and Lower Eocene sandstone – siltstone and clastic limestone flysch, 11 – Campanian-Maastrichtian carbonaceous deposits, 12 – Upper Turonian-Maastrichtian carbonaceous deposits, 13 – Aptian and Albian sandstone- siltstone flysch, 14 – Turonian-Santonian calc-alkalic basalts, andesite-basalts, their tuffs and limestones, 15 – nappes, 16 – reversed faults and thrusts, 17 – Tbilisi fault, 18 – old hidden deep fault, 19 – shatter zone of the deep fault (on geologic section AB), 20 – epicentre of Tbilisi earthquake of April 25, 2002. 21 – projection of the nearest boreholes on the plane of geologic section. From Gamkrelidze *et al.* (2008).

A4.10.3.2 Site conditions in the affected area

Figure A4.10.8 shows the map of the soil types that can be found in the Tbilisi area, generated by Slejko *et al.* (2008) based on the available borehole data, geological and geotechnical maps, as well as a map of quaternary deposits for the Tbilisi broader area. The soil type classification is based on the V_{s30} values, according to the specifications given by NEHRP provisions (BSSC, 1997), which can be easily related to those of Eurocode 8 (CEN, 2004). In the figure, both NEHRP soil class A, with $V_{s30} > 1,500$ m/s, and NEHRP soil class B, with $760 < V_{s30} < 1,500$, correspond to the EC8 definition of rock ($V_{s30} > 800$ m/s). NEHRP soil class C corresponds to stiff soils with $360 \text{ m/s} < V_{s30} < 760 \text{ m/s}$ (EC8 soil class B). NEHRP soil classes D and E correspond to soft soils with $180 < V_{s30} < 360$ and $V_{s30} < 180$ m/s, respectively, the equivalent of EC8 soil classes C and D. As observed from the map, Tbilisi is situated mostly on rock and stiff soils whose V_{s30} values would correspond to soil categories I ($V_{s30} > 800$ m/s) and II ($300 \text{ m/s} < V_{s30} < 800 \text{ m/s}$) of the building code in force (PN 01.01-09, 2009).

Figure A4.10.9 depicts the average shear wave velocity to a depth of 30 meters (V_{s30}) for the studied area, as calculated by the United States Geological Survey (USGS) V_{s30} Map Server using topographic slope as a proxy (Wald & Allen, 2007). As observed in the map, the V_{s30} values corresponding to the STBO station are around 650 - 700 m/s, which would correspond to PN 01.01-09 (2009) category II, or NEHRP class C, in relatively good agreement with Figure A4.10.8.

According to the analysis of Gabrichidze *et al.* (2004) of the data from 100 boreholes, the soil types that are most common in Tbilisi are rocky and semi-rocky (weathered and not weathered), gravel, clays, loams, sand loams (dense and subsiding), silty clay, lacustrine, and swampy fill soils, among others. Using the data from the same boreholes, Gabrichidze *et al.* (2004) performed one-dimensional equivalent linear site response analysis and compiled a map of the fundamental periods of vibration of soil deposits in the area of Tbilisi. Their results show that these lie in the range 0.1-0.3 seconds for most of the city, though four spots of increased periods are observed, mostly coinciding with the location of larger spectral acceleration values that will later be shown in Figure A4.10.16 and Figure A4.10.17. The largest spot lies to the north-east of the city and comprises large areas of periods between 0.3 and 0.5 seconds, and a rapid increase up to 1.3 seconds in a smaller spatial extent. Other two spots lie to the centre-west of the city and comprise areas of periods between 0.3 and 0.5 seconds, while a fourth smaller spot to the south reaches only up to 0.4 seconds.

No information has been found with respect to liquefaction susceptibility of soils in the area of Tbilisi. Rocks, which are predominant (Figure A4.10.8), are generally not prone to liquefaction. However, as Gabrichidze *et al.* (2004) reported the presence of other soil types (e.g. clays, loams, gravels), which under specific conditions could manifest liquefiable behaviour, no final conclusions could be drawn on this matter.

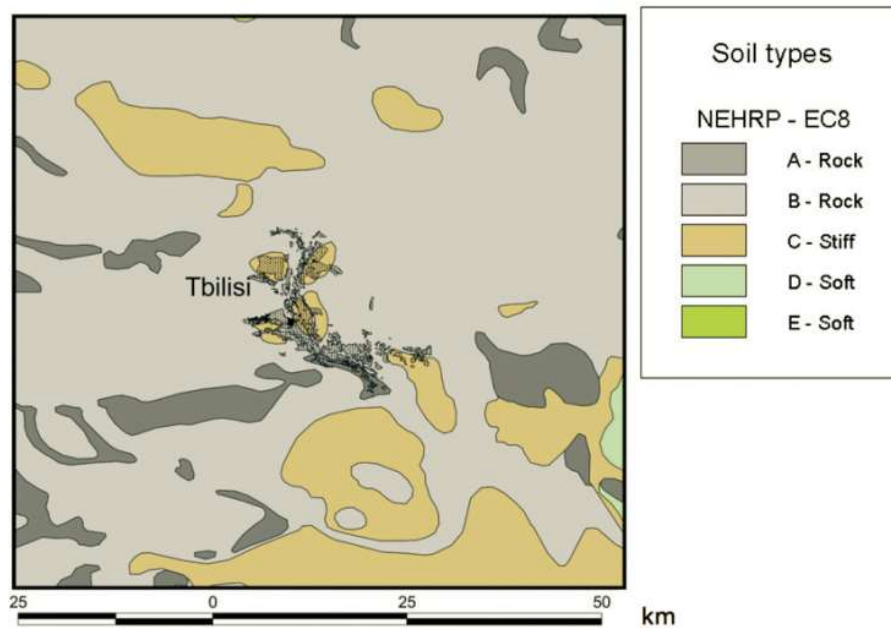


Figure A4.10.8. Soil types of the Tbilisi broader area according to the NEHRP provisions (BSSC, 1997) and Eurocode 8 (CEN, 2004). From Slejko *et al.* (2008).

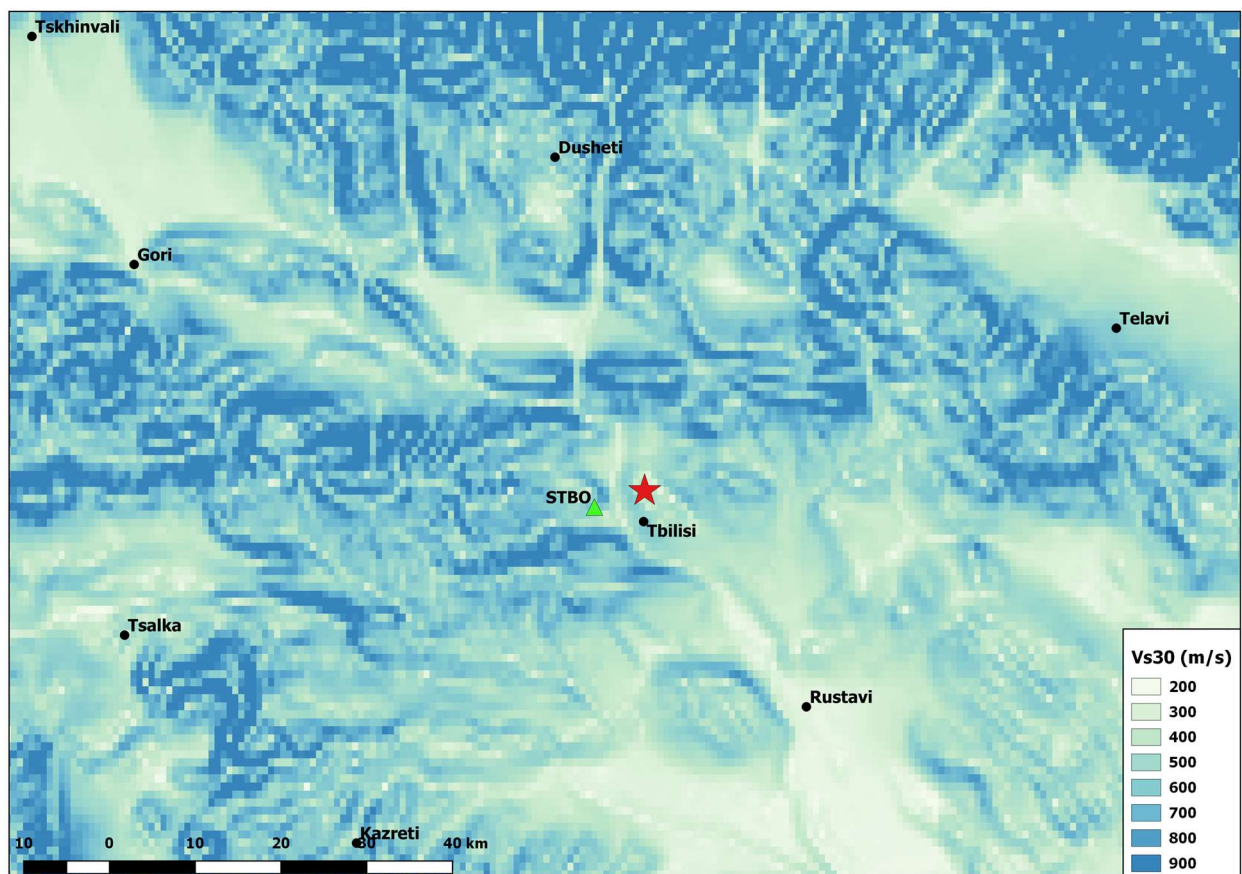


Figure A4.10.9. Estimation of Vs30 in the area around Tbilisi using topographic slope as a proxy. Taken from the USGS V_{s30} map server (Wald & Allen, 2007). Red star indicates the epicentre according to Varazanashvili *et al.* (2008); triangle indicates STBO station.

A4.10.4 Ground motions

A4.10.4.1 Intensity observations

The 2002 Tbilisi earthquake affected all the city districts and was felt as far as 130 km from the epicentre (Varazanashvili *et al.*, 2008). Figure A4.10.10(b) shows the macroseismic intensity map on the MSK-64 scale (Medvedev *et al.*, 1965) generated by Javakhishvili *et al.* (2004) using the answers to a questionnaire that was made available on the internet, and following the method proposed by the USGS, the Southern California Earthquake Center, and the California Division of Mines and Geology (2000). Tbilisi districts indicated by Arabic numbers in Figure A4.10.10 are listed in Table A4.10.5. As observed in Figure A4.10.10(b), maximum felt MSK intensities stretch in the NWN-SES direction, following the left bank of the Mtkvari river (Gamkrelidze *et al.*, 2008). Districts denoted by the numbers 2, 3, 4, 6, 7, 9 and 10 are entirely or partly enclosed by the isoseismal VII.

Taking into account the level of the induced damage and the fact that mostly low-rise, brick and stone apartment buildings corresponding to building vulnerability class B (on MSK-64 and EMS-98 scales) were affected by the earthquake, Gabrichidze *et al.* (2004) and Javakhishvili *et al.* (2004) concluded that the corresponding intensity for this seismic event would be VII according to both EMS-98 (Grünthal, 1998) and MSK-64 scale (Medvedev *et al.*, 1965).

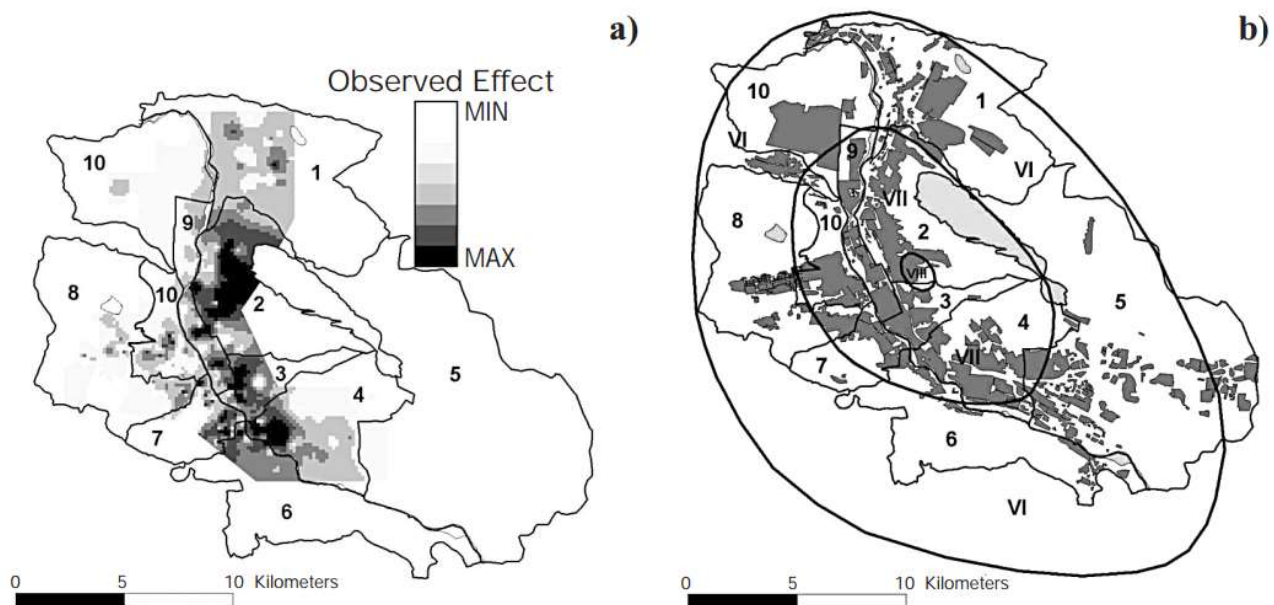


Figure A4.10.10. Macroseismic (MSK-64) intensity (Roman numbers) of the 2002 Tbilisi earthquake: a) relative effect according to the questionnaires, b) intensity map. Arabic numbers indicate the city districts as per Table A4.10.5. From Javakhishvili *et al.* (2004).

Table A4.10.5. List of Tbilisi Districts

Tbilisi Districts	
1	Gldani
2	Nadzaldevi
3	Chugureti
4	Isani
5	Samgori
6	Krtsanisi
7	Mtatsminda
8	Vake
9	Didube
10	Saburtalo

Gabrichidze *et al.* (2004) and Javakhishvili *et al.* (2004) analysed additional criteria in order to evaluate the maximum macroseismic intensity generated by this earthquake. Based on slightly different intensity prediction equations, the authors arrived to MSK intensities of around VII - VIII. The PGA recorded on a rock site at a distance of around 6 km from the epicentre was 0.11 g, which suggests intensity VII, while the PGA calculated on the surface (0.1 g-0.25 g) suggests slightly higher values, between VII and VIII. Gabrichidze *et al.* (2004) estimated maximum surface velocities in the range 10-25 cm/s and concluded that these correspond to intensity VII-VIII. Sliding and overturning of monuments in several graveyards was observed, implying intensity VIII. As there is no sufficient data in the city regarding geological indications associated to intensities as low as VI, such as cracks and landslides, Gabrichidze *et al.* (2004) concluded that, according to this criterion, intensities should have been equal to or lower than VI. All these considerations are summarised in Table A4.10.6.

Table A4.10.6. Macroseismic Intensity assessed by different criteria. From Gabrichidze *et al.* (2004).

Criteria	Macroseismic Intensity (MSK-64)
Intensity attenuation relation	VII-VIII
Recorded PGA on baserock	VII
Estimated PGA on the surface	VII-VIII
Estimated max. velocity on the surface	VII-VIII
Macroseismic data (grave yards)	VIII
Geological effects	<VI

The ShakeMap (Worden *et al.*, 2017) in terms of Modified Mercalli Intensities for this event is available at the website of the United States Geological Survey (USGS) and is depicted in Figure A4.10.11. As observed in the map, the highest intensity shown is 4.5 MMI. This value is significantly lower than those described above. Both epicentral locations according to the USGS and to Varazanashvili *et al.* (2008) are presented in the ShakeMap (see section A4.10.2.1). The highest MMI Intensity on the map is in better spatial agreement with the epicentre location assessed by Varazanashvili *et al.* (2008), possibly due to information from

STBO station (located closer to the latter) being the only observed data used to elaborate the ShakeMap. Due to this same reason, most of the ShakeMap largely relies on intensity prediction models.

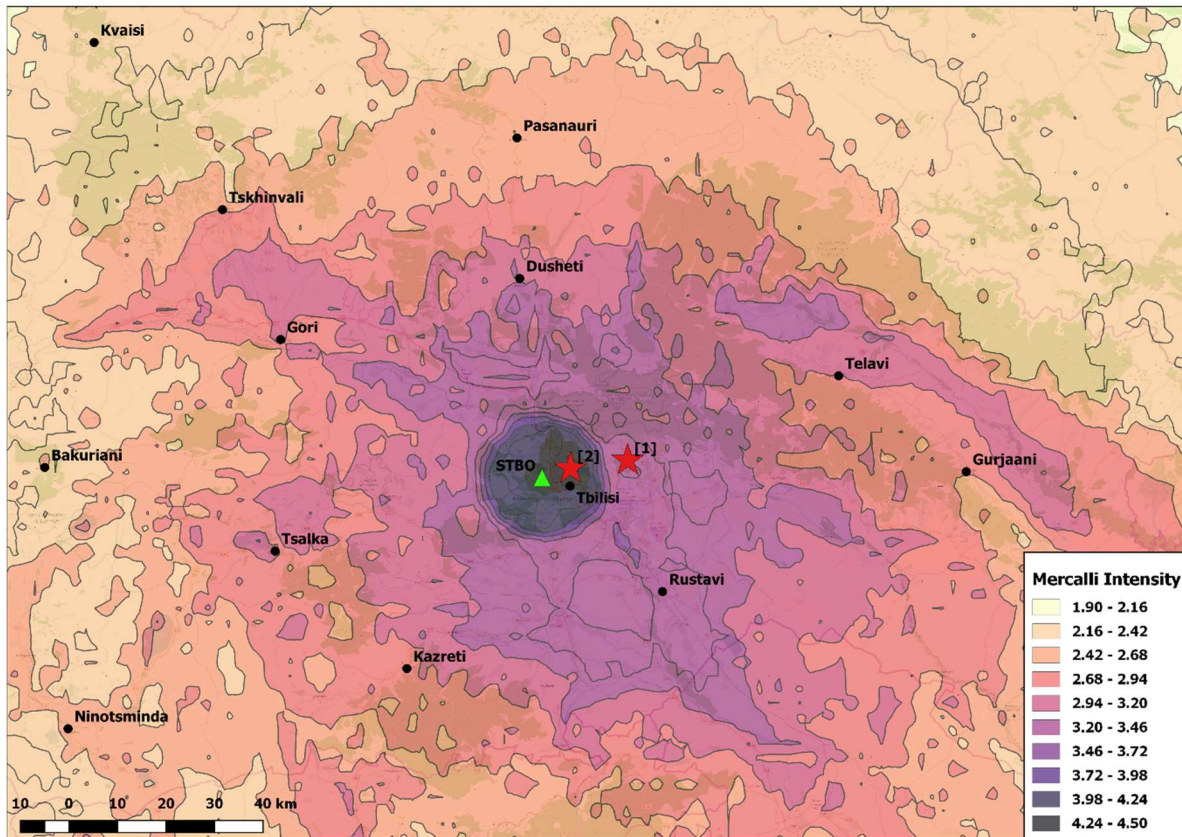


Figure A4.10.11. USGS ShakeMap in terms of Modified Mercalli Intensities (MMI) (28.01.2017). Red star (1) indicates epicentre according to the USGS; red star (2) indicates epicentre according to Varazanashvili et al. (2008). Triangle indicates STBO station.

A4.10.4.2 Ground motion recordings

This seismic event was recorded on a rock site at a distance of around 6 km to the west of the epicentre, at the STBO station of the seismic observatory of the Institute of Geophysics of the Georgian Academy of Sciences. The accelerograms were retrieved from the RESORCE ground motion database (Akkar *et al.*, 2014) and are presented in Figure A4.10.12. Table A4.10.7 summarizes some of the main characteristics of the waveforms recorded at the STBO station, processed using SeismoSignal (Seismosoft, 2016).

As shown in Figure A4.10.12 and Table A4.10.7, the highest recorded PGA was 108.54 cm/s^2 , and corresponds to the transversal component of the ground motion record. The dominant frequency corresponding to this accelerogram is around 5 Hz (0.2 seconds), which can be observed in the Fourier Amplitude graph in Figure A4.10.13, as well as in the pseudo-acceleration response spectrum of Figure A4.10.14.

The pseudo-acceleration and displacement response spectra for the two as-recorded horizontal components of the available accelerogram are shown in Figure A4.10.14 and Figure A4.10.15, respectively. Besides the peak corresponding to $T=0.2$ seconds described

above, a second less-significant peak can be observed in Figure A4.10.14 for the transverse component at $T=0.08$ seconds. A smaller peak can be observed as well for the longitudinal component at $T=0.12$ seconds.

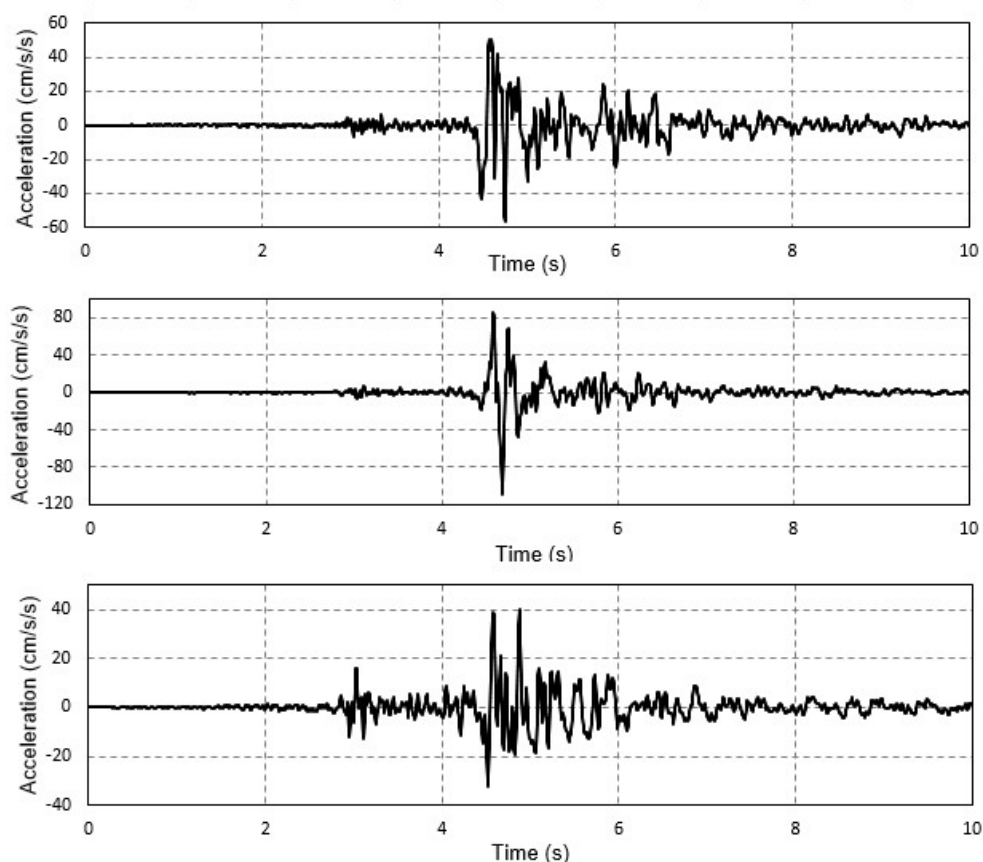


Figure A4.10.12. Longitudinal horizontal (top), transverse horizontal (centre) and vertical (bottom) acceleration time-histories recorded for the main shock at station STBO, in Tbilisi city, 6 km away from the epicentre. Epicentral distance based on epicentral coordinates assessed by Varazanashvili et al. (2008). Waveform data from RESORCE database (Akkar et al., 2014).

Table A4.10.7. Main characteristics of waveforms and recording station for the record of the main shock, available from the RESORCE database. L: longitudinal horizontal component. T: transverse horizontal component. V: vertical component.

Station	Station Name	Latitude	Longitude	Repi (km)	PGA (cm/s ²)			PGV (cm/s)			PGD (cm)		
					L (x)	T (y)	V (z)	L (x)	T (y)	V (z)	L (x)	T (y)	V (z)
STBO	Tbilisi - Seismic Observatory	41.733 °N	44.750 °E	6.1	56.910	108.540	40.281	3.276	2.956	1.585	0.372	0.186	0.101

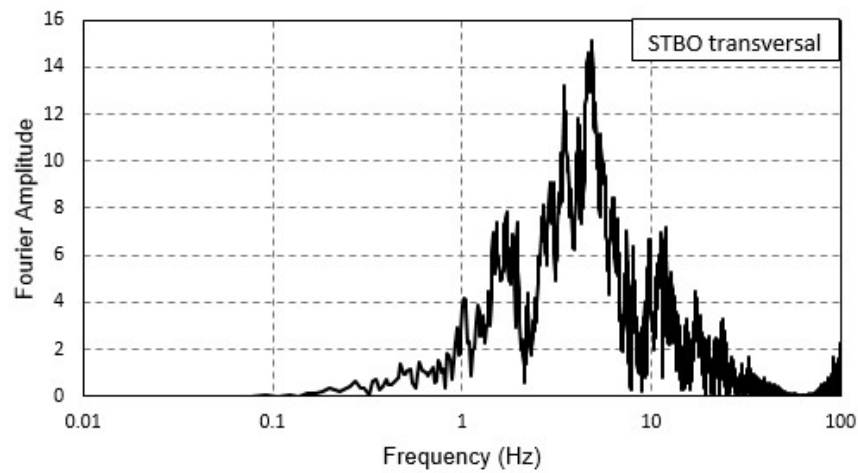


Figure A4.10.13. Fourier Amplitude for the transversal component of the acceleration time-history recorded for the main shock at station STBO, in Tbilisi city, 6 km away from the epicentre. Obtained with SeismoSignal (Seismosoft, 2016).

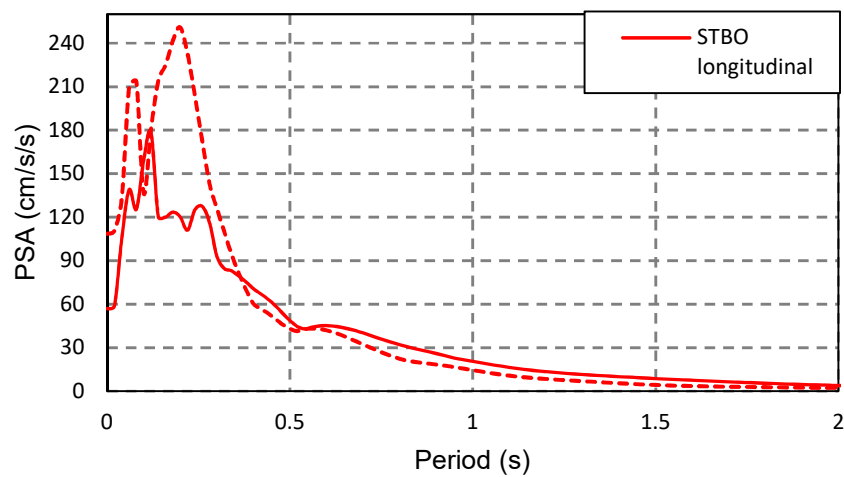


Figure A4.10.14. Pseudo-acceleration response spectra (5% of critical damping) for each of the two as-recorded horizontal components of the available accelerogram, obtained with SeismoSignal (Seismosoft, 2016).

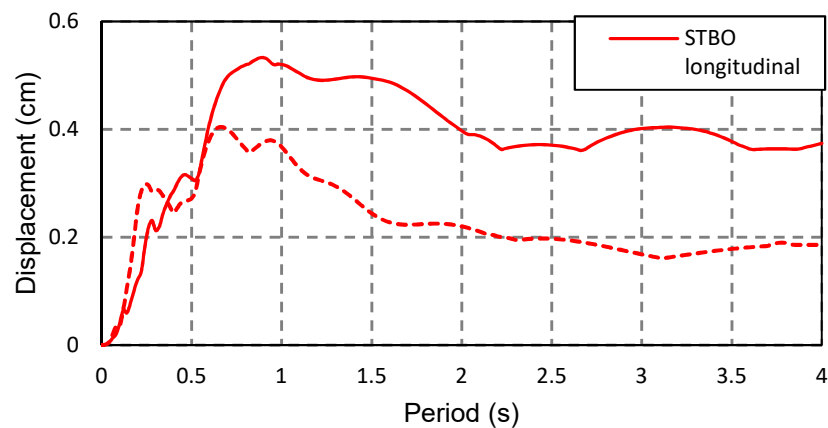


Figure A4.10.15. Displacement response spectra (5% of critical damping) for each of the two as-recorded horizontal components of the available accelerogram, obtained with SeismoSignal (Seismosoft, 2016).

A4.10.4.3 Inferred shaking levels

Using the record from station STBO as the input at bedrock, Gabrichidze *et al.* (2004) performed one-dimensional equivalent-linear site response analyses, and obtained spectral acceleration values for the longitudinal component of ground motion at the periods of 0.3 and 0.5 seconds, as shown in Figure A4.10.16 and Figure A4.10.17, respectively. These figures indicate that the spectral acceleration at station STBO was in the range between 0.09 g and 0.20 g for $T=0.3$ s and between 0.05 g and 0.1 g for $T=0.5$ s. Values of spectral acceleration corresponding to the lower bounds of these two ranges (*i.e.*, 0.09 g and 0.05 g) are in agreement with those shown in Figure A4.10.14 calculated directly from the longitudinal component of the record at the STBO station.

The PGA ShakeMap (Worden *et al.*, 2017) for this event, available from the United States Geological Service (USGS) website, is depicted in Figure A4.10.18. The highest PGA indicated on this map is 0.11 g, which is in agreement with the value recorded at the STBO station, the only observed data feeding its calculation (*i.e.*, it is mostly relying on prediction models). Just as for the case of Figure A4.10.11, the epicentre calculated by Varazanashvili *et al.* (2008) coincides better with the location of the maximum PGA than that of the USGS, possibly for the same reasons. Being the data from the STBO station the only recorded values available, and having no Did You Feel IT (DYFI) answers, the Ground Motion Prediction Equation (GMPE) of Zhao *et al.* (2006) was used for the calculation of the PGA ShakeMap. It is noted that this map does not match the estimations of Gabrichidze *et al.* (2004) of PGA values in the range 0.1-0.25 g for sites located over softer soils. Similarly, the maximum ShakeMap-derived Peak Ground Velocity (PGV) is equal to 0.75 cm/s and is much lower than the PGV recorded by the STBO station (see Table A4.10.7). The ShakeMap in terms of spectral acceleration indicates a maximum value of 0.0416 g at period of 0.3 seconds, which is lower than the value of ~0.09 g and ~0.126 g (Figure A4.10.14) calculated directly from the record at the STBO station for the longitudinal and transversal components, respectively. It is also lower than the range of spectral acceleration values obtained by Gabrichidze *et al.* (2004) and shown on map in Figure A4.10.16. The maximum ShakeMap-derived spectral acceleration at the period of 1 second is 0.0079 g, while at the period of 3 seconds its value is 0.0009 g.

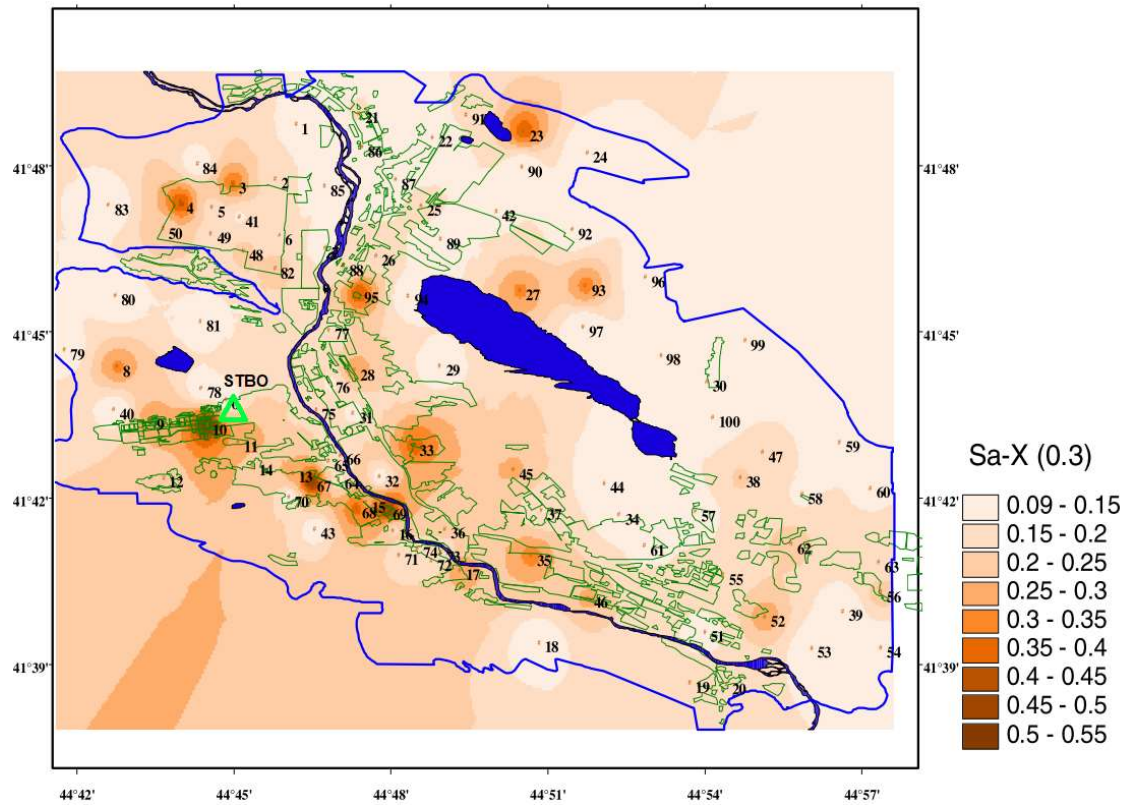


Figure A4.10.16. Spectral acceleration (5% of critical damping) at period of 0.3 seconds for the longitudinal (x) component of ground motion. From Gabrichidze *et al.* (2004).

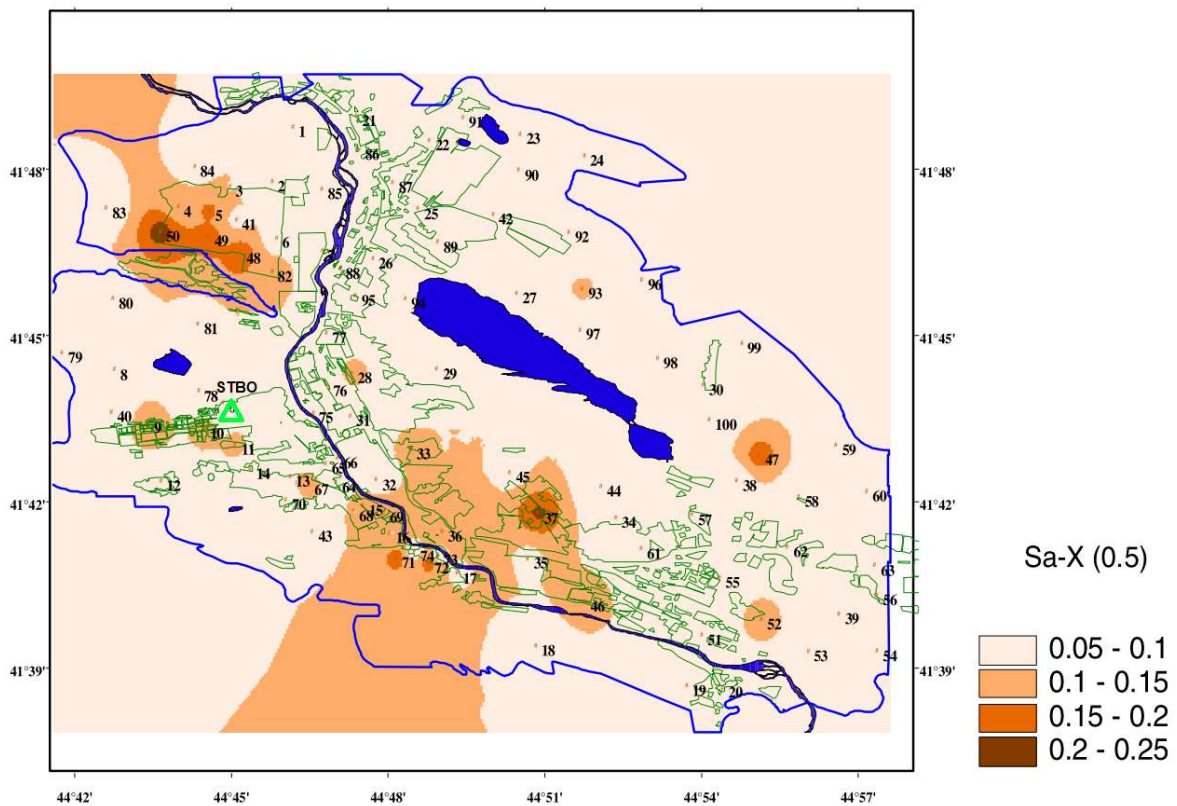


Figure A4.10.17. Spectral acceleration (5% of critical damping) at period of 0.5 seconds for the longitudinal (x) component of ground motion. From Gabrichidze *et al.* (2004).

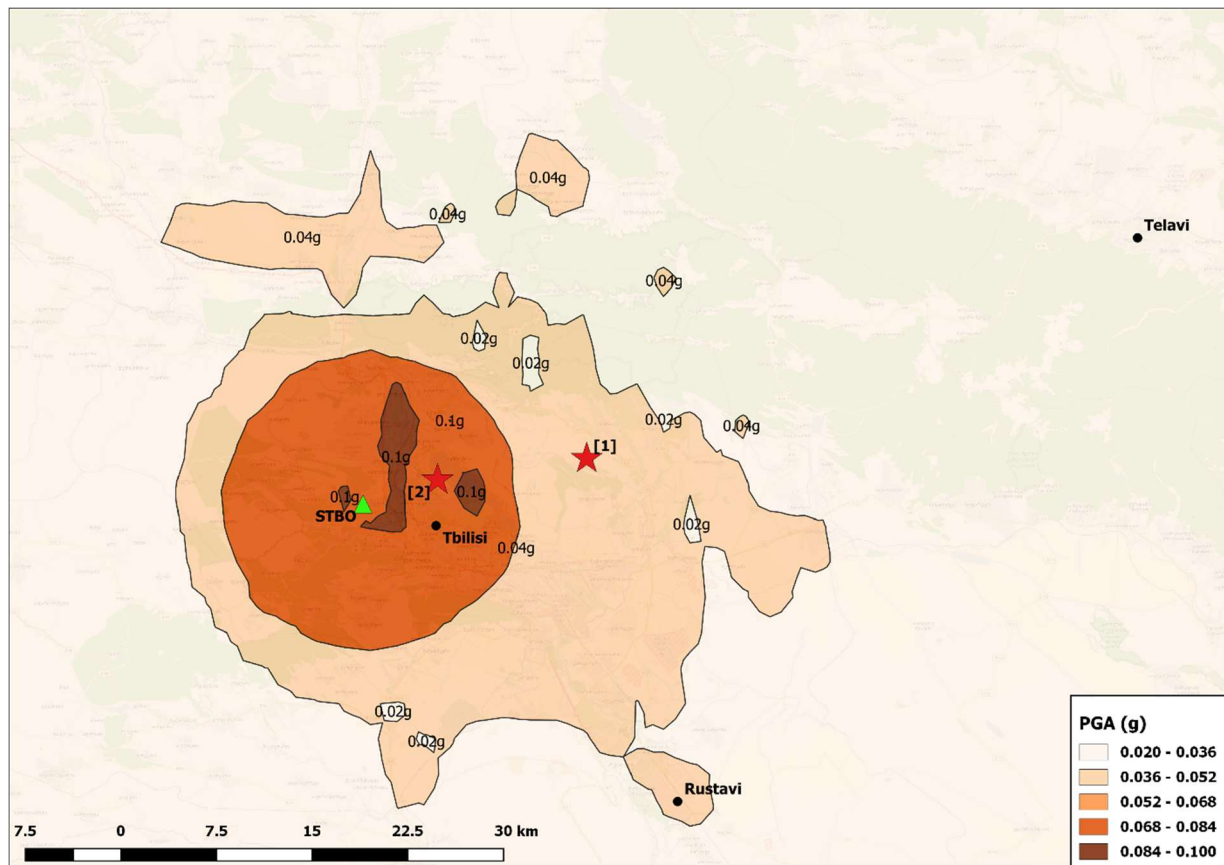


Figure A4.10.18. USGS Shake Map in terms of PGA (28.01.2017). Red star (1) indicates epicentre according to the USGS; red star (2) indicates epicentre according to Varazanashvili *et al.* (2008). Triangle indicates STBO station.

A4.10.4.4 Duration of ground shaking

The 5%-75% definition of the significant duration of the record from station STBO was calculated for its two horizontal components using the SeismoSignal software (Seismosoft, 2016). Results are shown in Table A4.10.8.

Table A4.10.8. Significant duration (5%-75% of Arias Intensity, in seconds) of the ground motion recorded at STBO station (waveforms from the RESORCE database, Akkar *et al.*, 2014).

Station	Station Name	Latitude	Longitude	Repi (km)	x component	y component
STBO	Tbilisi - Seismic Observatory	41.733 °N	44.750 °E	6.1	0.928	0.296

Estimations of earthquake significant durations were carried out using the models of Bommer *et al.* (2009) and Afshari & Stewart (2016) based on the 5%-75% Arias Intensity definition, as shown in Figure A4.10.19. Varazanashvili *et al.* (2008) estimated the average diameter of the rupture area of 3.5 ± 1 km and depth of 6.89 km. Considering these values, the depth to the rupture used for the model of Bommer *et al.* (2009) was approximated as 5.14 km. A series of distances were considered, including the closest distance from the fault rupture to the station STBO (approximately 7.7 km). Taking into account that the broader Tbilisi area is laying mostly on stiff soil ($360 \text{ m/s} < V_{s30} < 760 \text{ m/s}$) and rock ($V_{s30} > 760 \text{ m/s}$) (see Section A4.10.3.2), the V_{s30} values of 360 m/s, 760 m/s and 1500 m/s, corresponding

to the bounding limits of the definitions of soil types according to NEHRP, were used. A value of $V_{s30} = 700$ m/s is estimated from the USGS V_{s30} Map Server (Wald & Allen, 2007; see Figure A4.10.9) for the station STBO and is very close to the value of 760 m/s considered herein.

As can be observed in Figure A4.10.19, the significant durations calculated for Station STBO (Table A4.10.8) are closer to the predictions of the Bommer *et al.* (2009) equation than to those of the Afshari & Stewart (2016) one. They are also closer to the curves obtained using $V_{s30} > 760$ m/s than to those obtained using lower values of V_{s30} , as expected. Applying the predictive models using the distance from the Station STBO to the rupture, a 5.14 km depth to the top of the surface and V_{s30} of 700 m/s as estimated from the V_{s30} USGS Map (Figure A4.10.9), observed durations for the transversal (y) component (Table A4.10.8) are 2.05 and 3.10 standard deviations below the predictions of the models of Bommer *et al.* (2009) and Afshari & Stewart (2016), respectively.

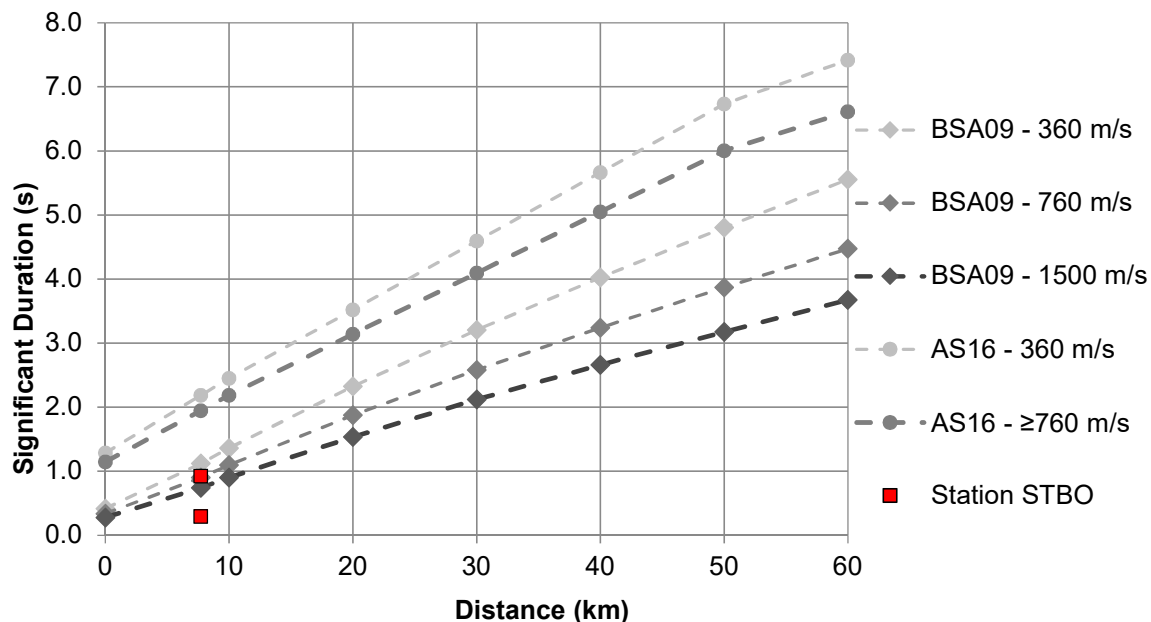


Figure A4.10.19. Estimation of the significant duration of the main shock, using prediction equations by Bommer *et al.* (2009, BSA) and Afhsari & Stewart (2016, AS), and significant duration calculated for the two horizontal components of the accelerogram recorded at the STBO station.

Highlighting how the short duration of the event had been beneficial for the exposed building stock, Gabrichidze *et al.* (2004) reported the following durations for the transversal component of ground motion recorded at the STBO station:

- bracketed duration (duration between the first and last excursions of 5% of PGA): 0.2 s;
- uniform duration (the total time during which the acceleration was larger than a value of 5% of PGA): 0.1 s;
- significant duration (based on the 5%-95% Arias Intensity definition): 2.4 s.

Jimsheladze *et al.* (2008) reported a duration of 3 seconds but did not provide information with respect to the definition of such duration, nor its location, though it is to be expected that they were referring to the area within the city of Tbilisi.

A4.10.5 Collateral earthquake hazards

A4.10.5.1 Surface rupture

No surface rupture has been documented for the 2002 Tbilisi earthquake. Varazanashvili *et al.* (2008) reported that the earthquake happened on a blind fault, covered by the Quaternary deposits of Mtkvari River.

Using empirical relations developed by Shebalin (1997), Riznichenko (1985) and Wells & Coppersmith (1994), Varazanashvili *et al.* (2008) estimated the rupture length to have been 3 ± 0.5 km, and the rupture diameter to have been 3.5 ± 1 km and around 5 km, respectively. When combined with the 6.89 km hypocentral depth calculated by the same authors, all these values are consistent with the lack of observation of surface rupture.

A4.10.5.2 Landslides

The area of Tbilisi is susceptible to landslides and the most active landslide zones are placed in the northern slope of Mtatsminda Hill, the Nutsubidze Plateau, the slopes of Mukhatgverdi Hill, a large area across the right bank of the Vere River, and the Khevdzmari Ravine near the Gldani village (Adeishvili *et al.*, 2011; United Nations Development Programme, UNDP, 2015). According to the findings of the National Environmental Agency, most of the landslides in this area are the result of inappropriate planning and construction of buildings and other infrastructure (Adeishvili *et al.*, 2011).

Adeishvili *et al.* (2011) reported the occurrence of geo-dynamic processes caused by the 2002 seismic event, though they did not specify the type of processes they were referring to. According to Galloway & Simpson (2003) and the Preliminary Determination of Epicenters (PDE) bulletin of the USGS, the roads in Tbilisi had been partially blocked due to landslides observed after the 2002 earthquake. However, it is not clear whether those authors were referring to landslide activity induced by the earthquake itself or to the landslides which are known to have been triggered by the extreme rainfall in the vicinity of Tbilisi in the months after the 2002 earthquake (UNDP, 2015).

A4.10.5.3 Liquefaction

No reports on liquefaction effects have been found.

A4.10.5.4 Settlements

According to Gabrichidze *et al.* (2004) and ICOMOS (2002/03), the earthquake caused the uneven subsidence of foundations and basement floors, though they do not explicitly state

to what extent this influenced the overall degree of damage observed. They note, however, that non-uniform settlements of foundations and subsidence of basement floors were observed prior to the earthquake as well, due to damaged underground water supply pipelines and to the infiltration of atmospheric water in foundation soils through damaged pavements.

A4.10.6 Exposed population

A4.10.6.1 Socio-economic setting

According to the 2016 Human Development Report (United Nations, 2016) the Human Development Index (HDI) for Georgia in 2015 was 0.769, while its Inequality-adjusted HDI (IHDI) was 0.672. This located Georgia in the 70th place in the world's ranking, while the Netherlands ranks 7th. Table A4.10.9 compares the HDI and IHDI for both countries based on the Human Development Reports for the years 2004 and 2016 (United Nations, 2004; 2016). The column "Adj. HDI" provides the HDI values given in the 2016 report for previous years, adjusted for data consistency in time. As observed from the adjusted HDI values given in the 2016 Human Development Report, the HDI Index for Georgia was trending upwards in recent years. Compared to the Netherlands, in year 2015, the HDI for Georgia was 16.77% smaller.

Table A4.10.9. Human Development Index and Inequality-adjusted Human Development Index for Georgia and the Netherlands.

Report	Data	Georgia				Netherlands			
		HDI	IHDI	Rank	Adj. HDI	HDI	IHDI	Rank	Adj. HDI
2004	2002	0.748	N/A	97	0.769	0.942	N/A	5	0.924
2016	2015	0.769	0.672	70	0.769	0.924	0.861	7	0.924

Due to its favourable topography and climate, two of Georgia's main economic activities are agriculture and, more recently, tourism. Other important sectors of Georgian economy are industry (especially that related to the production of construction materials), energy (hydropower provides most of the energy needs), transport and trade (Atlas of Natural Hazards & Risks of Georgia, 2012; Adeishvili *et al.*, 2011; Central Intelligence Agency, CIA, 2017).

After the declaration of Georgian independence in 1991, which followed the break-up of the Soviet Union, the economy of the country crumbled. This resulted in high unemployment rates as well as crime and corruption throughout the country. More stability within the country was gained after the Rose Revolution of 2003 (International Atomic Energy Agency (IAEA), 2002; Wikipedia 2017a, Wikipedia 2017b). A significant economic growth took place after the earthquake between the years 2004 and 2007, mostly as the result of large inflows of foreign investment (UNDP, 2014; CIA, 2017; International Monetary Fund, IMF, 2006). Conflicts with Russia in 2008 and the global financial crisis resulted in slow economic

growth. Even though the country's economy recovered from 2010 to 2016, unemployment remained high, and a considerable part of the population is still living in poverty (UNDP, 2014; CIA, 2017).

Table A4.10.10 presents a comparison between Georgia and the Netherlands in terms of GDP, GDP per capita and unemployment rate. Variations in GDP and unemployment rate for Georgia between the years 1996 – 2016 is presented in Figure A4.10.20 (World Economic Outlook Database (WEO), 2017). No information regarding the unemployment rate in Georgia for years 2016 and 2017 was available in the WEO (2017), but the National Statistics Office of Georgia (GeoStat, 2017a) reports 11.8 % of unemployment rate for year 2016.

Table A4.10.10. Gross domestic product (GDP), GDP per capita and unemployment rate for Georgia and the Netherlands, according to the World Economic Outlook Database (2017).

Indicator	Units	Georgia		Netherlands	
		2002	2017	2002	2017
Gross domestic product, current prices	Billion USD	3.40	13.72	467.02	762.69
Gross domestic product per capita, current prices	USD	776.79	3,715.39	28,919.20	44,654.23
Unemployment rate	%	12.59	N/A	3.67	5.40

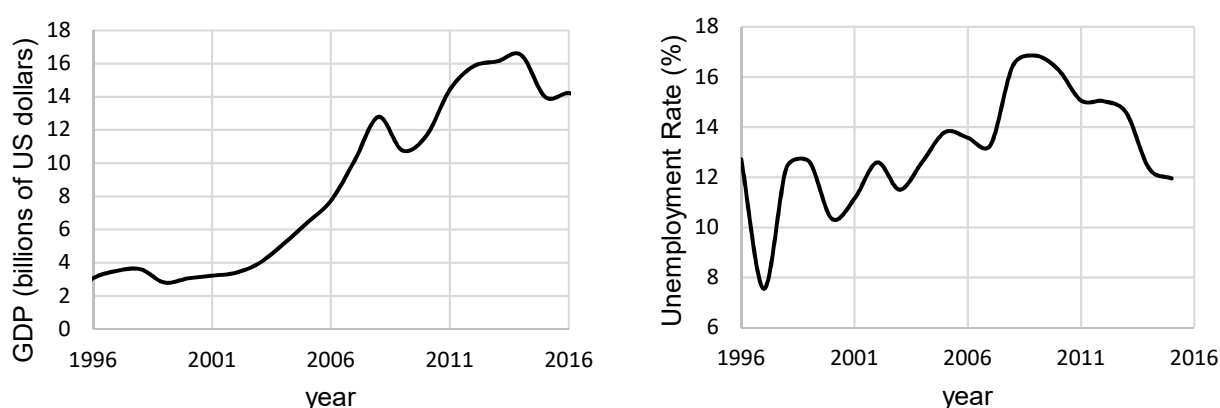


Figure A4.10.20. Gross domestic product (GDP) expressed in billions of US dollars (left) and unemployment rate expressed in percentages (right) for Georgia. Data from the World Economic Outlook Database (2017).

A4.10.6.2 Population density and distribution

Based on the general census of 2002, the population of the Tbilisi region was 1,081,679 people, of which 1,081,532 was urban and 147 was rural population (GeoStat 2017b). According to this data, the population of Tbilisi in 2002 represented 24.7 % of the total Georgian population.

The population density in the year 2000 according to Gridded Population of the World (GPW v4.0; CIESIN, 2016) for the area of Tbilisi is shown in Figure A4.10.21. As can be observed, the population density was around 5,100 persons/km² in the city.

The USGS EXPO-CAT human exposure database (Allen *et al.*, 2009) estimates that around 311,000 people were exposed to intensity MMI 5.5, most of which (99.88%) corresponded to urban population (Figure A4.10.22). A higher proportion of rural population is estimated for lower intensities of MMI 4 to MMI 5.5. This contrast in the urban/rural rates is to be expected, considering that some of the most relevant estimations of epicentral coordinates locate the source very close to the city. The number of people exposed to the highest MMI intensity of 6 was estimated in 980, all of them corresponding to urban population.

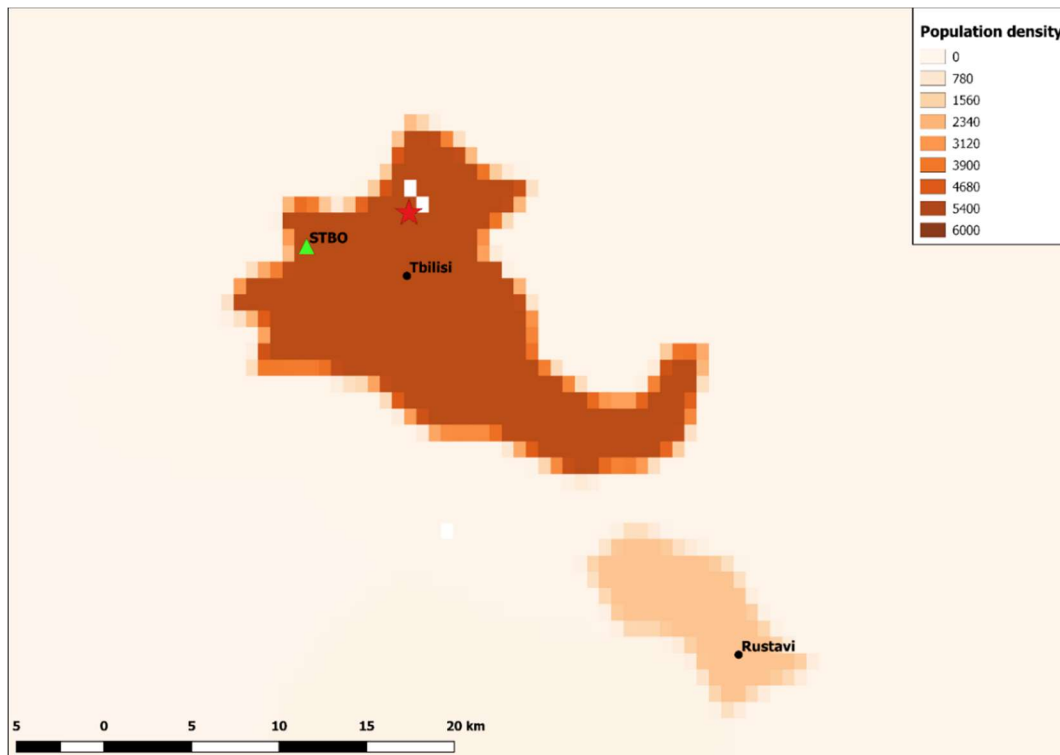


Figure A4.10.21. Population density (persons/km²) around the Tbilisi area in 2000. Data from Gridded Population of the World (GPW v4.0; CIESIN, 2016). The red star marks the epicentre of the main shock, according to Varazanashvili *et al.* (2008).

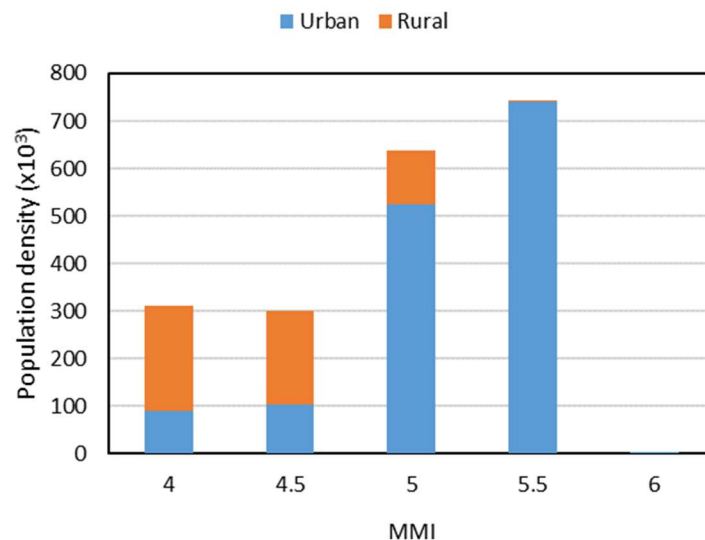


Figure A4.10.22. Disaggregation of estimated urban and rural population exposed to MMI IV to MMI VI. Data from USGS EXPO-CAT database (Allen *et al.*, 2009).

A4.10.6.3 Time of day of earthquake

The earthquake struck on a Thursday evening, at 22:41 local time. In this late hour of a week day, most of the Tbilisi population was probably in their homes, which implies risk of exposure to possible building collapses, falling ceiling debris, falling non-structural elements, etc. Considering that the greatest damage, in both qualitative and quantitative terms, was observed in residential buildings, the number of casualties was probably greater than what could have been the case had the earthquake occurred during the daytime. However, this reduction in casualties associated with the damage to residential buildings could have been offset by the additional casualties related to damage of administrative and public buildings, such as schools, kindergartens and hospitals. At the same time, the fact that the percentage of public buildings that were damaged is much lower than that of residential buildings could be as well counterbalanced by the higher occupation of the former.

A4.10.7 Characteristics of exposed building stock

A4.10.7.1 Seismic design codes

The seismic hazard of Georgia was first assessed while the country was under the rule of the USSR. The seismic hazard maps of 1937, 1957, 1968 and 1978 were compiled during this period (Chelidze *et al.*, 2002). As these maps were based on previously-observed maximum macroseismic intensities from past earthquakes, they were found to constantly underestimate seismic hazard levels associated with certain seismically active regions of the country that had not experienced major earthquakes in recent history. Each time a large event occurred, the map would be updated to account for the experienced levels of seismic hazard of the regions affected (Atlas of Natural Hazards & Risks of Georgia, 2012; Chelidze *et al.*, 2002; Ulomov, 1999).

The shift from the deterministic approach happened in the 1990s with the introduction of probabilistic seismic hazard assessment. Since then, many institutions and authors have developed their work on probabilistic seismic hazard and risk assessment of the Caucasian region (e.g., Balassanian *et al.*, 1999; Chelidze *et al.*, 2002; Slejko *et al.*, 2008; Varazanashvili *et al.*, 2012; Tsereteli *et al.*, 2014a; Tsereteli *et al.*, 2014b; Smit *et al.*, 2000). Under the scope of the GSHAP project (Giardini *et al.*, 1999), which took place between 1993 and 1999, the probabilistic seismic hazard of Caucasus was carried out (Balassanian *et al.*, 1999). This resulted in a map expressing seismic hazard in terms of the probability of exceedance of PGA and MSK-64 intensity with a 475-year return period. At around the same time, the Regional Seismology Department of the former Institute of Geophysics (Chelidze *et al.*, 2002) created the first probabilistic seismic hazard map specifically for Georgia, in terms of the same metrics, and for 1%, 2%, 5% and 10% probability of exceedance in 50 years. The probabilistic map expressing hazard with a 2,500-year return period (2% probability of exceedance in 50 years, Figure A4.10.3) was officially approved and adopted as a normative hazard map in PN 01.01-09 (2009), the Georgian building code, in 2009 (Tsereteli *et al.*, 2014a; Varazanashvili *et al.*, 2012; Atlas of Natural Hazards & Risks of Georgia, 2012).

Even though seismic design construction practices were implemented in Georgia in the 1950s, many of the earthquakes that affected the country in the late 20th/early 21st century (e.g., 1988, 1991, 1994, 1997, 2000, 2002) led to significant structural damage. Not only the old, non-conformant, part of the building stock was destroyed, but also the buildings that were constructed following specifications of seismic codes (International Science and Technology Center, ISTC, 2003). These were the so-called SNIIP seismic codes that had been used for regulation of seismic design and construction practices in all former Soviet Union countries, including Georgia. Until the country gained its independence in 1992, a series of SNIIP seismic standards were introduced, the latest of which was the SNIIP II-7-81 issued in 1982. Mkrtychev & Dzhinchvelashvili (2016) argue that the implementation of a deterministic, instead of probabilistic, approach for the assessment of seismic impacts led to inaccurate determination and, in many cases, underestimation of required seismic resistance of buildings constructed in compliance with this code. According to Armaghani (2011), the current seismic code of Georgia (PN 01.01-09), established in 2009, is still largely based on the old (SNIIP) code and is in a need of revision.

Armaghani (2011) emphasizes that Georgia does not have a unified system of design and construction regulations, as building codes used in practice represent a mix of various foreign (e.g. Soviet Union, American, British, German and other European) standards and lack any consistency. Due to their variety, enforcement of these codes is usually not controlled, and construction is performed by unskilled workers with the implementation of inexpensive, poor quality materials and construction methods, all of which contribute to the development of an unsustainable and inefficient building stock in Georgia (Armaghani, 2011). Though written in 2011, the report of Armaghani that informs on such poor conditions of the Georgian building stock and its building codes is likely to reflect the construction practices that were implemented even earlier, during the late 20th and the early 21st century.

A4.10.7.2 Building typologies

The diversity of architectural styles and building typologies in Tbilisi reflects the influences of the different cultures (Byzantine, West-European, Middle-Eastern, Soviet) throughout its history (International Council on Monuments and Sites, ICOMOS, 2001/02).

During the 19th century, Tbilisi downtown was built mostly in Western European style (Wikipedia, 2017b). Distinctive elements of residential dwelling houses were balconies and courtyards, mostly built out of wood and brick (Salukvadze & Gogishvili, 2009; UNESCO, 2007). During most of the 20th century, Soviet-style construction became typical, both for large public buildings and for low-cost mass housing. In order to address the needs of the increasing population of Tbilisi, communalization of dwelling space took place, which resulted in many people living in shared apartments known as *komunalkas*. Although it did not provide comfort for the city dwellers, the residential construction that was carried out during the period of Stalin sovereignty, until the late 1950s, was of good quality (Salukvadze & Gogishvili, 2009). From 1960s onwards, expansion of cheap mass housing took place. Standardized, prefabricated 4-5 storey concrete-panelled, usually poorly-constructed buildings known as *khrushchevkas*, were popular during this period (Salukvadze &

Gogishvili, 2009; Wikipedia, 2017b; Wikipedia, 2017c). Starting in the 1970s, better quality, high-rise buildings were constructed, but the general condition of the building stock was not significantly improved (Salukvadze & Gogishvili, 2009). In the period after the attainment of independence at the beginning of the 1990s, political, bureaucratic and financial restrictions did not allow for large investments in the real estate market, and most of the development in the construction sector was achieved in an illegal manner (Salukvadze & Gogishvili, 2009). Shutdown of the functional state construction sector and privatization of apartments led to tens of thousands of uncontrolled building projects to be carried out in Tbilisi. These constructions did not follow any building norms or took care of environmental and safety standards or building aesthetics. Additionally, low-quality vertical building extensions (VBE) contributed to the ongoing physical deterioration of existing buildings, to the extent that many are referred to as “vertical slums” (Salukvadze & Gogishvili, 2009; Wikipedia, 2017b). The situation changed in the mid-2000s when economic growth, property registration and reduced corruption led to the development of the real estate market and faster growing construction businesses (Salukvadze & Gogishvili, 2009). As emphasized by Tsereteli *et al.* (2014b), vulnerable infrastructure, growing population density and urban development contribute to increasing seismic risk in the city of Tbilisi.

The buildings that make up the “Tbilisi Historic District”, also known as the “Old Tbilisi”, that stretches on both sides of the River Mtkvari, including districts Nadzaladevi-Gldani; Mtatsminda-Krtsanisi; Didube-Chugureti (see Table A4.10.5), are in a vulnerable state. The Old Tbilisi is a 19th century urban fabric and consists of structures dating from the 5th to the 20th century with significant monumental and architectural value, though only a small percentage of the pre-19th century buildings remained after the Persian invasion of 1795 (Tbilisi.TV; ICOMOS, 2001/02). The houses are mostly single or two-storey and are made of a combination of wood and stone. A small number of brick and plaster buildings exist in the area as well, though they are not common (Palus & Zabawa-Krzywickowska, 2014). Many valuable Old Tbilisi historical buildings that deteriorated during the Soviet period were renovated in the 1980s (Salukvadze & Gogishvili, 2009). The Tbilisi Historic District was under the Worlds Monument Watch in 1998, 2000 and 2002 (World Monuments Fund, 2017), and was nominated for the inscription on the UNESCO World Heritage List in 1999, though it has not been included yet at the time of writing (October 2017). Despite its considerable architectural and urban value, the poor maintenance results in a relatively bad physical condition of the Old Tbilisi (ICOMOS 2001/02; 2002/03).

According to the PAGER Inventory Database v2.0 (Jaiswal & Wald, 2008), reinforced masonry bearing walls with wood or metal deck diaphragms are highly present (25%) in both urban and rural buildings (Figure A4.10.23). Besides this building type, in urban areas there is a high presence (20%) of precast panels, which are common for Soviet constructions. Other common urban typologies are unreinforced brick masonry and concrete block unreinforced masonry with either cement or lime mortar. The most common typology in Georgia for rural buildings is unreinforced brick masonry in lime mortar.

Gabrishidze *et al.* (2004) and Javakhishvili *et al.* (2004) report on the proportion of different building typologies that can be found in each district of Tbilisi (Figure A4.10.10), as shown in Table A4.10.11. According to the authors, the total building stock in the city consisted in

2004 of more than 45,000 residential properties, out of which a large proportion were low-rise brick and masonry, most likely constructed without any kind of seismic design (Gabrichidze *et al.*, 2004). According to Javakhishvili *et al.* (2004), they fall under building vulnerability class B on the EMS-98 (Grünthal, 1998) and MSK-64 (Medvedev *et al.*, 1965) scales. While the typologies are different from those used by the PAGER Inventory Database v2.0 (Jaiswal & Wald, 2008), Table A4.10.11 appears to be in agreement with the main structural types described above. The large-block structures mentioned in Table A4.10.11 are built of assembled prefabricated large-block masonry units usually made of natural or artificial stones or different types of concrete (light-weight, heavy, cellular and silicate). For exterior walls made of such blocks, the most common is the so called two-row sectioning system, where each floor of the building features two horizontal seams and the wall of each consecutive floor consists of three blocks (*i.e.* pier, sill and lintel block) (The Great Soviet Encyclopedia). Large-panel structures (Table A4.10.11) consist of prefabricated large slab elements. Exterior walls made of such panel elements usually cover one to two stories in height, while their width corresponds to that of one or two rooms. Similarly to large-block structures, panel-structures are usually made of various types of concrete, bricks and stones (*e.g.* hollow ceramic stone) (The Great Soviet Encyclopedia).

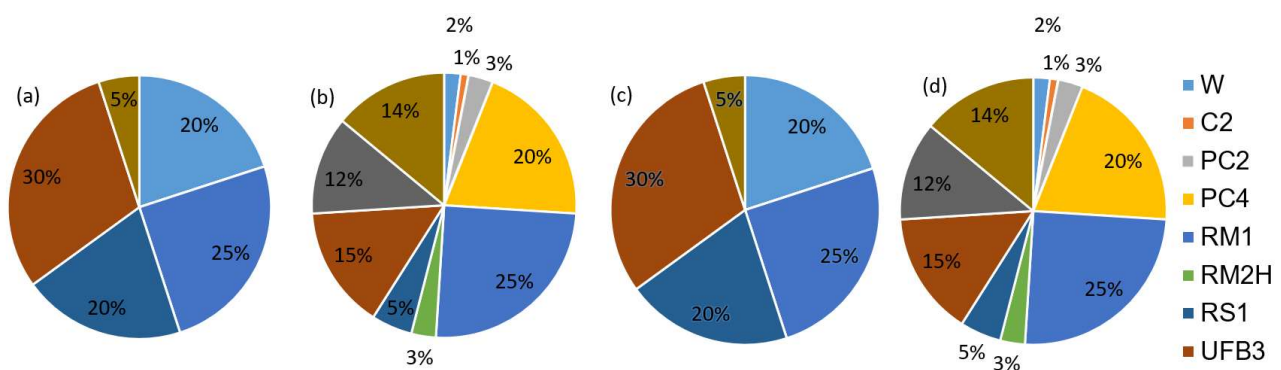


Figure A4.10.23. Proportion of buildings in Georgia belonging to each typology: (a) rural and residential, (b) urban and residential, (c) rural and non-residential, and (d) urban and non-residential. W: wood. C2: reinforced concrete shear walls. PC2: precast concrete frames with shear walls. PC4: precast panels (well-made of number of horizontal precast panels, construction from former Soviet Union countries). RM1: reinforced masonry bearing walls with wood or metal deck diaphragms. RM2H: reinforced masonry bearing walls with concrete diaphragms high-rise. RS1: local field stones dry stacked (no mortar) with timber floors, earth, or metal roof. UFB4: unreinforced fired brick masonry, cement mortar. UFB3: unreinforced brick masonry in lime mortar. UCB: concrete block unreinforced masonry with lime or cement mortar. Data from Jaiswal & Wald (2008).

According to Gabrichidze *et al.* (2004), the majority of schools in Tbilisi are 3-5 storey brick buildings constructed before 1950 and without consideration of seismic design, while a smaller number was constructed with MSK-64 design intensity VII in the period 1950-1990. Out of the total number of 202 schools, approximately 100 were constructed in compliance with standard projects from the 1960s onward, and can be associated with MSK-64 vulnerability classes B and C (Gabrichidze *et al.*, 2004).

Table A4.10.11. Most common types of buildings in Tbilisi in 2004. 1: 1-3 storey with brick walls; 2: 4-8 storey of brick; 3: 5-9 storey large-block; 4: 5-12 storey large-panel; 5: 5-16 storey prefabricated & cast in place RC frame; 6: 5-16 storey cast in place reinforced concrete. From Gabrichidze *et al.* (2004) and Javakhishvili *et al.* (2004).

District	Number of buildings in % by structural type							Total Number
	1	2	3	4	5	6	Other	
1. Gldani	77	2	11.2	8	1.5	0.2	0.1	2,630
2. Nadzaladevi	89.9	4	5	1	0.1	-	-	10,500
3. Chugureti	99.5	0.38	0.09	-	0.03	-	-	5,227
4. Isani	93	1	2.8	3	0.2	-	-	8,075
5. Samgori	74.3	11	8	6	0.2	-	0.5	3,685
6. Krtsanisi	96.5	1.3	2	-	0.2	-	-	3,100
7. Mtatsminda	95	4	0.8	-	0.2	-	-	3,000
8. Vake	82.7	10.3	5.5	0.3	1	-	0.2	3,564
9. Didube	80	3.2	10	5	1.8	-	-	1,390
10. Saburtalo	79	10.1	7	2.4	0.5	-	1	3,810

A4.10.7.3 Prior damage and retrofit

As mentioned in Section A4.10.7.2, in the period after Georgia's separation from the USSR in 1991, uncontrolled construction took place and many buildings were physically deteriorated due to the massive construction of low-quality vertical building extensions (VBE). At the same time, civil wars and armed conflicts with Russia in the 1990s resulted in many burned buildings and devastated infrastructure in Tbilisi (Gerkeuli, 2009). Considering as well decades-long under-maintenance of buildings found in the most affected part of the city, Old Tbilisi (ICOMOS, 2001/02), it is probable that considerable part of the Tbilisi building stock was already in a damaged state prior to the 2002 earthquake and that such pre-existing conditions made the consequences of the earthquake worse. An example of under-maintained buildings in the Tbilisi historic district that presented clear signs of damage prior to the earthquake is shown in Figure A4.10.24 (Hejazi, 2008).

Many buildings suffered from non-uniform settlements of foundations and subsidence of their basement floors prior to the earthquake, due to the damaged underground water supply pipelines that caused flooding of the basements, and to the infiltration of atmospheric water in foundation soils through damaged pavements (Gabrichidze *et al.*, 2004; ICOMOS, 2002/03).

Some of the brick masonry schools had been reinforced (mostly with steel bars) before the earthquake. According to Gabrichidze *et al.* (2004), this had a positive impact on their response to the earthquake loading.



Figure A4.10.24. Vernacular buildings in Betlemi Micro-Quarter in Tbilisi. Before (left) and after (right) the 2002 Tbilisi earthquake. From ICOMOS (2002/03).

A4.10.8 Damage observations

A4.10.8.1 Damage states

Most of the authors (Gabrichidze *et al.*, 2004; Javakhishvili *et al.*, 2004; Varazanashvili *et al.*, 2008) used the MSK-64 (Medvedev *et al.*, 1965) scale for the description of the damage states of buildings affected by this earthquake. Similar to the EMS-98 damage scale, the MSK-64 scale recognizes five damage grades, a description of which are given in Appendix II (Table A2.2.2).

The Ministry of Urbanization and Construction of Georgia made use of a three-grade scale for categorization of observed damage to buildings. Grade I was assigned to buildings with minor damage, grade II to those with significant structural damage, while major or complete damage to buildings was indicated as grade III (ReliefWeb, 2002b; 2002d).

A4.10.8.2 Damage statistics and description

As a result of the earthquake, thousands of buildings were damaged, including residential buildings, schools, kindergartens, hospitals, collective centres for internally displaced people, churches, cultural, administrative, and many other public buildings (ReliefWeb, 2002b; Gabrichidze *et al.*, 2004; Varazanashvili *et al.*, 2008). Most of the damage was concentrated in the old part of the city including Nadzaldevi-Gldani, Mtatsminda-Krtsanisi and Didube-Chugureti districts (see Figure A4.10.10 and Table A4.10.5), though it is noteworthy that no full collapses occurred during the earthquake (ICOMOS, 2002/2003; ReliefWeb, 2002b; Gabrichidze *et al.*, 2004). The highest level of damage was observed in old, low-rise (2- to 4-storey) brick and stone buildings that correspond to vulnerability class B buildings on both EMS and MSK scale, probably due to a combination of two reasons. Firstly, most of these buildings were built before the 1950s, without consideration of seismic load, and many of them were already damaged prior to the earthquake (Gabrichidze *et al.*, 2004; Javakhishvili *et al.*, 2004). Secondly, the natural frequencies of these buildings are

likely to have lied within the high-frequency range, of which the ground motion from this earthquake appears to have been especially rich, as pointed out in Section A4.10.4.2 and by Gabrichidze *et al.* (2004).

Gabrichidze *et al.* (2004) and ICOMOS (2002/03) report the following various degrees of damage:

- uneven subsidence of foundations;
- subsidence of basement floors;
- damage to already defective water-supply pipelines and subsequent flooding of already damp basements;
- cracking of brick arches in basements, and subsequent risk of further collapse;
- cracking and tilting of supporting walls;
- cracking of partition walls;
- falling of plaster;
- damage to connections between walls;
- damage to columns;
- partial destruction of masonry and brick lintels;
- failure of chimneys;
- disintegration of the structural unity of the buildings;
- collapse of semi-independent parts of buildings;
- collapse of parapets;
- loss of decorative façade elements, such as mouldings, cornices, stucco decoration elements, wooden open-work decoration details, metalwork elements, *etc.*;
- damage to roofs (e.g. shift of prefabricated roof slabs);
- collapse of cantilever eaves.

Examples for some of the kinds of damage listed above are shown in Figure A4.10.25 through Figure A4.10.27.



Figure A4.10.25. Damage to columns. Inst. of Mathematics (a); residential building in Kostava str. (b). From Gabrichidze *et al.* (2004).

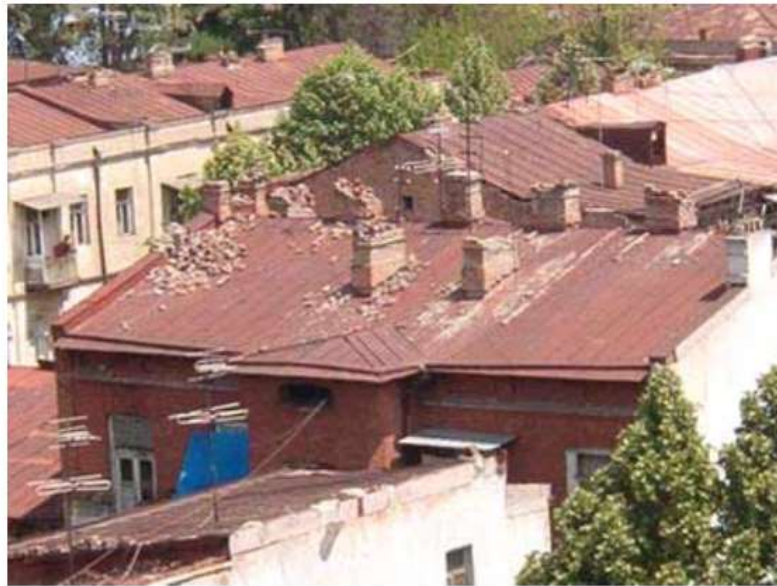


Figure A4.10.26. Damaged chimneys in Chugureti District. From Gabrichidze *et al.* (2004).

According to Gabrichidze *et al.* (2004), the Ministry of Urbanization and Construction of Georgia inspected more than 16,000 buildings after the earthquake and collected statistical information on their damage levels. Their findings, as reported by Gabrichidze *et al.* (2004), are presented below. It is noted that a report from ReliefWeb (2002c) mentions a larger number of buildings being assessed in Tbilisi. However, as Gabrichidze *et al.* (2004) provide the most comprehensive statistics, their numbers are reported in what follows.

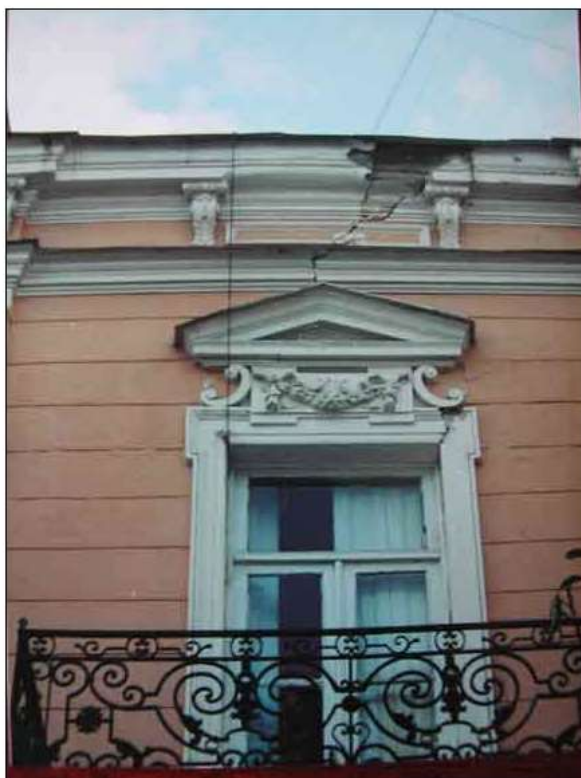


Figure A4.10.27. Damaged parapet of a residential house in Sololaki quarter (left) and Ikorta church of the Archangel after the earthquake (right). From ICOMOS (2002/03)

As shown in Table A4.10.12 and Figure A4.10.28, the number of inspected apartment buildings was around 15,500, of which around 73% suffered between moderate and heavy damage, and 25% presented only negligible to slight damage. Gabrichidze *et al.* (2004) report that, according to experts' opinions, more than 75,000 and 1,200 people lived in buildings that suffered MSK-64 damage grades 3 and 4, respectively.

Table A4.10.12. Number of residential buildings in different Tbilisi districts per MSK-64 damage grade. From Gabrichidze *et al.* (2004).

District	Damage Grade				
	1	2	3	4	5
1, 2. Gldani-Nadzaladevi	1934	2779	1936	63	-
9, 3. Didube-Chugureti	692	1536	1022	15	-
4, 5. Isani-Samgori	863	1102	851	12	-
6, 7. Krtsanisi-Mtatsminda	273	933	775	17	-
8, 10. Vake-Saburtalo	221	370	112	-	-
Total	3983	6720	4696	107	-

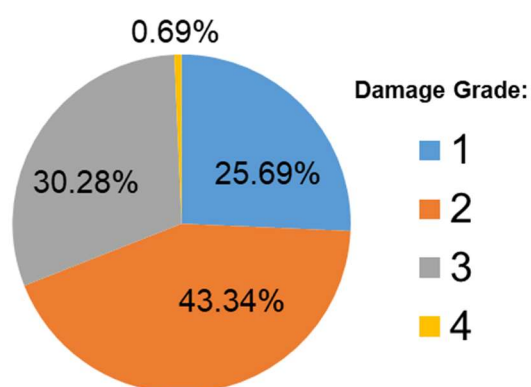


Figure A4.10.28. Percentage of residential buildings in Tbilisi (all districts included) per MSK-64 damage grade. 15,506 buildings in total. Data from Gabrichidze *et al.* (2004).

Around 530 public buildings including schools, kindergartens, higher education institutions, hospitals and clinics were assessed as well, of which 21% presented damage of grade 3 and 4. Other unspecified types of public buildings were also assessed (740 of them), of which 29% suffered damage grade 1, 45% damage grade 2 and 25% damage grade 3 (Gabrichidze *et al.*, 2004). At least five public buildings of cultural and historic significance and many administrative buildings were damaged (ReliefWeb, 2002b, 2002c).

All schools in Tbilisi (202) were inspected by teams of engineers. Large part of vulnerability class B schools suffered second grade damage, while most vulnerability class C schools suffered first grade damage. Statistical data on damage to school buildings is shown in Figure A4.10.29 (left) for 202 buildings (Gabrichidze *et al.*, 2004).

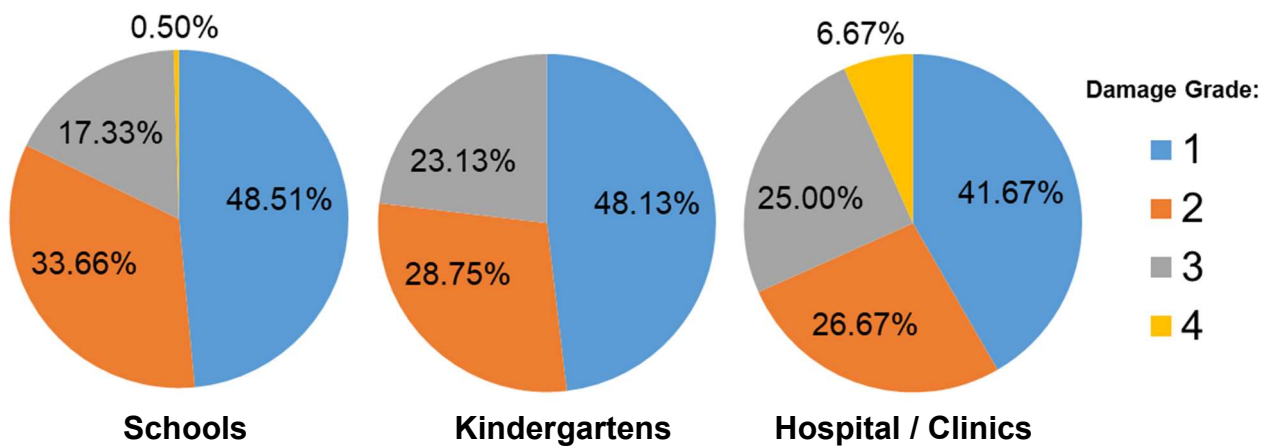


Figure A4.10.29. Percentage of school (left), kindergarten (centre) and hospital/clinic (right) buildings in Tbilisi (all districts included) per MSK-64 damage grade. Total of buildings: 202 (left), 160 (centre), 120 (right). Generated from data from Gabrichidze *et al.* (2004).

Many of the 160 assessed kindergartens were placed in residential, low-rise brick houses. Damage to infill walls (between columns and walls) was observed in some of the newly-constructed RC frames. Figure A4.10.29 (centre) shows the corresponding statistical data (Gabrichidze *et al.*, 2004).

The number of assessed hospitals and clinics was 120. At least nine hospitals suffered considerable damage (ReliefWeb, 2002b; 2002d). According to ReliefWeb (2002c), 76 healthcare-related buildings needed urgent repairs. The percentage of hospital and clinic buildings per damage grade, as reported by Gabrichidze *et al.* (2004), can be seen in Figure A4.10.29 (right).

Based on the information from a report from October 2002 (ReliefWeb, 2002c), 26 churches were assessed and some of them were found to be in a need of urgent repair. An example of a church that was heavily damaged by the earthquake and repaired afterwards is given in Figure A4.10.27 (right).

Many monuments of three graveyards in central Tbilisi were damaged, as exemplified in Figure A4.10.30 (Varazanashvili *et al.*, 2008; Gabrichidze *et al.*, 2004).



Figure A4.10.30. Shifted and overturned monuments in graveyards. From Gabrichidze *et al.* (2004).

Based on the preliminary results of a field survey, the Ministry of Urbanization and Construction of Georgia estimated that as many as 20% of dwellings had sustained either major or complete damage, corresponding to damage grade III on the three-grade scale described in section A4.10.8.1 (ReliefWeb, 2002b). These results indicate a much higher share of dwellings associated with the most-severe damage state, compared to that reported by Gabrichidze *et al.* (2004) (see Figure A4.10.28 and Table A4.10.12). Such discrepancy is understood considering that the initially estimated 20% were based on the incomplete information gathered in a first few days after the earthquake, when the assessed buildings were most probably those in the worst damage state.

Two water mains were damaged, and there was an electricity cut in some parts of the city after the earthquake. Mobile and landline phones were out of function for some hours following the main shock, but most probably due to overloading (ReliefWeb, 2002b).

In view of the comments found regarding how long it took for statistics on damage to be collected, it is likely that these contain the consequences not only from the main shock but also from the aftershocks that followed. According to Javakhishvili *et al.* (2004), large part of the old, low-rise brick/stone buildings suffered from additional damage caused by the aftershocks. Qualitative description of the extent of such aftershock-induced damage is not available but, considering that the magnitudes of aftershocks seem to have been relatively small, it is believed that most of the damage described within this section was possibly caused by the main shock.

In addition to aftershocks, continuous heavy rains during the following summer and snowfalls in the winter have also aggravated the condition of the damaged structures. Many foundations were weakened and existing cracks in the roofs and walls were widened (ICOMOS, 2002/03; ReliefWeb, 2002e).

Final numbers of damaged buildings are not clear from the available literature. Gabrichidze *et al.* (2004), who report on statistics for 15,506 residential buildings and 530 public buildings (16,036 total, a sub-set of, at least, 44,981 buildings), state that, even at the time of their writing, thousands of buildings had still not been inspected. This total number of buildings is similar to the 15,418 cases (13,099 extensively damaged plus 2,319 fully or partially destroyed buildings) reported by ReliefWeb (2002e) by the end of 2002, eight months after the earthquake. However, a later publication by Varazanashvili *et al.* (2008) states that around 40% of the building stock was damaged and indicates “around 50,000 buildings” in parenthesis, which can be interpreted as 50,000 buildings being the 40% of the total (which would then be 125,000). It is, of course, suspicious that the number reported in parenthesis is relatively close to 44,981, the building stock set for which Gabrichidze *et al.* (2004) presents a classification per typology (Table A4.10.11). Interpretation of these sources is rendered difficult by the fact that none of them specifies the exact extent of the area under study and only say “Tbilisi”, but its administrative boundaries have been modified in time (e.g., Salukvadze & Golubchikov, 2016). Following the numbers reported by Gabrichidze *et al.* (2004), 64.4% of the buildings suffered no damage or were not assessed, 0.3% suffered MSK damage grade (DG)1, 10.7% DG2, 15.3% DG3 and 9.3% DG4. Interpreting the 50,000

buildings as the 40% of the building stock from Varazanashvili *et al.* (2008) leads to 60.0% undamaged buildings, 9.6% with DG1, 19.2% with DG2 and 10.8% with DG3. These proportions are different from the aforementioned ones, albeit not substantially.

A4.10.8.3 Observed weaknesses

As explained in previous sections, a large proportion of the buildings in Tbilisi were systematically lacking proper level of maintenance and/or proper seismic design. Undoubtedly, this had a significant influence on the extent of the consequences of the 2002 earthquake.

According to Gabrichidze *et al.* (2004), old school buildings affected by this earthquake were characterized by a series of structural defects that negatively influenced their behaviour during the shaking. Large distance between capital transverse walls, high massive parapets, massive plaster in upper part of the walls and on the ceilings are some of the observed structural defects in such buildings. Some of the damaged kindergartens had infill walls constructed of silicate white brick, which is known to have low cohesion with mortar.

Damage observed in some of the reinforced-concrete buildings appeared to be directly related to the use of low-quality materials and the presence of design errors (Gabrichidze *et al.*, 2004).

A4.10.8.4 Damage distribution

The damage induced by the earthquake was mostly concentrated in the old part of the city (*i.e.* the Tbilisi Historic District), which encompasses Nadzaladevi-Gldani, Mtatsminda-Krtsanisi and Didube-Chugureti districts (districts 1, 2, 3, 6, 7, and 9 in Figure A4.10.10). This could be explained by its proximity to the epicentre, but mostly by the fact that a considerable part of the buildings in the Old Tbilisi consisted of low-rise brick and stone buildings that were particularly vulnerable to the high-frequency content of this earthquake (Gabrichidze *et al.*, 2004; Javakhishvili *et al.*, 2004; ReliefWeb, 2002b).

Gabrichidze *et al.* (2004) and Rekvava & Mdivani (2012) pointed out the influence of local site amplification effects on the consequences of this earthquake, though they did not directly link it to the spatial distribution of damage. Being the damage so extensive and the availability of information only in terms of broader districts and not at a sufficiently detailed scale, it is difficult to point at an obvious connection between the latter and the natural vibration periods of the soil columns calculated by Gabrichidze *et al.* (2004) and described in Section A4.10.3.2, or the soil types depicted in Figure A4.10.8. It is possible, however, to observe certain points in common between the maps depicted in Figure A4.10.10 and Figure A4.10.16, reproduced below as Figure A4.10.31 for clarity. From Table A4.10.11 it can be inferred that a large proportion of the buildings located in the most severely affected districts were 1-3 storey brick masonry structures, and that the spectral acceleration at an oscillator period of 0.3 seconds (Figure A4.10.16) can represent, at least in part, the kind of demands to which the latter were subject. As shown by the red polygons in Figure A4.10.31, peaks of large spectral demands can be observed at some of the areas marked as severely affected.

The red polygon also coincides with the alluvial quaternary deposits along both banks of the Mtkvari river depicted in Figure A4.10.7.

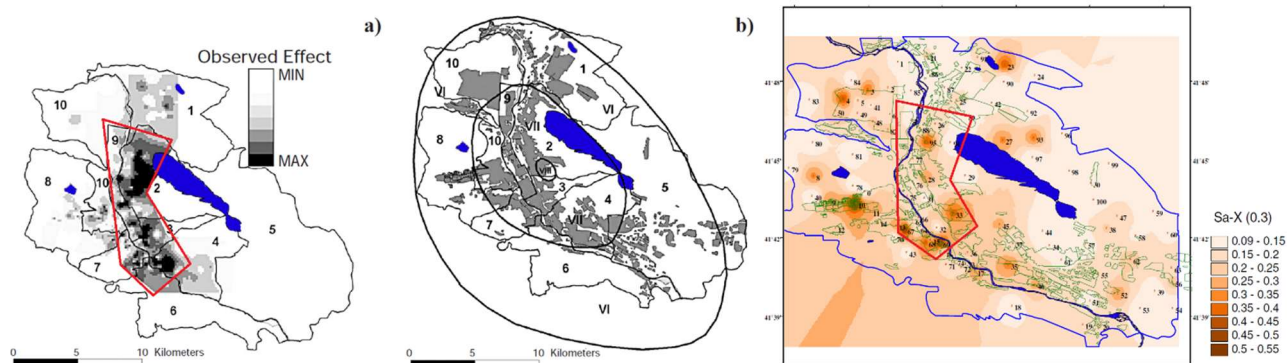


Figure A4.10.31. Relation between most damaged areas (left) and the spectral acceleration at $T=0.3$ s estimated through one-dimensional equivalent linear site-response analysis (right). Modified from Javakhishvili *et al.* (2004, left) and Gabrichidze *et al.* (2004, right).

A4.10.9 Casualties and losses

A4.10.9.1 Numbers of dead and injured

The number of reported deaths is different depending on the author and varies from 5 to over 8. USGS PAGER-CAT database (Allen *et al.*, 2009) and Javakahsvili *et al.* (2004) reported five deaths, while the International Disaster Database (EM-DAT), ReliefWeb (2002a, 2002b, 2002e) and ICOMOS (2002/03) report six people killed by the earthquake instead. Seven fatalities were reported by Gabrichidze *et al.* (2004) and Varazanashvili *et al.* (2008), while according to Godoladze *et al.* (2005) and Gamkrelidze *et al.* (2008) this number was more than eight.

The number of reported injuries varies as well. According to Gabrichidze *et al.* (2004), 30 people were injured as a consequence of this earthquake, which is lower than the 52 people reported by the USGS PAGER-CAT database (Allen *et al.*, 2009) and ReliefWeb (2002d). The EM-DAT database and ReliefWeb (2002a, 2002b) report 70 injuries, while the latter also reports about additional 200 people being identified with post-traumatic stress disorder.

EM-DAT website reports 19,156 persons affected by the earthquake, of which 1,086 were left homeless. According to Varazanashvili *et al.* (2008), the number of homeless people was 2,446. However, it is pointed out by Javakhishvili *et al.* (2004) that aftershocks caused additional damage to many old buildings and this resulted in as much as 69,000 homeless people from over 18,000 households. The observed discrepancy in the reported numbers of affected people also stems from the fact that consequences of the earthquake were felt long after its occurrence. Rainfall and snowfall, which followed in the months after the earthquake, caused additional damage to the buildings, leaving thousands of people without proper heating in the winter days. Many stayed in their unsafe homes, while those who were provided with temporary accommodation endured rather poor living conditions. While no official data appears to exist, some people affected by the earthquake claim that dozens of

deaths indirectly linked to the earthquake have occurred, referring to heart attacks, post-trauma and shock, angina pectoris, *etc.* (ReliefWeb, 2002e).

A4.10.9.2 Causes of casualties

According to ReliefWeb (2002a, 2002b) who reported causes of casualties for six people, three persons died from falling debris, one due to heavy injuries, and two from heart attacks. A witness reported to the Reuters news agency that her 18-year-old son and a young woman died while leaving the ground floor shop of a Soviet-style apartment block, due to the collapse of the roof (BBC, 2002).

A4.10.9.3 Estimates of economic losses

Gabrichidze *et al.* (2004) and Varazanashvili *et al.* (2008) report that the direct economic losses as a consequence of the earthquake exceeded 180 million USD. According to the former author, public buildings including educational institutions, hospitals, clinics and kindergartens suffered significant material losses amounting to more than 15 million USD. Approximately 8 million USD were the total material losses due to damage inspected in 202 school buildings, while the 160 investigated kindergartens were associated with total losses of 3.5 million USD (Gabrichidze *et al.*, 2004).

The International Disaster Database (EM-DAT) reports total losses as high as 350 million USD.

After the earthquake, the Extraordinary Committee for Resolving Disaster Results was formed and the Tbilisi Revival Foundation was established for the gathering of funds for emergency response to the earthquake (ICOMOS, 2002/03). An appeal to the international community was made for 525,854 USD for relief needs and 52.04 million USD for emergency rehabilitation actions. It was estimated that this amount of money would allow for the assistance of homeless families during the first six months, and for the repair, demolishing and reconstruction of the most severely damaged properties. However, the estimated cost for the full rehabilitation of damaged buildings was around 156.9 million USD in May 2002 (ReliefWeb, 2002b). Help was received from some domestic and international donors, and efforts were made to overcome the consequences of the earthquake and assist people. However, due to the absence of a disaster and risk preparedness plan, there was no proper coordination of actions of the state and private structures (ReliefWeb, 2002f; ICOMOS, 2002/03) and, even one year after the earthquake struck, many of the people were still without shelter and thousands of buildings were still unrepaired (Gabrichidze *et al.*, 2004). Many of the houses that could have been successfully repaired right after the earthquake were damaged beyond repair with the course of time, under the influence of aftershocks, rainfalls and snowfalls, as repairs were delayed. This resulted in higher economic losses than estimated at the beginning (ReliefWeb, 2002e).

A4.10.10 Discussion and conclusions

This **M**4.8 earthquake occurred on 25th April 2002, at 17:41 UTC (22:41 local time). The earthquake was of moderate magnitude but caused macroseismic effects as high as VII on the MSK-64 scale. The resulting extensive damage can be explained by the shallowness of the earthquake epicentre, the frequency content of the ground motion, amplified ground response due to local site effects, and the low quality of construction and maintenance of the exposed building stock. While around 64.4% of the buildings either suffered no damage or were not assessed, 0.3% suffered MSK damage grade (DG)1, 10.7% DG2, 15.3% DG3 and 9.3% DG4.

The horizontal acceleration recorded at a station located at approximately 6 km from the epicentre had a peak value of 0.11 g, and dominant frequencies of around 5 Hz, quite close to those of the low-rise brick and stone buildings located mostly in the old part of the city, which were the most severely damaged. Many of these buildings were already in poor condition prior to the earthquake, mostly because of bad construction practices, lack of maintenance and subsidence problems, and were further damaged by aftershocks and rainfalls.

While estimates of casualties vary, the most reliable sources suggest that six people died and 70 people were physically injured during the earthquake. Many more suffered from post-traumatic stress symptoms and were subject to poor living conditions afterwards, as thousands of households were left without their homes and many stayed in dwellings that were considered dangerous and unsafe. Due to lack of funds and the absence of a disaster preparedness plan and necessary normative documents to make the available help be directed to those who needed it, the earthquake resulted in a prolonged difficult social and economic situation in the country.

A4.10.11 References

A4.10.11.1 Bibliography

Adamia, S., A. Chabukiani, S. Kuloshvili & G. Maisuradze (2005). *Elicitation of alternative seismic sources interpretations and characterization*. ISTC CauSin Project CA-651, Final Report.

Adeishvili, M., T. Chachua, T. Gugushvili, Z. Jincharadze, E. Kakabadze & M. Sharabidze (2011). *GEO-Cities Tbilisi: An integrated environmental assessment of state and trends for Georgia's capital city*. Organization for Security and Co-operation in Europe (OSCE), United Nations Environment Programme (UNEP), and Environment and Security Initiative (ENVSEC). Available online at: <http://wedocs.unep.org/handle/20.500.11822/8796>. Last accessed: 7th December 2018.

Afshari, K. & J.P. Stewart (2016). Physically parameterized prediction equations for significant duration in active crustal regions. *Earthquake Spectra* **32**(4), 2057-2081.

Akhalbedashvili, A., K. Odishvili & V. Papalashvili (2004). *Tbilisi earthquake of 2002*. Publication of the Institute of Geophysics, Tbilisi, Georgia.

- Akkar, S., M.A. Sandikkaya, M. Senyurt, A.A. Sisi, B. Ö. Ay, P. Traversa, J. Douglas, F. Cotton, L. Luzi, B. Hernandez & S. Godey (2014). Reference database for seismic ground-motion in Europe (RESORCE). *Bulletin of Earthquake Engineering* **12**(1), 311–339.
- Allen, M., J. Jackson & R. Walker (2004) Late Cenozoic reorganization of the Arabia-Eurasia collision and the comparison of short-term and long-term deformation rates. *Tectonics* **23**(2), 1–16.
- Allen, T.I., D.J. Wald, P.S. Earle, K.D. Marano, A.J. Hotovec, K. Lin & M.G. Hearne (2009). An Atlas of ShakeMaps and population exposure catalog for earthquake loss modeling. *Bulletin of Earthquake Engineering* **7**(3), 701-718.
- Armaghani, B. (2011). *Georgian building codes assessment*. United States Agency for International Development (USAID), LEED AP, LEED Faculty, Global Sustainable Solution, L.L.C., Florida, USA. Available online at: http://pdf.usaid.gov/pdf_docs/pnadz453.pdf. Last accessed: 30th October 2017.
- Balassanian, S., T. Ashirov, T. Chelidze, A. Gassanov, N. Kondorskaya, G. Molchan, B. Pustovitenko, V.G. Trifonov, V.I. Ulomov, D. Giardini, M. Erdik, M. Ghafory-Ashtiany, G. Grünthal, D. Mayer-Rosa, V. Schenk & M. Stucchi (1999). Seismic hazard assessment for the Caucasus test area. *Annali di Geofisica* **42**(6), 1139-1151.
- Bardzimishvili, D. (1976). Hydrogeological conditions of Middle Eocene water-oil-bearing complex of Tbilisi environs (eastern part of Adjara-Trialeti zone) (In Russian). *Proceedings of VNIGNI, Georgian Department* **205**, 67–76.
- Bommer, J.J., P.J. Stafford & J.E. Alarcón (2009). Empirical equations for the prediction of the significant, bracketed, and uniform duration of earthquake ground motion. *Bulletin of the Seismological Society of America* **99**(6), 3217–3233.
- BSSC (Building Seismic Safety Council). (1997). *NEHRP recommended provisions for seismic regulations for new buildings. Part 1 – Provisions*. Washington D.C., USA.
- CEN (2004). *Eurocode 8: Design of structures for earthquake resistance - Part1: General rules, seismic actions and rules for buildings*. European Committee for Standardization, Brussels, Belgium.
- Center for International Earth Science Information Network - CIESIN - Columbia University (2016). Gridded Population of the World, Version 4 (GPWv4). Palisades, NY: NASA Socioeconomic Data and Applications Center. <http://dx.doi.org/10.7927/H4NP22DQ>
- Chelidze, T., Z. Javakhishvili, O. Varazanashvili, M. Elashvili, Y. Kolesnikov, T. Godoladze, N. Butikashvili & E. Ghlonti (2002). Seismic hazard assessment of Georgia (probabilistic approach). *Journal of Georgian Geophysical Society*. Available online at (last accessed 25th October 2017): http://drm.cenn.org/Hazard_assessment_files/eng/Seismic_hazard_assessment_of_Georgia.pdf
- Cisternas, A. & H. Philip (1997). Seismotectonics of the Mediterranean region and the Caucasus. In Giardini, D. & S. Balassanian (eds.): *Historical and prehistorical earthquakes in the Caucasus*. Kluwer Academic Publisher, the Netherlands.
- DeMets, C., R.G. Gordon, D.F. Argus & S. Stein (1990). Current plate motions. *Geophysical Journal International* **101**, 425–478.
- Gabrishidze, G., G. Lomidze, T. Mukhadze, A. Odisharia & I. Timchenko (2004). April 2002 epicentral earthquake in Tbilisi, Georgia. *Proceedings of the 13th World Conference on Earthquake Engineering*, August 1-6, Vancouver, B.C., Canada. Available online at (last accessed 30th October 2017): http://www.iitk.ac.in/nicee/wcee/article/13_1063.pdf

- Galloway, D. & B. Simpson (2003). A summary of earthquakes in 2002. *The Society for Earthquakes and Civil Engineering Dynamics (SECED) Newsletter* **17**(1), 1-8. Available online at: <https://www.seced.org.uk/images/newsletters/Newsletter%20vol%2017%20no%201.pdf>. Last accessed: 20th October 2017.
- Gamkrelidze, I., T. Giorgobiani, S. Kuloshvili, G. Lobjanidze & G. Shengelaia (1998). Active deep faults map and the catalogue for the territory of Georgia. *Bulletin of the Georgian Academy of Sciences* **157**, 80–85.
- Gamkrelidze, I., E. Nikolaeva, T. Godoladze & M. Elashvili (2008). *Tbilisi fault and seismic activity of Tbilisi Environs (Georgia)*. Proceedings of the A. Djanelidze Institute of Geology, Georgia.
- Gerkeuli, N. (2009). *Report on national urban policy in Georgia*. Draft report, Institute for European Studies, TSU, Tbilisi, Georgia. Available online at (last accessed 30th October 2017): http://webcache.googleusercontent.com/search?q=cache:fiAebelwkR8J:www.nispa.org/files/conferences/2009/papers/200906301514590.Gerkeuli_NATIONAL%2520URBAN%2520POLICY%2520N%2520GEORGIA.doc+&cd=1&hl=en&ct=clnk&gl=it&client=opera
- Giardini, D., G. Grünthal, K.M. Shedlock & P. Zhang (1999). The GSHAP global seismic hazard map. *Annali di Geofisica* **42**(6), 1225–1228.
- Godoladze, T.G., L. Hutchings, B. Foxal & Z. Javakhishvili (2005). Structural model of seismic hazard analysis of Tbilisi, Republic of Georgia. *Journal of the Georgian Geophysical Society* **10**(A), 77-82.
- Gotsadze, O., O. Varazanashvili & N. Butikashvili, (1990). *Seismic hazard assessment of Tbilisi* (in Russian). Report, Institute of Geophysics, Tbilisi, Georgia.
- Grünthal, G. (ed.) (1998). European Macroseismic Scale 1998 (EMS-1998). Cahiers du Centre Europeen de Geodynamique et de Seismologie 15, Centre Europeen de Geodynamique et de Seismologie, Luxembourg. Available online at (last accessed 30th October 2017): http://www.franceseisme.fr/EMS98_Original_english.pdf.
- Hejazi, M. (2008). The risks to cultural heritage in western and central Asia. *Journal of Asian Architecture and Building Engineering*, 239–245.
- Jaiswal, K.S. & D.J. Wald (2008). *Creating a global building inventory for earthquake loss assessment and risk management*. U.S. Geological Survey, Open-File Report 2008-1160. Available online at: <https://pubs.usgs.gov/of/2008/1160/>. Last accessed: 7th July 2017.
- Javakhishvili, Z., T. Godoladze, M. Elashvili, T. Mukhadze & I. Timchenko (2004). The Tbilisi earthquake of April 25, 2002 in the context of the seismic hazard of the Tbilisi urban area. *Bollettino di Geofisica Teorica ed Applicata* **45**(3), 169–185.
- Jimsheladze, T., N. Kapanadze & G. Melikadze (2008). Microtemperature observation in Tbilisi seismoactive region. *Journal of Georgian Geophysical Society* **12**(A), 75–80.
- Karakhanian, A.S., V.G. Trifonov, H. Philip, A. Avagyan, K. Hessami, F. Jamali, M.S. Bayraktutan, H. Bagdassarian, S. Arakelian, V. Davtian & A. Adilkhanyan (2004). Active faulting and natural hazards in Armenia, eastern Turkey and northwestern Iran. *Tectonophysics* **380**(3–4), 189–219.
- Medvedev, S., W. Sponheuer & V. Karnik (1965). *Seismic intensity scale, MSK 1964*. Academy of Sciences of the U.S.S.R., Soviet Geophysical Community, 13 pp.
- Mkrtychev, O. & G. Dzinchvelashvili (2016). Fundamental principles of earthquake resistance calculation to be reflected in the next generation regulations. *MATEC Web of Conferences* **86**: 5th International Conference “Integration, Partnership and Innovation in Construction Science and Education”, November 16-17, Moscow, Russia. Available online at: <https://www.matec->

- conferences.org/articles/mateconf/pdf/2016/49/mateconf_ipicse2016_01017.pdf. Last accessed: 30th October 2017.
- Palus, K. & J. Zabawa-Krzywicka (2014). Architecture of Tbilisi - on the borderline of two worlds. Part I. *Architecture Civil Engineering Environment (ACEE) Journal* **7**(4), 11–20.
- Philip, H., A. Cisternas, A. Gvishiani & A. Gorshkov (1989). The Caucasus: an actual example of the initial stages of continental collision. *Tectonophysics* **161**(1-2), 1–21.
- PN 01.01-09 (2009). *Building code: earthquake engineering. Construction norms and rules – “seismic resistant construction”*. Georgian Ministry of Economic Development, Tbilisi, Georgia. Available online at: <https://www.matsne.gov.ge/ka/document/view/86596> (in Georgian); http://iisee.kenken.go.jp/worldlist/66_Georgia/66_Georgia_Code.pdf (in English, without Annex 1). Last accessed: 17th October 2017.
- Rastsvetaev, L. (1989). Shifts and Alpine geodynamics in the Caucasus region. In Belov, A. & A. Satian (eds.): *The Caucasus geodynamics*. Nauka Publication House, Moscow, Russia.
- Rekvava, P. & K. Mdivani (2012). Modeling of ground motions for Tbilisi region with site effects. *Proceedings of the 7th International Conference on Material Technologies and Modeling (MMT)*, August 20-23, Ariel, Israel. Available online at: <https://www.ariel.ac.il/sites/conf/mmt/mmt-2012/Service%20files/papers/4-42-52.pdf>. Last accessed: 30th October 2017.
- Riznichenko, Y. (1985). *Problems of seismology*. Selected Papers, Nauka Publication House, Moscow, Russia.
- Salukvadze, J. & D. Gogishvili (2009). On the geography and typology of building construction in Tbilisi: before and after the crisis. *Proceedings of the 3rd International Workshop on Post-Communist Urban Geographies: Actors Shaping Urban Change*, September 17-19, Tartu, Estonia. Draft version available online at (last accessed 30th October 2017): http://webcache.googleusercontent.com/search?q=cache:QMP7APIIfH0J:www.ut.ee/sites/default/files/ut_files/B4_Salukvadze_Gogishvili.doc+&cd=1&hl=en&ct=clnk&gl=it&client=opera
- Salukvadze, J. & O. Golubchikov (2016). City as a geopolitics: Tbilisi, Georgia—A globalizing metropolis in a turbulent region. *Cities* **52**, 39-54.
- Seismosoft (2016). SeismoSignal - A computer programme for signal processing of strong-motion data.
- Shebalin, N. (1997). *Strong earthquakes*. Selected Papers, Academy of Mining Sciences, Moscow, Russia.
- Shengelia, I., Z. Javakhishvili & N. Jorjashvili (2011). Coda wave attenuation for three regions of Georgia (Sakartvelo) using local earthquakes. *Bulletin of Seismological Society of America* **101**(5), 2220–2230.
- Slejško, D., Z. Javakhishvili, A. Rebez, M. Santulin, M. Elashvili, P. L. Bragato, T. Godoladze & J. Garcia (2008). Seismic hazard assessment for the Tbilisi test area (eastern Georgia). *Bollettino di Geofisica Teorica ed Applicata* **49**(1), 37–57.
- Smit, P., V. Arzoumanian, Z. Javakhishvili, S. Arefiev, D. Mayer-Rosa, S. Balassanian & T. Chelidze (2000). The digital accelerograph network in the Caucasus. In Balassanian S., A. Cisternas & M. Melkumyan (eds.): *Earthquake hazard and seismic risk reduction. Advances in natural and technological hazards research*. Springer, Dordrecht, the Netherlands.
- SNiP-II-7-81 (1982). *Строительство в сейсмических районах. Нормы проектирования (Design standards and regulations for construction in seismic regions, in Russian)*. The State

- Committee for construction of the Council of Ministers of the U.S.S.R., Stroyizdat, Moscow. Available at (last accessed 28th September 2017): http://www.stroyventmash.ru/download/SNiP_II-7-81.pdf
- Trifonov, V.G., G.A. Vostrikov, R.V. Trifonov, A.S. Karakhanian & O.V. Soboleva (1999). Recent geodynamic characteristics in the Arabian-Eurasian and Indian-Eurasian collision region by active fault data. *Tectonophysics* **308**(1-2), 119–131.
- Tsereteli, N., V. Arabidze, O. Varazansahvili, T. Gugeshashvili, T. Mukhadze & A. Gventcadze (2014a). Vulnerability analysis and GIS based seismic risk assessment Georgia case. In Teodorescu H. N., A. Kirschenbaum, S. Cojocaru & C. Bruderlein (eds.): *Improving Disaster Resilience and Mitigation - IT Means Tools*. NATO Science for Peace Security Series C: Environmental Security, Springer, Dordrecht, the Netherlands.
- Tsereteli, N., V. Alania, O. Varazanashvili, V. Arabidze, N. Arevadze, T. Gugeshashvili & E. Tsereteli (2014b). The earthquake loss scenario for the city of Tbilisi. *Proceedings of the 2nd European Conference on Earthquake Engineering and Seismology*, August 25-29, Istanbul, Turkey.
- Ulomov, V. I. (1999). Seismic hazard of Northern Eurasia. *Annali di Geofisica* **42**(6), 1023–1038.
- United Nations, ed. (2004). *Human Development Report 2004 – Cultural liberty in today's diverse world*. Report of the United Nations Development Programme (UNDP), New York, United States.
- United Nations, ed. (2016). *Human Development Report 2016 – Human Development for Everyone*. Report of the United Nations Development Programme (UNDP), New York, United States.
- Varazanashvili, O., N. Tsereteli, S. Adamia, N. Butikashvili & T. Mukhadze (2008). Seismotectonic features of the April 25, 2002 Tbilisi, Georgia earthquake (Ms=4.6). *Journal of the Georgian Geophysical Society* **12**(A), 33–45.
- Varazanashvili, O., N. Tsereteli, A. Amiranashvili, E. Tsereteli, E. Elizbarashvili, J. Dolidze, L. Qaldani, M. Saluqvadze, S. Adamia, N. Arevadze & A. Gventcadze (2012). Vulnerability, hazards and multiple risk assessment for Georgia. *Natural Hazards* **64**(3), 2021–2056.
- Wald, D.J. & T.I. Allen (2007). Topographic slope as a proxy for seismic site conditions and amplification. *Bulletin of the Seismological Society of America* **97**, 1379–1395. Slope-based online map viewer available at: <http://usgs.maps.arcgis.com/apps/webappviewer/index.html?id=8ac19bc334f747e486550f32837578e1>. Data used herein downloaded from deprecated version last accessed on 25th June 2017.
- Weatherill, G. A., M. Pagani & J. Garcia (2016). Exploring earthquake databases for the creation of magnitude-homogeneous catalogues: tools for application on a regional and global scale. *Geophysical Journal International* **206**(3), 1652–1676.
- Wells, D. L. & K. J. Coppersmith (1994). New empirical relationships among magnitude, rupture length, rupture width, rupture area, and surface displacement. *Bulletin of the Seismological Society of America* **84**(4), 974–1002.
- Woessner, J., D. Giardini, H. Crowley, F. Cotton, G. Grünthal, G. Valensise, R. Arvidsson, R. Basili, M. B. Demircioglu, S. Hiemer, C. Meletti, R. W. Musson, A. N. Rovida, K. Sesetyan, M. Stucchi & The SHARE Consortium (2015). The 2013 European Seismic Hazard Model: Key Components and Results. *Bulletin of Earthquake Engineering* **13**(12), 3553–3596. Online data source: <http://www.efehr.org/en/home/>. Last accessed: 30th October 2017.
- Worden, C.B., E.M. Thompson, M. Hearne & D.J. Wald (2017). *ShakeMap V4 Manual: technical manual, user's guide, and software guide*. United States Geological Survey. Available online at: <http://usgs.github.io/shakemap/>.

Zare, M., H. Amini, P. Yazdi, K. Sesetyan, M.B. Demircioglu, D. Kalafat, M. Erdik, D. Giardini, M.A. Khan & N. Tsereteli (2014). Recent developments of the Middle East catalog. *Journal of Seismology* **18**, 749-772.

Zhao, J. X., J. Zhang, A. Asano, Y. Ohno, T. Oouchi, T. Takahashi, H. Ogawa, K. Irikura, H.K. Thio, P.G. Somerville & Y. Fukushima (2006). Attenuation relations of strong ground motion in Japan using site classification based on predominant period. *Bulletin of the Seismological Society of America* **96**(3), 712-732.

A4.10.11.2 Web references

BBC (2002): <http://news.bbc.co.uk/2/hi/europe/1951886.stm>. Last accessed: 25th June 2017.

Central Intelligence Agency (CIA): <https://www.cia.gov/index.html>

CIA (2017): The World Factbook (Georgia) (last accessed 25th June 2017):
<https://www.cia.gov/library/publications/the-world-factbook/geos/gg.html>

EM-DAT – The Emergency Events Database (Université Catholique de Louvain, Brussels, Belgium; Cred. Prof. Dr. D. Guha-Sapir): <http://www.emdat.be/>. Last accessed: 4th April 2018.

European-Mediterranean Seismological Centre (EMSC):
<https://www.emsc-csem.org/#2>

Geoportal of Natural Hazards and Risks in Georgia: <http://drm.cenn.org/index.php/en/>
Atlas of Natural Hazards & Risks of Georgia (2012) (last accessed 25th June 2017):
<http://drm.cenn.org/index.php/en/background-information/paper-atlas>

International Atomic Energy Agency (IAEA): <https://www.iaea.org>
IAEA (2002): 46th IAEA General Conference (2002) Documents (last accessed 25th June 2017):
<https://www.iaea.org/About/Policy/GC/GC46/Documents/>

International Council on Monuments and Sites (ICOMOS): <http://www.icomos.org/en/>
ICOMOS (2001/02): ICOMOS Report Georgia 2001/02 (last accessed 25th June 2017):
<http://www.icomos.org/risk/2001/geor2001.htm>
ICOMOS (2002/03): ICOMOS Report Georgia 2002/03 (last accessed 25th June 2017):
<http://www.icomos.org/risk/2002/georgia2002.htm>

International Monetary Fund (IMF): <http://www.imf.org/external/index.htm>
IMF (2006): Press Release: Statement by IMF Staff Mission to Georgia (last accessed 25th June 2017): <http://www.imf.org/en/News/Articles/2015/09/14/01/49/pr06276>

International Science and Technology Centre (ISTC): <http://www.istc.int>
ISTC (2003): Earthquake Resistant Reinforced Concrete Structures (last accessed 25th June 2017):
<http://www.istc.int/en/project/74C045D2D2AC700EC3256D0A0040FD33/>

International Seismological Centre (ISC): <http://www.isc.ac.uk/>

M. Nodia Institute of Geophysics, Georgian Academy of Sciences:
Main website: http://ig-geophysics.ge/index_eng.html
Earthquake Catalogue of Georgia 1250BC-2014: <http://ig-geophysics.ge/sector1-eng.html>. Last accessed 26th September 2017.

National Statistics Office for Georgia: <http://www.geostat.ge/>
GeoStat (2017a): Unemployment Rate (last accessed 25th June 2017):
http://www.geostat.ge/index.php?action=page&p_id=146&lang=eng
GeoStat (2017b): General Population Census (2002) (last accessed 25th June 2017):
http://www.geostat.ge/index.php?action=page&p_id=674&lang=eng

ReliefWeb: UN digital service providing info to humanitarian relief organizations: <http://reliefweb.int>
ReliefWeb (2002a): OCHA-Georgia Information Bulletin for the period 21-30 Apr 2002 (last accessed 25th June 2017): <http://reliefweb.int/report/georgia/ocha-georgia-information-bulletin-period-21-30-apr-2002>

ReliefWeb (2002b): Earthquake in Georgia: Appeal for emergency relief and rehabilitation (last accessed 25th June 2017): <https://reliefweb.int/report/georgia/earthquake-georgia-appeal-emergency-relief-and-rehabilitation>

ReliefWeb (2002c): OCHA-Georgia Information Bulletin for the period 01-10 Oct 2002 (last accessed 25th June 2017): <https://reliefweb.int/report/georgia/ocha-georgia-information-bulletin-period-01-10-oct-2002>

ReliefWeb (2002d): Georgia - Earthquake OCHA Situation Report No. 2 (last accessed 25th June 2017): <http://reliefweb.int/report/georgia/georgia-earthquake-ocha-situation-report-no-2>

ReliefWeb (2002e): Georgia: Quake victims protest (last accessed 25th June 2017): <http://reliefweb.int/report/georgia/georgia-quake-victims-protest>

Reliefweb (2002f): Georgia: Tbilisi earthquake victims waiting for assistance (last accessed 25th June 2017): <http://reliefweb.int/report/georgia/georgia-tbilisi-earthquake-victims-waiting-assistance>

Tbilisi.TV (last accessed 25th June 2017): <http://www.tbilisi.tv>

The Great Soviet Encyclopedia, retrieved on 12th January 2018 from The Free Dictionary: Large-Block Structures. (n.d.) The Great Soviet Encyclopedia, 3rd Edition. (1970-1979):

<https://encyclopedia2.thefreedictionary.com/Large-Block+Structures>.

Large-Panel Structures. (n.d.) The Great Soviet Encyclopedia, 3rd Edition. (1970-1979).

<https://encyclopedia2.thefreedictionary.com/Large-Panel+Structures>.

United Nations Educational Scientific and Cultural Organization (UNDP): <http://en.unesco.org>

UNESCO (2007): Tbilisi Historic District (last accessed 25th June 2017):

<http://whc.unesco.org/en/tentativelists/5233/>

United States Geological Survey (USGS): <https://earthquake.usgs.gov/earthquakes/>

Earthquake List, Maps and Statistics (last accessed 25th June 2017):

<https://earthquake.usgs.gov/earthquakes/eventpage/usp000b35x#executive>

The Preliminary Determination of Epicenters (PDE) Bulletin (last accessed 25th June 2017):

<https://earthquake.usgs.gov/data/pde.php>

United Nations Development Programme (UNDP) in Georgia: <http://www.ge.undp.org/>

UNDP (2014): Disaster Risk Reduction Capacity Report (last accessed 25th June 2017):

http://www.ge.undp.org/content/georgia/en/home/library/environment_energy/disaster-risk-reduction-capacity-assessment-report.html

UNDP (2015): Tbilisi Disaster Needs Assessment (last accessed 25th June 2017):

http://www.ge.undp.org/content/georgia/en/home/library/environment_energy/tbilisi-disaster-needs-assessment--2015.html

Wikipedia (2017a): https://en.wikipedia.org/wiki/Georgia_%28country%29

Last accessed 20th October 2017.

Wikipedia (2017b): https://en.wikipedia.org/wiki/Tbilisi#cite_ref-20.

Last accessed 20th October 2017.

Wikipedia (2017c): https://en.wikipedia.org/wiki/Stalinist_architecture.

Last accessed 20th October 2017.

World Economic Outlook Database (2017):

<https://www.imf.org/external/pubs/ft/weo/2017/01/weodata/index.aspx>

World Monuments Fund (WMF) (2017): Tbilisi Historic District (last accessed 25th June 2017):

<https://www.wmf.org/project/tbilisi-historic-district>

A4.11. November 2004 M5.0 Garda/Salò Earthquake, Italy

This earthquake occurred on 24th November 2004, at 22.59 UTC (23.59 local time), to the west of Garda Lake in Lombardy, northern Italy. While not causing any deaths and only a few minor injuries, damage to buildings was generally moderate but widespread, affecting 66 municipalities. The vulnerability of the masonry structures in the historical centres of the affected towns has been pointed as the main reason for the damage observed, though it is acknowledged that site effects are likely to have played a role in the amplification of ground motions.

A4.11.1 Tectonic and seismic setting

A4.11.1.1 Tectonic setting

This earthquake had its epicentre to the west of Garda Lake (*Lago di Garda* in Italian), in the vicinity of the town of Salò, in the northern Italian region of Lombardy. The area is located along the margin of the Southalpine chain, as shown in Figure A4.11.1, which formed as a consequence of the convergence of the African and Eurasian tectonic plates (Pessina *et al.*, 2006). The lake is surrounded by the Lombardian Prealps to the west and Mount Baldo to the east. It occupies a depression roughly oriented NNE-SSW that represents the boundary between the Lombardy basin to the west and the Venetian Plaform and Trento high ridge to the east, two very different geological settings of the Southern Alps (Massironi *et al.*, 2009; Baroni, 2017).

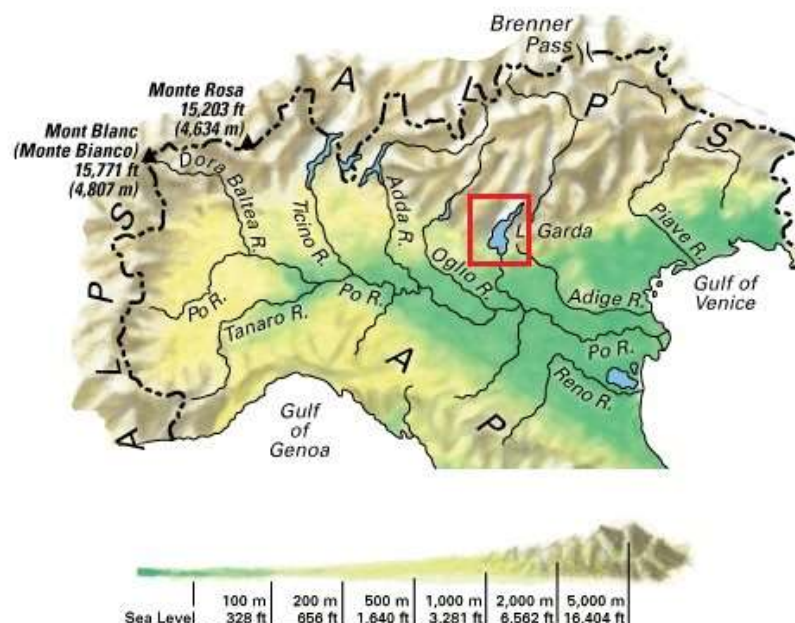


Figure A4.11.1. Topography of northern Italy. Red square broadly indicates the area affected by the 2004 Salò earthquake. Map modified from Mapsland (2018).

The main active tectonic structures of the Southalpine chain are usually blind thrusts (Pessina *et al.*, 2006). Of particular relevance in the area around Garda Lake is the

Giudicarie fault system, which is made up by a series of NNE-SSW trending thrusts, the main ones being shown in Figure A4.11.2. As illustrated, this system dominates the seismicity of the area, and it is believed to be responsible for the 2004 Salò earthquake.

Figure A4.11.2. Seismotectonic sketch of the area around Salò and to the west of Garda Lake. Modified from Pessina *et al.* (2007).

The area around Garda Lake in general, and the Giudicarie belt in particular, present low-to-moderate seismicity in comparison with other areas of Italy such as the Apennines. Nevertheless, a few moderate earthquakes have occurred, as can be observed in Figure A4.11.3. The plot depicts the seismicity observed in the period 1000-2014 within a 60-km radius from the epicentre of the 2004 Salò earthquake according to the 2015 version of the Parametric Catalogue of Italian earthquakes (CPTI15; Rovida *et al.*, 2016). As shown in Figure A4.11.2, the epicentres of many of these events are aligned with the Giudicarie system. The most important historic earthquakes were the 1117 Verona and 1222 Brescia-Verona ones, having reached Mercalli-Cancani-Sieberg (MCS) macroseismic intensities of up to IX, and VII-VIII, respectively (Massironi *et al.*, 2009; Rovida *et al.*, 2016). However, Figure A4.11.3 contains only 13 earthquakes with moment magnitudes equal to or greater than 5.0.

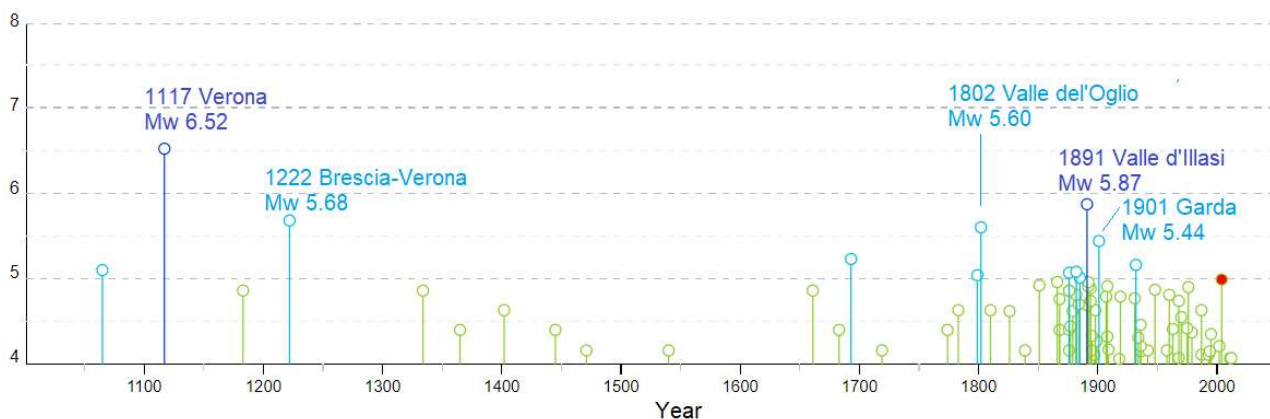


Figure A4.11.3. Seismicity observed in the period 1000-2014 within a 60-km radius from the epicentre of the 2004 Salò earthquake (red circle), according to CPTI15 (Rovida *et al.*, 2016).

A4.11.1.3 Seismic hazard

Figure A4.11.4 shows the seismic hazard map of Italy, as determined by the probabilistic seismic hazard assessment carried out by the National Institute of Geophysics and Volcanology of Italy (Istituto Nazionale di Geofisica e Vulcanologia, INGV), (Meletti, 2007; Meletti & Montaldo, 2007). According to this map, values of peak ground acceleration (PGA) on rock between 0.15 and 0.175 g have a 10% probability of exceedance in 50 years in the area affected by the 2004 Salò earthquake. The map in Figure A4.11.4 served as the basis to define the simplified seismic zonal classification map of 2015, which establishes homogeneous hazard per municipality, and according to which the region around Salò and to the west of Garda Lake is classified as Zone 2, to which PGA design values on rock between 0.15 and 0.25 g (with a 10% probability of exceedance in 50 years) are assigned (DPC, 2015). This classification was the same around the time of the earthquake (Dimova *et al.*, 2004).

Results of the Global Seismic Hazard Assessment Program (GSHAP; Giardini *et al.*, 1999), assign PGA values on rock with a 10% probability of exceedance in 50 years in the range 0.161-0.164 g to the area around Salò, which is in agreement with the values shown in Figure A4.11.4, though slightly closer to the lower bound of Seismic Zone 2. On the contrary, the more recent Seismic Hazard Harmonization in Europe (SHARE) project (Woessner *et al.*, 2015), assigns a PGA on rock with a 10% probability of exceedance in 50 years of 0.259 g to the town of Salò, which corresponds to the upper bound of said zone instead. The corresponding Uniform Hazard Spectrum is shown in Figure A4.11.5. Table A4.11.1 summarises all these values.

Table A4.11.1. Peak ground acceleration (PGA) values on rock with a 10% probability of exceedance in 50 years (475-year return period) according to different sources.

AREA	INGV	NTC (2008)	GSHAP	SHARE
Salò area	0.150-0.175 g	0.15-0.25 g	0.161-0.164 g	0.259 g

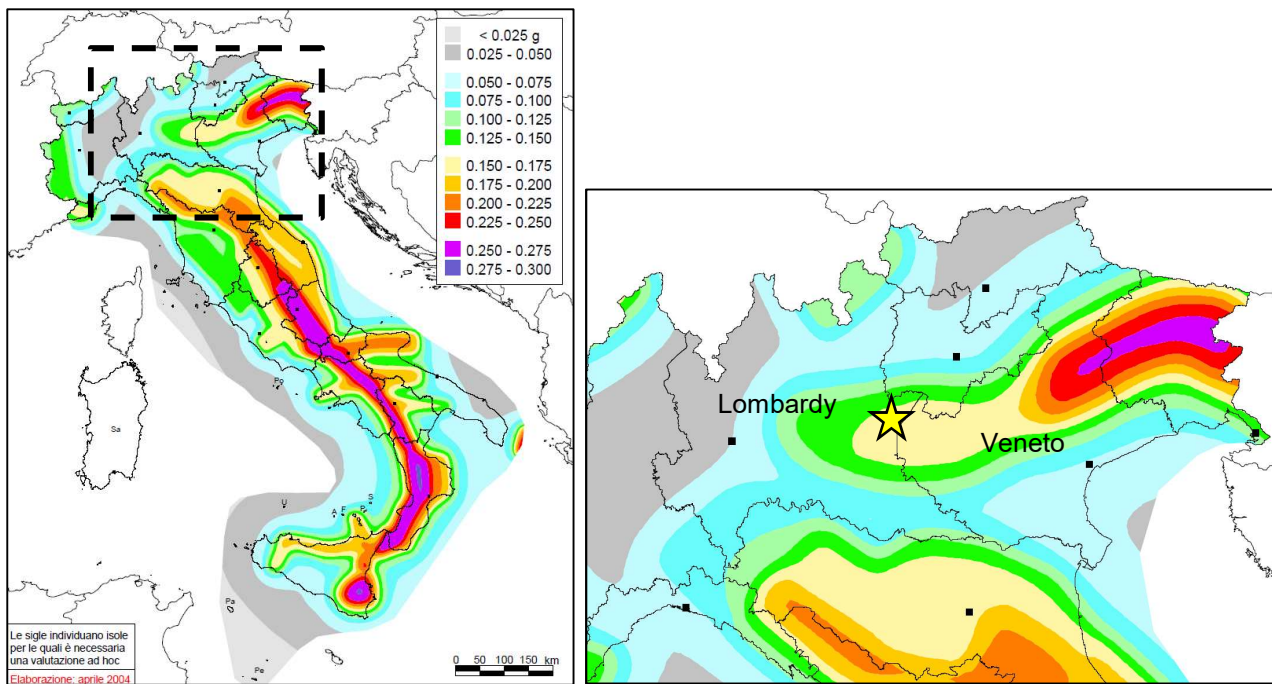


Figure A4.11.4. Seismic hazard map of Italy (left) with emphasis in the region around Garda Lake (right). Colours represent PGA values (g) on rock ($V_{s30}=800\text{m/s}$) with a 10% probability of exceedance in 50 years. Yellow star indicates epicentre of the 2004 Salò earthquake according to the INGV. Modified from INGV-Zone Sismiche (2006).

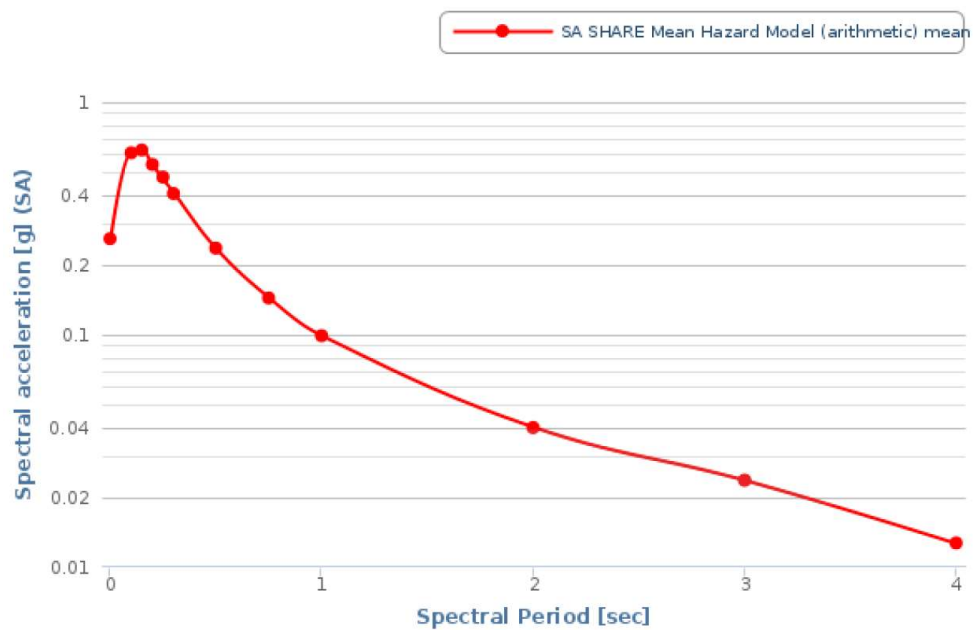


Figure A4.11.5. Uniform Hazard Spectrum for point 45.600°N 10.482°E (closest available to the town of Salò) according to SHARE (5% critical damping). Values correspond to PGA and spectral acceleration in rock with a 10% probability of exceedance in 50 years (mean).

A4.11.2 Earthquake source characteristics

A4.11.2.1 Location, depth and time

The main shock occurred on 24th November 2004, at 22.59 UTC (23.59 local time).

Several organizations and agencies report their own estimations of the epicentral coordinates and hypocentral depth. The information reported in the websites of the Italian National Institute of Geophysics and Volcanology (Istituto Nazionale di Geofisica e Vulcanologia, INGV), the National Earthquake Information Center (NEIC) of the United States Geological Service (USGS), the Global Centroid Moment Tensor Project (GCMT; Dziewonski *et al.*, 1981; Ekström *et al.*, 2012), the European-Mediterranean Seismological Centre (EMSC), the International Seismological Centre (ISC), and the Italian Centroid Moment Tensor dataset (Pondrelli *et al.*, 2006) is summarized in Table A4.11.2 and Figure A4.11.6. Also in the table are the coordinates obtained by Augliera *et al.* (2006) taking into consideration data from seismic stations that were not connected in real time to the national network. According to Pessina *et al.* (2007), the epicentral coordinates appear to be well constrained for this earthquake, but all depths in the range from 3 to 9 km yield similar root mean square errors.

Table A4.11.2. Epicentral coordinates and hypocentral depths from different sources.

Agency / Publication		Latitude	Longitude	Depth (km)
INGV	Istituto Nazionale di Geofisica e Vulcanologia	45.6850 °N	10.5210 °E	5.4
NEIC	National Earthquake Information Center, USGS	45.6260 °N	10.5590 °E	17.2
GCMT	Global Centroid Moment Tensor Project	45.5100 °N	10.4000 °E	12.0
EMSC	European-Mediterranean Seismological Centre (*)	45.6208 °N	10.5565 °E	5.0
ISC	International Seismological Centre	45.6405 °N	10.5817 °E	11.8
Italian CMT dataset (Pondrelli <i>et al.</i> , 2006)		45.6300 °N	10.7600 °E	15.4
Augliera <i>et al.</i> (2006), as reported in Pessina <i>et al.</i> (2007)		45.6890 °N	10.5240 °E	5.1

(*) Values reported in the EPOS Seismic Portal, as they appear to be a more up-to-date version than those directly found on the website of the EMSC.

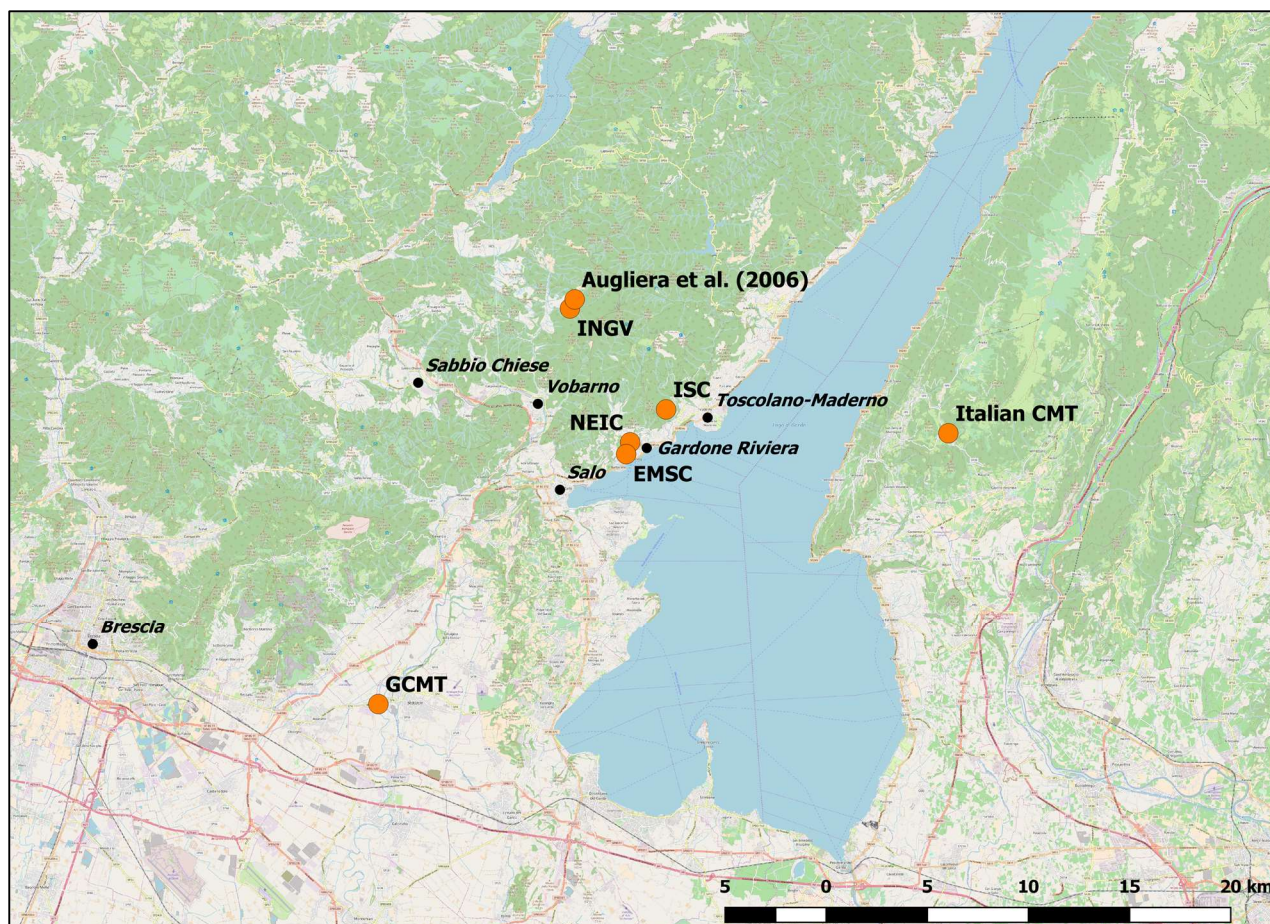


Figure A4.11.6. Estimates of epicentral coordinates according to different sources.

A4.11.2.2 Magnitude

Estimations of magnitude made by the same agencies are reported in Table A4.11.3.

Table A4.11.3. Estimations of moment magnitude (**M**), body-wave magnitude (**mb**) and surface-wave magnitude (**Ms**).

Agency / Publication		M	mb	ML	Ms
INGV	Istituto Nazionale di Geofisica e Vulcanologia	5.0	-	5.2	-
NEIC	National Earthquake Information Center, USGS	5.1	5.3	5.5	4.6
GCMT	Global Centroid Moment Tensor Project	5.0	5.3	-	4.6
EMSC	European-Mediterranean Seismological Centre	-	5.3	5.3	4.1
ISC	International Seismological Centre	-	5.2	-	4.5
Italian CMT dataset (Pondrelli <i>et al.</i> , 2006)		5.0	-	-	-

A4.11.2.3 Style-of-faulting

All sources agree that this earthquake presented a reverse mechanism, most likely associated to the Giudicarie thrust system (e.g., Dimova *et al.*, 2004; Pessina *et al.*, 2006). Table A4.11.4 and Figure A4.11.7 summarise the moment tensor solutions available, all of

which show a northwest-dipping plane believed to be the causative fault (Pessina *et al.*, 2006).

Table A4.11.4. Fault plane solutions and fault planes from different sources. Fault planes marked in gray are the preferred solution in each case.

Nodal Plane 1			Nodal Plane 2			Source
Strike	Dip	Rake	Strike	Dip	Rake	
217	25	52	78	71	106	NEIC (USGS) / GCMT
235	25	92	53	65	89	Pondrelli <i>et al.</i> (2006)
242	24	113	-	-	-	Augliera <i>et al.</i> (2006)

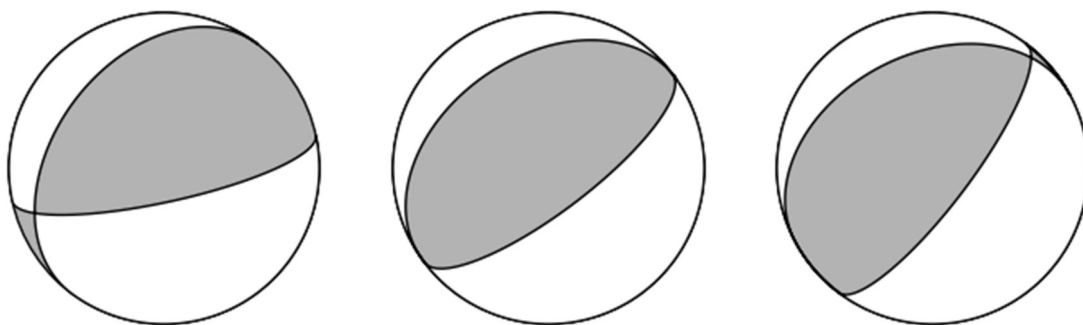


Figure A4.11.7. Focal mechanism of the main shock according to the USGS/GCMT (left), Pondrelli *et al.* (2006; centre), and Augliera *et al.* (2006, as reported by Pessina *et al.*, 2007; right).

A4.11.2.4 Stress drop

No information has been found on the stress drop associated with this earthquake.

A4.11.2.5 Foreshocks and aftershocks

Several sources report on the occurrence of a series of aftershocks, none of which was felt by the population (e.g., Pessina *et al.*, 2007), but no mention is made of any foreshocks.

Massa *et al.* (2009) make reference to 159 aftershocks with local magnitudes in the range 0.3-2.8 recorded by a temporary network installed from 25th November to the end of December 2004. Massa (2010) mentions 169 events in the range M_L 0.9-2.9. Pessina *et al.* (2007) report the occurrence of 187 events with local magnitudes in the range 0.3-2.8 between the occurrence of the main shock and the aftershock of 14th December 2004 at 09.30 UTC. Dimova *et al.* (2004) vaguely mention a series of minor aftershocks of magnitudes between 1.7 and 2.1, while Camassi *et al.* (2011) enumerate only twelve in the range M_L 1.6-2.7 that occurred up to 31st December 2004.

Figure A4.11.8 shows the location of the aftershocks with respect to the main shock, as presented by Massa *et al.* (2009). Pessina *et al.* (2007) have elaborated a very similar plot, further indicating a depth of around 8 to 12 km for most of the aftershocks and a depth of

5.1 km for the main shock. According to Massa *et al.* (2009), the location of the aftershocks is relatively accurate thanks to the density of the temporal network that recorded them.

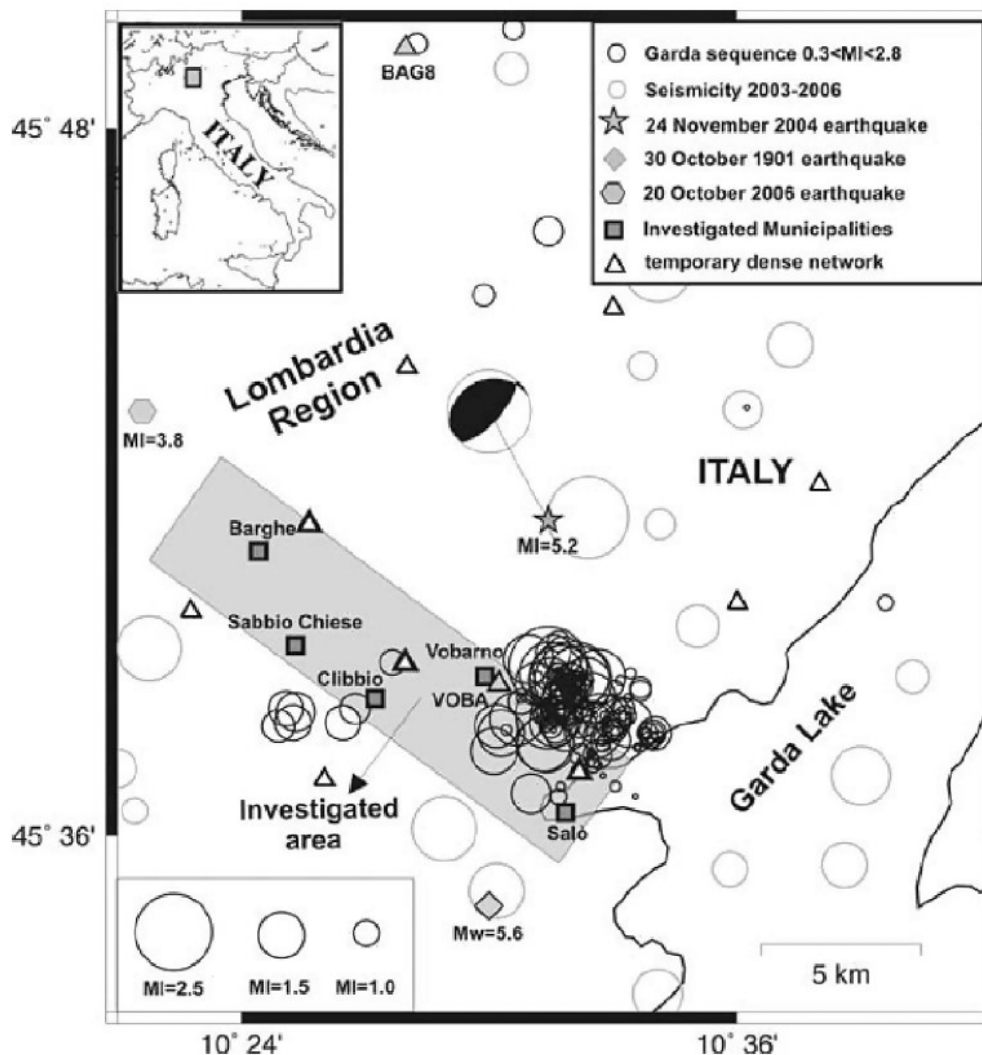


Figure A4.11.8. Location of the main shock (grey star with focal mechanism) and its aftershocks (black circles), the seismicity of the area from January 2003 onward and the location of other earthquakes of interest. Grey rectangle indicates area in which a microtremor survey was carried out. From Massa *et al.* (2009)

A4.11.2.6 Nature of earthquake

No reference has been found to this earthquake being of an origin other than tectonic.

A4.11.3 Geology and ground conditions in the affected area

A4.11.3.1 Regional geology and topography

Garda basin sits in a depression joining Po-Plain to southern Alps, which divides Lombardy basin (west) and Venetian Platform/Trento high ridge to east (Baroni, 2017). Initially formed during the Mesozoic, it has re-activated at several times in the past during the ongoing Alpine compression. The Garda depression is one of several along the southern margin of the Alps

whose canyons originate from deeply eroded rivers during the Late Miocene, during which time isolation of the Mediterranean basin from the Atlantic Ocean lowered sea-levels in the region. Marine deposits marking the filling of the Mediterranean in the early Pliocene indicate the transgression of the sea into the foothills of the Southern Alps approximately 4.04 – 3.81 Ma, which have subsequently been overlain by fluvial and fluvio-glacial sediments as the Lombardian plain has been uplifted. A complex history of tectonics stresses identified in the region indicate compression interspersed with periods of flexure induced tension (Scardia *et al.* 2014). The Giudicare fault system is a reactivation of an early Jurassic extensional region, under the current compressional tectonics.

The topography of the Alpine valleys surrounding Lake Garda on its western, northern and eastern Edges have been re-shaped by Pleistocene glaciations (0.9 Ma), which stretched as far south as the Po Plain. Glacial tills and fluvio-glacial deposits have largely characterised the region since the mid-Pleistocene. It is these deposits that form the frontal moraines surrounding the southern end of the lake (Berlusconi *et al.* 2013).

Figure A4.11.9 shows a general topographic map of the area most affected by the 2004 Salò earthquake. As can be observed, most of the towns and villages are located along the course of the Chiese river, which flows through the valleys of the generally mountainous landscape.



Figure A4.11.9. General topography of the area most affected by the 2004 Salò earthquake. From Pessina *et al.* (2013).

A4.11.3.2 Site conditions in the affected area

Site conditions in the area affected by the 2004 Salò earthquake have been thoroughly studied by Massa *et al.* (2009), who carried out a microtremor survey in the area enclosed by the grey rectangle in Figure A4.11.8. According to said authors, this area can be divided in two: a portion of the Sabbia valley, located between the towns of Barghe and Vobarno, and the southernmost section of the Alto Garda Bresciano region, which includes Salò.

According to Regione Lombardia (2002) and as summarised by Massa *et al.* (2009), the area located between Barghe and Vobarno is filled with the following kinds of deposits:

- present-day and recent alluvium with variable granulometry, spanning from clay to gravel;
- fluvial-glacial deposits of variable thickness (around 100 m maximum) with a strong presence of cobbles;
- alluvial terraces from the Pleistocene.

As shown in the simplified geological maps of Figure A4.11.10, there are numerous bedrock outcrops in the area, mostly consisting of dolomite and limestone. These are often covered by eluvium-colluvium debris deposits that are often subject to landslides (CNR-IRRS & Regione Lombardia – Servizio Geologico, 1996; Massa *et al.*, 2009). The area around Salò is characterised by NW-SE trending recent alluvium sediments and outcrops of fluvial-glacial and morainic deposits (CNR-IRRS & Regione Lombardia – Servizio Geologico, 1996; Massa *et al.*, 2009).

Figure A4.11.11 shows the number of people exposed to landslide hazard around the area affected by this earthquake, according to the Geographic Information System of the Italian National Statistics Institute (Istituto Nazionale di Statistica; GISTAT, 2018). As can be observed, south of the affected area landslide hazard is null, but it is certainly present around Salò and further north.

The horizontal-to-vertical noise ratios obtained by Massa *et al.* (2009) from their microtremor study are plotted in Figure A4.11.12, grouped into three frequency ranges and by location. The authors believe that the range 5-6.7 Hz represents old 2- to 3-storey masonry buildings, which were the most severely damaged. They observed the most significant amplifications in the towns of Barghe and Vobarno, and the weakest in Sàbbio Chiese and Salò. In terms of soil materials, the most marked amplifications were observed for the alluvium deposits and the debris fans, while rock had the flattest response and fluvial glacial deposits lied somewhere in between. The largest scatter in the resulting amplification factor was also observed for the alluvium deposits and the debris fans, as a consequence of their natural behaviour and variable thicknesses.

Figure A4.11.13 shows the V_{s30} global map elaborated by the USGS using topographic slope as a proxy for the area around Salò (Wald & Allen, 2007). The presence of the southern

Alps is evident from the high density of large values, as well as the notorious decrease to around 300-400 m/s along the valleys.

No studies regarding the liquefaction susceptibility of the area affected by this earthquake have been found.

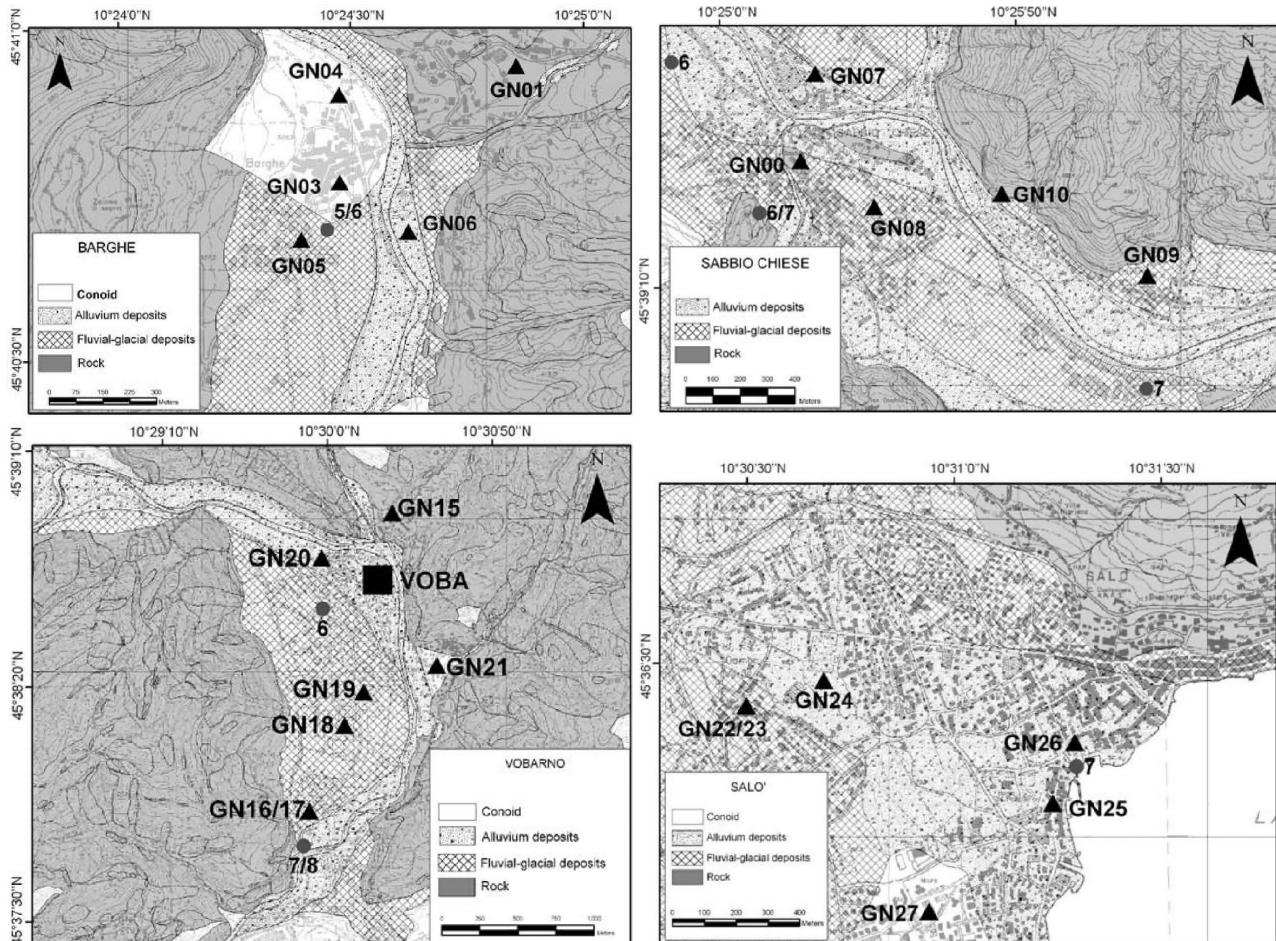


Figure A4.11.10. Simplified geological maps for the cities of Barghe (top left), Sàbbio Chiese (top right), Vobarno (bottom left) and Salò (bottom right). Black triangles indicate measurement points for the microtremor study. From Massa et al. (2009).

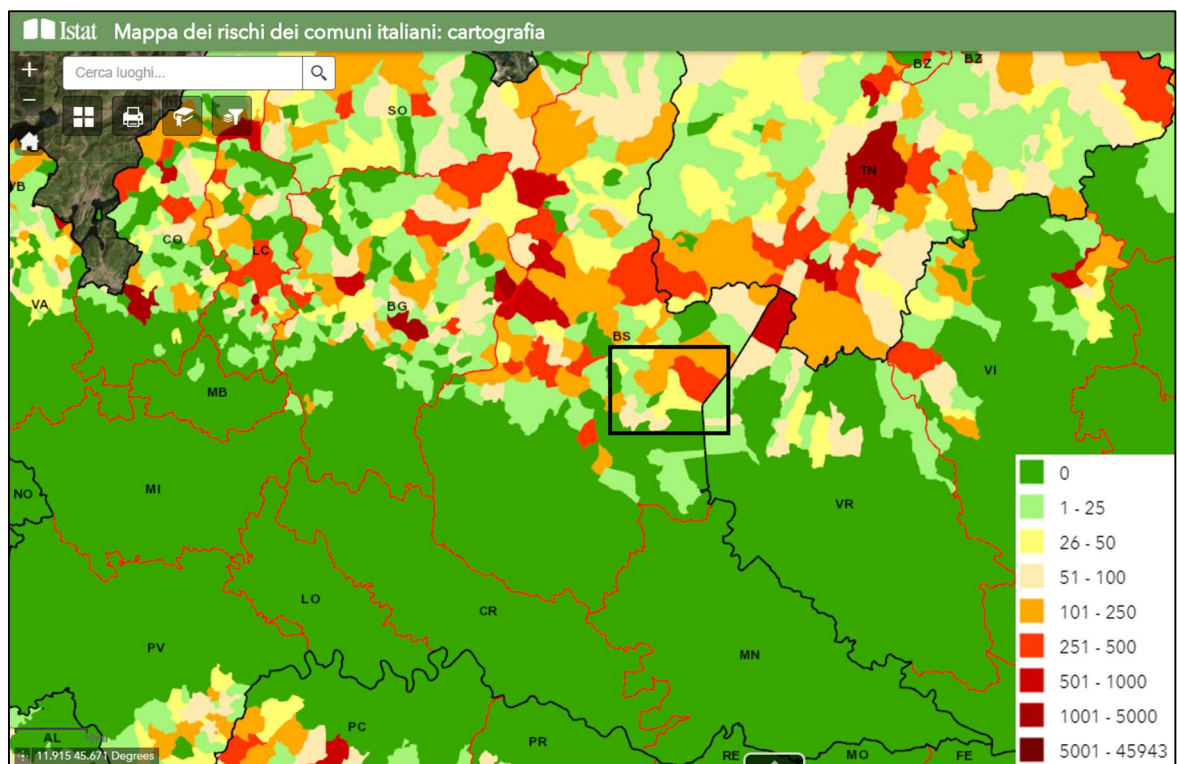


Figure A4.11.11. Population exposed to landslide hazard (colour scale). Rectangle approximately indicates the area affected by the 2004 Salò earthquake. Modified from GISTAT (2018).

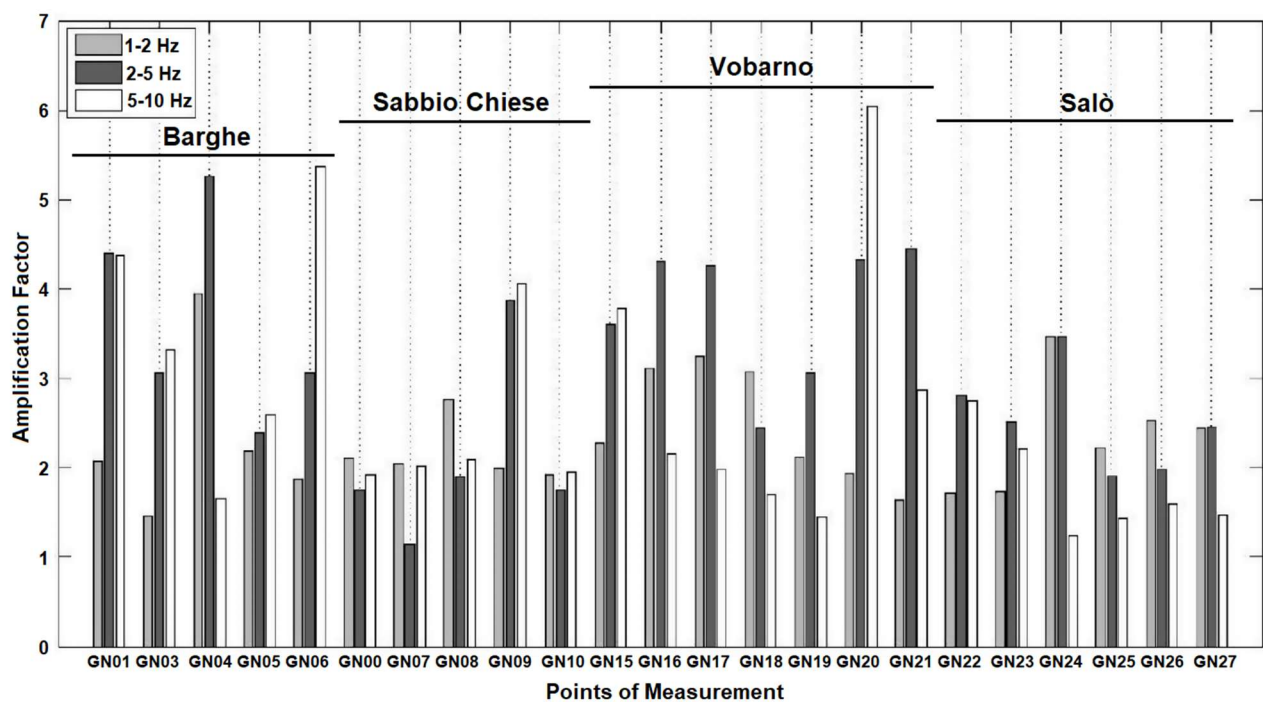


Figure A4.11.12. Amplification factors obtained from all microtremor measurement points. Modified from Massa *et al.* (2009).

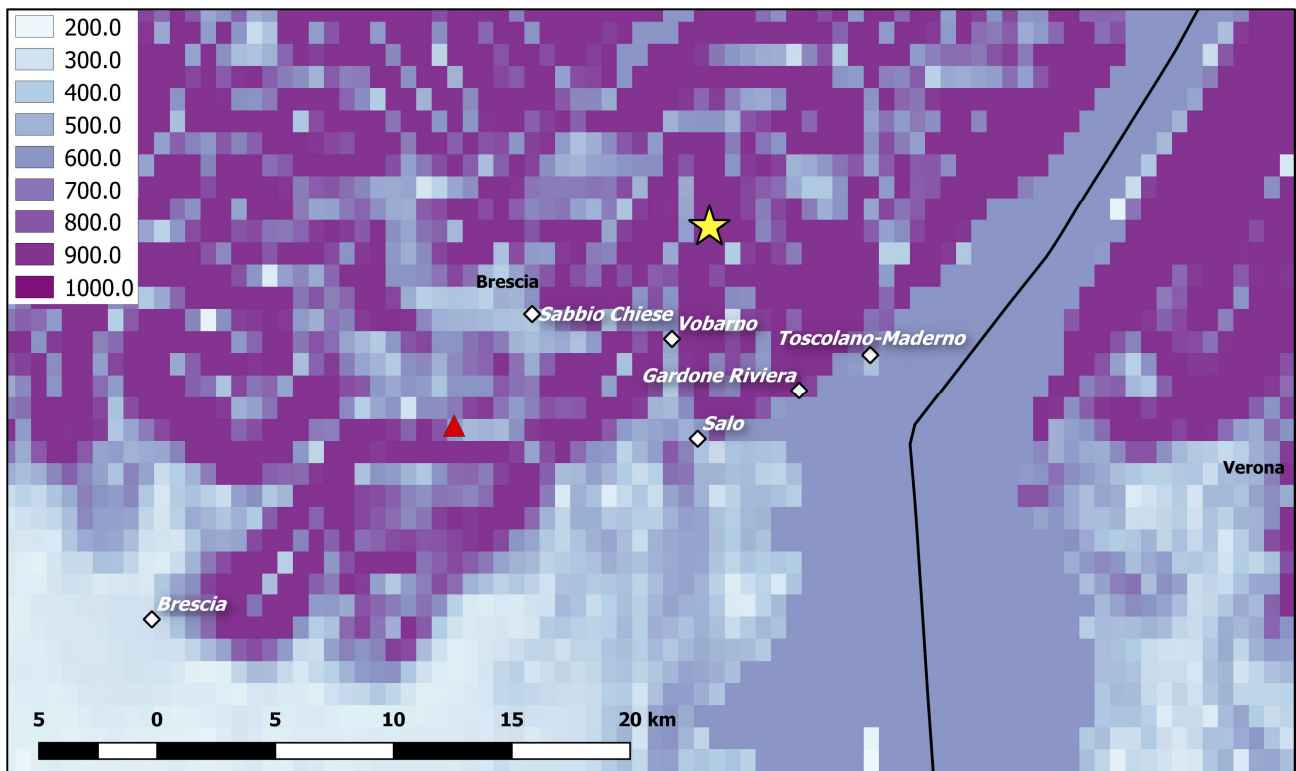


Figure A4.11.13. V_{s30} values estimated using topographic slope as a proxy. Data from the USGS V_{s30} map server (Wald & Allen, 2007). Yellow star denotes epicentre according to the INGV. Red triangle denotes location of station GVD.

A4.11.4 Ground motions

A4.11.4.1 Intensity observations

The 2004 Salò earthquake was largely felt in northern and central Italy, more specifically in the regions of Lombardy, Veneto, Piemonte, Liguria, Trentino, Emilia-Romagna and Toscana, Switzerland, Austria and Slovenia. According to Bernardini *et al.* (2005), the highest macroseismic intensities observed by the team who carried out the post-earthquake assessment were between VII and VIII of the Mercalli-Cancani-Sieberg scale (MCS; Sieberg, 1930) and occurred in Val Sabbia (small village between Clibbio and Carpeneda di Vobarno), Clibbio (small section of the town of Sàbbio Chiese) and Pompegnino (small section of the town of Vobarno). According to the same authors, the consequences observed would classify as intensity VII in the European Macroseismic Scale (EMS-98; Grünthal, 1998). Figure A4.11.14 shows the macroseismic intensity map according to the 2015 version of the Parametric Catalogue of Italian earthquakes (CPTI15; Rovida *et al.*, 2016), whose source is the publication by Bernardini *et al.* (2005).

Apart from the locations of the maximum observed intensity, Bernardini *et al.* (2005) explicitly mention the following:

- MCS intensity VII: Salò, Morgnaga (small section of the town of Gardone Riviera), Pavone (small section of Sàbbio Chiese), and Roè (Roè Volciano).

-

860

Several localities were subject to MCS intensities of VI and V-VI. Bernardini *et al.* (2005) highlight the particularly large extension of the area subject to MCS intensity of V. In total, 66 municipalities were strongly affected by this earthquake (Massa *et al.*, 2009; Pessina *et al.*, 2006).

Figure A4.11.15 shows the superposition of the CPTI15 MCS intensity datapoints (Rovida *et al.*, 2016; Bernardini *et al.*, 2005) and the USGS ShakeMap (Worden *et al.*, 2017) in terms of Modified Mercalli Intensity (MMI). The latter appears to be based purely on intensity prediction equations, as no data points are listed in the USGS website, and shows a maximum MMI of VI. As can be observed, there is some discrepancy between the direct observations of MCS intensities by the assessment team and the spatial pattern predicted by the ShakeMap.

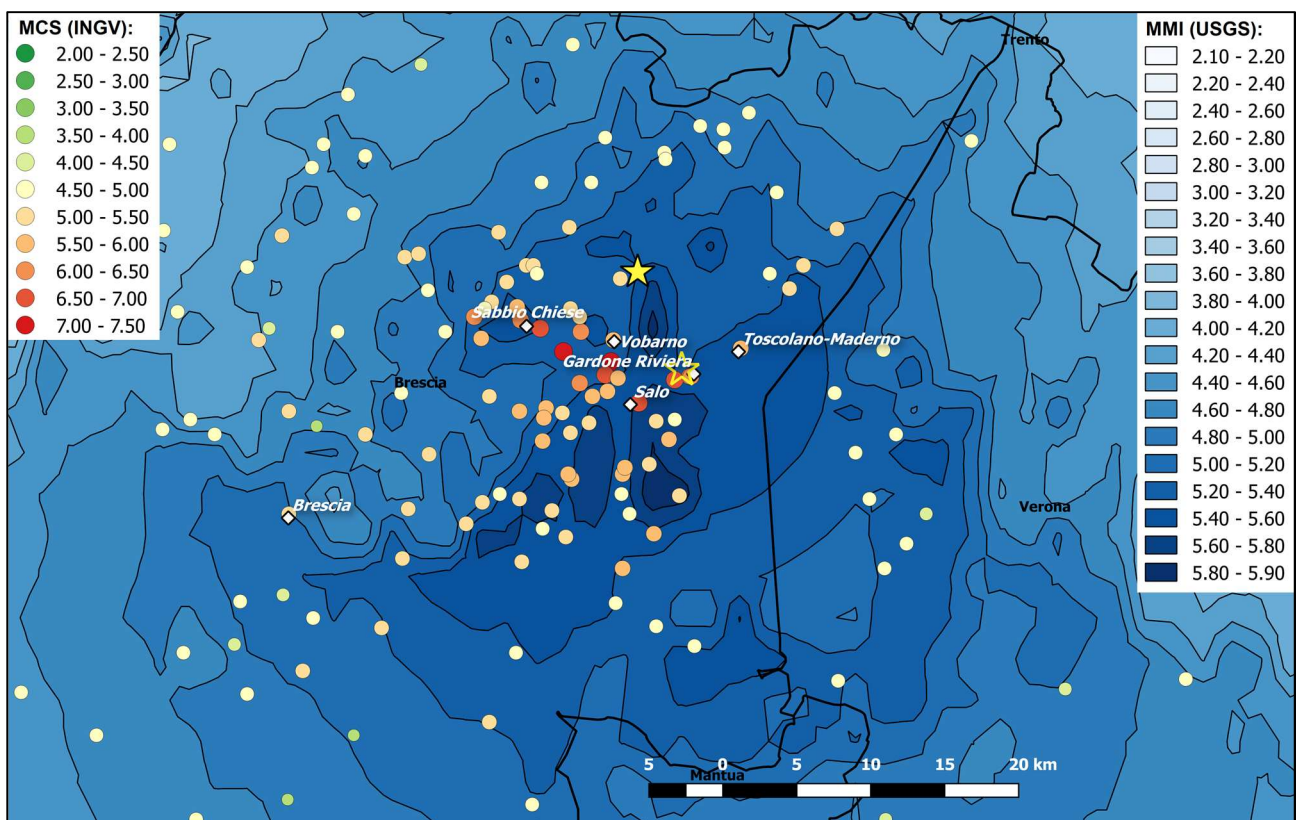


Figure A4.11.15. MCS macroseismic intensities observed according to CPTI15 (Rovida *et al.*, 2016) over USGS ShakeMap in terms of Modified Mercalli Intensity. Filled yellow star and hollow yellow star indicate the epicentral coordinates according to the INGV and the USGS, respectively.

A4.11.4.2 Ground motion recordings

The only near-field record of the 2004 Salò main shock was recorded at an analogue station (GVD) located in Vallio Terme on dolomitic bedrock covered only by a few metres of eluvial deposits, at around 13 to 14 km from the epicentre (Dimova *et al.*, 2004; Pessina *et al.*, 2007; Pergalani *et al.*, 2005). The maximum recorded PGA values were 72, 34 and 39 cm/s² along the north-south, east-west and vertical components respectively. These and other peak values from records in the far-field are summarised in Table A4.11.5. While most

sources make reference to these 72 cm/s^2 (e.g., Dimova *et al.*, 2004; Pessina *et al.*, 2007; Luzi *et al.*, 2016), it has called our attention that Augliera *et al.* (2010) mentions the same value, but then specifies that “*due to the lack of stations installed in the epicentral area, the first not saturated data was recorded, by a INGV-CNT velocimetric station, at an epicentral distance of 88 km*”, which seems to suggest that station GVD saturated. Moreover, while Dimova *et al.* (2004) state a value of 76 cm/s^2 in the text, a table in which they present a summary of peak values reports 159, 100 and 91 cm/s^2 for the north-south, east-west and vertical components of GVD station, respectively. A note mentions that acceleration values correspond to the digitized version of the recorded ground acceleration, obtained as a courtesy from the Italian Civil Protection. It has not been possible for us to find either this digitized version or further clarifications regarding this issue.

Table A4.11.5. Peak ground accelerations, velocities and displacements recorded at the five stations for which data is available from the Engineering Strong Motion Database (Luzi *et al.*, 2016).

Station	EC8 Soil	Repi (km)	PGA (cm/s^2)			PGV (cm/s)			PGD (cm)		
			E-W	N-S	Vert.	E-W	N-S	Vert.	E-W	N-S	Vert.
IT.GVD	A ^(*)	13.6	34.498	72.070	39.525	1.491	3.317	1.383	0.144	0.474	0.105
CH.VDL	A ^(*)	121.4	0.946	1.104	1.243	0.048	0.071	0.066	0.010	0.009	0.014
CH.LLS	A	174.0	0.357	0.273	0.321	0.028	0.032	0.027	0.008	0.009	0.010
IT.NOR	B	381.4	0.197	0.241	0.147	0.032	0.035	0.014	0.006	0.006	0.003
IT.GSG	B ^(*)	432.7	0.020	0.018	0.018	0.003	0.002	0.002	0.001	0.001	0.001

(*) V_{s30} not measured

Figure A4.11.16 and Figure A4.11.17 show the acceleration and displacement response spectra for the three components recorded at station GVD, whose waveforms are plotted in Figure A4.11.18. The N-S component presents relatively large spectral accelerations for periods in the range between 0.1 and 0.3 seconds, which, according to Massa *et al.* (2009), is typical of the buildings that suffered the most damage during this earthquake.

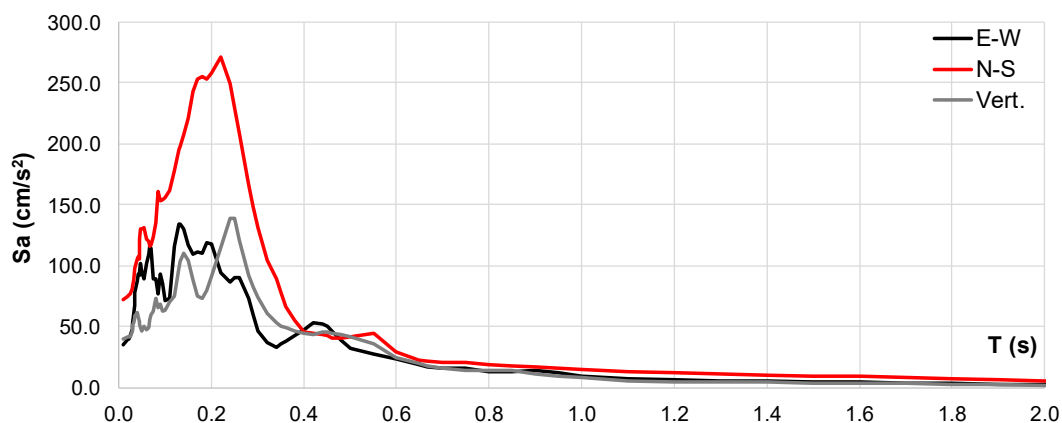


Figure A4.11.16. 5%-damped acceleration response spectra from the ground motions recorded at station GVD. Data from Luzi *et al.* (2016).

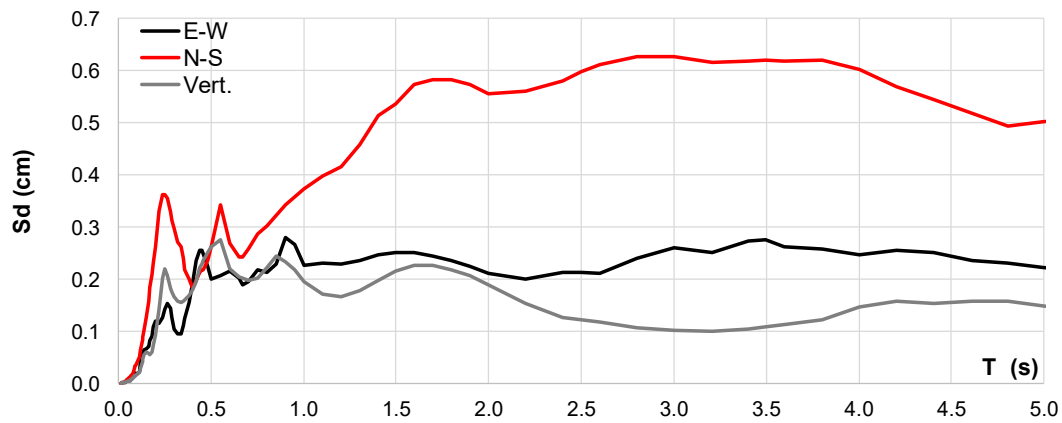


Figure A4.11.17. 5%-damped displacement response spectra from the ground motions recorded at station GVD. Data from Luzi *et al.* (2016).

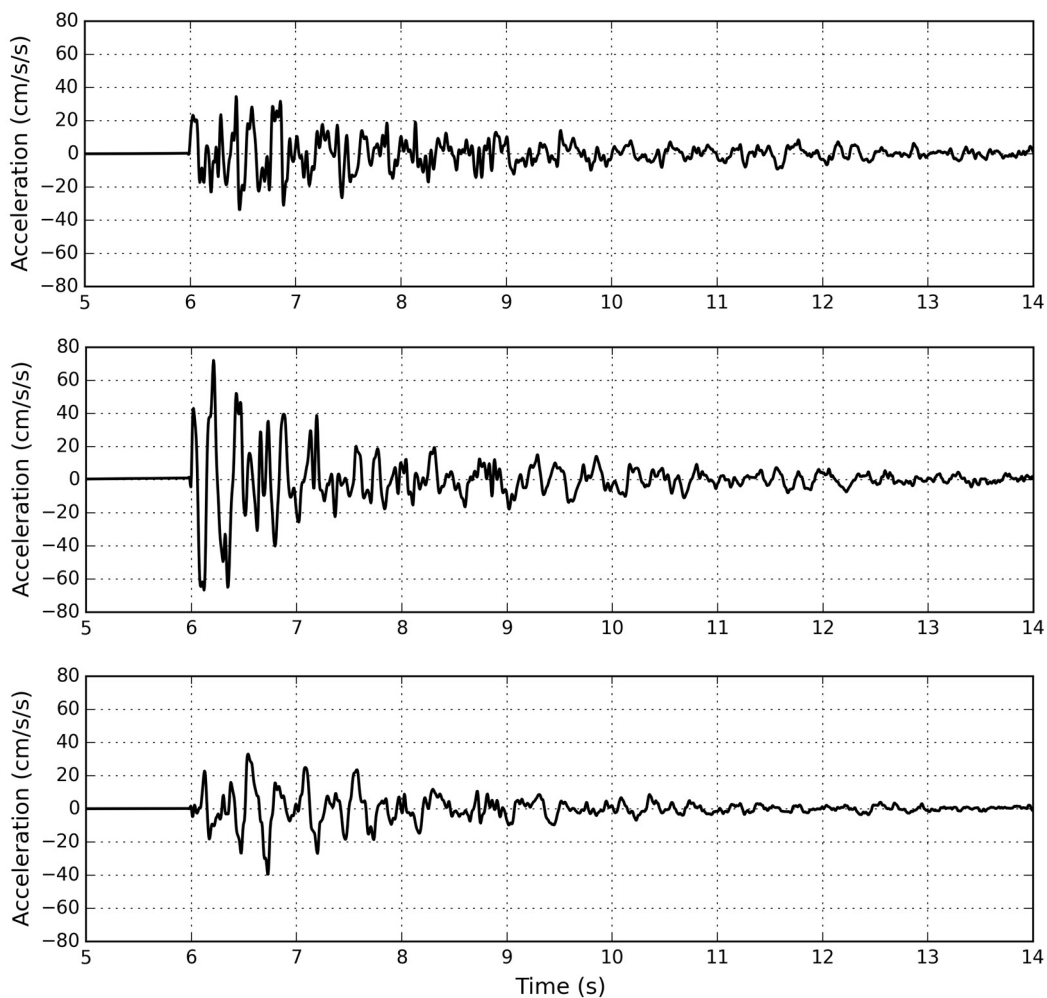


Figure A4.11.18. E-W (top), N-S (centre) and vertical (bottom) acceleration time-histories recorded at station GVD. Data from Luzi *et al.* (2016).

A4.11.4.3 Inferred shaking levels

Figure A4.11.19 shows the USGS ShakeMap (Worden *et al.*, 2017) in terms of PGA, together with the location of station GVD, where a maximum horizontal PGA of 72 cm/s^2

(0.073 g) was recorded. As can be observed, the values predicted by the ShakeMap are significantly lower than the latter.

Using a fault plane similar to that calculated by Augliera *et al.* (2006; Table A4.11.4), a rectangular rupture of 2.6 km by 2.5 km, calculated using the relationship by Wells & Coppersmith (1994), a depth to the top of the rupture of 10 km, based on unspecified seismological and geological data, and five alternative locations of the nucleation point, Pessina *et al.* (2006) carried out kinematic simulations of the rupture with the purpose of characterising the ground motion field likely to have been generated by the 2004 Salò earthquake. Figure A4.11.20 shows the two simulations that fit the best according to the authors, judged from their better agreement with macroseismic data and with the response spectra of the ground motions recorded at station GVD. Each of the two predict PGA values of 69.9 (Figure A4.11.20, left) and 105.0 cm/s^2 (Figure A4.11.20, centre) at the location of station GVD, the former being closer to the recorded one. According to these simulations, maximum horizontal PGA values between 200 and 250 cm/s^2 may have occurred on rock in the worst-shaken areas. Actual values are likely to have been higher due to site effects (Pessina *et al.*, 2006), with amplification factors easily ranging between 2 and 4 at many locations (see Figure A4.11.12).

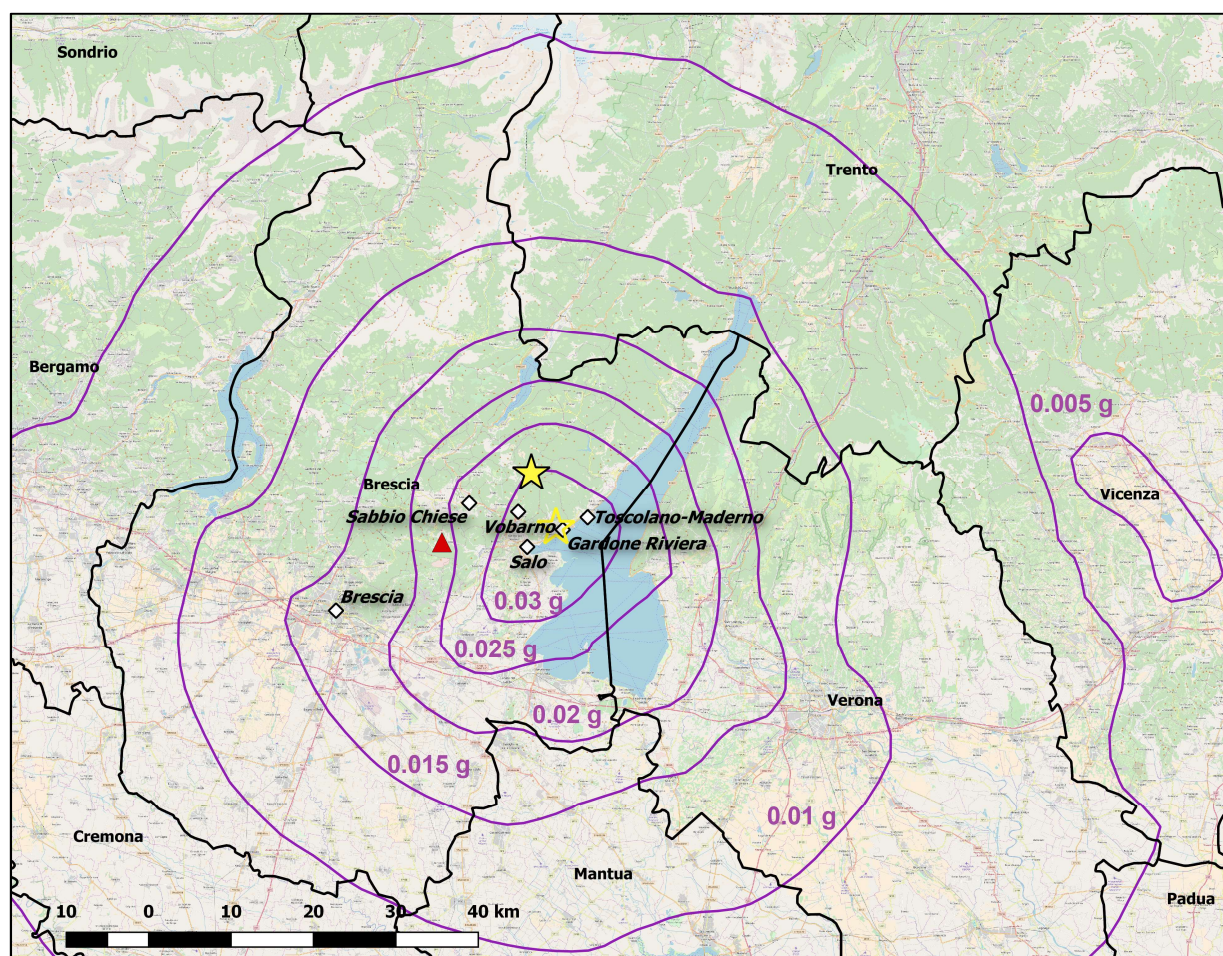


Figure A4.11.19. USGS ShakeMap PGA contours (purple lines) and location of recording station GVD (red triangle). Filled yellow star and hollow yellow star indicate the epicentral coordinates according to the INGV and the USGS, respectively.

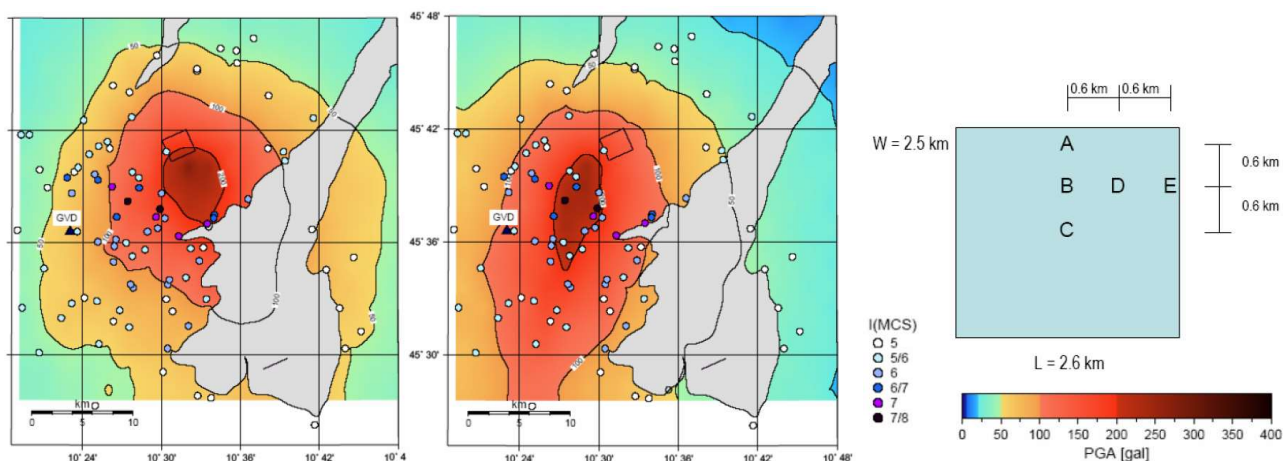


Figure A4.11.20. Synthetic horizontal PGA obtained by simulations (left: nucleation point B; centre: nucleation point D) and fault geometry with nucleation points (right). Blue triangle indicates location of station GVD. White-through-purple scale indicates MCS intensity. PGA in $\text{gal}=\text{cm/s}^2$. Modified from Pessina *et al.* (2006).

A4.11.4.4 Duration of ground shaking

Table A4.11.6 summarises the 5-75% of Arias intensity significant durations of the five records available from the Engineering Strong Motion Database (Luzi *et al.*, 2016), calculated using the OpenQuake ground motion toolkit (Weatherill, 2014). As can be observed, the release of energy close to the epicentre was relatively fast, a characteristic that is visible as well from the waveforms depicted in Figure A4.11.18.

Table A4.11.6. Significant duration (5-75% of Arias definition, seconds) of the ground motions recorded at the five stations for which data is available from the Engineering Strong Motion Database (Luzi *et al.*, 2016).

Station	EC8 Soil	Repi (km)	5-75% definition		
			E-W	N-S	Vert.
IT.GVD	A ^(*)	13.6	1.9	0.8	1.4
CH.VDL	A ^(*)	121.4	20.2	18.1	19.1
CH.LLS	A	174.0	28.7	29.2	30.0
IT.NOR	B	381.4	50.1	45.8	55.9
IT.GSG	B ^(*)	432.7	69.8	70.1	68.5

Estimations of earthquake significant durations can be obtained by means of prediction equations such as those of Bommer *et al.* (2009) and Afshari & Stewart (2016). Lacking more precise information, the values of V_{s30} that were used correspond to the limits between different Eurocode 8 (EC7; CEN, 2004) soil types. A value of 1000 m/s was used to represent soil A, which is defined by values above 800 m/s. A maximum of 600 m/s was used for the model of Afshari & Stewart (2016), as predicted durations do not change above it. A first attempt was carried out using a depth to the top of the rupture (Z_{tor}) of 10 km in the model of Bommer *et al.* (2009), as Pessina *et al.* (2006) selected said value for their simulations, based on seismological and geological data. However, as several depth estimations on Table A4.11.2 are much shallower, an alternative value of 4.6 km was

considered, a value that results from the 5.1-km depth calculated by Augliera *et al.* (2006), the geometry defined by Pessina *et al.* (2006), and the assumption of the hypocentre located in the middle of the rupture ($5.1 - 0.5 = 4.6$ km). The durations shown in Figure A4.11.21 are the ones stemming from this depth, and are larger than those calculated using 10 km. However, all durations calculated from far-field stations yield significantly larger values than those estimated, though it is noted that the model of Bommer *et al.* (2009) was derived for distances up to 100 km and is, thus, being applied outside of its range.

At around 13 km from the epicentre with a V_{s30} value of 1000 m/s, which is expected to represent the situation at station GVD, the model of Afshari & Stewart (2016) predicts a 2.1-s duration, while that of Bommer *et al.* (2009) predicts 1.1 to 1.5 seconds, using Z_{tor} of 10 km and 4.6 km, respectively. Given the small numbers, all these predictions seem reasonable when compared against the 0.8 and 1.9 seconds calculated for each of the two horizontal components at said station. However, very low values of V_{s30} would be needed to achieve the 1.9 seconds of the E-W component and unrealistically large values of V_{s30} would be required to achieve the 0.8 seconds of the N-S component instead, for any of the two depths used.

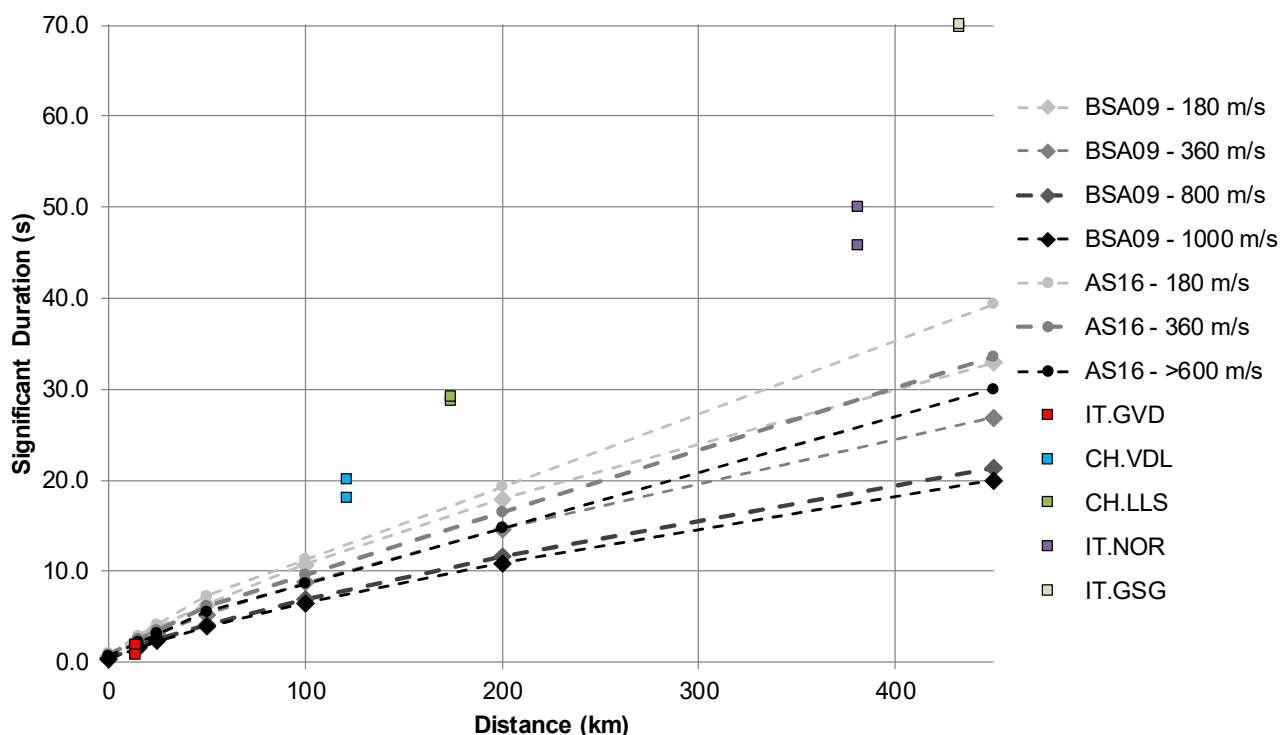


Figure A4.11.21. Estimation of the significant duration of the main shock using prediction equations by Bommer *et al.* (2009, BSA) and Afshari & Stewart (2016, AS), and significant duration calculated for the two as-recorded horizontal components of the five available accelerograms. Depth to the top of the rupture: 4.6 km.

La Repubblica (2004a) and GardaPost (2016) report a 25- to 30-second duration of the shaking, without specifying the location. Based on the significant durations calculated for the available ground motion records (Table A4.11.6) and the estimations obtained by means of prediction equations (Figure A4.11.21), these values seem quite large for the near-field, but feasible at distances larger than 100 km. However, as Corriere della Sera (2016) mentions

a 20-second duration in Milan, located slightly over 100 km from the epicentre, it is possible that La Repubblica (2004a) and GardaPost (2016) are also making reference to this location, without noting that duration is a function of distance.

A4.11.5 Collateral earthquake hazards

A4.11.5.1 Surface rupture

No surface rupture has been reported for this earthquake. This is in agreement with the hypocentral depths summarised in Table A4.11.2 and the source geometry described by Pessina *et al.* (2006).

Michetti *et al.* (2005) mention the occurrence of several cracks on the ground and on paved roads at Pompegnino and point out that their width was increasing due to heavy rains that occurred 5-6 days after the earthquake. They do not provide specifications on the origin of the cracks.

A4.11.5.2 Landslides

Michetti *et al.* (2005) observed multiple rockfalls at five sites and landslides at three other locations. The rockfalls involved a maximum volume of 100 cubic metres, while the landslides reached up to 1,000 cubic metres. The rockfalls at Clibbio damaged two houses and a main road (Dimova *et al.*, 2004; Camassi *et al.*, 2011; Michetti *et al.*, 2005).

A4.11.5.3 Liquefaction

According to Michetti *et al.* (2005), evidence of liquefaction and localised lateral spreading and settlement was observed in Salò. According to this source, a 30-cm fissure observed in Salò's harbour was due to the lateral spreading.

A4.11.5.4 Settlements

The only reference to settlements due to this earthquake is that by Michetti *et al.* (2005), associated to liquefaction and lateral spreading.

A4.11.6 Exposed population

A4.11.6.1 Socio-economic setting

According to the 2016 Human Development Data (United Nations, 2016), the Human Development Index (HDI) for Italy was 0.887 in 2015, latest data available, while its Inequality-adjusted HDI (IHDI) was 0.784. According to the world's ranking per HDI, Italy is currently located in the 26th place, while the Netherlands are ranked 7th. The two countries appear to have been more even around the year 2004, when the Salò earthquake occurred

Table A4.11.7 compares the HDI and IHDI for both countries, according to United Nations (2016).

Table A4.11.7. Human Development Index and Inequality-adjusted Human Development Index for Italy and the Netherlands. Data from United Nations (2006; 2016).

Report	Data	Italy				Netherlands			
		HDI	IHDI	Rank	Adj. HDI	HDI	IHDI	Rank	Adj. HDI
2006	2004	0.940	-	17	0.851	0.947	-	10	0.888
2016	2015	0.887	0.784	26	-	0.924	0.861	7	-

It is evident, as Figure A4.11.22 indicates, that both countries had followed a stable and growing economic course until 2008 when fluctuation started during the world's economic recession. Considering the size of Italy compared to the Netherlands, its economic power (GDP) is several times higher (Figure A4.11.22, left), but the GDP per capita of the Netherlands clearly exceeds that of Italy (Figure A4.11.22, right), placing the Netherlands high in the HDI and wealth ranking. Moreover, Italy has been more importantly affected by the 2008 crisis. Table A4.11.8 presents a comparison between Italy and the Netherlands in terms of gross domestic product (GDP), GDP per capita and unemployment rate for 2015.



Figure A4.11.22. GDP (left) and GDP per capita (right) fluctuation in US \$, for Italy and the Netherlands for the last 65 years according to World Bank national accounts data and the Organization for Economic Cooperation and Development (OECD) National Accounts data files (The World Bank Group, 2017).

Table A4.11.8. Gross domestic product (GDP), GDP per capita and unemployment rate in 2004 and 2015 for Italy and the Netherlands, according to the World Economic Outlook Database (2016)

Indicator	Units	Italy		Netherlands	
		2004	2015	2004	2015
Gross domestic product, current prices	Billions USD	1,800.76	1,815.76	651.42	750.70
Gross domestic product per capita, current prices	USD	31,319.73	29,866.62	40,008.33	44,322.83
Unemployment rate	%	7.983	11.908	5.665	6.89

Within Italy, the region of Lombardy (to which the communities to the west of Lake Garda belong) ranks third in terms of GDP per capita, after Trentino-South Tyrol and Aosta Valley, performing significantly better than the country as a whole (Statista, 2018). The main economic activity around Garda Lake is tourism, followed by agriculture (Zainoo, 2018).

A4.11.6.2 Population density and distribution

The area most affected by this earthquake does not present a high population density, especially when compared with nearby cities such as Brescia and Verona (see Figure A4.11.23). In the immediate vicinity of the epicentre of the 2004 earthquake, Salò is the most populated town. Table A4.11.9 summarises the population of the most affected localities in the year 2004.

Table A4.11.9. Population (number of inhabitants) of some of the most affected municipalities in the area of the earthquake. Data from Urbistat (2017).

Village	Population
Vobarno	7,600
Sàbbio Chiese	3,172
Salò	10,056
Villanuova sul Clisi	4,776
Toscolano Maderno	7,004
Roé Volciano	4,174

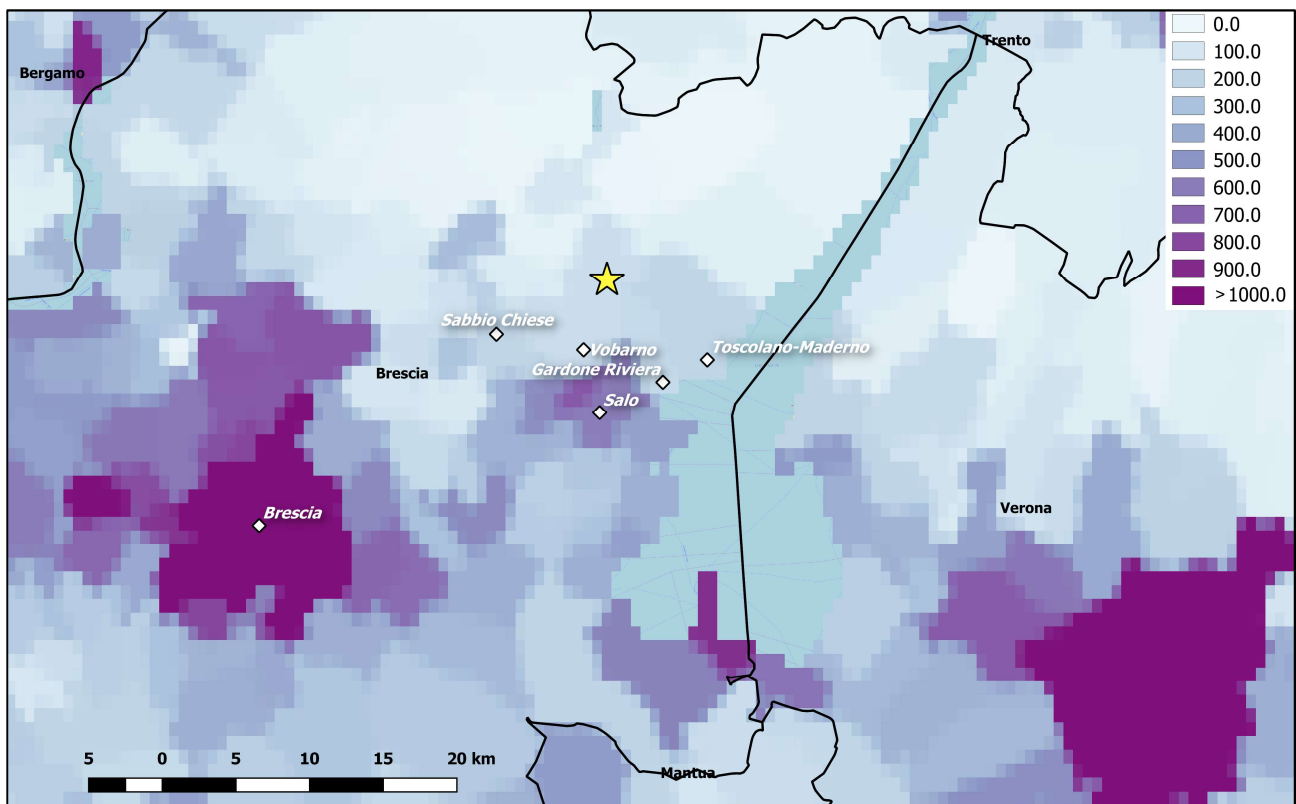


Figure A4.11.23. Population density (people/km²) in 2005 in the area around Salò, according to data from Gridded Population of the World v4.0 (CIESIN, 2016).

According to the EXPO-CAT database (Allen *et al.*, 2009), around seven million people are estimated to have been exposed to Modified Mercalli intensities of IV or larger caused by this earthquake, two thirds of which inhabit urban areas. When looking at higher intensities

the number drops significantly, the estimation being slightly over 200,000 people being exposed to MMI of VI or larger. It is noted that MMI values go up to 7.5 (*i.e.*, VII-VIII) for this earthquake in the EXPO-CAT database, but the USGS ShakeMap only reaches VI (Figure A4.11.15).

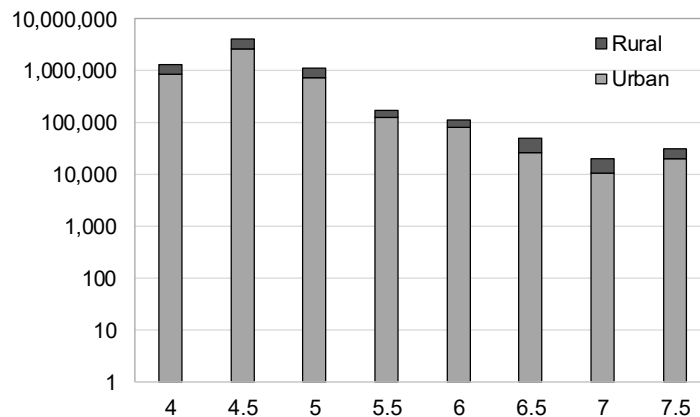


Figure A4.11.24. Estimation of total population exposed to different Modified Mercalli Intensities (MMI). Data from EXPO-CAT database (Allen *et al.*, 2009).

A4.11.6.3 Time of day of earthquake

This earthquake occurred at midnight (23.59 local time) of a Wednesday, when a large part of the population was asleep in their residencies. While La Repubblica (2004b) mentions falling debris as a cause of injury, it is not clear if this is associated to rubble falling onto the streets or inside the damaged buildings. The former would lead to the conclusion that the earthquake could have caused many more injuries had it occurred in the day time, when more people are in the streets, while the latter would suggest the opposite.

As Dimova *et al.* (2004) mention partial to severe damage in several schools and kindergartens, it is possible that more children could have been injured if the earthquake had occurred during the school hours. Similarly, the severe damage reported for a large number of churches suggests that occurrence of the earthquake during Mass service hours could have led to a larger number of injuries.

A4.11.7 Characteristics of exposed building stock

A4.11.7.1 Seismic design codes

The introduction of the seismic notion in the Italian regulations took place with the Royal Decree of 1927 following the destructive earthquakes of Reggio Calabria and Messina in 1908. As shown in Figure A4.11.25 (left), few areas were characterized as seismic in said document, mainly the ones affected by the earthquakes of 1908, with the rest of the Italian territory being covered by no legislation regarding earthquake resistant design. During the period between 1927 and 1962, when a law that provided construction details and redefined the distribution of seismic forces was passed, several Royal decrees were issued

characterizing new areas as seismic, describing anti-seismic techniques and modifying the mass proportions for the definition of seismic forces.

In 1971 the norm for the design and construction of reinforced concrete, prestressed concrete and steel structures was introduced. In 1974, regulation of private and public construction was made compulsory. In parallel, it was agreed that the seismic classification would be updated whenever the evolution of seismic knowledge demanded it. Soon, in 1975, the new construction code for seismic areas was approved by means of a ministerial decree. This code mainly allowed for the use of dynamic seismic analysis with the introduction of the elastic design spectrum, defined geotechnical criteria for the buildings foundation, and modified, again, the distribution of the seismic forces along the height of the buildings.

Seismological studies by the National Research Council (CNR) following the destructive earthquakes of Friuli – Venezia Giulia in 1976 and Irpinia in 1980, led to the proposal of a new seismic classification of the Italian territory approved by a series of decrees until 1984, when a probabilistic approach was applied for the division of Italy in three seismic zones (Figure A4.11.25, right). According to Dimova *et al.* (2004), it was in 1974 that the communities to the west of Garda Lake, including those that were most affected by the 2004 earthquake, were classified as belonging to Zone II, which implied the existence of a moderate hazard. However, Bernardini *et al.* (2005) mention 1986 as the year in which the area around Pompegnino was first classified as seismic.

In 1996, a ministerial decree established the seismic design with damage states as well as the dependence of the seismic forces on the dynamic characteristics of the buildings. In 2003, the 3rd-generation seismic code was introduced (Amadio, 2014), and the seismic classification of the country was updated in parallel (Figure A4.11.26, left). A fourth seismic class (the lowest) was then added, giving the possibility to the regions marked under this category to decide upon the obligation of designing their buildings to resist seismic action. Salò and the surrounding areas remained in Zone II (moderate-high), with design PGA values on rock between 0.15 and 0.25 g. This new code, compatible with Eurocode 8 (CEN, 2004), accounts for the ductility of the structure, the strength hierarchy among nodes and elements and the analysis at limit states.

A new code for design and construction, the NTC (2008), was introduced in 2008 and finally adopted in 2009, after the earthquake of L'Aquila. The NTC (2008), considered to be the norm of 4th generation (Amadio, 2014), is based on the principles of performance-based design with multiple limit states and is compatible with Eurocode 8 (CEN, 2004). Instead of the seismic zonation until then adopted, the territory was divided into a grid of 10x10-km cells, each of which is assigned a reference value of PGA on rock. This change led to the introduction of design seismic acceleration to areas that had been considered aseismic until then. The most recent update of this map was carried out in 2015 (Figure A4.11.26, right).

This section was elaborated with data from Amadio (2014), Balliana (2015) and Wikipedia (2017).

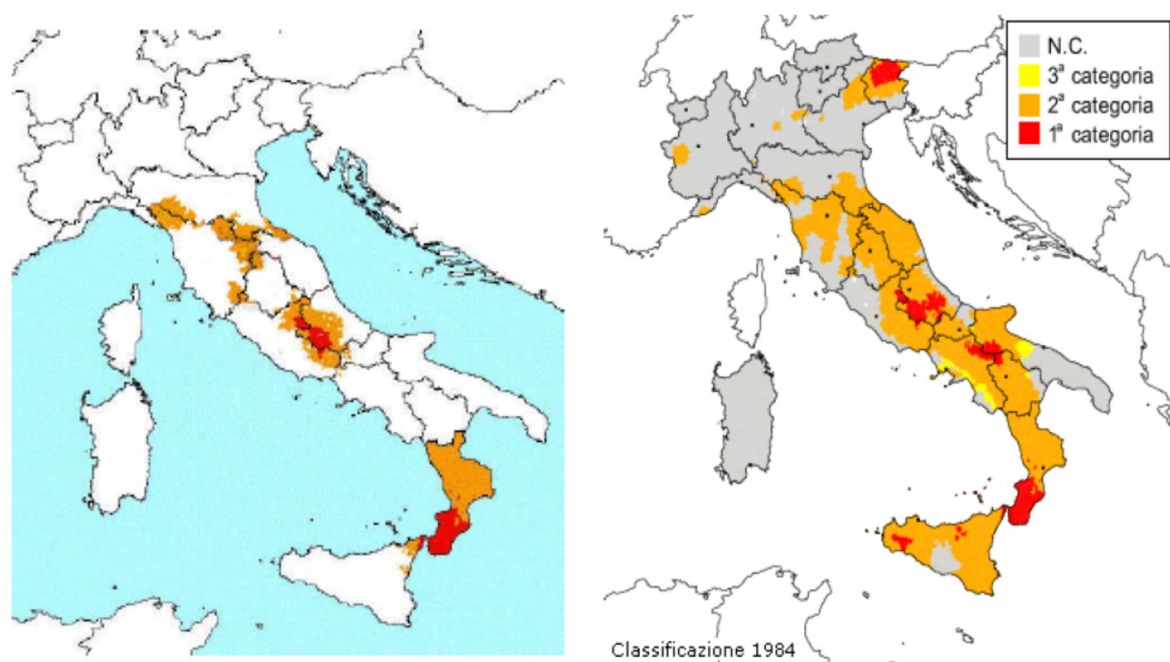


Figure A4.11.25. Seismic zonation of the Italian territory according to 1927 (left) and 1984 (right) norms. From Amadio (2014).

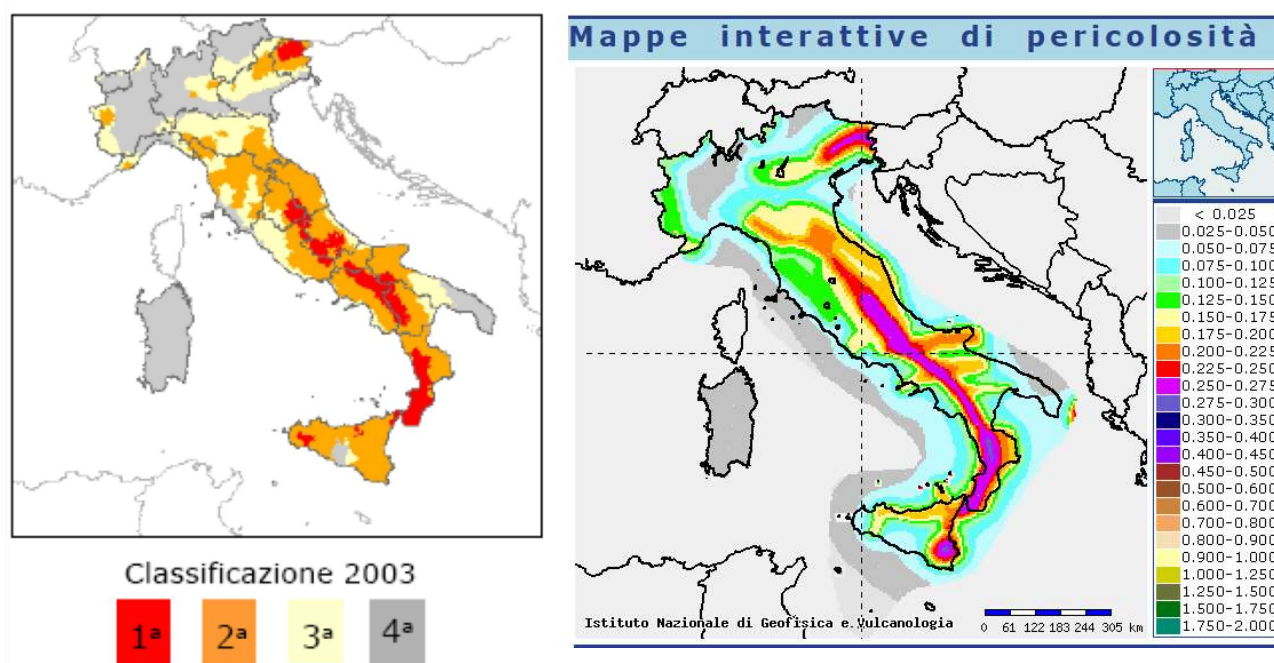


Figure A4.11.26. Seismic zonation of Italian territory according to 2003 norm (Amadio, 2014) (left) and 2015 update (right) (INGV-GIS, 2015).

A4.11.7.2 Building typologies

Data regarding typologies at the country level collected from the PAGER Inventory Database v2.0 (Jaiswal & Wald, 2008) for Italy are summarized in Figure A4.11.27. As can be observed, half of the Italian building stock is unreinforced brick masonry and the rest is composed by low to mid-rise ductile and non-ductile reinforced concrete frames. It is noted that the proportions reported are the same irrespective of whether it is rural/urban or

residential/non-residential building stock, which implies that data was not available for each individual category.

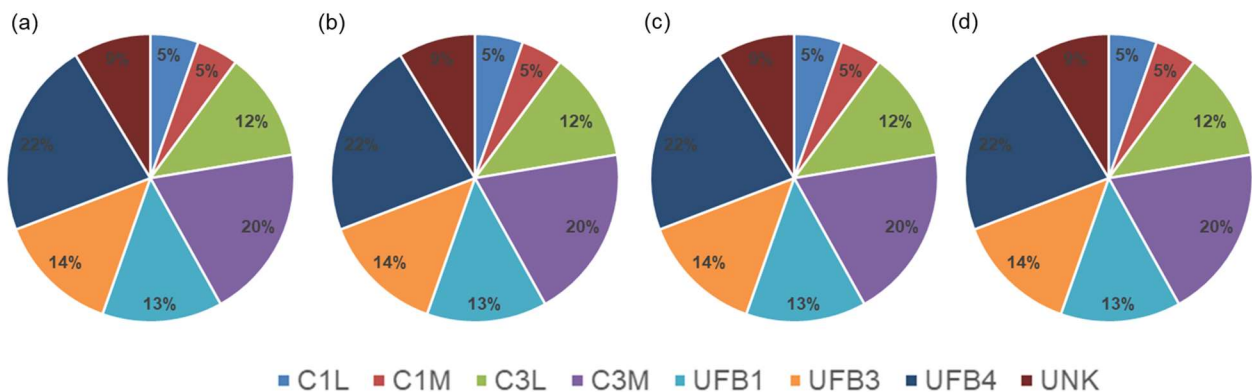


Figure A4.11.27. Proportion of building main typologies in Italy for (a) rural residential, (b) urban residential, (c) rural non-residential, (d) urban non-residential typologies: C1L: Ductile reinforced concrete moment frame with or without infill low-rise; C1M: Ductile reinforced concrete moment frame with or without infill mid-rise; C3L: Nonductile reinforced concrete frame with masonry infill walls low-rise; C3M: Nonductile reinforced concrete frame with masonry infill walls mid-rise; UFB1: Unreinforced brick masonry in mud mortar without timber posts; UFB3: Unreinforced brick masonry in lime mortar; UFB4: Unreinforced fired brick masonry, cement mortar; UNK: Not specified (unknown). 2002 data from USGS-PAGER, Jaiswal & Wald (2008).

According to Dimova *et al.* (2004), damage due to this earthquake was concentrated in the old historical centres of the affected localities, where most of the building stock consists of 2-storey (exceptionally 3-), 200- to 300-year old non-engineered masonry houses that have suffered from numerous structural modifications as time passed by. The authors describe these buildings as EMS-98 (Grünthal, 1998) vulnerability class A (the most vulnerable class, see Figure A2.1.1 in Appendix II). Predominance of 2- to 3-storey load-bearing masonry buildings in the area is supported by data from GISTAT (2018), however, this source indicates a median construction date of residential houses in the area of 1919-1945. Dimova *et al.* (2004) mention as well the presence of reinforced concrete (RC) structures with earthquake resistant design built after 1974 for a PGA of 0.07 g and assign an EMS-98 vulnerability class C to these, in view of the low design PGA value (less-vulnerable classes are usually assigned to RC buildings designed to withstand earthquake loads). According to GISTAT (2018), 45 to 64% of the residential buildings in the area are made of load-bearing masonry.

Pessina *et al.* (2006) summarise the vulnerability of the localities affected by this earthquake as per Table A4.11.10, the original source being a survey carried out by CNR-IRRS & Regione Lombardia (1996) that could not be retrieved for this work. Pessina *et al.* (2006) also point out the particularly high levels of vulnerability of historical centres and believe that an overall general good quality of construction can be assumed to exist outside of these.

Regione Lombardia (2018) characterises the building stock of the whole Lombardy region as being notably vulnerable due to its age, the most common structural typologies and the lack of maintenance.

Table A4.11.10. Vulnerability characterisation of the most affected localities. Data from Pessina *et al.* (2006).

Sections / Villages	MCS intensity	Vulnerability
Clibbio (Sàbbio Chiese)	VII-VIII	N/A
Pompegnino (Vobarno)	VII-VIII	N/A
Morgnaga (Gardone Riviera)	VII	Medium, High
Pavone (Sàbbio Chiese)	VII	Low
Roé Volciano	VII	Low, Medium, High
Salò	VII	Low, Medium

A4.11.7.3 Prior damage and retrofit

Camassi *et al.* (2011) state that the village of Val Sabbia, which comprises the small sections of Clibbio and Pompegnino that were particularly affected by this earthquake, had been damaged by previous seismic events that occurred in 1826, 1892, and 1898. No further details are given by the authors, but given the reported large presence of 200- to 300- year old masonry structures in the historical centres it might be inferred that some of these may have been damaged by those earthquakes and, perhaps, repaired.

Dimova *et al.* (2004) make reference to some buildings in Pavone having been retrofitted or partially rehabilitated shortly before the earthquake suffering structural damage. They attribute this to the interventions being focused on non-structural elements and not taking seismic design into consideration.

A4.11.8 Damage observations

A4.11.8.1 Damage states

No proper statistics in terms of established damage scales have been found in the literature. However, Bernardini *et al.* (2005) report that the maximum EMS-98 (Grünthal, 1998) macroseismic intensity observed was VII, which corresponds to the following description (see Table A2.1.1 of Appendix II):

- Many buildings of vulnerability class A (the most vulnerable) suffer damage of grade 3 (*i.e.*, moderate structural damage and heavy non-structural damage), and a few of grade 4 (*i.e.*, heavy structural damage and very heavy non-structural damage).
- Many buildings of vulnerability class B suffer damage of grade 2, and a few of grade 3.
- A few buildings of vulnerability class C sustain damage of grade 2.
- A few buildings of vulnerability class D sustain damage of grade 1.

For further details regarding EMS-98 (Grünthal, 1998) vulnerability classes and damage grades, please refer to Appendix II.

A4.11.8.2 Damage statistics and description

According to Pessina *et al.* (2006), the 2004 Salò earthquake caused damage to 3,500 residential buildings, 200 public buildings, and 300 churches, and left 2,200 people homeless. Massa *et al.* (2009) and Augliera *et al.* (2010) support this, as they mention damage to 3,700 buildings and 300 churches. Pessina *et al.* (2013) report that 500 residential buildings were damaged, of which 40 had to be demolished, and nearly 1,200 buildings “became unfit for use”, 10 of which were strategic for the public interest and more than 50 had either historic or artistic value. They mention as well the same 200 public buildings and 300 churches with damage. It is not clear why the total of 1,700 buildings is significantly lower than the 3,500 buildings reported by Pessina *et al.* (2006). The Significant Earthquake Database of the National Centers for Environmental Information of the National Oceanic and Atmospheric Administration (NOAA) of the United States estimates between 100 and 1,000 destroyed houses, a range that appears as small against all other more specific sources. The GardaPost news website, writing 12 years after the earthquake, appears to support the idea of many thousands of buildings damaged and provides more specific numbers: 3,649 private buildings, 315 religious buildings, and 183 public buildings, making a total of 4,147 damaged buildings (GardaPost, 2016). Acknowledging that the gathering of statistical data was not finished at the time of their writing, Dimova *et al.* (2004) report around 6,070 intervention requests and 1,187 evacuated people from 62 municipalities as of 1st December 2004.

According to Bernardini *et al.* (2005) and Dimova *et al.* (2004), the kinds of damage observed were the following:

- some partial collapses, mostly associated to abandoned or extremely unmaintained buildings (e.g., Figure A4.11.28, left);
- the fall of chimneys, roof tiles and plaster;
- diagonal shear cracking of masonry walls of different degrees of severity;
- out-of-plane deformation of masonry walls of different degrees of severity (e.g., Figure A4.11.28, right);
- failure of masonry due to the lack of seismic joints and the subsequent pounding (e.g., Figure A4.11.29, left; Figure A4.11.31, right);
- shear cracking of bell towers (e.g., Figure A4.11.30);
- cracking of windows piers;
- disintegration and failure of unconfined masonry under the structures of roofs (e.g., Figure A4.11.29, right);
- separation of masonry walls from RC slabs;
- light non-structural damage such as hairline cracks in masonry walls, fall of small pieces of plaster, and fall of loose bricks (e.g., Figure A4.11.31, left).

As mentioned earlier, most of the buildings that were most severely damaged were 2- to 3-storey load-bearing masonry structures with a certain antiquity and overall lack of maintenance. The most common weaknesses associated with these typologies are summarised in Section A4.11.8.3. Load-bearing masonry structures with RC slabs and RC frame structures suffered comparatively far less damage (Dimova *et al.*, 2004). The most common failure observed in the former were the cracking and falling of small pieces of plaster, while no major damage was generally observed in the latter. However, Bernardini *et al.* (2005) make reference to a more extensively damaged RC building in Pompegnino, and Dimova *et al.* (2004) mention considerable damage being observed in some relatively new buildings of Pavone, though no further explanations are given regarding their structural typology.

Though not reporting specific numbers, Dimova *et al.* (2004) provide the following detailed descriptions for five villages (or parts of) in terms of EMS-98 (Grünthal, 1998) damage states for different vulnerability classes:

- Vobarno: Dimova *et al.* (2004) classify it as EMS-98 intensity V and enumerate:
 - Very slight non-structural damage (mostly hairline cracks in plaster of the walls) in isolated buildings of vulnerability class A (the most vulnerable, the older masonry structures common of the historical centres) and class B.
 - A vertical crack in a masonry wall and the fall of plaster was observed in one building.
- Collio (small section of the town of Vobarno): Dimova *et al.* (2004) classify it as EMS-98 intensity V-VI and enumerate:
 - Many buildings of vulnerability class A and a few of class B suffered slight non-structural damage, mainly in the form of hairline cracks in the walls, fall of small pieces of plaster, and fall of loose bricks.
 - Cracking of masonry walls observed for a few buildings of vulnerability class A and isolated cases of class B.
 - Failure of one wall of a class C structure due to a non-engineered intervention.
- Pavone (small section of Sàbbio Chiese): Dimova *et al.* (2004) classify it as EMS-98 intensity VI. While stating that the historical centre and some relatively new buildings suffered “considerable damage”, they enumerate the following:
 - Many buildings of class A and a few buildings of class B suffered damage of grade 2.
 - Most buildings of class A and many buildings of class B suffered damage of grade 1.
- Pompegnino (small section of Vobarno): Dimova *et al.* (2004) classify it as EMS-98 VI-VII and enumerate:
 - Isolated buildings of class A suffered damage of grade 3.
 - Many buildings of class A and a few buildings of class B and C suffered damage of grade 2.
 - Many buildings of class B suffered damage of grade 1.
 - Isolated buildings of class C suffered damage of grade 2.

- Clibbio (small section of Sàbbio Chiese): Dimova *et al.* (2004) classify it as EMS-98 VI-VII, just like for Pompegnino, but the detailed enumeration is slightly different in this case:
 - Many buildings of class A and a few buildings of class B suffered damage of grade 2.
 - Most buildings of class A and many buildings of class B suffered damage of grade 1.
 - Isolated buildings of class C suffered damage of grade 2 (e.g., Figure A4.11.31, centre).

Figure A4.11.28 through Figure A4.11.31 show some examples of the damage observed in Pompegnino and Clibbio, the two most-affected locations to which an MCS intensity of VII-VIII was assigned (Bernardini *et al.*, 2005).



Figure A4.11.28. Collapse of masonry wall of poor quality (left) and out-of-plane deformation and cracking of masonry walls (right) in Pompegnino (MCS VII-VIII). From Dimova *et al.* (2004).



Figure A4.11.29. Failure of masonry due to pounding between buildings without seismic joints (left) and disintegration and failure of unconfined masonry under roof structures in Pompegnino (MCS VII-VIII). From Dimova *et al.* (2004).



Figure A4.11.30. Damage to the church of Clibbio (Sàbbio Chiese): general view (left; from Dimova *et al.*, 2004) and detail (right; from Bernardini *et al.*, 2005).



Figure A4.11.31. Fall of plaster and cracking of masonry wall in the school of Sàbbio Chiese (left), damage to infill masonry of an RC building in Clibbio (centre) and damage to load-bearing masonry in the junction between two neighbouring buildings in Salò (right). From Camassi *et al.* (2011; left) and Bernardini *et al.* (2005; centre and right).

Dimova *et al.* (2004) mention partial to severe damage in several schools and kindergartens, as well as severe damage to most churches.

According to Pessina *et al.* (2013), the electricity network, the water supply network and some segments of the secondary road network suffered from heavy damage, but provide no further details. Dimova *et al.* (2004) mention the closure of roads as well.

A4.11.8.3 Observed weaknesses

Dimova *et al.* (2004) mention the following weaknesses of the damaged building stock as having contributed or been responsible for the damage observed:

- Weak connections between unconfined masonry walls and the roofs, which led to the failure of the masonry and, in some cases, of the roof structures due to the loss of support.
- Insufficient in-plane stiffness of floors and roofs that did not allow for the redistribution of horizontal seismic forces across different walls.
- Lack of separation joints between different houses, which led to hammering effects.
- Irregular distribution of stiffness and mass in plan and in height.
- Non-engineered interventions and modifications.
- Weak bell towers.
- Slenderness of façades.
- Low quality of workmanship of masonry walls.

A4.11.8.4 Damage distribution

According to Franceschina *et al.* (2009), the directivity of the finite fault rupture had a significant influence over the asymmetric distribution of macroseismic intensities with respect to the epicentre, with highest intensities being observed to the south-west. While not having enough information to make further inferences, it calls our attention that the higher population density to the south and south-west of the epicentre does not seem to be taken into consideration in their analysis.

Acknowledging that the gathering of statistical data was not finished at the time of their writing, Dimova *et al.* (2004) report numbers of intervention requests and evacuated people for six villages as of 1st December 2004. Figure A4.11.32 summarises these data, showing, in red, the number of inhabitants of the village per intervention request and, in blue, the number of inhabitants per evacuated person. In this map, lower values indicate a higher impact than larger values. It is noted, though, that intervention requests do not necessarily imply that a damage state of significance was verified.

The microtremor study carried out by Massa *et al.* (2009) and described in Section A4.11.3.2 aimed at determining the existence or not of a link between the damage caused by the 2004 Salò earthquake and the site conditions in the area. While the investigation did highlight the role of alluvial deposits, fluvial-glacial deposits and debris fans in the amplification of ground motion, the nonparametric correlation analysis carried out by the authors suggests there is no clear correlation between surface geology and the spatial distribution of damage. As a consequence, Massa *et al.* (2009) conclude that the distribution of the damage observed was more highly influenced by the vulnerability of the building stock in the historic centres of the affected villages than by site conditions.

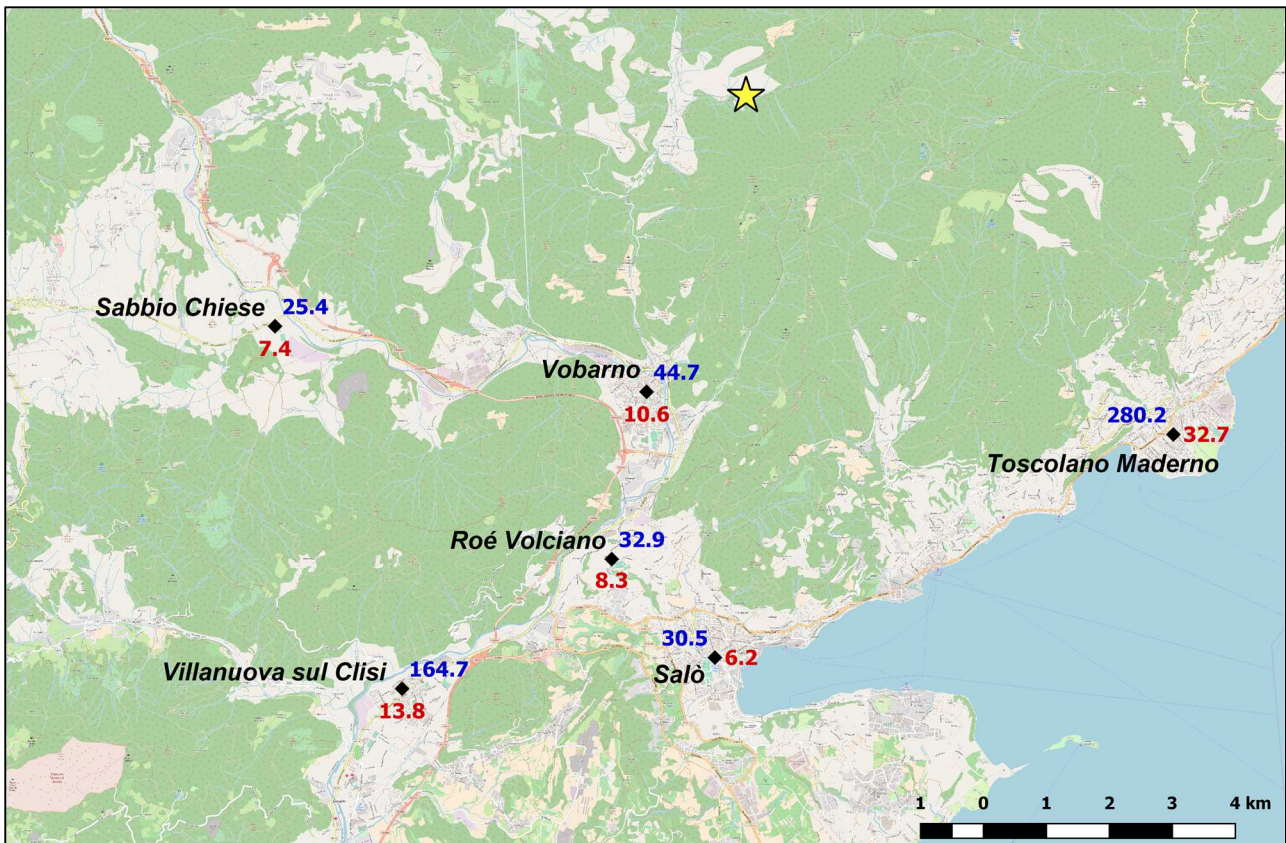


Figure A4.11.32. Number of inhabitants per intervention request (red) and per evacuated person (blue). Yellow star denotes epicentre according to INGV. Data from Dimova *et al.* (2004).

In contrast with the findings of Massa *et al.* (2009), Pessina *et al.* (2006) and Franceschina *et al.* (2009) state that local geological conditions could explain the discrepancies between observed intensities and those obtained from the simulations described in Section A4.11.4.3. However, it is noted that Pessina *et al.* (2006) used empirical relations to convert maximum PGA or PGV values into macroseismic intensities, and that the exact way in which they considered site conditions in their analysis is not clear.

Finally, Franceschina *et al.* (2009) mention the possible influence of soil-structure interaction on the extent of the damage observed, based on ambient noise observations of two damaged buildings and the soil conditions in Pompegnino.

A4.11.9 Casualties and losses

A4.11.9.1 Numbers of dead and injured

All sources agree on the lack of deaths related to this earthquake. However, reports on injuries are more incongruous. The NOAA database reports 9 injured, while the USGS says “at least nine” injured. La Repubblica (2004b), which presents a small chronology of the emergency response right after the earthquake, cites the chief of the Department of Civil Protection talking about 9 injured as well. However, an update from over 5 hours later mentions only 7. Corriere della Sera (2016) reports 7 as well at some point, but then

mentions “some dozens of people” having been slightly injured or bruised in Salò. GardaPost (2016) and La Repubblica (2004a) mention only 5 injured (four in Salò and one in Preseglie). From these discrepancies as well as the descriptions found, it appears that no severe injuries occurred.

A4.11.9.2 Causes of casualties

According to La Repubblica (2004b), one person was injured in Milan due to the fall of a window. According to the same source, the chief of the Department of Civil Protection mentioned someone being hurt by running away and others being hurt by falling debris. Corriere della Sera (2016) mentions one person being hurt while trying to protect a painting from being broken and “many others injured due to similar causes”, without any further specifications.

A4.11.9.3 Estimates of economic losses

Most sources make reference to 66 municipalities having been affected and an overall economic loss of around 215 million euros (e.g., Augliera *et al.*, 2010; Massa *et al.*, 2009; Pessina *et al.*, 2013). A non-scientific summary about seismic risk in the region of Lombardy mentions damage for around 200 million euros and highlights that this amount is significantly smaller than that caused by larger earthquakes in Italy (Regione Lombardia, 2018).

The NOAA database estimates losses in the range between 1 and 5 million United State dollars, which seems unlikely low, given the figures from other sources. This earthquake is not part of the EM-DAT database.

A newspaper article published by GardaPost (2016) on the twelfth anniversary of this earthquake contains a small summary of its financial cost, which is reproduced herein as Table A4.11.11. The reasons for the discrepancy between this final value of over 120 million euros and the aforementioned 215 million euros is not known. As can be observed, almost 50% of the costs is associated to the reparation of private buildings, while almost 30% and 18% correspond to churches and public buildings/infrastructures, respectively. To the authors' knowledge, private buildings insurance against earthquake damage is not compulsory in Italy, even at present time. According to Il sole 24 ore (2017), only 2.2% of Italian residences are currently insured for seismic risk. This translates into a very heavy financial burden that falls on the nation as a whole whenever a damaging event occurs, which is illustrated by the figures in Table A4.11.11. As an incentive to decrease the vulnerability of the building stock, fiscal relief has been agreed for the owners that opt for the seismic upgrade of their buildings (Il sole 24 ore, 2017).

Table A4.11.11. Financial cost of the 2004 Salò earthquake according to GardaPost (2016).

Cause	Amount (€)	Percentage
Autonomous accommodation (rent contribution for displaced persons)	2,252,912	1.9%
First aid interventions	5,194,423	4.3%
Private property restoration interventions	55,203,000	45.6%
Restoration of public buildings and infrastructures	21,260,614	17.6%
Church buildings restoration works	34,874,197	28.8%
Contributions to production activities	609,766	0.5%
Miscellaneous expenses	1,710,072	1.4%
Total amount committed	121,104,984	100%

A4.11.10 Discussion and conclusions

This **M5.0** earthquake occurred on 24th November 2004, at 22.59 UTC (23.59 local time), to the west of Garda Lake in Lombardy, northern Italy. Reaching a maximum MCS intensity of VII-VIII, it caused severe damage in an area that has seen destructive earthquakes in the past but nevertheless features much lower levels of seismicity than other regions in the country. No deaths and only 5 to 12 injuries resulted from this earthquake, despite the extensive material damage to over 4,000 buildings, including private residences, schools, churches and other public buildings. Only partial (not full) collapses were observed, but economic losses amounted to 120 to 215 million euros and at least 40 residential buildings are reported to have needed demolition. Other instances of damage included the fall of chimneys, the shear failure of masonry walls to different extents, the separation of masonry walls from reinforced concrete slabs, the disintegration of masonry supporting roof structures, and different kinds of non-structural damage.

Apart from the proximity to the epicentre, the amplification potential of the alluvial deposits, fluvio-glacial deposits and debris fans, as well as the dynamics of the rupture process, have been identified as relevant factors that explain the extent of the damage observed. However, most sources point at the extreme vulnerability of load-bearing masonry constructions dating from 200 to 300 years that are very common in the historical centres of small Italian towns as the main cause of the large number of affected buildings. The lack of seismic design of these structures combined with lack of maintenance appear to have played a fundamental role.

While landslides that occurred as a consequence of this earthquake caused damage to some houses and roads, they do not appear to have had an extreme relevance for the consequences observed.

A4.11.11References

A4.11.11.1 Bibliography

Afshari, K. & J.P. Stewart (2016). Physically parametrised prediction equations for significant duration in active crustal regions. *Earthquake Spectra* **32**(4), 2057-2081.

Allen, T. I., D. J. Wald, P. S. Earle, K. D. Marano, A. J. Hotovec, K. Lin & M. G. Hearne (2009). An Atlas of ShakeMaps and population exposure catalog for earthquake loss modeling. *Bulletin of Earthquake Engineering* **7**(3), 701-718.

Amadio (2014). *Evoluzione della normativa sismica (Evolution of the seismic norm, in Italian)*, Lecture slides, Department of Engineering and Architecture University of Trieste. Available online at: https://moodle2.units.it/pluginfile.php/84293/mod_resource/content/1/lezione%201.pdf. Last accessed: 24th December 2017.

Augliera P., E. D'Alema, S. Marzorati & M. Massa (2006). *Data set Garda 2004: elaborazione dati, installazione stazioni sismiche (Garda 2004 dataset: data elaboration, seismic stations installation, in Italian)*. Convenzione ProCiv-INGV 2004-2006 - Progetto S3: scenari di scuotimento in are di interesse prioritario e/o strategico, DPC-S3: Deliverable D12, DVD.

Augliera, P., E. D'Alema, S. Marzorati & M. Massa (2010). A strong motion network in northern Italy: detection capabilities and first analysis. *Bulletin of Earthquake Engineering* **8**, 1091-1104.

Balliana F. (2015) – Evoluzione normative sismica: <http://www.ingballiana.it/Normativa.html>. Last accessed: 27th December 2017.

Baroni, C. (2017). Lake Garda: an outstanding archive of Quaternary geomorphological evolution. In Soldati, M. & M. Marchetti (eds.): *Landscapes and landforms of Italy*. Springer International Publishing, 169-179.

Berlusconi, A., M.F. Ferrario, F. Livio, A.M. Michetti, C. Violante, E. Esposito, S. Porfido, P. Fiaccavento, L. Ripamonti & M. Roncoroni. (2013). Quaternary faults and seismic hazard in the Lake Garda area. *Ingegneria Sismica* 1-2, 10-35.

Bernardini, F., R. Camassi, V. Castelli, S. Del Mese, E. Ercolani, L. Giovani, A. Massucci, G. Milana, A. Rossi, A. Tertulliani & M. Vecchi (2005). Rilievo macrosismico del terremoto del Garda del 24 novembre 2004. *Ingegneria Sismica* **XXII**(2), 44-59.

Bommer, J.J., P.J. Stafford & J.E. Alarcón (2009). Empirical equations for the prediction of the significant, bracketed, and uniform duration of earthquake ground motion. *Bulletin of the Seismological Society of America* **99**(6), 3217-3233.

Boschi, E., E. Guidoboni, G. Ferrari, D. Mariotti, G. Valensise, P. Gasperini (2000). Catalogue of strong Italian earthquakes, 461 b.C. to 1997. *Annali di Geofisica* **43**, 609-868.

Camassi, R., A. Rossi, A. Tertulliani, V. Pessina & C. H. Caracciolo (2011). Il terremoto del 30 Ottobre 1901 e la sismicità del versante occidentale del Garda (The 30th October 1901 earthquake and the seismicity of the western sector of Garda Lake, in Italian). *Quaderni di Geofisica* **88**.

CEN (2004). *Eurocode 8: Design of structures for earthquake resistance - Part1: General rules, seismic actions and rules for buildings*. European Committee for Standardization, Brussels, Belgium.

Center for International Earth Science Information Network - CIESIN - Columbia University (2016). *Gridded Population of the World, Version 4 (GPWv4)*. Palisades, NY: NASA Socioeconomic Data and Applications Center. <http://dx.doi.org/10.7927/H4NP22DQ>.

CNR-IRRS & Regione Lombardia – Servizio Geologico (1996). *Determinazione del rischio sismico a fini urbanistici in Lombardia (Determination of seismic risk in Lombardy with urbanistic purposes, in Italian)*, 148 pp.

Dimova, S., E. Mola, P. Negro, A.V. Pinto & A. Colombo (2004). The Garda area (Italy) earthquake of 24 November 2004: A field report. *Report EUR 21513 EN of the European Commission Joint Research Centre, European Laboratory for Structural Assessment (ELSA)*, Ispra, Italy.

Dziewonski, A.M., T.-A. Chou & J. H. Woodhouse (1981). Determination of earthquake source parameters from waveform data for studies of global and regional seismicity. *Journal of Geophysical Research* **86**, 2825-2852.

Ekström, G., M. Nettles & A. M. Dziewonski (2012). The global CMT project 2004-2010: Centroid-moment tensors for 13,017 earthquakes. *Physics of the Earth and Planetary Interiors* **200-201**, 1-9.

Franceschina, G., V. Pessina, D. Di Giacomo, M. Massa, F. Mulargia, S. Castellaro & M. Mucciarelli (2009). La ricostruzione dello scuotimento del terremoto del Garda del 2004 ($M_L=5.2$) (Reconstruction of the ground shaking caused by the 2004 Garda earthquake, in Italian). *Bollettino della Società Geologica Italiana* **128**(1), 217-228.

Giardini, D., G. Grünthal, K.M. Shedlock & P. Zhang (1999). The GSHAP global seismic hazard map. *Annali di Geofisica* **42**(6), 1225-1228.

Grünthal, G. (ed.) (1998). *European Macroseismic Scale 1998 (EMS-98)*. Cahiers du Centre Europeen de Geodynamique et de Seismologie 15, Centre Europeen de Geodynamique et de Seismologie, Luxembourg.

Guidoboni, E. & A. Comastri (2005). *Catalogue of earthquakes and tsunamis in the Mediterranean area from the 11th to the 15th century*. Istituto Nazionale di Geofisica e Vulcanologia, Italy.

Jaiswal, K. & D.J. Wald (2008). *Creating a global building inventory for earthquake loss assessment and risk management*. Open File Report 2008-1160. U.S. Geological Survey, 110p. Available online at: <http://pubs.usgs.gov/of/2008/1160/>.

Luzi, L., R. Puglia, E. Russo & ORFEUS WG5 (2016). *Engineering Strong Motion Database, version 1.0*. Istituto Nazionale di Geofisica e Vulcanologia, Observatories & Research Facilities for European Seismology. doi: 10.13127/ESM.

Massa, M., S. Lovati, D. Di Giacomo, S. Marzorati, E. D'Alema & P. Augliera (2009). A Microtremor Survey in the Area Shooked by the M_L 5.2 Salò Earthquake (North Italy): An Empirical Approach to Determine the Effects of Ground Motions. *Journal of Earthquake Engineering* **13**(7), 1029-1046.

Massa, M. (2010). Selection of Empirical Green's Functions by waveform similarity analysis: An approach to predict ground motion in areas with saturated records. *Bulletin of the Seismological Society of America* **100**(4), 1513-1527.

Massironi, M., D. Zampieri, M. Bianchi, A. Schiavo, & A. Franceschini (2009). Use of PSInSAR™ data to infer active tectonics: Clues on the differential uplift across the Giudicarie belt (Central-Eastern Alps, Italy). *Tectonophysics* **476**(1), 297-303.

Meletti, C. (2007). Progetto S1: proseguimento della assistenza al DPC per il completamento e la gestione della mappa di pericolosità sismica prevista dall'Ordinanza PCM 3274/2003 e progettazione di ulteriori sviluppi, DPC-INGV S1 Project, Final Report, 70 pp. Available online at: http://esse1.mi.ingv.it/data/S1_Rendicontazione_Scientifica_finale_S1.pdf. Last accessed: 17th October 2017.

Meletti C. & V. Montaldo (2007). *Stime di pericolosità sismica per diverse probabilità di superamento in 50 anni: valori di ag* (Seismic hazard estimates for different probabilities of exceedance in 50 years: values of ag, in Italian). Progetto DPC-INGV S1, Deliverable D2. Available online at: <http://esse1.mi.ingv.it/d2.html>. Last accessed: 17th October 2017.

Michetti, A.M., F. Livio, K. Chunga, E. Esposito, D. Fanetti, R. Gambillara, S. Martin, F. Pasquaré, S. Porfido, G. Sileo & E. Vittori (2005). Ground effects of the M_L 5.2, November 24, 2004, Salò earthquake, Northern Italy, and the seismic hazard of the western Southern Alps. *Rendiconti della Società Geologica Italiana* **1**, 134-135.

Norme Tecniche per le Costruzioni (NTC), Gazzetta Ufficiale della Repubblica Italiana, n. 29 del 4 febbraio 2008 – Suppl. Ordinario n. 30 (NTC, 2008). Available online at: http://www.cslp.it/cslp/index.php?option=com_docman&task=doc_download&gid=3269&Itemid=10. Last accessed: 17th October 2017.

Pergalani, F., M. Compagnoni & V. Petrini (2005). Confronti tra l'utilizzo di accelerogrammi generati e registrati nella valutazione dei fenomeni di amplificazione sismica in Lombardia (Comparisons between the use of synthetic and recorded accelerograms in the evaluation of seismic amplification phenomena in Lombardy, in Italian). *Ingegneria Sismica* **3**(22), 36-51.

Pessina, V., G. Franceschina, P. Vannoli, L. Luzi & F. Pacor (2006). Damage distribution and seismological model of the November 24, 2004, Salò (Northern Italy) earthquake. *First European Conference on Earthquake Engineering and Seismology*, Geneva, Switzerland, 3-8 September.

Pessina, V., G. Franceschina, P. Augliera, M. Massa, D. Di Giacomo, S. Marzorati, E. D'Alema, S. Lovati & F. Pacor (2007). *Task 4 – Garda - Deliverable D13 – Scenari di scuotimento al bedrock a vari livelli di complessità* (Shaking scenarios at bedrock with different complexity levels, in Italian). DPC-S3 Project of the Civil Protection Direction, Italy.

Pessina, V., A. Tertulliani, R. Camassi, A. Rossi & G. Scardia (2013). The revision of the October 30, 1901 earthquake, west of Lake Garda (northern Italy). *Bollettino di Geofisica Teorica ed Applicata* **54**(1), 77-110.

Pondrelli, S., S. Salimbeni, G. Ekström, A. Morelli, P. Gasperini & G. Vannucci (2006). The Italian CMT dataset from 1977 to the present. *Physics of the Earth and Planetary Interiors* **159**(3-4), 286-303. Data available at: <http://rcmt2.bo.ingv.it/Italydataset.html>. Last accessed: 2nd May 2018.

Regione Lombardia (2002). *CD Progetto di Cartografia geoambientale, dati vettoriali, scala 1:10000* (Project of geo-environmental mapping, vector data, scale 1: 10000, CD in Italian). Comunità Montana Val Sabbia.

Rovida, A., M. Locati, R. Camassi, B. Lolli & P. Gasperini (2016). *CPTI15, the 2015 version of the Parametric Catalogue of Italian Earthquakes*. Istituto Nazionale di Geofisica e Vulcanologia, Italy. doi: <http://doi.org/10.6092/INGV.IT-CPTI15>.

Scardia, G., A. Festa, G. Monegato, R. Pini, S. Rogledi, F. Tremolada & F. Galadini (2015). Evidence for late Alpine tectonics in the Lake Garda area (northern Italy) and seismogenic implications. *Geological Society of America Bulletin* **127**(1-2) 113-130.

Sieberg, A. (1932). Geologie der Erdbeben. *Handbuch der Geophysik* **2**(4), 550-555.

United Nations, ed. (2006). *Human Development Report 2006 – Beyond scarcity: Power, poverty and the global water crisis*. Report of the United Nations Development Program (UNDP), New York, United States.

United Nations, ed. (2016). *Human Development Report 2016 – Human Development for everyone*. Report of the United Nations Development Program (UNDP), New York, United States.

Wald, D.J. & T.I. Allen (2007). Topographic slope as a proxy for seismic site conditions and amplification. *Bulletin of the Seismological Society of America* **97**, 1379–1395. Slope-based online map viewer available at: <http://usgs.maps.arcgis.com/apps/webappviewer/index.html?id=8ac19bc334f747e486550f32837578e1>.

Weatherill, G. A. (2014). *OpenQuake ground motion toolkit - User guide*. Global Earthquake Model (GEM). Technical Report.

Wells, D.L. & K.J. Coppersmith (1994). New empirical relationships among magnitude, rupture length, rupture width, rupture area, and surface displacement. *Bulletin of the Seismological Society of America* **84**, 974-1002.

Woessner, J., D. Giardini, H. Crowley, F. Cotton, G. Grünthal, G. Valensise, R. Arvidsson, R. Basili, M. B. Demircioglu, S. Hiemer, C. Meletti, R. W. Musson, A. N. Rovida, K. Sesetyan, M. Stucchi & The SHARE Consortium (2015). The 2013 European Seismic Hazard Model: Key Components and Results. *Bulletin of Earthquake Engineering* **13**(12), 3553–3596. Available online at: <http://www.efehr.org/en/home/>. Last accessed: 2nd May 2018.

Worden, C.B., M.C. Gerstenberger, D.A. Rhoades & D.J. Wald (2012). Probabilistic relationships between ground-motion parameters and Modified Mercalli Intensity in California. *Bulletin of the Seismological Society of America* **102**(1), 204-221.

A4.11.11.2 Web references

Corriere della Sera (2016) (last accessed 7th May 2018):

http://brescia.corriere.it/notizie/cronaca/16_agosto_25/terremoto-salo-lago-garda-brescia-2004-giornali-epoca-20da50fe-6abd-11e6-a743-cbace9857496.shtml?refresh_ce-cp

Department of Civil Protection (DPC, 2015) – Classificazione Sismica al 2015 (2015 Seismic Classification, in Italian) (last accessed 2nd May 2018):

Explanation: <http://www.protezionecivile.gov.it/jcms/it/classificazione.wp>.

Map: http://www.protezionecivile.gov.it/resources/cms/documents/A3_class20150416_r.pdf.

EM-DAT – The Emergency Events Database (Université Catholique de Louvain, Brussels, Belgium; Cred. Prof. Dr. D. Guha-Sapir): <http://www.emdat.be/>. Last accessed: 4th April 2018.

European-Mediterranean Seismological Centre (last accessed 2nd May 2018):

<https://m.emsc.eu/earthquake/earthquake.php?id=1459>.

EPOS Seismic Portal (2018) (last accessed 2nd May 2018):

http://www.seismicportal.eu/eventdetails.html?unid=20041124_0000024.

GardaPost (2016): <https://www.gardapost.it/2016/11/24/dodici-anni-fa-il-terremoto-di-salo/>. Last accessed: 5th May 2018.

GISTAT – Geographic Information System of the Italian National Statistics Institute (Istituto Nazionale di Statistica) (2018): <http://gisportal.istat.it/mapparischi/index.html?extent>. Last accessed 3rd May 2018.

Global Centroid Moment Tensor Project (GCMT): <http://www.globalcmt.org>. Last accessed: 9th May 2018.

Il sole 24 ore (2017) (last accessed 10th November 2017):

<http://www.ilsole24ore.com/art/impresa-e-territori/2017-08-21/rischio-terremoto-assicurato-solo-2percento-abitazioni-082738.shtml?uuid=AECSZXBC>.

INGV-Zone Sismiche (2006). Ordinanza PCM 3519 del 28 aprile 2006, All. 1b. Pericolosità sismica di riferimento per il territorio nazionale (Reference seismic hazard for the national territory, in Italian): <http://zonesismiche.mi.ingv.it>. Last accessed: 2nd May 2018.

INGV-Archivio Storico Macrosismico Italiano (Italian Historic Macroseismic Archive), this earthquake: https://emidius.mi.ingv.it/ASMI/event/20041124_2259_000. Last accessed: 2nd May 2018.

Istituto Nazionale di Geofisica e Vulcanologia – National Institute of Geophysics and Volcanology of Italy (INGV): <http://www.ingv.it/>. Last accessed: 16th February 2018.

La Repubblica (2004a) (last accessed 7th May 2018): <http://www.repubblica.it/2004/k/sezioni/cronaca/sismanord/sismanord/sismanord.html>.

La Repubblica (2004b) (last accessed 7th May 2018): <http://www.repubblica.it/2004/k/dirette/sezioni/cronaca/terrenord/terrenord/index.html?ref=search>.

Mapsland (2018) – Map of Italian topography: <https://www.mapsland.com/europe/italy/detailed-topography-map-of-italy>. Last accessed: 2nd May 2018.

National Geophysical Data Center / World Data Service (NGDC/WDS): Significant Earthquake Database. National Geophysical Data Center, National Oceanic and Atmospheric Administration (NOAA). DOI:10.7289/V5TD9V7K. <https://www.ngdc.noaa.gov/hazard/earthqk.shtml>. Last accessed: 24th December 2017.

Regione Lombardia (2018): <http://www.regione.lombardia.it/wps/wcm/connect/d6c07d07-95d0-4d13-a729-d87b93bf69f5/dossier.rischio.sismico.pdf?MOD=AJPERES&CACHEID=d6c07d07-95d0-4d13-a729-d87b93bf69f5>. Last accessed: 5th May 2018.

Statista (2018): <https://www.statista.com/statistics/658274/gross-domestic-product-gdp-per-capita-of-italy-by-region/>. Last accessed: 7th May 2018.

The World Bank Group (2017). World Bank Open Data: <http://data.worldbank.org>. Last accessed: 6th November 2017.

United States Geological Survey (USGS):
Website for this earthquake (last accessed 2nd May 2018):
<https://earthquake.usgs.gov/earthquakes/eventpage/usp000d94i#executive>.

Urbistat (2017): <https://ugeo.urbistat.com/AdminStat/it/it/demografia/popolazione/brescia/17/3>. Last accessed: 30th May 2017.

Wikipedia (2017): https://it.wikipedia.org/wiki/Classificazione_sismica_dell%27Italia (Italian seismic zonation, in Italian). Last accessed: 24th December 2017.

World Economic Outlook Database (2016):
<https://www.imf.org/external/pubs/ft/weo/2016/02/weodata/download.aspx>.
Last accessed: 6th November 2017.

Zainoo (2018): <https://www.zainoo.com/en/italy/lake-garda/geography-economy>.
Last accessed: 7th May 2018.

A4.12. April 2007 M4.0 Folkestone Earthquake, United Kingdom

This earthquake occurred on 28th April 2007, at 07:18 UTC (08.18 local time), and was the largest seismic event in the Dover Strait area since 9th January 1950. It was followed by 12 aftershocks with the last one occurring on 5th May. It caused damage to chimneys, brick masonry walls and plaster in the town of Folkestone, around 2 km away from the epicentre, and resulted in five roads evacuated and one injured person. It was the first time that emergency procedures were invoked by British authorities for a seismic event.

A4.12.1 Tectonic and seismic setting

A4.12.1.1 Tectonic setting

The United Kingdom (UK) is an intraplate island located along the West side of the Eurasian plate. Its seismicity and tectonic setting are affected by the collision between the African and Eurasian plates to the south and the divergence between the Eurasian and North American plates to the west of the country. These plate tectonic movements are responsible for the northwest-southeast oriented compressive stresses to which England and Wales are subject (Baptie, 2010; Chadwick *et al.*, 1996; Musson & Sargeant, 2007). The Variscan Front, which represents the northern extent of the Variscan Orogenic Belt and spans from southern Ireland to Northern France, determines the tectonic settings of the southern part of the country, where Folkestone is located. The regional tectonics of Folkestone and the Dover Strait area are dominated by this southwest dipping Variscan Front thrust with NW-SE orientation, as depicted in Figure A4.12.1 (Baptie, 2008a).

Folkestone lies along the boundary between the Mesozoic Weald Basin and the London-Brabant Massif. The former hosts faults that strike mainly northwest to southeast and are believed to have rejuvenated from Variscan thrusts (Lamplugh *et al.*, 1923; Plumtre, 1959), while the basement of the latter is expected to contain similarly-striking faults related to the Caledonian Orogeny. The Kent coalfield, which occupies a Carboniferous basin, underlies the Folkestone area and is bounded by the Variscan Front to the south (Dines, 1933; Bouroz, 1962).

Ottmöller *et al.* (2009) identify a northwest-trending fault believed to be connected to the Sangatte fault in the Dover Strait and mapped during the investigations carried out for the project of the Channel Tunnel (Warren & Harris, 1996) as the closest fault to the Folkestone earthquake. It represents the border between two blocks of the Variscan Front, and it is believed to dip west and cut through the Variscan unconformity (Warren & Harris, 1996; Ottmöller *et al.*, 2009). It is noted, however, that attribution of earthquakes to specific faults is particularly difficult in low-seismicity intraplate areas and that, due to its lack of continuous active deformation, the UK has no controlling faults (Musson, 2007).

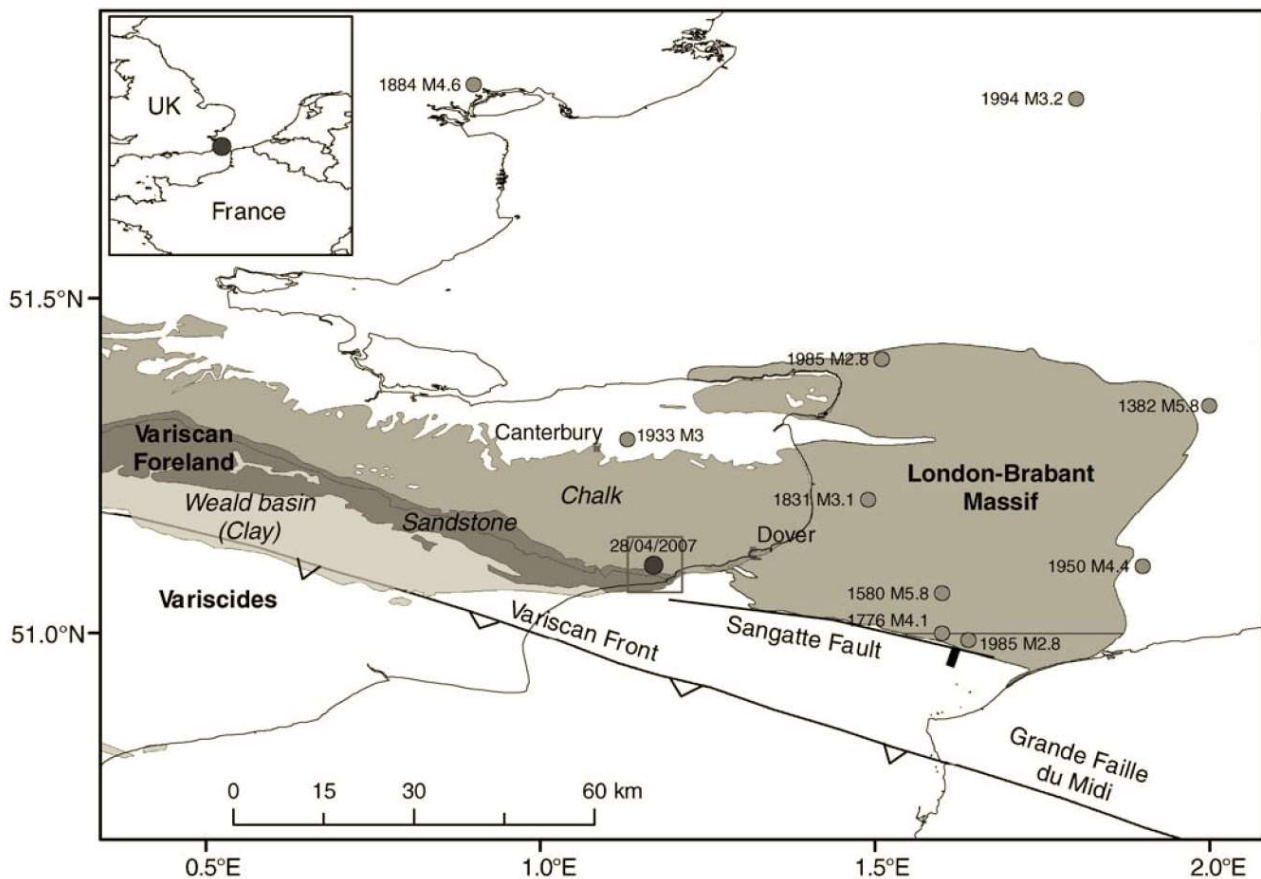


Figure A4.12.1. Tectonic map of the Folkestone Area. The epicentral locations of Folkestone earthquake and earthquakes with $M_L > 2.5$ are given by circles. From Ottemöller *et al.* (2009).

A4.12.1.2 Regional and local seismicity

Being an intraplate area, the seismicity of the UK is generally low (Musson & Sargeant, 2007). Documentation of seismic activity in the country exists for both the instrumental and historical periods, with increased rates being characteristic of the west (e.g. north-western England, western Scotland, Wales, Midlands, Cornwall, *etc.*) and the eastern part of the UK being associated with lower levels of seismicity. Nevertheless, the largest known – 1931 Dogger Bank (M_L 6.1) – and the most damaging – 1884 Colchester (M_L 4.6) – British earthquakes have occurred in the eastern part of the country (Baptie, 2008a; Sargeant *et al.*, 2008; Ottemöller *et al.*, 2009). Earthquakes of the size of the 1884 seismic event and greater occur every four years in the UK (Musson, 1994; Ottemöller *et al.*, 2009).

Until 2007, no earthquakes had been detected in the Folkestone area since the extensive installation of recording instruments with the capability to detect small-magnitude events in the late 1960s (Lovell & Henni, 1999; Musson, 2007). However, the Dover-Strait area is associated with a few historical seismic events, such as the earthquakes of 1382, 1449, 1580, 1776 and 1950 (Musson, 1994; Melville *et al.*, 1996; Musson & Winter, 1997). Both with estimated magnitudes of 5.8, the 1382 and the 1580 Dover Strait earthquakes were two of the largest British earthquakes in the historical record, and caused damage in an area spanning up to London (Baptie, 2008a; Musson & Walker, 2007). The epicentres of the earthquakes that happened in Kent and Dover-Straits from 1382 until the date of the Folkestone (2007) seismic event are depicted in Figure A4.12.2. The 2007 Folkestone

earthquake was the largest earthquake in Dover Strait region since 1950 (M_L 4.4) and the largest onshore seismic event that happened in the UK since the 2002 M_L 4.7 Dudley earthquake (Baptie *et al.*, 2005; Baptie, 2008a).

Whittaker *et al.* (1989) indicate that seismicity of the Dover Strait area might arise from the Belgian earthquake zone extending from the Lower Rhine graben westward across Belgium. However, as Chadwick *et al.* (1996) point out, relating seismicity to the geological settings of the UK represents a complex task. The reactivation of geological structures is related rather to their suitable orientation with respect to the present stress field than to the simple displacements associated with fault slipping.

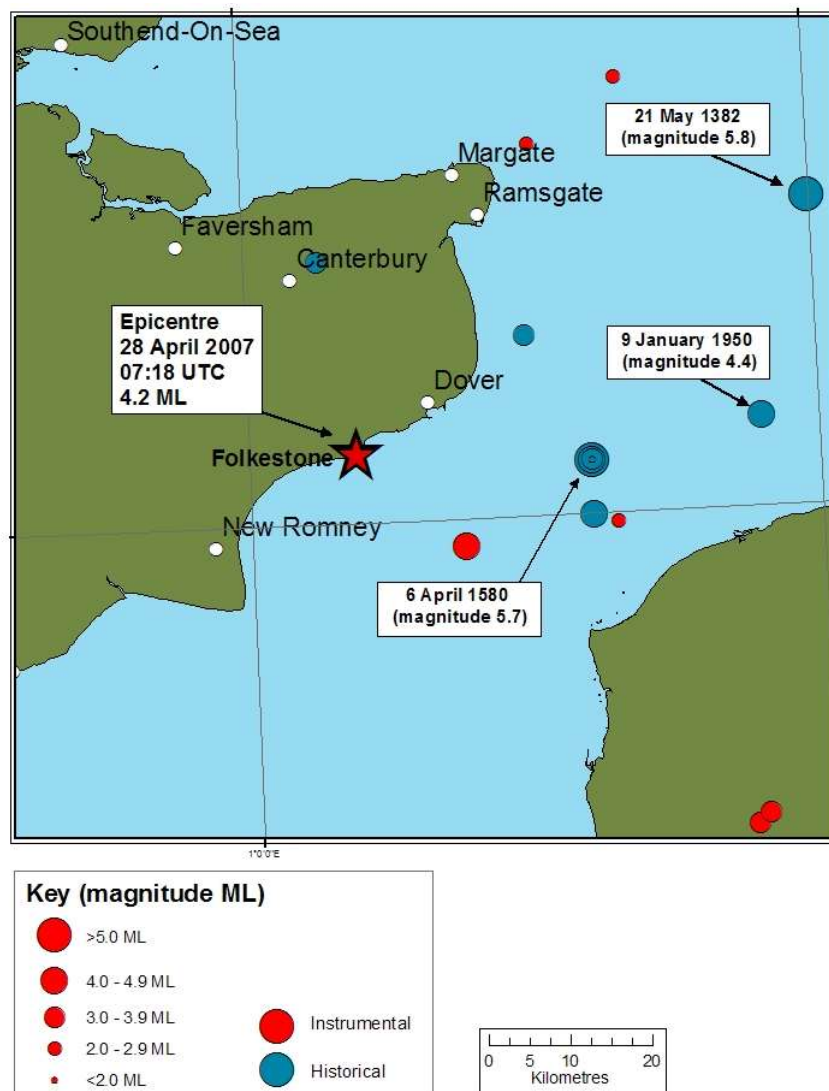


Figure A4.12.2. Historical and instrumental seismicity within 50 km of the Folkestone earthquake of 28 April 2007. Map includes seismic events from 1382 until 28 April 2007. From BGS (2007).

A4.12.1.3 Seismic hazard

The elaboration of the UK national seismic hazard map is managed by the British Geological Survey (BGS), the final goal being that of defining seismic zones to be used with Eurocode 8 (CEN, 2004). The official seismic hazard map (at the time of writing) representing the (geometric mean) peak ground acceleration (PGA) on rock with a 10% probability of

exceedance in 50 years (475 year return period) is shown in Figure A4.12.3 (left). Having been published in 2007, the catalogue used for its elaboration did not include the 2007 Folkestone earthquake. This map indicates values of PGA in the range between 0.00 g and 0.02 g for the Folkestone area. As a consequence of the overall low seismicity of the country, the delineation of areas with higher and lower seismic hazard only becomes visible considering lower probabilities of exceedance, such as on the map on the right of Figure A4.12.3, which clearly shows the difference between the western and eastern regions, as described earlier. According to this map, the values of PGA on rock with a 2% probability of exceedance in 50 years rise only to the range between 0.02 g and 0.04 for Folkestone. It is noted that using a minimum magnitude of **M4.5** might be resulting in a large proportion of the seismic activity of the UK being excluded from the model (Musson & Sargeant, 2007).

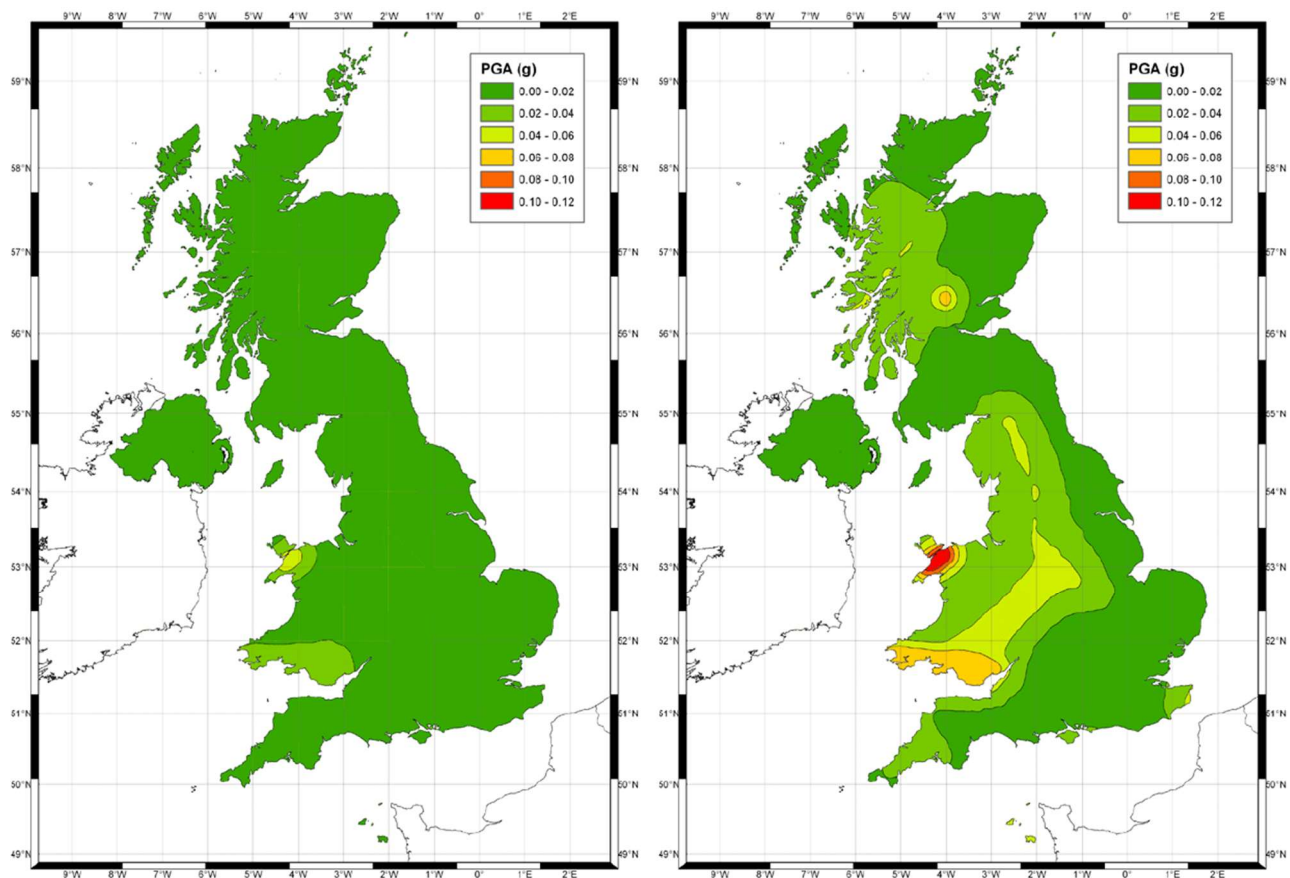


Figure A4.12.3. Peak ground acceleration (g) on rock with a 10% probability of exceedance in 50 years (475 years return period, left) and a 2% probability of exceedance in 50 years (2,500 years return period, right) for the United Kingdom. From Musson & Sargeant (2007).

Figure A4.12.4 shows the uniform hazard spectrum on rock with a 10% probability of exceedance in 50 years for coordinates 51.100 N and 1.182 E, which corresponds approximately to the location of Folkestone, according to the Seismic Hazard Harmonization in Europe (SHARE) project (Woessner *et al.*, 2015). As can be observed on the plot, the expected PGA on rock with a 10% probability of exceedance in 50 years is 0.025 g, which is slightly larger than the upper value of the range given by the national hazard map of the UK. According to the results from the Global Seismic Hazard Assessment Program (GSHAP), this value is 0.05 g for the Folkestone area (51.1N; 1.2E) (Giardini *et al.*, 1999).

All these results confirm the low levels of seismic hazard expected, which are in line with generally low levels of seismicity related to an intraplate area, far from any tectonic boundaries, within which the UK is positioned.

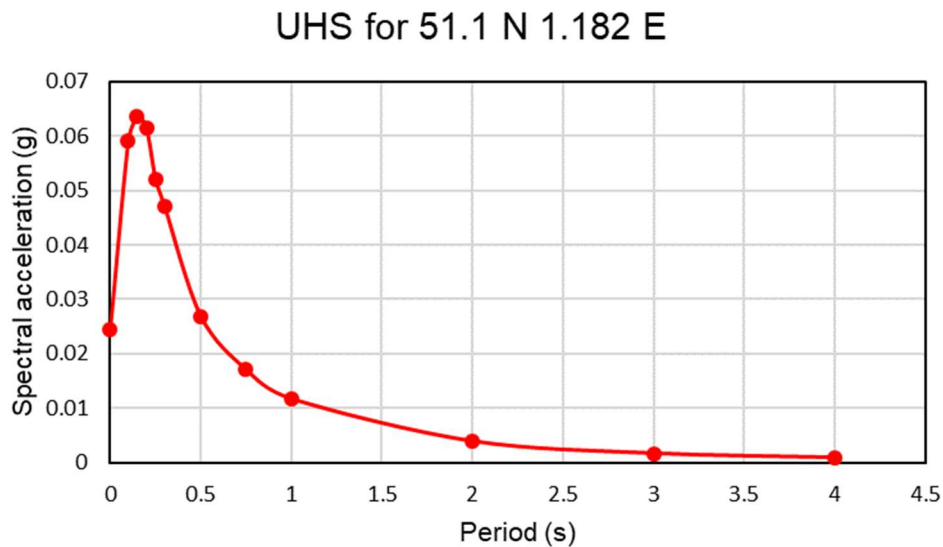


Figure A4.12.4. Uniform Hazard Spectrum for point 51.100 N and 1.182 E (corresponding, approximately, to the Folkestone area) according to SHARE, representing spectral acceleration values on rock with a 10% probability of exceedance in 50 years.

A4.12.2 Earthquake source characteristics

A4.12.2.1 Location, depth and time

The main shock occurred on 28th April 2007, at 07.18 UTC (08.18 local time).

The earthquake was recorded on many seismic stations within the UK as well as on stations spanning from Norway to Spain. This good azimuthal station coverage allowed for the determination of epicentral coordinates by the British Geological Survey (BGS) with a horizontal error of the order of 5 km (Otermöller *et al.*, 2009). Epicentral coordinates and focal depths reported in the websites of British Geological Survey (BGS), National Earthquake Information Center (NEIC) of the United States Geological Survey (USGS), International Seismological Centre (ISC) and European-Mediterranean Seismological Centre (EMSC) are given in Table A4.12.1 and shown on the map in Figure A4.12.5 (left). The 90% epicentral error ellipses computed by the BGS and the USGS, as plotted by Otermöller *et al.* (2009), are presented, in turn, in Figure A4.12.5 (right).

The presented BGS solution was calculated through local travel-time inversion by Otermöller *et al.* (2009), who also considered other ways of hypocentral depth assessment (*i.e.* moment tensor inversion, teleseismic depth phase and regional phase modelling) and concluded that 5.0 ± 2.0 km is their best estimate.

Table A4.12.1. Epicentral coordinates and hypocentral depths from different sources.

Agency / Publication		Latitude	Longitude	Depth (km)
BGS	British Geological Survey	51.1020 ° N	1.1690 °E	5.30
NEIC	National Earthquake Information Center, USGS	51.0850 ° N	1.0090 °E	10.00 (*f)
ISC	International Seismological Centre	51.0582 ° N	1.0721 °E	1.30
EMSC	European-Mediterranean Seismological Centre	51.0400 ° N	1.0000 °E	10.00

(*f) fixed parameter used for inversion

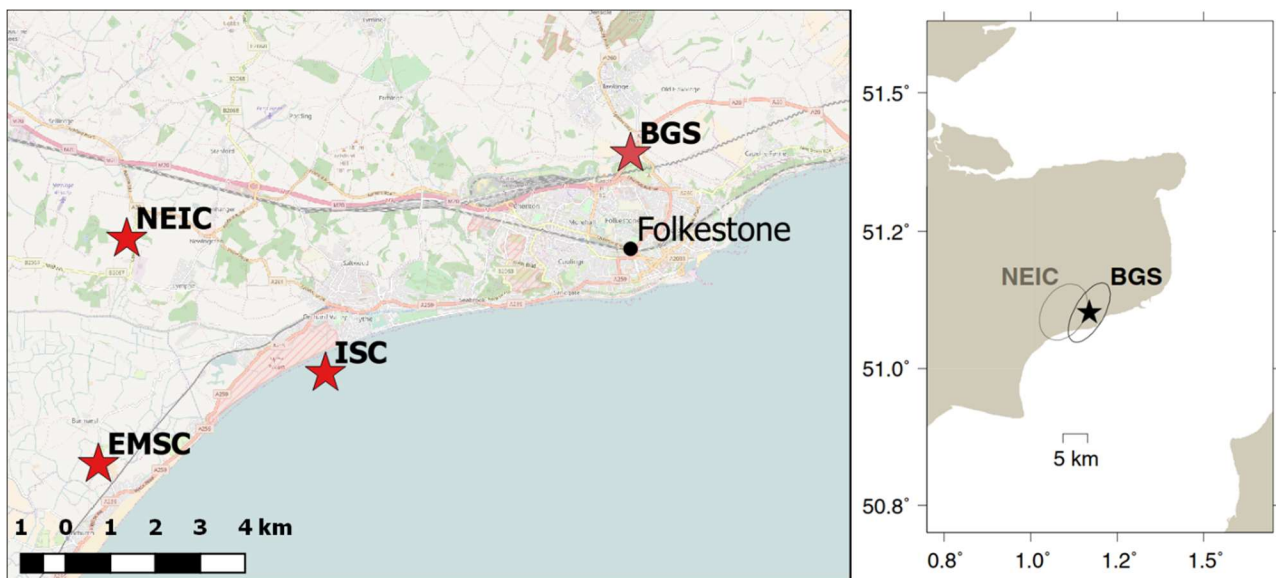


Figure A4.12.5. Estimations of epicentral coordinates (left) and epicentral error ellipse computed by BGS and NEIC (right, from Ottemöller *et al.*, 2009).

A4.12.2.2 Magnitude

Estimations of magnitude made by the same agencies are reported in Table A4.12.2.

The moment magnitude **M**4.0 and local magnitude M_L 4.3 reported in the website of the BGS were determined by Ottemöller *et al.* (2009) through moment tensor inversion. The local magnitude was computed based on the California scale of Hutton & Boore (1998), as it is the default one used in the UK. Ottemöller *et al.* (2009) also calculated the moment magnitude by means of spectral analyses and obtained a value of **M**3.8.

Table A4.12.2. Estimations of moment magnitude (M), body-wave magnitude (mb) and local magnitude (M_L).

Agency		M	mb	M_L
BGS	British Geological Survey	4.0	-	4.3
NEIC	National Earthquake Information Center, USGS	-	4.6	-
ISC	International Seismological Centre	-	4.6	-
EMSC	European-Mediterranean Seismological Centre	-	4.7	-

A4.12.2.3 Style-of-faulting

The moment tensor inversion solution of the BGS indicates a strike-slip mechanism with a strong normal component (Figure A4.12.6 and Table A4.12.3) (Ottemöller *et al.*, 2009). The nodal planes are indicating either right-lateral displacement on a plane striking WSW-ENE, or left-lateral displacement on a plane striking NNW-SSE. The NNW-SSE striking nodal plane conforms with the direction of the main faults affecting the Kent coalfield and the Variscan front, and consequently suggest a sub-structure of the latter as the causative fault. However, taking into account that the source radius is only 0.5 kilometres and that there is large uncertainty associated to the exact geometry of the Variscan front in the area around Folkestone, Ottemöller *et al.* (2009) remark that both striking planes should be considered as a possible solution.

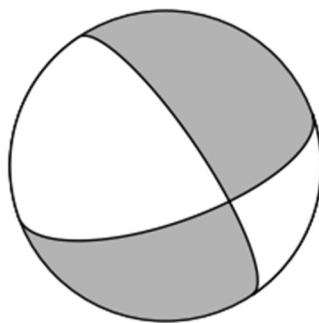


Figure A4.12.6. Focal mechanism for the Folkestone earthquake according to the BGS.

Table A4.12.3. Fault plane solutions and fault planes from BGS (2007).

Fault Plane 1			Fault Plane 2			Source
Strike	Dip	Rake	Strike	Dip	Rake	
326	69	-36	71	57	-155	British Geological Survey (BGS)

A4.12.2.4 Stress drop

Ottemöller *et al.* (2009) determined the stress drop of the mainshock from displacement source spectra using near surface attenuation from the aftershocks. The value of the calculated stress drop is 2.86 ± 2.40 MPa (28.6 ± 24 bars). Baptie (2008b) and Ottemöller & Sargeant (2010) also report a value of the stress drop of 3 MPa (30 bars) and 3 ± 3.4 MPa (30 ± 34 bars), respectively. This level of stress drop is much lower than 100 bars, which corresponds to a typical value observed from other intraplate earthquakes (Atkinson & Boore, 2006; Lay & Wallace, 1995).

A4.12.2.5 Foreshocks and aftershocks

According to Ottemöller *et al.* (2009) and the earthquake database of the BGS, the main shock was followed by twelve aftershocks with local magnitudes in the range between M_L 0.8 and M_L 1.7, their magnitudes having been calculated assuming that they have occurred

at the same location as the mainshock, due to eleven of them having been recorded only by the closest station, TFO, and only one counting with three different recordings. Sargeant *et al.* (2008), in contrast, mention only nine aftershocks in the range M_L 1.0 to M_L 1.8, and highlight that none were felt. Analysis of the cross correlation of aftershock waveforms by Ottemöller *et al.* (2009) shows that the mechanism is not necessarily the same for them all. A list of the aftershocks, date of their occurrence and magnitude is given in Table A4.12.4, while assuming their location being the same as that of the main shock.

While there is no evidence of foreshocks, several residents in the Folkestone area stated that they felt slight tremors in weeks before the mainshock (Kent News, 2007a).

Table A4.12.4. List of aftershocks with locations fixed to the main shock location (BGS).

Date	Time	Latitude	Longitude	Depth	Magnitude
28.04.2007	7:20	51.1020 ° N	1.1690 °E	5.3	1.7
28.04.2007	7:24	51.1020 ° N	1.1690 °E	5.3	1.1
28.04.2007	8:40	51.1020 ° N	1.1690 °E	5.3	1.0
28.04.2007	11:11	51.1020 ° N	1.1690 °E	5.3	1.7
28.04.2007	15:28	51.1020 ° N	1.1690 °E	5.3	0.9
29.04.2007	6:51	51.1020 ° N	1.1690 °E	5.3	1.4
29.04.2007	13:17	51.1020 ° N	1.1690 °E	5.3	0.8
01.05.2007	7:36	51.1020 ° N	1.1690 °E	5.3	1.4
02.05.2007	21:50	51.1020 ° N	1.1690 °E	5.3	1.5
02.05.2007	21:51	51.1020 ° N	1.1690 °E	5.3	1.4
04.05.2007	7:01	51.1020 ° N	1.1690 °E	5.3	1.3
05.05.2007	5:09	51.1020 ° N	1.1690 °E	5.3	1.2

A4.12.2.6 Nature of earthquake

The focal mechanism solution is indicating that the striking fault direction is in alignment with the main structures affecting the Variscan Front, and most of the authors do not question its tectonic origin. However, this earthquake has been included within the database of human-induced earthquakes of Wilson *et al.* (2017), who make reference to the possible triggering of the event by the change in gravitational stress components caused by increasing shingle accumulation in the harbour since 1806, as indicated by Klose (2007). According to the latter, by 2007 there was around 2.8×10^9 kg of accumulated material, which altered the stress at 2 km depth by 0.001-0.03 MPa.

A4.12.3 Geology and ground conditions in the affected area

A4.12.3.1 Regional geology and topography

Folkestone city lies in a valley between two cliffs, namely, the West and the East cliff. It is located in the southern boundary of the North Downs, which represent the ridge of chalk hills in the south-eastern part of the UK. The geology of this part of the UK consists of a deep Palaeozoic Platform overlaid by the deposits of the Mesozoic era (Jurassic and Cretaceous). The surface geology is related to the upper cretaceous rocks (Folkestone & Hythe Birds, 2017). The rock layers on which Folkestone is settled were deposited on the floor of the prehistoric shallow sea that existed at this part of Europe during the Cretaceous period (Warshaw *et al.*, 2006). The outcrops of the East cliff are the evidence of the Greensand beds, which were the first ones to be deposited on the shallow sea. The change of the chemical content of the sea resulted in deposits of Gault clay which have high content of fossil ammonites. Lastly, the late cretaceous Chalk Formations were created, forming the North Downs (Warshaw *et al.*, 2006).

The bedrock geology map of south-eastern part of the UK, downloaded from the website of the British Geological Survey (BGS, 2017), is presented in Figure A4.12.7. In the area surrounding Folkestone, the aforementioned layers of lower Greensand Formation, Gault Formation and Chalk can be observed. The grey chalk and white chalk subgroups can be easily identified, with the former being more evident in the high cliffs around Folkestone and the latter being more present at the eastern area surrounding the city of Dover.



Figure A4.12.7. Bedrock geology for the south-eastern part of the United Kingdom (BGS). Red star indicates the epicentre (according to the BGS); triangle indicates TFO station. From BGS (2017).

A4.12.3.2 Site conditions in the affected area

Superficial geology maps available from the website of the British Geological Survey (BGS, 2017) show that the area around Folkestone in south-eastern UK is covered by a formation of clay with flints, as well as brickearth and silt, all of which are superficial deposits from the Quaternary period, dating up to 5 million years. It is noted that silica flints observed in this area are probably accumulated in the chalk after its formation, which could be evidenced in the chalk cliffs present in Folkestone area (Folkestone & Hythe Birds, 2017).

According to the online map viewer of the website of the United Kingdom Soil Observatory (UKSO, 2017), the Folkestone area is mainly covered by sandstone and residual clay, more specifically, “sand to sandy loam and clay to clayey loam”. According to the same website, the sedimentary soil layers are expected to be of intermediate-to-deep depth. This is in agreement with the soil map available from the online Soilcapes map viewer of the Land Information System website (LandIS, 2017), which is presented in Figure A4.12.8 and indicates that Folkestone lies over “freely draining slightly acid loamy soils”, and the river bed consisting of “slowly permeable seasonally wet slightly acid but base-rich loamy and clayey soils”.

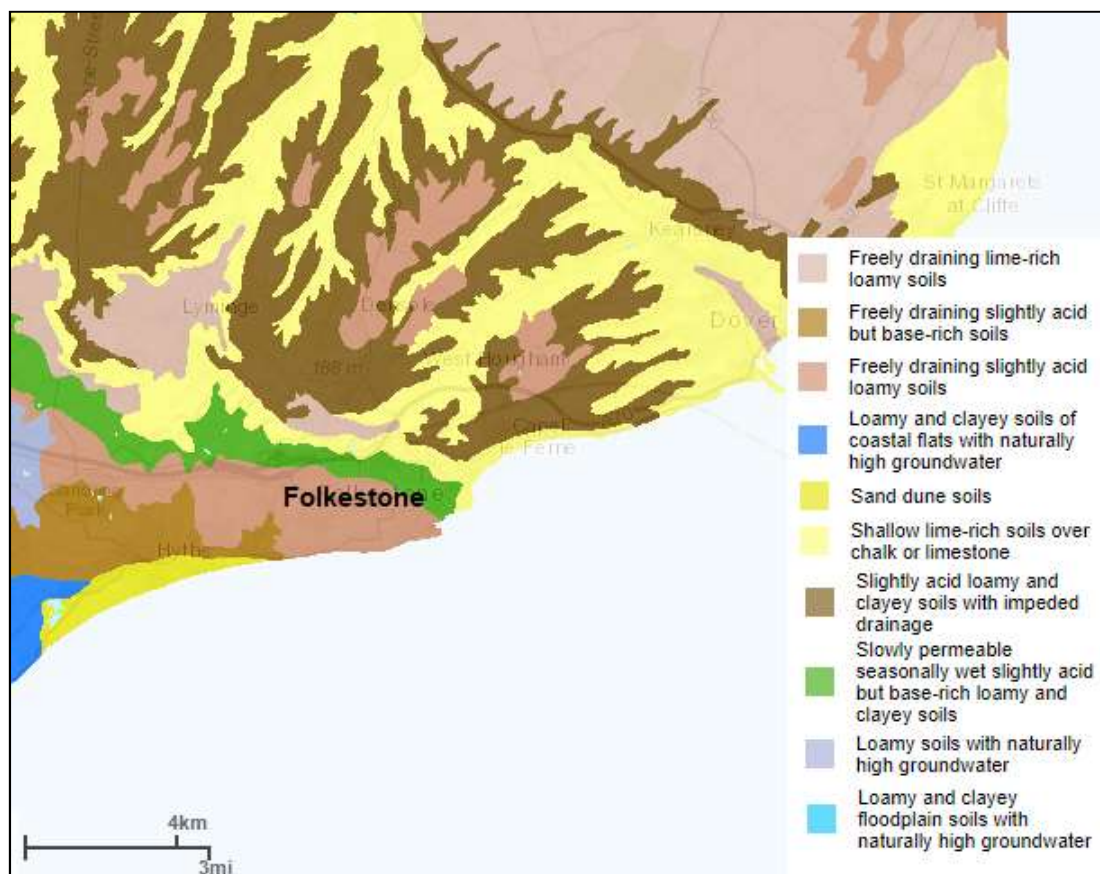


Figure A4.12.8. Soil map of the Folkestone area. From LandIS (2017).

Figure A4.12.9 shows the P-wave velocity model for the Folkestone area constructed by Ottemöller *et al.* (2009) combining data from different sources. The plot indicates the presence of chalk, sandstone, mudstone and limestone in the shallower layers corresponding to Mesozoic deposits.

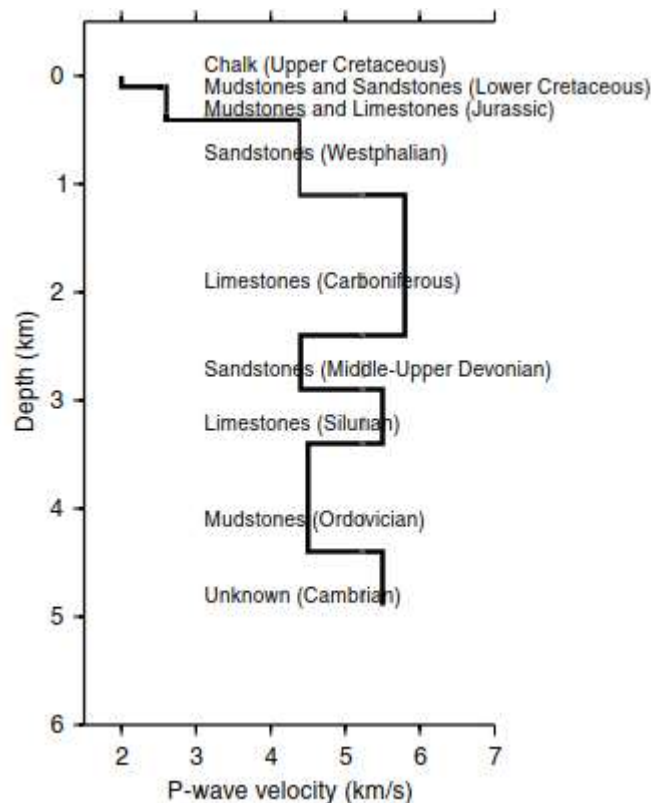


Figure A4.12.9. Shallow P-wave velocity model for Folkestone. Modified from Ottemöller *et al.* (2009).

Figure A4.12.10 depicts the average shear wave velocity to a depth of 30 meters (V_{s30}) for the studied area, as calculated by the United States Geological Survey V_{s30} Map Server using topographic slope as a proxy (Wald & Allen, 2007). It can be seen that velocities in the range between 300 and 400 m/s are measured at TFO seismological station location, while velocity at the epicentre is around 900 m/s. Sargeant *et al.* (2008) reported that the TFO station is located over soil type B according to Eurocode 8 (CEN, 2004) classification system (*i.e.*, V_{s30} in the range between 360-800 m/s), which is in agreement with the values shown in the V_{s30} USGS Map.

No specific studies regarding the susceptibility of this area to liquefaction have been found in the literature. While it appears that loam and clay are predominant and that sand, which is more likely to suffer from liquefaction triggered by seismic events, is not common, it is noted that liquefaction has been observed in saturated fine-grained soils in the past, depending mostly on their plasticity index (Boulanger & Idriss, 2006). The data regarding soil conditions gathered herein is, however, not sufficient to draw strong conclusions on this matter.

By means of analysis of the horizontal to vertical (H/V) spectral ratios for microtremors recorded at the TFO station (the closest station to the epicentre), Ottemöller *et al.* (2009) identified large amplifications at the frequencies of 0.4 and 3.9 Hz, and a small peak at 17 Hz, as shown in Figure A4.12.11. The latter is similar to the frequency (14.3 Hz) at which the horizontal PGA is observed at the TFO station.

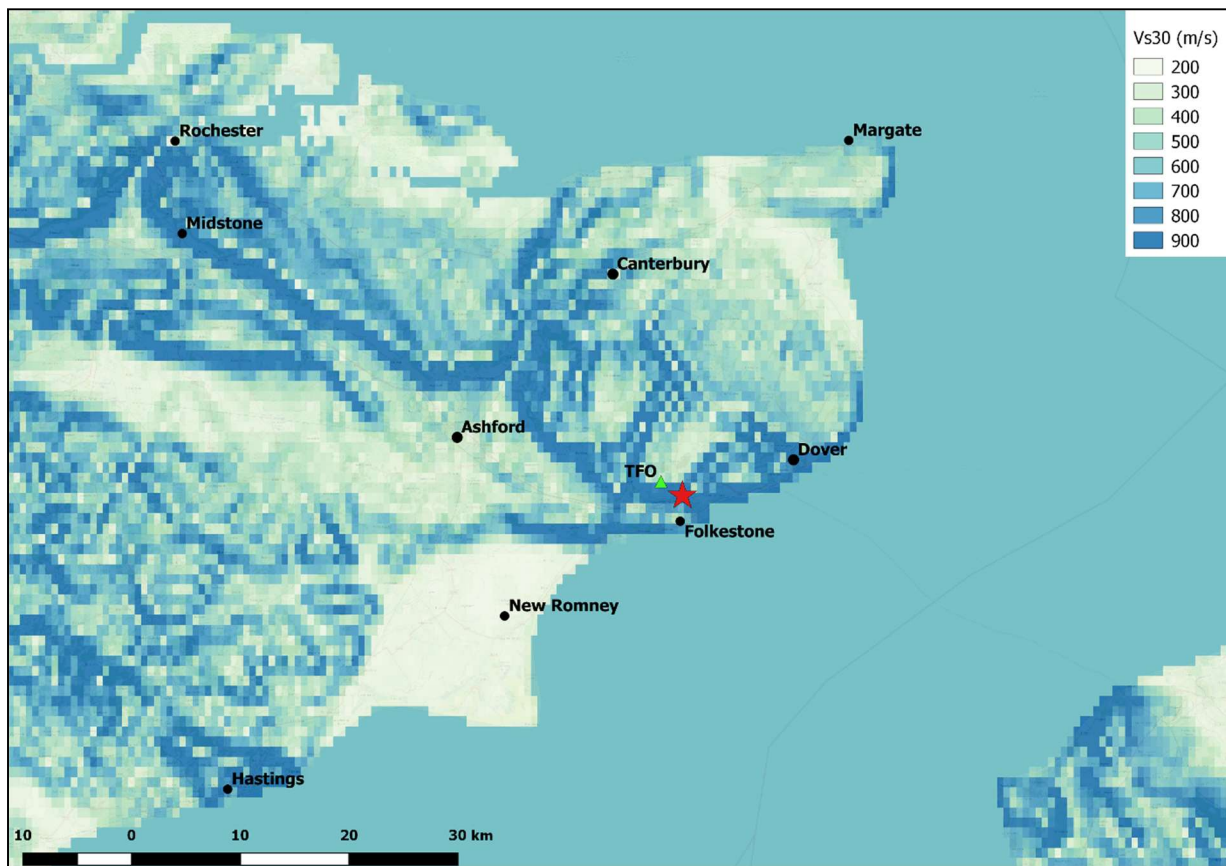


Figure A4.12.10. Estimation of V_{s30} in the area of Folkestone according to the USGS V_{s30} map server (Wald & Allen, 2007). Red star indicates epicentre (according to the BGS); triangle indicates TFO station.

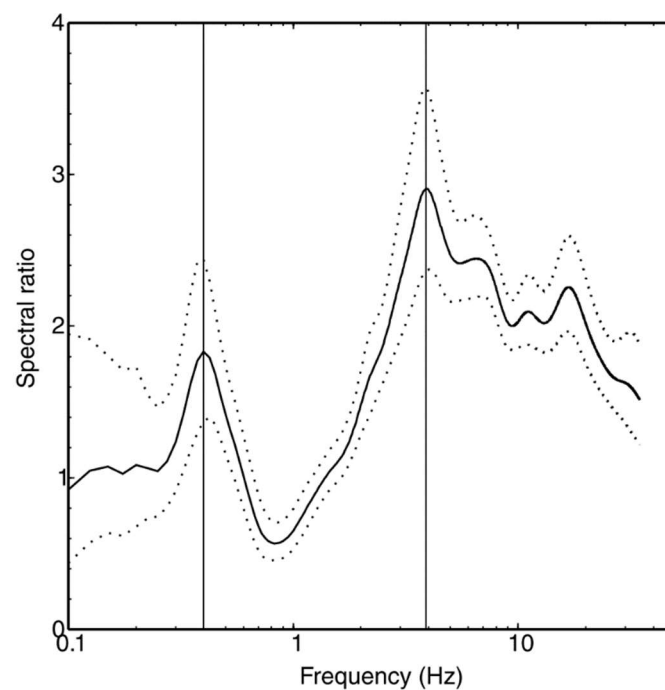


Figure A4.12.11. Spectral ratio of H/V- component ambient noise measurements at station TFO (\pm standard deviation). From Ottemöller *et al.* (2009).

A4.12.4 Ground motions

A4.12.4.1 Intensity observations

The online macroseismic questionnaire available on the British Geological Survey (BGS) webpage yielded more than 1,000 replies in the four days following the Folkestone earthquake, most of them coming from the county of Kent. The earthquake was reported to have been felt across much of Kent and the south-east UK, extending up to Norwich, 180 km to the North, and appears to have been little felt in France, to the South (Sargeant *et al.*, 2008). However, Sargeant *et al.* (2008) point out that the overall felt area appears to have been unusually small, as the intensity attenuation equation for the UK of Musson (2005) predicts much larger isoseismals of EMS-98 intensity IV and III than observed. Figure A4.12.12 illustrates this, by showing the isoseismals obtained by means of the online macroseismic survey in black, and those calculated with the intensity attenuation relation of Musson (2005) in grey. Interestingly, good spatial matching is obtained for isoseismals 6 and 5. Sargeant *et al.* (2008) suggest that this discrepancy might be due to the shallowness of this seismic event, in the sense that the near-field radiation of seismic energy was restricted to the upper, lower velocity part of the crust.

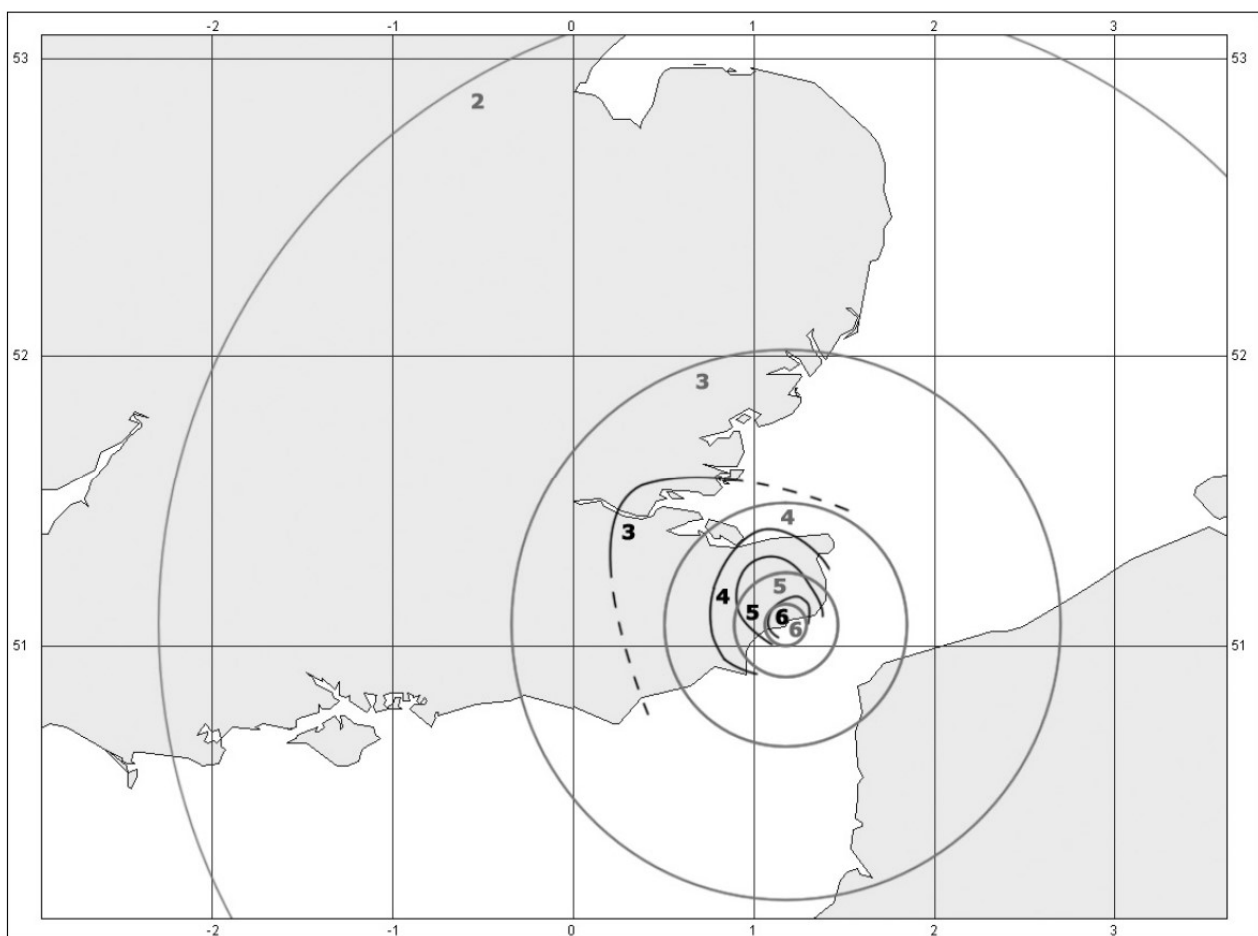


Figure A4.12.12. Isoseismals (EMS-98) of the Folkestone earthquake; black lines correspond to observed isoseismals from the online macroseismic survey and grey lines correspond to modelled isoseismals obtained with the intensity attenuation relation for the UK of Musson (2005). From Sargeant *et al.* (2008).

The maximum assigned macroseismic intensity was the matter of an extensive debate by Sargeant *et al.* (2008), mostly related to the interpretation of the EMS-98 scale (Grünthal, 1998). The two main issues under discussion were the consideration of cracks and partial collapse of chimneys as being structural or non-structural damage, and the actual vulnerability class of the building stock, the two resulting alternatives being maximum EMS-98 intensities of VI or VII. Sargeant *et al.* (2008) finally concluded that an EMS-98 intensity of VI was the most reasonable estimate for the most heavily damaged areas of Folkestone. These and those with an assigned intensity of V are marked in the map of Figure A4.12.13.



Figure A4.12.13. Areas with assigned EMS-98 intensities of 5 and 6 based only on the results of the field survey after the Folkestone earthquake (considering chimneys as non-structural components). From Sargeant *et al.* (2008).

The USGS ShakeMap (Worden *et al.*, 2017) in terms of Modified Mercalli Intensities (MMI), seemingly calculated using only the Intensity Prediction Equation (IPE) of Atkinson & Wald (2007) and no observed data, is presented in Figure A4.12.14 (USGS, 2017a). According to this map, a maximum intensity of around 5.7 MMI is expected to have been attained, which is similar to the aforementioned intensity levels reported by Sargeant *et al.* (2008). However, compared to the findings of the BGS online macroseismic survey, the location of the highest intensity in the USGS ShakeMap is shifted to the south-west (towards New Romney), which is consistent with the discrepancies in epicentral locations reported by these two agencies.

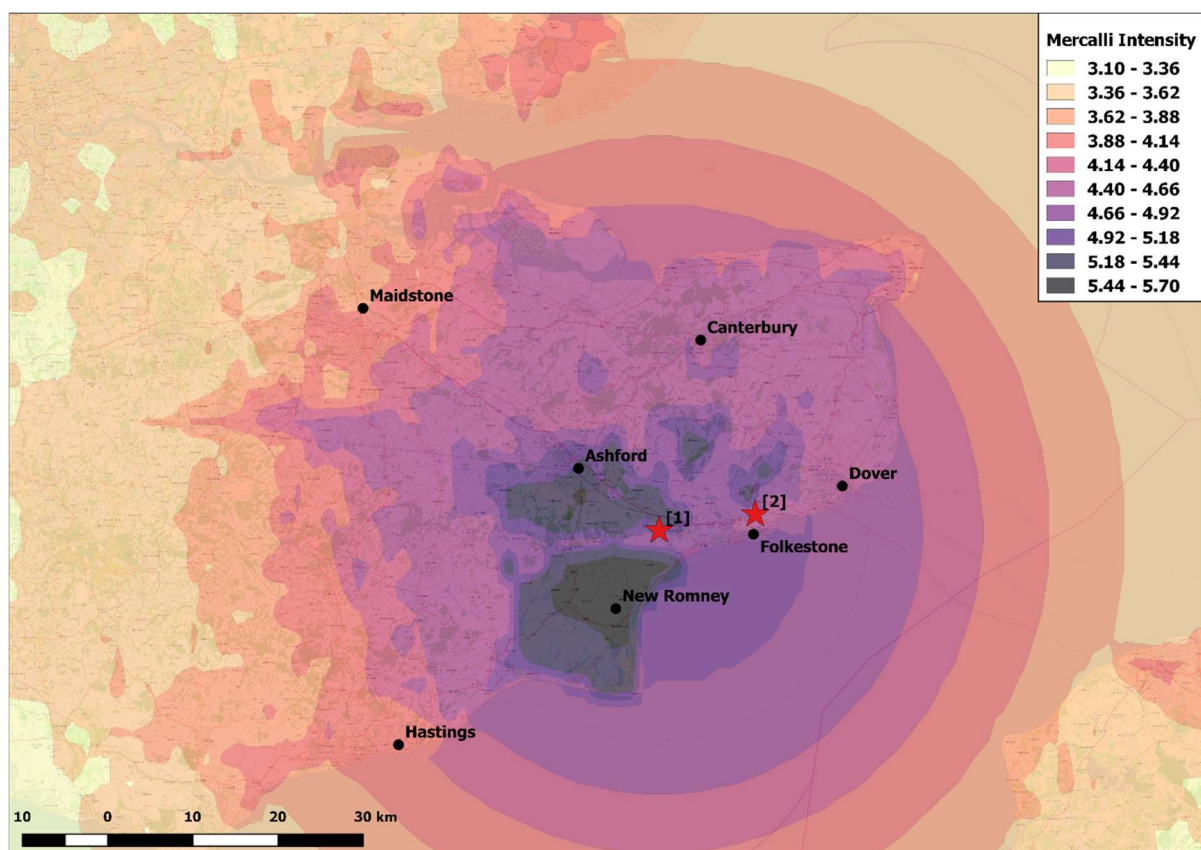


Figure A4.12.14. USGS ShakeMap (2017a) in terms of Modified Mercalli Intensities (MMI). Red stars indicate epicentre according to the USGS [1] and according to the BGS [2].

A4.12.4.2 Ground motion recordings

The Folkestone earthquake was recorded by many broadband stations, as 15 UK stations were operational during the event (Ottemöller *et al.*, 2009). Figure A4.12.15 presents a map with most of the stations from the UK that recorded this event, while some of their corresponding seismograms are shown in Figure A4.12.16.

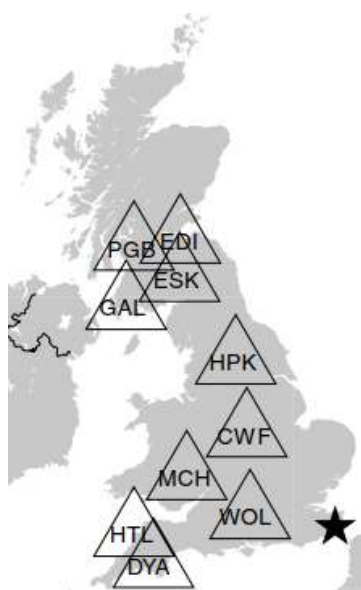


Figure A4.12.15. Map of broadband stations used for moment tensor inversion by Ottemöller *et al.* (2009). Star indicates epicentre. From Ottemöller *et al.* (2009).

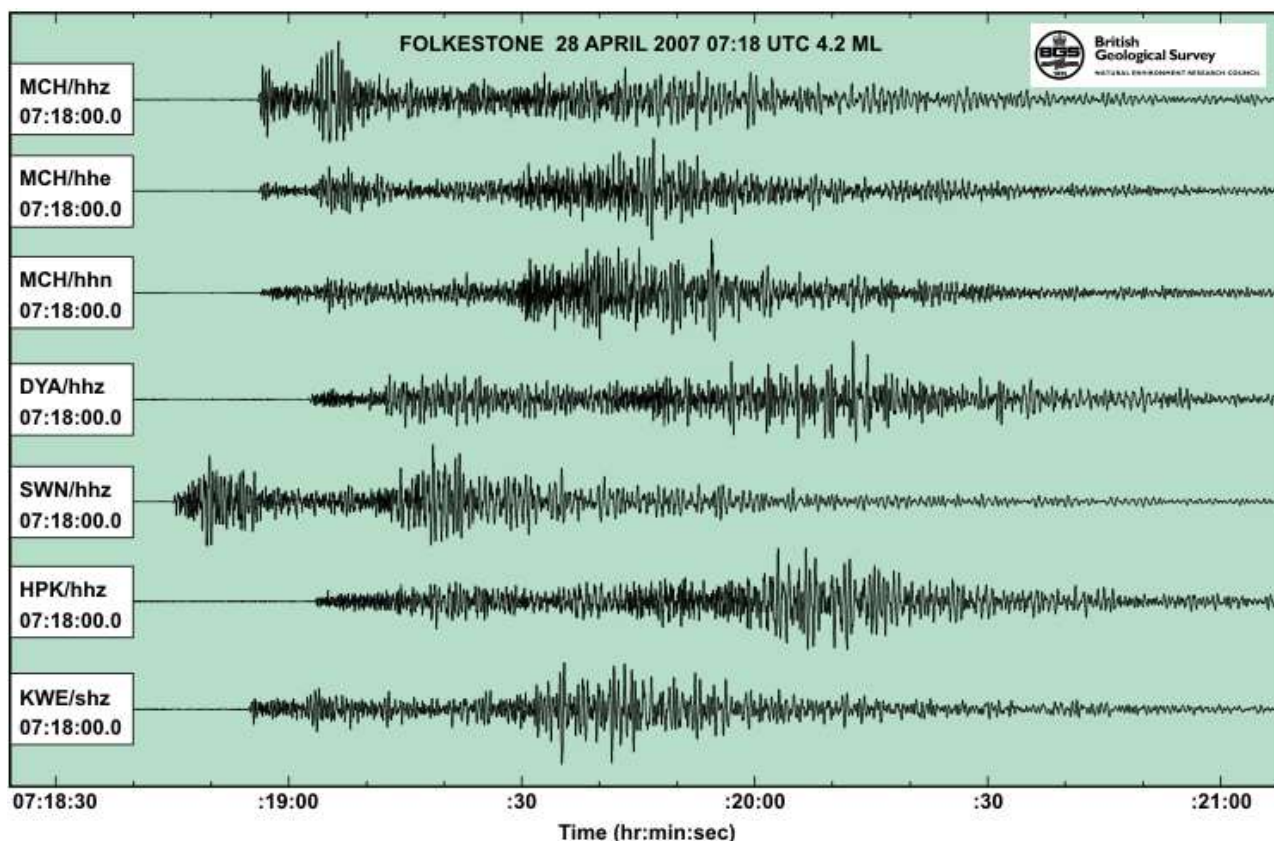


Figure A4.12.16. Seismograms of the Folkestone earthquake as recorded by the BGS instruments. From BGS (2007).

The closest recording station (TFO) was located at a distance between 5 and 8 km north-west from the hypocentre (Ottemöller *et al.*, 2009). According to the bedrock and superficial geology maps (see Figure A4.12.7), the bedrock at the TFO station is chalk, while superficial geology indicates sandy clay with flints.

Figure A4.12.17 presents the horizontal acceleration, velocity and displacement time histories recorded at the TFO station (Sargeant *et al.*, 2008). It can be observed that the north—south component of horizontal acceleration reaches a value of 0.118 g, which is the strongest horizontal PGA ever recorded in the UK up to the time of writing (May 2017). As for the vertical component, accelerations, velocities and displacements have attained values of 0.036 g, 0.53 cm/s, and 0.02 cm, respectively.

Elastic acceleration response spectra for a 5% damping ratio for the recording of station TFO are plotted in Figure A4.12.18. The higher spectral amplitudes at low periods and smaller spectral amplitudes at higher periods indicate that high-frequency content is dominant, which is expected for a near-field record of a small magnitude earthquake (Sargeant *et al.*, 2008).

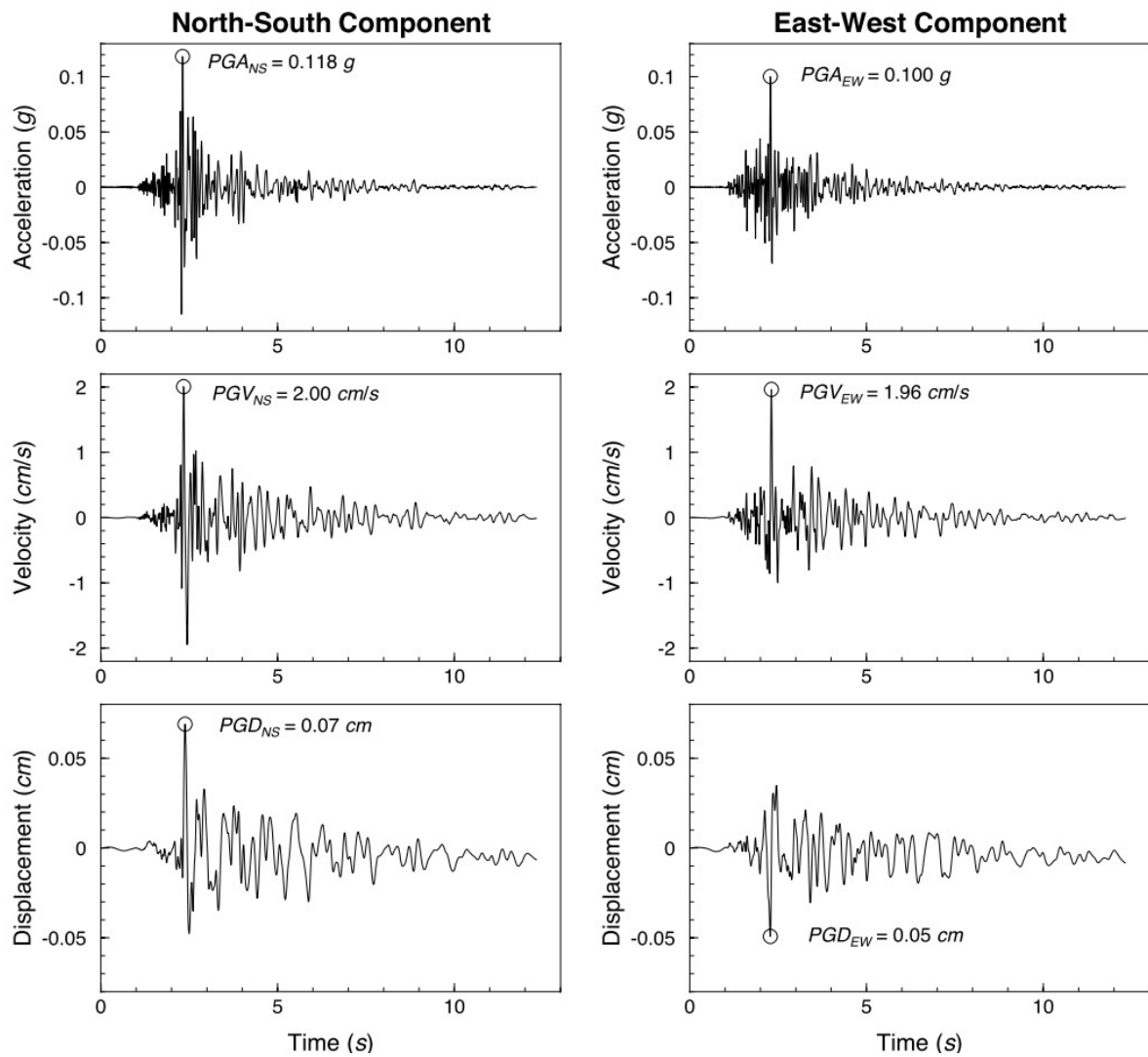


Figure A4.12.17. Horizontal acceleration, velocity and displacement time-histories recorded at station TFO. From Sargeant *et al.* (2008).

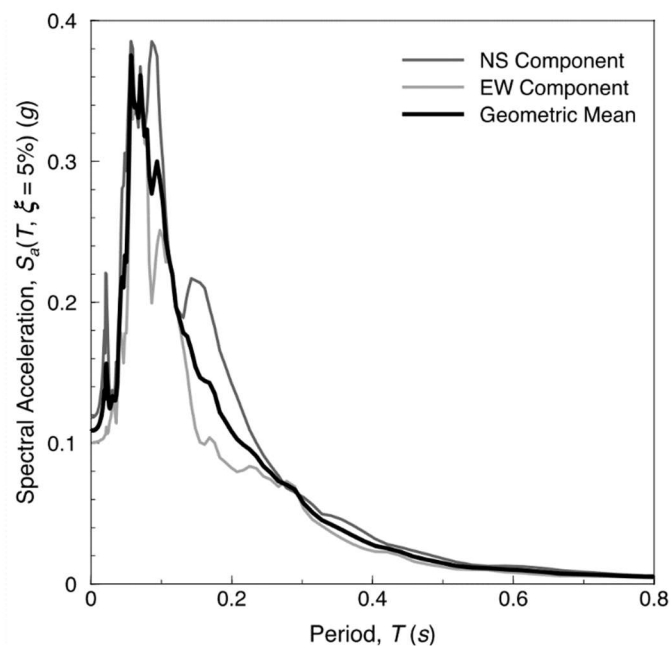


Figure A4.12.18. Elastic 5% damped acceleration response spectra for the accelerograms recorded at station TFO. From Sargeant *et al.* (2008).

Sargeant *et al.* (2008) made a comparison between the geometric mean response spectra and Eurocode 8 (CEN, 2004) type II design spectra for various damping levels, as presented in Figure A4.12.19. Being anchored to the PGA of the recorded motions, the site class factor is not included in the determination of the code spectrum, but corner periods corresponding to site class B, to which the site conditions at station TFO are inferred to belong, are used.

As can be observed, code-based spectra appear as unconservative at the short periods and conservative at the long periods, when compared to the observed spectra. Bearing in mind that the EC8 type II spectrum was developed based on earthquakes of magnitudes close to M_s 5.5, the difference in the obtained results is expected (Sargeant *et al.*, 2008).

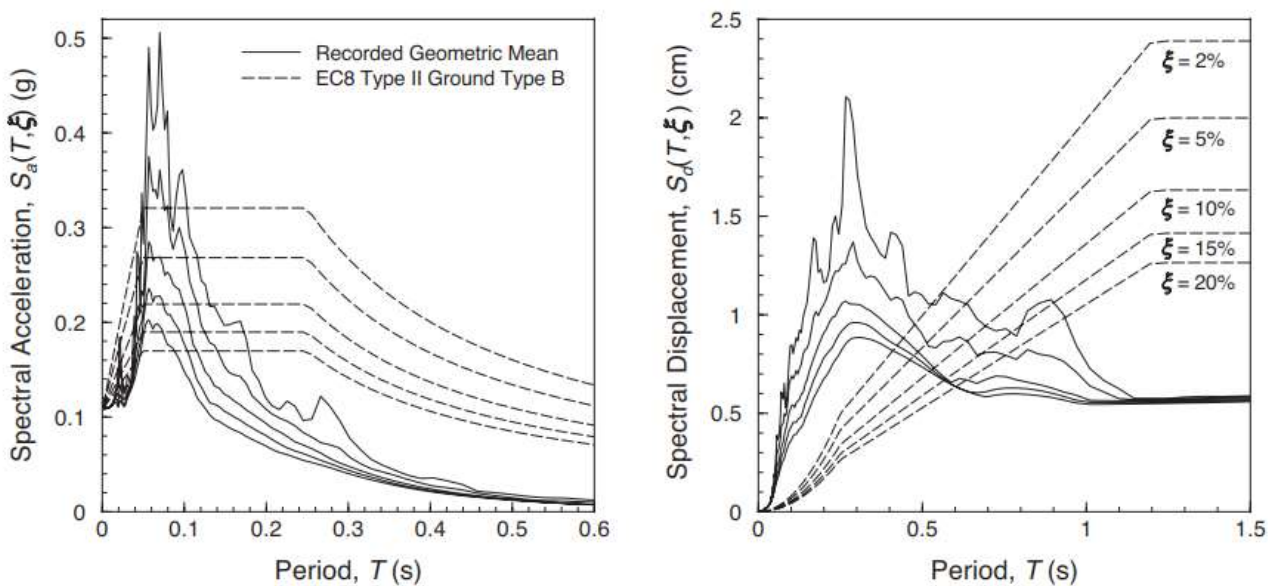


Figure A4.12.19. Comparison of the geometric mean of the acceleration (left) and displacement (right) spectra recorded at station TFO for different levels of damping with the design spectra type II based on Eurocode 8. From Sargeant *et al.* (2008).

Figure A4.12.20 presents a series of comparisons carried out by Arango *et al.* (2012) for the PGA values recorded in the different stations with respect to the median predictions (\pm two standard deviations) of four different ground motion prediction equations (GMPEs): Akkar & Bommer (2010) and Bommer *et al.* (2007), developed for shallow crustal events in Europe and the Middle East, Boore & Atkinson (2008) and its modification by Atkinson & Boore (2011), for shallow crustal events, and Atkinson & Boore (2006) for stable continental regions of eastern North America. All the GMPEs fit the data reasonably well. The Boore & Atkinson (2008) equation fits the observed data over a broad range of distances. The magnitude-dependent stress drop version of Atkinson & Boore (2006) equation over predicts the data at larger distances (200 to 400 km), while the Boore & Atkinson (2008) equation modified for crustal events under predicts this data. When adjusted to the Folkestone earthquake estimated stress drop of around 3.0 MPa (30 bars), the Atkinson & Boore (2006) equation provides better fit to the data. As can be observed, the accelerations recorded at large distances were very small.

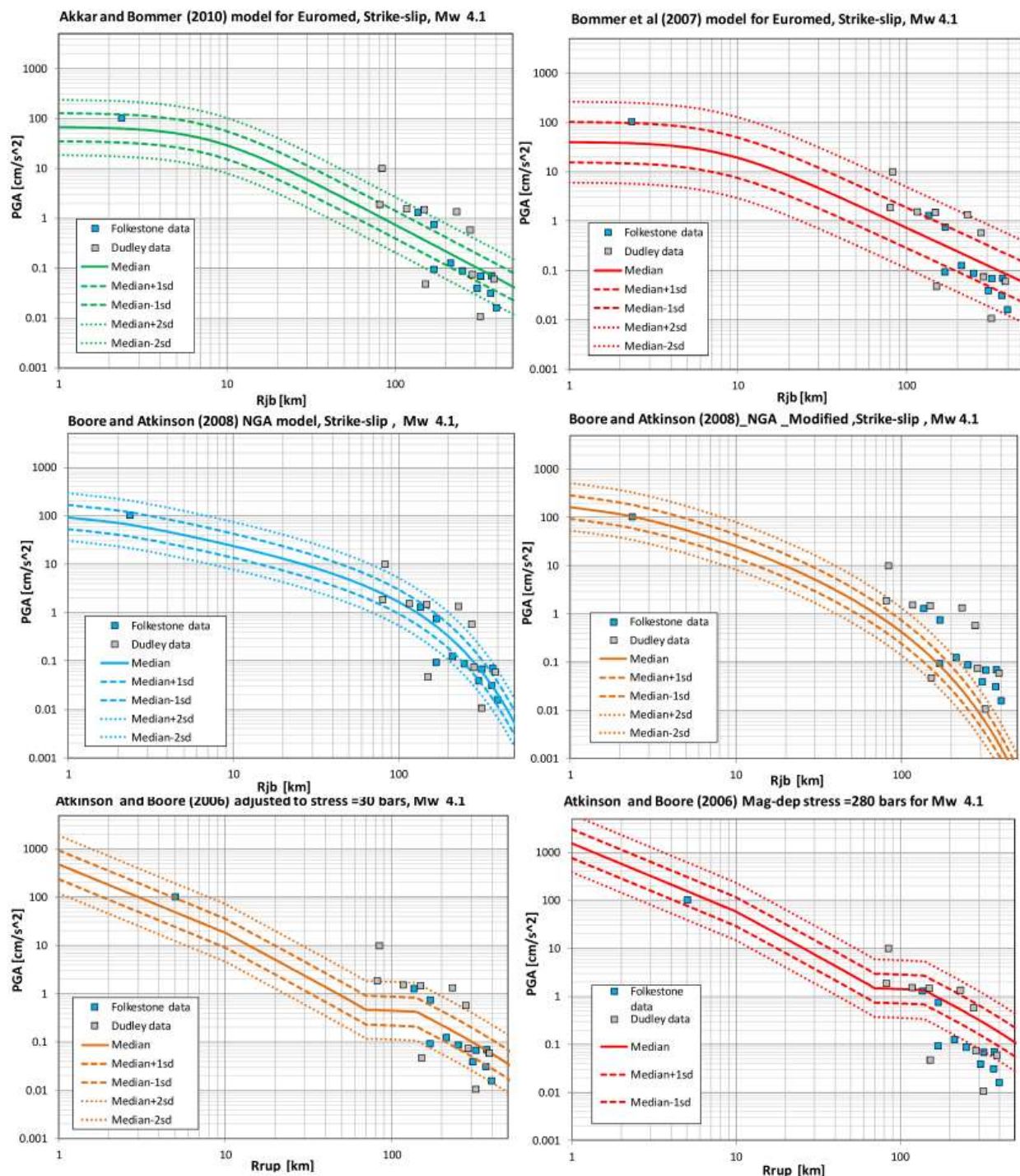


Figure A4.12.20. Comparison of data recorded during the Folkestone earthquake with median PGA values at rock predicted by different GMPEs. Ignore grey squares labelled Dudley. From Arango *et al.* (2012).

A4.12.4.3 Inferred shaking levels

Applying the relation given by Wald *et al.* (1999), Sargeant *et al.* (2008) estimated that Modified Mercalli Intensities of around 5.6 to 5.9 could be expected at station TFO, based on the peak ground accelerations recorded at the site.

In view of their results from the H/V analysis (see section A4.12.3.2), Ottemöller *et al.* (2009) believe that site amplification is likely to have played a role in the ground motions observed

at station TFO, and that the similarity of the geology at the site of said station and that of Folkestone, as well as their epicentral distances (around 2 km), may suggest that similar site amplification effects may have occurred in the district of Foord, one of the most damaged areas of Folkestone.

Figure A4.12.21 presents the USGS ShakeMap (Worden *et al.*, 2017) in terms of peak ground acceleration, seemingly calculated using only the GMPE of Atkinson & Boore (2006) and the Ground Motion/Intensity Conversion Equation of Atkinson & Kaka (2007). This map indicates PGA values as high as 0.22 g in the area close to the epicentre, much larger than that recorded at the TFO station. The maximum estimated Peak Ground Velocity (PGV) is equal to 6.29 cm/s while the maximum derived Spectral Acceleration (SA) is taking values of 0.17 g at a period of 0.3 s, 0.02 g at 1 s and 0.0015 g at 3 s.

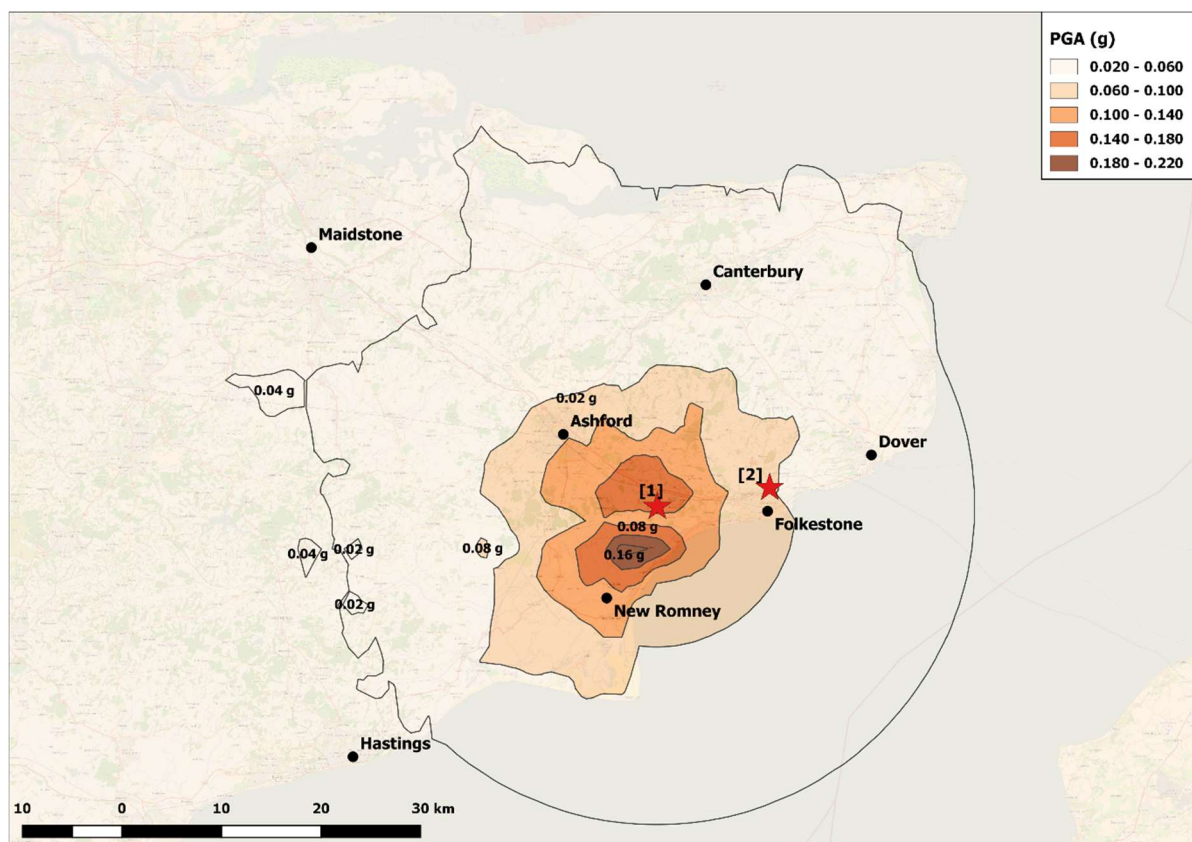


Figure A4.12.21. USGS ShakeMap (2017a) in terms of PGA. Red stars indicate epicentre according to the USGS [1] and according to the BGS [2].

A4.12.4.4 Duration of ground shaking

It was reported by Sargeant *et al.* (2008) that the 5-95% of Arias intensity definition of the significant duration of the earthquake at station TFO, around 5 km away from the hypocentre, was 2.58 s and 3.11 s for the N-S and E-W components, respectively.

Estimations of significant ground motion durations were carried out using the models of Bommer *et al.* (2009) and Afshari & Stewart (2016) based on the 5-75% Arias Intensity definition, as shown in Figure A4.12.22. Taking into account the 0.5 (± 0.1) km source radius estimated by Ottemöller *et al.* (2009) and the 5.3 km hypocentral depth reported by the BGS,

the depth to the top of the rupture used for the model of Bommer *et al.* (2009) was 4.8 km. A range of distances to the fault rupture and velocities of 180 m/s, 360 m/s and 800 m/s, which correspond to the boundaries of the Eurocode 8 (CEN, 2004) definitions of soil types, were considered. These values are also representative of those shown in Figure A4.12.10 for the cities of New Romney, Ashford and Folkestone, respectively. Higher values of significant duration ($D_{5-75\%}$) are obtained using the model of Afshari & Stewart (2016) than that of Bommer *et al.* (2009).

Additionally, the 5-95% Arias Intensity definition of significant duration ($D_{5-95\%}$) was calculated for the TFO station, which is located on soil type B based on the Eurocode 8 classification system (V_{s30} values in the range between 360-800 m/s), as reported by Sargeant *et al.* (2008). As can be observed, the resulting durations range between 1.44 and 3.92 seconds, and the values of significant durations reported by Sargeant *et al.* (2008) fall within this range. The duration reported by Sargeant *et al.* (2008) is within [0.65, 1.63] and [-0.14, -0.84] standard deviations of the models of Bommer *et al.* (2009) and Afshari & Stewart (2016), respectively.

All these values are significantly shorter than the 10 seconds reported by the residents to the media (Galloway, 2008), though it is usually the case that people perceive earthquakes to be longer than they really are.

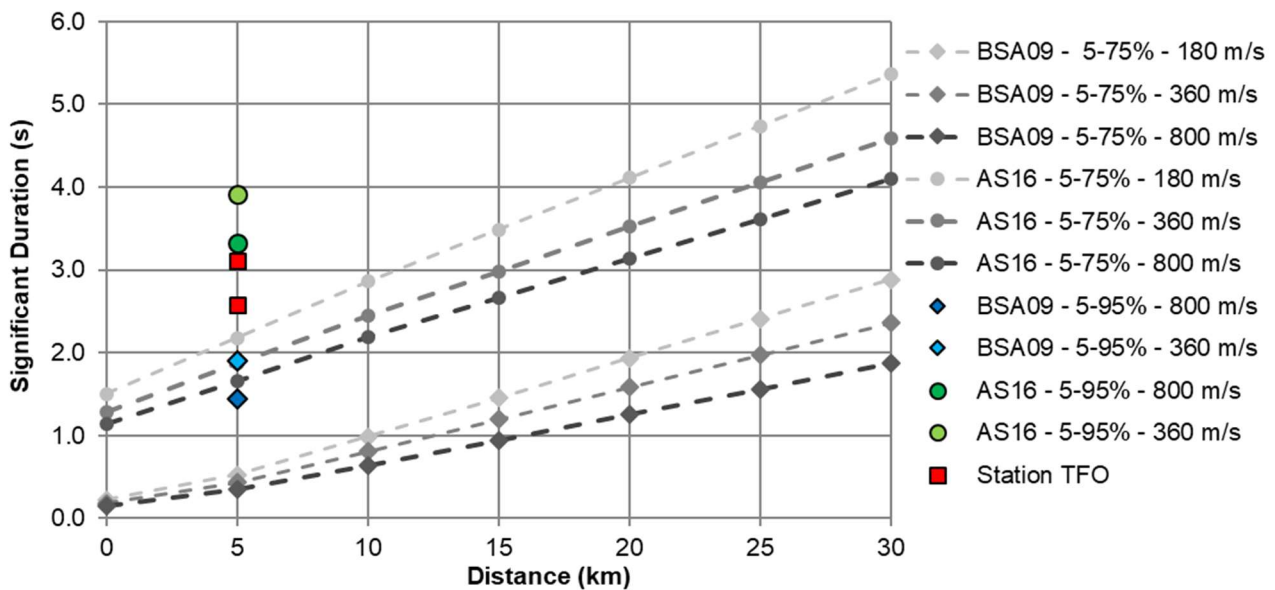


Figure A4.12.22. Estimation of the significant duration of the main shock, using prediction equations by Bommer *et al.* (2009, BSA) and Afshari & Stewart (2016, AS) and values reported by Sargeant *et al.* (2008) for the two as-recorded components of Station TFO.

A4.12.5 Collateral earthquake hazards

A4.12.5.1 Surface rupture

No surface rupture has been documented neither for the 2007 Folkestone earthquake nor for any other British earthquake (Baptie, 2010). This is consistent with the 0.5 (\pm 0.1) km source radius estimated by Ottemöller *et al.* (2009) and the 5.3 km hypocentral depth reported by the BGS.

A4.12.5.2 Landslides

At the same day of the earthquake, a 300-metre-long crack appeared in a cliff near Barton on Sea, a village in the district of New Forest, around 200 km to the west of the epicentre. It was feared that it could trigger large landslide movements. However, authorities did not draw strong conclusions on the correlation between the earthquake and the crack (BBC, 2007b).

A4.12.5.3 Liquefaction

No reports on liquefaction effects have been found.

A4.12.5.4 Settlements

Ground settlements are only mentioned in reports for this earthquake making reference to pre-existing conditions that may have had an influence on the vulnerability of the building stock, but not caused by the earthquake itself (Sargeant *et al.*, 2008, additional unpublished material courtesy of Dr. G. Weatherill).

A4.12.6 Exposed population

A4.12.6.1 Socio-economic setting

According to the 2016 Human Development Data (United Nations Development Program, 2017), the Human Development Index (HDI) for the United Kingdom in 2015 was 0.909, while its Inequality-adjusted HDI (IHDI) was 0.836 (Table A4.12.5). This located the UK in the 16th place in the world's ranking, while the Netherlands ranks 7th. The following table compares the HDI and IHDI for both countries for a series of Human Development Reports (United Nations, 2008, 2009, 2010, 2016) covering the time around which the Folkestone earthquake occurred. The column "Adj. HDI" provides the HDI values given in the 2016 report for previous years, adjusted for data consistency in time. According to the 2016 report, the UK saw a drop in its (adjusted) HDI during the years 2010-2013, but started a recovery process after that, while the Netherlands have experienced a steady increase over the whole period. The HDI for the UK was around 1.6% smaller than that of the Netherlands in 2015.

The economy of the UK is greatly influenced by the automotive and aerospace industries, which represent a significant part of the British manufacturing sector. Additionally, the UK

has the third-highest share of global pharmaceutical research and development expenditures (Ministerial Industry Strategy Group Pharmaceutical Industry, 2009; Department for Business Innovation and Skills, 2011). Due to the Great Recession, the unemployment rate in the UK increased from 5.4% in May 2008, to 7.8% in May 2009, and was followed by a peak of 8.4% in the second part of year 2011. In 2015 the annual growth rate of wages and salaries was 3.9% and had steadily increased since its lowest value of 0.2% in 2009 (Office for National Statistics).

Table A4.12.5. Human Development Index and Inequality-adjusted Human Development Index for the United Kingdom and the Netherlands.

Report	Data	United Kingdom				Netherlands			
		HDI	IHDI	Rank	Adj. HDI	HDI	IHDI	Rank	Adj. HDI
2007	2005	0.946	N/A	16	0.892	0.953	N/A	9	0.905
2008					0.895				0.906
2009	2007	0.947	N/A	21	0.895	0.964	N/A	6	0.906
2010	2010	0.849	0.766	26	0.902	0.890	0.818	7	0.911
2016	2015	0.909	0.836	16	0.909	0.924	0.861	7	0.924

Table A4.12.6 presents a comparison between the United Kingdom and the Netherlands in terms of GDP, GDP per capita and unemployment rate for the years 2007 and 2016, according to World Economic Outlook Database (WEO, 2016).

Table A4.12.6. Gross domestic product (GDP), GDP per capita and unemployment rate for the United Kingdom and the Netherlands, according to the World Economic Outlook Database (2016).

Indicator	Units	United Kingdom		Netherlands	
		2007	2016	2007	2016
Gross domestic product, current prices	Billion USD	3,064.350	2,649.890	840.583	769.930
Gross domestic product per capita, current prices	USD	49,973.920	40,411.710	51,311.400	45,210.240
Unemployment rate	%	5.350	4.962	4.161	6.700

A4.12.6.2 Population density and distribution

In Figure A4.12.23, population density, according to Gridded Population of the World (GPW v3; CIESIN, 2005) is depicted for Folkestone and the areas spreading north-west from the epicentre. The most damaged area was the Foord district of Folkestone, for which the estimated population density is around 300 persons/km² (in a 2.5-arcmin resolution¹). Based on data from year 2011, the population of Folkestone was 46,698 people (Office for National Statistics).

The USGS EXPO-CAT database (Allen *et al.*, 2009) estimates that around 390,400 people were exposed to a MMI intensity of IV and 257,543 people were exposed to intensities

¹ The maximum density in the area increases up to 9990 people/km² in the newer GPW 4.0 (0.5-arcmin resolution).

between IV and V, of which 81.7% and 76.8% was urban population, respectively (Figure A4.12.24). Around 180,000 people were exposed to MMI intensities of V or higher, and only 3,700 people were exposed to the highest observed MMI intensity of VI.

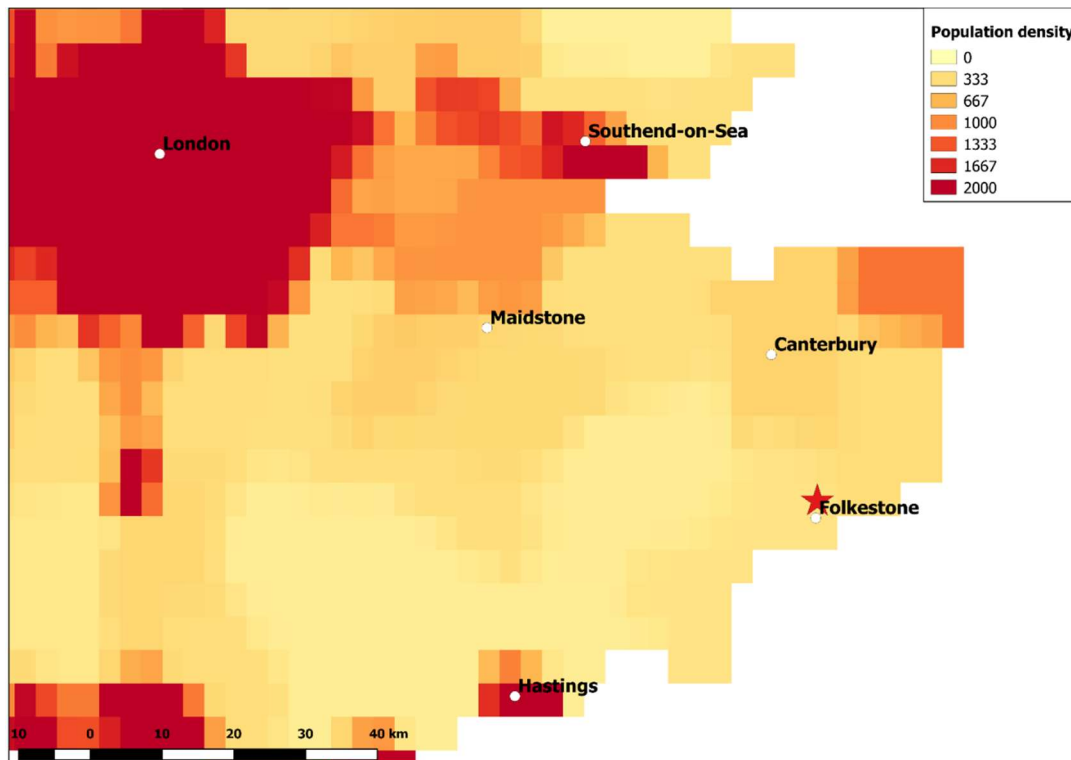


Figure A4.12.23. Population density (persons/km²) around the Folkestone area in the year 2000. Data from Gridded Population of the World (GPW v3.0; CIESIN, 2005). The red star marks the epicentre of the main shock, according to the BGS. Last category includes 2000 ppl/km² and more.

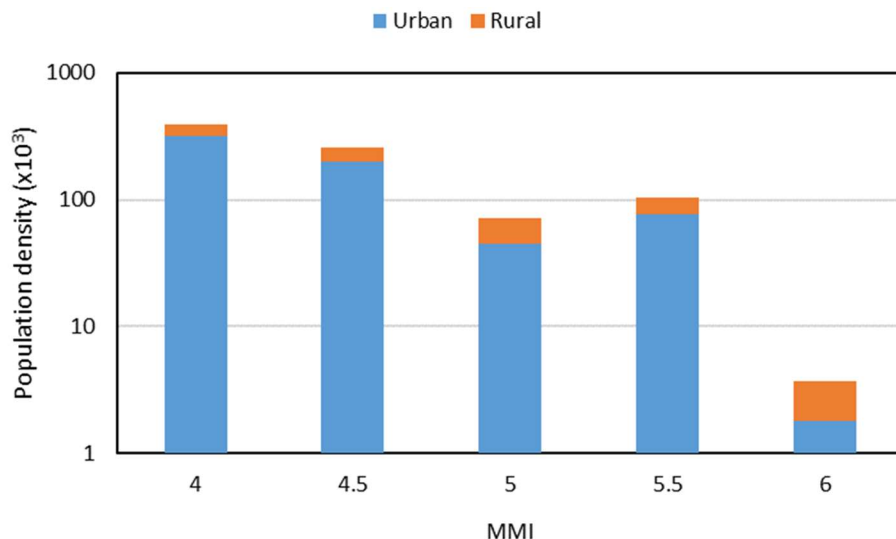


Figure A4.12.24. Disaggregation of urban and rural population exposed to MMI IV to MMI VI. Data from USGS EXPO-CAT database (Allen *et al.*, 2009).

A4.12.6.3 Time of day of earthquake

The earthquake struck on a Saturday morning at 08.18 local time. At that time, most people were at their homes. Since the earthquake did not produce extensive internal damage

except for cracks on the walls, people stayed safe inside. However, many of them panicked and feared aftershocks, and so went out to observe the damage on the external parts of their homes. Both the temporary loss of power to the main city and the closure of roads whilst debris was cleared meant that most businesses in Folkestone were closed on Saturday morning (the busiest trading period of the week) until about midday, and resulted in non-negligible costs related to business interruption (Weatherill, 2017, personal communication).

The influence of the earthquake striking on a non-school day is not fully clear, as ceiling plaster cracked and fell in several classrooms at Harvey Grammar School, but available imagery suggests that only minor injuries, if any, could have occurred (Sargeant *et al.*, 2008, additional unpublished material courtesy of Dr. G. Weatherill).

A4.12.7 Characteristics of exposed building stock

A4.12.7.1 Seismic design codes

Before the implementation of Eurocode 8 (CEN, 2004) provisions in 2008-2009, only structures considered to be critical were designed for seismic action in the UK. Within this category lie nuclear power plants, which have been designed seismically since the 1980s, major dams and offshore structures (Booth, 2010). The design of tanks was covered by British Standards before the implementation of Eurocode 8 as well. But even after the introduction of Eurocode 8 there was no considerable change in the treatment of standard structures with respect to required seismic design (Booth, 2010). It is generally accepted that, due to the low seismicity of the UK, there is no need for the application of Eurocode 8 provisions, except for structures whose failure would lead to particularly high human losses or have considerable impact over the environment, the economy or the safety of the country. Some guidance with respect to the criteria to determine whether a building in the UK should be designed for seismic action or not is provided in document PD 6698:2009 (British Standard Institution (BSI), 2009), which contains complementary information on the use of Eurocode 8 and is published by the British Standards Institution, but does not have the status of a British Standard (Booth, 2010).

With the aim of making the application of Eurocode 8 provisions possible, a national seismic hazard map was developed and adopted for the UK in 2007 (Musson & Sargeant, 2007). This map is the first UK national hazard map for which seismic source models were primarily based on neotectonic considerations (described by Chadwick *et al.*, 1996) rather than on historical seismicity alone. The map is depicted in Figure A4.12.3 (left) and presents PGA with a 10% probability of exceedance in 50 years (*i.e.* 475 years return period).

Though Eurocode 8 was implemented in the UK only within the last decade, hazard maps have been developed for the country since the 19th century. O'Reilly (1884) made the first attempt towards seismic mapping with the hazard expressed solely through the frequency of earthquake occurrence (Musson & Sargeant, 2007). According to Musson & Sargeant (2007), the first recognizable hazard map of the UK was the one of Lilwall (1976), which

depicted macroseismic intensities with a 200-year return period. With the development of nuclear industry during the 1980s, the knowledge of British seismicity was improved and probabilistic seismic hazard assessment (PSHA) procedures started developing. Ove Arup (1993) used PSHA to estimate the seismic hazard for 11 cities in the UK, though this was not enough for the development of a full hazard map (Musson & Winter, 1997; Musson & Sargeant, 2007). A set of hazard maps for the offshore British area, developed through a collaboration between the BGS and Arup during 1992, were the first maps for which the probabilistic method was fully used (Musson, 2012). Soon after, the first hazard maps based on a comprehensive and detailed hazard study were elaborated for the whole country by Musson & Winter (1997). One of these maps represents hazard in terms of EMS intensities with a return period of 475 years, while the other indicates PGA levels with a return period of 10,000 years (Figure A4.12.25). In the former, EMS 6 was corresponding to high, EMS 5 to moderate and EMS 4 and 3 to low hazard areas. In the latter, average hazard values were in the range between 0.10 g and 0.15 g, and only some areas with higher hazard levels attain PGA values higher than 0.25 g.

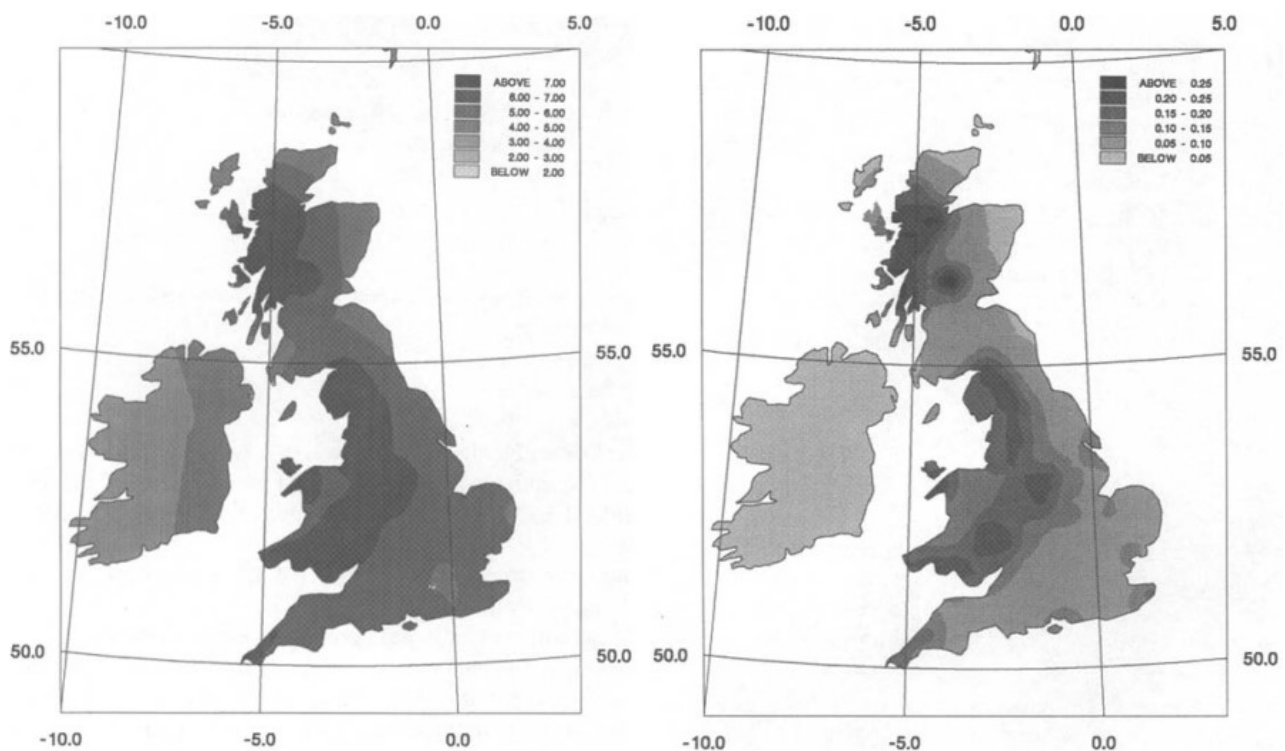


Figure A4.12.25. Seismic hazard maps of the UK representing EMS intensity values with a 10% probability of exceedance in 50 years (left) and PGA values with a 0.5% probability of exceedance in 50 years (10,000 years return period, 10^{-4} annual probability) of Musson & Winter (1997).

While earthquake design is generally not considered critical in the UK, wind has been taken into consideration for the design of structures since 1944, when the first code of practice for wind loads (BSI, 1944) was issued by the British Standards Institution (Hill *et al.*, 2013). Considerable changes in wind design requirements were implemented in revised versions of the code, which were published in 1952, 1972, 1986, and 1997. Wind actions that should be considered during the structural design of buildings are currently defined by the part 1-4 of the acting Eurocode 1 (BS EN 1991-1-4:2005+A1:2010) (BSI, 2005), which is accompanied by the National Annex (BSI, 2008). According to Gething (2010), wind design

loads have more than doubled with respect to those specified by the 1944 code, while for some of the UK regions (*i.e.* London, the South East, the East of England and Northern Ireland) their value has more than tripled.

A4.12.7.2 Building typologies

According to the PAGER Inventory Database v2.0 (Jaiswal & Wald, 2008), the most common typology of urban, rural, residential and non-residential buildings in the UK is unreinforced masonry, as shown in Figure A4.12.26. Comparably, non-ductile reinforced concrete frames and steel structures are less prevalent in the UK and are more typical for non-residential buildings. According to Sargeant *et al.* (2008), most residential buildings in the UK are likely to fall under vulnerability class B on the EMS-98 scale (Grünthal, 1998), though it is acknowledged that the actual vulnerability may vary from A to C, depending on the construction quality.

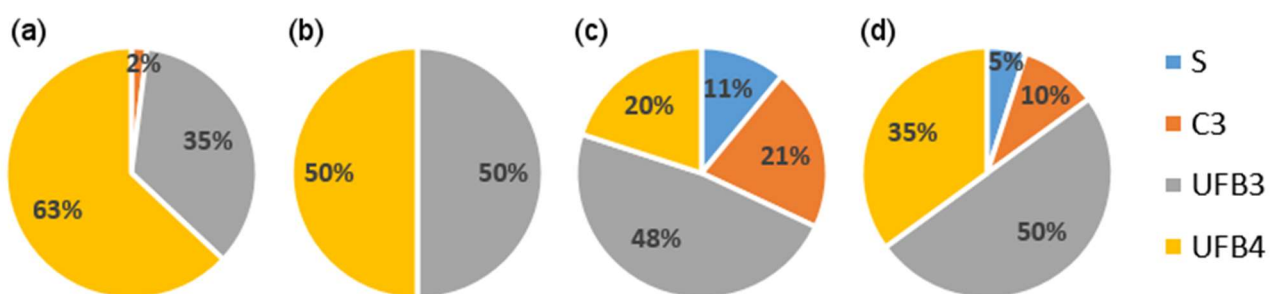


Figure A4.12.26. Proportion of buildings in the UK belonging to each typology: (a) urban and residential, (b) rural and residential, (c) urban and non-residential, and (d) rural and non-residential. UFB4: unreinforced fired brick masonry, cement mortar. UFB3: unreinforced brick masonry in lime mortar. C3: non-ductile reinforced concrete frame with masonry infill walls. S: steel. Data from Jaiswal & Wald (2008).

Figure A4.12.27 shows the ages of construction, building types and occupancy types of the building stock of the Shepway district, to which Folkestone belongs. With 31.3% against 23.8%, the proportion of buildings built before 1919, which tend to be less well-maintained than newer constructions, is much higher than the national average (Sargeant *et al.*, 2008; Shepway District Council, 2001). Similarly, the percentage of detached dwellings and converted flats is higher in the Shepway district when compared to the national UK level.

Figure A4.12.28 depicts the distribution of age of construction for the three main categories of tenure types that can be distinguished within the UK private dwelling sector: owner-occupied, housing association and privately-rented. Privately-rented tenure type has the oldest dwelling age profile, with the percentage of these buildings built before 1919 in the Shepway district being 71%, significantly higher than the 53% measured at the national level. It is noted that older dwellings, converted and terraced building types, and private rented tenure type, all of which are very common in the Shepway, are generally associated with poorer conditions and lack of maintenance. Consequently, the housing stock in the Shepway district is found to be in generally poorer conditions than the national average. The unfitness rate of the buildings in the Shepway district is 10%, which is slightly higher than the national average of 7%. Based on the private sector condition survey (Shepway District

Council, 2001), out of all subareas of the Shepway district, Folkestone presents the highest unfitness rate (17%).

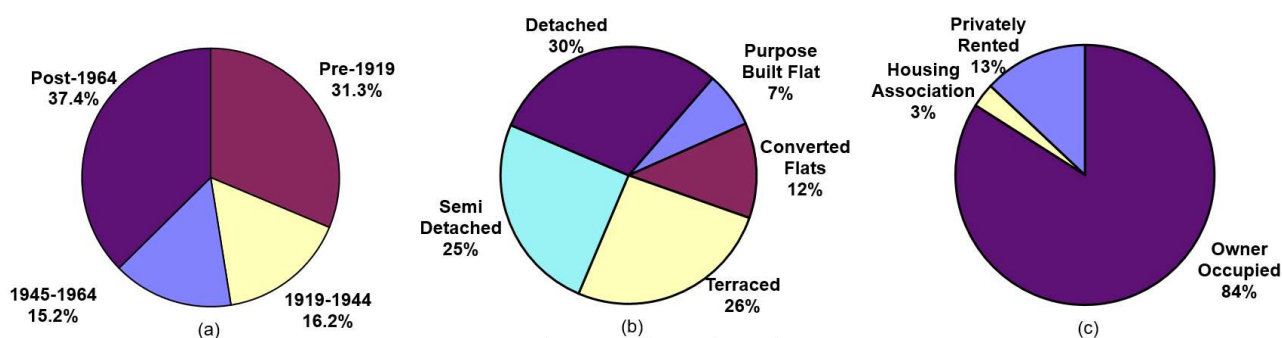


Figure A4.12.27. Age of construction (a), building types (b) and occupancy types (c) of the building stock of the Shepway district. Data from Shepway District Council (2001).

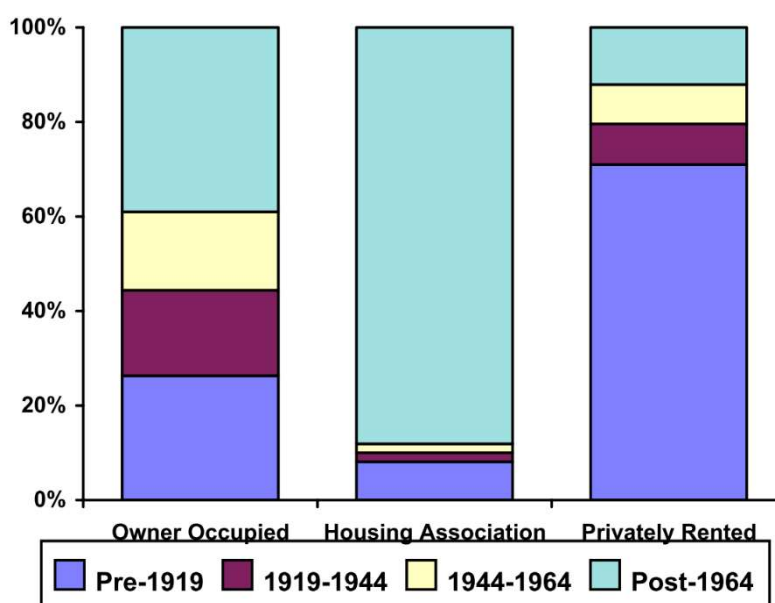


Figure A4.12.28. Tenure by date of construction in the Shepway district. From Shepway District Council (2001).

While a detailed characterization of the typologies existing in Folkestone is not available, Sargeant *et al.* (2008) provide some details regarding the two most common kinds of structures that can be found in the most affected areas of Folkestone. These are two- and three-storey unreinforced brick residential properties built during the Late Victorian/early Edwardian (1870-1919) and the interwar (1920-1939) periods. During the former, the typical constructions consisted of solid walls of fired clay brick bonded with lime or cement-lime mortar, with timber rafters and floor joists generally not tied to the brickwork, usually possessing large brick chimneys. Similar construction practices were kept during the interwar period, though the use of mortar made of a mixture of cement and lime resulted in an improvement of the strength of walls and chimneys (Sargeant *et al.*, 2008). Additionally, cavity walls started to become common during this period and finally became mandatory in 1935. By the early 21st century, cavity walls constructed in this early years presented deterioration of the wall ties due to exposure to damp (Sargeant *et al.*, 2008, additional unpublished material courtesy of Dr. G. Weatherill).

A4.12.7.3 Prior damage and retrofit

Taking into account the old age of the building stock in Folkestone, it is probable that damage of the dwellings prior to the earthquake was present, particularly in the form of cracking as a consequence of bombing during the Second World War. An example of this is Harvey Grammar School, located north-west of the main damaged area, whose façade was bombed during the WW II and later rebuilt. This school was damaged during the Folkestone earthquake, possibly due to the plane of weakness created locally between the old school building and the newer rebuilt façade (Sargeant *et al.*, 2008).

Many of the chimneys damaged by the Folkestone earthquake were already in need of re-pointing before the earthquake, as in many cases the original lime mortar had dissolved away, leaving loosened bricks (Sargeant *et al.*, 2008, additional unpublished material courtesy of Dr. G. Weatherill). In some cases, the repointing had already been carried out with cement mortar, which is less flexible than the original lime mortar (Sargeant *et al.*, 2008).

It should be pointed out as well that the Shepway Council building control team had previously reported occurrences of flood and settlement damage for the areas in which the greatest earthquake damage was observed. It is possible that this may have led to the existence of weaknesses before the Folkestone earthquake struck (Sargeant *et al.*, 2008, additional unpublished material courtesy of Dr. G. Weatherill).

A4.12.8 Damage observations

A4.12.8.1 Damage states

With the purpose of estimating the levels of macroseismic intensity experienced in the Folkestone area due to this earthquake, Sargeant *et al.* (2008) made use of the EMS-98 damage scale (Grünthal, 1998), details of which can be found in Section 3.8.1 of Chapter 3 and Appendix II.

Additionally, the Shepway District Council classified buildings using five damage categories, as follows:

- Category 1: unoccupiable properties that pose a high level of risk to the public, with immediate action being required.
- Category 2: similar to Category 1, but with a lower risk of collapse and injury.
- Category 3: cracks.
- Category 4: buildings that had been assessed and made safe, after having been originally assigned to Category 1.
- Category 5: unconfirmed reports of damage.

It is noted that the Folkestone earthquake seems to have been the first time that assessment of structures in terms of categories of earthquake damage was carried out in the UK.

A4.12.8.2 Damage statistics and description

Immediately after the earthquake, damage surveys were conducted by the media, the local council, and engineers from Imperial College London and the firm Ove Arup. The British Geological Survey and engineers and seismologists from several British universities then continued the survey on 1st May and 2nd May. The work of Sargeant *et al.* (2008) collected the findings of all of these and is used to describe the damage observed in what follows.

Figure A4.12.29 shows the map of the main damaged area, located approximately 2 km away from the epicentral coordinates calculated by the BGS and surveyed during 1st and 2nd May. Table A4.12.7 presents a summary of the damage observed in each of the areas marked with letters on the map, elaborated from the descriptions of Sargeant *et al.* (2008) as well as additional material not published in Sargeant *et al.* (2008), courtesy of Dr. G. Weatherill. As neither source provides numbers of cases of the types of damage observed, the column labelled “quantification” preserves the wording used by the authors.

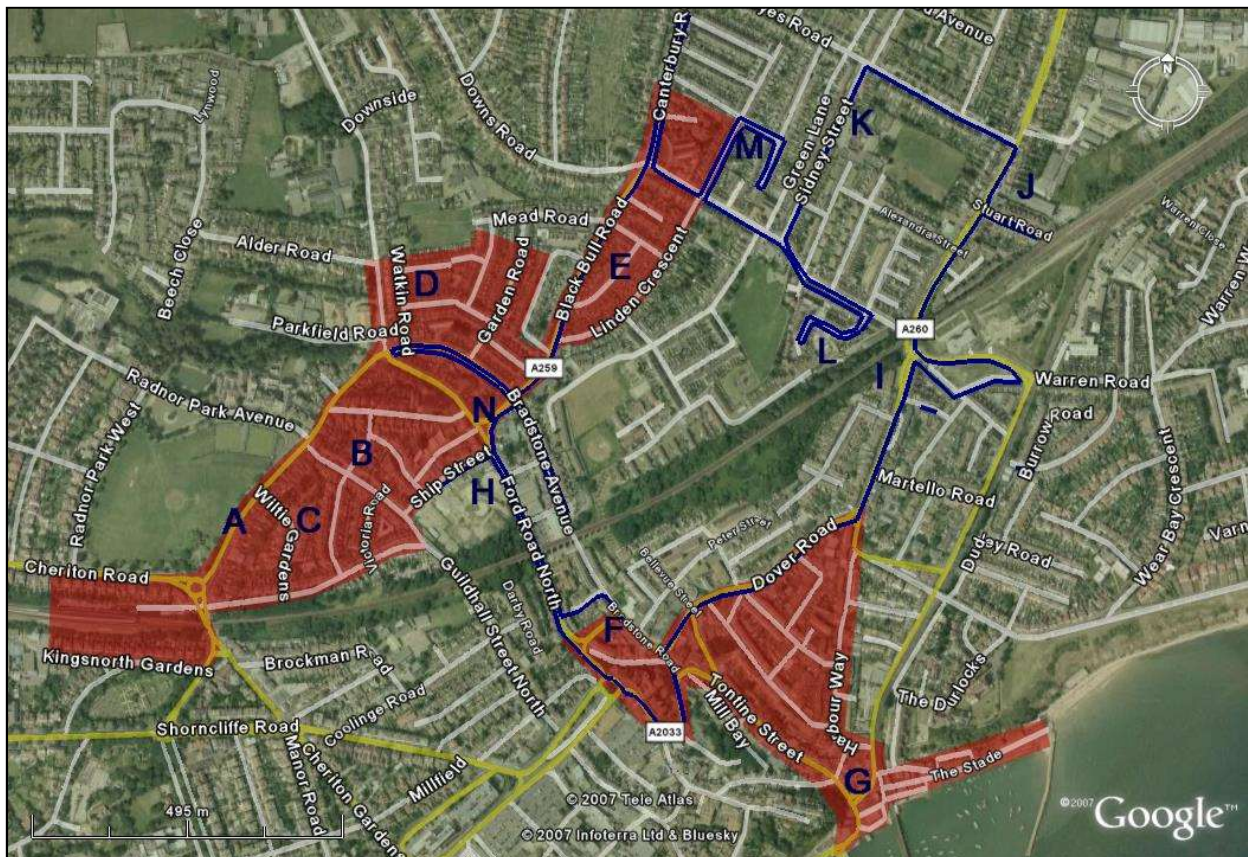


Figure A4.12.29. Map of the main damaged area following the Folkestone earthquake. Shaded area is area of reconnaissance survey on 1st May. Dark blue line represents track of the detailed survey on 2nd May. Letters are indicating damaged areas mentioned in the text. From Sargeant *et al.* (2008), colour version courtesy of Dr. Graeme Weatherill.

Table A4.12.7. Damage observed in Folkestone, from descriptions by Sargeant *et al.* (2008).

Area	Place	Building Stock	Observed Damage	Quantification	Source
A	west and south of Radnor Park	1930s-style 3-storey detached houses	Dislodged chimney pots, not fallen.	On isolated properties.	a
	Radnor Park Road	1930s-style 2- and 3-storey semi-detached houses	Dislodged chimney bricks. Extensively cracked chimney stacks.	Most properties.	a
			Partial or complete collapse of chimney stacks. Consequent dislodging and/or breaking of roof tiles.	Many properties.	a
			2-4 mm wide cracks in plasterwork and brickwork of exterior walls.	Some properties.	a
B	south-east of Radnor Park Road	mixed ^(c)	Dislodged chimney pots and bricks. Full collapse of chimney stacks.	Extensive.	b
	Radnor Park Crescent, Bournemouth Gardens, St. John's Church Road	early Edwardian terraced and 1930s-style semi-detached ^(c)	Full collapse of chimney stacks.	More than 50%.	b
C	Wiltie Gardens	early 20 th century 4-st. building	Long narrow cracks in plasterwork.	One specific building.	b
D	north of Pavilion Road and Radnor Park Road	terraced houses	Many reports of damage, not so evident from the exterior. Minor cracking of exterior plasterwork.	N/A	a
		semi-detached houses	Many reports of damage, more evident from the exterior.	N/A	a
E	east and parallel to Black Bull Road	terraced houses	Damage to chimneys.	High density of damage.	a
F	Grace Hill	3-storey residential apartment masonry building	10-15 mm wide crack in exterior wall extending through the roof line	One specific building.	a, b
	Grace Independent Baptist Church and School	building with vertical irregularity	Severe internal damage (no details). Vertical crack along the front.	One specific building.	a
G	Tontine Street and Tram Road	mix of pre-war and post-war buildings ^(c)	N/A	A few cases.	a
G-H	harbor, railway lines, viaducts, tunnels		-	None.	a, b
H	north end of Foord Road	terraced houses	Damage to chimneys. 1-2 mm wide in exterior walls.	N/A	b
	main commercial district	N/A	N/A	A few cases.	b
I	along Dover Road	terraced houses	Significant chimney damage.	Isolated cases.	a, b
	smaller roads connected to Dover Road	terraced houses	Cracks on façade.	Two cases.	b
		terraced houses	Cracks in the gable end of end-of-terraced houses.	Isolated cases.	a
J	Stuart Road	terraced houses	Partial or complete collapse of chimney stacks. Consequent damage to roof tiles.	One third.	a, b
K	west of Dover Road, along Sidney Street and Canterbury Road	1930s-style terraced houses	Partial or complete collapse of chimney stacks. 10-mm wide cracks in non-collapsed chimney stacks.	Many properties.	a, b
	Canterbury Road	1930s-style 3- and 4-storey semi-detached houses in good conditions	Partial collapse of chimney stacks.	Nearly 50%	a, b
L	Gladstone Road (south of Canterbury Road)	early Edwardian 2-storey terraced houses ^(c)	"Among the most badly damaged". Partial or complete collapse of chimney stacks. Consequent damage to roof tiles.	N/A	b
		early Edwardian 2-storey terraced house ^(c)	Extensive cracking in ceilings of most rooms. Partial collapse of chimney stack and damage to roof tiles. Differential movement between layers of bricks.	One specific building.	b
M	Marshall Street	1930s-style terraced houses	Partial or complete collapse of chimney stacks. Minor cracking in exterior plasterwork	"The highest density".	b
		1960s house in between 1930s terraced houses	Cracks at joint between older and newer construction.	One specific building.	b
N	Black Bull Road, Radnor Park Road and Foord Road junction	late-Victorian and early 20 th century terraced houses, with seemingly low maintenance	Partial collapse of chimney stacks.	"Not as high" as in A, B and K.	a
Not shown	Harvey Grammar School (2 km west of main damage)	built in 1912, façade bombed during WWII and rebuilt in 1945	Ceiling plasterwork cracked and fallen. 3-4 mm wide crack between older building and newer façade, through brickwork and mortar joints. Cracks radiant from windows	One specific building.	a, b
Not shown	close to Channel Tunnel Terminal (north-west of city)	1950s-style terraced houses with stream running nearby	Cracks in interior plaster. 3-4 mm wide crack across entire front of one house. Dislodged bricks in chimney stacks.	"A small terrace".	b

Sources:

a) Sargeant *et al.* (2008)b) Additional material not published in Sargeant *et al.* (2008), courtesy of Dr. G. Weatherillc) Additional material not published in Sargeant *et al.* (2008) with further verification from Google Street View, courtesy of Dr. G. Weatherill

The most common type of damage caused by this earthquake was the dislodgement of chimney clay pots and/or bricks. In most roads, chimney damage was observed in 10-20% of buildings, while in some others this percentage was as high as 60-70% (Sargeant *et al.*, 2008). In some of the properties chimney collapse resulted in secondary damages to the roof tiles and, rarely, to the roof structure.

Interior plaster cracking along joints of ceiling plaster board panels and diagonal cracking of plaster above door frames are other instances of non-structural damage that were commonly observed. Structural damage was minor and was observed just in a few locations where vertical cracking of walls and lintels was evident (Sargeant *et al.*, 2008).

It is interesting to note that the damage was not observed in masonry buildings of younger age, likely due to the implementation of good construction practices (Sargeant *et al.*, 2008).

Most of the damage was concentrated within the Foord district of Folkestone, though there were some rare cases of isolated instances of damage observed outside this area. Two examples of this are a property located 3 kilometres north-west from Folkestone, in the vicinity of the Pent stream and the Channel Tunnel Terminal, and Harvey Grammar School, also located around 2 km away from the most damaged area. The former consisted of a small terrace of 1950's masonry properties, one of which presented a large horizontal crack (3-4 mm width) across its entire front, and could not be occupied (Sargeant *et al.*, 2008, additional unpublished material courtesy of Dr. G. Weatherill). In the case of Harvey Grammar School, a 2-meter long, 3-4 mm wide vertical crack was observed at the joint of the front and sidewall, as shown in Figure A4.12.30. As mentioned in Section A4.12.7.3, it is suspected that the small crack may have been a consequence of the existence of a plane of weakness between the original building and the newer façade, rebuilt after World War II, potentially aggravated by the earthquake. An example of cracked and fallen plaster, which was observed in most of the classrooms, is shown in Figure A4.12.31 (Sargeant *et al.*, 2008, additional unpublished material courtesy of Dr. G. Weatherill).

The most damaged area was that enclosed by Radnor Park and Canterbury Road (letters A, B, C, D, E, F and G in Figure A4.12.29). Most of the reported and observed damage was related to dislodged or fallen chimney pots, cracking and partial or full collapse of chimney stacks, dislodged bricks and their falling from the roof, dislodgement and/or breaking of roof tiles caused by the above, cracking of bricks and plaster (Sargeant *et al.*, 2008, additional unpublished material courtesy of Dr. G. Weatherill). Scaffolding was erected on some of the properties and remedial measures were taken for the prevention of chimney stack collapses. In Figure A4.12.32, an example of evident fractures in plaster and brick at the corners of the doors and windows observed in Radnor Park Road (label A in Figure A4.12.29) is depicted. An example of a collapsed chimney and the subsequent damage to roof tiles is presented in Figure A4.12.33.

The type of damage observed during a survey that was conducted specifically for the properties classed as damage category 1 by the Shepway District Council was similar to the one observed in general, as mentioned above, though of higher degree. The typical dwellings in the surveyed areas were terraced houses from the 1930s. Some of the most

badly damaged properties were observed in area L, while area M presented the highest density of damaged residences. Examples of the damage observed in these areas are shown in Figure A4.12.34, which depicts an interior crack of more than one meter in length and three millimetres in width, and Figure A4.12.35, in which a crack that radiated from the joint between the newer (1960) property and older (1930) property is shown. The latter was most probably the result of differential shaking and vibration of these two houses (Sargeant *et al.*, 2008, additional unpublished material courtesy of Dr. G. Weatherill).



Figure A4.12.30. Harvey Boy's Grammar School: vertical cracking exacerbated by the earthquake strong shaking. Courtesy of Dr. Graeme Weatherill.



Figure A4.12.31. Harvey Boy's Grammar School: cracked and fallen plaster observed in the classroom. Courtesy of Dr. Graeme Weatherill.



Figure A4.12.32. Cracks in masonry observed in Radnor Park Road. Photograph credit: G. Weatherill. From Sargeant *et al.* (2008), colour version courtesy of Dr. Graeme Weatherill.



Figure A4.12.33. Chimney stack and damage to roof tiles. Photograph credit: G. Weatherill. From Sargeant *et al.* (2008), colour version courtesy of Dr. Graeme Weatherill.



Figure A4.12.34. Cracking of interior of property in Gladstone Road. Photograph credit: S.L. Sargeant, courtesy of Dr. G. Weatherill.



Figure A4.12.35. Cracking at junction between terrace house style (to right) and a 1960s inserted replacement property. Photograph credit: P.W. Burton, courtesy of Dr. G. Weatherill.

As mentioned in section A4.12.4.1, Sargeant *et al.* (2008) present a debate regarding whether the damage observed in Folkestone should be considered as EMS-98 damage grade 1 (no structural damage, slight non-structural damage) or 2 (slight structural damage with moderate non-structural damage). While damage grade 1 seems to better describe what was observed in the buildings themselves (*i.e.*, hairline cracks in very few walls, fall of small pieces of plaster, very few cases of fall of loose stones from upper parts of buildings), damage grade 2 explicitly covers the partial collapse of chimneys, which was extensively observed. However, the remaining criteria that characterise damage grade 2, namely, cracks in many walls and fall of fairly large pieces of plaster, was not observed, with the exception of a very small number of buildings. According to Sargeant *et al.* (2008), there

were many observations of buildings with vulnerability class B suffering damage of grade 1, very few observations of damage grade 2, and no damage to buildings with vulnerability class C.

In spite of the relevance of this debate, Sargeant *et al.* (2008) do not present detailed observation counts and statistics of damage states. What are, however, available are statistics regarding the responses from the public received for the online questionnaire of the BGS for the most damaged 5x5 km square area, which contains Folkestone. The questionnaire resulted in 200 replies in the form of “yes, it was observed in my property”, “no, it was not” and “no answer/cannot tell”. The results of the questionnaire are shown in Table A4.12.8. As observed from this table, small cracks in the plaster are reported by more than half of the observers, while a third of them reported large cracks. More than 75% of the respondents observed fall of small objects, while 89 of 200 reported books falling from shelves (Sargeant *et al.*, 2008).

Table A4.12.8. Summary of reports of strong effects and damage from Folkestone for the most damaged 5x5 km square area. From Sargeant *et al.* (2008).

Effect	Yes	No	N/A
Objects shifted	164	14	22
Books etc. fall	89	52	59
Furniture shifted	37	99	64
Furniture topples over	9	127	54
Small cracks in plaster	114	14	72
Large cracks in plaster	58	49	93
Fall of small pieces of plaster	83	35	82
Fall of large pieces of plaster	17	75	108
Fall of stones	60	58	82
Small cracks in brickwork	67	42	91
Large cracks in brickwork	31	68	101
Fall of free-standing walls	7	91	102
Fall of chimneys	40	75	85
House walls partly collapse	10	98	92

The additional, unpublished material of Sargeant *et al.* (2008), courtesy of Dr. G. Weatherill, contains statistical information on damage for 1,358 dwellings of the Folkestone area. According to this data, no damage was reported for around 40% of all the 1,358 dwellings for which information is available. The rest (60%) of the dwellings had reported damage and were categorized into five damage states according to the classification system of Shepway District Council (section A4.12.8.1), as follows:

- Category 1: 7%
- Category 2: 12%

- Category 3: 14%
- Category 4: 25%
- Category 5: 2%.

Given the definition of Category 4 (section A4.12.8.1), the total percentage of dwellings that were in a need of immediate assessment was 32% (7% dwellings of Category 1 and 25% dwellings of Category 4). It is noted that the word “dwelling” is being used herein to indicate individual postal addresses, which is what was noted in the survey. In this sense, a semi-detached house is, for example, counted as two dwellings. Apartment blocks were not assessed (Weatherill, *pers. comm.*).

Due to the damage suffered, some of the homes were evacuated. The Kent Fire and Rescue Service reported more than 400 emergency calls regarding issues concerning structural damage and gas smells (BBC, 2007a). EDF Energy reported that several thousand customers had lost electric power after the earthquake, but that the service was quickly restored (The Guardian, 2007; Sargeant *et al.*, 2008). Immediately after the shaking, residents gathered outside their homes due to fear of possible aftershocks (The Guardian, 2007).

It is noted that, due to the type of damage observed, it was not always possible for the surveyors to determine if all instances had been directly caused by the earthquake, other causes, or the worsening effects of the earthquake over pre-existing damage. In this respect, the exact number of damaged buildings is uncertain (Weatherill, 2017, *pers. comm.*). While the statistical information available for 1,358 dwellings indicates 815 damaged dwellings, a newspaper article citing the Association of British Insurers speaks of 1,300 affected homes (KentOnline, 2017), and another article mentions “about 1,500 properties” (KentOnline, 2007).

A4.12.8.3 Observed weaknesses

While there may have been a few factors playing a role in the consequences of this earthquake, the most outstanding weakness seems to be related to chimneys, not only because of their intrinsic slenderness and usual lack of seismic design, but also because a great proportion of them were poorly maintained and had lost mortar or suffered from sulphur intrusion (Sargeant *et al.*, 2008). Additionally, the overall poorer state of the building stock in comparison with the national average described in section A4.12.7.2 can be considered a weakness, though the report by the Shepway District Council (2001) does not specify what kind and level of deterioration was observed.

A4.12.8.4 Damage distribution

Sargeant *et al.* (2008) investigated the influence of site effects on the spatial distribution of damage observed in Folkestone. With this aim, they compared the latter with the geological map of the area, which indicates presence of superficial quaternary unconsolidated deposits, as shown in Figure A4.12.36 (A). However, due to its scale (1:50,000) and the fact

that the area under analysis is an urban area covered with manmade construction, said map cannot be expected to accurately indicate the location of superficial deposits in this context. Thus, Sargeant *et al.* (2008) compiled an additional map (Figure A4.12.36 (B)) using topographic curvature analysis to identify the areas from which unconsolidated deposits are expected to erode and the areas in which these are likely to accumulate. Comparing the two maps given in Figure A4.12.36, and Table A4.12.9, the authors concluded that the terrain-derived map indicates a higher proportion of damaged properties underlain by unconsolidated accumulated deposits than the geological map (*i.e.* 59% against 12%). While still considering their results satisfactory, the authors warn about the influence of the presence of mainline railway, roads and motorways on this kind of analysis.

Along similar lines though not conducting a specific study about it, Musson & Walker (2007) point out the possible role of site amplification along the course of the Pent culverted river. Additionally, Ottemöller *et al.* (2009) mention that site amplification effects similar to those observed in their H/V analysis at TFO station may have had an influence on the damage observed in Folkestone, though Sargeant *et al.* (2008) believe that this H/V analysis does not allow to draw conclusions with respect to the influence of site amplification in Folkestone.

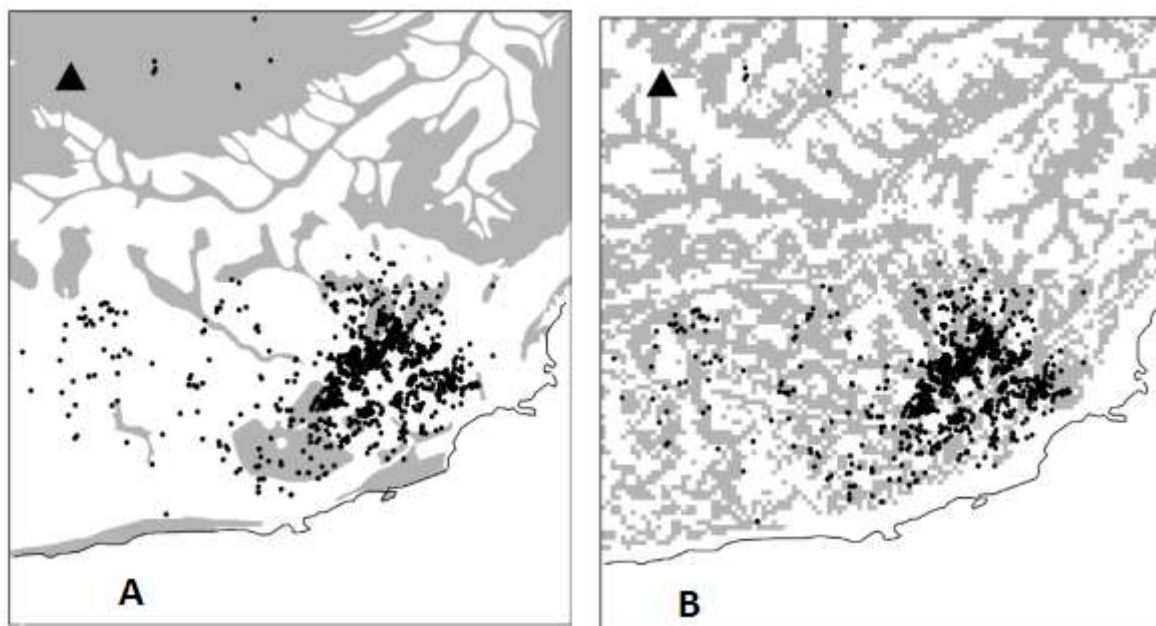


Figure A4.12.36. (A) 1:50,000 superficial geology map of the area, with mapped deposits shaded in grey; (B) Terrain analysis map; grey areas represent concave-upward landforms with accumulated unconsolidated deposits. From Sargeant *et al.* (2008).

Table A4.12.9. Number of damaged properties coinciding with unconsolidated deposits for the traditional geological map and the accumulated material model. Taken from Sargeant *et al.* (2008).

Geological Model	Number of properties	Significant damage (Category 1)	Unassessed (reportedly) damage
All property	1,326	778 (59%)	548 (41%)
Properties underlain by traditionally mapped superficial deposits	165 (12%)	93 (7%)	72 (5%)
Properties underlain by accumulation model	778 (59%)	467 (35%)	311 (23%)

The map in Figure A4.12.37 shows the spatial distribution of the damage in terms of the five-level classification system of the Shepway District Council described in section A4.12.8.1, for buildings for which this information is available (unpublished material of Sargeant *et al.*, 2008, courtesy of Dr. G. Weatherill). As can be observed, the highest density of damaged structures is associated with the area denoted with letter M in Figure A3.2.31, corresponding to Marshal Street. Most of the buildings in this area were classified as category four, meaning that they were in need of immediate action after the earthquake. High densities of damaged residences are observed in other parts of the Foord district as well (e.g. the area around Broadmead Road, Black Bull Road, Radnor Park Road, Canterbury Road, *etc.*).

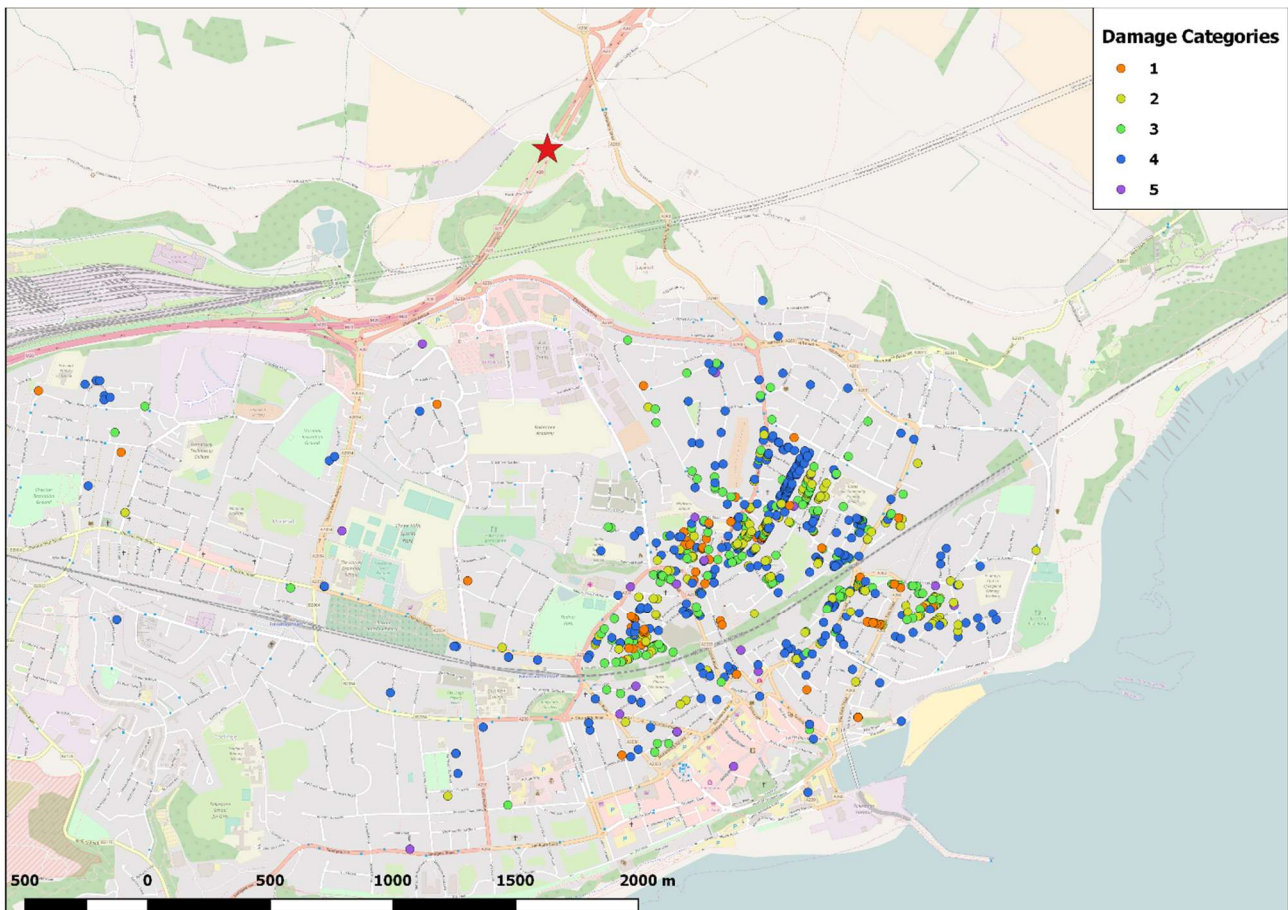


Figure A4.12.37. Distribution of damage produced by Folkestone earthquake. Red star indicates the epicentre according to the BGS. Data courtesy of Dr. G. Weatherill.

A4.12.9 Casualties and losses

A4.12.9.1 Numbers of dead and injured

The police reported to The Guardian (2007) that they received no reports of serious injuries. According to the south-east coast ambulance service, one woman in her 30s suffered a minor head injury and neck pain and was taken to the hospital. Salvation Army Minister Captain Peter West reported to The Guardian (2007) that many people were upset and confused, but no serious trauma was evident. Folkestone and Hythe Conservative Member of Parliament Michael Howard stated that they “have got off remarkably lightly”, considering

that no serious injuries nor real devastating damage to property was produced by the earthquake (BBC, 2007a).

Based on the information available at the International Disaster Database (EM-DAT) website, the total number of people affected by the Folkestone earthquake was 4,501. EM-DAT reports no dead or homeless people, and only one injured person. This one injury is also mentioned by Sargeant *et al.* (2008).

A4.12.9.2 Causes of casualties

As a consequence of this earthquake, only one person was injured and suffered minor head injuries due to falling masonry (Sargeant *et al.*, 2008).

A4.12.9.3 Estimates of economic losses

The estimated damage based on the International Disaster Database (EM-DAT) is 60,000,000 US dollars. Kent News (2007b) and KentOnline (2007) reported that the repair bill could be as high as £20 million, while the total cost of the damage according to estimates of insurers was around £10 million (KentOnline, 2017). The Association of British Insurers (ABI) claimed that the insurance cost for the damage could reach “single figure millions” (BBC, 2007a), though they have also reported to KentOnline (2017) that the exact cost of the damage to 1,300 affected homes was not known, since the data was not kept at the time of the earthquake. These monetary values of the economic losses correspond to the time of the earthquake occurrence.

Both the temporary loss of power to the main city and the closure of roads whilst debris was cleared resulted in substantial costs related to business interruption (Weatherill, 2017, personal communication).

A4.12.10 Discussion and conclusions

This **M4.0** earthquake occurred on 28th April 2007, at 07:18 UTC (08.18 local time), and was the most damaging seismic event in the UK for some decades. While it was felt over a rather restricted area for an event of its magnitude, the maximum EMS-98 intensity was between VI and VII, and the north-south component of the horizontal acceleration recorded at the station closest to the epicentre reached the highest PGA ever observed in the UK (0.118 g) at the time of writing, a value significantly larger than indicated by the national hazard map for usual design recurrence periods.

Damage was mostly concentrated in Folkestone, where many properties suffered partial or total chimney collapse and fine cracks in brick masonry walls and plaster. Only some partial collapses and falls of free-standing walls were reported within the most damaged area. The number of affected properties seems to have ranged between around 800 to 1,500, though most instances of damage were not serious. The observed damage can be explained by the shallowness of this seismic event, its proximity to the town of Folkestone, the large amplitude

of spectral accelerations in the short period range, and the poorer condition of the building stock in this part of the UK with respect to the national average, both regarding the buildings themselves and, in particular, their chimneys. While the distribution of superficial unconsolidated deposits is likely to have played a role in the amplification of ground motions, results cannot be considered conclusive.

Only one person was injured by falling masonry, though minor additional injuries could have occurred had the earthquake happened during a school day. Expected to have been in the order of tens of millions, the extent of the monetary loss is not fully known but was certainly influenced by the downtime costs incurred by local businesses.

A4.12.11 References

A4.12.11.1 Bibliography

Afshari, K. & J. P. Stewart (2016). Physically parameterized prediction equations for significant duration in active crustal regions. *Earthquake Spectra* **32**(4), 2057-2081.

Akkar, S. & J. J. Bommer (2010). Empirical equations for the prediction of PGA, PGV, and spectral accelerations in Europe, the Mediterranean Region, and the Middle East. *Seismological Research Letters* **81**, 195–206.

Allen, T. I., D. J. Wald, P. S. Earle, K. D. Marano, A. J. Hotovec, K. Lin & M. G. Hearne (2009). An Atlas of ShakeMaps and population exposure catalog for earthquake loss modeling. *Bulletin of Earthquake Engineering* **7**(3), 701–718.

Arango, M. C., M. W. Free & Z. A. Lubkowski (2012). Comparing predicted and observed ground motions from UK earthquakes. *15th World Conference on Earthquake Engineering (15WCEE)*, September 24-28, Lisboa, Portugal.

Atkinson, G. M. & D. M. Boore (2006). Earthquake Ground-Motion Prediction Equations for eastern North America. *Bulletin of the Seismological Society of America* **96**(6), 2181–2205.

Atkinson, G.M. & D. M. Boore (2011). Modifications to existing GMPE in light of new data. *Bulletin of the Seismological Society of America* **101**(3), 1121-1135.

Atkinson, G. M. & S. I. Kaka (2007). Relationships between felt intensity and instrumental ground motion in the Central United States and California. *Bulletin of the Seismological Society of America* **97**, 497–510.

Atkinson, G. M. & D. J. Wald (2007). ‘Did you feel it?’ Intensity data: A surprisingly good measure of earthquake ground motion. *Seismological Research Letters* **78**, 362–368.

Baptie, B. (2008a). *UK earthquake monitoring 2007/2008*. British Geological Survey, Commissioned Report OR/08/072, 42 pp. Available online at (last accessed 7th July 2017):
http://www.earthquakes.bgs.ac.uk/publications/annual_reports/2008_19th_annual_report.pdf.

Baptie, B. (2008b). *UK earthquake monitoring 2008/2009*. British Geological Survey, Commissioned Report OR/08/072, 52 pp. Available online at (last accessed 7th July 2017):
http://www.earthquakes.bgs.ac.uk/publications/annual_reports/2009_20th_annual_report.pdf.

Baptie, B. (2010). Seismogenesis and state of stress in the UK. *Tectonophysics* **482**(1–4), 150–159.

- Baptie, B. L., L. Ottemöller, S. Sargeant, G. Ford & A. O'Mongain (2005). The Dudley earthquake of 2002: A moderate sized earthquake in the UK. *Tectonophysics* **401**, 1–22.
- Bommer, J. J., P. J. Stafford & J. E. Alarcón (2009). Empirical equations for the prediction of the significant, bracketed, and uniform duration of earthquake ground motion. *Bulletin of the Seismological Society of America* **99**(6), 3217–3233.
- Bommer, J. J., P. J. Stafford, J. E. Alarcon & S. Akkar (2007). The influence of magnitude range on empirical ground-motion prediction. *Bulletin of the Seismological Society of America* **97**(6), 2152–2170.
- Boore, D. M. & G. M. Atkinson (2008). Ground-motion prediction equations for the average horizontal component of PGA, PGV, and 5%-damped PSA at spectral periods between 0.01 s and 10.0 s. *Earthquake Spectra* **24**(1), 99–138.
- Booth, E. (2010). Eurocode 8 — Design of structures for earthquake resistance. In Roberts, J. (eds.): *The essential guide to Eurocodes transition* (part 10). British Standards Institution (BSI), pp 171–181. Available online at: <http://shop.bsigroup.com/upload/eurocodes/pdf/BIP2197/Part-10.pdf>. Last accessed: 7th July 2017.
- Boulanger, R. W. & I. M. Idriss (2006). Liquefaction susceptibility criteria for silts and clays. *Journal of Geotechnical and Geoenvironmental Engineering* **132**(11), 1413–1426.
- Bouroz, A. (1962). Contribution a l'etude de la structure du bassin houiller du Boulonnais. (Contribution to the study of the structure of the Boulonnais coal basin, in French). *Annales de la Société géologique du Nord* **82**, 27–37.
- British Standards Institution (BSI, 1944). *Code of Practice, CP4*. London, United Kingdom.
- British Standards Institution (BSI, 2005). *Eurocode 1: Actions on structures. General actions. Wind actions. BS EN 1991-1-4:2005+A1:2010*. London, United Kingdom.
- British Standards Institution (BSI, 2008). *UK National Annex to Eurocode 1. Actions on structures. General actions. Wind actions. NA to BS EN 1991-1-4:2005+A1:2010*. London, United Kingdom.
- British Standards Institution (BSI, 2009). *Recommendations for the design of structures for earthquake resistance to BS EN 1998. PD 6698:2009*. London, United Kingdom.
- CEN (2004). *Eurocode 8: Design of structures for earthquake resistance-Part1: General Rules, seismic actions and rules for buildings*. European Committee for Standardization, Brussels, Belgium.
- Center for International Earth Science Information Network - CIESIN - Columbia University, United Nations Food and Agriculture Programme - FAO, and Centro Internacional de Agricultura Tropical - CIAT (2005). Gridded Population of the World, Version 3 (GPWv3). Palisades, NY: NASA Socioeconomic Data and Applications Center (SEDAC). <http://dx.doi.org/10.7927/H4639MPP>. Last accessed: 7th July 2017.
- Chadwick, R. A., T. C. Pharaoh, J. P. Williamson & R. M. W. Musson (1996). *Seismotectonics of the UK*. British Geological Survey, Technical Report WA/96/3C, Keyworth, Nottingham, United Kingdom. Available online at: <http://nora.nerc.ac.uk/7994/1/WA96003.pdf>. Last accessed: 7th July 2017.
- Dines, H. G. (1933). *The sequence and structure of the Kent Coalfield*. Summary of Progress of the Geological Survey of Great Britain and the Museum of Practical Geology for the year 1932 (part II), London, United Kingdom. Available at: <http://pubs.bgs.ac.uk/publications.html?pubID=B00240>. Last accessed: 7th July 2017.

- Galloway, D. D. (2008). *Bulletin of British earthquakes 2007*. British Geological Survey, Internal Report OR/08/048. Available online at (last accessed 7th July 2017): <http://www.earthquakes.bgs.ac.uk/publications/bulletins/Eqbull2007.pdf>.
- Gething, B. (2010). *Design for future climate: opportunities for adaptation in the built environment*. Technology Strategy Board, Report, Swindon, United Kingdom. Available online at (last accessed 9th October 2017): http://www.cakex.org/sites/default/files/documents/tsb-climatechangereport-0510_final1.pdf
- Giardini, D., G. Grünthal, K. M. Shedlock & P. Zhang (1999). The GSHAP global seismic hazard map. *Annali di Geofisica* **42**(6), 1225–1228.
- Grünthal, G. (1998). *European Macroseismic Scale 1998 (EMS-1998)*. Cahiers du Centre Europeen de Geodynamique et de Seismologie 15, Centre Europeen de Geodynamique et de Seismologie, Luxembourg. Available online at (last accessed 7th July 2017): http://www.franceseisme.fr/EMS98_Original_english.pdf.
- Hill, M., D. Gatey & N. Peiris (2013). Damage observations in the UK from windstorm Ulli and implications for building codes and loss estimation. *Proceedings of the 6th European & African Conference on Wind Engineering*, July 7-13, Cambridge, UK. Available online at (last accessed 9th October 2017): <http://www.iawe.org/Proceedings/EACWE2013/M.Hill.pdf>
- Hutton, L. K. & D. Boore (1998). The MI scale in Southern California. *Bulletin of the Seismological Society of America* **77**, 2074–2094.
- Jaiswal, K. S. & D. J. Wald (2008). *Creating a global building inventory for earthquake loss assessment and risk management*. U.S. Geological Survey, Open-File Report 2008-1160. Available online at: <https://pubs.usgs.gov/of/2008/1160/>. Last accessed: 7th July 2017.
- Klose, C. D. (2007). Coastal land loss and gain as potential earthquake trigger mechanism in SCR's. *AGU Fall Meeting Abstracts*. San Francisco, California, USA.
- Lamplugh, G. W., F. L. Kitchin & J. Pringle (1923). *The concealed Mesozoic rocks in Kent*. Memoirs of the Geological Survey, HMSO, London, United Kingdom. Available online at (last accessed 7th July 2017): <http://pubs.bgs.ac.uk/publications.html?pubID=B01998>.
- Lay, T. & T. C. Wallace (1995). *Modern global seismology*. Academic Press, San Diego, California.
- Lilwall, R. C. (1976). *Seismicity and seismic hazard in Britain*. Seismological Bulletin, Institute of Geological Sciences (Great Britain), HMSO, London, United Kingdom.
- Lovell, J. H. & P. H. O. Henni (1999). *Historical seismological observatories in the British Isles*. British Geological Survey, Technical Report WL/99/13, Edinburgh, Scotland, UK. Available online at: <http://www.earthquakes.bgs.ac.uk/hazard/pdf/wl9913.pdf>. Last accessed: 7th July 2017.
- Melville, C. P., A. Levret, P. Alexandre, J. Lambert & J. Vogt (1996). Historical seismicity of the Strait of Dover - Pas de Calais. *Terra Nova* **8**, 626–647.
- Musson, R. M. W. (1994). *A catalogue of British earthquakes*. British Geological Survey, Global Seismology Report WL/94/04.
- Musson, R. M. W. (2005). Intensity attenuation in the UK. *Journal of Seismology* **9**, 73–86.
- Musson, R. M. W. (2007). British earthquakes. *Proceedings of the Geologists' Association* **118**(4), 305–337.
- Musson, R. M. W. (2012). Interpreting intraplate tectonics for seismic hazard: A UK historical perspective. *Journal of Seismology* **16**(2), 261–273.

Musson, R. M. W. & S. L. Sargeant (2007). *Eurocode 8 seismic hazard zoning maps for the UK*. British Geological Survey, Technical Report CR/07/125N, 70 pp. Available online at: http://www.earthquakes.bgs.ac.uk/hazard/UK_seismic_hazard_report.pdf. Last accessed: 7th July 2017.

Musson, R. M. W. & W. Winter (1997). Seismic hazard maps for the UK. *Natural Hazards* **14**, 141–154.

Musson, R. & A. Walker (2007). Folkestone earthquake 28 April 2007. *The Society for Earthquake and Civil Engineering Dynamics (SECED) Newsletter* **20**(2), 1–16.

O'Reilly, J. P. (1884). Catalogue of the earthquakes having occurred in Great Britain and Ireland during historical times. *Transactions of the Royal Irish Academy* **28**, 285–316.

Ottmöller, L. & S. L. Sargeant (2010). Ground-motion difference between two moderate-size intraplate earthquakes in the United Kingdom. *Bulletin of the Seismological Society of America* **100**(4), 1823–1829.

Ottmöller, L., B. Baptie & N. J. P. Smith (2009). Source parameters for the 28 April 2007 Mw 4.0 earthquake in Folkestone, United Kingdom. *Bulletin of the Seismological Society of America* **99**(3), 1853–1867.

Ove Arup (1993). *Earthquake hazard and risk in the UK*. Technical Report, Ove Arup & Partners, London.

Plumtre, J. H. (1959). Underground waters of the Kent Coalfield. *Transactions of the American Institute of Mining and Metallurgical Engineers* **119**(3), 155–169.

Sargeant, S. L., P. J. Stafford, R. Lawley, G. Weatherill, A. J. S. Weston, J. J. Bommer, P. W. Burton, M. Free, R. M. W. Musson, T. Kuuyuor & T. Rossetto (2008). Observations from the Folkestone, U.K., earthquake of 28 April 2007. *Seismological Research Letters* **79**(5), 672–687.

Shepway District Council (2001). *Private sector house condition survey*. Managed Services and Consultancy, Draft Final Report.

United Nations, ed. (2008). *Human Development Report 2007/2008 - Fighting climate change: human solidarity in a divided world*. Report of the United Nations Development Programme (UNDP), New York, United States.

United Nations, ed. (2009). *Human Development Report 2009 - Overcoming barriers: human mobility and development*. Report of the United Nations Development Programme (UNDP), New York, United States.

United Nations, ed. (2010). *Human Development Report 2010 – The real wealth of nations: pathways to human development*. Report of the United Nations Development Programme (UNDP), New York, United States.

United Nations, ed. (2016). *Human Development Report 2016 – Human Development for Everyone*. Report of the United Nations Development Programme (UNDP), New York, United States.

Wald, D.J. & T.I. Allen (2007). Topographic slope as a proxy for seismic site conditions and amplification. *Bulletin of the Seismological Society of America* **97**, 1379–1395. Slope-based online map viewer available at: <http://usgs.maps.arcgis.com/apps/webappviewer/index.html?id=8ac19bc334f747e486550f32837578e1>. Data used herein downloaded from deprecated version last accessed on 7th July 2017.

Wald, D. J., J. Quitoriano, T. H. Heaton & H. Kanamori (1999). Relationship between peak ground acceleration, peak ground velocity and Modified Mercalli Intensity in California. *Earthquake Spectra* **15**(3), 557–564.

Warren, S. T. & C. S. Harris (1996). An interpretation of the structural geology. In Harris C. S., M. B. Hart, P. M. Varley & C. D. Warren (eds.): *Engineering geology of the Channel Tunnel*. Thomas Telford Publishing, London, United Kingdom.

Warshaw, J., O. Bradbury, L. Cartell & S. Beech (2006). *Conservation area appraisal- Folkestone*. Conservation Architecture and Planning, Headley, Hampshire, UK. Available online at: <https://www.capstudios.co.uk/documents/081217FinalAdobe8sm.pdf>. Last accessed: 7th July 2017.

Whittaker, A., N. R. Brereton, C. J. Evans & R. E. Long (1989). Seismotectonics and crustal stress in Great Britain. In Gregersen, S., P. Basham (eds.): *Earthquakes at North-Atlantic passive margins: Neotectonics and postglacial rebound*. Proceedings of the NATO Advanced Research Workshop, May 9-13 (1988), Vordingborg, Denmark, 393–411.

Wilson, M.P., G.R. Foulger, J.G. Gluyas, R.J. Davies & B.R. Julian (2017). HiQuake: The human-induced earthquake database. *Seismological Research Letters* **88**(6), 1560-1565. Database available at: <http://inducedearthquakes.org/>. Last accessed: 5th February 2018.

Woessner, J., D. Giardini, H. Crowley, F. Cotton, G. Grünthal, R. Arvidsson, R. Basili, M. B. Demircioglu, S. Hiemer, C. Meletti, R. M. W. Musson, A.N. Rovida, K. Sesetyan, M. Stucchi & The SHARE Consortium (2015). The 2013 European Seismic Hazard Model: Key Components and Results. *Bulletin of Earthquake Engineering* **13**(12), 3553–3596. Online data source: <http://www.efehr.org/en/home/>. Last accessed: 10th October 2017.

Worden, C.B., E.M. Thompson, M. Hearne & D.J. Wald (2017). *ShakeMap V4 Manual: technical manual, user's guide, and software guide*. United States Geological Survey. Available online at: <http://usgs.github.io/shakemap/>.

A4.12.11.2 Web references

BBC (2007a): http://news.bbc.co.uk/2/hi/uk_news/england/6605095.stm. Last accessed: 7th July 2017

BBC (2007b): http://news.bbc.co.uk/2/hi/uk_news/england/dorset/6603547.stm. Last accessed: 7th July 2017

British Geological Survey (BGS): <https://www.bgs.ac.uk/>
BGS (2007): Report for the 28-Apr-2007 Folkestone event (last accessed 7th July 2017): http://www.earthquakes.bgs.ac.uk/education/reports/folkestone/folkestone_28_april_2007.htm
BGS (2017): BGS Geology 625k (DiGMapGB-625) data downloads (last accessed 7th July 2017): http://www.bgs.ac.uk/products/digitalmaps/dataInfo.html#_625

Department for Business Innovation and Skills (BIS, 2011): <http://webarchive.nationalarchives.gov.uk/20121212135622/http://www.bis.gov.uk/policies/business-sectors/biotechnology-pharmaceuticals-and-healthcare/pharmaceutical>
Last accessed: 7th July 2017

European-Mediterranean Seismological Centre (EMSC): <https://www.emsc-csem.org/>. Last accessed: 7th July 2017

Folkestone & Hythe Birds (2017): <http://www.folkestonebirds.com/Sites/Geology.pdf>. Last accessed: 7th July 2017

International Seismological Centre (ISC):

<http://www.isc.ac.uk/>

Last accessed: 7th July 2017

Kent News (2007a):

<https://web.archive.org/web/20070531231344/http://www.kentnews.co.uk/kent-news/People-felt-tremors-in-the-weeks-leading-up-to-Earthquake-newsinkent3638.aspx>

Last accessed: 7th July 2017

Kent News (2007b):

<http://www.kentnews.co.uk/news/earthquake-clean-up-costs-could-hit-16320million-1-1031489>

Last accessed: 7th July 2017

KentOnline (2007):

<http://www.kentonline.co.uk/folkestone/news/cost-of-the-quake---1500-build-a29468/>

Last accessed: 7th July 2017

KentOnline(2017):

<http://www.kentonline.co.uk/folkestone/news/remembering-day-that-rocked-our-124738/>

Last accessed: 7th July 2017

LandIS (2017):

<http://www.landis.org.uk/soilscapes/index.cfm>

Last accessed: 7th July 2017

Ministerial Industry Strategy Group Pharmaceutical Industry (2009):

http://webarchive.nationalarchives.gov.uk/20130107105354/http://www.dh.gov.uk/prod_consum_d/h/groups/dh_digitalassets/%40dh/%40en/%40ps/documents/digitalasset/dh_113133.pdf

Last accessed: 7th July 2017

Office for National Statistics (ONS):

<https://www.ons.gov.uk>

Last accessed: 5th May 2017

The Guardian (2007):

<https://www.theguardian.com/uk/2007/apr/28/theobserver.uknews>

Last accessed: 7th July 2017

The International Disaster Database (EM-DAT):

<http://www.emdat.be/database>

Last accessed: 5th May 2017

United Kingdom Soil Observatory (UKSO, 2017):

<http://mapapps2.bgs.ac.uk/ukso/home.html>

Last accessed: 7th July 2017

United Nations Development Program (2017):

<http://hdr.undp.org/en/data>

Last accessed: 7th July 2017

United States Geological Survey (USGS): <https://earthquake.usgs.gov/>

USGS (2017a): Website for the Folkestone event (last accessed 7th July 2017):

<https://earthquake.usgs.gov/earthquakes/eventpage/usp000fase#executive>

World Economic Outlook Database (WEO, 2016):

<https://www.imf.org/external/pubs/ft/weo/2016/02/weodata/index.aspx>

Last accessed: 7th July 2017

A4.13. August 2017 M3.9 Ischia earthquake, Italy

This earthquake occurred on 21st August 2017, at 18.57 UTC (20.57 local time), on the volcanic island of Ischia in the Tyrrhenian Sea, west-southwest of Naples, Italy. It is the strongest event to have occurred in this area since 1883. Very few aftershocks of low magnitude were recorded and no foreshock activity was reported. The degree of localized damage in the hilly part of Casamicciola Terme was disproportionally high (I_0 =VIII on the EMS scale) for the moderate magnitude of the earthquake, while macroseismic intensities of IV-V were reported in most of the island. The shallowness and proximity of the hypocentre, site effects and the resonance of the ground motion with the local building typologies are some of the reasons for the extensive damage observed, together with the vulnerability of the structures due to poor design and construction quality.

A4.13.1 Tectonic and seismic setting

A4.13.1.1 Tectonic setting

The area which hosted the Ischia Island earthquake of 21st August 2017 is situated in the volcanic field of the Campania Plain (Piana Campana), in southern Italy (Figure A4.13.1), a NW-SE trending graben which subsided up to 5 km during the Plio-Quaternary (Acocella *et al.*, 2001). The latter was formed as a consequence of the extensional movement of NW-SE trending normal faults bounding the eastern margin of the Tyrrhenian basin, as well as NE-SW normal-to-strike-slip fault systems (Acocella & Funiciello, 1999). Ischia and its neighboring islands, Procida and Vivara, along with the Phlegrean Fields (Campi Flegrei) and Mt. Vesuvius-Somma, constitute a volcanic complex which lies on the western margins of Piana Campana, crossing it in an east-west direction. The resolved strain field suggests a N-S to NE-SW extensional regime with a deformation rate of around 70 nanostrain/year in the region of Ischia Island (INGV G.D.L. 2017; Devoti *et al.*, 2010, 2017; Tibaldi & Vezzoli, 1998).

The island of Ischia is a product of effusive and explosive volcanic activity that began over 150ka (ka = thousand years) ago, initially in a submarine environment. Gradually, the main morphological feature in the middle of the island, Mt. Epomeo, was formed. A significant eruption that occurred 55ka ago, known in the literature as the “Monte Epomeo Green Tuff” event (Brown *et al.*, 2008), was followed by the collapse of the magmatic chamber and the formation of a caldera which was wholly or partially submerged into the sea (Capaldi *et al.*, 1976; De Vita *et al.*, 2006). However, during the past 33ka magma started to refill the magmatic reservoir, pushing the overlying crust upwards, uplifting Mt. Epomeo by 900 m to a present height of around 787m above sea level (Orsi *et al.*, 1991; Paoletti *et al.*, 2013). Mt. Epomeo is surrounded by faults striking roughly tangentially to its periphery, as shown in Figure A4.13.2: NW-SE and SW-NE faults at its SW and SE sides, respectively, N-S subvertical faults to its west, and inland-dipping EW-trending reverse faults to the north (Orsi *et al.*, 1991; Paoletti *et al.*, 2013).

That of the “resurgent block” (Figure A4.13.3) is considered among the various existing models as the most likely to explain the structure and morphology of Mt. Epomeo, according to volcanic, structural, seismic, hydrothermal, geophysical and geochemical evidence (Paoletti *et al.*, 2013). The mountain is rising along high-angle, inland-dipping reverse faults at the margins, within a locally compressional stress regime, as a result of an increase in pressure in the upper part of a shallow magmatic reservoir. The largest deformation occurs along its boundaries. Due to an asymmetry in the vertical displacement, the uplifted block is tilted by 15° towards the southwest, with outward-dipping normal faults in its interior facilitating the movement of magma through a locally extensional regime. Another model proposed by some authors (e.g., Carlino *et al.*, 2006; Carlino, 2012) is that of the “resurgent dome”, in which the uplift of the block is due to the growth of a laccolith that causes the crust to bend almost elastically, with the largest deformation occurring at the centre of the dome. In that case, the block is uplifted in a more symmetrical fashion (Paoletti *et al.*, 2013).

Based on the shallowness of the seismicity observed in the island and data indicating the existence of a high geothermal gradient, Carlino *et al.* (2006) believe the depth of the Brittle-Ductile Transition (BDT) zone to be approximately 2 to 3 km in the north of the island. Carlino *et al.* (2010) believe that the southern part of the island is less seismically active than the northern part due to its even higher geothermal gradient favouring slow-slip phenomena.

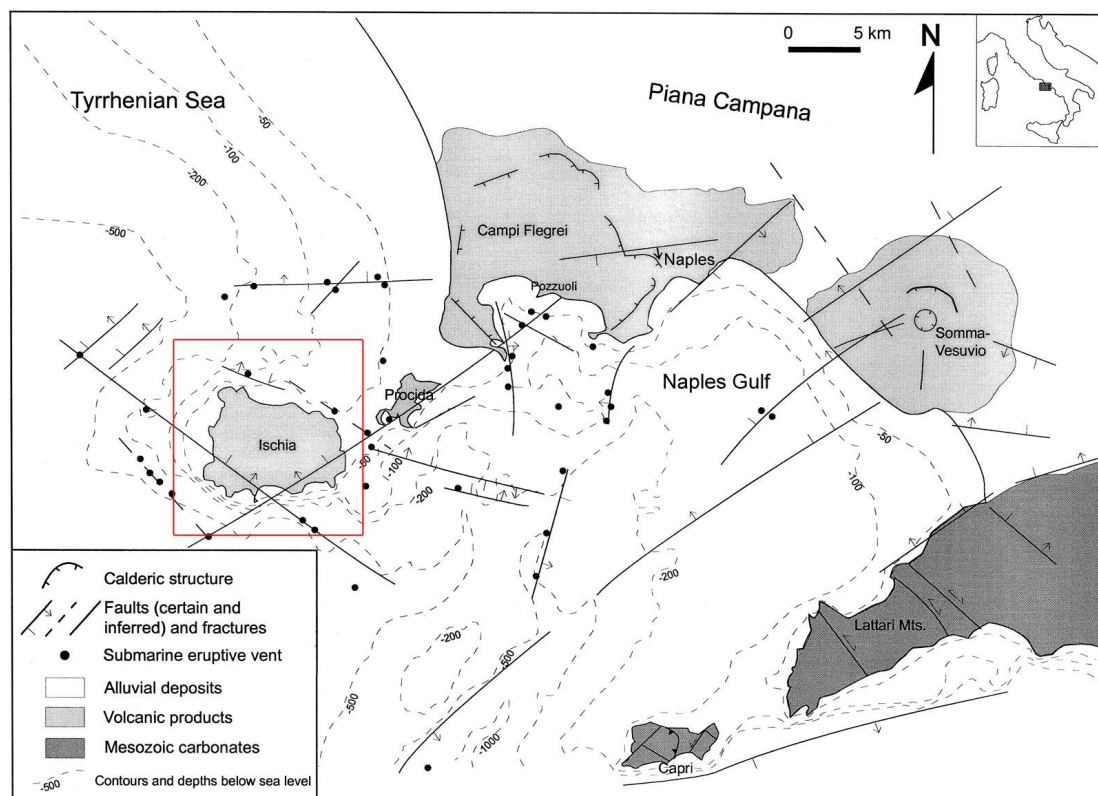


Figure A4.13.1. Tectonic map of the Naples gulf and the volcanic complexes of Ischia-Procida-Campi Flegrei and Somma-Vesuvio, by the southwest margins of the Tyrrhenian Sea. The red rectangle encloses Ischia Island. Figure modified after Acocella & Funiciello (1999).

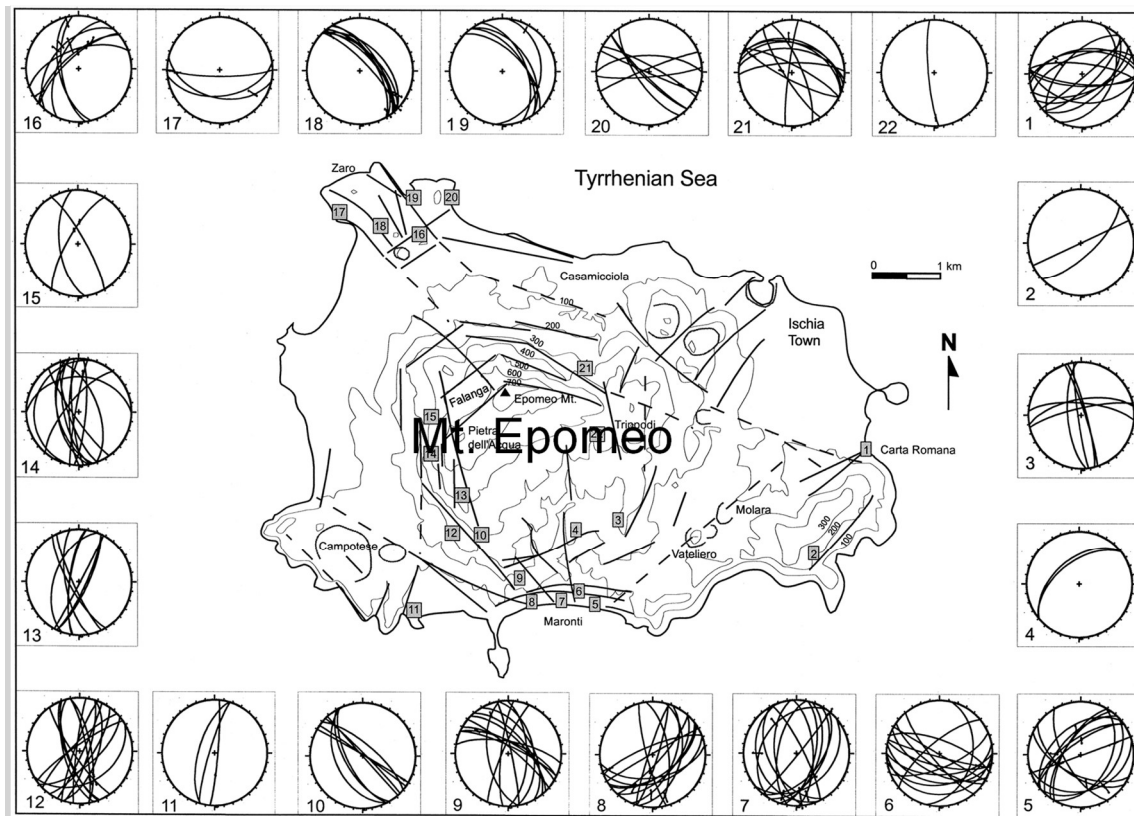


Figure A4.13.2. Mapped faults on Ischia Island and spatially grouped fault plane slickenside measurements at 22 points, represented by lower hemisphere projections on stereonets. From Acocella & Funiciello (1999).

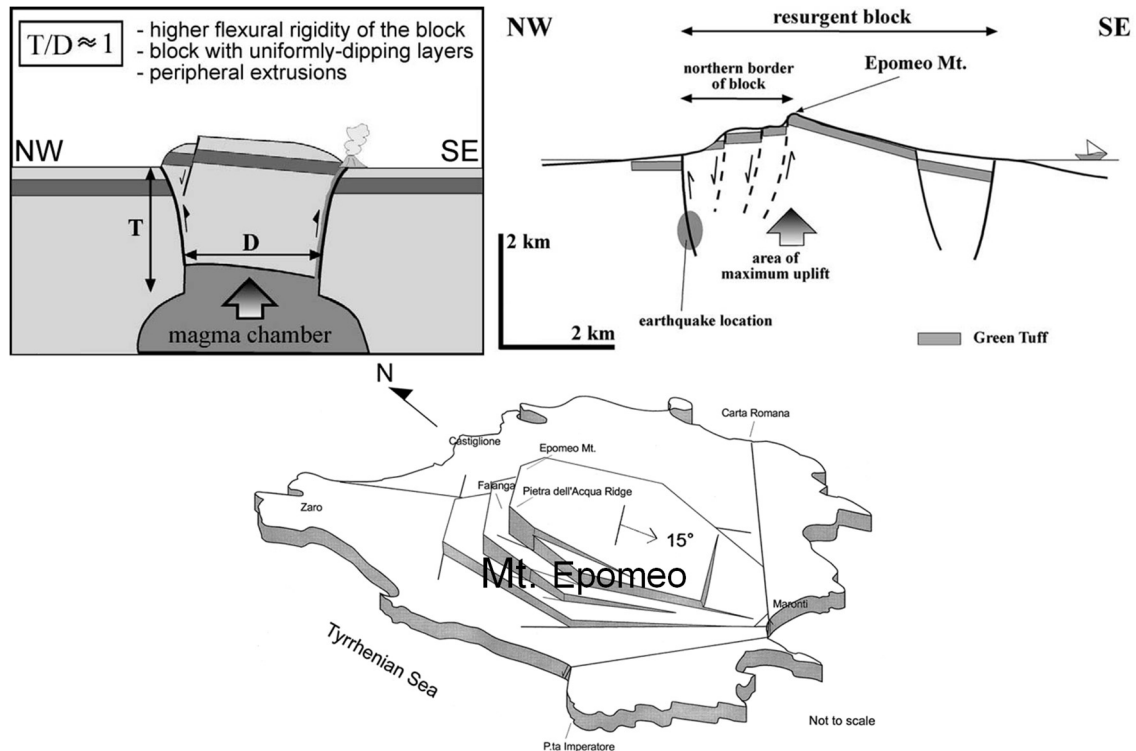


Figure A4.13.3. The resurgent block model (top left, from Acocella *et al.*, 2001). Sketch of the present state of Mt. Epomeo according to the resurgent block model (top right, modified from Acocella & Funiciello, 1999). Block diagram of the island of Ischia and Mt. Epomeo's 15° tilt towards the southeast (bottom, modified from Acocella & Funiciello, 1999).

A4.13.1.2 Regional and local seismicity

The broader region of the Gulf of Naples is generally characterized by low seismicity, as illustrated in Figure A4.13.4, mainly due to the relatively low strain rate and the absence of large active faults, though the effects of it being located at the margins of the National Seismological Network of Italy over the detectability of small earthquakes should not be overlooked. The Gulf of Naples is situated in a region where deep seismicity ($H > 300 \text{ km}$) is detected at the lowest part of the Wadati-Benioff zone due to the subduction that occurs along the Calabrian Arc (Sartori, 2003). However, shallow microseismicity is not absent. For example, rich activity has been observed in Campi Flegrei, mainly related to the uprising of magmatic fluids or gases through pre-existing faults (e.g., Di Luccio, 2015).

Figure A4.13.5 shows the local seismicity of Ischia Island where, until 2017, the earthquake rate had been estimated to be about 5 events of magnitude lower than 2.5 per year since 1999 (INGV-Terremoti, 2017a), while the energy release has also been low (INGV G.D.L., 2017). The seismicity is also characterized by focal depths shallower than 3 km (INGV G.D.L., 2017), which is consistent with the estimations for the BDT zone at roughly 2 km.

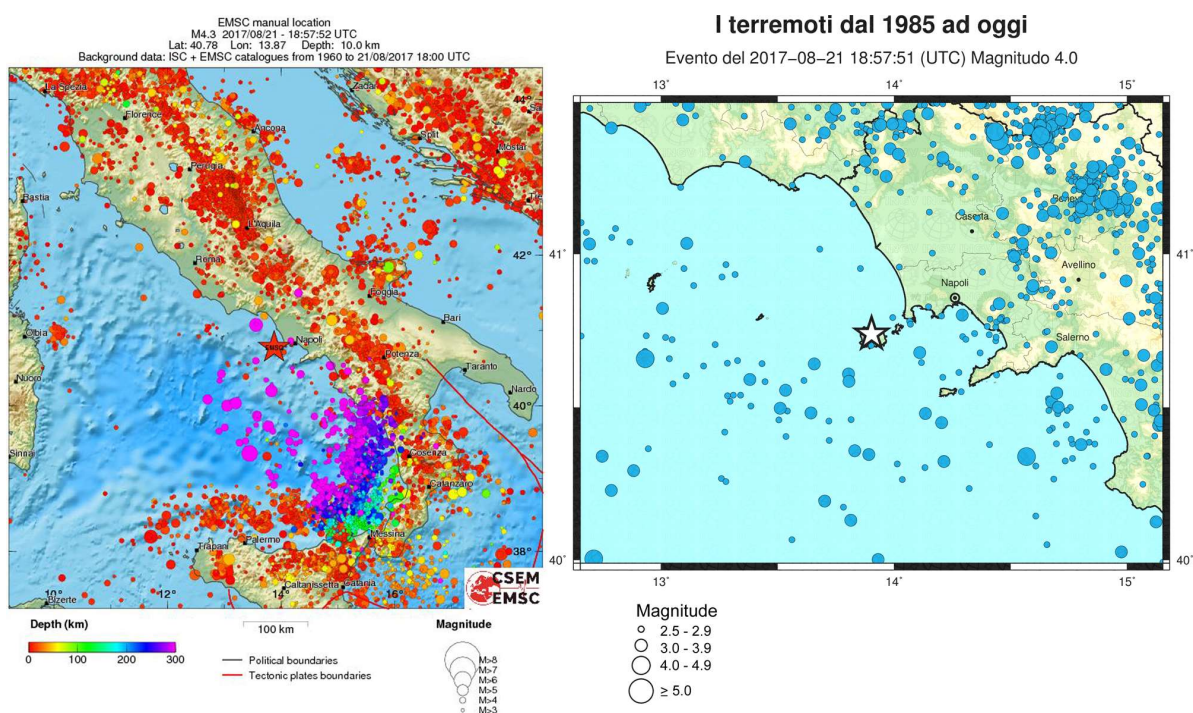


Figure A4.13.4. Seismicity of Italy since 1960 (left, red star indicates epicentre of the 2017 Ischia earthquake; CSEM/EMSC, 2017) and regional seismicity ($M \geq 2.5$) of the broader area of the Gulf of Naples for the period 1985-2017 (right, white star indicates epicentre; INGV, 2017).

Historically, it's been the northern part of Ischia that has suffered the most from earthquakes. Table A4.13.1 shows the intensities as reported in the municipality of Casamicciola Terme (referred to as Casamicciola in what follows), the largest settlement of Ischia, located along the northern coast of the island, for events that have occurred since 1762. During the 19th century there have been several cases of reported earthquakes that caused severe damage in Casamicciola. Well documented cases of strong earthquakes include those of 1762, 1796,

1828, 1881, and 1883 (INGV G.D.L., 2017). The latter also marked the last time that a significant seismic event had occurred on the island until 2017.

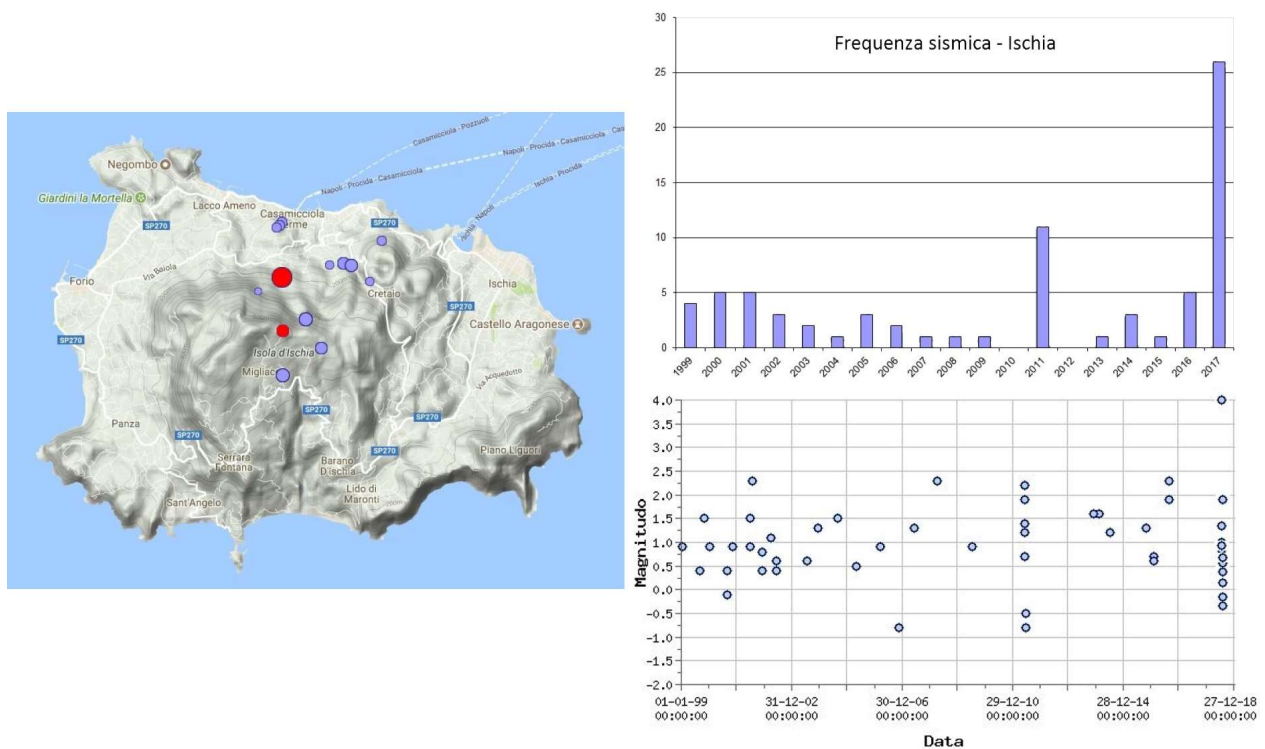


Figure A4.13.5. Location of epicentres (left), histogram of yearly number (top) and distribution of magnitudes (bottom) of the local seismicity on Ischia Island for the period 1999-2017. Epicentres in red in the left panel are for the mainshock ($M_d=4.0$) of 21/08/2017 and its largest recorded aftershock ($M_d=1.9$) on 23/08/2017. Figure modified after INGV G.D.L. (2017).

The earthquake of 28th July 1883 was the strongest and deadliest event in the seismic history of Ischia. It cost the life of 2,333 people, with 1,235 deaths and 451 injured in Casamicciola alone, where a maximum Mercalli-Cancani-Sieberg Intensity (MCS) of 10 was observed and 80% of the buildings were destroyed (CFTI4MED; CPTI15). This event has been widely used as a reference for studies on the macroseismic field on Ischia Island (e.g., Cubellis *et al.*, 2004; Carlino *et al.*, 2010) and slope instability hazard (Della Seta *et al.*, 2012; Paparo & Tinti, 2017). While the damage was extensive in the northern part of the island, it was only limited in its eastern part (INGV G.D.L., 2017). It should be noted that this event is registered with **M5.8** in many catalogues but, along with the magnitudes of other historic events in Italy, it is likely overestimated and subject to revision (INGV G.D.L., 2017). A more conservative value of **M4.26**, estimated using attenuation laws applicable for the volcanic region of Mt. Etna (Azzaro *et al.*, 2011), is currently accepted for the 1883 event (CPTI15; Rovida *et al.*, 2016). Several significant damaging aftershocks occurred in the two months following July 1883, in contrast to the 2017 Ischia earthquake, which produced only few minor aftershocks that were not felt by the population (INGV G.D.L., 2017).

Table A4.13.1. Reported earthquake intensities (MCS) in Casamicciola since the year 1762. Data from CPTI15 (Rovida *et al.*, 2016).

Year	Month	Day	Mw	Epicentral area	Intensity at Casamicciola	Epicentral Intensity
1762	7	23	3.50	Isola d 'Ischia	6-7	6-7
1796	3	18	3.88	Isola d 'Ischia	8	8
1828	2	2	4.01	Isola d' Ischia	9	8-9
1841	3	6	3.25	Isola d' Ischia	6	5-6
1863	1	30	2.87	Isola d' Ischia	5	4
1867	8	15	2.99	Isola d' Ischia	5-6	4-5
1881	3	4	4.14	Isola d' Ischia	9	9
1883	7	28	4.26	Isola d' Ischia	10	9-10
1892	11	16	4.40	Isola di Ponza	0	5-6
1893	1	25	5.15	Vallo di Diano	0	7
1905	9	8	6.95	Calabria centrale	2	10-11
1913	10	4	5.35	Molise	4	7-8
1927	5	25	4.98	Sannio	3	6
1927	10	11	5.20	Marsica	2	7
1930	7	23	6.67	Irpinia	5	10
1930	10	30	5.83	Senigallia	0	8
1933	9	26	5.90	Maiella	2-3	9
1990	5	5	5.77	Potentino	3	N/A

A4.13.1.3 Seismic hazard

Figure A4.13.6 shows the seismic hazard map of Italy, as determined by the probabilistic seismic hazard assessment carried out by the National Institute of Geophysics and Volcanology of Italy, the INGV, (Meletti, 2007; Meletti & Montaldo, 2007) and reported in the official Italian Technical Construction Norms (NTC, 2008). This hazard map has been elaborated based on the seismic source zonation (SSZ) model ZS9 of Meletti *et al.* (2008), in which Ischia Island, along with the Gulf of Naples, Campi Flegrei and Mt. Vesuvius, is characterised as a volcanic area, with predominant normal faulting, effective depth of 3km and maximum observed magnitude **M**5.78. The map in Figure A4.13.6 served as the basis to define the simplified seismic zonal classification map of 2015, which establishes homogeneous hazard per municipality, and according to which the region of Naples, including Ischia, is classified as Zone 2, to which PGA design values on rock between 0.15 and 0.25 g (with a 10% probability of exceedance in 50 years) are assigned (DPC, 2015). More in detail, Ischia lies mostly within the 0.125 – 0.150 g zone and partly within the 0.150-0.175 g zone (ISTAT, 2017) with a gradient increasing from SW towards NE, as shown in Figure A4.13.7 (right).

Results of the Global Seismic Hazard Assessment Program (GSHAP; Giardini *et al.*, 1999), assign a PGA value on rock with a 10% probability of exceedance in 50 years of 1.209 m/s² (0.123 g) to the area around Casamicciola (Figure A4.13.7, left), which is in agreement with the aforementioned national values.

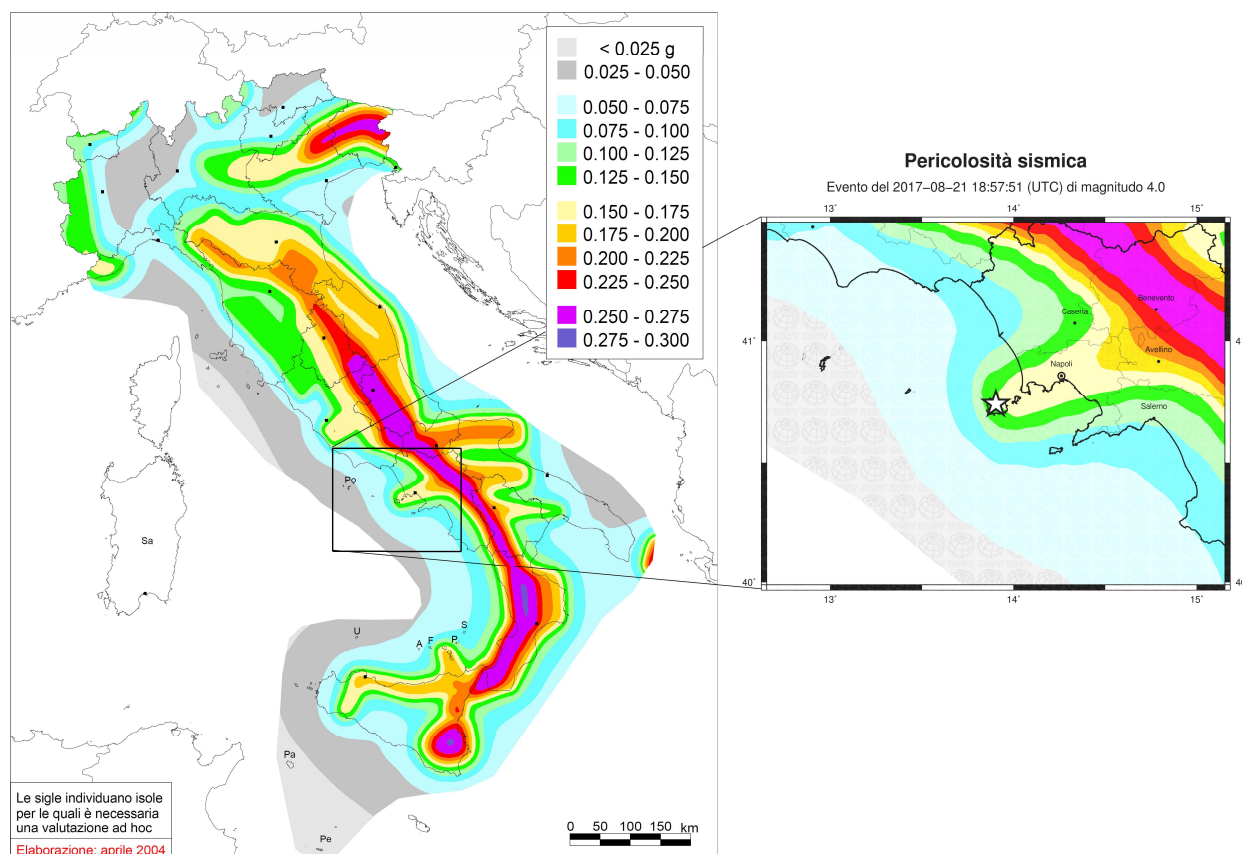


Figure A4.13.6. Seismic hazard map of Italy (left) with emphasis in the region of mid-western Campania Plain (inset, right). Colours represent PGA values (g) on rock ($V_{s30}=800\text{m/s}$) with a 10% probability of exceedance in 50 years. Figure modified after Meletti & Montaldo (2007) (INGV-Zone Sismiche, 2006).

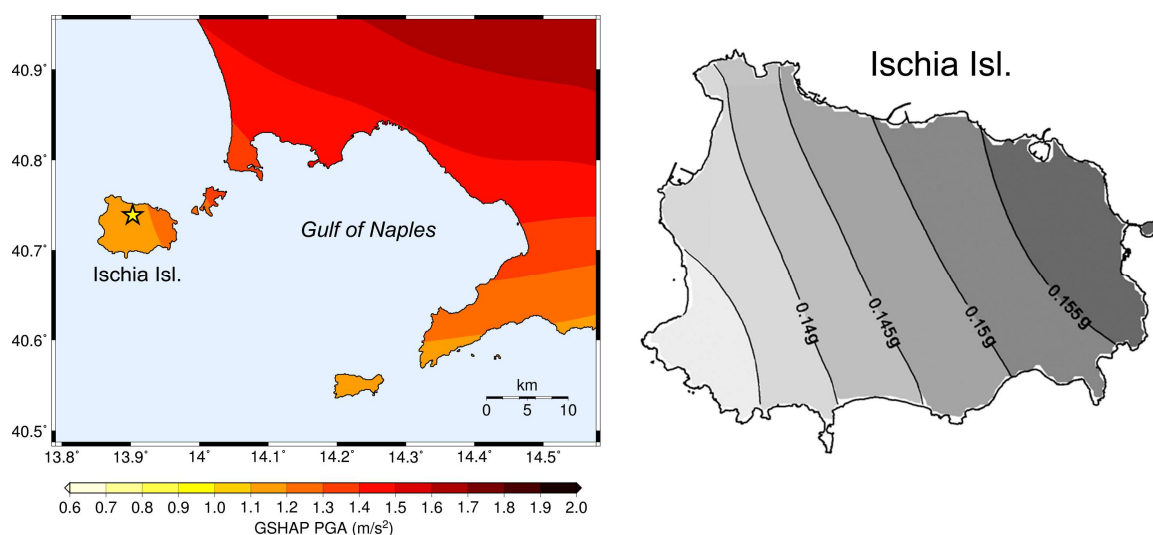


Figure A4.13.7. PGA (left: m/s^2 , right: g) values with a 10% probability of exceedance in 50 years in Ischia Island from GSHAP data (Giardini *et al.*, 1999; left) and as given by the Italian seismic norms (NTC, 2008), modified after Rapolla *et al.* (2010; right).

In the results for the more recent Seismic Hazard Harmonization in Europe (SHARE) project (Woessner *et al.*, 2015; Figure A4.13.8), higher PGA values on rock ($V_{s30}=800\text{ m/s}$) with a 10% probability of exceedance in 50 years are proposed for Ischia Island, in the range 0.300-0.325 g. When looking in detail at the seismogenic sources used for SHARE (EFEHR-

EPOS, 2017) and comparing them with those of the ZS9 model used for Italy (Meletti *et al.*, 2008) it stands out that the area sources comprising Ischia and the broader area around Naples have similar shapes in both models, but very different assigned maximum magnitudes. While in ZS9 seismic source 928 is assigned a maximum **M**5.78, SHARE considers that up to around **M**7 would be possible. This main difference is likely to hold a large influence in the divergence of the results from the two hazard models.

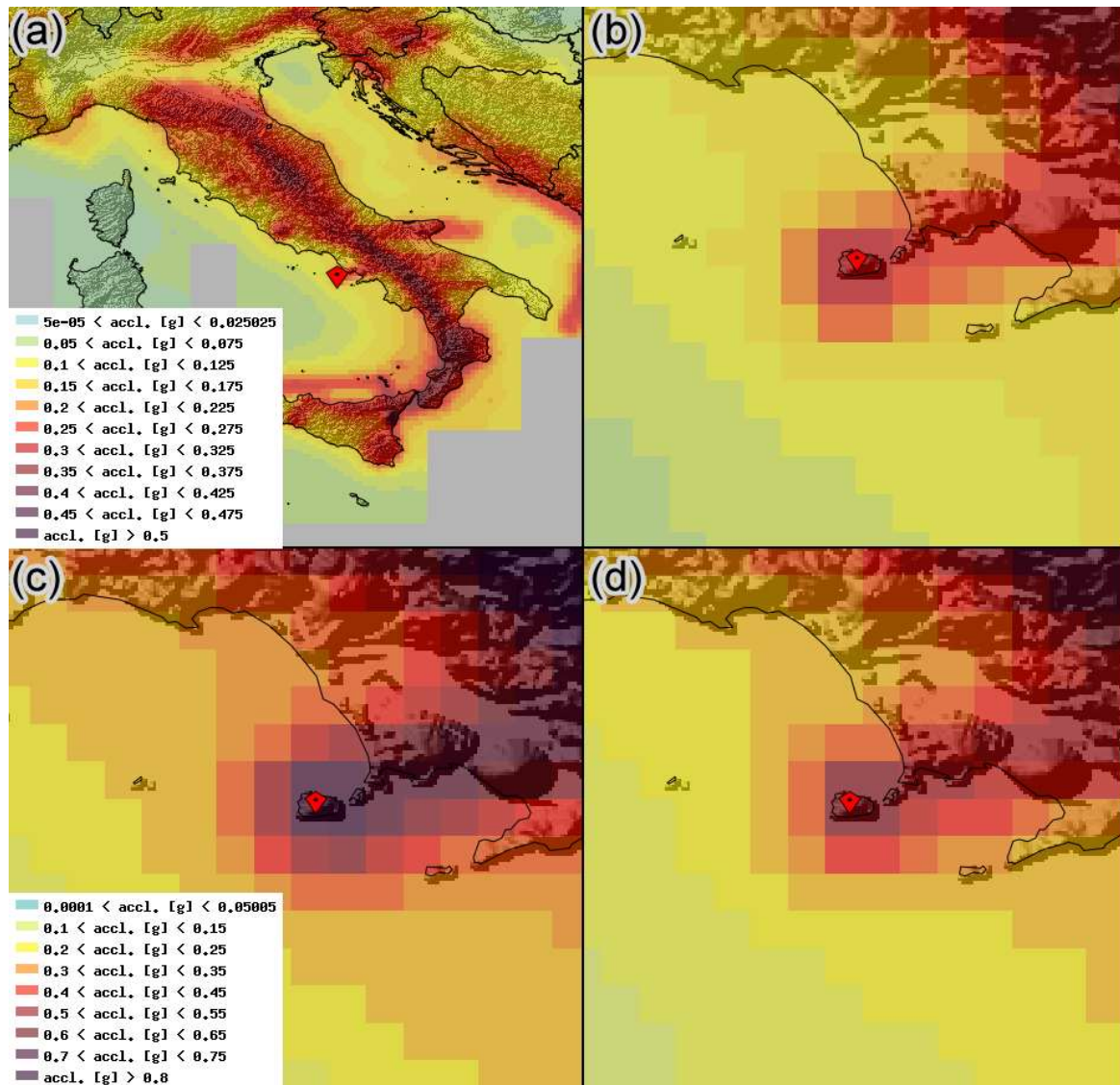


Figure A4.13.8. Mean hazard map according to the SHARE project (Woessner *et al.*, 2015): (a) PGA on rock for Italy and (b) for the broader area of Ischia Island, (c) pseudo-spectral acceleration for $T=0.15$ s and (d) for $T=0.25$ s, with 10% probability of exceedance in 50 years (475-year return period).

The uniform hazard spectra curve of spectral acceleration (S_a) on Ischia Island according to SHARE is much higher than the corresponding Eurocode 8 (EC8; CEN, 2004) Type II design spectrum with input PGA of 0.175 g on rock (maximum value according to the seismic zonation map, ISTAT, 2017), as it is observed in Figure A4.13.9. The latter is compatible with the NTC (2008) proposed elastic design spectrum. The various estimates of existing

hazard models for PGA on rock with 10% probability of exceedance in 50 years (475 years of recurrence period) are summarized in Table A4.13.2.

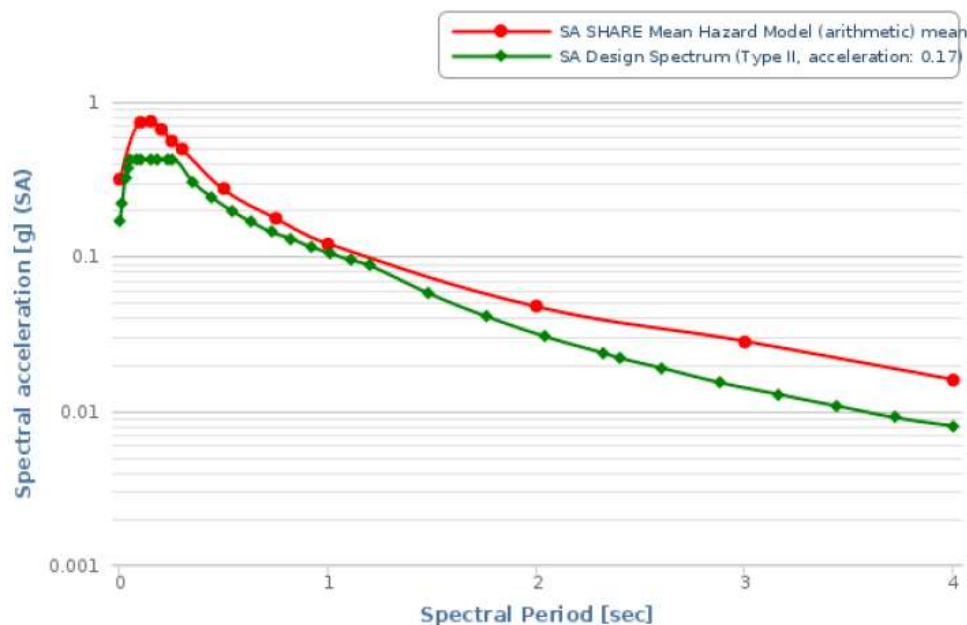


Figure A4.13.9. Rock site design spectra (5% damping) for the closest available coordinates to the city of Casamicciola according to SHARE (red line) and Type II Eurocode 8 (EC8; CEN, 2004) (green line). From SHARE project (Woessner *et al.*, 2015).

Table A4.13.2. Peak ground acceleration (PGA) values on rock with a 10% probability of exceedance in 50 years (475-year return period), according to different studies.

AREA	NTC (2008)	GSHAP	SHARE
Casamicciola	0.125-0.175 g	0.120 g	0.300-0.325 g

A4.13.2 Earthquake source characteristics

A4.13.2.1 Location, depth and time

This earthquake occurred on 21st August 2017, at 18.57 UTC (20.57 local time).

The location procedure for the 2017 Ischia earthquake has presented numerous challenges. Initial solutions by various institutes, including the INGV, reported an epicentre approximately 3 km offshore, with a (fixed) focal depth of 10 km. However, macroseismic evidence indicated that the solution had to be revised, as the distribution of ground effects and damage was mainly localized on the northern part of the island, not by the coasts but inland, towards the northern side of Mt. Epomeo (INGV G.D.L., 2017).

The problems and various attempts at relocating the mainshock are described in detail by INGV G.D.L. (2017). To begin with, being Ischia a small island 30 km WSW of Naples, at the margins of the Italian national seismological network, its azimuthal coverage is poor and the uncertainties have to be constrained mostly using data from the few available stations

which are installed on the island. There is a permanent local network of three operational digital stations, with one of them, IOCA, located at the Observatory of Casamicciola, very close to the most damaged “red zone” area, and the other two (IMTC, Forio Monte Corvo; IFOR, Forio Punta Imperatore) on the south-west. In addition, there are three more stations equipped with analogue instruments, OC9 and FO9, located close to IOCA and IFOR, and station CAI (Castello Aragonese) at the easternmost edge of the island. Station IOCA recorded the earthquake, but its signal on the velocimeter became saturated as soon as the P-waves arrived, allowing only for P-waves to be picked for the preliminary solution (INGV G.D.L., 2017). In addition to this, the transmission from stations IMTC and IFOR was interrupted during the earthquake, leaving a gap on the continuity of the records. Due to all this, the preliminary location had to be solved using only a local P-wave arrival on Ischia, with the consequent difficulties in constraining the focal depth, since it proved difficult to pick the S-waves on other stations of the national network (INGV G.D.L., 2017). Further attempts were made using different values of fixed focal depth between 1 and 10 km, which shifted the epicentre by 1-2 km along the western coast (Figure A4.13.10, right, rectangles).

As different location algorithms were trialled and more data became available, including the non-saturated accelerometric records from IOCA station, it was possible to refine the solution, arriving finally to a hypocentre located beneath the hilly part of Casamicciola at a focal depth of around 1.7 km (INGV G.D.L., 2017). This solution, delivered on 25th August 2017 by the INGV, is compatible with the shallow depth of the BDT zone and correlates better with the macroseismic observations.

Table A4.13.3 and Figure A4.13.10 (left) gather the hypocentral coordinates finally reported by the INGV, the Unites States Geological Survey (USGS) and the European Mediterranean Seismological Centre (EMSC).

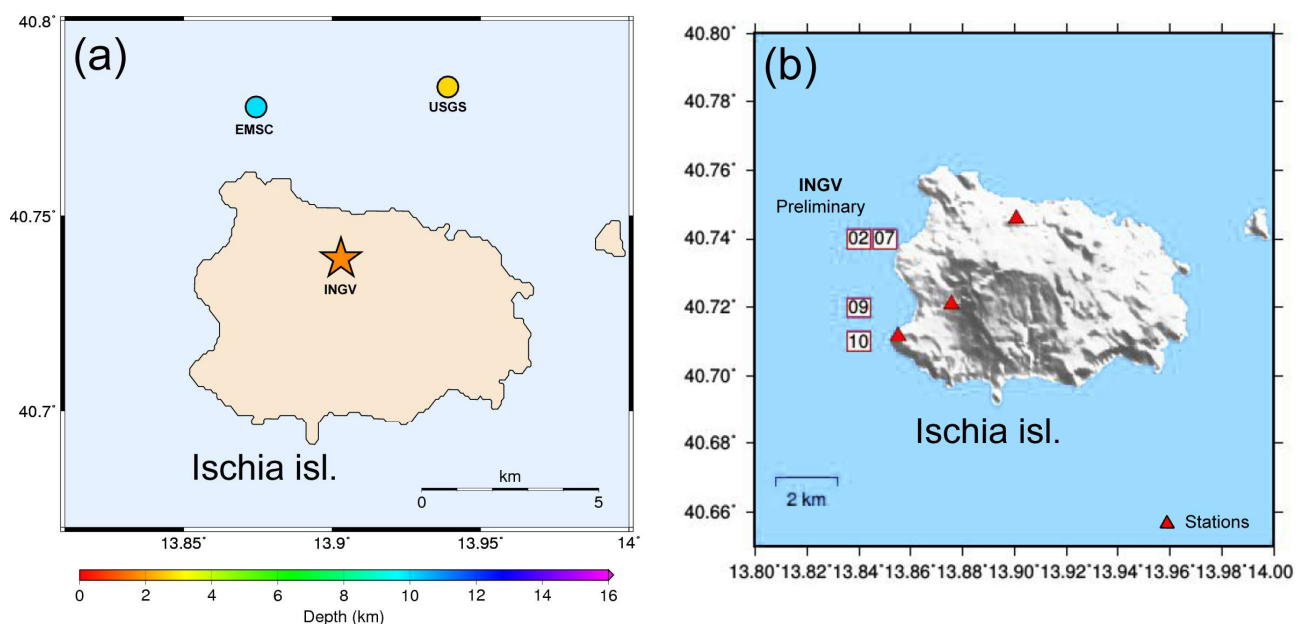


Figure A4.13.10. Maps presenting the different estimates for the epicentral coordinates of the 2017 Ischia earthquake by the various agencies listed in Table A4.13.3; star marks the final solution of the INGV (left). Different attempts of the INGV to better constrain the hypocentre (rectangles with numbers indicating the focal depths of the respective solutions and red triangles representing the digital permanent local stations) (INGV G.D.L., 2017; right).

Table A4.13.3. Epicentral coordinates of the 2017 mainshock and hypocentral depths from different sources.

Agency / Publication		Latitude	Longitude	Depth (km)
INGV	Istituto Nazionale di Geofisica e Vulcanologia	40.739 °N	13.903 °E	1.7
NEIC	National Earthquake Information Center, USGS	40.783 °N	13.939 °E	2.7
EMSC	European Mediterranean Seismological Centre	40.778 °N	13.874 °E	10.0 (*f)

(*f) fixed parameter used for inversion

A4.13.2.2 Magnitude

As with the hypocentral location, the estimation of the magnitude has also been difficult (INGV G.D.L., 2017). The initially reported magnitude was $M_L=3.6\pm0.2$, based on the distribution of local magnitude estimates shown in Figure A4.13.11. Duration magnitude, calibrated for the stations of the broader volcanic region in terms of seismic wave attenuation, was determined at $M_d=4.0\pm0.3$ and was considered more accurate. Moment magnitude was then determined to be **M3.8** by the post-earthquake assessment group of the INGV (INGV G.D.L., 2017), though a final value of **M3.9** is reported in the institution's website and is, thus, adopted herein (INGV CNT, 2017). Estimates for the magnitude of the 2017 Ischia mainshock by various agencies and authors are reported in Table A4.13.4.

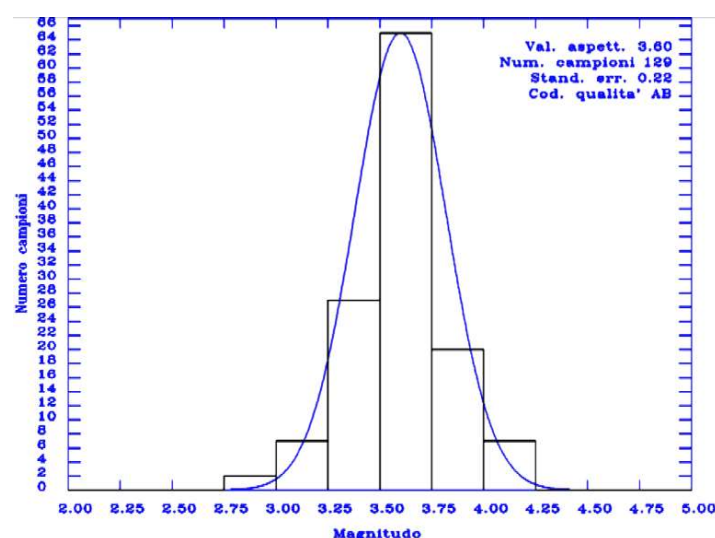


Figure A4.13.11. Distribution of calculated local magnitude values per station. From INGV G.D.L. (2017).

Table A4.13.4. Estimations of moment magnitude (**M**), body-wave magnitude (m_b), local magnitude (M_L) and duration magnitude (M_d) for the Ischia 2017 mainshock as reported by various agencies.

Agency / Publication		M	m_b	M_L	M_d
INGV	Istituto Nazionale di Geofisica e Vulcanologia	3.9	-	3.6	4.0
NEIC	National Earthquake Information Center, USGS	-	4.2	-	-
EMSC	European Mediterranean Seismological Centre	-	4.3	-	-





A4.13.2.3 Style-of-faulting

The determination of the focal mechanism was equally affected by the poor azimuthal coverage of the seismological network, the relatively small magnitude of the event and its shallow focal depth. If this earthquake was a repetition of the 28th July 1883 event, it would have been expected to occur on a SW-NE trending, NW-dipping normal fault, probably with a dip-slip faulting mechanism (INGV G.D.L., 2017).

Table A4.13.5 summarizes the available solutions for the focal mechanism of the main shock, as determined by the INGV (the only available source at the time of writing, December 2017) using different methods. The automatic Regional Centroid Moment Tensor (RCMT) and Time-Domain Moment Tensor (TDMT) solutions indicate a significant strike-slip component, with **M**3.8 and a small non-double-couple component being attributed to noise (INGV G.D.L., 2017). A manual TDMT solution after selection of certain components of stations from the South Apennines and imposing a pure double-couple solution results in a pure dip-slip normal solution with E-W striking nodal planes and **M**4.0 (INGV G.D.L., 2017). However, all of the above have a centroid depth at 8 km, which is incompatible with the preferred hypocentral solution and the BDT zone restrictions.

An alternative solution for the faulting mechanism was derived by the INGV using InSAR data modelling that revealed significant subsidence of 3.6-4.0 cm near the epicentre (Figure A4.13.12, top). A slip model that likely explains the observed deformation was calculated by non-linear inversion showing a north-dipping normal fault and slip between the depths of 200 and 980 m (last row in Table A4.13.5; Figure A4.13.12) (INGV G.D.L., 2017). At the time of writing (December 2017), moment tensor results are considered inconclusive for this event.

Table A4.13.5. Focal mechanism solutions determined by INGV using different methods (INGV G.D.L. (2017)). The north-dipping planes (likely to be the fault) are indicated in grey.

Nodal Plane 1			Nodal Plane 2			Centroid Depth (km)	Beachball	Source (method)
Strike	Dip	Rake	Strike	Dip	Rake			
241	48	-7	335	85	-138	8.0		INGV (quick RCMT)
37	65	-46	151	49	-146	5.0		INGV (TDMT-auto)
275	45	-85	88	45	-95	8.0		INGV (TDMT-manual)
263	51	-92	86	39	-88	0.53		INGV (InSAR model)

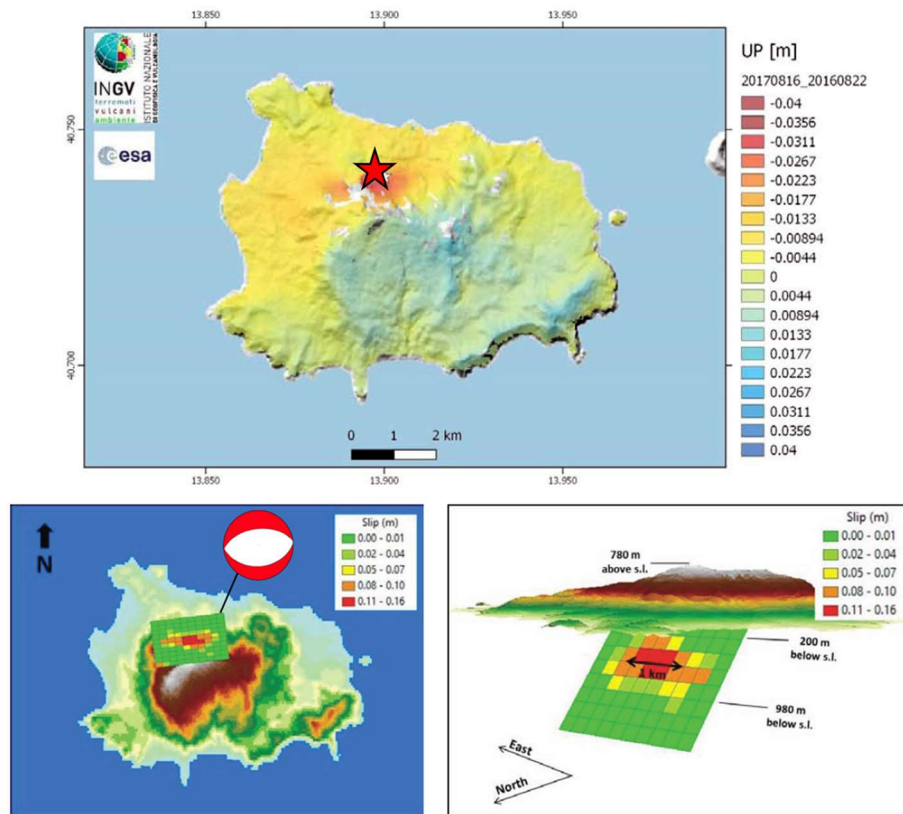


Figure A4.13.12. Vertical deformation on Ischia resolved using SAR images, showing subsidence of the order of 4cm (top); modelling of an E-W south-dipping causative source by non-linear inversion of the InSAR deformation (bottom left); same in a 3D view, as seen from the north-west end of Ischia Island (bottom right). Modified after INGV G.D.L. (2017).

A4.13.2.4 Stress drop

No estimates of stress drop have been found in the current scientific literature for this earthquake.

A4.13.2.5 Foreshocks and aftershocks

Unfortunately, due to the blackout in the island that followed the seismic shock, no recordings of early strong aftershocks are available by local stations other than IOCA (ISI, 2017). Therefore, no aftershock locations are found in the bulletins of the INGV, the EMSC, the ISC or the USGS. Looking at the continuous waveforms of the closest seismological station, IOCA, very few aftershock signals were observed. No foreshocks have been registered either in any bulletin.

Some 27 aftershocks of low magnitude are reported in the technical report of the INGV G.D.L. (2017). For most of these events, which are depicted in Figure A4.13.13, the location could not be determined, as they were only recorded by less than 2 stations. For the rest, only the duration magnitude, M_d , could be estimated, assuming a similar hypocentre to that of the mainshock. The largest recorded aftershock occurred on 23rd August 2017 (INGV G.D.L., 2017), and had magnitude $M_d=1.9$ and its epicentre estimated a few hundred meters south of the relocated epicentre of the mainshock (see Figure A4.13.5, left).

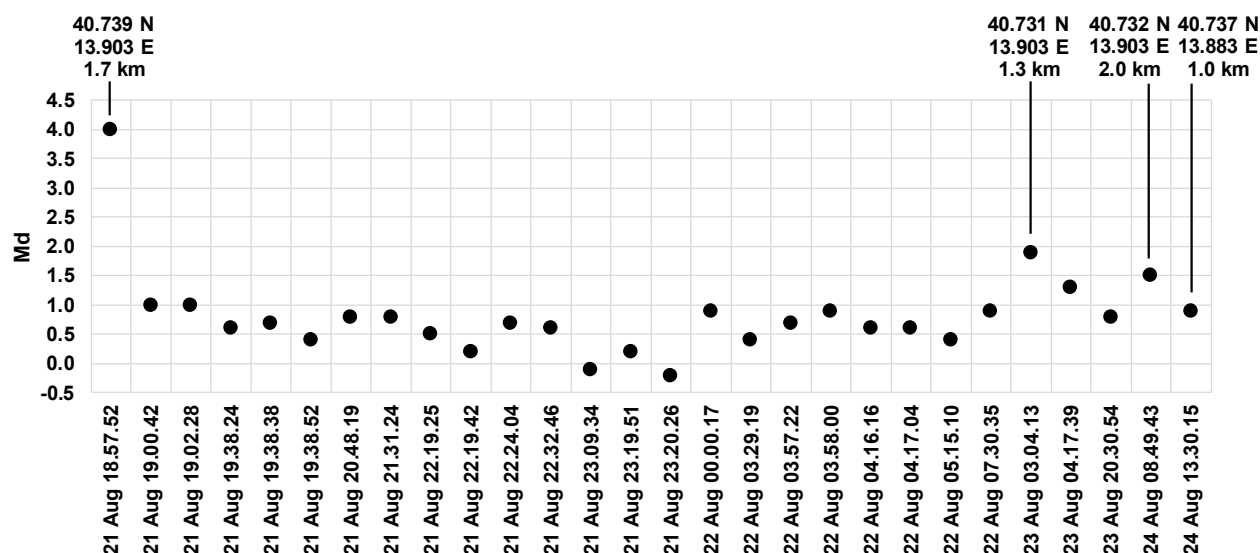


Figure A4.13.13. Seismic events recorded in Ischia from 21st August 2017 until 30th August 2017. Hypocentral coordinates indicated when available. Data from INGV G.D.L. (2017).

A4.13.2.6 Nature of earthquake

This earthquake occurred in a volcanic region, in an area previously hit by earthquakes of similar magnitude, such as the one of 28th July 1883. Although its focal mechanism cannot be constrained by seismological data, non-linear inversion of deformation observed by InSAR and GPS observations suggest that the source is compatible with north-dipping normal faulting, in agreement with a known seismogenic source of Ischia, registered in the DISS database (DISS, 2017). Moreover, anomalies on tilt measurements were observed about two minutes before the occurrence of the mainshock (INGV-Terremoti, 2017c). These would support the idea of triggering of the earthquake by local changes in the stress field due to displacement of magma or circulation of hydrothermal fluids, which also caused deformation on the surface. Given the measured extensional strain rate in the region, a likely contribution of active volcanism to the stress loading or triggering of the fault, and no published evidence to suggest that it may have been triggered by anthropogenic activity, this earthquake is considered to be purely of natural origin.

A4.13.3 Geology and ground conditions in the affected area

A4.13.3.1 Regional geology and topography

Ischia Island is a volcanic complex, being, on its most part, the result of a series of effusive and explosive volcanic eruptions that began over 150 thousand years ago, with its alkali-potassic magma sharing a common origin with that of other Campania volcanoes, such as the Campi Flegrei, Procida and Vivara islands (Aiello *et al.*, 2012). With a total surface area of 42km², it is composed of landslide deposits, marine sediments and volcanic rocks, represented by alkali-trachytes, trachybasalts, latites and phonolites (Manzo *et al.*, 2006). The volcanism in the Phlegraean Volcanic District is related to the regional Pliocene and

At the surface, the whole eastern section of Ischia Island is covered by extensive pumice formations due to the highly explosive eruptions, fed by alkali-trachytic magmas, occurred in the western border of Ischia graben (Capaldi *et al.*, 1976). The normal faults in the interior of the resurgent block of Mt. Epomeo act as pathways for the emission of fumaroles, while hot springs are distributed primarily along the coast (Carlino *et al.*, 2014).

The topography of Ischia Island is dominated by Mt. Epomeo, which is currently raised at 786 m above sea level. It is also characterized by many landslides, including some catastrophic avalanche events with the most significant one having occurred about 5,000 years ago at the southern flank of the island, covering an area of 250-300km² (Chiocci & de Alteriis 2006). As many as 27 shallow landslide events have been associated to earthquakes that occurred from the mid-18th to the early 20th century (Caccavale *et al.*, 2017). It is noteworthy, however, that a historically recorded landslide that occurred in 1228 in the area of Lacco Ameno, killing more than 700 people in the Fango area by a lahar deposit (Della Seta *et al.*, 2012), is reported by many studies as being induced by a significant earthquake (MCS IX-X; Cubellis *et al.*, 2004), but the latter is disputed (INGV G.D.L., 2017).

A4.13.3.2 Site conditions in the affected area

The area most severely hit by the 2017 Ischia earthquake was the hilly part of Casamicciola, near the epicentre, according to the final solution of INGV G.D.L. (2017). Besides being very close to the epicentre and the focal depth of the earthquake being very shallow, local site conditions are likely to have played a considerable role in the amplification of the strong motion. According to the global USGS V_{s30} model, developed using topographic slope as a proxy (Wald & Allen, 2007; Figure A4.13.15), this area reportedly has high V_{s30} values of around 900 m/s. However, this model does not take into account the volcanic nature of the rocks but only the topography, while its resolution is too coarse.

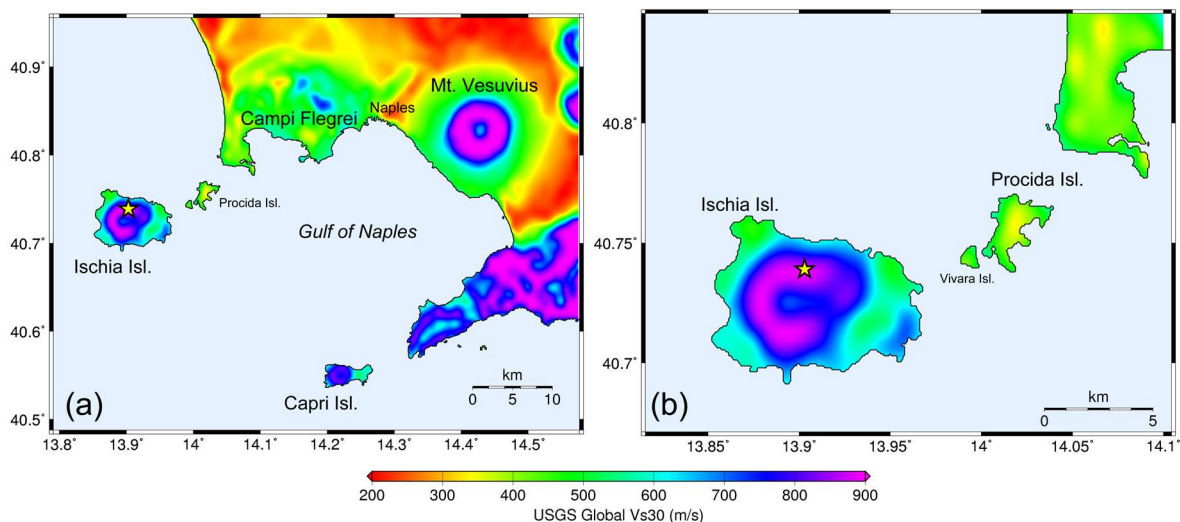


Figure A4.13.15. Map of V_{s30} (m/s) drawn using data from the USGS Global V_{s30} model (Wald & Allen, 2007) (a) for the broader area of the Gulf of Naples and (b) for the broader area of Ischia Island. The star marks the final epicentral solution (INGV G.D.L., 2017) of the 2017 earthquake.

The more detailed V_{s30} map of Figure A4.13.16 has been elaborated by Caccavale *et al.* (2017) for the purpose of earthquake-induced landslide hazard zoning of the Phlegrean Islands, of which Ischia is one. The meizoseismal (*i.e.*, most affected) zone, as identified by Azzaro *et al.* (2017), is completely within an area characterized by V_{s30} in the range 180-200m/s. Although the coastal areas have lower values of around 100-150m/s, the Marina di Casamicciola was not as severely hit by the earthquake as the hilly part of the town, an effect likely related to the resonance of the prevalent high frequency values of the ground motion with the natural frequencies of the low-rise local buildings, influenced by the volcanic rock.

According to Caccavale *et al.* (2017), the topographic amplification factor in the affected area is close to 1.0, though it can reach 1.2 in some localised sites. The meizoseismal zone is, however, within an area of medium to high susceptibility to earthquake-induced landslide hazard, characterized by debris deposits (Rapolla *et al.*, 2010) or reworked tuffs lithology (Carlino *et al.*, 2010), and overlaps with the area of interest for landslides during the 1881 and 1883 earthquakes (Figure A4.13.17). This type of lithology, such as debris deposits, tuff, (re-worked) pyroclastic deposits, categorized as “Ground type C: Debris deposits, Deposits of dense or medium-dense soil” by Rapolla *et al.* (2010), has an S-wave velocity of about 180-360 m/s. Likewise, Caccavale *et al.* (2017) classifies “pyroclastic deposits (also with palaeosoils); pumice and ash layers; slope debris; un-welded scoriae and loose pyroclastic deposits” as EC8 lithological Class C with $V_{s30}=280$ m/s. Table A4.13.6 summarizes the classification of Ischia lithologies according to the EC8 (CEN, 2004) soil taxonomy and their respective V_{s30} values. It should be noted, however, that the strong heterogeneity of the soils is such that it would require detailed seismic microzonation in the epicentral area to better determine zones with very localized, significant site effects.

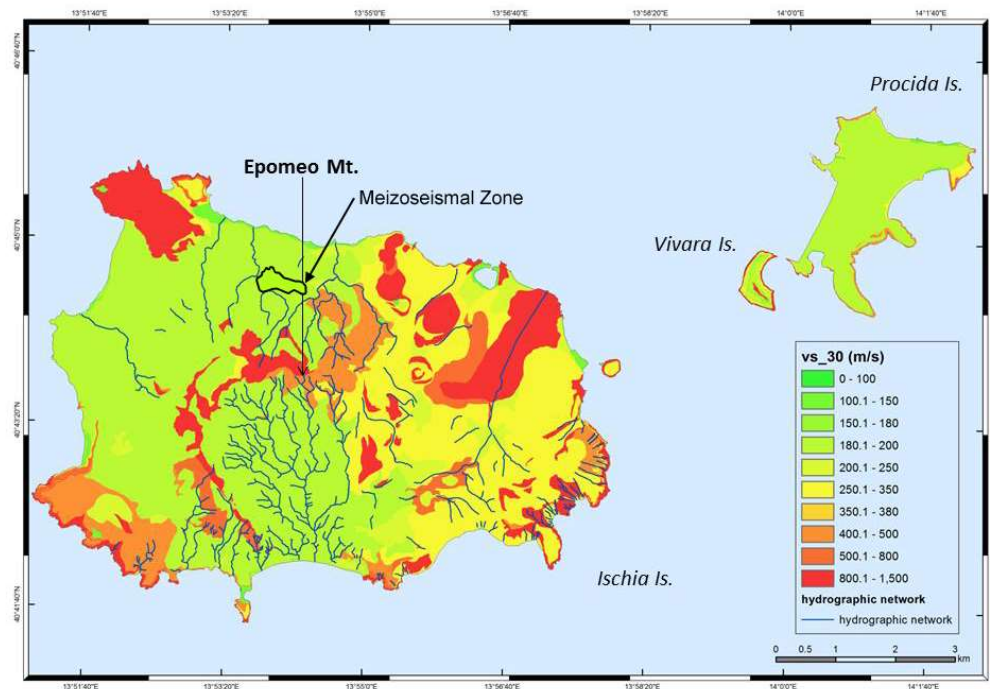


Figure A4.13.16. Detailed V_{s30} values of Ischia, Procida and Vivara islands. Meizoseismal zone black polygon after QUEST (Azzaro *et al.*, 2017). Modified from Caccavale *et al.* (2017).

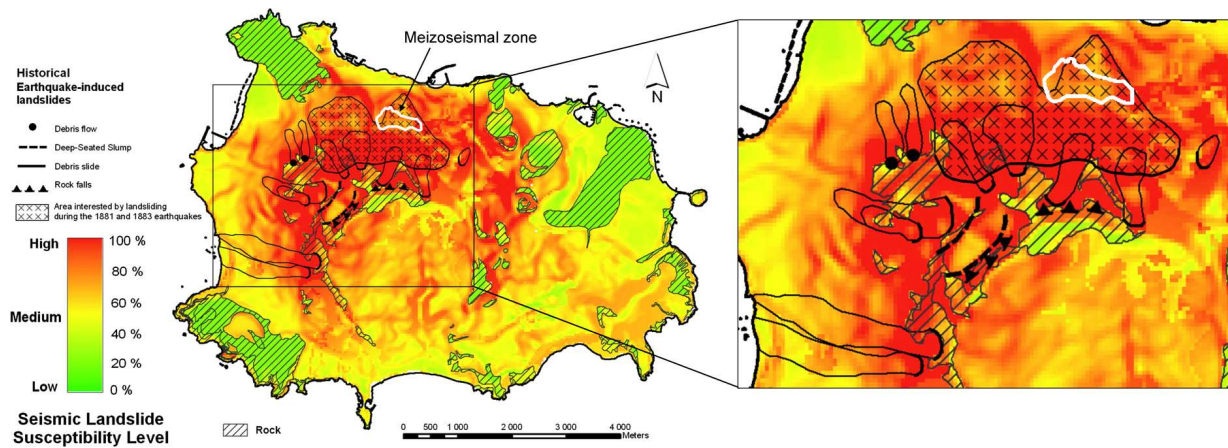


Figure A4.13.17. Map of seismic landslide susceptibility level on Ischia Island. The meizoseismal zone white polygon is after QUEST (Azzaro *et al.*, 2017). Modified after Rapolla *et al.* (2010).

Table A4.13.6. V_{s30} average value ranges for each lithological class in Ischia. From Caccavale *et al.* (2017).

EC8 Classes	V_{s30} (m/s) range	V_{s30} (m/s) average reference value	Lithologies
A1	>1500	1500	lava
A2	800 - 1500	1150	fractured lava; lithified yellow tuff; lava with welded scoriae; welded tuff
B1	400 - 800	600	tuff with pyroclastic deposits; welded brecciae and scoriae; lithified pyroclastic deposits
B2	350 - 500	425	Partly lithified pyroclastic deposits; stratified tuff; brecciae; marine silty sandstones with tuffites
C	180 - 380	280	pyroclastic deposits; pumice and ash layers; slope debris; unwelded scoriae and loose pyroclastic deposits
D	150 - 250	200	eluvial-colluvial pyroclastic deposits; sandy and silty beach deposits; ash deposits with reworked soils; landslide, debris and colluvial deposits
E	100 - 200	150	loose reworked pyroclastic deposits, dump materials and reworked soils

Ambient noise H/V ratios calculated for the IOCA site (Figure A4.13.18; Cultrera *et al.*, 2017) reveal significant amplification (7.5) in the frequency range 1.5 - 2.0 Hz (*i.e.*, periods of 0.5 s to 0.7 s), whereas such pronounced amplification frequencies were not encountered in other locations on the island, implying local site effects in the epicentral region and strong lateral variation in the seismic response due to the spatial heterogeneity of the volcanic deposits. The respective amplification in the 1.5-2.0 Hz band at station IOCA for the mainshock was about 11 (INGV G.D.L., 2017).

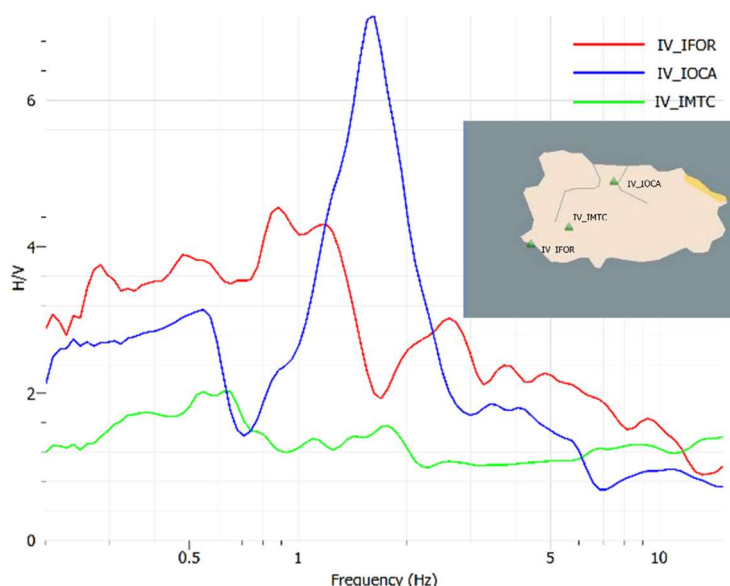


Figure A4.13.18. H/V ratios at three sites in Ischia. From Cultrera *et al.* (2017).

The susceptibility to earthquake-induced landslides has been studied in detail by Rapolla *et al.* (2010) and Caccavale *et al.* (2017) producing maps of the respective hazard (Figure A4.13.17). The most dangerous areas, with susceptibility >60%, covering the 8% of the island's surface (Rapolla *et al.*, 2010), include the broader northern and western slopes of Mt. Epomeo, where numerous historical landslide events have been registered.

No studies on the susceptibility to liquefaction on Ischia Island have been found in the scientific literature. It is, however, considered a potential effect that could be triggered by landslides, and could then, in turn, transform the latter into avalanches of debris flow (Nocentini *et al.*, 2015).

A4.13.4 Ground motions

A4.13.4.1 Intensity observations

One of the most distinctive characteristics of this earthquake is the very localized damage that was observed in the epicentral area. The first information was available from the online questionnaires of the “hai sentito il terremoto?” (“have you felt the earthquake?”) service of the INGV (HSIT, 2017) for which 507 answers from 133 communities were registered. As shown in the map on the left of Figure A4.13.19, this resulted in a distribution of MCS intensities VI-VII in the northern part of Ischia, in the communities of Casamicciola and Lacco Armeno, III-IV in the rest of the island and Procida island, and III (barely felt) in the mainland. When the intensity is measured in the European Macroseismic Scale (EMS-98), the highest intensity is VI in the aforementioned mainly affected communities, III-IV in the rest of the island and III to none in the closest mainland (Figure A4.13.19, right). A substantial drop of intensity from VI-VII to III-IV is clearly observed within the island of Ischia itself and it highly indicates the localized site effects discussed in Section A4.13.3.2. Being based on only 15 answers over 10 blocks, macroseismic intensities derived from the analogous Did You Feel

It? (DYFI) service of the USGS (2017) cannot be considered fully trustworthy. Nevertheless, the resulting intensity values plotted against their corresponding hypocentral distances in Figure A4.13.20 (left), illustrate the inconsistency between the observed intensities at distances between 10 and 100 km and the expected ones, estimated according to the intensity attenuation law of Atkinson & Wald (2007). The overall tendency is confirmed by the denser MCS intensity observations by HSIT (2017) plotted over epicentral distance (Figure A4.13.20, right), which also show a rapid attenuation of intensity at distances greater than 10 km.

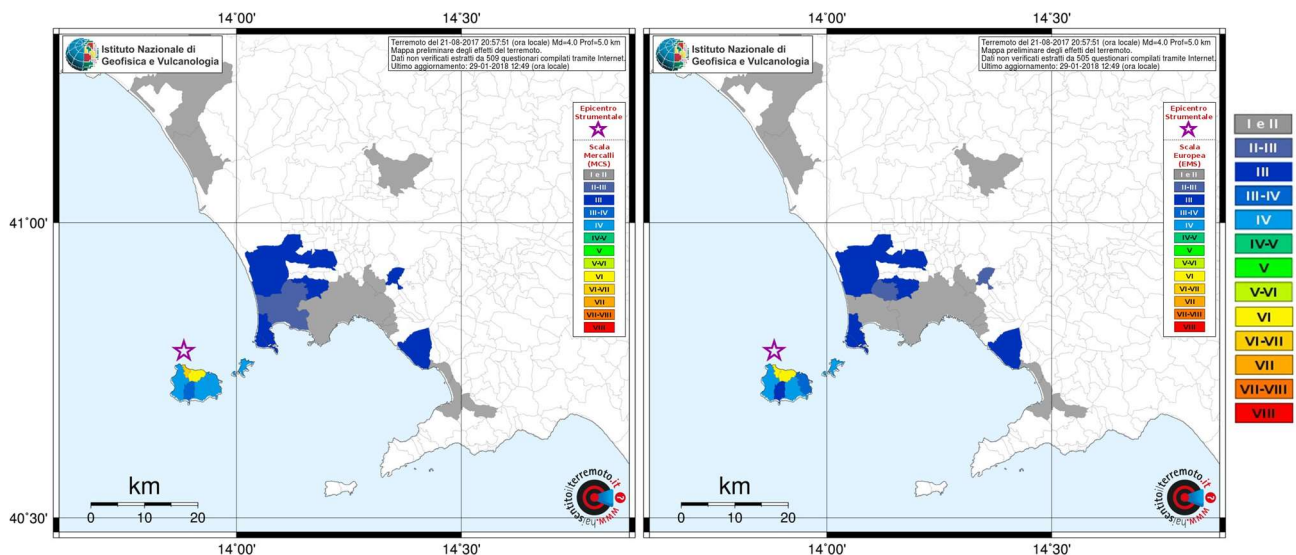


Figure A4.13.19. Spatial distribution of intensity in MCS scale (left) and EMS-98 scale (right) according to the results of over 500 answered “did you feel the earthquake” questionnaires, from HSIT (2017). The star shows a preliminary epicentre solution.

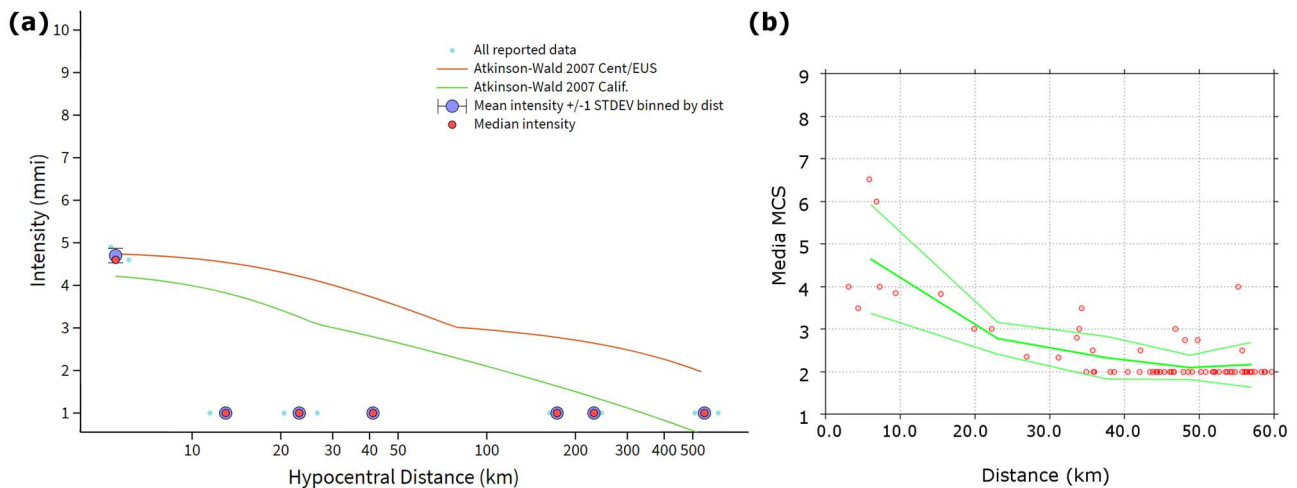


Figure A4.13.20. Intensity attenuation with distance: (a) MMI prediction according to the model of Atkinson & Wald (2007; green and red lines) and DYFI answers from USGS (2017); (b) MCS data points from HSIT (2017, red circles) and average intensity $\pm 1\sigma$ (green lines). Modified from USGS (2017) and HSIT (2017).

On-site damage observations carried out by Azzaro et al. (2017) during a series of macroseismic field investigations allowed for the elaboration of a more detailed description of the spatial distribution of intensity on the island, as shown in Figure A4.13.21. The most

affected area was a hilly part of Casamicciola, with maximum EMS-98 intensity of VIII, which is referred to as the “Red Zone” (“zona rossa” on the map of Figure A4.13.21) due to the great concentration of damage. Other localities where the shaking was strong and the effects relatively important were Fango (in Lacco Ameno) and Bagni (in Casamicciola), each to the west and east of the Red Zone, both with assigned EMS-98 intensities of VII, and Marina di Casamicciola (in Casamicciola), with EMS-98 VI, while in the rest of the island the EMS intensities varied between IV and V. The lowest intensities have been attributed to areas where no damage was observed, based on the testimonials of locals and transitory effects. The spatial distribution of the macroseismic observations is compatible with the outcome of the online macroseismic questionnaires (Figure A4.13.19, right), although higher intensity values are inferred from the field investigations.

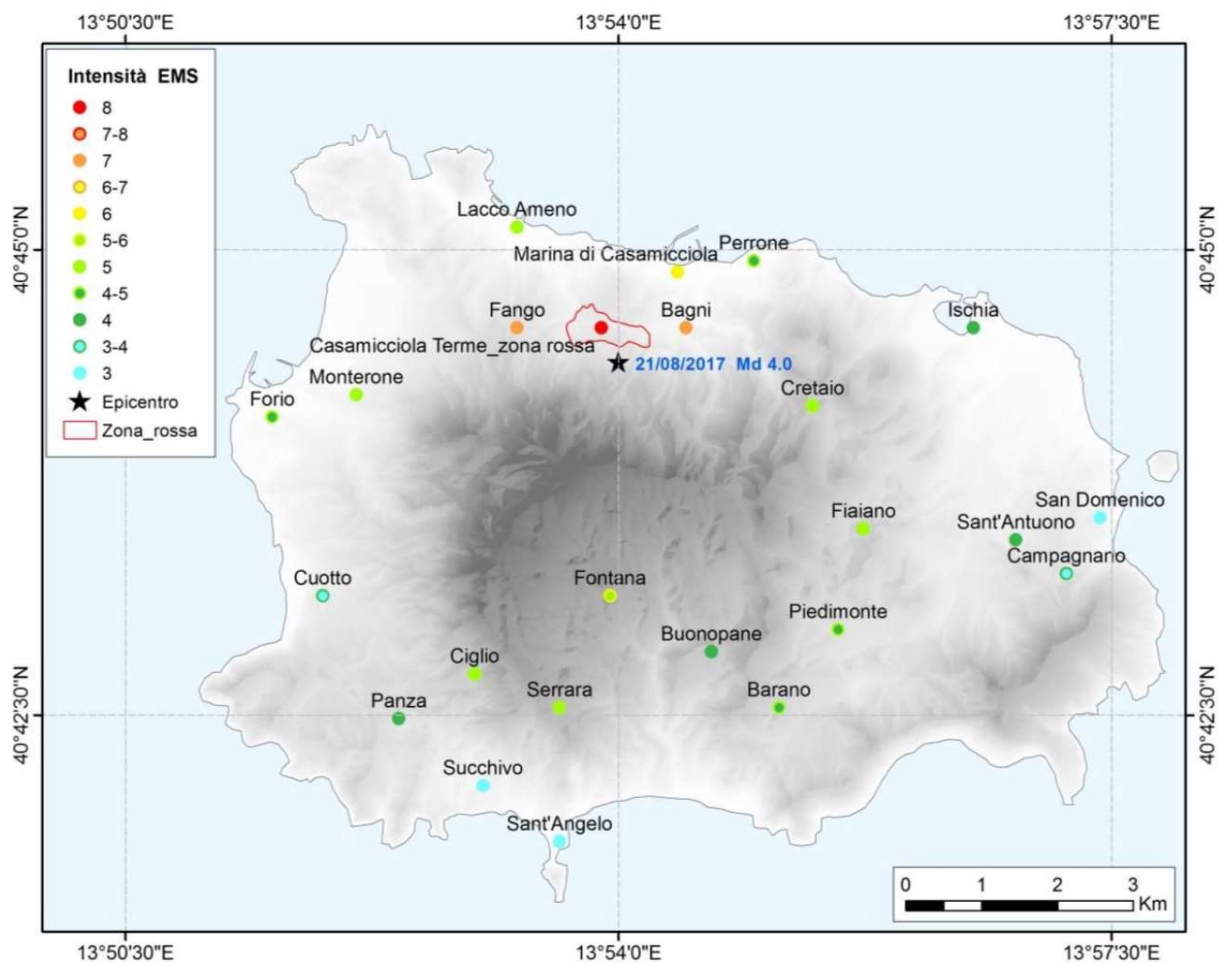


Figure A4.13.21. EMS-98 intensity observations on Ischia Island derived from macroseismic field observations. The meizoseismal “red zone” (zona rossa) is enclosed with a red curve. From Azzaro *et al.* (2017).

Verderame *et al.* (2017) have elaborated an isoseismal map for the most affected area of Casamicciola and Lacco Ameno, using the attenuation law developed by Carlino *et al.* (2010) for MCS macroseismic intensities reported by Cubellis & Luongo (1998) and Cubellis *et al.* (2004) for the earthquake of Ischia in 1883, and considering the peak ground accelerations recorded at IOCA station by means of the empirical relation of Faenza & Michelini (2010). The law of Carlino *et al.* (2010) has been specifically developed for the island, taking into account both its geological and seismological characteristics (shallow

events of low magnitude). Assuming a direct equivalence between the EMS-98 and MCS macroseismic scales as per Musson *et al.* (2010), Verderame *et al.* (2017) concluded that the intensity distribution theoretically derived, which is shown in Figure A4.13.22, is in agreement with that observed on-site (Figure A4.13.21) at the epicentral Red Zone and the localities of Fango and Marina di Casamicciola, whereas the derived isoseismals appear to overestimate the effects to the west, at Lacco Ameno.

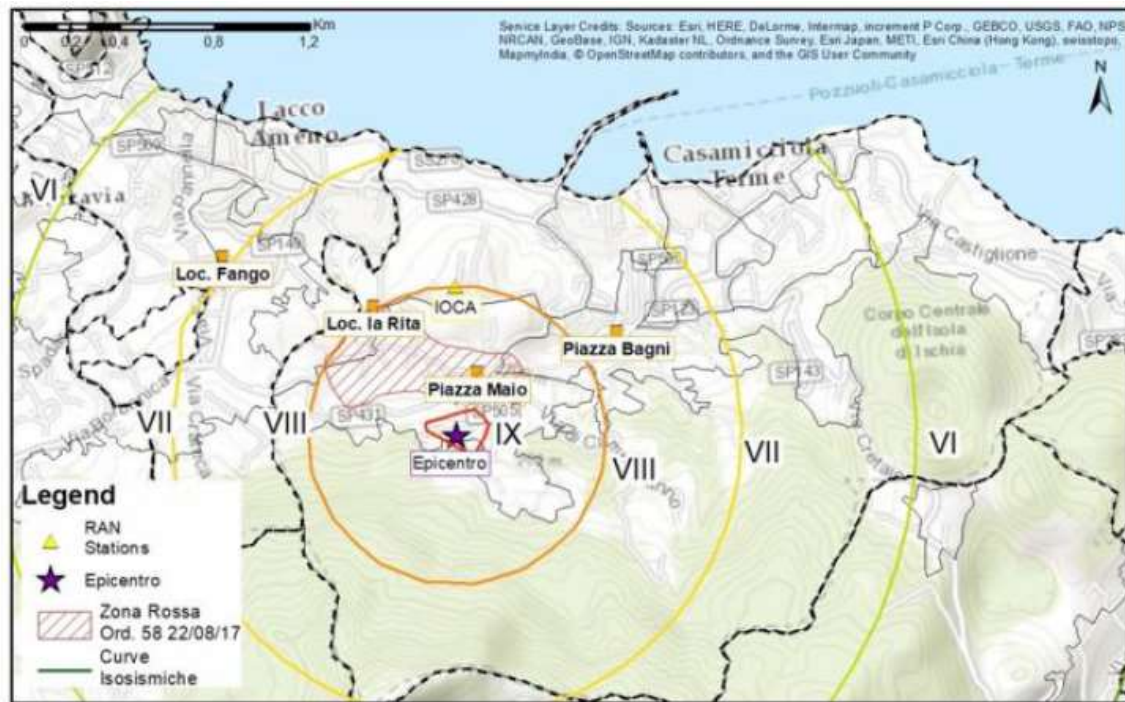


Figure A4.13.22. MCS intensity isoseismals derived with the attenuation law of Carlino *et al.* (2010) and the conversion model of Faenza & Michelini (2010). From Verderame *et al.* (2017).

The INGV generated different ShakeMaps in terms of MCS instrumental intensity for this event, based on different assumptions and/or methodologies. First, the ground motion prediction equations (GMPEs) that are normally used for the development of Italian ShakeMaps (that of Michelini *et al.*, 2008, and the regional scaling relationships of Malagnini *et al.*, 2000, 2002, and Morasca *et al.*, 2006) were applied, resulting in the map shown in Figure A4.13.23 (left). Due to the very high value of acceleration recorded at the IOCA station, in comparison with those predicted by the GMPEs and the trends of other recordings at larger distances, this measurement was considered to be an outlier and was neglected by the algorithm for the intensity prediction process. As a result, when compared with the macroseismic investigations, the maximum intensities at the epicentral area are underestimated, as explained by INGV G.D.L. (2017). Moreover, site effects, particularly relevant during this event, cannot be properly implemented yet in the ShakeMap calculations and the soil response is only taken into account via a standardized grid of V_{s30} values.

The second approach applied after the abovementioned problem was identified, namely the dismissal of the only available local observation at station IOCA as an outlier and the low predicted intensity on Ischia, the GMPE derived by Tusa & Langer (2016), appropriate for volcanic areas (derived with data from Mt. Etna), was used to develop the map of Figure A4.13.23 (right). This version reflects better the higher intensities (VI-VII) observed at the

epicentral area by taking into account the recorded PGA at IOCA station. However, an overestimation of the intensities in the rest of the island is observed, considering that no other record is used as input for a better calibration of the results at larger epicentral distances within the island itself. INGV G.D.L. (2017) concludes that none of the ShakeMaps is able to fully capture the observed intensities simultaneously at all sites, due to the lack of data points within the island.

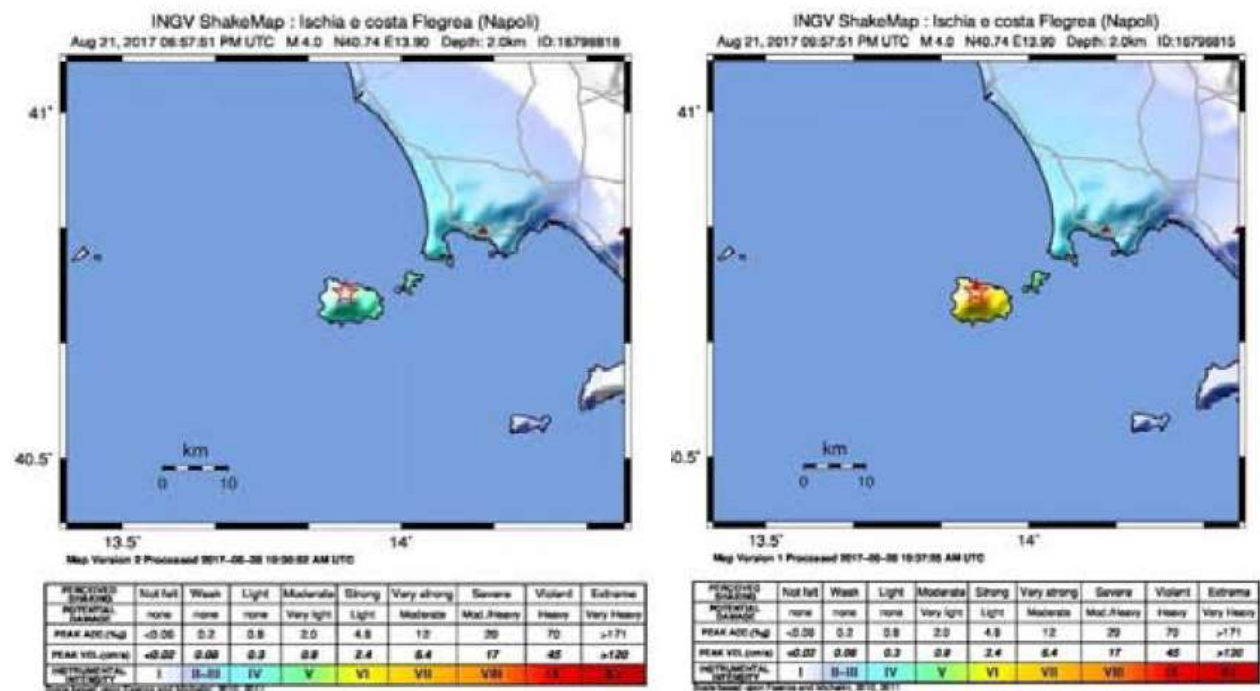


Figure A4.13.23. Instrumental MCS Intensity ShakeMap focused in the area of Ischia, derived using the standard GMPEs for Italian ShakeMaps (Michelini *et al.*, 2008; left) and the Tusa & Langer (2016) GMPE for volcanic zones (right). From INGV G.D.L. (2017).

A4.13.4.2 Ground motion recordings

The 2017 Ischia earthquake was recorded by 35 strong motion instruments that belong to the INGV. The recorded waveforms and the results of their analysis are available through the Engineering Strong Motion Database (ESM, 2017; Luzi *et al.*, 2016). Of the 35, 12 are classified as records of bad quality, and only one of them, that of IOCA station, has PGA values larger than 0.1 cm/s², as the remainder correspond to stations located on the mainland more than 56 km away from the epicentre. Iervolino *et al.* (2017) report the existence of two other records on the mainland whose PGA values reach 0.49 and 0.20 cm/s², at distances of 19.9 and 26 km, respectively, as shown in Figure A4.13.24. It is not known why these records are not available within the EMS database.

The maximum values of PGA were recorded at the IOCA station, which is located in the centre of Casamicciola (Figure A4.13.24), at low topography (altitude of 123 m, ESM, 2017), 0.8 km away from the epicentre calculated by the INGV and reported in Table A4.13.3 (8.5 km according to the CSEM/EMSC estimate) and 0.5 km away from the most affected area, according to INGV G.D.L. (2017). According to ESM (2017), it is situated on EC8 soil type B. However, this characterization was obtained from geological considerations, without a

direct measurement of shear-wave velocities (ESM, 2017; Iervolino *et al.*, 2017). According to the V_{s30} map of Caccavale *et al.* (2017) shown in Figure A4.13.16, IOCA station lies over soils with V_{s30} in the range 180-200 m/s, which would correspond to EC8 soil type C instead.



Figure A4.13.24. Location of the IOCA station on the island and of the closest stations (CAFL, CMSN) on the mainland. Modified from Iervolino *et al.* (2017).

Figure A4.13.25 and Figure A4.13.26 depict corrected acceleration, velocity and displacement time series of the three ground motion components recorded at IOCA station, whose peak values are summarised in Table A4.13.7. Figure A4.13.27 presents the respective 5% damped spectral pseudo-acceleration, pseudo-velocity and displacement spectra. As pointed out by Iervolino *et al.* (2017), both horizontal components present a peak in the spectral acceleration and spectral velocity at around 0.5-0.6 seconds. Based on the results of Cultrera *et al.* (2017) shown in Figure A4.13.18, Iervolino *et al.* (2017) believe that this isotropic amplification is likely due to site effects, as ambient noise measurements yielded the highest site amplification values at periods around 0.5-0.67 s.

Table A4.13.7. Corrected PGA, PGV and PGD per recorded component of ground motion at IOCA station, as reported by EMS (2017).

COMPONENT	PGA (g)	PGV (cm/s)	PGD (cm)
East-West	0.275	17.8	2.31
North-South	0.188	11.5	1.72
Vertical	0.270	11.8	1.46

The peak ground and spectral values of the vertical component of ground acceleration are relatively high, compared to the horizontal components, especially up to a period of 0.40 s, after which the vertical pseudo-acceleration decreases abruptly. A large peak with values above 0.85 g can be observed at around 0.26 seconds, whilst high spectral accelerations

greater than 0.5 g are observed across periods from 0.15 through 0.3 s (Figure A4.13.27). As ISI (2017) discuss that the building stock of Ischia is mainly composed by 2-3 storey masonry buildings with eigenperiods up to 0.3 s, it appears that a large part of the building stock was subject to these particularly large vertical accelerations that jeopardize the masonry walls integrity and significantly decrease their lateral resistance.

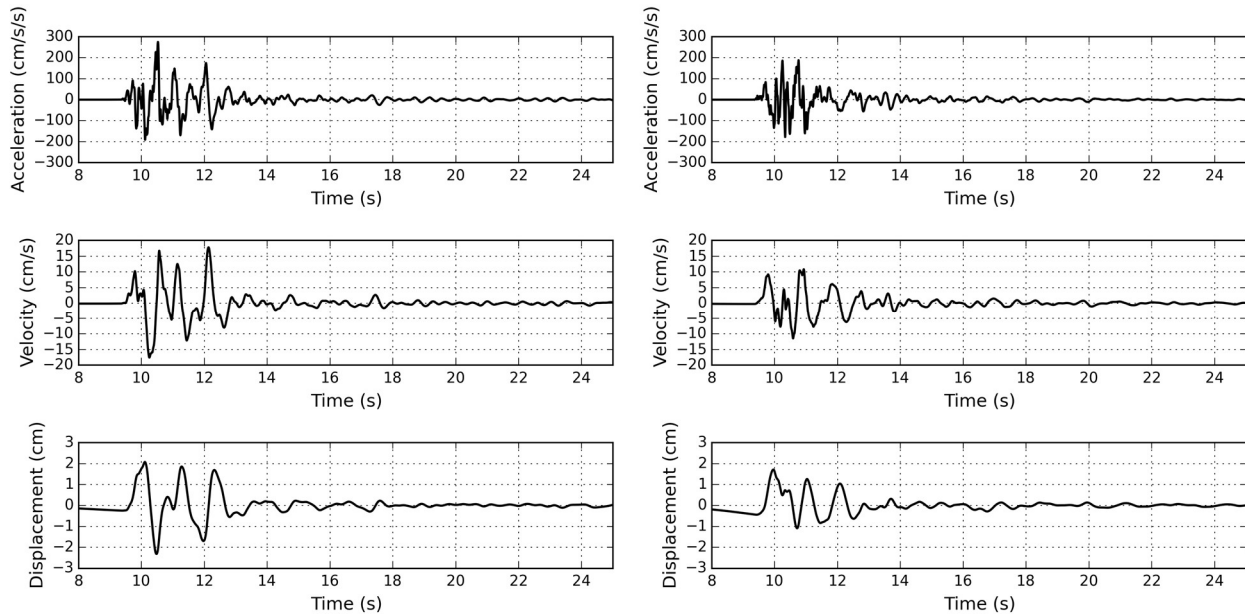


Figure A4.13.25. Corrected recordings of ground acceleration (top), velocity (centre) and displacement (bottom) for the east-west (left) and north-south (right) components of Ischia earthquake at IOCA station (epicentral distance 0.8 km). Waveforms from ESM (Luzi *et al.*, 2016).

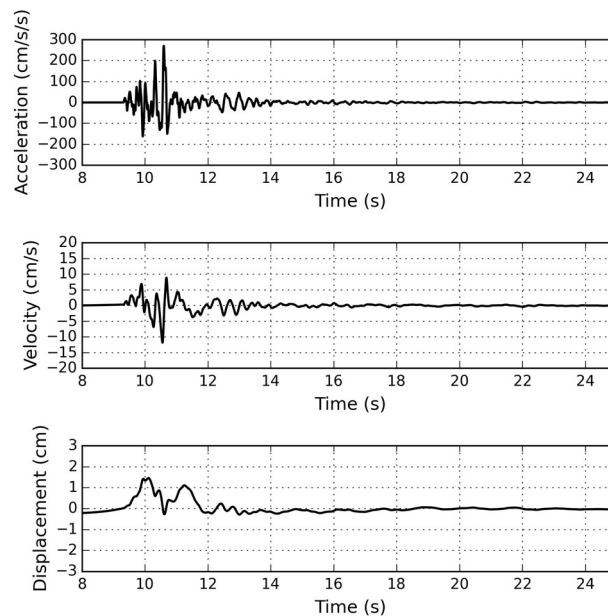


Figure A4.13.26. Corrected recordings of ground acceleration (top), velocity (centre) and displacement (bottom) for the vertical component of Ischia earthquake at IOCA station (epicentral distance 0.8 km). Waveforms from ESM (Luzi *et al.*, 2016).

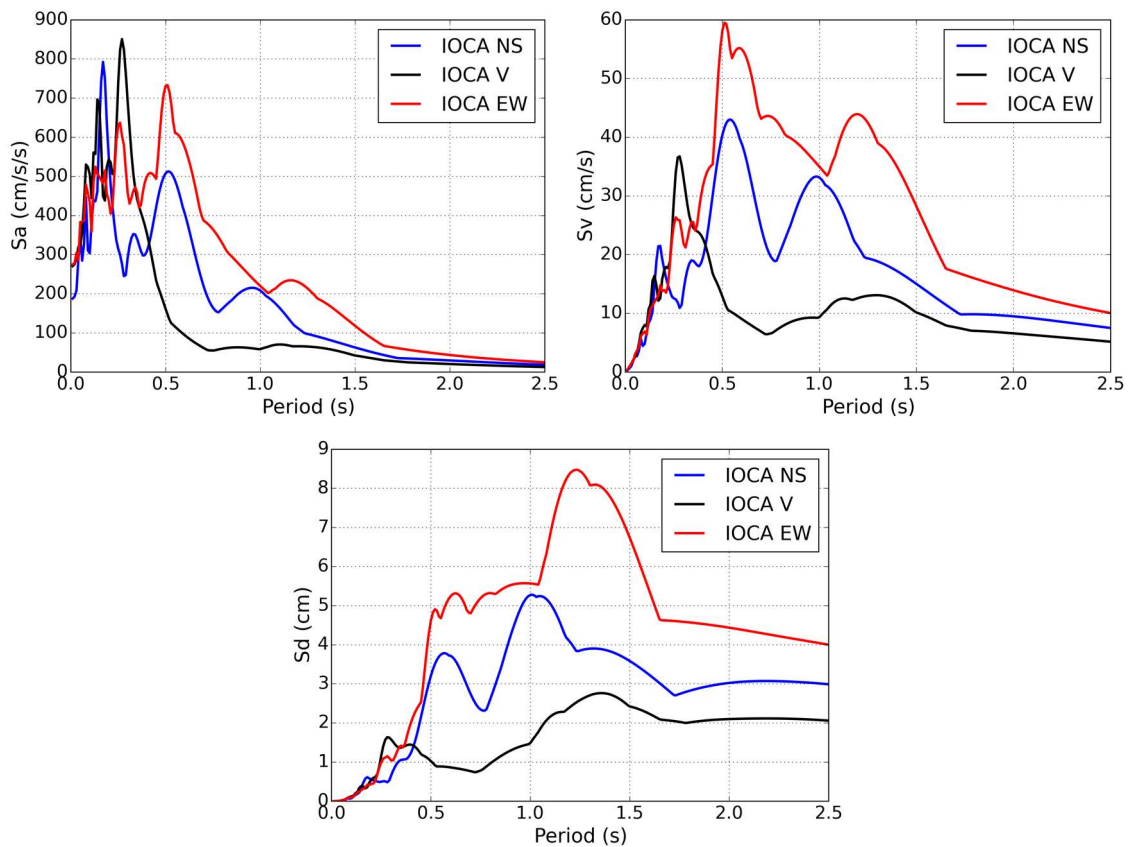


Figure A4.13.27. 5% damping pseudo-acceleration (top left), pseudo-velocity (top right) and displacement (bottom) spectra of the three components of the IOCA recording. Waveforms from ESM (Luzi *et al.*, 2016).

The magnitude of the vertical component becomes evident when compared against the 475-year return period vertical elastic design spectrum of NTC08 for soil B, as shown in Figure A4.13.28 (right). At the same time, the spectral accelerations of the horizontal components are closer to the corresponding elastic design spectrum of NTC08 for soil B, though they largely exceed it at a broad range of periods, particularly in the case of the east-west component (Figure A4.13.28, left). According to Iervolino *et al.* (2017), these exceedances are likely due to the proximity of the station to the epicentre, the shallow hypocentral depth and local site effects. It is noted that both plots in Figure A4.13.28 use soil type B as a reference because this is the soil type indicated for IOCA station, though if soil type C were to be more appropriate according to the discussion presented earlier, the conclusions from these comparisons could change.

The recorded PGAs shown in the pseudo-acceleration response spectra of the recordings at the two closest stations on the mainland (19.9 and 26.0 km, Figure A4.13.24) are not larger than 0.0005 g, suggesting a rapid attenuation of the ground motion (Iervolino *et al.*, 2017; Figure A4.13.29). This effect is attributed to the moderate magnitude, the shallow depth, and the volcanic nature of the soil of the area. The spectra at both stations are typical for recordings at such a distance from the epicentre exhibiting relatively uniform spectral amplitudes at a broad period range.

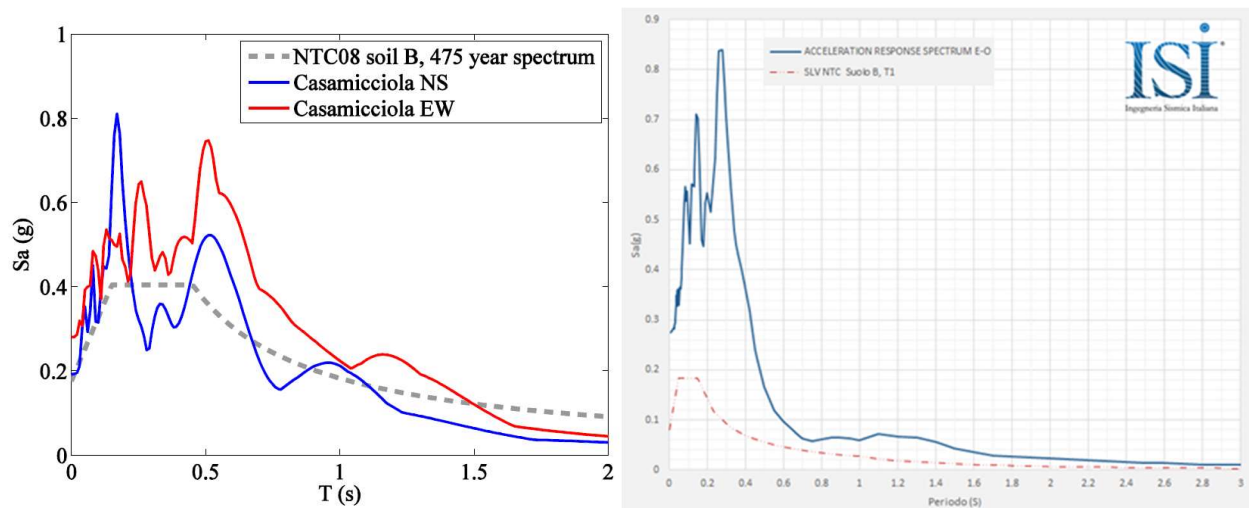


Figure A4.13.28. Horizontal acceleration spectra (5% damping) of IOCA record versus horizontal design elastic spectrum for the NTC08 Life Safety Limit State (SLV, 475-year return period) at soil B, from Iervolino *et al.* (2017) (top). Vertical acceleration response spectrum for the same record (blue line) versus vertical design spectrum for the NTC08 Life Safety Limit State (SLV, 475-year return period) at soil B (red dashed line), modified from ISI (2017) (bottom).

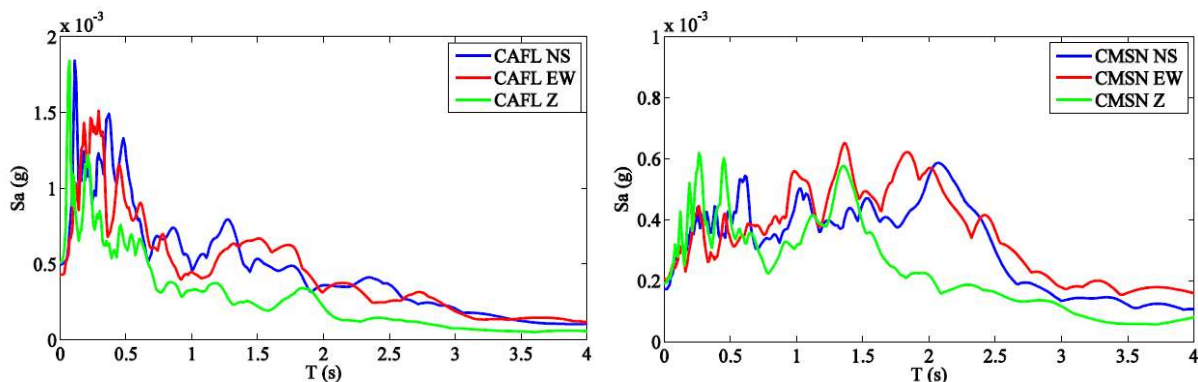


Figure A4.13.29. 5% damped pseudo-acceleration spectra of the three components of the ground motion for recordings in Arco Felice (CAFL) (left); and Monte Sant'Angelo (CMSN) (right). From Iervolino *et al.* (2017).

Comparisons carried out by Iervolino *et al.* (2017) between the geometric mean and larger horizontal response spectra of the mainshock at IOCA and two theoretical GMPEs for shallow near-field earthquakes determined for volcanic regions by Tusa & Langer (2016) and Ambraseys *et al.* (1996), valid in the context of Italian hazard studies, show that the recorded ground motion is above the theoretical median and lies close to two standard deviations in both cases, when a local magnitude M_L of 4.3 is used (black lines in Figure A4.13.30). This was the first estimate of magnitude reported by the INGV, which was later downgraded to M_L 3.6. When using the latter, both spectra exceed the +2 standard deviations at most medium-to-long periods (grey lines in Figure A4.13.30). Different results might be obtained if using soil type C rather than B, as discussed earlier. Iervolino *et al.* (2017) point out that the local exceedance of the +2 standard deviations of the model by Tusa & Langer (2016) for periods around 0.5-0.6 seconds supports the suspicion that local site conditions played a significant role in the amplification of ground motions, as discussed above.

Iervolino *et al.* (2017) carried out similar comparisons with the response spectra of stations CAFL and CMSN, assuming soil type B due to lack of further information, and found that the geometric means of both agree relatively well with the median prediction of Tusa & Langer (2016) for M_L 3.6, while the larger horizontal spectra are mostly below -2 standard deviations of the model of Ambraseys *et al.* (1996), irrespective of the magnitude used. Iervolino *et al.* (2017) award this to the model of Tusa & Langer (2016) being specific for volcanic regions, while that of Ambraseys *et al.* (1996), is incapable of capturing the rapid attenuation of the ground motion at volcanic soils. While not mentioned by Iervolino *et al.* (2017), it is also noted that M_L 3.6 lies comfortably within the range of magnitudes for which the former was derived, while the latter used data from earthquakes with surface-wave magnitude M_s equal to or larger than 4.0.

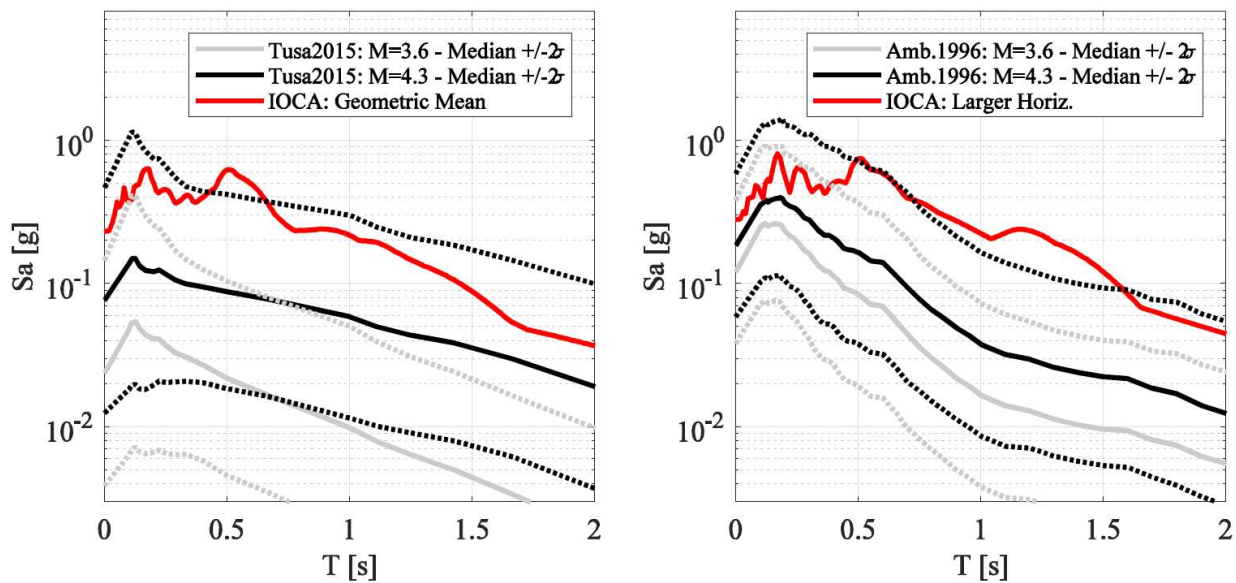


Figure A4.13.30. Comparison between the 5% damped geometric mean (left) and larger horizontal (right) spectral acceleration (S_a , g) recorded at IOCA station and predicted by the Tusa & Langer (2016; left) and Ambraseys *et al.* (1996, right) GMPEs. From Iervolino *et al.* (2017).

The INGV (INGV-Terremoti, 2017b) carried out further comparisons in terms of horizontal PGA against the model of Bindi *et al.* (2011) for crustal active areas and that of Tusa & Langer (2016), as shown in Figure A4.13.31. As can be observed, the model of Tusa & Langer (2016) matches better the observations on EC8 soil type A (Figure A4.13.31, left), while it slightly overestimates PGA values at long distances on EC8 soil type B (Figure A4.13.31, right). The one data point at less than 1 km on the plot on the right of Figure A4.13.31 corresponds to IOCA station and lies clearly above the predictions from both models, which could be due either to local site conditions and/or the effect of a soil of quality worse than B at IOCA, as it has been suggested by Caccavale *et al.* (2017). For all other cases, observed values are significantly lower than predicted by the model of Bindi *et al.* (2011). From these plots it becomes clear that the propagation of the co-seismic energy has been abruptly attenuated by Iervolino *et al.* (2017), attributed to the shallow focal depth of the event, its low magnitude and the anelastic properties of the volcanic environment.

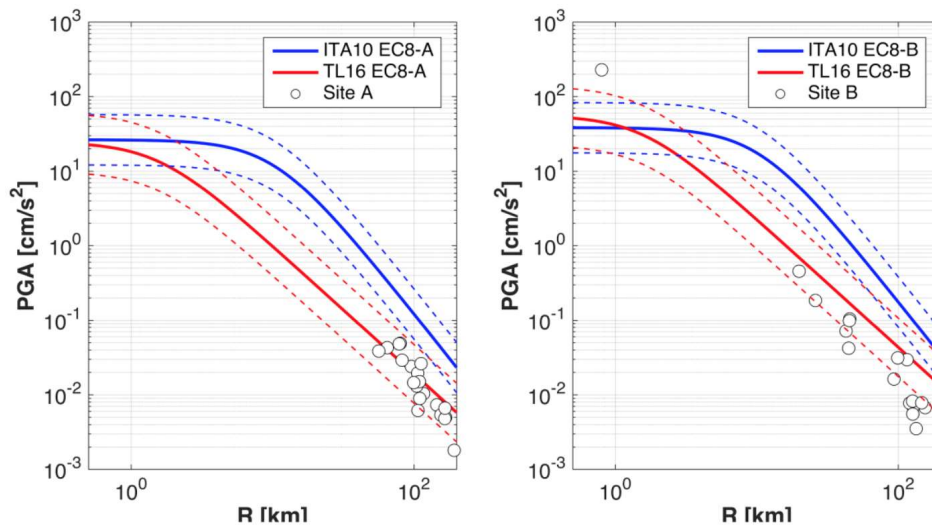


Figure A4.13.31. Comparison of PGA observations (open circles) and attenuation laws (blue lines for the model of Bindi *et al.*, 2011, red lines for the model of Tusa & Langer, 2016) for sites located on rock (EC8 soil A, left) and hard soil (EC8 soil B, right). From INGV-Terremoti (2017b).

A4.13.4.3 Inferred shaking levels

The generation of ShakeMaps in terms of PGA and PGV by the INGV faced the same difficulties as explained in Section A4.13.4.1 for the case of the macroseismic intensities (INGV G.D.L., 2017). Several versions of the maps were created, varying the GMPE used and forcing the consideration of the values measured at IOCA station. Unfortunately, the resolution of the maps contained within the report by INGV G.D.L. (2017) makes it almost impossible to visually infer values of ground motion, and the final version of the maps available online (INGV-ShakeMaps, 2017) does not specify the colour scale used, which appears to be different from that used for the intensities. No other inferred ground motions have been found in the literature.

A4.13.4.4 Duration of ground shaking

According to Iervolino *et al.* (2017), the 5-95% of Arias definition of significant duration of ground motion at stations CAFL and CMSN (Figure A4.13.24) was 45.0 s and 79.7 s, respectively. For the case of IOCA station, processing of the waveforms available from the ESM database (2017) yields 2.85, 3.59 and 2.73 seconds for the east-west, north-south and vertical components, according to the same definition.

Estimations of earthquake significant durations were obtained using the empirical relations proposed by Bommer *et al.* (2009) and Afshari & Stewart (2016) (Figure A4.13.32). Significant durations were determined in terms of the 5-75% definition of Arias intensity for a range of epicentral distances covering the island of Ischia and for V_{s30} values mainly corresponding to the average reference ones of A, B, C and E EC8 soil categories, reported for Ischia by Caccavale *et al.* (2017) (Table A4.13.6). For the model of Bommer *et al.* (2009), a depth to the top of the rupture of 0.2 km was used, in accordance with the slip model derived by INGV G.D.L. (2017). For epicentral distances ranging 0-15 km, the estimates obtained by means of the equation of Afshari & Stewart (2016) seem to better match the

values for 5-75% of Arias intensity recorded at IOCA (Table A4.13.8), than those obtained with the model of Bommer *et al.* (2009). This is expected, as the former was derived using data from earthquakes with moment magnitude in the range 3.0-7.9, while the latter only considered events with magnitude above **M**4.8.

Table A4.13.8 shows the significant duration of the record from the nearest IOCA station available from the ESM Database (2017), calculated for each component using SeismoSignal (Seismosoft, 2016).

Table A4.13.8. Significant duration (5-75% of Arias Intensity, in seconds) of the 2017 mainshock recorded at IOCA station, 0.8 km away from the epicentre, determined using SeismoSignal (Seismosoft, 2016) and the waveforms from ESM (2017)¹.

COMPONENT	Duration (s)
IOCA East-West	2.08
IOCA North-South	1.07
IOCA Vertical	0.80

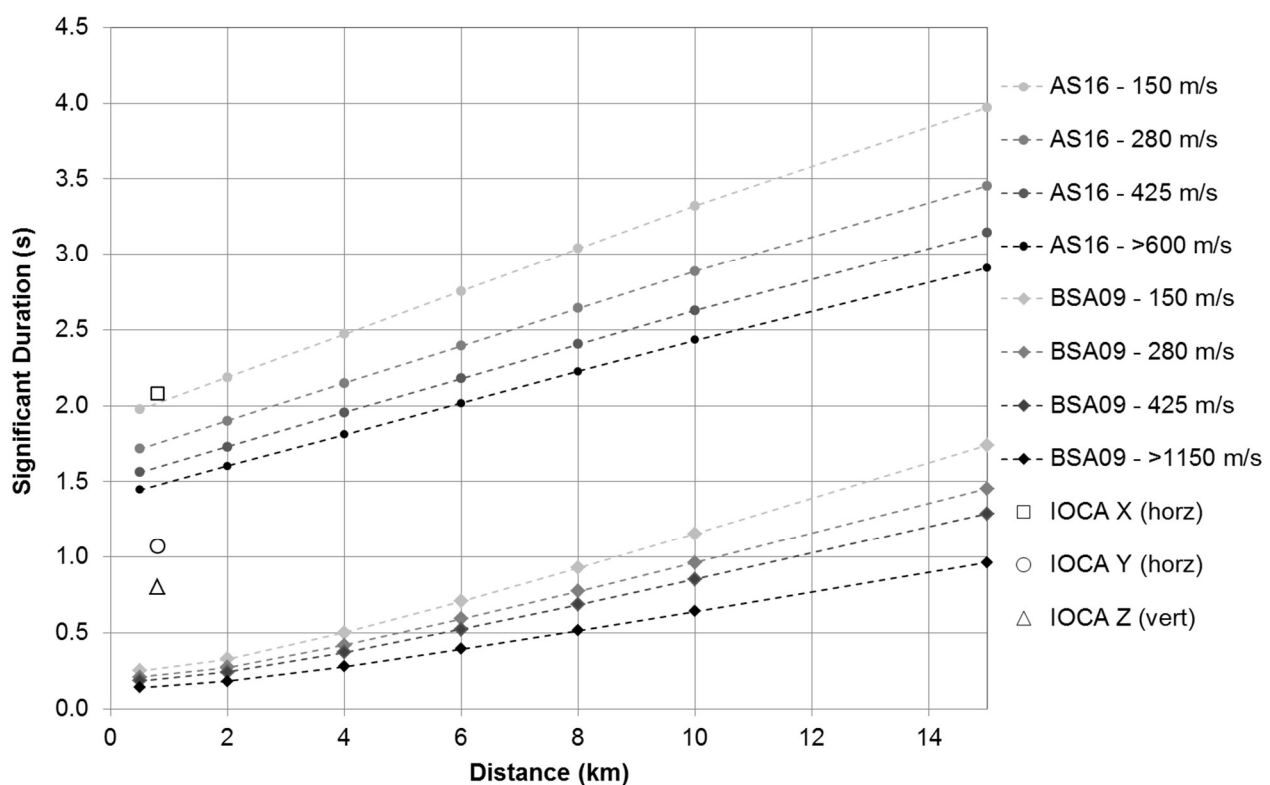


Figure A4.13.32. Estimation of the significant duration of the 2017 mainshock in Ischia, using prediction equations by Bommer *et al.* (2009, BSA) and Afshari & Stewart (2016, AS). Stand-alone markers indicate observed 5-75% of Arias intensity significant duration at IOCA station.

¹ Calculated as per a previous version of this report with **M**3.8 instead of **M**3.9.

A4.13.5 Collateral earthquake hazards

A4.13.5.1 Surface rupture

Even though the earthquake's hypocenter was very shallow, its magnitude was too small for the main rupture to reach the surface. However, it did produce secondary cracks in directions NE-SW to E-W (N60E through N110E), either due to the dynamic ground motion or to static deformation disrupting the softer shallow layers, also causing a subsidence of $4 \text{ cm} \pm 1 \text{ cm}$ that was measured via InSAR in an area about 1 km south of Casamicciola and Lacco Ameno (INGV G.D.L., 2017).

A4.13.5.2 Landslides

Several cases of landslides and rockfalls have been reported for this event by Di Manna *et al.* (2017) in their technical report for the Italian National Institute for Environmental Protection and Research (ISPRA). Rock detachments and collapses of green tuff were observed along a dirt road and through a forest of chestnuts (points 322 and 323 in Figure A4.13.61). The first collapse was characterized by a total volume of less than 1 m^3 , with 3 main grey-yellowish tuff blocks with dimensions $40 \times 20 \times 20 \text{ cm}$, $20 \times 10 \times 10 \text{ cm}$ and $10 \times 5 \times 5 \text{ cm}$, and various small fragments with size of the order of 1 cm. The second collapse was characterized by a large block of tuff with dimensions $200 \times 100 \times 100 \text{ cm}$, and other blocks with dimensions smaller than 100 cm. The detachment occurred from an escarpment with a height of about 4-5 m. INGV G.D.L. (2017) has also observed fall of tuff blocks between the localities of Fango and Piazza Maio, as well as limited landslides of volcanic material from the slopes of the roads.

At the fumarole between Montagnone and Montecito (points 330 and 331 in Figure A4.13.61) a 30-40-cm wide and 20-30-cm high partial detachment at the edge of the slope was observed for a length of about 70 cm. Another landslide occurred along the escarpment on the right bank of Senigallia valley, in the upstream sector of Via Nizzola (point 335 in Figure A4.13.61). This was composed of green tuff material with an estimated total volume of $50\text{-}60 \text{ m}^3$.

A4.13.5.3 Liquefaction

No evidence of liquefaction has been reported for this event.

A4.13.5.4 Settlements

Di Manna *et al.* (2017) observed the subsidence of foundations of some new and recently repaired buildings in Fango. As shown in Figure A4.13.53, this led to damage of the supported structures. Moreover, Di Manna *et al.* (2017) interpret the few surface cracks appeared on the surface of paved roads and the cultivated land, at times continuous inside the houses, as a hint of differential ground settlement. A water pipe was damaged at the location of a road crack.

A4.13.6 Exposed population

A4.13.6.1 Socio-economic setting

According to the 2016 Human Development Data (United Nations, 2016), the Human Development Index (HDI) for Italy was 0.887 in 2015, latest data available, while its Inequality-adjusted HDI (IHDI) was 0.784. According to the world's ranking per HDI, Italy is currently located in the 26th place, while the Netherlands are ranked 7th. Table A4.13.9 compares the HDI and IHDI for both countries, according to United Nations (2016).

Table A4.13.9. Human Development Index and Inequality-adjusted Human Development Index for Italy and the Netherlands, from United Nations (2016).

Report	Data	Italy			Netherlands		
		HDI	IHDI	Rank	HDI	IHDI	Rank
UNDP (2016)	2015	0.887	0.784	26	0.924	0.861	7

It is evident, as Figure A4.13.33 indicates, that both countries had followed a stable and growing economic course until 2008 when fluctuation started during the world's economic recession. Considering the size of Italy compared to the Netherlands, its economic power (GDP) is several times higher (Figure A4.13.33, left), but the GDP per capita of the Netherlands clearly exceeds that of Italy (Figure A4.13.33, right), placing the Netherlands high in the HDI and wealth ranking. Moreover, Italy has been more importantly affected by the 2008 crisis. Table A4.13.10 presents a comparison between Italy and the Netherlands in terms of gross domestic product (GDP), GDP per capita and unemployment rate for 2015.



Figure A4.13.33. GDP (left) and GDP per capita (right) fluctuation in US \$, for Italy and the Netherlands for the last 65 years according to World Bank national accounts data and the Organization for Economic Cooperation and Development (OECD) National Accounts data files (The World Bank Group, 2017).

According to Statista (2017), the region of Campania, to which the island of Ischia belongs, ranks 17th (out of 20 Italian regions) in GDP per capita for the year 2017, with 17,077 euro (almost half of the GDP per capita of the country as a whole). Regarding the average income per person, the communities of Ischia vary between 13,800 and 16,800 euro per year, according to TWIG Blog (2017), which reports data from MEF (2015), with the country's average income per person in 2015 equal to 20,690 euro, in growth by 1.3% since 2014. It

is evident again that Ischia, following the economy of the region of Campania, is placed among the less privileged areas of Italy in financial terms. Its economy is mainly based on tourism, commerce and other associated activities, as the occupation per resident mainly reveals (ISTAT, 2011). The permanent residents are also occupied by other activities, such as trading, information services, scientific and technical services, to name some.

Table A4.13.10. Gross domestic product (GDP), GDP per capita and unemployment rate during 2015 for Italy and the Netherlands, according to the World Economic Outlook Database (2016)

Indicator	Units	Italy	Netherlands
Gross domestic product, current prices	Billions USD	1,815.76	750.696
Gross domestic product per capita, current prices	USD	29,866.62	44,322.83
Unemployment rate	%	11.908	6.89

A4.13.6.2 Population density and distribution

The island of Ischia belongs to the province of Naples that is a part of the region of Campania. The total population of Campania is 5,766,810 people with density of 420.83 people per km², while the province of Naples has 3,054,956 permanent residents with 2,591.3 persons per km².

Details on the population of the communities of Ischia and the neighboring island of Procida are given in Table A4.13.11 according to the 2011 census (ISTAT, 2011) in descending order of EMS-98 intensity as estimated in Figure A4.13.21. In Figure A4.13.34, the respective communities are mapped. It is evident that the most affected communities of Casamicciola and Lacco Ameno are densely populated.

In all communities included in Table A4.13.11, the EMS-98 intensity observed is equal to or higher than IV, according to the EMS-98 intensity map of Figure A4.13.21, except for the community of Serrara Fontana, within which some localities experienced intensities larger than V while some others were subject to intensity III. The total affected population that corresponds to these communities is 73,868 registered persons. The population of the communities of the mainland that hardly felt the earthquake (I~III) are not considered in this number. However, having the earthquake occurred at the peak of the touristic season, an additional 150,000 tourists are believed to have been on the island, according to The Guardian (2017).

Due to the recent date of the earthquake no information on population exposure is yet available from public disaster databases.

Table A4.13.11. Population and population density in 2011 for the communities of Ischia and the neighboring island of Procida. Data from ISTAT (2011).

District	Population	Population density (people/km ²)
Casamicciola	8,685	1,381.5
Lacco Ameno	5,988	2,251.1
Forio	18,044	1,268.7
Barano d'Ischia	10,114	901.6
Ischia	18,147	2,295.7
Serrara Fontana	3,098	941.1
Procida	9,792	2,403.2

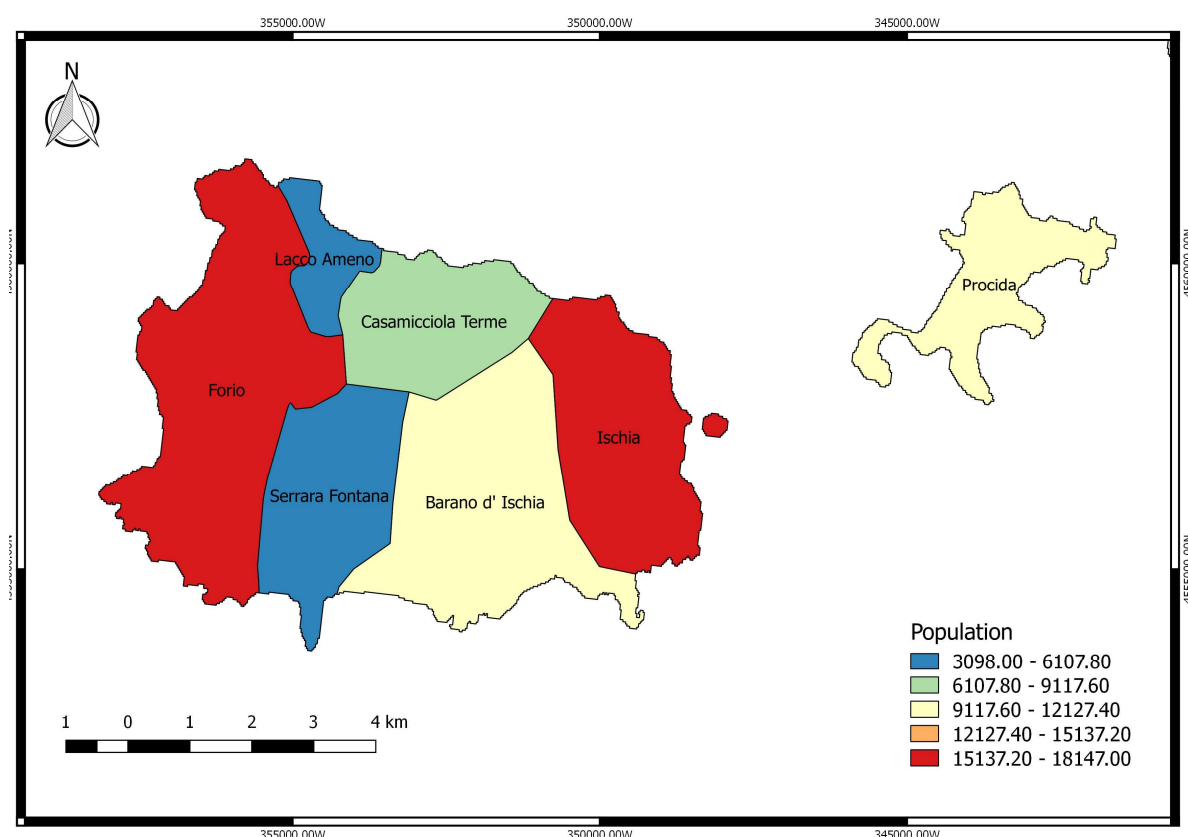


Figure A4.13.34. Population distribution within the communities of Ischia and Procida (data from ISTAT, 2011).

A4.13.6.3 Time of day of earthquake

The earthquake hit the area of Casamicciola at 20.57.51 local time, during the peak of the summer touristic period for the island. As mentioned by The Guardian (2017), that was typically the time of dinner for locals and tourists and many people were indoors. Considering that some of the casualties were among the visitors of the island, should the earthquake have occurred during another season, or at a time of the day in which most tourists could have been outdoors at the beach, the aftermath could have been less negative in terms of casualties.

Due to the shallowness of the hypocentre, the rumble of the P-waves came simultaneously with the main shock which was followed by a total blackout (ISI, 2017), creating additional panic among the population.

A4.13.7 Characteristics of exposed building stock

A4.13.7.1 Seismic design codes

The introduction of the seismic notion in the Italian regulations took place with the Royal Decree of 1927 following the destructive earthquakes of Reggio Calabria and Messina in 1908. As shown in Figure A4.13.35 (left), few areas were characterized as seismic in said document, mainly the ones affected by the earthquakes of 1908, with the rest of the Italian territory being covered by no legislation regarding earthquake resistant design. During the period between 1927 and 1962, when a law that provided construction details and redefined the distribution of seismic forces was passed, several Royal decrees were issued characterizing new areas as seismic, describing anti-seismic techniques and modifying the mass proportions for the definition of seismic forces. It was in 1935 that the community of Casamicciola was included among the seismic areas of the country.

In 1971 the norm for the design and construction of reinforced concrete, prestressed concrete and steel structures was introduced. In 1974, regulation of private and public construction was made compulsory. In parallel, it was agreed that the seismic classification would be updated whenever the evolution of seismic knowledge demanded it. Soon, in 1975, the new construction code for seismic areas was approved by means of a ministerial decree. This code mainly allowed for the use of dynamic seismic analysis with the introduction of the elastic design spectrum, defined geotechnical criteria for the buildings foundation, and modified, again, the distribution of the seismic forces along the height of the buildings.

Seismological studies by the National Research Council (CNR) following the destructive earthquakes of Friuli – Venezia Giulia in 1976 and Irpinia in 1980, led to the proposal of a new seismic classification of the Italian territory approved by a series of decrees until 1984, when a probabilistic approach was applied for the division of Italy in three seismic zones (Figure A4.13.35, right). It was in 1981 that the communities of Ischia, Barano d'Ischia, Lacco Ameno, Forio, Serrara Fontana were classified as belonging to Zone II, which implied the existence of a moderate hazard.

In 1996, a ministerial decree established the seismic design with damage states as well as the dependence of the seismic forces on the dynamic characteristics of the buildings. In 2003, the 3rd-generation seismic code was introduced (Amadio, 2014), and the seismic classification of the country was updated in parallel (Figure A4.13.36, left). A fourth seismic class (the lowest) was then added, giving the possibility to the regions marked under this category to decide upon the obligation of designing their buildings to resist seismic action. Ischia remained in Zone II (moderate-high), with design PGA values on rock between 0.15 and 0.25 g. This new code, compatible with Eurocode 8 (CEN, 2004), accounts for the

ductility of the structure, the strength hierarchy among nodes and elements and the analysis at limit states.

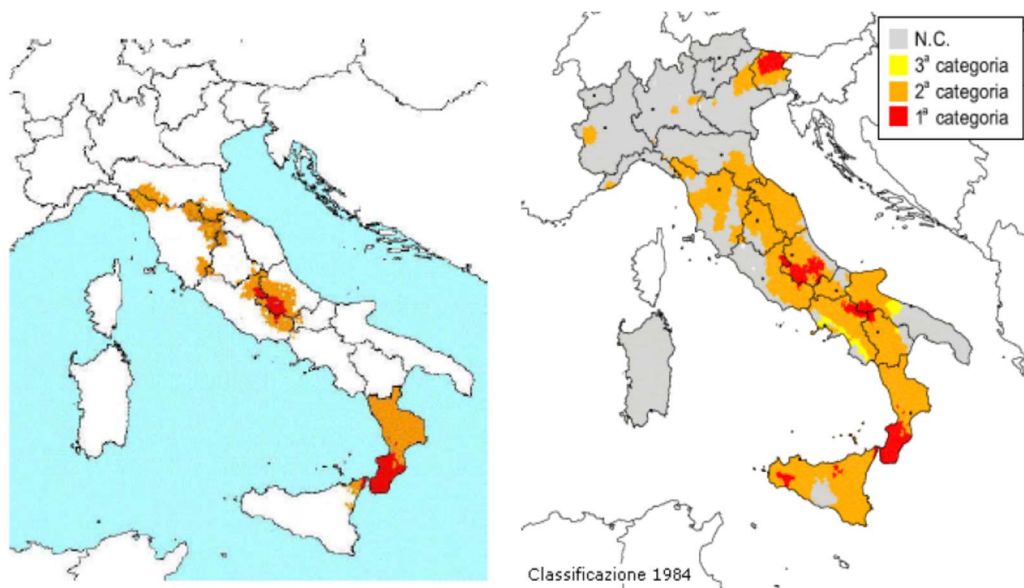


Figure A4.13.35. Seismic zonation of the Italian territory according to 1927 (left) and 1984 (right) norms. From Amadio (2014).

A new code for design and construction, the NTC (2008), was introduced in 2008 and finally adopted in 2009, after the earthquake of L'Aquila. The NTC (2008), considered to be the norm of 4th generation (Amadio, 2014), is based on the principles of performance-based design with multiple limit states and is compatible with Eurocode 8 (CEN, 2004). Instead of the seismic zonation until then adopted, the territory was divided into a grid of 10x10-km cells, each of which is assigned a reference value of PGA on rock. This change led to the introduction of design seismic acceleration to areas that had been considered aseismic until then. The most recent update of this map was carried out in 2015 (Figure A4.13.36, right).

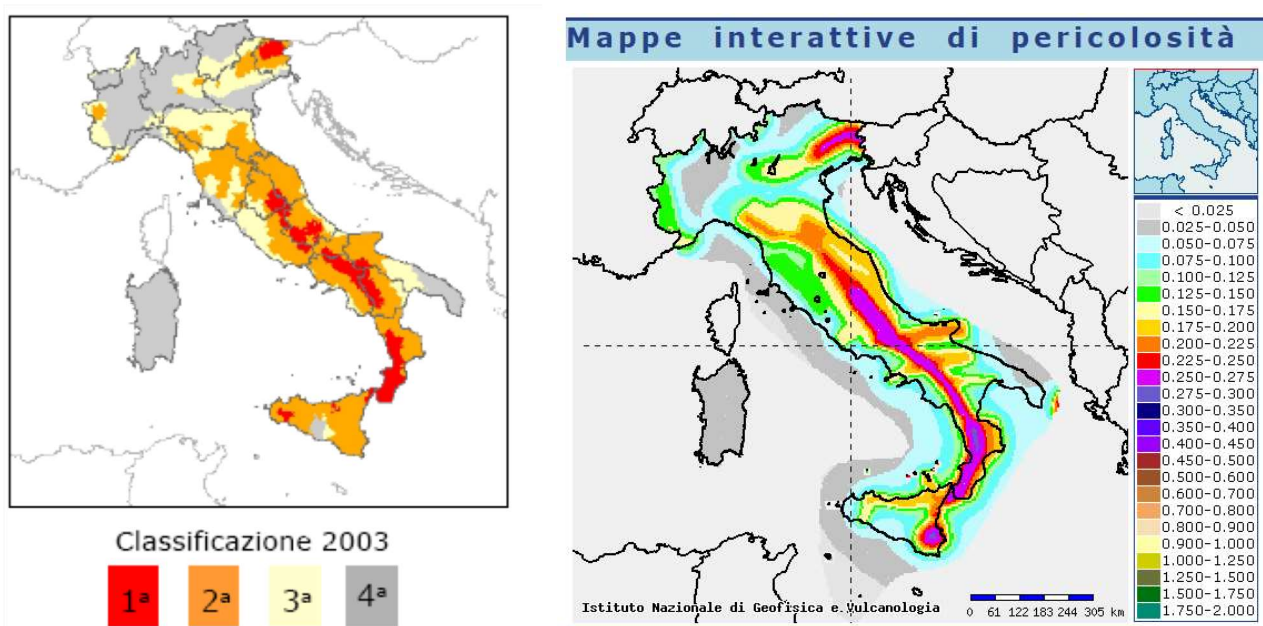


Figure A4.13.36. Seismic zonation of Italian territory according to 2003 norm (Amadio, 2014) (left) and 2015 update (right) (INGV-GIS, 2015).

This section was elaborated with data from ISI-Normative (2013), Amadio (2014), Balliana (2015) and Wikipedia (2017).

A4.13.7.2 Building typologies

Data regarding typologies at the country level collected from the PAGER Inventory Database v2.0 (Jaiswal & Wald, 2008) for Italy are summarized in Figure A4.13.37. As can be observed, half of the Italian building stock is unreinforced brick masonry and the rest is composed by low to mid-rise ductile and non-ductile reinforced concrete frames. It is noted that the proportions reported are the same irrespective of whether it is rural/urban or residential/non-residential building stock, which implies that data was not available for each individual category.

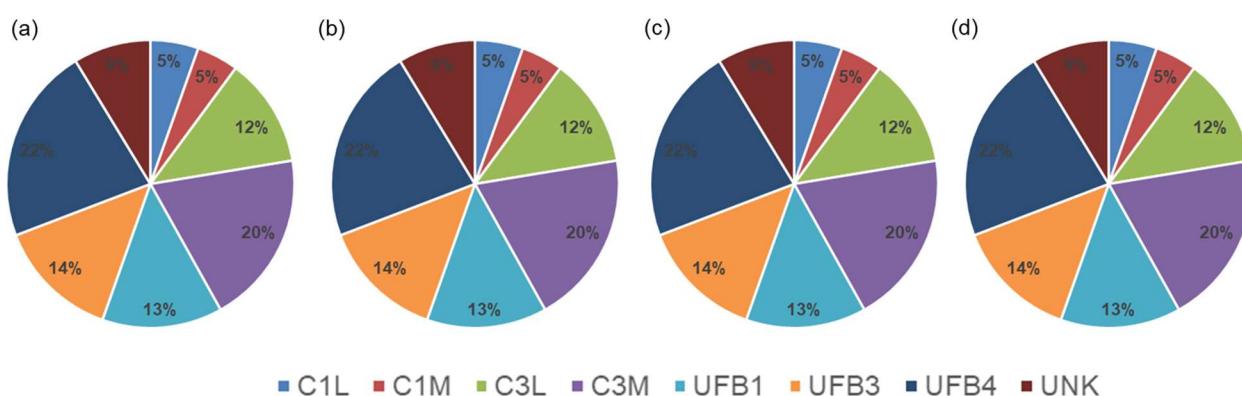


Figure A4.13.37. Proportion of building main typologies in Italy for (a) rural residential, (b) urban residential, (c) rural non-residential, (d) urban non-residential typologies: C1L: Ductile reinforced concrete moment frame with or without infill low-rise; C1M: Ductile reinforced concrete moment frame with or without infill mid-rise; C3L: Nonductile reinforced concrete frame with masonry infill walls low-rise; C3M: Nonductile reinforced concrete frame with masonry infill walls mid-rise; UFB1: Unreinforced brick masonry in mud mortar without timber posts; UFB3: Unreinforced brick masonry in lime mortar; UFB4: Unreinforced fired brick masonry, cement mortar; UNK: Not specified (unknown). 2002 data from USGS-PAGER, Jaiswal & Wald (2008).

The World Housing Encyclopedia (2014) includes in its database seven building typologies present on the Italian territory, whose main characteristics are listed in Table A4.13.12. One of the reports available in the website for the WHE-GEM Building taxonomy (2017) describes a representative type of reinforced concrete building in Italy: a 4- to 6-storey residential or commercial building with reinforced concrete infilled frames as lateral resisting system, constructed in the 1950-1960s. This typology matches the description of multi-storey reinforced concrete (RC) buildings typology in Table A4.13.12.

The distribution of buildings per construction material and construction period is illustrated in Figure A4.13.38 and Figure A4.13.39 for the communities of Ischia and the island of Procida, according to the data available from ISTAT (2011). It is evident that masonry is the prevailing bearing material for all the communities. Moreover, it is revealed that the majority of the building stock of all the communities and especially of the most affected localities of Casamicciola and Lacco Ameno was erected between 1960 and 1990.

Table A4.13.12. Building typologies in Italy according to the World Housing Encyclopedia (2014).

Building type	Age	Material	Height / number of dwellings	Found in	Damage by earthquakes
Multi-storey tower masonry with stone pillars and wood or arched beams (Casa Torre)	More than 200 years	Masonry: Stone Walls: Rubble stone (field stone) in mud/lime mortar or without mortar. Timber floor and roof	3-4 storeys / single dwelling	Urban areas (e.g. Tuscany)	Damaged at $M_L \geq 4.5$
Single-family stone masonry house	100-200 years	Masonry: Stone Masonry Walls: Rubble stone (field stone) in mud/lime mortar or without mortar; vaulted masonry floor, timber roof	2-5 storeys; single dwelling; terraced houses	Urban areas (e.g. Centro Italia)	Damaged at $M \geq 5.6$, $I \geq VI$
Single-family historic brick masonry house (centro storico)	100-200 years	Masonry: Earthen/Mud/Adobe/Rammed Earth Walls: Mud walls	2-3 stories; single dwelling; terraced houses	Urban areas (e.g. Central Italy)	Damaged at $I \geq VII$
Multi-storey RC buildings	25-60 years	Structural Concrete: Moment Resisting Frame: Designed for gravity loads only, with URM infill walls; Rigid floor and roof	4-10 stories; 20-49 units	Urban / suburban areas	Damaged at $M \geq 5$; $I \geq VI$
Brick masonry farmhouse with a "dead door"	100-200 years	Unreinforced Masonry Walls: Brick masonry in mud/lime mortar	2 stories; single dwelling	Rural areas (e.g. Emilia Romagna)	Damaged at $M \geq 4.5$; $I \geq VI$
Unreinforced stone wall rural housing	More than 200 years	Wooden Structure: Load-bearing Timber Frame: Wood frame (with special connections); rubble stones for infill	4 stories; single dwelling	Urban areas (e.g. Central Italy)	Damaged at $M \geq 5.1$; $I \geq VII$
Lower and middle class residential building in rural areas of Central Italy	76-100 years	Masonry: Stone Masonry Walls: Rubble stone (field stone) in mud/lime mortar or without mortar; vaulted masonry floor or timber, timber roof	4 stories; single dwelling	Rural areas (e.g. Central Italy)	Damaged at $M \geq 6$; $I \geq IX$

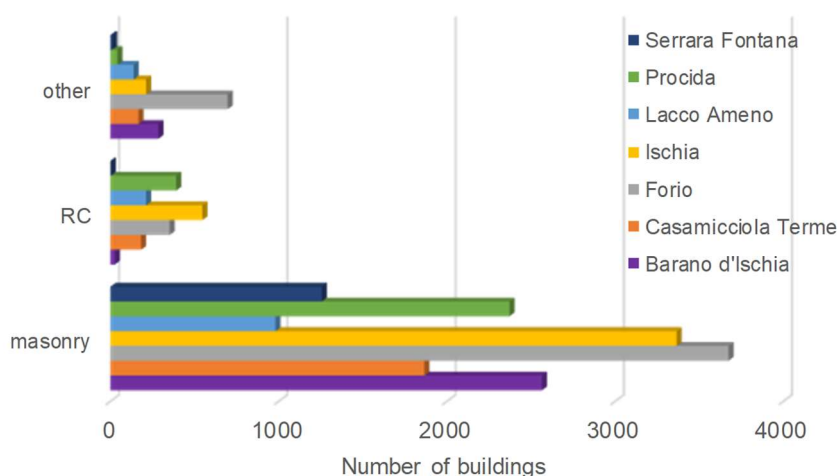


Figure A4.13.38. Number of buildings per construction material for the communities of Ischia and Procida. From ISTAT (2011).

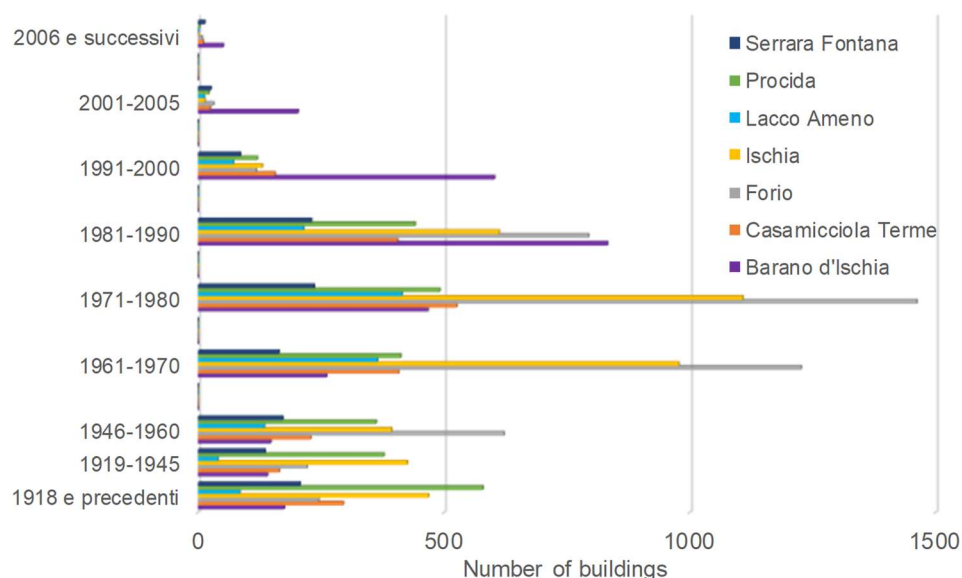


Figure A4.13.39. Number of buildings per construction period for the communities of Ischia and Procida. From ISTAT (2011).

The maps of Figure A4.13.40, Figure A4.13.41 and Figure A4.13.42 illustrate the distribution of the exposed building inventory of the most affected communities of Casamicciola and Lacco Ameno, according to Verderame *et al.* (2017). It is confirmed again that the prevailing structural system is bearing masonry walls, which make up around 80% of a total of 3252 residential buildings in the two communities (Verderame *et al.*, 2017) with a greatest presence of reinforced concrete buildings in the northern districts of Lacco Ameno (Figure A4.13.40). Furthermore, the building stock of the area is composed by low-rise buildings (1- to 2-storeys) (Figure A4.13.41), mainly dating more than 30 years (Figure A4.13.42). Higher concentration of older buildings is observed in the districts of the port of both communities, while some new constructions of both masonry and reinforced concrete can be inferred from the juxtaposition of maps of Figure A4.13.40 and Figure A4.13.42.

Verderame *et al.* (2017) classified the building stock of the two most affected communities of Casamicciola and Lacco Ameno according to their EMS-98 vulnerability class, which ranges from A through F, the former corresponding to the most vulnerable (Grünthal, 1998). For the buildings in reinforced concrete, this classification was carried out as a function of their construction period, which should reflect their level of seismic design. The buildings erected prior to 1935 in Casamicciola and prior to 1981 in Lacco Ameno (dates in which these areas started to be considered as seismically active), have been assigned to vulnerability class C, while those erected after said dates were assigned to class D. Regarding the buildings in masonry, there is a large variability in the level of vulnerability, depending on the material itself and the horizontal diaphragms. In view of this, Verderame *et al.* (2017) followed a simplified approach for their classification, based on the work of Di Pasquale *et al.* (2005), who studied the correlation between the vulnerability of the masonry buildings and their construction period, and defined five time-windows with different probabilities of being associated to the three most representative vulnerability classes, as shown in Table A4.13.13.

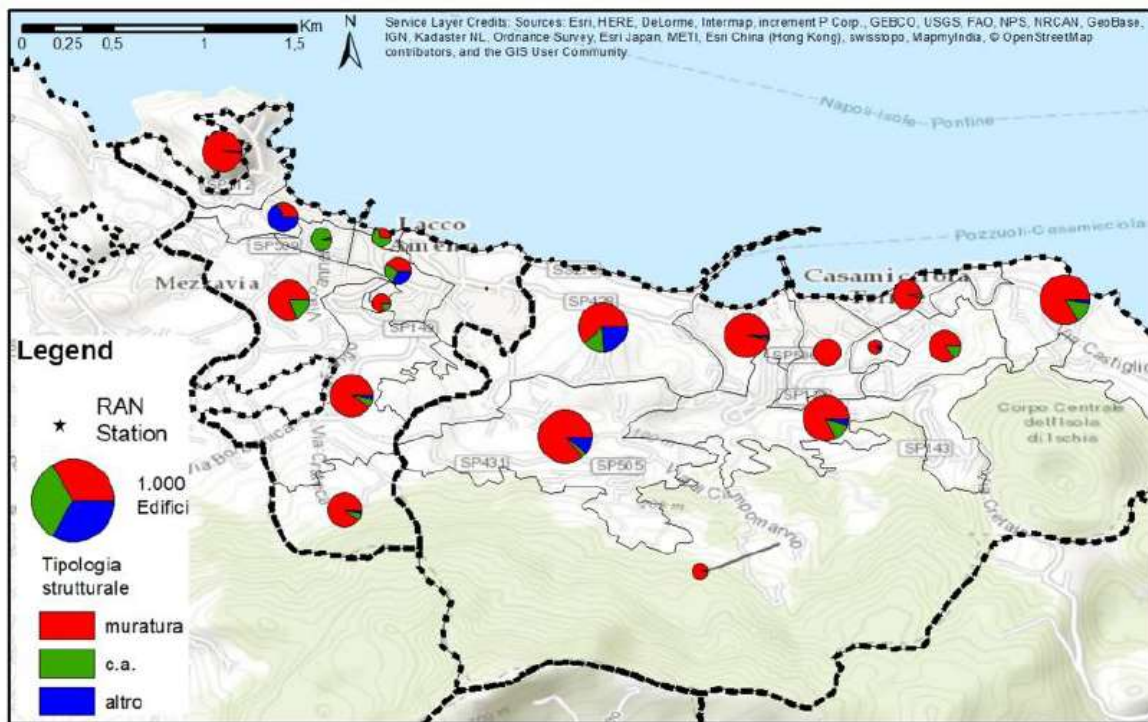


Figure A4.13.40. Distribution of construction material of buildings per cadastral sector of the most affected communities of Casamicciola and Lacco Ameno. Red: masonry. Green: reinforced concrete. Blue: other. From Verderame *et al.* (2017).

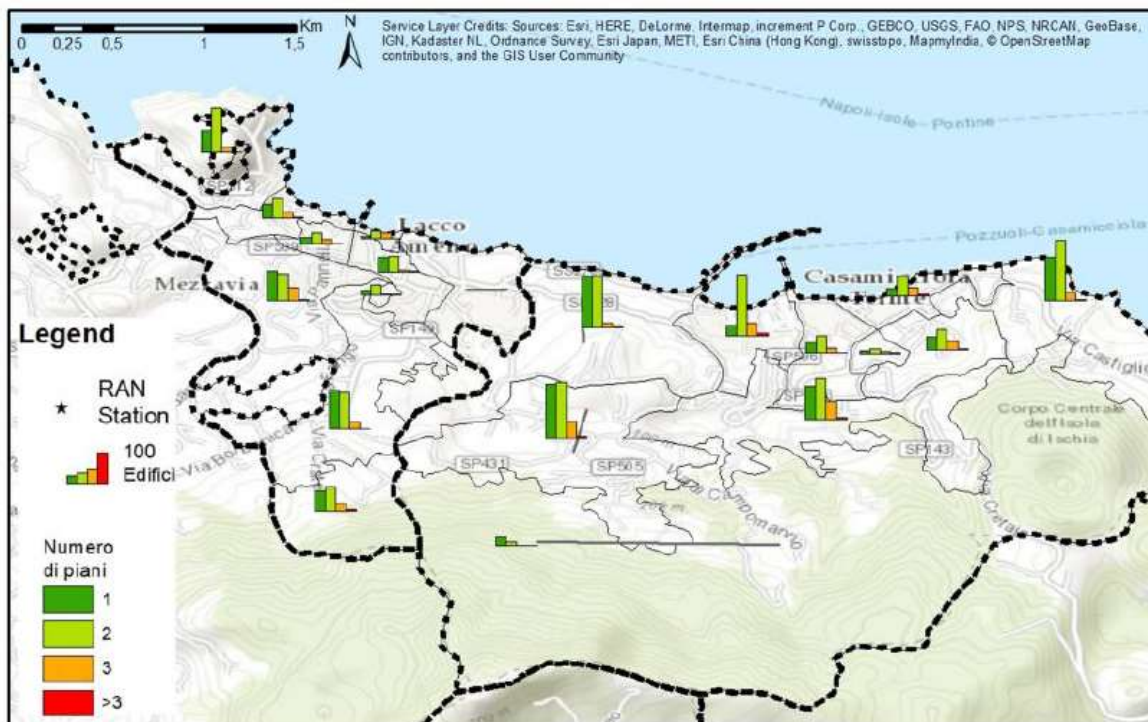


Figure A4.13.41. Distribution of number of storeys of buildings (green: 1 storey, red: more than 3 storeys) per cadastral sector of the most affected communities of Casamicciola and Lacco Ameno. From Verderame *et al.* (2017).

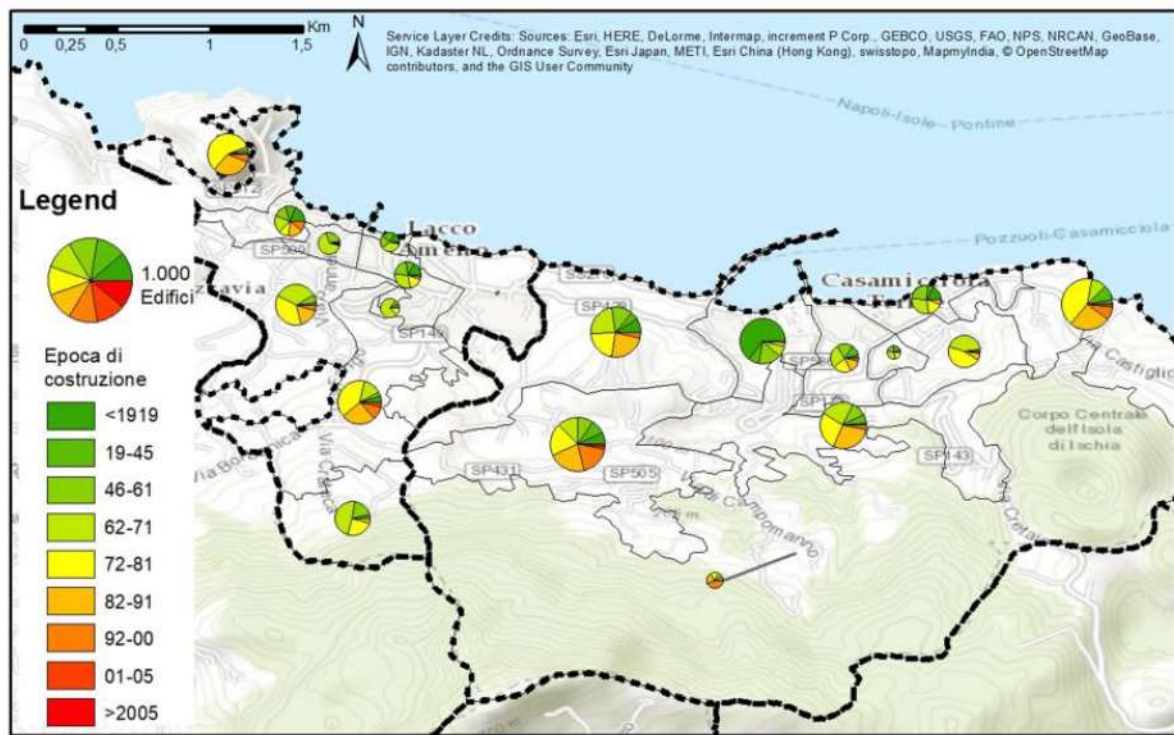


Figure A4.13.42. Distribution of construction period of buildings (green: before 1919, red: after 2005, colours in between show only the last two digits of the years) per cadastral sector of the most affected communities of Casamicciola and Lacco Ameno. From Verderame *et al.* (2017).

The resulting number of buildings classified per vulnerability class for the most affected localities and their proportions are listed in Table A4.13.14 and Table A4.13.15. Considering the entire building stock of both communities as a whole, it is concluded that 15.9% of it belongs to class A, 29.3% in class B, 49.8% in class C and 5.0% in class D. The distribution of the buildings per vulnerability class is mapped in Figure A4.13.43. A majority of masonry buildings of vulnerability class C is observed, in agreement with the conclusions from the technical team of the PLINIUS Centre of Studies mission (Zuccaro *et al.*, 2017), who reported as well a “notable presence” of buildings class B. The QUEST (Quick Earthquake Survey) team of the INGV (Azzaro *et al.*, 2017) also identified a majority of masonry buildings, mainly in tuff bricks with no strengthening elements, and classified them as class B. The latter authors also comment on a small presence of masonry buildings of class A and RC) buildings of class C. The prevalence of unreinforced masonry buildings in volcanic rock has been also recognized by the mission of the National and Kapodistrian University of Athens (NKUA) (Lekkas *et al.*, 2017), being, however, more conservative in the vulnerability class attribution between A and B.

Table A4.13.13. Probabilities per vulnerability class in correlation to construction period, according to Di Pasquale *et al.* (2005).

Construction period	Probability per Vulnerability class		
	A	B	C
<1919	74%	23%	3%
1919-1945	52%	40%	8%
1946-1960	25%	47%	28%
1961-1971	4%	31%	65%
1972-1991	2%	19%	79%

Table A4.13.14. Number of buildings per vulnerability class in the most affected localities, according to Verderame *et al.* (2017).

Community	A	B	C	D	Total
Casamicciola	420	671	970	157	2218
Lacco Ameno	145	369	799	21	1334
Total	565	1040	1769	178	3552

Table A4.13.15. Percentage of buildings per vulnerability class in each of the two most affected localities and for their summation, from the data in Table A4.13.14

Community	A	B	C	D	Total
Casamicciola	18.9%	30.3%	43.7%	7.1%	100%
Lacco Ameno	10.9%	27.7%	59.9%	1.6%	100%
Total	15.9%	29.3%	49.8%	5.0%	100%

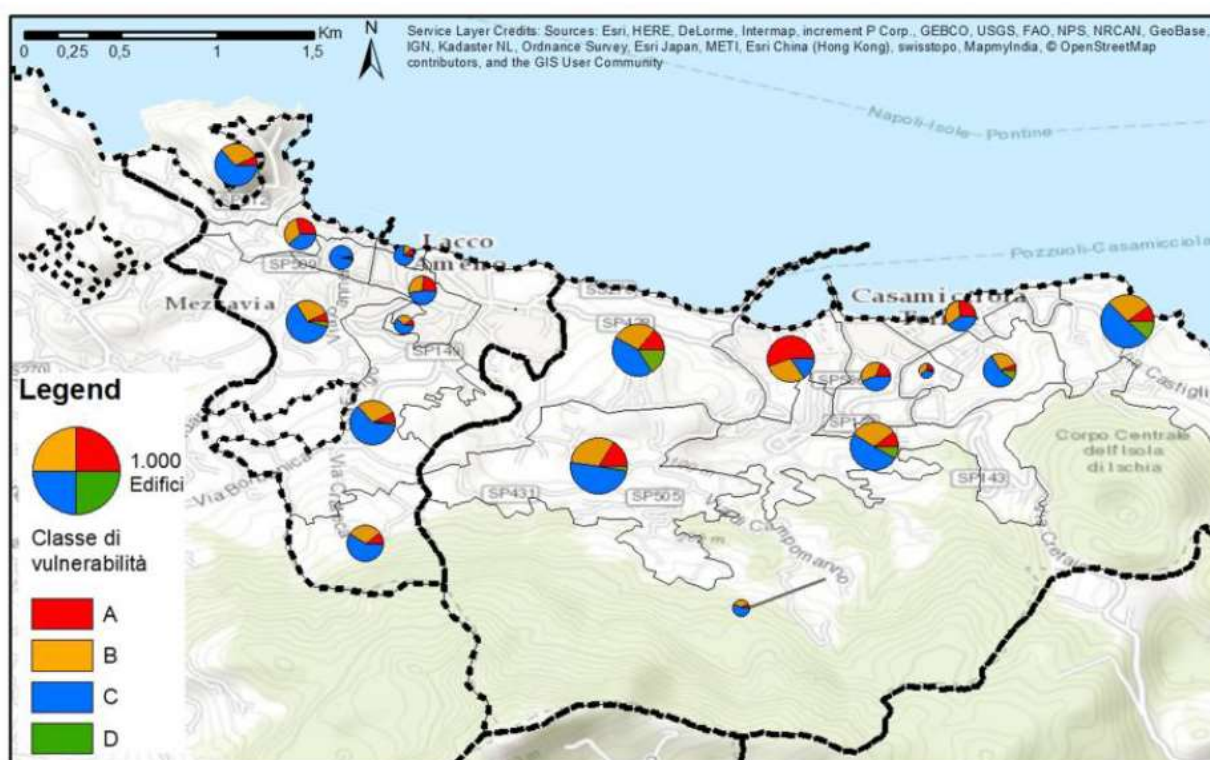


Figure A4.13.43. Distribution of seismic vulnerability of buildings per cadastral sector of the most affected communities of Casamicciola and Lacco Ameno. Vulnerability classes indicated by the colour scale on the left. From Verderame *et al.* (2017).

Overall, the main structural typologies encountered may be categorized as follows:

- a) Low-rise unreinforced masonry buildings using local volcanic material (tuff bricks) with lack of seismic design and detailing (Lekkas *et al.*, 2017). The older buildings are usually built between the end of the 19th century and the beginning of the 20th, and may have undergone structural modifications (e.g., addition of staircase, replacement of floor with rigid slabs, etc.) (Zuccaro *et al.*, 2017). According to Di Manna *et al.* (2017), these are made of heterogeneous rubble stones, often bound together with earth mortar of low quality and in low quantity. Heterogeneity is also encountered in the more recent structures, according to Di Manna *et al.* (2017), in which stones of different nature and dimensions are used, occasionally in combination with hollow bricks. Inadequate connections between intersecting walls, as well as floor– or roof–wall anchorage was also observed.
- b) Low-rise buildings erected between the 1960s and 1980s in unreinforced masonry or with a mixed system of bearing masonry with RC elements, and horizontal diaphragm of hollow bricks (Zuccaro *et al.*, 2017).
- c) 2- to 4-storey RC frame buildings with brick infill walls (Lekkas *et al.*, 2017).
- d) Buildings with dual structural systems (Lekkas *et al.*, 2017): the primary bearing material is masonry at the perimeter walls while a secondary timber frame is developed internally in height (Figure A4.13.51). Di Manna *et al.* (2017) comment, however, that a unique case of this locally so-called “telaio beneventano” was encountered. They assume that this was potentially born after incorporation of an existing timber structure to a newer masonry one, rather than a conceived seismically resistant system.

An interesting observation of QUEST (Azzaro *et al.*, 2017), during their on-site investigation, is mentioned, with respect to the complexity of the building stock and the structural modifications that this has undergone during the years. This is also supported by Di Manna *et al.* (2017) who make reference to enlargements and additions in height that buildings have undergone with use of different material and bearing systems. It is characteristic that these additions are often put in place without properly accounting for the adjacent existing structure in terms of connections, seismic joints or compatibility of deformations.

Extensive discussion has taken place in the newspapers, the political and the scientific circles with respect to the “illegal” nature of these modifications (e.g., floor elevation) or even of new constructions that lack of permissions and control of regulations. It is characteristic what Euronews (2017) report on the illegal building in Ischia, quoting the words of the environmental group Legambiente who underlines that “Ischia has always been a symbol of illegal construction, random overconstruction and impunity” and that Campania region as a whole “is the worst in Italy for breaking the rules around coastal construction”. It is reported that around 600 buildings should be demolished as illegal in Ischia and, instead, between 2001 and 2011 only 4% of the ones that had been identified were removed. In addition, the use of material and techniques of questionable quality is strongly speculated in many of the

recent constructions, together with their erection in non-appropriate location, with no respect to existing regulations (Athensvoice, 2017; La Repubblica-Cronaca, 2017). The latter is further supported by M. Stucchi and other scientists (Terremoti e grandi rischi, 2017) who highlight that even the “legal” buildings of the area, often non-conforming to the seismic regulations, are to be considered as dangerous as much as the “illegal” ones.

A4.13.7.3 Prior damage and retrofit

Not many details on prior damage or retrofit of the built environment are available. Only Di Manna *et al.* (2017) mention that during the damage surveys it has been possible to identify masonry buildings with strengthening interventions in the past, such as the addition of steel rods under the roof (Figure A4.13.44, left). They have recognized, as well, buildings that have undergone interventions for enlargement during which attempts for structural upgrade with RC elements have been endeavoured, such as the example on Figure A4.13.44 (right).



Figure A4.13.44. Masonry building with addition of steel rods under the roof (left), and enlargement of building with attempts of structural strengthening by means of RC elements (right). From Di Manna *et al.* (2017).

A4.13.8 Damage observations

A4.13.8.1 Damage states

As discussed in Section A4.13.4.1, EMS-98 intensities of IV to VIII have been observed on the island, based on the site surveys and testimonies of the locals (Azzaro *et al.*, 2017). As explained in Appendix II (Table A2.1.1), the EMS-98 scale defines an intensity value according to the degrees of damage that buildings of different vulnerability classes experience. According to this scheme, the EMS-98 intensity of VIII observed in Ischia implies that:

- many buildings of vulnerability class A (the most vulnerable) suffered damage of grade 4 and a few suffered damage of grade 5;
- many buildings of vulnerability class B suffered damage of grade 3 and a few suffered damage of grade 4;

- many buildings of vulnerability class C suffered damage of grade 2 and a few suffered damage of grade 3;
- a few buildings of vulnerability class D sustained damage of grade 2.

All available reports with macroseismic site surveys (Zuccaro *et al.*, 2017; INGV G.D.L., 2017 and Azzaro *et al.*, 2017) provide statistics without specifying the damage scale used, though it can be assumed to be equivalent to EMS-98. Damage statistics with respect to the usability characterization of the buildings after the post-earthquake investigation with the Italian AeDES/GI-AeDES methodology (Italian Civil Protection Department, DPC, 2000) are also reported (DPC, 2017). According to this, a first-level judgement is made with respect to the buildings' usability, as described in Table A4.13.16.

Table A4.13.16. Usability classes and description as per the Italian AeDES form (DPC, 2000) (translation as per Masi *et al.*, 2016).

Usability class	Usability outcome	Damage description
A	Usable building	All parts of the building can be used without any threat to the inhabitants, without any short-term countermeasures.
B	Temporarily unusable building (totally or partially), but usable with short-term countermeasures	The building, in its current state, is at least partially unusable, but it may be sufficient to implement short-term countermeasures in order to reduce the risk to the inhabitants to an acceptable level.
C	Partially unusable building	The damage in some parts of the building could present an elevated risk to the occupants.
D	Temporarily unusable building requiring a more detailed investigation	Temporarily unusable building requiring a more detailed investigation. The building shows characteristics such that it is not possible to judge the building usability. A further, more detailed inspection is required.
E	Unusable building	The unusability of the building is due to structural, non-structural or geotechnical risk.
F	Unusable building because of external risk	The unusability is due to severe external risk, without any significant damage to the building itself.

A4.13.8.2 Damage statistics and description

Being this a recent event, no detailed scientific databases are yet available with a confirmed number of damaged buildings.

By 15th September 2017, a total number of 1,746 buildings in the three affected communities of Casamicciola, Lacco Ameno and Forio had been surveyed by the post-seismic damage assessment campaign, under the coordination of the Civil Protection Department, for characterization of their usability (DPC, 2017). Among these, 513 buildings were classified as usable (class A, see Section A4.13.8.1), 92 as unusable due to external risk (A-F), 688 as unusable with or without external risk (B-BF-C-CF-D-DF), 349 as temporarily and/or partially unusable with or without external risk (E-EF) and 104 with no outcome, as depicted in Figure A4.13.45. Their disaggregation with respect to their occupancy type and use is illustrated in Figure A4.13.46. It is noted that the site inspections of public buildings, schools and other structures that could accommodate population preceded the verifications of the residential buildings. In total, 1,071 private buildings and 58 public buildings, including

schools, were classified as temporarily or permanently unusable. The DPC (2017) reports that the characterisation of another 200 buildings was still pending by 15th September, while the total number of requests for inspection had been 2,341 up to that date. The DPC highlights that this does not necessarily correspond to 2,341 individual buildings, as more than one request per building may have been received. Taking into consideration all this together with the total of 3,552 buildings reported in Table A4.13.14, it is not clear what the situation of the remaining ~1,800 buildings not covered by Figure A4.13.45 is.

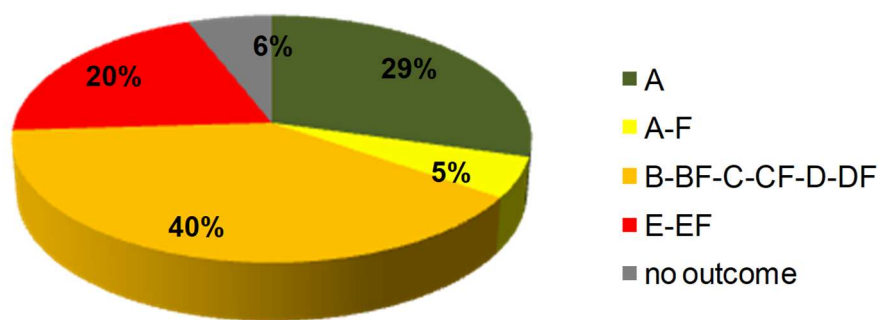


Figure A4.13.45. Distribution of 1,746 buildings surveyed until 15th September 2017 with respect to their usability. Data from DPC (2017).

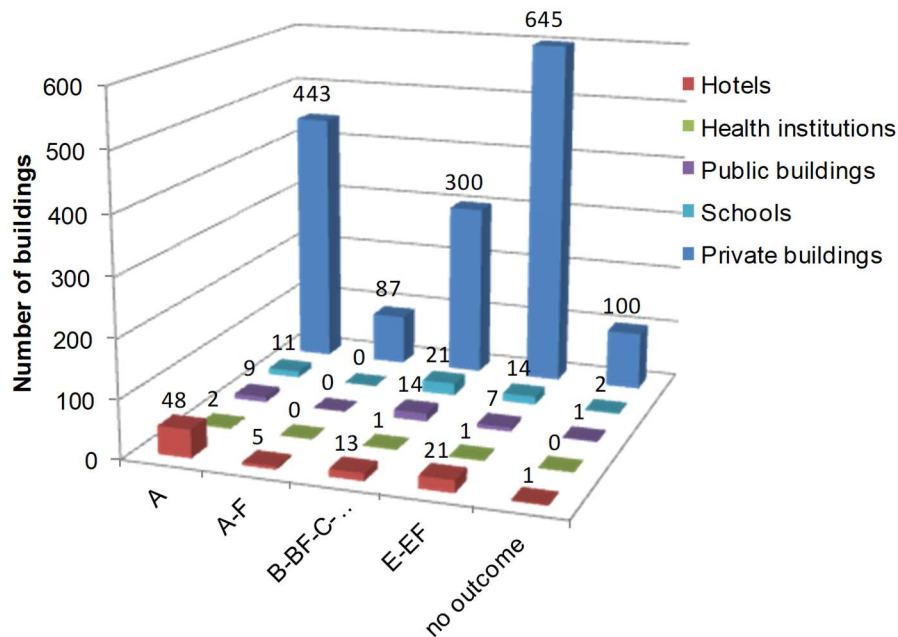


Figure A4.13.46. Disaggregation of 1,746 buildings surveyed until 15th September 2017 per occupancy and usability. Data from DPC (2017).

From the fast survey of 21 structures belonging to the Ministry of Cultural Heritage carried out during the first week after the earthquake, 3 buildings were found to be severely damaged, 7 with medium-severe damage and the remaining 11 with slight damage, as DPC (2017) reports. Reference is also made, by the same document, to the damage at the archeological site of the Archeological Museum of Pitaecusa in Villa Arbusto (Lacco Ameno). The results from more surveys carried out the successive days, as well as the findings of the more detailed Level II assessment of the churches of the island, have not been yet published at the time of writing (December 2017).

Zuccaro *et al.* (2017) carried out surveys in the epicentral and most affected area between the localities of Fango and Piazza Maio (see Figure A4.13.22 for location). They analysed externally some of the buildings lying within their survey zone and assigned damage levels equivalent to the EMS-98 damage scale to them. Their first results are given in Figure A4.13.47. Considering that no specific numbers are provided, others than the graph of Figure A4.13.47, some qualitative results may be deduced. Among the analysed buildings (around 65), prevalence of moderate (D2) and substantial to heavy (D3) damage is observed, with 70% of the buildings falling into either of these two categories, while around 20% of them are classified as having very heavy damage (D4) or being destroyed (D5).

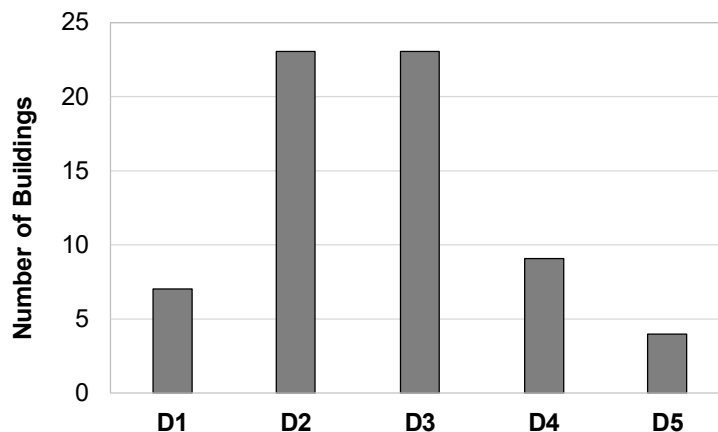


Figure A4.13.47. Damage states of buildings analysed by Zuccaro *et al.* (2017).

Damage to buildings can be described separately per structural typology present in the affected area. Most of the damage is concentrated in buildings of unreinforced masonry bearing walls, which correspond to the most vulnerable elements of the local building inventory (Section A4.13.7.2). Lekkas *et al.* (2017) mention that masonry buildings suffered “slight non-structural to very heavy” damage. Azzaro *et al.* (2017) report three total collapses (Figure A4.13.48, left) and several partial collapses (Figure A4.13.48, right) of this kind of structure throughout the meizoseismal area. They classify as EMS-98 damage state 3 or “substantial to heavy” damage the following damage configurations observed in considerable number: diagonal cracks (Figure A4.13.49), loss of verticality of walls, out-of plane wall failures (Figure A4.13.50, left), expulsion and delamination of wall wythes (Figure A4.13.50, centre, right), and corner failures due to the disintegration of walls. The façade wall and the bell tower of a church in the locality of Rita of Casamicciola were severely damaged. In addition, less important effects have been noted as well, such as hairline cracks to the plaster or detachment of plaster, and falls of non-structural elements such as cornices or chimneys.

Zuccaro *et al.* (2017) comment that the out-of-plane failure of the walls was not a common type of failure during the earthquake of Ischia and, instead, diagonal shear cracking (Figure A4.13.49) appeared more often. The authors interpret this observation as a hint of “good box-like behaviour, high masonry quality and good interlock of cantonal walls”. Moreover, they attribute the detachment of the wall corners to the good restraint of the walls. These explanations are rather contradictory to the descriptions of Di Manna *et al.* (2017), included in Section A4.13.7.2, who discuss the low-quality masonry and poor interlocking of walls.



Figure A4.13.48. Total (left) and partial (right) collapse in the red zone of Casamicciola. From Azzaro *et al.* (2017).



Figure A4.13.49. Diagonal shear cracks in masonry buildings. From D'Ambra *et al.* (2017; left) and Zuccaro *et al.* (2017; right).



Figure A4.13.50. Out-of plane wall failure in Fango at Lacco Ameno (left); masonry expulsion and diagonal cracks in Casamicciola red zone (centre); delamination of wythes and corner failure (right). From Azzaro *et al.* (2017; left and centre) and Di Manna *et al.* (2017; right).

Both teams of Lekkas *et al.* (2017) and Zuccaro *et al.* (2017) have dedicated comments to the building with the dual system of Figure A4.13.51, highlighting that, despite the partial collapse of the masonry walls, the timber frame sustained the roof and prevented a more extensive collapse of the structure as a whole.



Figure A4.13.51. Damage to the masonry walls of the dual system building (Lekkas *et al.*, 2017).

Lekkas *et al.* (2017) briefly report that only non-structural damage has been observed in RC buildings, while Azzaro *et al.* (2017) specify that limited cases of damage states 1 or 2 are observed in these typologies. D'Ambra *et al.* (2017) have noticed cracks, detachment (Figure A4.13.52, left) and collapse (Figure A4.13.52, right) of the infill panel of some RC buildings.



Figure A4.13.52. Detachment (left) and collapse (right) of infill panels of RC buildings. From D'Ambra *et al.* (2017).

Subsidence of the foundations was observed by Di Manna *et al.* (2017) in some new and recently repaired buildings in Fango (Figure A4.13.53).

Horizontal cracks, running parallel to the intermediate floors or the roof, have also been observed in both masonry and RC buildings (Figure A4.13.54) and have been interpreted by Zuccaro *et al.* (2017) as a result from the combined effect of storey drifts and the large vertical component of the ground motion. In fact, several evidences of the high vertical component have been registered in the built environment, as illustrated by Figure A4.13.55

(Lekkas *et al.*, 2017), as well as to non-structural elements (Zuccaro *et al.*, 2017). Damage to the latter consisted mainly on the overturning of parapet walls located along the side of the street (Figure A4.13.56, left), detachment and overturning of a staircase, as well as horizontal cracks at columns (Figure A4.13.56, right).



Figure A4.13.53. Subsidence of foundation of a residence in Fango (Di Manna *et al.*, 2017).



Figure A4.13.54. Horizontal crack at floor level due to story drift (Zuccaro *et al.*, 2017)



Figure A4.13.55. Damage in different buildings evidencing the impact of the high vertical seismic component (Lekkas *et al.*, 2017).



Figure A4.13.56. Collapse of parapet side walls (left) (Di Manna *et al.*, 2017); rotation of tuff stone column (centre) (INGV G.D.L., 2017); collapse of house retaining wall (right) (INGV G.D.L., 2017).

Another type of damage is reported by Zuccaro *et al.* (2017) and concerns cracks in adjacent buildings due to hammering due to staggered floors and lack of seismic joints, such as shown in Figure A4.13.57.



Figure A4.13.57. Damage to adjacent buildings due to hammering (Zuccaro *et al.*, 2017)

While most of the damage reports elaborated by different teams after the earthquake focused mainly on buildings, there are also relevant mentions of collapses of retaining stone walls, ruptures, damage to non-structural elements, rockfalls and landslides. The collapse of several dry-stone walls (“parracine” in Italian) is of particular importance for the island of Ischia, which counts more than 5 km of walls, dating more than 100 years (Ischia land, 2015). They are built using a traditional technique, with local lava or tuff stones with dimensions between 10-20cm and 30-50cm, with no use of mortar or other binder, and are characteristic of the Mediterranean architecture. Their role is important in demarcating the rural territory, serving as separation for properties, soil retaining and prevention of surface runoff. Several walls of this kind partially collapsed in sections of 1-2 m up to 3-4 m, got inclined or the stones lost their interlocking, as shown in Figure A4.13.58 (Di Manna *et al.*,

2017). This severely jeopardizes the stability of the structures themselves, in case of strong precipitations, as well as of the retained soils.

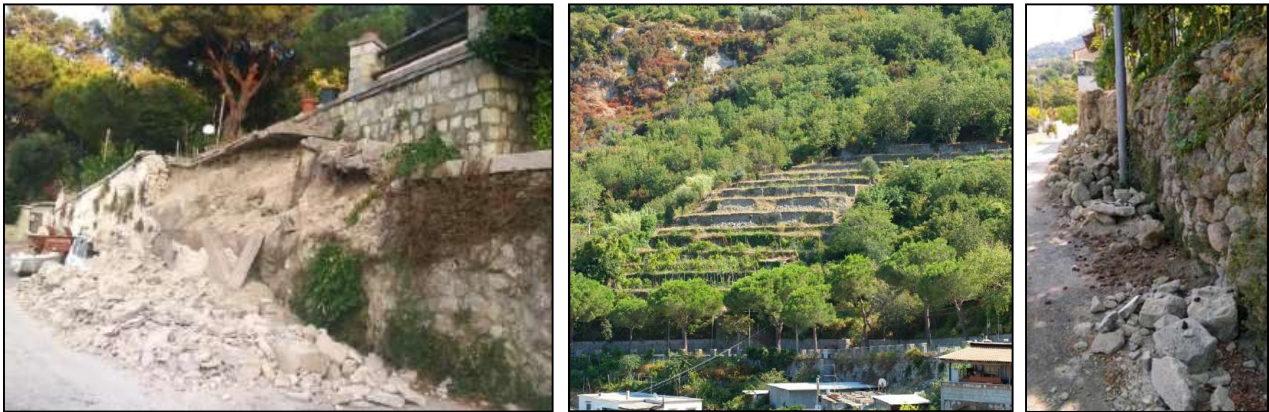


Figure A4.13.58. Collapse of house retaining wall (left), and partial collapse of dry stone walls at the hilly area between localities of Fango and Maio (centre) and in Casamicciola (right). From INGV G.D.L. (2017; left and right) and Di Manna *et al.* (2017; centre).

As discussed in Section A4.13.5.1, a few surface cracks appeared on the surface of paved roads and the cultivated land, at times continuous inside the houses (Di Manna *et al.*, 2017). In the latter, the crack seems to have developed along the joint of adjacent buildings or within parts of the same building erected in different periods of time. Di Manna *et al.* (2017) interpret this type of damage as a hint of differential ground settlement. A water pipe was damaged at the location of a road crack.

The detaching of rocks described in Section A4.13.5.2 caused limited damage. Some of their consequences were the bending and breaking of chestnut trees located downhill, the obstruction of a box-shaped concrete culvert and damage to water pipes (Di Manna *et al.*, 2017; INGV G.D.L., 2017).

A4.13.8.3 Observed weaknesses

As discussed in Sections A4.13.7.2 and A4.13.8.2, the building stock of Ischia is characterised by the presence of many illegal constructions, the common use of poor-quality materials and inappropriate construction detailing and design for a seismically active area. For example, Di Manna *et al.* (2017) list photographic examples of buildings with poor wall-to-wall and wall-to-floor connections. Although it has not been possible to attribute the reason of collapse or extensive damage to the illegal nature of each of these buildings, a strong influence of the latter over the former is being openly discussed (*e.g.*, Euronews, 2017; La Repubblica-Cronaca, 2017).

A4.13.8.4 Damage distribution

In total, from the information provided by DPC (2017) by 15th September 2017, the number of buildings declared permanently or temporarily, partially or fully unusable is listed in Table A4.13.17 per surveyed community. The corresponding population that needed immediate assistance in the hotels has been also included. The usability outcome per community is

depicted in Figure A4.13.59. It is noted, again, that 150 surveys in Casamicciola and 50 in Lacco Ameno were still pending.

Table A4.13.17. Immediately unusable surveyed buildings per affected community (see Figure A4.13.34) and corresponding displaced population. From DPC (2017).

Communities	Immediately unusable	Displaced population
Casamicciola	804	739
Lacco Ameno	35	307
Forio	290	15

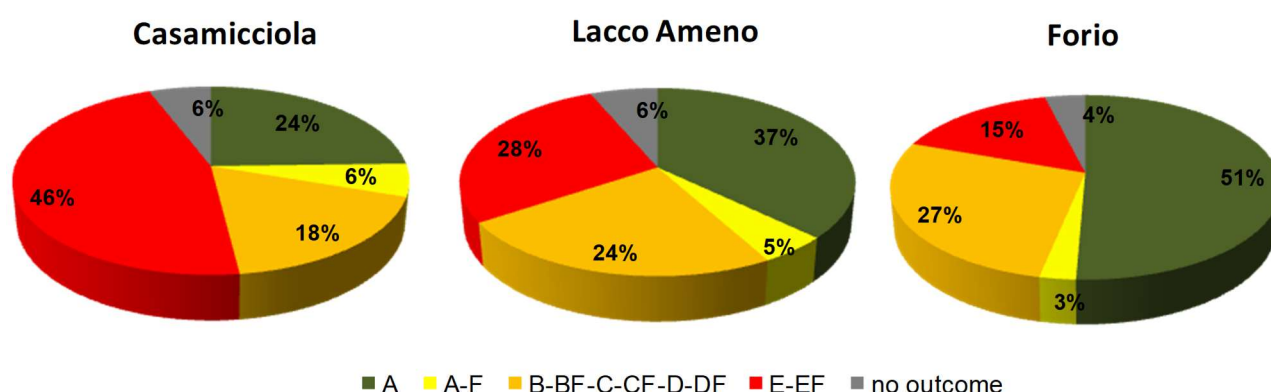


Figure A4.13.59. Distribution of buildings per post-earthquake usability (see Section A4.13.8.1). The 100% corresponds to the total surveyed buildings (1156 in Casamicciola, 488 in Lacco Ameno and 75 in Forio). Data from DPC (2017).

From the post-seismic usability surveys discussed above, as well as the macroseismic investigations and attribution of intensities (see Section A4.13.4.1), the most affected communities were Casamicciola and Lacco Ameno. Some damage has been also registered in Forio (see Figure A4.13.34 for location) to the west of the island. The damage has been mainly concentrated in an area delineated by the localities of Fango (in Lacco Ameno), Rita, Piazza Maio and Piazza Bagni (in Casamicciola) (see Figure A4.13.22 for location), within which a so-called “red zone” was delineated north of the epicentre (Figure A4.13.21).

The damage classified by Azzaro *et al.* (2017) as EMS-98 grade 3, as described in Section A4.13.8.2, is mainly concentrated in the red zone. Moreover, several buildings were affected in the locality of Fango, where two total collapses of highly vulnerable buildings have occurred as well (Azzaro *et al.*, 2017). Slight to moderate damage was reported in Piazza Bagni (Zuccaro *et al.*, 2017), probably due to better quality of the built environment. Less pronounced is the damage in the coastal area of Casamicciola (e.g., Marina di Casamicciola, Perrone). It is clearly observed that the extent and severity of damage decreases when moving far from the epicentral area towards the city centre of Lacco Ameno (Zuccaro *et al.*, 2017). Light damage has been reported in the communities of Serrara Fontana and Forio, to the west and south-east of the red zone, respectively, while no damage was observed in the community of Ischia (see Figure A4.13.34 for location). The map of Figure A4.13.60 depicts the EMS-98 damage states of some of the affected buildings that were externally inspected by Zuccaro *et al.* (2017) in the red zone between

the localities Fango, La Rita and Piazza Maio. Unfortunately, information regarding soil types and seismological aspects of the earthquake are not available at the same scale to be able to make a comparison or cause/effect inferences.

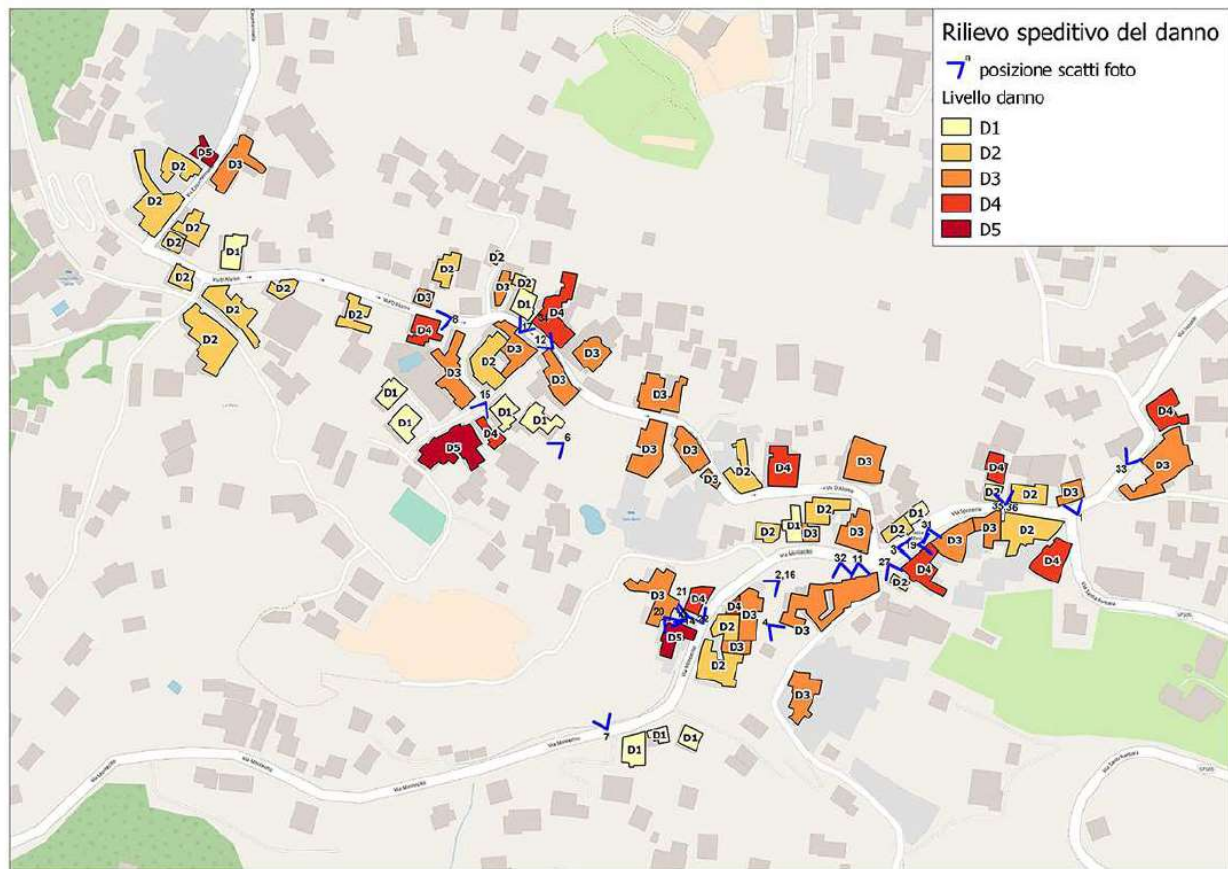


Figure A4.13.60. Classification of buildings per estimated damage state (D1, yellow, slight damage, through D5, red, destruction). From Zuccaro *et al.* (2017).

Di Manna *et al.* (2017) elaborated a more comprehensive map for the red zone in Casamicciola, showing occurrences of damage not only to buildings but also to geotechnical structures, land masses and water pipes, as shown in Figure A4.13.61. In this map, surface ruptures on the paved roads, cultivated land or buildings are marked in yellow circles, the location of landslides and rockfalls is indicated in green, mainly in the hilly area to the south of Fango, and several collapses of dry stone walls are indicated in blue. The water main damage (in orange) is located in an area of several ground ruptures. Finally, some of the damaged buildings surveyed are marked with triangles, distinguishing between cases of collapses (red) and damage to non-structural elements (purple).

As previously mentioned, several authors (*e.g.*, Cultrera *et al.*, 2017; INGV G.D.L., 2017) indicate that site effects are likely to have played a significant role in the large amplitudes of ground motion observed in the near field for an earthquake of this magnitude. The geological (Figure A4.13.14) and V_{s30} (Figure A4.13.16) maps of Ischia, reproduced below as Figure A4.13.62 for clarity, can readily support the suspicions of the authors. The correspondence between the areas that were most severely damaged and the loose unconsolidated younger volcanic deposits with very low values of V_{s30} shown in Figure A4.13.62 in green suggests

that these are likely to have been responsible for the large acceleration demands recorded. Similarly, the presence of older volcanic rocks to the east (in red in Figure A4.13.62, left) with higher V_{s30} (yellow/orange/red in Figure A4.13.62, right) can explain the lack of site amplification in this direction.

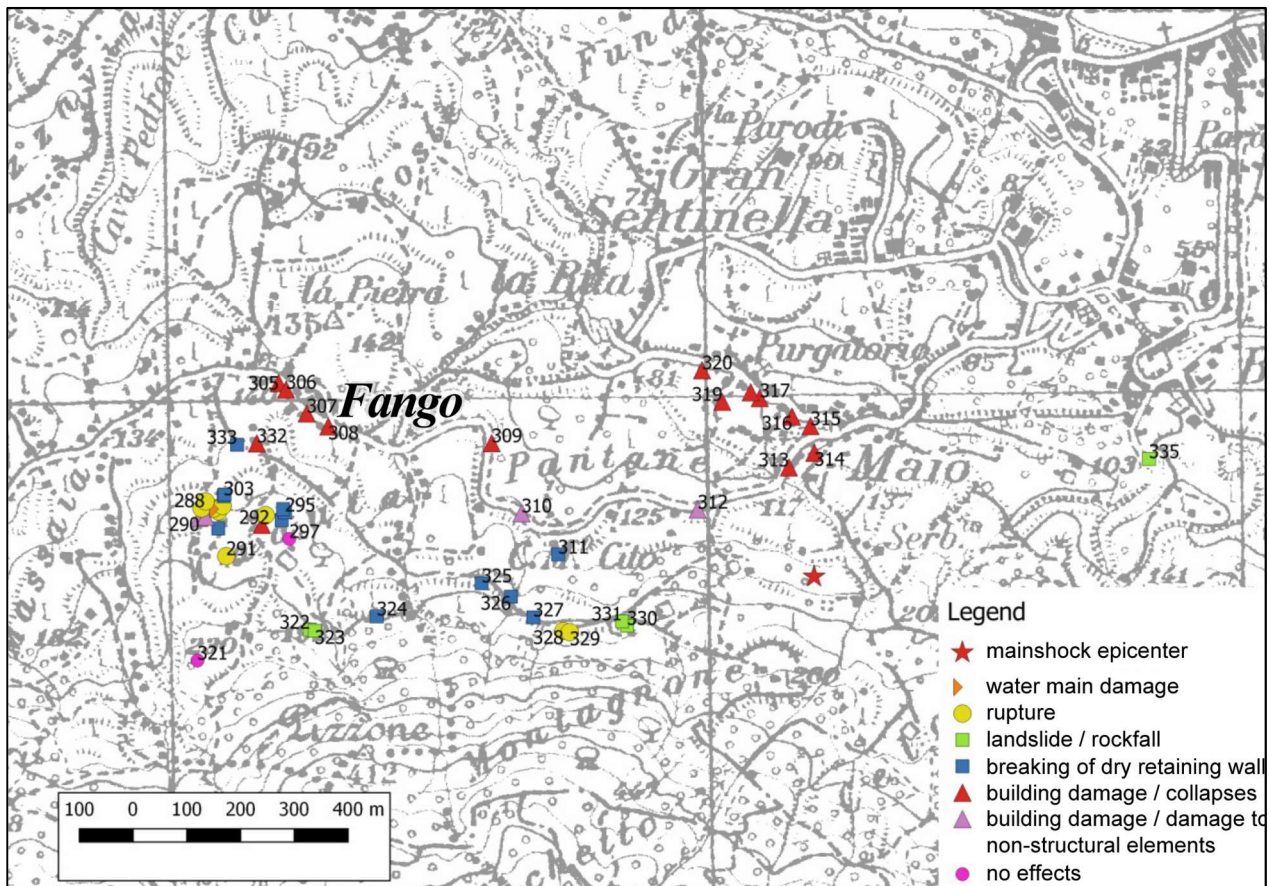


Figure A4.13.61. Distribution of observed effects in the man-made and natural environment of the “red zone” (localities of Fanco and Piazza Maio). Translated from Di Manna *et al.* (2017).

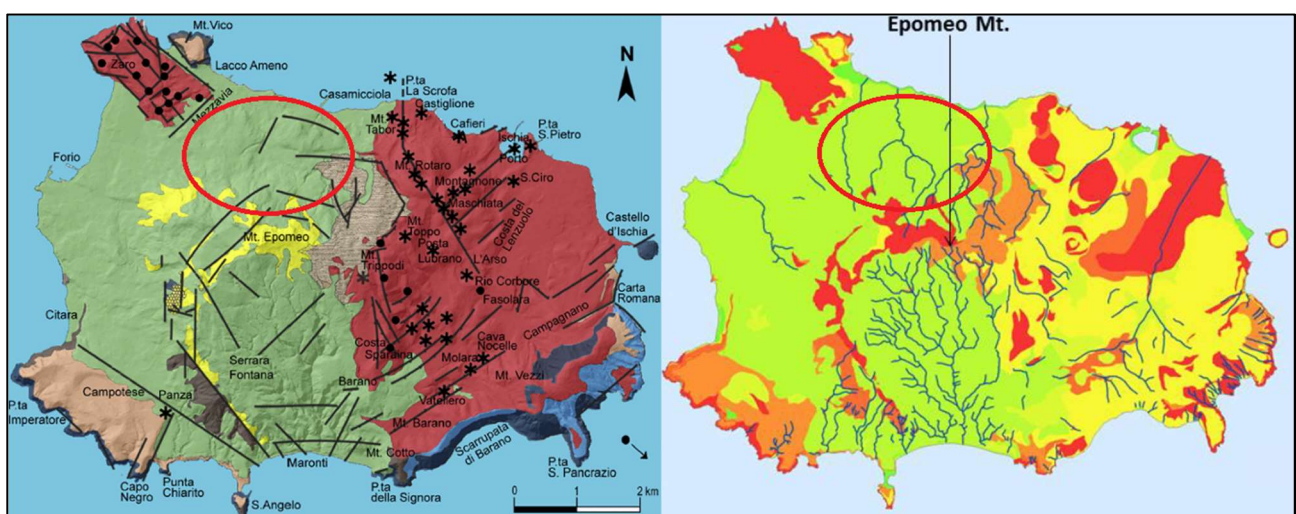


Figure A4.13.62. Relation between most damaged areas and the geological (left) and site (right) conditions of the island of Ischia. Most damaged areas approximately enclosed by red ellipse. Modified from De Vita *et al.* (2013, left) and Caccavale *et al.* (2017, right).

A4.13.9 Casualties and losses

A4.13.9.1 Numbers of dead and injured

In total, 42 injuries, among which one was severe and 16 required hospitalization, and 2 dead persons have been identified (La Repubblica-Napoli, 2017a; DPC, 2017; NOAA, 2017). One of the dead persons was a tourist on the island. The DPC (2017) reports that 5 members of the same family were safely pulled out of the rubble, while La Repubblica-Napoli (2017a) and Earthquake-report (2017) mention that 7 to 10 people were declared missing under the rubble at the time of the earthquake. According to the EM-DAT database (2017), a total of 2,639 people were somehow affected by this earthquake.

A4.13.9.2 Causes of casualties

One of the women died after having been hit by the falling cornice of a church while entering the church (La Repubblica-Napoli, 2017c). The second woman, visiting the island, died after being trapped under the rubble when the house that accommodated her collapsed (La Repubblica-Napoli, 2017c).

No further details are provided upon the causes of injuries but it may be inferred that they are the victims of collapse of houses and fall of debris. The DPC (2017) mentions that the deaths and the severe injuries were due to building collapses.

A4.13.9.3 Estimates of economic losses

At the time of writing (December 2017), no overall estimates of economic loss have been found.

What has been mostly reported, in terms of figures, is the number of displaced population that has finally established at around 1,600 people (La Repubblica-Napoli, 2017b), initially reported them to exceed 2,500 (The Guardian, 2017). More precisely, the activity report of DPC (2017) describes that 1,544 people were assisted during the emergency phase of the earthquake and in total 1,061 people had to be displaced at long term due to inaccessibility of their dwellings. By 15th September 2017 (time of writing of DPC (2017) report), 1,129 buildings had been classified as temporarily or permanently unusable. These figures are given herein so as to provide a picture of the impact, directly related to the economic loss.

A few days after the earthquake, Il sole 24 ore (2017a) reported that 7 million euro from the national Italian budget had been allocated to aid families affected by the emergency in Ischia. A subsidy up to 900 € per month has been agreed to be provided to every family (according to their number of members), whose dwelling has been partially or fully collapsed, in order to host themselves at their own initiative. The expected duration of this financial assistance is not clear in the sources. Special conditions are anticipated for elder or handicap people.

Regarding the immediate impact of the earthquake on the local economy, it is highlighted that the island was hit at the peak of the touristic summer season. Around 1500 visitors fled the island the next day, while a few days later large discounts in touristic offers were observed, with the purpose of attracting new visitors (Il mattino, 2017a). Yet, a small drop or cancellation in the hotel bookings was registered overall, according to the same source. On the other hand, Il mattino (2017b) mentioned some days later that the cancellations after the earthquake were a great shock for the local economy and that massive dismissals of the employees in the touristic sector were expected. The same source highlights the uncertainty of 20,000 employees and more than 2,000 small to medium enterprises that were facing the risk of shutting down. Meanwhile, it estimated a loss of 40 million euros for Ischia and, in total, financial damage of 120 million euros for the economy of the entire region.

To the authors' knowledge, while private buildings insurance against earthquake damage is not compulsory in Italy, it is anyway available from different private insurers. During the past years, there has been a continuous debate on the topic of compulsory disaster insurance. Only 2.2% of Italian residences are currently insured for seismic risk, what corresponds to 176,000 house owners (Il sole 24 ore, 2017b). With respect to the companies with industrial buildings, an increase of 18% has been registered compared to 2016, what is translated into 600 billion euros potential insured loss (Il sole 24 ore, 2017b). As an incentive to decrease the vulnerability of the building stock, fiscal relief has been agreed for the owners that opt for the seismic upgrade of their buildings (Il sole 24 ore, 2017b).

A4.13.10 Discussion and conclusions

The damaging 21st August 2017 **M**3.9 Ischia Island earthquake, which largely affected the settlement of Casamicciola, was not surprising given the geodynamics of this active volcanic area. The region has produced shallow events of similar magnitudes in the past and, in particular, the catastrophic 1883 **M**4.3 earthquake, whose seismogenic source was likely the same as that of the 2017 event.

The source characteristics of the 2017 mainshock were difficult to obtain and required the combination of seismological recordings, InSAR imagery and the application of several modern sophisticated techniques. The preferred solution of the National Institute of Geophysics and Volcanology of Italy (INGV) placed the earthquake onshore Ischia at a very shallow depth of around 2km, south of Casamicciola, at the northern hills of Mt. Epomeo, 30km WSW of Naples. Ground motions have been considered as abruptly attenuated, attributed to the shallow focal depth of the event, its low magnitude and the anelastic properties of the volcanic environment. No foreshock activity was reported, whilst very few aftershocks of low magnitude were recorded in the vicinity of the main shock.

The main shock reached a maximum EMS-98 intensity of VIII in the epicentral area, which comprised a few hundred meters between Casamicciola and Lacco Ameno, and it abruptly dropped elsewhere onshore Ischia down to IV. Maximum horizontal and vertical PGA values of 0.28 and 0.27 g, respectively, were recorded less than 1 km away from the epicentre. Damage has been recorded for 1,129 buildings (as reported on 15th September 2017)

among which several total and partial collapses were observed. Forty-two people were injured, two died from buildings collapses, at least five were safely pulled-out of the rubble and around 1,060 were left permanently or long-term homeless. It is possible that the time at which the earthquake occurred may have played a negative role in the resulting casualties, as large numbers of people were probably congregated inside or around buildings for dinner.

The effects of the earthquake are considered largely adverse with respect to its small-to-moderate magnitude. Reasons for this are likely:

- The proximity of the source to the affected structures and the shallow focal depth, focusing most of the released energy near the epicentral area.
- Amplification of the seismic motion in the 1.5-2.0 Hz band due to site effects.
- Particularly high vertical component at period close to the natural dynamic characteristics of the local building stock (low-rise masonry buildings).
- Vulnerability of structures, especially older masonry ones constructed with no seismic design. The influence of widespread illegal construction and the poor-quality of the materials was extensively discussed.

A4.13.11References

A4.13.11.1 Bibliography

Acocella, V. & R. Funiciello (1999). The interaction between regional and local tectonics during resurgent doming: the case of the island of Ischia, Italy. *Journal of Volcanology and Geothermal Research* **88**, 109–123.

Acocella, V., F. Cifelli & R. Funiciello (2001). The control of overburden thickness on resurgent domes: insights from analogue models. *Journal of Volcanology and Geothermal Research* **111**, 137–153.

Afshari, K. & J. Stewart (2016). Physically parametrized prediction equations for significant duration in active crustal regions. *Earthquake Spectra* **32**(4), 2057-2081.

Aiello, G., E. Marsella & S. Passaro (2012). Stratigraphic and structural setting of the Ischia volcanic complex (Naples Bay, Southern Italy) revealed by submarine seismic reflection data. *Rendiconti Lincei* **23**, 387–408.

Ambraseys, N.N., K.A. Simpson & J.J. Bommer. (1996). Prediction of horizontal response spectra in Europe. *Earthquake Engineering & Structural Dynamics* **25**, 371–400.

Amadio (2014). *Evoluzione della normativa sismica (Evolution of the seismic norm, in Italian)*, Lecture slides, Department of Engineering and Architecture University of Trieste. Available online at: https://moodle2.units.it/pluginfile.php/84293/mod_resource/content/1/lezione%201.pdf. Last accessed: 24th December 2017.

Ambraseys, N.N., K.A. Simpson & J.J. Bommer (1996). Prediction of horizontal response spectra in Europe. *Earthquake Engineering & Structural Dynamics* **25**, 371–400.

- Atkinson, G.M. & D.J. Wald (2007). "Did You Feel It?" intensity data: A surprisingly good measure of earthquake ground motion. *Seismological Research Letters* **78**, 362-368.
- Azzaro, R., S. D'Amico & T. Tuve (2011). Estimating the magnitude of historical earthquakes from macroseismic intensity data: new relationships for the volcanic region of Mount Etna (Italy). *Seismological Research Letters* **82**, 533–544.
- Azzaro, R., S. Del Mese, L. Graziani, A. Maramai, G. Martini, S. Paolini, A. Screpanti, V. Verrubbi, L. Arcoraci & A. Tertulliani (QUEST) (2017). *Rilievo macrosismico per il terremoto dell'isola di Ischia del 21 agosto 2017 (Macroseismic survey for the earthquake on the island of Ischia on the 21st August 2017, in Italian)*. Final report. Istituto Nazionale di Geofisica e Vulcanologia, doi:10.5281/zenodo.886047. Available online at (last accessed 12th February 2018): <http://www.questingv.it/images/rilievimacrosismici/Casamicciola%20report%20finale.pdf>.
- Bindi, D., F. Pacor, L. Luzi, R. Puglia, M. Massa, G. Ameri and R. Paolucci (2011), Ground motion prediction equations derived from the Italian strong motion database. *Bulletin of Earthquake Engineering* **9**(6), 1899-1920.
- Bommer, J.J., P.J. Stafford & J.E. Alarcón (2009). Empirical equations for the prediction of the significant, bracketed, and uniform duration of earthquake ground motion. *Bulletin of the Seismological Society of America* **99**(6), 3217-3233.
- Brown, R.J., G. Orsi & S. de Vita (2008). New insights into Late Pleistocene explosive volcanic activity and caldera formation on Ischia (southern Italy). *Bulletin of Volcanology* **70**, 583–603.
- Caccavale, M., F. Matano & M. Sacchi (2017). An integrated approach to earthquake-induced landslide hazard zoning based on probabilistic seismic scenario for Phlegrean Islands (Ischia, Procida and Vivara), Italy. *Geomorphology* **295**, 235–259.
- Capaldi, G., L. Civetta & P. Gasparini (1976). Volcanic history of the Island of Ischia (South Italy). *Bulletin Volcanologique* **40**, 11–22.
- Carlino, S. (2012). The process of resurgence for Ischia Island (southern Italy) since 55 ka: the laccolith model and implications for eruption forecasting. *Bulletin of Volcanology* **74**, 947–961.
- Carlino, S., E. Cubellis, G. Luongo & F. Obrizzo (2006). On the mechanics of caldera resurgence of Ischia Island (southern Italy). In Troise, C., G. De Natale & C.R.J. Kilburn (eds.): *Mechanisms of activity and unrest at large calderas*. Geological Society, London, Special Publications **269**, 181–193.
- Carlino, S., E. Cubellis & A. Marturano (2010). The catastrophic 1883 earthquake at the island of Ischia (southern Italy): macroseismic data and the role of geological conditions. *Natural Hazards* **52**, 231–247.
- Carlino, S., R. Somma, A. Troiano, M. G. Di Giuseppe, C. Troise & G. De Natale (2014). The geothermal system of Ischia Island (southern Italy): Critical review and sustainability analysis of geothermal resource for electricity generation. *Renewable Energy* **62**, 177–196.
- CEN (2004). *Eurocode 8: Design of structures for earthquake resistance - Part1: General rules, seismic actions and rules for buildings*. European Committee for Standardization, Brussels, Belgium.
- Chiocci, F. L. & G. de Alteriis (2006). The Ischia debris avalanche: first clear submarine evidence in the Mediterranean of a volcanic island prehistorical collapse. *Terra Nova* **18**, 202–209.
- Civetta, L., G. Gallo & G. Orsi (1991). Sr- and Nd-isotope and trace-element constraints on the chemical evolution of the magmatic system of Ischia (Italy) in the last 55 ka. *Journal of Volcanology and Geothermal Research* **46**, 213–230.

Cubellis E. & G. Luongo (1998). *Il terremoto del 28 luglio 1883 a Casamicciola nell'isola d'Ischia – "Il contesto fisico" (The earthquake of 28th July 1883 at Casamicciola in the island of Ischia – the physical context, in Italian)*. Monografia No1, Servizio Sismico Nazionale, Istituto Poligrafico e Zecca dello Stato, Rome, 49-123

Cubellis, E., S. Carlino, R. Iannuzzi, G. Luongo & F. Obrizzo (2004). Management of historical seismic data using GIS: The Island of Ischia (Southern Italy). *Natural Hazards* **33**, 379–393.

Cultrera, G., D. Famiani, G. Milana, S. Amoroso, B. Angioni, P. Bordoni, L. Cantore, F. Cara, R. Cogliano, M. D'Amico, G. Di Giulio, D. Di Naccio, C. Felicetta, A. Fodarella, S. Lovati, L. Luzi, C. Mascandola, M. Massa, A. Mercuri, F. Pacor, M. Pischiutta, S. Pucillo, R. Puglia, G. Riccio, G. Tarabusi, M. Vassallo (INGV EMERSITO W.G., 2017). *Evento sismico Ischia 2017, Rapporto n.1 (2017 Ischia seismic event, Report n.1, in Italian)*. Available online at (last accessed 16th February 2018): https://ingvterremoti.files.wordpress.com/2017/08/rapporto_1_emersito_ischia2017.pdf.

D'Ambra, C., A. Prota, M. Di Ludovico & G. Manfredi (2017). *Rapporto fotografico relativo ai danni subiti da alcuni edifici a seguito dell'evento sismico del 21 agosto 2017 presso isola d'Ischia- M=4.0 (Photo report of damage suffered by some buildings following the seismic event of 21st August 2017 in the island of Ischia - M = 4.0, in Italian)*, Rete dei Laboratori Universitari di Ingegneria Sismica (Reluis), Naples, Italy.

Della Seta, M., E. Marotta, G. Orsi, S. de Vita, F. Sansivero & P. Fredi (2012). Slope instability induced by volcano-tectonics as an additional source of hazard in active volcanic areas: the case of Ischia island (Italy). *Bulletin of Volcanology* **74**, 79–106.

Department of Civil Protection (DPC, 2000). *Manuale per la compilazione della scheda di 1° livello di rilevamento danno, pronto intervento e agibilità per edifici ordinari nell'emergenza post-sismica (AeDES) (Manual for the compilation of the 1st level of damage detection, intervention and usability for ordinary buildings in post-seismic emergency, in Italian)*, Department of Civil Protection, Roma, Italy, 121 pp. Available online at (last accessed: 12th November 2017): http://www.protezionecivile.gov.it/resources/cms/documents/2_LRManualeAedes_31_ottobre_GU.pdf.

Department of Civil Protection (DPC, 2017). *Rapporto di attività inerenti la gestione emergenziale connessa con gli eventi sismici nel territorio dell'isola di Ischia (Report of activities related to the emergency management of the seismic events in the Ischia region, in Italian)*. Activity report, Mod. 3, Department of Civil Protection, Roma, Italy. Available online at (last accessed: 12th November 2017): <http://www.camera.it/temiap/2017/09/22/OCD177-3050.pdf>.

De Vita, S., F. Sansivero, G. Orsi & E. Marotta (2006). Cyclical slope instability and volcanism related to volcano-tectonism in resurgent calderas: The Ischia island (Italy) case study. *Engineering Geology* **86**, 148–165.

De Vita, S., M. A. Di Vito, C. Gialanella & F. Sansivero (2013). The impact of the Ischia Porto Tephra eruption (Italy) on the Greek colony of Pithekoussai. *Quaternary International* **303**, 142–152.

Devoti, R., G. Pietrantonio, A. R. Pisani, F. Riguzzi, E. Serpelloni, I. Eds, M. Beltrando, A. Peccerillo, M. Mattei & S. Conticelli (2010). Present day kinematics of Italy. *Journal of the Virtual Explorer* **36**, 1–27.

Devoti, R., N. D'Agostino, E. Serpelloni, G. Pietrantonio, F. Riguzzi, A. Avallone, A. Cavaliere, D. Cheloni, G. Cecere, C. D'Ambrosio, L. Falco, G. Selvaggi, M. Métois, A. Esposito, V. Sepe, A. Galvani & M. Anzidei (2017). A combined velocity field of the mediterranean region. *Annals of Geophysics* **60**, S0215.

Di Luccio, F., N. A. Pino, A. Piscini & G. Ventura (2015). Significance of the 1982-2014 Campi Flegrei seismicity: Preexisting structures, hydrothermal processes, and hazard assessment. *Geophysical Research Letters* **42**, 7498–7506.

- Di Manna, P., G. M. Monti, L. Olivetta, E. Vittori, E. Esposito & C. Violante (2017). *Ricognizione degli effetti indotti dal terremoto di Casamicciola del 21 agosto 2017 M4.0 (Recognition of the effects of the Casamicciola earthquake at 21st August 2017 M4.0, in Italian)*. ISPRA – Istituto Superiore per la Protezione e la Ricerca Ambientale, Relazione Tecnica, Roma, Italy. Available online at: http://www.isprambiente.gov.it/files2017/notizie/relazione_tecnica_ispra_ischia_casamicciola.pdf. Last accessed: 17th October 2017.
- Di Pasquale G., G. Orsini, R.W. Romeo (2005). New Developments in seismic risk assessment in Italy. *Bulletin of Earthquake Engineering* **3**(1), 101-128.
- Faenza, L. & A. Michelini (2010). Regression analysis of MCS intensity and ground motion parameters in Italy and its application in ShakeMap. *Geophysical Journal International* **180**(3), 1138-1152.
- Giardini, D., G. Grünthal, K.M. Shedlock & P. Zhang (1999). The GSHAP global seismic hazard map. *Annali di Geofisica* **42**(6), 1225-1228.
- Grünthal, G. (ed.) (1998). European Macroseismic Scale 1998 (EMS-98). *Cahiers du Centre Européen de Géodynamique et de Séismologie* **15**, Centre Européen de Géodynamique et de Séismologie, Luxembourg, 99 pp.
- Iervolino, I., Baltzopoulos G., Chioccarelli E. (2017) *Preliminary engineering report on ground motion data of the Aug 21st 2017 Ischia earthquake V3.2*. DOI: 10.13140/RG.2.2.31712.99842. Available online at: <http://www.reluis.it>. Last accessed: 14th February 2018.
- INGV Grupo di Lavoro sul terremoto dell'isola di Ischia (INGV G.D.L., 2017). *Rapporto di sintesi preliminare sul terremoto dell'Isola d'Ischia (Casamicciola) M4.0 del 21 Agosto 2017 (6 Settembre 2017) (Preliminary Report on the earthquake of the island of Ischia M4.0 on the 21 August 2017, in Italian)*, Istituto Nazionale di Geofisica e Vulcanologia, doi:10.5281/zenodo.886044. Available online at: https://ingvterremoti.files.wordpress.com/2017/09/rapporto-di-sintesi-sul-terremoto-6-settembre-2017_1.pdf. Last accessed: 20th December 2017.
- Jaiswal, K. & D.J. Wald (2008). *Creating a global building inventory for earthquake loss assessment and risk management*. Open File Report 2008-1160. U.S. Geological Survey, 110p. Available online at: <http://pubs.usgs.gov/of/2008/1160/>.
- Lekkas, E., S. Mavroulis & P. Karydis (2017). *The Mw 4.0, August 21, 2017 Ischia (Italy) Earthquake: a minor earthquake with high intensities*. Scientific Report, Newsletter of Environmental, Disasters and Crises Management Strategies, National & Kapodistrian University of Athens, Greece. Available online at: https://edcm.edu.gr/images/documents/Ischia_EQ_2017_Newsletter.pdf. Last accessed: 12th November 2017.
- Luzi, L., R. Puglia, E. Russo & ORFEUS WG5 (2016). Engineering Strong Motion Database. Istituto Nazionale di Geofisica e Vulcanologia, Observatories & Research Facilities for European Seismology. Available online at: <http://esm.mi.ingv.it/>.
- Malagnini, L., R.B. Herrmann, M. Di Bona (2000). Ground motion scaling in the Apennines (Italy). *Bulletin of the Seismological Society of America* **90**, 1062-1081.
- Malagnini, L., A. Akinci, R.B. Herrmann, N.A. Pino, L. Scognamiglio (2002). Characteristics of the ground motion in northeastern Italy. *Bulletin of the Seismological Society of America* **92**(6), 2186-2204.
- Manzo, M., G. P. Ricciardi, F. Casu, G. Ventura, G. Zeni, S. Borgström, P. Berardino, C. Del Gaudio & R. Lanari (2006). Surface deformation analysis in the Ischia Island (Italy) based on spaceborne radar interferometry. *Journal of Volcanology and Geothermal Research* **151**, 399–416.

Meletti, C. (2007). Progetto S1: proseguimento della assistenza al DPC per il completamento e la gestione della mappa di pericolosità sismica prevista dall'Ordinanza PCM 3274/2003 e progettazione di ulteriori sviluppi, DPC-INGV S1 Project, Final Report, 70 pp. Available online at: http://esse1.mi.ingv.it/data/S1_Rendicontazione_Scientifica_finale_S1.pdf. Last accessed: 17th October 2017.

Meletti C. & V. Montaldo (2007). *Stime di pericolosità sismica per diverse probabilità di superamento in 50 anni: valori di ag* (Seismic hazard estimates for different probabilities of exceedance in 50 years: values of ag, in Italian). Progetto DPC-INGV S1, Deliverable D2. Available online at: <http://esse1.mi.ingv.it/d2.html>. Last accessed: 17th October 2017.

Meletti, C., F. Galadini, G. Valensise, M. Stucchi, R. Basili, S. Barba, G. Vannucci & E. Boschi (2008). A seismic source zone model for the seismic hazard assessment of the Italian territory. *Tectonophysics* **450**, 85–108.

Masi, A., G. Santarsiero, A. Digrisolo, L. Chiauuzzi & V. Manfredi (2016). Procedures and experiences in the post-earthquake usability evaluation of ordinary buildings. *Bollettino di Geofisica Teorica ed Applicata* **57**(2), 199-220.

Michellini, A., L. Faenza, V. Lauciani & L. Malagnini (2008). Shakemap implementation in Italy. *Seismological Research Letters* **79**(5), 688–697.

Morasca, P., L. Malagnini, A. Akinci, D. Spallarossa & R.B. Herrmann (2006). Ground motion scaling in the western Alps. *Journal of Seismology* **10**, 315-333.

Musson, M.W., G. Grünthal & M. Stucchi (2010). The comparison of macroseismic intensity scales. *Journal of Seismology* **14**(2), 413-428.

Nocentini, M., V. Tofani, G. Gigli, F. Fidolini & N. Casagli (2015). Modeling debris flows in volcanic terrains for hazard mapping: the case study of Ischia Island (Italy). *Landslides* **12**, 831–846.

Norme Tecniche per le Costruzioni (NTC), Gazzetta Ufficiale della Repubblica Italiana, n. 29 del 4 febbraio 2008 – Suppl. Ordinario n. 30 (NTC, 2008). Available online at: http://www.cslp.it/cslp/index.php?option=com_docman&task=doc_download&gid=3269&Itemid=10. Last accessed: 17th October 2017.

Orsi, G., G. Gallo & A. Zanchi (1991). Simple-shearing block resurgence in caldera depressions. A model from Pantelleria and Ischia. *Journal of Volcanology and Geothermal Research* **47**, 1–11.

Paoletti, V., M. D'Antonio & A. Rapolla (2013). The structural setting of the Ischia Island (Phlegrean Volcanic District, Southern Italy): Inferences from geophysics and geochemistry. *Journal of Volcanology and Geothermal Research* **249**, 155–173.

Paparo, M. A. & S. Tinti (2017). Analysis of seismic-driven instability of Mt. Nuovo in the Ischia Island, Italy. *Bulletin of the Seismological Society of America* **107**, 750–759.

Rapolla, A., V. Paoletti & M. Secomandi (2010). Seismically-induced landslide susceptibility evaluation: Application of a new procedure to the island of Ischia, Campania Region, Southern Italy. *Engineering Geology* **114**, 10–25.

Rovida, A., M. Locati, R. Camassi, B. Lolli & P. Gasperini (eds.) (2016). CPTI15, the 2015 version of the Parametric Catalogue of Italian Earthquakes. Istituto Nazionale di Geofisica e Vulcanologia, Italy. DOI:10.6092/INGV.IT-CPTI15. Available online at: https://emidius.mi.ingv.it/CPTI15-DBMI15/index_en.htm.

Sartori, R. (2003). The Tyrrhenian back-arc basin and subduction of the Ionian lithosphere. *Episodes*, **26**, 217-221.

Seismosoft (2016). *SeismoSignal 2016* – A computer program for signal processing of strong-motion data, available from <http://www.seismosoft.com>.

Tibaldi, A. & L. Vezzoli (1998). The space problem of caldera resurgence: an example from Ischia Island, Italy. *Geologische Rundschau* **87**, 53–66.

Tusa, G. & H. Langer (2016). Prediction of ground motion parameters for the volcanic area of Mount Etna. *Journal of Seismology* **20**, 1–42.

United Nations, ed. (2016). *Human Development Report 2016 – Human Development for everyone*. Report of the United Nations Development Program (UNDP), New York, United States.

Verderame G., C. Del Gaudio, M. Di Domenico & P. Ricci (2017). *Rapporto relativo ad una preliminare predizione del danno agli edifici residenziali di Casamicciola Terme e Lacco Ameno a seguito del sisma del 21.08.2017, ore 20.57, M=4.0 (v.2.0 aggiornamento al 30 agosto 2017) (Report on a preliminary prediction of damage at residential buildings of Casamicciola Terme and Lacco Ameno after the earthquake of 21.08.2017, at 20.57, M=4.0, in Italian, v2.0 update of 30th August 2017)*. Dipartimento di Strutture per l'Ingegneria e l'Architettura – DiSt Università degli Studi di Napoli Federico II. Available online at: <http://biblus.acca.it/download/reluis-rapporto-relativo-ad-una-preliminare-predizione-del-danno-agli-edifici-residenziali-di-ischia/>. Last accessed: 7th November 2017.

Wald, D.J. & T.I. Allen (2007). Topographic slope as a proxy for seismic site conditions and amplification. *Bulletin of the Seismological Society of America* **97**, 1379–1395. Slope-based online map viewer available at: <http://usgs.maps.arcgis.com/apps/webappviewer/index.html?id=8ac19bc334f747e486550f32837578e1>.

Woessner, J., D. Giardini, H. Crowley, F. Cotton, G. Grünthal, G. Valensise, R. Arvidsson, R. Basili, M. B. Demircioglu, S. Hiemer, C. Meletti, R. W. Musson, A. N. Rovida, K. Sesetyan, M. Stucchi & The SHARE Consortium (2015). The 2013 European Seismic Hazard Model: Key Components and Results. *Bulletin of Earthquake Engineering* **13**(12), 3553–3596. Available online at: <http://www.efehr.org/en/home/>. Last accessed: 16th November 2017.

Zuccaro G., F. Cacace, S. Nardone & M. IacuanIELLO (2017). *Critical analysis of typologies, damage and collapse mechanism after the Casamicciola earthquake of 21 August 2017*. Report of the Mission of the PLINIUS Study Centre, Università degli Studi di Napoli Federico II. Available online at: http://plinivs.it/wp-content/uploads/2017/09/report_en.pdf. Last accessed: 16th February 2018.

A4.13.11.2 Web References

Athensvoice (2017): http://www.athensvoice.gr/world/368780_giati-katastrafikan-tosa-polla-spitia-sto-seismo-tis-iskia-ti-dilose-o-epikefalis. Last accessed: 8th November 2017.

Balliana F. (2015) – Evoluzione normative sismica: <http://www.ingballiana.it/Normativa.html>. Last accessed: 27th December 2017.

Centre Sismologique Euro-Méditerranéen (CSEM/EMSC): <http://www.emsc-csem.org/>. Last accessed: 17th October 2017.

Catalogue of Strong Earthquakes in Italy 461 B.C. – 1997 and Mediterranean Area 760 B.C. – 1500 (CFTI4MED) – Information regarding the 1883 earthquake (last accessed 16th February 2018): <http://storing.ingv.it/cfti4med/quakes/11949.html>.

CPTI15, the 2015 version of the Parametric Catalogue of Italian Earthquakes (CPTI15) – Information regarding earthquakes in Ischia: https://emidius.mi.ingv.it/CPTI15-DBMI15/place/IT_60014. Last accessed: 17th October 2017.

Database of Individual Seismogenic Sources – ITIS068: Casamicciola Terme (DISS, 2017): http://diss.rm.ingv.it/dissnet/CadmoDriver?_action_do_single=1&_state=find&_token=NULLNULLNULL&_tabber=0&_page=pGGSources_d&IDSource=ITIS068. Last accessed: 17th October 2017.

Department of Civil Protection (DPC, 2015) – Classificazione Sismica al 2015 (2015 Seismic Classification, in Italian) (last accessed 17th October 2017): http://www.protezionecivile.gov.it/resources/cms/documents/A3_class20150416_r.pdf.

Earthquake-report (2017): <https://earthquake-report.com/2017/08/21/minor-earthquake-tyrrhenian-sea-on-august-21-2017/>. Last accessed: 10th November 2017.

European Facilities for Earthquake Hazard and Risk – European Plate Observing System – ESHM13 seismogenic sources (EFEHR-EPOS, 2017) (last accessed 14th February 2018): <http://www.efehr.org/en/Documentation/specific-hazard-models/europe/seismogenic-sources/>.

EM-DAT – The Emergency Events Database (Université Catholique de Louvain, Brussels, Belgium; Cred. Prof. Dr. D. Guha-Sapir): <http://www.emdat.be/>. Last accessed: 11th December 2017.

Engineering Strong Motion Database (ESM): <http://esm.mi.ingv.it>.
ESM – 2017 Ischia event (last accessed: 17th October 2017): http://esm.mi.ingv.it/DYNA-stage/CadmoDriver?_action_do_single=1&_criteria=CZ001%3d%20AZ014itaca_event_idIAZ021E_MSC%2d20170821_0000072%27&_page=ACC_Events_D&_rock=INVALID&_state=find&_tabber=3.

Euronews (2017): <http://www.euronews.com/2017/08/28/illegal-building-and-the-ischia-earthquake>. Last accessed: 8th November 2017.

Hai Sentito Il Terremoto (HSIT, 2017) (Last accessed 17th October 2017): <http://www.haisentitoilterremoto.it/repository/16796811/index.html>.

Il mattino (2017a) (last accessed 10th November 2017): https://www.ilmattino.it/napoli/cronaca/ischia_dopo_terremoto_fioccano_le_offerte_attirare_turisti-3200202.html.

Il mattino (2017b) (last accessed 24th December 2017): https://www.ilmattino.it/napoli/citta/ischia_terremoto_turismo_disdette_40_milioni-3215219.html.

Il sole 24 ore (2017a) (last accessed 10th November 2017): http://www.ilsole24ore.com/art/notizie/2017-08-29/sisma-ischia-sette-milioni-i-primi-interventi-192221.shtml?uuid=AE1AkTJC&refresh_ce=1.

Il sole 24 ore (2017b) (last accessed 10th November 2017): <http://www.ilsole24ore.com/art/impresa-e-territori/2017-08-21/rischio-terremoto-assicurato-solo-2percento-abitazioni-082738.shtml?uuid=AECSZXBC>.

Ingegneria Sismica Italiana (ISI-Normative, 2017):
Website for this earthquake (last accessed: 17th October 2017): <http://www.ingegneriasismicaitaliana.com/it/3/news/1059/terremoto-dellaisola-di-ischia-del-21-agosto-2017-prime-valutazioni-sismiche-e-macrosismiche/#title>.

Ischia land (2015): <https://www.ischia.land/le-parracine-ischitane-i-muri-a-secco-dellisola-dischia/>. Last accessed: 11th November 2017.

Istituto Nazionale di Geofisica e Vulcanologia – National Institute of Geophysics and Volcanology of Italy (INGV): <http://www.ingv.it/>. Last accessed: 16th February 2018.

INGV Centro Nazionale Terremoti (INGV CNT) (2017): <http://cnt.rm.ingv.it/en/event/16796811>. Last accessed: 8th April 2019.

INGV-GIS (2015). Mappe interattive di pericolosità sismica (Interactive maps of seismic hazard): <http://esse1-gis.mi.ingv.it/>. Last accessed: 15th November 2017.

INGV-ShakeMaps for this event (last accessed: 4th November 2017):
<http://shakemap.rm.ingv.it/shake/16796811/intensity.html>

INGV-Terremoti (2017a) - Terremoto dell'Isola d'Ischia del 21 agosto 2017: elaborazione dati INGV presentata alla Commissione Grandi Rischi (CGR) del 25 agosto 2017 (Earthquake on the Island of Ischia on 21 August 2017: INGV data processing presented to the Great Risks Commission (CGR) on 25 August 2017, in Italian) (last accessed: 17th October 2017):
<https://ingvterremoti.wordpress.com/2017/08/25/terremoto-dellisola-dischia-del-21-agosto-2017-elaborazione-dati-ingv-presentata-alla-commissione-grandi-rischi-cgr-del-25-agosto-2017/>.

INGV-Terremoti (2017b) - Il terremoto di Casamicciola del 21 agosto 2017: osservazioni sul moto del suolo (The Casamicciola earthquake of 21 August 2017: observations on ground motion, in Italian) (last accessed: 17th October 2017): <https://ingvterremoti.wordpress.com/2017/09/14/il-terremoto-di-casamicciola-del-21-agosto-2017-osservazioni-sul-moto-del-suolo/>.

INGV-Terremoti (2017c) - La deformazione del suolo ad Ischia rilevata dalla Rete tiltmetrica (The deformation of the soil in Ischia detected by the tiltmetric network, in Italian) (last accessed 15th December 2017): <https://ingvterremoti.wordpress.com/2017/12/12/la-deformazione-del-suolo-ad-ischia-rilevata-dalla-rete-tiltmetrica/>.

INGV-Zone Sismiche (2006). Ordinanza PCM 3519 del 28 aprile 2006, All. 1b. Pericolosità sismica di riferimento per il territorio nazionale (Reference seismic hazard for the national territory, in Italian): <http://zonesismiche.mi.ingv.it>. Last accessed: 17th October 2017.

Istituto Nazionale di Statistica – Dati Censimento Popolazione Abitazioni (ISTAT, 2011): <http://dati-censimentopopolazione.istat.it/Index.aspx?lang=it>. Last accessed: 6th November 2017.

Istituto Nazionale di Statistica – GIS portal (ISTAT, 2017):
<http://gisportal.istat.it/mapparischi/index.html?extent>. Last accessed: 9th November 2017.

La Repubblica-Cronaca (2017) (last accessed 10th November 2017):
http://www.repubblica.it/cronaca/2017/08/22/news/terremoto_ischia_morire_per_scossa_di_bassa_magnitudo-173587827/.

La Repubblica-Napoli (2017a) (last accessed 10th November 2017):
http://napoli.repubblica.it/cronaca/2017/08/21/news/scossa_di_terremoto_panico_a_ischia-173550278/. Last accessed: 10th November 2017.

La Repubblica-Napoli (2017b) (last accessed 10th November 2017):
http://napoli.repubblica.it/cronaca/2017/09/21/news/terremoto_a_ischia_un_mese_dopo_1800_gli_sfolati_-176111150/.

La Repubblica-Napoli (2017c) (last accessed 10th November 2017):
http://napoli.repubblica.it/cronaca/2017/08/22/news/ischia_un_sondino_per_alimentare_i_due_bambini-173591045/.

Ministry of Economy and Finance (MEF, 2015) (last accessed 6th November 2017):
http://www1.finanze.gov.it/finanze2/analisi_stat/index.php?opendata=yes.

National Geophysical Data Center / World Data Service (NGDC/WDS): Significant Earthquake Database. National Geophysical Data Center, National Oceanic and Atmospheric Administration (NOAA). DOI:10.7289/V5TD9V7K. <https://www.ngdc.noaa.gov/hazard/earthqk.shtml>. Last accessed: 24th December 2017.

Statista (2017): <https://www.statista.com/statistics/658274/gross-domestic-product-gdp-per-capita-of-italy-by-region/>. Last accessed: 6th November 2017.

The Guardian (2017): <https://www.theguardian.com/world/2017/aug/21/earthquake-strikes-italian-island-of-ischia-with-one-reported-dead>. Last accessed: 6th November 2017.

The World Bank Group (2017). World Bank Open Data: <http://data.worldbank.org>. Last accessed: 6th November 2017.

Terremoti e grandi rischi (2017): <https://terremotiegrandirischi.com/2017/08/22/ischia-torre-annunziata-percezione-del-rischio-e-magnitudo-m-stucchi/#comments>. Last accessed: 9th November 2017.

Twig Blog (2017): <http://twig.pro/la-classifica-dei-redditi-dei-comuni-italiani-del-2015/>. Last accessed: 6th November 2017.

United States Geological Survey (USGS):
Website for this earthquake: <https://earthquake.usgs.gov/earthquakes/eventpage/us2000aaaae>. Last accessed: 17th October 2017.

WHE-GEM Building taxonomy reports (2017): <http://www.world-housing.net/related-projects/share-your-knowledge-of-buildings/building-taxonomy-summary-reports>. Last accessed: 7th November 2017.

Wikipedia (2017): https://it.wikipedia.org/wiki/Classificazione_sismica_dell'Italia. Last accessed: 24th December 2017.

World Economic Outlook Database (2016):
<https://www.imf.org/external/pubs/ft/weo/2016/02/weodata/download.aspx>. Last accessed: 6th November 2017.

World Housing Encyclopedia (2014): Results for Italy: <http://db.world-housing.net/list/?country=Italy>. Last accessed: 7th November 2017.